

Lecture Notes in Mechanical Engineering

Krishna Mohan Singh

Sushanta Dutta

Sudhakar Subudhi

Nikhil Kumar Singh *Editors*

Fluid Mechanics and Fluid Power, Volume 1


Select Proceedings of FMFP 2022

 Springer

Lecture Notes in Mechanical Engineering

Series Editors


Fakher Chaari, National School of Engineers, University of Sfax, Sfax, Tunisia

Francesco Gherardini , Dipartimento di Ingegneria “Enzo Ferrari”, Università di Modena e Reggio Emilia, Modena, Italy

Vitalii Ivanov, Department of Manufacturing Engineering, Machines and Tools, Sumy State University, Sumy, Ukraine

Mohamed Haddar, National School of Engineers of Sfax (ENIS), Sfax, Tunisia

Editorial Board

Francisco Cavas-Martínez , Departamento de Estructuras, Construcción y Expresión Gráfica Universidad Politécnica de Cartagena, Cartagena, Murcia, Spain

Francesca di Mare, Institute of Energy Technology, Ruhr-Universität Bochum, Bochum, Nordrhein-Westfalen, Germany

Young W. Kwon, Department of Manufacturing Engineering and Aerospace Engineering, Graduate School of Engineering and Applied Science, Monterey, CA, USA

Justyna Trojanowska, Poznan University of Technology, Poznan, Poland

Jinyang Xu, School of Mechanical Engineering, Shanghai Jiao Tong University, Shanghai, China

Lecture Notes in Mechanical Engineering (LNME) publishes the latest developments in Mechanical Engineering—quickly, informally and with high quality. Original research reported in proceedings and post-proceedings represents the core of LNME. Volumes published in LNME embrace all aspects, subfields and new challenges of mechanical engineering.

To submit a proposal or request further information, please contact the Springer Editor of your location:

Europe, USA, Africa: Leontina Di Cecco at Leontina.dicecco@springer.com

China: Ella Zhang at ella.zhang@springer.com

India: Priya Vyas at priya.vyas@springer.com

Rest of Asia, Australia, New Zealand: Swati Meherishi at swati.meherishi@springer.com

Topics in the series include:

- Engineering Design
- Machinery and Machine Elements
- Mechanical Structures and Stress Analysis
- Automotive Engineering
- Engine Technology
- Aerospace Technology and Astronautics
- Nanotechnology and Microengineering
- Control, Robotics, Mechatronics
- MEMS
- Theoretical and Applied Mechanics
- Dynamical Systems, Control
- Fluid Mechanics
- Engineering Thermodynamics, Heat and Mass Transfer
- Manufacturing Engineering and Smart Manufacturing
- Precision Engineering, Instrumentation, Measurement
- Materials Engineering
- Tribology and Surface Technology

Indexed by SCOPUS, EI Compendex, and INSPEC.

All books published in the series are evaluated by Web of Science for the Conference Proceedings Citation Index (CPCI).

To submit a proposal for a monograph, please check our Springer Tracts in Mechanical Engineering at <https://link.springer.com/bookseries/11693>.

Krishna Mohan Singh · Sushanta Dutta ·
Sudhakar Subudhi · Nikhil Kumar Singh
Editors

Fluid Mechanics and Fluid Power, Volume 1

Select Proceedings of FMFP 2022

 Springer

Editors

Krishna Mohan Singh
Department of Mechanical and
Industrial Engineering
IIT Roorkee
Roorkee, Uttarakhand, India

Sushanta Dutta
Department of Mechanical and
Industrial Engineering
IIT Roorkee
Roorkee, Uttarakhand, India

Sudhakar Subudhi
Department of Mechanical and
Industrial Engineering
IIT Roorkee
Roorkee, Uttarakhand, India

Nikhil Kumar Singh
Department of Mechanical and
Industrial Engineering
IIT Roorkee
Roorkee, Uttarakhand, India

ISSN 2195-4356

ISSN 2195-4364 (electronic)

Lecture Notes in Mechanical Engineering

ISBN 978-981-99-7826-7

ISBN 978-981-99-7827-4 (eBook)

<https://doi.org/10.1007/978-981-99-7827-4>

© The Editor(s) (if applicable) and The Author(s), under exclusive license to Springer Nature Singapore Pte Ltd. 2024

This work is subject to copyright. All rights are solely and exclusively licensed by the Publisher, whether the whole or part of the material is concerned, specifically the rights of translation, reprinting, reuse of illustrations, recitation, broadcasting, reproduction on microfilms or in any other physical way, and transmission or information storage and retrieval, electronic adaptation, computer software, or by similar or dissimilar methodology now known or hereafter developed.

The use of general descriptive names, registered names, trademarks, service marks, etc. in this publication does not imply, even in the absence of a specific statement, that such names are exempt from the relevant protective laws and regulations and therefore free for general use.

The publisher, the authors, and the editors are safe to assume that the advice and information in this book are believed to be true and accurate at the date of publication. Neither the publisher nor the authors or the editors give a warranty, expressed or implied, with respect to the material contained herein or for any errors or omissions that may have been made. The publisher remains neutral with regard to jurisdictional claims in published maps and institutional affiliations.

This Springer imprint is published by the registered company Springer Nature Singapore Pte Ltd.

The registered company address is: 152 Beach Road, #21-01/04 Gateway East, Singapore 189721, Singapore

Paper in this product is recyclable.

Contents

Fluid Flow and Heat Transfer

Experimental Modelling to Measure the Seat Leakage in Shutdown System of PFBR	3
Piyush Kumar Aggarwal, Indranil Banerjee, V. Vinod, and S. Raghupathy	
Performance of Water-Based Loop Heat Pipe at Different Ambient Conditions for Thermal Management in Terrestrial Applications	15
Shail N. Shah, Fagun A. Pithadiya, and Sanjay V. Jain	
Investigation of Inlet Blockage in the Central Subassembly of a Sodium-Cooled Fast Reactor	27
Yadu Narendran, K. Natesan, K. Devan, and A. John Arul	
Experimental Investigation of PHP with Hybrid Nanofluid for EV Battery Thermal Management	37
Nikhil S. Mane, Siddhartha Tripathi, and Vadiraj Hemadri	
Numerical Study of SiO₂–Water Nanofluid Jet Impingement on Heated Surface	49
Ketan Atulkumar Ganatra and Achintya Mukhopadhyay	
An Updated Review of Heat Transfer Enhancement Techniques in Tube-Type Heat Exchangers	65
Manoj Kumar Diwaker and Arvind Kumar	
Effect of Housing Design Modifications on Fluid Flow and Heat Transfer Characteristics of Electrical Motor Casing: A Numerical Study	79
P. Sai Bhargav, M. Ganapathi, and K. Arul Prakash	
A Numerical Investigation for Heat Transfer Enhancement Using Convergent and Divergent Shape Orifice Geometry of Synthetic Jet	93
Mangesh Chaudhari and Omkar Gaonkar	

Performance Evaluation of a Thermal Energy Storage System with Stainless Steel Encapsulated Phase Change Material	105
A. Surya, M. Chandraesh, N. Nallusamy, and R. Prakash	
Understanding the Heat Transfer Characteristics and Axis Switching Phenomenon in High Aspect Ratio Elliptical Orifice Impinging Synthetic Jets	117
Pawan Sharma, Prakhar Bharadwaj, Kshitij Bhat, K. A. Vyvaswath, Bhavya Dalal, Pradeep K. Singh, Santosh K. Sahu, and Harekrishna Yadav	
Numerical Investigation of Exergy and Entropy Analysis for W/EG-Based Non-newtonian Hybrid Nanofluid for Helically Corrugated Tube Heat Exchanger	127
Ayush Painuly, Niraj K. Mishra, and Prabhakar Zainith	
Experimental and Numerical Investigation of a Device for Localized Cooling	139
S. V. H. Nagendra and D. V. S. Bhagavanulu	
Study of MHD Stagnation Point Flow of Casson Fluid with Non-linear Radiation and Non-uniform Heat Source	153
Snehal D. Patel and Harshad. R. Patel	
Heat Transfer Enhancement Using Passive Technique	173
Adarsh Shinde, Rishi Choudhary, Siddhi Bairagi, Vaibhavi Chandankar, Shruti Dhadi, Sanchitee Rokade, and M. B. Chaudhari	
A Review on Heat Pipe-Assisted Thermal Management Systems in Electrical Vehicles for Lithium-Ion Batteries	185
Rajat Kumar, Ankur Dwivedi, and Varun Goel	
Design to Avoid Dry Out in a Flat Heat Pipe Based on Cu Foam	195
Nitish Kumar Tripathi, Prafulla P. Shevkar, Chitransh Atre, and Baburaj A. Puthenveetil	
Framework with Data-Analytic for Fault Detection and Performance Prediction of a Steam Boiler: A Case Study	201
Nivedita Wagh and Sudhir Agashe	
Design of Liquid Cooled Pin-Fin Heat Sink for High Voltage Electric Vehicle	213
Akhil Suresh, N. Jinesh, J. K. Antony, and Arun Issac	
Establishment of Thermal Mixing Behavior in Grid Plate of FBRs 1 & 2	227
Amit K. Chauhan, M. Rajendrakumar, and K. Natesan	

Velocity Slip and Temperature Jump in Homogeneous and Heterogeneous Porous Medium 241
 Krishan Sharma, Subrata Kumar, and P. Deepu

Insights from a Nonlinear and Corresponding Linear Model of a Pulsating Heat Pipe 253
 Alok Kumar, Govind Maurya, Nadeem Ahmed, and Suneet Singh

Heat Transfer Evaluation Method for RC Members at Standard Fire Scenario 265
 Banti A. Gedam

Enhanced Melting Behavior of Phase Change Material (PCM) in a Rectangular Cavity: Effect of Fin 277
 Anjan Nandi, Nirmalendu Biswas, and Aparesh Datta

Determining the Best Passive Heat Transfer Enhancement Technique in Circular Pipe Heat Exchangers with the MCDM Technique 289
 Soumith Voddepalli, Sujit Nath, and Agnimitra Biswas

Thermo-Diffusion and Heat Generation Effects on Unsteady MHD Flow of Nanofluid in a Perforated Vertical Medium 303
 Harshad Patel, Akhil Mittal, and Tejal Nagar

Critical Thickness of the Phase Change Material (RT-42) for Temperature Management of 18,650 Li-Ion Cell Undergoing Rapid Discharging 321
 Vivek Saxena, Akhalesh Sharma, Santosh K. Sahu, and Shailesh I. Kundalwal

Effect of Orientation on the Thermal Performance of a PCM-Based Finned Heat Sinks 337
 Ch. Ravi Shankar and Y. Naresh

Thermal Performance Analysis of Cross-Finned Heat Sinks Using Nano-Enhanced Phase Change Material 347
 Vivek Saxena, Anuj Kumar, Harshit Ziniwal, Gaurav Nagar, Santosh K. Sahu, and Shailesh I. Kundalwal

Numerical Investigation on Performance of CPU Heat Sinks 361
 Vedant Kanate, Arjun Pardeshi, Falguni Charde, Krushna Kolase, Adinath Bhise, and Pramod Kothmire

Modelling of Phase Change Material Embedded Li-Ion Battery Pack Under Different Load Conditions Using Equivalent Circuit Model 373
 Mazhar Hussain, Mohd. Kaleem Khan, and Manabendra Pathak

Heat Transfer Enhancement in Miniature Channels with Micro-fin Having Varying Fin Height Along the Axis of Flow	387
Rohit Kumar and Manmohan Pandey	
Thermo-Hydraulic Evaluation of Isothermally Heated Bluff Bodies with Different Shapes	401
Bibhu Bhusan Sha, Rajiva Lochan Mohanty, Dishant Chandrakant Patel, and Mihir Kumar Das	
Study of the Effect of Single-Phase Flow Conditions on FAC for Various Feeder Bend Geometries of Pressurized Heavy Water Reactor (PHWR)	415
K. Premsai, Niraj Uttam, A. Moorthi, and Ankit Bangar	
Deployment of Helical Fins for Heat Transfer Enhancement in Internal Flows	431
Yatharth Lilhare, Amit Arora, and Himanshu Jangid	
Numerical Study on Heat Transfer Through Semi-Circular Grooved Microchannel	443
Anshul Rajput, Zahoor Bhat, Yogesh M. Nimdeo, and Harish Pothukuchi	
Numerical Study of Combined Phase Change Material and Natural Air Cooling System for Lithium-Ion Battery Thermal Management	457
Indra Kumar Lokhande, Deepyaman Chakraborty, and Nishant Tiwari	
Flow and Heat Transfer Phenomena Through Porous Media Under Turbulent Regime	471
Shaik Dilshad Begum, G. Trilok, and N. Gnanasekaran	
Numerical Investigation of Heat Transfer Characteristics of CO₂ in a Vertical Divergent Tapered Annular Channel	483
Ashok Kumar Gond, Dipankar Narayan Basu, and Amaresh Dalal	
A Numerical Study on the Combined Effect of Y-Shaped Fin and Alumina Nanoparticles on PCM Solidification	495
S. Abhinand, Amrita Sharma, and Hardik Kothadia	
Effect of Interruption on a Shrouded Fin Heat Sink: A Numerical Study	509
Rahul Ray, Aurovinda Mohanty, and Pandab Patro	
Study on Melting of Beeswax Dispersed with Ferro-Nanoparticles Inside a Square Annulus Cavity Under an External Magnetic Field	521
Amit Kumar Ghosh and Pabitra Halder	
Numerical and Experimental Analysis of Liquid Cold Plate Thermal Management System for High-Powered Electronics	533
Rehan Ansari, Mohammad Saqlain Fakhr, Osama Khan, Uzair Sain, and Arnab Ganguly	

Investigation on Passive Thermal Management Using Phase Change Materials Encapsulated Over 18,650 Lithium-Ion Battery 549
 Saumendra Nath Mishra, Siddhartha Banerjee, Sourav Sarkar, Achintya Mukhopadhyay, and Swarnendu Sen

Thermal and Hydraulic Study of Mini-Channel with Irregular Surface Topology 563
 Vishwajeetsinh Rahevar, Prayag Desai, Sheetal Pandya, Amit Arora, and Niraj Shah

Thermo-hydraulic Assessment of Fin Profiles in Internally Finned Tubes 573
 Himanshu Jangid, Amit Arora, and Yatharth Lilhare

Loss of Electric Power Supply Transient in an Irradiation Test Loop of HFRR 587
 Amitanshu Mishra, Paban Kumar Guchhait, and Samiran Sengupta

Toward Analysis of Corium Hydraulics in Liquid Sodium 595
 Ram Kumar Maity, T. Sundararajan, M. Rajendrakumar, and K. Natesan

Effect of Porous-Fin on Performance Enhancement of Shell-Tube Latent Heat Thermal Storage System 609
 C. Suresh and Sandip K. Saha

Effect of an Asymmetrically Confined Rotating Cylinder on Heat Transfer 623
 Shruti Gautam, Aruna Thakur, and Pooja Thakur

Flow and Heat Transfer Investigation of Liquid Heat Sink for an IGBT Module 637
 Puja Koch, Alankrita Singh, and Sudhakar Subudhi

Numerical Investigation of Laminar Fluid Flow and Heat Transmission in a Filleted Grooved Channel 649
 Ananya Mandal, Auronil Mukherjee, Soumen Chakraborty, and Supratim Saha

Local Heat Transfer and Fluid Flow Characteristics Over Cylinder in the Presence of Vortex Generator Acting as Flow Guides 663
 Arravaram Lakshman, Sandeep Mantri, and Satyanand Abraham

Estimating Baking Time for a Bakery Furnace Using Radiation Network Analysis 677
 Guru Bachan Satsangi, Sunny Jagdish Shiyal, Bamaniya Jayesh Pravinbhai, Narayan Jaiswal, and Amit Patel

Experimental Investigation of Elliptical Air-Jet Impingement on Metal-Foamed Surface 691
 Pradeep Kumar Singh, Jaykumar Joshi, Pawan Sharma, and Santosh Kumar Sahu

Comparative Numerical Analysis of ZnO and Ag/ZnO Nanofluids Flowing Through Automobile Radiator 701
 Sandip Dhupal, Krantisinha Jagtap, Shubham Malkunjkar, Mahesh Shindge, and Surendra D. Barewar

Role of Buoyancy and Acceleration Parameters in the Heat Transfer Deterioration of Supercritical Carbon-Dioxide Under Natural Circulation 715
 Kapil Bodkha, D. S. Pilkhwal, and N. K. Maheshwari

Experimental Investigations on the Thermal Contact Conductance Using Al₂O₃ Nanoparticles in the Interfacial Material 729
 Rajesh Choudhary, Aman Singh, Aditya Kumar, and Sudhakar Subudhi

Propulsion and Power

Design and Analysis of Optimized Solid Propellant Grain 743
 Mohammed Akbar and Prabhat Dattakumar Phondekar

Role of Piezoelectric Coupling Factor on FIV-Based Energy Harvesting of a Piezoelectric Flag 759
 Rajanya Chatterjee, Chhote Lal Shah, Sayan Gupta, and Sunetra Sarkar

Flow Features of Propeller Wakes Impinging on a Circular Disk Through Unsteady Simulations 769
 Bhavin Patel and Rajesh Ranjan

Experiment on Hydraulic Power Take-Off Unit (PTO) for Point Absorber Wave Energy Converter (PA-WEC) 781
 Shivam Gupta, Sumana Ghosh, Parmod Vaishnav, Priti Sarkar, Deepak Kumar, and Bharat Sitaram Mendhe

Micro-hydropower Generation for Sustainable Development: A Review 791
 Anmol Jamakhandikar, Rahul Kumar Painter, Ashish Doshi, and Mukund Bade

Numerical Investigation of Unsteady Performance of a High-Pressure Transonic Turbine Stage of a Small Engine 801
 Ssheshan Pugazhendhi and Shyama Prasad Das

Effect of Divergence Angle, Carrier Gas, and Back Pressure on Species Separation Using Convergent Divergent Micro-Nozzle 817
 Manu K. Sukesan, Ashok Kumar, and S. R. Shine

The Effect of Hot Gas Injection on Thrust Vector Control in a Double-Divergent Nozzle—A Numerical Investigation	829
B. S. Bijo and S. Kumar Ranjith	
Study and Computational Analysis of RS-25 Engine's Nozzle and Find Out Data of RS-25 Engine	845
Jaykumar I. Adalja, Krutarth T. Soni, Mehul K. Rana, and Jignesh R. Vala	

About the Editors

Prof. Krishna Mohan Singh is Professor in the Department of Mechanical and Industrial Engineering at Indian Institute of Technology (IIT) Roorkee. His research interests include the areas of computational mechanics, development of novel parallel algorithms, meshfree methods, shape and topology optimization, fluid dynamics, DNS/LES of turbulent flows, CAE, computer-aided analysis and design of thermo-fluid and multi-physics systems, computational fluid dynamics, modeling and simulation of flow and heat transfer in turbomachines, transport and energy systems.

Prof. Sushanta Dutta is Professor in the Department of Mechanical and Industrial Engineering at Indian Institute of Technology (IIT) Roorkee. His research interests are in the areas of experimental fluid mechanics, experimental heat transfer, optical measurement techniques, active and passive control of flow field, wake dynamics, turbulence study, Schlieren, HWA, PIV, LCT, PSP, microfluidics and heat transfer augmentation using phase change material.

Prof. Sudhakar Subudhi is Professor in the Department of Mechanical and Industrial Engineering at Indian Institute of Technology (IIT) Roorkee. His research interests are in the area of experimental heat transfer and fluid mechanics, heat transfer enhancement of natural and forced convection in water/nanofluids, natural ventilation and unconventional energy systems.

Dr. Nikhil Kumar Singh is Assistant Professor in the Department of Mechanical and Industrial Engineering at Indian Institute of Technology (IIT) Roorkee. His broad research interests include direct numerical simulations of two-phase flows and phase change, computational fluid dynamics and heat transfer, numerical methods and turbulent flows.

Fluid Flow and Heat Transfer

Experimental Modelling to Measure the Seat Leakage in Shutdown System of PFBR



Piyush Kumar Aggarwal, Indranil Banerjee, V. Vinod, and S. Raghupathy

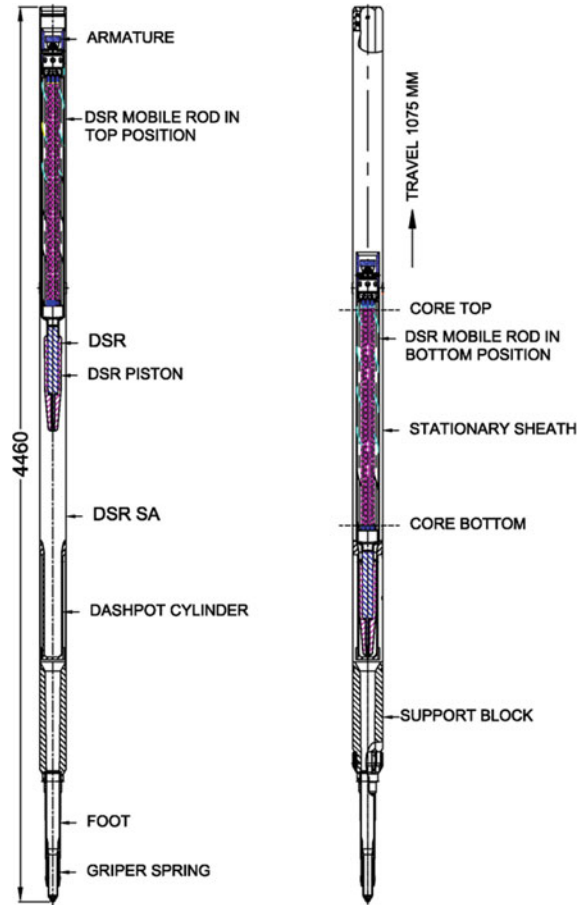
1 Introduction

Prototype Fast Breeder Reactor (PFBR), which is sodium-cooled Fast Breeder Reactor (FBR), has two independent fast-acting and diverse reactor shutdown systems for controlling the power and shutting down the reactor. These are Control and Safety Rod (CSR) shutdown system and Diverse Safety Rod (DSR) shutdown system. CSR shutdown system is used for controlling the reactor power as well as shutting down the reactor, whereas the DSR shutdown system is used only for shutting down the reactor [1]. Nine neutron absorber rods are provided in CSR shutdown system and three neutron absorber rods are provided in DSR shutdown system. In case of Safety Control Rod-Accelerated Movement (SCRAM), the electromagnet gets de-energized in both the shutdown systems. In CSR shutdown system, CSR with lifting mechanism is released, while in DSR shutdown system, mobile DSR alone falls under gravity and finally deposited on their respective dashpot of the sub-assembly, to shut down the reactor [2]. In case of CSR system failed to act, DSR system is self-sufficient to shut down the reactor. The schematic of the DSR in normal operating condition and deposited condition is shown in Fig. 1. DSR contains Boron Carbide (B_4C) with enrichment of 65% of B-10 isotope, which is a neutron absorber. DSR in the deposited condition absorb neutrons, which are generated due to nuclear fission reaction inside the reactor core. The neutrons absorbed in B-10 result in an (n, α) reaction. This process liberates heat and produces helium gas. The maximum amount of heat that can be generated in DSR is estimated as 1 MWt.

To remove this amount of generated heat, a minimum sodium coolant flow rate of 3 kg/s shall pass through the mobile DSR. The schematic of flow path at this condition is illustrated in Fig. 2. It can be seen from this figure that there are two parallel flow paths: (i) through mobile DSR and (ii) through DSR–dashpot interface.

P. K. Aggarwal (✉) · I. Banerjee · V. Vinod · S. Raghupathy
India Gandhi Centre for Atomic Research, Kalpakkam, Tamil Nadu 603102, India
e-mail: piyushaggarwal786@gmail.com

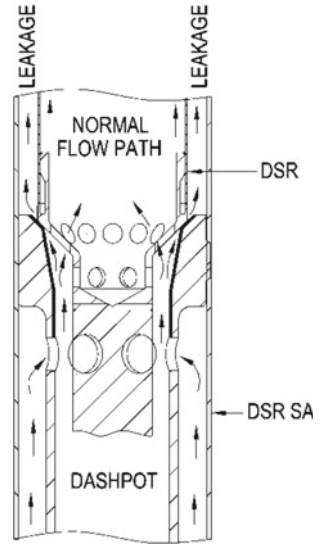
Fig. 1 Schematic of DSR in normal operating condition and deposited condition



The flow between these two parallel paths is apportioned according to their relative hydraulic resistance. Required coolant flow through mobile DSR shall be more than 95% of the total flow and less than 5% of the total flow is allowed to leak through the DSR–dashpot interface.

Therefore, it is required to measure the leakage rate of sodium through DSR–dashpot interface to validate the design. However, carrying out the studies in sodium is costly, time-consuming and requires complicated safety procedure to be followed. Hence, the studies are carried out using water as working fluid in a geometrically similar model due to the closeness of hydraulic properties of sodium and water. However, these water model studies require careful investigation of similarity criteria to arrive at the appropriate test parameters and extrapolation of experimental results into prototype system. Sometimes experiments can be further simplified by simulating the zone of interest only. The present study has been conducted to measure the

Fig. 2 Schematic of flow path in DSRSA when DSR is deposited on dashpot



leakage rate experimentally through DSR–dashpot interface region by only simulating the geometrical features of interface region. The relation between pressure drop and the seat leakage was developed which will be useful for designing the future DSRSA system.

2 Dimensional Analysis and Similarity Criteria

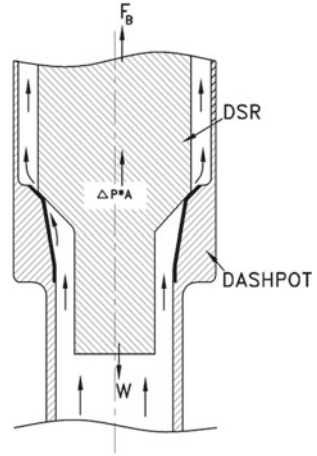
The total flow rate through DSRSA is apportioned between the DSR mobile assembly and DSR–dashpot seat according to their respective flow path resistance. The pressure loss across the mobile DSR at various operating conditions was measured in earlier water model experiment simulating the full-scale DSRSA. This pressure loss value can be used in a simplified experimental model simulating only the DSR–dashpot region to measure the leakage flow rate. Various forces acting on DSR when it is deposited on dashpot are shown in a schematic diagram shown in Fig. 3. The pressure drop across DSR–dashpot interface which is a metal-to-metal contact surface is function of liquid properties (density and viscosity), surface roughness, geometrical features, velocity of liquid leaking through the seat, and contact pressure as stated in Eq. 1.

$$\Delta P = f(\rho, \mu, \varepsilon, D, V, P_C). \tag{1}$$

The force acting on contact area can be expressed as

$$P_C A_C \sin\theta = (W - F_B - \Delta P \times A_p). \tag{2}$$

Fig. 3 Schematic diagram of the experimental model



Using dimensional analysis and choosing, ρ , V , and D as repeating variables, following non-dimensional numbers can be formed:

- (1) Euler number: $Eu = \left(\frac{\Delta P}{\rho V^2} \right)$.
- (2) Reynolds number: $Re = \left(\frac{\rho V D}{\mu} \right)$.
- (3) Relative surface roughness: $\bar{\epsilon} = \left(\frac{\epsilon}{D} \right)$.
- (4) Non-dimensional contact pressure: $P_c^* = \left(\frac{P_c}{\rho V^2} \right)$.

Applying Buckingham Pi theorem, it can be written

$$Eu = f(Re, \bar{\epsilon}, P_c^*). \quad (3)$$

Therefore, in model testing above-mentioned non-dimensional numbers are required to be simulated along with the simulation of geometrical similarity. Calculation of required process parameters in a 1:1 scale water model simulating the DSR–dashpot region and transposition of measured leakage rate through DSR–dashpot interface into reactor condition were carried out using the following procedures:

Step-I: The equivalent differential pressure across the seating interface in the model can be found out from Eu and Re similitudes.

From Eu similitude, it can be written that,

$$\Delta P_m = \left(\frac{\rho_m}{\rho_p} \right) \times \left(\frac{V_m}{V_p} \right)^2 \times \Delta P_p. \quad (4)$$

*The Subscript 'm' is used for model and 'p' is used for prototype.

From Re similitude, it can be written that,

$$\left(\frac{V_m}{V_p}\right) = \left(\frac{\rho_p}{\rho_m}\right) \times \left(\frac{\mu_m}{\mu_p}\right). \quad (5)$$

The equivalent differential pressure in model across DSR–dashpot interface at nominal leakage rate in reactor can be estimated from Eq. 6 which is deduced by combining Eqs. 4 and 5.

$$\Delta P_m = \left(\frac{\rho_p}{\rho_m}\right) \times \left(\frac{\mu_m}{\mu_p}\right)^2 \times \Delta P_p. \quad (6)$$

Differential pressure across DSR–dashpot interface in reactor (ΔP_p) is equal to the pressure drop across mobile DSR assembly when DSR is deposited on dashpot. This is because these are two parallel flow paths. In earlier experiment, the pressure drop across mobile DSR in reactor at nominal flow rate of 3.18 kg/s was estimated for the following two cases:

Case 1: $\Delta P_p = 5.58$ kPa, when DSR is deposited on dashpot and the lifting mechanism for DSR is at the top most position, not attached to DSR.

Case 2: $\Delta P_p = 7.6$ kPa, when DSR is deposited on dashpot and the lifting mechanism for DSR is engaged with the DSR, prior to lifting it.

These values are used to estimate the differential pressure requirement across the seating interface in the model.

Step-2: The contact pressure at seat in the model shall be equal to the contact pressure of prototype.

$$(P_c)_m = (P_c)_p. \quad (7)$$

$(P_c)_p$, which is contact pressure at DSR–dashpot interface in prototype, can be estimated using Eq. 2.

$$(P_c)_p = \frac{1}{(A_c)_p \sin\theta} \{(W - F_B - A_p \times \Delta P) \times\}_p,$$

where

$A_p = 9.33 \times 10^{-3} \text{ m}^2$ (contact diameter is 109 mm).

$A_c = 1.712 \times 10^{-3} \text{ m}^2$ (lateral contact width 5 mm).

$\theta = 45^\circ$.

$W_B = W - F_B = 45 \times 9.81 \text{ kg m/s}^2$ (apparent wt. in sodium at 400 °C).

The values of contact pressure for the above-mentioned two cases are as follows:

(a) For case 1, $\Delta P_p = 5.58$ kPa,

$$(P_c)_p = \frac{1}{1.712 \times 10^{-3} \times 0.707} \{(45 \times 9.81) - 9.33 \times 10^{-3} \times 5.58 \times 10^3\}$$

$$= 321.7 \text{ kPa}$$

(b) For case 2, $\Delta P_p = 7.6$ kPa,

$$(P_C)_P = \frac{1}{1.712 \times 10^{-3} \times 0.707} \{ (45 \times 9.81) - 9.33 \times 10^{-3} \times 7.6 \times 10^3 \}$$

$$= 306.1 \text{ kPa}$$

To maintain the equivalent contact pressure in model as found out using Eq. 7, the equivalent weight of DSR in model can be estimated from the following equation:

$$(P_C)_m = \frac{1}{(A_C)_m \times \text{Sin}45^\circ} \{ (W - F_B - A_P \times \Delta P) \}_m, \quad (8)$$

$$(W - F_B)_m = [(P_C \times A_C) \sin 45^\circ + (\Delta P)(A_P)]_m. \quad (9)$$

In the present experimental setup, only DSR–dashpot region is simulated in the model and full DSR is not simulated. A small portion of the DSR foot is immersed in water, and hence, the buoyancy force acting on the model is neglected. Therefore, Eq. 9 can be modified as follows:

$$W_m = [0.707 \times (P_C)(A_C) + (\Delta P)(A_P)]_m. \quad (10)$$

Step-3: The leakage mass flow rate in the model (\dot{m}_m) can be measured for differential pressure (ΔP_m) across seating interface. The flow through the narrow gap of DSR seating on dashpot is expected to be viscous dominant. Therefore, viscous forces and inertial forces will be characterizing the leakage flow through seating. Hence, the leakage mass flow rate can be extrapolated to reactor condition using Re similitude shown in the following equation:

$$\dot{m}_p = \rho_p \times V_p \times A_p.$$

Also using Eq. 5,

$$V_p = \left(\frac{\rho_m}{\rho_p} \right) \times \left(\frac{\mu_p}{\mu_m} \right) V_m$$

$$\dot{m}_p = \rho_p \left(\frac{\rho_m}{\rho_p} \right) \times \left(\frac{\mu_p}{\mu_m} \right) \times V_m \times A_p = \left(\frac{\mu_p}{\mu_m} \right) \times \dot{m}_m. \quad (11)$$

Density and dynamic viscosity of water at 55 °C and sodium at 400 °C are tabulated in Table 1. These values are considered for estimation of the required value of ΔP_m , $(P_C)_m$, and $(W)_m$ by using Eqs. 6, 7, and 10 and tabulated in Table 2.

Table 1 Hydraulic properties of water and sodium for test conditions

	Dynamic viscosity (kg/m-s)	Density, (kg/m ³)
Water at 55 °C	0.50×10^{-3}	986
Sodium at 400 °C	0.281×10^{-3}	857

Table 2 Equivalent pressure drop and required weight of DSR in model for different test conditions

Test conditions using water at 55 °C	ΔP_m (kPa)	$(P_c)_m$ (kPa)	$(W)_m$ (kg)
Case 1: $\Delta P_p = 5.58$ kPa	15.35	321.7	54.3
Case 2: $\Delta P_p = 7.6$ kPa	20.91	306.1	57.6

3 Description of Experimental Model and Methodology

A 1:1 scale simplified model of DSR–dashpot interface has been fabricated to conduct the experimental leakage rate measurements in water. The apparent weight of actual DSR in sodium at 400 °C is 45 kg in PFBR. The DSR–dashpot leakage measurement testing is conducted by maintaining the same apparent weight of DSR as in prototype, which is 45 kg, instead of 54.3 kg estimated weight for model testing mentioned in Table 2. However, the differential pressure (ΔP_m) across the seating interface was simulated as per Table 2. The less simulated weight of mobile DSR will give less sitting pressure in water testing compared to the prototype for simulated differential pressure across the seating interface. Since, additional wt. will further reduce the leakage and this weight will provide conservative measurement of leakage flow. Leakage flow was measured at various differential pressures across DSR–dashpot interface. In model test setup, DSR weight is simulated with a solid rod. The seating portion of DSR–dashpot interface is fabricated exactly same as in PFBR DSR–dashpot seating interface profile with same hard-facing material. The schematic of fabricated DSR and dashpot is shown in Fig. 4.

The schematic of experimental test setup is shown in Fig. 5.

A water tank of 1.75 m³ was used to maintain the leakage flow. An immersion-type, rod heater was used to raise the water temperature. Temperature of water was monitored continuously. To achieve the desired flow rate and hence differential pressure, compressed air was used to increase the pressure inside the tank. A pressure transmitter (PT) was provided to measure the gauge pressure at the entry to DSR–dashpot interface. Tape heaters and insulation were provided on the connecting pipe between test setup and tank to maintain the constant water temperature.

The photographic view is shown in Fig. 6. The experiment was conducted at water temperature of 55–60 °C. Filtered water was used during the experiment, and suspended particle of size < 10 micron was expected after filtration. Subsequent to this, the water tank was pressurized using compressed air. A pressure transmitter was connected at dashpot to measure gauge pressure inside the dashpot. Differential pressure across DSR–dashpot is equal to the measured gauge pressure since the dashpot outlet is open to atmosphere. Leakage flow rate was measured by water

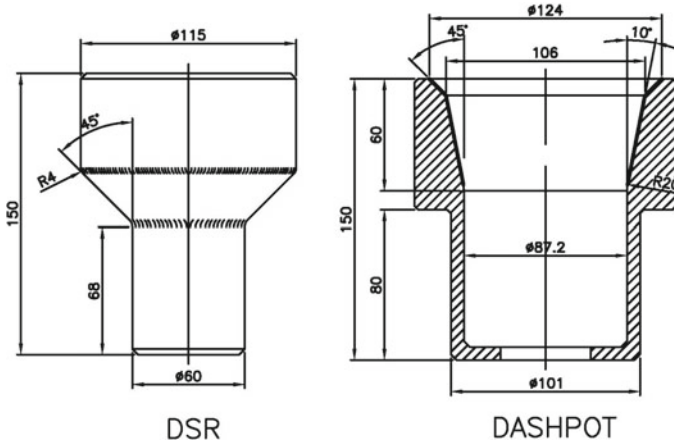


Fig. 4 DSR–dashpot interface in model

Fig. 5 Schematic of the experimental setup

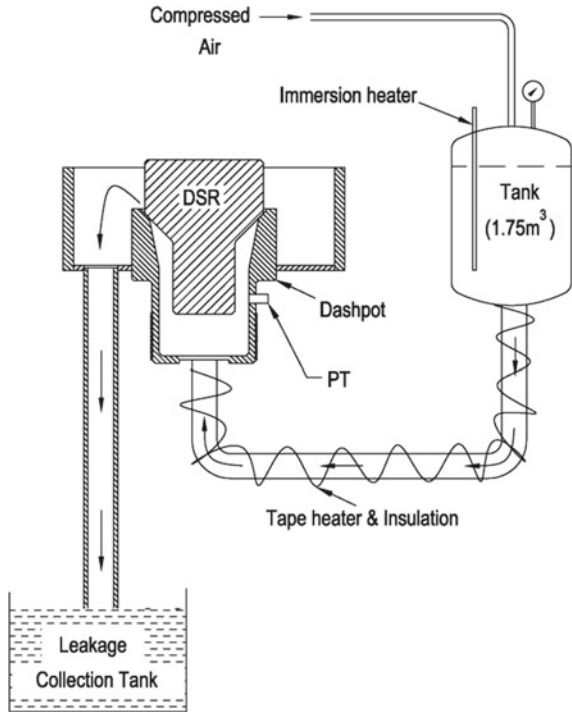
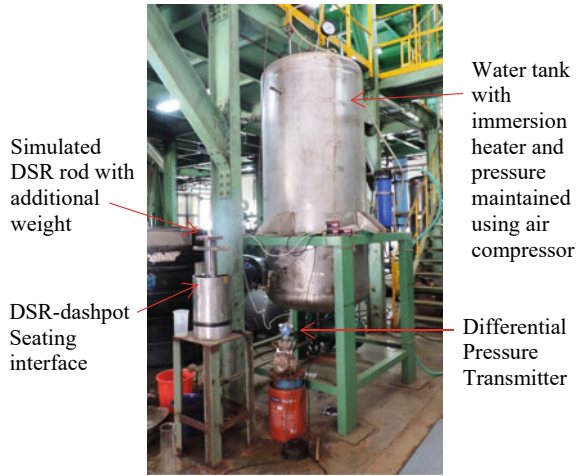


Fig. 6 Photographic view of the experimental setup



volume collection method. The leakage flow rate was measured at different differential pressure conditions. Experimental leakage measurement tests were conducted with random alignment of the DSR sitting on dashpot.

4 Results and Discussions

Measurement of leakage rate has been carried out for a wide range of differential pressure across DSR–dashpot interface. The plot for differential pressure across DSR–dashpot interface versus leakage mass flow rate of water is presented in Fig. 7.

It can be seen from the above figure that the leakage rate is a strong function of the DSR orientation inside dashpot. Even a minor change in DSR sitting orientation on dashpot can alter the leakage rate significantly. There is a contact between DSR and dashpot interface, which is not allowing the DSR to tilt significantly. However, during free seating of DSR on dashpot at different orientations, minor tilting of DSR happens, which breaks the surface contact at interface and significant leakage happens. Therefore, DSR is lifted manually, rotated, and positioned freely number of times in its seat on dashpot to get the maximum leakage. The legend corresponding to Test-2 in Fig. 7 shows the upper bound of the leakage flow rate.

All the experimental data have been transposed to reactor condition using the similitude laws as discussed in previous section. The sodium leak rate (g/s) vs. differential pressure across DSR–Dashpot interface for reactor conditions is shown in Fig. 8. The upper bound characteristic is also plotted in this figure to estimate the maximum possible leakage rate. It can be seen from this figure that the maximum sodium leakage rate considering the upper bound curve fit equation for case—1 ($\Delta P = 5.58$ kPa) is 15 g/s which is around 0.5% of the total flow rate (3.18 kg/s) through DSRSA, and for case—2 ($\Delta P = 7.6$ kPa), the maximum leakage rate is found to be

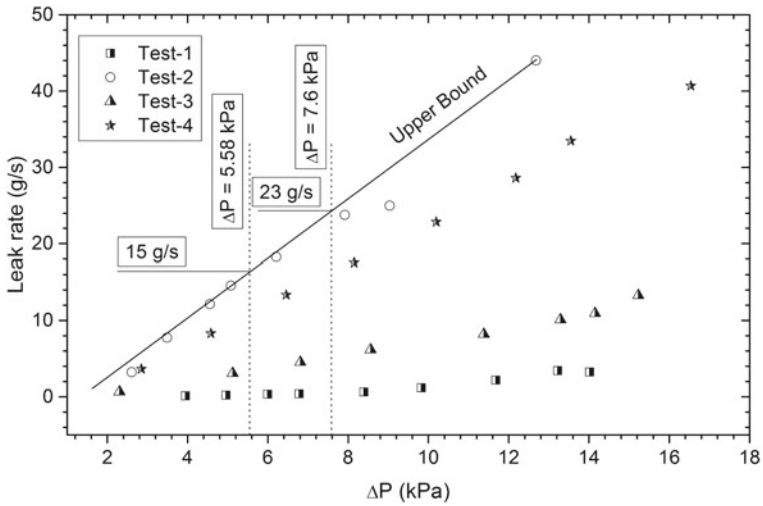


Fig. 7 Water leakage across DSR–dashpot seating with varying differential pressures

23 g/s which is 0.72% of the rated flow rate. These leakage rates are much lower than the maximum allowable limit of leakage flow through DSR–dashpot interface which is 5% of the nominal flow rate through DSRSA in reactor.

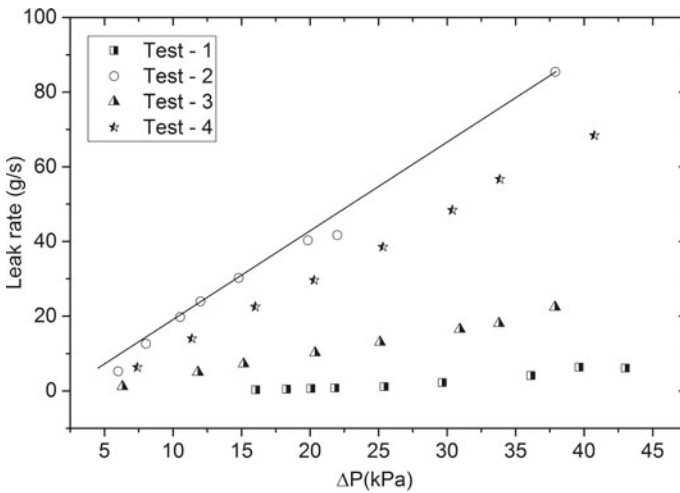


Fig. 8 Leakage rate versus pressure drop across DSR–dashpot

5 Conclusion

A study has been carried out to estimate the leakage rate through DSR–dashpot interface when DSR is deposited on the dashpot. The pressure drop in test model has been simulated using Eu and Re numbers. A correlation has been derived to estimate the weight of DSR in testing condition, to generate the same amount of contact pressure on the seat as in PFBR. It was observed from the experiment that even slight change on the sitting orientation of DSR can alter the leakage rate significantly. Thus, DSR is positioned at different orientations and water leakage rate has been measured. The experimental measurement has been carried out with water at higher temperature. All the experimental measurement data were transposed using appropriate similitude laws. An upper bound characteristic curve is also established. Since the data scatter is very high due to orientation of DSR inside dashpot, an uncertainty analysis was also carried out. The estimated maximum sodium leakage rate through DSR–dashpot interface at pressure drop of 5.58 kPa (corresponding to the situation of DSR sitting on dashpot just after shutdown) is found to be 21.5 g/s which is only 0.7% of nominal flow rate (3.18 kg/s). Subsequently, the sodium leakage was also estimated for other condition which represents the situation of DSR deposited in dashpot and lifting mechanism is attached with it. As mentioned earlier, the corresponding pressure drop across DSR–dashpot interface is 7.6 kPa. At this pressure drop, maximum leakage rate is found to be 32.9 g/s which is 1.03% of the rated flow rate. These leakage rates are much lower than the allowable limit of 5% of the nominal flow rate through DSRSA in reactor.

Nomenclature

W	Weight of the mobile DSR	[kg]
F_B	Buoyancy force acting on mobile DSR due to full submergence in sodium	[kg m/s ²]
W_A	Apparent weight	[kg]
A_P	Projected area of DSR	m ²
A_C	Contact area of the lateral contact surface	m ²
ΔP	Pressure drop across DSR–dashpot interface (seating)	N/m ²
θ	Angle of inclined contact surface	degree
ρ	Density of the liquid	[kg/m ³]
μ	Dynamic viscosity of the liquid	kg/m-s
ε	Roughness of the contact surface	mm
D	Characteristic length representing geometrical features	m
V	Velocity of leakage flow	m/s
P_C	Contact pressure at DSR–dashpot interface	N/m ²

References

1. Vijayashree R et al (2010) Design, development, testing and qualification of diverse safety rod and its drive mechanism for a prototype fast breeder reactor. *J Eng Gas Turbines Power* 132(10)
2. Nimala Sundaran M et al (2017) Experimental seismic qualification of diverse safety rod and its drive mechanism of prototype fast breeder reactor. In: International conference on fast reactors and related fuel cycles: next generation nuclear systems for sustainable development, IAEA, Vienna (Austria), FR17, June 2017

Performance of Water-Based Loop Heat Pipe at Different Ambient Conditions for Thermal Management in Terrestrial Applications



Shail N. Shah, Fagun A. Pithadiya, and Sanjay V. Jain

1 Introduction

The twenty-first century has seen a rise in the importance of thermal management issues in several industrial applications. Due to miniaturization and an increase in heat-generating equipment, various industries including the space industry, electronics, mobile, laptop, supercomputers, etc., are experiencing problems with thermal management. Loop heat pipes absorb heat from the heated surface, converting the working fluid to vapor as a result. LHP has a wick structure to enable fluid flow back to the evaporator in a variety of orientations. LHP was developed first time in 1972 at the Ural Polytechnical Institute of Thermal Physics by Maydanik et al. [1]. They tested an LHP with a length of 1.2 m and a capacity of around 1 kW.

Conventional heat pipe (HP) consists of single evaporator and condenser section and the primary wick. The addition of secondary wick and C.C. in LHP is the primary structural change between HP and LHP. Transport lines in LHP separate the heat source from the heat sink, increasing LHP's flexibility. Insufficient liquid in the primary wick causes a dry-out condition. In this situation, the pressure differential between the C.C. and the evaporator causes liquid to flow from the C.C. through the secondary wick to the evaporator section and then to the primary wick, allowing the LHP to absorb more heat from the heat source as shown in Fig. 1.

Conventional heat pipes have significant length and dry-out constraints, whereas LHP can operate at larger heat loads and over longer distances between the evaporator and condenser portions. Nakamura et al. [2] investigated long-distance heat transfer for heat loads of 1000 W and up to 10 m length.

Water-based LHP can be used for terrestrial applications like thermal management in mobile, laptop, defense, air conditioning. Ambient condition has significant effect

S. N. Shah · F. A. Pithadiya · S. V. Jain (✉)

Department of Mechanical Engineering, Institute of Technology, Nirma University, Ahmedabad, India

e-mail: sanjay.jain@nirmauni.ac.in

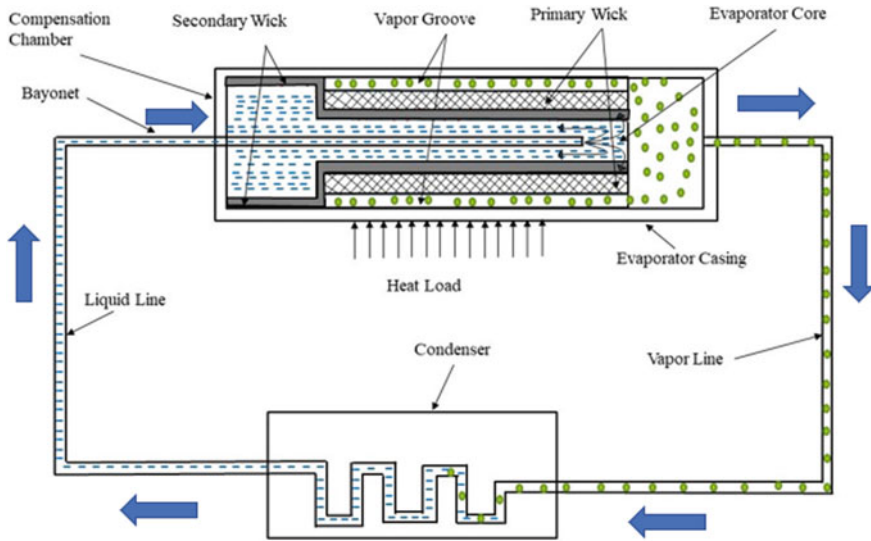


Fig. 1 Schematic diagram of LHP

on the performance of LHP as it will vary heat exchange and overall loop temperature based on the amount of heat load to be removed from the source.

2 Literature Review and Objective

Mathematical modeling of LHP has been done over the years in two segments: single-phase analysis and two-phase analysis. Single-phase analysis of LHP was done in initial years for mathematical modeling to understand the working of LHP by Kaya et al. [3]. Later, Hoang et al. [4] developed first two-phase analysis model of ammonia-based LHP for space application. Water-based LHP for terrestrial application is under immense research since last half decade. Flat-plate LHP was developed by Tsai et al. [5] for better gripping on electronic components and better heat transfer. It was found to be less efficient than conventional LHP, but better flexibility was obtained for mounting. Singh et al. [6] analyzed water-based miniature LHP (mLHP) for computer CPU cooling. It was concluded that a mLHP can be employed to thermally regulate electronic devices with small footprints and high heat flux chipsets. Vasiliev et al. [7] analyzed use of LHP for high-power electronic components. It was discovered that the vapor groove fabrication affects the mean pore diameter and wick porosity on the surface of vapor removal grooves. LHP for server cooling was analyzed by Maydanik et al. [8]. Various condenser cooling techniques were tested using miniature ammonia LHPs and a CPU thermal simulator. Choi et al. [9] analyzed water-based LHP for electronic cooling with sintered porous wick. Hu et al. [10] developed 3D-printed

wick and performance of LHP was found to be in line with sintered wick structure. In order to explain the two-phase heat transfer coefficient and pressure decrease in depth, Adoni et al. [11] created a steady-state model using the energy and mass conservation equations. Different structural modifications have been carried out over the years to meet customer requirement as well as to improve performance of LHP [12–14]. Micro and miniature LHPs have been developed to meet miniature cooling requirement for terrestrial applications [15, 16].

The performance of LHP is significantly impacted by the environment. The literature study revealed that only a small number of researchers have thoroughly investigated the combined effects of ambient condition on various LHP characteristics. Novelty of the present work is the combined analysis of water-based LHP for effect of ambient conditions (i.e., 10, 22, and 40 °C) on the parameters like steady-state operating temperature (SSOT), condenser outlet temperature (T_{co}), liquid line outlet temperature (T_{lo}), two-phase pressure drop across condenser (i.e., $\Delta P_{2\phi}$), heat exchange from compensation chamber (C.C.), and liquid line to ambient (i.e., $Q_{c.c.-amb}$, $Q_{L.L.-amb}$) and resistance of LHP (R_{LHP}).

3 Mathematical Modeling of Loop Heat Pipe

In the present study, to analyze performance of loop heat pipe with water as a working fluid, several dimensional parameters were taken from the literature for the validation purpose as mentioned in Table 1.

The total heat load (Q_1) distribution in the system is the addition of evaporator heat transfer (Q_{evap}), heat leak from evaporator compensation chamber ($Q_{Heatleak}$), heat transfer from compensation chamber to ambient, and heat transfer from liquid line to ambient as per Eq. (1).

$$Q_1 = Q_{evap} + Q_{Heatleak} + Q_{L.L.-amb} + Q_{c.c.-amb}. \quad (1)$$

Table 1 LHP dimensional parameters

Component	Dimension (OD/ID length)	Unit
Evaporator	$\Phi 42/32 \times 100$	mm
C.C	$\Phi 42/32 \times 100$	mm
Vapor line	$\Phi 6/4 \times 220$	mm
Liquid line	$\Phi 6/4 \times 150$	mm
Condenser	$\Phi 6/4 \times 300$	mm
Wick	$\Phi 30/20 \times 100$	mm
Porosity	30.9	%
Pore radius	54	μm

Evaporator wall temperature (T_{evp}) can be calculated as per Eq. (2) from the natural convection phenomenon.

$$T_{\text{evp}} = T_{\text{amb}} + \frac{Q_1}{h_{\text{air}}A}. \quad (2)$$

Temperature of vapor (T_{h}) at evaporator section was calculated using Eq. (3).

$$T_{\text{h}} = T_{\text{evp}} - (T_{\text{evp}} - T_{\text{evpsat}})e^{\left(\frac{-h_{\text{evp}}A\Delta L}{mC_pL}\right)}, \quad (3)$$

where A is evaporator wall area (m^2).

Liquid line outlet temperature (T_{lo}) was found using Eq. (4) by applying resistance method.

$$T_{\text{lo}} = T_{\text{amb}} + (T_{\text{co}} - T_{\text{amb}})e^{\left(\frac{-L}{mRc_p}\right)}. \quad (4)$$

Two-phase analysis along the condenser section was done using Lockhart methodology [4]. For the analysis, Eqs. (5–7) were used.

$$\Delta P_{2\Phi} = \int_{x_{\text{out}}}^{x_{\text{in}}} \frac{\Phi_1^2 f_l (1-x)^2}{2D\rho_l} \left(\frac{m}{A}\right)^2 \left[\frac{dz}{dx}\right] dx, \quad (5)$$

$$\Phi_1 = \left[1 + \left[\frac{C}{X}\right] + \left[\frac{1}{X^2}\right]\right], \quad (6)$$

$$X = \left[\frac{f_l}{f_g}\right]^{0.5} \left[\frac{\rho_g}{\rho_l}\right]^{0.5} \left[\frac{1-x}{x}\right]. \quad (7)$$

Resistance of loop heat pipe (R_{LHP}) was calculated using Eq. (8).

$$R_{\text{LHP}} = \frac{T_{\text{evp}} - \frac{(T_{\text{cc}} + T_{\text{co}})}{2}}{Q_1}. \quad (8)$$

Single-phase pressure drop in vapor line and liquid line was calculated using Eq. (9) and pressure drop in wick structure was found using Eq. (10).

$$\Delta P = \left(\frac{8\mu mL}{\pi\rho r^4}\right), \quad (9)$$

$$\Delta P_{\text{w}} = \frac{\mu m \ln\left(\frac{D_{\text{ow}}}{D_{\text{iw}}}\right)}{2\pi\rho L_{\text{wick}} K_{\text{wick}}}. \quad (10)$$

Heat exchange from compensation chamber and heat leak from evaporator to wick were calculated using Eqs. (11–13).

$$Q_{c.c.-amb} = \frac{(T_{cc} - T_{amb})}{R_{cc}}, \quad (11)$$

$$Q_{sc} = mC_p(T_{cc} - T_{lo}), \quad (12)$$

$$Q_{Heatleak} = \frac{2\pi K_{eff}L_{wick}\Delta T_{wick}}{\ln\left(\frac{D_{ow}}{D_{iw}}\right)}. \quad (13)$$

3.1 Algorithm of Mathematical Modeling

Mathematical model for the analysis of LHP was developed in MATLAB software by using the algorithm as per Fig. 2. Steady-state convergence criteria were used. For the convergence, $Q_{Heatleak} - Q_{sc} - Q_{c.c.-amb} \leq 0.001$ criteria need to be satisfied. To find thermophysical properties like k , C_p , μ , h_{fg} , σ , and ρ , fifth-order polynomial equations were used [11]. For the passive flow along the loop, maximum capillary pressure needs to be greater than total pressure drop along the loop.

4 Results and Discussion

4.1 Validation of Two-Phase Model

To analyze performance of loop heat pipe, mathematical model was developed as per algorithm shown in Fig. 2. The model was developed in MATLAB software, and the results were validated with experimental model of Hu et al. [10]. Figure 3 shows the comparison of evaporator temperature with experimental model of Hu et al. [10].

The evaporator temperature increased as heat load was increased. T_{evp} increased by 52.91 °C as heat load was increased from 20 to 160 W.

Figure 4 shows the validation of resistance of loop heat pipe with experimental model of Hu et al. [10]. Resistance of LHP decreased as heat load was increased. R_{LHP} decreased by 0.26 KW⁻¹ when heat load was increased from 20 to 160 W. For the average evaporator temperature, the deviation between the present model and the model of Hu et al. [10] was found to be 3.96%.

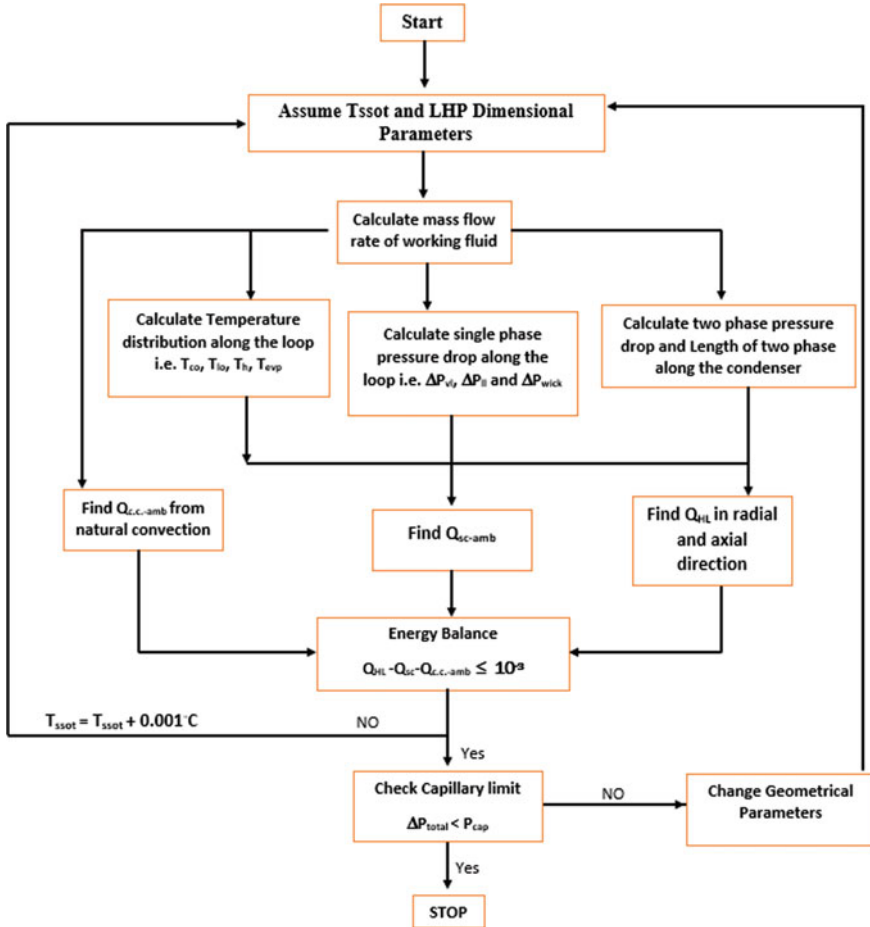


Fig. 2 Algorithm of mathematical modeling

4.2 Effect of Ambient Condition on LHP

Effect of different ambient condition (10 °C, 22 °C, and 40 °C) on SSOT, T_{lo} , T_{co} , $Q_{L.L.-amb}$, $Q_{c.c.-amb}$, and R_{LHP} was analyzed and explained in this section.

Figure 5 shows the variation of SSOT, T_{lo} , and T_{co} at different ambient conditions. It was observed that as heat load was increased from 20 to 160 W, temperature of the system increased. SSOT, T_{co} , and T_{lo} increased by 35.2, 21.51, and 18.59 °C at ambient temperature of 22 °C. It can be seen that loop temperature increased with increase in ambient temperature because of higher heat transfer rate between ambient and system. At 160 W, increment of 24.4 °C, 11.9 °C, and 13.92 °C was seen in SSOT, T_{co} , and T_{lo} when ambient temperature was increased from 10 °C to 40 °C. The same phenomenon was observed by Hu et al. [10].

Fig. 3 Validation of evaporator temperature

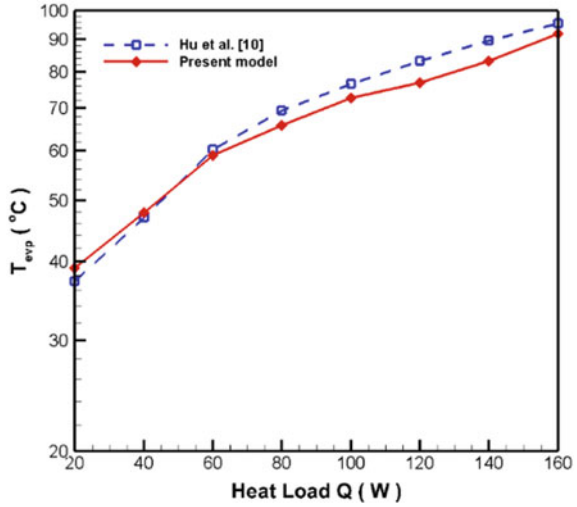
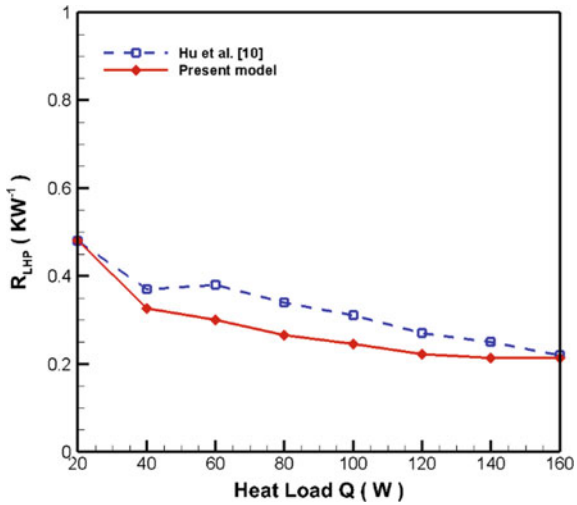


Fig. 4 Validation of resistance of LHP



Effect of ambient temperature on $Q_{c.c.-amb}$ is shown in Fig. 6. When ambient temperature was increased from 10 °C to 40 °C, heat transfer from compensation chamber to ambient was observed to be decreasing. As ambient temperature increased, temperature difference was observed to be decreasing because heat transfer from compensation chamber to ambient decreased. At 160 W, $Q_{c.c.-amb}$ decreased by 0.36 W when ambient temperature was increased from 10 °C to 40 °C.

Ambient temperature has significant effect on heat transfer from liquid line to ambient. Heat transfer from liquid line to ambient depends on temperature difference between condenser outlet temperature and ambient temperature as shown in Fig. 7.

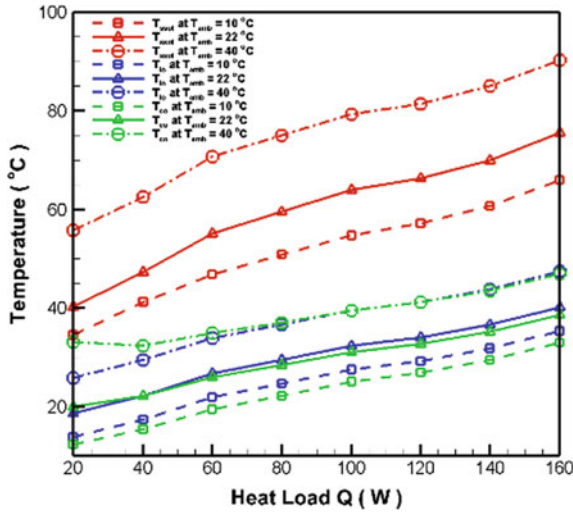


Fig. 5 Variation in SSOT, T_{lo} , T_{co} with heat load at different T_{amb}

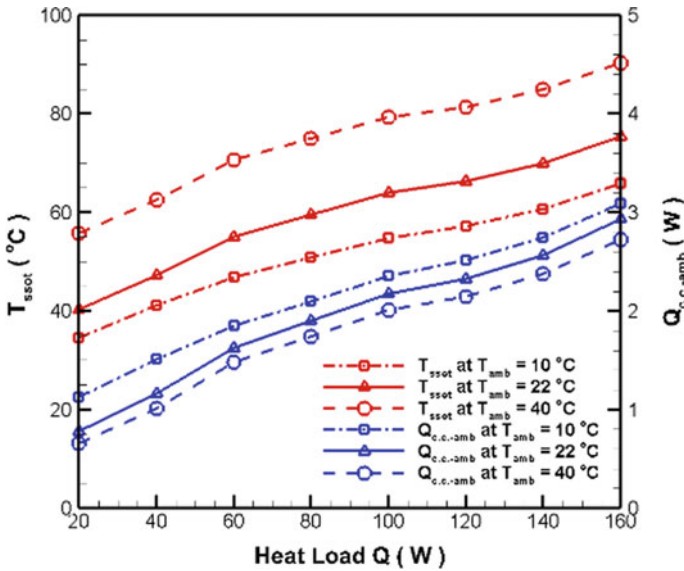


Fig. 6 Effect of T_{amb} on $Q_{c.c.-amb}$

At lower ambient temperature, $Q_{LL,-amb}$ increased as ΔT increased. As ambient temperature was increased from 10 °C to 40 °C, ΔT decreased and $Q_{LL,-amb}$ also decreased. At 22 °C ambient temperature, $Q_{LL,-amb}$ increased by 0.28 W when heat load was increased from 20 to 160 W.

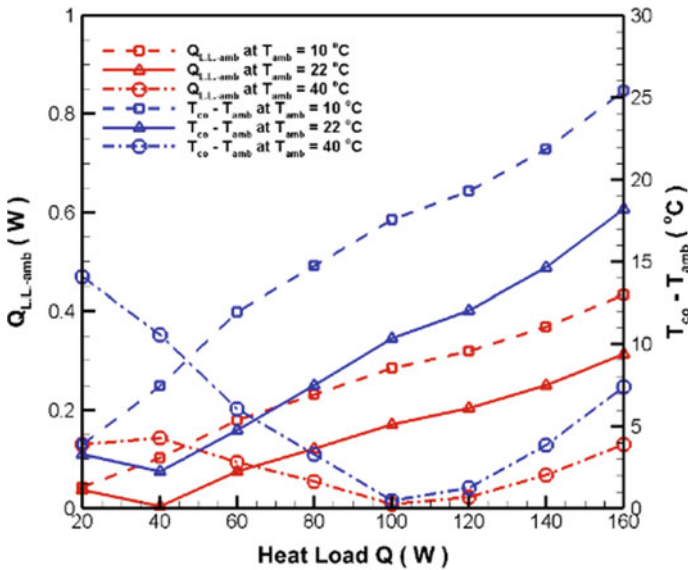


Fig. 7 Effect of T_{amb} on $Q_{L.L.-amb}$

Ambient temperature has significant effect on two-phase pressure drop across the condenser section. Effect of ambient temperature on two-phase pressure drop is shown in Fig. 8. As ambient temperature increased, length of two-phase along the condenser section increased that led to increased two-phase pressure drop across the condenser section. Two-phase pressure drop increased by 103.85 Pa when ambient temperature was increased from 10 °C to 40 °C at 160 W heat load. Effect of ambient condition on the resistance of loop heat pipe is shown in Fig. 9. Resistance of loop heat is inversely proportional to the heat load and directly proportional to the temperature difference between evaporator wall temperature and condenser temperature (Eq. (8)).

Resistance reduces with increasing heat load. As ambient temperature rises, temperature difference also rises, which causes to have higher resistance at specific heat load with rise in ambient temperature. At heat load of 20 W, R_{LHP} increased by 0.67 KW^{-1} when ambient temperature increased from 10 °C to 40 °C.

5 Conclusions

In the present study, mathematical model was developed to analyze the performance of loop heat pipe with different ambient conditions. The mathematical model was found in-line with the experimental model of Hu et al. [10] with the variation of 3.96% in terms of evaporator temperature. The major conclusions drawn from the study are as under:

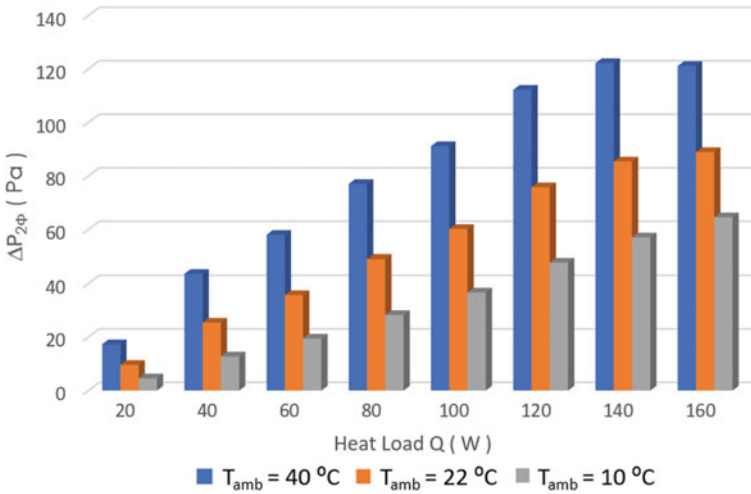


Fig. 8 Comparison of $\Delta P_{2\phi}$ at different heat loads

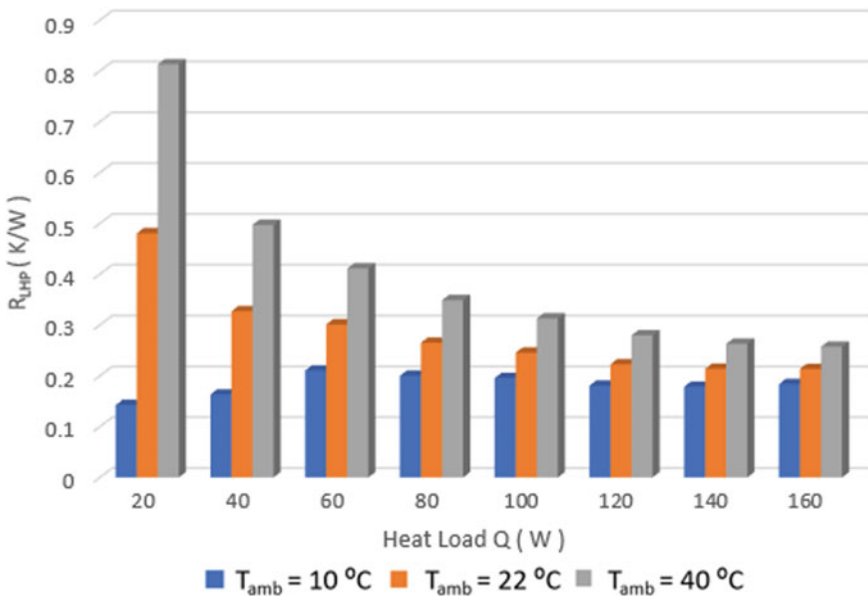


Fig. 9 Comparison of thermal resistance at different heat loads

- When ambient temperature was increased from 10 °C to 40 °C, SSOT, T_{co} , and T_{lo} increased by 24.4 °C, 11.9 °C, and 13.92 °C.
- Ambient temperature has significant effect on two-phase pressure drop along the condenser section.

- At 160 W of heat load, two-phase pressure drop increased by 103.84 Pa when ambient temperature increased from 10 °C to 40 °C.
- Resistance of LHP decreases with increase in heat load and increases with increase in ambient temperature.
- Heat transfer from C.C. to ambient and from liquid line to ambient decreased by 0.36 W and 0.28 W temperature, respectively, when ambient increased from 10 °C to 40 °C at 160 W heat load.

Nomenclature

A	Surface Area of Evaporator	[m ²]
amb	Ambient	
C_p	Specific Heat	[kJ kg ⁻¹ K ⁻¹]
D_{ow}	Outer Diameter of Wick	[m]
D_{iw}	Inner Diameter of Wick	[m]
evp	Evaporator	
f	Darcy Friction Factor	
h_{fg}	Latent Heat	[kJ kg ⁻¹]
h_{air}	Heat Transfer Coefficient of air	[W m ⁻² K ⁻¹]
k	Thermal Conductivity of Working Fluid	[W m ⁻¹ K ⁻¹]
K_{wick}	Permeability of Wick	
K_{eff}	Effective Thermal Conductivity of Wick	[W m ⁻¹ K ⁻¹]
L_{wick}	Length of Wick	[m]
m	Mass Flow Rate of Working Fluid	[kg s ⁻¹]
ΔP	Single-Phase Pressure Drop	[Pa]
ΔP_W	Pressure Drop Across Wick	[Pa]
$\Delta P_{2\phi}$	Two-phase Pressure Drop	[Pa]
Q_1	Applied Heat Load	[W]
Q_{evap}	Evaporator Heat Transfer	[W]
$Q_{c.c.-amb}$	Heat Transfer from Compensation Chamber to Ambient	[W]
Q_{sc}	Heat Transfer of Sub-cooling	[W]
$Q_{Heatleak}$	Heat Leakage from Evaporator to Wick	[W]
$Q_{L.L.-amb}$	Heat Transfer from Liquid Line to Ambient	[W]
r	Pore Radius	[μm]
R_{LHP}	Resistance of LHP	[K W ⁻¹]
R_{cc}	Resistance of Compensation Chamber	[K W ⁻¹]
T_h	Temperature of Vapor	[°C]
T_{lo}	Liquid Line Outlet Temperature	[°C]
T_{evp}	Evaporator Wall Temperature	[°C]
T_{cc}	Temperature of Compensation Chamber	[°C]
T_{co}	Condenser Outlet Temperature	[°C]
T_{amb}	Ambient Temperature	[°C]

T_{ssot}	Steady-State Operating Temperature	[°C]
x	Quality of Working Fluid	
X	Lockhart Constant	
ρ	Density	[kg m ⁻³]
μ	Dynamic Viscosity	[Pa s]
ϕ_1	Two-phase Multiplier	
σ	Surface Tension	[N m ⁻¹]

References

1. Maydanik Y et al (1985) Heat transfer apparatus. U.S. Patent No. 4515209
2. Nakamura K, Odagiri K, Nagano H (2016) Study on a loop heat pipe for a long-distance heat transport under anti-gravity condition. *Appl Therm Eng* 107:167–174
3. Kaya T, Hoang TT, Ku J, Cheung MK (1999) Mathematical modeling of loop heat pipes. 37th *Aerosp Sci Meet Exhib* 13(3)
4. Hoang TT (1999) AIAA 99-3448 mathematical modeling of loop heat pipes with two-phase pressure drop. In: 33rd thermophysics conference, 28 June–1 July, 1999, Norfolk, VA
5. Tsai M, Yu C, Kang S, Rd Y, Ext T (2005) Flat plate loop heat pipe with a novel evaporator structure dissipation problems, and take heat away from the heat vapor line. *Heat Pipes Vap Chamb*, pp 21–24
6. Singh R, Akbarzadeh A, Dixon C, Mochizuki M, Riehl RR (2007) Miniature loop heat pipe with flat evaporator for cooling computer CPU. *IEEE Trans Components Packag Technol* 30(1):42–49
7. Vasiliev L et al (2009) Loop heat pipe for cooling of high-power electronic components. *Int J Heat Mass Transf* 52(2):301–308
8. Maydanik Y, Verzhinin S, Pastukhov V, Fried S (2010) Loop heat pipes for cooling systems of servers. *IEEE Trans Components Packag Technol* 33(2):416–423
9. Choi J, Sano W, Zhang W, Yuan Y, Lee Y, Borca-Tasciuc D (2013) Experimental investigation on sintered porous wicks for miniature loop heat pipe applications. *Exp Therm Fluid Sci* 51(2):271–278
10. Hu Z, Wang D, Xu J, Zhang L (2020) Development of a loop heat pipe with the 3D printed stainless steel wick in the application of thermal management. *Int J Heat Mass Transf* 161
11. Adoni A, Ambirajan A, Jasvanth V, Kumar D, Dutta P (2010) Theoretical and experimental studies on an ammonia-based loop heat pipe with a flat evaporator. *IEEE Trans Components Packag Technol* 33(2):478–487
12. He S, Zhou P, Liu W, Liu Z (2020) Experimental study on thermal performance of loop heat pipe with a composite-material evaporator for cooling of electronics. *Appl Therm Eng* 168
13. Li J, Lin F, Wang D, Tian W (2013) A loop-heat-pipe heat sink with parallel condensers for high-power integrated LED chips. *Appl Therm Eng* 56(2):18–26
14. Li J, Lv L (2015) Performance investigation of a compact loop heat pipe with parallel condensers. *Exp Therm Fluid Sci* 62:40–51
15. Shioga T, Mizuno Y (2015) Micro loop heat pipe for mobile electronics applications. *Annu IEEE Semicond Therm Meas Manag Symp*, pp 50–55
16. Anand A, Jaiswal A, Ambirajan A, Dutta P (2018) Experimental studies on a miniature loop heat pipe with flat evaporator with various working fluids. *Appl Therm Eng* 144:495–503

Investigation of Inlet Blockage in the Central Subassembly of a Sodium-Cooled Fast Reactor



Yadu Narendran, K. Natesan, K. Devan, and A. John Arul

1 Introduction

The fast breeder reactors (FBRs) are expected to provide a sustainable and environmentally beneficial energy system, and they constitute the second stage of India's three-stage nuclear power program. Among various FBR concepts pursued throughout the world, sodium-cooled fast reactors (SFRs) with a closed fuel cycle were chosen by India for commercial development. In SFR, each fuel pin is wound by helical spacer wire around the clad. The fuel pins are closely arranged in a triangular pitch and housed inside a hexagonal sheath. When the reactor is working at normal operating conditions, heat generated by the fuel pins is transferred to the coolant flowing through the space between the fuel pins of the SA. The continuous flow of the coolant in the SA should be maintained for safe reactor operation.

A blockage in the SA will disrupt the designed power-to-flow ratio. The sources of flow blockage are excessive pin deformation due to swelling, fragments from failed fuel, oil ingress into the primary sodium circuit, foreign materials, spacer wire snapping, leftover during fabrication, and chemical products during operation. A coolant flow blockage in a SA can result in local sodium boiling, dryout, and melting of clad and fuel. It is known that a local melting caused by any fault in the SA level might propagate, resulting in a whole core accident. Therefore, coolant flow blockages are considered one of the initiating events of Core Disruptive Accidents (CDAs), which involve the melting of the whole core. Therefore, analysis of flow blockages is crucial in nuclear safety studies. Several measures are included into the core design to detect such blockages. The reactor power is monitored by a number of neutron detectors. The sodium temperatures at the fuel SA exits are monitored using thermocouples. For a gradually forming inlet blockage, the amount of reduction in

Y. Narendran (✉) · K. Natesan · K. Devan · A. John Arul
Indira Gandhi Centre for Atomic Research, A CI of Homi Bhabha National Institute, Kalpakkam,
Tamil Nadu 603102, India
e-mail: yadunarendran@gmail.com; yadun@igcar.gov.in

the flow rate of the coolant can affect the detection time, coolant boiling time, and the extent of void propagation.

It is essential to understand the phenomena which influence accidents from initiation to termination. The occurrence of sodium boiling plays a significant role in the course of events, rate of progression of accident, and amount of damages taking place in an accident. In a SFR, sodium voiding could cause positive reactivity feedback, which will increase the power of the reactor. Detailed modeling for sodium boiling is essential for any SFR severe accident analyses. Therefore, a sodium boiling model is crucial for the analysis of total inlet blockages of SA.

2 Literature Review and Objective

The investigation on blockage of SA of fast reactor is important for nuclear safety studies. A total instantaneous blockage (TIB) event has occurred in the Fermi-I reactor owing to a blockage of the coolant input to the SA by Zirconium plates [1]. Several experimental and numerical studies were reported on coolant blockage in the SA of SFR. The SCARABEE-N in-pile experiment program was carried out at the Cadarache SURT facility to study the characteristics of a TIB accident in the SA of SFR [2]. The program had different experimental groups corresponding to various phenomena occurring during TIB. The program observed the absence of violent fuel coolant interaction and axial fuel ejection. MOL-7C in-pile local blockage experiments were conducted in the BR-2 reactor in Belgium, using fuel burnup as the primary parameter [3]. The experiments showed that the local blockages are not self-limiting if the fuel burnup is significant, and without reactor trip, rapid damage progression would occur. J. L. Manzano et al. studied the ability to detection of rapid inlet blockages in the PEC reactor SA using the boiling model BLOW-3A [4]. The authors conducted an investigation on the effects of inlet flow reduction on the time of coolant boiling, clad melting, fuel melting, and the time of detection by temperature monitoring thermocouple at the outlet of the SA.

There were numerical studies conducted on coolant flow blockages in medium-sized SFR. P. Chellapandi et al. reported that the SCRAM parameter reached the threshold limit before the maximum clad hot spot is below 1073 K for 32% of inlet flow blockage for all rates of inlet flow reduction [5]. The extent of flow reduction greater than 95% is not permissible for any flow rate reduction. R. K. Maity et al. conducted thermal hydraulic studies to analyze the temperature dilution experienced in the core-temperature monitoring system of a SFR [6]. The study concluded that flow reductions within 7% and 12% are detected in fuel and blanket SA, respectively. M. Naveen Raj et al. analyzed the effect of planar blockage in the SA using three-dimensional CFD model and concluded that the transient is detectable by monitoring the discrepancies in the outlet temperature profile [7]. In a TIB, the inlet of the fuel SA is totally blocked instantaneously and is regarded as a theoretical envelope of all smaller blockages. The consequence of TIB in a medium-sized SFR is investigated

and detection of the accident is ensured by temperature rise in the neighboring SA sodium outlet [8, 9].

There have been several methods developed for modeling sodium boiling [10]. Two-fluid models can account for the observed phenomena such as thermal non-equilibrium of phases, and slip flow compared to simple models such as homogeneous-equilibrium models. Therefore, a two-fluid sodium boiling model can predict complex phenomena associated with SFR accidents in detail. The two-fluid sodium boiling model developed by M. R. Granziera et al. validated satisfactorily with experimental data [11].

Although there were studies regarding different aspects of blockages of SA, limited study is reported on the effect of blockage level in a SA on boiling time, dryout time, and clad melting time. This study aims to predict the events occurring during inlet blockage of a SA such as sodium boiling, clad dryout, and clad melting. Time of detection of the accident by the sodium outlet temperature monitoring thermocouples is also predicted. The effect of blockage growth is investigated through a parametric study.

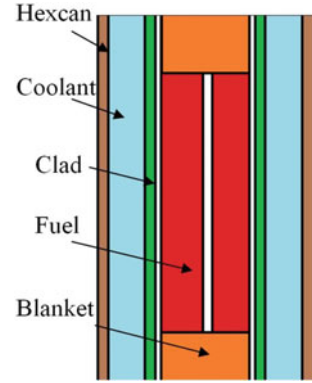
3 Modeling

In the present study, the single-pin approach is used to model the SA of the reactor. The approach has been used for severe accident analysis in the literature [12]. In this approach, all the fuel pins of a SA are assumed to behave the same. Therefore, a single fuel pin of average SA power, average coolant channel area, and corresponding hexcan wall represents a SA as shown in Fig. 1. Details regarding the division of grids, governing equations, and solution strategy of heat transfer calculation of fuel, clad, and blanket regions can be found in [9]. To model the sodium boiling, one-dimensional two-fluid model is adopted. Conservation equation of mass, momentum, and energy of vapor phase over a control volume is given by [11]:

$$\begin{aligned} \frac{\partial}{\partial t} \int_V \alpha \rho_v dV + \int_{A_{z+}} \alpha \rho_v U_v dA - \int_{A_{z-}} \alpha \rho_v U_v dA \\ = \int_V (S_e - S_c) dV, \end{aligned} \quad (1)$$

$$\begin{aligned} \frac{\partial}{\partial t} \int_V \alpha \rho_v U_v dV + \int_{A_{z+}} \alpha \rho_v U_v^2 dA - \int_{A_{z-}} \alpha \rho_v U_v^2 dA \\ - \oint_{A_v} P \cdot \hat{k} \cdot \hat{n} dA = - \int_{A_w} f_v dA - \int_V \alpha \rho_v g dV + \int_V M_v dV, \end{aligned} \quad (2)$$

Fig. 1 Schematic of single-pin approach



$$\begin{aligned}
 & \frac{\partial}{\partial t} \int_V \alpha \rho_v \left(e_v + \frac{1}{2} U_v^2 \right) dV + \int_{A_{z+}} \alpha \rho_v U_v \left(e_v + \frac{1}{2} U_v^2 \right) dA \\
 & - \int_{A_{z-}} \alpha \rho_v U_v \left(e_v + \frac{1}{2} U_v^2 \right) dA = \int_V Q_v dV - \int_V \alpha \rho_v g U_v dV \\
 & - \int_{A_w} \vec{U}_v \cdot \vec{f}_v dA + \int_{A_v} P \cdot \hat{n} \cdot \vec{U}_v dA - \int_V P \frac{\partial \alpha}{\partial t} dV + \int_{A_i} q_{vi} dA.
 \end{aligned} \quad (3)$$

Conservation equations of liquid phase are similar to the above equations, where vapor properties are replaced with liquid properties. The resulting six conservation equations are simplified and discretized as described in [11]. The Newton iteration scheme is used for the solution of discretized equations with solution vector as:

$$X = [\alpha, P, T_v, T_l, U_v, U_l]. \quad (4)$$

If the discretized conservation equations are defined as $F_p(X) = 0$, the iteration procedure can be derived as:

$$\sum_{q=1}^{q=6} \left(\frac{\partial F_p}{\partial x_q} \right)_{x^k} (x_q^{k+1} - x_q^k) = -F_p(X^k), \quad p = 1, \dots, 6. \quad (5)$$

The resulting sets of equations are solved using the solution procedure and correlations as described in [11].

4 Results and Discussion

4.1 Validation

The BI1 loss of flow (LOF) test data is used for the validation of the model developed. The test was conducted in the CABRI reactor and was used for the validation of various codes developed for SFR accident modeling [13]. The BI1 test was an in-pile LOF experiment using a single-mixed oxide test pin irradiated in the PHENIX reactor with a maximum burnup of 1 at.%. Details of the pin properties are given in Table 1.

The initial conditions of the experiment are given in Table 2. The transient was initiated by the reduction of mass flow rate in the test section by reducing the pump head. The reduced mass flow results in rapid rise of temperature in the test channel. Sodium boiling is observed to occur at the top of fuel region at time 20.2 s. The boiling causes sudden decrease inlet mass flow rate. Eventually, voided region expanded to lower part of the pin and clad dryout is observed.

The model developed is able to simulate regions from lower blanket to upper blanket of the test pin. Initial conditions are achieved by giving the steady-state flow rate as input. Non-uniform heat generation in the pin along the axial direction is incorporated. After establishing close results for steady-state values, the transient phase is simulated by giving inlet flow rate and pressure outlet as boundary condition as given in [13].

The predicted evolution of boiling front of sodium along the axial length is compared with experimental data in Fig. 2. Since the present model does not has

Table 1 Details of the test pin

Parameter	Value (mm)
Clad inner diameter	6.595
Clad outer diameter	7.605
Fuel inner diameter	0
Fuel outer diameter	6.4
Upper blanket length	99.5
Lower blanket length	200.2
Fuel length	748.8

Table 2 Details of CABRI BI1 experiment initial condition

Parameter	Value
Fissile power	36230W
Inlet mass flow rate	0.161 kg/s
Temperature at BFC	676 K
Temperature at TFC	859 K

Fig. 2 Comparison of evolution of sodium boiling front predicted by present calculation against experimental data [13] along the axial length of the pin

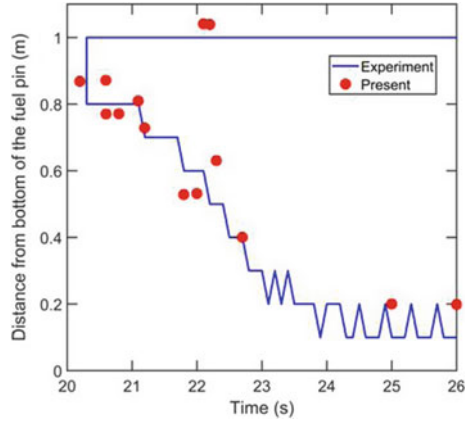
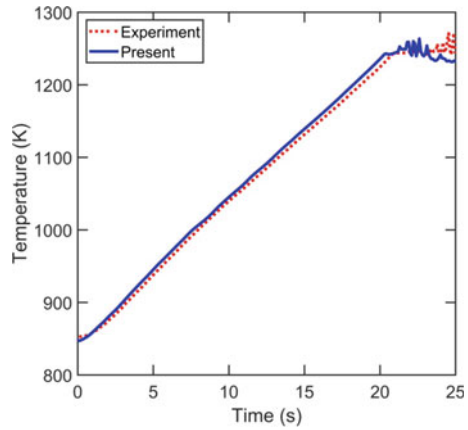


Fig. 3 Comparison of sodium temperature evolution predicted by present calculation against experimental data [13] at 77 cm from bottom of the fuel column

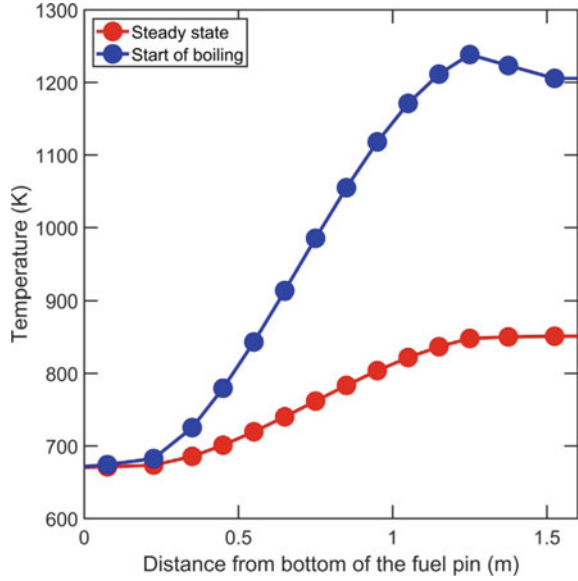


the capability to model beyond the top blanket region, the evolution of boiling front above the fuel region is not predicted accurately. The calculated evolution of temperature with time at 77 cm from bottom of the fissile column is in good agreement with that of experimental data as shown in Fig. 3.

4.2 Analysis of Rapid Inlet Blockage

After validation of the model with experimental data, a detailed analysis on inlet blockage in the central SA of a medium-sized SFR is conducted. Geometrical data and initial input conditions used for the present analysis are same as in [9]. In the present analysis, neutronics effects and inter-SA heat transfer are not incorporated. The dilution of temperature reading at sodium outlet and finite thermocouple time

Fig. 4 Comparison of temperature distribution of sodium along the axial length of the pin at steady-state condition and at the time of boiling ($\tau = 8s$ and $F = 0$)



constant are neglected. Steady-state condition is achieved through transient approach. The blockage scenario is simulated by giving the coolant inlet flow rate as boundary condition keeping the outlet pressure constant at steady-state value. Inlet flow rate is given by the following expression [4]:

$$m(t) = m_0[F + (1 - F) \exp(-t/\tau)], \tag{6}$$

where τ is the time constant of blockage formation; m_0 is the initial mass flow rate; $m(t)$ is instantaneous mass flow rate; $F = m_r/m_0$; and m_r is residual mass flow rate. As the flow rate of the coolant reduces, temperature of the core components increases. For $\tau = 8s$ and $F = 0$, 10 K rise in the sodium outlet temperature is occurred at 0.8 s. Figure 4 compares the temperature distribution along the axial length of the pin at start of the transient (steady state) and the temperature distribution during the time of incipient boiling at 10.4 s. At the time of start of boiling, blockage was 73.72%. It is observed that the boiling starts at the top of the fissile region. As the outlet pressure is lower, voiding is faster in the top blanket region. As the time progresses, the boiling front progresses downward in the fissile region as shown in Fig. 5 which depicts the boiling front evolution with time along the axial length of the pin. Dryout is first observed at the top of the fissile region at 15.21 s. Dryout is immediately followed by clad melting. It is assumed that when all the radial meshes of the clad at a particular location is melted, clad motion starts. The code terminates at the time when clad motion starts at 17.6 s. Thus, clad motion is initiated before the boiling front progresses to bottom of the fissile region.

A parametric study of effect of τ on time of detection, time of start of sodium boiling, and start of molten clad motion is conducted and the results are depicted in

Fig. 5 Sodium boiling front evolution along the axial length of the pin ($\tau = 8s$ and $F = 0$)

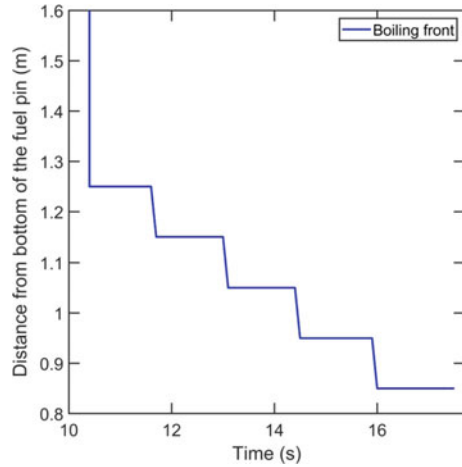


Fig. 6. Accident detection time, boiling start time, and clad motion start time are used to obtain the regions as shown in Fig. 6. It is clear from the figure that the accident is detected by the rise of sodium outlet temperature by 10 K well before the sodium boiling is initiated. Heat balance calculation showed that 5.23% blockage could cause 10 K rise in the sodium outlet temperature. For lower values of τ , blockage formation is rapid. Therefore, detection, boiling, and clad motion are observed to occur at higher blockage percentage. For higher values of τ , flow rate reduction is gradual and blockage percentage on which various phenomena occur has less influence on τ . A parametric study on the effect of values of F (0–0.4 with interval of 0.05) for $\tau = 4$ is conducted. As the F increased, time of detection, boiling, and clad motion increased. For $F = 0.2$ to 0.3, a steady-state boiling is achieved and did not progress to dry out. At $F = 0.35$, boiling did not occur at all. This variation is because, as F increases, the residual mass flow rate increases. At higher values of F , the residual coolant flow is sufficient to maintain a new steady-state condition with higher coolant temperature distribution.

5 Conclusions

To investigate the inlet blockage in a SA of a SFR, one-dimensional two-fluid sodium boiling model is developed. The model is added to previously developed single-pin thermal model. The developed model is validated with CABRI B11 loss of flow experimental data. The inlet blockage in the central SA of a medium-sized SFR is analyzed using the developed model. For 8 s of blockage formation time constant, detection of the accident by sodium outlet temperature monitoring thermocouple occurs at 0.8 s. The boiling front evolution of the coolant and temperature distribution of the core components is predicted. The parametric study showed that blockage

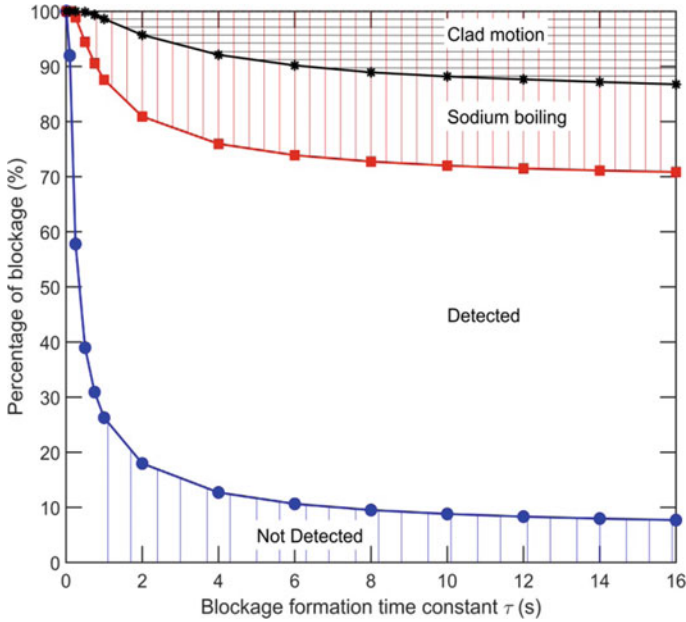


Fig. 6 State map of occurrence of various phenomena as a function of blockage formation time constant (τ) and percentage of blockage at $F = 0$

percentage at the time of detection, time of boiling, and time of clad motion is less sensitive as blockage formation time constant (τ) increases. The blockage is detected before boiling is started at all values of τ . As the value of F increases, the blockage may lead to steady-state boiling or steady-state single-phase flow at an elevated temperature distribution.

Nomenclature

- P Pressure [N/m^2]
- U_{vz} Axial component of vapor velocity [ms^{-1}]
- U_v Vapor velocity [ms^{-1}]
- U_l Liquid velocity [ms^{-1}]
- Q Instantaneous flow rate [$\text{m}^3 \text{s}^{-1}$]
- Q_0 Initial flow rate [$\text{m}^3 \text{s}^{-1}$]
- τ Flow halving time constant [s]
- t Time [s]
- T_v Vapor temperature [K]
- T_l Liquid temperature [K]
- α Void fraction

ρ_v	Vapor density [kgm^{-3}]
g	Acceleration due to gravity [ms^{-2}]
S	Mass exchange rate [$\text{kgs}^{-1} \text{m}^{-3}$]
M	Momentum exchange rate [$\text{kgm}^{-2} \text{s}^{-2}$]
f_v	Frictional force per area [$\text{kgm}^{-1} \text{s}^{-2}$]
q_v	Heat flux through interfaces [Wm^{-2}]
Q_v	Volumetric heat generation rate [Wm^{-3}]
e_v	Specific energy of vapor [Jkg^{-1}]

References

1. Waltar AE, Todd DR, Tsvetkov PV (2011) Fast spectrum reactors. Springer
2. Kayser G, Charpenel J, Jamond C (1998) Summary of the SCARABEE-N subassembly melting and propagation tests with an application to a hypothetical total instantaneous blockage in a reactor. Nucl Sci Eng 128:144–185
3. Schleisiek K, Aberle J, Homann C, Schmuck I, Maschek W, Rahn A, Romer O, Schmidt L, Borms L, Verwimp A (1998) The Mol-7C in-pile local blockage experiments: main results, conclusions, and extrapolation to reactor conditions. Nucl Sci Eng 128:93–143
4. Manzano D, Bianchini G, Struwe D (1987) Detectability limits of rapid inlet blockages in high powered subassemblies of the PEC reactor, science and technology of fast reactor safety. Thomas Telford Publishing, pp 1–275
5. Chellapandi P, Velusamy K (2015) Thermal hydraulic issues and challenges for current and new generation FBRs. Nucl Eng Des 294:202–225
6. Maity RK, Velusamy K, Selvaraj P, Chellapandi P (2011) Computational fluid dynamic investigations of partial blockage detection by core-temperature monitoring system of a sodium cooled fast reactor. Nucl Eng Des 241:4994–5008
7. Raj MN, Velusamy K (2018) Investigations on thermal hydraulic consequences of planar blockage in a prototype sodium cooled fast reactor fuel subassembly. Prog Nucl Energy 104:47–59
8. Ravi L, Velusamy K, Chellapandi P (2016) Conjugate heat transfer investigation of core damage propagation during total instantaneous blockage in SFR fuel subassembly. Ann Nucl Energy 90:371–388
9. Narendran Y, Natesan K, Devan K, Arul AJ, Vikram G (2022) Modeling of neutronics and thermal-hydraulic aspects during total instantaneous blockage of central fuel subassembly in a fast reactor. Ann Nucl Energy 175:109187
10. Tsige-Tamirat H, Perez-Martin S, Pfrang W, Anderhuber M, Gerschenfeld A, Laborde L, Mikiatyuk K, Peniguel C, Mimouni S (2022) A review of models for the sodium boiling phenomena in sodium-cooled fast reactor subassemblies. J Nucl Eng Radiat Sci 8
11. Granziera MR, Kazimi MS (1980) A two dimensional, two fluid model for sodium boiling in LMFBR fuel assemblies. MIT Energy Laboratory
12. Fukano Y (2015) SAS4A analysis on hypothetical total instantaneous flow blockage in SFRs based on in-pile experiments. Ann Nucl Energy 77:376–392
13. Bandini G, Ederli S, Perez-Martin S, Haselbauer M, Pfrang W, Herranz L, Berna C, Matuzas V, Flores AF, Girault N, et al (2018) ASTEC-Na code: thermal-hydraulic model validation and benchmarking with other codes. Ann Nucl Energy 119:427–439

Experimental Investigation of PHP with Hybrid Nanofluid for EV Battery Thermal Management



Nikhil S. Mane, Siddhartha Tripathi, and Vadiraj Hemadri

1 Introduction

The use of electric vehicles (EVs) has dramatically increased in response to global warming concerns and fossil fuel depletion. Lithium-ion (LI) batteries are the primary choice for EV energy storage as they have high-energy storage density and durability. Among different designs of LI batteries, cylindrical-shaped 18,650 battery cells are the preferred choice for batteries in several electric cars and bikes due to their cost and flexibility in design. These batteries are also used for grid energy storage, electronics, and aviation. The high-energy requirements of certain applications can be met by connecting these cells in parallel or series in the form of modules. Even though these batteries are accepted for several applications, their thermal management is challenging for engineers.

In LI batteries, energy is stored in the form of chemical energy and converted into electric energy during energy consumption. Hence, chemical to electric and vice versa cyclic energy conversion occurs during the charging–discharging process. This cyclic energy conversion during battery operation generates heat as a by-product which, if accumulated, increases the battery's temperature. High operating temperatures of batteries reduce their life and performance and lead to thermal runaway. Thermal runaway is a chain reaction that occurs due to the high temperature of the battery, which can potentially result in battery explosion and fire hazards [1]. The heat generation in batteries depends upon the discharge rate of the battery. Hence, operating at high loads results in an increase in the operating temperatures. Different techniques have been used to remove this heat so that the safe and efficient functioning of the batteries is ensured. These methods include forced air convection, immersion cooling, thermosyphon, and heat pipes.

N. S. Mane (✉) · S. Tripathi · V. Hemadri
Department of Mechanical Engineering, BITS Pilani K K Birla Goa Campus, Zuarinagar,
Sancoale, Goa 403726, India
e-mail: p20180023@goa.bits-pilani.ac.in

To develop battery cooling systems, researchers have employed either one or a combination of various cooling techniques. Pesaran [2] listed the three thermal functions of an ideal battery cooling system: It should remove the heat generated in the battery, provide heating if required, and protect the battery from rapid temperature fluctuations. The battery cooling system should also take into account the energy loss, size, cost, and weight of the system [3]. The cooling of batteries with forced air convection can only be effective with low discharge rates. Li et al. [4] used forced convection and herringbone fins to cool the cylindrical LI battery module (12 batteries), working at 1–4 C discharge rate. They found a 17.92% decrease in the maximum temperature difference in the battery module. A few studies have also focused on using phase change material (PCM) with different convection heat transfer enhancement techniques for battery cooling. Sun et al. [5] used longitudinal and cylindrical-shaped fins in combination with PCM for battery cooling. They used an electric heater to simulate the LI batteries citing safety-related reasons. They found efficient cooling performance at 20W heat generation.

Karimi et al. [6] utilized Ag nanoparticle-mixed PCM for battery cooling. They observed a 70% reduction in the temperature difference between the battery and PCM with the addition of nanoparticles. They concluded that using nanoparticles mixed with PCM can be an effective technique for BTMS. Wang et al. [7] conducted an experimental study on prismatic battery cooling using an L-shaped heat pipe. They found that heat pipes are viable battery cooling devices and can maintain battery temperature below 40°C for 10 W/cell heat generation and below 70 °C for 20–40 W/cell heat generation. Zhao et al. [8] successfully designed a cooling system for a cylindrical battery pack using air-cooled heat pipe. They too used phase change material to ensure better heat collection from the batteries. They observed the reduction in temperature to be around 29%. Mbulu et al. [9] investigated the feasibility of water-cooled L and I-shaped heat pipes for cooling LI batteries. It was observed that heat pipes remove more than 92.18% of generated heat and reduce the battery temperature by 5 °C.

Heat pipes have different variants as thermosyphons, wicked heat pipes, flat heat pipes, loop heat pipes, and PHPs. All these variants have their unique functioning characteristics and applications. Among the different variants, PHP is a promising design due to its simple structure, design flexibility, high orientation independence, and availability of a wider range of working fluids [10]. Qu et al. [11] investigated the different shapes of pulsating heat pipes (I, inverted U, and N) for cooling electric vehicle batteries. Results show that N-shaped and inverted U-shaped designs show the best performance. They also found that a reduction in adiabatic length reduces the start-up temperature. Few of the available studies focus on investigating the effect of working fluids on PHP performance. Burban et al. [12] studied the effect of working fluids (acetone, methanol, water, and n-pentane) on the ability of PHP to cool the EV batteries at different inclinations (0° and 45°). They found that with methanol, PHP performance is improved at higher temperatures.

The use of nanofluids as working fluids in thermal applications has increased in recent years as nanofluids have superior thermal properties compared to their base fluids. Mane et al. [13] showed that CuO + Fe₃O₄-water (0.1 wt.%) nanofluid has

superior thermal conductivity, wettability, and viscosity compared to water. They also predicted that a collective effect of these properties delivers better thermal performance in cooling applications. The use of nanofluids has been shown to improve the performance of different designs of heat pipes. Liu et al. [14] used CuO–water nanofluid to study the heat transfer characteristics of a flat heat pipe. Jia et al. [15] investigated the effect of SiO₂–water nanofluid (0.05–0.5 wt.%) on the heat transfer performance of PHP. They observed that though at a lower fraction, the PHP shows performance enhancement, at a higher fraction of nanoparticles, the thermal performance of PHP depreciates. They also observed that thermal resistance decreases with increased evaporator heat input. Recently, Jajarm et al. [16, 17] studied the effect of nanofluids on the performance of PHP. They found that the PHP performance improves with nanofluids, and start-up temperatures can be considerably reduced.

The PHP performance with nanofluids needs further experimentation as reliable data showing the PHP performance improvement and reduction in start-up temperature with nanofluids can potentially lead to their increased acceptability in several applications. Also, there is a scarcity of literature available on the effect of nanofluids on PHP performance with inclination angle and heat inputs. Given these shortcomings, a parametric study is conducted to study the thermal performance of the PHP designed for 18,650 battery cell modules. In this work, we explore the effect of working fluid (CuO + Fe₃O₄–water nanofluid and water) and PHP inclination (90°, 45°, and 0°) on PHP performance. The concentration of CuO + Fe₃O₄–water nanofluid is maintained at 2 wt.%, and the filling ratio of PHP is maintained at 60%.

2 Materials and Methods

Figure 1a, b show the conceptual design of PHP for the cooling of 18,650-cell module whose performance is explored in this work. The PHP is designed to occupy the gap in the module of six 18,650 cells arranged in an offset pattern. The offset pattern is the preferred cylindrical battery arrangement in most applications because of its low space occupancy. The internal diameter of the PHP copper pipe is 3.76 mm, and the outer diameter is 4.76 mm. The total height of PHP is 214 mm, including the evaporator (82 mm), adiabatic section (50 mm), and condenser (82 mm). The distance between two adjacent pipes of PHP geometry is 30 mm. Figure 1c gives detailed information on the dimensions of the PHP. The PHP is fabricated using a copper tube and joined through brazing. It should be noted that during the fabrication of PHP, utmost care should be taken to avoid dents or any obstructions to fluid flow, which can seriously hamper PHP operations. The concept of the PHP as a battery cooling device is such that the evaporator portion of PHP will receive heat from the cells, which is then transferred to the condenser through the PHP. At the condenser, cooling will take place through forced air convection.

In this work, heat supplied by the cell is simulated using an electric heater fabricated using a nichrome wire. This heater covers approximately the same area of the evaporator as that of a 18,650-cell module. The heat generation in the 18,650 cells

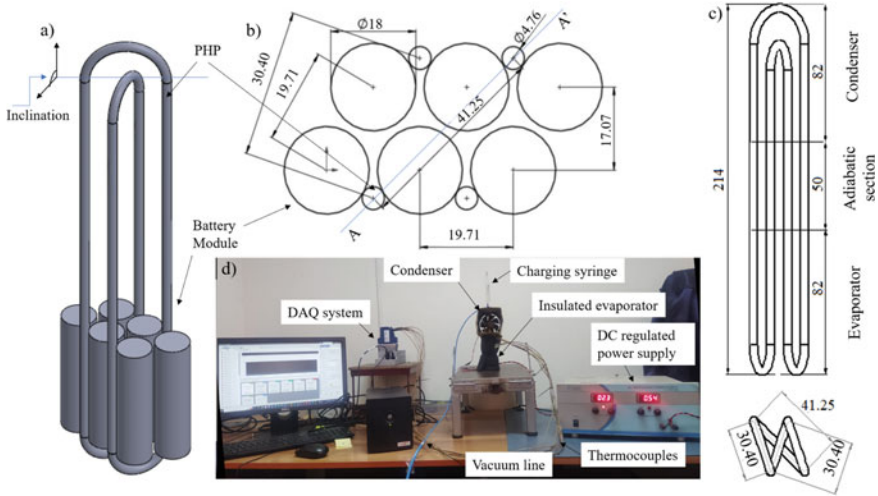


Fig. 1 **a** Conceptual design of PHP in the module of six cylindrical 18,650 LI batteries for cooling, **b** conceptual arrangement of PHP with respect to cylindrical LI batteries during cooling, **c** detailed dimensions of PHP, **d** experimental setup of the present study

is based on the state of charge, rate of discharge, and life of the battery; hence, heat supplied to the heater is maintained between 5 and 20 W so that the actual range of heat generation of six 18,650 cells is covered. The heat input of this heater is varied using a DC-regulated power supply. An electric fan ($90 \times 90 \text{ mm}^2$) attached to a square duct is used for cooling the condenser. All the components of the experimental setup can be observed in Fig. 1 d.

Water and $\text{CuO} + \text{Fe}_3\text{O}_4$ -water nanofluid (2 wt.%) is used as working fluid in PHP. The nanofluid is prepared by mixing 2 wt.% of 50 nm $\text{CuO} + \text{Fe}_3\text{O}_4$ nanoparticles (1 wt.% each) in water. The nanofluid concentration is decided based on the literature stating that to improve the boiling characteristics of the fluid, at least 1 wt.% nanoparticle concentration should be maintained [18]. Gum Arabica is used as a dispersant to obtain an excellent colloidal dispersion. The effectiveness of Gum Arabica in obtaining excellent nanofluid stability is discussed in our previous work [19]. The dispersant (0.2 wt.%) and nanoparticles are properly mixed in water using a mechanical stirrer. After this, 2-h ultrasonication using an ultrasonicator (20 kHz frequency) is conducted to reduce the size of nanoparticle agglomerates. The prepared nanofluid is then charged into PHP through a three-way valve using a syringe after thoroughly vacuuming the PHP using a vacuum pump (ultimate pressure: 0.002 mbar). The charging volume of each working fluid is maintained at 60% of the total space in PHP. The temperatures of PHP are recorded using four T-type thermocouples each on the condenser and evaporator and data acquisition system. The temperatures are recorded throughout the trial at the interval of 1 s. The effect of PHP inclination on thermal performance is also studied in the present work. The different inclinations of PHP along the vertical axis perpendicular to line AA' (as shown in Fig. 1) are

obtained by mounting it on the variable inclination platform. For each PHP inclination trial, the desired position is locked on the platform so that PHP makes the desired angle with a horizontal position. The angle of inclination is measured using a digital inclinometer (accuracy: $\pm 0.2\hat{A}^\circ$).

Once the working fluid is charged, the heat is supplied to the evaporator. The heat is supplied in the step-up manner (5, 10, 15, and 20 W), where each power input is maintained for 30 min before increasing to the next step. After the trial, the inclination angle is changed, and the procedure is repeated. The obtained data from the experiments are then analyzed, and thermal resistance (R_{th}) is calculated using Eq. (1).

$$R_{th} = \frac{T_E - T_C}{Q}, \quad (1)$$

where T_C and T_E are average values of condenser and evaporator temperatures. Q is the heat supplied to the PHP evaporator. Each experiment is repeated three times, and average values of R_{th} are presented here. The uncertainties observed in experimental measurements are calculated [20], and the maximum uncertainty (U) is $\pm 1.0024\%$.

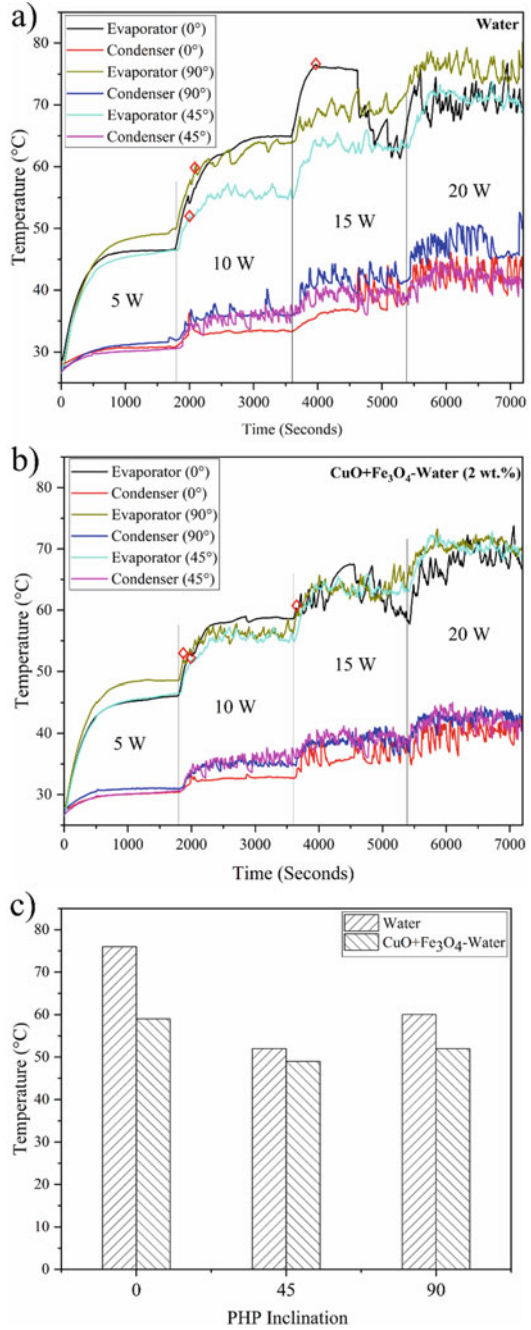
3 Results and Discussion

3.1 Start-Up of PHP

The start-up temperature is the temperature at which flow pulsation initiates in the PHP; hence, at this point, the thermal resistance of the PHP significantly decreases and effective cooling begins. The suitability and acceptance of PHP for any application strongly depend on PHP's start-up temperature as it decides the temperature at which PHP delivers its best performance. The working fluid temperature starts to rise when heat is received at the PHP evaporator. When the temperature reaches the start-up point, a continuous flow of liquid and vapor slug occurs in the PHP. This flow is induced due to the vaporization of a small part of the working fluid, which also increases the pressure, thus aiding the flow in PHP. This pulsatory flow can be recognized by the fluctuations observed in PHP temperatures, as shown in Fig. 2. During vapor slug and liquid flow in the PHP, the high temperature of vapor bubbles leads to localized heating and cooling of the PHP surface for a short period. This leads to temperature fluctuations on the PHP surface. When the amount of heat supplied increases, the vapor generation increases, leading to increased pressure and high velocity of liquid–vapor slug pulsations. This increased pulsation frequency is seen in Fig. 2a, b through increased temperature fluctuations at higher heat input.

It is observed here that the evaporator temperature attained by the 5W heat supply is not enough to reach the start-up temperature. In most of the experimental runs at different parameters, the PHP start-up takes place at 10W. Hence, at 5W, heat transfer

Fig. 2 Start-up temperatures of PHP with **a** water compared to **b** CuO + Fe₃O₄-water nanofluid and pulsation initiation in PHP at different inclinations. **c** Lower start-up temperature of PHP at 45° inclinations and with CuO + Fe₃O₄-water nanofluid



from the evaporator to the condenser section occurs through only conduction of the PHP body as the start-up of PHP is not attained. For the horizontal position, the PHP start-up temperature is 76 °C with water and 58 °C for CuO + Fe₃O₄-water nanofluid (2 wt.%). For the vertical position (90°) and 45° inclined position, the start-up temperature for both working fluids is comparable, but with nanofluid, more uniform and continuous temperature fluctuations are observed.

The pulsation characteristics of the PHP are also influenced by the PHP inclination. With both the working fluids, PHP in the horizontal (0°) position showed a considerable delay in the start-up. In the horizontal position of the PHP, the evaporator space is not entirely filled with working fluids as is the case in 45° and 90° positions. Only a portion of the heat supplied to the evaporator is received by the working fluid, which increases the evaporator temperature without the start-up of the PHP. This delays the vapor slug and liquid, and a high temperature is required to start the PHP. Compared to 45° and 90° positions, the performance of PHP in a horizontal position is inferior and cannot work effectively for LI battery cooling. It can be concluded from this observation that PHP is not favorable in horizontal orientation.

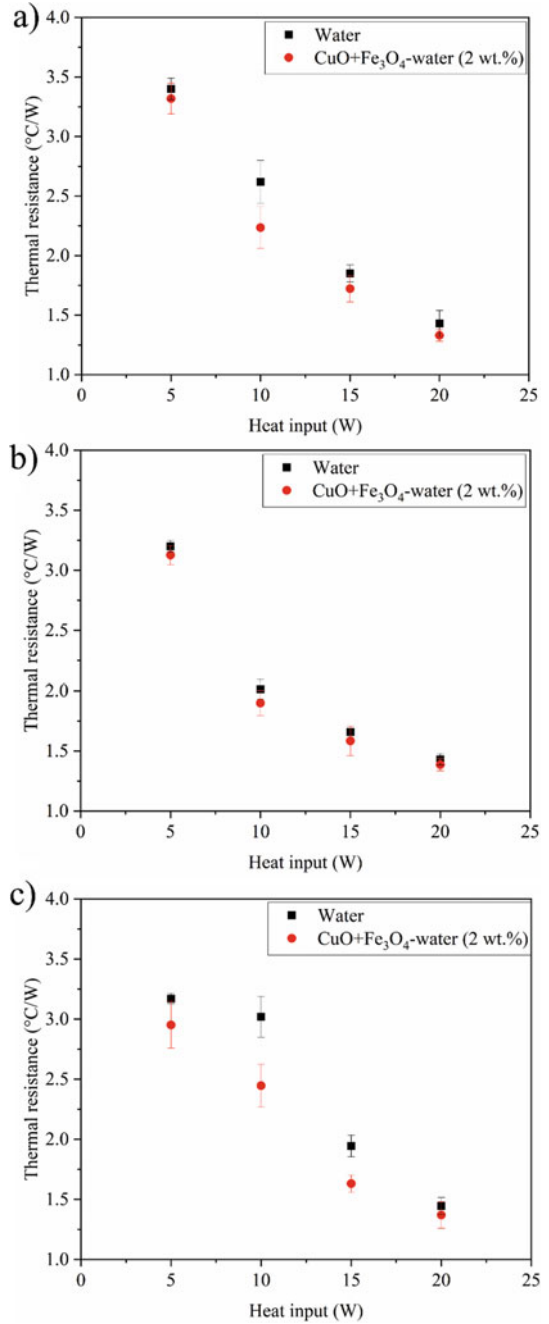
Figure 2c shows the start-up temperature of the PHP with different working fluids and PHP inclinations. It is observed that at all the PHP inclinations studied, the start-up temperature is lower for CuO + Fe₃O₄-water nanofluid than water. This shows that with nanofluids PHP can effectively be used for applications at lower temperatures. Figure 2c also illustrates the effect of PHP inclination on the start-up temperature. The start-up temperature is lowest at 45° PHP inclinations for both the working fluids. The lowest start-up temperature of the PHP is observed to be 49°C for CuO + Fe₃O₄-water nanofluid at a 45° inclined position. This shows that the PHP can be used to maintain the temperature of the 18,650 LI batteries in a safe range (45–50°C). However, further investigation is still required to reduce PHP's start-up temperature below 45°C so that effective intensified cooling takes place earlier than the safe temperature range.

3.2 Effect of Working Fluid on the PHP Performance

The thermal resistance of the PHP with water and with nanofluid is compared to investigate the effect of working fluid on the performance of PHP. The impact of working fluid and heat input on the thermal resistance of PHP is shown in Fig. 3.

It can be observed that the thermal resistance of PHP decreases when CuO + Fe₃O₄-water nanofluid (2 wt.%) is used compared to water. During this study, PHP with nanofluids has an average 7.8% lower thermal resistance than PHP with water. The decreased thermal resistance of PHP with nanofluid results from the high thermal conductivity of nanofluid due to the Brownian motion of nanoparticles. The decreased thermal resistance of PHP can also be attributed to the deposition of nanoparticles on the evaporator surface; these particles act as nucleation sites and assist in boiling. The altered wettability of the surface with nanofluids also promotes boiling [21].

Fig. 3 Decrease in thermal resistance with heat input and superior thermal performance of PHP with CuO + Fe₃O₄-water nanofluid PHP with **a** 90° (vertical), **b** 45°, and **c** 0° (horizontal) inclination



All these phenomena and altered properties of working fluid due to nanoparticles collectively lead to the decreased thermal resistance of PHP with nanofluids.

At 5 W heat input where PHP has not reached start-up temperature, the thermal resistance of PHP with both working fluids is comparable at 90° (vertical) and 45° inclined positions. This is because of the lack of pulsations at low heat input when the heat transfer takes place purely through conduction in the PHP body. At starting temperature with 10 W heat input, the fluid boiling and flow pulsation phenomenon come into play, and thermal resistance decreases. The CuO + Fe₃O₄-water nanofluid (2 wt.%) has better thermal properties and also nanoparticles assist the boiling which reduces the PHP thermal resistance compared to water. With increased heat input, the boiling and flow pulsations intensify, and the thermal resistance decreases continuously.

Figure 3 also shows that the PHP inclination also influences the thermal resistance of the PHP. The average thermal resistance values show that at 45° inclination, PHP performs better than vertical and horizontal positions. The higher pressure required for start-up at the vertical position and the higher empty space of the evaporator in the horizontal position contributes to their marginally diminished performance in the respective orientations.

4 Conclusions

Experimental investigation on pulsating heat pipe designed for cooling lithium-ion battery module is conducted with different working fluids (CuO + Fe₃O₄-water nanofluid and water) and PHP inclination (90°, 45°, and 0°). The conclusions drawn from this study are:

- Use of CuO + Fe₃O₄-water nanofluid considerably reduces the start-up temperature of the PHP for all the inclination positions investigated in this study.
- For all the PHP inclinations, nanofluids reduce the thermal resistance of PHP. For all the trials in this study, PHP resistance is decreased by an average value of 7.8% with CuO + Fe₃O₄-water nanofluid (2 wt.%) compared to water.
- PHP performance is best at 45° inclinations, while the highest thermal resistance and high start-up temperature are observed at the horizontal position.
- In this study, the lowest start-up temperature observed is 49°C; since it is within safe temperature limits, it provides confidence for the application of PHP for LI battery cooling. With further investigation, the start-up temperature can be further reduced to provide more efficient cooling to LI batteries at lower temperatures, i.e., ~ 45°C.

Acknowledgements The authors would like to thank BITS Pilani K. K. Birla Goa Campus for funding this work under the Additional Competitive Grant.

Nomenclature

Q	Heat input W
R_{th}	Thermal resistance °C/W
T	Temperature °C
U	Uncertainty-
$Wt.$	Weight fraction

References

- Vetter J, Novák P, Wagner M, Veit C, Möller K, Besenhard J et al (2005) Ageing mechanisms in lithium-ion batteries. *J Power Sour* 147(2005):269–281
- Pesaran A (2001) Battery thermal management in EVs and HEVs: issues and solutions. In: *Advanced automotive battery conference* 10
- Fayaz H, Afzal A, Samee A et al (2022) Optimization of thermal and structural design in lithium-ion batteries to obtain energy efficient battery thermal management system (BTMS): a critical review. *Arch Computat Methods Eng* 29:129–194
- Li C, Li Y, Gao L, Garg A, Li W (2021) Surrogate model-based heat dissipation optimization of air-cooling battery packs involving herringbone fins. *Int J Energy Res* 45(7):8508–8523
- Sun Z, Fan R, Yan F, Zhou T, Zheng N (2019) Thermal management of the lithium-ion battery by the composite PCM-Fin structures. *Int J Heat Mass Transf* 145:118739
- Karimi G, Azizi M, Babapoor A (2016) Experimental study of a cylindrical lithium ion battery thermal management using phase change material composites. *J Energy Storage* 8:168–174
- Wang Q, Jiang B, Xue QF, Sun HL, Li B, Zou HM, Yan YY (2015) Experimental investigation on EV battery cooling and heating by heat pipes. *Appl Therm Eng* 88:54–60
- Zhao J, Lv P, Rao Z (2017) Experimental study on the thermal management performance of phase change material coupled with heat pipe for cylindrical power battery pack. *Exp Thermal Fluid Sci* 82:182–188
- Mbulu H, Laonual Y, Wongwises S (2021) Experimental study on the thermal performance of a battery thermal management system using heat pipes. *Case Stud Therm Eng* 26:101029
- Mameli M, Besagni G, Markides C (2022) Innovations in pulsating heat pipes: from origins to future perspectives. *Appl Therm Eng* 203:117921
- Qu J, Wang C, Li X, Wang H (2018) Heat transfer performance of flexible oscillating heat pipes for electric/hybrid-electric vehicle battery thermal management. *Appl Therm Eng* 135:1–9
- Burban G, Ayel V, Alexandre A, Lagonotte P, Bertin Y, Romestant C (2013) Experimental investigation of a pulsating heat pipe for hybrid vehicle applications. *Appl Therm Eng* 50(1):94–103
- Mane N, Hemadri V (2022) Experimental investigation of stability, properties and thermo-rheological behaviour of water-based hybrid CuO and Fe₃O₄ nanofluids. *Int J Thermophys* 43:1–22
- Liu Z, Xiong J, Bao R (2007) Boiling heat transfer characteristics of nanofluids in a flat heat pipe evaporator with micro-grooved heating surface. *Int J Multiphase Flow* 33:1284–1295
- Jia H, Jia L, Tan Z (2013) An experimental investigation on heat transfer performance of nanofluid pulsating heat pipe. *J Therm Sci* 22:484–490
- Jajarm A, Goshayeshi H, Bashirmezahad K (2022) Experimental study of thermal performance of a newly designed pulsating heat pipe with Fe₃O₄ nanofluid-exposed magnetic field and corrugated evaporator. *Int J Thermophys* 43:40

17. Jajarm A, Goshayeshi H, Kazem B (2022) Experimental study on heat transfer enhancement of carboxylate multi-wall carbon nanotubes in a 3D pulsating heat pipe with a corrugated evaporator. *Nanoscale Microscale Thermophys Eng*
18. Taylor R, Phelan P (2009) Pool boiling of nanofluids: comprehensive review of existing data and limited new data. *Int J Heat Mass Transf* 52(23–24):5339–5347
19. Mane N, Tripathi S, Hemadri V (2022) Effect of biopolymers on stability and properties of aqueous hybrid metal oxide nanofluids in thermal applications. *Colloids Surf, A* 643:128777
20. Holman JP (1978) *Experimental methods for engineers*. McGraw-Hill Inc.
21. Barber J, Brutin J, Tadrist L (2011) A review on boiling heat transfer enhancement with nanofluids. *Nanoscale Res Lett* 6:280

Numerical Study of SiO₂–Water Nanofluid Jet Impingement on Heated Surface



Ketan Atulkumar Ganatra and Achintya Mukhopadhyay

1 Introduction

Jet impingement is widely used technique in many industries. This technique finds applications in cooling of metal sheets, gas turbine blade cooling, drying of textile, etc. Recently liquid jet impingement has gained much interest among researchers due to higher heat transfer as compared to air jet impingement. The use of nanofluids (mixture of water and solid particles) improves further heat transfer as compared to liquid jets due to enhanced thermo-hydraulic properties such as viscosity, density, and thermal conductivity.

The experimental study for liquid jet impingement using nanofluids was reported in [1–3] and numerical study was reported in [4, 5].

Lv et al. [1, 2] investigated jet impingement on circular heated surface. The nanofluid used was mixture of Al₂O₃–water and SiO₂–water. The particle size was 30 nm for SiO₂ and Al₂O₃. The Al₂O₃ volume fraction ranged from 0– to 2% and the SiO₂ volume fraction ranged from 0 to 3% in nanofluid. The Reynolds number was 5000–13,000 and separation distance ratio spanned from 2 to 5. Higher heat transfer was observed with increasing Reynolds number and particle volume fraction in nanofluid. Maximum 61 and 40% enhancement in heat transfer coefficient was observed for Al₂O₃–water and SiO₂–water nanofluid. The Nusselt number correlation was also suggested. Kareem et al. [3] in their investigation used CuO–water nanofluid as working fluid for jet impingement. The CuO volume fraction in nanofluid ranged from 0 to 0.3%. The particle size was 50 nm. Nusselt number was enhanced by 2.9% for the range of particle volume fraction.

Manca et al. [4] used Al₂O₃–water nanofluid for confined jet impingement. The particle volume fraction was in 0–5% range. The jet was rectangular with laminar flow characteristics having jet Reynolds number 100–400. The thermal condition of

K. A. Ganatra (✉) · A. Mukhopadhyay
Department of Mechanical Engineering, Jadavpur University, Kolkata, West Bengal, India
e-mail: ketanganatra0@gmail.com

target surface was uniform temperature. The single phase property model was used for numerical solution of conservation equations. Pumping power was 3.9 times higher with 5% particle volume fraction as compared to pure water jet impingement. Allauddin et al. [5] used Al_2O_3 –water nanofluid in their study. The $VF = 0-0.1$ and $Re = 1200-40,000$. Maximum 28% enhancement of Nu_S was reported while no change in the flow was observed with the use of nanofluid.

Extreme literature is available for jet impingement on flat surface using air as working fluid. However very less study has undertaken which involves nanofluid as the working fluid. Further the previous study employing nanofluid involves Al_2O_3 as mixture particles for nanofluid. The present study aims at numerical analysis of thermo-hydraulic behaviour of heated surface under impinging slot jet using SiO_2 –water nanofluid.

2 Problem Statement

The computational domain used for numerical simulation is shown in Fig. 1. The slot jet width (L) is 5 mm. The jet temperature (T_J) is 300 K and the target surface temperature (T_P) is 320 K. The Reynolds number is 10,000 and separation distance (S) is 30 mm ($S/L = 6$). The velocity profile at jet inlet is fully developed. The velocity profile is obtained using separate computational domain for slot jet with ratio of jet height to jet width as 64 [6]. The 5% of flow turbulence intensity is assumed at jet inlet [6–8].

The following dimensionless parameters are used in the analysis,
 Reynolds Number (Re)

$$Re = \frac{\rho UL}{\mu_f} \tag{1}$$

Nusselt Number (Nu)

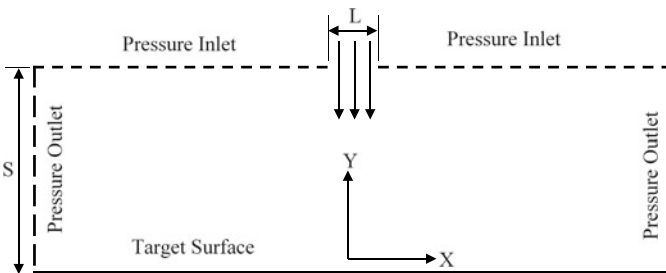


Fig. 1 2D computational domain used for present numerical study

$$\text{Nu}_X = \frac{q_X}{(T_P - T_J) k_f} \frac{L}{k_f} \quad (2)$$

Friction Factor (f)

$$f = \frac{\tau_m}{\frac{1}{2} \rho U^2} \quad (3)$$

Performance Index (PI)

$$\text{PI} = \frac{(\text{Nu}_a)_{nf} / (\text{Nu}_a)_w}{(f)_{nf} / (f)_w} \quad (4)$$

3 Fluid Properties

The nanofluid is mixture of water and solid nanoparticles. The resultant mixture properties are calculated from the following expressions,

$$\rho_{nf} = \gamma \rho_p + (1 - \gamma) \rho_w \quad (5)$$

$$(\rho C_p)_{nf} = \gamma (\rho C_p)_p + (1 - \gamma) (\rho C_p)_w \quad (6)$$

The Eqs. (5) and (6) are taken from [1].

The thermal conductivity of the nanofluid is evaluated from the following expression [9]

$$k_{nf} = k_w (4.97\gamma^2 + 2.72\gamma + 1) \quad (7)$$

There are number of models available in literature for the calculation of mixture dynamic viscosity. The following three models are used to compare the different models,

$$\frac{\mu_{nf}}{\mu_w} = \frac{1}{(1.552\gamma^2 - 2.5\gamma + 1)} \quad (8)$$

$$\log_e \frac{\mu_{nf}}{\mu_w} = \frac{2.7\gamma^2 + 2.5\gamma}{1 - 0.609\gamma} \quad (9)$$

$$\mu_{nf} = \mu_w (7.349\gamma^2 + 2.5\gamma + 1) \quad (10)$$

Appropriate reference for Eqs. (8–10) are [10–12].

Table 1 Water and nanofluid properties

VF	ρ (kg/m ³)	Cp (J/kgK)	k (W/mK)
0	998.20	4182.00	0.6
0.01	1010.41	4090.11	0.6166
0.02	1022.63	4000.42	0.6338
0.03	1034.85	3912.85	0.6516
0.04	1047.07	3827.33	0.6700
0.05	1059.29	3743.78	0.6890

Table 2 Dynamic viscosity of nanofluids using different models

VF	Dynamic viscosity $\times 10^{-6}$ (kg/ms)			
	[10]	[11]	[12]	Average
0.01	1018.29	1018.57	1018.55	1018.47
0.02	1044.58	1045.69	1045.56	1045.28
0.03	1071.89	1074.49	1074.04	1073.47
0.04	1100.29	1105.06	1103.97	1103.11
0.05	1129.84	1137.53	1135.36	1134.25

The density and specific heat of SiO₂ solid nanoparticles are 2220 kg/m³ and 745 J/kgK [13]. The nanofluid properties at different volume fraction of nanoparticles are shown in Table 1.

The dynamic viscosity of water is 998×10^{-6} kg/ms. The dynamic viscosity of nanofluid is shown in Table 2.

4 Different Zones Related to Jet Impingement

The structure of the fluid flow is identified as either before jet impingement or after jet impingement. The different zones are shown in Fig. 2.

Before a jet strikes the target surface, there are three zones related to fluid flow distribution. They are (i) potential core region, (ii) developing zone, and (iii) fully developed zone. The velocity profile is not fully developed in potential core region. The length of potential core for slot jet impingement is 4.7–7.7 times the nozzle width [14]. The jet velocity profile will be fully developed and does not change in the fully developed zone.

When the fluid particles start approaching the target surface, their velocity starts decreasing and the pressure starts increasing. The pressure is maximum at stagnation point (central location of target surface). The stagnation region is identified as region from the start of maximum pressure up to the location where the gauge pressure is zero [15]. In present study, it is identified as the location where maximum friction

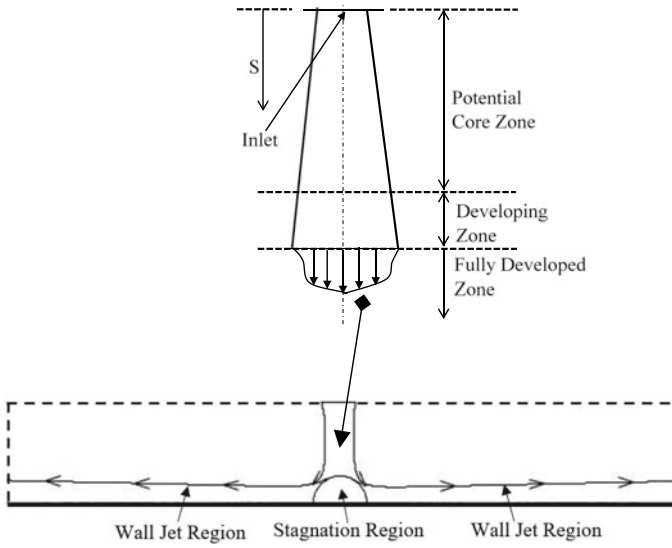


Fig. 2 Different zones concerning to jet impingement

factor (f) occurs. The flow direction then changes from the wall perpendicular to wall parallel direction which is known as wall jet region.

5 Mathematical Modelling

The mathematical modelling is carried out with the assumptions of 2D steady state, turbulent and incompressible flow with single phase properties. The governing equations for conservation of mass, momentum and energy are,

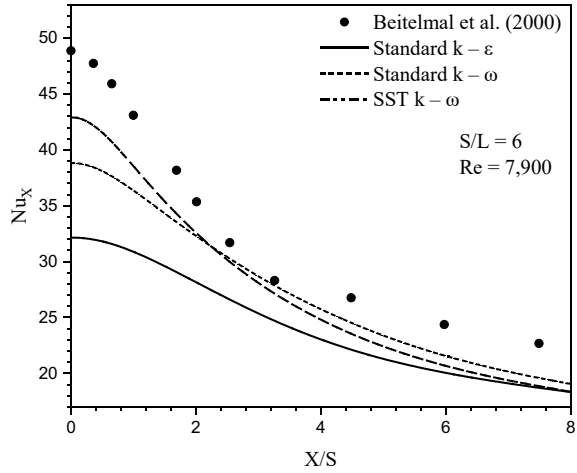
$$\frac{\partial}{\partial x_i} u_i = 0$$

$$\rho u_j \frac{\partial u_i}{\partial x_j} = -\frac{\partial p}{\partial x} + \frac{\partial}{\partial x_j} \left[\mu \left(\frac{\partial u_i}{\partial x_j} + \frac{\partial u_j}{\partial x_i} \right) - \rho \overline{u_i' u_j'} \right]$$

$$\rho u_j \frac{\partial T}{\partial x_j} = \frac{\partial}{\partial x_j} \left[\frac{\mu}{Pr} \frac{\partial T}{\partial x_j} - \rho \overline{T' u_j'} \right]$$

The finite volume open source CFD toolbox [16] is used for the solution of governing equations.

Fig. 3 Comparison of experimental and numerical results



In order to select a turbulence model, the numerical results are compared with experimental results of [17] in Fig. 3. The SST k—ω model has least error at stagnation point ($X/S = 0$). The error indicates the absolute value of difference in experimental and numerical results. In the wall jet region beyond $X/S = 2$, standard k—ω and SST k—ω predict almost the same numerical results. Hence overall SST k—ω model [18] works well and therefore it is used for modelling turbulent flow.

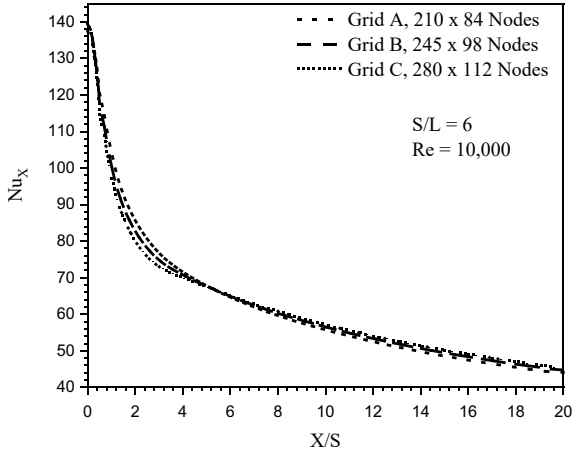
6 Grid Sensitivity Test

Three different grids are used to carry out the grid sensitivity test. The numerical results of the local Nusselt number for three different grids is shown in Fig. 4. There is no significant change in numerical results. Hence the numerical results are independent from the Grid Size.

7 Results and Discussion

The present study involves numerical analysis for SiO_2 –water nanofluid jet impingement on heated surface. The effect of following parameters on friction factor (f), Nusselt number in the plate direction, stagnation Nusselt number, average Nusselt number and Performance Index (PI) is discussed in the following sections.

Fig. 4 Numerical results showing grid sensitivity test



7.1 Effect of Particle Volume Fraction

Figure 5 shows the friction factor (ratio of wall shear stress to dynamic pressure) profile in X —Direction. Higher particle volume fraction results in larger wall shear stress both in wall jet region and stagnation region. The dynamic viscosity of nanofluid is higher as compared to water. Further dynamic viscosity increases with increasing particle volume fraction in nanofluid. The higher dynamic viscosity results in larger wall shear stress. The friction factor (f) is zero at stagnation point due to all kinetic energy is converted to pressure energy. Then it increases in the stagnation region. It has maximum value at particular location. Then it decreases in the wall jet region.

Figure 6 shows Nusselt number variation in X —Direction. The Nusselt number is maximum at stagnation point and it further decreases in wall jet region. This variation is general in nature and does not depend on particle volume fraction. The Nusselt number (at stagnation point and in wall jet region) increases with increasing solid particle volume fraction in nanofluid. The higher turbulence induced due to presence of solid nanoparticle leads to enhancement in heat transfer.

Figures 7 and 8 show turbulent kinetic energy in domain ($VF = 0$ and $VF = 0.05$). Higher ' k ' is observed in domain (both stagnation region and wall jet region) for $VF = 0.05$ as compared to $VF = 0$. The maximum value of ' k ' (for $VF = 0$) is 0.25, 0.1, and 0.1 in potential core region, stagnation region and wall jet region. The maximum value of ' k ' (for $VF = 0.05$) is 0.28, 0.2, and 0.2 in potential core region, stagnation region and wall jet region. This increased ' k ' leads to enhanced heat transfer.

Figure 9 shows effect of particle volume fraction on stagnation and average Nusselt number. Higher particle volume fraction leads to increased stagnation and average Nusselt number. Nu_s is increased by 2.1% for $VF = 0.01$ and 14% for $VF = 0.05$ as compared to pure water jet impingement. Similarly Nu_a gets increased by 2.4% and 14.3% at $VF = 0.01$ and $VF = 0.05$ as compared to pure water. Allauddin et al.

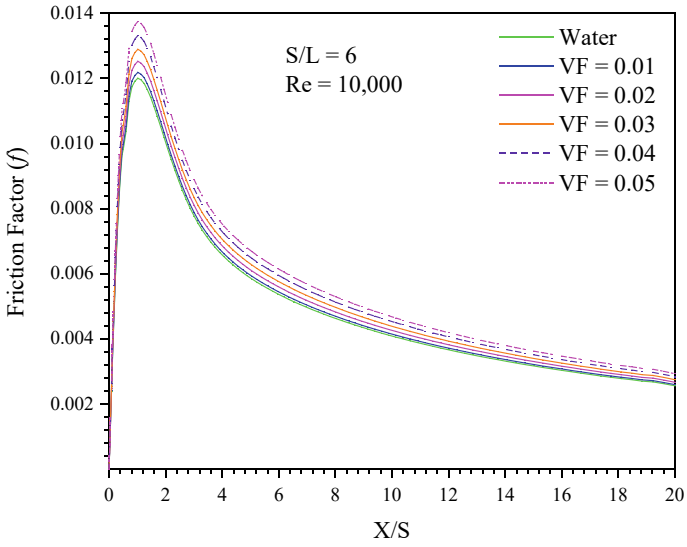


Fig. 5 Effect of particle volume fraction on friction factor (f) distribution in X —Direction

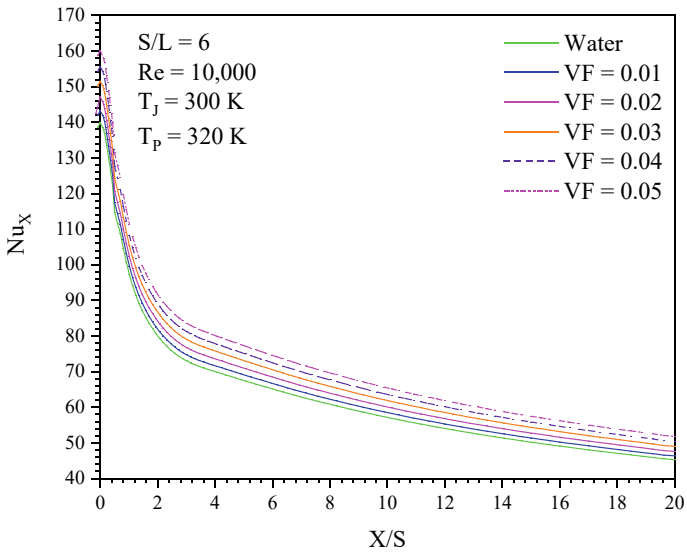


Fig. 6 Effect of particle volume fraction on local Nusselt number distribution

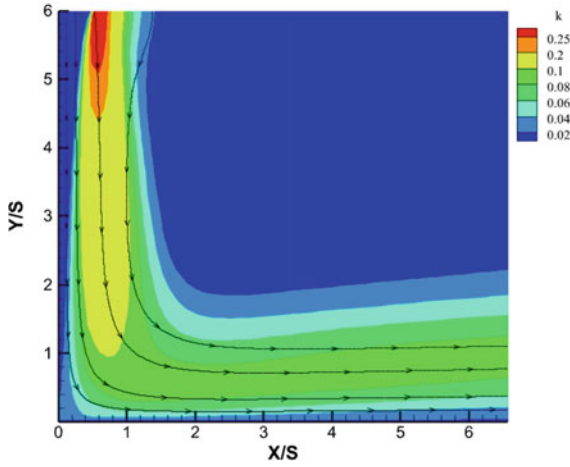


Fig. 7 Turbulence kinetic energy distribution (VF = 0)

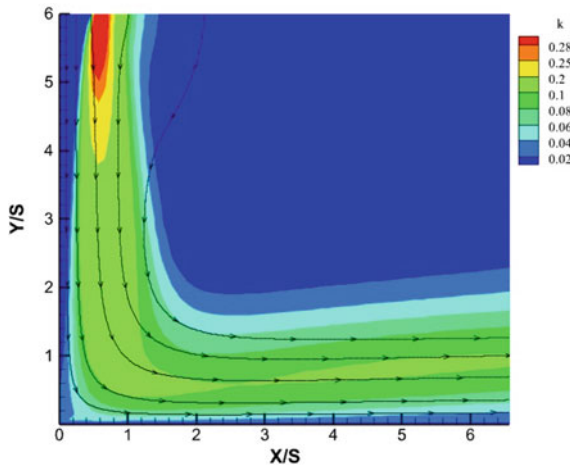


Fig. 8 Turbulence kinetic energy distribution (VF = 0.05)

[5] observed 28% increase in Nu_S for $Re = 29,000 - 40,000$ and $VF = 0.1$ in their study. The enhancement of Nu_S in our study is less as compared to [5] because Re and VF are very low in our case.

Figure 10 shows the PI variation for different particle VF. Since higher VF leads to increased Nu as well as f as shown in Figs. 5 and 6. Higher f leads to higher pumping power requirement. Hence the PI is defined to consider the combined effect of VF on both f and Nu . PI is increased with increasing particle VF. PI gets increased to 1.02 and 1.14 for $VF = 0.01$ and $VF = 0.05$. Ahmadi et al. [19] reported the optimum value of PI as 1.14 in their numerical study for Al_2O_3 —water nanofluid.

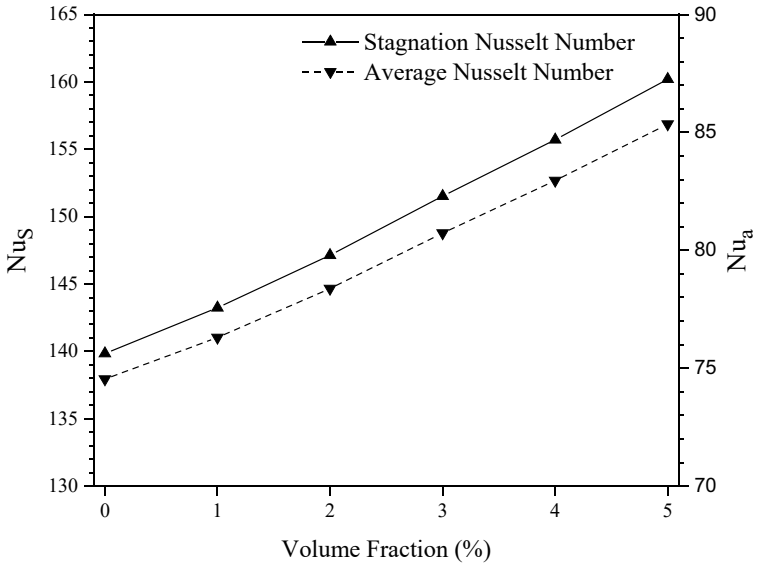


Fig. 9 Particle volume fraction effect on Nu_s and Nu_a

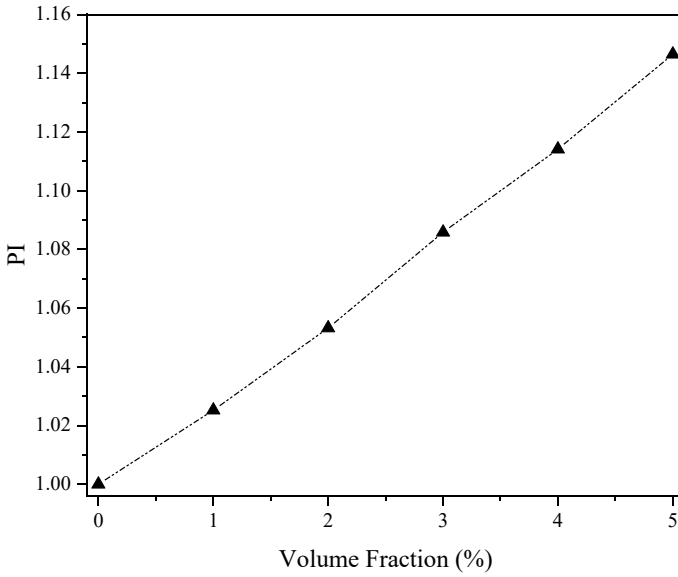


Fig. 10 Effect of particle volume fraction on Performance Index (PI)

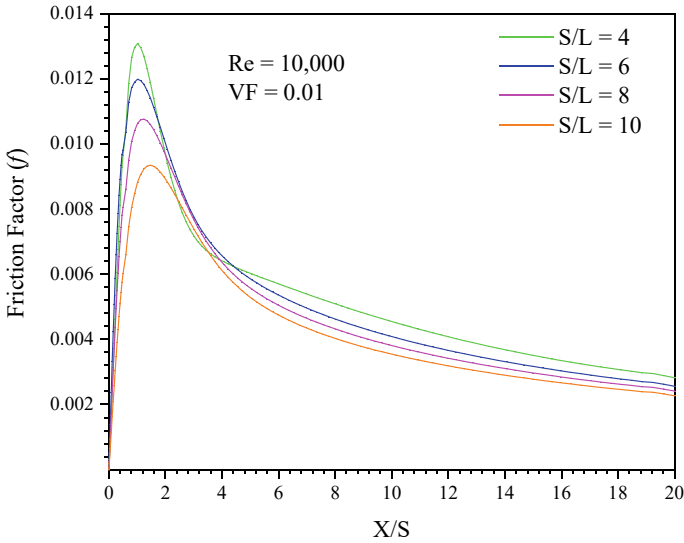


Fig. 11 Effect of S/L on friction factor (*f*) distribution in X—Direction

7.2 Effect of Separation Distance (S/L)

Figure 11 shows the effect of S/L at Re = 10,000 and VF = 0.01 on friction factor (*f*) distribution in X—Direction. The friction factor (*f*) decreases with increasing S/L both in stagnation region and in wall jet region. It is because when S/L increases, the flow velocity decreases with increasing separation distance. Hence the flow kinetic energy is reduced in wall jet region which reduces shear resistance. When comparison is made between maximum friction factor (*f*), it reduces by 30% with change in S/L from 4 to 10.

It can be seen that maximum value of friction factor (*f*) is slightly shifted in the positive X—Direction with increasing S/L. This is due to larger jet spreading with higher S/L.

It should be noted that for S/L = 4, the friction factor (*f*) is lower as compared to S/L = 6, 8 and 10 in between X/S = 2 – 4. This shows the existence of potential core region [14]. Hence friction factor is reduced between X/S = 2 – 4.

The effect of S/L on the local Nusselt number distribution in plate direction is shown in Fig. 12. In wall jet region, Nusselt number is highest for S/L = 4 and progressively reduces with increasing S/L. However in stagnation region, the trend is slightly changed due to existence of potential core region.

Figure 13 shows the S/L effect on stagnation Nusselt number (Nu_S) for VF = 0 – 0.05. The general observation is Nu_S gets decreased with increasing S/L. In present study, with the increasing S/L, Nu_S attains maxima at particular S/L value and then after it decreases. The Nu_S is maximum at S/L = 6 and minimum at S/L = 4. The maximum heat transfer should be at the end of potential core region [14]. In the

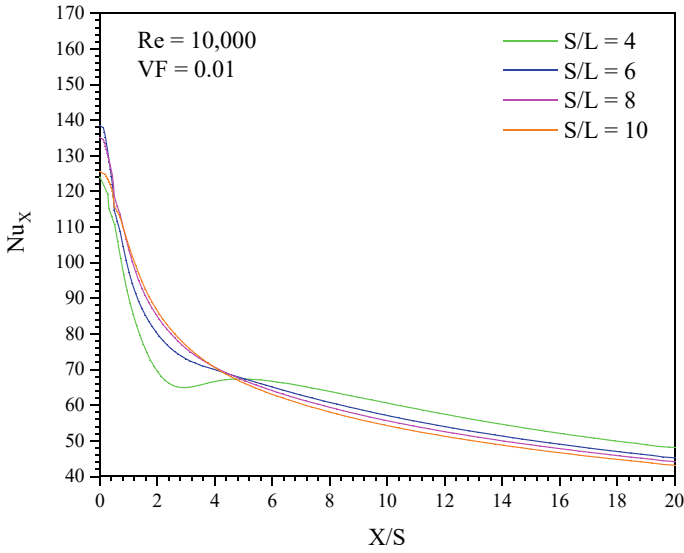


Fig. 12 Effect of S/L on Nusselt number distribution in X —Direction

present study, maximum Nu_S is found for $S/L = 6$. The Nu_S for $S/L = 4, 8$ and 10 as compared to that for $S/L = 6$ (maximum heat transfer) gets decreased by 13, 3 and 10%.

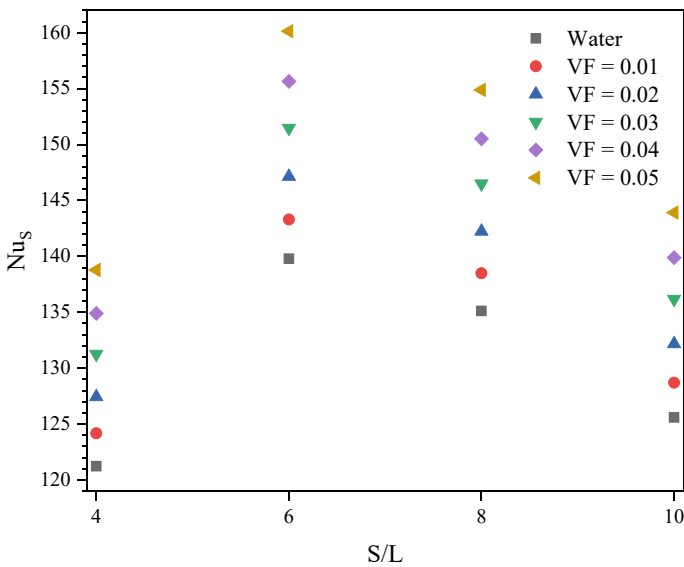


Fig. 13 Effect of S/L on Nu_S for water and nanofluid with different particle volume fraction

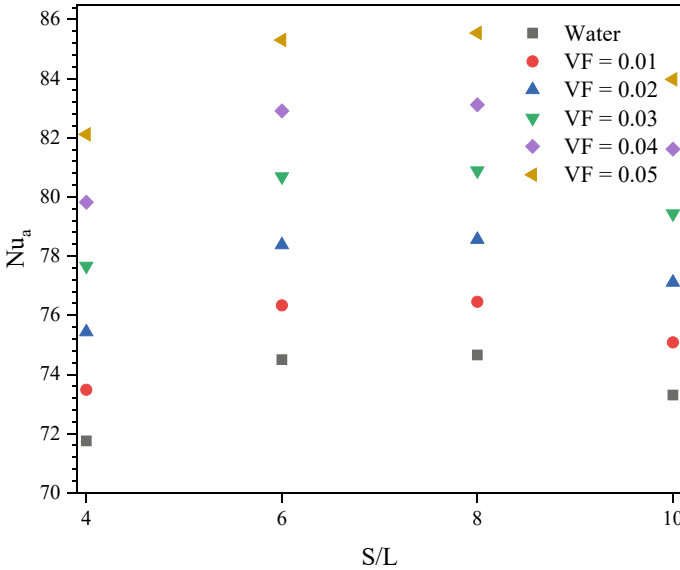


Fig. 14 Effect of S/L on Nu_a for water and nanofluid with different particle volume fraction

The variation in Nu_a with S/L for different VF is shown in Fig. 14. The Nu_a is maximum for $S/L = 6$. The study for air jet impingement shows maxima of average Nusselt number for $S/L = 6$ [6]. The Nu_a for $S/L = 4$ and 10 as compared to that for $S/L = 6$ (maximum heat transfer) gets decreased by 3.7 and 1.6%. However very negligible change in Nu_a is observed for $S/L = 6$ and $S/L = 8$.

The above discussed variation of Nu_s and Nu_a with S/L remains unaffected by particle VF.

The S/L does not have significant impact on PI and hence it is graphically not shown here.

8 Conclusion

The numerical study using SiO₂–water nanofluid for slot jet impingement on heated surface has performed using finite volume code. The Reynolds number is fixed as 10,000. The effect of solid particle volume fraction and separation distance has been investigated leading to the following conclusions,

1. Friction Factor (f) increases with increasing VF in nanofluid.
2. Nusselt number increases with increased solid particles volume fraction.
3. Nu_a gets increased by 2.4 and 14.3% as particle VF in nanofluid increased to 1 and 5%.
4. Friction Factor (f) decreases with increasing S/L ratio.

5. Nu_s and Nu_a are maximum for $S/L = 6$.
6. S/L does not have significant impact on PI.
7. The increasing particle VF results in improvement of PI indicates the overall improvement in system efficiency.

Nomenclature

C_p	Specific Heat (J/kgK)
f	Friction Factor
k	Thermal Conductivity (W/mK)
k	Turbulence Kinetic Energy (m^2/s^2)
L	Slot Width (m)
Nu	Nusselt Number
PI	Performance Index
q	Wall Heat Flux (W/m^2)
Re	Reynolds Number
S	Separation Distance (m)
T	Temperature (K)
U	Velocity Magnitude m/s)
VF	Volume Fraction
X	X—Coordinate (m)
Y	Y—Coordinate (m)

Greek Symbols

μ	Dynamic Viscosity (kg/ms)
ρ	Density (kg/m^3)
ω	Specific Dissipation Rate (s^{-1})
τ	Wall Shear Stress (N/m^2)
γ	Volume Fraction

Suffix

a	Average
f	Fluid
J	Jet
m	Mean
nf	Nanofluid

<i>p</i>	Particle
<i>P</i>	Plate
<i>S</i>	Stagnation Point
<i>W</i>	Water
<i>X</i>	In <i>X</i> —Direction

References

1. Lv J, Chang S, Hu C, Bai M, Wang P, Zeng K (2017) Experimental investigation of free single jet impingement using Al₂O₃—water nanofluid. *Int Commun Heat Mass Transf* 88:126–135
2. Lv J, Hu C, Bai M, Zeng K, Chang S, Gao D (2017) Experimental investigation of free single jet impingement using SiO₂—water nanofluid. *Exp Thermal Fluid Sci* 84:39–46
3. Kareem ZS, Balla HH, AbdulWahid AF (2019) Heat transfer enhancement in single circular impingement jet by CuO—water nanofluid. *Case Stud Therm Eng* 15:100508
4. Manca O, Ricci D, Nardini S, Lorenzo GD (2016) Thermal and fluid dynamic behaviors of confined laminar impinging slot jets with nanofluids. *Int Commun Heat Mass Transf* 70:15–26
5. Allauddin U, Mahrukh M, Rehman NU, Haque ME, Uddin N (2018) Numerical investigation of heat transfer by an impinging jet using alumina—water nanofluid. *Numer Heat Transf Part A Appl* 74(8):1486–1502
6. Gori F, Bossi L (2000) On the cooling effect of an air jet along the surface of a cylinder. *Int Commun Heat Mass Transf* 27(5):667–676
7. Ganatra KA, Singh D (2019) Comparison of various RANS models for impinging round jet cooling from a cylinder. *ASME—J Heat Transf* 141(6):064503
8. Ganatra KA, Singh D (2020) Numerical investigation of effect of semi-circular confinement bottom opening angle for slot jet impingement cooling on heated cylinder. *Int J Therm Sci* 149:106148
9. Maiga SEB, Nguyen CT, Galanis N, Roy G (2004) Heat Transfer behaviours of nanofluids in a uniformly heated tube. *Superlattices Microstruct* 35:543–557
10. Bruijn HD (1942) The Viscosity of suspensions of spherical particles—the fundamental η — c and φ relations. *Wiley Online Library* 61(12):863–874
11. Vand V (1948) Viscosity of solutions and suspensions—I—theory. *J Phys Chem* 52(2):277–299
12. Vand V (1948) Viscosity of solutions and suspensions—II—experimental determination of the viscosity concentration function of spherical suspensions. *J Phys Chem* 52(2):300–314
13. Azmi WH, Sharma KV, Sarma PK, Mamat R, Anuar S, Rao VD (2013) Experimental determination of turbulent forced convection heat transfer and friction factor with SiO₂ nanofluid 51:103–111
14. Hrycak P (1981) Heat transfer from impinging jets: a literature review. AFWAL-TR 81-3054. New Jersey
15. Brahma RK, Faruque O, Arora RC (1991) Experimental investigation of mean flow characteristics of slot jet impingement on a cylinder. *Springer* 26:257–263
16. OpenFOAM User Guide (v2106), OpenCFD Limited (2021)
17. Beitelmal AH, Saad MA, Patel CD (2000) The effect of inclination on the heat transfer between a flat surface and an impinging two dimensional air jet. *Int J Heat Fluid Flow* 21:156–163
18. Menter FR, Kuntz M, Langtry R (2003) Ten years of industrial experience with the SST turbulence model, turbulence. *Heat Mass Transf* 4:625–632
19. Ahmadi H, Moghari RM, Esmailpour K, Mujumdar AS (2016) Numerical investigation of semi-confined turbulent slot jet impingement on a concave surface using an Al₂O₃—water nanofluid. *Appl Math Model* 40:1110–1125

An Updated Review of Heat Transfer Enhancement Techniques in Tube-Type Heat Exchangers



Manoj Kumar Diwaker and Arvind Kumar

1 Introduction

The use of energy has grown as a result of improvement of living standards, industrialization, and urbanization. In this new city modernization era, researchers face new challenges of saving and efficiently utilizing energy. Since heat is low-grade energy, its use must be optimized, and hence intentionally and more thermally, efficient systems are being developed. The performance of the heat exchanger determines thermal control, energy savings, and materials savings. Heat exchangers are one of the most versatile thermal systems which have household, industrial, and commercial applications [1]. Heat exchange devices such as parabolic trough collectors in solar water heaters, radiators in automobiles, compressors are examples that use only single-phase fluid for heat exchange. When thermal systems are operated at extremely high temperatures or subjected to intense heat, their life span and performance decrease. If a thermal system fails before its expected life span, it might be hazardous from the safety point of view. Compatibility, performance, and life are all factors that must be considered. For this purpose, the thermal system components having high heat exposure must be cooled to guarantee dependability, performance, and longevity. The supply of external energy might be challenging to regulate in some circumstances [2]. For this purpose, nanofluids are being used, which contain solid nanometer-sized (generally less than 100 nm) nanoparticles (Al_2O_3 , TiO_2 , WO_3 , Ag, Au, GNP, Cu, MgO , ZnO , SiO_2 , SWCNT, MWCNT, etc.) dispersion in a base fluid [3]. Thermal characteristics of base fluids such as thermal conductivity, heat capacity, density, viscosity are greatly influenced by distributed solid metallic and non-metallic nanoparticles [4, 5].

M. K. Diwaker (✉) · A. Kumar
Department of Mechanical and Industrial Engineering, MANIT Bhopal, Bhopal 462003, India
e-mail: manoj.diwaker2007@gmail.com

2 Literature Review and Objective

As the demand for high heat transfer rates grows, several ways for heat transfer augmentation are being explored developed accordingly. Researchers are making attempts to create new approaches that improve heat transfer rates while minimizing pressure loss [6]. Heat transfer augmentation techniques are broadly classified into two categories: active and passive. To increase the heat transfer rate, the active methods require some external power. External power can be provided to either the heated surface or the fluids, depending on the system needs. The altered flow pattern of the liquid inside the tube results from the augmented heat transfer. The alteration inflow pattern is due to the turbulence promoters. These turbulence promoters assist the boundary layer disruption and better mixing of fluids and consequently the enhanced heat transfer rate [7]. Artificial roughness [8, 9], ribs [10], baffles [11, 12], rib-groove [12], blocks, fins [13], obstacles [14], and use of different type of swirl flow devices [14–23] are all examples of turbulence promoters that have been included in this study. Because passive methods may be simply implemented in the existing heat exchangers, they are preferred over active methods. Researchers have proposed a number of ways for improving heat transfer in heat exchangers. An attempt has been made in this study to outline the different studies that deal with the application of passive methods in tubular heat.

The thermal performance factor, also known as the performance evaluation criterion or the performance index, is used to estimate the tubular heat exchanger's performance [24]. It depends on the heat transfer coefficient as well as the friction factor. This parameter can be written as follows:

$$\text{TPF, PEC, PI}(\eta) = \frac{\frac{\text{Nu}}{\text{Nu}_o}}{\left(\frac{f}{f_o}\right)^{\frac{1}{3}}} \text{ where, } \text{Nu} = \frac{hD}{k}, f = \frac{2D\Delta P}{L\rho V^2}.$$

The terms Nu , f , Nu_o , and f_o stands for Nusselt number and friction factors for enhanced tube and plain tube, respectively [25, 26].

In the case of performance evaluation of heat transfer from extended surfaces or the fins, the term effectiveness is more commonly used. The effectiveness of the exchanger is defined as the ratio of heat transfer with fin and without fin. Mathematically, it can be expressed as:

$$\varepsilon = \frac{q_f}{hA_{fb}\Delta T} = \frac{Q_{\text{fin}}}{Q_{\text{without fin}}},$$

where ' q_f ' is the heat transfer rate with fin.

3 Methods

Intensification methods are mainly classified into active and passive methods. The active method necessitates the use of an external source of energy to help in heat transmission. Active strategies include surface vibration, pulsing flow, and the injection of an electric field. Using active techniques, it is more challenging to create and construct a compact and efficient heat exchanger. However, these techniques have the advantage of allowing the flow to be controlled and modified according to the system's requirements [27].

The passive method requires no extra energy to accelerate heat transfer. However, the fluid turbulence promoters block the path of the fluid, which needs extra pumping power. This pumping power is added to the previously required pumping power. This method is widely used in industries because it can be used in the existing heat exchanger. Surface or geometrical changes to the flow are commonly used in passive methods by adding fins, inserts, or extra devices. These devices improve the heat transfer coefficient by disrupting fluid flow behavior leading to increased pumping power requirement. However, there are also some techniques like small height ribs suggested to reduce the pumping power requirements. Small height ribs increase the effective area of heat transfer and with less amount of pumping power. These ribs do not disrupt the main flow [4]. Some other techniques like the use of swirl flow devices, vortex generators, and the use of nanofluid are also included in the present study.

3.1 Classification of Passive Methods

Passive methods of heat exchange are further classified into following headings:

- A. Artificial roughness.
- B. Extended surfaces.
- C. Swirl flow devices.
- D. Vortex generators.
- E. Use of nanofluid.
- A. Artificial Roughness

Artificial roughness is the alteration to the tube's wall surface. These are small height repeated corrugation, ribs, dots, etc., protruded to the tube wall surface, which creates local wall turbulence (Fig. 1), for example, sand power roughened surfaces [8]. To decrease friction loss, the heights of roughness components (ribs, dots, etc.) are maintained modest in relation to the diameter of the tube.

This section discusses the effect of various roughness geometries: Naphon et al. [30] investigated the impact of helical ribs in a double-pipe heat exchanger (DPHE) experimentally.

Helical ribs have a substantial influence on thermohydraulic performance, according to their results. However, any type of flow obstruction, which contributes

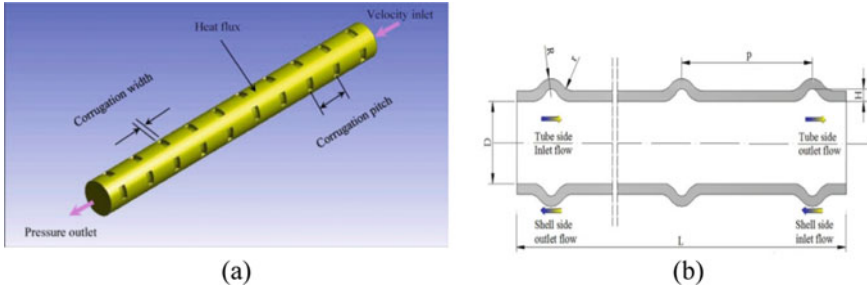
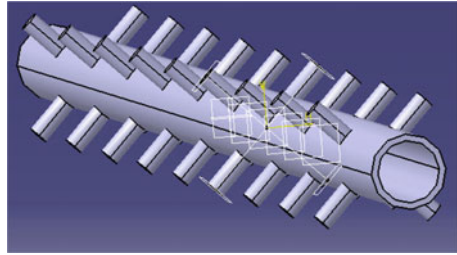


Fig. 1 a Corrugated tube [28] b geometrical parameters of corrugated tube [29]

to the turbulence generation, also augments the pressure drop across the boundaries. Meng et al. [31] used computational and experimental methods to study the thermal performance factor of discrete double-inclined ribs tubes (DDIR tube). According to their findings, the DDIR tube offers a superior overall thermohydraulic performance factor than the normal tube. Han et al. [32] investigated the single corrugated tube numerically using response surface methodology. Their result revealed that increasing the resistance to the flow increases the TPF and the friction factor. Their results indicate that the optimum values of the friction factor ratio are $f/f_o = 1.22$ while thermal performance factor $\eta = 1.42$ for $Nu/Nu_o = 1.2$. Garcia et al. [33] performed their experiments with three types of artificially roughened tubes: corrugated tubes, wire coils, and dimpled tubes. The feature of roughness tubes, according to their findings, has a greater influence on pressure drop than thermohydraulic performance. Rainieri and Pagliarini et al. [34] studied the TPF of tube's walls corrugation. Their result revealed that helical corrugation produces a significant swirl component at a higher Reynolds number, but the effect is not too much on heat transfer rate. Kathait and Patil et al. [35] found that enlarging the gaps in a specified corrugation pattern significantly augments the heat transfer rate irrespective of Reynolds number. They had examined the impact of a discrete corrugated rib roughened tube with an altered tube surface on TPF. Discrete double-inclined ribs (DDIR) tube has been examined by Li et al. [36]. Their investigations were focused on the behavior of heat exchange and resistance to the flow in turbulent conditions. Compared to a plain tube, the heat transfer rate was found to increase up to 120%, and the pressure drop was found enhanced up to 250%. Promvong et al. [37] investigated coupled ribs type and winglet-type VGs with air. Heat transmission and friction loss are higher when the angle of attack is larger than when it is smaller. Vicente et al. [38] investigated the heat transfer rate and friction factor of corrugated tubes. They discovered that the corrugated tubes show much better thermohydraulic performance under the same flow circumstances than the smooth tubes. The friction factor coefficient increased by 20–300%, while the Nusselt number increased by up to 250%. Buchlin [39] examined heat TPF of perforated ribs experimentally in the range of Reynolds number 30000–60,000. They have compared the different types of perforated Plexiglas ribs. Their results reveal that the pitch ratio five and open area

Fig. 2 Typical geometries of circular tube with extended surfaces [49]



ratio 0.53 perform the best. The impact of transverse perforated ribs on the friction factor and the thermal energy exchange has been investigated by Nuntadusit et al. [40].

B. Extended Surfaces

This is one of the successful ways because the effective heat transfer area and the flow turbulence are increased. These approaches rely on expanded surfaces, such as fins. Extended surfaces significantly increase pressure loss, needing a high amount of pumping power. A few examples of extended surfaces are shown in Fig. 2.

Mohammed et al. [41] studied the thermohydraulic performance of the louvered strip inserts in DPHE. They have also varied the nanofluids. Their results reveal that the enhanced tubes have the Nusselt number approximately four times higher than the plain tube. The impact of backward configuration on the heat transfer rate ranges 367–411%. Vermahmoudi et al. [42] performed the investigation with Fe_2O_3 nanofluid. The heat exchanger chosen for the study was air-cooled. Their results show an augmented heat transfer coefficient if the concentration of the nanoparticles and Reynolds number increases. The louvered strips put in a concentric tube heat exchanger were examined by Eiamsa-ard et al. [43]. They found that using louvered strips results in a greater heat transmission rate than using a plain tube. When using a louvered strip with a backward layout, the total enhancement ratio is 9–24% higher than when using a forward arrangement. The thermohydraulic performance of curved trapezoidal winglets was studied by Zhou and Ye et al. [44] They examined the impact on the thermohydraulic performance of various types of winglets. The highest TPF was observed in the case of the delta winglets and the curves of trapezoidal winglets. Eiamsa-ard and Promvonge et al. [45, 46] found the highest TPF 1.19 in the case of double side delta wings. Two types of VGs have been examined by Torii et al. [47] in a fin-tube heat exchanger. Chompookham et al. [48] investigated the heat transmission and friction loss characteristics of coupled wedge ribs and winglet-type vortex generators (WVGs). They observed that the linked ribs and WVGs increased the heat transfer rate and friction loss over the smooth channel significantly.

C. Swirl Flow Devices

A swirl device decreases the thickness of the boundary layer by creating the secondary flow in the form of vortices in the existing axial flow. The velocity profiles near the walls are modified by the secondary flow. Other researchers have looked into swirl

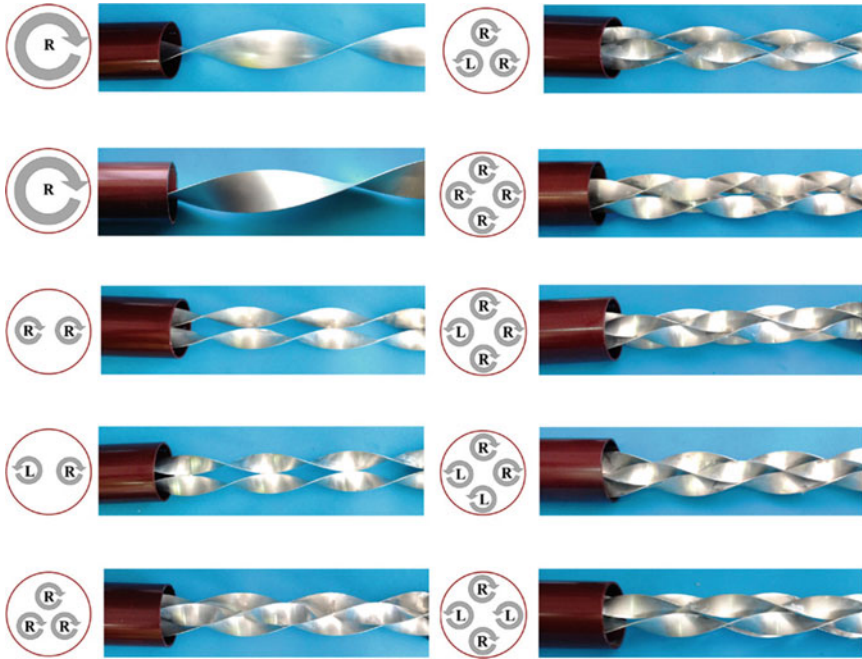
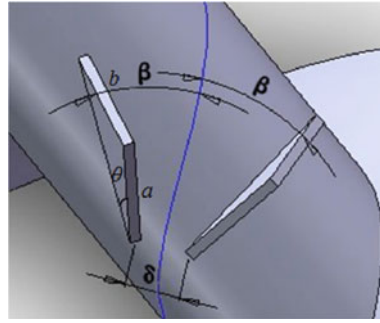


Fig. 3 Inner tube fitted with multiple inserts [44]

flow devices, including conical rings, helical wire, and twisted tapes. Some of the examples of swirl flow devices have been shown in Fig. 3.

Aluminum-twisted tapes with a thickness of 1 mm have been used by Naphon et al. [30] to investigate the TPF of DPHE. Hot and cold water has been used as the working fluid in the investigation. Their findings show that twisted tape inserts have a considerable influence on heat transmission and friction factor in tubular-type heat exchangers. Short length twisted tapes have been used by Yadav et al. [50] in concentric tube U-bend heat exchangers. The smooth tube's performance assessment criterion, on the other hand, was 1.3–1.5 times larger than that of the enhanced heat exchanger. Esparza and Rojas [51] improved the overall performance of heat exchangers by using helical wire coils placed within a circular pipe. From their results, they concluded that by the increase of pitch ratio, the friction factor decreases. As turbulators, Karakaya and Durmus et al. [52] used conical-shaped springs. They discovered that when the conical angle rises, the exergy loss decreases. This is because the addition of tabulators to the flow medium results in augmented thermo-hydraulic performance. Hatami et al. [53] investigated several heat exchanger designs for improving the waste heat recovery from diesel exhaust. In order to strengthen TPF, Hatami et al. [54] employed a finned tube and a vortex generator. In air to water double-pipe heat exchanger, Sheikholeslami et al. [55] examined the impact of flow turbulence on the thermohydraulic performance of heat exchangers. They also employed an agitator to improve heat transfer efficiency.

Fig. 4 Geometrical parameters of vortex generators [60]



D. Vortex Generators (VGs)

Creating vortex in the flow direction is another effective way in the different types of turbulence promotion. The vortex forms the secondary flow, breaking the thermal boundaries layers in the previously developed flow and extracting heat from the core flow. Cans, winglets, barriers, and other VGs devices have all been studied. Some of the examples of vortex generators have been shown in Fig. 4.

Torri et al. [47] studied winglet-type VGs in a circular tube fin-tube heat exchanger. The “common flow up” configuration was utilized to employ previously unused orientation. For enhanced tube wake control, Joardar et al. [56] evaluated the impact of arrays in specific orientations. The single row winglet arrangement causes the rate of heat transfer to increase up to 16.5–44%. On the other hand, the three-row vortex generator generates the heat transfer rate increased up to 29.9–68.8%. To obtain the best settings, the Taguchi method was used. Habchi et al. [57] used statistics to assess the performance of a trapezoidal wing with a bottom excavation. Since the excavation lowers the resistance to the flow, the cavity reduces the area of contact between the vortex generators and the wall exposed to the heat. This phenomenon reduces the conduction heat flux which enhances the convective heat transfer rates. A numerical analysis of the thermal–hydraulic performance of rectangular winglets with punched holes in the channel wall was conducted. Wu and Tao [58] investigated the impact of the punched hole and concluded that the Nusselt number is a little higher (approximately 1.1%). The friction factor was found relatively lesser (about 1.2%) than the case without pierced holes. The low-speed recirculation zone is located right after the VG, where the front holes have a minor impact on heat transfer and flow drag. Guobing Zhou et al. [59] performed an experiment to examine the performance of flat and curved VGs with and without punched holes. They have concluded that the resistance to the flow was found to be lowered in every flow regime.

E. Use of Nanofluids

Some of the researchers have also investigated the thermal performance of the heat exchangers with nanofluids. Nanofluids are the nanometer-sized particles (generally) dispersed in the base fluid such as water, ethylene glycol. These nanofluids may be utilized in existing heat exchangers without any modification.

In a DPHE, Al_2O_3 /water nanofluid along with trapezoidal cut has been examined by Prasad et al. [61]. The flow regime has been considered turbulent. In their studies, the annulus side heat transfer rate has been found higher than that of the tube side because of secondary flow. Their studies also indicated that when the concentration and twist ratio of nanofluids rise, heat transmission and pressure decrease. In addition, Chandra Sekhara Reddy [62] investigated the flow characteristics of TiO_2 /water/E.G. nanofluid in DPHE. They have used the wire coils for turbulence enhancement. They claimed the heat transfer intensified by with a factor 10.73 in the case of volume concentration of 0.03%. The heat transfer enhancement for the same concentration of nanofluid with wire coils, on the other hand, was 13.85 and 10.89%, respectively. Wu Zan et al. [63] investigated water heat transfer and pressure drop in helical DPHEs using different water/aluminum nanofluids. According to the researchers, the critical Reynolds number does not affect the influence of nanofluids. According to them, no other factors like Brownian motion, thermophoresis, and diffusion phoresis are competitively significant than that of the thermophysical properties of the nanofluid. According to the researchers, these nanofluids may be termed homogeneous phases. Demir et al. [64] numerically examined the effect of TiO_2 and Al_2O_3 in concentric tube heat exchangers. The researchers discovered that using high-concentration nanofluids enhances heat transfer rate and decreases pressure. Furthermore, the studies showed that even modest concentrations of nanofluids might increase heat transfer rates. Mohammed et al. [41] have used the various nanofluids along with louvered strips in the DPHE. The nanofluids examined were Al_2O_3 , CuO , SiO_2 , and ZnO , with concentrations ranging from 1 to 4% and diameters varying from 20 to 50 nm. According to reports, the front design enhanced heat transfer by 367–411%.

4 Conclusions

The passive techniques are narrowed in its scope. Overviews of current developments in the field of heat transfer enhancement have been done. The findings of the researches are summarized in this study.

- To improve heat transfer rates, several components such as roughness, winglets, coiled wires, twisted tapes, corrugated tubes, fins have been employed. They all augment the heat transfer by disturbing the boundary layer.
- Nanofluids are gaining popularity as a result of its better thermophysical characteristics relative to conventional working fluids.
- Researchers are primarily focused on either active or passive techniques but very rarely on the combination of both. This needs further exploration. The review reveals that researchers have investigated both experimentally and numerically various techniques of heat transfer augmentation in simple tube-type heat exchangers by modifying the geometry of insert for different types of working fluids using variable parameters of insert for laminar and turbulent flow.

- Also, various types of nanofluids like Al_2O_3 , TiO_2 , WO_3 , Ag, Au, GNP, Cu, MgO, ZnO, SiO_2 , SWCNT, MWCNT, etc., have been used in the analysis.
- Researchers have, in general, investigated the impact of twisted tapes, vortex generators, extended surfaces in circular cross-section tubes. Rectangular, square, elliptical cross-sectional tubes can be chosen for studies.
- The type of profile cut and space ratio on the inserts also play a significant role that needs further investigations.
- Also, induced vibration techniques have been implemented in very few investigations.
- However, a number of researches in the field of heat transfer augmentation in tubular-type exchangers using passive methods are reported, and there are still scopes of further studies. For example, the effect of the variation in the insert profile, type of nanofluid, variation in the nanofluid concentration, type of tube corrugation, type of vortex generators, type of extended surfaces, etc., can be explored further. Also, the effects of the combination of these variations can be chosen for future studies.

Acknowledgements The corresponding author acknowledges the fellowship support given by the Ministry of Education (MoE), Government of India.

Abbreviations

Nomenclatures

A	Cross-sectional flow area
A_o	Outer surface area of the heat exchanger, (m^2)
c_p	Specific-heat capacity at constant pressure
d	Hydraulic diameter of the inner pipe, (m)
h	Convective heat transfer coefficient, ($\text{W}/\text{m}^2\text{K}$)
k	Thermal conductivity (W/mK)
L	Rib length (m)
L^*	Rib length ratio
m	Mass flow rate of the fluid, (kg/s)
p	Pitch ratio
Pe	Peclet Number
Nu	Nusselt number
ΔP	Pressure drop
P^*	Rib pitch ratio
T_h	Hot fluid inlet temperature, ($^\circ\text{C}$)
T_c	Cold fluid inlet temperature, ($^\circ\text{C}$)
Q	Rate of heat transfer, (W)
r	Radius of pipe, (m)

Greek symbols

α	Rib inclined angle ($^{\circ}$)
β	Winglet angle ($^{\circ}$)
μ	Dynamic viscosity, (N-s/m ²)
η	Performance index
ε	Effectiveness
ρ	Density
ϕ	Volume fraction of nanoparticles (%)

Abbreviations

ACT	Asymmetric corrugated tube
CHTC	Convective heat transfer coefficient
DPHE	Double-pipe heat exchangers
HTR	Heat transfer rate
Exp	Experimental
EG	Ethyl glycol
Num	Numerical
MWCNT	Multi-wall carbon nanotube
PEC	Performance evaluation criteria
SWCNT	Single-wall carbon nanotube
SCT	Symmetric corrugated tube
VC	Volume concentration
VGs	Vortex generators
TT	Twisted tape
THPI	Thermohydraulic performance index

Subscripts

avg	Average
<i>b</i>	Bare pipe
<i>bf</i>	Base fluid
<i>c</i>	Cold
<i>h</i>	Hot
<i>i</i>	Inner
<i>nf</i>	Nanofluid
<i>np</i>	Nanoparticle
<i>o</i>	Outer
<i>cw</i>	Cold water

<i>hw</i>	Hot water
<i>s</i>	Smooth tube
<i>ct</i>	Corrugated tube

References

1. Dandoutiya BK, Kumar A (2021) CFD analysis for the performance improvement of a double pipe heat exchanger with twisted tape having triangular cut. *Energy Sources Part A Recover Util Environ Eff* 1–19. <https://doi.org/10.1080/15567036.2021.1946215>
2. Singh SK, Kumar A (2020) Advances in heat transfer enhancement using twisted tape inserts with and without nanofluid. *Int J Mech Prod Eng Res Dev* 10(1):157–174. <https://doi.org/10.24247/ijmperdfeb202014>
3. Dandoutiya BK, Kumar A (2019) A review on nano fluids for solar collector application. *SSRN Electron J* 1–10. <https://doi.org/10.2139/ssrn.3442589>
4. Alam T, Kim MH (2018) A comprehensive review on single phase heat transfer enhancement techniques in heat exchanger applications. *Renew Sustain Energy Rev* 81(August 2016):813–839. <https://doi.org/10.1016/j.rser.2017.08.060>
5. Sidik NAC, Muhamad MNAW, Japar WMAA, Rasid ZA (2017) An overview of passive techniques for heat transfer augmentation in microchannel heat sink. *Int Commun Heat Mass Transf* 88(September):74–83. <https://doi.org/10.1016/j.icheatmasstransfer.2017.08.009>
6. Lotfi B, Sundén B, Wang Q (2016) An investigation of the thermo-hydraulic performance of the smooth wavy fin-and-elliptical tube heat exchangers utilizing new type vortex generators. *Appl Energy* 162:1282–1302. <https://doi.org/10.1016/j.apenergy.2015.07.065>
7. Alam T, Kim MH (2017) A critical review on artificial roughness provided in rectangular solar air heater duct. *Renew Sustain Energy Rev* 69(July 2016):387–400. <https://doi.org/10.1016/j.rser.2016.11.192>
8. Poongavanam GK, Kumar B, Duraisamy S, Panchabikesan K, Ramalingam V (2019) Heat transfer and pressure drop performance of solar glycol/activated carbon based nanofluids in shot peened double pipe heat exchanger. *Renew Energy* 140:580–591. <https://doi.org/10.1016/j.renene.2019.03.059>
9. Meng JA, Liang XG, Chen ZJ, Li ZX (2005) Experimental study on convective heat transfer in alternating elliptical axis tubes. *Exp Therm Fluid Sci* 29(4):457–465. <https://doi.org/10.1016/j.expthermflusci.2004.04.006>
10. Singh P, Pandit J, Ekkad SV (2017) Characterization of heat transfer enhancement and frictional losses in a two-pass square duct featuring unique combinations of rib turbulators and cylindrical dimples. *Int J Heat Mass Transf* 106:629–647. <https://doi.org/10.1016/j.ijheatmasstransfer.2016.09.037>
11. Nanan K, Thianpong C, Pimsarn M, Chuwattanakul V, Eiamsa-ard S (2017) Flow and thermal mechanisms in a heat exchanger tube inserted with twisted cross-baffle turbulators. *Appl Therm Eng* 114:130–147. <https://doi.org/10.1016/j.applthermaleng.2016.11.153>
12. Eiamsa-ard S, Ruengpayungsak K, Thianpong C, Pimsarn M, Chuwattanakul V (2019) Parametric study on thermal enhancement and flow characteristics in a heat exchanger tube installed with protruded baffle bundles. *Int J Therm Sci* 145(November 2017):106016. <https://doi.org/10.1016/j.ijthermalsci.2019.106016>
13. Tang W, Li W (2020) Frictional pressure drop during flow boiling in micro-fin tubes: a new general correlation. *Int J Heat Mass Transf* 159. <https://doi.org/10.1016/j.ijheatmasstransfer.2020.120049>
14. Promvong P, Koolnapadol N, Pimsarn M, Thianpong C (2014) Thermal performance enhancement in a heat exchanger tube fitted with inclined vortex rings. *Appl Therm Eng* 62(1):285–292. <https://doi.org/10.1016/j.applthermaleng.2013.09.031>

15. Sheikholeslami M, Gorji-Bandpy M, Ganji DD (2015) Review of heat transfer enhancement methods: focus on passive methods using swirl flow devices. *Renew Sustain Energy Rev* 49:444–469. <https://doi.org/10.1016/j.rser.2015.04.113>
16. Zheng N, Yan F, Zhang K, Zhou T, Sun Z (2020) A review on single-phase convective heat transfer enhancement based on multi-longitudinal vortices in heat exchanger tubes. *Appl Therm Eng* 164(May 2019):114475. <https://doi.org/10.1016/j.applthermaleng.2019.114475>
17. Sharifi K, Sabeti M, Rafiei M, Mohammadi AH, Shirazi L (2018) Computational fluid dynamics (CFD) technique to study the effects of helical wire inserts on heat transfer and pressure drop in a double pipe heat exchanger. *Appl Therm Eng* 128:898–910. <https://doi.org/10.1016/j.applthermaleng.2017.08.146>
18. Vashistha C, Patil AK, Kumar M (2016) Experimental investigation of heat transfer and pressure drop in a circular tube with multiple inserts. *Appl Therm Eng* 96:117–129. <https://doi.org/10.1016/j.applthermaleng.2015.11.077>
19. Huu-Quan D et al (2020) Experimental investigation on the hydrothermal attributes of MWCNT/water nanofluid in the shell-side of shell and semi-circular tubes heat exchanger. *Appl Therm Eng* 176(January):108304. <https://doi.org/10.1016/j.ijmecsci.2019.04.026>
20. Esmaeilzadeh E, Almohammadi H, Nokhosteen A, Motezaker A, Omrani AN (2014) Study on heat transfer and friction factor characteristics of γ -Al₂O₃/water through circular tube with twisted tape inserts with different thicknesses. *Int J Therm Sci* 82(1):72–83. <https://doi.org/10.1016/j.ijthermalsci.2014.03.005>
21. Promvong P, Skullong S (2020) Thermo-hydraulic performance in heat exchanger tube with V-shaped winglet vortex generator. *Appl Therm Eng* 164(April 2019):114424. <https://doi.org/10.1016/j.applthermaleng.2019.114424>
22. Wu X, Zhang W, Gou Q, Luo Z, Lu Y (2014) Numerical simulation of heat transfer and fluid flow characteristics of composite fin. *Int J Heat Mass Transf* 75:414–424. <https://doi.org/10.1016/j.ijheatmasstransfer.2014.03.087>
23. Huisseune H, T'Joen C, De Jaeger P, Ameer B, De Schampheleire S, De Paep M (2013) Performance enhancement of a louvered fin heat exchanger by using delta winglet vortex generators. *Int J Heat Mass Transf* 56(1–2):475–487. <https://doi.org/10.1016/j.ijheatmasstransfer.2012.09.004>
24. Omid M, Farhadi M, Jafari M (2017) A comprehensive review on double pipe heat exchangers. *Appl Therm Eng* 110:1075–1090. <https://doi.org/10.1016/j.applthermaleng.2016.09.027>
25. Singh SK, Kumar M, Kumar A, Gautam A, Chamoli S (2018) Thermal and friction characteristics of a circular tube fitted with perforated hollow circular cylinder inserts. *Appl Therm Eng* 130:230–241. <https://doi.org/10.1016/j.applthermaleng.2017.10.090>
26. Hasanpour A, Farhadi M, Sedighi K (2014) A review study on twisted tape inserts on turbulent flow heat exchangers: the overall enhancement ratio criteria. *Int Commun Heat Mass Transf* 55:53–62. <https://doi.org/10.1016/j.icheatmasstransfer.2014.04.008>
27. Singh SK, Kumar A (2019) An effect of twisted tape with nanofluid on the performance of double pipe heat exchanger: a comprehensive review. *Int J Mech Prod Eng Res Dev* 9(1):531–540. <https://doi.org/10.24247/ijmpdrfeb201951>
28. Saikia SS et al (2020) Optimum number and arrangement of evacuated-tube solar collectors under various operating conditions. *Sol Energy* 30(September):123542. <https://doi.org/10.1016/j.solener.2020.09.056>
29. Liu J, Gao J, Gao T, Shi X (2013) Heat transfer characteristics in steam-cooled rectangular channels with two opposite rib-roughened walls. *Appl Therm Eng* 50(1):104–111. <https://doi.org/10.1016/j.applthermaleng.2012.05.003>
30. Naphon P (2006) Heat transfer and pressure drop in the horizontal double pipes with and without twisted tape insert. *Int Commun Heat Mass Transf* 33(2):166–175. <https://doi.org/10.1016/j.icheatmasstransfer.2005.09.007>
31. Ding T, Meng Z, Chen K, Fan G, Yan C (2020) Experimental study on flow characteristic of thimble heat exchanger applied to passive residual heat removal system of molten salt reactor. *Appl Therm Eng* 165(November 2019):114619. <https://doi.org/10.1016/j.applthermaleng.2019.114619>

32. Han H, Li B, Shao W (2014) Multi-objective optimization of outward convex corrugated tubes using response surface methodology. *Appl Therm Eng* 70(1):250–262. <https://doi.org/10.1016/j.applthermaleng.2014.05.016>
33. García A, Solano JP, Vicente PG, Viedma A (2012) The influence of artificial roughness shape on heat transfer enhancement: corrugated tubes, dimpled tubes and wire coils. *Appl Therm Eng* 35(1):196–201. <https://doi.org/10.1016/j.applthermaleng.2011.10.030>
34. Rainieri S, Bozzoli F, Cattani L, Pagliarini G (2013) Compound convective heat transfer enhancement in helically coiled wall corrugated tubes. *Int J Heat Mass Transf* 59(1):353–362. <https://doi.org/10.1016/j.ijheatmasstransfer.2012.12.037>
35. Kathait PS, Patil AK (2014) Thermo-hydraulic performance of a heat exchanger tube with discrete corrugations. *Appl Therm Eng* 66(1–2):162–170. <https://doi.org/10.1016/j.applthermaleng.2014.01.069>
36. Li XW, Meng JA, Guo ZY (2009) Turbulent flow and heat transfer in discrete double inclined ribs tube. *Int J Heat Mass Transf* 52(3–4):962–970. <https://doi.org/10.1016/j.ijheatmasstransfer.2008.07.027>
37. Pethkool S, Eiamsa-ard S, Kwankaomeng S, Promvong P (2011) Turbulent heat transfer enhancement in a heat exchanger using helically corrugated tube. *Int Commun Heat Mass Transf* 38(3):340–347. <https://doi.org/10.1016/j.icheatmasstransfer.2010.11.014>
38. Vicente PG, García A, Viedma A (2004) Experimental investigation on heat transfer and frictional characteristics of spirally corrugated tubes in turbulent flow at different Prandtl numbers. *Int J Heat Mass Transf* 47(4):671–681. <https://doi.org/10.1016/j.ijheatmasstransfer.2003.08.005>
39. Buchlin JM (2002) Convective heat transfer in a channel with perforated ribs. *Int J Therm Sci* 41(4):332–340. [https://doi.org/10.1016/S1290-0729\(02\)01323-6](https://doi.org/10.1016/S1290-0729(02)01323-6)
40. Nuntadusit C, Wae-hayee M, Bunyajitradulya A, Eiamsa-ard S (2012) Thermal visualization on surface with transverse perforated ribs. *Int Commun Heat Mass Transf* 39(5):634–639. <https://doi.org/10.1016/j.icheatmasstransfer.2012.03.001>
41. Mohammed HA, Hasan HA, Wahid MA (2013) Heat transfer enhancement of nanofluids in a double pipe heat exchanger with louvered strip inserts. *Int Commun Heat Mass Transf* 40(1):36–46. <https://doi.org/10.1016/j.icheatmasstransfer.2012.10.023>
42. Vermahmoudi Y, Peyghambarzadeh SM, Hashemabadi SH, Naraki M (2014) Experimental investigation on heat transfer performance of Fe₂O₃/water nanofluid in an air-finned heat exchanger. *Eur J Mech B/Fluids* 44:32–41. <https://doi.org/10.1016/j.euromechflu.2013.10.002>
43. Eiamsa-ard S, Promthaisong P, Thianpong C, Pimsarn M, Chuwattanakul V (2016) Influence of three-start spirally twisted tube combined with triple-channel twisted tape insert on heat transfer enhancement. *Chem Eng Process Process Intensif* 102:117–129. <https://doi.org/10.1016/j.cep.2016.01.012>
44. Eiamsa-ard S et al (2018) Convective heat transfer and pressure drop of aqua based TiO₂ nanofluids at different diameters of nanoparticles: data analysis and modeling with artificial neural network. *Int J Therm Sci* 96(April):106398. <https://doi.org/10.1016/j.applthermaleng.2016.09.027>
45. Eiamsa-ard S, Promvong P (2007) Enhancement of heat transfer in a circular wavy-surfaced tube with a helical-tape insert. *Int Energy J* 8(1):29–36
46. Eiamsa-ard S, Nuntadusit C, Promvong P (2013) Effect of twin delta-winged twisted-tape on thermal performance of heat exchanger tube. *Heat Transf Eng* 34(15):1278–1288. <https://doi.org/10.1080/01457632.2013.793112>
47. Torii K, Kwak KM, Nishino K (2002) Heat transfer enhancement accompanying pressure-loss reduction with winglet-type vortex generators for fin-tube heat exchangers. *Int J Heat Mass Transf* 45(18):3795–3801. [https://doi.org/10.1016/S0017-9310\(02\)00080-7](https://doi.org/10.1016/S0017-9310(02)00080-7)
48. Chompookham T, Thianpong C, Kwankaomeng S, Promvong P (2010) Heat transfer augmentation in a wedge-ribbed channel using winglet vortex generators. *Int Commun Heat Mass Transf* 37(2):163–169. <https://doi.org/10.1016/j.icheatmasstransfer.2009.09.012>
49. Zhang L et al (2017) Effects of the arrangement of triangle-winglet-pair vortex generators on heat transfer performance of the shell side of a double-pipe heat exchanger enhanced by helical

- fins. *Heat Mass Transf und Stoffuebertragung* 53(1):127–139. <https://doi.org/10.1007/s00231-016-1804-7>
50. Yadav V, Baghel K, Kumar R, Kadam ST (2016) Numerical investigation of heat transfer in extended surface microchannels. *Int J Heat Mass Transf* 93:612–622. <https://doi.org/10.1016/j.ijheatmasstransfer.2015.10.023>
 51. Muñoz-Esparza D, Sanmiguel-Rojas E (2011) Numerical simulations of the laminar flow in pipes with wire coil inserts. *Comput Fluids* 44(1):169–177. <https://doi.org/10.1016/j.compfluid.2010.12.034>
 52. Karakaya H, Durmuş A (2013) Heat transfer and exergy loss in conical spring turbulators. *Int J Heat Mass Transf* 60(1):756–762. <https://doi.org/10.1016/j.ijheatmasstransfer.2013.01.054>
 53. Nakhchi ME, Hatami M, Rahmati M (2020) Experimental investigation of heat transfer enhancement of a heat exchanger tube equipped with double-cut twisted tapes. *Appl Therm Eng* 180(April):115863. <https://doi.org/10.1016/j.applthermaleng.2020.115863>
 54. Hatami M, Ganji DD, Gorji-Bandpy M (2014) A review of different heat exchangers designs for increasing the diesel exhaust waste heat recovery. *Renew Sustain Energy Rev* 37:168–181. <https://doi.org/10.1016/j.rser.2014.05.004>
 55. Sheikholeslami M, Ganji DD, Gorji-Bandpy M (2016) Experimental and numerical analysis for effects of using conical ring on turbulent flow and heat transfer in a double pipe air to water heat exchanger. *Appl Therm Eng* 100:805–819. <https://doi.org/10.1016/j.applthermaleng.2016.02.075>
 56. Joardar A, Jacobi AM (2008) Heat transfer enhancement by winglet-type vortex generator arrays in compact plain-fin-and-tube heat exchangers. *Int J Refrig* 31(1):87–97. <https://doi.org/10.1016/j.ijrefrig.2007.04.011>
 57. Habchi C et al (2012) Enhancing heat transfer in vortex generator-type multifunctional heat exchangers. *Appl Therm Eng* 38:14–25. <https://doi.org/10.1016/j.applthermaleng.2012.01.020>
 58. Wu JM, Tao WQ (2008) Numerical study on laminar convection heat transfer in a rectangular channel with longitudinal vortex generator. Part A: verification of field synergy principle. *Int J Heat Mass Transf* 51(5–6):1179–1191. <https://doi.org/10.1016/j.ijheatmasstransfer.2007.03.032>
 59. Zhou G, Feng Z (2014) Experimental investigations of heat transfer enhancement by plane and curved winglet type vortex generators with punched holes. *Int J Therm Sci* 78:26–35. <https://doi.org/10.1016/j.ijthermalsci.2013.11.010>
 60. Naik H, Tiwari S (2018) Effect of winglet location on performance of fin-tube heat exchangers with inline tube arrangement. *Int J Heat Mass Transf* 125:248–261. <https://doi.org/10.1016/j.ijheatmasstransfer.2018.04.071>
 61. Prasad PVD, Gupta AVSSKS, Deepak K (2015) Investigation of trapezoidal-cut twisted tape insert in a double pipe U-Tube heat exchanger using Al₂O₃/Water nanofluid. *Procedia Mater Sci* 10(Cnt 2014):50–63. <https://doi.org/10.1016/j.mspro.2015.06.025>
 62. Chandra Sekhara Reddy M, Vasudeva Rao V (2014) Experimental investigation of heat transfer coefficient and friction factor of ethylene glycol water based TiO₂ nanofluid in double pipe heat exchanger with and without helical coil inserts. *Int Commun Heat Mass Transf* 50:68–76. <https://doi.org/10.1016/j.icheatmasstransfer.2013.11.002>
 63. Wu Z, Wang L, Sundén B (2013) Pressure drop and convective heat transfer of water and nanofluids in a double-pipe helical heat exchanger. *Appl Therm Eng* 60(1–2):266–274. <https://doi.org/10.1016/j.applthermaleng.2013.06.051>
 64. Demir H, Dalkilic AS, Kürekci NA, Duangthongsuk W, Wongwises S (2011) Numerical investigation on the single phase forced convection heat transfer characteristics of TiO₂ nanofluids in a double-tube counter flow heat exchanger. *Int Commun Heat Mass Transf* 38(2):218–228. <https://doi.org/10.1016/j.icheatmasstransfer.2010.12.009>

Effect of Housing Design Modifications on Fluid Flow and Heat Transfer Characteristics of Electrical Motor Casing: A Numerical Study



P. Sai Bhargav, M. Ganapathi, and K. Arul Prakash

Nomenclature

A	Area m^2
C_p	Specific Heat $J/kg.K$
FVM	Finite Volume Method
\bar{h}	Average heat transfer coefficient $W/m^2.K$
k	Thermal conductivity $W/m.K$
L	Length m
\dot{m}	Mass flow rate kg/s
Δp	Pressure drop Pa
PMSM	Permanent Magnet Synchronous motor
q	Heat flux W/m^2
Q	Heat transfer rate W
t	Thickness mm
T	Temperature K
u, v, w	Flow velocity components m/s
V	Volume m^3
W	Width m
x_i	Cartesian coordinates

Greek Letters

ρ	Density kg/m^3
μ	Kinematic viscosity $kg/m.s$

P. Sai Bhargav (✉) · M. Ganapathi · K. Arul Prakash
Department of Applied Mechanics, IIT Madras, Chennai 600036, India
e-mail: am20s044@smail.iitm.ac.in

γ	Fillet angle $^{\circ}$
α	Semi-angle of trapezoid $^{\circ}$

Subscripts

a	Air
avg	Average
b	Base
d	Design (1, 2, 3)
f	Fluid
fr	Frame
m	Mean
in	Inlet
out	Outlet
R	Reattachment
s	Surface
S	Solid
w	Wall

1 Introduction

The thermal performance of electric motors is of utmost importance to ensure safe and reliable operation. During the motor operation, there is considerable heat generation in various motor components, such as the windings, stator, and rotor core. These losses range from a few watts to many kilowatts [1]. In a Totally enclosed fan-cooled (TEFC) motor, all the motor components are made inert from the environment. A cooling fan removes heat by blowing high-velocity air over the motor housing [2]. In heavy-duty applications, the motor housing consists of extended surfaces to improve heat transfer.

Helies [3] performed detailed theoretical and experimental studies for TEFC motors. The author proposed a correlation to determine the average heat transfer coefficient based on geometrical parameters and fluid velocity. A detailed experimental study on the heat transfer capability of finned frames with a different number of fins and dimensions has been performed in [4]. The results indicate that the heat transfer coefficients can be improved by as much as 20% by the appropriate selection of housing design.

2 Literature Review and Objective

Chen et al. [5] numerically studied a single fin and optimized parameters, such as fin pitch, height, and thickness. The authors concluded that the proper choice of these parameters could reduce thermal resistance by more than 50%. A novel simplified 2D FEA model to optimize the housing structure has been suggested by Ulbrich et al. [6], and its promise is established by comparison to detailed CFD studies. Moon et al. [7] conducted numerical studies to optimize additional design parameters such as duct shape through the rotor core and dimensions of the fan cover. Wong and Indran [8] numerically demonstrated the effect of adding a fillet to a plate-fin heat sink subjected to impinging flow. The thermal performance improved by as much as 13%, and larger improvements were observed at a larger fillet radius. Hussain et al. [9] extended this study to plate-fin heat sinks with fillet profiles subjected to parallel flows. Compared to impinging flow design, the base temperature and thermal resistance were reduced by 7.5 and 18%, respectively.

From the literature review, numerous studies have focused on optimizing fin parameters and housing design. However, the effect of modifying the fin design (contrary to fin parameters) has received less attention. Therefore in this paper, 3D numerical studies on three different housing designs have been investigated using the finite volume method (FVM)-based commercial tool ANSYS Fluent®. The effect of a fillet profile of different fillet angles is investigated. Base temperature (T_b), average heat transfer coefficient (\bar{h}), and pressure drop (Δp) are considered as the parameters of interest to analyse all the housing designs.

3 Numerical Procedure

3.1 Geometry

The typical housing of a TEFC motor consists of an annular frame (to which axial fins are attached), a conduit box to enclose wirings, and various flanges for mounting. To simplify the analysis, the geometry composed of only an annular frame ($t_{fr} = 10$ mm) with 48 equidistant fins has been analysed. Figure 1a, b represents the geometry of the housing and trapezoidal cross-section of the fin. The radius and length of the base are 140.5 and 150 mm, respectively. This base configuration is referred to as Design 1 for the rest of this paper.

Design 2: Finned housing with fillet profile

Design 1 is modified by adding a fillet to the base of the two consecutive fins specified by the fillet angle, γ (Fig. 1c). The material removed from the base is added to the top of the fin, increasing its length. This process is referred to as volume compensation, and a similar procedure, as detailed in [9], has been adopted. The housing with fillet profile of 60° has been referred to as design 2. The fillet angles considered in this study are detailed in 4.2.

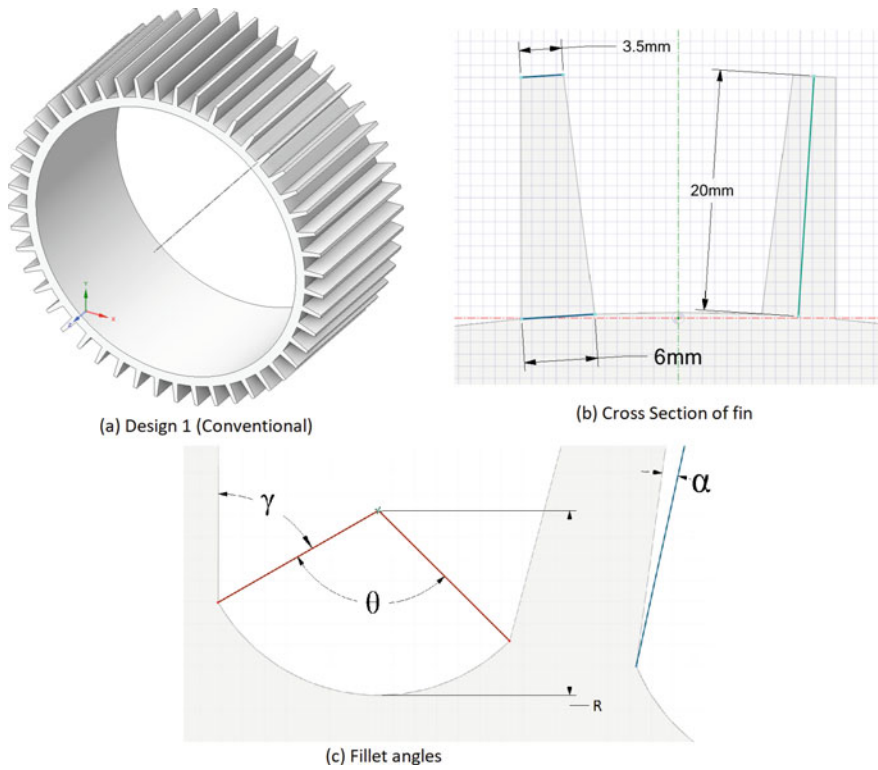


Fig. 1 a Geometry of design 1, b cross-section of fin, and c fillet angles

Design 3: Finned housing with fillet profile and a thin central strip

Design 3 is similar to design 2 except that the material removed from the base of the fin is used for two purposes: to add a thin central strip ($t_{cs} = 1mm$) and the increased length of fins.

Figure 2 represents the 45° sector of these designs. Table 1 summarizes the volume and surface area of all the housings. The volume of the housing remains the same, and more importantly, the surface area improves significantly for the proposed designs. Thus, the thermal performance is expected to increase for the proposed designs. The fluid flow is also expected to be altered through the housing.

3.2 Computational Domain and Boundary Conditions

Noting the circumferential symmetry of the geometry, only the 45° sector composed of the solid and fluid domain has been considered as the computational domain.

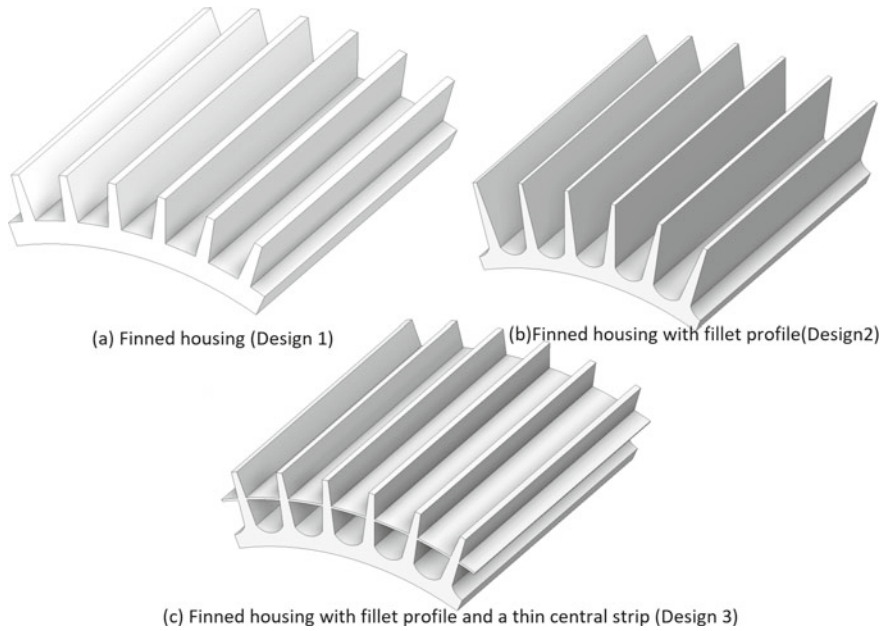


Fig. 2 The 45° sectors of **a** design 1, **b** design 2, and **c** design 3

Table 1 Geometric properties of the designs

Design	Volume ($V, \times 10^4 \text{mm}^3$)	Surface area (A_s, mm^2)
1	25.7	55,028
2	25.68	77,075
3	25.72	94,884

Figure 3 depicts the computational domain considered for design 1. Similar computational domains are considered for the other designs by replacing them with the respective solid regions.

The boundary conditions used for all the designs are summarized in Table 2. The base is subjected to a constant wall heat flux. To get a good approximation for the heat flux, the base of the frame is subjected to, a simple conduction problem with convective boundary condition is solved. An air-cooled 3 kW PMSM motor with all the motor components modelled as suggested in [10] and empirical correlation [3] for the convective BC is used. The heat loss through the base obtained from this procedure is used as constant heat flux ($q_w = 5241 \text{W/m}^2 \text{K}$) in this study. As this procedure holds no further bearing, it is not described in detail.

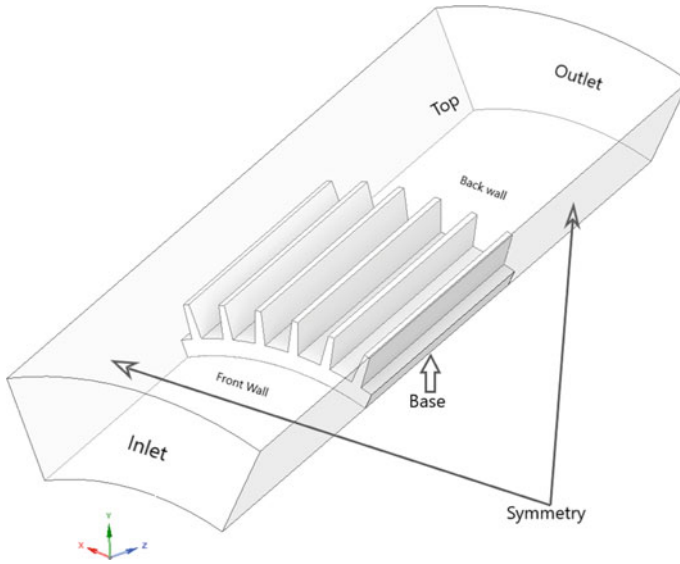


Fig. 3 Computational domain

Table 2 Boundary conditions

Region	Velocity BC	Thermal BC
Inlet	$u = v = 0; w = v_{in}$	$T = 313K$
Outlet	$p = p_{out}$	–
Base	–	$q_w = -k_s \frac{\partial T_s}{\partial n}$
Coupled walls	$u = v = w = 0$	$T_f = T_s; -k_f \frac{\partial T_f}{\partial n} = -\frac{\partial T_s}{\partial n}$
Symmetric planes	–	$-k_s \frac{\partial T_s}{\partial n} = 0$
Other walls	$\frac{\partial u}{\partial n} = 0$	$-k_s \frac{\partial T_s}{\partial n} = 0$

3.3 Numerical Modelling

The FVM-based, ANSYS Fluent 20.2[®] has been utilized to discretize the domain and the governing equations. The problem under consideration is a three-dimensional (3D) conjugate heat transfer problem. The convective medium is air ($\rho_f = 1.127 \text{ kg/m}^3$, $\mu_f = 1.9181 \text{ kg/m.s}$) and Aluminium alloy 6061 ($\rho_s = 2719 \text{ kg/m}^3$, $k_s = 202.4 \text{ W/m.K}$) is used for the housing material. The following assumptions simplify the analysis:

1. The fluid flow is steady and incompressible.
2. The fluid properties are assumed to be constant and depend upon its mean temperature.
3. Radiation heat transfer is neglected.

4. The viscosity-induced heat generation is not considered.

Under these assumptions, the governing equations for mass, momentum, and energy are reduced to:

$$\frac{\partial u_i}{\partial x_i} = 0 \quad (1)$$

$$\rho_f u_j \frac{\partial u_i}{\partial x_j} = -\frac{\partial p}{\partial x_j} + \frac{\partial}{\partial x_j} \tau_{ij} \quad (2)$$

where, $\tau_{ij} = \left[\mu \left(\frac{\partial u_i}{\partial x_j} + \frac{\partial u_j}{\partial x_i} \right) - \rho_f u'_i u'_j \right]$ (3)

$$u_j \frac{\partial}{\partial x_j} T_f = (\alpha + \alpha_T)_f \frac{\partial}{\partial x_j} \left(\frac{\partial T_f}{\partial x_j} \right) \quad (4)$$

The standard $k - \Omega$ SST model has been used for turbulence modelling. For the solid domain, the Laplace equation has been solved.

$$\frac{\partial}{\partial x_j} \left(\frac{\partial}{\partial x_j} T_s \right) = 0 \quad (5)$$

The second-order upwind scheme discretizes momentum and energy equations. The SIMPLE algorithm for pressure-velocity coupling is employed. The relative residuals for x, y, and z velocities are set to 10^{-5} , and for the energy equation, it is restricted to 10^{-7} . The average heat transfer coefficient (\bar{h}) is computed as follows:

$$\bar{h} = \frac{Q}{A_s(T_b - T_m)} \quad (6)$$

$$Q = m C_{p,a} (\dot{T}_{\text{out}} - T_{\text{in}})_f \quad (7)$$

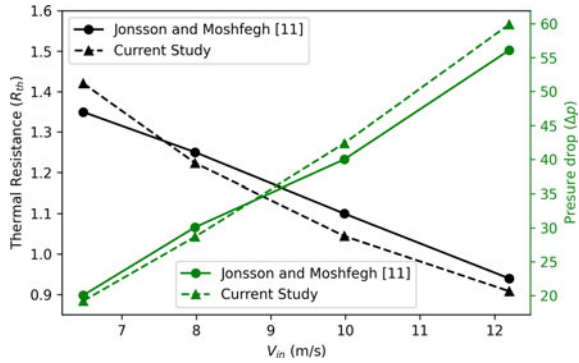
$$T_m = \frac{T_{\text{avg}} + T_b}{2} \quad (8)$$

$$T_{\text{avg}} = \frac{(T_{\text{in}} + T_{\text{out}})_f}{2} \quad (9)$$

The thermal performance factor (η) has been defined as follows:

$$\eta = \frac{\bar{h}_d / \bar{h}_1}{(\Delta p_d / \Delta p_1)^{(1/3)}} \quad (10)$$

Fig. 4 Validation of thermal resistance and pressure drop



3.4 Validation

Detailed grid independent studies have been performed on all designs. Grids, where no notable variation in parameters of interest, are considered for all the represented results. The grids used in the current study vary from 3.2 to 5.6 million elements. The numerical model is validated against Jonsson and Moshfegh’s experimental results [11]. Numerical results (Fig. 4) indicate a maximum discrepancy of 5.2 and 6.8% in thermal resistance and pressure drop, respectively, indicating excellent agreement with experimental results.

4 Results and discussion

4.1 Effect of Fillet

To understand the effect of the addition of fillet, a finned frame with a fillet profile 600 added to the base of the fin without volume compensation (fillet unadjusted) is compared to design 1. Table 3 illustrates the key differences in the observed flow features at an inlet velocity of $V_{in} = 2.29\text{m/s}$. There is a reduction in the length and width of reattachment regions formed at the base of the fin (Fig. 5). This can be attributed to the smoother fluid transition as it approaches the fin. The base temperature reduces by 5%; interestingly, the pressure drop also reduces slightly (2.74%). One would expect a decrease in temperature as the surface area increases by 2.75%. The pressure drop is reduced due to the removal of sharp corners, where skin friction coefficients are usually high.

Effect of Volume Compensation Fig. 6 represents the velocity contours for the volume compensated fin. Regions close to the base are disturbed due to reattachment regions, and as the boundary layer grows along the length of the housing, the velocity gradient zone is set up. The increased length of the fin due to volume compensation is exposed to regions of high ambient velocity. Velocity, arguably the most critical

Table 3 Comparison of flow features

Feature	Design 1	Fillet unadjusted
A_s (mm ²)	55,028	56,450
T_b (C)	126.93	120.86
Δp (Pa)	4.74	4.61
L_R (mm)	101	90
w_R (mm)	11	10.54

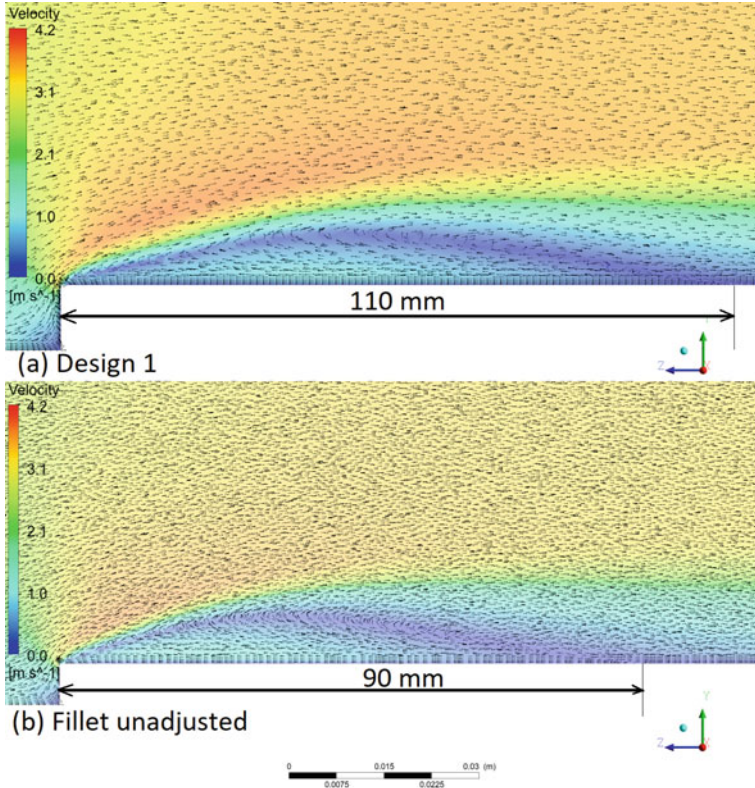


Fig. 5 Comparison of reattachment lengths (L_R) at the base of fin **a** design 1 and **b** fillet unadjusted

factor, increases heat transfer. This explains the increase in heat transfer coefficients and the significant reduction in base temperature.

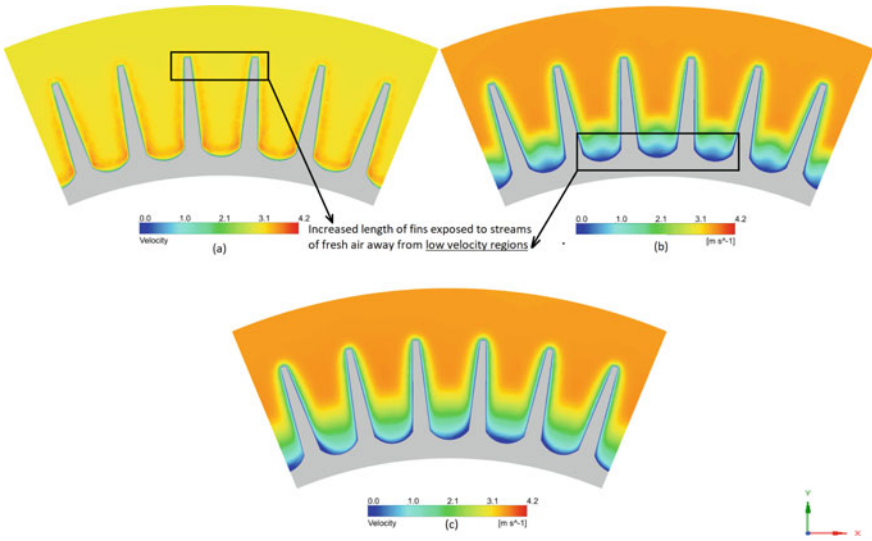
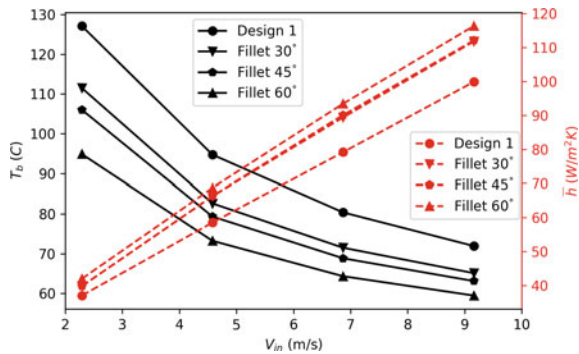


Fig. 6 Velocity Contours at the a front, b middle, and c back face of the fin

4.2 Effect of Fillet Angles

Three different fillet angles (γ) 30° , 45° , and 60° are considered. Figure 7 represents the housing’s base temperature and average heat transfer coefficient variation with different fillet angles along with design 1. The results indicate an improvement in heat transfer coefficient and reduction in base temperature over design 1. The improvements also increase with an increase in the fillet angle. Housing with a fillet angle of 60° exhibits superior performance across velocities. This can be attributed to the substantial increase in surface area, improving heat transfer. The results also indicate that the relative improvements in performance reduce with an increase in velocity.

Fig. 7 Comparison of base temperature and heat transfer coefficient for different fillet angles



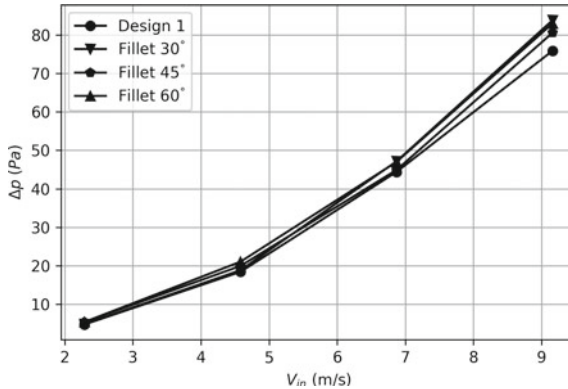


Fig. 8 Comparison of pressure drop at different fillet angles

However, reducing the order $10\text{ }^{\circ}\text{C}$ can significantly improve the life of electrical and electronic components. In particular, the heat transfer coefficient improves in the range of, $5 - 16.5\text{W/m}^2\cdot\text{K}$ and base temperature reduces in the range of $12\text{--}32\text{ }^{\circ}\text{C}$ for the 60° fillet case over design 1. It is also interesting to see that the heat transfer coefficient for fillet 30° and fillet 45° remains nearly the same across velocities. This indicates that heat transfer coefficients do not need to improve with increased surface area. However, the base temperature is lower for the fillet 45° because of higher surface area than the fillet 30° .

Figure 8 represents the variation of total pressure drop across velocities. The pressure drop increases for all cases with an increase in velocity. The pressure drop value is on the lower side for design 1. Due to an increase in the surface area, the skin friction drag increases and, consequently, the total pressure drop. However, the maximum increase occurs for fillet 60° and is approximately 10% higher than design 1.

4.3 Effect of Addition of Thin Strip (Design 3)

The addition of a thin strip along with the fillet profile to the fin improves heat transfer. This is due to the substantial increase in surface area ($\approx 72\%$). Additionally, Fig. 9 depicts the interesting flow phenomenon observed. The reattachment region formed at the base of the fin is suppressed, $L_R = 35\text{mm}$, $w_R = 5.5\text{mm}$ and a narrower region is formed above the strip. A small wake region on the downstream side of the strip is also observed.

Referring to Fig. 10, the lowest base temperatures are observed for design 3, closely followed by design 2, and the performance improvement could be mainly attributed to the surface area enhancement. In particular, the base temperature decreases in the range of $15.5 - 40.5^{\circ}\text{C}$ in comparison to design 1 for the range

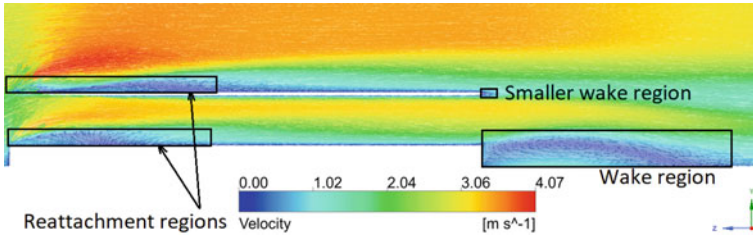
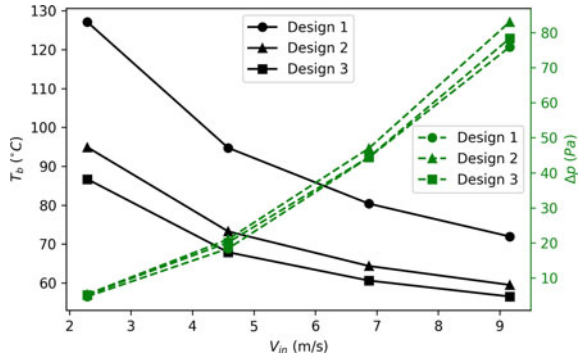


Fig. 9 Flow features observed due to the addition of a thin strip

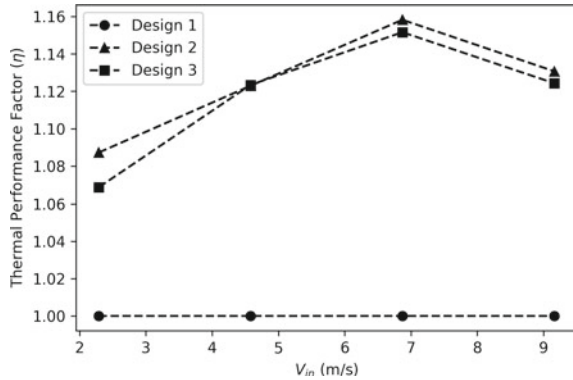
Fig. 10 Comparison of base temperature and pressure drop for three designs



of velocities considered. The highest pressure drop is observed for design 2. The pressure drop for design 3 closely follows design 1; thus, adding a thin strip does not increase the pressure drop considerably.

To summarize the combined thermohydraulic performance, the thermal performance factor for all the housings is represented in Fig. 11. The thermal performance factor indicates the superior performance of design 2. On average, a combined improvement of 12.5% in the thermohydraulic performance over design 1 is observed. Design 3 also closely follows design 2 at higher velocities; an average improvement of 11.7% is observed.

Fig. 11 Thermal performance factor for three designs



5 Conclusion

Three-dimensional numerical studies have been performed on three different housing designs, each occupying the same volume. The effect of a fillet profile of different fillet angles is investigated. The numerical results can be summarized as follows:

- The addition of fillet alone reduces the base temperature by 5 °C and decreases pressure drop compared to design 1. However, the effect of volume compensation is more significant, and the base temperature decreases by 32 °C.
- With an increase in the fillet angle, the heat transfer performance increases and, consequently, the pressure drop.
- For design 2, the base temperature decreases in the range of 12 – 32 °C and heat transfer coefficient improves in the range of 5 – 16.5W/m².K over design 1.
- For design 3, the base temperature decreases in the range of 15.5 – 40.5 °C over design 1.
- The thermal performance factor indicates an improvement of 12.5 and 11.7% for design 2 and design 3, respectively.

Acknowledgements The authors acknowledge the support of Ms. Veena P. and Prof. Kamalesh Hatua, Department of Electrical Engineering, IIT Madras, for their inputs on the electric motor housing and their thermal management.

References

1. Wang X, Li B, Gerada D, Huang K, Stone I, Worrall S, Yan Y (2022) A critical review on thermal management technologies for motors in electric cars. *Appl Therm Eng* 201:117758
2. Wei T (2014) *Mechanical design of electric motors*, CRC press
3. Heiles F (1952) Design and arrangement of cooling fins. *Elektrotechnik und Maschinenbau* 69:42–48

4. M An'IV, Juan AT (2008) Heat transfer and thermal design of finned frames for TEFC variable-speed motors. *IEEE Transact Industr Electron* 55:3500–3508
5. Chen YC, Chen BC, Chen CL, Jimmy QD (2005) Cfd thermal analysis and optimization of motor cooling fin design. *Heat Transfer Summ Conferen* 47330:625–629
6. Ulbrich S, Kopte J, Proske J (2018) Cooling fin optimization on a TEFC electrical machine housing using a 2-d conjugate heat transfer model. *IEEE Trans Industr Electron* 65:1711–1718
7. Moon SH, Jung YH, Kim KW (2016) Numerical investigation on thermal-flow characteristics of a totally enclosed fan cooled induction motor
8. Wong K-C, Indran S (2013) Impingement heat transfer of a plate fin heat sink with fillet profile. *Int J Heat Mass Transf* 65:1–9
9. Ammar AH, Basim F, Basima SK, Hossein T (2019) Numerical investigation of heat transfer enhancement in plate-fin heat sinks: effect of flow direction and fillet profile. *Case Stud Therm Eng* 13:100388
10. Tikadar A, Johnston D, Kumar N, Joshi Y, Kumar S (2021) Comparison of electro-thermal performance of advanced cooling techniques for electric vehicle motors. *Appl Therm Eng* 183:116182
11. Jonsson H, Moshfegh B (2001) Modeling of the thermal and hydraulic performance of plate fin, strip fin, and pin fin heat sinks influence of flow bypass. *IEEE Trans Compon Packag Technol* 24(2):142–149

A Numerical Investigation for Heat Transfer Enhancement Using Convergent and Divergent Shape Orifice Geometry of Synthetic Jet



Mangesh Chaudhari and Omkar Gaonkar

1 Introduction

Nowadays, there is a great demand for electronic devices occupying less space in the system and which are compact in size. However, due to this requirement, the shoot-up in operating temperatures occurs in the system, which reduces the overall performance of system. For the electronic devices to operate effectively and without malfunctioning, a proper heat removal system ought to be placed in the device. Generally, for heat removal, heat sinks are used with air as a working medium. Air as a working fluid is most advantageous in terms of cost, availability, and reliability. This traditional forced-air cooling is facing problems for next-generation electronic gadgets due to constraints of space and cooling requirement. Synthetic jets can be potentially used to overcome these drawbacks for cooling applications. Synthetic jets can be used as an effective cooling device for next-generation electronics.

When a fluid is alternately ejected and sucked from the cavity by the motion of a diaphragm, the synthetic jet is formed. During the motion of diaphragm, suction and ejection of the working takes place into the closed cavity. During ejection, the vortices are detached from the edges of the orifice and travel into the medium. These vortices covalence with each other to form a jet known as a synthetic jet. In this manner, the synthetic jet is formed that synthesizes a jet of fluid through entrainment of the ambient fluid.

M. Chaudhari (✉) · O. Gaonkar
Department of Mechanical Engineering, VIT Pune, Pune 411037, India
e-mail: chaudharimb@gmail.com; mangesh.chaudhari@vit.edu

2 Literature Review and Objective

Chaudhari et al. [1] noticed that the average heat transfer coefficient is affected by the orifice diameter and also stated that it increases with a decrease in the thickness of the orifice plate. The maximum heat transfer was found to be 11 times more than the heat transfer coefficient for natural convection. Chaudhari et al. [2] studied the effect of orifice shape in synthetic jet-based impingement cooling. They considered the square, rectangular, and circular shape orifices. They found that square and circular orifices behave similarly qualitatively and rectangular orifice behaves differently. Also, it was found that a square orifice gives maximum heat transfer coefficient at larger axial distances and a rectangular orifice performs better at smaller axial distances. Pavlova et al. [3] stated that synthetic jet is up to three times better than continuous jet cooling for heat removal from the surface. The high-frequency ($f = 1200$ Hz) synthetic jet removes heat better than the low-frequency ($f = 420$ Hz) jet for small distances between the synthetic jet and the heated surface, whereas low-frequency jet can be more effective at larger distances. In work by Mangate et al. [4] study on heat transfer and acoustics of impinging synthetic jet using diamond and oval shape, orifice was done. The study showed that the maximum average heat transfer coefficient was 17% and 7% more in diamond and oval shape orifices, respectively, than a circular orifice. Mane et al. [5] performed axisymmetric numerical simulations and experimental measurements of synthetic jet cavities using piezoelectric composite diaphragms, Bimorph and Thunder. The system is modelled using an RNG k- ϵ model. The simulated results for the Bimorph diaphragm are in good agreement with the experimental data with differences up to = 15% but under-predict the results for Thunder by more than 30%. Jain et al. [6] numerically investigated an axisymmetric synthetic jet. Modelling of a moving diaphragm was done using three methods, i.e., with a velocity boundary condition, with a moving piston boundary condition, and with a moving wall boundary condition. From the numerical results, it was seen that change in the orifice geometry affects the synthetic jet more than the cavity geometry. Chaudhari et al. [7] presented experimental results for the effect of excitation frequency on the synthetic jet flow for cavities of different depths and different orifice diameters. It is shown that results are more sensitive to changes in the orifice diameter as compared to changes in the cavity depth. Firdaus et al. [8] analysed the amplitude motion of the diaphragm of the synthetic jet at different frequencies and measured the enhancement of heat transfer. Here, maximum frequency was observed at resonance frequency which had the highest amplitude. A large vortex formation was recorded during the ejection stroke for the resonance frequency which gave the maximum temperature drop and a higher heat transfer coefficient. Tang and Zhong [9] studied 2D numerical simulations for flow generated by a synthetic jet actuator consisting of a circular orifice for the laminar case and fully turbulent case. The flow in the cavity was included in the computation and velocity boundary condition was applied at the diaphragm. Also, four turbulent models were tested for the fully turbulent case and it was found that the RNG k- ϵ and Standard k- ω model gives close results to experimental data. Laouedj et al. [10] investigated the performance of the moving

boundary technique which is one of the different techniques implemented to reproduce the flow behaviour of a 3D synthetic jet. The results in form of averaged velocity components, as well as the phase, averaged quantities are compared to experimental measurement. Liu et al. [11] studied the heat transfer enhancement of diffuser-shaped orifice. The results showed that at the small jet to heated surface spacing, the highest heat transfer of 600 opening angle diffuser improved approximately 30% compared to straight and round orifice.

In this study, numerical analysis of synthetic jet is done to enhance the performance using various parameters. The numerical analysis is conducted for various parameters. An average heat transfer coefficient is determined for varying axial distance amongst the orifice exit and heated surface and validated with existing experimental results. Also, the average ejection and suction velocities are validated for a given actuation frequency. The geometrical parameter like convergent shape and divergent shape orifice is considered whilst the thickness of the orifice plate is also varied. ANSYS Fluent (academic) software is used for numerical simulations.

3 Numerical Modelling

The computational software, geometry and mesh details, boundary conditions, dynamic meshing for moving diaphragm, turbulence model, and other simulation parameters are described in this section.

3.1 *Geometry and Mesh*

The ANSYS Fluent (academic) software is used for 2D simulations of synthetic jet. The geometry can be considered as two regions. The first one is the cavity containing the diaphragm, cavity walls, and orifice. And the second region comprises the ambient air, where the ejection of air from the cavity through the orifice takes place due to the vibration of the diaphragm on the heated surface. For vibrating diaphragm, moving wall boundary condition is applied using a UDF and the cavity and orifice are considered as walls. A pressure inlet and pressure outlet boundary conditions are considered in the ambient air region and the heated surface and other surfaces are considered as walls as shown in Fig. 1. Also, the axisymmetric boundary condition (Fig. 2) is used to divide the geometry in half to reduce computational time. A triangular unstructured mesh is used for all regions and refinement is applied at the walls to capture the velocity variations near the walls. The ambient air region changes as the axial distance changes, making the geometry change. So, for all types of geometry change, same type of mesh is used as shown in Fig. 3. The mesh is created using Ansys mesher and this mesh is then translated to fluent for setup.

Fig. 1 Computational geometry and boundary conditions used in the present work

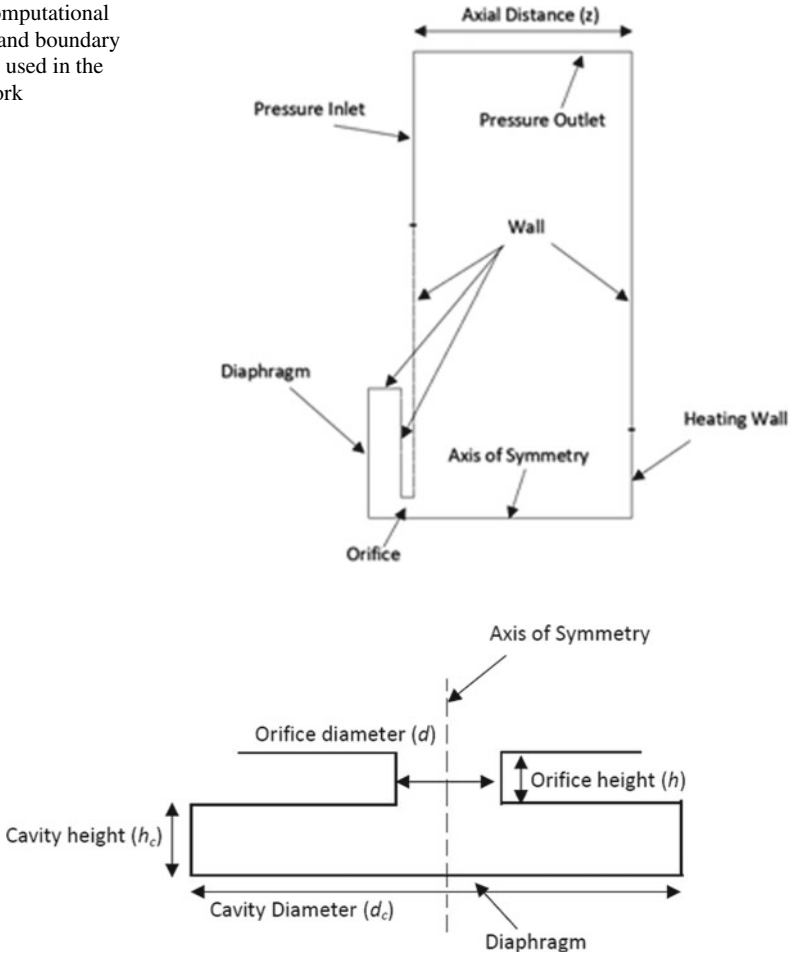


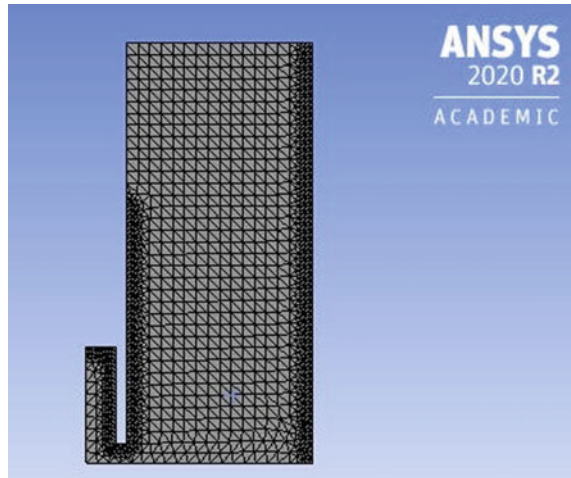
Fig. 2 Cavity and orifice region with geometric details

3.2 *Fluent Parameters*

The mesh is being developed using the workbench software, which is exported into Fluent software. It uses a control volume-based technique to convert the governing Navier–Stokes differential equations at each node cell into algebraic equations. These equations can be solved through iteration. The segregated, unsteady, axisymmetric solver is used with a first-order implicit time scheme. This is unconditionally stable with respect to time step size.

The segregated solver mainly used for incompressible flows solves the algebraic equations sequentially. In research by Tang et al. [9], it is concluded that $k-\epsilon$ RNG turbulence is capable of dealing with flows with large and rapid changing

Fig. 3 Computational mesh used in present work



strain rates, so the $k-\varepsilon$ RNG model is used for turbulence modelling in this work. For a pressure–velocity coupling, pressure-implicit with the splitting of operators (PISO) based on a higher degree of approximation is chosen. This algorithm significantly reduces convergence difficulties associated with a highly distorted skewed mesh. Tang et al. [9] concluded that PISO algorithm improves transient calculations although it requires more computational time. Second-order upwind spatial discretization is used for the momentum and energy and first-order upwind is used for turbulent kinetic energy and turbulent dissipation rate. The under-relaxation parameters are kept at 0.3, 1.0, and 0.7 for pressure, density, and momentum, respectively. The turbulent specifications for the pressure inlet and pressure outlet are set using the intensity and viscosity ratio with values of 5% intensity and turbulent viscosity ratio of 10.

3.3 Diaphragm Boundary Conditions

For a moving wall, the dynamic mesh is used for which the tri- unstructured mesh is the requirement. The dynamic mesh method of smoothing and remeshing is used in the present work. The dynamic mesh zone of the diaphragm is defined using a UDF, which controls the position of each node on the diaphragm. In this study, a moving boundary condition is utilized and the movement of the diaphragm is defined using a logarithmic approximation, for such a case, the instantaneous shape of the oscillating diaphragm is described as

$$\delta(r, t) = \frac{\delta_c}{2} \left[1 - \frac{4r^2}{D_c^2} + \frac{8r^2}{D_c^2} \ln \left(\frac{2r}{DC} \right) \right] \cos(2\pi ft) \quad (1)$$

where, δ_c is the diaphragm centre, peak-to-peak displacement, r is the distance from the centre of the diaphragm, d_c is the diaphragm diameter r , and f is the actuation frequency. Differentiating above Equation, the instantaneous logarithmic diaphragm velocity is derived.

$$\delta(r, t) = \frac{\delta_c}{2} \left[1 - \frac{4r^2}{D_c^2} + \frac{8r^2}{D_c^2} \ln\left(\frac{2r}{DC}\right) \right] \sin(2\pi ft) \tag{2}$$

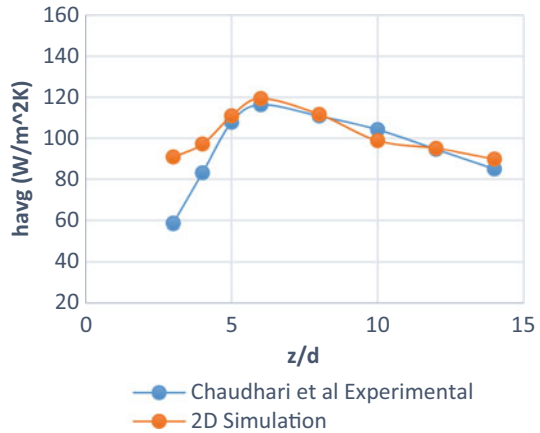
3.4 Validation of Numerical Results

The experimental results by Chaudhari et al. [1] are considered for validation of numerical results. In this work, the experimental setup consisted of a synthetic jet with an 8 mm single orifice, 50 mm cavity diameter, and 1.52 mm amplitude of diaphragm. Also, the length orifice plate was 110 mm, the height of an orifice was 2.4 mm, and the size of the heating surface was 40×40 mm with a diaphragm vibrating at 200 Hz. This whole setup is considered for 2D geometry and similar boundary conditions are applied for numerical simulations. The numerical simulation results and experimental results of z/d versus h_{avg} are plotted in a graph as shown in Fig. 4. The variation in the numerical results from experimental results is within 10% and thus, it can be said that the numerical model is validated and can be used for further work.

Chaudhari et al. [1] have given the empirical correlation (Eq. 3) for a certain range of non-dimensional parameters.

$$\frac{Nu_{avg}}{Pr^{0.333}} = 7.624(Re)^{0.792} \left(\frac{L}{d}\right)^{-2.186} \left(\frac{R}{d}\right)^{2.258} \left(\frac{z}{d}\right)^{-0.632} \tag{3}$$

Fig. 4 Validation of the numerical model with experimental results of Chaudhari et al. [1] for 8 mm single orifice synthetic jet at 200 Hz



3.5 Numerical Steps Involved

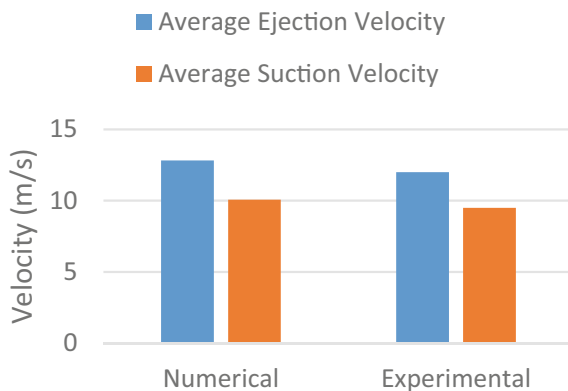
A 2D geometry is modelled in Ansys design modeller as shown in Fig. 1. The 2D geometry is then meshed using Ansys mesher and the boundary conditions are given as mentioned in above section. Then, the mesh is translated to fluent for setup. The fluent parameters are given in the setup. Boundary conditions are given as mentioned in the above section. Continuity, momentum, and energy equation are used for the simulations. K- ϵ RNG model is used for turbulence modelling. For a pressure-velocity coupling, pressure-implicit with the splitting of operators (PISO) based on a higher degree of approximation between the iterative corrections for pressure and velocity is chosen. The under-relaxation parameters are kept default at 0.3, 1.0, and 0.7 for pressure, density, and momentum, respectively. Diaphragm boundary condition is mentioned in above section. Post-processing of the results are viewed in the Ansys post-processor. The results, counters, etc. are seen in Ansys post-processing.

Also, the experimental results for velocity by Chaudhari et al. [7] are also considered for validation of numerical results. Here, the results are validated for average suction and average ejection velocities for the same experimental setup mentioned above and for 300 Hz frequency. The numerical simulation results and experimental results for average ejection and average suction velocities are plotted in graph as shown in Fig. 5. The variation in the numerical results from experimental results is within 10% and thus, it can be said that the numerical model is validated and can be used for further work.

4 Results and Discussions

In this section, numerical results of synthetic jet with varying orifice geometry are presented. A graph of average ejection and average suction velocity is plotted for different orifice geometry and also for the average heat transfer coefficient.

Fig. 5 Validation of the numerical model with experimental results of Chaudhari et al. [7] at 300 Hz



4.1 Flow Measurement

The flow velocities of the synthetic jets at 1 mm away from orifice are measured at 300 Hz frequency to study the effect of the diverging divergent-shaped and convergent-shaped orifice (Fig. 6). For the first case during the ejection stroke, the divergent-shaped orifice acts as a diffuser, creating a lower pressure drop and during the suction stroke, the convergent-shaped orifice acts as a nozzle, creating a higher pressure drop. High velocity of the flow is observed in ejection stroke, and the suction stroke developed low velocity [11].

Therefore, during the ejection stroke, the diversion-shaped orifice gives higher velocity of flow, giving a high-ejection flow rate. Similarly, for the second case that is for a convergent-shaped orifice during the ejection stroke, it acts as a nozzle, creating a higher pressure drop. During the suction stroke, the nozzle-shaped orifice acts as a diffuser, creating a lower pressure drop.

Therefore, during the ejection stroke, the convergent nozzle-shaped orifice had lower velocity and during the suction, the stroke had higher flow velocities comparatively. The plot showing these changes in velocities is shown in Fig. 7.

From Fig. 7, it is observed that the average ejection velocity from the orifice is more in diverging divergent-shaped orifice than that of the converging convergent-shaped orifice. A percentage increase of 39.53% was observed in ejection velocity for 2.4 mm orifice height when compared with the normal circular orifice. And for $h = 4.8$ mm, the percentage increase is 58.73%. It is also observed that the suction velocity reduces when compared to the normal circular orifice. A percentage decrease of 49.66% was observed for 2.4 mm orifice height, whereas 76.53% for 4.8 mm orifice height.

For the converging nozzle-shaped orifice, the ejection velocities are less compared to the suction velocities. Here, a percentage decrease of 43.44% was observed in ejection velocity when compared to the circular orifice for 2.4 mm height, and 50.54% reduction for 4.8 mm orifice height. Also, an increase of 21.73% was observed for average suction velocity for 2.4 mm and 14.86% for 4.8 mm orifice height.

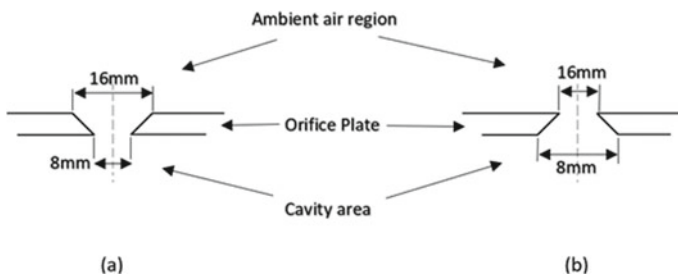
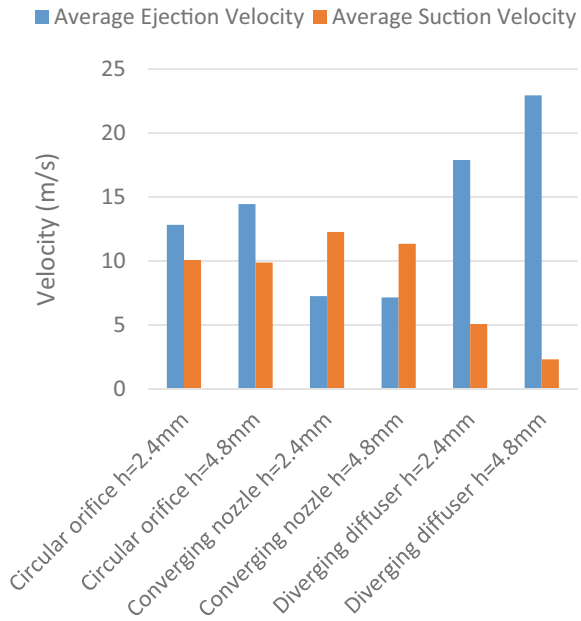


Fig. 6 **a** Divergent-shaped orifice. **b** Convergent-shaped orifice

Fig. 7 Variation in average ejection and suction velocities for different orifice geometry

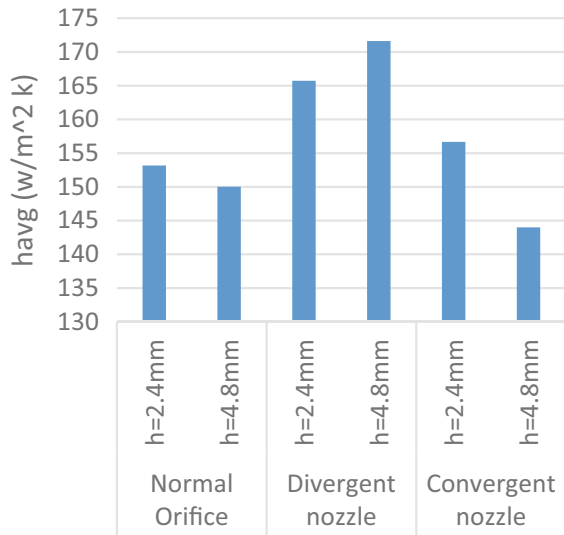


4.2 Heat Transfer Results

A numerical study was performed where the synthetic jet impinged on the heated surface and the average heat transfer coefficient from the heated wall is calculated. The simulation was performed for different orifice geometry as specified earlier. The plot showing these results is shown in Fig. 7.

From Fig. 8, it is observed that the average heat transfer coefficient is more for diverging type divergent-shaped orifice than a circular and convergent-shaped orifice. A percentage increase of 8.2% in heat transfer coefficient was observed for 2.4 mm orifice height when compared to normal circular orifice and 14.39% for 4.8 mm orifice height. Similarly, 2.28% increase was observed for converging nozzle-shaped orifice for 2.4 mm height. But a decrease of 4.02% was seen for 4.8 mm height in the nozzle-shaped orifice. A maximum heat transfer coefficient of 171.62W/m²K was obtained for a diverging divergent-shaped for $h = 4.8$ mm and a minimum value of 144.01W/m²K was observed for convergent-shaped orifice for $h = 4.8$ mm.

Fig. 8 Variation in average heat transfer coefficient for different orifice geometry



5 Conclusion

In the current study, heat transfer and velocity measurements are investigated for a diffusion-shaped orifices and nozzle-shaped orifices of synthetic jet. Following are the conclusions:

1. From divergent-shaped orifices, average ejection flow velocity is higher than that from round and convergent-shaped orifices.
2. Heat transfer enhancement of approximately 14% is observed using divergent-shaped orifices over that of round orifices was observed.
3. The divergent-shaped orifice produced the highest heat transfer.
4. Orifice thickness changes on the heat transfer performance considerably. The heat transfer coefficient increases for divergent-shaped orifice as the thickness increases. But for circular and divergent-shaped orifice, heat transfer coefficient reduces as the thickness increases.

References

1. Chaudhari MB, Puranik B, Agrawal A (2010) Heat transfer characteristics of synthetic jet impingement cooling. *Int J Heat Mass Transf* 53:1057–1069
2. Chaudhari MB, Puranik B, Agrawal A (2010) Effect of orifice shape in synthetic jet-based impingement cooling. *Exp Therm Fluid Sci* 34:246–256
3. Pavlova A, Amitay M (2006) Electronic cooling with synthetic jet impingement. *J Heat Transfer* 128:897–907

4. Mangate LD, Chaudhari MB (2015) Heat transfer and acoustic study of impinging synthetic jet using diamond and oval shape orifice. *Int J Therm Sci* 89:100–109
5. Poorna M, Karla M, Ali R, Robert B, Nicolas C (2007) Piezoelectric actuators as synthetic jets: cavity dimension effects. *J Intell Mater Syst Struct* 18
6. Jain M, Puranik B, Agrawal A (2011) A numerical investigation of effects of cavity and orifice parameters on the characteristics of a synthetic jet flow. *Sens Actuat A* 165:351–366
7. Chaudhari M, Verma G, Puranik B, Agrawal A (2009) Frequency response of a synthetic jet cavity. *Exp Therm Fluid Sci* 33(3):439–448
8. Firdaus SM, Abdullah MZ, Abdullah MK, Fairuz ZM (2019) Heat transfer performance of a synthetic jet at various driving frequencies and diaphragm amplitude. *Arab J Sci Eng* 44(2):1043–1055
9. Tang H, Zhong S (2005) 2D numerical study of circular synthetic jets in quiescent flows. *Aeronaut J* 109(1092):89–97
10. Samir L, Abbès A, Abdelilah B (2012) New analysis in 3d-synthetic jets within numerical investigation using cfd validation code: moving boundary techniques. *Energy Procedia* 19:226–238
11. Liu Y-H, Chang T-H, Wang C-C (2016) Heat transfer enhancement of an impinging synthetic air jet using diffusion-shaped orifice. *Appl Therm Eng* 94:178–185

Performance Evaluation of a Thermal Energy Storage System with Stainless Steel Encapsulated Phase Change Material



A. Surya, M. Chandraesh, N. Nallusamy, and R. Prakash

1 Introduction

The energy demand for our globe is increasing due to industrialization, and in people's lifestyles, more energy is consumed for heating and cooling applications. We have to move technology that contributes to less carbon footprint and less usage of fossil fuels, since they are depleting and their prices are more fluctuating, affecting the global economy. The utilization of solar thermal energy for heating, cooling, and generating power has more potential to solve the energy crisis. But the problem with renewable energy sources is that they are seasonal and time-dependent. The TES systems can help these scenarios by storing the thermal energy for our application.

The packed bed latent heat thermal energy storage (LHTES) system, one type of thermal energy system, has been drawing attention due to its straightforward design and effective heat transfer during heat charging and discharging. In addition to acting as a buffer between energy supply and demand, the packed bed LHTES arrangement may effectively utilize solar energy and industrial waste heat. PCM-based thermal storage systems receive greater attention nowadays. However, the poor thermal conductivity of those materials is the issue to be resolved. Practical design constraints of the storage tank, extended heat transfer surface area, and immersion of nanoparticles are the predominant methods to improve the heat transfer rate and the PCM's storage capacity within a short period; at the same time, it has to store the energy for a long while.

A. Surya · M. Chandraesh · R. Prakash (✉)
Department of Mechanical Engineering, Sri Sivasubramaniya Nadar College of Engineering,
Kalavakkam, Chennai 603110, India
e-mail: prakashr@ssn.edu.in

N. Nallusamy
School of Engineering, Shiv Nadar University Chennai, Kalavakkam, Chennai 603110, India

2 Literature Review and Objective

Research focuses on improving thermal stratification, energy efficiency, thermal performance, and the amount of energy stored to equip TES efficiently. An experimental evaluation of Thermal Stratification of a packed bed latent heat storage is done using adipic acid encapsulated in aluminum spheres. It is observed that the low flow rate (4 ml/s) for different set heater temperatures shows the best variation of the stratification number profile comparatively with higher flow rates of 8 and 12 ml/s at different set heater temperatures, and they concluded that the effect of flow rate is significant on thermal stratification than that of charging set heater temperature [1]. For a comprehensive model, thermally stratified storage tank, a convection number needs to be paired with geometric information. CFD is also valid but costlier in computation time, and 1-D models with empirical correlations are the most effective solution [2]. The different geometrical configuration of thermal energy storage plays a crucial role in enhancing system performance.

An experimental setup of radial-bed thermal energy storage is developed and investigated at 49.7 kWh and operating temperatures between 25 and 700 °C. The pressure drop is less comparatively and has an overall thermal efficiency of 71.8% [3]. The performance of TES with a single stainless steel tube, a steel tube with longitudinal fins, and a copper tube with helical fins. It is observed that they obtained an average storage capacity value of 47.2 kWh/m³ during the charging process, and the heat transfer is improved in a heat exchanger with fins by increasing the heat exchange power factor by a factor of 10 [4]. A theoretical investigation was done on the effects of water inlet velocity, tank aspect ratio, and temperature difference, and the result concluded that thermal stratification improves with an increase in temperature difference, decrease in inlet velocities, and higher aspect ratios [5]. In a numerical investigation based on the hexagonal circle configuration impacts of geometric parameters, it is found that the packed bed has a better thermal storage design than the shell and tube units [6]. The 2D model of a cylindrical-shaped double-coiled, vertical HWS tank is simulated in Ansys fluent and validated against experimental data in charging mode. It is observed that the stratification improves when the heat source is at the upper position [7]. A numerical study has been done by varying the length, the radius of the TES tank, and the number of spheres in a packed bed. PCM is encapsulated in spheres, and it is concluded that the L/R value resulted in higher phase change and storage effectiveness [8]. A study observed that the FCC (Face Centre Cubic lattice packing) has better thermal performance than body center cubic and simple cubic packing [9]. In a study of a district cooling system, in which PCM is incorporated numerically analyzed, it is concluded that the effect of PCM on thermal stratification during charging is insignificant and enhanced during discharging. It is improved [10]. By investigating novel medium PCM NaNO₃-KNO₃ (55–45 wt%) in packed bed latent heat storage, it has been observed that with the continuous increase in the air temperature inside the TES tank, the temperature difference inside the tank is initially relatively higher. However, it gradually decreases, and the charging efficiency is improved by controlling the initial and final temperature [11]. The thermal

performances at a different flow rate of HTF (4, 6, 8 ml/s) and three various PCM (adipic acid, erythritol, and eutectic solder) among these three PCM erythritols have observed high energy efficiency, and efficiency decreases for all PCM when the flow rate is increased [12].

The work aims to improve the heat transfer of phase change material and analyze the thermal performance of compact thermal energy storage systems for domestic hot water applications with affordable and readily available materials.

3 Materials and Methodology

Water and granulated paraffin wax are employed, respectively, as the HTF and PCM. Stainless steel (SS) spherical balls without solid internal fins and with solid internal fins are used to encapsulate the PCM. Tables 1 and 2 show the thermophysical parameters. Each ball has an outside diameter of 75 mm, and a thickness of 2 mm and is filled with PCM. The internal solid fin has dimensions of 90 mm diameter and 8 mm thickness. Each spherical stainless steel in both ball configurations contains 140 g of PCM. The storage tank is made of stainless steel and has a height of 0.51 m with a diameter of 0.31 m. The storage tank is divided into four parts with a height of 0.1 m. The entire system uses asbestos rope with a thickness of 0.03 m as its thermal insulation material. 8 kg of paraffin wax and 15 kg of water were used in this study.

Figures 1 and 2, respectively, show the schematic layout of the experimental system and the thermal storage tank. The system has the components as a constant temperature bath with electrical heaters, a TES tank, a rotameter for flow rate control, flow control valves, a resistance temperature detector (RTD) sensor connected with a temperature indicator to measure the temperatures at four stages of the tank, PCM temperatures, inlet, and outlet. Meshes were provided between two different layers,

Table 1 Thermophysical properties of HTF and SS

Parameter	HTF	SS
Density (ρ), [kg/m ³]	979.5	7930
Specific heat (Cp), [kJ/kg.K]	4.189	0.510
Thermal conductivity (k), [W/m.K]	0.66	16.2

Table 2 Thermophysical properties of PCM [13]

Parameter	Value	
Melting temperature (T _m), [°C]	61	
Latent heat of fusion (L _m), [kJ/kg]	213	
Density (ρ), [kg/m ³]	Solid: 861	Liquid: 778
Thermal conductivity (k), [W/m.°C]	Solid: 0.4	Liquid: 0.15
Specific heat (Cp), [kJ/kg.°C]	Solid: 1.850	Liquid: 2.384

and 50 mm space was provided for proper water flow at the top and bottom of the storage tank.

HTF is initially heated through electrical heaters and circulated to flow at 70 °C to the storage tank with flow rates of 2, 4, and 6 L/min from the constant temperature

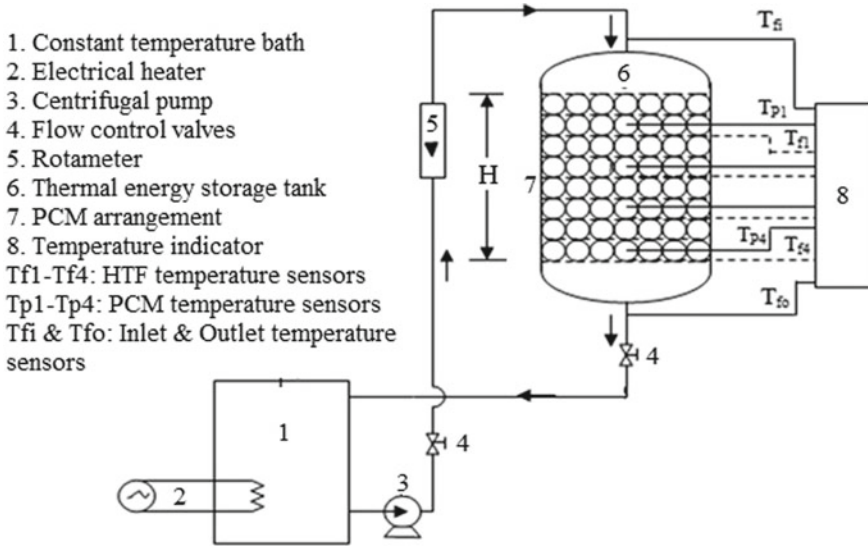


Fig. 1 Schematic layout of the experimental system

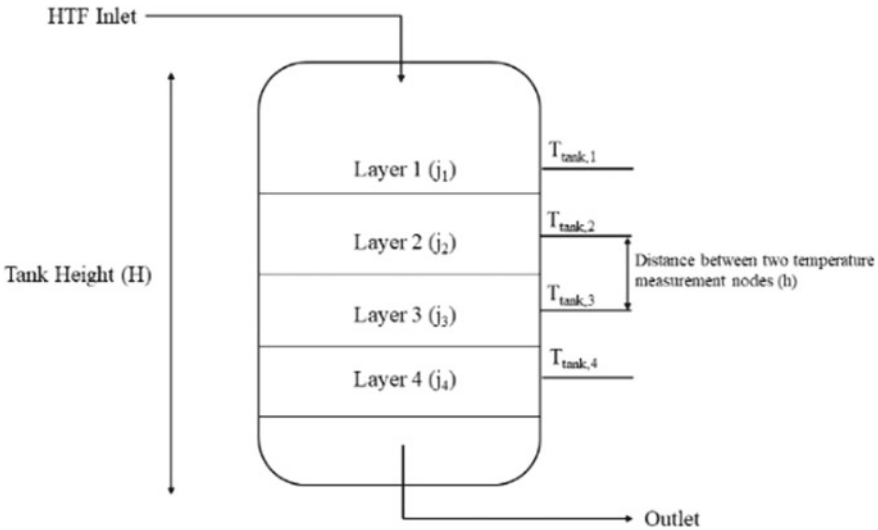


Fig. 2 Schematic layout of the storage tank

bath (CTB). Every ten minutes, the temperature of HTF and PCM is noted at all four stages of the tank; moreover, inlet and outlet temperatures are also indicated. The flow once stopped when all temperatures reached the HTF inlet temperature, which means the tank was fully charged.

Thermophysical properties of heat transfer fluid, stainless steel, and paraffin wax were tabulated in Tables 1 and 2.

3.1 Uncertainty Analysis

Holman offered the expression to analyze experimental uncertainty investigation in Eq. 1 [14]. Data points from various instruments/devices in the study are used to simulate the possibility of measurement error. The accuracy of the independent is shown in Table 3.

$$\sigma = \sqrt{\left[\left(\frac{\partial y}{\partial c_1} d_1 \right)^2 + \left(\frac{\partial y}{\partial c_2} d_2 \right)^2 + \left(\frac{\partial y}{\partial c_3} d_3 \right)^2 + \dots + \left(\frac{\partial y}{\partial c_n} d_n \right)^2 \right]} \quad (1)$$

Overall experimental uncertainty in the heat storage of the system is calculated as 1.423%. The value of uncertainty was considered suitable for the experiment.

4 Results and Discussion

During the experimental process, the CTB is integrated with the TES section, and the inlet HTF is allowed to flow with the inlet temperature of 70 °C for all three flow rates. The temperature of the HTF inside the CTB is constantly monitored. The most influential parameters are the mass flow and inlet temperature of HTF. In this study, energy calculations and the storage tank's stratification analysis were considered the thermal performance evaluation parameters.

Table 3 Accuracy of independent variables

Independent variables	Accuracy [±]
Temperature	0.1 °C
Mass of PCM	0.1 kg
Mass of HTF	0.1 kg
Mass flow rate	2.0%

4.1 Liquefaction Fraction of PCM

The Liquefaction fraction of the paraffin wax over melting time can be expressed by Eq. (2).

$$\phi = \begin{cases} 0, & \text{for } T_p \leq T_s \\ \frac{T_p - T_s}{T_1 - T_s}, & \text{for } T_s < T_{PCM} < T_1 \\ 1, & \text{for } T_p \geq T_1 \end{cases} \quad (2)$$

Figure 3 shows PCM liquefaction for solid internal fins and without fins configuration balls at different flow rates. It is observed from Fig. 3 that the liquefaction initially increases gradually concerning with time, then it liquefies as fast as possible. Due to the high heat transfer surface, an internal solid fin ball melts the PCM more quickly than without fin balls. Table 4 provides the actual liquefaction duration of each test condition. From Table 4, while increasing the flow rate from 2 to 4 L/min and 6 L/min, the liquefaction time lessened by 21.04 and 31.57% for no fined balls, and 23.53 and 41.18% for fin patterned balls, respectively.

Fig. 3 Liquefaction of PCM concerning the time

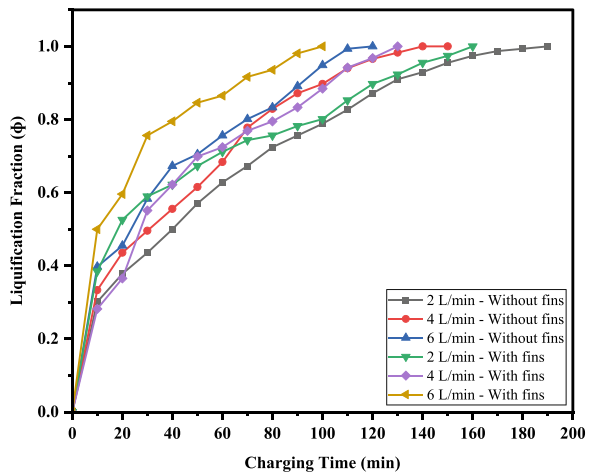
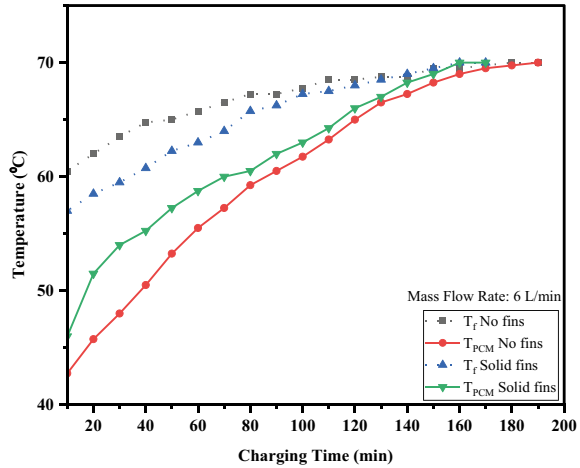


Table 4 Liquefaction duration at different test conditions

Pattern	Description	2 L/min	4 L/min	6 L/min
No fins	Liquefaction time (min)	190	150	130
	Reduction in time (%)	–	21.04	31.57
Solid internal fins	Liquefaction time (min)	170	130	100
	Reduction in time (%)	–	23.53	41.18

Fig. 4 Temperature profile during charging



4.2 Temperature Profile

Figure 4 shows the charging temperature profile comparison of the 6 L/min flow rate for no fins and internal solid fin configuration balls. The average temperature of four layers is used to plot the graph. Initially, the PCM absorbs high temperatures and gradually increases over time. Increasing the mass flow rate moderately impacts the charging duration of the system.

4.3 Storage Analysis of the System

The system was designed to store 4800 kJ (theoretically) of energy to supply hot water to a family of four members with an average temperature of 45 °C. And it was assumed as half of the energy (i.e., 2400 kJ) is stored as sensible heat, and another half of the energy (i.e., 2400 kJ) is stored as latent heat. The actual storage capacity is denoted by Eq. 3 and 4.

The heat storage capacity of HTF can be expressed as follows:

$$q_{sensible} = m_{HTF} \times C_{p_{HTF}} \times (T_f - T_i)_{HTF} \tag{3}$$

The heat storage capacity of PCM can be expressed as follows,

$$q_{latent} = m \times [C_{p_s}(T_f - T_m) + (\times L_m) + C_{p_s}(T_f - T_m)] \tag{4}$$

The overall heat storage capacity of the system is the sum of the heat storage capacity of sensible heat and latent heat. It is expressed in Eq. 5; it is constant for all the test conditions of this study. Experimental heat storage varies concerning the

flow rate and fin configuration.

$$Q_{\text{overall}} = Q_{\text{sensible}} + Q_{\text{latent}} \tag{5}$$

From the above expressions, the actual heat storage as sensible heat is 2449.395 kJ, latent heat is 2170.390 kJ, and the maximum possible storage capacity of the system is 4620 kJ.

The experimental heat storage of the system under different conditions can be determined by the following equations Eq. 6–8.

$$\text{Cumulative heat stored: } Q_{\text{cum}} = \sum_{i=1}^n Q_{\text{sen.}} + Q_{\text{lat.}} \tag{6}$$

$$Q_{\text{sensible}} = [m C_p (T_2 - T_1)]_{\text{HTF}} \tag{7}$$

$$Q_{\text{latent}} = m [C_{p_s}(T_2 - T_1) + L_m + C_{p_s}(T_2 - T_1)] \tag{8}$$

Figure 5 shows the system’s cumulative heat stored at different test conditions. It is observed from the figure that increasing the mass flow rate and providing fins moderately influenced the storage amount. At the same charging period, the 6 L/min conditions stored more energy than the 2 L/min conditions in both fin configuration cases.

Table 5 represents the amount of cumulative heat stored at different test conditions. Moreover, the ratio between the cumulative heat stored and theoretical energy storage can be expressed as the actual energy efficiency of the system, and the ratio between cumulative heat stored and maximum heat storage capacity is described as the capacitive energy efficiency of the system.

Fig. 5 Cumulative heat stored by the system

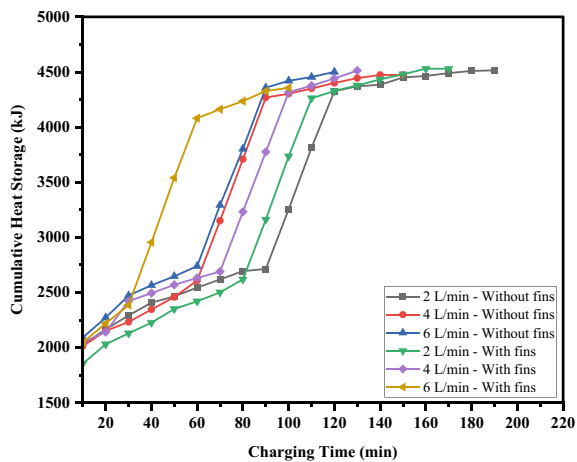


Table 5 Storage analysis of the test conditions

Pattern	Flow rate (L/min)	Q _{cum} (kJ)	Efficiency (η _{actual}) (%)	Efficiency (η _{capacitive}) (%)
No fins	2	4514.995	94.06	97.71
	4	4473.062	93.18	96.82
	6	4500.685	93.76	97.42
Solid internal fins	2	4529.259	94.36	98.04
	4	4512.819	97.53	97.67
	6	4356.430	90.76	94.29

4.4 Stratification Analysis

The ratio between the mean of the temperature gradients at any given time interval and the most significant mean temperature gradient for the charging/discharging process is known as the stratification number, according to Fernández-Seara et al. It is derived from the following expression in Eq. 9–11.

$$Str = \frac{(\partial T / \partial y)_t}{(\partial T / \partial y)_{t=0}} \tag{9}$$

where,

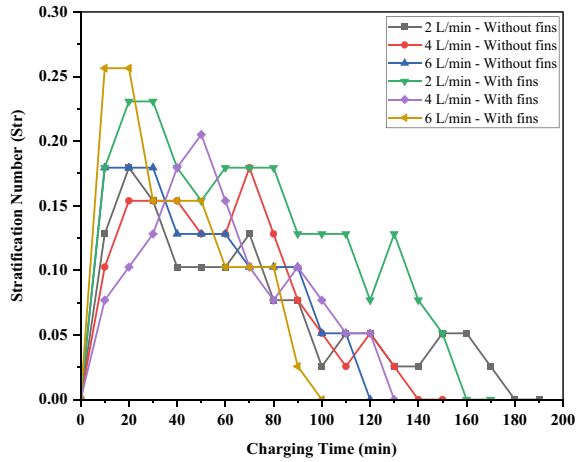
$$\left(\frac{\partial T}{\partial y}\right)_t = \frac{1}{N - 1} \left\{ \sum_{j=1}^{N-1} \left[\frac{T_j - T_{j+1}}{\Delta h} \right] \right\} \tag{10}$$

$$\left(\frac{\partial T}{\partial y}\right)_{t=0} = \frac{T_i - T_{ini}}{(N - 1) \Delta h} \tag{11}$$

Figure 6 shows the stratification number as the time function for all mass flow rates of both fin configurations. During the charging process, the stratification was higher for the solid internal fin configuration with a flow rate of 6 L/min due to the water temperature difference between the two stages of the storage tank. It is observed that the stratification is low when the flow rate is less. The stratification number will rise during the charging process as it moves along, peaking at a value that will begin to fall. When the stratification number reaches its maximum, the storage tank’s outlet temperature rises above its starting point. The degradation of thermal stratification in the TES tank is represented by the drop in temperature difference after the peak.

Richardson number is an efficient stratification performance indicator that takes into account many features of storage systems, such as tank geometry, velocity, and the temperatures at the top and bottom layers of the tank. Richardson’s number is substantially less than 1; buoyancy has no bearing on the flow. When it exceeds unity, buoyancy predominates. It is expressed by Eq. 12, 13. It is the ratio between

Fig. 6 Stratification number during the charging



buoyancy and mixing forces.

$$Ri = \frac{g\beta H(T_{top} - T_{bottom})}{v_{sf}^2} \tag{12}$$

where,

$$v_{sf} = \frac{\dot{V}}{\pi r^2} \tag{13}$$

Table 6 provides the Richardson number concerning with superficial velocity of the experimental conditions. Table 6 shows that the Ri greater than 0.25 is a stable test environment, damping the mechanical turbulence [15].

Table 6 Richardson number comparison

Configuration	\dot{m} (L/min)	v_{sf} (m/s)	Ri
No fins	2	0.0657	5.061
	4	0.1315	1.356
	6	0.1976	0.596
Internal solid fins	2	0.0657	7.930
	4	0.1315	1.758
	6	0.1976	0.848

5 Conclusion

The performance analysis of the thermal storage tank is presented in this paper. For better charging and storage time reduction, the heat transfer surface of the stainless steel encapsulation was increased by providing solid internal fins. The system's capacity is calculated as 4620 kJ and stored at almost 4481.207 kJ (i.e., 97%) on average.

- The charging duration is lessened by increasing the flow rates from 2 to 4 and 2 to 6 L/min to 21.04 and 31.57% without fin configuration balls. For solid internal fin configuration balls, the duration lessened by 23.53 and 41.18% while increasing the flow rate by 2 to 4 L/min and 2 to 6 L/min.
- While providing fins in the encapsulation, reduce the charging time to around 10.05, 13.33, and 23.07% for 2, 4, and 6/min, respectively. However, it does not have a significant effect on the process. Hence, the mass flow rate is influenced more than the fin configuration.
- Stratification analysis shows that the tank is highly stratified when the flow rate is 6 L/min.
- Richardson's number range declares that the charging process is stable and mechanical turbulence is dampened. And buoyancy force dominates the flow for 2 and 4 L/min flow rate conditions. Then the 6 L/min flow condition is entirely turbulent due to the value being less than unity, and buoyancy has no effect in this condition.
- It is concluded that increasing the heat transfer surface area of encapsulation and flow rate of HTF moderately improves the system's thermal performance.
- In the future, overall energy–exergy analysis, the influence of heat transfer numbers, and the effect of encapsulation material on storage also be considered for detailed thermal performance evaluation.

Nomenclature

g	Acceleration due to gravity [m.s ⁻²]
Q_{cum}	Cumulative heat stored [kJ]
η	Efficiency [%]
T_f	Final temperature [°C]
h	Height of each layer [m]
T_i	Initial temperature [°C]
\dot{m}	Mass flow rate [L/min]
Φ	Melt fraction
T_m	Melting temperature [°C]
N	Number of layers
r	Radius of the inlet pipe [m]

Ri	Richardson number
Cp	Specific heat [$\text{kJ.kg}^{-1}.\text{°C}^{-1}$]
Str	Stratification number
v_{sf}	Superficial velocity [m.s^{-1}]
j	Temperature measuring point
β	Thermal expansion coefficient [K^{-1}]
σ	Uncertainty [%]
\dot{V}	Volumetric flow rate [$\text{m}^3.\text{s}^{-1}$]

References

1. Ashmore M, Katlego L, Robert L, Denis O, Karidewa N (2018) Thermal stratification performance of a packed bed latent heat storage system during charging. In: E3S web of conferences, vol 64, p 03001, EDP sciences
2. Rendall J, Abu-Heiba A, Gluesenkamp K, Nawaz K, Worek W, Elatar A (2021) Nondimensional convection numbers modeling thermally stratified storage tanks: Richardson's number and hot-water tanks. *Renew Sustain Energy Rev* 150:111471
3. Trevisan S, Wang W, Guedez R, Laumert B (2022) Experimental evaluation of an innovative radial-flow high-temperature packed bed thermal energy storage. *Appl Energy* 311:118672
4. Caron-Soupart A, Fourmigué JF, Marty P, Couturier R (2016) Performance analysis of thermal energy storage systems using phase change material. *Appl Therm Eng* 98:1286–1296
5. Karim A, Burnett A, Fawzia S (2018) Investigation of stratified thermal storage tank performance for heating and cooling applications. *Energies* 11(5):1049
6. Liang H, Niu J, Annabattula RK, Reddy KS, Abbas A, Luu MT, Gan Y (2022) Phase change material thermal energy storage design of packed bed units. *J Energy Storage* 51:104576
7. Kumar K, Singh S (2021) Investigating thermal stratification in a vertical hot water storage tank under multiple transient operations. *Energy Rep* 7:7186–7199
8. Aziz NA, Amin NAM, Majid MSA, Bruno F, Belusko M (2022) Optimising a packed bed phase change material of spheres using effectiveness-number of transfer unit method. *J Energy Storage* 49:104019
9. Duan Z, Zhang Z, Wang J, Cao X, Zhang J (2020) Thermal performance of structured packed bed with encapsulated phase change materials. *Int J Heat Mass Transf* 158:120066
10. Oró E, Castell A, Chiu J, Martin V, Cabeza LF (2013) Stratification analysis in packed bed thermal energy storage systems. *Appl Energy* 109:476–487
11. Wang W, He X, Shuai Y, Qiu J, Hou Y, Pan Q (2022) Experimental study on thermal performance of a novel medium-high temperature packed-bed latent heat storage system containing binary nitrate. *Appl Energy* 309:118433
12. Mawire A, Lefenya TM, Ekwomadu CS, Lentswe KA, Shobo AB (2020) Performance comparison of medium temperature domestic packed bed latent heat storage systems. *Renew Energy* 146:1897–1906
13. Nallusamy N, Roy R, Surya A (2019) Experimental investigation on heat transfer enhancement of latent heat storage system containing spherical capsules with internal hollow and solid fins. In: AIP conference proceedings, vol 2161, no 1, p 020001, AIP Publishing LLC
14. Holman JP, Gajda WJ (2001) *Experimental methods for engineers*. McGraw-Hill, New- York
15. Schnelle Jr, K. B. (2003). *Atmospheric diffusion modeling*.

Understanding the Heat Transfer Characteristics and Axis Switching Phenomenon in High Aspect Ratio Elliptical Orifice Impinging Synthetic Jets



Pawan Sharma, Prakhar Bharadwaj, Kshitij Bhat, K. A. Vyvaswath, Bhavya Dalal, Pradeep K. Singh, Santosh K. Sahu, and Harekrishna Yadav

1 Introduction

Technological innovation in electronics is leading to smaller components with better performance and higher heat fluxes than ever before. As far as the reliability and optimum performance of these devices are concerned, the conventional cooling techniques are becoming inadequate for handling these intense heat fluxes. As a result, there is a need for compact and high-efficiency cooling devices. Impingement jets have attracted great interest recently for heat removal [1]. Impingement cooling at maximum flow speed is known to offer heat transfer coefficients up to three times that of conventional convective cooling [2]. Among impingement jet cooling methods, synthetic jet cooling has received significant attention because of the enhanced mixing due to its transient nature. SJs are found to be superior to continuous jets in terms of entrainment rate due to the rapid formation of periodic vertical structures in SJ [3]. Especially among SJs, the enhanced entrainment and mixing properties of Non-circular SJs are better than those of axisymmetric jets [4]. Synthetic Jet Actuators are novel active flow control zero-net-mass-flux (ZNMF) devices [1], i.e., the mass ejected by the actuator cavity during ejection is equal to the mass sucked during the suction stroke. SJs have significant momentum flux, i.e., there is a net-momentum addition due to the movement of the diaphragm. When an SJ is ejected through a non-axisymmetric orifice, the shape of the jet fluctuates as it flows downstream due to self-induced deformations of the vortex rings [5]. This phenomenon of the rotation of the jet shape in symmetric vortex rings is called axis

P. Sharma (✉) · P. Bharadwaj · K. Bhat · K. A. Vyvaswath · B. Dalal · P. K. Singh · S. K. Sahu · H. Yadav
Department of Mechanical Engineering, Indian Institute of Technology Indore, Indore 453552, India
e-mail: phd1901203008@iiti.ac.in

switching. This change in cross-section shape increases downstream, away from the jet origin. The shape change is such that the forms remain almost similar to the jet opening, with its major and minor axis rotated at angles concerning the jet origin. Axis switching is of great significance for heat transfer applications and has been observed in rectangular jets [6], elliptic jets [4, 7], and other more complicated non-circular jets [8, 9]. Depending on initial conditions at the jet inlet, the cross-section of non-circular jets can evolve in the expansion region of the jet between the orifice exit and the impingement plate [5, 6]. It takes place through shapes similar to that at the jet inlet, with its major and minor axis rotated at angles depending on the jet geometry.

2 Literature Review and Objective

Synthetic Jets (SJ) have a vast potential to meet the cooling demand for future electronic applications. The main advantages of SJ cooling are its simple structure, low weight, low power consumption, and its high reliability in operations without the need for a dedicated plumbing system, since SJs are generated directly from the ambient fluid [5]. Axis switching is a phenomenon that is extensively studied in the case of non-axisymmetric impingement jets. Reodikar et al. [10] considered compressible impingement jets from different orifice geometries to study the mechanism of axis switching and its influence on heat transfer characteristics. They found that the phenomenon of axis switching is prevalent in elliptic jets at low orifice-to-plate ratios ($z/D \approx 2$), and elliptic jets mostly undergo an axis switch of 90 degrees. At larger z/D values, they reported that the jet section becomes axisymmetric regardless of the initial shape or aspect ratio at the orifice exit. They attributed this phenomenon to differential velocity gradients and jet spreading. It is seen that most of the work on elliptic impingement jet cooling focuses on lower aspect ratios. Gutmark and Grinstein [10] reported that the evolution of the jets strongly depends on multiple initial conditions at the elliptic nozzle exit, such as thickness distribution at the nozzle lip, non-uniformity of shear-layer thickness, the eccentricity measured by the nozzle geometrical aspect ratio, and Reynolds and Mach numbers. Shi et al. [7] studied the influence of various initial conditions on the behavior of elliptic jets experimentally. With a laser-induced fluorescence and 2D stereoscopic particle image velocimetry, they concluded that the entrainment ability of the elliptical synthetic jet is greater than that of the circular synthetic jet and increases with the orifice aspect ratio ($AR \leq 4$) and Reynolds number. On the other hand, Reodikar et al. [9] reported that the heat transfer characteristics of circular and non-circular jets are comparable and observed a better performance for the case of circular jets in all conditions. In addition to this, Lee and Lee's [11] experimental study of local heat transfer distribution of elliptic impinging jet found that for higher orifice-to-plate distance ($z/D > 6$), the heat transfer rates of the elliptic impinging jet are lower than those for the circular jet in the stagnation region. They argued that the cause of this phenomenon is that, in the central area, most of the momentum of the elliptic jet is lost before arriving

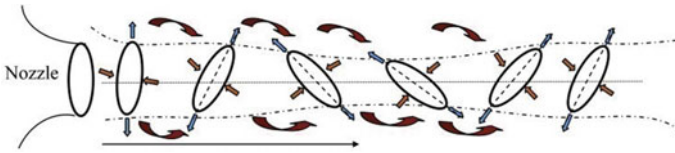


Fig. 1 Axis switching (Reodikar et al. [9])

at the impingement plate due to significant entrainment and substantial mixing with the ambient fluid. Additionally, they correlated the Nusselt number for the nozzle aspect ratio and the nozzle-to-plate spacing as $Nu \propto AR^{-0.082} z/D^{-0.077}$. Straccia and Farnsworth [6] studied the axis switching phenomenon for moderate orifice aspect ratios ($AR = 13, 19$) of a jet expelled from a synthetic jet actuator with a rectangular orifice. They used stereoscopic particle image velocimetry in addition to a Biot-Savart velocity induction solver to study the effect of orifice shape on vortex dynamics and axis switching. They reported that for $AR > 6$, the jet axis switched once and did not complete the axis switching cycle as opposed to jets with lower AR , which switched axis 2–3 times before the vortices lost coherence. They found a double peak in the mean jet centerline velocity profile, which became more prominent with increasing AR . A literature survey suggests a significant amount of studies on elliptic jet impingement. However, most studies consider only a lower aspect ratio ($AR < 4$) of an elliptic orifice. On the other hand, the effects of higher aspect ratios in rectangular orifices on impinging jets' dynamics and heat transfer characteristics have been studied in great detail. The objective of the present study is to investigate the influence of higher orifice aspect ratios ($AR = 10, 14$) on the axis switching behavior and the heat transfer characteristics of the elliptic jet. The present study experimentally analyzes the local and average Nu over the impingement plate and studies the temperature variation on the impingement plate (Fig. 1).

3 Materials and Methods

The experimental setup comprises a Synthetic Jet Actuator (SJA) assembly, hot-wire anemometry, an IR thermal imaging setup along with a heated foil, as shown in Fig. 2. The SJ actuator assembly uses a loudspeaker of 133 mm diaphragm size and a 15 mm diameter orifice plate ($t/d = 0.33$). A power oscillator (SI-28DR) supplies the input sinusoidal signal to the SJ actuator. The amplitude of the input signal is maintained constant ($= 4.5V_{rms}$). The frequency of SJ actuation is fixed as 40 Hz (i.e., its resonance frequency). A constant temperature hot-wire anemometer (Mini CTA 54 T42) with a single wire probe is employed to measure the flow velocity at the orifice exit. A 120×120 mm size matte finish test foil (SS material, AISI-304) is heated by a direct current power source for a constant heat flux of 2.5 kW/m^2 . The back side of the test surface is painted with flat black paint to achieve uniform emissivity ($\epsilon = 0.95$). The thermal imaging technique with an IR camera (FLIR:

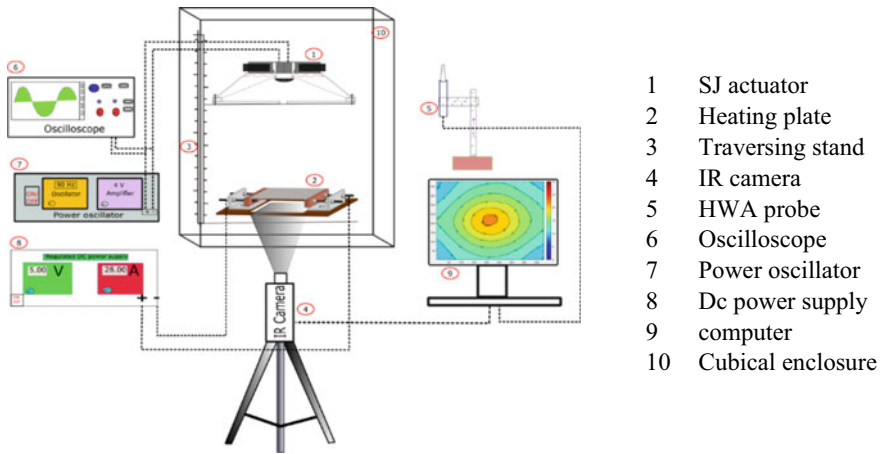


Fig. 2 Schematic of the experimental setup used in present investigation

A655sc) is used to study the heat transfer characteristics by gauging the temperature of the test surface. The IR camera measures temperatures from 0 to 2000 °C with an uncertainty of 1.5%. A calibration technique elaborated in [12] is employed to obtain the emissivity of 0.95 from the IR camera setup.

Apart from this, a stepper motor-controlled traversing stand is used to maintain the surface distance between the orifice plate and heated foil. All the experiments are conducted in an enclosed environment to abstain from surrounding effects. The ambient temperature (T_a) during the experimental investigation is measured with a pre-calibrated K-type thermocouple by placing it in the enclosed chamber of the experimental setup.

3.1 Data Reduction

The centerline mean velocity is measured by the instantaneous velocity during the ejection stroke (half cycle) calculated as follows

$$U_0 = \frac{1}{T} \int_0^{T/2} u(t) dt \quad (1)$$

The Reynolds number (Re) based on mean centerline velocity can be calculated as

$$Re = \frac{U_0 \times d}{\nu} \quad (2)$$

where d is the orifice diameter and ν is the kinematic viscosity of the fluid.

The Average Nusselt (Nu_{avg}) number is computed as follows:

$$Nu_{avg} = \frac{h_{avg} \times d}{k_f} \quad (3)$$

where, k_f is the thermal conductivity of fluid.

The average heat transfer coefficient (h_{avg}) can be calculated as

$$h_{avg} = \frac{q_{conv}}{(T_s - T_a)} \quad (4)$$

Here, T_s and T_a are the temperature of test foil and its ambience, respectively, while q_{conv} is the net heat supplied to the test specimen.

$$q_{conv} = q_j - q_{loss}; \quad q_j = \frac{V \times I}{A} \quad (5)$$

q_j , while q_{loss} denotes the total heat loss from the target surface. The net supplied heat flux (q_j) is calculated by the supplied voltage (V) and current (I) across the test foil.

The heat loss from the target surface is obtained by no-flow experiment [13] and the corresponding equation for heat loss w.r.t ($T_s - T_a$) is stated as below for $T_a = 32$ °C.

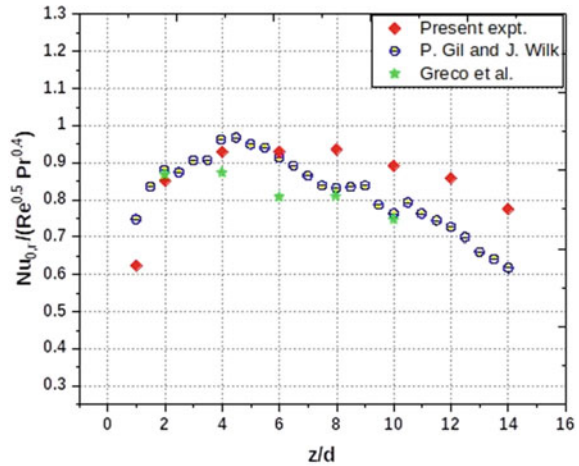
$$Q_{loss} = 0.23143 \times (T_s - T_a) - 0.31364 \quad (6)$$

A maximum of 21.1% heat loss is computed, which combines the heat loss due to natural convection and radiation from the foil surface (from both top and rear surface). The maximum uncertainty associated with q_{conv} and Nu_0 is found to be ± 3.95 and $\pm 4.53\%$, respectively as calculated based on Coleman and Steel [14].

4 Results and Discussion

In this section, heat transfer characteristics of the circular orifice ($AR = 1$) are compared to elliptical orifices ($AR = 10, 14$). All the orifices have the same effective orifice area among the studied orifices. The effective orifice diameter D is taken to be 15 mm based on our previous study [12], and the Reynolds number (Re) for the present investigation is calculated to be 8986.

Fig. 3 Results of reduced stagnation point Nusselt number as compared to the literature data



4.1 Validation Study

The results of heat transfer characteristics in the case of synthetic jet impingement cooling are compared to available literature data to evaluate the correctness of the experimental method. The reduced stagnation point Nusselt number ($Nu_{0,r}$) is considered for comparison to different experimental conditions. A 150 mm size diaphragm synthetic jet actuator with $V_{rms} = 1$ to 6 V, $Re = 3600$ to 22,950, and $L_0 = 0.84$ to 170.5 were used by Gil and Wilk [15]. In another study, Greco et al. [16] used an SJ actuator with a diaphragm size of 208 mm operating at $Re = 5250$ and $L_0/d = 5$ to 20. The current validation study employs a 133 mm diaphragm size actuator operating at $V_{rms} = 4$. The comparative heat transfer results are shown in Fig. 3 and the results closely match with the heat transfer results obtained by Gil and Wilk [15] and Greco et al. [16] (Fig. 4).

4.2 Effect of AR on Local and Average Nu

The distribution of local Nu on the heated surface is shown in Fig. 5a–d for different orifice-to-surface spacings ($z/d = 1, 3, 6, 10$). In Fig. 5a–d, local Nu is shown for orifices of different aspect Ratios (AR): $AR = 1$ (circular orifice) and $AR = 10, 14$ (elliptic orifice). The local Nu along the major and minor axis is plotted on the right and left side of the stagnation point, respectively, in each of the plots Fig. 5a–d. For all the orifices, the local Nu is observed to be largest at the stagnation point ($r/d = 0$), and then it decreases away from the stagnation point and reaches a local minimum at $r/d = 2.67$. For $z/D = 1$, a bell-shaped curve is observed for the case of $AR = 10$ on both the major and the minor axis. But such a shape of Nu is observed only on the major axis in the case of $AR = 14$. The Nu of $AR = 10$ and $AR = 14$ is higher than the

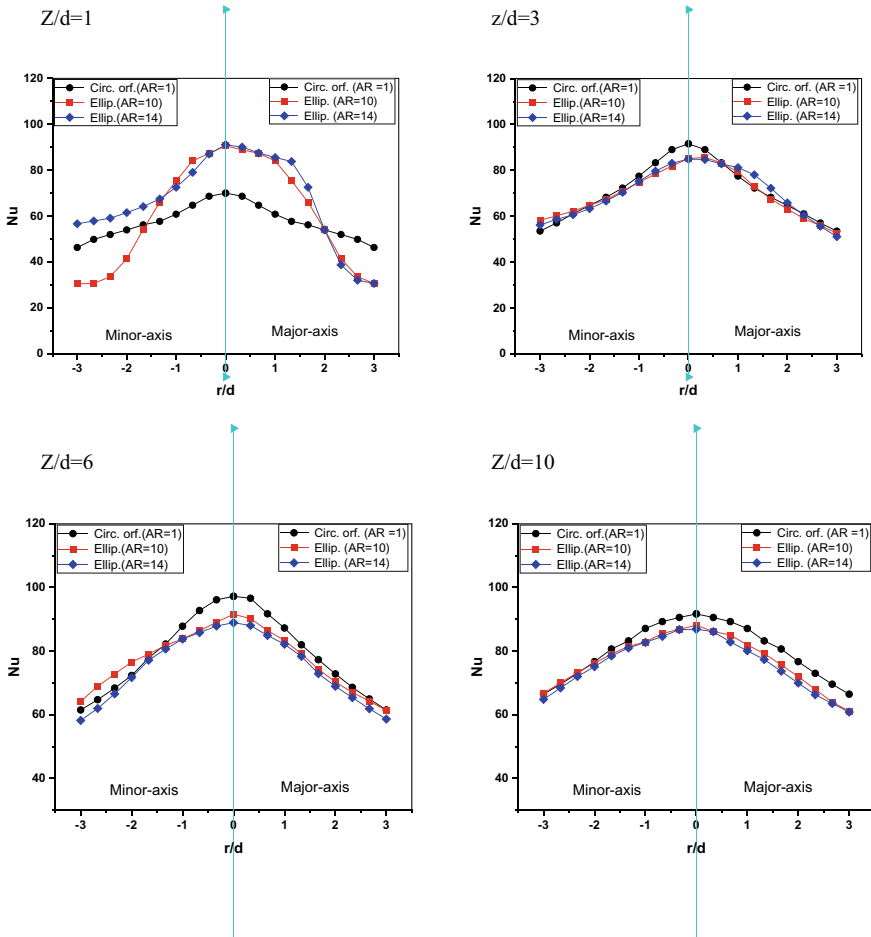


Fig. 4 Distribution of local Nusselt Number for various r/d and z/d values

Nu for circular orifice near the stagnation region, but the Nu for $AR = 10, 14$ is lower otherwise. High AR elliptic jets perform 28% better cooling in the near-field ($z/D = 1$). The Nu of $AR = 10$ and 14 has similar values closer to the stagnation region. For all the cases $z/D = 3, 6, 10$, the circular orifice performs better local cooling, as evident by a higher local Nu . In the case of far-field, The $AR = 10$ elliptic jet has higher Nu values than the jet with $AR = 14$ and thus, performs cooling better.

Figure 6 shows the line average Nusselt number (Nu_{l-avg}) variation on the Major (X) axis and Minor (Y) axis for the different aspect ratios ($AR = 1, 10, 14$) with the z/D values. The Nu_{l-avg} for the circular orifice ($AR = 1$) gradually increases and decreases after a certain point, whereas for elliptic orifices, a double peak is observed. Both plots show that, at low z/D values, Nu_{l-avg} is minimum. This is a consequence of low entrainment of surrounding air due to walling of the orifice and the heated surface.

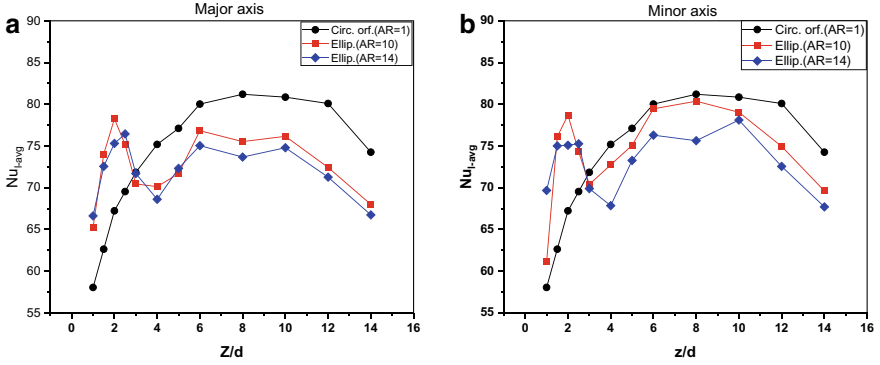


Fig. 5 Line average Nusselt number of studied orifices along **a** major axis, **b** minor axis

Additionally, at the near-field, the formed vortices fail to escape, and the recirculation decreases the heat transfer rate. However, for higher surface spacing ($z/D = 12$ to 14), Nu starts to decrease again due to a decrease in the kinetic energy and jet turbulence in the far-field region. So, the maximum heat transfer is obtained in the intermediate field ($z/d = 6$ to 10). The higher aspect ratio elliptic jets offer a higher Nu at lower z/D distances than circular orifices, similar to the findings of Bhapkar et al. [4]. This is due to the high spreading rate of elliptical orifices as compared to circular orifices. Among $AR = 10$ and 14 , the elliptic jet with $AR = 10$ performs better cooling than $AR = 14$, evident for the Nu_{l-avg} plots.

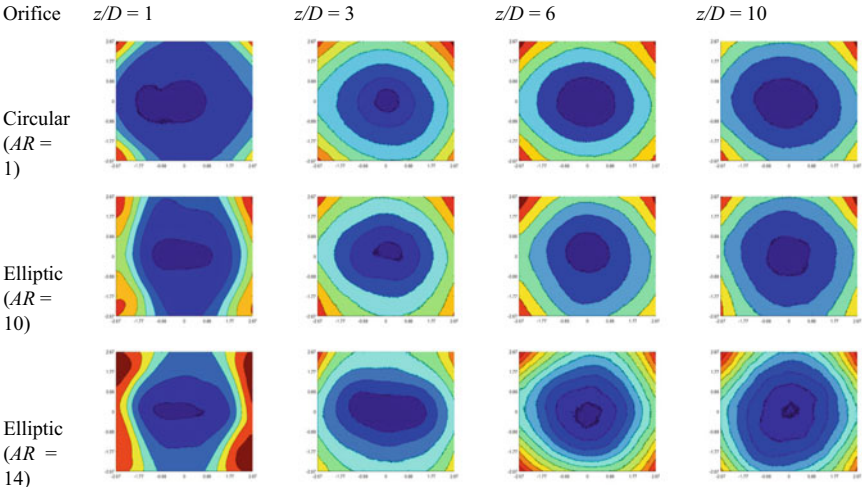


Fig. 6 Local temperature contour maps for different aspect ratios and orifice to surface distances

4.3 Axis Switching

In Fig. 5a,b, at the near-field ($z/D = 1,3$), the local Nu values for the major axis of the $AR = 14$ jet are higher than the minor axis Nu measurements. This suggests that the cooling is highly localized and similar to the shape of the orifice. This is also clearly apparent from the Fig. 6 showing IR thermography plots for $z/D = 1,3$ with $AR = 14$. As the jet progresses downstream, for values of $z/D = 6$ and 10 , the minor axis Nu values are slightly higher than the major axis plots. The IR thermography contour plots also depict a similar behavior. The heat transfer characteristics of the elliptic jets change with the axial distances. This suggests that axis switching is observed even in the case of higher AR elliptic jets.

5 Conclusion

This experimental study investigates the influence of the elliptic orifice aspect ratio on local heat transfer between a smooth flat plate and the impinging jet of air at different nozzle-to-plate distances. The following conclusions are drawn from this study:

1. Higher aspect ratio jets offer higher Nu values at low z/D values than axisymmetric orifices. For $z/D = 1$, elliptic jets offered 28% higher heat transfer rate in the stagnation region than the circular jet. Thus, high aspect ratio elliptic jets perform better cooling in the near-field region of the jet.
2. Circular jets produce a single peak in the Nu_{avg} vs. z/D plot, which lies in the mid-field region ($z/D = 6$ to 10). Contrary to this, elliptic jets ($AR = 10,14$) produce double peaks lying in near-field ($z/D = 1$ to 3) and mid-field regions ($z/D = 6$ to 10).
3. Axis switching is observed even for synthetic jets ejected from high aspect ratio ($AR = 10,14$) elliptic orifices.

Nomenclature

D	Orifice diameter[mm]
t	Orifice plate thickness[mm]
Nu	Nusselt Number
z/D	Dimensionless orifice to surface distance
r/D	Dimensionless radial distance
ε	Emissivity
Re	Reynolds number
V_{rms}	Root mean square amplitude [V]

T_s	Surface temperature of test foil [$^{\circ}\text{C}$]
T_a	Ambient temperature [$^{\circ}\text{C}$]
V	Voltage drop across foil [V]
I	Flowing current across foil [A]

References

1. Sharma P, Singh PK, Sahu SK, Yadav H (2021) A critical review on flow and heat transfer characteristics of synthetic jet. *Trans Indian Natl Acad Eng* [Internet]. Springer, pp 1–32. Retrieved from: <https://link.springer.com/article/https://doi.org/10.1007/s41403-021-00264-5>
2. Zuckerman N, Lior N (2006) Jet impingement heat transfer: physics, correlations, and numerical modeling. *Adv Heat Transf* 39
3. Smith BL, Glezer A (1998) The formation and evolution of synthetic jets. *Phys Fluids* 10:2281–2297
4. Bhapkar US, Srivastava A, Agrawal A (2014) Acoustic and heat transfer characteristics of an impinging elliptical synthetic jet generated by acoustic actuator. *Int J Heat Mass Transf Elsevier* 79:12–23
5. Gorman JM, Sparrow EM, Abraham JP (2014) Slot jet impingement heat transfer in the presence of jet-axis switching. *Int J Heat Mass Transf Pergamon* 78:50–57
6. Straccia JC, Farnsworth JAN (2021) Axis switching in low to moderate aspect ratio rectangular orifice synthetic jets. *Phys Rev Fluids Am Physic Soc* 6:1–26
7. Shi XD, Feng LH, Wang JJ (2019) Evolution of elliptic synthetic jets at low Reynolds number. *J Fluid Mech Cambridge Univ Press* 868:66–96
8. Zhong S, Garcillan L, Pokusevski Z, Wood NJ (2004) A PIV study of synthetic jets with different orifice shape and orientation. In: 2nd AIAA flow control conference, pp 1–13
9. Reodikar SA, Meena HC, Vinze R, Prabhu SV (2016) Influence of the orifice shape on the local heat transfer distribution and axis switching by compressible jets impinging on flat surface. *Int J Therm Sci Elsev Masson* 104:208–224
10. Gutmark EJ (1999) Flow control with noncircular jets. *Ann Rev Fluid Mech* [Internet]. 31:239–72. Retrieved from: <https://doi.org/10.1146/annurev.fluid.31.1.239>
11. Lee J, Lee SJ (2000) The effect of nozzle aspect ratio on stagnation region heat transfer characteristics of elliptic impinging jet. *Int J Heat Mass Transf* 43:555–575
12. Sharma P, Sahu SK, Yadav H (2022) Experimental investigation of flow and thermal characteristics of synthetic jet issuing from sharp- edged orifices. *Exp Heat Transf* [Internet]. Taylor & Francis, pp 1–25. Retrieved from: <https://doi.org/10.1080/08916152.2022.2105449>
13. Yogi K, Krishnan S, Prabhu SV (2021) Experimental investigation on the local heat transfer with an unconfined slot jet impinging on a metal foamed flat plate. *Int J Therm Sci* [Internet]. 169. Retrieved from: <https://www.sciencedirect.com/science/article/pii/S001793102033341X>
14. Coleman HW, Steele WG (2018) Experimentation, validation, and uncertainty analysis for engineers. John Wiley & Sons
15. Gil P Wilk J (2020) Heat transfer coefficients during the impingement cooling with the use of synthetic jet. *Int J Therm Sci Elsevier* 147:106132
16. Greco CS, Paolillo G, Ianiro A, Cardone G, de Luca L (2018) Effects of the stroke length and nozzle-to-plate distance on synthetic jet impingement heat transfer. *Int J Heat Mass Transf Elsevier* 117:1019–1031

Numerical Investigation of Exergy and Entropy Analysis for W/EG-Based Non-newtonian Hybrid Nanofluid for Helically Corrugated Tube Heat Exchanger



Ayush Painuly, Niraj K. Mishra, and Prabhakar Zainith

1 Introduction

A non-Newtonian fluid can be defined as those substances whose viscosity is a function of shear strain rate and the shear stress have a non-linear dependency on shear rate. These fluids are widely used in petroleum, pharmaceutical, food and chemical industries. Due to their nature, such fluids have a low Reynolds number as well as a high Prandtl number values [1], resulting in notably low heat transfer rates. Various heat transfer enhancement methods are effective in increasing the performance of the heat exchanger when dealing with these fluids. There are three general thermal performance enhancement classifications: passive, active and a combination of the two, of which, the more commonly used method is the passive method. Passive methods include employing different types of surface modification to increase the turbulence within the flowing fluid [2]. Modification of the heat transfer surface increases the heat transfer area as well as reduces the thickness of the boundary layer near the surface, thereby improving the heat transfer rate as well as reducing the size and operating cost of the heat exchanger.

2 Literature Review and Objective

Few researchers have compounded two or more techniques and observed the merits and demerits of using more than one passive method at a time. Ahmed et al. [3] experimentally and numerically studied SiO₂-water nanofluid inside a sinusoidal,

A. Painuly · N. K. Mishra (✉) · P. Zainith
Department of Mechanical Engineering, NIT Uttarakhand, Srinagar, Uttarakhand 246174, India
e-mail: nkm.iitg@gmail.com

trapezoidal and a plane channel at different volume fractions ranging from 0 to 1%. The work investigated that Nusselt number increases on rising the volume fraction of nanoparticles with a pressure drop penalty. Naphon and Wiriyasart [4] investigated the heat transfer and flow features of TiO_2 -water nanofluid inside a HCT in the presence of magnetic field and pulsating flow. The disturbance is created in the flow due to the corrugation followed by the magnetic field. The study suggested that the combined heat transfer technique can be used to cool electronic gadgets.

Several studies have been reported on entropy generation rate and exergy analysis using nanofluids through a corrugated passage. Fadodun et al. [5] numerically investigated entropy generation rate in SWCNT- H_2O flowing through an inwardly corrugated tube under turbulent conditions. The study considers the effect of volume fraction of nanoparticle, e/d_h ratio on Bejan number and rate of entropy generation. The author reveals that increment in the corrugation amplitude enhances viscous entropy generation but does not influence the thermal entropy generation much. Pavlovic et al. [6] experimentally investigated the exergy efficiency of TiO_2 , CuO , Cu and Al_2O_3 with water and oil as base fluids inside a corrugated absorber tube. The results indicated that the exergy efficiency is higher for oil-based nanofluids, while high thermal performance is achieved for water-based nanofluids. Moreover, CuO -oil nanofluid shows the maximum exergetic efficiency among all. Saleh and Sundar [7] investigated the effect of particle volume fraction and volume flow rates on entropy generation and exergy efficiency of Ni -water nanofluid under laminar conditions inside a corrugated plate heat exchange. The total entropy generation and exergy destruction decrease on increasing the particle concentration in the base fluid.

As per the published literature, exergy analysis of hybrid non-Newtonian nanofluid inside a helically corrugated tube has not been performed in the past. Most of the investigations have estimated the first law analysis which is not sufficient in the engineering applications as it only manifests the thermal performance and not the irreversibility associated with the process taking place. Whereas, the second law analysis evaluates the loss of work potential during the heat transfer process as well as the level of energy degraded. Thus, the present study focuses upon the second law analysis of TiO_2 - SiO_2 (20:80) hybrid nanoparticle mixed with water-ethylene glycol (60:40) to form a non-Newtonian hybrid nanofluid inside a helically corrugated tube under turbulent conditions. Thermal properties of the hybrid nanofluid have been calculated using correlations in the literature and then ANSYS FLUENT 19.0 is used to simulate the model for examining the effect of volume flow rate (Q) of the hybrid nanofluid, volume fraction (φ) of hybrid nanoparticles inside the base fluid and e/d_h ratio of the helically corrugated tube.

3 Materials and Methods

A schematic diagram of HCT section used in the current study is shown in Fig. 1. ANSYS FLUENT 19.0 is used to examine the rate of entropy generation and second law efficiency of fluid flow inside a HCT.

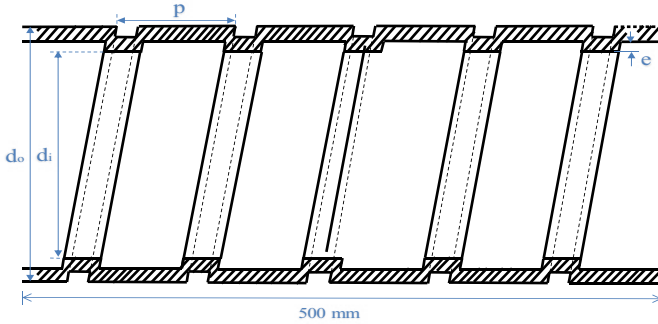


Fig. 1 Sectional view of HCT

Table 1 represents the geometrical parameters of the corrugated tubes used in the current study. Hybrid nanoparticle $\text{TiO}_2\text{-SiO}_2$ (80:20) is dispersed in a solution of water-ethylene glycol (60:40) to form a hybrid nanofluid. Hybrid nanofluid is passed through various HCTs at three different e/d_h ratios and three different nano particle mixing ratios under turbulent conditions over a range of volume flow rate (Q) of the nanofluid of 15 to 25 lpm. The results of HCT are compared to a smooth tube of length 500 mm and diameter of 22 mm.

A constant heat flux of 25 kW/m^2 is maintained on the copper wall. While using a corrugated tube, the effect of e/d_h ratio is more dominant than p/d_h . Therefore, the present study is focused upon the effect of e/d_h ratio of the HCT used. Moreover, increasing the concentration of SiO_2 in the hybrid nanofluid used increases the heat transfer rate which attains a maximum value at a volume ratio of 20:80 [8]. Table 2 represents the thermal properties of the base fluid and hybrid nanofluid at different volume fractions.

Moreover, the flow is assumed to be 3-D, unsteady and fully developed with fluid inlet temperature as 298 K. The hybrid nanofluid is incompressible, non-Newtonian

Table 1 Geometrical parameters of the ST and HCT

	HCT-1	HCT-2	HCT-3
L	500	500	500
d_i	19	20	20.5
d_o	26	27.5	28.5
e	1.10	1.54	1.98
p	6.6	6.6	6.6
e/d_h	0.05	0.07	0.09
p/d_h	0.30	0.30	0.30

Table 2 Thermal properties of base fluid and hybrid nanofluids at different volume fractions

	Base fluid	1%	3%	5%
C_p (J/kg.K)	3670	3585	3560	3524
ρ (kg/m ³)	1044	1060	1068	1123
K (W/mK)	0.4076	0.4896	0.5462	0.6081
μ (Ns/m ²)	0.00207	0.002122	0.002225	0.002329

and the model is assumed to be a single-phase mixing model. The thermal conductivity of the wall is constant throughout and is invariant with temperature. Acceleration due to gravity is 9.81 m/s² in the negative y-direction and heat transfer due to gravity is neglected.

3.1 Governing Equations

Nusselt number, Friction factor and Reynolds number are calculated as:

$$Nu = \frac{hd_h}{k} \quad (1)$$

$$f = \frac{\Delta P}{\frac{1}{2}\rho u^2 \left(\frac{L}{d_h}\right)} \quad (2)$$

Entropy generation rate can be determined by using Eq. (3).

$$\dot{S}_g = \dot{S}_f + \dot{S}_t \quad (3)$$

The frictional entropy generation rate (\dot{S}_f) and thermal entropy generation rate (\dot{S}_t) are determined by using the Eq. (4) and (5), respectively [9].

$$\dot{S}_f = \frac{8fL\dot{m}^3}{d_h^5(T_{out} - T_{in})(\pi\rho)^2} \ln \frac{T_{out}}{T_{in}} \quad (4)$$

$$\dot{S}_t = \frac{\dot{q}^2 d_h^2 L}{Nu.kT_{in}T_{out}} \quad (5)$$

The second law efficiency is defined as the ratio of exergy recovered to the exergy expanded. It is a helpful measure of effectiveness of a system that goes beyond the first law analysis constraints.

$$\eta_{II} = \frac{\text{ExergyRecovered}}{\text{ExergyExpanded}} = 1 - \frac{\text{ExergyDestruction}}{\text{ExergyExpanded}} \quad (6)$$

That is,

$$\eta_{II} = 1 - \frac{T_a \dot{S}_g}{\left(1 - \frac{T_a}{T_s}\right) \dot{q} \pi d_h L} \quad (7)$$

3.2 Grid Independence Test

The grid test is performed over HCT-2 using TiO₂-SiO₂-based W/EG non-Newtonian hybrid nanofluid ($\varphi = 1\%$). Table 3 shows the variation in Nusselt number with mesh elements at 15 lpm. The k- ϵ model is used to simulate the results with enhanced walled treatment. Six different mesh sizes are tested with 8.75×10^5 , 9.87×10^5 , 1.15×10^6 , 1.36×10^6 , 1.55×10^6 and 1.75×10^6 elements. On increasing the mesh elements beyond 5,203,188, Nusselt number increases by 0.085 and 0.114% for mesh elements 1.55×10^6 and 1.75×10^6 , respectively. So further increasing the mesh elements will only increase the simulation time with negligible changes in the Nusselt number. Typically, 1.36×10^6 mesh elements are chosen for the current fluid flow analysis using HCT-2 under turbulent conditions. The mesh close to the wall has been refined enough to properly capture the thermal and velocity boundary layers.

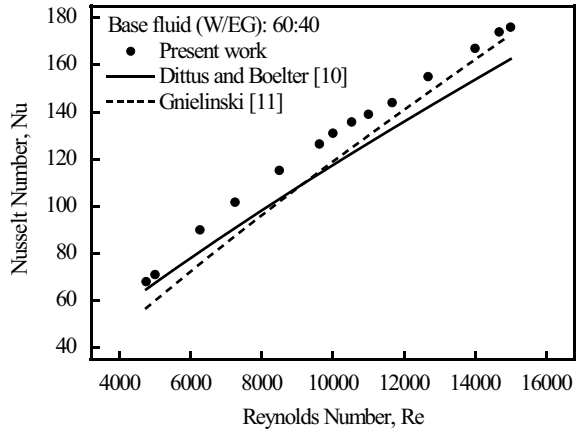
4 Results and Discussion

Entropy generation rate and second law efficiency have been investigated for a non-Newtonian hybrid nanofluid flowing through various HCTs under turbulent conditions. Numerical results have been validated from equations present in the previous literature [10, 11] using a base fluid inside a smooth tube (ST) for the Nusselt number and friction factor (Fig. 2).

Table 3 Grid Independence test at a volume flow rate of 15 lpm for HCT-2

<i>Nu</i>	Mesh elements					
	8.75×10^5	9.87×10^5	1.15×10^6	1.36×10^6	1.55×10^6	1.75×10^6
<i>HCT-2</i>	208.8	209.12	209.9	210.9	211.08	211.14

Fig. 2 Comparison of present work of the base fluid inside ST to other experimental data in the literature



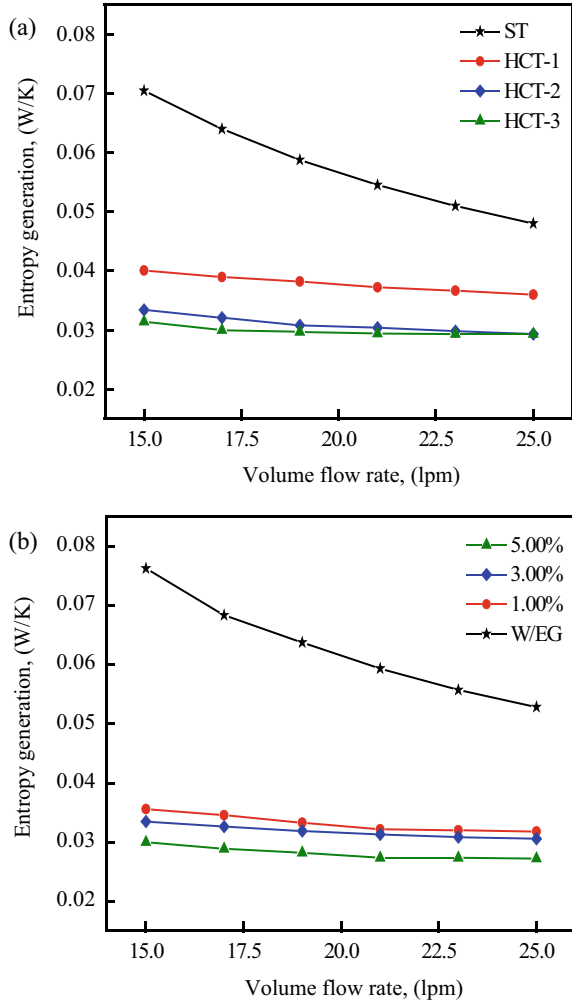
4.1 Rate of Entropy Generation

Herein, variation of rate of entropy generation with respect to Q , e/d_h ratio and ϕ has been discussed. Entropy generation rate is evaluated using Eq. (3) by adding rate of frictional entropy generation and rate of thermal entropy generation. Moreover, frictional entropy generation rate (\dot{S}_f) and thermal entropy generation rate (\dot{S}_t) are calculated using Eqs. (4) and (5), respectively. The data simulated from ANSYS FLUENT 19.0 is used to calculate (\dot{S}_f) and (\dot{S}_t) for the fluid flow. A constant heat flux of $25,000 \text{ W/m}^2$ is maintained over the walls of the HCT.

Figure 3a,b illustrates the entropy generation rate of hybrid nanofluids verses Q for a range of e/d_h ratio and ϕ , respectively. The total irreversibility is reduced by adding corrugation and employing hybrid nanofluids. It is a promising result from the point of view of the second law of thermodynamics. Moreover, greater corrugation heights and higher volume fractions show lower entropy generation rate. Thus, minimum entropy production of the HCT is at the condition, when $e/d_h = 0.09$, $\phi = 5\%$ and $Q = 25 \text{ lpm}$. Furthermore, \dot{S}_f increases by 75 to 160% with increase in e/d_h and Q of the hybrid nanofluid. As the value of e/d_h increases from 0.05 to 0.09, the value of friction factor increases due to increase in viscous losses and geometric resistance near the wall surface. The average increment in \dot{S}_f over smooth tube is 71.5, 115.2 and 151.1% for $e/d_h = 0.05$, 0.07 and 0.09, respectively. It further increases as the volume fraction of hybrid nanofluid increases in the base fluid. The increase in \dot{S}_f is about 7 to 38% depending upon ϕ and the Q of the fluid. As the incorporation of particles increases, the viscous property of the fluid increases significantly. This allows friction losses to dominate the flowing fluid and greatly increases the friction factor, resulting in increase in \dot{S}_f .

Unlike frictional entropy generation, thermal entropy generation rate decreases with the increase in e/d_h and ϕ . Due to uneven surface created by the increase in e/d_h ratio, the heat transfer is enhanced by increasing the turbulence and contact period of flowing fluid with the HCT. As a consequence, rate of thermal entropy

Fig. 3 Variation of entropy generation with **a** e/d_h ratio and **b** ϕ at different lpm



generation decreases by 27 to 56% on increasing the Q and e/d_h ratio. The average increment in \dot{S}_f is 35, 43.9 and 50.2% for $e/d_h = 0.05, 0.07$ and 0.09 , respectively. Moreover, on increasing ϕ , the temperature difference between the HCT wall and the mean fluid temperature decreases with further decrease in the \dot{S}_t . An increase in mean flow velocity pitches the turbulent flow intensity which increases the average Nusselt number and significantly reduces \dot{S}_t around 42 to 61% over a range of Q .

4.2 Second Law Efficiency

The second law efficiency increases with the corrugation height and volume flow rate. Exergy efficiency of a smooth tube and corrugated tubes with different corrugation height is shown in Fig. 4a. A decrease in entropy generation and irreversibility leads to an increase in η_{II} . According to the single-phase mixing model, where the fluid particles and nanoparticles have no relative motion, the fluid motion plays a major role in enhancing the heat transfer. It can be seen that the geometry of the HCT is such that it enhances the collision of fluid particles on the walls of HCT and the vortex flow within the corrugation ribs. This vortex motion of the fluid generates another overall swirl motion throughout the HCT, which leads to better heat transfer rate and lower entropy production rate. Moreover, at higher lpm, proper mixing of the fluid occurs due to stronger secondary flow. As secondary flow gets stronger, the rate of thermal entropy production decreases. Evidently, higher η_{II} is achieved at greater corrugation heights. It increases from 64.7 to 85.2% as smooth tube is replaced by HCT-3 at 25 lpm.

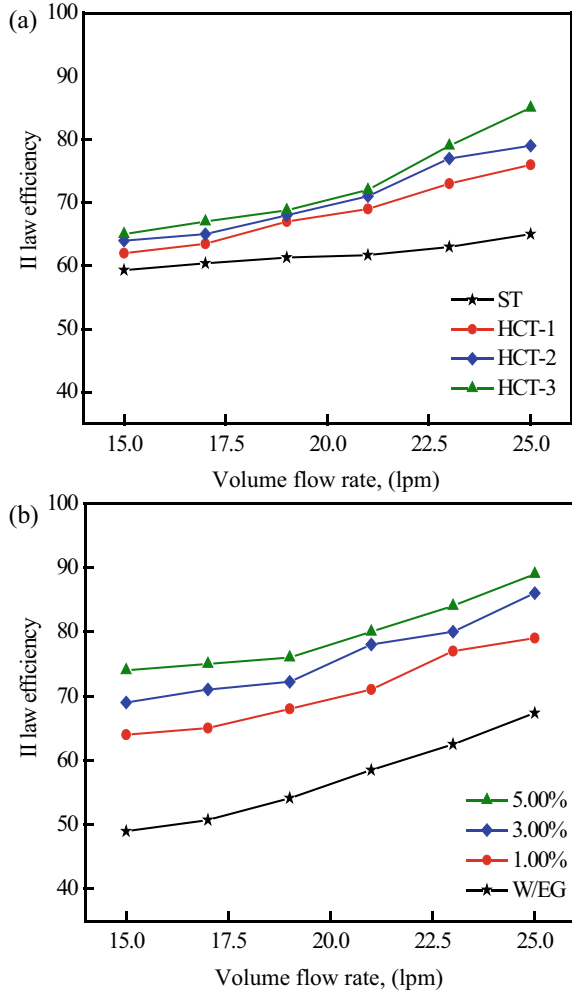
It further increases as the base fluid is replaced by hybrid nanofluids as shown in Fig. 4b. As the particle volume fraction within the base fluid increases, the rate of heat transfer within the nanofluid also increases. This further reduces the radial temperature gradient and increases the intensity of the collision of fluid with the HCT walls, making the temperature profile more uniform. Due to the more uniform temperature profile and enhanced heat transfer rate, the entropy production rate is lower at higher volume fractions. The mean increment in η_{II} with respect to the base fluid is about 24.4, 33.9 and 40.5% for $\varphi = 1, 3$ and 5, respectively. η_{II} enhances from 67.3 to 89.2% by employing hybrid nanofluid in place of base fluid inside a HCT at 25 lpm.

5 Conclusion

The entropy, exergy and II law efficiency of a water-ethylene glycol (60:40)-based $\text{TiO}_2\text{-SiO}_2$ hybrid nanofluid has been investigated numerically inside helically corrugated tubes under turbulent conditions. Variation of volume fraction of nanoparticles, volume flow rate and corrugation height are studied. From the numerical results, following conclusions can be made:

1. The thermal boundary layer gets disturbed due to corrugation, resulting in a drop in temperature gradient. Moreover, the profound use of nanofluids inside a corrugated tube reduces the irreversibility associated with the system.
2. The use of nanofluids inside a HCT reduces the rate of thermal entropy production, while increasing the frictional entropy generation rate. However, with this hybrid system, the total entropy of the system decreases.

Fig. 4 The II law efficiency versus volume flow rate at different **a** e/d_h ratio and **b** ϕ



3. Irreversibility due to friction losses increases on adding nanoparticles inside the base fluid, while it decreases as the volume flow rate of the hybrid nanofluid decreases under turbulent conditions.
4. The η_{II} increases to 51.2% by employing hybrid nanofluid concerning the base fluid at 25 lpm inside the HCT.

Nomenclature

ST Smooth tube–

<i>HCT</i>	Helically corrugated tube–
<i>l</i>	Lengthmm
<i>d</i>	Diametermm
<i>d_h</i>	Hydraulic diametermm
<i>p</i>	Pitch of HTCmm
<i>e</i>	Corrugation heightmm
<i>f</i>	Friction factor–
<i>Nu</i>	Nusselt number–
<i>T</i>	TemperatureK
<i>T_a</i>	Ambient temperatureK
<i>t</i>	Temperature ⁰ C
<i>h</i>	Heat transfer coefficientW/m ² K
<i>k</i>	Thermal conductivityW/mK
<i>u</i>	Velocitym/s
\dot{S}_g	Rate of entropy generationW/K
<i>lpm</i>	Liter per minutel/min
<i>q</i>	Heat fluxkW/m ²
ϕ	Volume fraction–
ρ	Density, kg/m ³ kg/m ³

References

1. Chhabra RP, Richardson JF (2011) Non-Newtonian flow and applied rheology: engineering applications. Butterworth-Heinemann
2. Zainith P, Mishra NK (2022) Evaluation of thermal performance of conically shaped micro helical tubes using non-Newtonian nanofluids-a numerical study. *J Therm Sci Eng Applicat* 14(8):1–30
3. Ahmed MA, Yusoff MZ, Ng KC, Shuaib NH (2015) Numerical and experimental investigations on the heat transfer enhancement in corrugated channels using SiO₂–water nanofluid. *Case Stud Therm Eng* 6:77–92
4. Naphon P, Wiriyasart S (2018) Pulsating flow and magnetic field effects on the convective heat transfer of TiO₂-water nanofluids in helically corrugated tube. *Int J Heat Mass Transf* 125:1054–1060
5. Fadodun OG, Amosun AA, Okoli NL, Olaloye DO, Ogundeji JA, Durodola SS (2021) Numerical investigation of entropy production in SWCNT/H₂O nanofluid flowing through inwardly corrugated tube in turbulent flow regime. *J Therm Anal Calorim* 144(4):1451–1466
6. Pavlovic S, Bellos E, Loni R (2018) Exergetic investigation of a solar dish collector with smooth and corrugated spiral absorber operating with various nanofluids. *J Clean Prod* 174:1147–1160
7. Saleh B, Sundar LS (2021) Experimental study on heat transfer, friction factor, entropy and exergy efficiency analyses of a corrugated plate heat exchanger using Ni/water nanofluids. *Int J Therm Sci* 165:106935
8. Painuly A, Mishra NK, Zainith P (2022) Heat transfer enhancement in a helically corrugated tube by employing w/eg based non-newtonian hybrid nanofluid under turbulent conditions. *J Enhanc Heat Transf* 29(1):1–25
9. Jarungthammachote S (2010) Entropy generation analysis for fully developed laminar convection in hexagonal duct subjected to constant heat flux. *Energy* 35(12):5374–5379

10. Dittus FW (1930) Heat transfer in automobile radiators of the tubler type. Univ Calif Pubs Eng 2:443
11. Gnielinski V (1976) New equations for heat and mass transfer in turbulent pipe and channel flow. Int Chem Eng 16(2):359–368

Experimental and Numerical Investigation of a Device for Localized Cooling



S. V. H. Nagendra and D. V. S. Bhagavanulu

1 Introduction

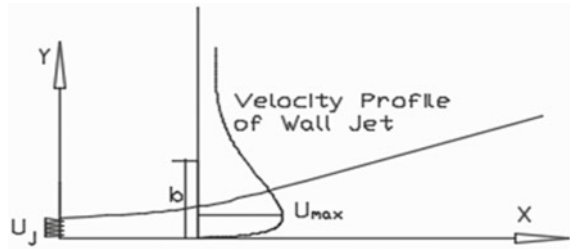
Air comfort has turned into a fundamental need in the present days. The heating or cooling load for any design is assessed based on the volume of the space considered. Mostly, the whole space does not require such consideration [1, 2]. There is targeted zone of the space, where the comfort necessity is really required. If the condition can be controlled or kept up just in these required areas of the space at that point, an exceptional amount of energy can be spared. In this paper, numerical simulation and experimental results have been presented. Wall-bounded flow, generally known as wall jet, is investigated [3]. For clarity, it is referenced that the outcome acquired from the code has been validated by experiments. The wall jet is a term used for a fluid flow when it passes over a surface issued from a nozzle or an orifice [3]. The configuration used in the current investigation is plane wall jet. It is also defined as when fluid flow tangentially spread over a surface issued from an orifice or a nozzle, and then it is termed as plane wall jet (Fig. 1).

2 Methodology

Plane wall jet is generated using a jet tunnel with a velocity of 2 m/s and volumetric flow rate of 0.045 m³/s. The Reynolds number at the exit of the orifice is 20,242. A curved plate of radius 3 m with an initial straight portion of length 5 times of characteristic length is taken. A total pressure probe connected to a micro manometer

S. V. H. Nagendra · D. V. S. Bhagavanulu (✉)
Department of Mechanical Engineering, Gyan Ganga Inst. of Technology and Sciences,
Jabalpur 482001, India
e-mail: bhagavanulu@gmail.com

Fig. 1 Configuration of a plane wall jet system



records the velocity values at different sections, namely, 1, 2, 3, 4, 5, 10, 15, 20 h. The probe is connected to a traverse apparatus with a span of 1.4 m and is moved in all the three directions. The micro manometer has the range of 0–5 m/s with 1.99–199.9 Pa. The temperature is recorded using single point thermistor-based probe with a composition of NiCr-Ni (Make: testo). The range of the thermometer is –50 to 150 degree Celsius with ± 0.1 °C accuracy.

The numerical analysis is performed on ANSYS fluent academic research version. The physical model implemented to capture the flow dynamics is K-Epsilon with standard wall function [1]. Convergence criteria are $1e-4$ and $1e-6$ for N-S and energy equation, respectively. Grid size is optimized on the basis of grid independence test, which is 715,246. The inflation layers taken are thirty and the boundary layer thickness is approx. 16 mm. Approximately 1742 iterations were taken for convergence. A hot body is placed at the room temperature of 300 K. The temperature of incoming fluid is maintained at 288 K. The thermal values are recorded at two different stations: one on the hot body and a 12×12 virtual grid of size 2.4×2.0 m defined in front of the hot body.

3 Design Aspects

The design of the device is done on the cad tool namely Autodesk inventor educational version. The important parts of the device assembly are (a) horizontal plate, (b) curved surface attached in front of horizontal plate, (c) scissor jack mechanism to control the length of horizontal plate, (d) stepper motors to drive the scissor mechanism and to control the curvature radius of the curved surface, (e) flexible supports for curved surface, (f) ceiling attachment support with height adjustment grooves, (g) orifice with aspect ratio adjustment mechanism. The parts from ‘a’ to ‘f’ are shown in Fig. 2 and part ‘g’ is shown in Fig. 3. Front view of the device is shown in Fig. 3. The device works as follows: a low temperature fluid flows over the horizontal surface ‘a’ and then passes over a curved surface ‘b’. The fluid flows over the curved surface and then concentrated over a localize zone. The relative position of horizontal surface ‘a’ and curved surface ‘b’ controlled by the scissor jack mechanism ‘c’ and flexible

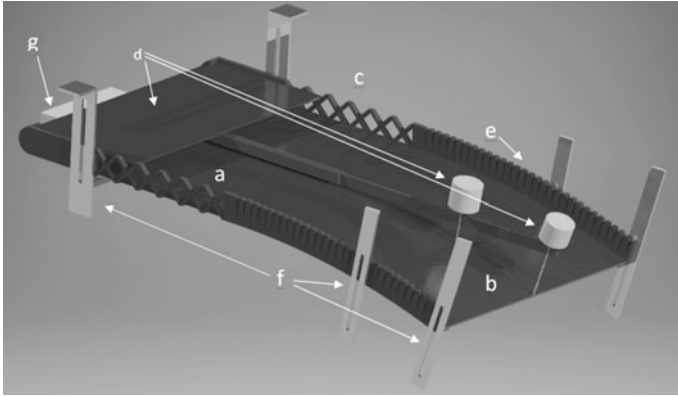
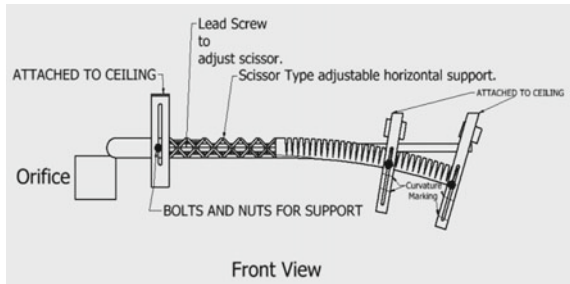


Fig. 2 The 3d cad model of localized cooling device

Fig. 3 The front view of the mechanism with annotations

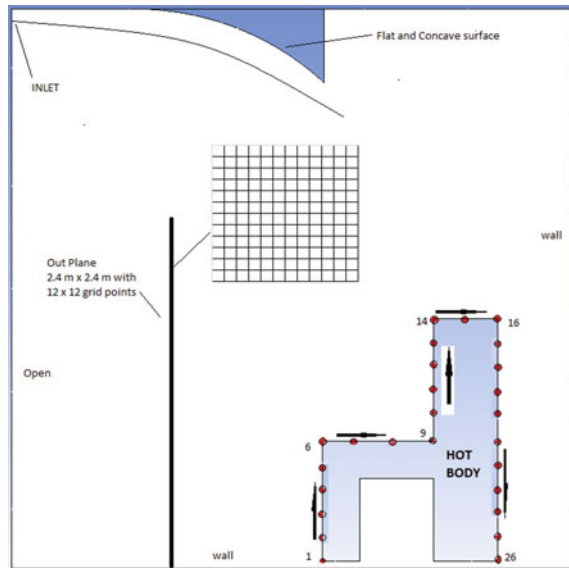


support 'e' will help to target the fluid over the desired zone. The aspect ratio will control the incoming velocity and horizontal distance of plane surface and curvature radius of the curved surface will control the decay of velocity. Both the surface will be insulated and polished, so that there will be no heat transfer [4].

4 Results

Experimental and numerical results are presented in the form of graphs and contours. The computational domain is shown in the Fig. 4. The domain physical resembles a $3.04 \times 3.04 \times 3.04$ m standard room size.

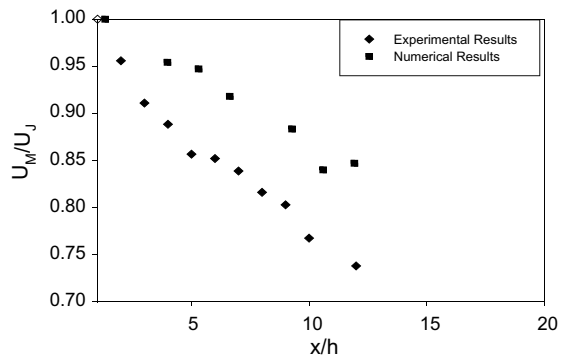
Fig. 4 The experimental setup with temperature points



4.1 Maximum Velocity Decay

Figure 4 shows the maximum velocity decay, which is plotted between U_m/U_j and x/h . It is observed that the potential core region existed upto 4 h. The flow does not have radial decay region as the total length of the surface is not sufficient and existed only up to 10 h. Characteristic decay region exists from 5 to 10 h as observed in both the cases [5]. Thereafter, the flow changes from wall jet to free jet. The decay rate is slower in case of numerical results, which is $n -0.34$, whereas the experimental results are much faster, i.e., -0.37 compared to the numerical results (Fig. 5).

Fig. 5 The Decay of Maximum velocity in the direction of the flow



4.2 Mean Velocity Profiles and Contours

Figures 6 and 7 show the experimental and numerical results of mean velocity profiles. It shows good agreement with existing literature Glauert [3, 6]. The maximum velocity point shows a little shift towards the wall side in the concave region when compared to the plane surface. And it is due to the centripetal force caused on the surface of concavity. It is found to be $y/b = 0.35$ when compared to plane surface, that is $y/b = 0.37$. Figure 8 shows how to the lateral velocity profile at station 15 h and compares it to free jet solution and found to be in good correlation. At this station, the jet converts from wall jet to free jet. The velocity profiles are not drawn after this section, as it does not correlate to any standard equation.

The velocity contour is represented in the XY plane and YZ plane. Levels of contours are taken as 20. Streamline is also presented on the centre plane with 250 seed points equally spaced on the face. Figure 9 shows that velocity distribution on

Fig. 6 Experimental results of the mean velocity profiles in the longitudinal direction (1–10 h)

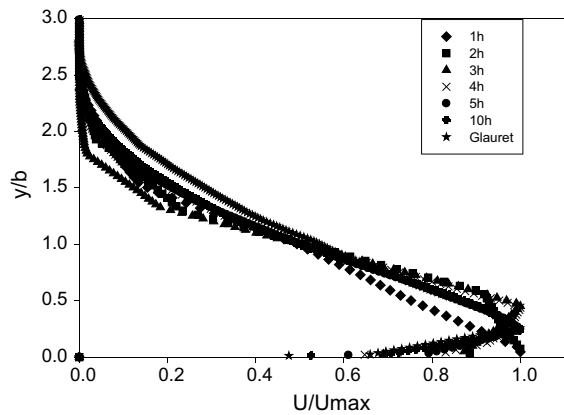


Fig. 7 Numerical results of the mean velocity profiles in the longitudinal direction (1–10 h)

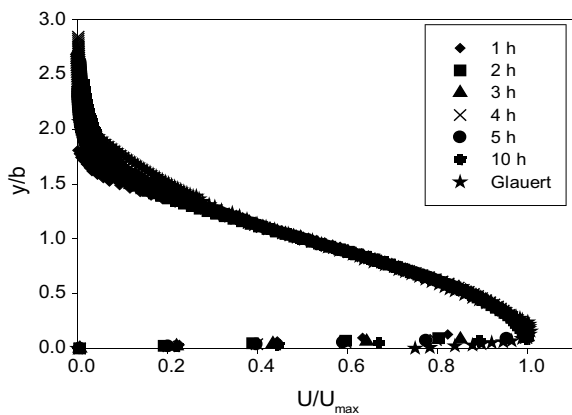
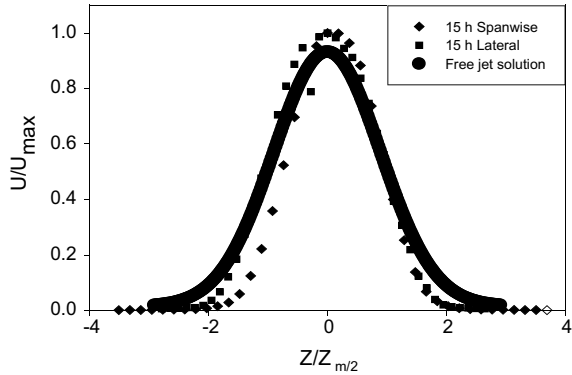


Fig. 8 The experimental values mean velocity profiles on spanwise and lateral direction at 15 h



the centre plane and can be seen that the fluid passing over the curved surface acts tangentially on a specific zone, where the hot body is placed. It can also be observed that the fluid velocity is de-accelerating sufficiently near the target, which results in ergonomic air velocity required to avoid any discomfort in case the hot body is taken as a human body.

Figures 10, 11, 12, 13 show the velocity contours on the Y–Z plane normal to the surface in direction of flow. It clearly shows that whilst fluid passes over the surface, it shows the characteristics of wall jet, but when it leaves the surface, it starts to transform into free jet. It is also seen that the jet is growing more in lateral direction i.e. in Z direction more when compared to the longitudinal direction.

Figure 14 shows the streamlined profile of fluid on the centre plane. It shows good agreement with the existing literature of fluid flow dynamics on such physical domain.

Fig. 9 Velocity contour on XY plane

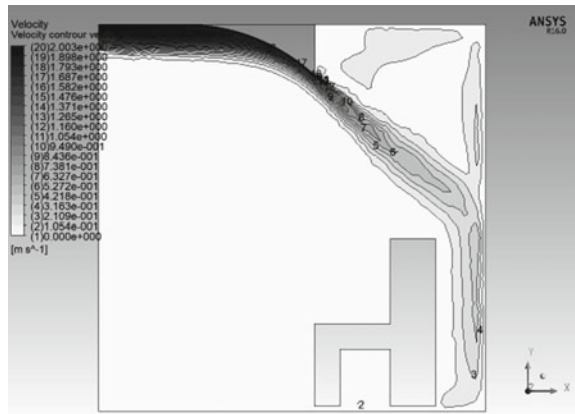


Fig. 10 Velocity contour on YZ plane at 1 h



Fig. 11 Velocity contour on YZ plane at 3 h



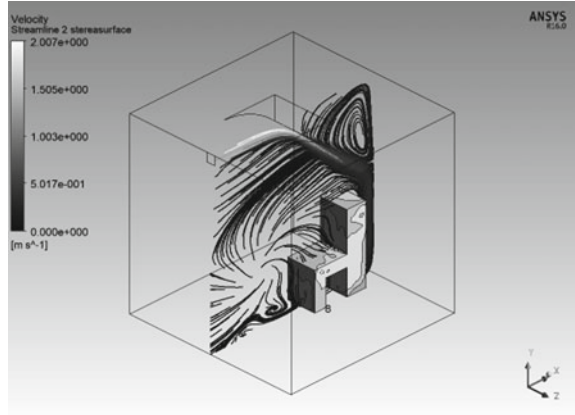
Fig. 12 Velocity contour on YZ plane at 5 h



Fig. 13 Velocity contour on YZ plane at 15 h



Fig. 14 Streamline velocity profile on XY plane



4.3 Growth of Half Width

Figure 15 shows the half-width growth on the longitudinal direction. It is plotted between b/h and x/h . The numerical results are slower and are about 0.027 whereas the experimental results show 0.034 linear growth rate constant. The lateral growth rate will be minimum twice the rate of longitudinal growth rate [3], which is out of the scope of measurement in the current measurements.

Fig. 15 The growth scales of the wall jet in longitudinal direction

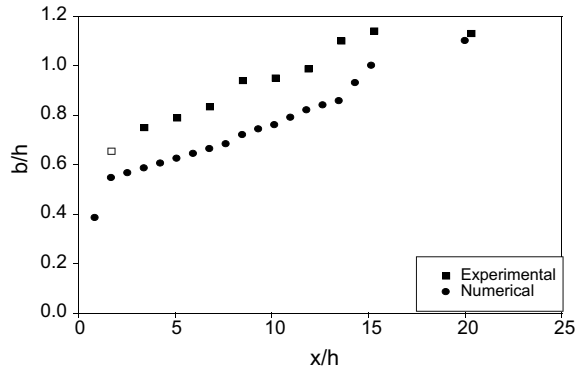
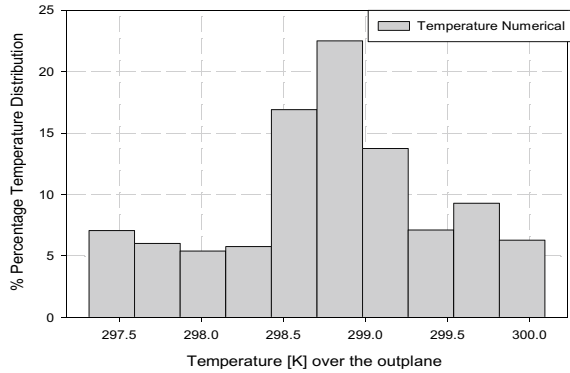


Fig. 16 Numerical results of percentage temperature distribution over the 12×12 grid plane



4.4 Temperature Distribution

Figures 16 and 17 show the percentage distribution of temperature on the plane of inspection as shown in Fig. 4. Numerical results show that average temperature is about 298.7 K. About 53% of the investigation plane shows temperature range of 298.5–299 K in the numerical results. The experimental results show the range of 299.8–300.4 K, which is about 51%.

Figure 18 shows the temperature values at 26 different points located on the hot body as defined in Fig. 4. Wall adjacent temperature is recorded and calculated and shown in the form of graph. It is clearly observed that numerical results show lower temperature when compared to experimental results. The average temperature of 26 points near the wall of hot body is 300.3 K in numerical results, whereas it is 307 K in the case of experimental results.

The contour of temperature is drawn on XY plane and YZ plane, respectively. Figure 19 shows the temperature distribution on the centre plane. It shows that there is significant decrease in temperature of hot body from 310 to 303.6 K.

Figures 20, 21, 22 discussed on the distribution temperature over the YZ plane, at 10, 15 and 20 h. The contour shows that the temperature near the body is high and reducing as the air moves away from the hot body with increase in temperature, which confirms the heat transfer from the surface of hot body. The same can be seen in Fig. 23, which shows streamline with temperature as variable.

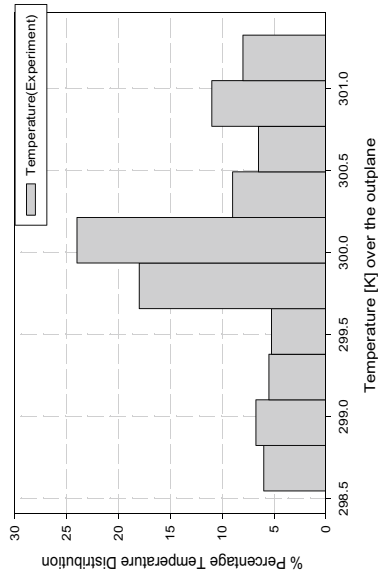


Fig. 17 Experimental results of percentage temperature distribution over the 12×12 grid plane

Fig. 18 Temperature over the hot body at different points

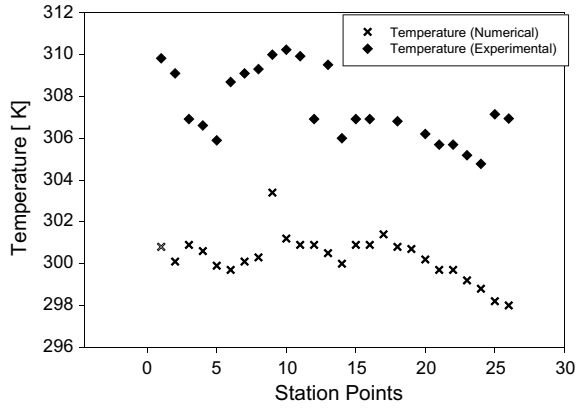


Fig. 19 Thermal contour on XY plane

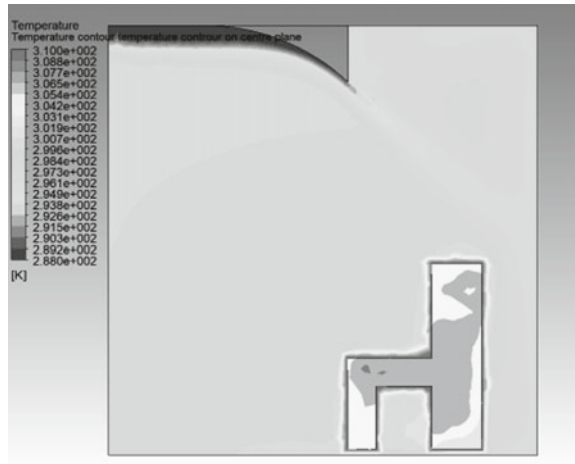


Fig. 20 Thermal contour on YZ plane at 10 h

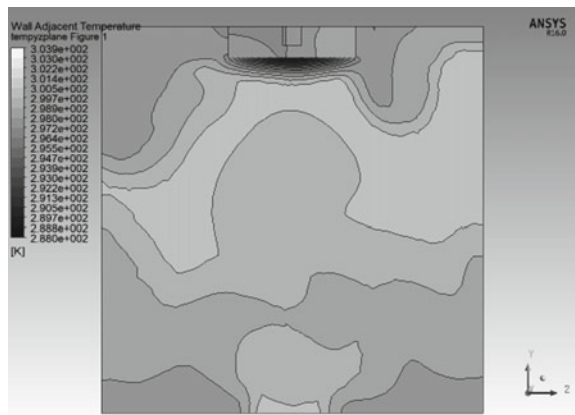


Fig. 21 Thermal contour on YZ plane at 15 h

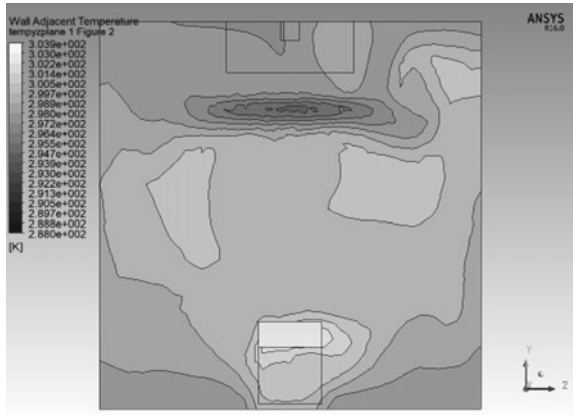


Fig. 22 Thermal contour on YZ plane at 20 h

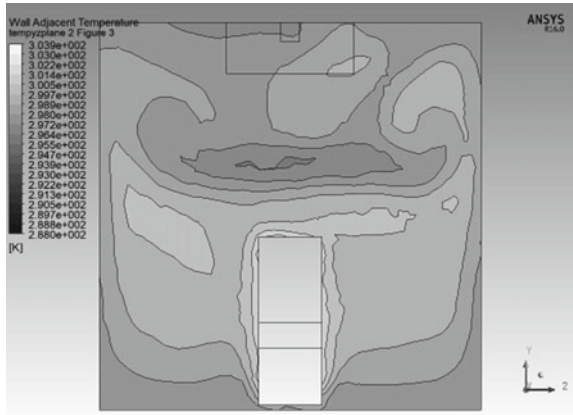
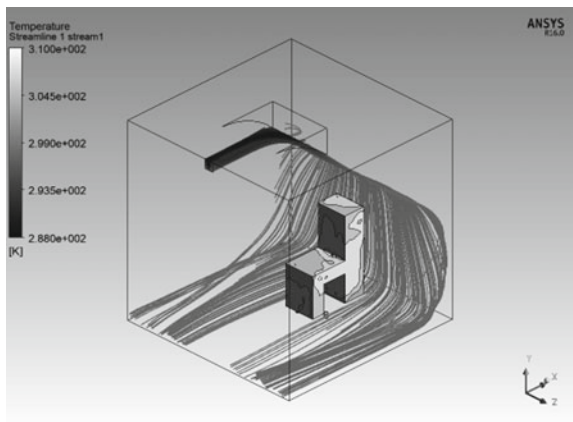


Fig. 23 3D streamline representation with temperature variable



5 Conclusion

The investigation gives an appreciable overview of the dynamics of the fluid over the design. It is observed that as the design is capable of concentrating the fluid over the hot body, convective heat transfer occurs resulting in lowering the temperature. The mean velocity profiles agree well with Glauert. The maximum velocity point has a slight shift near to the wall in the concave region. Decay exponent follows the power law. The half-width scale follows the linear behaviour of growth. The lateral spread of the jet agrees with free jet configuration.

The longitudinal and lateral growth of jet play an important role in the heat transfer. As the width increases, the surfaces of the hot body in contact with the cold fluid will increase, which results in the increase in average heat transfer. By lowering the aspect ratio of orifice, the half-width growth will reduce in the longitudinal direction due to the centripetal effect of the concave surface, but the lateral growth will be higher when compared to longitudinal growth. The decay of maximum velocity also plays an important role in deciding the aspect ratio. As the aspect ratio of orifice decreases, the decay of velocity will also slow down. For the comfort velocity, the optimum aspect ratio has to be set in the present case, that is 1.0. So to control the flow, three parameters have to be adjusted, which are aspect ratio, the horizontal length of plate and radius of the curved surface. Further, the numerical results exhibit that the system efficiently concentrating the fluid in the desired direction. The velocity distribution over the plane also correlates well with the wall jet flow and free jet behaviour.

References

1. Heschl C, Sanz W, Klanatsky P (2005) Implementation and comparison of different turbulence models for three dimensional wall jets with FLUENT CFD Forum, Bad Nauheim
2. Srivajana W (2003) Effect of air velocity on thermal comfort in hot and humid climates. *J Sci Technol* 8
3. Glauert MB (1956) The wall jet. *J Fluid Mech* 1:625–643
4. Nagenda SVH, Nanda Prasant, Bhagavanulu DVS (2019) A System for cooling a space. Retrieved from <https://ipindiaservices.gov.in/PublicSearch/PublicationSearch/PatentDetails>
5. Nagendra Prasant Nanda SVH, Bhagavanulu DVS (2017) Numerical study of 3-dimensional wall jet on curved surfaces. *Int J Appl Eng Res* 5604–5609
6. Nagendra SVH, Bhagavanulu DVS, Nanda P (2017) Computational study of three dimensional wall jet on concave surface. In: Saha A, Das D, Srivastava R, Panigrahi P, Muralidhar K (eds) *Fluid mechanics and fluid power—contemporary research lecture notes in mechanical engineering*. Springer, New Delhi

Study of MHD Stagnation Point Flow of Casson Fluid with Non-linear Radiation and Non-uniform Heat Source



Snehal D. Patel and Harshad. R. Patel

1 Introduction

The research area in the direction of non-Newtonian fluids has received much attention in recent years. The reason behind the study is its numerical practical uses in the fields of engineering and industry, particularly, crude oil extraction process from petroleum products. The various flow problems involving the variety of non-Newtonian fluids have been studied by several researchers. In Newtonian fluid models, the connection between stress and shear strain rate is linear, in contrast to non-Newtonian fluids' claim that it is non-linear. In terms of investigation of flow field characteristic, comparing non-Newtonian fluids to Newtonian fluids is complex as well as challenging just because of mathematical modelling that produces the highly non-linear PDEs. The different non-Newtonian fluids models developed periodically as per the need and demand of various industries. Out of some well-known fluids models, the Casson fluid model demonstrates yield stress in the constitutive equation and depicts shear thinning. In order to forecast the flow behavior, Casson [1] invented the Casson fluid in 1959. Casson fluids include honey, tomato sauces, jellies, concentrated fruit liquids and human blood. For the mathematical modelling of such types of problems, the researchers have employed this model [2, 3]. Bird et al. [4] and Fung [5] provided descriptions of the equations for the Bingham plastic fluid and Casson fluids, respectively. The flow of non-Newtonian fluids, when heat transfer is taking place, is a crucial topic of research. The authors [6] considered the flow in porous medium. In chemical industries, pharmaceutical industries, biological industries and food industries, understanding the heat transfer characteristics of such fluids moving through different geometrical shapes is crucial. Irvine and Karni [7] have considered rheological property measurements, whereas Lawal and Majumdar [8] studied the effect of viscous dissipation. For a variety of geometries

S. D. Patel (✉) · Harshad. R. Patel
Department of Mathematics, UVPCE Ganpat University, Mehsana, India
e-mail: sdp01@ganpatuniversity.ac.in

and flow conditions, the Casson fluid problems with energy equation were explored by many researchers periodically [9–16]. The investigation of stretching sheet has received a lot of attention due to their importance in various industries for manufacturing process like plastic sheet production, paper and polymer production, petroleum production etc. One of the most crucial stages in above said process is the heat transfer characteristic in flow problem because in such procedures, the cooling rate during this process is very import as far as the quality of final product is concerned. The key parameter which is used to manage the cooling rate is the MHD parameter. Since the joint phenomenon of heat and mass transfer problems with chemical reactions is also important in many industrial production processes. First introduce the idea of boundary layer flow on stretched surface proposed by Crane [17]. Many researchers [18–25] have extended this pioneering work of Crane by taking into account diverse physical circumstances and various fluids. Kandasamy et al. [26] discussed thermal stratification of MHD flow in stretched surface. Later on, Cortell [27] reported numerical analysis in viscoelastic fluid flowing under the effect of a porous stretching sheet. The 2D MHD Maxwell flow discussed by Hayat [28] and the HAM method are employed to solve flow equations. Similar kind of work was done by considering thermal radiation by [29–31]. In many physical problems, the importance of heat generation or absorption is very crucial. The exponential heat source has several uses in both business and engineering. There are many industrial applications and processes, such as nuclear gas turbine, missiles, propulsion devices and air crafts where radiative heat transfer is frequently used. In space technology, it is crucial to understand how different flows are affected by radiation from heat transfer. Animasaun et al. [32] discussed HAM method for similar research works. Ali [33] reported heat generation and heat absorption by giving analytic solution of MHD fluid flow, which is continuously moving vertical permeable surface. The non-linear thermal radiation effect in the MHD flow model explained by [34, 35]. The variable heat source and sink of MHD flow past over different surfaces were discussed by Prakash and Kumar [36, 37] in their study. Sivasankaran et al. [38] explained thermal radiation and irregular heating on MHD Casson fluid by numerical.

2 Mathematical Formulation

We considered 2D steady laminar bio-convective stagnation point MHD flow through porous media. We suppose that the fluid's velocity will be $u_w(x) = ax$. In addition to this, T_w is fluid's temperature and C_w is the fluid's concentration at $y = 0$. In Fig. 1, the co-ordinate x -axis is considered parallel to surface and y -axis is taken perpendicular to it. The physical sketch of the problem (Fig. 1) depicts the magnetic field B_0 , which is applied to the perpendicular direction of x - axis. The Casson fluid's constitutive equation can be expressed as:

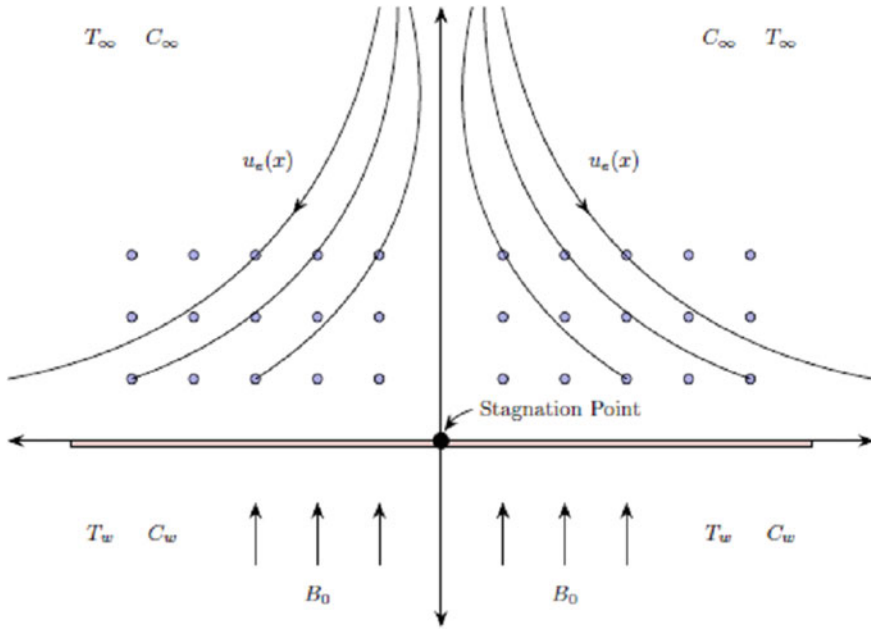


Fig. 1 Sketch of the problem

$$\tau_{ij} = \begin{cases} 2\left(\mu B + \frac{P_y}{\sqrt{2\pi}}\right)e_{ij} & \pi > \pi_c \\ 2\left(\mu B + \frac{P_y}{\sqrt{2\pi_c}}\right)e_{ij} & \pi < \pi_c \end{cases} \quad (1)$$

In this equation, the value of P_y is given by

$$P_y = \frac{\mu B \sqrt{2\pi}}{\gamma} \quad (2)$$

According to Batchelor’s [39] definition of viscosity, for Newtonian systems is mathematically expressed as below.

$$\tau^* = \frac{\partial u}{\partial y} \quad (3)$$

For Non-Newtonian Casson fluid flow, we considered $\pi > \pi_c$

$$\mu = \mu_B + \frac{P_y}{\sqrt{2\pi}} \quad (4)$$

The set of flow equations is as below:

$$\frac{\partial u}{\partial x} + \frac{\partial v}{\partial y} = 0 \quad (5)$$

$$u \frac{\partial u}{\partial x} + v \frac{\partial u}{\partial y} = u_e \frac{du_e}{dx} + \frac{\mu \left(1 + \frac{1}{\gamma}\right)}{\rho} \frac{\partial^2 u}{\partial y^2} - \frac{\sigma B_0^2}{\rho} + g\beta_C(C - C_\infty) - \frac{\mu\phi}{\rho k'}(u_e - u) + g\beta_T(T - T_\infty) \quad (6)$$

$$u \frac{\partial T}{\partial x} + v \frac{\partial T}{\partial y} = \left(\frac{k_2}{\rho c_p}\right) \frac{\partial^2 T}{\partial y^2} + \left(\frac{\sigma B_0^2}{\rho c_p}\right) u^2 - \frac{1}{\rho c_p} \frac{\partial q_r}{\partial y} + q''' \quad (7)$$

$$u \frac{\partial C}{\partial x} + v \frac{\partial C}{\partial y} = \frac{D_T}{T_w} \frac{\partial^2 T}{\partial y^2} + D_B \frac{\partial^2 C}{\partial y^2} - K(C - C_\infty) \quad (8)$$

The problem's suitable boundary conditions are given by

$$\begin{aligned} -k_2 \frac{\partial T}{\partial y} &= h_f(T_f - T), u = u_w = ax^n, C = C_w, v = 0 \text{ as } y \rightarrow 0 \\ T &\rightarrow T_\infty, u \rightarrow u_e = bx, C \rightarrow C_\infty \text{ as } y \rightarrow \infty \end{aligned} \quad (9)$$

For radiation, we may write the Rosseland approximation [40] expression as below.

$$q_r = -\frac{16\sigma^*}{3k^*} T^3 \frac{\partial T}{\partial y} \quad (10)$$

We differentiate Eq. (10) with respect to y

$$\frac{\partial q_r}{\partial y} = -\frac{16\sigma^*}{3k^*} \left[3T^2 \frac{\partial T}{\partial y} + T^3 \frac{\partial^2 T}{\partial y^2} \right] \quad (11)$$

By putting the value of Eq. (11) in the Eq. (7)

$$\begin{aligned} u \frac{\partial T}{\partial x} + v \frac{\partial T}{\partial y} &= \left(\frac{k_2}{\rho c_p}\right) \frac{\partial^2 T}{\partial y^2} + \left(\frac{\sigma B_0^2}{\rho c_p}\right) u^2 \\ &+ \frac{1}{\rho c_p} \frac{16\sigma^*}{3k^*} \left[3T^2 \frac{\partial T}{\partial y} + T^3 \frac{\partial^2 T}{\partial y^2} \right] + q''' \end{aligned} \quad (12)$$

The last term in Eq. (3) represents the irregular heat source and heat sink [41], which is mathematically written as

$$q''' = \frac{k_2 u_w(x)}{x\nu} [A_1(T_w - T_\infty) f' + B_1(T - T_\infty)] \quad (13)$$

One thing is clear that if $A_1 > 0, B_1 > 0$, then it is the case of internal heat source. If $A_1 < 0, B_1 < 0$, then it is the case of heat sink.

By introducing following similarity transformations, the set of revised form of governing equations, which is dimensionless is as below.

$$\eta = \sqrt{\frac{a(n+1)}{2\nu}} x^{\frac{n-1}{2}} y, T = T_\infty\{\theta(\theta_w - 1)\}, C(\eta) = \frac{C - C_\infty}{C_w - C_\infty}$$

$$u = ax^n F'(\eta), v = \sqrt{\frac{a(n+1)}{2\nu}} x^{\frac{n-1}{2}} \left[F(\eta) + \frac{n-1}{n+1} \eta F'(\eta) \right] \tag{14}$$

As a result, the dimensionless form of all the governing equations mentioned above is provided by

$$\left(1 + \frac{1}{\gamma}\right) F''' + F''F - \left(\frac{2n}{n+1}\right) f'^2 + \frac{2\lambda}{n+1} \left(\theta + \overset{\vee}{N} C\right) - \frac{2}{n+1} \left(M^2 + \frac{1}{k_1}\right) (1 - F') + A^2 = 0 \tag{15}$$

$$\theta'' + Nr \left[\{1 + (\theta_w - 1)\theta\}^3 \theta'' + 3(\theta_w - 1)\theta'^2 \{1 + (\theta_w - 1)\theta\}^2 \right] + Pr(F\theta' - \theta F') + Pr E_c M^2 F'^2 + A^* F' + B^* \theta = 0 \tag{16}$$

$$C'' + Sc(FC' - CF') + ScSr\theta'' - K_r S_c C = 0 \tag{17}$$

The relevant boundary conditions are

$$F(\eta) = 0, F'(\eta) = 1, C(\eta) = 1, \theta'(\eta) = 1 \text{ as } \eta \rightarrow 0$$

$$F'(\eta) \rightarrow A, C(\eta) \rightarrow 0, \theta(\eta) \rightarrow 0 \text{ as } \eta \rightarrow \infty \tag{18}$$

Different appropriate parameters namely are given below,

$$\lambda = \frac{Gr_x}{Re_x^2}, \overset{\vee}{N} = \frac{Gr_x^*}{Gr_x}, Gr_x = \frac{g\beta_T(T_w - T_\infty)x^3}{\nu^2}, Gr_x^* = \frac{g\beta_C(C_w - C_\infty)x^3}{\nu^2},$$

$$M^2 = \frac{\sigma B_0^2}{a\rho x^{n-1}}, Nr = \frac{16\sigma^* T_\infty^3}{3k^* k_2}, \frac{1}{Pr} = \frac{k_2}{\rho c_p}, A = \frac{b}{a}, Sc = \frac{\nu}{D_B},$$

$$\frac{1}{k_1} = \frac{\mu\theta}{k'}, Sr = \frac{D_m K_T(T_w - T_\infty)}{\nu(C_w - C_\infty)}, D_f = \frac{D_m K_T(C_w - C_\infty)}{\nu c_s c_p(T_w - T_\infty)}$$

3 Solution of the Problem by HAM Method

The aforementioned ODE Eqs. (15) to (17), along with conditions (Eq. 18), the HAM is employed for finding the solution which was initially suggested by Liao [42]. To establish the permitted range of convergence for the series solution, the appropriate \hbar -curve is plotted. The range of these \hbar -curves is also displayed below. The auxiliary linear operators and few initial guesses needed in order to get the HAM solution are listed below. The set of initial guesses is;

$$F_0(\eta) = \eta A + (1 - A)(1 - e^{-\eta}) \quad (20)$$

$$\theta_0(\eta) = e^{-\eta} \quad (21)$$

$$C_0(\eta) = e^{-\eta} \quad (22)$$

The set of linear operators is

$$L_F = \frac{\partial^3 F}{\partial \eta^3} - \frac{\partial F}{\partial \eta} \quad (23)$$

$$L_\theta = \frac{\partial^2 \theta}{\partial \eta^2} - \theta \quad (24)$$

$$L_C = \frac{\partial^2 C}{\partial \eta^2} - C \quad (25)$$

Which are satisfying the below given equations.

$$L_F(a + be^\eta + ce^{-\eta}) = 0$$

$$L_\theta(de^\eta + ee^{-\eta}) = 0$$

$$L_C(fe^\eta + ge^{-\eta}) = 0 \quad (26)$$

where a, b, c, d, e, f, g are the arbitrary constants.

3.1 The Skin-Friction, Sherwood Number and Nusselt Number

The mathematical expression of Skin-friction co-efficient, the Sherwood number formula and the Nusselt number formula are written as below.

$$\begin{aligned}
 R_e^{\frac{1}{2}} C_{F_x} &= \sqrt{\frac{n+1}{n}} \left(1 + \frac{1}{\gamma}\right) F''(0), \\
 R_e^{-\frac{1}{2}} Nu_x &= -\sqrt{\frac{n+1}{n}} \theta''(0) \\
 R_e^{-1/2} Sh_x &= -C'(0)
 \end{aligned}
 \tag{27}$$

where, the local Reynolds numbers are $R_{ex} = u_w \frac{x}{\nu}$.

3.2 Convergence Analysis

After drawing h-curves of auxiliary parameters, we are able to find the range of convergence from these Figs. 2, 3 and 4.

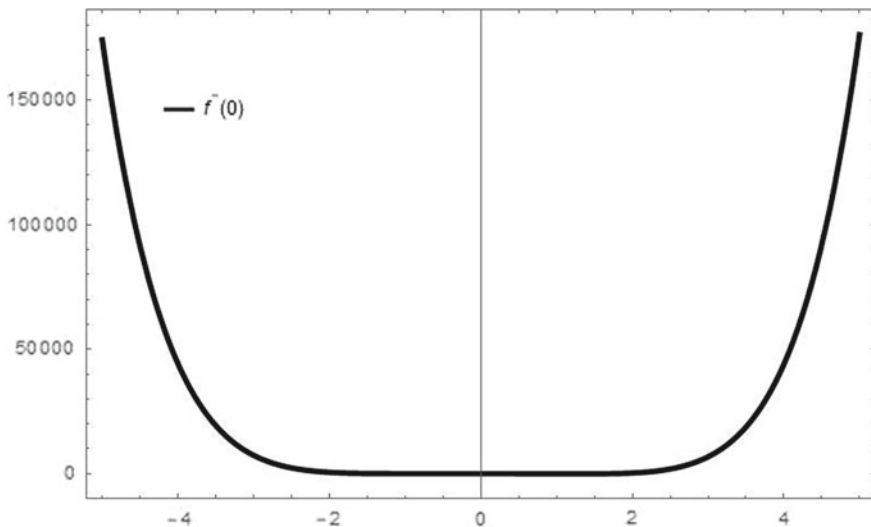


Fig. 2 h curve on $F''(0)$

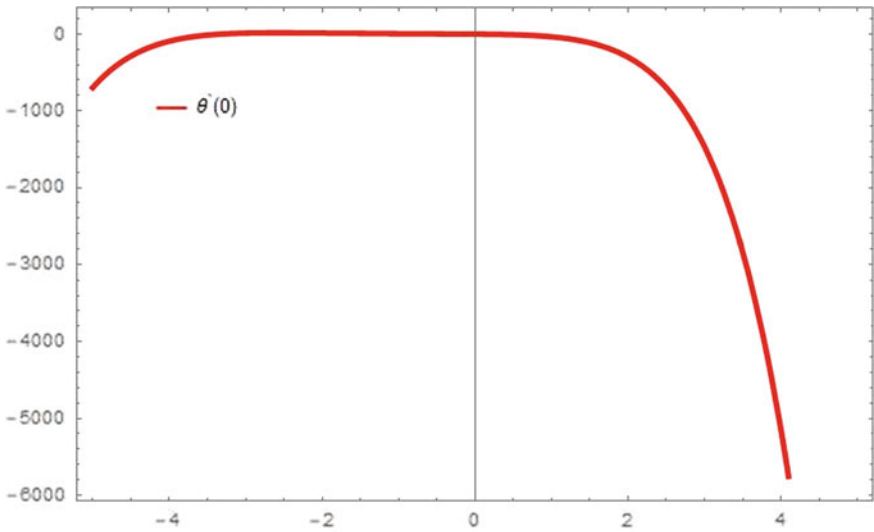


Fig. 3 h curve on $\theta'(0)$

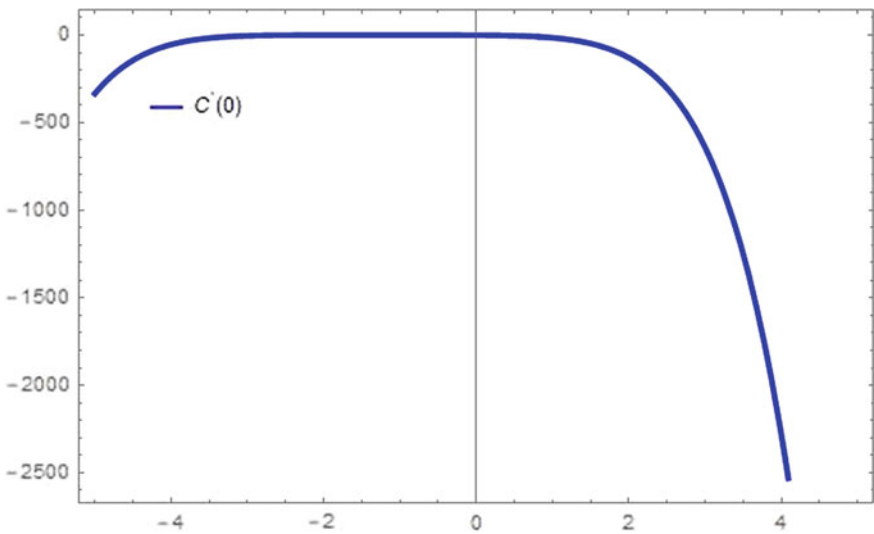


Fig. 4 h curve on $C'(0)$

4 Results and Discussion

For better understanding of the effect of different physical parameters, numerical results are obtained and presented graphically in Figs. 5, 6, 7, 8, 9, 10, 11, 12, 13, 14, 15, 16, 17, 18 and 19. Figure 5 gives the relationship between the magnetic

parameter (M) and fluid's velocity. We found that velocity of the fluid increased. Figure 6 displayed the significant impact on Casson fluid parameter (γ). As γ is improved, the yield stress is reduced, which results in flowing movement that has slowed down. With an increase in Casson fluid parameter, fluid physically becomes more viscous, it means that fluid viscosity increases. Figure 7 exhibits that when permeability parameter (k) is increased, we found fall in velocity curve. The effect of ratio of velocity parameter (A) is shown in Fig. 8. The velocity distribution is increased, as this parameter is increased.

Figure 9 shows the non-linear radiation effect on heat transfer process. Initially, the temperature field is positively impacted by the non-linear radiation parameter, then it decreases. The effect of mixed convection parameter (λ) on momentum is described in Fig. 10. One observation is that when the bio-convection parameter is high, the velocity also boosted in a direct proportion. The θ_w temperature ratio parameter tends to diminish the curve of temperature field, we can observe this fact in Fig. 11. Figure 12 clearly indicates that there is an increment, if the buoyancy force parameter (\tilde{N}) is incremented. Figure 13 is sketched for concentration profiles respectively with different values of chemical reaction parameter (Kr). We observed that both profiles fall down when the value of the value of this parameter is incremented. Figure 14 depicts the effects of Eckert number on heat transfer process. It is seen that Eckert number tends to improve the flow and heat transfer process. This contributes to the improvement of the thermal boundary layers. Figures 15 and 16 illustrate that the motion of the fluid and heat transfer process increase as the heat sink parameter (B_1) increases. This result strongly agrees with the real situation. In general, higher values

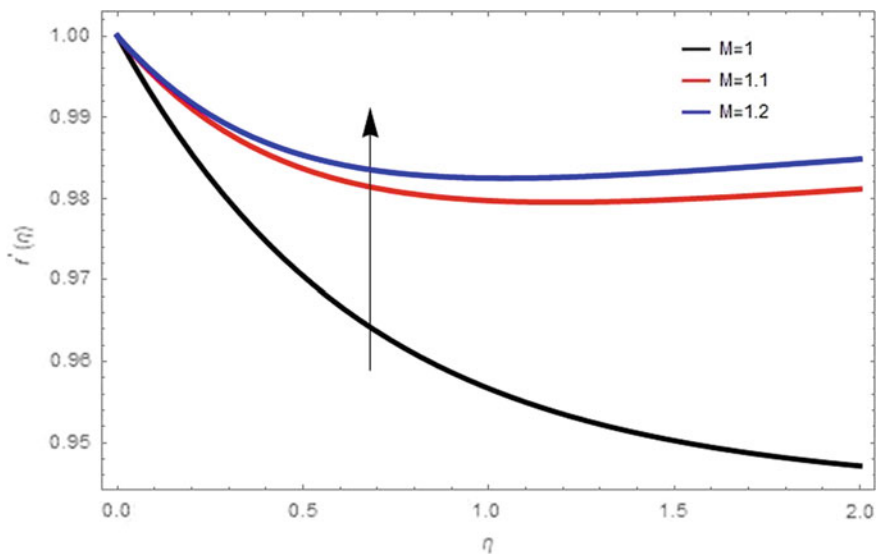


Fig. 5 M on F'

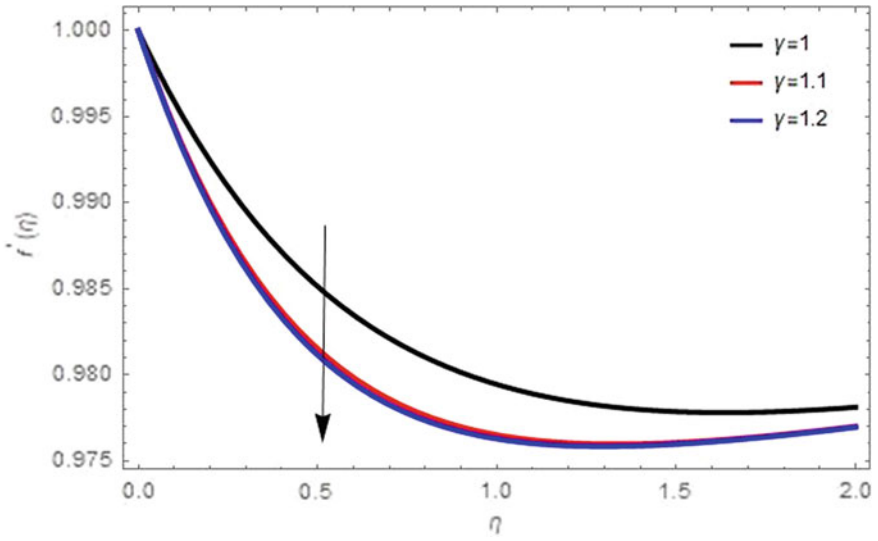


Fig. 6 γ on F'

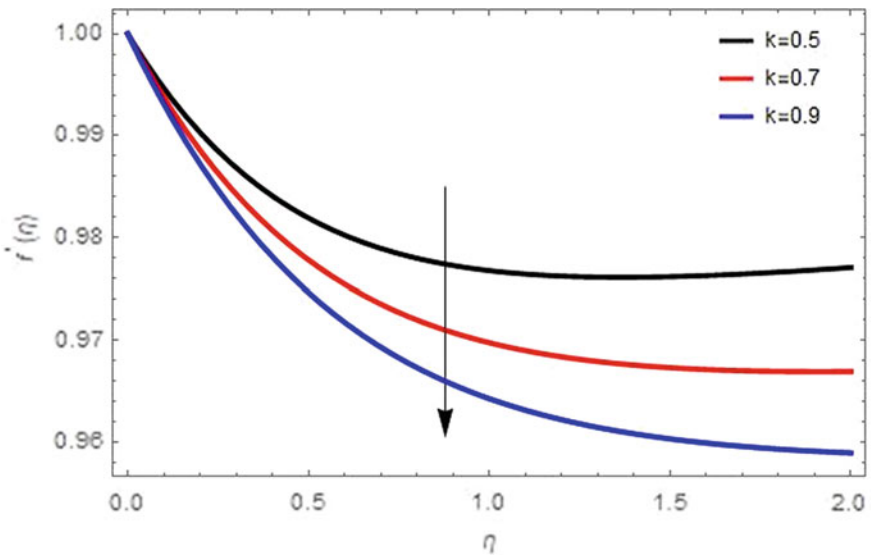


Fig. 7 k on F'

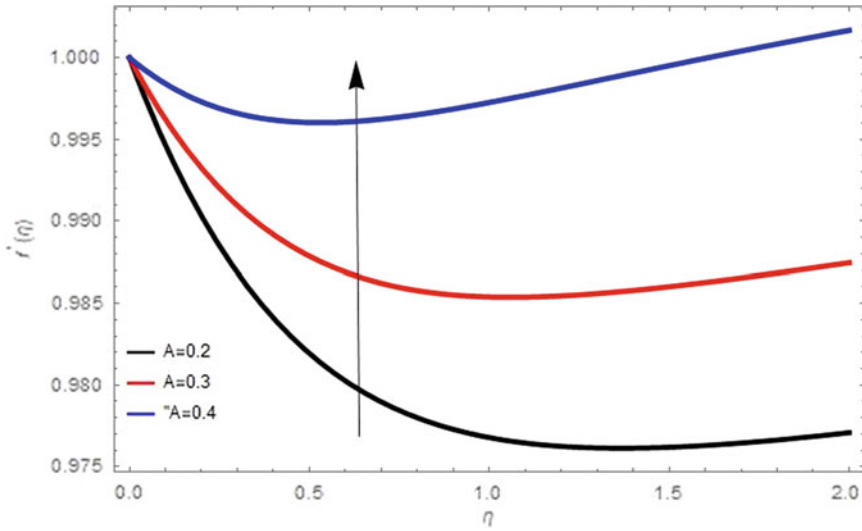


Fig. 8 A on F'

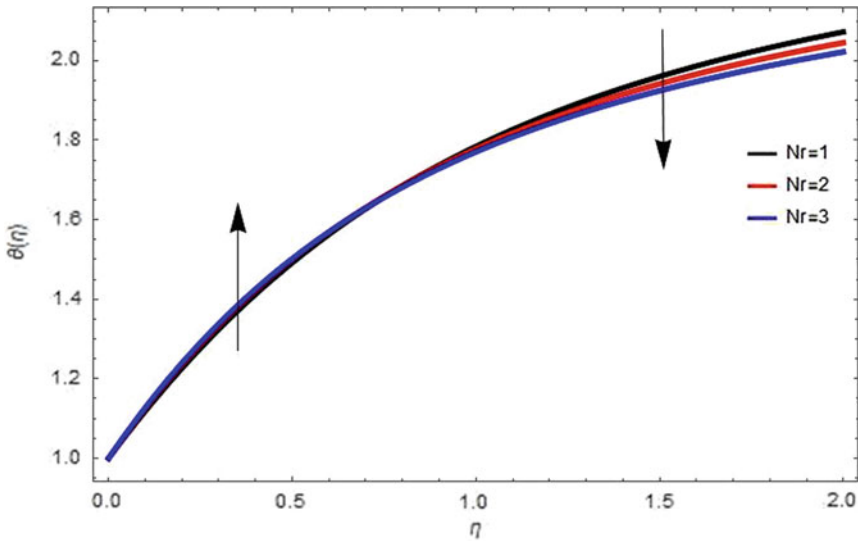


Fig. 9 Nr on θ

of the irregular heat sink parameter improve temperature profiles. We've observed an improvement in temperature profiles and velocity curves, because it generates internal energy in the flow. Similar trend for irregular heat source parameter (A_1) is represented in Figs. 17 and 18. Figure 19 illustrates that increasing the Soret number (Sr) increases concentration and its thickness.

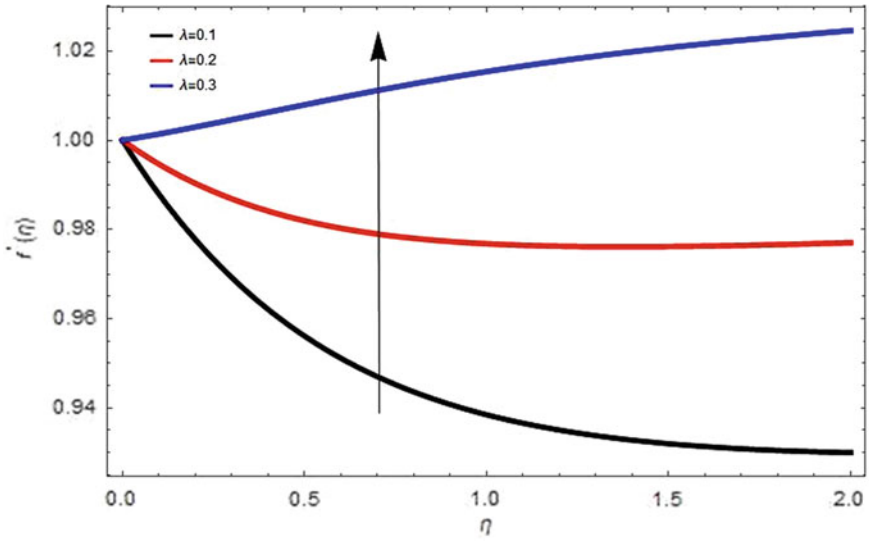


Fig. 10 λ on F'

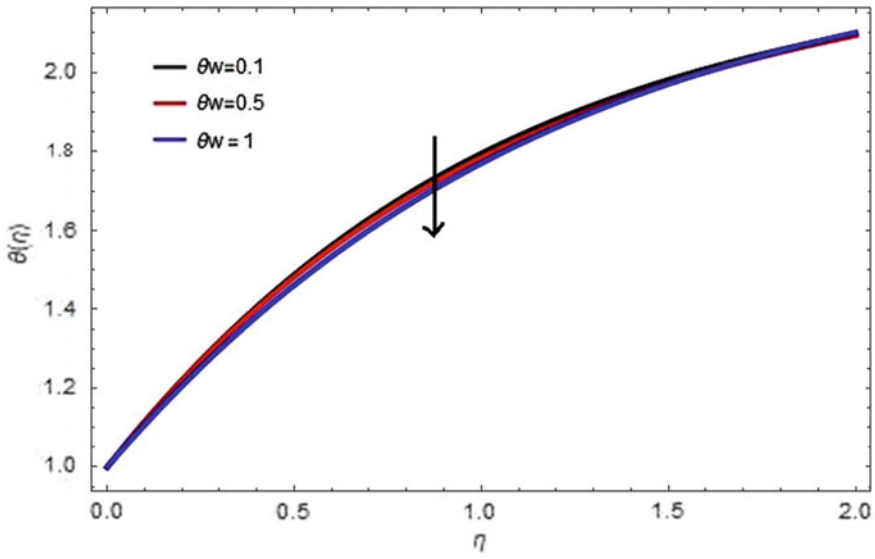


Fig. 11 θ_w on θ

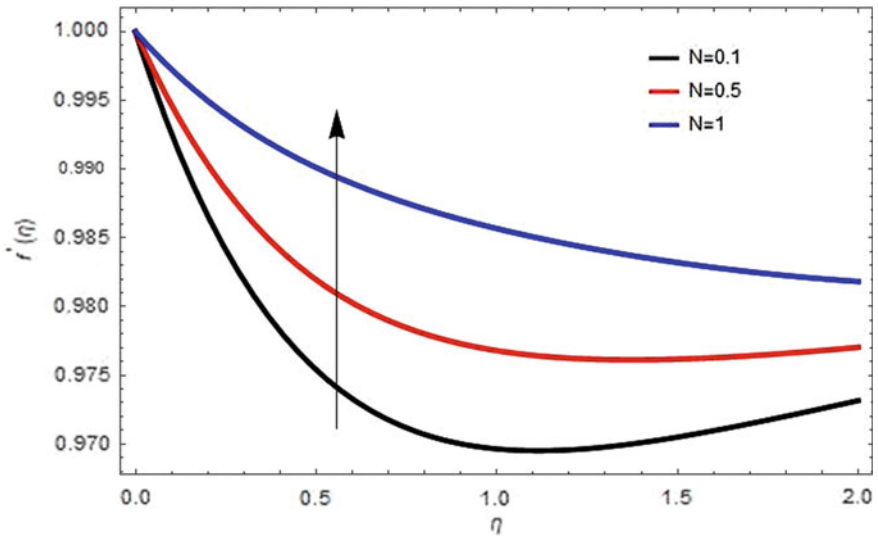


Fig. 12 N on F'

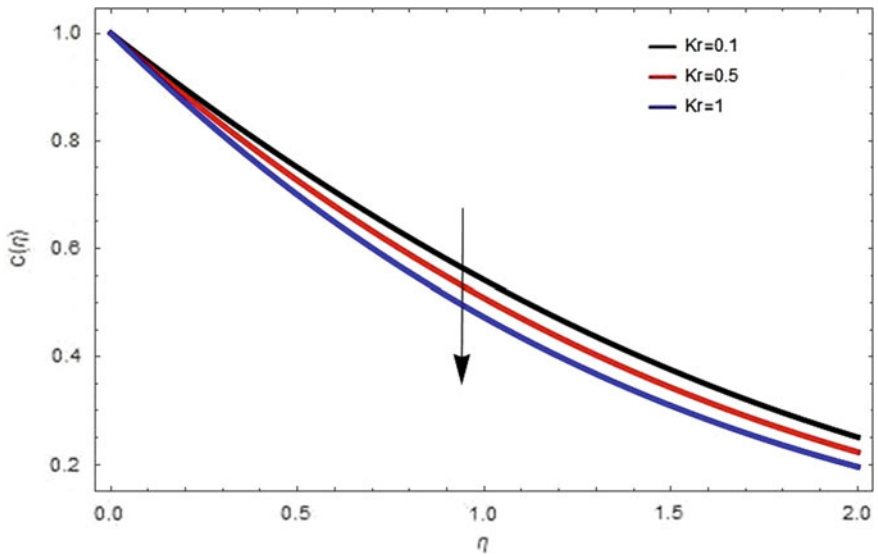


Fig. 13 K_r on C

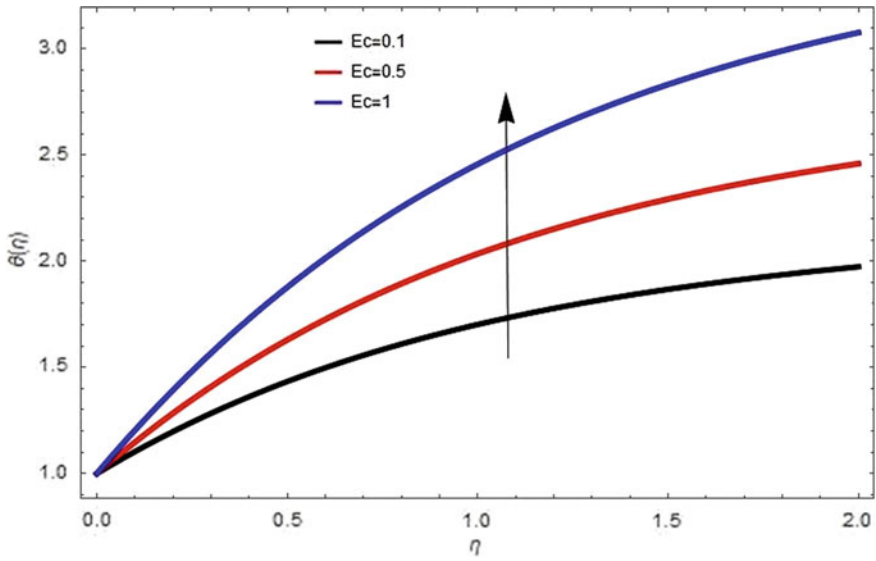


Fig. 14 E_c on θ

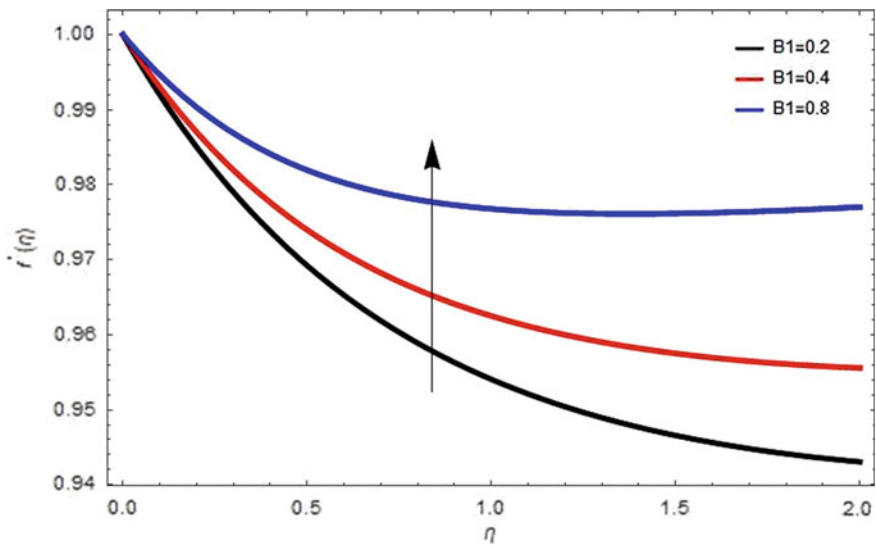


Fig. 15 B_1 on F'

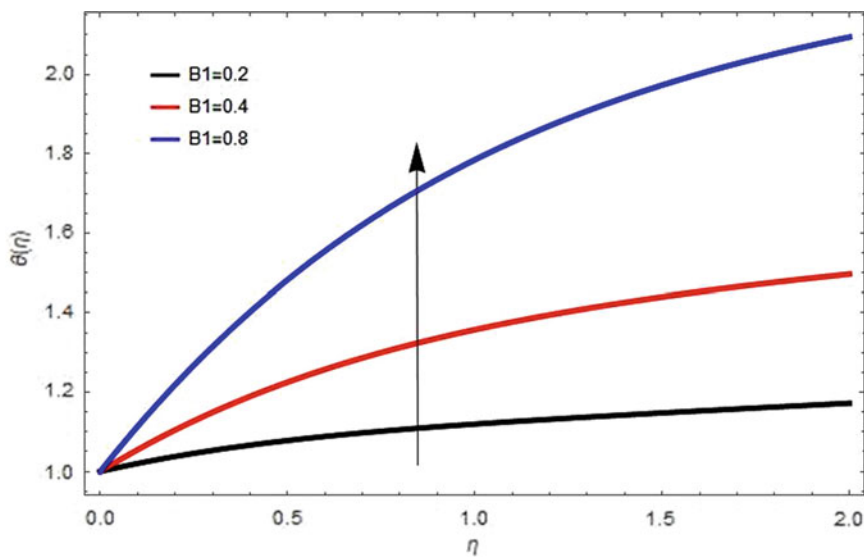


Fig. 16 B_1 on θ

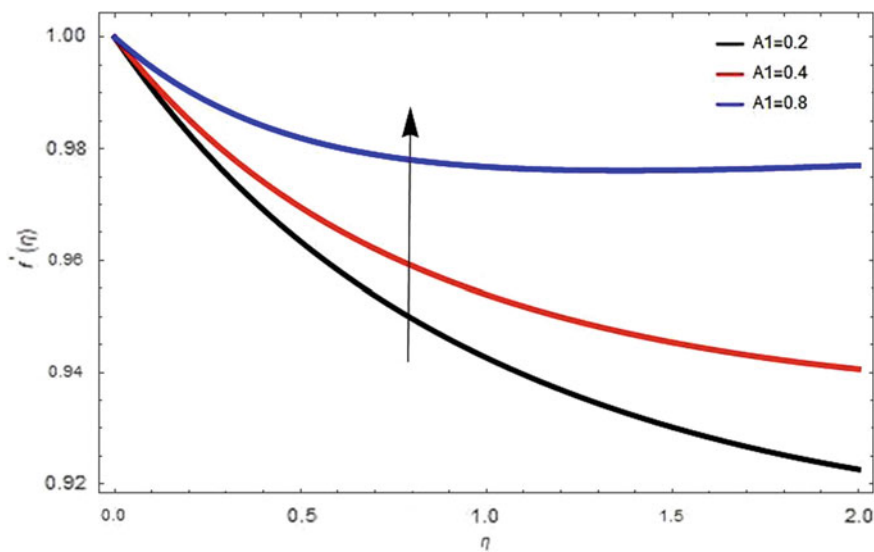


Fig. 17 A_1 on F'

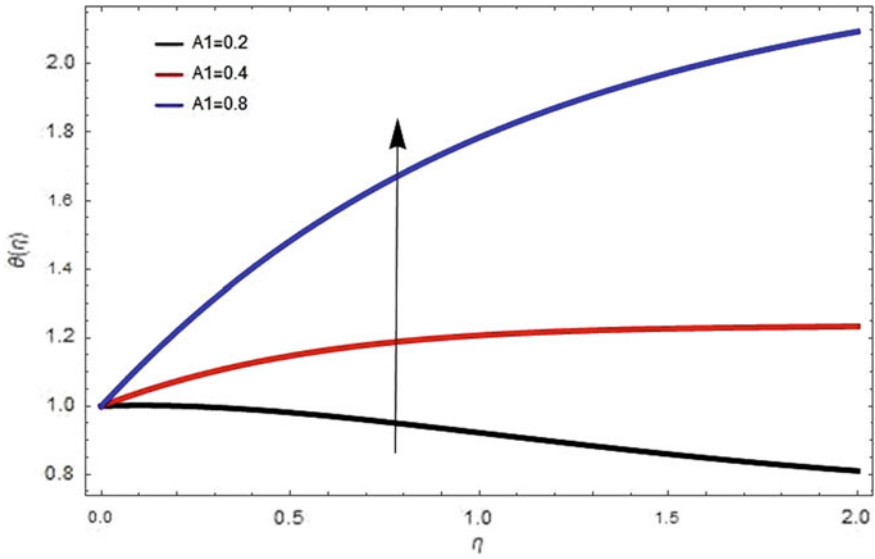


Fig. 18 A_1 on θ

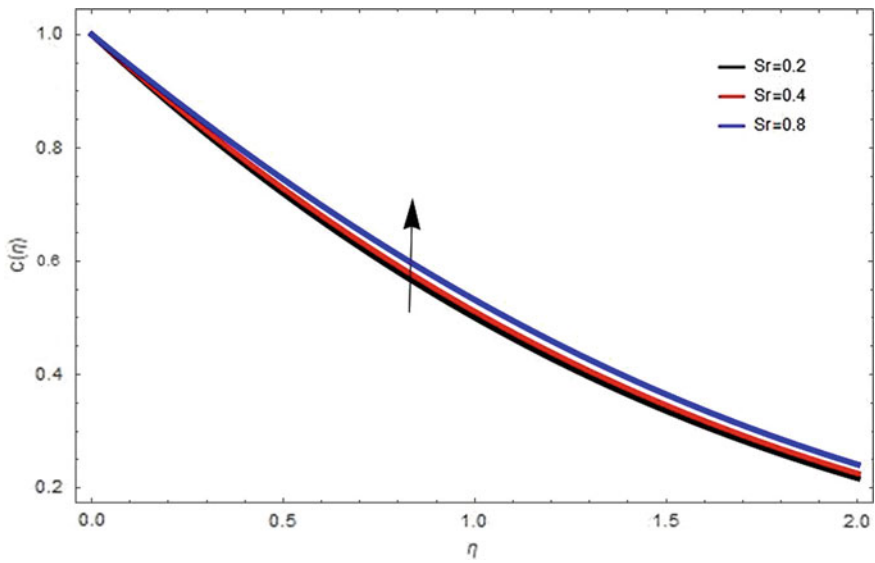


Fig. 19 S_r on C

5 Conclusion

The key findings result of the current study are listed below:

- The magnetic parameter, heat sink parameter and bio-convection parameter tend to improve accelerated the flow.
- On the other hand, the velocity distribution is decreased by Casson fluid parameter, permeability parameter and reaction parameter.
- When the heat source parameter, heat sink parameter and Eckert number are augmented, the temperature fields rise.
- The temperature profile seems to be coming down when the values of temperature ratio parameter are increased. In the case of thermal radiation parameter, we found mixed change on temperature curve.
- The concentration boundary layer falls down as chemical reaction parameter increases, reverse trend is observed in the curve when the Soret number is incremented.

Nomenclature

η	Similarity variable
γ	Casson fluid parameter
λ	Mixed or Bio-convection parameter
μ	Dynamic viscosity
μ_B	Plastic dynamic viscosity
ν	Kinematic viscosity co-efficient
ϕ	Porosity of the porous medium
π	Deformation rate of component
π_c	π 'S Critical value
ρ	Fluid's density
σ	Electrical conduction
σ^*	The Stefan-Boltzmann number
τ^*	Shear stress
θ	Fluid's temperature (Dimensionless)
$\theta(\eta)$	The non-dimension temperature function
θ_w	Temperature ratio parameter
N^{\sim}	Buoyancy force parameter
A	Velocities' ratio
a	The rate of stretching
b	The free stream velocity rate
B_0	Uniform magnetic field
C	Species concentration
$C(\eta)$	Concentration function (Dimensionless)

cp	(At constant pressure) the Specific heat
cs	Concentration susceptibility
C_w	Fluid's concentration at surface
D	Mass diffusion co-efficient
D_B	Brownian motion
D_F	Mass diffusion number (Dufour number)
D_T	Thermophoresis diffusion co-efficient
ei_j	Deformation rate of (i, j) th component
$F'(\eta)$	Dimensionless velocity function
$F(\eta)$	Stream function (Dimensionless)
g	Gravitational acceleration
H	Heat generation parameter
hf	Convective heat transfer co-efficient
k	Permeability parameter
k^*	Mean absorption co-efficient
K_2	Thermal conductivity
K_T	Thermal diffusion ratio
M	Magnetic parameter
n	Power-law exponent
Nr	Thermal radiation
Pr	Prandtl number
Py	Fluid's yield stress
q'''	Heat source/sink
qr	Radiative Heat flux
Sr	Thermo diffusion number (Soret number)
T	Fluid's temperature
$u_e(x)$	Free stream velocity
u_w	Stretching velocity

References

1. Casson N (1959) Rheology of disperse, systems
2. Blair GWS (1959) Nature 183(4661):613–614
3. Copley AL, Stainsby G et al (1960) Flow properties of blood and other biological systems
4. Bird RB, Stewart WE, Lightfoot EN, Meredith RE (1961) J Electrochem Soc 108(3):78C
5. Fung YC, Skalak R (1981) Biomechanics: mechanical properties of living tissues
6. Dash RK, Mehta KN, Jayaraman G (1996) Int J Eng Sci 34(10):1145–1156
7. Kakaç S, Shah RK, Aung W (1987) Handbook of single-phase convective heat transfer
8. Lawal A, Mujumdar AS (1987) Adv Transp Processes 5:352–443
9. Shaw S, Reddy Gorla RS, Murthy P, Ng C-O (2009) Pulsatile Int J Fluid Mech Res 36(1)
10. Venkatesan J, Sankar DS, Hemalatha K, Yatim Y (2013) J Appl Math 2013
11. Mukhopadhyay S, Mandal IC (2014) Chin Phys B 23(4):044702
12. El-Dabe NT, Ghaly AY, Rizkallah RR, Ewis KM, Al-Bareda AS (2015) J Appl Math Phys 3(06):649

13. Manjunatha PT, Gireesha BJ, Prasannakumara BC (2017) *Int J Appl Comput Math* 3(1):293–310
14. Gireesha BJ, Archana M, Prasannakumara BC, Gorla RSR, Makinde OD (2017) *Int J Num Methods Heat Fluid Flow*
15. Archana M, Gireesha BJ, Prasannakumara BC, Gorla RSR (2018) *Nonlinear Eng* 7(2):91–101
16. Kumar KG, Archana M, Gireesha BJ, Krishnamurthy MR, Rudraswamy NG (2018) *Results Phys* 8:694–701
17. Crane LJ (1970) *ZAMP* 21(4):645–647
18. Pavlov KB *Gidrodinamika M* (1974) *Magnitnaya Gidrodinamika* 4(1):146–147
19. Gupta PS, Gupta AS (1977) *Can J Chem Eng* 55(6):744–746
20. Rajagopal KR, Na TY, Gupta AS (1984) *Rheol Acta* 23(2):213–215
21. Kumar Sankara K, Watson LT (1985) *Z Angew Math Phys* 36(6):845–853
22. Char M-I et al (1988) *J Math Anal Appl* 135(2):568–580
23. KV, Rollins D (1992) *Int J Non-linear Mech* 27(2):265–277
24. Chamkha AJ (2000) *Chem Eng J* 76(2):159–168
25. Afify AA (2004) *Heat Mass Transf* 40(6):495–500
26. Kandasamy R, Periasamy K, Sivagnana Prabhu KK (2005) *Int J Heat Mass Transf* 48(21–22):4557–4561
27. Cortell R (2007) *Chem Eng Process-Process Intensification* 46(10):982–989
28. Hayat T, Abbas Z, Ali N (2008) *Phys Lett A* 372(26):4698–4704
29. Kataria HR, Patel H (2016) *Alex Eng J* 55(1):583–595
30. Bala P, Reddy A (2016) *Ain Shams Eng J*, 593–602
31. Eid MR, Mabood F (2021) *J Mech Eng Sci* 235(22):6099–6110
32. Animasaun IL, Adebile EA, Fagbade AI (2016) *Journal of the Nigerian Mathematical Society* 35(1):1–17
33. Chamkha AJ (2003) *Int Commun Heat Mass Transfer* 30(3):413–422
34. Abdul Hakeem AK, Kalaivanan R, Vishnu Ganesh N, Ganga B (2014) *Ain Shams Eng J* 5(3):913–922
35. Hayat T, Shaheen U, Shafiq A, Alsaedi A, Asghar S (2015) *Marangoni. AIP Adv* 5(7):077140
36. Prakash J, Durga Prasad P, Vinod Kumar G, RVMSS Kumar K, Varma SVK (2016) *Int J Eng Sci Invent* 5(7):12–23
37. Kumar KA, Ramana Reddy JV, Sugunamma V, Sandeep N (2018) *Alex Eng J* 57(1):435–443
38. Sivasankaran S, Bhuvanewari M, Alzahrani AK (2020) *Alex Eng J* 59(5):3315–3323
39. Batchelor CK, Batchelor GK (2000) *An introduction to fluid dynamics*. Cambridge University Press
40. Rosseland S (1931) *Springer-verlag, Berlin*
41. Khader MM, Sharma RP (2021) *Math Comput Simul* 181:333–350
42. Liao S (2003) *Introduction to the homotopy analysis method*. CRC

Heat Transfer Enhancement Using Passive Technique



Adarsh Shinde, Rishi Choudhary, Siddhi Bairagi, Vaibhavi Chandankar, Shruti Dhadi, Sanchitee Rokade, and M. B. Chaudhari

1 Introduction

Heat transfer enhancement is the study of improving the rate of heat transfer mainly achieved by increasing the rate of heat transfer either by active methods comprising the supply of external power to the system, for instance, ultrasonic enhancement, electro hydrodynamic or by passive methods which include modifying the surface of system, altering physical parameters changing flow of fluid, insertion of additives. Furthermore, a compound method comprises both active and passive techniques. One such passive heat enhancement technique is twisted tape inserts that modify flow of fluid within the channel which promotes turbulent and transverse flow coercing both convective and conductive modes of heat transfer.

2 Literature Review and Objective

Kumar et al. [1] reviewed heat transfer enhancement with twisted tape and provided a criteria of performance for various tape inserts, the objective being to provide a review of the work conducted on plain twisted tape, modified twisted tape and modified twisted tape geometry. By considering the insights from pressure drop and heat transfer investigations of various tape inserts, this survey aims to be an intensive literature summary for all the feasible research topics on the case. The paper highlights the effectiveness of plain and modified twisted tape in laminar flow, as in this case, thermal resistance is not confined to a limited region, however, a pressure drop penalty is observed in turbulent flow. Whereas in the case of twisted tape with

A. Shinde (✉) · R. Choudhary · S. Bairagi · V. Chandankar · S. Dhadi · S. Rokade · M. B. Chaudhari
Department of Mechanical Engineering VIT Pune, Pune, India
e-mail: adarsh.shinde21@vit.edu

modified geometry, more turbulence is generated which results in an increased rate of heat transfer when compared to plain and modified twisted tape. Sarada et al. [2] experimentally investigated the characteristics of heat transfer and friction in turbulent flow in a horizontal tube with inside diameter 27.5 mm by varying the width of twisted tapes under the condition of constant wall heat flux with air as fluid medium. The experiment aimed to decrease pressure drops, which is apparent in the case of full width tapes, without causing any profound changes in rate of heat transfer with the goal of lessening material usage. In the results, it was evident that with the insertion of twisted tape, Nusselt number improved significantly due to secondary flow, at greater Reynolds numbers and low twist ratios. The overall enhancement ratio of the tubes with reduced width twisted tape insert was attained 1.39. Mahdi et al. [3] investigated experimentally and numerically, the improvement of heat transfer in inclined and horizontal single tube heat exchanger before and after the addition of variant copper tape inserts which included V-cut twisted tape (V-TT) and alternate axis twisted tape with variant twist ratio ($\gamma = 4.0$ and 6.0). Under the condition of $Re = 1056\text{--}2002$, distilled water was made to flow through an insulated tube, using fiberglass at the outer surface for minimal thermal losses. This study resulted in a substantial increase of 16–27% in the coefficient of heat transfer than the smooth tube. It was also concluded that as compared to V-cut insert, the alternate axis insert gives enhanced performance of heat transfer. Liu and Sakr [4] summarized different methods and inserts used in heat exchangers. After several experiments and research on several types of inserts, including wire coil, swirl generators, conical ring and rib, it was perceived that as compared to empty tube full length twisted tape (FLTT), the pressure drop increased by 185% by doing necessary changes in the geometry of the tape. At the same twist ratio, lower pressure drop is yielded by Multiple short length twisted tapes (MSLTTs) when compared to FLTT. Performance of twisted tape inserts is better in laminar flow than in turbulent flow. The shape of the insert plays a significant role while selecting the tube inserts. If the pressure drop penalty is taken into consideration, then better overall performance is given by wire coil.

The current research focuses on a computational study for enhancement of heat transfer using commercial software. For heat transfer enhancement, twisted tape of different non-conducting material is used in the current work. The heat transfer enhancement is predicted by the validated model. It is observed that the non-conducting material for the twisted tape gives better performance as compared to the conducting material.

Further research is going on for the different flow and geometric parameters.

3 Materials and Methods

Figure 1 represents tube geometry having length of 400 mm and 0.487 thickness with twisted tape inserted in it of 26 mm. The analysis is conducted for two different widths of tape inserts (26 and 10 mm).

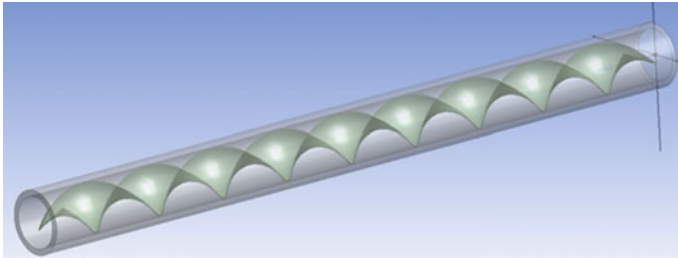


Fig. 1 Design of plain copper tube with twisted tape of insert of width 26 mm

Figure 2 shows a tube having twisted tape of 10 mm inserted in it. PEEK and PTFE materials were found suitable to study heat transfer characteristics of non-conducting tape inserts. Their properties are as follows:

Table 1 shows various properties of materials. It consists of density, specific heat and thermal conductivity of copper, PEEK and PTFE.

A grid independence study was conducted prior to the analysis. Result Variations are not significant after the market cell size, hence, this edge sizing number of divisions was considered as the better mesh for calculation. This mesh size would give better results with less time as compared to finer mesh. Hence, for the current work, 50 divisions were selected for the edge sizing.

Figure 3 represents the variation in the outlet velocity of fluid with respect to change in number of Mesh Nodes. It denotes the optimum number of Mesh Nodes beyond which there is minimal variation in results.

Figure 4 represents the variation in Nusselt number with respect to change in number of Mesh Nodes. The simulations for system configurations were finely

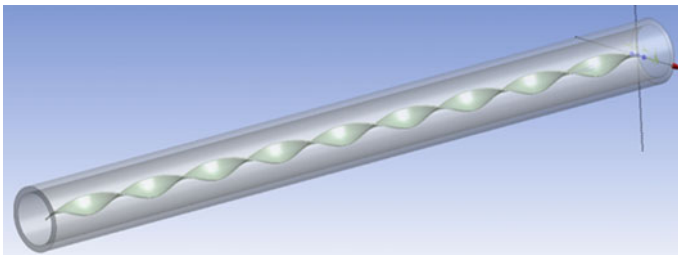


Fig. 2 Design of plain copper tube with twisted tape of insert of width 10 mm

Table 1 Properties of materials

Properties	Copper	PEEK	Teflon
Density [kg/m ³]	8978	1320	2200
Cp (specific heat) [J/Kg-K]	381	1340	1090
Thermal conductivity [W/m-K]	387.6	0.25	0.3

Fig. 3 Variation in outlet velocity with change in number of mesh nodes

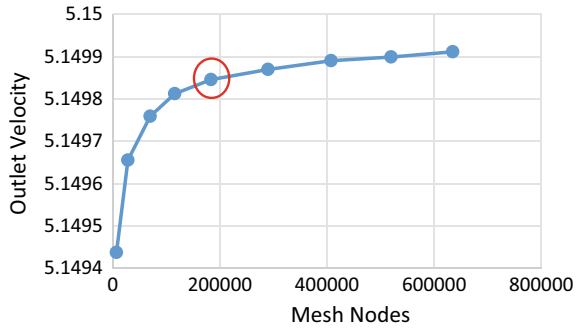
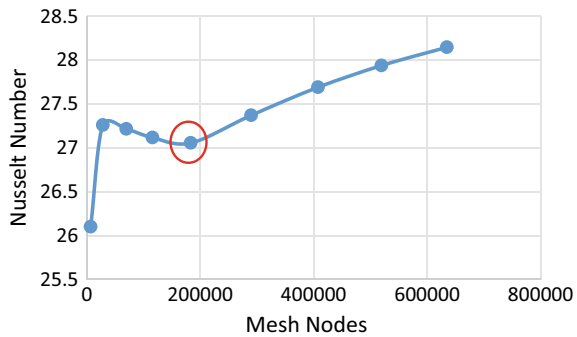


Fig. 4 Variation in Nusselt number with change in number of mesh nodes



meshed using the commercial software ANSYS 21.2.0. for accurate results. In this setup, SST k-omega viscous model was selected. For a copper pipe with inner diameter 27.5 mm, materials PEEK and PTFE were used for twisted tape insert. Necessary boundary conditions at inlet and outer wall surface were given. Solid domain, fluid domain and tape insert were assigned with respective materials. For analysis, a SIMPLE algorithm was used. The model was run for varying Reynolds number with air as working fluid. The governing equations used for this analysis are as follows:

$u = u\hat{i} + v\hat{j} + w\hat{k}$, where u is the velocity vector used in governing equations as mentioned below:

The mass conservation or continuity equation is as follows:

$$\frac{\partial u}{\partial x} + \frac{\partial v}{\partial y} + \frac{\partial w}{\partial z} = 0 \tag{1}$$

The governing momentum conservation equations in 3D are as follows:

$$\rho \left(\underline{u} \frac{\partial \underline{u}}{\partial x} + \underline{v} \frac{\partial \underline{u}}{\partial y} + \underline{w} \frac{\partial \underline{u}}{\partial z} \right) = -\frac{\partial p}{\partial x} + \mu \left(\frac{\partial^2 \underline{u}}{\partial x^2} + \frac{\partial^2 \underline{u}}{\partial y^2} + \frac{\partial^2 \underline{u}}{\partial z^2} \right) - \rho \left[\frac{\partial}{\partial x} (\underline{u}^2) + \frac{\partial}{\partial y} (\underline{u}'\underline{v}') + \frac{\partial}{\partial z} (\underline{u}'\underline{w}') \right]. \tag{2}$$

$$\rho \left(\underline{u} \frac{\partial v}{\partial x} + \underline{v} \frac{\partial v}{\partial y} + \underline{w} \frac{\partial v}{\partial z} \right) = -\frac{\partial p}{\partial y} + \mu \left(\frac{\partial^2 v}{\partial x^2} + \frac{\partial^2 v}{\partial y^2} + \frac{\partial^2 v}{\partial z^2} \right) - \rho \left[\frac{\partial}{\partial x} (\underline{u}'v') + \frac{\partial}{\partial y} (\underline{v}'^2) + \frac{\partial}{\partial x} (\underline{v}'w') \right] + S_{my}. \quad (3)$$

$$\rho \left(\underline{u} \frac{\partial w}{\partial x} + \underline{v} \frac{\partial w}{\partial y} + \underline{w} \frac{\partial w}{\partial z} \right) = -\frac{\partial p}{\partial z} + \mu \left(\frac{\partial^2 w}{\partial x^2} + \frac{\partial^2 w}{\partial y^2} + \frac{\partial^2 w}{\partial z^2} \right) - \rho \left[\frac{\partial}{\partial x} (\underline{u}'w') + \frac{\partial}{\partial x} (\underline{v}'w') + \frac{\partial}{\partial y} (\underline{w}'^2) \right]. \quad (4)$$

where, S_{my} is the combined source term due to the body forces. The energy conservation equation is as follows:

$$\rho \cdot \text{div}(Eu) = -\text{div}(pu) + \left[\frac{\partial(u\tau_{xx})}{\partial x} + \frac{\partial(u\tau_{yx})}{\partial y} + \frac{\partial(u\tau_{zx})}{\partial z} + \frac{\partial(v\tau_{xy})}{\partial x} + \frac{\partial(v\tau_{yy})}{\partial y} + \frac{\partial(v\tau_{zy})}{\partial z} + \frac{\partial(w\tau_{xz})}{\partial x} + \frac{\partial(w\tau_{yz})}{\partial y} + \frac{\partial(w\tau_{zz})}{\partial z} \right] + S_E. \quad (5)$$

where, E is the specific energy of fluid.

4 Results and Discussion

Heat Transfer Coefficient and Nusselt number increase when twisted tapes are used in the tube. This is due to the rapid mixing of flow, which generates high turbulence intensity and enhances heat transfer. The enhancement in heat transfer occurs due to the thinning of the boundary layer as a result of the spiral motion of the fluid (Fig. 5).

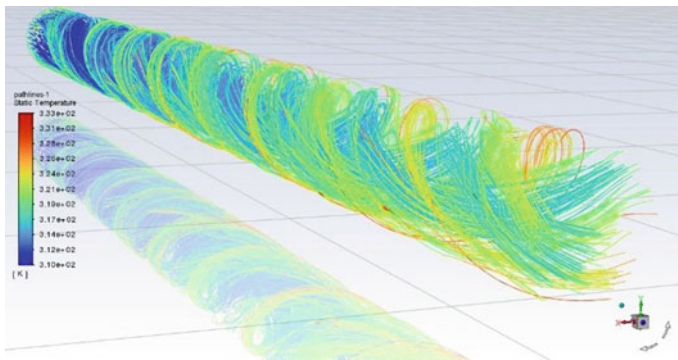


Fig. 5 CFD analysis of fluid flow through pipe with tape insert (26 mm)

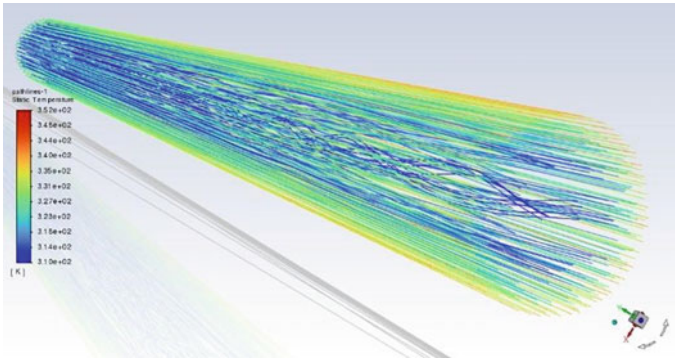


Fig. 6 CFD analysis of fluid flow through pipe with tape insert (10 mm)

A decline in heat transfer enhancement is observed with reduction in tape width (10 mm) as the spiral motion of the fluid is decreased near edges (Fig. 6). This results in vortex formation only at the center of the pipe. Whereas, the tape insert of 26 mm width causes the spiral motion of fluid up to the edges of the pipe, resulting in higher vortex formation and rise in heat transfer enhancement (Fig. 5).

Heat transfer increases to a greater extent when insulators such as PEEK and Teflon are used as compared to metals, mainly Aluminum. This is mainly due to insulating materials (PEEK and Teflon) allowing minimal accumulation of heat within them, thereby a large amount of heat in the pipe is absorbed by the fluid. This increases the temperature of fluid, which further enhances heat transfer.

Figure 7 shows the validation of the current model with the experimental results of Sarda et al. [2] and the Dittus Boelter equation. It shows that the predicted results by the current model have a maximum error of 6.16%. The same model is used to predict the heat transfer by using twisted tape for various flow and geometric parameters (Table 2).

It is observed from Fig. 8 that, for twisted tape of 26 mm width and 0.486 mm thickness at a constant pitch of 82.5 mm by using PEEK and PTFE as tape material, the percent increase in Nusselt number for non-conducting materials as compared to plain tube was observed to be 135–160%. Whereas, when compared to tape insert of Aluminum material of same width and under same conditions (Sarada et al. 2010), there is an enhancement of heat transfer by 75–110%. This improvement in Nusselt number is attained due to the same flow physics and the lower conductivity of the material (Tables 3 and 4).

Figure 9 shows that under similar conditions with the width of the twisted tape changed to 10 mm, the rise in Nusselt number was observed to be 25–30% compared to plain tube and 20% when compared to aluminum tape insert (Tables 5 and 6).

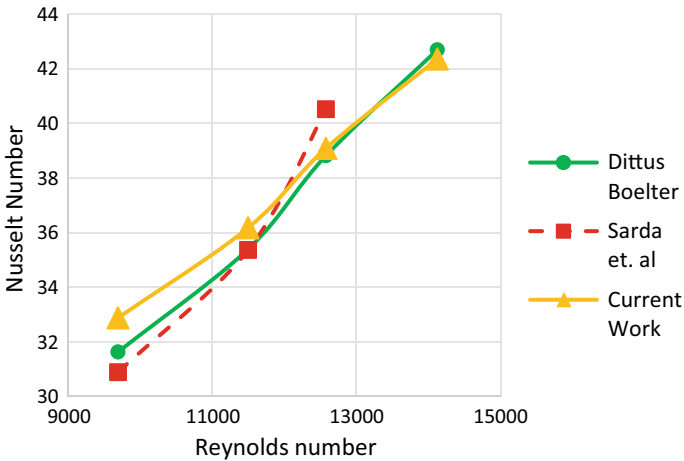


Fig. 7 Validation of current model with previous work (Sarada et al. [2]) and Dittus Boelter correlation for plain tube

Table 2 Obtained Nusselt no. and heat transfer coefficient from the work

Reynolds No.	Nusselt No.			Heat transfer coefficient	
	Dittus Boelter	Sarda et al.	Current work	Dittus Boelter	Current work
9697	31.62	30.88	32.87	27.82	28.92
11,500	35.39	35.36	36.17	31.14	31.93
12,578	38.809	40.51	39.08	34.149	34.3903
14,122	42.687		42.35	37.5643	37.27

The comparison of Nu number and Re number for 26 and 10 mm width tape insert can be seen in Fig. 10. It is realized that, despite the enhancement of Nusselt number using 10 mm tape width, it was considerably lower when compared to rise in Nusselt number observed with 26 mm width tape insert. The percent reduction in the low width tape insert (10 mm), in contrast with its counterpart (26 mm) was 37–44%. These results correspond to the work of Sarada et al. [2] (Tables 7 and 8).

5 Conclusions

The computational analysis showcases an enhancement of Nusselt number when traditional conducting material for twisted insert is replaced with insulating/non-conducting material (PTFE & PEEK) in a circular pipe of 27.5 mm inner diameter for two widths of tape inserts (26 and 10 mm) under constant wall heat flux with the

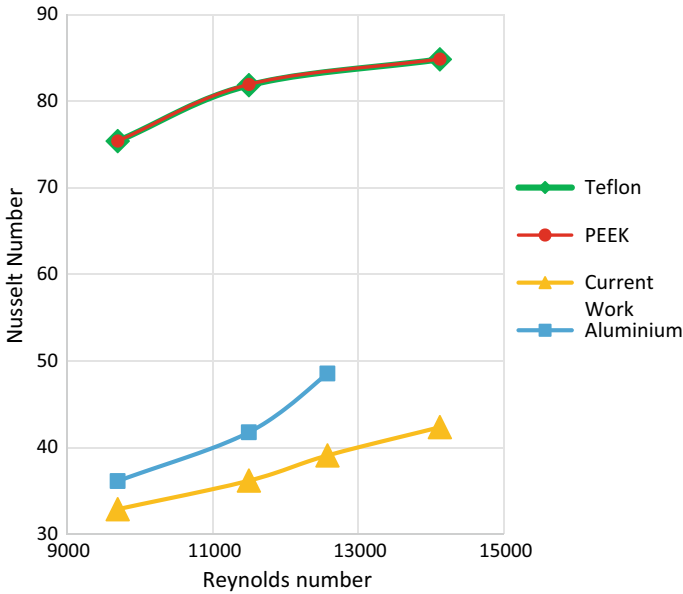


Fig. 8 Comparison of Nusselt number to different Reynolds number with/without twisted tape insert of 26 mm width for PEEK and PTFE

Table 3 Comparison of Nu of plain tube to Nu of tube with 26 mm width twisted tape (PEEK)

Reynolds No.	Nusselt No.		Heat transfer coefficient	
	Plain tube	26 mm width tape	Plain tube	26 mm width tape
9697	32.87	75.42	28.92	66.37
11,500	36.17	81.96	31.93	72.03
14,122	42.35	84.88	37.27	74.7

Table 4 Comparison of Nu of plain tube to Nu of tube with 26 mm width twisted tape (Teflon)

Reynolds No.	Nusselt No.		Heat transfer coefficient	
	Plain tube	26 mm width tape	Plain tube	26 mm width tape
9697	32.87	75.41	28.92	66.36
11,500	36.17	81.86	31.93	72.03
14,122	42.35	84.85	37.27	74.67

variation of Reynolds number from 9000 to 14,500. Conclusions drawn from this study are:

1. The computational data of Nusselt number for plain tube were validated with empirical calculations with maximum deviation of 3.95%.

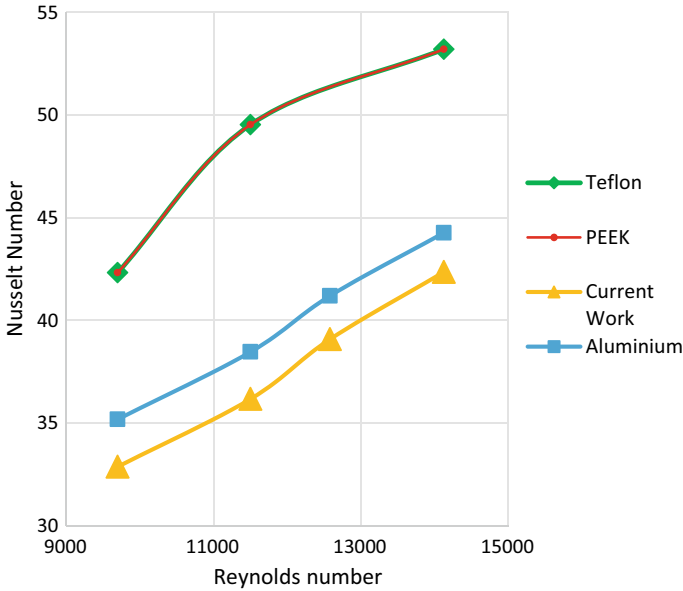


Fig. 9 Comparison of Nusselt number to Reynolds number with/without twisted tape insert of 10 mm width for PEEK and PTFE

Table 5 Comparison of Nu of plain tube to Nu of tube with 10 mm width twisted tape (PEEK)

Reynolds No.	Nusselt No.		Heat transfer coefficient	
	Plain tube	10 mm width tape	Plain tube	10 mm width tape
9697	32.87	42.32	28.92	37.24
11,500	36.17	49.53	31.93	43.59
14,122	42.35	53.2	37.27	46.81

Table 6 Comparison of Nu of plain tube to Nu of tube with 10 mm width twisted tape (Teflon)

Reynolds No.	Nusselt No.		Heat transfer coefficient	
	Plain tube	10 mm width tape	Plain tube	10 mm width tape
9697	32.87	42.32	28.92	37.24
11,500	36.17	49.53	31.93	43.59
14,122	42.35	53.2	37.27	46.81

2. Compared to 26 mm width of tape insert, Nusselt number decreased by 37–44% for 10 mm width tape insert.
3. Results for both PEEK and PTFE were observed to be analogous due to the similarity in their properties, the only difference is PTFE being considerably cheaper than PEEK.

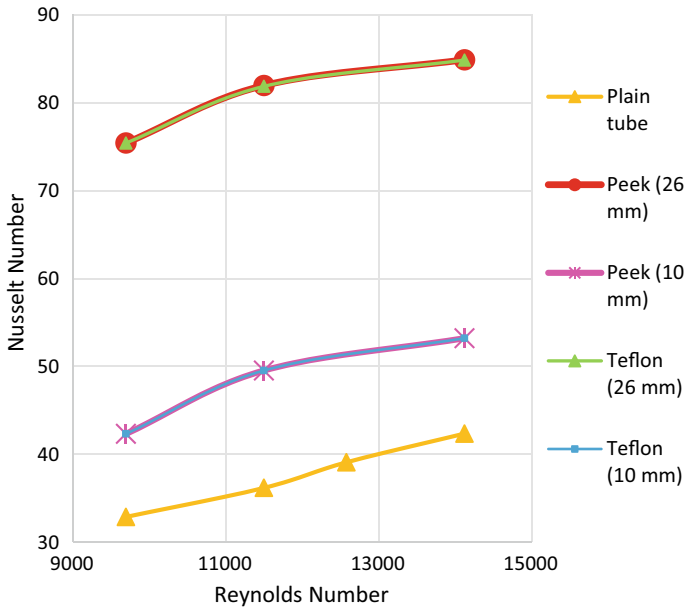


Fig. 10 Comparison of Nusselt number with Reynold’s number for 26 mm and 10 mm width twisted tape for PEEK and PTFE

Table 7 Comparison of Nu of 26 mm width tape to Nu of 10 mm width tape (PEEK)

Reynolds No.	Nusselt No.		Heat transfer coefficient	
	26 mm width tape	10 mm width tape	26 mm width tape	10 mm width tape
9697	75.42	42.32	66.37	37.24
11,500	81.96	49.53	72.03	43.59
14,122	84.88	53.2	74.7	46.81

Table 8 Comparison of Nu of 26 mm width tape to Nu of 10 mm width tape (Teflon)

Reynolds No.	Nusselt No.		Heat transfer coefficient	
	26 mm width tape	10 mm width tape	26 mm width tape	10 mm width tape
9697	75.41	42.32	66.36	37.24
11,500	81.86	49.53	72.03	43.59
14,122	84.85	53.2	74.67	46.81

Nomenclature

- Nu Nusselt number
- Re Reynolds number

ν	Kinematic viscosity of air [m^2/s]
ϵ_C	Emissivity of Copper
μ	Dynamic Viscosity [$\text{kg}/\text{m}\cdot\text{s}$]
η	Over all enhancement ratio
ρ_w	Density of water [kg/m^3]
ρ_a	Density of air [kg/m^3]

References

1. Kumar NC, Murugesan P (2012) Review on twisted tapes heat transfer enhancement. *Int J Sci Eng Res* 3(4):1–9
2. Sarada SN, Raju ASR, Radha KK, Sunder LS (2010) Enhancement of heat transfer using varying width twisted tape inserts. *Int J Eng Sci Technol* 2(6):107–118
3. Liu S, Sakr M (2013) A comprehensive review on passive heat transfer enhancements in pipe exchangers. *Renew Sustain Energy Rev* 19:64–81
4. Mahdi AS, Al-Musawi STA, Kadhim ZK, Hussain HM, Habeeb LJ (2020) Heat transfer enhancement by using twisted tape in horizontal and an inclined tube. *J Mech Eng Res Dev* 43(3):106–124

A Review on Heat Pipe-Assisted Thermal Management Systems in Electrical Vehicles for Lithium-Ion Batteries



Rajat Kumar, Ankur Dwivedi, and Varun Goel

1 Introduction

Electric Vehicles (EVs) are the highly encouraging choice for a green and clean atmosphere as the globe relies increasingly on renewable energy sources and batteries hold uniform energy better. The task for EVs is to create a battery that can sustain long-range, efficient driving, and rapid charging. LIBs are the best power source for EVs. Li-ion batteries are eco-friendly, have no gassing issues and are safe. Temperature and ambient factors affect a LIB's performance, life, and safety. LIBs can function safely at a temperature limit of 20–60 °C. BTMS is necessary to protect batteries from overheating and temperature rise [1]. A BTMS maintains the batteries' optimal operating temperature range with uniform cell and packs temperature distribution. Weight, compactness, complexity, cost, and dependability of the system must also be addressed. Thermal management systems include liquid, air, heat pipe, PCM, and hybrid cooling. Heat pipes are popular because of their excellent heat transmission rate, low maintenance and cheap cost, long lifespan, and lightweight. Heat pipes are basic passive cooling systems with fluid transfer. Heat pipes can be employed for cooling EVs [2, 3]. Heat pipe-aided cooling techniques for battery units have been examined by researchers due to their superior heat dissipation effectiveness over inadequate air convection, heavy liquid pump cooling, and PCM's lower thermal conductivity. [4]. The thermal conductivity of a heat pipe is about 100 times higher than a simple copper pipe. Heat pipes are a low-cost, long-lasting, lightweight, and thermally conductive passive cooling technology [5]. The major goals of BTMS are to keep the temperature of the battery cell below the permitted T_{\max} , reduce ΔT_{\max} , and keep battery cell temperatures within the working limit for the ideal battery system performance. Various types of BTMS are air-cooled [6], water-cooled [7],

R. Kumar (✉) · A. Dwivedi · V. Goel

Department of Mechanical Engineering, National Institute of Technology Hamirpur, Hamirpur, Himachal Pradesh 177005, India

e-mail: rajatr2020@nith.ac.in

thermo-electric cooled [8], PCM cooled [9], and HP-cooled [5]. The BTMS should be lightweight, inexpensive, compact in size, efficient, and low maintenance cost. BTMS should function with low power and a broad temperature range. Among all types of BTMS, heat pipe cooling is a superior BTMS owing to its high thermal conductivity, high heat transfer rate, wide temperature range, no external power required, low maintenance required, and high thermal performance.

2 Literature Review

Heat Pipes (HPs) are very effective heat exchangers that are utilized in many different types of thermal devices. Aluminum and copper are superb heat conductors and can be used to make heat pipes. The heat pipe has a wide range of applications, including electronics cooling, aviation cooling, air conditioning, energy production, chemical processing, and solar thermal system cooling. Heat pipes often transmit heat by altering the coolant state. Hence, choosing the proper working fluid is crucial to increasing the thermal effectiveness of the heat pipe. HPs are often filled with fluids like water, acetone, alcohol, ethylene, and glycol to dissipate heat from HP. In most cases, HP is a circular shape with an inner wick structure. Before sealing, the pipe is emptied and then charged with operating coolant [10]. HP has no mechanical components for functioning. HP typically comprises three parts: evaporator, adiabatic, and condenser portion, as shown in Fig. 1. Heat input is given to the evaporator in which fluid starts its phase from liquid to vapor then vapor transfers to the condenser via the adiabatic part. In the condenser, heat is released to the surroundings. HPs use a capillary wicking action to flow fluid from the condenser unit to the evaporation portion. Sintered powder (SP), groove structure, screen mesh, etc. are types of wick structures used in HPs. HPs have become more popular in many industries, such as consumer electronics, defense, aerospace, medical, automotive, food, telecommunications, and others. Circular HP, flat HP, L-type HP, loop HP, and oscillating/pulsating HP are types of heat pipes. Nowadays various research is going on battery thermal management systems using heat pipes [5].

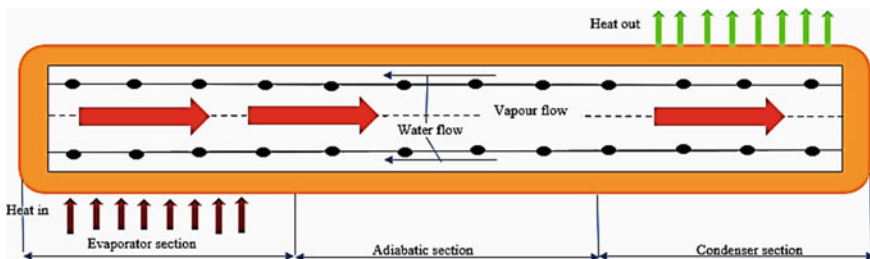


Fig. 1 Achematic diagram of a heat pipe

2.1 Heat Pipe-Assisted BTMS

The HP has various wick structures which consist of sintered powder (SP), screen mesh, and groove structure. HP works on the principle of capillary action which helps fluid return to the evaporator from the condenser unit. A lot of research on heat pipe-assisted BTMS is going on across the world. L-shape, circular, flat, loop heat pipe, etc. HP-BTMS are briefly discussed in this section. C-rate is utilized to determine the discharge and charge rate of a battery. Greco et al. [11] developed a 1-D mathematical simulation for heat pipe-based BTMS in LIB. 18 circular HPs made up of copper having a diameter of 10 mm are considered for the system. Groove wick structure and ammoniac working fluid for HP were chosen. Prismatic LIB having 20 Ah capacity was considered in the design. A single heat pipe's maximum heat transfer capacity is set to 400 W. The heat pipe system cooled battery temperature by 27.6 °C, whereas forced convection was expected at 51.5 °C. Heat pipes enable a better cooling technique than forced air cooling. Tran [12] experimentally investigated heat pipe cooling for LIB in hybrid electrical vehicles. 14 cylindrical cells with 142 mm height, 38 mm diameter, and 6.5 Ah capacity made up the battery simulator. The battery cooling wall was a copper plate with a heat pipe attached. Copper Plate has an identical temperature as the temperature of a battery wall. The evaporator temperature was beyond 50 °C for both 54 W and 84 W input powers. The evaporator temperature was controlled at 46 °C when the heat produced by the cell was modest. Moreover, the AMESim model revealed that the cell temperature was 49.70 °C, which is extremely near to the maximum range of the battery's working temperature limit. Gan et al. [13] numerically studied a heat pipe-assisted TMS of a LIB using a thermal equivalent circuit model (TECM). Various inlet working fluid temperatures, coolant flow rates, and discharge rates are used to verify the TECM. The 18,650 LIBs are considered in this study. Three HPs are positioned in between a row of batteries. The HP (copper–water sintered) has an outside 6 mm diameter and 91 mm length. T_{\max} and ΔT_{\max} were observed to be 33 °C and 4.83 °C, respectively. The T_{\max} lowered by around 14 °C as compared to natural cooling at of 5C discharge rate. Yao et al. [14] analyzed numerically the performance of refrigerant and HP-BTMS combined with air conditioning of EV. A rectangular LiFePO_4 battery having a capacity of 7 Ah was used in this study. Flat heat pipe comprised of aluminum and acetone as a working fluid was selected. The findings show that at the specific temperatures (25, 30, and 35 °C), the maximum battery temperature could be maintained below 40 °C and ΔT_{\max} between cells could be maintained below 3 °C. Feng et al. [15] studied the strain of HP-BTMS. A battery unit comprising of 24 cylindrical cells and a circular copper HP with sintered wick structure was selected. Maximum battery temperature was 17.5 °C achieved with fins and ΔT_{\max} was controlled at 6.5 °C. Yuan et al. [16] evaluated the temperature characteristics of HP-BTMS. LiFePO_4 battery with 10 Ah capacity was used. A tubular heat pipe (copper-sintered water) was selected. T_{\max} was 32.2 °C achieved and maximum temperature difference was below 4 °C. Using a dual heat pipe, heat collecting plate, and forced air circulation reduces battery temperature. Gan et al. [17] numerically analyzed HP-BTMS for

cylinder-cell batteries. 24 cylindrical cells and L-shaped heat pipe (copper-sintered water) were considered. The metal sleeves in the form of waves are employed to link heat pipes with batteries. The outcomes revealed that the flow rate has a substantial effect on battery pack T_{\max} but has a minimal effect on temperature uniformity. 0.5 Lmin^{-1} coolant flow rate is suggested at 2C discharge rate. The maximum battery temperature was $45 \text{ }^\circ\text{C}$ achieved and battery pack's ΔT_{\max} may be maintained at around $5 \text{ }^\circ\text{C}$. Mbulu et al. [18] examined the effectiveness of HP-assisted BTMS. Battery is replaced by electric heater heated at 30, 40, 50, and 60 W using I and L-shaped heat pipes. Water was employed to chill the condenser portions of the HPs at mass flow rates of 0.017, 0.033, and 0.05 kg/s. The findings showed that the developed HP-assisted BTMS can maintain T_{\max} lower than $54 \text{ }^\circ\text{C}$ and ΔT_{\max} under $5 \text{ }^\circ\text{C}$ at 60W. It could transfer more than 92.18% of the heat produced. Putra et al. [19] investigated the effectiveness of BTMS by employing a loop heat pipe (LHP) for EVs. A cartridge heater having a capacity of 400W was used instead of battery for heat generation. Copper LHP with stainless steel screen mesh wick structure was used. With a 60% filling ratio, acetone, alcohol, and distilled water were employed as coolants. The flat plate LHP performed best using acetone as the working fluid with 1.60 W/cm^2 heat flux load. The thermal resistance attained was $0.23 \text{ W/}^\circ\text{C}$. The highest temperature of evaporator was around $50 \text{ }^\circ\text{C}$ with acetone and alcohol, within the working temperature limit of LIB. Behi et al. [20] numerically analyzed the BTMS using heat pipes in Evs. Forced fluid cooling, natural air cooling, and HP cooling methods are suggested to cool the lithium titanate (LTO) cell. L-shaped copper HP with SP wick structure and water as coolant is selected. The outcomes stated that a HP delivered 30% of the desired cooling capacity at 8C. When compared to natural air cooling and liquid cooling system, HP cooling method performed improved while lowering the battery pack temperature by 30% and 32.5%, respectively. Moreover, the T_{\max} could be maintained under $37.1 \text{ }^\circ\text{C}$ and ΔT_{\max} closed to $4.9 \text{ }^\circ\text{C}$. Liang et al. [21] studied the performance of HP-aided BTM system. HP-BTMS thermal performance is tested from 15 to $35 \text{ }^\circ\text{C}$ ambient temperature. Two surrogate batteries made up of heater and aluminum blocks were used. The copper HP with SP wick structure having water as coolant is used. Heat input power varied from 20 to 50 W is used for this study. Results revealed that when the atmospheric temperature falls below $24 \text{ }^\circ\text{C}$, the thermal efficiency of HP-aided BTMS marginally improves. By lowering the temperature of coolant, the thermal efficiency of HP-BTMS is maintained at the same level when the atmospheric temperature is below $35 \text{ }^\circ\text{C}$. The T_{\max} may be kept below $45 \text{ }^\circ\text{C}$, while ΔT_{\max} is lower than $5 \text{ }^\circ\text{C}$ at 50 W. Lie et al. [22] studied the effectiveness of heat pipe-based BTMS. The LiFePO_4 battery with 12.5 Ah capacity was used. Flat HP (copper-sintered water) was considered at room temperature of $40 \text{ }^\circ\text{C}$. BTMS reduces the T_{\max} and ΔT_{\max} by $29.5 \text{ }^\circ\text{C}$ and $8 \text{ }^\circ\text{C}$, respectively compared to conventional battery cooling of the battery surface. Maximum battery temperature was $41.6 \text{ }^\circ\text{C}$ achieved and battery pack's temperature difference could be controlled under $2.9 \text{ }^\circ\text{C}$. Based on type of HP, HP material, of wick structure type, type of coolant, battery type and capacity, T_{\max} and ΔT_{\max} of the battery were analyzed and mentioned in Appendix 1.

2.2 *Oscillating Heat Pipe (OHP) Assisted BTMS*

Oscillating Heat pipe (OHP) has a wickless structure and is light in weight compared to previously discussed heat pipes. The pipe is drained and then partially filled with a coolant, which forms vapor–liquid slugs and plugs. The vapor–liquid /bubble-slug mechanism transfers heat from one end of this tube by pulsating method to the other. The filling ratio (FR) is very important in OHP-based BTMS. FR is defined as the working fluid volume ratio to HP's total volume. Various researchers conducted an experiment on OHP-based BTMS to examine the thermal pattern of batteries using a TMS. Rao et al. [30] explored the thermal performance of batteries with heat pipes for e-vehicles. The rectangular heater made of aluminum is the same size as a real LiFePO_4 power battery. Copper tubes with an external 5 mm diameter were used to create the Oscillating heat pipes (OHP). Oscillating heat pipes have a wickless structure and are lighter than other heat pipes. The overall length of a HP is 18 mm. Water as a coolant and the FR of water is 50% in HPs being selected. Heat input power was varied from 10 to 60 W for this system. The T_{\max} may be maintained under 50 °C when the heat generation rate is below 50 watts. The ΔT_{\max} is less than 5 °C with a 30 W rate of heat generation. A detailed study of various parameters affecting T_{\max} and ΔT_{\max} of OHP-based BTMS is mentioned in Appendix 2.

2.3 *Heat Pipe-Phase Change Materials (HP-PCM) Assisted BTMS*

Hybrid system which consists of HP-PCM-assisted BTMS is more efficient than simple HP-aided BTMS. Various researchers experimentally/numerically performed the thermal performance of hybrid system by combining HP with PCM-based BTMS. Zhao et al. [33] fabricated and investigated heat pipe/phase change material (HP/PCM) combined BTM system. Six heat pipes (copper-sintered water) with circular fins were considered and paraffin/ethylene glycol (EG) was used as PCM. The results demonstrated that PCM temperature management is more effective than air based BTM. The T_{\max} of HP/PCM PCM-assisted could be maintained at 42 °C for a lengthier time than air cooling and PCM cooling systems under similar circumstances. By filling PCM, the ΔT_{\max} could be decreased by around 33.6%, and by integrating PCM with HP, it can decrease by a further 28.9%. ΔT_{\max} of HP/PCM combined BTM could be adjusted to be under 5 °C. A detailed study of various parameters affecting T_{\max} and ΔT_{\max} of HP/PCM-based BTMS (hybrid system) is mentioned in Appendix 2.

3 Discussions

The excessive heat of the battery reduces its capacity and cycle life while also elevating the probability of an explosion or accident. Researchers discovered that the LIBs function brilliantly from 25 to 50 °C temperature limit. Therefore, BTMS is essential to keep the T_{\max} within the appropriate limit. Despite extensive studies on BTMS over the last few years, the expected result of the battery has yet to be realized. Comparing battery performance using various kinds of BTMS is difficult as various scholars examined using cylindrical and prismatic types of batteries with different discharging/charging rates (0.5–8C), varying capacities (1.96–55 Ah), different input power (10–120 W), and ambient temperatures (15–35 °C). Heat pipe-assisted thermal management method and hybrid cooling technique for a battery are discussed in this article. Heat pipes are a low-cost, long-lasting, lightweight, and thermally conductive passive cooling technology. Flat HP, L-shaped HP, micro-HP, and circular HP-assisted BTMS are discussed in Sect. 2.1. Screen mesh, sintered copper powder, and groove-type structure are used as wick structure in heat pipe-assisted BTMS. Water, methanol, acetone, and ethanol as the coolant used in HP-assisted BTMS. The maximum Battery temperature and ΔT_{\max} are maintained at around 55 °C and 5 °C, respectively. Oscillating heat pipe-aided BTMS is discussed in Sect. 2.2. Among various working fluids, water with a 50% filling ratio and three turns of OHP gave the best results i.e., keeping T_{\max} at 46.5 °C and ΔT_{\max} at 5 °C. HP/PCM-BTMS (Hybrid systems) are considered in Sect. 2.3. Water, air, and acetone are used as coolants in HPs. Paraffin and ethylene glycol (EG) are used as PCM. Water as coolant, and 50% FR for HP and paraffin PCM are suggested for HP/PCM-aided BTMS to control T_{\max} and ΔT_{\max} around 42 °C and 5 °C, respectively.

4 Concluding Remarks

LIBs have extended cycle life and high energy density which makes them a suitable candidate for use as storage devices in electrical vehicles. LIBs are sensitive to temperature, therefore, BTMS is required to maintain the T_{\max} and the ΔT_{\max} . BTMS is a very essential part of a battery with high energy density. Air-cooled, water-cooled, PCM cooling HP cooling, thermoelectric cooling, and hybrid cooling are types of BTMS. Among all these, heat pipe-assisted BTMS is superior in terms of better heat conductivity, high heat transfer rate, wide temperature range, etc. L-shape, circular, flat, and loop, and oscillating heat pipes are types of heat pipes. Sintered powder, screen mesh, and groove are types of wick structures used in HP-based BTMS. Water, alcohol, methanol, acetone, ethanol, etc. are used as coolants in HPs. OHP-based BTMS has an advantage over other HP-aided BTMS due to its wickless structure and lightweight property. The number of turns of OHP is 3, FR is 30–50%, and a condenser above the evaporator is suggested. The thermal effectiveness of HP-aided

BTMS can be further enhanced by adding PCM to make a hybrid system subjected to PCM leakage issues.

Nomenclature

- LIBs* Lithium-ion batteries
- BTMS* Battery thermal management system
- HP* Heat pipe
- OHP* Oscillating heat pipe
- PCM* Phase change material
- SP* Sintered powder
- T_{max} Maximum battery temperature (°C)
- ΔT_{max} Maximum temperature difference (°C)
- D Outer diameter of heat pipe (mm)
- L_e Length of evaporator (mm)
- L_c Length of condenser (mm)
- L_t Total length (mm)

Appendix 1: Summary of some relevant studies on Heat pipe-based BTMS

Authors	Analysis type	Type of HP	HP material	Wick structure	Working fluid	T_{max} (°C)	ΔT_{max} (°C)
Liang et al. [21]	Experimental	Circular and flattened	Copper	Sintered powder	Water	45	5
Wang et al. [23]	Experimental	L-shape circular	Copper	Sintered powder	Water	41.1	5
Ye et al. [24]	Numerical	Flat heat pipe	Copper	Sintered powder	Water; methanol; ethanol	45	5
Zhao et al. [25]	Experimental	Flat heat pipe	Aluminum	Groove	Acetone	30	1.1
Wang et al. [26]	Numerical	Flat heat pipe	Copper	Sintered powder	Water	27.6	1.08
He et al. [27]	Numerical	L-shape circular	Copper	Sintered powder	Water	37.6	3.7

(continued)

(continued)

Authors	Analysis type	Type of HP	HP material	Wick structure	Working fluid	T_{\max} (°C)	ΔT_{\max} (°C)
Smith et al. [28]	Experimental	Flat heat pipe	Copper	Sintered powder	Water	55	5
Dan et al. [29]	Numerical	Micro heat pipe	Aluminum	Groove	Acetone	40	2

Appendix 2: Summary of some relevant studies on heat pipe and PCM-based BTMSs

Authors	Analysis type	HP type	Working fluid	Filling ratio (%)	PCM used	T_{\max} (°C)	ΔT_{\max} (°C)
Rao et al. [30]	Experimental	OHP	Water	50	–	50	5
Qu et al. [31]	Experimental	OHP	DI-water	50	–	50	5
Wei et al. [32]	Experimental	OHP	Water; ethanol; binary fluid mixtures	30–50	–	46.5	2.1
Zhao et al. [33]	Experimental	OHP	Water	50	Paraffin	42	5
Chen et al. [34]	Numerical	Flat HP	Air	–	Paraffin/EG	50	4.3
Wang et al. [35]	Experimental	OHP	Acetone	50	Paraffin	50	5

References

1. Tete PR, Gupta MM, Joshi SS (2021) Developments in battery thermal management systems for electric vehicles: a technical review. *J Energy Storage* 35:102255
2. Ghanbarpour M, Khodabandeh R, Vafai K (2017) An investigation of thermal performance improvement of a cylindrical heat pipe using Al₂O₃ nanofluid. *Heat Mass Transf* 53(3):973–983

3. Siddique A, Mahmud S, Van Heyst B (2018) A comprehensive review of a passive (phase change materials) and an active (thermoelectric cooler) battery thermal management system and their limitations. *J Power Sources* 401:224–237
4. Karimi D, Behi H, Jaguemont J, Sokkeh A, Kalogiannis T, Hosen S, Van Mierlo J (2020) Thermal performance enhancement of phase change material using aluminum-mesh grid foil for lithium-capacitor modules. *J Energy Storage* 30:101508
5. Faghri A (1995) *Heat pipe science and technology*. Global Digital Press
6. Xie J, Ge Z, Zang M, Wang S (2017) Structural optimization of lithium-ion battery pack with forced air-cooling system. *Appl Therm Eng* 126:583–593
7. Huo Y, Rao Z (2015) The numerical investigation of nanofluid based cylinder battery thermal management using lattice Boltzmann method. *Int J Heat Mass Transf* 91:374–384
8. Krüger L, Limperich DG (2012) Energy consumption of battery cooling in hybrid electric vehicles
9. Duan X, Naterer F (2010) Heat transfer in phase change materials for thermal management of electric vehicle battery modules. *Int J Heat Mass Transf* 53(23–24):5176–5182
10. Pathak S, Kumar R, Goel V, Pandey A, Tyagi V (2022) Recent advancements in thermal performance of nano-fluids charged heat pipes used for thermal management applications: a comprehensive review. *Appl Therm Eng* 119023
11. Greco A, Cao D, Jiang X, Yang H (2014) A theoretical and computational study of lithium-ion battery thermal management for electric vehicles using heat pipes. *J Power Sources* 257:344–355
12. Tran H, Harmand S, Sahut B (2014) Experimental investigation on heat pipe cooling for hybrid electric vehicle and electric vehicle lithium-ion battery. *J Power Sources* 265:262–272
13. Gan Y, Wang J, Liang J, Huang Z, Hu M (2020) Development of thermal equivalent circuit model of heat pipe-based thermal management system for a battery module with cylindrical cells. *Appl Therm Eng* 164:114523
14. Yao M, Gan Y, Liang J, Dong D, Ma L, Liu J, Li Y (2021) Performance simulation of a heat pipe and refrigerant-based lithium-ion battery thermal management system coupled with electric vehicle air-conditioning. *Appl Therm Eng* 191:116878
15. Feng L, Zhou S, Li Y, Wang Y, Zhao Q, Luo C, Wang G, Yan K (2018) Experimental investigation of thermal and strain management for lithium-ion battery pack in heat pipe cooling. *J Energy Storage* 16:84–92
16. Yuan W, Yan Z, Tan Z, Chen W, Tang Y (2016) Heat-pipe-based thermal management and temperature characteristics of Li-ion batteries. *Can J Chem Eng* 94(10):1901–1908
17. Gan Y, He L, Liang J, Tan M, Xiong T, Li Y (2020) A numerical study on the performance of a thermal management system for a battery pack with cylindrical cells based on heat pipes. *Appl Therm Eng* 179:115740
18. Mbulu H, Laoonual Y, Wongwises S (2021) Experimental study on the thermal performance of a battery thermal management system using heat pipes. *Case Stud Therm Eng* 26:101029
19. Putra N, Ariantara B, Pamungkas A (2016) Experimental investigation on performance of lithium-ion battery thermal management system using flat plate loop heat pipe for electric vehicle application. *Appl Therm Eng* 99:784–789
20. Behi H, Karimi D, Jaguemont J, Ghanbarpour M, Behnia M, Van Mierlo J (2020) Thermal management analysis using heat pipe in the high current discharging of lithium-ion battery in electric vehicles. *J Energy Storage* 32:101893
21. Liang J, Gan Y, Li Y (2018) Investigation on the thermal performance of a battery thermal management system using heat pipe under different ambient temperatures. *Energy Convers Manage* 155:1–9
22. Lei S, Shi Y, Chen G (2020) Heat-pipe based spray-cooling thermal management system for lithium-ion battery: experimental study and optimization. *Int J Heat Mass Transf* 120494
23. Wang Q, Jiang B, Xue F, Sun L, Li B, Zou H, Yan Y (2015) Experimental investigation on EV battery cooling and heating by heat pipes. *Appl Therm Eng* 88:54–60
24. Ye Y, Shi Y, Saw H, Tay A (2016) Performance assessment and optimization of a heat pipe thermal management system for fast charging lithium-ion battery packs. *Int J Heat Mass Transf* 92:893–903

25. Zhao R, Gu J, Liu J (2015) An experimental study of heat pipe thermal management system with wet cooling method for lithium-ion batteries. *J Power Sources* 273:1089–1097
26. Wang L, Zhao Y, Quan Z, Liang J (2021) Investigation of thermal management of lithium-ion battery based on micro heat pipe array. *J Energy Storage* 39:102624
27. He L, Tang X, Luo Q, Liao Y, Luo X, Liu J, Li Y (2022) Structure optimization of a heat pipe-cooling battery thermal management system based on fuzzy grey relational analysis. *Int J Heat Mass Transf* 182:121924
28. Smith J, Singh R, Hinterberger M, Mochizuki M (2018) Battery thermal management system for electric vehicle using heat pipes. *Int J Therm Sci* 134:517–529
29. Dan D, Yao C, Zhang Y, Zhang H, Zeng Z, Xu X (2019) Dynamic thermal behavior of micro heat pipe array-air cooling battery thermal management system based on thermal network model. *Appl Therm Eng* 162:114183
30. Rao Z, Wang S, Wu M, Lin Z, Li F (2013) Experimental investigation on thermal management of electric vehicle battery with heat pipe. *Energy Convers Manage* 65:92–97
31. Qu J, Wang C, Li X, Wang H (2018) Heat transfer performance of flexible oscillating heat pipes for electric/hybrid-electric vehicle battery thermal management. *Appl Therm Eng* 135:1–9
32. Wei A, Qu J, Qiu H, Wang C, Cao G (2019) Heat transfer characteristics of plug-in oscillating heat pipe with binary-fluid mixtures for electric vehicle battery thermal management. *Int J Heat Mass Transf* 135:746–760
33. Zhao J, Rao Z, Liu C, Li Y (2016) Experimental investigation on thermal performance of phase change material coupled with closed-loop oscillating heat pipe (PCM/CLOHP) used in thermal management. *Appl Therm Eng* 93:90–100
34. Chen K, Hou J, Song M, Wang S, Wu W, Zhang Y (2021) Design of battery thermal management system based on phase change material and heat pipe. *Appl Therm Eng* 188:116665
35. Wang Q, Rao Z, Huo Y, Wang S (2016) Thermal performance of phase change material/oscillating heat pipe-based battery thermal management system. *Int J Therm Sci* 102:9–16

Design to Avoid Dry Out in a Flat Heat Pipe Based on Cu Foam



Nitish Kumar Tripathi, Prafulla P. Shevkar, Chitransh Atre,
and Baburaj A. Puthenveettil

1 Introduction

The flat heat pipe or Thermal Ground Plane (TGP) is a passive device which maintains the temperature of electronic chips or any other heat-generating components by absorbing their heat from the one end, i.e., the evaporator section, and removes the heat at the other end, called the condenser section, without any other external energy needed. The components of a heat pipe are a closed rectangular cavity formed by joining the top and bottom plate made of copper material, a wick structure made of copper foam, and a small amount of working fluid free from condensable gases, which is in equilibrium with its own vapour. Typical heat pipes work on a simple principle of condensation and evaporation of the working fluid occurring in a closed system. Heat is transferred from evaporator to condenser by converting the liquid to vapour, utilizing the latent heat of the working fluid [1–3]. In the previous work, we showed that copper foam can be used instead of sintered powder based as the porous media [4]. Since the minimum porosity (ϵ) to avoid dry out decreases with an increase in mean pore diameter (d_p), for a given length of the heat pipe (L_{TGP}) and maximum heat flux (Q_{max}), larger pore sizes as would occur in copper foam seem to be desirable.

The present work proposes a design methodology to avoid dry out of the flat heat pipe where copper foam is used as the porous media. A rectangular copper cavity encloses the porous media fixed on the cavity's bottom surface (Fig. 1). The space above the porous media surface and the cavity top wall forms the vapour region [5]. The degassed liquid will be filled in the porous media. Heat absorbed from the hot chip by the fluid evaporates it to form vapour on the evaporator side. This vapour will move to the condenser region of the chamber, where it condenses on the porous

N. K. Tripathi (✉) · P. P. Shevkar · C. Atre · B. A. Puthenveettil
Department of Applied Mechanics, IIT Madras, Chennai 600036, India
e-mail: nitishkumartripathi7@gmail.com

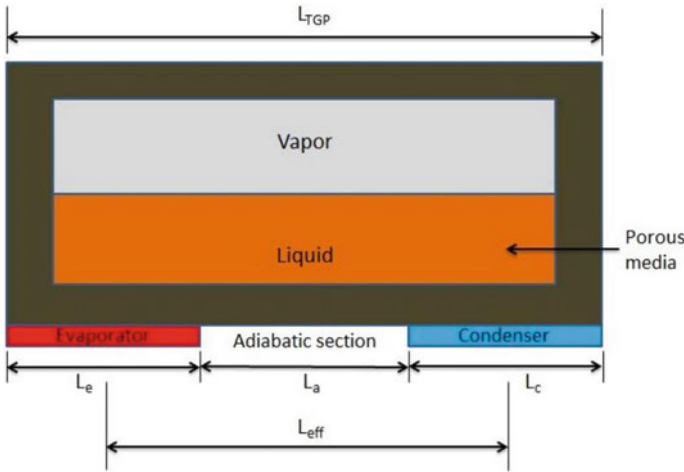


Fig. 1 Schematic of the heat pipe

media and returns through the porous media to the evaporator region by capillary motion [3].

The following design calculations were done for a Thermal Ground Plane (TGP) with porous media made of copper foam. The geometry considered is shown in Fig. 1. The minimum capability of the device is to maintain the temperature of the MMIC to less than 150 °C removing about 20 W from a size of 5 mm × 5 mm. The device's thickness is 3.5 mm and the length 3 cm, the exact values are expected to be the outcome of the design process explained in the upcoming section.

2 Methodology

For a heat pipe to work properly without dry out, the net capillary pressure difference between the evaporator and the condenser region (ΔP_c) must be greater than or equal to the sum of the pressure losses in the system [4, 5] i.e.,

$$\Delta P_c \geq \Delta P_1 + \Delta P_v + \Delta P_b \quad (1)$$

Here, ΔP_1 is the pressure drop due to the viscous resistance of the liquid, ΔP_v is the pressure drop due to viscous resistance in the vapour, and ΔP_b is the hydro static pressure head. The capillary pressure (ΔP_c) is given by the Young–Laplace equation,

$$\Delta P_c = C_1 \frac{2\sigma}{r_p} \quad (2)$$

where, σ = surface tension of water in (N/m) at 115 °C, r_p = mean wick pore radius

$$r_p = \frac{0.0254}{2\text{PPI}} \epsilon \quad (3)$$

with $\epsilon = 0.95$ and $C_1 = 0.5$, an empirical value for porous media dependent on the contact angle and the standard deviation of the pore diameter [6]. Since the flow is laminar, using Hagen–Poiseuille equation, ΔP_1 in (1) is

$$\Delta P_1 = \frac{\dot{m} \mu_1 L_{\text{eff}}}{K \rho_1 A_{\text{wick}}}. \quad (4)$$

Here, \dot{m} = mass flow rate (kg/s), μ_1 = dynamic viscosity of the liquid (Pa s), L_{eff} = effective length of TGP (m), which is equal to $L_a + 0.5(L_e + L_c)$ (see Fig. 1), ρ_1 = density of water (kg/m³), A_{wick} = area of cross-section of the wick (m²), and K is the permeability in (m²). The permeability of the copper foam, which appears in (4) can be obtained from [7] as

$$K = \frac{K_r}{r_p}, \quad (5)$$

where K_r is the ratio of permeability vs porosity [7] and r_p from (3). We extrapolate the data from Table 5 of the paper [7] by using power law curve fit to obtain the value of

$$K_r = \frac{0.56E^{-14}}{\epsilon^2 - 75.07 \epsilon + 0.4601} \quad (6)$$

where $\epsilon = 0.95$.

We assume that all the heat supplied by the chip to the heat pipe is carried away by \dot{m} kg/s of water vapour, which condenses at the condenser and flows back through the porous media to the evaporator end. The mass flow rate (kg/s) of liquid through the porous media $\dot{m} = Q_{\text{HP}}/h_{\text{fg}}$ with Q_{HP} = heat flux, and the latent heat of vapourization of water $h_{\text{fg}} = 2336130$ J/kg. In (1), the pressure drop in the vapour chamber due to viscous resistance (ΔP_v) is approximated by,

$$\Delta P_v = \frac{32\mu_v L_{\text{eff}} \dot{m}}{d_v^2 \rho_v A_{\text{vap}}}, \text{ assuming laminar flows} \quad (7)$$

Here, μ_v is the dynamic viscosity of water vapour in kg/ms at 0.3 bar, hydraulic diameter of vapour channel, $d_v = 4 \times A_{\text{vap}} / 2 \times (W_v + H_v)$ where W_v & H_v are width and height of vapour chamber in m, ρ_v = vapour density in kg/m³, and A_{vap} is the area of cross-section of the vapour chamber. ΔP_b in (1) is considered as the static pressure head over the length of the heat pipe L_{TGP} , multiplied by a factor g_f to take into account of the acceleration of the heat pipe.

$$\Delta P_b = \rho_1 g L_{\text{TGP}} g_f, \quad (8)$$

where $L_{\text{TGP}} = L_a + L_e + L_c$.

Table 1 Input parameters during the study

μ_l (Pa s)	ρ_l (kg/m ³)	μ_v (Pa s)	ρ_v (kg/m ³)	d_v (mm)
2.36×10^{-4}	946.74	1.3×10^{-5}	0.191	0.0019

3 Results and Discussion

Simulations were conducted with the values of properties and parameters shown in Table 1. These properties were chosen at a pressure of 0.3 bar, assuming the vapour pressure of water at the average mean temperature. The evaporator temperature is considered to be at 150 °C and the condenser temperature 80 °C, so that the properties are evaluated at a mean temperature of 115 °C, the saturation temperature at 0.3 bar pressure. This assumption needs to be relaxed in future calculations where a temperature model is coupled to a pressure model. Equations 1–8 were solved for a range of pores per inch $130 \leq \text{PPI} \leq 500$ of copper foam. Figure 2 shows the limiting heat flux Q_{HP} that would result in dry out for various L_{TGP} , when the PPIs are changed over the range $130 < \text{PPI} < 490$. The Fig. 2 gives the amount of dry out heat flux, when $L_{TGP} = 3$ cm for various PPI. It is clear that for a 20 W heat removal over a distance of 3 cm, the porous media needs to have a PPI of 170 or more. The Fig. 2 also gives the maximum length that the heat pipe can transport a given heat flux without dry out for a Cu foam of specified PPI. For a given heat flux, larger PPI implies larger L_{TGP} . Figure 3 shows the max heat transferable for a length 3 cm. A higher PPI of copper foam is needed if we increase the g_f , i.e., gravity factor, with the help of linear interpolation, we found that $Q_{max} = 0$ at $g_f = 1$ and the length of TGP = 3 cm for the copper foam of 70 PPI. From Fig. 3, the copper foam of 450 PPI has $Q_{max} = 176$ W at $g_f = 1$ and $Q_{max} = 122$ W at $g_f = 3$. A 30% decrease in Q_{max} with increase in the gravity factor is observed. Similarly for $g_f = 3$ and $g_f = 5$, the decrease in maximum heat flux for 450PPI is 45%. Hence, with increase in g_f , the heat flux value will decrease.

4 Conclusions

In the paper, we have presented a design methodology that gives the parameters of the heat pipe which dry out can be prevented in the flat heat pipe for a given length of the flat heat pipe, PPIs, and maximum heat flux. Equating capillary pressure with the viscous pressure drop in the porous media and the vapour section, we find out the dry out length for various heat fluxes and PPIs of copper foam. We find that at a fixed porosity 95% for the 3 cm optimum dry out length of the flat heat pipe when 20 W of heat flux is to be removed from the chip of area 5×5 mm². For a length of 3 cm and 450 PPI of copper foam, the increase in g_f from 1 to 5 decreases the maximum heat flux from 176W to 67 W for the $g_f = 1$ to $g_f = 5$.

Fig. 2 Variation of maximum heat flux with length of the heat pipe for various pores per inch (PPI) for a heat pipe using Cu foam

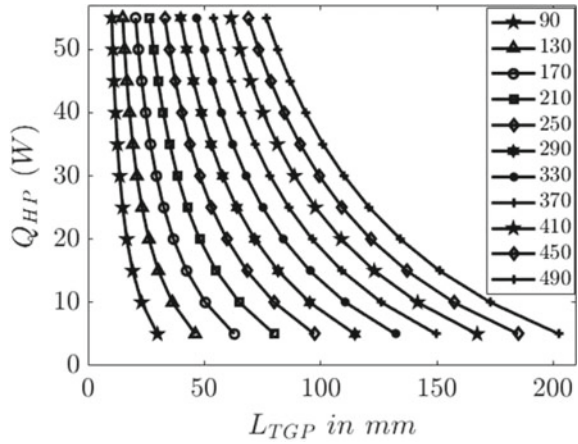
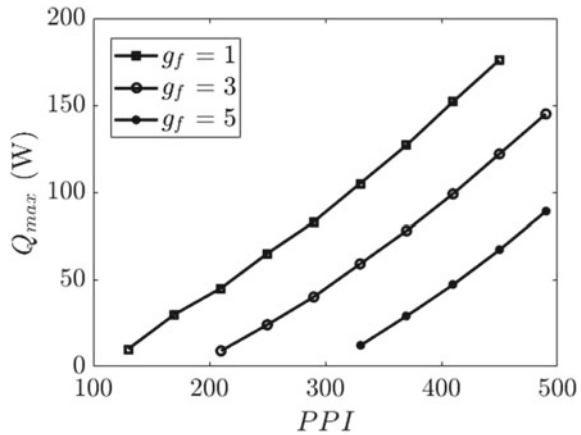


Fig. 3 Maximum heat transferable for various pores per inch (PPI) at the value of porosity ($\epsilon = 0.95$) for a length of TGP ($L_{tgp} = 3$ cm, with $g_f = 1, 3$ and 5



Acknowledgements We gratefully acknowledge the financial support of DST, the Government of India through their grants IMP/2018/001167. We acknowledge the support of Usha P Verma S ‘G’, Advanced Systems Laboratory (ASL), DRDO, and Astra Microwave Products Ltd.

Nomenclature

- L_{TGP} Length of the TGP [m]
- g_f Gravity Factor
- r_p Radius of the pore size [m]
- μ_1 Dynamic viscosity of water [Pa s]
- ρ_1 Density of water [kg/m³]
- ϵ Porosity

μ_v	Dynamic viscosity of water [Pa s]
ρ_v	Density of vapour [kg/m^3]
g	Gravity [m/s^2]
A_{vap}	Area of cross-section of the vapour chamber [m^2]
L_a	Length of adiabatic section [m]
L_e	Length of evaporator section [m]
L_c	Length of condenser section [m]
H_v	Height of the vapour region [m]
W	Width of wick [m]
σ	Surface tension of water [N/m]
K	Permeability [m^2]

References

1. Chi SW (1976) Heat pipe theory and practice, Series in thermal and fluids engineering. McGraw-Hill, New York
2. Dunn PD, Reay DA (1976) Heat pipes. Pergamon Press, Oxford
3. Faghri NA (1995) Heat pipe science and technology. Taylor & Francis
4. Tripathi N, Shevkar PP, Atre C, Puthenveetil BA (2022) A design procedure for sintered copper flat heat pipes. In: Proceedings of ICFTES22 (NIT Calicut, Kerala INDIA), 2022
5. Ababneh MT, Gerner FM, Chamarthy P, de Bock Shakti P, Chauhan, Deng T (2014) Thermal-fluid modeling for high thermal conductivity heat pipe thermal ground planes. J Thermophys Heat Transf 28(2)
6. De Bock HPJ, Varanasi K., Chamarthy P., Deng T., Kulkarni A., Rush BM, Russ BA, Weaver SE, Frank M. Gerner, Experimental investigation of micro/nano heat pipe wick structures. In: ASME International mechanical engineering congress and exposition, proceedings IMECE2008 (2008), no. 67288, pp 991–996
7. Shirazy MRS, Fréchet LG (2013) Capillary and wetting properties of copper metal foams in the presence of evaporation and sintered walls. Int J Heat Mass Transf 58(1–2):282–291

Framework with Data-Analytic for Fault Detection and Performance Prediction of a Steam Boiler: A Case Study



Nivedita Wagh and Sudhir Agashe

1 Introduction

The performance of the boiler is generally predicted using steam pressure which helps to obtain its efficiency. This pressure is affected by the quality of combustion and scaling, etc. Heat content of the steam is a function of the steam pressure. It is therefore possible to predict the performance of a boiler through pressure prediction. The expected steam pressure is highly affected by the faults developed in the boiler unit. It is therefore important to identify the faults to have a better prediction of pressure. The present work reports the data-driven framework for steam pressure prediction and fault diagnosis in the steam boiler.

2 Literature Review and Objective

The literature review of the frameworks for fault-finding and data-driven models for performance prediction is presented here. Qin et al. [1] proposed an indirect failure prediction method for predicting boiler failures in thermal power plant. Machine learning to improve the efficiency in industrial boilers for fault detection, diagnosis and prognosis is reported by Meng et al. [2]. They argued that the knowledge of an expert or an engineer is helpful to diagnose the faults if output data is collected. But this approach is not able to identify the new faults that occur in the system.

Data-driven frameworks are widely used by many researchers for different processes. Among others, scenario based stochastic model is used by Niknam et al. [3] to predict the load demand, output power of wind, photo-voltaic units and

N. Wagh (✉) · S. Agashe

Department of Instrumentation and Control Engineering, College of Engineering Pune,
Pune 411005, India

e-mail: wagnivedita1984@gmail.com

market price. A novel self-adaptive probabilistic modification strategy is proposed to improve the performance of the algorithm. Kim et al. [4] proposed a framework and some methodologies for thermal performance analysis, which differs from conventional performance monitoring. Furnace temperature control in the power plant boiler using data-driven framework is reported by Zhenhao et al. [5]. Dual-optimized adaptive model predictive control (DoAMPC) technique based on the data analytics is used here. It is argued that results based on experimental data using DoAMPC analysis can be used to control the boiler furnace temperature with small errors. Li and Wang [6] proposed data-driven framework with five main variables which affect the boiler performance.

Neural network approaches are powerful in the modeling of engineering applications. These approaches are reported in the literature for implementation of the data-driven framework. Heydar et al. [7] used it to predict target output through two input data sets. They argued that it is possible to analyze and make recommendations for optimizing boilers in the gas refinery complex using response-surface method (RSM). Principal Component Analysis (PCA) is effectively used by Zhang and Niu [8] for realizing the remote diagnosis of the running state of the power station unit. They set up the data interface of power plant, which completes the calculation and analysis of power plant data in a timely and efficient manner. To check the effectiveness of the air compressor system, Benedetti et al. [9] proposed a novel methodology with the help of statistical modeling and control charts. The statistical regression is used here to construct a baseline of the energy behavior. The control charts are used to validate the baseline and to identify the optimal operating conditions and energy consumption patterns. It also identifies the degradation in energy performance due to specific faults. Nikula et al. [10] focused on performance improvement of steam boilers by enhancing its efficiency, for which he developed a data-driven framework. Their framework helps to identify the performance with respect to expected performance. They also carried out fault detection with the help of exponentially weighted moving average (EWMA) charts.

It is noticed from the literature review that the development of correlations using any statistical procedure largely depends on the accuracy of selection of the variables which govern the processes. There is good amount of literature available for the selection of such variables which dominate the performance of any process [6, 11, 12, 13].

Thus, the literature reports the performance prediction of boiler using models which are either physical law-based or data-driven. The physical law-based models are derived from many assumptions. The literature also reports the fault-finding frameworks based on data-driven model. However, the framework including both fault finding and performance prediction is rarely reported in the literature. *This work therefore is an attempt to present a generalized data driven framework for a boiler with an aim to identify the faults through the understanding of the boiler performance in terms of steam pressure.* To be more specific, the aim of the present work is to provide a generalized data-driven framework that can detect the fault in key performance parameter and predict the steam pressure of a boiler and its deviation from the actual boiler pressure. Such a data-driven framework is useful for

plant operators and supervisors for taking up precautionary measures. The proposed framework is developed using in-house pilot plant boiler.

3 Methodology

Physical law-based control is the traditional method for process control [14]. The major focus of this method is on the optimization of the process. However, present study proposes a data-driven framework to identify the faults through the understanding of the boiler performance in terms of steam pressure. This framework helps to detect the statistically out of control process by monitoring the deviation from the expected pressure. The expected pressure data may be used to have a better performance. The framework also proposes a mechanism which gives better expected pressure estimate during monitoring. The correctness of the data obtained during experiments is ensured through an uncertainty analysis. The variable ranking is then carried out to understand the most dominant parameters which affect the estimation of steam pressure. The scatter plots are then plotted to understand the trends of variation between target variable and highly ranked variables. The regression analysis is then carried out to obtain the data-driven mathematical models for prediction of estimated pressure. Various models are obtained by considering combinations of different parameters affecting the estimated pressure. The new data which is obtained through another set of experiments is then projected in these models for the purpose of testing. During this testing, the various statistical parameters like R^2 , adjusted R^2 , p -value, t -value, RMS value and standard error are obtained for various models. The comparison of is made based on statistical parameters to obtain the best model.

The exponentially weighted moving average (EWMA) charts are then developed to ensure that the steam generation process is not uncontrolled. The best model thus obtained is then further tested by introducing the numerical fault in the data.

The framework is shown in Fig. 1. The variable ranking approach is effectively used to implement such a framework. Responses of multiple regressions are used to predict the steam pressure. Both system identification and monitoring parts include a variable ranking approach. During the monitoring part, the statistical parameters such as adjusted multiple coefficient of determination, also called adjusted R^2 , are observed. The major advantage of the adjusted R^2 is to understand if the added new independent variable is really an explaining variable or a noise. The F-test is also carried out as it determines whether a significant relationship exists between the dependent variable and the set of all the independent variables. The t-test is done to determine whether each of the individual independent variable is significant or not. The estimation of the expected steam pressure is based on the responses from a multiple linear regression model and the historical maximum steam pressure in previous process states.

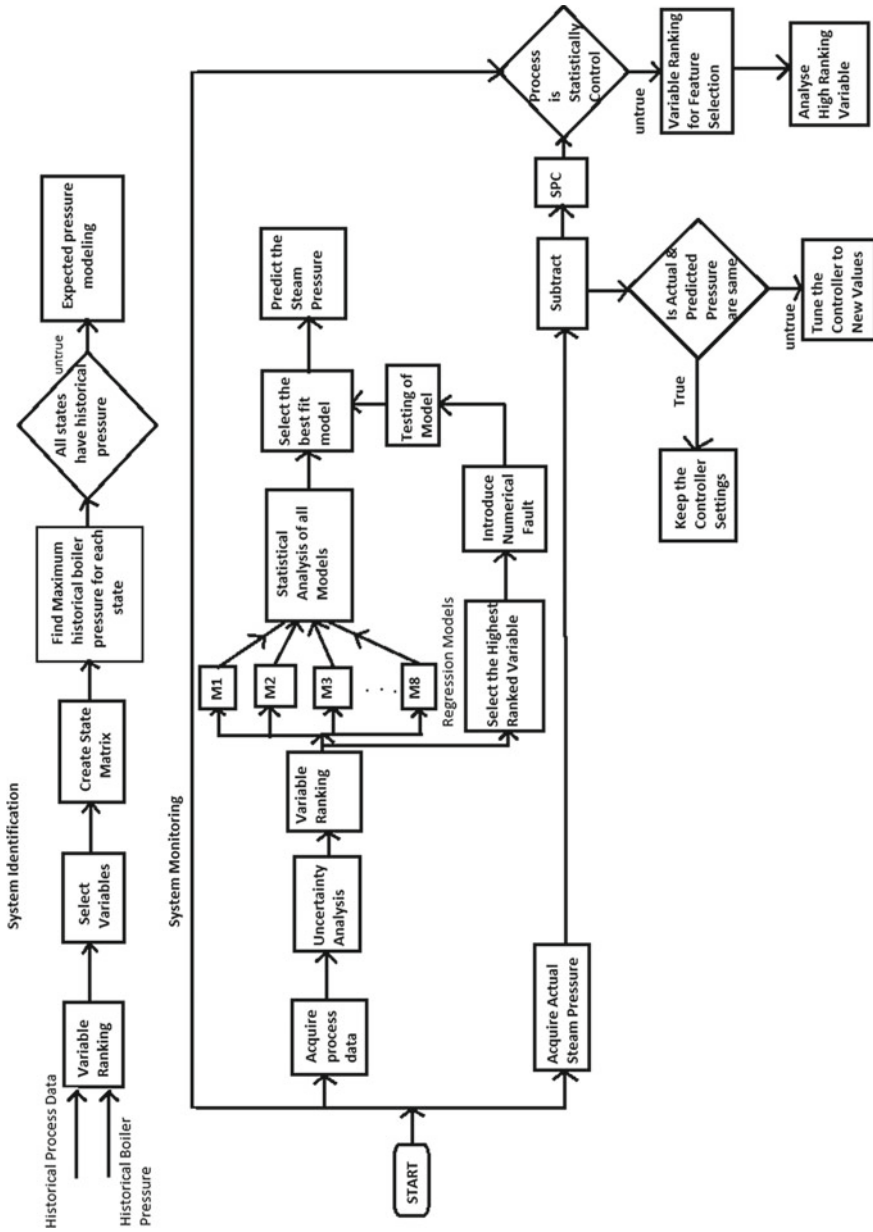


Fig. 1 Structure of proposed framework for identification and monitoring part

4 Results and Discussion

The framework for boiler pressure prediction is implemented with a laboratory-based pilot plant. The pilot plant is in the advanced process laboratory of *College of Engineering Pune* (India). The boiler is in cascade with heat exchanger unit where the cold water is supplied through inner pipe and steam flows through outer pipe of the heat exchanger, where the steam transfers heat to cold water [15]. The variables consisted of measurements of steam pressure, steam temperature, volumetric flow of steam and water level in the drum. The target variable is the instantaneous steam pressure, although it is measured as well. The data was acquired from a period of normal process operation. Total 3.0 h of data were used for system identification and 7.0 h of data were used for monitoring. The sampling time was 0.25 s. The steam pressure of the boiler is shown in Figure 2 for the identification and monitoring periods. It is noticed that the boiler takes around 2500 s to build up the pressure which then varies between 2.4 and 3.6 bar. The fluctuations in the pressure during monitoring period are also noticeable.

4.1 System Identification and Monitoring

All the possible parameters that affect the boiler pressure were tested in variable ranking which suggested that the steam flow rate and steam temperature have the highest value of similarity metric. Hence, these two parameters were selected to train the multiple linear regression models. Further, the pilot plant boiler unit was operated to obtain the data for developing the scatter plots (not shown). It is noticed that the relationship between steam pressure and steam temperature as well as steam flow

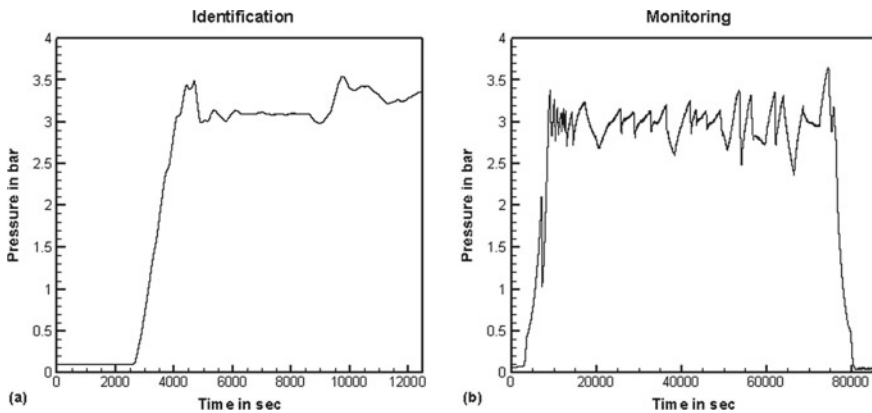


Fig. 2 Steam pressure of boiler for system identification and monitoring part of the framework

rate is linear. Thus, steam temperature and steam flow rate are selected for developing the multiple linear regression (MLR) models for boiler.

The highest ranking variables were used for developing the state matrices. The regression coefficients are obtained through WEKA. The estimates of expected pressure are set in two dimensional arrays where each dimension belongs to one of the variables from steam flow rate or steam temperature (not shown). It is noticed that the maximum pressure reaches to 0.35 MPa at the state variables of about 145 °C steam temperature and flow rate of 5.76 kg/hr.

The comparison of variation of actual pressure with the pressure predicted with the help of multiple regressions is presented in Fig. 3. Data for total of 12500 s is used for prediction of expected pressure. It has been observed that the predicted pressure by regression model is close to the actual boiler drum pressure. However, the prediction overshoots in between 9500 and 10,000 s. Overall the regression graph is unstable in nature. If extensive data is available for such type of operation, then the accuracy of the model will further improve. Further, the deviation between the expected pressure and actual pressure is demonstrated through EWMA chart for the identification period. Selecting the value of λ , which is exponential smoothing factor, is based on experience. The value of λ close to zero means the forecast for the next time instant is approximately equal to the forecast of the previous time instant. Hence, selecting the appropriate value of λ is the key to accurate forecasting with EWMA method. The weighting factor λ gives the rate at which the older data enters into the calculations of the EWMA statistics. A higher value of λ discounts older observation faster. In pilot plant boiler case, the λ value is set at four different values 0.7, 0.3, 0.2 and 0.05.

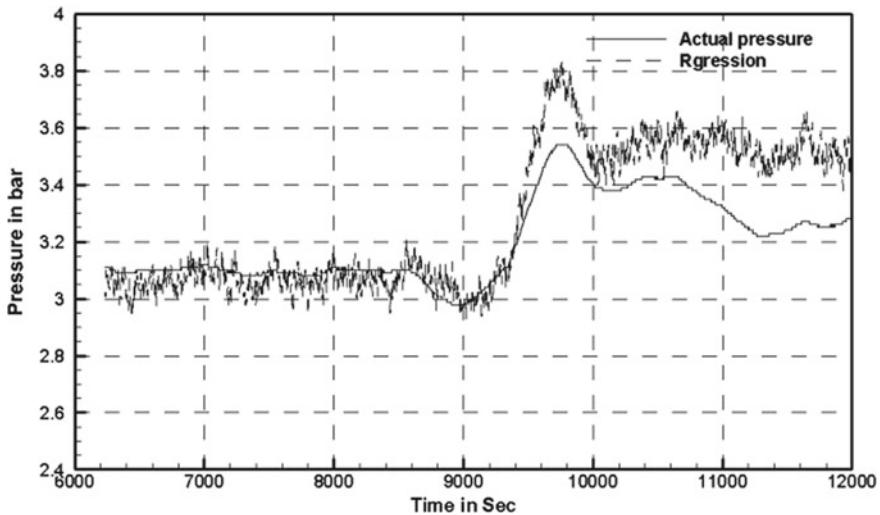


Fig. 3 Comparison of actual boiler pressure and the pressure predicted using multiple regression analysis for system identification

The action lines are calculated using equation $T \pm 3\sqrt{\frac{\lambda}{2-\lambda}}\sigma$. The deviation in the actual and predicted pressure is more in the case of larger λ value. Hence EWMA chart for $\lambda = 0.05$ is presented here in Fig. 4. It is noticed that the process is statistically out of control which may be due to small amount of data used for the system identification. It is therefore proposed to make use of large amount of data for further update of the model and its analysis as a part of system monitoring.

The monitoring framework of the system is further implemented to obtain the better model for pressure prediction. It is observed during the system identification that the prediction of steam pressure is statistically out of control when the model obtained through regression analysis is implemented. In this section, the implementation of monitoring framework for expected steam pressure is presented. The data used for the monitoring framework is for about 7.0 h with the time step of 0.25 s which gives data for approximately 80,000 time instances. The combinations of different independent variables form a unique model as listed in Table 1. Regression analysis

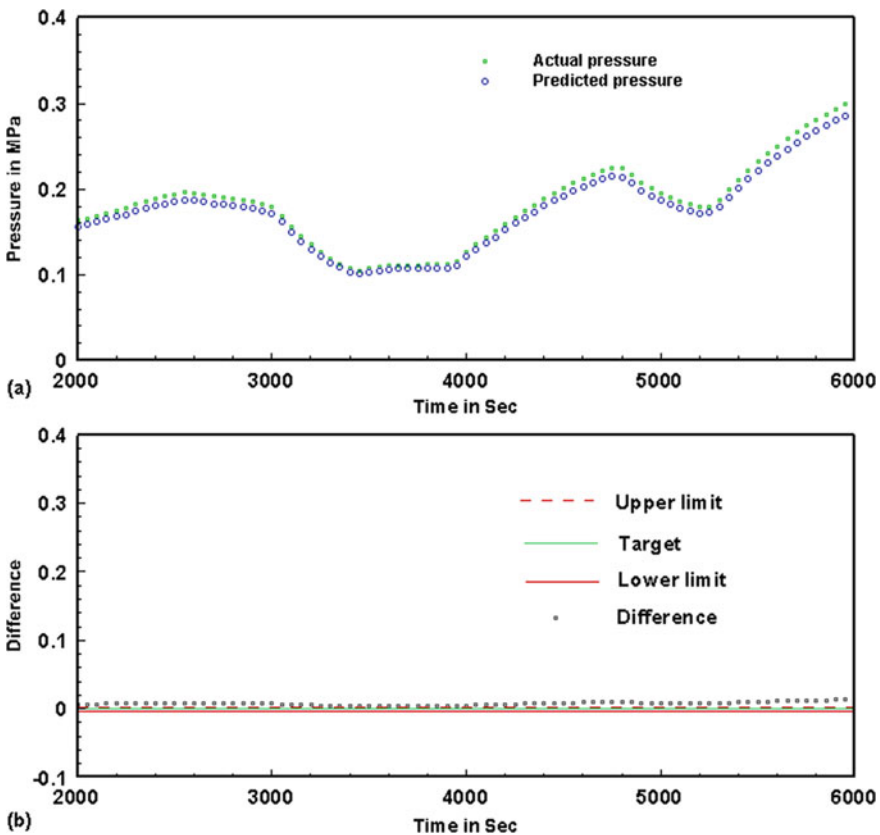


Fig. 4 Steam pressure monitoring using EWMA chart for $\lambda = 0.05$ indicating **a** variation of pressure with time and **b** variation of difference between actual and predicted pressure with time

Table 1 Different multiple regression models and their corresponding independent variables

Name of the model	Independent variables of the model
MLR2A	Steam temperature and steam flow rate
MLR2B	Steam temperature and volume of steam
MLR2C	Steam temperature and volume of water
MLR3A	Steam temperature, steam flow rate and volume of steam
MLR3B	Steam temperature, steam flow rate and volume of water
MLR3C	Steam temperature, volume of steam and volume of water
MLR4	Steam temperature and steam flow rate, volume of steam and volume of water

is carried out using PYTHON code developed in-house. The regression coefficients are obtained using multiple linear regression models. In nomenclature of the models, MLR stands for multiple linear regression; the number in the model indicates number of independent variables considered with variants A, B and C.

The coefficients of the MLR2 models and the corresponding statistical results are presented in Table 2 as representative results. These results are useful to provide the mathematical equations and overall accuracy of these models. However, this analysis is insufficient to understand the usefulness of these models for monitoring and control of the steam generation process. This can be done through EWMA chart of the data considered for monitoring. Further, the variation of predicted actual pressure is obtained through different MLR models (Not shown). It is noticed that MLR2A provides under prediction of the steam pressure and MLR2B and MLR2C give higher values of predicted pressure which is the requirement of good mathematical model to determine predicted pressure. MLR3A, MLR3B, MLR3C and MLR4 give the values of predicted pressures which are lower than actual pressure. Thus, although these models are statistically superior to MLR2B and MLR2C models, the under prediction of steam pressure restricts their use for monitoring and control of the steam generation process.

4.2 Monitoring Through Fault Introduction

This section demonstrates the effect of drift faults (introduced numerically) on the predicted pressure and on the EWMA chart for MLR2A, MLR2B and MLR2C models. The data used for monitoring period is considered here. The effect of the steam flow rate on the expected pressure is almost negligible, which was indicated by the relatively small regression coefficient $\beta_2 = 0.0230$. The steam temperature has a major impact on expected pressure, which was indicated by comparatively higher regression coefficient of $\beta_1 = 0.1066$ for MLR2A, $\beta_1 = 0.1103$ for MLR2B and $\beta_1 = 0.1102$ for MLR2C. Therefore, it is proposed to manipulate the steam temperature by linearly varying it from its mean value in upward and downward directions, total

Table 2 Results for MLR2A, MLR2B and MLR2C models

Statistical parameters	Selected attributes or independent variables for the models		
	Steam temperature, steam flow rate and volume of steam (MLR3A)	Steam temperature, steam flow rate and volume of water (MLR3B)	Steam temperature, volume of steam and volume of water (MLR3C)
Regression coefficients	$\beta_0 = - 11.9978$ $\beta_1 = 0.1070$ $\beta_2 = 0.0172$ $\beta_3 = - 74.6926$	$\beta_0 = - 13.5793$ $\beta_1 = 0.1070$ $\beta_2 = 0.0170$ $\beta_3 = 74.4709$	$\beta_0 = - 191.984$ $\beta_1 = 0.1092$ $\beta_2 = 8400.986$ $\beta_3 = 8475.33$
R-squared	0.961	0.961	0.960
Adjusted R-squared	0.961	0.961	0.960
F-statistic	4.219×10^5	4.218×10^5	4.066×10^5
t-statistic	Intercept = - 754.244 ST = 958.593 SF = 118.096 VS = -51.045	Intercept = - 411.842 ST = 958.480 SF = 115.548 VW = 50.982	Intercept = - 115.335 ST = 988.604 VS = 105.381 VW = 108.039
Standard error	Intercept = 0.016 ST = 0.000 SF = 0.000 VS = 1.463	Intercept = 0.033 ST = 0.000 SF = 0.000 VW = 1.461	Intercept = 1.665 ST = 0.000 VS = 79.720 VW = 78.447
P-Value	Intercept = 0.00 ST = 0.000 SF = 0.000 VS = 0.000	Intercept = 0.00 ST = 0.000 SF = 0.000 VW = 0.000	Intercept = 0.0 ST = 0.000 VS = 0.000 VW = 0.000

by 10 °C. This restriction of 10 °C is used because with this the temperature reaches its maximum value in the monitored data. This introduction of numerical fault in the temperature data is presented in Fig. 5. The continuous horizontal lines indicate the limits of the operational range of temperature. The dotted line is for mean steam temperature. The purpose of introducing such a fault is to understand the robustness of these models while implementing them for monitoring the steam pressure.

The effects of introduction of fault in the steam temperature through linear upward and downward drift on the expected pressure as predicted by MLR2A, MLR2B and MLR2C is understood through corresponding EWMA charts (not shown). It is observed that with increase or decrease in the temperature, the expected pressure changes correspondingly in case of all the three models under consideration. The steam temperature values of the drift down become closer to the upper limit of the operational range. Similar types of effects are observed for the expected pressure obtained using all three models. It is thus argued that MLR2A, MLR2B and MLR2C models with steam temperature as the major influencing parameter are the robust models which provide better values of predicted steam pressure. Among these three models, MLR2B and MLR2C are proposed to be best suited as these models predict the steam pressure which is closer to and higher than the actual pressure.

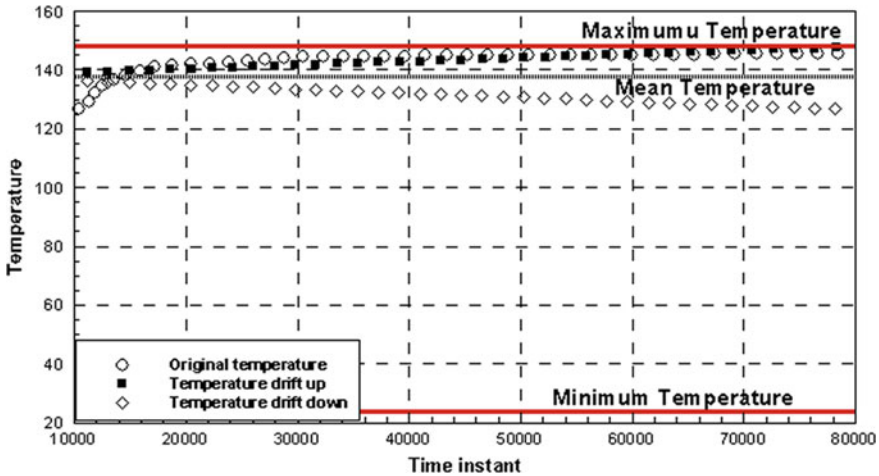


Fig. 5 Fault introduction in the data in terms of steam temperature

5 Conclusion

A data-driven framework based on large amount of historical data is proposed for fault detection in a boiler performance. In the present work, various combinations of independent parameters such as steam temperature, steam flow rate, volume of steam and volume of water are used to obtain different data-driven models such as MLR2A, MLR2B, MLR2C, MLR3A, MLR3B, MLR3C and MLR4. It is observed that MLR2B and MLR2C are the only models which provide pressure prediction higher than the actual pressure. The over prediction of the pressure with minimum residual and standard error is the characteristics of a good model. Further, the response of MLR2 models is therefore tested with the introduction of numerical fault in the highly ranked key performance parameter which is steam temperature in this case. The models respond well with the data having numerical faults. The authors are able to bring out a data-driven framework for fault prediction in the boiler and its performance monitoring, which is not readily available in the literature.

References

1. Qin H, Yin S, Gao T Luo H (2020) A data-driven fault prediction integrated design scheme based on ensemble learning for thermal boiler process. *IEEE Int Conf Ind Technol (ICIT)* 639–644
2. Meng Y, Wu X, Oladejo J, Dong X, Zhang Z, Deng J, Yan Y, Zhao H, Lester E, Wu T, Pang Heng C (2021) Application of machine learning in industrial boilers: fault detection, diagnosis and prognosis. *ChemBioEng* 8(5):1–10

3. Niknam T, Azizipanah-Abarghooee R, Narimani MR (2012) An efficient scenario-based stochastic programming framework for multi-objective optimal micro-grid operation. *Appl Energy* 99:455–470
4. Kim H, Na MG, Heo G (2014) Application of monitoring, diagnosis, and prognosis in thermal performance analysis for nuclear power plants. *Int J Nucl Eng Technol* 46:737–752
5. Zhenhao T, Haiyang Z, Ping C, Shengxian C, Zhiyong Z (2017) Data analytics based dual-optimized adaptive model predictive control for the power plant boiler. *Math Probl Eng* 9, Article ID 8048962
6. Wang JG, Shieh SS, Jang SS, Wong DSH, Wu CW (2013) A two-tier approach to the data-driven modelling on thermal efficiency of a BFG/coal co-firing boiler. *Fuel* 111:528–534
7. Heydar M, Milad S, Mohammad Hossein A, Ravinder K, Shahabodini S (2019) Modelling and efficiency optimization of steam boilers by employing neural networks and response-surface method (RSM). *J Math Spec Issues Hybrid Mach Learn Techn Appl Real Eng Appl Math* 7(7):629
8. Zhang H, Niu X (2020) Preliminarily realize the remote diagnosis of the running state of the power station unit with principal component analysis based on java program. *IOP Conf Ser Earth Environ Sci* 512:012126
9. Benedetti M, Bonfà F, Introna V, Santolamazza A, Ubertini S (2019) Real time energy performance control for industrial compressed air systems: methodology and applications. *Energies MDPI Open Access J* 12(20):1–28
10. Nikula RP, Ruusunen M, Kauko L (2016) Data-driven framework for boiler performance monitoring. *Int J Appl Energy* 183:1374–1388
11. Chandok JS, Kar IN, Tuli S (2008) Estimation of furnace exit gas temperature (FEGT) using optimized radial basis and back-propagation neural networks. *Int J Energy Convers Manag* 49:1989–98
12. Song Z, Kusiak A (2007) Constraint-based control of boiler efficiency a data mining approach. *IEEE Trans Ind Inf* 3:73–83
13. Shieh SS, Chang YH, Jang SS, Ma MD, Huang TS (2010) Statistical key variable analysis and model-based control for the improvement of thermal efficiency of a multi-fuel boiler. *Fuel* 89:1141–9
14. Astrom KJ, Bell RD (2000) Drum-boiler dynamics. *Automatica* 36:363–378
15. Wagh N, Agashe SD (2021) Data driven frameworks for system identification of a steam generator. In: *Data management, analytics and innovation proceedings of ICDMAI 2021*, vol 71. Kolkata, India, pp 2–451

Design of Liquid Cooled Pin–Fin Heat Sink for High Voltage Electric Vehicle



Akhil Suresh, N. Jinesh, J. K. Antony, and Arun Issac

1 Introduction

According to a European Union assessment, the transport industry is responsible for roughly 28% of total carbon dioxide (CO₂) emissions, with road transport accounting for more than 70% of transport sector emissions. As a result, most developed country governments encourage the usage of Electric Vehicles (EVs) to reduce air pollution, CO₂ and other greenhouse gases. More specifically, they promote sustainable and efficient transportation through a variety of initiatives, primarily through tax breaks, purchase incentives or other special measures such as free public parking or free use of highways. Even though governments promote the Electric Vehicle some barriers are there to EVs growth.

Use of semiconductor devices as power modules in the inverter of EVs increases its efficiency. Module size of these inverters is decreasing day by day, so the density and switching frequency of power semiconductors are increasing, and heat density within a system is also increasing. This creates a non-uniform temperature distribution in inverter.

These semiconductor devices are sensitive to high temperature. If the temperature crosses the barrier temperature of power module, it gets damaged. So proper cooling technique must be used to avoid overheating and hence increase the life of device.

Currently, different heat sink models are available, nowadays Inverter modules are becoming lower in size, and for that power, MOSFET or IGBT are used. These power modules produce large amount of heat. Each inverter is made of customized power modules so their cooling techniques will also vary. Here study is conducted

A. Suresh (✉) · N. Jinesh · J. K. Antony
Department of Mechanical Engineering, RIT Pampady, Kottayam 686501, India
e-mail: akhilsureshkizhuvallickal10@gmail.com

A. Issac
Department of Thermal System, Entuple E Mobility PVT LTD, Trivandrum 695016, India

for a 60 kW power rated inverter. In this study, effect of compartment configuration is compared with effect of multiple inlet and outlet configurations.

2 Methodology

In this chapter the methodology adopted for designing the heat sink and analyzing the designed model is discussed. The chapter includes the details of design of heat sink and details of CFD analysis of the designed model. The losses used for design calculations are 3 kW for continuous load (Fig. 1).

3 Design of Heat Sink

In this section, the methods and procedures used for design of heat sink are discussed. In order to get a good heat sink, geometry different heat sink models are studied. All the designs are made using Spaceclaim.

During design of inverter, heat sink following parameters are to be considered:

- **Fluid flow rate inside the Heat sink:** Flow rate has a significant effect on the Heat dissipation capacity of a Heat sink. If the flow rate is too less, then less amount of heat will be removed. If the flow rate is too high, it will not get sufficient time to take away the heat from pins. So an Optimum Flow rate is to be found out to get a proper cooling [3].
- **Flow distribution at the inlet and outlet:** Flow distribution at the inlet and outlet must be turbulent in nature, so that maximum heat can be removed quickly [4].
- **Pin material:** While selecting Pin material, one should note that it has good thermal conductivity, less weight and less corrosive. It should not be reacted with the fluid flowing through it [5].
- **Arrangement of Pins:** Pins can be arranged either in normal way or staggered way. Staggered way helps to create more turbulence in the system [1].
- **Spacing between Pins:** While selecting spacing between the pins, one should also check the manufacturability of the system. Also, the spacing in both x and y directions should be calculated.

The inverter used in this study is a 3Phase MOSFET based inverter. From its data sheet, maximum junction temperature is 150 °C. Also the temperature of the coolant flowing inside the heat sink must be lower than 85 °C. From the 3D model, dimensions of base plate can be obtained, which is the connecting component between inverter and heat sink. The length and width of the base plate is given as 150 mm and 140 mm respectively. So the heat sink should be created using the dimensions 150 mm length and 140 mm width. The thickness of base plate is given as 20 mm.

Based on the base plate dimensions initially heat sink is modelled with length 150 mm, width 140 mm, total height 50 mm, thickness at each wall 5 mm and pin

height 40 mm. Initially, geometries without fillet at the corners were designed. Then pins with different cross sections are created (Fig. 2).

When the shape was changed from Rectangular to Circular the no of pins that can be created using same cross sectional area and similar spacing is more. For circular shape, we can create 77 pins while using rectangular pins only 68 pins can be created.

In order to find the variation in temperature while increasing no of pins, models are created with changing spacing between the pins. Finally to study the variations in changing the base thickness, geometries with different base thickness are created.

4 CFD Analysis of Designed Heat Sink

This section discusses the methodologies and procedures used for heat sink CFD analysis. Different heat sink models are investigated in order to obtain a decent heat sink shape with higher heat dissipation. ANSYS Fluent is used for all of the analyses.

Heat is transported between the metal base plate and the solid fins by heat conduction and is subsequently expelled through the liquid in the channels via forced convection. The analysis is simplified by the following assumptions.

- Single-phase, incompressible, laminar turbulent flow is considered. For each heat sink configuration, the Re varies while the coolant volume flow rate is fixed.
- The thermo-physical properties of the solid and fluid stay constant, that is, they are temperature independent.
- Natural convection and radiation heat transmission are not taken into account.
- Can neglect the effects of gravitational force and heat dissipation produced by viscosity.
- The thermal contact resistance that develops between the solid walls is insignificant.
- Each heat sink's surface has good insulating properties.

Under these assumptions, the three-dimensional steady governing equations of this conjugated heat transfer problem are given as follows:

Momentum equations of the coolant [2]:

$$\rho_c \left(u \frac{\partial u}{\partial x} + v \frac{\partial u}{\partial y} + w \frac{\partial u}{\partial z} \right) = -\frac{\partial p}{\partial x} + \mu_c \left(\frac{\partial^2 u}{\partial x^2} + \frac{\partial^2 u}{\partial y^2} + \frac{\partial^2 u}{\partial z^2} \right) \quad (1)$$

$$\rho_c \left(u \frac{\partial v}{\partial x} + v \frac{\partial v}{\partial y} + w \frac{\partial v}{\partial z} \right) = -\frac{\partial p}{\partial y} + \mu_c \left(\frac{\partial^2 v}{\partial x^2} + \frac{\partial^2 v}{\partial y^2} + \frac{\partial^2 v}{\partial z^2} \right) \quad (2)$$

$$\rho_c \left(u \frac{\partial w}{\partial x} + v \frac{\partial w}{\partial y} + w \frac{\partial w}{\partial z} \right) = -\frac{\partial p}{\partial z} + \mu_c \left(\frac{\partial^2 w}{\partial x^2} + \frac{\partial^2 w}{\partial y^2} + \frac{\partial^2 w}{\partial z^2} \right) \quad (3)$$

where ρ_c , μ_c and p represent the density of the coolant, dynamic viscosity of the coolant and the pressure of coolant respectively.

4.1 Meshing

The designed model must be meshed with good quality. In this study, Fluent meshing is directly used. Figure 3 shows the body after surface meshing. Skewness is one of the parameter which determines mesh quality. Skewness is defined as the difference in shape between the cell and an equilateral cell of equivalent volume. Highly skewed cells might make the solution unstable and reduce accuracy. A maximum value greater than 0.95 may cause convergence problems and necessitate modifying solver controls, such as lowering under-relaxation factors and/or switching to the pressure-based coupled solver. In all the designed models, obtained skewness value is in the range of 0.4 and 0.8. Then inflation is added at the fluid boundaries.

Fig. 1 Work flow diagram

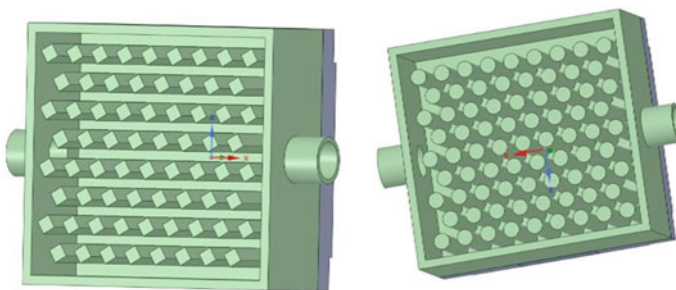
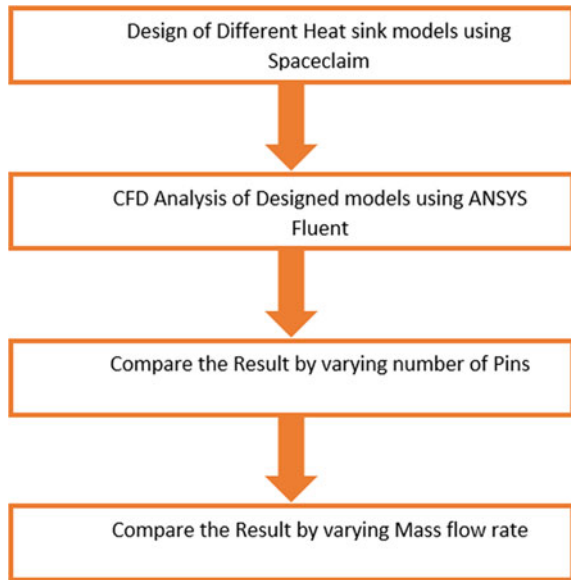


Fig. 2 Geometry with rectangular and circular pins

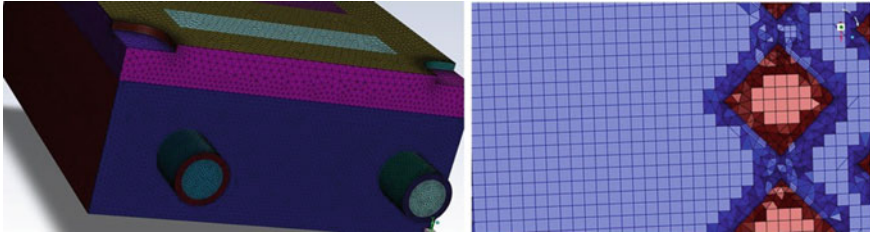


Fig. 3 Geometry after meshing with inflation layers

Table 1 Grid independence study

Number of nodes	Maximum base plate temperature
20,138,525	135.7565
22,190,775	135.2141
23,474,195	135.2149
24,270,991	135.2616
30,830,785	135.3945

After adding inflation layer volume mesh is created with Hexcore elements. Hexcore meshing is a hybrid meshing technique that creates tetrahedral cells close to the boundaries and Cartesian cells inside the domain’s core. Then meshes with good orthogonal quality and skewness are obtained. If any of the above mesh quality measure is not acceptable, then the body should be remeshed. In all the geometries which are created, these mesh qualities are achieved.

Grid independence study is conducted to make sure that the created mesh is enough for the analysis.

Table 1 shows the maximum base plate temperature obtained when mesh size was changed. Figure 4 shows the variation of maximum base plate temperature with change in number of nodes.

4.2 Boundary Conditions

As per the Geometry, three heat sources are present in the inverter. So to define heat source, three surfaces are created with uniform size (90 mm length and 24 mm width). Total power loss is 3 kW. So the boundary condition at the heat source is given as Wall heat flux.

$$\text{Wall heat flux} = \frac{P_{\text{loss}}}{3A_{\text{hs}}}$$

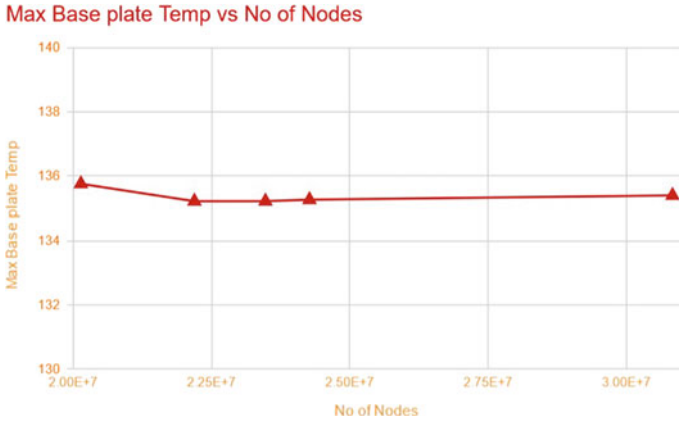


Fig. 4 Maximum base plate temperature versus number of nodes

where P_{loss} is the Total Power loss from inverter during continuous load, A_{hs} is the Area of heat source. The obtained wall heat flux value is 462962.963 W/m^2 .

The material used for making the heat sink is Aluminium (LM6). Its density is 2719 kg/m^3 , specific heat at constant pressure (C_p) is 960 J/KgK and thermal conductivity K is 202.4 W/mK . The coolant used in this study is Water-Ethylene Glycol (50/50). It's density is 1111.4 kg/m^3 , Specific heat at constant pressure (C_p) is 3283 J/KgK , Thermal Conductivity K is 0.252 W/mK and Viscosity 0.0157 kg/ms .

The total heat taken away by the fluid can be calculated by,

$$Q = \dot{m}C_p\Delta T$$

where Q is the total power loss (3000 W), \dot{m} is the mass flow rate, (C_p) is 3283 J/KgK for water Ethylene Glycol mixture and ΔT is the difference in temperature of fluid at inlet and outlet. Using these value, obtained mass flow rate is 0.04568 kg/s . The inlet temperature is taken as 331 K ($58 \text{ }^\circ\text{C}$).

4.3 Analysis Setup

In this study steady state analysis is carried out since this work deals with continuous load only. Turbulence model used in this study is $K-\omega$ -SST model along with energy equation. The $k-\omega$ SST model predicts flow separation better than most RANS models and explains its good performance under adverse pressure gradients. It can account for the primary shear stress transport in adverse pressure gradient boundary layers. Because of its high accuracy to expense ratio, it is the most often used model in the industry. Solver scheme used is coupled (pressure-velocity) type with second

order upwind. Convergence condition used in this study is residuals values should be $\leq 10e - 6$. Also convergence is checked by Area Weighted average of Temperature and Volume averaged Temperature of Heated bodies.

5 Results and Discussion

In this chapter, results obtained at the end of analysis are discussed. Results of steady state analysis with different geometries by changing shape and size of pins are discussed in separate subsections. Results by changing number of pins is discussed in a sub section. Also, results obtained while studying the influence of multiple inlets and inlet outlet positions are discussed in another subsection. Results obtained by changing mass flow rate are also discussed.

5.1 Initial Geometry Results

After steady state analysis on initial geometry with rhombus shaped pins (5 mm \times 5 mm) without fillet, the following results were obtained.

As from the Table 2, maximum base plate temperature is 202 °C which is very must high. The limiting junction temperature of the power module is 150 °C. For safe operation, the base plate temperature should be below 120 °C, since some extra layers are present in between power module and base plate and these surfaces also create thermal resistance. The inlet fluid temperature was 58 °C. The outlet temperature was 83.1 °C which gives a rise of 25.1 °C. As per the data sheet of inverter, maximum coolant temperature must be 85 °C. Here the temperature is closer to the limiting value.

Pins at the central portion have comparatively lesser heat compared to pins near to walls. A good amount of heat is taken away by the coolant.

In this case, recirculation is seen at the corners to avoid this fillets are provided at the corners and modified geometry is analyzed.

Table 2 Temperature distribution

Area-weighted average at	Temperature (°C)
Inlet	58
Outlet	83.1
Heat source temperature	191
Pins	118
Wall wetted temperature	131
Max base plate temperature	202

Table 3 Effect of changing size of pins and spacing between pins

S. No.	Specification	Inlet Temp. (C)	Change in Temp. (C)	Base Plate Max Temp. (C)	HTC total (W/m ² K)
1	Pin Size—5 × 5 Spacing in X and Y direction 4 mm	58	26	204.18017	186.26478
2	Pin Size—4 × 4 Spacing in X and Y direction 4 mm	58	26.3	200.73824	182.46344
	Pin Size—3 × 3 Spacing in X and Y direction 4 mm	58	26	202.99843	180.64065
3	Pin Size—3 × 3 Spacing in X and Y direction 3 mm	58	24.5	183.71774	173.77255

5.2 Results by Changing Size and Spacing of Pins

In order to find the best pin size and Pin spacing, a study is conducted by changing the size of pins and Spacing between the pins. Rhombus shaped pins were created for the study.

As from Table 3, the best geometry is obtained when the size of pins is minimum, and spacing between the pins is also minimum. When the size of pins and spacing between pins are reduced the number of pins that can be incorporated in the geometry increases and this leads to decrease in base plate temperature and good heat dissipation. The study is limited to these sizes because of manufacturing constraints. If we reduce the pin size less than 3 × 3 mm and spacing in XY direction to 2 mm during large-scale production, it will be very difficult for manufacture.

5.3 Effect of Changing Number of Pins

A study is conducted to find the effect of changing number of pins. Circular shaped pins are selected for this study because circular pins showed the best results than rhombus shaped pins. Number of pins in the model is changed by changing the spacing between the pins and keeping same cross sectional area. All the pins are made up of diameter 3 mm. In this study, mass flow rate given at the inlet is 0.18272 kg/s.

Table 4 shows the temperature variation while changing number of pins. As the number of pins increases, temperature on the base plate gets reduced. This is because surface area which comes in contact with the fluid increases and thereby increases the heat transfer rate. Figure 5 shows the variation of base plate temperature with change in number of pins.

When the number of pins is changed from 137 to 791, temperature change of 77 °C is observed, which shows 39.4% percentage reduction in temperature.

Table 4 Effect of changing number of pins

No. of pins	Max base plate Temp	Difference with reference Temp*	Percentage Reduction
137	196.3185	61.3185	–
173	191.43549	56.43549	2.487289787
188	181.63522	46.63522	7.4793155
263	158.57722	23.57722	19.22451526
295	156.28436	21.28436	20.39244391
409	141.13157	6.13157	28.1109167
581	129.36015	– 5.63985	34.1069996
791	118.84279	– 16.15721	39.46429399

*Reference temperature is taken as 135 °C

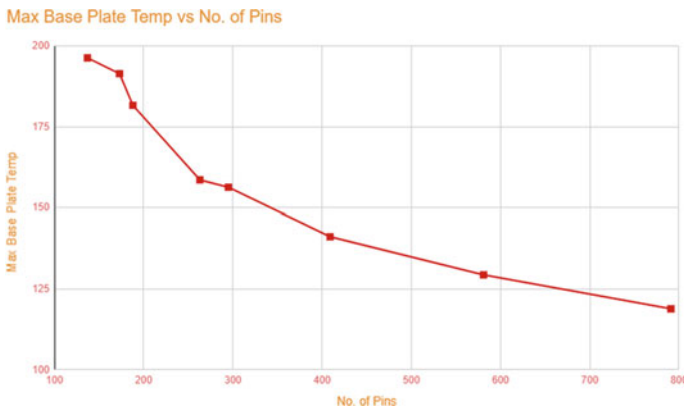


Fig. 5 Maximum base plate temp versus number of pins

5.4 One Inlet and One Outlet with Compartment Structure

Since the previous model gives good heat dissipation properties, the model with three compartment and single inlet is studied.

Table 5 shows the temperature distribution in one inlet one outlet with three compartment configuration. The temperature on the base plate is very less in this case. In the previous case outlet mass flow rate 0.27408 kg/s. So here, inlet mass flow rate is selected as 0.27408 kg/s in this case.

Figure 6 shows the velocity distribution in single inlet with three compartment case. From the fig itself, it is clear that turbulence is seen at the inlet portion. This enhances heat transfer rate. So this three compartment structure is useful in the heat sink configuration. Some bump like projections are provided in the middle and last compartment to guide the fluid to centre portion. The height of total heat sink is

Table 5 Temperature distribution one inlet and one outlet with three compartments

Area—weighted average at	Temperature (°C)
Inlet	58
Outlet	61
Pins in 1st compartment	69
Pins in 2nd compartment	70
Pins in 3rd compartment	70
Wall wetted temperature	73
Heat source temperature	94
Max base plate temperature	115

reduced to 30 mm because in the previous studies, there was not much effect on the top portion of the heat sink. Fillet is provided at each pins base. It will increase the surface area and there by enhance heat transfer.

From Fig. 6, it is clear that uniform cooling is taking place in this model. The major advantage of this model over previous model is it requires less connectors and other parts. Also temperature is reduced to 115 °C which is very much safe for the Power module (Fig. 7).

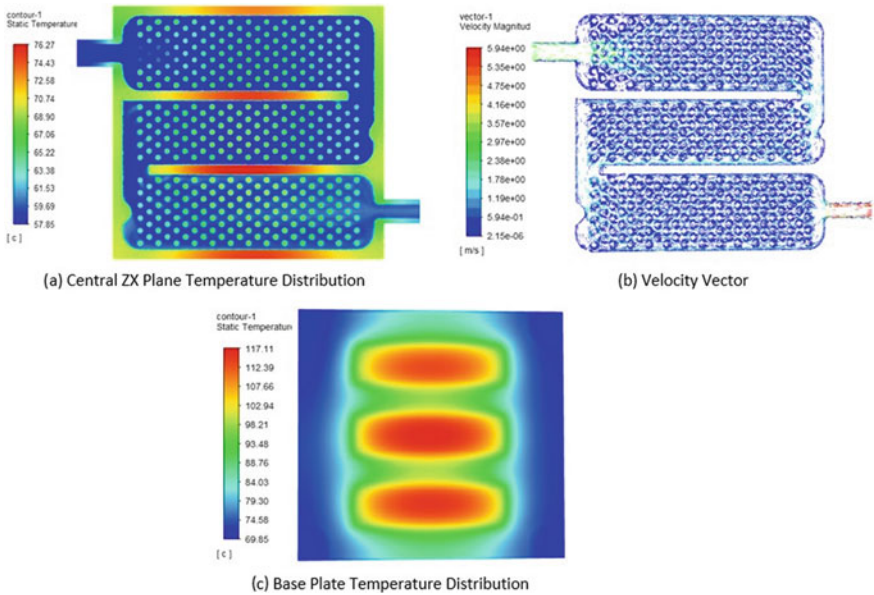


Fig. 6 Temperature and velocity distribution

Fig. 7 Thickness and area of heat sink

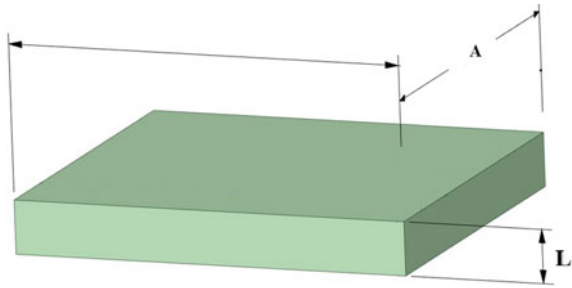


Table 6 Effect of changing thickness of heat sink

Heat sink Thickness (mm)	Max base plate Temp	Total HTC
2.5	120.56431	558.07191
5	122.00918	558.81923
7.5	124.1193	559.01021
10	125.91641	563.20081

5.5 Reducing Thickness of Heat Sink

Study is conducted by reducing thickness of heat sink. By reducing the thickness of heat sink at the contact region with the base plate, temperature on the base plate gets reduced.

This is due to decrease in Thermal resistance;

$$\text{Thermal resistance} = \frac{L}{KA}$$

where L is the length to be covered (Thickness) in metre, K Thermal Conductivity of the material, A Contact area of the heat transferring surface. Table 6 shows the results obtained by varying thickness of heat sink. When the thickness of heat sink is reduced to 2.5 mm from 10 mm a temperature drop of 6 °C is seen, which means a percentage reduction of 4.25%. Based on these values, it is clear that heat sink should have minimum thickness.

5.6 Changing Mass Flow Rate

In order to understand the effect on changing mass flow rate study is conducted by varying mass flow rate. Based on the given power loss and properties of ethylene glycol water mixture, calculated mass flow rate is 0.04568 kg/s. Results obtained after changing mass flow rate are shown in Table 7.

Table 7 Effect of changing mass flow rate

Mass flow rate	Max base-plate Temp	Difference with Reference Temp*	Percentage Reduction
0.04568	147.518	12.518	–
0.0912	131.54563	– 3.45437	10.82740411
0.13704	124.51149	– 10.48851	15.59573069
0.18272	120.56431	– 14.43569	18.2714584
0.2284	117.9127	– 17.0873	20.06894074
0.27408	115.85582	– 19.14418	21.4632655

*-Reference temperature is taken as 135 °C

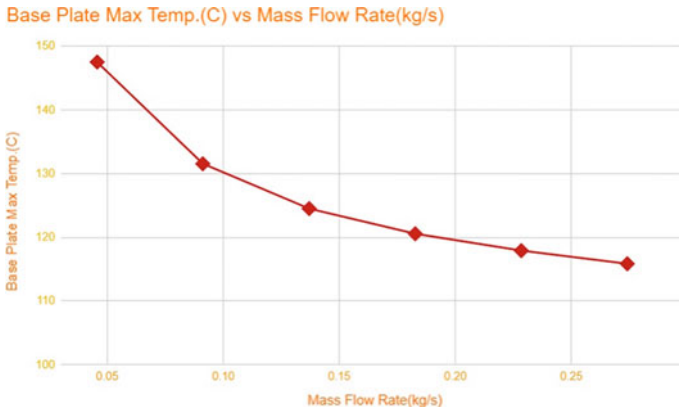


Fig. 8 Maximum base plate temp versus mass flow rate

Figure 8 shows the variation of base plate temperature with change in number of pins.

When the mass flow rate is changed from 0.04568 to 0.27408, temperature change of 31.66 °C is observed, which shows 21.46% reduction in Temperature.

6 Conclusions

The performance of liquid cooled Pin–Fin heat sink for inverter by changing shape of pins, size of pins and mass flow rate of liquid is studied. The total power loss is estimated as 3 kW (continuous load) and based on power loss, mass flow rate is obtained which is 0.04568 kg/s. The Pin–Fin type Heat sink model is selected for the cooling. The fluid used as coolant is ethylene glycol water mixture (50/50). The material used to create heat sink is aluminium. The effect of changing shape of

pins, size of pins, spacing between pins, thickness of heat sink and mass flow rate is studied.

- As the number of pins increases, temperature on base plate reduces. When the number of pins changed from 137 to 791, temperature change of 77 °C is observed, i.e. a percentage reduction of 39.4%.
- As the base plate thickness is reduced to 2.5 mm from 10 mm, thermal resistance is reduced where temperature on base plate is reduced by 4.25%.
- As mass flow rate increases, the temperature on base plate decreases gradually, when mass flow rate is changed from 0.04568 kg/s to 0.27408 kg/s a temperature drop of 44 °C (21.5% reduction) is observed in the base plate. This temperature decrease is sufficient for this parametric study and hence mass flow rate of 0.27408 kg/s (14.7964729 L/min) is taken for further study.

In the future scope, the above conclusions show that for an inverter with 3 kW loss in continuous load, liquid cooling system with Ethylene Glycol-Water (50–50) as fluid can be fabricated.

Acknowledgements This work is supported by Entple E Mobility PVT LTD Bangalore.

Nomenclature

ρ_c	Coolant density
μ_c	Coolant dynamic viscosity
P	Coolant pressure
C_{pc}	Coolant specific heat capacity

References

1. Baumann M, Lutz J, Wondrak W (2011) Liquid cooling methods for power electronics in an automotive environment. In: Proceedings of the 2011 14th European conference on power electronics and applications. IEEE, pp 1–8
2. Cengel Y, Cimbala J (2013) Ebook: Fluid mechanics fundamentals and applications (si units). McGraw Hill
3. Mademlis G, Orbay R, Liu Y, Sharma N, Arvidsson R, Thiringer T (2021) Multidisciplinary cooling design tool for electric vehicle sic inverters utilizing transient 3d-cfd computations, eTransportation 7:100092
4. Shahsavar A, Shahmohammadi M, Askari IB (2021) CFD simulation of the impact of tip clearance on the hydrothermal performance and entropy generation of a water-cooled pin-fin heat sink. Int Commun Heat Mass Transf 126:105400
5. Wilde J, Staiger W, Thoben M, Schuch B, Kilian H (1998) Integration of liquid cooling, thermal and thermomechanical design for the lifetime prediction of electrical power modules. Tech report, SAE Technical Paper

Establishment of Thermal Mixing Behavior in Grid Plate of FBRs 1 & 2



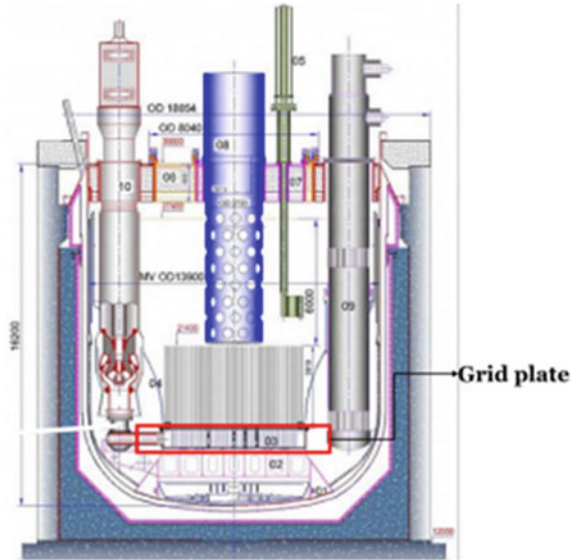
Amit K. Chauhan, M. Rajendrakumar, and K. Natesan

1 Introduction

India is witnessing the advanced commissioning stage of the Prototype Fast Breeder Reactor (PFBR), at the nuclear island in Kalpakkam. PFBR is the typical Liquid Metal cooled Fast Breeder Reactor (LMFBR) which formulates the second stage of the Indian Nuclear Program (INPP). There are three stages of INPP, conceptualized based on the strategy to enhance fuel utilization using a closed fuel cycle [1]. While the first stage of INPP was commenced with the induction of Pressurized Heavy Water Reactors (PHWRs) fueled by natural uranium, LMFBRs form the second stage of INPP which is fueled by plutonium obtained from first stage reactors. The third stage of INPP would include thermal advance reactors using uranium 233 fuel obtained from the second stage by utilizing thorium as a fertile material in the LMFBRs core. Fast Breeder Reactors (FBRs 1 & 2) are the twin units of commercial LMFBRs, currently, in the design stage at Kalpakkam [2]. FBRs 1 & 2 are 500 MWe, pool-type reactors with few design modifications carried out compared to PFBR to enhance the safety features, viz., three primary sodium pumps (PSPs) unlike two in PFBR. Figure 1 shows the cross-sectional view of FBR 1 & 2. Primary liquid sodium is pumped into the inlet plenum called grid plate through a diffusor, spherical header, and primary pipes [3], 4. Figure 2 shows the top and side views of the grid plate. There are 3 spherical headers corresponding to 3 PSPs. Each spherical header is connected to the grid plate through two primary pipes, hence totaling 6 primary pipes. The location of all 6 primary pipes is symmetrical with respect to the reactor axis. As all 6 inlets are symmetric to the axis, the inlet conditions of the coolant are the same during normal operation of the reactor. Liquid sodium from the grid plate flows upward through the sub-assemblies against gravity and extracts heat from Sas [5].

A. K. Chauhan (✉) · M. Rajendrakumar · K. Natesan
Thermal Hydraulic Section, Thermal Hydraulics Division, Reactor Design and Technology Group, Indira Gandhi Centre for Atomic Research, Kalpakkam, Kanchipuram 603102, India
e-mail: amitchauhan@igcar.gov.in

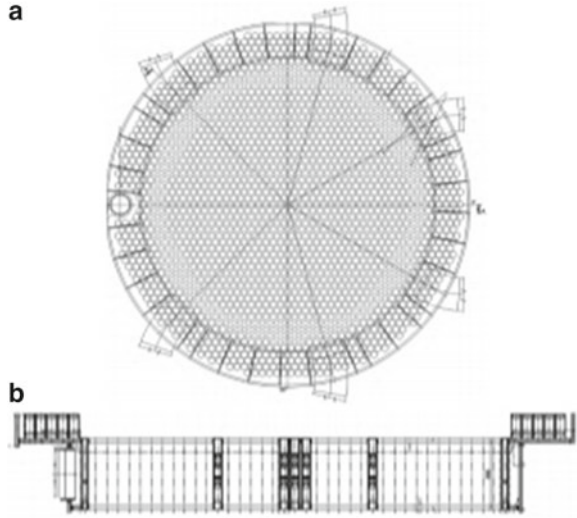
Fig. 1 Crossectional view of FBR 1 & 2. Grid plate is highlighted



During any undesired transient event in the secondary circuit of FBRs 1 & 2 will result in asymmetry in the inlet condition of primary sodium to grid plate. Consequently, the outlet temperature of sodium from SAs would vary from normal values. The safety of the reactor is ensured by monitoring SCRAM parameters during its operation. Rise in the central SA outlet temperature $\Delta\theta_{CSAM}$ is one of such important SCRAM parameters that is influenced during such asymmetrical conditions of the inlet to grid plate. If the temperature rise in $\Delta\theta_{CSAM}$ is 5 °C, it raises an alarming situation and if the value is 10 °C, then reactor SCRAM and finally shut down. Proper mixing of sodium inside the grid plate would reduce $\Delta\theta_{CSAM}$ due to enhanced heat transfer properties. It is essential to estimate the mixing behavior of coolant inside the grid plate before it enters SAs in the core.

Jalali and Fadaei [6] proposed a unique feature of the ability to add an independent and diverse shutdown system into the reactor core in the new design of grid plate for Tehran reactor [6]. CFD study was carried out to establish the flow and thermal parameters for different operating conditions. Peng et al. [7] carried out an experiment on a scaled-down model of a small modular reactor to estimate the flow and mixing characteristics in the reactor core [7]. Tong et al. [8] carried out a CFD study to analyze the flow and mixing characteristics in the reactor vessel of a nuclear reactor [8]. With an extensive survey of the available open literature, it is observed that the mixing behavior of the flow in grid plate or inlet plenum is not reported to our knowledge. It is essential to establish the flow mixing behavior inside the grid plate of the reactor toward its design. As mentioned earlier, good mixing would enhance the heat transfer of liquid metal as a coolant in the plenum and SAs in the core. To this end, a detailed 3D CFD study of the grid plate for FBRs 1 & 2 is carried out to

Fig. 2 Crossectional view of grid plate: **a** top view and **b** crossectional view



establish the mixing behavior of liquid sodium during any undesired transient event in the secondary circuit. This forms the objective of the present study.

2 Methodology

2.1 Physical Modeling and Meshing

The grid plate (GP) of FBR 1 & 2 is enclosed cylindrical volume with top and bottom plates placed axially, as shown in Fig. 2. While the bottom plate seals the GP absolutely without any opening, the top plate has an opening corresponding to individual SA depending on the flow zone. In between the top and bottom plate [Height = 835 mm], there are sleeves as many as SAs numbers, with numbers of holes azimuthally at a certain height, depending on its position with respect to flow zoning. There are 2091 numbers of sleeves [including 2 vacant SAs positions]. Multiple holes in sleeves (hole size and number depend on the position of the sleeve with respect to flow zoning) allow sodium crossflow inside it and vertically upward into the SA. A typical fuel (FSA), blanket (BSA), and absorber rod (ARSA) SA sleeve’s cross-sectional view are shown in Fig. 3. It is decided to model all 2091 sleeves to capture the effect of sleeves on the hydraulics of sodium flow inside GP. The holes in the sleeves are modeled as a single slot to overcome the complexity of modeling and meshing. However, the slot flow area is equal to the total flow area of the holes, which is ensured in modeling. The integrated 3D computational domain of grid plate with 6 nos. of primary pipes for FBR 1 & 2 is developed using the commercial modeling tool ANSYS SPACE CLAIM [9]. The primary pipe is modeled to account for the

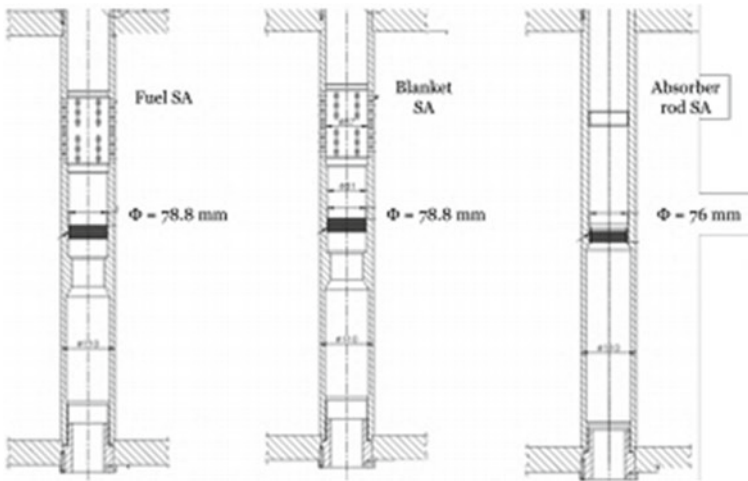


Fig. 3 Crosssectional view of sleeve for FSA, BSA, and ARSA of FBR 1 & 2

effects of the non-radial entry velocity into GP. Figure 4 shows the 3D computational domain developed. Figure 5 shows a typical 3D mesh for the GP generated. A 2D hexahedral mesh is generated on the bottom plate and subsequently, it is extruded axially to generate the 3D mesh. A finer mesh near the wall is generated to capture the near-wall effect accurately. Also, mesh quality and y^+ value (considered between 30 and 300 [10]) are respected near the wall region. The standard logarithmic wall function approach is used to capture the velocity profile near the wall accurately. The primary pipe circular cross-section is difficult to model in this scenario. To overcome this, 2D mesh cells on the outer surface of the grid plate are selected in a pattern that resembles a circular cross-section. Also, number of the 2D cells selected is finalized to ensure the total flow area is equal to the flow area of the primary pipe. The mesh quality is maintained at close to 1 (i.e., orthogonality: 1 being good quality and 0 being bad quality). Also, the aspect ratio of the mesh is maintained at nearly 45. Since the domain is very complex due to its geometrical dimension variation, a single mesh with fine discretization is considered. The computational domain has dimensions as low as 15 mm, and as large as 850 mm, hence resulting in the complexity of handling the mesh size. There is a total of 50 million hexahedral elements generated as shown in Fig. 5.

2.2 Computational Methodology

Figure 6 shows the boundary condition specified in the computational domain. A mass flow rate of 1399.5 kg/s through each pipe in normal operating conditions is imposed as the inlet boundary condition. However, a zero-gauge pressure gradient

Fig. 4 A3D computational domain with all nomenclature

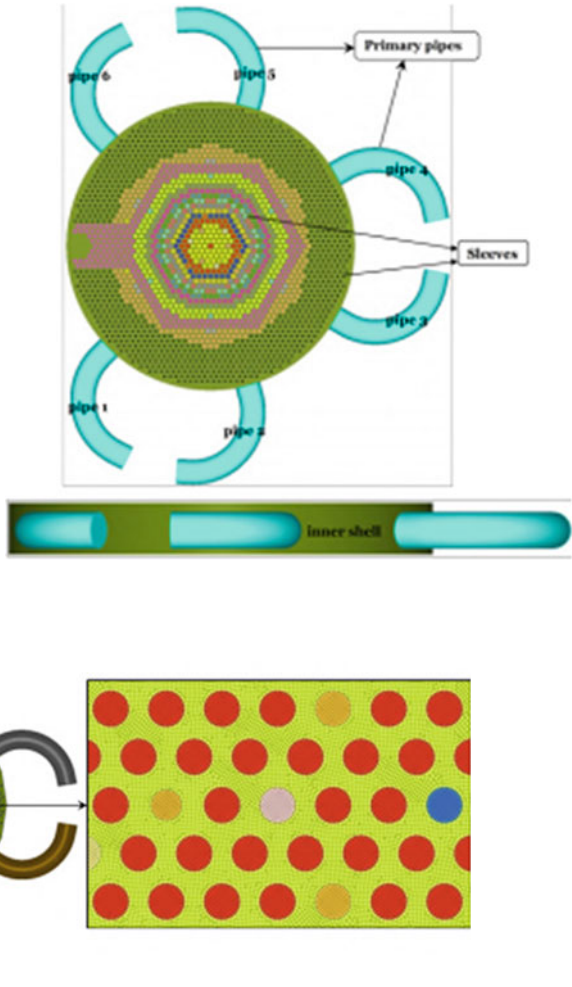
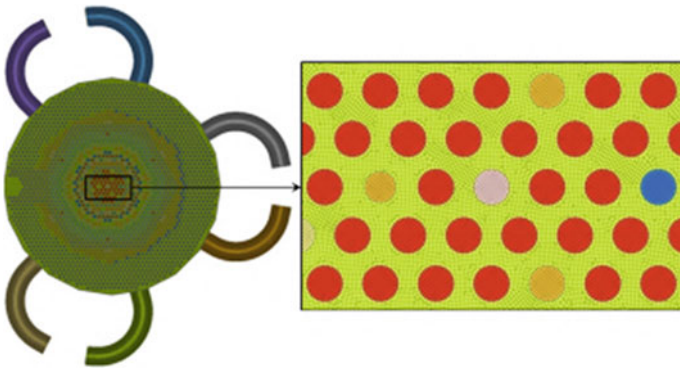


Fig. 5 A3D mesh generated in the domain



is imposed at the outlet boundary. Also, the pressure drop along the SA is taken care of in the present modeling of GP. At the outlet section, (pressure loss coefficient) K of the corresponding zone is provided to ensure the designed flow through the respective SA.

All surface walls of the computational domain are imposed with no-slip and adiabatic boundary conditions. A liquid sodium temperature of $397\text{ }^\circ\text{C}$ is considered the inlet temperature of a primary pipe, at which the coolant's properties are estimated. The present study assumes a steady and incompressible flow of liquid sodium in GP. The density and dynamic viscosity of sodium is assumed constant at 857.7 kg/m^3 and $2.82 \times 10^{-4}\text{ kg/ms}$, respectively. Table 1 shows flow zones in FBR 1 & 2

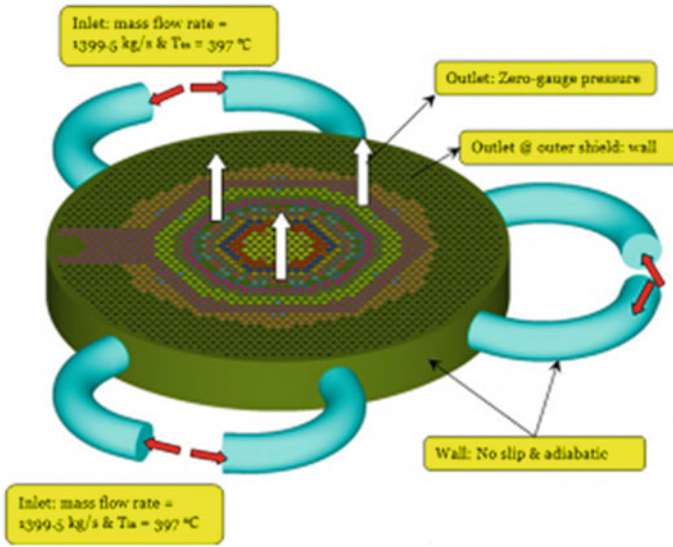


Fig. 6 Boundary conditions imposed on the computational domain

and corresponding K values of SAs. Figures 7 and 8 show core configuration and flow zoning structure of FBR 1 & 2 reactor. The hydraulic resistance of the orifice is selected based on the required flow rate through the SA. The same is simulated here by specifying K at the outlet boundary condition as aforementioned. The hydraulic resistance is calculated using Eq. 1. The flow through the reflector SA, absorber rod SA, and storage SA are not modeled, as a low flow rate leads to very high input K values for these SA ($\approx 10^5$). Higher K values introduce instability in the solution process.

$$\Delta P = K \frac{(\rho U^2)}{2} \quad (1)$$

where, ΔP is the pressure drop across the SA (64 mlc of sodium), ρ is the density of liquid sodium at $T = 397$ °C, and U is the velocity of liquid sodium at the inlet of SA. Turbulence in the flow is modeled by eddy viscosity-based standard high Re standard $k-\epsilon$ turbulence model used to assess the effect of turbulence in fluid flow [11]. It is reported [12] that the second-moment closure models perform better than the eddy viscosity-based models for flows with significant swirls. However, the second-moment closure models suffer from a serious drawback that they are many times unstable although they are superior to the eddy viscosity-based models in predicting local flow features. This forms the basis for the selection of the turbulence model. The pressure term is discretized using the PRESTO scheme. The momentum, energy, turbulent kinetic energy, and turbulent dissipation rate are discretized using

Table 1 Overall flow allocation in the expected equilibrium core

SA type	N _z	N _{SA}	m/SA (kg/s)	K
Fuel inner	1	52	33.3	28.8
	2	36	31.2	33.5
	3	30	28.6	49.3*
Fuel outer	4	30	33.3	29.5
	5	36	28.4	40.5
	6	24	23.4	59.6
	7	30	20.3	79.3
Blanket	8	27	6.2	1209.3*
	9	30	4.9	1360.3
	10	66	4.3	1767.2
	11	72	3.5	2665.5
CSR	12	9	3	3626.9
DSR	13	3	3	3628.8
HSAR	14	3	5	1307.2
Reflector	15	156	0.3	363,079.2
Inner B ₄ C	16	266	0.3	362,593.5
Storage	17	221	2.5	8643.2*
Storage FF	18	12	0.5	130,690.6@
Diluents	19	0	10.1	320.4
	20	0	7.5	580.4
ICSA	21	0	8.1	497.8
Source	22	3	9	403.4
Purger		6	0.3	363,024.6@
Total			1112	

N_z is the zone number, N_{SA} is the number of SAs in the respective flow zone. *K value modified to obtain desired flow in the respective zone. @: Outlet corresponding to these SAs are converted to wall, B₄C is absorber rod, FF is storage for failed fuel, ICSA is central SA, CSR, DSR and HSAR are control and diverse safety rods

a second-order upwind scheme. Governing equations for the fluid flow are solved with convergence criteria of 10⁻⁶. ANSYS FLUENT 19.2 [10] is used to carry out the CFD simulation. The conservation equation of mass, momentum, and energy are as follows:

Conservation of mass:

$$\frac{\partial}{\partial x_j}(\rho u_j) = 0 \tag{2}$$

Conservation of momentum:

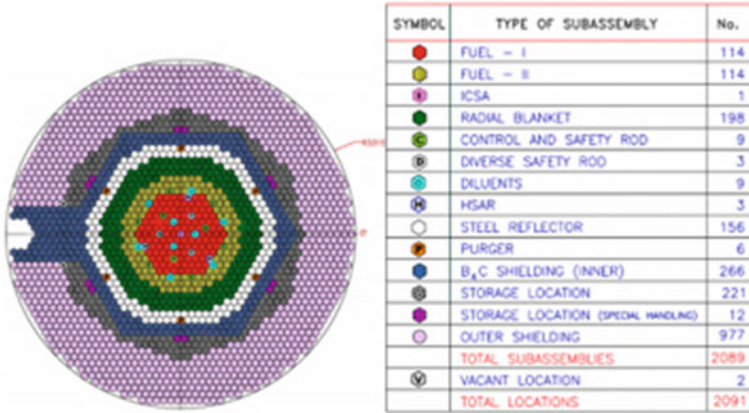
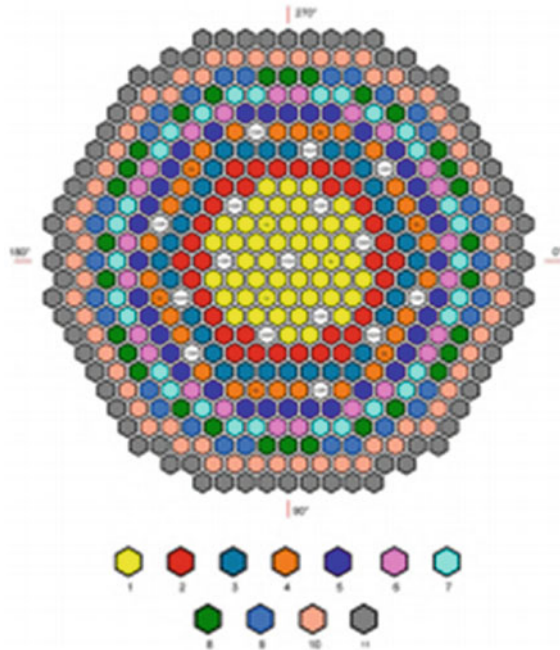


Fig. 7 Core configuration of FBR 1 & 2

Fig. 8 Flow zoning for FBR 1 & 2



$$\frac{\partial}{\partial x_j} (\rho u_j u_i - \tau_{ij}) = -\frac{\partial P}{\partial x_i} \tag{3a}$$

$$\tau_{ij} = 2\mu s_{ij} - \frac{2}{3}\mu \frac{\partial u_k}{\partial x_k} \delta_{ij} - \overline{\rho u'_i u'_j} \tag{3b}$$

$$s_{ij} = \frac{1}{2} \left(\frac{\partial u_i}{\partial x_j} + \frac{\partial u_j}{\partial x_i} \right) \quad (3c)$$

where, ρ is the fluid density, u_j is the fluid velocity in the three space directions, x_j is space coordinates, p is the pressure, and τ_{ij} is the total shear stress (laminar + turbulent).

Turbulent kinetic energy (k):

$$\frac{\partial}{\partial x_j} (\rho k u_j) = \frac{\partial}{\partial x_j} \left(\left(\mu + \frac{\mu_t}{\sigma_k} \right) \left(\frac{\partial k}{\partial x_j} \right) \right) + P_k - \rho \quad (4)$$

Dissipation rate (ε):

$$\frac{\partial}{\partial x_j} (\rho \varepsilon u_j) = \frac{\partial}{\partial x_j} \left(\left(\mu + \frac{\mu_t}{\sigma_\varepsilon} \right) \left(\frac{\partial \varepsilon}{\partial x_j} \right) \right) + \frac{C_{\varepsilon 1} \varepsilon P_k}{k} - C_2 \frac{\rho^2}{k} \quad (5)$$

where, σ_k and σ_ε are turbulent Prandtl numbers of k and ε respectively, P_k is the shear production of turbulence, $C_{\varepsilon 1}$ and $C_{\varepsilon 2}$ are constants of turbulence model having values 1.44 and 1.92 respectively and μ is the dynamic viscosity of the fluid. μ_t is the turbulent viscosity calculated from k and ε as:

$$\mu_t = C_\mu \frac{k^2}{a} \quad (6)$$

where, the constant C_μ is 0.09.

In the present study, to evaluate the mixing of sodium inside GP, 3 scenarios are considered, viz., **Case#1**, reference case where the inlet temperature of liquid sodium is same in all 6 primary pipes, **Case#2** refers to the condition when sodium inlet temperature at two of six primary pipes is higher by 10 °C, and **Case#3** refers to the condition when sodium inlet temperature at four of six primary pipes is higher by 10 °C.

3 Results and Discussions

Aforementioned, three different scenarios are simulated and corresponding analyses of the results are presented in this section. In case#1, inlet temperature T_{Na} , in the primary sodium is the same in all 6 primary pipes to GP. As expected, the sodium temperature remains the same in the whole domain. This case is simulated as the reference case to compare the variation in the other two cases. The velocity contour plot for case#1, at the outlet section and at midplane [i.e., an axial distance of 0.415 m from the bottom surface of GP] is shown in Fig. 9. The maximum velocity of ≈ 10 –11 m/s is observed near the outlet of the primary pipe. The velocity vectors of sodium near two of the primary pipes are shown in Fig. 10. The total pressure drop in the

grid plate, i.e., from an inlet of the primary pipes to the outlet section of the central sub-assembly, is estimated to be 9.05 mlc.

In case#2, the T_{Na} , in two out of six primary pipes is considered higher by 10 °C, while the other four pipes have primary sodium at the same inlet temperature. Figure 11 shows temperature distribution at the outlet section of the GP. The smudging of the interface because of heat diffusion is visible. The thermal interface formed sees the temperature of sodium ranging from 397 to 407 °C. It can be seen that the high-temperature region is localized (nearly 120° sector) near the interface, and global mixing is not observed. In case#3, it is assumed that the inlet temperature of primary sodium is higher by 10 °C in four primary pipes, while the other two pipes

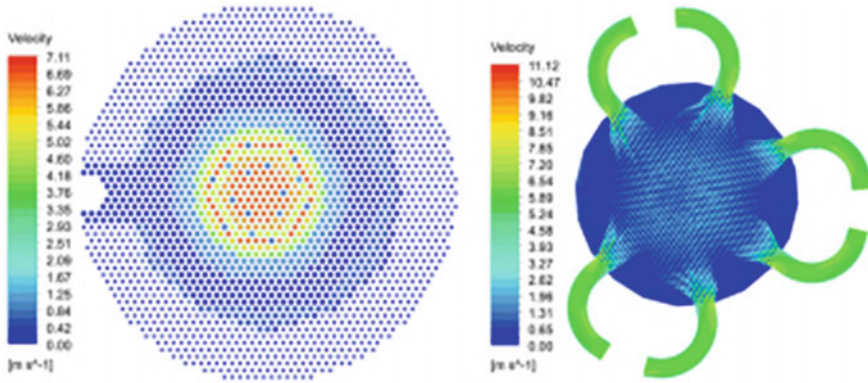
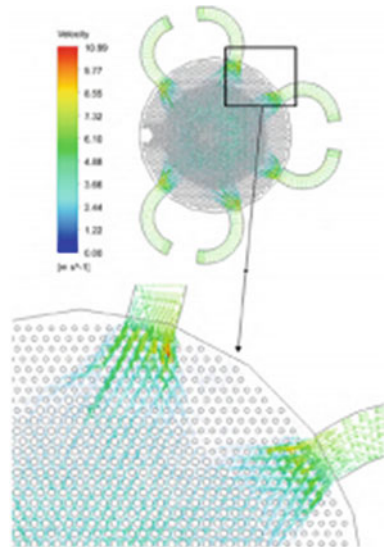


Fig. 9 Velocity contour plot for case#1

Fig. 10 Velocity vector plot for case#1



have sodium temperature at 397 °C. The temperature distribution at the outlet plane of the grid plate and the whole domain is shown in Fig. 12. The interface formed at the IVTP location and other ends at 240°, due to thermal diffusion, remains nearly the same as in case#2 (see Fig. 11).

To quantify the mixing of hot and cold primary sodium inside the grid plate, the average temperature at the inlet of SAs is estimated at every 30° sector of the domain and for every flow zone. Figure 13 shows the sectorial division for different flow zones and the primary pipes' location. The mass average temperature sector wise is calculated as given in Eq. 7.

To appreciate the thermal mixing, outlet temperature for case#2 and case#3 are compared with nondimensionalized temperature (θ) as defined in Eq. 8.

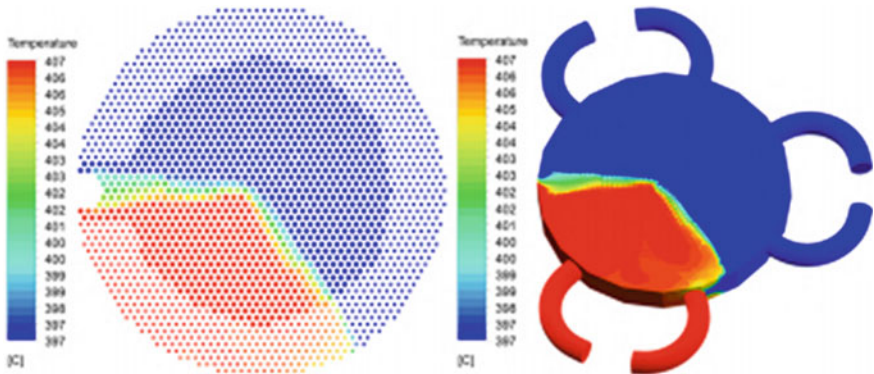


Fig. 11 Temperature distribution in the grid plate for case#2

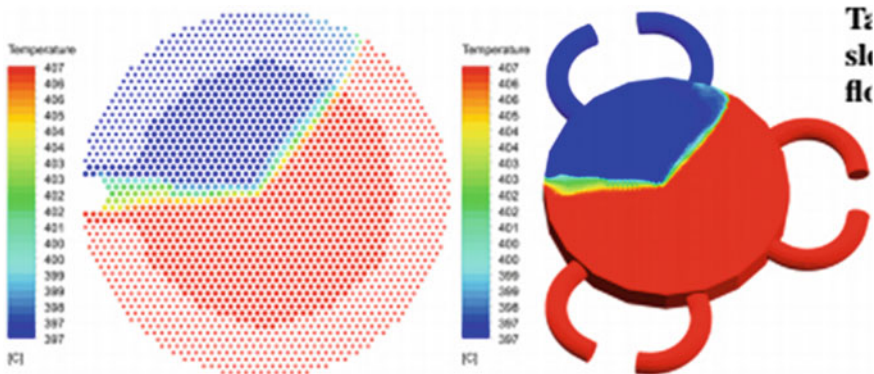
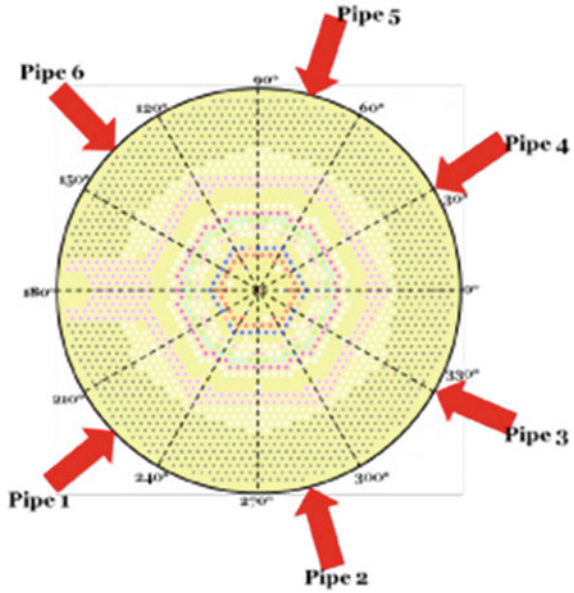


Fig. 12 Temperature distribution in the grid plate for case#3

Fig. 13 Angular positioning of 30° sectors for respective flow zones at the outlet plane of the grid plate



$$\text{mass weighted average temperature} = \frac{\int T\rho|\vec{v}d\vec{A}|}{\int \rho|\vec{v}d\vec{A}|} \tag{7}$$

where, T is the sodium temperature, ρ is density, v is velocity, and A is the area at the outlet plane of the grid plate

$$\theta = \frac{T_{\text{case}}}{T_{\text{mean}}} \tag{8}$$

where, θ is non—dimensional temperature, T case is the temperature of the corresponding case, T mean is mean temperature calculated as Eq. 9.

$$T_{\text{mean}2} = T_{\text{ref}} + \frac{\Delta T}{3} \text{ for case\#2} \tag{9}$$

$$T_{\text{mean}3} = T_{\text{ref}} + \frac{2\Delta T}{3} \text{ for case\#3} \tag{10}$$

where, T_{ref} is the temperature of the reference case, and ΔT is the inlet temperature rise, i.e., 10 °C.

$T_{\text{mean}2}$ and $T_{\text{mean}3}$ values are calculated to be 400.3 °C and 403.7 °C, respectively. θ close to 1 represents perfect mixing condition, while θ away from 1 represents inadequate mixing. Table 2 shows the average temperature at the outlet plane (SA inlet) for 12 different sectors for a typical flow zone#8. For each sector, an inlet

Table 2 Temperature (°C) evolution at the outlet of sleeves of grid plate represented sector wise for a typical flow zone#8 for equilibrium core of FBR 1 & 2

Sector	Case#2	Case#3	T _{case2}	T _{case3}
1	397.01	407.01	0.992	1.008
2	397	405.2	0.992	1.004
3	397	397.28	0.992	0.984
4	397	397.1	0.992	0.984
5	397	397.01	0.992	0.984
6	397.74	397.6	0.994	0.985
7	406.13	406.27	1.014	1.006
8	406.97	407	1.017	1.008
9	406.9	407	1.016	1.008
10	406.21	407	1.015	1.008
11	397.97	407	0.994	1.008
12	397	407	0.992	1.008

temperature of the flow zone is averaged using Eq. 8. The table also gives θ , which quantifies the mixing as a departure from the perfectly mixed condition. For case#2, the primary pipes 1 and 2 supply sodium at higher temperatures; similarly, for case 3, the primary pipes 1, 2, 3, and 4 supply sodium at higher temperatures. In case#2, sectors 7, 8, 9, and 10 are affected, and there is a temperature rise in the SA inlet in these sectors as given in Table 2. This is as expected because affected primary pipes 1 & 2 are in the vicinity of these sectors. Similarly, for case 3, sectors 6, 7, 8, 9, 10, 11, 12, 1 & 2 have a temperature rise in the SA inlet, which is in the vicinity of affected primary pipes 1–4. For the central SA, the SA inlet temperature is 398.8 °C for case#2 and 404.9 °C for case#3. Accordingly, the θ_{CSAM} values could increase by 1.8 °C and 7.9 °C for case#2 and case#3, respectively. This shows that as far as the central SA is concerned, there is nearly perfect mixing in the sodium streams reaching it from various pumps.

4 Conclusion

A 3D thermal hydraulic analysis is carried out for the grid plate of FBR 1 & 2 to establish and quantify the thermal mixing of primary sodium inside the GP. The study is carried out when there is a differential temperature among different primary pump outlets to simulate thermal mixing behavior during unexpected transients in secondary sodium loops. Based on the analysis of the nominal condition, the pressure drop offered by the grid plate (with primary pipes) is established to be 9.05 mlc. In either case, analyzed in the present study, the rise in sodium outlet temperature at the central SA θ_{CSAM} location in GP is found to be lower than its critical value

of 10 °C, thereby representing nearly perfect mixing in the streams reaching from various pumps.

References

1. Sinha RK, Kakodkar A (2006) Design and development of the AHWR—the Indian thorium fuelled innovative nuclear reactor. *Nucl Eng Des* 236:683–700
2. Puthiyavinayagam P, Selvaraj P, Balasubramaniyan V, Raghupathy S, Velusamy K, Devan K, Nashine BK, Sureshkumar KV, Padmakumar G, Varathrajan S, Mohankrishnan P, Srinivasan G, Bhaduri AK (2017) Development of fast breeder reactor technology in India. *Progress Nucl Energy* 101:19–42
3. Chetal SC, Chellapandi P, Puthiyavinayagam P, Raghupathy S, Balasubramaniyan V, Selvaraj P, Mohanakrishnan P, Raj B (2011) Current status of fast reactor and future plans in India. *Energy Procedia* 7:64–73
4. Puthiyavinayagam P, Devan K, Aithal SR, Athmalingam S, Vijayashree R, Raghupathy S, Velusamy K, Theivarajan N, Usha S, Bhaduri AK (2018) Advanced design features of mox fuelled future Indian SFRs, FR 17. *Int Atomic Energy Agency* 51(6)
5. Natesan K, Kasinathan N, Velusamy K, Selvaraj P (2006) Thermal hydraulic investigations of primary coolant pipe rupture in an LMFBR. *Nucl Eng Des* 236(11):1165–1178
6. Jalali HR, Fadaei AH (2017) Proposition of innovative and safe design of grid plate for Tehran research reactor. *Ann Nucl Energy* 106:11–32
7. Peng F, Su Q, Xing J, Lu D, Wang C, Gu H (2021) Experimental study on flow distribution and mixing at the core inlet of double loop small module reactor. *Ann Nucl Energy* 252:1080–1088
8. Tong LL, Hou LQ, Cao XW (2021) Analysis of the flow distribution and mixing characteristics in the reactor pressure vessel. *Nucl Eng Technol* 53:93–102
9. Spaceclaim, User guide, ANSYS 19.2. 2 (2019)
10. Fluent, User guide, ANSYS 19.2. 2 (2019)
11. Spalding DB, Launder BE (1974) Numerical computation of turbulent flows. *Comp Methods Appl Mech Eng* 13:269–289
12. Hanjalic K, Tropea C, Jakirlic S (2002) Modeling rotating and swirling turbulent flows: a perpetual challenge. *AIAA J* 40:1984–1996

Velocity Slip and Temperature Jump in Homogeneous and Heterogeneous Porous Medium



Krishan Sharma, Subrata Kumar, and P. Deepu

Nomenclature

F	Pressure coefficient
f	Darcy friction factor
F_t	Thermal accommodation coefficient
F_v	Tangential momentum accommodation coefficient
G	Pressure gradient
K	Permeability of porous matrix
K_0	Characteristic permeability
k	Thermal conductivity of fluid
Kn	Knudsen number, λ/R
M	Ratio of effective viscosity to fluid viscosity, μ_e/μ
Nu	Nusselt number
p	Pressure
Pr	Prandtl number
q_w	Wall heat flux
R	Microtube radius
r	Radius coordinate
Re_D	Reynolds number
T	Fluid temperature
T_e	Entry fluid temperature
T_m	Bulk mean temperature
T_w	Wall temperature
u	Fluid velocity
z	Longitudinal coordinate

K. Sharma (✉) · S. Kumar · P. Deepu
Department of Mechanical Engineering, IIT Patna, Bihta 801103, India
e-mail: krishan.pme16@iitp.ac.in

Greek Symbols

α	Velocity slip coefficient,
α_v	Momentum slip factor
α_t	Temperature jump factor
β	Temperature jump coefficient
γ	Specific heat ratio
η	Dimensionless radial coordinate, r/R
θ	Dimensionless temperature
λ	Mean free path
σ	Porous media shape parameter

1 Introduction

Recent advancements in micro-fabrication and the shrinking of electronic devices have reignited interest in microscale gas transport phenomena at the microscale. Modeling of the fluid flow and heat transfer through such tiny devices requires the incorporation of velocity slip, temperature jump, and recently identified problems [1, 2]. Multichip units of supercomputers and small electronic devices employ the hyper porous media to cool their tiny components. Modeling fluid flow and heat transfer in such small devices (size of few hundred millimeters) involves the incorporation of temperature jump, velocity slip, and recently identified issues. A rarefied gaseous flow through tiny narrow channels violates the no-slip requirement of the classical continuum approach [3]. In such a flow gas velocity is non-zero at the wall boundaries and there is a temperature differential between the neighboring gas layer and the wall. The Knudsen number (Kn) is a measure of the degree of rarefaction in a rarefied gaseous flow. It is the ratio of the mean free path (λ) to the representative physical length scale of the flow domain. Based on the amount of rarefaction, four models exist: the continuum flow regime ($Kn \leq 10^{-3}$), the slip-flow regime ($10^{-3} < Kn \leq 10^{-1}$), the transition flow regime ($10^{-1} < Kn \leq 10$), and the free molecular regime ($Kn > 10$) [4, 5]. In the continuum flow regime, the Navier–Stokes and energy equations are applicable with no-slip conditions at the boundaries [2]. In the slip-flow regime, the N-S equations can still be applied as long as the appropriate boundary conditions for the velocity slip and temperature jump are considered at the walls [6]. In addition, the N-S equation is not relevant for the transition and free molecular regime; instead, the kinetic theory of gas must be used. In this paper, we are interested in the slip-flow regime (i.e., $10^{-3} < Kn \leq 10^{-1}$).

Most of the studies on heat transfer slip flow have only been conducted with homogeneous porous media. As far as we are aware, no research has been done that encompasses the analytical analysis of flow in heterogeneous porous media with rarefied gas flow.

Therefore, the present study fills the gap by providing precise analytical results on convective heat transfer in a circular microtube while taking into consideration homogeneous/heterogeneous permeability along with the condition of velocity slip, temperature jump, and uniform wall heat flux. Fluid flow and heat transfer are modeled using the Brinkman momentum equation and thermal energy equation. Heterogeneous permeability is introduced in power-law fashion i.e., $K = K_0\eta^n$. Two cases are considered (i) $K = K_0$ (homogeneous porous medium) and (ii) $K = K_0\eta$ (heterogeneous porous medium). The exact solution for velocity, temperature, and Nusselt number are derived and compared for both cases.

2 Mathematical Formulation

A schematic representation of a micro-tube channel filled with saturated porous media in cylindrical coordinates (r, z) is shown in Fig. 1. The flow of rarefied gas is in the positive z - direction. The tube wall is considered impermeable at $r = R$, and subjected to a uniform heat flux q_w . The current study makes the following presumptions:

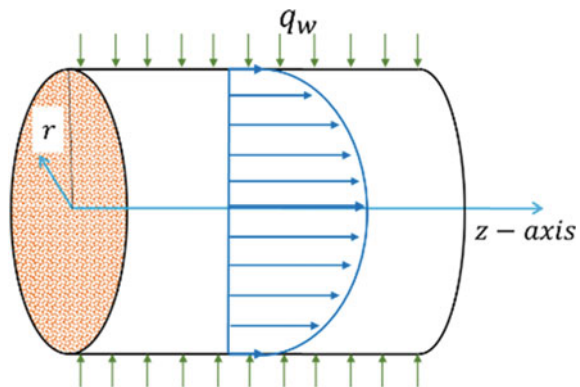
- Steady, incompressible, unidirectional laminar flow is considered.
- The flow is fully developed (hydrodynamically and thermally).
- Axial thermal conduction is assumed to be negligible.
- Natural convection, radiative heat transfer, and thermal dispersion are negligible.

Under the above stated conditions, the Brinkman momentum equation and thermal energy equation in cylindrical coordinates are written as.

Brinkman momentum equation

$$\mu_{\text{eff}} \left(\frac{\partial^2 u}{\partial r^2} + \frac{1}{r} \frac{\partial u}{\partial r} \right) - \frac{\mu}{K} u - \frac{\partial p}{\partial z} = 0 \tag{1}$$

Fig. 1 Schematic of a circular micro-tube filled with a porous medium



Thermal energy equation

$$\frac{k}{\rho c_p} \left(\frac{\partial^2 T}{\partial r^2} + \frac{1}{r} \frac{\partial T}{\partial r} \right) = u \frac{\partial T}{\partial z} \quad (2)$$

Here u is the velocity, K is the permeability, μ_{eff} is the effective viscosity, μ is the fluid viscosity, p is the pressure, and k , T , ρ and c_p are the thermal conductivity, temperature, density of the fluid, and specific heat respectively.

The velocity slip at the wall and finiteness of the velocity at the center of the microtube are associated boundary conditions with the momentum equation (Eq. 1). To account for the rarefaction effect of gaseous flow, the tube wall uses the following velocity slip boundary condition.

$$u_{f,w} - u_w = -\alpha_v \lambda \left. \frac{\partial u}{\partial r} \right|_{\text{wall}}, \quad \alpha_v = \frac{2 - F_v}{F_v} \quad (3)$$

where $u_{f,w}$ is the velocity of the fluid layer immediately adjacent to the tube wall, u_w is the wall velocity, λ is the mean free path, F_v is the tangential momentum accommodation coefficient, and α_v is the momentum slip factor. It is worth noting that for stationary wall, $u_w = 0$.

Temperature jumps at the wall and finite temperature at the center of the microtube are the boundary conditions corresponding to the thermal energy equation (Eq. 2). The temperature of the wall and the temperature of the nearby gas layer are different. The gradient in the local temperature is proportional to their difference. The boundary condition for the temperature jump is thus as follows:

$$T_{f,w} - T_w = -\alpha_t \lambda \left. \frac{\partial T}{\partial r} \right|_{\text{wall}}, \quad \alpha_t = \frac{2 - F_t}{F_t} \frac{2\gamma}{\gamma + 1} \frac{1}{\text{Pr}} \quad (4)$$

Here T_w is the wall temperature, $T_{f,w}$ is the temperature of the fluid layer immediately adjacent to the wall, γ is the specific heat ratio, F_t is the thermal accommodation coefficient, Pr is the Prandtl number, and α_t is the temperature jump factor. Physically, F_v and F_t values range from 0 to 1. The value of F_v and F_t depends on the temperature, pressure and surface finish and must be determined experimentally. F_v and F_t are often assumed to be equal to one in majority of studies. However, experimental observation indicates that both coefficients value are less than one [5]. Therefore, present work considers both F_v and F_t 0.85, as suggested by Bahrami et al. [5].

In order to consider the heterogeneity, we use the assumption that permeability is power-law dependent on the radial coordinate, i.e., $K(\eta) = K_0 \eta^n$. Here n represents a real number. Let us assume that the pressure gradient is constant ($G = -\partial p / \partial z$) and rewriting Eq. (1) in dimensionless form as shown below

$$\eta^n \frac{d^2 \tilde{u}}{d\eta^2} + \eta^{n-1} \frac{d\tilde{u}}{d\eta} - \sigma^2 \tilde{u} = -\frac{\eta^n}{M} \quad (5)$$

where $\eta = \frac{r}{R}$, $\tilde{u} = \frac{\mu u}{GR^2}$, $\sigma = \frac{1}{\sqrt{Da}}$, $Da = \frac{K_0}{R^2}$. Here Da is the Darcy number, K_0 is the characteristic permeability and σ is the porous medium shape parameter [7, 8]. It is quite difficult to construct a closed-form solution of Eq. (5) with a general value of n . Hence, we investigate only two cases: (i) homogeneous porous medium ($n = 0$ i.e., $K = K_0$) and (ii) heterogeneous porous medium ($n = 1$ i.e., $K = K_0\eta$).

The mean velocity is given by

$$u_m = \frac{2}{R^2} \int_0^R ur dr \tag{6}$$

With uniform heat flux q_w in fully developed flow, the first law of thermodynamics prescribes the following constant axial temperature gradient [9].

$$\frac{\partial T}{\partial z} = \frac{2q_w}{\rho c_p R u_m} \tag{7}$$

The bulk mean temperature is given by

$$T_m = \frac{2}{R^2 u_m} \int_0^R uTr dr. \tag{8}$$

Using Eq. (7) and the following definitions of dimensionless temperature, Nusselt number, and dimensionless velocity

$$\theta = \frac{T - T_w}{T_m - T_w}, \quad Nu = \frac{2Rq_w}{k(T_w - T_m)}, \quad \hat{u} = \frac{u}{u_m} = \frac{\tilde{u}}{\tilde{u}_m} \tag{9}$$

the dimensionless form of the thermal energy equation (Eq. (2)) reads

$$\frac{d^2\theta}{d\eta^2} + \frac{1}{\eta} \frac{d\theta}{d\eta} = -\hat{u}Nu \tag{10}$$

The velocity slip and temperature jump boundary condition in dimensionless form can be written as

$$\tilde{u}(1) = -\alpha \left. \frac{\partial \tilde{u}}{\partial \eta} \right|_{\eta=1}, \quad \alpha = \alpha_v Kn \tag{11}$$

$$\theta|_{\eta=1} = -\beta \left. \frac{\partial \theta}{\partial \eta} \right|_{\eta=1}, \quad \beta = \alpha_t Kn \tag{12}$$

Here Kn , α and β are the Knudsen number, velocity slip coefficient, temperature jump coefficient respectively.

3 Theoretical Analysis

3.1 Case I: Homogenous Porous Medium

In the case of uniform permeability $n = 0$, subsequently, Eq. (5) becomes

$$\frac{d^2\tilde{u}}{d\eta^2} + \frac{1}{\eta} \frac{d\tilde{u}}{d\eta} - \sigma^2\tilde{u} + \frac{1}{M} = 0 \tag{13}$$

Utilizing the boundary conditions, solution to Eq. (13) gives

$$\tilde{u} = \frac{1}{M\sigma^2} \left(1 - \frac{I_0(\sigma\eta)}{\alpha\sigma I_1(\sigma) + I_0(\sigma)} \right) \tag{14}$$

where I_ζ is the first-kind ζ th ordered modified Bessel function. Introducing non-dimensional mean velocity \tilde{u}_m stated by

$$\tilde{u}_m = 2 \int_0^1 \tilde{u}\eta d\eta \tag{15}$$

And solving \tilde{u}_m further velocity \hat{u} is defined as

$$\hat{u} = \frac{\tilde{u}}{\tilde{u}_m} = \frac{\sigma(I_0(\sigma) - I_0(\eta\sigma) + \alpha\sigma I_1(\sigma))}{\sigma I_0(\sigma) + (-2 + \alpha\sigma^2)I_1(\sigma)} \tag{16}$$

Now we move toward the heat transfer analysis. Applying the boundary conditions, thermal energy equation (Eq. (10)) gives

$$\theta = \frac{-Nu}{4\sigma} \left(\frac{(4 + (-1 + \eta^2 - 2\beta)\sigma^2)I_0(\sigma) - 4I_0(\eta\sigma) + \sigma((-1 + \eta^2)\alpha\sigma^2 + \beta(4 - 2\alpha\sigma^2))I_1(\sigma)}{\sigma I_0(\sigma) + (-2 + \alpha\sigma^2)I_1(\sigma)} \right) \tag{17}$$

Finally using the dimensionless bulk mean temperature equation

$$2 \int_0^1 \hat{u}\theta\eta d\eta = 1, \tag{18}$$

and substituting Eqs. (16) and (17) in Eq. (18), we get the expression for Nusselt number as a function of slip coefficient and shape parameter

$$\text{Nu} = \frac{8(\sigma I_0(\sigma) + (-2 + \alpha\sigma^2)I_1(\sigma))^2}{A_1 I_0(\sigma)^2 + 2A_2 I_0(\sigma)I_1(\sigma) + A_3 I_1(\sigma)^2} \quad (19)$$

where

$$A_1 = (-24 + (1 + 4\beta)\sigma^2)\sigma$$

$$A_2 = 24 - 8(\alpha + \beta)\sigma^2 + \alpha(1 + 4\beta)\sigma^4$$

$$A_3 = (8 + 16\beta + \alpha(32 - 16\beta\sigma^2 + \alpha(1 + 4\beta)\sigma^4))\sigma$$

For cases $Kn = 0$ i.e., $\alpha = \beta = 0$, Nu reduces to

$$\text{Nu} = \frac{8\sigma^3(I_2(\sigma))^2}{\sigma(-24 + \sigma^2)(I_0(\sigma))^2 + 48I_0(\sigma)I_1(\sigma) + 8\sigma(I_1(\sigma))^2} \quad (20)$$

Which shows agreement with Eq. (16) of Sharma et al. [10].

3.2 Case II: Heterogeneous Porous Medium

When $n = 1$, Eq. (5) becomes

$$\eta \frac{d^2 \tilde{u}}{d\eta^2} + \frac{d\tilde{u}}{d\eta} - \sigma^2 \tilde{u} = -\frac{\eta}{M} \quad (21)$$

Applying the BCs yields

$$\tilde{u} = \frac{1 + \eta\sigma^2}{M\sigma^4} - \frac{B_1 I_0(2\sqrt{\eta}\sigma)}{M\sigma^4(I_0(2\sigma) + \alpha\sigma I_1(2\sigma))} \quad (22)$$

The mean velocity is

$$\tilde{u}_m = \frac{B_2 I_0(2\sigma) + B_3 I_1(2\sigma)}{3M\sigma^7(I_0(2\sigma) + \alpha\sigma I_1(2\sigma))} \quad (23)$$

Thus, the velocity profile becomes

$$\hat{u} = \frac{3\sigma^3((1 + \eta\sigma^2)(I_0(2\sigma) + \alpha\sigma I_1(2\sigma)) - B_1 I_0(2\sqrt{\eta}\sigma))}{B_2 I_0(2\sigma) + B_3 I_1(2\sigma)} \quad (24)$$

Similarly, the temperature solution

$$T = \frac{\text{Nu}}{12\sigma} \left(\frac{B_4 I_0(2\sigma) + 36B_1 I_0(2\sqrt{\eta}\sigma) + \sigma \left(B_5 I_1(2\sigma) - 18B_1 \left(\frac{2\sqrt{\eta} I_1(2\sqrt{\eta}\sigma)}{\sigma(2+\beta)I_2(2\sigma) - 2\eta I_2(2\sqrt{\eta}\sigma) + \beta\sigma I_3(2\sigma)} \right) \right)}{B_2 I_0(2\sigma) + B_3 I_1(2\sigma)} \right) \quad (25)$$

Finally utilizing the compatibility Eq. (18), Nu expression is

$$\text{Nu} = \frac{120\sigma (B_2 I_0(2\sigma) + B_3 I_1(2\sigma))^2}{\sigma B_6 I_0(2\sigma)^2 + 2B_7 I_0(2\sigma) I_1(2\sigma) + \sigma B_8 I_1(2\sigma)^2} \quad (26)$$

where

$$B_1 = (1 + (1 + \alpha)\sigma^2)$$

$$B_2 = (6 + (9 + 6\alpha)\sigma^2 + 2\sigma^4)\sigma$$

$$B_3 = -6 - 6(2 + \alpha)\sigma^2 - 3(2 + \alpha)\sigma^4 + 2\alpha\sigma^6$$

$$B_4 = -36 - 18(2 + 2\alpha - \beta)\sigma^2 - 9(-1 + \eta^2 - 2(2 + \alpha)\beta)\sigma^4 - 4(-1 + \eta^3 - 3\beta)\sigma^6$$

$$B_5 = 36 + 36(1 + \alpha)\sigma^2 - 9(-1 + \eta^2)\alpha\sigma^4 - 4(-1 + \eta^3)\alpha\sigma^6 + 6\beta(-3 - 3(2 + \alpha)\sigma^2 - 3\sigma^4 + 2\alpha\sigma^6)$$

$$B_6 = -317520 - 144(3328 + 2220\alpha - 15\beta)\sigma^2 - 144(1314 + 15\alpha^2 + \alpha(1151 - 30\beta) - 45\beta)\sigma^4 + 9(-3249 + 700\beta + 144\alpha(-23 + 5\beta) + 16\alpha^2(-13 + 15\beta))\sigma^6 - 144(12 + 3\alpha^2 - 15\beta - 2\alpha(-8 + 5\beta))\sigma^8 + 40(1 + 6\beta)\sigma^{10}$$

$$B_7 = 158760 + 72(4451 + 30\alpha - 30\beta)\sigma^2 - 72(-2836 + 2175\alpha^2 + 105\beta + \alpha(983 + 60\beta))\sigma^4 - 72(-649 + 130\beta + 30\alpha(21 + 4\beta) + 2\alpha^2(527 + 15\beta))\sigma^6 - 9(8\alpha^2(166 + 15\beta) + 8(-59 + 65\beta) + \alpha(921 + 420\beta))\sigma^8 + 144(5\alpha^2(-1 + \beta) - 5\beta + \alpha(-4 + 5\beta))\sigma^{10} + 40(\alpha + 6\alpha\beta)\sigma^{12}$$

$$B_8 = -144\alpha(1 + \sigma^2)(-2190 - (2149 + 30\beta)\sigma^2 - (518 + 45\beta)\sigma^4)$$

$$\begin{aligned}
& -(56 + 5\beta)\sigma^6 + 10\beta\sigma^8) \\
& + \alpha^2\sigma^2(315360 + 72(4339 + 30\beta)\sigma^2 + 144(529 + 15\beta)\sigma^4 \\
& + (7767 - 900\beta)\sigma^6 - 144(-1 + 5\beta)\sigma^8 + 40(1 + 6\beta)\sigma^{10}) \\
& + 72(1 + \sigma^2)^2(-41 - 22\sigma^2 + 6\sigma^4 + 30\beta(1 + \sigma^2)^2)
\end{aligned}$$

Similarly, for cases $Kn = 0$ i.e., $\alpha = \beta = 0$, Nu reduces to

$$Nu = \frac{-120\sigma^3\left((6 + 9\sigma^2 + 2\sigma^4)I_0(2\sigma) - 6(1 + \sigma^2)_0^2 F_1[2, \sigma^2]\right)^2}{\sigma(317520 + 479232\sigma^2 + 189216\sigma^4 + 29241\sigma^6 + 1728\sigma^8 - 40\sigma^{10})I_0(2\sigma)^2 - 144(1 + \sigma^2)(2205 + 2246\sigma^2 + 590\sigma^4 + 59\sigma^6)I_0(2\sigma)I_1(2\sigma) - 72\sigma(1 + \sigma^2)^2(-41 - 22\sigma^2 + 6\sigma^4)I_1(2\sigma)^2} \quad (27)$$

is in complete agreement with the Eq. (26) of Sharma et al. [10].

4 Results and Discussion

Figure 2 demonstrates that an increase in the velocity slip coefficient (α) leads to an increase in Nusselt number, as an increase in the velocity slip at the wall indicates an increase in velocity, which results in a greater convective heat transfer. Moreover, Fig. 2 shows that an increase in the temperature jump coefficient (β) decreases the Nusselt number because an increase in slip reduces the temperature gradient at the wall, which implies decreasing heat transfer. Plots for the case of homogeneous porous media are depicted as solid colored lines and as dotted colored lines for heterogeneous porous media. Figure 2 depicts that for a given value of σ , Nusselt number is larger in case of heterogeneous permeability than the homogeneous permeability. It is because in case of heterogeneous permeability, there exists a larger temperature gradient at the wall compared to homogeneous permeability.

Apart it is clear from the Fig. 2a–c that for a fixed velocity slip coefficient (α) and temperature jump coefficient (β), Nusselt number (Nu) increases with increases in shape parameter (σ). The same can be explained further in more detail in Fig. 3.

Figure 3 depicts the Nusselt number (Nu) vs shape parameter (σ) plot at different Knudsen number (Kn) for the homogeneous (solid lines) as well as heterogeneous permeability case (dashed lines). It is to be noted that the values of Nusselt number for uniform permeability are confined between 4.36 ($\sigma \rightarrow 0$, Plane Poiseuille flow) and 8 ($\sigma \rightarrow \infty$, plug flow or Darcy flow) and between 4.36 and 12 for heterogeneous permeability. This is consistent with the results of Sharma et al. [10]. As we know that velocity slip coefficient and temperature jump coefficient are functions of Knudsen number (Kn) (Eq. 12). $Kn = 0$ represents zero slip and temperature jump at the wall.

Fig. 2 Effect of α , β and σ parameters on Nu for $K = K_0$ (solid lines) and $K = K_0\eta$ (dashed lines)

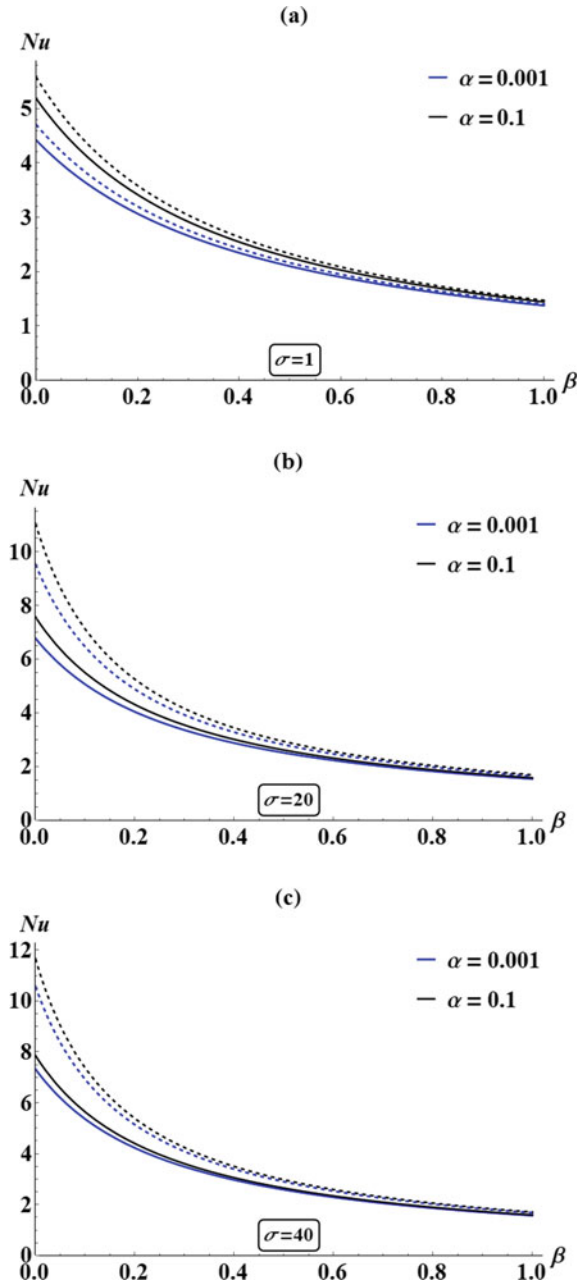
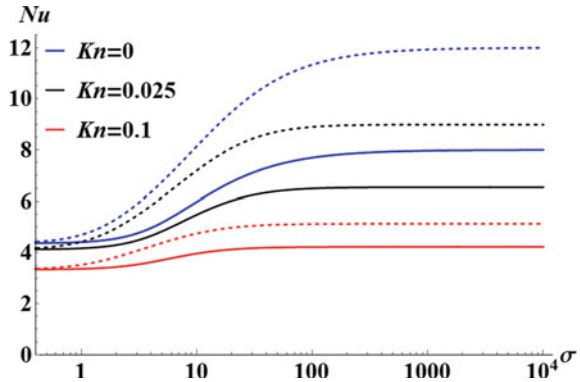


Fig. 3 Effect of Kn and σ on Nu for $K = K_0$ (solid lines) and $K = K_0\eta$ (dashed lines)



It is clear from the figure that for a given value of shape parameter (σ), an increase in Knudsen number (Kn), Nusselt number (Nu) drops.

5 Conclusion

Steady fully developed rarefied gaseous flow is investigated in a micro-tube channel filled with porous medium. Exact solutions are derived for velocity, temperature, and Nusselt number. The reported results for homogeneous and heterogeneous permeability scenario for a typical case of $Kn = 0$, validates the available literature data on flow and heat transfer in porous medium with no slip at the wall.

Results show the higher heat transfer in cases of heterogeneous permeability case than the uniform permeability scenario. The observation that Nu is higher in the heterogeneous permeability case than in the homogeneous permeability scenario serves as a confirmation of the same.

For the condition of $\sigma \rightarrow 0$ & ∞ respectively, present solution can be used to predict a clear fluid flow (i.e., Plane Poiseuille flow) and plug flow or Darcy flow. This is because for $\sigma \rightarrow 0$ & ∞ , Brinkman momentum equation reduces to the clear fluid flow and Darcy model equation respectively.

References

1. T.A.A.X.W. Randall, F.B.R.O. Warrington Jr, Laminar Forced Convection In A Circular Tube With Constant Heat Flux And Slip Flow, *Microscale Thermophys. Eng.* 1 (1997) 303–320
2. Z. Duan, Y.S. Muzychka, Slip flow heat transfer in annular microchannels with constant heat flux, *J. Heat Transfer.* 130 (2008)
3. J.J. Shu, J. Bin Melvin Teo, W. Kong Chan, Fluid velocity slip and temperature jump at a solid surface, *Appl. Mech. Rev.* 69 (2017). <https://doi.org/10.1115/1.4036191>

4. Renksizbulut M, Niazmand H, Tercan G (2006) Slip-flow and heat transfer in rectangular microchannels with constant wall temperature. *Int J Therm Sci* 45:870–881
5. Bahrami H, Bergman TL, Faghri A (2012) Forced convective heat transfer in a microtube including rarefaction, viscous dissipation and axial conduction effects. *Int J Heat Mass Transf* 55:6665–6675
6. Larrodé FE, Housiadas C, Drossinos Y (2000) Slip-flow heat transfer in circular tubes. *Int J Heat Mass Transf* 43:2669–2680
7. Hooman K, Ranjbar-Kani AA (2004) A perturbation based analysis to investigate forced convection in a porous saturated tube. *J Comput Appl Math* 162:411–419. <https://doi.org/10.1016/j.cam.2003.08.031>
8. K. Sharma, D. P, S. Kumar (2022) Magnetohydrodynamic flow and heat transfer filled with homogeneous and heterogeneous porous medium. *Heat Transf Res* 54:35–53. <https://doi.org/10.1615/heattransres.2022045564>
9. Incropera F, DeWitt D, Bergman T, Lavine A (2007) *Fundamentals of heat and mass transfer*. Wiley, New York
10. Sharma K, Deepu P, Kumar S (2020) Convective heat transfer in a tube filled with homogeneous and inhomogeneous porous medium. *Int Commun Heat Mass Transf* 117:104791. <https://doi.org/10.1016/j.icheatmasstransfer.2020.104791>

Insights from a Nonlinear and Corresponding Linear Model of a Pulsating Heat Pipe



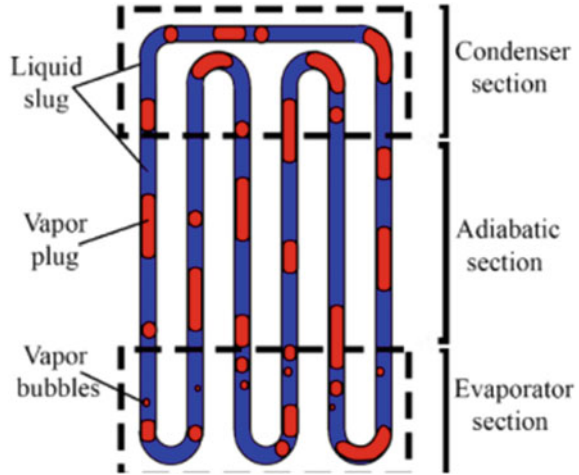
Alok Kumar, Govind Maurya, Nadeem Ahmed, and Suneet Singh

1 Introduction

Pulsating flow provides an enhancement in heat transfer due to increased surface area for the heat transfer mechanism [1]. In order to obtain self-sustained oscillations of the flow, many designs of the heat exchangers have been proposed by changing the size and the shape of the pipe as well as by changing the working fluid [2]. It has been observed that a partially filled capillary-size pipe can provide sustained oscillations in industrial applications dealing with miniature sizes such as electronic cooling requiring relatively small-sized heat exchangers. Therefore, among various heat exchangers for electronic cooling at the circuit level, heat pipe has played a prominent role. Pulsating heat pipe (PHP), as shown in Fig. 1, is a meandering tube with multiple U-shape turns with an evaporator and a condenser section. The wick-less structure and the smaller size compared to other heat transfer devices make it a perfect choice for thermal management applications. Although heat pipe technology is used across industrial applications, the requirement of self-sustained oscillations can only be satisfied using the pulsating heat pipe [3]. Therefore, understanding the PHP dynamics is crucial to use it in more sensitive applications like space applications and electronics. The analysis of the operating dynamics was initially based on the experimental findings and the start-up process. Once the threshold value of the applied heat to initiate the pulsating process in the system was calculated, other challenges like optimizing the working parameters like the critical diameter, and width of the liquid thin film were posed [4]. Theoretical analysis of the PHP started with the mathematical modeling of the system using basic conservation equations. The modeling of the oscillating position of the liquid slug is done using the spring-mass

A. Kumar (✉) · G. Maurya · N. Ahmed · S. Singh
Fluid Flow Systems Simulation Lab, Department of Energy Science and Engineering, IIT
Bombay, Mumbai 400076, India
e-mail: alok.kumar@iitb.ac.in

Fig. 1 Schematic diagram of a pulsating heat pipe [7]



system [5]. The simple design, yet complex phenomena in a PHP pose several difficulties in modeling the system. Various coupled processes like capillary size, phase change, friction, and surface tension result in a complicated problem to analyze [6]. Therefore, the results from the linearized mathematical models fail to produce real phenomena. The present work provides a comparative analysis of a nonlinear and corresponding linear model using bifurcation analysis. The impact of additional bifurcation points and possible changes on the operating dynamics are discussed in detail using the phase portrait and the temporal evolution analysis.

2 Mathematical Modeling

The mathematical modeling of the PHP (primarily based on [8]) consists of the momentum conservation equation for the liquid slug, the energy balance equation of the vapor plug, and the continuity equation. The momentum conservation equation for the liquid slug can be written by adding all the force components acting on the slug in the control volume shown in the figure, as follows,

$$\frac{d^2x_i}{dt^2} = \frac{1}{m_l}(P_g A - P_e A - \rho_g g L_1 A \sin \theta + F_f) \quad (1)$$

where x_i is the position of the liquid slug, P_g and P_e vapor pressure and external pressure respectively. This formulation has been made assuming the fact that the capillary forces at each meniscus are equal and opposite resulting in zero net capillary force across the plug. The friction force F_f depends on the flow type. For $Re_w \ll 4$, it follows the Poiseuille profile as,

$$F_f = -8\pi \mu L_1 \dot{x}_i = c\dot{x}_i, \quad \text{where } c = -8\pi \mu L_1 \quad (2)$$

Although, it is the simplest form of friction force that will provide a qualitatively rich insight into the dynamics. Energy conservation of a general control volume consisting of a liquid slug squeezed between two vapor plugs can be written as,

$$\frac{dT_g}{dt} = \frac{1}{c_v m_g} \left(\dot{m}_g (c_p T_{g,sat} - c_v T_g) - P_{g,sat} A \dot{x}_i + \dot{Q}_g \right) \quad (3)$$

The energy conservation equation for the vapor bubble is given in Eq. 3 whose terms correspond to the energy added by phase change, mechanical work done by the liquid plug, and the amount of heat transferred from the wall respectively. Where T_g is the averaged temperature of the vapor bubble which is usually overheated i.e., $T_g > T_{g,sat}$. m_g is the mass of bubbles and \dot{m}_g is the net rate of evaporation. Isothermality (where \dot{Q}_g is taken in a way such that $\dot{T}_g = 0$) and adiabaticity (where $\dot{Q}_g = 0$) are the two limiting conditions for temperature evolution. The mass conservation equation can be explained using the phase change phenomena. For the phase change modeling, a globally accepted simplified approach in terms of thermal resistance has been adopted.

$$\dot{Q} = \frac{(T_w - T_{g,sat})}{R_{th}}, \quad \text{since } \dot{Q} = \dot{m}_g \times H_v, \quad \dot{m}_g = \frac{\dot{Q}}{H_v} = \frac{(T_w - T_{g,sat})}{R_{th} H_v} \quad (4)$$

The wall temperature profile should be a continuous function of the space variable in the axial length. Therefore, a profile with an arctangent function (shown in Eq. 5) may provide a relatively close representation of the wall temperature obtained by experimental data.

$$T_w(x) = \frac{T_{HL}}{\pi} \arctan \left(-\frac{\pi |T'_{wc}|}{T_{HL}} (x - x_c) + \frac{T_H + T_L}{2} \right) \quad (5)$$

where $|T'_{wc}|$ is the temperature gradient and $T_{HL} = T_H - T_L$. Here, x is the space variable in the axial length and x_c is the point of the inflection.

$$|T'_{wc}| = \left(\frac{-dT_w}{dx} \right)_{x=x_c}, \quad \text{where } x_c = \frac{T_{HL}}{\pi |T'_{wc}|} \tan \left[\frac{\pi (T_{g,sat,0} - \frac{1}{2}(T_H + T_L))}{T_{HL}} \right] \quad (6)$$

Thus the rate of vapor mass flow can be written as,

$$\dot{m}_g(x_i) = \frac{\frac{T_{HL}}{\pi} \tan^{-1} \left(-\frac{\pi |T'_{wc}|}{T_{HL}} (x - x_c) + \frac{T_H + T_L}{2} \right) - T_{g,sat}}{H_v R_{th}} \quad (7)$$

where the saturation temperature of the vapor bubble

$$T_{g,sat} = \left[\left(\frac{1}{T_{g,sat,0}} \right) - \frac{R_g}{H_v} \ln \left(\frac{P_g}{P_{g,0}} \right) \right]^{-1}$$

2.1 Nonlinear System

Equations (1), (3), and (7) collectively form the system of equations representing the dynamics of a PHP. Since stability analysis is performed around the equilibrium, the system is converted into perturbation equations. This system of perturbation equations is then converted to the dimensionless system of equations. The non-dimensionalization of the perturbation terms has been done in perturbation form only. The dimensionless system of equations is written as follows:

$$\ddot{\tilde{x}}_i = \widetilde{\nabla P}_g + \tilde{F}_f, \tag{8}$$

$$\dot{\widetilde{\nabla m}}_g = \widetilde{T}_{HL} \tan^{-1}[-\widetilde{T}'_{wc}(\tilde{x}_i - \tilde{x}_c)] + \widetilde{C}_{th} - \left(\frac{T_{g,0}}{m_{g,0}\omega_n H_v R_{th}} \right) \widetilde{\nabla T}_{g,sat} \tag{9}$$

$$\begin{aligned} \dot{\widetilde{\nabla T}}_g &= \frac{\gamma_{th}(\widetilde{\nabla T}_{g,sat} + \widetilde{\nabla T}_{g,sat,0}) - (1 + \widetilde{\nabla T}_g) \dot{\widetilde{\nabla m}}_g}{1 + \widetilde{\nabla m}}_g \\ &\quad - \frac{(1 - \gamma_{th})(1 + \widetilde{\nabla P}_g)\dot{\tilde{x}}_i}{1 + \widetilde{\nabla m}}_g + \frac{\dot{\tilde{Q}}_g}{1 + \widetilde{m}}_g \end{aligned} \tag{10}$$

Equations 8–10 form the system of nonlinear ordinary differential equations which is consisting of all major thermophysical processes involved in the transient operation. Both the limiting conditions of isothermality and adiabatic indicate that Eq. 10 vanishes and Eq. 9 converts to the following equation,

$$\dot{\widetilde{\nabla m}}_g = \widetilde{T}_{HL} \tan^{-1}[-\widetilde{T}'_{wc}(\tilde{x}_i - \tilde{x}_c)] + \widetilde{C}_{th} \tag{11}$$

The above system of equations (Eqs. 8 and 11) is converted into a system of three first-order ordinary differential equations. The equilibrium points for the given nonlinear system (obtained by putting the right-hand side equal to zero) are $\dot{\tilde{x}}_i = 0$, $\tilde{x}_i = \widetilde{\nabla m}_g$, $\because \ddot{\tilde{x}}_i = 0$, and $\tilde{x}_i = \tilde{x}_c - (|\widetilde{T}'_{wc}|)^{-1} \tan(-\widetilde{C}_{th}/\widetilde{T}_{HL})$, $\because \widetilde{\nabla m}_g = 0$. Further, the system with replaced temperature profile is called the linear model. Although the wall temperature equation is linearized, the model still retains its nonlinearity because of the nonlinearity present in other equations. This nonlinear system of perturbations is valid for both high and low Reynolds numbers.

2.2 Linear System

The linear and actual temperature profile

The vapor plug is always at high temperature whereas the liquid slug remains at low temperature. This transition from high to low does not occur all of a sudden. Although the temperature shifts from high to low in a continuously decreasing fashion which asymptotically approaches the extreme values, it can be approximated with a linear temperature profile as shown in Fig. 2. The deviation between the two profiles is only on the extreme values which can be ignored without any loss of generality. Also, the assumption of the linear profile is suitable to reduce the complexity.

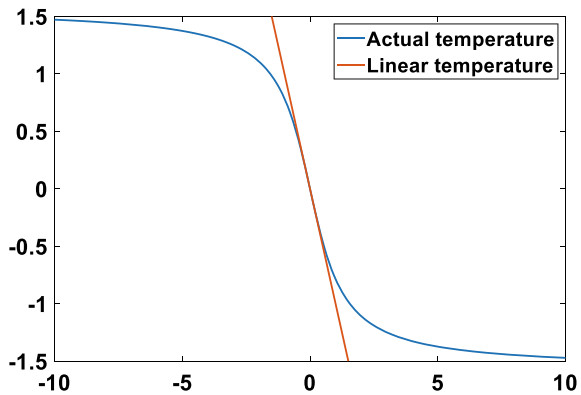
The assumption can be supported by the argument that the asymptotic approach of the temperature at both the walls creates an extra number of singularities in the mathematical system which further complicates the real dynamics. After considering the linear temperature profile, the system has two equilibrium points, $(0, 0, 0)$ and $(c, 0, c)$, which are obtained using three conditions: (1) $\tilde{\sigma} \neq 0, \tilde{x}_i = 0, ,$ (2) $\tilde{\sigma} = 0, \tilde{x}_i \neq 0,$ and (3) $\tilde{\sigma} = 0, \tilde{x}_i = 0,$ where c is any given constant. The linear system obtained after the linearization around the equilibrium points is given by:

$$\ddot{\tilde{x}}_i \approx -\tilde{x}_i + \widetilde{\nabla m}_g - 2\zeta_f \dot{\tilde{x}}_i \tag{12}$$

$$\widetilde{\nabla m}_g \approx -2\tilde{\sigma} \tilde{x}_i \tag{13}$$

where $\tilde{\sigma} = \frac{\frac{1}{2} \widetilde{T_{HL}} |T'_{wc}|}{1 + (\tilde{x}_c T'_{wc})^2} = \frac{L_{g,0} |T'_{w,0}|}{3m_{g,0} \omega_n H_v R_{th}}$

Fig. 2 The linear and actual wall temperature profiles



3 Results and Discussion

Both models have been numerically solved using the Runge–Kutta method. Detailed bifurcation analysis has been performed using *MATCONT* which reveals a series of bifurcation points. Discussion on all of them is beyond the scope of the present work. Rather, to explore any possible route to chaos, the Zero-Hopf point has been chosen and the presence of any hidden attractor is analyzed using the phase portraits.

3.1 Phase-Portrait

The position-velocity phase portrait of the liquid slug shows a completely different phenomenon with both models. The phase portrait shown in red in Fig. 3 corresponds to the linear mode, whereas the other shown in the zoomed view is for the nonlinear model. The linear model captures the oscillatory motion but the trajectory continues to grow beyond the physical limit. The nonlinear model explains the amplitude of the oscillatory behavior appropriately. The oscillations converge to a constant amplitude limit cycle.

The system shows different operating characteristics for different parameter values. The parameter space has been divided into three sub-regions using the trichotomy property. The temporal evolution and the phase portraits for all three subregions have been plotted in Fig. 4. The temporal evolution of the linear model in all three conditions ($\tilde{\sigma} \{ \zeta_f, \tilde{\sigma} = \zeta_f, \text{ and, } \tilde{\sigma} \} \zeta_f$) shows that the friction coefficient works as a damper to the system. In other words, if the friction coefficient dominates the amplitude of the oscillations starts decreasing and vice versa for the phase change coefficient. The phase portrait also shows an inward spiral, a perfect ellipse, and an

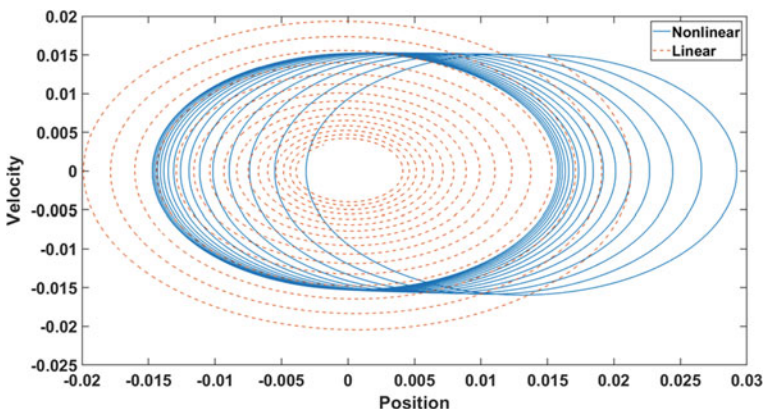
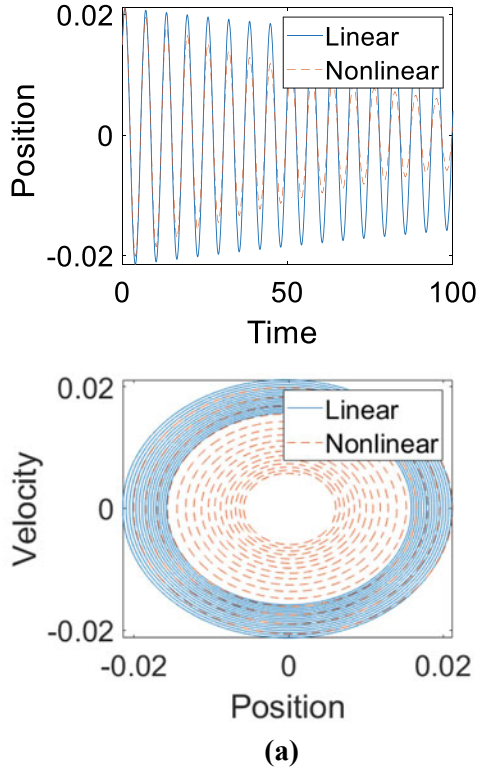


Fig. 3 Phase portrait between the position and velocity of the liquid slug in the linear and nonlinear models

Fig. 4 The temporal evolution and phase portrait between the position and the velocity of the liquid slug in the linear (blue) and nonlinear (red) model, (a) for $\tilde{\sigma} < \zeta_f$, (b) for $\tilde{\sigma} = \zeta_f$, and (c) for $\tilde{\sigma} > \zeta_f$

1. For $\tilde{\sigma} < \zeta_f$

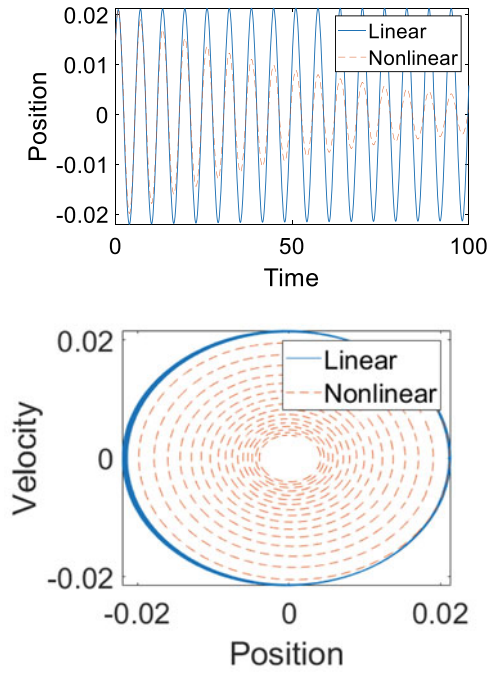


outward spiral for the respective conditions. But, for the nonlinear model, both the temporal and the phase portrait show a decaying nature of the oscillations which represents the actual feature of the operating characteristics.

The change in the nature of the oscillations from the linear to the nonlinear model indicates that the sudden changes in the equilibrium points will also vary from the linear to the nonlinear model. Therefore, as the linear model provides a definite form of the pattern in the equilibrium point, to understand the same for the nonlinear system, bifurcation analysis is used. It has been found that the nonlinear model has a Zero-Hopf bifurcation point in addition to the Generalized Hopf bifurcation in the linear model [9]. In order to explore any possibility of a hidden attractor due to this additional ZH point, the phase space has been utilized.

Fig. 4 (continued)

2. For $\tilde{\sigma} = \zeta_f$



(b)

3. For $\tilde{\sigma} > \zeta_f$

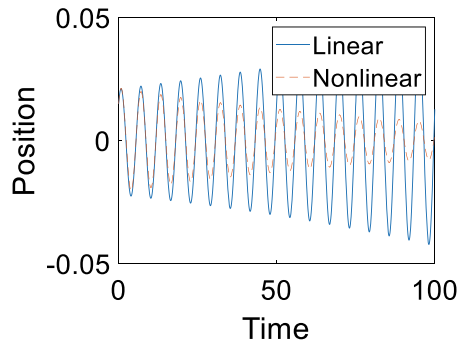
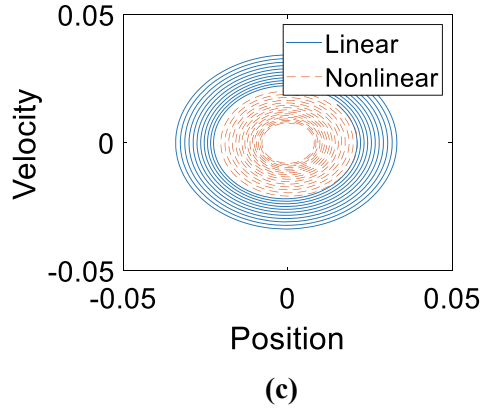


Fig. 4 (continued)



3.2 Hidden Attractor

An attractor is called a hidden attractor if its basin of attraction does not intersect with small neighborhoods of equilibria, otherwise, it is called a self-excited attractor [10]. The chaotic regime of a PHP has been identified by experimental studies but no theoretical work is present that deals with the onset of a chaotic region [11]. Among several methods to detect the presence of a hidden attractor, one is due to the presence of simultaneous occurrence of the ZH and GH bifurcation points [9].

3.3 Phase-Portrait of the Hidden Attractor

A three-dimensional portrait of the position, velocity, and mass flow rate at three different parameters is shown in Fig. 5. The parameter values have been chosen in the vicinity of the ZH point. For $\tilde{\sigma} = 0.6, \zeta_f = 0.55$, the phase portrait is showing an outward spiral which finally settles to a constant amplitude LC (blue in Fig. 5). A double frequency is observed (red) at $\tilde{\sigma} = 0.7, \zeta_f = 0.92$ which corresponds to the Period-doubling bifurcation. The switch from a constant amplitude LC to the double frequency oscillations is observed but the onset of this switch is not visible. Therefore, to address the question of the source for the double frequency of the oscillations, a portrait at the ZH point is drawn (shown in green) and it is found that this parameter value retains the trajectory for a certain period around the green portrait. This phenomenon shows a possible presence of a hidden attractor in the parameter space which provides a possible route to chaos.

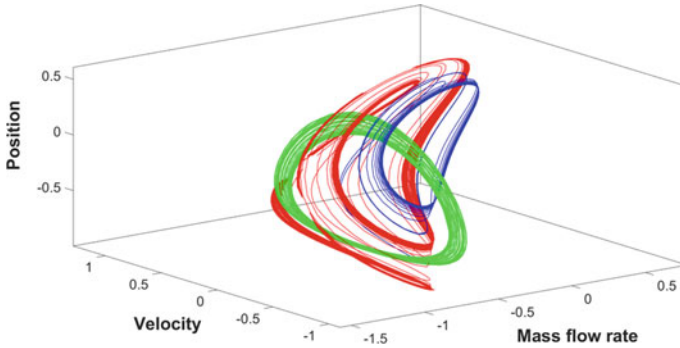


Fig. 5 Three dimensional portrait of the position, velocity, and mass flow rate representing a possible hidden attractor in green

4 Conclusion

The bifurcation analysis provides a qualitative understanding of the operating dynamics of a pulsating heat pipe provided. The linear model captures the oscillatory behavior but fails to explain the limiting character of the amplitude of the oscillations. On the other hand, the nonlinear model captures the said character perfectly and shows a constant amplitude limit cycle. Varying both parameters simultaneously reveals an additional bifurcation i.e., GH in the nonlinear model. The simultaneous presence of GH and ZH makes the dynamics complex and a possible presence of a hidden attractor due to the ZH is explained using a 3D phase portrait of all three state variables at three different parameter values. A short-term revolving of the trajectory on the given parameter value indicates a probable presence of a hidden attractor responsible for making the system chaotic.

Nomenclature

A	Area of the tube [m^2]
c_p, c_v	Specific heat capacities [$\text{J} \cdot \text{kg}^{-1} \text{K}^{-1}$]
F_f	Friction force [kg m s^{-2}]
g	Gravitational acceleration [ms^{-2}]
L	Length [m]
m	Mass flow rate [kg s^{-1}]
P	Pressure [Pa]
Q_g	Applied Heat [Wm^{-2}]
Re	Reynolds number
R_{th}	Thermal resistance
T	Temperature [$^{\circ}\text{C}$]

t/τ	Dimension/non-dimensional time
x_i	Position of the liquid slug [m]
\dot{x}_i	Velocity of the liquid slug [ms^{-1}]
ρ	Density of the working fluid [kg m^{-3}]
θ	Inclination angle
μ	Viscosity of the working fluid [Pa s]
σ	Phase change coefficient
ζ_f	Friction coefficient

Acronyms

<i>BP</i>	Branch Point
<i>GH</i>	Generalized Hopf
<i>LPC</i>	Limit Point of Cycles
<i>LC</i>	Limit Cycle
<i>NS</i>	Neimar-Sacker
<i>PD</i>	Period Doubling
<i>PHP</i>	Pulsating Heat Pipe
<i>SBPHP</i>	Single Branch Pulsating Heat Pipe
<i>ZH</i>	Zero Hopf

Subscripts and Superscripts

<i>c</i>	Critical
<i>g</i>	Gas
<i>l</i>	Liquid slug
<i>o</i>	Equilibrium
<i>sat</i>	Saturation
<i>sat, o</i>	Saturation at the equilibrium
<i>w</i>	Wall
∇	Relative difference between the equilibrium value and the transient value
\sim	Dimensionless quantity
\cdot	Rate of change of the quantity

References

1. Ye Q, Zhang Y, Wei J (2021) A comprehensive review of pulsating flow on heat transfer enhancement. *Appl Therm Eng* 196:117275. <https://doi.org/10.1016/j.applthermaleng.2021.117275>
2. Jiang B (2010) Analysis on mechanism of heat transfer enhancement by vibration and experimental research on a new type of vibrational heat transfer component. Shandong Univ, Jinan, PRC
3. Shafii MB, Faghri A, Zhang Y (2001) Thermal modeling of unlooped and looped pulsating heat pipes. *J Heat Transfer* 123(6):1159–1172. <https://doi.org/10.1115/1.1409266>
4. Yang XS, Karamanoglu M, Luan T, Koziel S (2014) Mathematical modeling and parameter optimization of pulsating heat pipes. *J Comput Sci* 5(2):119–125. <https://doi.org/10.1016/j.jocs.2013.12.003>
5. Nikolayev VS (2021) Physical principles and state-of-the-art of modeling of the pulsating heat pipe: a review. *Appl Therm Eng* 195:117111. <https://doi.org/10.1016/j.applthermaleng.2021.117111>
6. Vasiliev LL (2005) Heat pipes in modern heat exchangers. *Appl Therm Eng* 25(1):1–19. <https://doi.org/10.1016/j.applthermaleng.2003.12.004>
7. Sharma M, Singh Sikarwar B (2019) Flow and heat transfer of fluid in a pulsating heat pipe. *J Phys Conf Ser* 1369(1):012019. <https://doi.org/10.1088/1742-6596/1369/1/012019>
8. Tessier-Poirier A, Monin T, Léveillé É, Monfray S, Formosa F, Fréchette LG (2019) How evaporation and condensation lead to self-oscillations in the single-branch pulsating heat pipe. *Phys Rev Fluids* 4(10):1–34. <https://doi.org/10.1103/PhysRevFluids.4.103901>
9. Kumar A, Singh S (2023) Bifurcation analysis of a pulsating heat pipe. *Int J Therm Sci*. <https://doi.org/10.1016/j.ijthermalsci.2023.108384>
10. Kuznetsov NV, Leonov GA (2014) Hidden attractors in dynamical systems: systems with no equilibria, multistability and coexisting attractors. *IFAC Proc* 47(3):5445–5454. <https://doi.org/10.3182/20140824-6-ZA-1003.02501>
11. Song Y, Xu J (2009) Chaotic behavior of pulsating heat pipes. *Int J Heat Mass Transf* 52(13–14):2932–2941. <https://doi.org/10.1016/j.ijheatmasstransfer.2009.02.030>

Heat Transfer Evaluation Method for RC Members at Standard Fire Scenario



Banti A. Gedam

1 Introduction

Incidents of accidental fire in high-rise building structures are increasing significantly. In such conditions, fire resistance rating evaluation of RC members constructed by NSC and HSC is important for safety and evacuation measures [1]. However, fire resistance rating evaluation is associated with an appropriate heat transfer model, which mainly helps to determine the real-time temperature-dependent concrete properties [2]. Existing code and standard practices, i.e., NBC [3], IS 456 [4], and IS 1642 [5] are preliminary developed for NSC and deal with fire resistance rating in terms of nominal concrete cover provision, which does not associate with heat transfer nor performance-based evaluation considering recent structural requirements.

The type of fire load depends on a building compartment shape and size, and on the characteristics of different combustible and hazardous materials used. However, in building the most severe fire load can be observed as a cellulosic fire after the initial combustion of materials and this has been acknowledged in full flag development in IS 3809 [6], ISO 834 [7], BS 476-22 [8], and ASTM E119 [9] as standard time–temperature curves shown in Fig. 1.

Such a fire load may lead to a very serious threat for the RC members either damaged/collapsed and may affect their service life too after the fire impact. Heat transfer evaluation of RC members to obtain structural stability and integrity against failure at standard fire load is often a requirement. Therefore, this paper is addressing the most important problem solution of a heat transfer evaluation for RC members at standard fire load.

B. A. Gedam (✉)

Department of Civil Engineering, Sardar Vallabhbhai National Institute of Technology,
Ichchhanath, Surat, Gujarat 395007, India

e-mail: bantiagedam@gmail.com

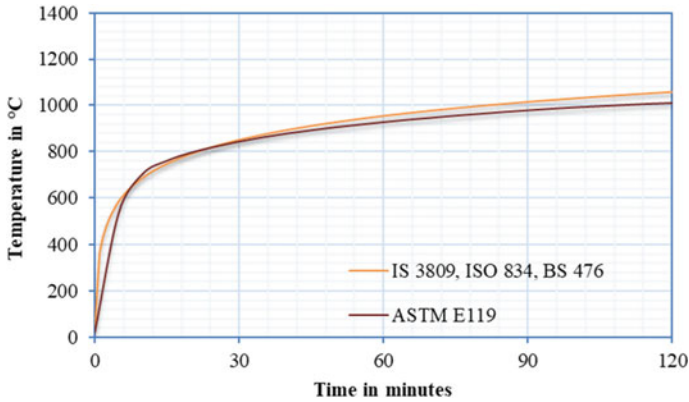


Fig. 1 Standard time–temperature fire loads as per IS 3809, ISO 834, BS 476, and ASTM E119

2 Literature Review and Objective

For the fire-resistant rating of RC members, many analytical and numerical research studies were observed for evaluating the RC member behavior by employing the heat transfer method [10–13]. Some research studies [14–19] also reported an empirical approach to heat transfer analysis, which limits their application use specifically for RC beams at standard fire load.

It is worth noting that all research studies exhibited the applicability of the heat transfer model, specifically developed either for the column or beam with the limitation of fire exposure conditions and time. Also, though computational and advanced numerical approaches are available to solve the heat transfer problem, the problem still exists due to consideration of material homogeneity and non-consideration of aggregate effect. Thermally induced concrete properties of NSC and HSC are completely different [20] and considering all heating mechanisms with appropriate concrete thermal properties for heat transfer evaluation makes it more complex in transient heating conditions.

Therefore, this paper is focusing on the existing problem for heat transfer evaluation of NSC and HSC RC members at standard fire load and the development of a simple heat transfer model to evaluate temperature transmission in RC members in one-dimensional (1D) and two-dimensional (2D) up to 280 min.

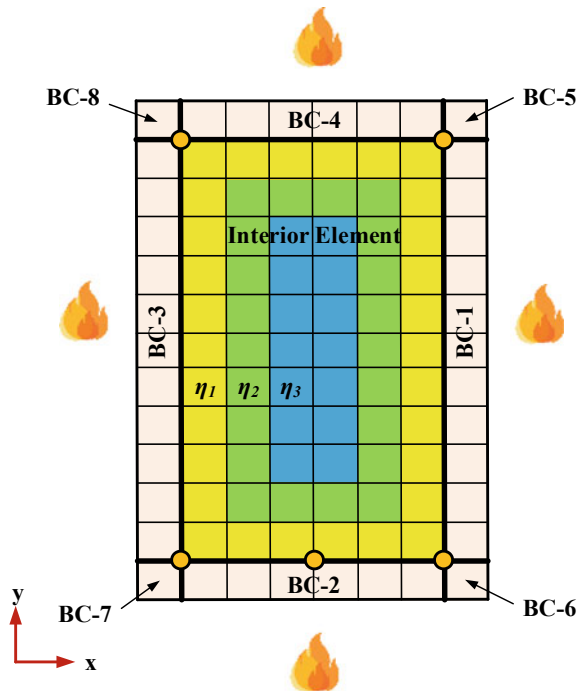
3 Heat Transfer Model

It is worth noting that when an RC member comes in contact with fire the numerical problem comprises unsteady state heat transfer at the transient heating boundary condition, which makes the problem more complex for obtaining numerical estimating results. In real practical situations, RC member boundary exposure to fire through a space air gap in which two basic heating mechanisms, i.e., convection and radiation predominantly act on the exposed face. However, with the relationship between these two mechanisms, the heat transfers within the RC member are due to the conduction mechanism which is in an unsteady state due to transient heating boundary conditions. In such a way, the heat transfer analysis simultaneously complies with three basic heating mechanisms with the association of concrete thermal properties at transient heating conditions.

To develop a heat transfer model for RC members, a finite difference method is being used. It is assumed that the RC member is exposed to fire on four sides shown in Fig. 2, and accordingly assumption has been made for heat transfer model development which requirements are as follows:

1. All RC members are considered completely solid, homogeneous, isotropic, have constant material properties, and are discretized into a number of elements of the same size and shape.

Fig. 2 Schematic diagram of RC member in discretized and different boundary heating elements



2. Each discretized element node physically interacts with each other by heating mechanisms in a standard fire scenario.
3. All exposed surfaces of RC member to fire is considered as a boundary condition and comes in contact with fire by two heating mechanism, i.e., convection and radiation.
4. Each internal element node is associated with boundary elements that transfer the heat by conduction mechanism.

In numerical evaluation, the partial differential for heat conduction yields Eq. 1 as a two-dimensional analysis, where the addition of convection and radiation for boundary elements becomes Eq. 2. However, as seen in Fig. 2 various boundaries, i.e., BC-1 to BC-4 and BC-5 to BC-6 shows similarity with fire exposure condition, hence only one boundary conditions BC-4 and BC-5 have been numerically elaborated.

$$\frac{\partial^2 T}{\partial x^2} + \frac{\partial^2 T}{\partial y^2} = \frac{\rho \cdot C_p}{k} \frac{\partial T_f}{\partial t} \tag{1}$$

$$\underbrace{\left(\frac{\partial^2 T}{\partial x^2} + \frac{\partial^2 T}{\partial y^2} \right)}_{\text{Conduction}} + \underbrace{h \Delta x (T_\infty - T_{m,n})}_{\text{Convection}} + \underbrace{\varepsilon \cdot \sigma \Delta x (T_s^4 - (T_{m,n} + 274)^4)}_{\text{Radiation}} = \frac{\rho \cdot C_p}{k} \frac{\partial T_f}{\partial t} \tag{2}$$

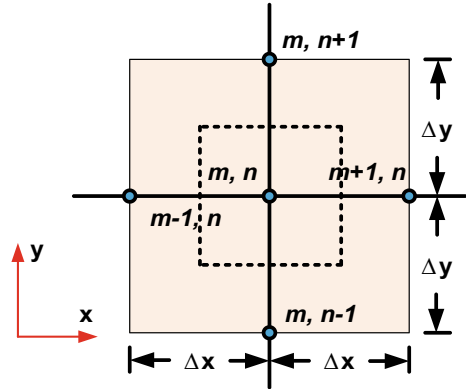
3.1 Internal Elements

Figure 3 presents internal element nodes consisting of subscript ‘m’ as the x-coordinate and the subscript ‘n’ as the y-coordinate. Using the Laplace Eq. 2 with the pertinent element as four node points with size $\Delta x = \Delta y$, the second order derivative approximated as Eqs. 3 and 4. The time derivative approximately is shown in Eq. 5. If the associated element node temperatures are known at any specific time intervals, then the temperature at increment time Δt can be easily calculated by using Eq. (6). Therefore, for the square grid, the temperature becomes Eq. 7.

$$\left. \frac{\partial^2 T}{\partial x^2} \right]_{m,n} \approx \frac{\left. \frac{\partial T}{\partial x} \right]_{m+1/2,n} - \left. \frac{\partial T}{\partial x} \right]_{m-1/2,n}}{\Delta x} = \frac{T_{m+1,n} + T_{m-1,n} - 2T_{m,n}}{(\Delta x)^2} \tag{3}$$

$$\left. \frac{\partial^2 T}{\partial y^2} \right]_{m,n} \approx \frac{\left. \frac{\partial T}{\partial y} \right]_{m,n+1/2} - \left. \frac{\partial T}{\partial y} \right]_{m,n-1/2}}{\Delta y} = \frac{T_{m,n+1} + T_{m,n-1} - 2T_{m,n}}{(\Delta y)^2} \tag{4}$$

Fig. 3 Internal element nodes nomenclature as 2D heat transfer



$$\frac{\partial T_f}{\partial t} \approx \frac{\Delta T}{\Delta t} = \frac{T_{m,n}^p - T_{m,n}}{\Delta t} \tag{5}$$

$$\frac{T_{m+1,n} + T_{m-1,n} - 2T_{m,n}}{(\Delta x)^2} + \frac{T_{m,n+1} + T_{m,n-1} - 2T_{m,n}}{(\Delta y)^2} = \frac{1}{\alpha} \frac{T_{m,n}^p - T_{m,n}}{\Delta t} \tag{6}$$

$$T_{m,n}^p = \tau [T_{m+1,n} + T_{m-1,n} + T_{m,n+1} + T_{m,n-1} - 4T_{m,n}] + T_{m,n} \tag{7}$$

However, due to homogeneous RC member Eq. 7 considering concrete fully pure dense, which analysis results introduced error in prediction. This is because the concrete in real conditions is highly heterogeneous due to the type of concrete materials used when studied at the microscopic level [21, 22] and this significantly influenced the temperature distribution field within the RC member. Hence, the empirical coefficient of density diffusivity in θ term has been introduced. The modified Eq. 8 for internal node heat transfer calculation has been obtained from Eq. 7.

$$T_{m,n}^p = \tau \cdot \theta \cdot [T_{m-1,n} + T_{m+1,n} + T_{n-1,m} + T_{n+1,m} - 4T_{m,n}] + T_{m,n} \tag{8}$$

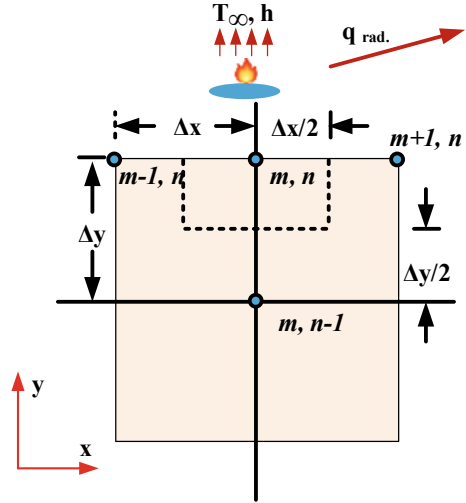
where, $\tau = \frac{k \cdot \Delta t}{0.31 \cdot \rho \cdot C_p \cdot \Delta x^2}$ and $\theta = \frac{(\eta_m \times 0.25 + 0.75)}{10}$

3.2 External and Corner Elements

Figure 4 presents external element nodes which are associated with convection and radiation heating condition. Considering Eq. 2, the energy balance on a node (m, n) is becoming with complete heat transfer mechanisms given in Eq. 9.

$$h \Delta x (T_\infty - T_{m,n}) + \varepsilon \cdot \sigma \Delta x (T_s^4 - (T_{m,n} + 274)^4)$$

Fig. 4 External element nodes nomenclature of BC-4 as 2D heat transfer



$$\begin{aligned}
 &+ k \frac{\Delta y}{2} \frac{T_{m-1,n} - T_{m,n}}{\Delta x} + k \frac{\Delta y}{2} \frac{T_{m+1,n} - T_{m,n}}{\Delta x} \\
 &+ k \Delta x \frac{T_{m,n-1} - T_{m,n}}{\Delta y} = \rho \Delta x \frac{\Delta y}{2} C_p \left[\frac{T_{m,n}^p - T_{m,n}}{\Delta t} \right] \tag{9}
 \end{aligned}$$

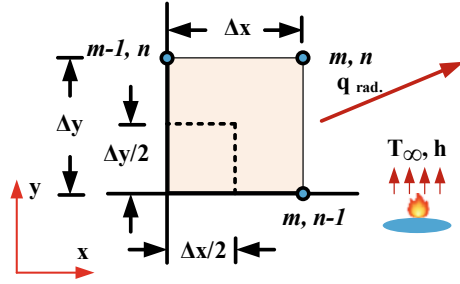
Simplifying the Eq. 9 by $\Delta x = \Delta y$, thermal diffusivity $\alpha = \frac{k}{\rho \cdot C_p}$ and divided $\frac{k}{2}$, the corresponding temperature $T_{m,n}^p$ is become Eq. 10.

$$\begin{aligned}
 T_{m,n}^p &= T_{m,n} \left[1 - 4\tau - 2\tau \frac{h\Delta x}{k} \right] \\
 &+ \tau \left[T_{m,n+1} + T_{m,n-1} + 2T_{m-1,n} + \frac{2h\Delta x}{k} T_\infty + 2 \cdot \varepsilon \cdot \sigma \frac{\Delta x}{k} (T_s^4 - (T_{m,n} + 274)^4) \right] \tag{10}
 \end{aligned}$$

Figure 5 presents corner element nodes which is also associated with convection and radiation heating condition. Now, space coordinate $\Delta x = \Delta y$ for corner element volumetrically affected as $\Delta x/2 = \Delta y/2$, then the corner temperature calculation on a node (m, n) is becoming as Eq. 11.

$$\begin{aligned}
 &h \left(\frac{\Delta x}{2} + \frac{\Delta y}{2} \right) (T_\infty - T_{m,n}) + \varepsilon \cdot \sigma \left(\frac{\Delta x}{2} + \frac{\Delta y}{2} \right) (T_s^4 + (T_{m,n} + 274)^4) \\
 &+ k \frac{\Delta y}{2} \frac{T_{m-1,n} - T_{m,n}}{\Delta x} + k \frac{\Delta y}{2} \frac{T_{m+1,n} - T_{m,n}}{\Delta x} + k \Delta x \frac{T_{m,n-1} - T_{m,n}}{\Delta y} \\
 &= \rho \Delta x \frac{\Delta x}{2} \frac{\Delta y}{2} C_p \left[\frac{T_{m,n}^p - T_{m,n}}{\Delta t} \right] \tag{11}
 \end{aligned}$$

Fig. 5 Corner element nodes nomenclature of BC-5 as 2D heat transfer



Simplifying the Eq. (11) by $\Delta x = \Delta y$, thermal diffusivity $\alpha = \frac{k}{\rho \cdot C_p}$ and divided $\frac{k}{4}$, The corresponding numerical equation for $T_{m,n}^p$ becomes

$$T_{m,n}^p = T_{m,n} \left[1 - 4\tau - 4\tau \frac{h\Delta x}{k} \right] + 2\tau \left[T_{m-1,n} + T_{m,n-1} + \frac{2h\Delta x}{k} T_\infty + 2 \cdot \varepsilon \cdot \sigma \frac{\Delta x}{k} (T_s^4 - (T_{m,n} + 274)^4) \right] \quad (12)$$

4 Heat Transfer Evaluation

Heat transfer model prediction accuracy was validated with the experimental measured results. However, this model was developed for 2D heat transfer evaluation, but the type of fire exposure condition and developed numerical equations of boundary condition also fascinated 1D heat transfer evaluation. Therefore, RC shear walls and RC beams exposed to standard fire have been considered as case studies. For predicting the temperature transmission in RC shear walls and columns, available details of RC members, i.e., material and cross-sectional size were incorporated into the heat transfer model and evaluated in the computational platform using excel programming. The properties adopted for evaluating heat transfer in NSC and HSC RC members are shown in Table 1.

4.1 Case Study I: 1D Heat Transfer Analysis of Shear Walls Exposed to ISO 834 Fire from One Side

Ngo et al. [23] performed experimental studies on NSC and HSC RC walls of size 2400 mm in length, 1000 mm wide, and 150 mm thick that were exposed on one side at standard fire load ISO 834 up to 120 min. Figures 6 and 7 show experimental measured results along with heat transfer model prediction results for NSC and HSC

Table 1 Thermal properties consideration for heat transfer evaluation

Independent variables	NSC	HSC
Fire exposure condition	ISO/ASTM	ISO/ASTM
Heat transfer coefficient in convection, h_c (W/m ² K)	8	8
Emissivity, ϵ	0.85	0.85
Moisture content, μ (%)	0% more than 200 °C	0% more than 200 °C
Thermal conductivity, k (W/mK)	0.6	0.8
Specific heat, C_p (J/kgK)	1100	1100
Stefan-Boltzmann Constant, σ (W/m ² K ⁴)	5.67×10^{-8}	5.67×10^{-8}

shear walls. The experimental measured results show that though the size of the shear walls is the same, the heat transfer rate increment with respect to the exposure time is completely different. This is due to the thermal properties, in which HSC thermal conductivity is higher than that of the NSC, which comprises a density of 2434 kg/m³ for HSC and 2262 kg/m³ for NSC resulting in the high rate of heat transfer in RC shear wall can be observed. This implies that the HSC structural member has more difficulty maintaining their stability and integrity against collapse in severe fire exposure conditions.

It is observed that the prediction of temperature variation with respect to standard time–temperature heating conditions is a good prediction using the thermal properties from Table 1 for NSC and HSC in the heat transfer model. However, for NSC and HSC shear walls, an initial time period of up to 60 min and later either overpredicted or underpredicted heat transfer rate at different locations from the fire exposure side. This is due to both conditions’ heat transfer equations being associated with constant

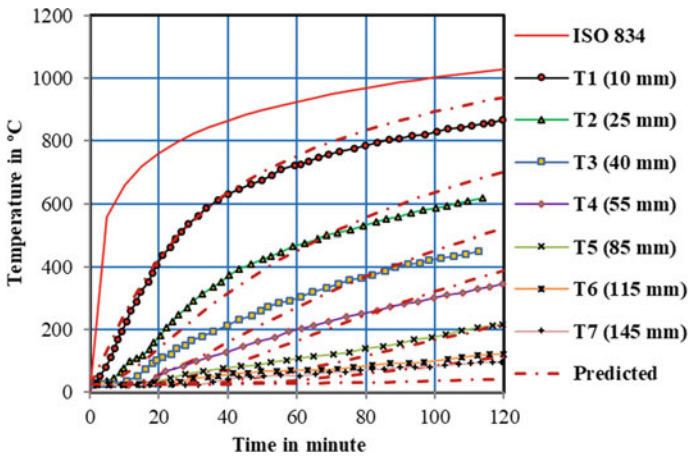


Fig. 6 Heat transfer evaluation for NSC RC shear wall as 1D heat transfer from fire exposure surface

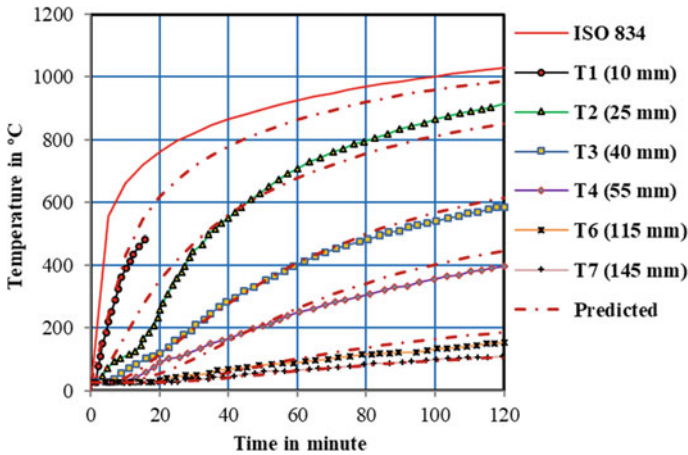


Fig. 7 Heat transfer evaluation for HSC RC shear wall as 1D heat transfer from fire exposure surface

thermal properties, in which diffusivity is identical and does not relate to variable temperature-dependent thermal induced properties of NSC and HSC.

Nonlinear temperature-dependent properties of concrete in the iterative process of the heat transfer model make the simulation more complex and time-consuming in nature, hence constant value had been assimilated to be used in the heat transfer model to keep simple and reliable results. In quantitatively maximum overpredicting or underpredicting results were observed as less than $\pm 8\%$ difference at any point with respect to the time-temperature fire load. This implies that the proposed heat transfer model is efficient in predicting temperature variation in RC members at one side of fire exposure conditions.

4.2 Case Study II: 2D Heat Transfer Analysis of RC Column Exposed to ASTM Fire from Four Side

Kodur et al. [24] performed experimental studies on RC columns of size 305 mm square cross-section and 3810 mm height exposure to standard fire load ASTM maximum up to 280 min. Figures 8 and 9 show experimental measured results along with heat transfer model prediction results for NSC and HSC. Similar results of the high rate of heat transfer for the HSC RC column than the NSC RC column were observed, which comprised a density of 2431 kg/m^3 for HSC and 2294 kg/m^3 for NSC.

Basically, this difference is attributed due to the thermal properties of NSC and HSC, in which HSC has higher compactness with lower porosity at low water content improves density and enhances thermal conductivity. Thus, the heat transfer rate

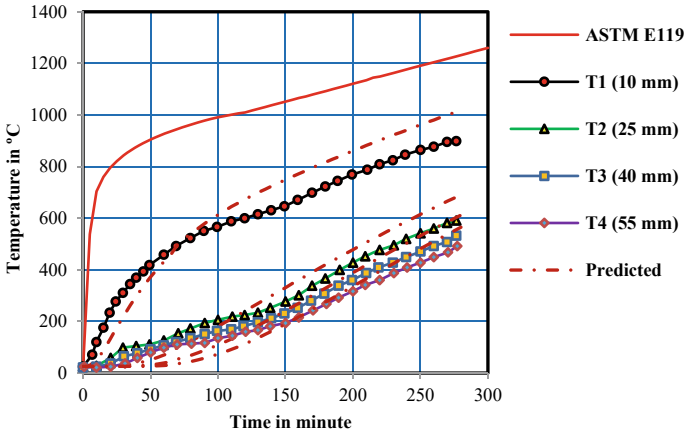


Fig. 8 Heat transfer evaluation for NSC RC column as 2D heat transfer from fire exposure surface

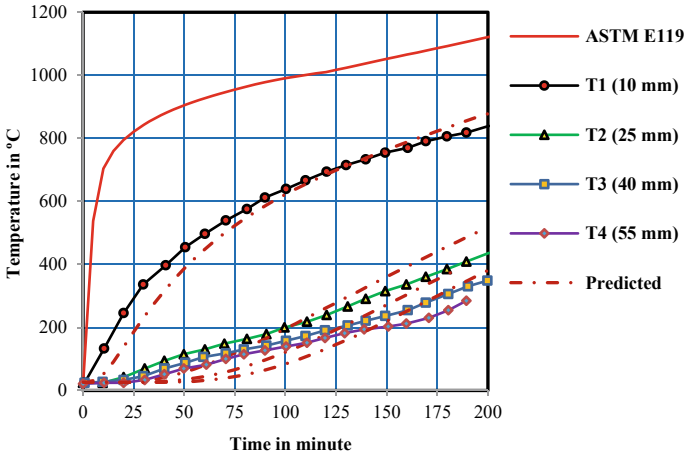


Fig. 9 Heat transfer evaluation for HSC RC column as 2D heat transfer from fire exposure surface

increases resulting in the temperature transmission at the HSC column being higher than that of the NSC column.

As seen in Figs. 8 and 9, it is observed that in 2D heat transfer both same size RC column exposure to ASTM standard fire load, RC column made by HSC reveals very early failure with respect to temperature at 180 min, whereas for the same temperature profile approximates at RC column mode by NSC at 277 min. This implies that the proposed heat transfer model also is efficient in predicting temperature variation in RC members at four sides of fire exposure conditions.

5 Conclusions

Based on the present research, it can draw the main relevant conclusions in heat transfer evaluation of RC members are as follows:

1. The standard fire load and exposure conditions significantly affected the temperature variation within NSC and HSC RC members, and HSC members often encounter more severe conditions than NSC members.
2. Thermal properties of concrete, i.e., thermal conductivity, specific heat, and density play a significant role in the rate of heat transmission within RC members.
3. The developed heat transfer model is helpful in accurately predicting 1D and 2D heat transfer problems for NSC and HSC RC members. The quantitatively maximum overpredicting or underpredicting results were observed as less than $\pm 8\%$ difference at any point with respect to the time temperature.

Acknowledgements The author wishes to express their gratitude and sincere appreciation to the authority of the Council of Scientific and Industrial Research (CSIR), India in Project No. MLP072002 for financing this research work. Also, for several ongoing research projects associated with the FBR in Civil Infrastructure and Engineering during his service period in Fire Safety Engineering, CSIR—Central Building Research Institute, Roorkee.

Nomenclature

α	Thermal diffusivity [mm/s]
ε	Emissivity
$\Delta x = \Delta y$	Size of elements [mm]
μ	Moisture content [%]
θ	Heat transfer coefficient
τ	Stability equation of heat tranfere model [kg/m ³]
σ	Stefan-Boltzmann constant [W/m ² K ⁴]
C_p	Specific heat [J/kgK]
hc	Convective heat transfer coefficient [W/m ² K]
k	Thermal conductivity [W/mK]
$T_{m,n}^p$	Temperature in element [°C]

References

1. Gedam BA (2021) Fire resistance design method for reinforced concrete beams to evaluate fire-resistance rating. Structures 33:855–877
2. EN 1992-1-2, Eurocode 2 (2004), Design of concrete structures—Part 1–2: General rules—Structural fire design., Commission of European Communities, Brussels

3. NBC (2016) National building code of India, vol 1. Bureau of Indian Standards, New Delhi, India
4. IS 456 (2000) Plain and reinforced concrete – code of practice. Bureau of Indian Standards, 1–100
5. IS 1642, 1989, Code of practice for fire safety of buildings (general) – Details of construction.”, Bureau of India Standards, New Delhi.
6. IS 3809, Fire resistance test for structures. Bureau of Indian Standards, 1979, 1–14.
7. ISO 834, Fire resistance test element – Elements of building construction – Part 1: General requirements, 1999, 1–25.
8. BS 476–22, 1978, Fire test on building materials and structures, Methods for determination of the fire resistance of load bearing elements of construction.
9. ASTM E119, Standard test method for fire tests of building construction and materials, ASTM International, 2016, pp. 1–36.
10. Kodur et al (2010) Energy based time equivalent approach for evaluating fire resistance of reinforced concrete beams. *Fire Saf J* 45(4):211–220
11. Gao et al (2013) Finite element modeling of reinforced concrete beams exposed to fire. *Eng Struct* 52:488–501
12. Gao et al (2017) Fire resistance of RC beams under design fire exposure. *Mag Concr Res* 69(8):402–423
13. Kumar P, Kodur VKR (2017) Modeling the behavior of load bearing concrete walls under fire exposure. *Constr Build Mater* 154:993–1003
14. U. Wickstrom, A very simple method for estimating temperatures in fire exposed structures, *New Technology to Reduce Fire Losses and Costs*. Ed., Grayson. S. J. and Smith, D.A., Elsevier Applied Science, London, UK, 1986, pp. 186–194.
15. Lie TT, Irwin RJ (1993) Method to calculate the fire resistance of reinforced concrete columns with rectangular cross section. *ACI Struct J* 90(1):52–60
16. Desai SB (1998) Design of reinforced concrete beams under fire exposure conditions. *Mag Concr Res* 50(1):75–83
17. Abbasi A, Hogg PJ (2005) A model for predicting the properties of the constituents of a glass fibre rebar reinforced concrete beam at elevated temperatures simulating a fire test. *Compos B Eng* 36(5):384–393
18. Kodur V, Baolin Y, Dwaikar M (2013) A simplified approach for predicting temperature in reinforced concrete members exposed to standard fire. *Fire Saf J* 56:39–51
19. Gao WY, Dai JG, Teng JG (2014) Simple method for predicting temperatures in reinforced concrete beams exposed to a standard fire. *Adv Struct Eng* 17(4):573–589
20. Kodur VR, Sultan MA (2003) Effect of temperature on thermal properties of high-strength concrete. *J Mater Civ Eng* 15(2):101–107
21. Gedam BA, Bhandari NM, Upadhyay A (2016) Influence of supplementary cementitious materials on shrinkage, creep, and durability of high-performance concrete. *J Mater Civ Eng* 28(4):04015173
22. Gedam BA (2019) Time-dependent behaviour prediction of the prestressed HPC I-girder. *Eng Struct* 201:109763
23. Ngo et al (2013) Testing of normal- and high-strength concrete walls subjected to both standard and hydrocarbon fires. *ACI Struct J* 110(3):1–8
24. Kodur VKR, Cheng FP, Wang TC, Sultan MA (2003) Effect of strength and fiber reinforcement on fire resistance of high-strength concrete columns. *J Struct Eng* 129(2):253–259

Enhanced Melting Behavior of Phase Change Material (PCM) in a Rectangular Cavity: Effect of Fin



Anjan Nandi, Nirmalendu Biswas, and Aparesh Datta

1 Introduction

Extensive research has been conducted on the utilization of various renewable energy sources. Because of developing digitalized businesses, unstable crude oil supply, rising fossil fuel prices, and concerns about high carbon emissions into the environment and global warming, energy demand is at an all-time high right now. It is crystal clear that the output of any renewable energy system is not much. This fact necessitates a reliable and efficient energy system for converting renewable energy into useful energy. In recent years, application phase change materials (PCMs) have been used as latent heat storage units (LHSU) for various thermal systems to utilize renewable energy. Therefore, the effectiveness of PCM-based thermal systems is one of the most relevant topics in the modern era. However, most of the available PCMs have low thermal conductivity, so the latent heat storage is less for a limited time. Several researchers have attempted (numerically as well experimentally) to utilize the PCM efficiently.

With the above context, Rieger et al. [1] investigated the melting of a phase change material analytically and experimentally and they found similar results of liquid fraction with respect to time both experimentally and numerically. Nanoparticles, porous material, nano-encapsulated PCMs, and extended surface (fin) are some of the procedures to enhance thermal conductivity and many researchers studied these enhancements methodologies [2]. For the enhancement of LHSU, Elgafy and Lafdi [3] experimentally and analytically studied the use of carbon nanofibers as nanoparticles and found out that the nanofibers enhanced the PCM performance. Akhmetov

A. Nandi · N. Biswas (✉)

Department of Power Engineering, Jadavpur University, Salt Lake, Kolkata 700106, India
e-mail: biswas.nirmalendu@gmail.com

A. Datta

Department Mechanical Engineering, NIT Durgapur, Durgapur 713209, India

et al. [4] experimentally and Abdulateef et al. [5] numerically investigate the solidification and melting process using Al_2O_3 as nanoparticles (NPs). They found that the thermal conductivities were improved using the nanoparticles. Yu et al. [6], Kim et al. [7], and Senobar et al. [8] used NePCM combined with highly conductive porous media to enhance the thermal performance of LHSU. Experimentally, they found out that the metal foam enhances more than NPs and their combination is more effective than using only metal foam or NPs. Encapsulated PCMs are also used to store thermal energy as an energy storage system. Athawale et al. [9] numerically predicted the melting characteristics of an encapsulated PCM when a heat transfer fluid (HTF) is subjected to an encapsulated PCM capsule. From the numerical investigation, an optimum value for which the melting point is at its lowest can be found. Kamkari and Groulx [10] experimentally observed the PCMs' melting characteristics with a rectangular fin with various inclination angles. Results show that it will be more effective if the bottom wall is the heated wall. Xu et al. [11] numerically studied the optimization of horizontal fins to improve the performance of the PCM in a square section. They found that the thermal conductivity of the material of the fin and its thickness does not affect the critical values of the total length. Nakhchi and Esfahani [12] numerically investigate the improvement of the PCM with downward and upward step fins. The results show downward step fins can increase up to 56.3% at 800 s and 65.5% at 3600 s faster than conventional horizontal fins. Many researchers try to find effective ways to enhance the PCMs' performance, and using rectangular fins is one of them.

Although there is a vast pool of literature on the different techniques for enhancing the thermal behavior of PCMs, still many fundamental aspects are scary. To bridge this gap, the present numerical work is formulated to investigate the enhanced thermal behavior of phase change materials (PCMs) utilizing a rectangular fin placed vertically in a rectangular cavity filled with paraffin wax (RT-45). This study mainly focuses on the melting behavior of PCMs without a fin, a single fin, and a double fin attached to a top heated cavity. The volume of the PCM and total surface area of fins were kept constant.

2 Numerical Modeling

2.1 Physical Model

PCM is contained in a rectangular cavity with a horizontal length of $L = 80$ mm and a vertical height of $B = 40$ mm, which is shown in Fig. 1. A constant temperature ($T_w = 343$ K) was maintained on the top wall of the chamber, which is greater than the PCM's melting point (T_m). All other walls of the chamber are adiabatic. For zero fin, L is considered as 78 mm and the B as 40 mm for the sake of making the volume constant for the PCM. Two other physical domains are also studied, one with a single fin and another with a double fin. For the single fin, the fin's position is at

Fig. 1 Schematic diagram of the set-up

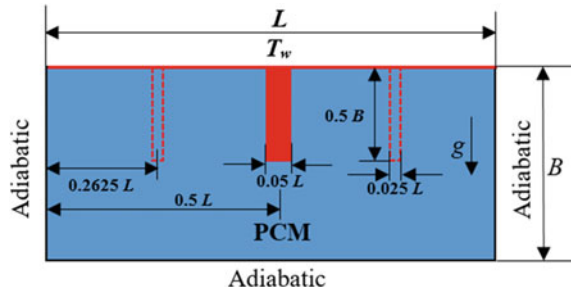


Table 1 Thermo-physical properties of paraffin wax (RT45) [14] and fin material (copper) [13]

Properties	RT-45	Copper
Density (Kg/m ³)	880	8978
Specific heat (J/Kg K)	3028 (solid) 2333 (liquid)	381
Thermal conductivity (W/m K)	0.2415	387.6
Viscosity (Kg/m s)	0.0256	–
Thermal expansion factor (1/K)	1.25×10^{-4}	–
Latent heat (J/kg)	1.397×10^5	–
Solidus temperature (K)	308	–
Liquidus temperature (K)	322	–

the center of the top wall with a 20 mm ($0.5B$) projected length and 4 mm ($0.05L$) of a thickness (t). For the double fin, the fin’s positions are 21 mm ($0.2625L$) from the left wall and 21 mm from the right wall. The length is kept at $0.5B$ mm but the thickness is reduced to $0.025L$. The initial temperature of the whole domain is considered to be 300 K. Paraffin wax (RT-45) is used as a PCM and copper (Cu) is used as a material for the fin as well as the top heated wall. The thermo-physical properties are specified in Table 1.

2.2 Mathematical Description

The governing equations are used to define the heat flow in the PCM and the equations are solved numerically. For the solid–liquid phase change process, the enthalpy–porosity model is used to identify the PCM and fin region. The governing equations [13] are as follows:

$$\text{Continuity equation : } \frac{\partial u}{\partial x} + \frac{\partial v}{\partial y} = 0 \tag{1}$$

Momentum equation:

$$\rho \left(\frac{\partial u}{\partial t} + u \frac{\partial u}{\partial x} + v \frac{\partial u}{\partial y} \right) = \mu \left(\frac{\partial^2 u}{\partial x^2} + \frac{\partial^2 u}{\partial y^2} \right) - \frac{\partial \rho}{\partial x} - \frac{\mu}{K} u + A_{mush} \frac{(1-f)^2}{f^3 + \delta} u \quad (2)$$

$$\begin{aligned} \rho \left(\frac{\partial v}{\partial t} + u \frac{\partial v}{\partial x} + v \frac{\partial v}{\partial y} \right) &= \mu \left(\frac{\partial^2 v}{\partial x^2} + \frac{\partial^2 v}{\partial y^2} \right) - \frac{\partial \rho}{\partial y} - \frac{\mu}{K} v \\ &+ A_{mush} \frac{(1-f)^2}{f^3 + \delta} v + \rho_{ref} g \beta (T - T_{ref}) \end{aligned} \quad (3)$$

Energy equation:

$$\begin{aligned} \left[(1-\varepsilon)(\rho C_p)_{fin} + \varepsilon(\rho C_p)_{PCM} \right] \frac{\partial T}{\partial t} + \varepsilon \rho_{PCM} \Delta h \frac{\partial f}{\partial t} \\ + (\rho C_p)_{pcm} \left(u \frac{\partial T}{\partial x} + v \frac{\partial T}{\partial y} \right) = \lambda_{eff} \left(\frac{\partial^2 T}{\partial x^2} + \frac{\partial^2 T}{\partial y^2} \right) \end{aligned} \quad (4)$$

$$\begin{cases} f = 1 & T > T_m \\ f = \frac{T-T_s}{T_m-T_s} & T_s < T < T_m \\ f = 0 & T < T_s \end{cases} \quad (5)$$

The total enthalpy is defined as the summation of sensible heat capacity and the latent heat of phase change, which is defined as: $H = h + fL$.

The sensible enthalpy is as follows:

$$h = h_{ref} + \int_{T_{ref}}^T C_p dT \quad (6)$$

Here, h_{ref} is the sensible enthalpy of PCM (at T_{ref}).

3 Numerical Method

For the numerical simulation, various computations have been conducted in a 2D geometry using the finite volume-based Ansys FLUENT [13] solver. The size of the PCM cavity is 80×40 mm. The mesh structure is selected as a quadrilateral cell. For the selection of the correct mesh, a mesh independent test is carried out considering five different grid sizes 80×40 , 120×60 , 160×80 , 200×100 , and 240×120 . The grid size 160×80 with 13,041 nodes and 12,800 number of elements is the best choice for the accurate solution and also considering the time required per solution. After the grid independence, the time independence study was done with five different time step sizes, likely 2, 1, 0.5, 0.2, and 0.1 s. Of these, 0.5 s is the

best suitable for getting the optimum value. The PCM density was presumed to be constant (the density at solidus temperature was used) and by using the Boussinesq approximation, the buoyancy effect. For the solution, the SIMPLE scheme is used for pressure–velocity coupling. For the pressure correlation equation, PRESTO is used. Standard initialization is utilized for solution initialization. The optimum value of 0.5 s was used for the time step size (s) and 140 iterations were used per time step.

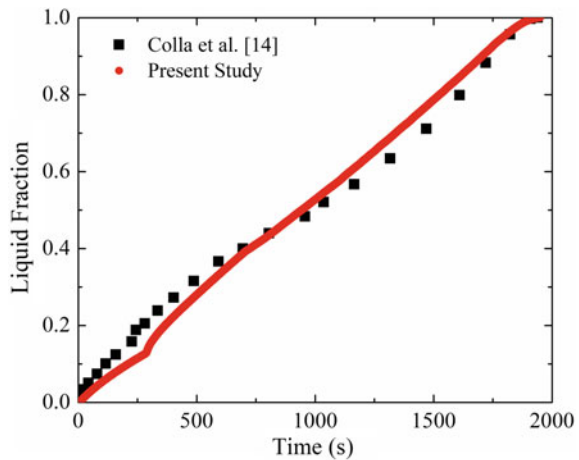
4 Results and Discussion

The purpose of this study is to enhance the performance of the LHSU with a fixed area of the fin and PCM volume. The effect of the fin surface area and number of fins on the melting behavior is analyzed meticulously.

4.1 Validation Study

For the numerical verification of the present solver, the published work of Colla et al. [14] containing pure PCM RT 45 is simulated and the liquid fraction with time is plotted in Fig. 2. It shows a good agreement with the present study. This comparison confirms the accuracy of the present solver.

Fig. 2 Validation of present study with numerical work of Colla et al. [14] for pure RT 45



4.2 Effect of Fin Surface Area

In this work, the initial temperature of the heated wall as well as fins is set at 300 K. Three cases have been studied in this work. One is without a fin, and the other two are with a single fin and a double fin, respectively. In the cases of single and double fins, the surface area of the copper fins is kept constant at 80 mm^2 . For the single fin, the length of the fin is taken as $0.5 B$ and the thickness (t) is $0.05 L$. For the double fin, the length of the fins is taken as $0.5 B$ and the thickness as $0.025 L$. Therefore, for the fixed fin length, the thickness of the fins is varied. From the simulated results, it is observed that the complete PCM melting time required for the no-fin case is 19,445.5 s, which is shown in Fig. 3.

The single fin takes 10,041 s and the double fin takes 8261 s to melt the PCM entirely. As this is a two-dimensional numerical study, the calculated heated wall length for the case without a fin is 78 mm; for the single fin and the double fin including the fin as a heated surface, it is 120 mm and 160 mm, respectively. It can be found that as the heated wall length increases the melting time decreases. The melting time per mm heated wall for the no-fin, single fin, and double fin conditions are 249.30 s/mm, 83.675 s/mm, and 51.63 s/mm respectively when the total volume of the PCM is considered $78 \times 40 \times 1 \text{ mm}^3$ as shown in Fig. 4.

In the present study, the melting for the PCM has been divided into three parts. The first part, where the slope is high (from an angle of 90 to 75° with a positive X-axis), is called the fast melting zone. The second part, where the slope is moderate (from an angle of 75 to 60°), is the moderate melting zone. The last part (where the angles are from 60 to 0°) is called the slow melting zone. In the absence of a fin, these three zones are promptly visible; the fast melting zone is up to 1500 s (up to 0.185 liquid fraction). The moderate melting zone is considered until 8000 s (up to 0.64 liquid fraction), and the slow melting zone is considered until the end of the full melting. In the case of single fins, the fast melting zone is up to liquid fraction 0.44, the rest is a moderate melting zone, and there is no slow melting zone. In the case of a double

Fig. 3 Liquid fraction versus time (s) for without fin, single fin, and double fin

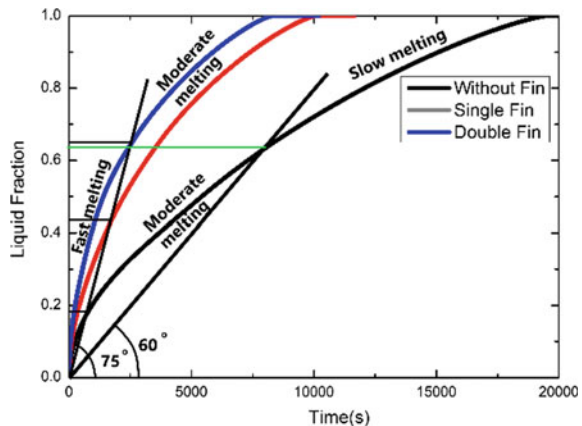
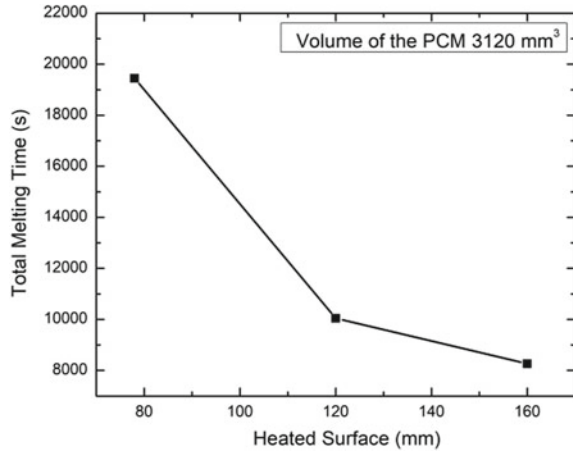


Fig. 4 Comparison of total melting time with heated surface length at constant PCM volume



fin, the fast melting zone is up to liquid fraction 0.64, the rest is a moderate melting zone, and like the single fin, there is no slow melting zone here. With this analysis, we can observe that by increasing the contact surface length of the fin and the PCM, the melting time decreases. When comparing single fin to no-fin, the fast melting zone expands drastically from liquid fraction 0.185–0.44; the moderate melting zone also expands, but there is no slow melting zone. Again, when double fins are compared with single fins, the change is not that significant. Results show that the fast melting zone increases from a liquid fraction of 0.44–0.64 and the moderate melting zone also decreases. For the PCM melting process, two modes of heat transfer are significant: one is conduction, and the other is natural convection. The fast melting zone is the initial zone for PCM melting, this fast melting happened due to conduction. Because the heated wall was in direct contact with the PCM, conduction took precedence over natural convection. For moderate melting zones, the heated wall is not that close to the wall, so natural convection dominates over conduction. As conduction is the fastest process for heat transfer, the moderate melting zone’s slope is not as sharp as before, and a decreasing curve appears. For the slow melting zone, natural convection highly dominates over the conduction, as the heated wall is far from this zone. This is the slowest zone of the entire melting zone. As the RT-45 is a phase change material, it changes from solid to liquid and a reverse flow of heat occurs as shown in Fig. 5.

The above facts are due to the density difference; when solid PCM gets heated and converted to liquid, the heated liquid has less density than the liquid PCM, so the less dense liquid tries to go above the surface and push the cold liquid PCM downwards. Hence, a circular heat flow loop has been created throughout the rectangular cavity. For this reason, when the cavity height is increased, the rate of liquid fraction decreases. If the contact surface area of the heated wall and the fin with the PCM increases, the liquid fraction rate also increases. When the heated wall length increased from 78 mm (in the case of no-fin) to 120 mm (in the case of a single fin), a 48.36% reduction in total melting time can be observed. When the heated wall length

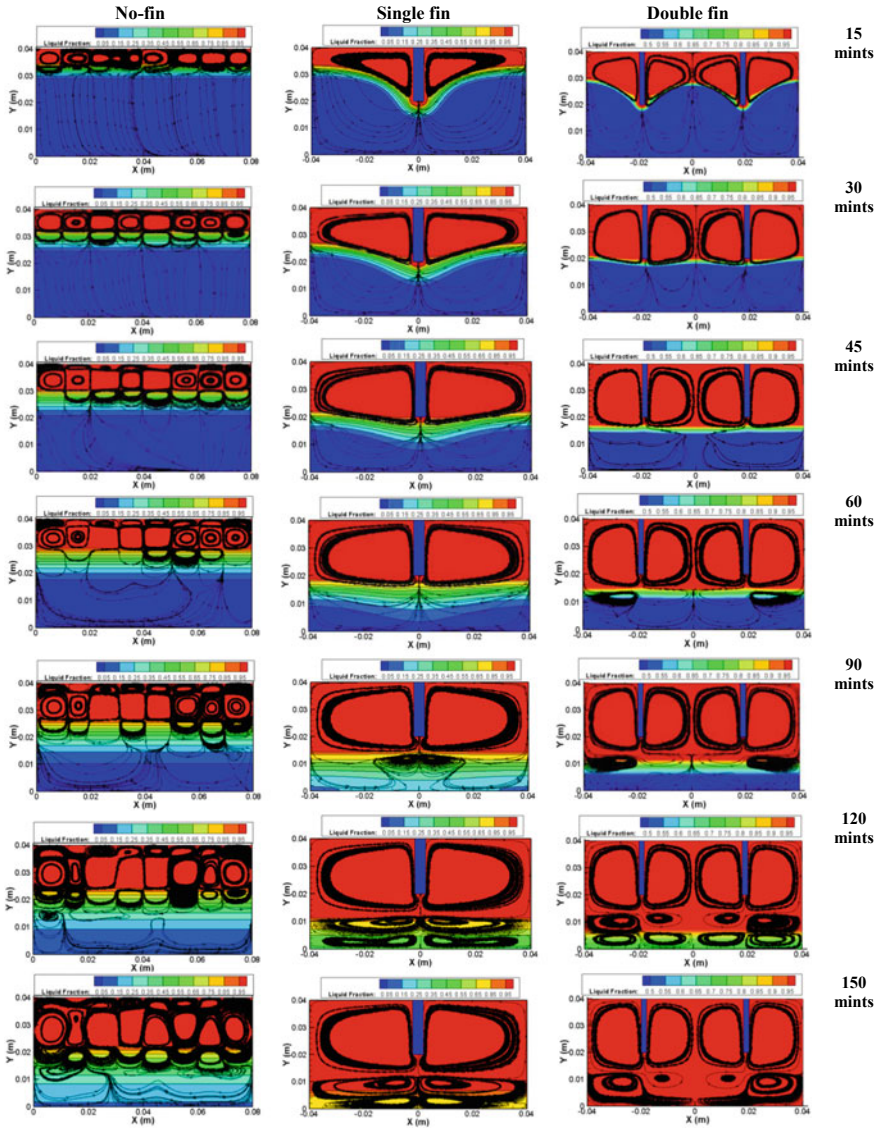


Fig. 5 Liquid fraction contour with stream trace lines at the various time frames with no-fin, single fin, and double fins

increases from 120 to 160 mm (in the case of double fins), a reduction of 17.73% of the total melting time can be seen.

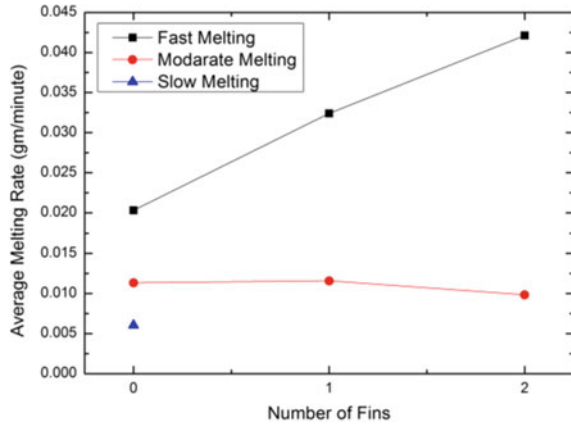
The three zones and the stream trace line contours can be vividly observed in Fig. 5 at different time intervals. During the initial stage after 15 min, heat transfer is conduction dominated, and it is observed that many circular circulation loops

are formed near the heated wall. The extreme left loop shows an anti-clockwise movement, and very next to it, a clockwise rotation can be seen, and this continues up to the extreme right. In the case of a 30-min time frame, the second set of circulation is generated. The heat is moved forward by this set of second loops. As the extreme left of the first set of loops was anti-clockwise, the second set of extreme left loops is clockwise in rotation, the very next is anti-clockwise, and so on. In the 45 min time frame, the first set of loops enlarged and the natural convection dominated. In this time frame, it can be seen that the third set of very small circulation loops has been generated at the contact surface of the heated wall. For a 90 min time frame, all three sets of loops are slightly enlarged, and push each loop toward the bottom which helps to transfer the heat downward. In the case of 120 min, the first and third sets of loops slightly enlarged, but the second set of loops enlarged more than the previous, and the fourth set of loops just appeared at the bottom of the second loop. At 150 min, it can be seen that some of the first set of loops try to fuse with the second set of loops, which tries to enhance the heat transfer by natural convection. The fourth set of loops can be seen to enlarge their loop size. Thus, there is a continuous change in the circular shape and its size.

4.3 Effect of Number of Fins

The effect of the number of fins is also analyzed. The volume of PCM remains constant throughout the case study, and the fin surface area does too. Figure 5 depicts the melting contour with stream trace lines for the comparison of no-fin, single fin, and double fin. It is observed that two circulation loops have been generated in the case of a single fin at 15 min. A clockwise loop on the right side of the fin and an anti-clockwise loop on the left. It is clear that in 15 min, there has been more melting than when there is no-fin. At 30 min, the loop got enlarged, and the melting front at the center remained constant, while the melting front on the side rose, giving the loop the appearance of an inverted hill. Up to 60 min of the same phenomena can be witnessed. After then, there is a gradual melting process. As two oppositely oriented second sets of the loop are produced at the bottom of the tip of the fin at 90 min, it is seen that the melting front of the middle of the tip does not expand significantly, however, the melting front of the side increases more than the middle front. These two loops actually push the heat upward. The third set of the loop is generated 120 min below the second set of the loop, and the second set of the loop enlarges. At 150 min, the first set of loop sizes remains the same, the second set of loop sizes increases, and it pushes down the third set of loop sizes so that the third set of loop sizes decreases. In the case of a double fin, four loops have been generated. The adjacent stream trace loop of the left fin is anti-clockwise, and the right is clockwise. The adjacent stream trace loop of the right fin is anti-clockwise, and the right is clockwise. These loops expand up to 45 min. At 60 min, the second set of loops has begun to form at the top corner of the two fins. It can be seen that these loops expand up to 90 min. The third set of loops has been generated at the bottom of the second set of loops, which can

Fig. 6 Variation of average melting rate with number of fins of different mode of melting



be seen in Fig. 5 at 120 min. The first set of loops does not enlarge since the second set of loops develops. At 150 min, the whole PCM liquefied, and the corner loop of the second set of loops was merged with the third set of loops. One other significant thing is that the mushy zone interface for zero fins is slightly larger than a single fin and way larger than a double fin. As the contact surface area is smaller for the zero-fin case, the mushy zone interface is higher. For the single fin, the contact surface area is increased and the mushy zone decreases, and for the double fin, the contact surface area increases more than the other two, so the mushy zone interface is small. When the mushy zone is away from the contact surface, it gradually increases. Therefore, as the contact surface area increases, the mushy zone decreases, i.e., heat transfer is pretty high. The fast melting zone increases significantly with the increase of the number of fins, though the moderate melting zone does not change that much and it slightly decreases with the increase of the number of the fin as shown in Fig. 6. The slow melting zone is only present for the zero fin condition.

5 Conclusions

This work is attempting to investigate the enhanced heat transfer performance of a phase change materials (PCMs) utilizing rectangular fin placed vertically in a rectangular cavity filled with paraffin wax (RT-45). The PCM volume and surface area of the fin remain constant throughout the cases. Numerical results are obtained from a rectangular geometry with a top heated wall at 343 K and all the other three surfaces being insulated walls. The effect of heated contact surface area and the number of fins have been studied. The volume of the PCM is considered 3120 mm³ in all cases. The following conclusions were derived from this present work:

- When the heated surface is increased from 78 to 120 mm, the melting time reduces by 48.36 percent. Further, the increase in heated surface wall length increases from 120 to 160 mm, and the melting time reduces by 17.73%.
- The melting profile for the no-fin can be divided into three zones: a fast melting zone, a moderate melting zone, and a slow melting zone. However, when the single fin or double fin is added, the fast melting zone increases, and the slow melting zone is omitted. This is due to the increase in heated contact surface area. As the contact surface area increases, the fast melting zone increases due to increased heat transfer due to conduction between the heated surface and corresponding PCM.
- The average melting speed for the fast melting increases as the number of fins or heated surface area increases. For moderate melting, the average melting speed does not change significantly (it slightly decreases).
- As the heated surface length increases, the total melting time decreases. However, the rate of reduction in the total melting time decreases with the increase in heated surfaces.
- With the increase in contact heated surface, the area mushy zone decreases and the mushy zone area increases when is away from the contact heated surface. Results show as the contact heated surface increases; heat transfer increases thus mushy zone decreases.
- The average melting speed depends on the number of sets of circulation loops. As the number of sets of loops increases, the average melting rate decreases. When the heated surface area increases, the number of sets of circulation loops decreases.

Acknowledgements The first author acknowledges the financial support from the SERB-SRG project fund of the Government of India.

Nomenclature

u, v	X and y velocity components [m/s]
x, y	Cartesian coordinates [m]
T	Time [s]
A_{mush}	Mushy zone constant [$\text{kg m}^{-3} \text{s}$]
F	Liquid fraction
C_p	Specific heat [$\text{J Kg}^{-1} \text{K}^{-1}$]
Δh	Latent heat of fusion [K J Kg^{-1}]

References

1. Rieger H, Projahn U, Bareiss M, Beer H (1983) Heat transfer during melting inside a horizontal tube. *J Heat Transfer* 105(2):226–234
2. Khademi A, Shank K, Mehrjardi SAA, Tiari S, Sorrentino G, Said Z, Chamkha AJ, Ushak S (2022) A brief review on different hybrid methods of enhancement within latent heat storage systems. *J Energy Storage* 54:105362
3. Elgafy A, Lafdi K (2005) Effect of carbon nanofiber additives on thermal behavior of phase change materials. *Carbon* 43:3067–3074
4. Akhmetov B, Navarro ME, Seitov A, Kaltayev A, Bakenov Z, Ding Y (2019) Numerical study of integrated latent heat thermal energy storage devices using nanoparticle-enhanced phase change materials. *Sol Energy* 194:724–741
5. Abdulateef AM, Jaszczur M, Hassan Q, Anish R, Niyas H, Sopian K, Abdulateef J (2021) Enhancing the melting of phase change material using a fins–nanoparticle combination in a triplex tube heat exchanger. *J Energy Storage* 35:102227
6. Yu J, Yu ZC, Tang CL, Chen X, Song QF, Kong L (2016) Preparation and characterization of composite phase change materials containing nanoparticles. *Kemija U Industriji Casopis Kemi'cara I Kemijskih Inženjera Hrvatske* 65:605–612
7. Kim HG, Kim YS, Kwac LK, Shin HJ, Lee SO, Lee US, Shin HK (2019) Latent heat storage and thermal efficacy of carboxymethyl cellulose carbon foams containing Ag Al, carbon nanotubes, and graphene in a phase change material. *Nanomaterials* 9:158
8. Senobar H, Aramesh M, Shabani B (2020) Nanoparticles and metal foams for heat transfer enhancement of phase change materials: a comparative experimental study. *J Energy Storage* 32:101911
9. Athawale V, Bhattacharya A, Rath P (2021) Prediction of melting characteristics of encapsulated phase change material energy storage systems. *Int J Heat Mass Transf* 181:121872
10. Kamkari B, Groulx D (2018) Experimental investigation of melting behaviour of phase change material in finned rectangular enclosures under different inclination angles. *Exp Thermal Fluid Sci* 97:94–108
11. Xu Y, Zheng ZJ, Yang C, Cai X (2021) Intelligent optimization of horizontal fins to improve the melting performance of phase change materials in a square cavity with isothermal vertical wall. *J Energy Storage* 44:103334
12. Nakhchi ME, Esfahani JA (2020) Improving the melting performance of PCM thermal energy storage with novel stepped fins. *J Energy Storage* 30:101424
13. ANSYS Inc (2015) ANSYS fluent theory guide 12.0
14. Colla L, Ercole D, Fedele L, Mancin S, Manca O, Bobbo S (2017) Nano-phase change materials for electronics cooling applications. *ASME J Heat Transf* 139:052406–052411

Determining the Best Passive Heat Transfer Enhancement Technique in Circular Pipe Heat Exchangers with the MCDM Technique



Soumith Voddepalli, Sujit Nath, and Agnimitra Biswas

1 Introduction

Heat transfer systems or heat exchangers form a core component of almost every industry, making them one of the most sought-after in research and development. Heat exchangers have applications all over the Energy Sector, Manufacturing, Agriculture, Electronics, Refrigeration, Air Conditioning, Transportation, Food, Pharmaceuticals, etc. [1] With the increasing population, depleting energy resources, and increasing technological needs, there is an imminent need for more efficient heat exchangers to reduce energy usage. Heat transfer enhancement techniques increase the thermal performance of heat exchangers.

Heat transfer enhancement in these heat exchangers is usually done by either modifying geometrical parameters or altering flow parameters. It can be done passively or actively. In passive heat transfer enhancement, no external energy is used to improve heat transfer, whereas in active heat transfer enhancement, external energy is used to improve heat transfer.

Active techniques [2] include electro-hydrodynamics, jet impingement, mechanical inserts, fluid vibration, etc. The electrohydrodynamic (EHD) technique involves coupling an electric field with the fluid domain, creating fluid displacement, and increasing heat transfer. In jet impingement, fluid projection at high velocity creates a thinner boundary layer improving the heat transfer coefficient. Mechanical aids such as rotating heat exchangers create swirl flow to improve heat transfer. Surface vibration enhances natural and forced convection and reduces cavitation to increase heat transfer. The vibration method controls fluid motion near the wall surface to improve heat transfer.

Passive methods [3] don't use any external power for heat transfer augmentation. They improve heat transfer by minimizing thermal resistance, and they do that by

S. Voddepalli (✉) · S. Nath · A. Biswas
Department of Mechanical Engineering, NIT Silchar, Silchar 788010, India
e-mail: voddepalli_rs@mech.nits.ac.in

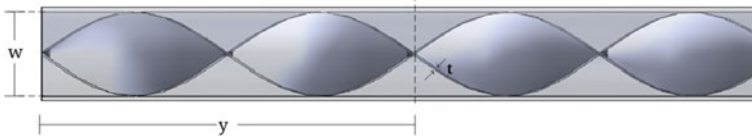


Fig. 1 Twisted tape

modifying the existing fluid flow pattern using devices, additives, and surface and geometrical changes. Passive techniques include increasing the roughness of the surface, treating the surface, increasing the surface area for heat transfer, causing swirl flow inside tubes, using twisted tubes, using additives like nanoparticles to increase conduction in fluid, etc. The downside of passive methods is that the pressure drop also increases, which creates limitations in using passive methods.

There are also compound methods in which two or more active or passive techniques are used together to increase thermal performance further.

Active methods are expensive and complicated for practical applications and supplying power. Active methods showed less potential compared to passive techniques. Passive techniques are used widely for heat transfer augmentation for ease of application and low cost. Circular pipe heat exchangers use either active/passive techniques for heat transfer enhancement or improving thermal performance.

Twisted tapes, Coil wire, Conical inserts, Nozzle turbulators, Ring turbulators, wavy tapes, Louvered strips, Baffles, Swirl generators, Grooved and ribbed pipes, nanofluids, etc. are a few passive heat transfer techniques [3].

Twisted tapes are a highly used and most researched passive heat transfer enhancement technique. Twisted tapes are flat pieces of solid material twisted axially. They are inserted in the flow to enhance heat transfer. They are used widely in heat exchangers because they increase heat transfer with a low-pressure loss penalty compared to other methods. Twisted tapes are easily manufacturable, low cost, and easily employable in thermal systems. Twisted tapes are modified to increase their thermal performance further.

Selecting the best heat transfer enhancement technique for circular pipe heat exchangers depending on its requirement, is vital. Although much research is done on finding new and improved passive heat transfer techniques, no effort is made to find the best passive technique to cater to any particular application. MCDM (Multi-Criteria Decision Making) can help make decisions where several conflicting criteria are considered. MCDM method helps to choose the best alternatives, i.e., passive heat transfer technique, with several criterion, the best one can be obtained by analyzing the different scopes, and weights for the criteria, and optimum ones were chosen using any multi-criteria decision-making techniques.

2 Literature Review and Objective

Twisted tape generally induces swirl flow which causes heat transfer enhancement. The twisted tape increases heat transfer for the following reasons. Twisted tape increases flow velocity by creating partitions and restricting the flow by its geometry. Twisted tape reduces the hydraulic diameter, increasing the heat transfer coefficient. The use of twisted tape has a longer flow path created by the spiral flow motion. The twisted tape creates secondary fluid motion, mixing the fluid and increasing heat transfer. The twisted tape can also act as the fin, increasing the surface area for heat transfer [3].

Even though twisted tape improves heat transfer, pressure loss is comparatively higher than the plain tube. The twisted tapes' thermal performance can still be further enhanced by modifying the geometrical parameters of twisted tape. Twisted tapes are perforated, axially rotated, attached with baffles/ribs, dimpled, cut centrally or peripherally, winged centrally or peripherally, corrugated, serrated, trimmed, etc., to improve thermal performance.

Short-length twisted tapes [4] occupy only part of the tube. Swirl flow is created at the start of the pipe and deteriorates along the tube. Its thermal performance is less than that of twisted tape.

Thianpong et al. [5] proposed twisted perforated tape to improve the thermal performance of the classic twisted tape. Heat transfer enhancement increases with the decrease in the pitch ratio of perforations as the turbulent intensity decreases with an increase in pitch ratio. The friction factor also increases with a decreased pitch ratio due to less fluid flow mixing when the space between perforation decreases.

Wongcharee et al. [6] proposed an alternate axis twisted tape, rotated axially along the tube for heat transfer enhancement. Nusselt number and friction factor are higher in alternate axis twisted tape compared to classic twisted tape. Nusselt number increases with the increase in twist angle (θ).

Eiamsa-ard and Promvonge [7] performed experimental analysis on Screwtape/Helical tape with and without core rod. The thermal performance factor is higher in Screwtape without a core rod, making the core rod obsolete.

Eiamsa-ard et al. [8] experimented on helically twisted tapes and compared them to conventional helical tapes. Nusselt number and friction factor increase as the helical pitch ratio of helically twisted tape.

Tapered twisted tapes [9] have gradually reduced width along with the flow. Nusselt number and friction factor decrease with increased taper angle (θ).

Kurhade et al. [10] performed experiments on twisted corrugated tape to study the effect of varying twisted ratios compared to the plain tube. They found that the Nusselt number and friction factor are high at lower twist ratios due to higher swirl intensity and longer flow length.

Eiamsa-ard et al. [11] performed studies on the tube with twin twisted tapes with co-swirl and counter-swirl flow arrangements compared to single twisted tape. Nusselt number and friction factor are higher in the counter-swirl flow arrangement than in the co-swirl flow arrangement. The thermal performance factor is increased

up to 25% in the counter-swirl arrangement than in the co-swirl arrangement, which can be attributed to a higher increase in the Nusselt number.

Chokphoemphun et al. [12] performed studies on two single, dual, triple, and four quadruple twisted tape arrangements in co-swirl and counter-swirl arrangements. It can be found that the counter-swirl arrangement has better thermal performance than the co-swirl arrangement.

Eiamsa-ard and Promvonge [13] performed experimental analysis on serrated twisted tapes. The thermal performance factor is higher in serrated twisted tape than in common twisted tape.

Studies have been done on rectangular [14], square [15], trapezoidal [16], U-shaped [17], and V-shaped/triangular cuts [18] on the periphery of twisted tape to improve the thermal performance of the twisted tape. The thermal performance factor of all the peripheral cut twisted tape is higher than common twisted tape.

Bhattacharyya et al. [19] performed numerical analysis on center-trimmed twisted tape with four different width ratios. It is found that thermal performance in the center-trimmed twisted tape is higher than typical twisted tape.

Saysroy and Eiamsa-ard [20] performed numerical analysis on central square-cut twisted tape with five different perforation width ratios and three perforation length ratios. Nusselt number and friction factor increase with decreasing width ratio and length ratio, but the thermal performance factor is highest at the largest width ratio and smallest length ratio.

Oni et al. [21] performed numerical analysis on elliptical, circular, and triangular perforations of the same area at the center of the twisted tape. Nusselt number and friction factor are higher in triangular cut twisted tape followed by circular and elliptical.

Chang et al. [22] performed experimental analysis on broken, twisted tapes. Nusselt number and friction factor increase with a decrease in the twist ratio.

Eiamsa-ard et al. [23] performed experimental analysis on center delta wings with three angles of attack. Nusselt number and friction factor increase with the angle of attack, and the thermal performance factor is also highest in the largest angle of attack.

Zheng et al. [24] performed numerical analysis on twisted tape with dimples on one side and protrusions on the other. They observed that the protruded side has less thermal performance than the dimpled side.

Murugesan et al. [25] performed an experimental analysis on twisted tape with wire nails and compared it to classic twisted tape. Twisted tape with wire nails has a higher Nusselt number, friction factor, and thermal performance than classic twisted tape.

Hayat et al. [26] performed numerical analysis on trapezoidal ribs on twisted tape with three slant angles. Nusselt number and friction factor increase with the slant angle, but the thermal performance factor is higher in the smallest slant angle.

Although many works have been done on modified twisted tapes, there is no guideline for selecting better insert designs based on different technical and economic criteria. The present study selects the best twisted tape based on energy and economic parameters.

3 Materials and Methods

3.1 Correlation Analysis

In research, correlation analysis is a statistical technique for calculating and measuring the strength of the linear relationship between two variables.

The change in one variable caused by a change in the other is calculated using correlation analysis. A high correlation indicates a strong connection between the two variables, whereas a low correlation indicates a weak connection.

Pearson Correlation Analysis is the ratio between the covariance of two variables and the product of their standard deviations; the correlation coefficient always lies between -1 and 1 .

$$r = \frac{\sum (x_i - \bar{x}) - (y_i - \bar{y})}{\sqrt{\sum (x_i - \bar{x})^2 (y_i - \bar{y})^2}} \quad (1)$$

r = Pearson Correlation coefficient

x_i = values of the x-variable in a sample

\bar{x} = mean of the values in x-variable

y_i = values of the y-variable in a sample

\bar{y} = mean of the values in y-variable

3.2 Anova

An ANOVA test can be used to determine whether an experiment's results are significant.

In one-way ANOVA, two independent groups are compared using the F-distribution. The test's null hypothesis is that the two means are the same. As a result, a significant result indicates that the two means are not equal.

In ANOVA, the Sum of Square (SS), degrees of freedom (df), Mean Square (MS), F-value, p-value, and F-critical are calculated.

Suppose F-statistic is greater than the F-critical value. In that case, the test is significant, the p-value should be less than α (0.05), the result is statistically important, and the null hypothesis is generally rejected in favor of the alternative hypothesis.

The calculations of the hypothesis test are shown,

$$SS_{\text{betweengroups}} = \sum_j \frac{(\sum_i y_{ij})^2}{I_j} - \frac{\left(\left(\sum_j \sum_i y_{ij} \right)^2 \right)}{I} \tag{2}$$

$$SS_{\text{withingroup}} = \sum_j \sum_i y_{ij}^2 - \sum_j \frac{(\sum_i y_{ij})^2}{I_j} \tag{3}$$

$$DF_{\text{betweengroups}} = J - 1 \tag{4}$$

$$DF_{\text{withingroup}} = I - J \tag{5}$$

$$MS_{\text{betweengroups}} = \frac{SS_{\text{betweengroups}}}{DF_{\text{betweengroups}}} \tag{6}$$

$$MS_{\text{withingroup}} = \frac{SS_{\text{withingroup}}}{DF_{\text{withingroup}}} \tag{7}$$

$$F = \frac{MS_{\text{betweengroups}}}{MS_{\text{withingroup}}} \tag{8}$$

3.3 Multiple-criteria Decision-Making (MCDM)

The Technique for Order of Preference by Similarity to Ideal Solution (TOPSIS) is a prevalent MCDM technique used extensively for making decisions by researchers because of its applicability in various problems. The TOPSIS method’s core point is to evaluate the choices based on the positive and negative ideal solutions. In TOPSIS, an alternative has the smallest distance to the positive ideal solution and the largest distance to the negative ideal solution [27].

The steps of the TOPSIS are as follows,

Step 1: Determine ‘m’ alternatives and ‘n’ criteria.

Step 2: Find the weight (w) of every criterion considering

$$\sum_{j=1}^n w_j = 1 \tag{9}$$

Step 3: Generating decision matrix (D).

Step 4: Normalizing the decision matrix (R)

$$R = (r_{i,j})_{m \times n} = \sqrt{\sum_{j=1}^n \frac{x_{i,j}}{x_{i,j}^2}}, i = 1, 2, \dots, m; ; j = 1, 2, \dots, n \quad (10)$$

Step 5: Generating a weighted normalized decision matrix (V)

$$V = (v_{i,j})_{m \times n} = w_j r_{i,j}, i = 1, 2, \dots, m; j = 1, 2, \dots, n \quad (11)$$

Step 6: Find ideal solutions for the positive (A +) and the negative (A -).

$$A^+ = (v_1^+, v_2^+, \dots, v_n^+) = \left(\left(\max_i v_{i,j} \mid j \in I \right), \left(\max_i v_{i,j} \mid j \in J \right) \right) \quad (12)$$

$$A^- = (v_1^-, v_2^-, \dots, v_n^-) = \left(\left(\max_i v_{i,j} \mid j \in I \right), \left(\max_i v_{i,j} \mid j \in J \right) \right) \quad (13)$$

where $i = 1, 2, \dots, m, j = 1, 2, \dots, n$

Step 7: Using the Euclidian distance, determine the separation measures for each option.

The Positive ideal distance is

$$d^+ = \sqrt{\sum_{j=1}^n (v_{i,j} - v_j^+)^2}, i = 1, 2, \dots, n \quad (14)$$

The Negative ideal distance is

$$d^- = \sqrt{\sum_{j=1}^n (v_{i,j} - v_j^-)^2}, i = 1, 2, \dots, m \quad (15)$$

Step 8: Calculate the relative closeness (C)

$$C_i = \frac{d_i^-}{d_i^+ + d_i^-}, i = 1, 2, \dots, m, C_i = [0, 1] \quad (16)$$

Step 9: Sort the choices accordingly and choose each option based on the C_i value. The best option is the one with the highest C_i score.

3.4 Sensitivity Analysis

Sensitivity analysis determines how target variables are affected based on changes in other variables known as input variables. Sensitivity analysis is performed to determine how rankings change with changing criteria weights.

4 Results and Discussion

To rank, the different modified twisted tapes, surface-volume ratio, Reynolds number, Nusselt number, friction factor, and cost per thermal performance factor are used to judge against each other.

Twenty-one different twisted tapes are taken from available literature to rank among each other. Geometrical configuration and flow configuration for each insert is taken at optimized configuration or maximum thermal performance factor. i.e., Surface to volume ratio, Reynolds number, Nusselt number, and friction factor of the twisted tapes are considered at highest thermal performance.

Before conducting MCDM analysis, a correlation test and ANOVA are performed to check the collinearity among each other and to eliminate any non-contributing criteria, respectively. Twenty-one modified Twisted Tapes (TT) are taken in the present study to rank among each other (Table 1).

4.1 Correlation Analysis

Pearson correlation Analysis was conducted to measure the statistical relationship, or association, between two continuous variables (Table 2).

This table shows that the Reynolds and Nusselt numbers are highly correlated (0.41) compared to others.

4.2 Anova

ANOVA follows correlation analysis to find the variance among and within the groups. A one-way ANOVA will tell you if at least two groups are different from each other (Table 3).

As F -statistic is greater than the F -critical value, the test is significant, and the p -value is less than α (0.05). So, there is no need to eliminate any criteria for MCDM analysis.

4.3 Topsis

We will perform TOPSIS, in which the Nusselt number, Reynolds number, and Surface to Volume ratio should be maximum, and the Friction factor and Cost should be minimum for maximum heat transfer enhancement. So, to maximize every criterion, friction factor, and cost were considered inverse for the calculation to be easier. Each criterion is given equal weightage (Table 4).

Table 1 Modified twisted tapes with criteria

		S/V	Re	Nu	f	Cost/TPF
1	Tapered TT	2.39	6000	26	0.086	0.691
2	Alternate axis perforated TT	3.13	3000	92	0.046	0.095
3	Helically twisted TT	8.33	6000	91	0.12	0.913
4	Peripheral rectangular cut TT	1.20	20,000	301	0.06	0.597
5	Peripheral triangular cut TT	1.86	3000	122	0.29	0.433
6	Serrated TT	2.92	4000	71	0.18	1.906
7	Peripheral U cut TT	1.90	3000	121	0.231	0.437
8	Peripheral square cut TT	1.90	3000	115	0.22	0.434
9	Peripheral trapezoidal cut TT	1.59	6000	55	0.03	1.209
10	Central square cut TT	4.61	7000	176	0.125	0.085
11	Crosscut TT	3.47	5000	90	0.1	0.076
12	Central triangular cut TT	2.60	5000	94	0.18	0.264
13	Center trimmed TT	2.67	5000	31	0.2	0.184
14	Peripheral trapezoidal wing TT	2.92	5000	245	0.325	0.343
15	Twin delta wing TT	3.13	5000	200	0.32	0.252
16	Quadruple co & counter swirls TT	4.55	5000	125	0.75	0.039
17	Dimpled TT	2.28	5000	250	0.11	0.828
18	Corrugated TT	2.15	5000	40	0.036	3.449
19	Louvered TT	2.95	5000	400	0.375	0.170
20	Nailed TT	2.53	3000	45	0.28	1.024
21	Broken TT	4.03	5000	100	0.2	0.515

Table 2 Pearson Correlation Analysis

	S/V	Re	Nu	f	Cost/TPF
S/V	1				
Re	-0.3	1			
Nu	0.14	0.41	1		
f	0.30	-0.24	0.24	1	
Cost/TPF	-0.33	-0.01	-0.33	-0.37	1

Table 3 ANOVA analysis

Source of variation	SS	Df	MS	F stat	P-value	F crit
Between groups	4.89 E + 08	4	1.22 E + 08	49.04	9 E-23	2.462
Within groups	2.49 E + 08	100	2,493,317			
Total	7.38 E + 08	104				

Table 4 Ranking by TOPSIS

	Ranking
Tapered TT	13
Alternate axis perforated TT	5
Helically twisted TT	12
<i>Peripheral rectangular cut TT</i>	1
Peripheral triangular cut	19
Serrated TT	16
Peripheral U cut TT	18
Peripheral square cut TT	20
Peripheral trapezoidal cut TT	2
Central square cut	6
Crosscut TT	10
Central triangular cut TT	14
Center trimmed TT	15
Peripheral trapezoidal wing TT	9
Twin delta winged TT	11
Quadruple co & counter swirl TT	8
Dimpled TT	7
Corrugated	4
Louvered	3
Nailed	21
Broken twisted tape	17

Rankings showed that peripheral rectangular cut twisted tape is the most preferable of all modified twisted tapes.

4.4 Sensitivity Analysis

Sensitivity analysis is performed after MCDM to determine how rankings change with changing criteria weights (Table 5).

Alternative four rankings didn't change with the varying weights, making it preferable in different situations where some criteria are given more weightage than others.

Sensitive analysis shows that peripheral rectangular cut twisted tapes are preferable to others even when the Nusselt number is given more weightage than friction factor, surface to volume ratio, Reynolds number, Cost/TPF, and vice versa.

Table 5 Sensitivity analysis

(0.3, 0.3, 0.15, 0.15, 0.1)	(0.25,0.25, 0.2, 0.2, 0.1)	(0.2, 0.2, 0.2, 0.2, 0.2)	(0.15, 0.15, 0.25, 0.25, 0.2)	(0.1, 0.1, 0.3, 0.3, 0.2)
16	15	15	15	14
6	5	5	5	4
12	12	12	12	12
1	1	1	1	1
20	20	20	19	19
15	16	17	20	20
18	18	18	17	16
19	19	19	18	18
7	6	7	7	5
2	2	3	3	6
5	7	6	6	7
13	13	13	13	13
14	14	14	14	15
8	10	10	10	10
9	11	11	11	11
3	4	2	2	3
10	9	9	9	9
11	8	8	8	8
4	3	4	4	2
21	21	21	21	21
17	17	16	16	17

5 Conclusions

An analytical study has been done on twenty-one twisted tape inserts to find the best passive heat transfer enhancement technique. MCDM analysis is performed to find the preferable twisted tape design among them.

Pearson Correlation Analysis showed that the Reynolds and Nusselt numbers are highly correlated at a factor of 0.41. ANOVA analysis showed that no two criteria need to be eliminated as F-statistic is greater than the F-critical value and the p-value is less than α (0.05). Peripheral rectangular cut twisted tape with S/A of 1.2, Nusselt number of 301, a friction factor of 0.06, Reynolds number of 0.06, and cost/TPF of 0.597 was the top-ranked alternative after performing TOPSIS. Sensitivity analysis also showed that Peripheral rectangular cut twisted tape was ranked top with varying criteria weights.

Present analysis on modified Twisted tape inserts can be expanded to rank different passive techniques to find the best possible technique for an application by using required criteria and weights based on its requirement.

Acknowledgements The authors would like to thank the Mechanical Department of NIT Silchar for providing the required infrastructure to conduct research.

Nomenclature

Nu	Nusselt number
F	Friction factor
TPF	Thermal performance factor
Re	Reynolds number
S/V	Surface to volume ratio 1/m
$Cost/TPF$	Cost per thermal performance factor Rs

References

1. Varun MO, Garg H, Nautiyal S, Khurana N, Shukla MK (2016) Heat transfer augmentation using twisted tape inserts: a review. *Renew Sustain Energy Rev* 63:193–225
2. Sheikholeslami M, Gorji-Bandpy M, Ganji DD (2015) Review of heat transfer enhancement methods: focus on passive methods using swirl flow devices. *Renew Sustain Energy Rev* 49:444–469
3. Liu S, Sakr M (2013) A comprehensive review on passive heat transfer enhancements in pipe exchangers. *Renew Sustain Energy Rev* 19:64–81
4. Eiamsa-ard S, Thianpong C, Eiamsa-ard P, Promvonge P (2009) Convective heat transfer in a circular tube with short-length twisted tape insert. *Int Commun Heat Mass Transf* 36(4):365–371

5. Thianpong C, Eiamsa-Ard P, Eiamsa-Ard S (2012) Heat transfer and thermal performance characteristics of heat exchanger tube fitted with perforated twisted-tapes. *Heat Mass Transf und Stoffuebertragung* 48(6):881–892
6. Wongcharee K, Eiamsa-ard S (2011) Enhancement of heat transfer using CuO/water nanofluid and twisted tape with alternate axis. *Int Commun Heat Mass Transf* 38(6):742–748
7. Eiamsa-ard S, Promvong P (2007) Heat transfer characteristics in a tube fitted with helical screw-tape with/without core-rod inserts. *Int Commun Heat Mass Transf* 34(2):176–185
8. Eiamsa-ard S, Yongsiri K, Nanan K, Thianpong C (2012) Heat transfer augmentation by helically twisted tapes as swirl and turbulence promoters. *Chem Eng Process Process Intensif* 60:42–48
9. Piriyarungrod N, Eiamsa-ard S, Thianpong C, Pimsarn M, Nanan K (2015) Heat transfer enhancement by tapered twisted tape inserts. *Chem Eng Process Process Intensif* 96:62–71
10. Kurhade DBNS, Dange MM (2015) Effect of wavy (Corrugated) twisted tape inserts on heat transfer in a double pipe heat exchanger. *Int J Innov Eng Res Technol* 2(1)
11. Eiamsa-ard S, Thianpong C, Eiamsa-ard P (2010) Turbulent heat transfer enhancement by counter/co-swirling flow in a tube fitted with twin twisted tapes. *Exp Therm Fluid Sci* 34(1):53–62
12. Chokphoemphun S, Pimsarn M, Thianpong C, Promvong P (2015) Thermal performance of tubular heat exchanger with multiple twisted-tape inserts. *Chinese J Chem Eng* 23(5):755–762
13. Eiamsa-Ard S, Promvong P (2010) Thermal characteristics in round tube fitted with serrated twisted tape. *Appl Therm Eng* 30(13):1673–1682
14. Salam B, Biswas S, Saha S, Bhuiya MMK (2013) Heat transfer enhancement in a tube using rectangular-cut twisted tape insert. *Procedia Eng* 56:96–103
15. Murugesan P, Mayilsamy K, Suresh S (2010) Turbulent heat transfer and pressure drop in tube fitted with square-cut twisted tape. *J Chem Eng* 18(4):609–617
16. Murali G, Nagendra B, Jaya J (2020) CFD analysis on heat transfer and pressure drop characteristics of turbulent flow in a tube fitted with trapezoidal-cut twisted tape insert using Fe₃O₄ nano fluid. *Mater Today Proc* 21:313–319
17. Murugesan P, Mayilsamy K, Suresh S (2011) Heat transfer and friction factor in a tube equipped with u-cut twisted tape insert. *Jordan J Mech Ind Eng* 5(6)
18. Murugesan P, Mayilsamy K, Suresh S, Srinivasan PSS (2011) Heat transfer and pressure drop characteristics in a circular tube fitted with and without V-cut twisted tape insert. *Int Commun Heat Mass Transf* 38(3):329–334
19. Bhattacharyya S, Chattopadhyay H, Bandyopadhyay S (2016) Numerical study on heat transfer enhancement through a circular duct fitted with centre-trimmed twisted tape. *Int J Heat Technol* 34(3):401–406
20. Saysroy A, Eiamsa-ard S (2017) Periodically fully-developed heat and fluid flow behaviors in a turbulent tube flow with square-cut twisted tape inserts. *Appl Therm Eng* 112:895–910
21. Oni TO, Paul MC (2016) Numerical investigation of heat transfer and fluid flow of water through a circular tube induced with divers' tape inserts. *Appl Therm Eng* 98:157–168
22. Chang SW, Yang TL, Liou JS (2007) Heat transfer and pressure drop in tube with broken twisted tape insert. *Exp Therm Fluid Sci* 32(2):489–501
23. Eiamsa-ard S, Wongcharee K, Eiamsa-ard P, Thianpong C (2010) Thermohydraulic investigation of turbulent flow through a round tube equipped with twisted tapes consisting of centre wings and alternate-axes. *Exp Therm Fluid Sci* 34(8):1151–1161
24. Zheng L, Xie Y, Zhang D (2017) Numerical investigation on heat transfer performance and flow characteristics in circular tubes with dimpled twisted tapes using Al₂O₃-water nanofluid. *Int J Heat Mass Transf* 111:962–981
25. Murugesan P, Mayilsamy K, Suresh S (2010) Heat transfer and friction factor studies in a circular tube fitted with twisted tape consisting of wire-nails. *Chinese J Chem Eng* 18(6):1038–1042

26. Hayat MZ, Nandan G, Tiwari AK, Sharma SK, Shrivastava R, Singh AK (2021) Numerical study on heat transfer enhancement using twisted tape with trapezoidal ribs in an internal flow. *Mater Today Proc* 46:5412–5419
27. Behzadian M, Khanmohammadi S, Otaghsara M, Yazdani M, Ignatius J (2012) A state-of-the-art survey of TOPSIS applications. *Expert Syst Appl* 39(17):13051–13069

Thermo-Diffusion and Heat Generation Effects on Unsteady MHD Flow of Nanofluid in a Perforated Vertical Medium



Harshad Patel, Akhil Mittal, and Tejal Nagar

Nomenclature

nf	Nanofluid
ρ_{nf}	Density
μ_{nf}	Dynamic viscosity
k_{nf}	Thermal conductivity
$(\rho C_p)_{nf}$	Thermal conductivity
k_f	Velocity field
ϕ	Nanoparticle volume fraction
k	Permeability
u	Velocity
θ	Temperature
C	Concentration
G	Acceleration due to gravity
c_p	Specific heat at constant pressure
D	Mass diffusivity
Nr	Thermal radiation
Sr	Soret number
Pr	Prandtl number
Gm	Mass Grash of number

H. Patel (✉)

U.V Patel College of Engineering, Ganpat University, Kherva, Gujarat, India
e-mail: harshadpatel2@gmail.com

A. Mittal
Gujarat Arts and Science College, Ahmedabad, India

T. Nagar
Gujarat Technological University, Ahmedabad, India

Gr Thermal Grash of number
T Time

1 Introduction

This paper's discussion covered the nanofluid flow and heat transfer solution. The thickness of the thermal border increases as thermal radiation increases. The operating temperature can be determined by industrial operations. Jaafar et al. [1] discussed the hybrid nanofluid with the effects of thermal radiation. The purpose of this work is to examine the steady flow and heat transfer of the nonlinearly stretching/shrinking hybrid nanofluid under the influence of magnetic field, thermal radiation, and suction. Dual solutions were found, and it was shown that water has better heat transmission capabilities than both nanofluids and hybrid nanofluids. Aly et al. [2] and Wahid et al. [3] worked on these concepts. To improve heat transmission within the other flow effects taken into consideration, this study advises dropping the nanofluid concentration and growing thermal radiation. Many researchers like, Raza et al. [4] and Mahabaleshwar et al. [5] considered MHD flow of with different physical parameter effects. It is explored how physical characteristics such as temperature, skin friction coefficient, micro-rotation, and local Nusselt number affect non-dimensional velocity, non-dimensional skin friction coefficient, and other fluid flow parameters with an analytical closed form solution with duality. Waqas et al. [6] described the nanofluid flow with nonlinear thermal radiation. They deduced from the results that velocity increases as solid volume fraction increases. Furthermore, higher thermal Biot number estimates result in a rise in fluid temperature. Kumar et al. [7] and Sivasankaran et al. [8] discussed natural convective. In this paper, the radiation parameter tends to improve velocity and temperature profiles. The processing of magnetic nanoparticles in the chemical and metallurgical sectors is appropriate for the simulations that are currently being used. Higher Casson liquid parameter values are found to exhibit thermal stratification when radiation is present. As the values of the Casson liquid parameter and radiation parameter increase, the kinematic energy increases. Mustafa et al. [9] define the Buoyancy effects on the MHD nanofluid flow, whereas Hayat et al. [10] considered mixed convective peristaltic flow with thermal deposition. Large wavelength and low Reynolds number conditions have been used to study heat and mass transport. The resulting nonlinear systems are mathematically resolved. The graphical representations demonstrate the growing influence of temperature through mixed convection as well as the behavior of concentration as it decreases due to thermal deposition and positive chemical reaction. The effects of chemical reaction and heat generation on MHD flow discussed by [11–16]. The three-dimensional flow is more impact in real life situation as compared to one- and two-dimensional flow. Yang et al. [17] considered three-dimensional flow of natural convection in porous medium whereas, Rizwana et al. [18] considered the mixed convectional stagnation point flow. However, when nano-iron oxide was added, the

absolute viscosity increased, and as the temperature rose, the absolute viscosity trended downward. Younes et al. [19] represented the Nanofluids and its applications. The need for a deeper understanding of the different elements that affect thermal conductivity has increased as a result of recent developments in tailoring nanofluids to acquire specific thermophysical features. Any material that is on the nanoscale combined with a base fluid is referred to as a nanofluid. Although research into the creation and usage of nanofluids has grown significantly over the past ten years, there are still very few commercially viable uses for these materials, with the majority of research concentrating on theoretical and fundamental science studies. The numerous uses of nanofluids are briefly covered in this review. It primarily focuses on a discussion of the many factors that have been discovered to have a substantial impact on thermal conductivity and thermal behavior in general. Recently, Gandhi et al. [20] and Sheikholeslami et al. [21] discussed heat generation effects on MHD flow with different physical conditions.

The novelty of research work is to thermos-diffusion, heat generation, thermal radiation, and chemical reaction effects on MHD flow of nanofluid in perforated vertical medium. Using the similarity transformation, the governing systems of PDE's has been transformed into ODE's and the resultant problem is solved by Laplace Transform and Inverse Laplace transform. The flow phenomenon has been characterized with the help of graphs.

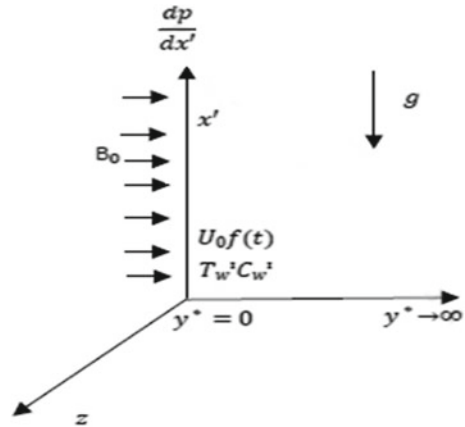
2 Mathematical Formulation of the Problem

One-dimensional flow of nanofluid in the presence of external magnetic field, radiation, reaction, and pressure is studied through perforated vertical medium, Fig. 1 clearly mentions the co-ordinate system. The flow is confined with $y' > 0$. A transverse magnetic field B_0 is applied in y' - directions. It is assumed that at time $t' \leq 0$, T'_{∞} (temperature) and C'_{∞} (concentration), respectively. At the time $t' > 0$, the velocity $u_0 f(t)$, temperature T'_w , and concentration C'_w , respectively.

The following assumptions are made for the flow:

- (1) The term defined by dissipation (viscous) is neglected in the temperature equation as compared to the term of conduction.
- (2) The Dufour and Soret influence in the equation of concentration and temperature is neglected since the assumption of concentration level is low in convectional fluid flows.
- (3) The effect of the pressure gradient ($\frac{dp'}{dx'}$) on the velocity of the fluid was studied.

Fig. 1 Sketch of the problem



By Boussinesq approximation the governing momentum, energy, and concentration equation is given below:

$$\rho_{nf} \frac{\partial u'}{\partial t'} = \mu_{nf} \frac{\partial^2 u'}{\partial y'^2} - \sigma_{nf} B_0^2 u' - \frac{\sigma_{nf} \varphi}{k'} u' + g(\rho\beta'_T)_{nf} (T' - T'_\infty) + g(\rho\beta'_C)_{nf} (C' - C'_\infty) - \frac{dP'}{dx'} \quad (1)$$

$$\frac{\partial T'}{\partial t'} = \frac{k_{nf}}{(\rho c_p)_{nf}} \frac{\partial^2 T'}{\partial y'^2} - \frac{1}{(\rho c_p)_{nf}} \frac{\partial q_r}{\partial y'} + \frac{Q(T' - T_0)}{(\rho c_p)_{nf}} \quad (2)$$

$$\frac{\partial C'}{\partial t'} = D \frac{\partial^2 C'}{\partial y'^2} - k_2(C' - C'_\infty) \quad (3)$$

where,

$$\rho_{nf} = (1 - \varnothing)\rho_f + \varnothing\rho_s, \quad (4)$$

$$\mu_{nf} = \frac{\mu_f}{(1 - \varnothing)^{2.5}}, \quad (5)$$

$$\sigma_{nf} = \sigma_f \left[1 + \frac{3(\sigma - 1)\varnothing}{(\sigma + 2) - (\sigma - 1)\varnothing} \right], \quad (6)$$

$$\sigma = \frac{\sigma_s}{\sigma_f}, \quad (7)$$

$$(\rho\beta)_{nf} = (1 - \varnothing)(\rho\beta)_f + \varnothing(\rho\beta)_s, \quad (8)$$

$$k_{nf} = k_f \left[1 - 3 \frac{\varnothing(k_f - k_s)}{2k_f + k_s + \varnothing(k_f - k_s)} \right], \tag{9}$$

$$(\rho c_p)_{nf} = (1 - \varnothing)(\rho c_p)_f + \varnothing(\rho c_p)_s, \tag{10}$$

With

$$u' = 0, T' = T'_\infty, C' = C'_\infty; \text{asy}' \geq 0 \text{ and } t' \leq 0$$

$$u' = u_0 f(t), T' = T'_w, C' = C'_w; \text{ast}' > 0 \text{ and } y' = 0$$

$$u' \rightarrow 0, T' \rightarrow T'_\infty, C' \rightarrow C'_\infty; \text{asy}' \rightarrow \infty \text{ and } t' > 0 \tag{11}$$

Using the Rosseland approximation, Eq. (2) can be written as,

$$\frac{\partial T'}{\partial t'} = \frac{k_{nf}}{(\rho c_p)_{nf}} \frac{\partial^2 T'}{\partial y'^2} - \frac{1}{(\rho c_p)_{nf}} \frac{16\sigma^* T_\infty'^3}{3k^*} \frac{\partial^2 T'}{\partial y'^2} + \frac{Q(T' - T'_\infty)}{(\rho c_p)_{nf}} \tag{12}$$

where,

$$q_r = -\frac{4\sigma^*}{3k^*} \frac{\partial T'^4}{\partial y'} \tag{13}$$

$$T'^4 \cong 4T_\infty'^3 T' - 3T_\infty'^4 \tag{14}$$

$$q_r = -\frac{4\sigma^*}{3k^*} \frac{\partial(4T_\infty'^3 T' - 3T_\infty'^4)}{\partial y'} \tag{15}$$

The dimensionless quantities are introduced:

$$\begin{aligned} y &= \frac{U_0 y'}{v}, u = \frac{u'}{U_0}, t = \frac{t' U_0^2}{v}, \theta = \frac{(T' - T'_\infty)}{(T'_w - T'_\infty)}, \\ C &= \frac{(C' - C'_\infty)}{(C'_w - C'_\infty)}, k = \frac{k' U_0^2}{V^2}, Gr = \frac{V_g \beta'_T (T'_w - T'_\infty)}{U_0^3}, \\ M &= \frac{\sigma B_0^2 V}{\rho U_0^2}, Gm = \frac{V_g \beta'_C (C'_w - C'_\infty)}{U_0^3}, Pr = \frac{\mu C_p}{k}, \\ Sc &= \frac{v}{D}, Kr = \frac{V k_2}{U_0^2}, P = \frac{P'}{\rho U_0^2}, X = \frac{x' U_0}{V}, \mu = V \rho \end{aligned} \tag{16}$$

Applying the variables (16) on Eq. (1–3), we obtained the non-dimensional system of PDE's with conditions as follows:

$$\frac{\partial u}{\partial t} = \frac{\partial^2 u}{\partial y^2} - \left(M + \frac{1}{k} \right) u + G_r \theta + G_m C - \frac{dP}{dx} \tag{17}$$

$$\frac{\partial \theta}{\partial t} = \frac{1 + Nr}{Pr} \frac{\partial^2 \theta}{\partial y^2} + H_1 \theta \tag{18}$$

$$\frac{\partial C}{\partial t} = \frac{1}{Sc} \frac{\partial^2 C}{\partial y^2} - KrC \tag{19}$$

With

$$u = C = \theta = 0 \text{ as } y \geq 0, t \leq 0$$

$$u = f(t), C = 1, \theta = 1, \text{ as } y = 0, t > 0$$

$$u \rightarrow 0, C \rightarrow 0, \theta \rightarrow 0, \text{ as } y \rightarrow \infty, t > 0 \tag{20}$$

System becomes:

$$\frac{\partial u}{\partial t} = a_1 \frac{\partial^2 u}{\partial y^2} - \left(a_3 M + \frac{a_1}{k} \right) u + a_2 G_r \theta + G_m a_5 C - \frac{dP}{dx} \tag{21}$$

$$\frac{\partial \theta}{\partial t} = a_4 \frac{\partial^2 \theta}{\partial y^2} + H_1 \theta, \tag{22}$$

$$\frac{\partial C}{\partial t} = \frac{1}{s_c} \frac{\partial^2 C}{\partial y^2} - KrC, \tag{23}$$

With,

$$u = 0, \theta = 0, C = 0; \text{ as } y \geq 0 \text{ and } t \leq 0; \tag{24}$$

$$u = f(t), \theta = 1, C = 1; \text{ as } y = 0, t > 0; \tag{25}$$

$$u \rightarrow 0, \theta \rightarrow 0, C \rightarrow 0 \text{ as } y \rightarrow \infty, t > 0; \tag{26}$$

3 Solution of the Problem

The governing dimensionless Eqs. (21–26) are a system of PDE’s. The Laplace transform is used to finding the solutions of said problem.

3.1 Solution of Temperature Profiles

$$\theta_{(y,t)} = f_2(y, t) \tag{27}$$

3.2 Solution of Concentration Profiles

$$C_{(y,t)} = f_5(y, t) \tag{28}$$

3.3 Solution of Velocity Profiles

$$u_{(y,t)} = g_4(y, t) + g_2(y, t) + g_1(y, t) - g_3(y, t) \tag{29}$$

where,

$$g_{i=1to4}(y, t) = L^{-1}G_{i=1to4}(y, s) \text{ and } f_{i=1to8}(y, t) = L^{-1}F_{i=1to8}(y, s) \tag{30}$$

$$g_1(y, t) = d_8 f_1(y, t) - d_8 f_2(y, t) + d_{14} f_3(y, t) - d_{14} f_4(y, t) \tag{31}$$

$$g_2(y, t) = d_{10} f_1(y, t) - d_{10} f_5(y, t) + d_{16} f_7(y, t) - d_{16} f_6(y, t) \tag{32}$$

$$g_3(y, t) = d_{12} f_1(y, t) - \frac{d_{12}}{S} + d_{12} f_8(y, t) - \frac{d_{12}}{d_1 + S} \tag{33}$$

$$g_4(y, t) = L^{-1} \left\{ F(S) e^{-\sqrt{\frac{d_1+s}{a_1}} y} \right\} \tag{34}$$

$$f_1(y, t) = \frac{1}{2} \left[e^{-y\sqrt{\frac{d_1}{a_1}}} \operatorname{erfc} \left(\frac{y}{2\sqrt{d_1 t}} - \sqrt{d_1 t} \right) + e^{y\sqrt{\frac{d_1}{a_1}}} \operatorname{erfc} \left(\frac{y}{2\sqrt{d_1 t}} + \sqrt{d_1 t} \right) \right] \tag{35}$$

$$f_2(y, t) = \frac{1}{2} \left[e^{-iy\sqrt{\frac{H_1}{a_4}}} \operatorname{erfc}\left(\frac{y}{2\sqrt{a_4 t}} - i\sqrt{H_1 t}\right) + e^{iy\sqrt{\frac{H_1}{a_4}}} \operatorname{erfc}\left(\frac{y}{2\sqrt{a_4 t}} + i\sqrt{H_1 t}\right) \right] \tag{36}$$

$$f_3(y, t) = \frac{e^{-d_{13}t}}{2} \left[e^{-y\sqrt{\frac{1}{a_1}(d_1-d_{13})}} \operatorname{erfc}\left(\frac{y}{2\sqrt{a_1 t}} - \sqrt{(d_1 - d_{13})t}\right) + e^{y\sqrt{\frac{1}{a_1}(d_1-d_{13})}} \operatorname{erfc}\left(\frac{y}{2\sqrt{a_1 t}} + \sqrt{(d_1 - d_{13})t}\right) \right] \tag{37}$$

$$f_4(y, t) = \frac{e^{-d_{13}t}}{2} \left[e^{-y\sqrt{\frac{1}{a_4}(-H_1-d_{13})}} \operatorname{erfc}\left(\frac{y}{2\sqrt{a_4 t}} - \sqrt{(-H_1 - d_{13})t}\right) + e^{y\sqrt{\frac{1}{a_4}(-H_1-d_{13})}} \operatorname{erfc}\left(\frac{y}{2\sqrt{a_4 t}} + \sqrt{(-H_1 - d_{13})t}\right) \right] \tag{38}$$

$$f_5(y, t) = \frac{1}{2} \left[e^{-y\sqrt{KrSc}} \operatorname{erfc}\left(\frac{y\sqrt{Sc}}{2\sqrt{t}} - \sqrt{Krt}\right) + e^{y\sqrt{KrSc}} \operatorname{erfc}\left(\frac{y\sqrt{Sc}}{2\sqrt{t}} + \sqrt{Krt}\right) \right] \tag{39}$$

$$f_6(y, t) = \frac{e^{-d_{15}t}}{2} \left[e^{-y\sqrt{Sc(Kr-d_{15})}} \operatorname{erfc}\left(\frac{y\sqrt{Sc}}{2\sqrt{t}} - \sqrt{(Kr - d_{15})t}\right) + e^{y\sqrt{Sc(Kr-d_{15})}} \operatorname{erfc}\left(\frac{y\sqrt{Sc}}{2\sqrt{t}} + \sqrt{(Kr - d_{15})t}\right) \right] \tag{40}$$

$$f_7(y, t) = \frac{e^{-d_{15}t}}{2} \left[e^{-y\sqrt{\frac{1}{a_1}(d_1-d_{15})}} \operatorname{erfc}\left(\frac{y}{2\sqrt{a_1 t}} - \sqrt{(d_1 - d_{15})t}\right) + e^{y\sqrt{\frac{1}{a_1}(d_1-d_{15})}} \operatorname{erfc}\left(\frac{y}{2\sqrt{a_1 t}} + \sqrt{(d_1 - d_{15})t}\right) \right] \tag{41}$$

$$f_8(y, t) = \frac{e^{-d_1 t}}{2} \left[\operatorname{erfc}\left(\frac{y}{2\sqrt{a_1 t}}\right) + \operatorname{erfc}\left(\frac{y}{2\sqrt{a_1 t}}\right) \right] \tag{42}$$

$$\begin{aligned} F_1(y, s) &= \frac{1}{s} e^{-y\sqrt{\frac{d_1+s}{a_1}}}, & F_2(y, s) &= \frac{1}{s} e^{-y\sqrt{\frac{s-H_1}{a_4}}}, \\ F_3(y, s) &= \frac{1}{(s+d_{13})} e^{-y\sqrt{\frac{d_1+s}{a_1}}}, & F_4(y, s) &= \frac{1}{(s+d_{13})} e^{-y\sqrt{\frac{s-H_1}{a_4}}}, \\ F_5(y, s) &= \frac{1}{s} e^{-y\sqrt{Sc(Kr+s)}}, & F_6(y, s) &= \frac{1}{s+d_{15}} e^{-y\sqrt{Sc(Kr+s)}}, \\ F_7(y, s) &= \frac{e^{-y\sqrt{\frac{d_1+s}{a_1}}}}{(s+d_{15})}, & F_8(y, s) &= \frac{1}{d_1+s} e^{-y\sqrt{\frac{d_1+s}{a_1}}} \end{aligned} \tag{43}$$

4 Result and Discussion

For better understanding of the physics, we find the numerical solutions of said problem and analyze the different physical parameter effects through the graphs.

A crucial physical metric for determining how nanoparticles affect fluid flow and heat transfer rate is the volume fraction. Figures 2 and 3 show how the volume Fraction affects the water nanofluid reduced velocity field and increased temperature field, for Fe_3O_4 /water nanofluid. Physically, the performance of fluid viscosity appeared to be improved by the higher values of the nanoparticle volume fraction.

The velocity curve of the uniform velocity is shown in Fig. 4. According to the Figure, as M rises, velocity gradually drops off in the distance. The existence of external magnet within the fluid causes this slowing of fluid motion. When a magnetic field works perpendicular to the flow of a fluid that conducts electricity, a Lorentz force is applied against motion. As a result, the fluid's field tends to slow down due to this force of resistance. Observation and our physical reality are thus consistent. Figure 5 depicts the impact of permeability (κ) on the velocity profile when the plate moves erratically. This result suggests that as rises, velocity increases. The temperature profile is depicted in figures with heat generation parameter H in Figs. 6, 7. It is concluded that heat creation causes the velocity field and temperature

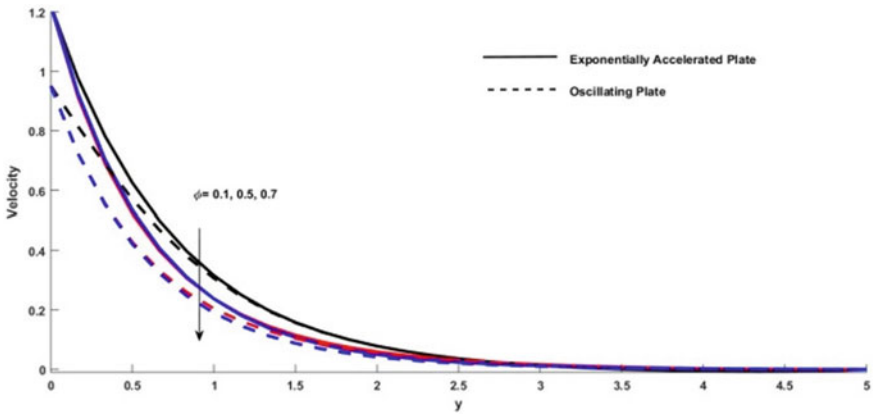


Fig. 2 u for \varnothing

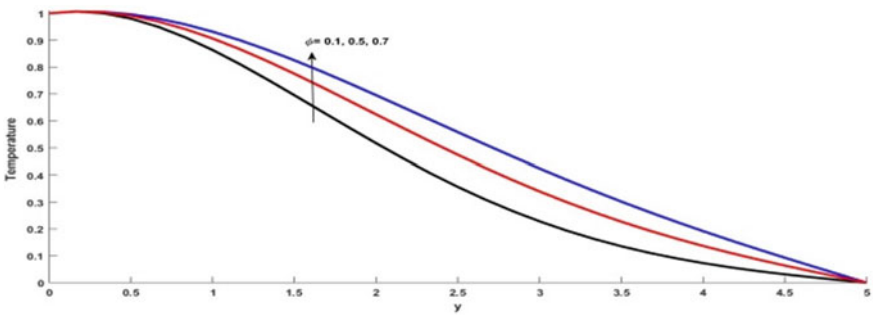


Fig. 3 θ for \varnothing

distribution to increase. Due to this existence of a heat generation, more energy is produced which leads to improve the values of heat transfer process as well as velocity. The effects Nr on heat transfer process and momentum which are seen in Figs. 8, 9. It has been observed that, thermal radiation tends to improve motion of the fluid as well as heat transfer process. This result is strongly agreed with real situation because fluid thickness decrease with increasing the radiation which leads to accelerated the fluid flow. Figure 10 illustrates how Pr effects on the velocity field, demonstrating how the temperature field falls as Prandtl number rises. In terms of physics, Prandtl number leads to pure convection extension, and the effective Prandtl number informs us of the material resistance to shear flow. The impact of Sc on the motion of the fluids and mass transfer process which is represented by Figs. 11, 12. As can be seen, the concentration and velocity profiles' values drop as the Schmidt number rises. The physically depicts the mass momentum transfer of the fluid. Figures 13, 14 show how changes in the mass and heat Grashof numbers, Gm and Gr , respectively, affect velocity distribution. These figures illustrate how an increase in the mass and heat Grashof numbers causes an improved in the velocity field. Grashof number is a straightforward technique to measure the opposing force physically because it is a ratio of buoyant and viscous forces. Figures 15, 16 shows the effects of Kr on velocity and concentration profiles, this graph shows how the velocity and concentration field decreases. The boundary layer thickness of concentration changes with Kr , while the momentum boundary layer does not. A velocity profile's effects on the pressure gradient (P) are seen in Fig. 17. For increased pressure gradient values, it is seen that the velocity curve drops.

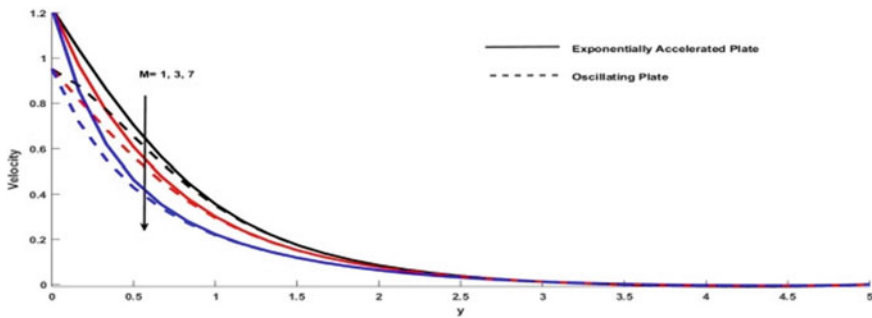


Fig. 4 u for M

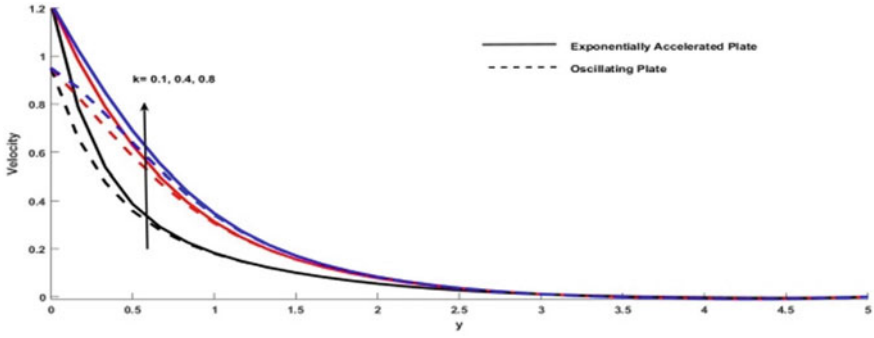


Fig. 5 u for k

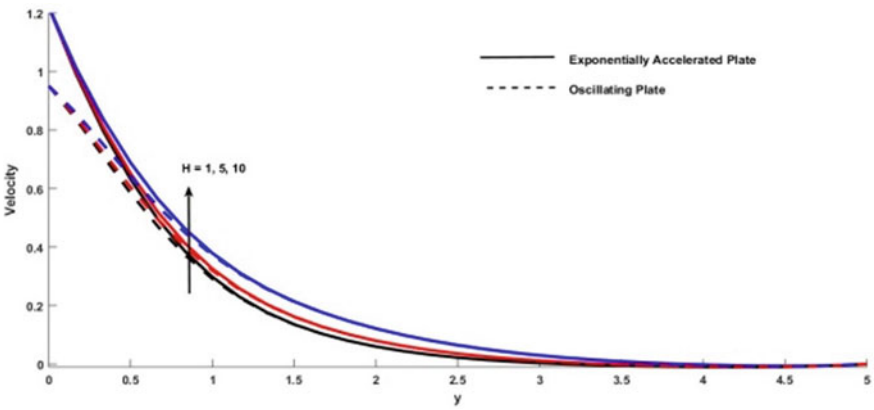


Fig. 6 u for H

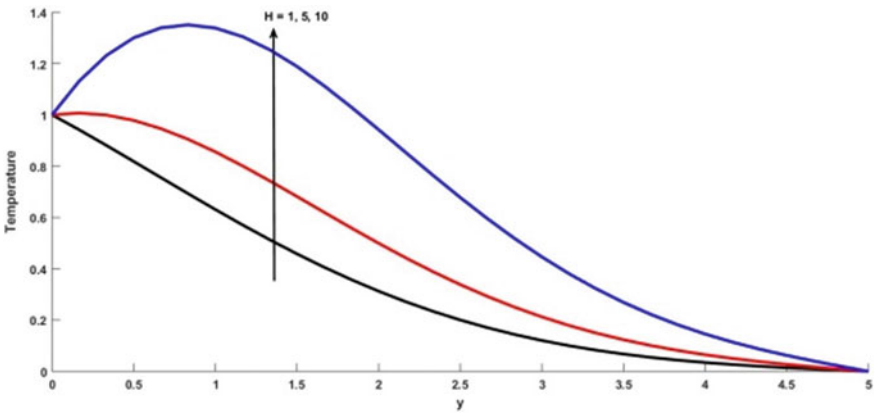


Fig. 7 θ for H

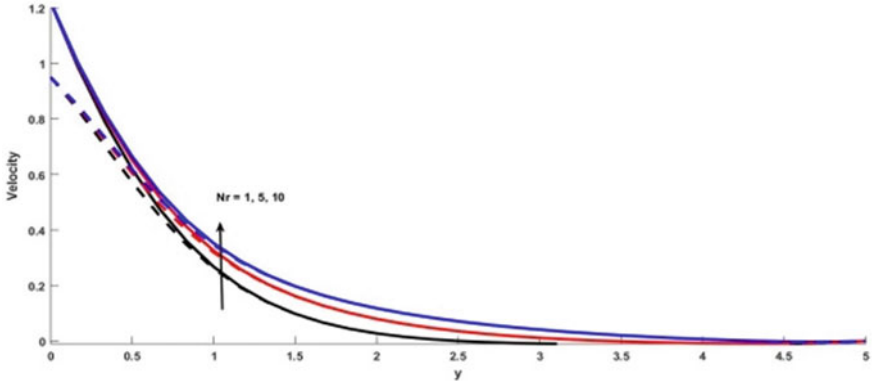


Fig. 8 u for Nr

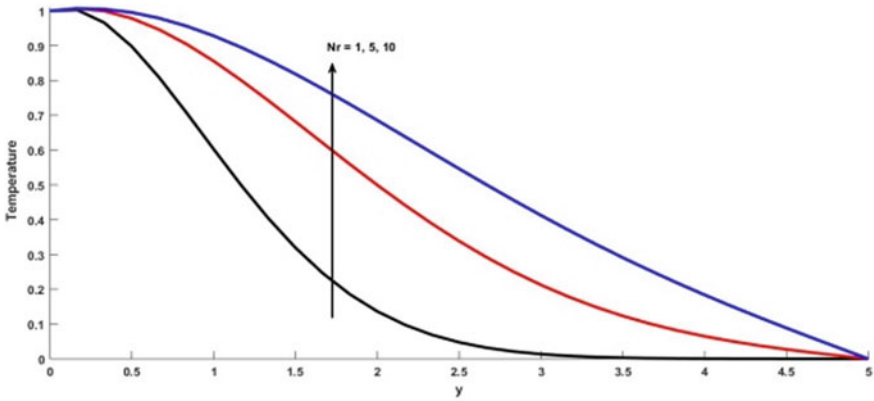


Fig. 9 θ for Nr

5 Conclusions

The concluding remark as follow:

- The motion of fluid accelerated due to the increasing values of permeability, heat generation parameter, thermal radiation parameter, mass Grashof number, and heat Grashof number.
- The volume fraction, magnetic field, and pressure gradient tends to reduce the flow of motion.
- Heat generation, volume fraction, and radiations tend to improve the heat transfer process.
- The mass transfer process delayed with chemical reaction parameter.

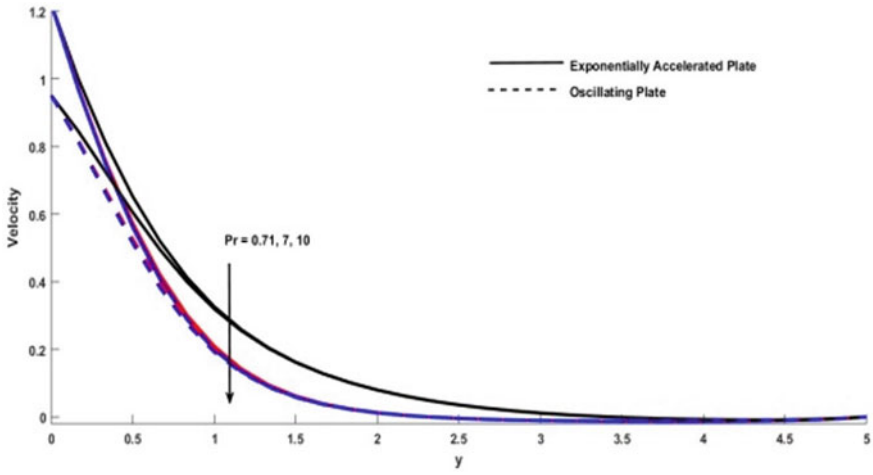


Fig. 10 u for Pr

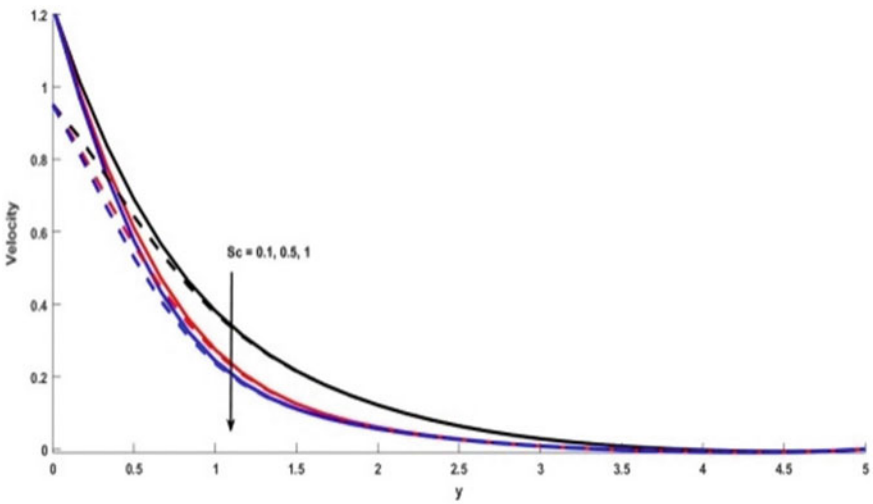


Fig. 11 u for Sc

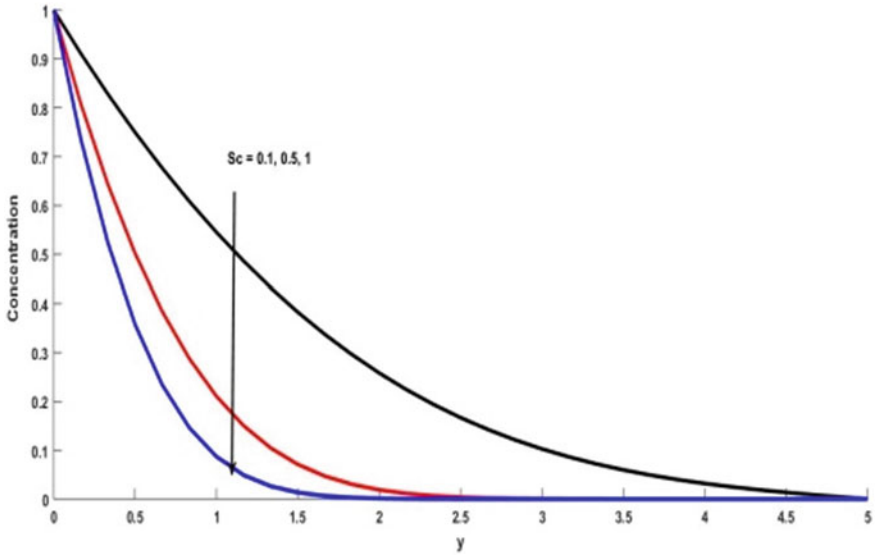


Fig. 12 C for Sc

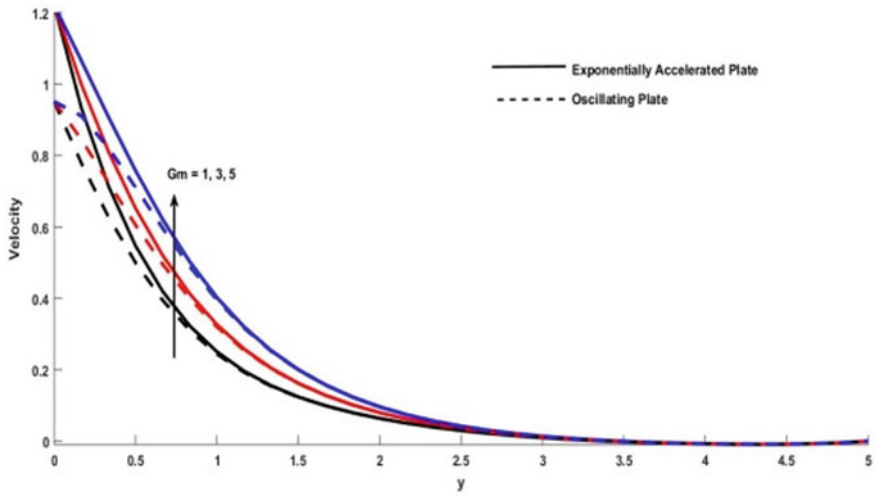


Fig. 13 u for Gm

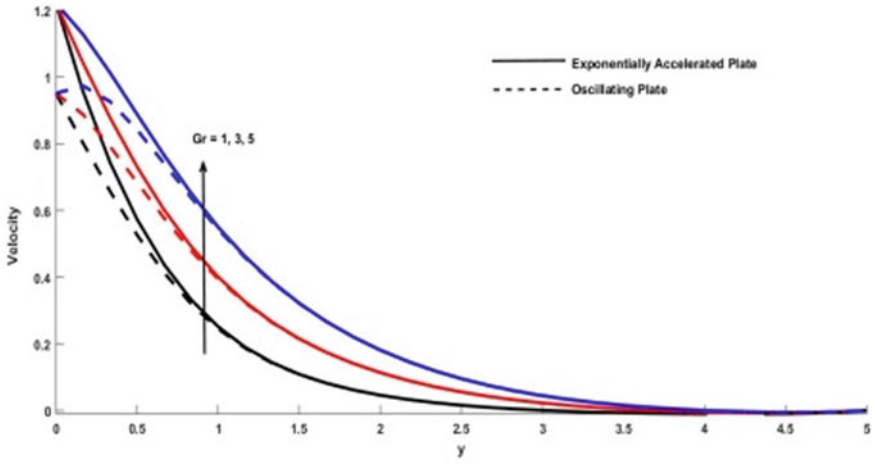


Fig. 14 u for Gr

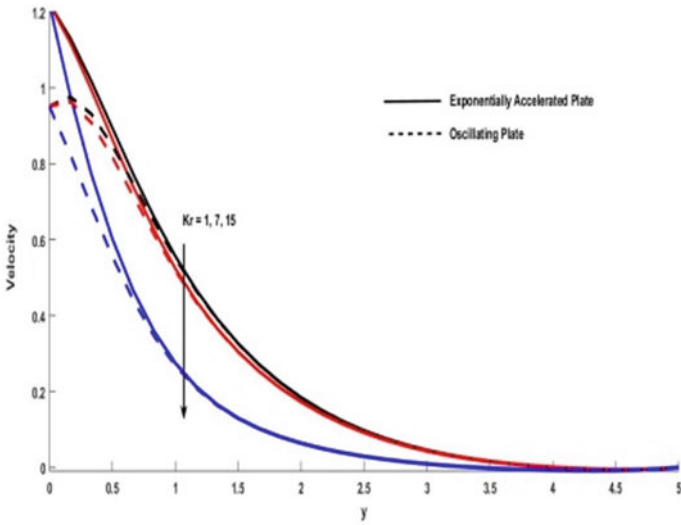


Fig. 15 u for Kr

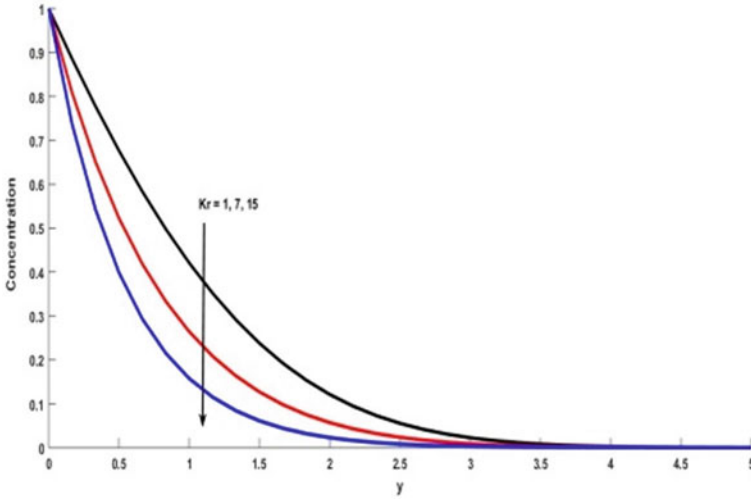


Fig. 16 C for Kr

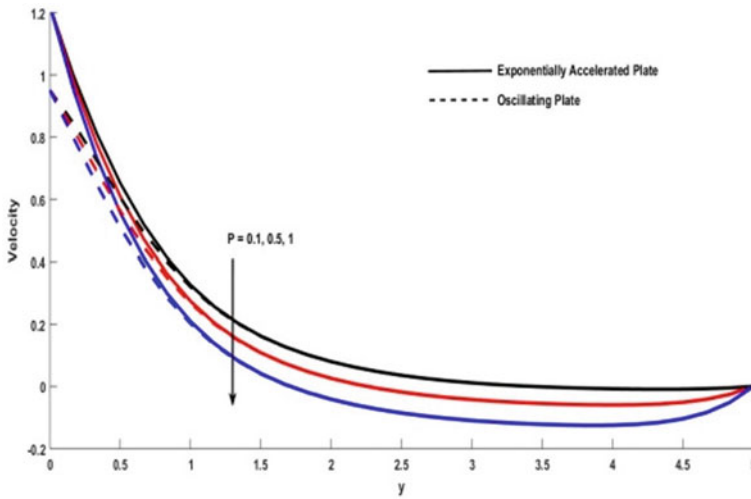


Fig. 17 u for P

References

1. Jaafar I, Waini A, Jamaludin R, Nazar I (2022) Pop. Chin J Phys 79:13–27
2. Aly EH, Mahabaleshwar US, Anusha T, Usafzai WK, Pop I (2022) Therm Sci Eng 32:101294
3. Wahid NS, Arifin NM, Bachok N, Pop I (2022) Chin J Phys 77:378–392
4. Raza R, UIhaq SS, Shah S, Alansari M (2022) Int Commun Heat Mass Transfer 131:105785
5. Mahabaleshwar S, Sneha KN, Chan A, Zeidan D (2022) Int Commun Heat Mass Transfer 135:106080

6. Waqas H, Yasmin S, Muhammad T, Imran M (2021) *J Market Res* 14:2579–2585
7. Anilkumar M, Reddy Y, Rao VS, Goud S (2021) *Case Stud Therm Eng* 24:100826
8. Sivasankaran S, Bhuvanawari M, Alzahrani AK (2020) *Alex Eng J* 59:3315–3323
9. Mustafa M, Khan JA, Hayat T, Alsaedi A (2017) *Int J Heat Mass Transf* 108:1340–1346
10. Hayat T, Tanveer A, Alsaedi A (2016) *Int J Heat Mass Transf* 96:474–481
11. Ravindran R, Ganpathirao M, Pop I (2014) *Int J Heat Mass Transf* 73:743–751
12. Kandasamy R, Periasamy K, Prabhu KK (2005) *Int J Heat Mass Transf* 48:4557–4561
13. Krishna MV, Ahmad NA, Aljohani AF (2021) *Alex Eng J* 60:3467–3484
14. Wahid NS, Arifin NM, Pop I, Bachok N, Ezad M (2022) *Alex Eng J* 61:3323–3333
15. Reddy JV, Sugunamma V, Sandeep N, Sulochana C (2016) *J Niger Mathematic Soc* 35:48–65
16. Khashi NS, Arifin NM, Nazar R, Hafidzuddin E, Wahi N, Pop I (2020) *Chin J Phys* 64:251–263
17. Yang X, Shao Q, Hoteit H, Carrera J, Younes A (2021) *Adv Water Resour* 155:103992
18. Rizwana R, Hussain A, Nadeem S (2021) *Int Commun Heat Mass Transfer* 124:105285
19. Younes H, Mao M, Sohel SM, Lou D, Hong H, Peterson GP (2022) *Appl Therm Eng* 207:118202
20. Sharma BK, Gandhi R (2022) *Propul Pow Res* 22:276–292
21. Sheikholeslami M, Kataria HR, Mittal AS (2018) *J Mol Liq* 257:12–25

Critical Thickness of the Phase Change Material (RT-42) for Temperature Management of 18,650 Li-Ion Cell Undergoing Rapid Discharging



Vivek Saxena, Akhalesh Sharma, Santosh K. Sahu,
and Shailesh I. Kundalwal

1 Introduction

Li-ion cells create heat due to electrochemical processes. The literature reports that operation temperature affects battery performance. This non-uniform temperature impacts charge–discharge and electrochemical activity, reducing cell lifespan and safety. The recommended operating temperature of lithium-ion batteries is 10–45 °C, and the greatest temperature gradient should be below 5 °C [1, 2]. The working range beyond this reduces battery performance and life. Using a thermal management approach to regulate battery temperature is critical. A well-designed and proven TMS prevents temperature rise and monitors cell temperature gradient, assuring battery safety, reliability, and long life. Researchers have tried air-cooled systems [3], liquid-cooled systems [4, 5], cold plates [6, 7], heat pipes [8], and hybrid systems [9, 10] to cool battery packs. Air-cooled systems are simple, lightweight, and inexpensive, but their performance is generally inadequate owing to air’s limited thermal conductivity, which causes uneven cell temperature distribution. Due to their efficiency and temperature homogeneity, liquid cooling systems are a suitable alternative for thermal control of battery modules. Nissan Leaf, Tesla Model 3, Tesla Model X, Chevrolet Bolt, Audi R8 e-Tron, and Chevrolet Spark employ liquid and air cooling. Liquid-cooled systems include high starting costs, complicated designs, coolant leaks, and active maintenance difficulties. Literature shows extensive effort in PCM battery thermal control. Sun et al. [11] evaluated cylindrical and longitudinal fins for cylindrical cell heat control. The scientists employed a cylindrical heating element to replicate a cylindrical cell; adding fins increased the batteries’ operational duration at optimal temperature. A unique arc-shaped finned was claimed to increase working time by 157, 189, and 238% for the same simulated cell at 20, 30, and 40 °C. Huang

V. Saxena (✉) · A. Sharma · S. K. Sahu · S. I. Kundalwal
Department of Mechanical Engineering, Indian Institute of Technology Indore, Indore, India
e-mail: phd2001103003@iiti.ac.in

© The Author(s), under exclusive license to Springer Nature Singapore Pte Ltd. 2024
K. M. Singh et al. (eds.), *Fluid Mechanics and Fluid Power, Volume 1*, Lecture Notes
in Mechanical Engineering, https://doi.org/10.1007/978-981-99-7827-4_26

321

et al. [12] studied 25 parallel 18,650 lithium-ion batteries with PCM cooling. The cooling performance of PCM composites increases with their thermal conductivity and latent heat, but subsequently saturates. With MFs in the PCM, a porosity of 0.94 shows a temperature gradient of less than 1 °C. Alipanah and Xianglin [13] evaluated the thermal performance of several PCMs and MF-PCM matrices under simulated battery discharging circumstances at 400, 600, and 800 W/m². Higher diffusivity PCM keeps the battery cooler, while adding a metal matrix improves thermal management system performance. Choudhari et al. [14] evaluated the thermal management of a Panasonic NCR18650PF Li-ion cell with different fin shapes integrated with PCM. Wang et al. [19] studied prismatic Li-ion battery thermal conductivity, viscosity, latent heat, and PCM thickness. A temperature reduction of 7.26 K is observed for a 5C discharge rate (C rating determines the charging/discharging rate of the battery); the authors concluded that increasing thermal conductivity and latent heat would not necessarily assist the thermal management system.

Li-ion thermal modelling is crucial to understand thermal dynamics. Multiscale multi-domain modelling has become common for batteries [7]. This method unites the many battery length scales for determining temperature distribution. MSMD modelling strategies use empirical and physics-based electrochemical sub-models such as the equivalent circuit model (ECM), the Newman, Tiedemann, Gu, and Kim (NTGK) model, and the Newman Pseudo-two-dimensional (P2D) model [15]. In MSMD models, empirical to basic physics-based electrochemical sub-models like as NTGK, ECM, and P2D exist. MSMD has recently acquired prominence for numerical battery modelling. ANSYS fluent and COMSOL have included these battery models for more precise simulations. Although 2D-3D thermal modelling has been used to predict active and passive battery cooling, knowledge gaps exist. Several researches have combined PCM with battery models, however multiscale domain modelling is limited, notably for batteries embedded with PCM.

2 The Test Rig

Commercially available cylindrical Li-ion cell (make: SONY VTC5—18,650 type) of 2.6 Ah capacity has been used in the current investigation. The cell has an 18 mm diameter and 65 mm height. To charge and discharge the cell, a combination of programmable DC power supply (make: BK PRECISION, 9115, USA) and a DC electronic load (make: BK PRECISION, 8510B, USA) has been used. The power supply and electronic load has a capacity of 0–60 V/0–60 A and 0–120 V/0–120 A, respectively (Fig. 1).

K type thermocouples (1/36 SWG with Teflon coating, supplier: Excel Thermal Instruments India) have been used to measure the temperature. The insulating sleeve of the cell is removed to paste the thermocouples on the surface of the cell and four thermocouples are pasted maintaining an equidistance between them. The temperature data is recorded using Agilent 34972A (make: USA) data acquisition system with a recording frequency of 5 s. The battery is tested in the ambient temperature

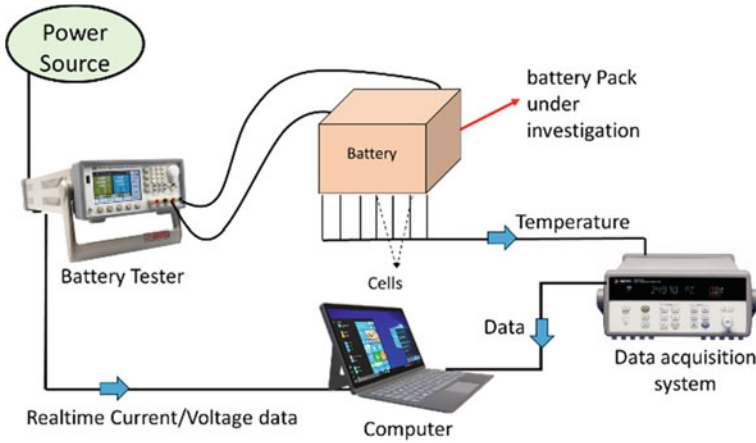


Fig. 1 Schematic of test facility

conditions in the present investigation. Constant current-constant voltage (CC-CV) methodology has been adopted to charge the cell. The cell is first charged at 0.3C until it reaches 4.1 V. The tester maintains 4.1 V until C/10 taper current approaches zero. After being fully charged for 30 min, the battery is drained at a constant C rate. In this research, rapid discharge rate of 4C and 3C has been used. Before every discharge, the battery is fully charged utilizing the aforesaid procedure. After fully discharging any C-rate battery, it's rested for four hours before the next experiment. Every charge–discharge test is repeated twice to verify the repeatability of the experiments. The transient voltage–capacity response and the temperature rise response during both the discharge rates has been used to validate the numerical model. Table 1 below presents the specification of SONY VTC5 18,650 Li-ion cell.

Table 1 Cell specifications

Specification	Value	Unit
Rated capacity	2.6	Ah
Nominal voltage	3.6	V
Charge cut-off	4.1	V
Discharge cut-off	2.5	V
Maximum discharge current	10	A
Capacity	9	Wh
Weight	44.3	gms

3 The Numerical Model

The battery packs have been modelled in ANSYS fluent using the NTGK approach of the MSMD model. The governing equations for which are:

$$\frac{\partial \rho C_p T}{\partial t} - \nabla \cdot (k \nabla T) = \sigma_+ |\nabla \phi_+|^2 + \sigma_- |\nabla \phi_-|^2 + \dot{q}_{ech} \quad (1)$$

$$\nabla \cdot (\sigma_+ \nabla \phi_+) = -J_{ech} \quad (2)$$

$$\nabla \cdot (\sigma_- \nabla \phi_-) = J_{ech} \quad (3)$$

The electrical conductivities of the positive and negative electrodes are denoted by σ_+ and σ_- , respectively. These are the electrode potential fields: ϕ_+ and ϕ_- . J_{ech} and q_e represent the volumetric current transmission and joule heat production rates, respectively. As shown in equation, the NTGK sub-model provides a semi-empirical relationship between the present transfer rate and the potential fields.

$$J_{ech} = aY[U - (\phi_+ - \phi_-)] \quad (4)$$

Here, a represents the battery's specific volume, Y represents the inverse slope of the V-I curve, and U represents the open circuit voltage. Y and U are represented as a function of DOD in the following Eqs. 5–7.

$$Y = \left[\sum_{n=0}^5 a_n (\text{DOD})^n \right] \exp\left(-C_1 \left(\frac{1}{T} - \frac{1}{T_{\text{ref}}}\right)\right) \quad (5)$$

$$U = \left[\sum_{n=0}^5 b_n (\text{DOD})^n \right] - C_2(T - T_{\text{ref}}) \quad (6)$$

$$\text{DoD} = \frac{V}{3600 Q_{\text{Ah}}} \int_0^t J dt \quad (7)$$

In the present investigation, the empirical parameters are estimated by conducting experiments with the same cell and then using the parameter estimation tool in ANSYS Fluent. The electrochemical heat production is denoted by the Eq. 8.

$$\dot{q}_{ech} = J_{ech} \left[U - (\phi_+ - \phi_-) - T \frac{dU}{dT} \right] \quad (8)$$

The cell in this concept is physically separated into two domains: active and inactive. The active zone is a homogenous region that manifests all electrodes and the separator, regardless of their varying material qualities, and is the zone for electrochemical processes that lead to electrochemical heat. Copper is the material utilized for the negative tab and aluminium is used as positive tab. The commonly employed enthalpy-porosity model is employed for the formulation of PCM melting processes. The Boussinesq approximation is used to represent the influence of natural convection, assuming the fluid is incompressible and Newtonian. Below are the governing equations.

Continuity:

$$\frac{\partial \rho_f}{\partial t} + \nabla \cdot \rho_f \vec{V} = 0. \quad (9)$$

Momentum:

$$\frac{\rho_f}{\varepsilon} \frac{\partial \vec{V}}{\partial t} + \frac{\rho_f}{\varepsilon^2} (\vec{V} \cdot \nabla) \vec{V} = -\nabla P + \frac{\mu_f}{\varepsilon} (\nabla^2 \vec{V}) - \rho_{f,ref} \beta_f \varepsilon (T - T_{ref}) \vec{g} - \vec{S} - \vec{F}. \quad (10)$$

The energy equation for the coupled heat transfer is:

$$\frac{\partial \varepsilon \rho_f C_{pf} T_f}{\partial t} + \nabla \cdot (\rho_f C_{pf} \vec{V} T) = \nabla \cdot (K_e \nabla T) - S_L. \quad (11)$$

A_m indicates the zone between constant and mushy, which amplifies the suppressing effect. This explains the nature of PCM melting; the constant value ranges from 10^4 to 10^7 . For the simulations at hand, the number 10^5 is used (Fig. 2).

$$S = A_m \frac{(1 - \lambda)^2}{\lambda^3 + 0.001} \quad (12)$$

Here, a constant value of 0.001 is added in the denominator to avoid zero in the number. The porosity value of an individual cell is defined by a term called melt fraction (λ) which helps in tracking the melting of PCM. A value of 0 indicates a solid state of PCM, while 1 denotes the completely melted PCM. The porosity value in case of only PCM is 1, so that the effect of porous media is eliminated, further λ is defined as:

$$\lambda = \frac{\Delta H}{L_f} = \begin{cases} 0 & \text{if } T < T_{solidus} \\ 1 & \text{if } T > T_{solidus} \\ \frac{T - T_{solidus}}{T_{liquidus} - T_{solidus}} & \text{if } T_{solidus} < T < T_{liquidus} \end{cases} \quad (13)$$

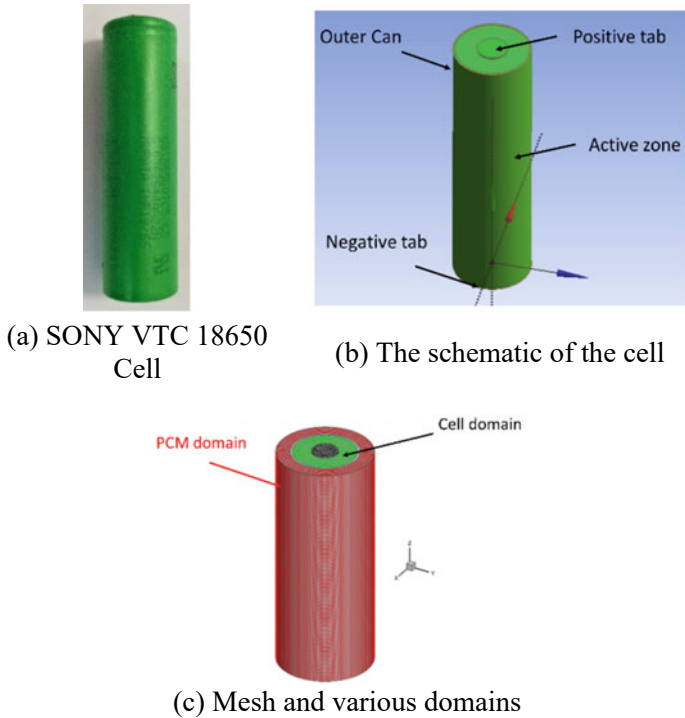


Fig. 2 Description of the cell

Table 2 Mesh sensitivity analysis

Testing conditions	Element size = 0.4 mm, No. of elements = 587,385	
	$\Delta T = 1 \text{ s } (\%)$	$\Delta T = 0.5 \text{ s } (\%)$
Deviation (%) with reference	0.166	0.0432

Total enthalpy is:

$$H = h + \Delta H, \text{ where } h = h_{\text{ref}} + \int_{T_{\text{ref}}}^T c_{pf} dT. \tag{14}$$

The grid and time independence analyses of the present inquiry are conducted as presented in Table 2. Consideration is given to a discharge rate of 4C for the analysis. Initially, three grid sizes were examined for a fixed time step of 2S; it was determined that a mesh containing 587,385 elements is precise enough for simulations. Moreover, two distinct time steps of 1 s and 0.5 s were examined for any variation in numerical findings. The reference conditions correspond to a mesh size of 0.2 mm having

Table 3 Material properties [14]

Material	Property	Value
Cell material	Density	1113 kg/m ³
	Specific heat	503 J/kg-K
	Thermal conductivity	$k_r = 0.413$ $k_\theta = 1.78$ $k_z = 1.78$ W/m K
PCM RT-42	Density	760 kg/m ³
	Specific heat	2000 J/kg-K
	Thermal conductivity	0.2 W/m K
	Melting heat	165,000 J/kg
	Transition temperature	311 K (solidus) 316 K (liquidus)

1,136,773 elements. It should be noticed that increasing grid and time-step refinement increases calculation time without significantly altering the findings. Thus, a 1S time step is chosen for numerical simulations. The selection of PCM change material plays a crucial role in the thermal management of Li-ion cells. In the current simulations, paraffin that was RT-42 has been used. The properties are tabulated in the Table 3.

4 Results and Discussion

4.1 Validation of the Numerical Model

The current numerical model is validated by conducting in-house experiments with a single SONY VTC5 Li-ion cell. Figure 3 illustrates the voltage–time transient response of the cell for two different rapid discharging rate of 4C and 3C.

The lower and upper cut-off limit are 2.5 and 4.1 V. The results from the current simulations are matching well with the experimental test data. The temperature rise response from the current numerical model is compared with the test data in Fig. 4. The maximum temperature of the cell reaches up to 56 and 48 °C for the rapid discharge rate of 4C and 3C. The current numerical model accurately captures the temperature rise of the cell as can be seen from the above figure.

4.2 Effect of PCM Thickness on the Temperature Rise

To determine the critical thickness required to control the cell temperature to the optimum working limit, eight different thicknesses of the PCM domain have been considered. The variation in the PCM domain thickness is considered from 0.5 mm

Fig. 3 Validation of the test set-up

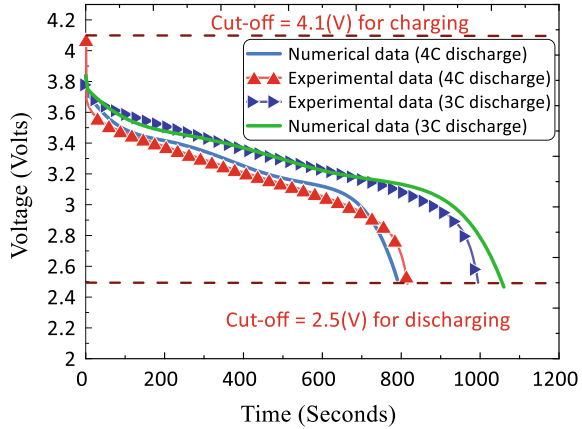
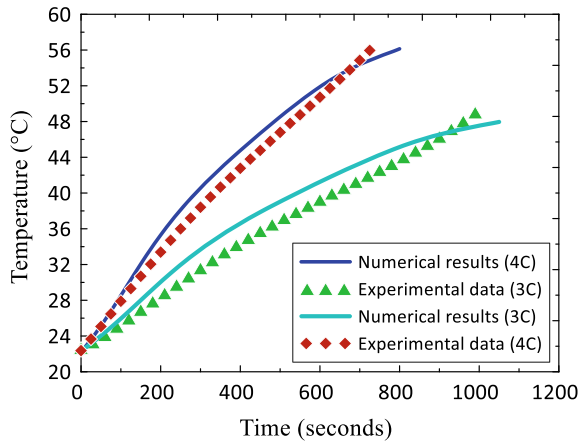


Fig. 4 Thermal performance of unfinned heat sink



to 4 mm. The peak rapid discharge rate of 4C has been considered to determine the optimum PCM thickness. PCM can be an effective tool to control the cell temperature; however, a minimum thickness needs to be provided for effective cooling (Fig. 5).

For 1 mm thickness, the PCM completely melts as can be seen from the figure. Beyond a PCM thickness of 2.5 mm there is no significant decrement in the results. It is essential to track the amount of PCM melted during the discharge process. Any amount of unmelted PCM has the capability to absorb further heat from the cell domain. Figure 6 presents the amount of the PCM melted after the complete discharge of the cell. For a thickness of 0.5 mm, the PCM completely melts even before the complete discharge of the cell. For a thickness of 2 mm, about 50% of the PCM remains unmelted. The temperature contour plots for a thickness of 0.5 mm, 1 mm, 2.5 mm, and 4 mm have been presented in Figs. 7a–d, respectively.

Fig. 5 Effect of PCM thickness

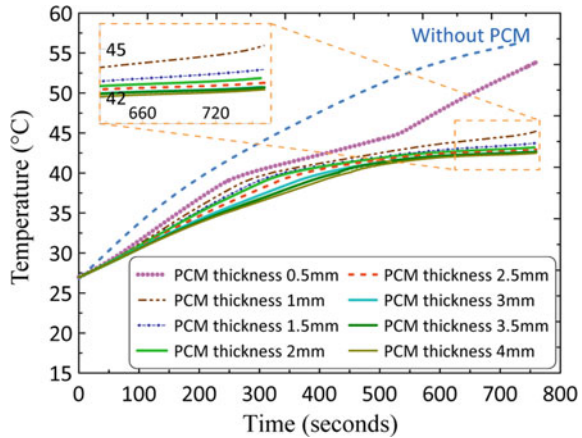
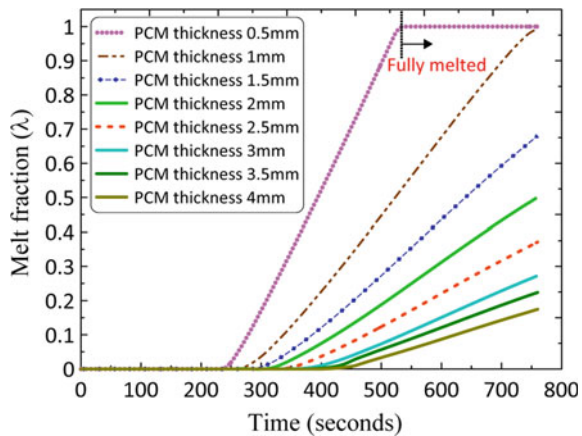


Fig. 6 Melting behaviour of PCM for various thickness

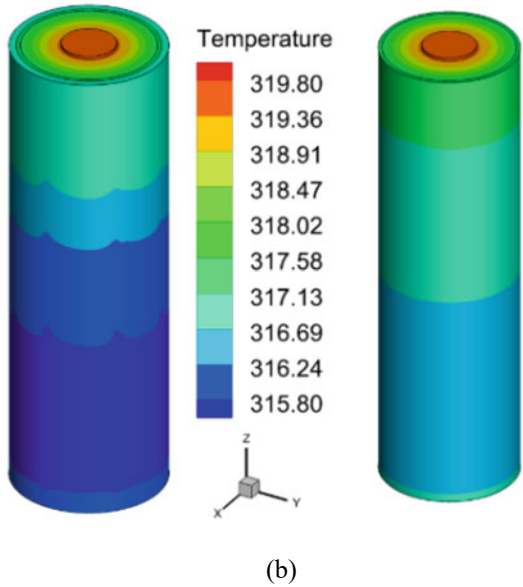
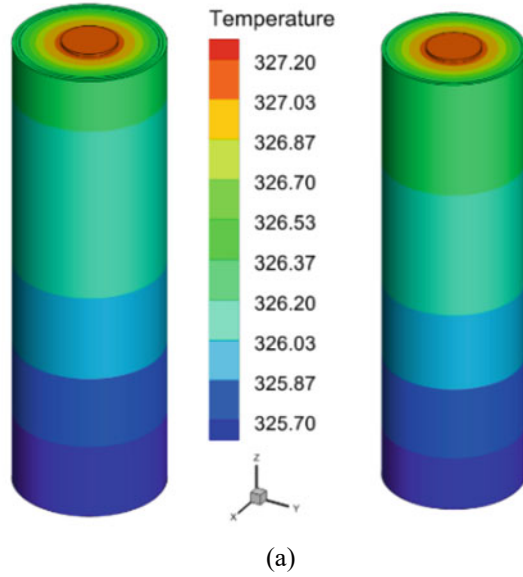


In all the Figs. 7a–d, the contour result on the left side is for the complete domain, i.e. including the cell and the PCM domain, whereas the right side depicts the temperature of the cell domain only. Keeping the PCM thickness of 2.5 mm, the cell is further tested for profile test to mimic a more realistic scenario.

4.3 Cell Under Profile Test

During the profile testing following discharge sequence is modelled to check the thermal performance of PCM embedded battery cell. During an actual discharge scenario in an EV, the charge/discharge process is very dynamic according to loading conditions and vehicle acceleration. In the current case, the cell is subjected for a discharge by 3C for 120 s followed by discharge by 5C for 60 s. After the discharge

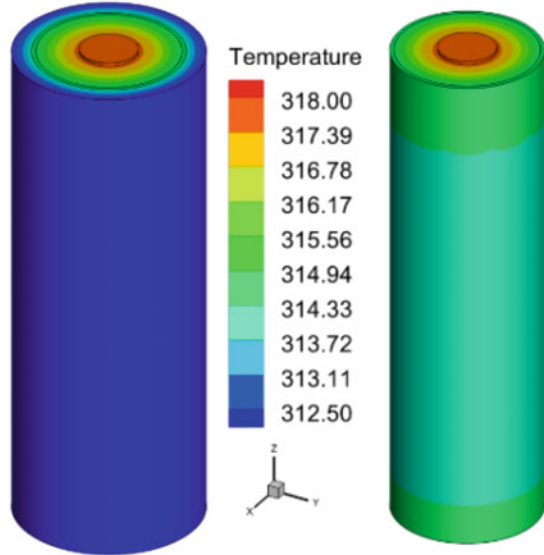
Fig. 7 **a** Temperature contours 0.5 mm thickness, **b** temperature contours 1 mm thickness, **c** temperature contours 2 mm thickness, **d** temperature contours 4 mm thickness



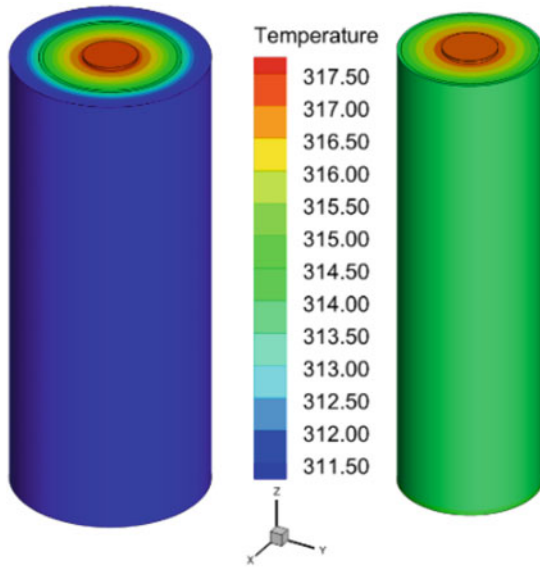
by 60 s, the cell is allowed to rest for 60 s and then three such cycles are repeated. Finally, the cell is completely discharged by using a high discharge rate of 8C.

The voltage and the state of charge (SOC) response of the cell is illustrated in Fig. 8. Both the SOC and voltage have been presented in the same figure. The temperature rise during the profile test is depicted in the Fig. 9. It is evident that even

Fig. 7 (continued)



(c)



(d)

in the aggressive discharge conditions, the PCM can control the cell temperature. The maximum temperature at the end of the discharge is 44.8 °C. The temperature contours and the melt contours for the profile test have been presented in Fig. 10a–b, respectively. The complete cell-PCM domain and an x - y plane within both the domain are presented. From Fig. 10a, temperature inside the cell domain remains within the optimum temperature. The peak temperature is reported in the tabs zone; however, this is because of the increased current density in the tab zones. The melt contour in Fig. 10b depicts the amount of PCM melted at the end of the profile test. The average melting in the whole domain was 60.5% after the complete discharge of the cell.

Fig. 8 Voltage and SOC during profile test

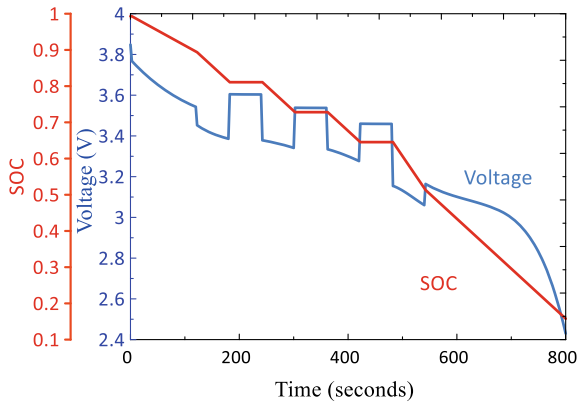


Fig. 9 Temperature rise during the profile test

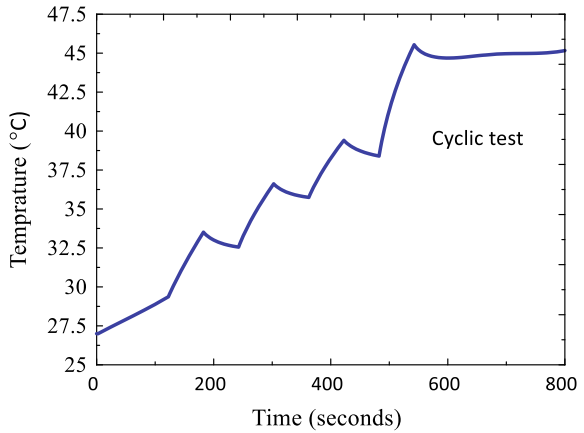
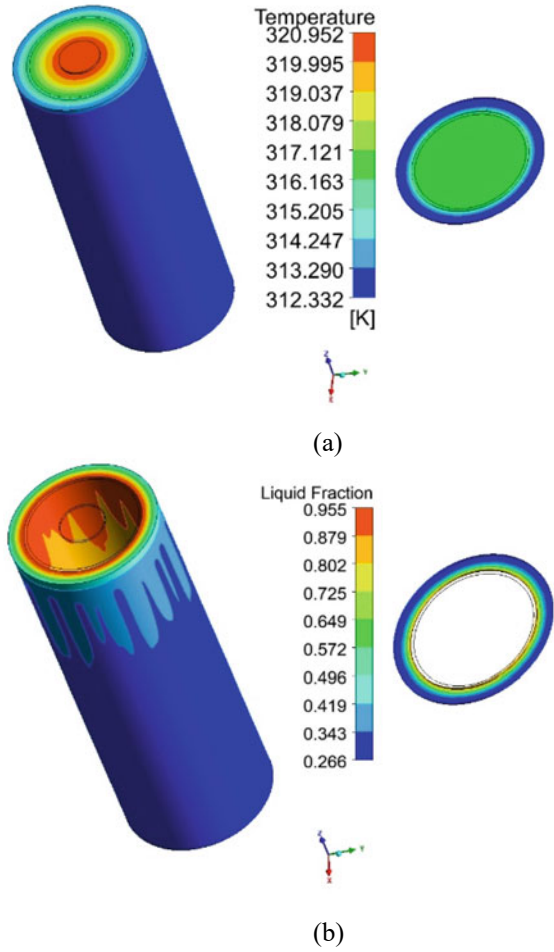


Fig. 10 **a** Temperature at the end of profile test, **b** melt at the end of profile test



5 Conclusions

A cylindrical 18,650 Li-ion cell was modelled in the current investigation. The cell model was validated using the in-house experiments for a rapid discharge of 4C and 3C. PCM was utilized to curtail the temperature rise in the cell due to rapid discharging. The PCM is found to be an effective candidate for the temperature management of the cell. The optimum value of thickness of the PCM domain was found to be 2.5 mm. For the optimum thickness, the profile test simulations were carried out to mimic the transient discharging behaviour from the cell, where the PCM was able to hold the cell in the optimum temperature range. The present

research demonstrates the effectiveness of multiscale modelling approach for accurate modelling of the Li-ion cells and the unmatched candidature of PCM for the battery thermal management applications.

Acknowledgements The first author would like to thank and acknowledge the research grant from Prime Minister's Research Fellowship (PMRF), Govt. of India.

Nomenclature

C_p	Specific heat capacity (J/kg-K)
g	Acceleration due to gravity (m/s ²)
H	Specific enthalpy (J/kg)
j	Current density (A/m ³)
I	Current (A)
V	Voltage (Volt)
k	Thermal conductivity (W/m K)
L	Latent heat (J/kg)
p	Pressure (Pa)
Q	Total heat (W)
g	Gravitational acceleration (m/s ²)
T	Temperature (K)
BTMS	Battery thermal management system
A_m	Mushy zone constant
S	Source term in momentum equation
SOC	State of charge
PCM	Phase change material
DOD	Depth of discharge

Greek Symbol

λ	Melt fraction
ρ	Density (kg/m ³)
σ	Electrical conductivity (S/m)
μ	Dynamic viscosity (kg/m-s)
β	Thermal expansion coefficient (1/K)

References

1. Saxena V, Dey H, Kumar A, Sharma A, Sahu SK, Kundalwal I (2021) Numerical investigation of phase change material enhanced Li-ion battery pack using the dual potential multi-scale multi-dimensional (MSMD) approach. In: Proceedings of 26th National 4th International ISHMT-ASTFE Heat and Mass Transfer Conference Dec 17–20. IIT Madras, Chennai, 600036, Tamil Nadu, India, pp 1519–1525. <https://doi.org/10.1615/IHMT-2021.2290>
2. Patel JR, Rathod MK (2020) Recent developments in the passive and hybrid thermal management techniques of lithium-ion batteries. *J Power Sources* 480(July):228820. <https://doi.org/10.1016/j.jpowsour.2020.228820>
3. Kirad K, Chaudhari M (2021) Design of cell spacing in lithium-ion battery module for improvement in cooling performance of the battery thermal management system. *J Power Sources* 481(September 2020):229016. <https://doi.org/10.1016/j.jpowsour.2020.229016>
4. Sheng L et al (2019) Numerical investigation on a lithium ion battery thermal management utilizing a serpentine-channel liquid cooling plate exchanger. *Int J Heat Mass Transf* 141:658–668. <https://doi.org/10.1016/j.ijheatmasstransfer.2019.07.033>
5. Zhao C, Cao W, Dong T, Jiang F (2018) Thermal behavior study of discharging/charging cylindrical lithium-ion battery module cooled by channeled liquid flow. *Int J Heat Mass Transf* 120:751–762. <https://doi.org/10.1016/j.ijheatmasstransfer.2017.12.083>
6. Xu X, Tong G, Li R (2020) Numerical study and optimizing on cold plate splitter for lithium battery thermal management system. *Appl Therm Eng* 167(September 2019):114787. <https://doi.org/10.1016/j.applthermaleng.2019.114787>
7. Zhang H, Li C, Zhang R, Lin Y, Fang H (2020) Thermal analysis of a 6s4p Lithium-ion battery pack cooled by cold plates based on a multi-domain modeling framework. *Appl Therm Eng* 173(March):115216. <https://doi.org/10.1016/j.applthermaleng.2020.115216>
8. Smith J, Singh R, Hinterberger M, Mochizuki M (2018) Battery thermal management system for electric vehicle using heat pipes. *Int J Therm Sci* 134(June 2017):517–529. <https://doi.org/10.1016/j.ijthermalsci.2018.08.022>
9. Al-Zareer M, Dincer I, Rosen MA (2019) Development and analysis of a new tube based cylindrical battery cooling system with liquid to vapor phase change. *Int J Refrig* 108:163–173. <https://doi.org/10.1016/j.ijrefrig.2019.08.027>
10. Ding B, Qi ZH, Mao CS, Gong L, Liu XL (2020) Numerical investigation on cooling performance of PCM/cooling plate hybrid system for power battery with variable discharging conditions. *J Therm Anal Calorim* 141(1):625–633. <https://doi.org/10.1007/s10973-020-09611-0>
11. Sun Z, Fan R, Yan F, Zhou T, Zheng N (2019) Thermal management of the lithium-ion battery by the composite PCM-Fin structures. *Int J Heat Mass Transf* 145:118739. <https://doi.org/10.1016/j.ijheatmasstransfer.2019.118739>
12. Huang R, Li Z, Hong W, Wu Q, Yu X (2020) Experimental and numerical study of PCM thermophysical parameters on lithium-ion battery thermal management. *Energy Rep* 6:8–19. <https://doi.org/10.1016/j.egy.2019.09.060>
13. Alipanah M, Li X (2016) Numerical studies of lithium-ion battery thermal management systems using phase change materials and metal foams. *Int J Heat Mass Transf* 102:1159–1168. <https://doi.org/10.1016/j.ijheatmasstransfer.2016.07.010>
14. Choudhari VG, Dhoble AS, Panchal S (2020) Numerical analysis of different fin structures in phase change material module for battery thermal management system and its optimization. *Int J Heat Mass Transf* 163:120434. <https://doi.org/10.1016/j.ijheatmasstransfer.2020.120434>
15. Ansys Fluent Theory Guide (2021) Ansys Fluent Theory Guide 15317(November)
16. Luo J, Zou D, Wang Y, Wang S, Huang L (2022) Battery thermal management systems (BTMs) based on phase change material (PCM): a comprehensive review. *Chem Eng J* 430(P1):132741. <https://doi.org/10.1016/j.cej.2021.132741>
17. Zhang SS, Xu K, Jow TR (2003) The low temperature performance of Li-ion batteries. *J Power Sources* 115(1):137–140. [https://doi.org/10.1016/S0378-7753\(02\)00618](https://doi.org/10.1016/S0378-7753(02)00618)

18. Ramadass P, Haran B, White R, Popov BN (2002) Capacity fade of Sony 18650 cells cycled at elevated temperatures: part I. Cycling performance. *J Power Sources* 112(2):606–613. [https://doi.org/10.1016/S0378-7753\(02\)00474-3](https://doi.org/10.1016/S0378-7753(02)00474-3)
19. Wang Y, Wang Z, Min H, Li H, Li Q (2021) Performance investigation of a passive battery thermal management system applied with phase change material. *J Energy Storage* 35(January). <https://doi.org/10.1016/j.est.2021.102279>

Effect of Orientation on the Thermal Performance of a PCM-Based Finned Heat Sinks



Ch. Ravi Shankar and Y. Naresh

1 Introduction

As portable electronic devices become a necessary part of life, they operate in different orientations rather than a fixed one. While using, electronic chips produce enough heat that might disturb or damage the functioning of the whole device. So, effective thermal management for the electronic chip is in the limelight for researchers. Recent studies say that PCM-based heat sinks can be used for the thermal management of electronic devices [1]. As the PCM has brighter properties like high latent heat, large specific heat capacity, and low volumetric expansivity suits the application. But the significant pullback is the poor thermal conductivity of PCM. Still, it can be enhanced with thermal conductivity enhancers (TCE) like providing fins [2, 3], adding nano-particles [4], using metal foams [5], or coupling with a heat pipe [6]. But portable devices are continuously subjected to changes in orientation from time to time while used, and thermal management is vital with orientation changes.

2 Literature Review and Objective

A lump of literature is available on the study of the effect of orientation on PCM-based heat sinks with different fin configurations as TCEs at different power levels at a fixed fill ratio [7, 8]. Although the literature is available on heat sinks with varying configurations of the fin with orientations up to 90°. However, the investigations on the effect of orientation (up to 180°) on thermal performance have not been

Ch. Ravi Shankar (✉) · Y. Naresh
Department of Mechanical Engineering, Sardar Vallabhbhai National Institute of Technology,
Surat 395007, India
e-mail: p21me018@med.svnit.ac.in

adequately addressed in the literature. Hence, in the present study, an attempt has been made to investigate the thermal performance of various heat sinks under a 99% fill ratio at different power levels. Further, investigations have been carried out on the best configuration at different orientations, i.e., from 0 to 180°.

3 Experimental Setup and Procedure

The aluminum-made bare cylindrical heat sink has an outer diameter of 58 mm, height of 55 mm, and a wall thickness of 5 mm and is used for the experimental investigations. For the central stem heat sink, the stem of diameter 5 mm is fabricated for the central stem heat sink. 2 mm thickness fins are used for three fin and four fin heat sink configurations. The heat sink partitions are fabricated using an end milling process. The pictorial view of each heat sink is shown in the Fig. 1. This developed in-house experimental test facility is shown in Fig. 2. To overcome the drawback of low thermal conductivity of PCM, four fins of the thickness of 2 mm are provided longitudinally and used as thermal conductivity enhancers. Calibrated K-type thermocouples are used to measure the temperature of the base and walls of the heat sink. A total of 10 thermocouples are used to monitor the heat sink performance, i.e., two at the base of the heat sink (taking an average of these), three at the wall (taking the average of these), three to measure the PCM temperature, and two to measure the room temperature. The nichrome wire heater is attached at the bottom to mimic the heat generation effect from an electronic chip. Insulation is provided at the bottom of the heat sink using cork to transfer the maximum heat in one dimensional, i.e., to the heat sink. The top of the heat sink is covered by an acrylic cap that also provides transparency to capture the melt fronts. The properties of PCM and aluminum heat sink are mentioned below in table [1]. The uncertainty analysis using error propagation method is performed to determine the consistency of the experiments. It is calculated that the uncertainty in power for heat input level of 8 W, the voltage of 4.94 V, and current reading of 1.620 A gives ± 0.1704 W.

The experiments are conducted at four different power levels (6, 8, 10, and 12 W) and five different orientations (0°, 45°, 90°, 135°, and 180°) at a constant fill ratio of 99%. The orientation is varied by the setup shown in Fig. 1b, and the spirit level ensures the zero level. All sets of experiments are conducted at the controlled room temperature of 25 °C (Table 1).

4 Results and Discussion

This section denotes the experimental results of all fin configuration heat sinks subjected to different power input levels. From the experiments, the charging times for bare heat sink, central stem, three fins, and four fins are 5165, 5575, 4720, and 4905 s, respectively. Similarly, discharging times for bare heat sink, central stem,

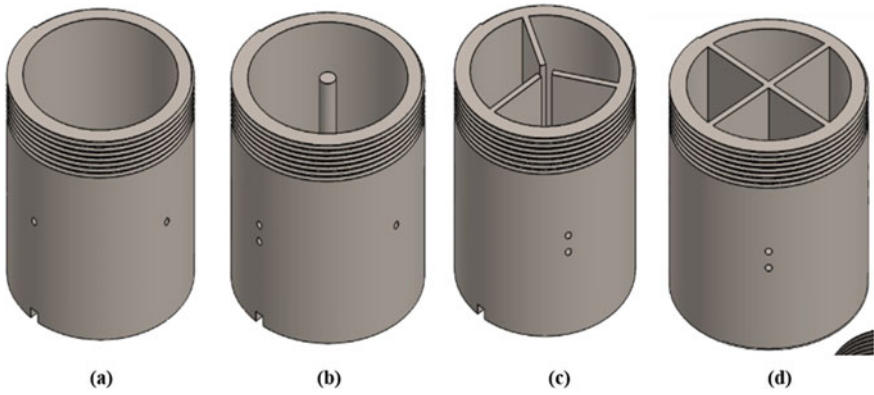
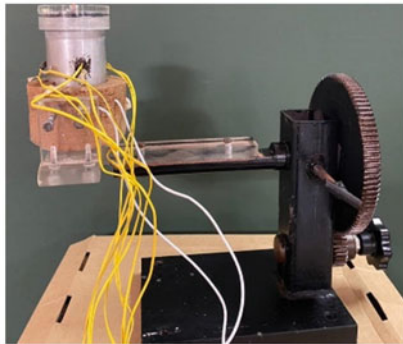


Fig. 1 A3-D view of **a** bare heat sink **b** heat sink with central stem **c** heat sink with three fins with a central gap for provision of heat pipe **d** heat sink with four fins



(a)



(b)

Fig. 2 Photograph of **a** experimental setup **b** orientation setup

Table 1 Material properties used in the current study

Material	Thermal conductivity (W/mK)	Specific heat (kJ/kgK)	Latent heat (kJ/kg)	Melting point (°C)	Density (kg/m ³)
n-eicosane	0.39 (solid) 0.157 (liquid)	1.9 (solid) 2.2 (liquid)	237.4	36.5	810 (solid) 770 (liquid)
Aluminum	202.4	0.87		660.4	2719

three fins, and four fins are 27,880, 26,765, 22,900, and 19,965 s at the same power level (i.e., 8 W). The charging times are on the higher sides for bare and stem heat sink cases compared with the other two cases. However, the discharging time is too high for the bare and the stem heat sink case. Therefore, the overall effectiveness (charging time and discharging time) of the four fin heat sink case is higher compared with all the configurations considered in the present study. Hence, further studies are carried out on the four-finned heat sink.

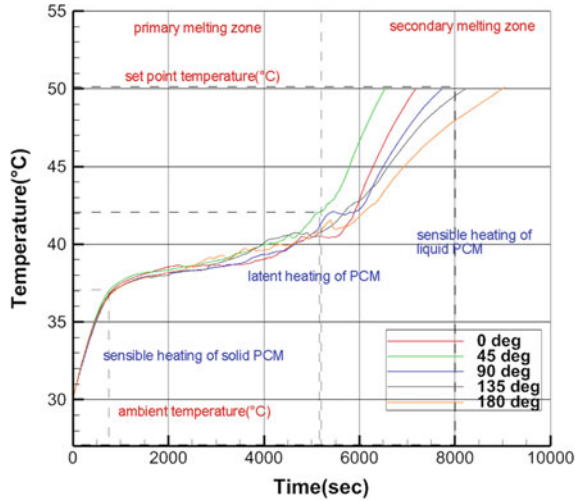
The in-depth orientation analysis on thermal performance is studied because the portable devices are continuously subjected to changes in orientation during usage. For a given power input at each orientation, the charging and discharging times variation with respect to time are measured. Charging time is the time to reach the set point temperature from room temperature, and discharging time is the time taken to reach the room temperature from the set point temperature under natural convection conditions. In the current study, the set point temperature is 50 °C as humans can easily carry and operate the portable device comfortably below 50 °C [9]. Experimental results show that for a four fin heat sink at a power level of 6W, the charging times are 7190, 6540, 7745, 8230, 9045 s at 0°, 45°, 90°, 135°, and 180°, respectively. The discharging times at the same power input level are 17,870, 19,560, 17,015, 18,050, and 16,720 s at 0°, 45°, 90°, 135°, and 180°, respectively. The above readings show that the charging time and discharging time is less in the 180° case. At the 180° orientation, the charging time values are 9045, 5735, 3620, and 2895 s at 6 W, 8 W, 10 W, and 12 W, respectively. Incidentally, these are the maximum values of charging time at different power levels. At 0° orientation, the direction of heat input is opposite to gravitational force. As time passes, the PCM layer adjacent to the walls of the heat sink melts and forms a thin layer between solid PCM and walls. But, as the liquid quantity is too small, there are no significant buoyancy forces inside the heat sink. Thus, the viscous force dominates, and conduction is the predominant heat transfer. The temperature change induces a density change, too, due to buoyancy force (which dominates viscous force with the increase in liquid fraction). A continuous movement of fluid exists from the bottom to the top, as the high temperature and lighter fluid at the heat sink's base comes up, inducing the convection currents inside the heat sink. This gets stronger as the liquid fraction increases. In this whole phase, convection heat transfer is predominant, and buoyancy force acts in the opposite direction to gravity and in the direction of convection current, thus resulting in lower charging times. At 180°, the phenomenon changes; now, the heat input is in the same direction as gravity. As time passes, melted liquid PCM drops due to downward

gravity force; as the lighter PCM settles down, no buoyancy forces are acting, and there is no bulk movement of PCM and hence no convection inside the heat sink. The heat transfer from base to solid PCM is through pure conduction; as the thermal conductivity of PCM is low, the heat transfer rate is maximum through the fins and thus resulting in large charging times.

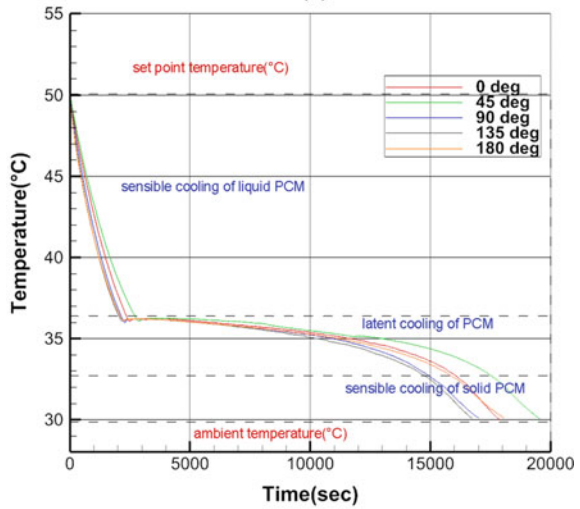
The variations of charging and discharging cycles of a PCM-based finned heat sink is shown in Fig. 3a, b at a power level of 6W at different orientations. The sensible heating of solid PCM is observed at 37 °C at around 850 s. Latent heating of PCM is observed up to 5300 s where a large amount of heat is absorbed, and then sensible heating of liquid PCM takes place, thus reaching the set point temperature and completing the charging cycle at around 9045 s at 180° orientation. In the discharging cycle, the sensible cooling of liquid PCM takes place until 2000s, and these lines are much sloppy than the sensible cooling of solid PCM, as the temperature gradients are higher at set point temperature to ambient temperature and hence PCM at walls cools faster. Latent cooling is continuous up to about 13,000 s, and the sensible cooling of solidified PCM is observed until reaching the temperature of 30 °C, taking 18,050 s at 180° orientation. The graph shows that the one with an ample charging time of 9045 s and less discharging time of 18,050 s is obtained at 180° orientation and hence considered the best orientation. The same trends are observed at other power levels too.

For performance evaluation of a PCM-based heat sink, a heat sink with working fluid as air is taken as the baseline. To quantify the performance of the heat sink, the dimensionless parameter called enhancement ratio for the charging cycle, reduction ratio for discharging cycle, and effectiveness for the overall performance of heat sink is introduced [6]. The enhancement ratio is the ratio of the charging time of the heat sink with PCM to the charging time of the heat sink without PCM. The reduction ratio is the ratio of discharging time of a heat sink without PCM to the discharging time of the heat sink with PCM. Figure 4a shows the enhancement ratio values of four fin heat sink under different orientations at a power level of 8W, and the enhancement ratio values at all power levels are given in Table 2. The reduction ratio values are plotted in Fig. 4b with respect to orientation at a power level of 8W, and for all power levels, the values are given in Table 3. The effectiveness of the heat sink is calculated as the product of the enhancement and reduction ratios. The values are plotted for the 8W power level plotted, as shown in Fig. 5. From the plots, the HS has an enhancement ratio of 6.036 at 180°, which is the largest at the given power levels compared with other orientations, and the reduction ratio of 0.184 is obtained at 180°. The effectiveness of 1.110 shows superiority at the same orientation. In sum, for the different power levels, it is inferred that enhancement, reduction ratios, and effectiveness are on the higher side at 180°.

Fig. 3 Base time and temperature history of HS with four fins at different orientations **a** charging cycle **b** discharging cycle



(a)



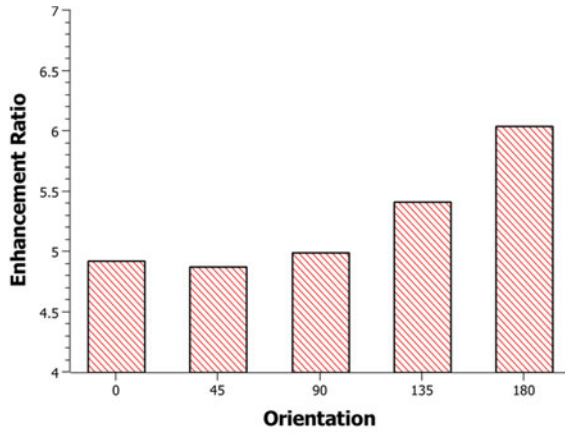
(b)

5 Conclusions

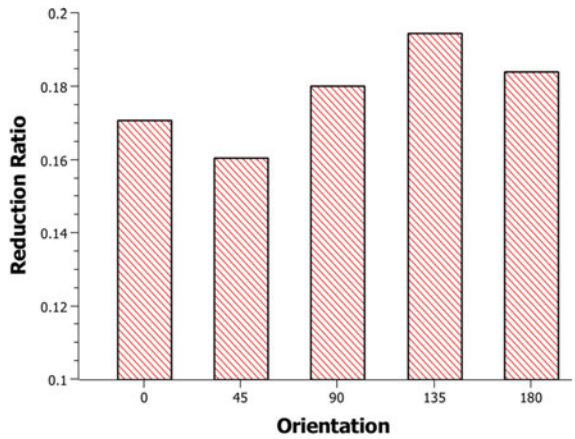
An in-house experimental test facility is developed to conduct heat transfer experiments on finned heat sinks at different power levels. The orientation of the heat sink is changed between 0° and 180° and the following conclusions are made:

- i. Four-finned heat sink has shown significant results in charging and discharging compared with the other three cases.

Fig. 4 **a** Enhancement
b reduction ratios of HS with
four fin at different
orientations at 8 W power
level



(a)



(b)

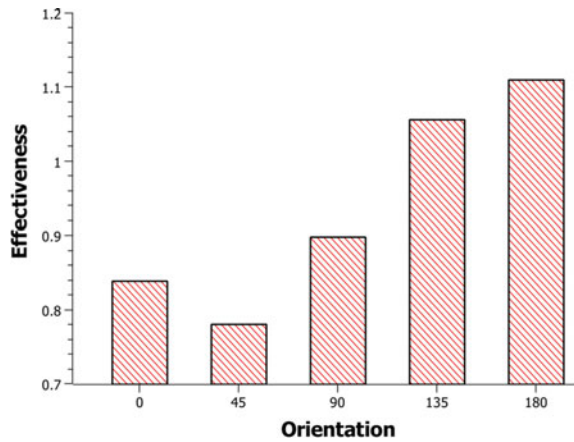
Table 2 Enhancement ratio
of PCM-based heat sink at
different orientations and
different power levels

Orientation	10 W	12 W
0°	5.092	5.345
45°	5.042	5.327
90°	5.157	5.336
135°	5.085	5.252
180°	5.171	5.411

Table 3 Reduction ratio of PCM-based heat sink at different orientations and different power levels

Orientation	10 W	12 W
0°	0.1896	0.1992
45°	0.1641	0.1774
90°	0.198	0.1972
135°	0.2075	0.2108
180°	0.2842	0.2074

Fig. 5 Effectiveness of HS with four fin at different orientations at power level of 8 W



- ii. Among all the orientations, 180° orientation shows superior performance with an enhancement ratio of 6.036 and a reduction ratio of 0.184 at the 8 W power level.
- iii. For a power level of 8 W at 180° orientation, the overall effectiveness of the heat sink is found to be 1.11 and the same trend is observed at all other power levels.

References

- Hodes M, Weinstein RD, Pence SJ, Piccini JM, Manzione L, Chen C (2002) Transient thermal management of a handset using phase change material (PCM). *J Electron Packag* 124(4):419–426. <https://doi.org/10.1115/1.1523061>
- Baby R, Balaji C (2012) Experimental investigations on phase change material based finned heat sinks for electronic equipment cooling. *Int J Heat Mass Transf* 55:8. <https://doi.org/10.1016/j.ijheatmasstransfer.2011.11.020>
- Arshad A, Ali HM, Yan WM, Hussein AK (2018) An experimental study of enhanced heat sinks for thermal management using n-eicosane as phase change material. *Appl Therm Eng* 15. <https://doi.org/10.1016/j.applthermaleng.2017.12.066>
- Manoj Kumar P, Saminathan R, Sumayli A, Mittal M, Abishek AS, Atharsh Kumar AS, Reddy TDK, Rinawa ML (2022) Experimental analysis of a heat sink for electronic chipset cooling

- using a nano improved PCM (NIPCM). *Mater Today Proc* 56:1527–1531. <https://doi.org/10.1016/j.matpr.2022.01.178>
5. Baby R, Balaji C (2013) Experimental investigations on thermal performance enhancement and effect of orientation on porous matrix filled PCM based heat sink. *Int Commun Heat Mass Transf* 46:27–30. <https://doi.org/10.1016/j.icheatmasstransfer.2013.05.018>
 6. Marri GK, Balaji C (2021) Experimental and numerical investigations on a phase change material based heat sink with symbiotically joined heat pipe. *Heat Transf Eng* 42(1):23–40. <https://doi.org/10.1080/01457632.2019.1685241>
 7. Akula R, Balaji C (2021) Thermal performance of a phase change material-based heat sink subject to constant and power surge heat loads: a numerical study. *J Therm Sci Eng Appl* 13(3):031014. <https://doi.org/10.1115/1.4047944>
 8. Marri GK, Balaji C (2022) Effect of phase change temperatures and orientation on the thermal performance of a miniaturized PCM heat sink coupled heat pipe. *Exp Heat Transf*:1–23. <https://doi.org/10.1080/08916152.2022.2073487>
 9. Dreyfuss HD, Tilley AR (1993) *The measure of man and woman: human factors in design*. Whitney Library of Design

Thermal Performance Analysis of Cross-Finned Heat Sinks Using Nano-Enhanced Phase Change Material



Vivek Saxena, Anuj Kumar, Harshit Ziniwal, Gaurav Nagar, Santosh K. Sahu, and Shailesh I. Kundalwal

1 Introduction

Passive thermal management systems (PTMS) have made their way into the field of thermal energy storage due to the ever-increasing demand for more energy and the requirement of small high-energy density systems, including space systems [1], textile [2, 3], medicine [4], electronics cooling [5, 6], and transportation industries because they have better thermophysical, kinetic and economic parameters [7, 8]. By maintaining the temperature at a constant level, heat is absorbed during the solid–liquid transition phase. Active thermal management system (ATMS) is the counterpart of PTMS, but due to the requirement of external power to function, PTMS is currently under investigation. In the area of PTMS, the PCM is one of the frequently employed because of its high latent heat capacity. Compared with other sensible heat energy systems, PCMs have a heat storage capacity that is nearly 7–9 times more [9]. The style and composition of the heat sinks have an impact on PCM performance. PCM can be divided into three groups: organic, inorganic and eutectic. Organic PCMs have a number of favourable qualities, including a high specific heat capacity, a considerable latent heat value and repeatability or reusability [10]. PCM has a drawback due to its reduced thermal conductivity, which slows down the rate at which heat is transmitted despite these benefits. Metallic fins, nanoparticles and metal foams are just a few methods that are used to impact the thermal conductivity to get around this. As a thermal conductivity enhancer (TCE), fins have been widely used in several experiments on heat sinks and few critical studies are described in the next section.

V. Saxena (✉) · H. Ziniwal · G. Nagar · S. K. Sahu · S. I. Kundalwal
Department of Mechanical Engineering, Indian Institute of Technology Indore, Indore, India
e-mail: phd2001103003@iiti.ac.in

A. Kumar
Department of Mechanical Engineering, Indian Institute of Technology, Bombay, India

2 Literature Review and Objective

PCM-based heat sinks containing metallic foams and internal fins was experimentally examined by Kumar et al. [11]. It was determined that a heat sink with circular pin fins may effectively cool electronic components. The same authors [12] also conducted an experimental study on how adding nanoparticles improved the thermal performance. According to this study, heat sinks with square pin fins perform better in terms of thermal management and adding nanoparticles significantly improved heat sink performance. Experimental research on heat sinks with plate fins integrating nanoparticles was conducted by Kothari et al. [13]. The study suggested that adding 2% nanoparticles to a heat sink would increase its operational time by a factor of 1.48. Hosseinirad et al. [14] investigated the impact of fin closeness on the thermal performance of heat sinks. It has been claimed that heat sinks with both straight and wavy fins collectively perform worse than those with only straight or only wavy fins. The fin-embedded PCM was investigated on battery thermal management system. The improvement in cycling stability of bischofite as a thermal energy storage material was investigated by Gutierrez et al. [15]. Sahoo et al. [16] examined orthotropic fins enhance heat transfer like TCE. The authors examined variation between thermal conductivity and TCE volume fraction. It is evident from the literature that several investigations have been made employing combination of phase change material with fins and nanoparticles. However, inclusion of cross-finned heat sink in combination with nanoparticles has been rarely explored. The aim of the present investigation is to examine the thermal performance of combination of nanoparticles and cross-fins to get the maximum operation time. Here, five different cross-finned heat sinks have been used with two different weight fractions of nanoparticles in a hybrid combination to evaluate the thermal performance.

3 Materials and Methodology

Figure 1a outlines the experimental test rig with all the accoutrements. Figure 1b depicts the different heat sinks used in the present investigation. The heat sink assembly includes a base plate heater (make: Sunrise Products India, dimensions: $100 \times 100 \times 4$), and CNC-milled (Emcomill E350, Austria) cross-finned heat sinks (Aluminium-6061). An acrylic sheet (thermal conductivity: $0.19 \text{ W m}^{-1} \text{ K}^{-1}$) of 4 mm thickness is used to cover the top surface and glass-wool is employed to provide the insulation. The wall thickness of cross-finned heat sink is varied such that the volume fraction of 6.60% is maintained in each case. The power supply in system contains a DC power source (make: Aplab L3260, 0–30 V/0–40 A, India) and is controlled by setting the current and voltage. K type thermocouples (1/36 SWG with Teflon coating, supplier: Excel Thermal Instruments India) have been used to measure the temperature. The temperature data is recorded using Agilent 34972 A (make: USA) data acquisition system with a recording frequency of 10 s.

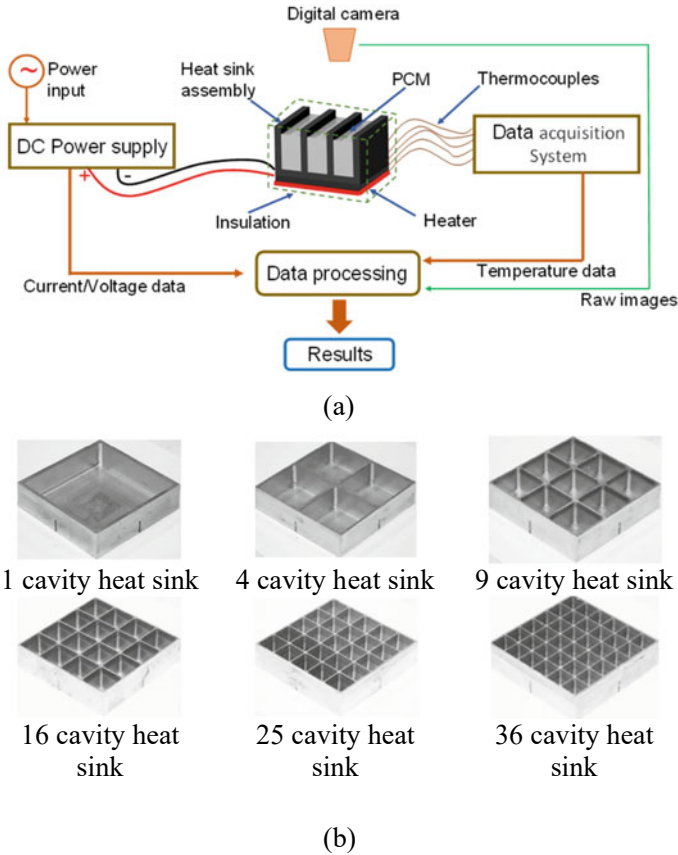


Fig. 1 a Test rig, b cross-finned heat sinks

The instruments uncertainty is as follows: temperature $\pm 0.3\text{ }^\circ\text{C}$, voltage $\pm 0.1\text{ V}$, current $\pm 0.1\text{ A}$ and input heat flux $\pm 4.12\%$. The dimensions of the heat sink configurations are tabulated in Table 1. The selection of the phase change material can be based on the targeted operating range of the device which needs thermal management solution. It is essential that the phase transition temperature of the phase change material should be below the critical operating temperature of the electronic device. Other important properties include high specific heat and latent heat, chemical and thermal stability with negligible sub-cooling effect. In the present investigation, paraffin wax (make: Sigma-Aldrich, USA) whose melting point lies between $53\text{--}58\text{ }^\circ\text{C}$ has been used. The peak summer temperature in India can reach up to $45\text{--}48\text{ }^\circ\text{C}$ and hence a lower melting range of PCM might not be useful in some geographical regions. Al_2O_3 (APS: $30\text{--}50\text{ nm}$) and CuO (APS: $30\text{--}50\text{ nm}$) nanoparticles with purity of 99.9% are purchased from Nano-labs India.

Table 1 Dimensions of the heat sink

Cavity	t_{base}	t_{wall}	t_{fin}	Cavity dimensions
1	2 mm	3 mm	–	$93 \times 93 \times 23$
4		2 mm	3 mm	$46.5 \times 46.5 \times 23$
9			1.5 mm	$31 \times 31 \times 23$
16			1 mm	$23.25 \times 23.25 \times 23$
25			0.75 mm	$18.6 \times 18.6 \times 23$
36			0.60 mm	$15.5 \times 15.5 \times 23$

Table 2 Thermophysical properties [11–13, 17]

Material	Density	Specific heat	Latent heat	Viscosity	Thermal conductivity
Aluminium	2719	0.896	–	–	218
PCM (paraffin wax, M. P. 53–58 °C)	900	2.2	200	0.0235	0.18
CuO	6300	0.55	–	–	33
Al ₂ O ₃	3500	0.76	–	–	36

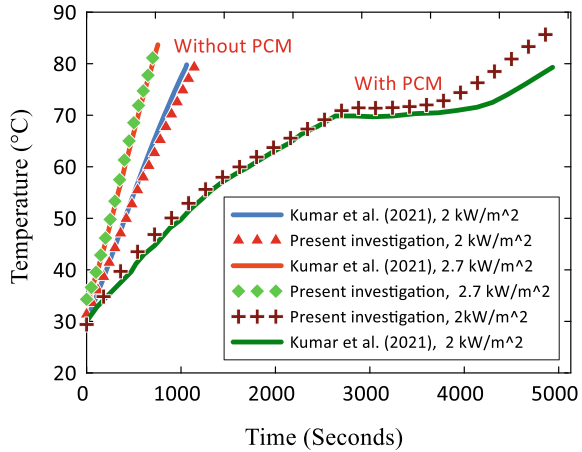
The main thermophysical properties are tabulated in Table 2. The preparation methodology of NePCM is as follows: at first, using a digital weighing machine, the amount of solid PCM and nanoparticles is determined. PCM and nanoparticles are weighed, and then the PCM is melted using the hot plate. Nanoparticles are gradually mixed with melted paraffin wax while being agitated on a magnetic stirrer (REMI, 2MLH, India) for one hour at 500 RPM and then sonicated for about 1 h using a probe type sonicator (make: Athena 950 W, India) to ensure uniform distribution of the particles. It should be noted that the amount of the PCM/NePCM is kept same in all the heat sinks to evaluate the comparative performance. The PCM/NePCM-based HS assembly is then fixed with thermocouples in the necessary locations before allowing the material to solidify. At the bottom of the HS, the plate heater is fixed. Using Ohm's law to manage the current and voltage, heat flux is delivered from the DC source. For all situations, the HS is maintained in a horizontal position throughout the testing.

4 Results and Discussion

4.1 Set-Up Validation and Effect of PCM

The validation of the test set-up is employed using the earlier research carried out by Kumar et al. [11, 12] in the same test facility. As can be seen in Fig. 2, the results from the current experiments have been compared with both with and without phase change

Fig. 2 Validation of the test set-up



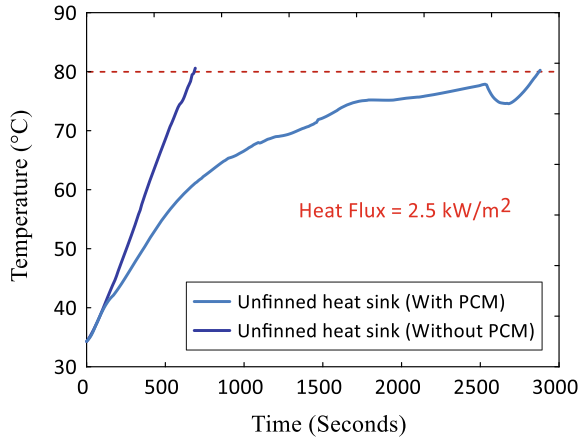
materials in the heat sink. For validation experiments the paraffin wax (make: sigma Aldrich, melting range 58–62 °C) was used with input heat flux range of 2–2.7 kW/m².

The average deviation of present investigation remains below 10%. The analysis findings reveal a pattern that resembles that seen in other studies on heat sinks of a comparable size [11–13]. To clearly distinguish the effect of using PCM, a comparative result has been presented in Fig. 3. Figure 3 compares the performance of unfinned heat sink with/without PCM for an input heat flux of 2.5 kW/m². For a critical temperature of 80 °C, the working time with the heat sink saturated with PCM is much longer than without PCM. The high latent heat of the PCM assists in absorbing significant amount of heat from the heat sink thus maintaining its temperature lower for a longer duration of time. The time to reach the critical temperature for without PCM and with PCM is about 740 and 2820 s, respectively, which is more than 250% enhancement in working time with the heat sink.

4.2 Effect of Concentration of Nanoparticles on Thermal Performance of Different Heat Sinks

In this section, the effect of concentration of nanoparticles on the thermal performance of different heat sinks has been discussed. As discussed earlier, a heat flux of 2.5 kW/m² is used to conduct the experiments. Figure 4a–f illustrates the transient temperature–time behaviour of unfinned heat sink, 1 cavity heat sink, 4 cavity heat sink, 9 cavity heat sink, 16 cavity heat sink, 25 cavity heat sink and 36 cavity heat sink. The average temperature of the bottom of the heat sinks have been presented in all the figures. For unfinned heat sink, it can be seen that the maximum operating

Fig. 3 Heat sink performance with/without PCM



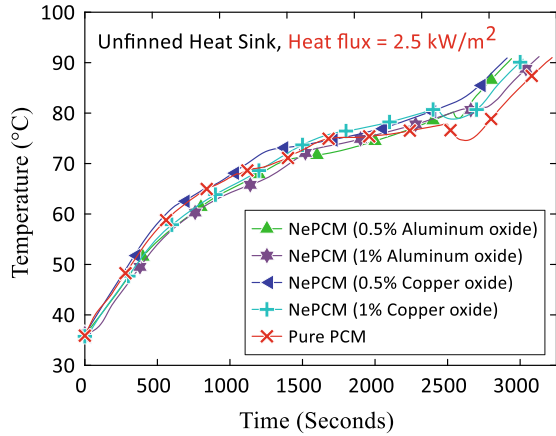
time is reported by pure PCM followed by 1% Al_2O_3 , 1% CuO , 0.5% Al_2O_3 and 0.5% CuO .

The time to reach the critical temperature of 90 °C in the same order is 3220, 3120, 3020, 2940 and 2910 s. In the case of 4 cavity heat sink (Fig. 4b), all the different NePCM and PCM take nearly the same time to reach the targeted temperature. No significant difference can be seen after 2500 s. The time to reach 90 °C in this case is 3170, 3160, 3130, 3120 and 3110 s. Clearly, the performance of this heat sink is not significantly affected by combination of nanoparticles in the phase change material. For the case of 9 cavity heat sink, the best performance is observed by pure PCM followed by 1% CuO , 0.5% Al_2O_3 , 1% Al_2O_3 and 0.5% CuO . The result can be seen in Fig. 4c.

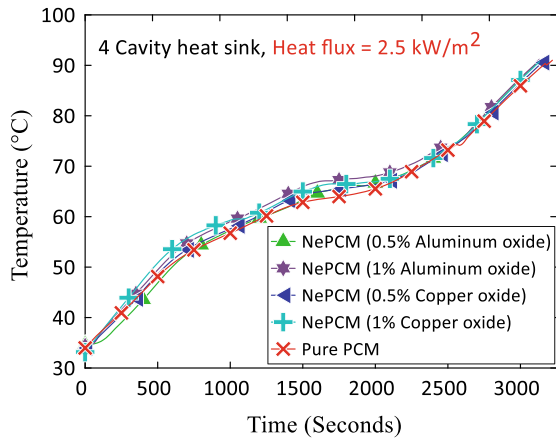
Using Fig. 4d–e, it can be seen that for 16 and 25 cavity heat sinks, the best performance is obtained by using 1% Al_2O_3 and pure PCM and the shortest time is reported by NePCM having 0.5% Al_2O_3 and rest of the NePCMs follow a similar trend. The 36 cavity heat sinks report the best performance by pure PCM followed by 1% CuO and rest of the NePCMs depict similar behaviour.

The PCM embedded with nanoparticles may not be useful in every scenario, but the performance depends significantly on the heat sink type. As the number of fins increases, the heat conduction path increases. This also increases the effective thermal conductivity of the composite PCM. This delay in reaching a certain set point temperature is also due to more uniform melting in heat sinks with fins which helps in better management of temperature.

Fig. 4 **a** Performance of unfinned HS, **b** performance of 4 cavity HS, **c** performance of 9 cavity HS, **d** Performance of 16 cavity HS, **e** performance of 25 cavity HS, **f** performance of 36 cavity HS



(a)



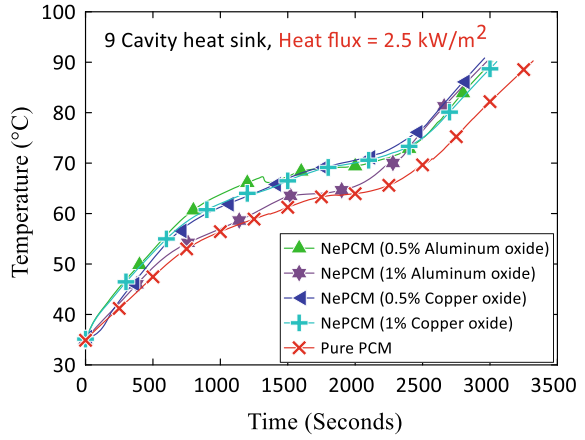
(b)

4.3 Effect of Heat Sink Arrangement on Thermal Performance of PCM/NePCM

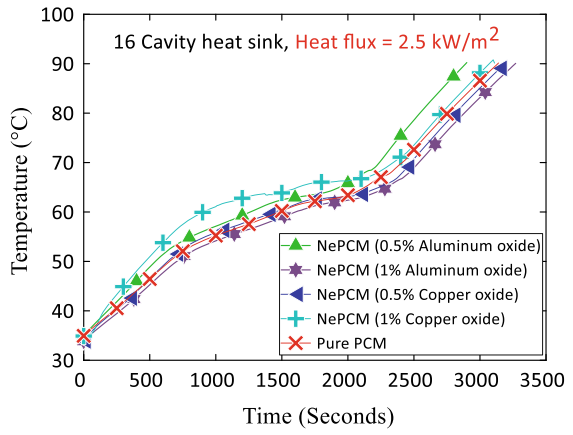
Here, the results are presented by comparing the performance of all the type of heat sinks for each type of NePCM and pure PCM individually. Figure 5a depicts the thermal performance analysis of all the heat sinks for the case of pure PCM. It can be seen that the time to reach the set point temperature increases as the number of fins increases.

The average base temperature remains highest in the case of pure PCM and lowest in the case of 36 cavity heat sink. Clearly, addition of fins has a significant impact on the thermal performance of the heat sink. In the case of NePCM having 0.5% CuO,

Fig. 4 (continued)

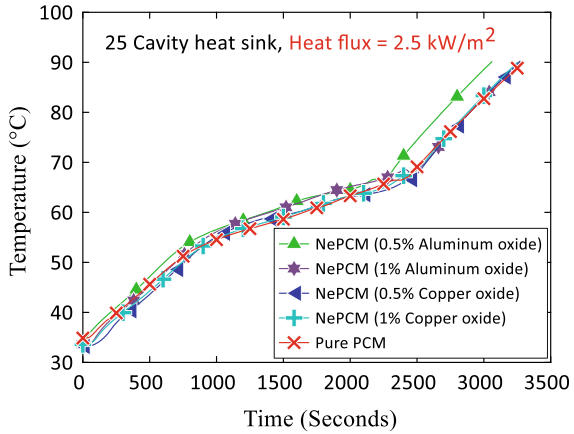


(c)

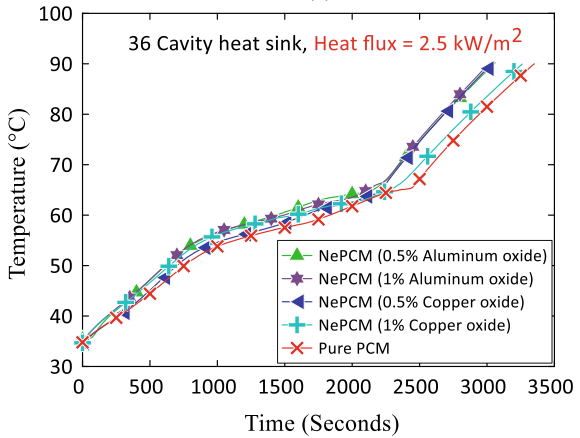


(d)

Fig. 4 (continued)



(e)

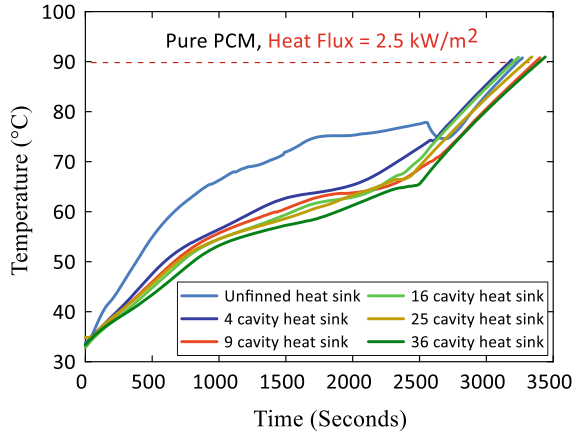


(f)

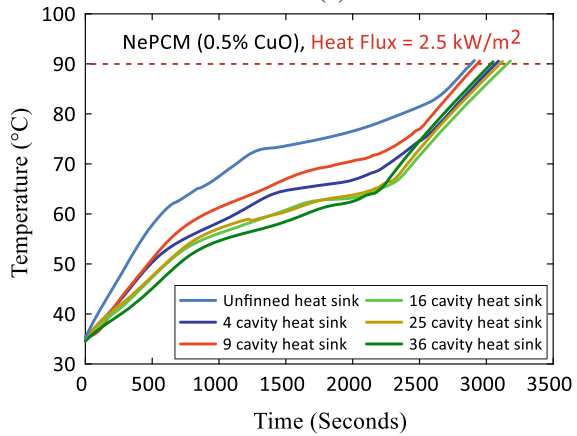
the similar trend is observed as in previous case. The lowest temperature is obtained for highest number of fins and highest in the case of unfinned heat sink. However, it should be noted that the time to reach the targeted temperature of 90 °C is lower in the present case when compared with the case of pure PCM. This is because of the enhanced thermal conductivity of the PCM due to the presence of CuO particles.

For the case of 0.5% Al₂O₃, there is no significant difference in the performance of heat sinks except for unfinned and 16 cavity heat sink. Surprisingly, the same trend is not observed in the present case. The best performance is reported by 16 cavity heat sink for the case of 1% Al₂O₃ (as can be seen in Fig. 5d). The results for NePCM 1% CuO have been presented in Fig. 5e. The lowest average temperature is reported for the case of 36 cavity heat sink and the highest for unfinned heat sink. It should be noted that the time to reach the set point temperature increases as the concentration of the nanoparticles increases, i.e. irrespective of the heat sink,

Fig. 5 a: Performance of pure PCM, **b** performance of NePCM (0.5% CuO), **c** performance of NePCM (0.5% Al₂O₃), **d** performance of NePCM (1% Al₂O₃), **e** performance of NePCM (1% CuO)



(a)



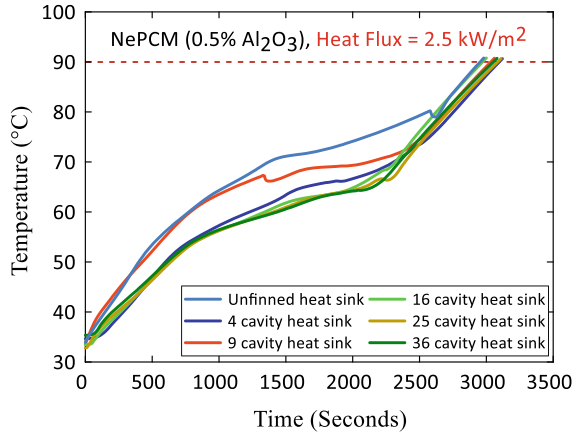
(b)

the addition of nanoparticles increases the time to reach the set point temperature. However, in some of the cases, a general conclusion cannot be made because the thermal performance of various NePCMs vary with different heat sinks.

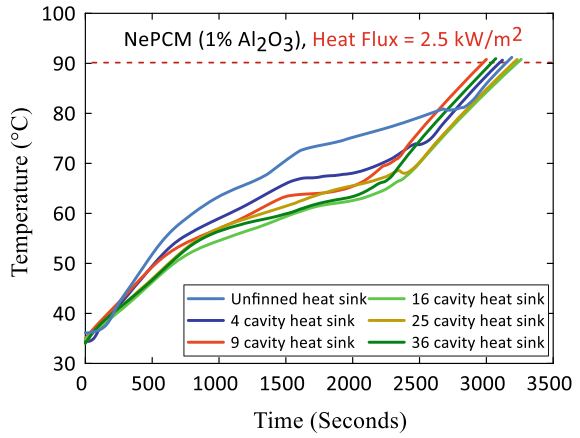
5 Conclusions

The present study reported the thermal performance of PCM/NePCM based on CuO and Al₂O₃ nanoparticles. Six different heat sinks for a constant heat flux input of 2.5 kW/m² have been taken to carry out all the experiments. PCM-based HS extends the duration of operation, resulting in a lower HS base temperature than an empty HS. The following conclusions are made from this experimental investigation:

Fig. 5 (continued)

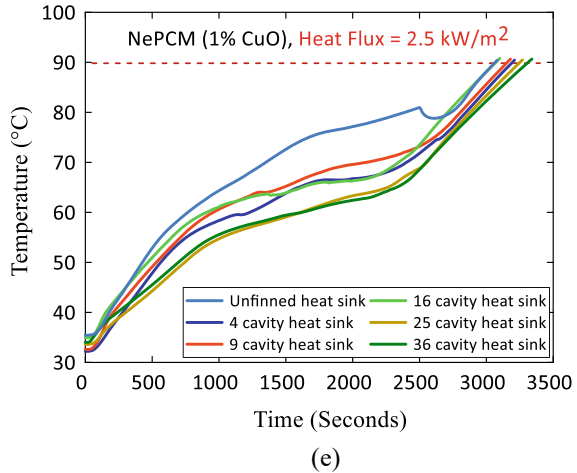


(c)



(d)

Fig. 5 (continued)



- For pure PCM, the best performance is obtained by 36 cavity heat sink and least by unfinned heat sink.
- It is observed that as the concentration of nanoparticles increases, the thermal performance increases.
- HS with a greater number of fins performs better for less nanoparticle concentration and HS with less number of fins for higher concentration.
- For 0.5% CuO, nearly comparable maximum operating time is reported by 4×4 , 5×5 and 6×6 heat sinks, while for 1% CuO 6×6 outperforms other heat sink configuration.
- For 0.5% Al_2O_3 , the maximum time to reach the critical temperature is reported from 3×3 heat sink followed by 2×2 , 5×5 and 6×6 configurations of heat sink.
- The overall best performance is achieved by 6×6 , i.e. 36 cavity heat sink using pure PCM followed by 1% Al_2O_3 . However, the operating time for both the cases is closer.

The present research demonstrates the combined use of cross-fins and nanoparticles for management applications. It is observed that the addition of nanoparticles in combinations with fins may not always improve the thermal performance. Therefore, a trade-off analysis needs to be performed between the number of fins and concentration of nanoparticles to get the maximum performance.

Acknowledgements The first author would like to thank and acknowledge the research grant from Prime Minister's Research Fellowship (PMRF), Govt. of India.

Nomenclature

PCM	Phase change material
NePCM	Nano-enhanced phase change material
SPT	Set point temperature
HS	Heat sink
APS	Average particle size (nm)
TCE	Thermal conductivity enhancer
q''	Heat flux (kW/m ²)
ΔT	Temperature difference (°C)

References

1. Kim TY, Hyun BS, Lee JJ, Rhee J (2013) Numerical study of the spacecraft thermal control hardware combining solid-liquid phase change material and a heat pipe. *Aerosp Sci Technol* 27(1):10–16. <https://doi.org/10.1016/J.AST.2012.05.007>
2. Sarier N, Onder E (2012) Organic phase change materials and their textile applications: an overview. *Thermochim Acta* 540:7–60. <https://doi.org/10.1016/J.TCA.2012.04.013>
3. Demirbağ S, Aksoy SA (2016) Encapsulation of phase change materials by complex coacervation to improve thermal performances and flame retardant properties of the cotton fabrics. *Fibers Polymers* 17(3):408–417. <https://doi.org/10.1007/S12221-016-5113-Z>
4. Lv Y, Zou Y, Yang L (2011) Feasibility study for thermal protection by microencapsulated phase change micro/nanoparticles during cryosurgery. *Chem Eng Sci* 66(17):3941–3953. <https://doi.org/10.1016/J.CES.2011.05.031>
5. Sebzali MJ, Rubini PA (2007) The impact of using chilled water storage systems on the performance of air cooled chillers in Kuwait. *Energy Build* 39(8):975–984. <https://doi.org/10.1016/J.ENBUILD.2006.11.004>
6. Kandasamy R, Wang XQ, Mujumdar AS (2007) Application of phase change materials in thermal management of electronics. *Appl Therm Eng* 27(17–18):2822–2832. <https://doi.org/10.1016/J.APPLTHERMALENG.2006.12.013>
7. Fang X, Zhang Z, Chen Z (2008) Study on preparation of montmorillonite-based composite phase change materials and their applications in thermal storage building materials. *Energy Convers Manage* 49(4):718–723. <https://doi.org/10.1016/J.ENCONMAN.2007.07.031>
8. Li M, Kao H, Wu Z, Tan J (2011) Study on preparation and thermal property of binary fatty acid and the binary fatty acids/diatomite composite phase change materials. *Appl Energy* 88(5):1606–1612. <https://doi.org/10.1016/J.APENERGY.2010.11.001>
9. Abhat (1983) Low temperature latent heat thermal energy storage: heat storage materials. *Solar Energy* 30(4):313–332. [https://doi.org/10.1016/0038-092X\(83\)90186-X](https://doi.org/10.1016/0038-092X(83)90186-X)
10. Kothari R, Sahu SK, Kundalwal SI, Mahalkar P (2021) Thermal performance of phase change material-based heat sink for passive cooling of electronic components: an experimental study. *Int J Energy Res* 45(4):5939–5963. <https://doi.org/10.1002/er.6215>
11. Kothari KR, Sahu SK, Kundalwal SI (2021) A comparative study and optimization of phase change material based heat sinks for thermal management of electronic components. *J Energy Storage* 43. <https://doi.org/10.1016/j.est.2021.103224>
12. Kumar A, Kothari R, Sahu SK, Kundalwal SI (2021) Thermal performance of heat sink using nano-enhanced phase change material (NePCM) for cooling of electronic components. *Microelectronics Reliability* 121. <https://doi.org/10.1016/j.microrel.2021.114144>

13. Kothari R, Sahu SK, Kundalwal SI (2021) Investigation on thermal characteristics of nano enhanced phase change material based finned and unfinned heat sinks for thermal management system. *Chem Eng Process* 162. <https://doi.org/10.1016/j.cep.2021.108328>
14. Hosseinirad E, Khoshvaght-Aliabadi M (2021) Proximity effects of straight and wavy fins and their interruptions on performance of heat sinks utilized in battery thermal management. *Int J Heat Mass Transf* 173. <https://doi.org/10.1016/j.ijheatmasstransfer.2021.121259>
15. Ushak GS, Galleguillos H, Fernandez A, Cabeza LF, Grágeda M (2015) Use of polyethylene glycol for the improvement of the cycling stability of bischofite as thermal energy storage material. *Appl Energy* 154:616–621. <https://doi.org/10.1016/j.apenergy.2015.05.040>
16. Sahoo SK, Rath P, Das MK (2016) Numerical study of phase change material based orthotropic heat sink for thermal management of electronics components. *Int J Heat Mass Transf*. <https://doi.org/10.1016/j.ijheatmasstransfer.2016.07.063>
17. Serrano A, Duran M, Dauvergne JL, Doppiu S, Del Barrio EP (2021) Tailored transition temperature plastic crystals with enhanced thermal energy storage capacity. *Solar Energy Mater Solar Cells* 220:110848. <https://doi.org/10.1016/j.solmat.2020.110848>

Numerical Investigation on Performance of CPU Heat Sinks



Vedant Kanate, Arjun Pardeshi, Falguni Charde, Krushna Kolase, Adinath Bhise, and Pramod Kothmire

1 Introduction

A heat sink is a heat dissipation tool with an outwardly extending base of fins. Air velocity, material selection, fin design, and surface treatment are just a few examples of the variables that affect heat sink performance. When a cheap heat-generating device is in use, a heat sink removes and distributes the heat to maintain the chip's ideal operating temperature. Convection, radiation, and conduction are the three modes of transport. The flow removes the heat by changing the enthalpy across the surface once the heat enters the fins. The entire system may be destroyed if the inexpensive overheated without the use of a heat sink. Due to its high thermal conductivity and ease of machining, aluminum is the most often used material for heat sinks. Heat sinks are used widely in many different industries to cool components, not just computers.

Three mathematically constructed heat sinks with lattice topology were the subject of an experimental and numerical study on forced convection heat transfer in [1] Mohammad Khalil. In [2], the topology optimization method is used in the bionic domain to create two topological heat sinks with two different goals in mind in order to enhance the thermal performance of heat sinks. One objective is to minimize the temperature difference and pressure drop, another is to minimize the average temperature and pressure drop. CFD analysis of hot spots in copper metal foam flat heat pipes for electronic cooling applications was done by Brahim and Jemni [3], and the results suggest that the locations of hotspots closest to walls are the most crucial. Alam [4] conducted a numerical analysis on CPU heat sink cooling using micro-pin fins with a triangular shape. At various Re , the pressure coefficient and heat transmission were measured. The investigation came to the conclusion that an increase in air flow velocity improves heat extraction from CPUs by raising the

V. Kanate (✉) · A. Pardeshi · F. Charde · K. Kolase · A. Bhise · P. Kothmire
School of Mechanical Engineering, MIT Academy of Engineering, Alandi Pune 412105, India
e-mail: vkkanate@mitaoe.ac.in

Nusselt number. The numerical analysis of a phase change material (PCM)-based heat sink with internal fins was presented by Shatikian in [5]. The fins' thickness here ranges from 0.5 to 4 mm. The fin-to-PCM layer ratio is maintained constant. The base's temperature fluctuates from 60 to 240 °C over the PCM's mean melting point. Carbajal's [6] quasi-three-dimensional investigation of the thermal performance of a flat heat pipe revealed that it successfully distributed heat evenly on the structure's condenser side.

2 Literature Review and Objective

Hosseinizadeh et al. [7] compared heat sinks with and without PCM in the paper [7]: Experimental and Numerical Study on Performance of PCM-based Heat Sink with Different Configuration of Internal Fins, and came to the conclusion that while increasing fin thickness only slightly improves PCM melting rate and increasing power input has the opposite effect. Koito et al. [8] Shuichi Torii performed a numerical analysis on a flat plate type heat pipe known as a "vapor chamber" in order to experimentally verify thermal fluid phenomena in the chamber. Here, the temperature decrease inside the vapor chamber is calculated and the capillary pressure head required to circulate the working fluid is estimated.

Irshadrshad et al. [9] contrasts a heat sink's use of phase transition material (PCM). Power levels, the number of fins, fin height, and fin thickness are all taken into consideration. The increase in fin height and number, according to the results, demonstrates an improvement in thermal performance as a whole. The rate at which the PCM melted increased as power levels rose. El Ghandouri et al. [10] performs a numerical analysis of the corrugated fin-based heat transfer and cooling of a heat-generating vertical base.

Corrugated fins are used in a numerical assessment of the heat dissipation and cooling of a heat-generating vertical base. The outcomes demonstrate that the finned heat sinks that have been suggested can increase the heat transfer coefficient. Additionally, the system's overall thermal performance was enhanced.

The majority of the aforementioned articles concentrate on determining the pressure coefficients when Reynold's numbers are changed, however, most of them use specific geometry hotspots rather than the complete geometry to perform the analysis. Some publications only discuss the layout and spacing of the fins.

The scope of the current study is a numerical and experimental study on the effect of fin arrangement on:

1. Temperature drop.
2. Average heat flux.
3. Average heat transfer coefficient.

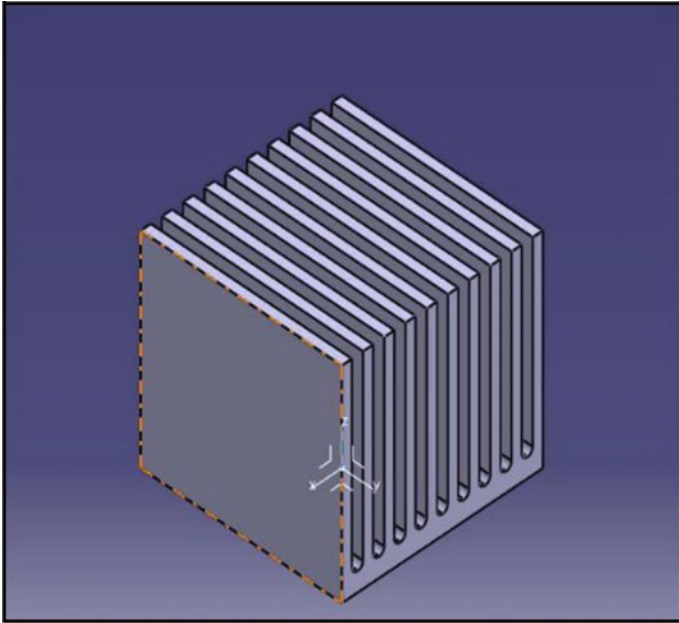


Fig. 1 Conventional fin arrangement

3 Materials and Methods

3.1 Geometry

The geometries are modeled in CATIA V5. Three different geometries were created. The base dimensions for all the geometries are standard, i.e., 37.5X37.5. Figures 1, 2 and 3 show the three different geometries.

3.2 Meshing and Material

Meshing is done in Ansys 19.2. The size of the mesh is 0.7 mm as shown in Fig. 4. A mesh independence study is carried out between temperature drop vs mesh size and minimum temperature vs mesh size. The results for the same are displayed in Fig. 5. The mesh independence study shows that the temperature drop around the fins first increases with a decrease in mesh size to size 1.5 mm, decreases till size 1 mm, and later increases till size 0.7 mm and then stays constant.

It also shows that the minimum temperature decreases with a decrease in mesh size to size 1.5 mm, increases to 1 mm, and later decreases again to 0.7 mm and then remains constant. The material used for designing the heat sink is aluminum since

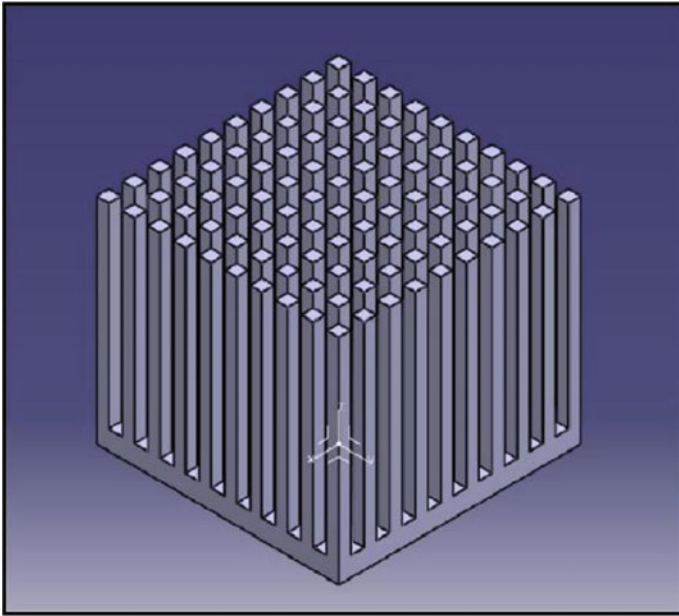


Fig. 2 Split fin arrangement

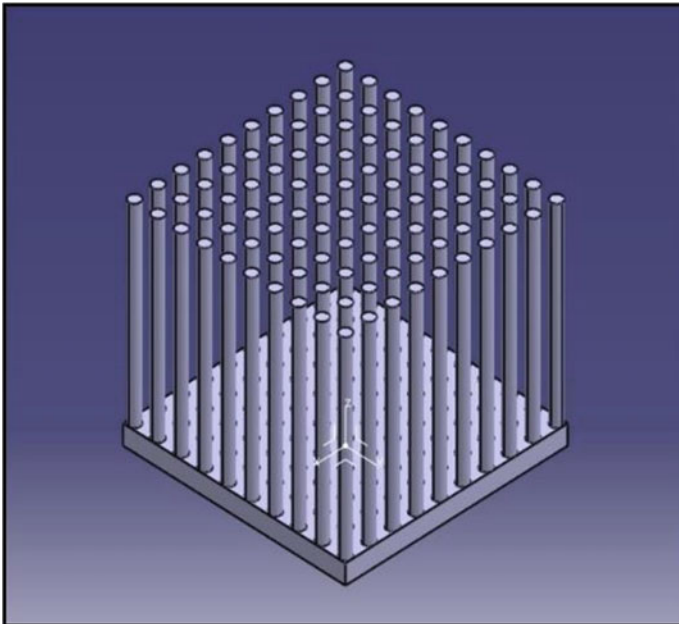


Fig. 3 Pin fin arrangement

Fig. 4 Mesh of conventional fin geometry

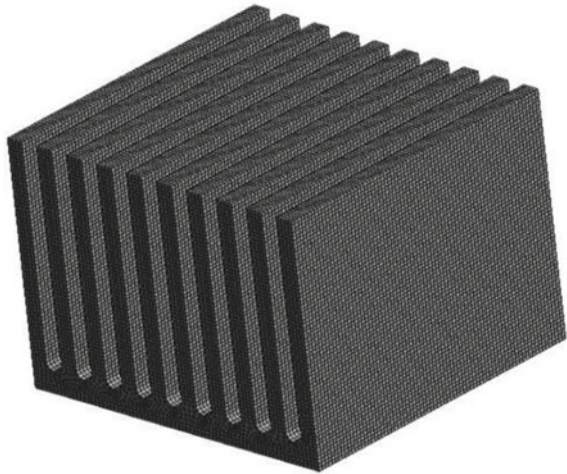
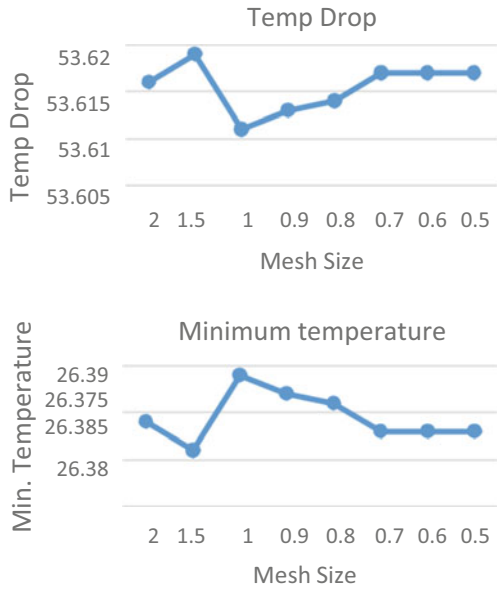


Fig. 5 Mesh independence study between mesh size and temperature drop



the material has good machinability, good thermal conductivity, is cheaper than other materials like copper, and is light in weight.

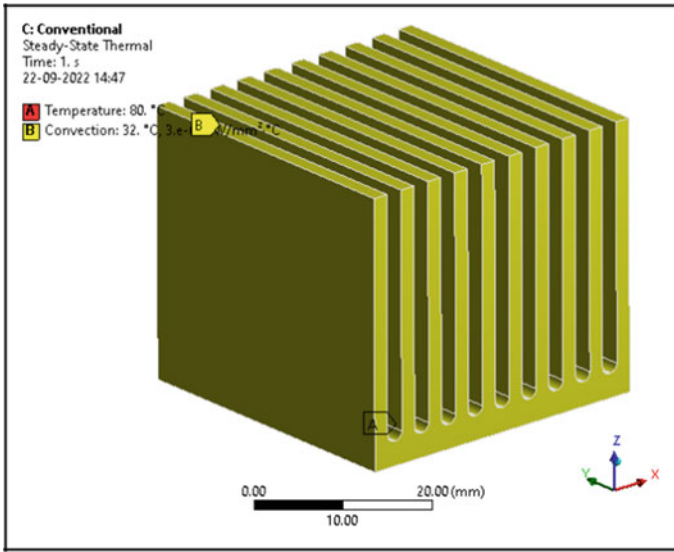


Fig. 6 Boundary conditions for conventional fin

3.3 *Boundary Conditions*

CPU heat sinks absorb heat from the CPU and transfer it to the surrounding, hence keeping the CPU cool and decreasing the chances of thermal throttling. As the CPU is the source of the heat, it is located at the base of the heat sink.

As shown in Figs. 6, 7 and 8, the base of the heat sink is given a temperature of 80 °C, while keeping the ambient temperature to be 32 °C. The other surfaces of the heat sink body are given the convective film coefficient of $3.0 \times 10^{-4} \text{ W/m}^2 \text{ } ^\circ\text{C}$.

3.4 *Output Parameters*

All the input parameters shown in boundary conditions and the output parameters obtained from the analysis are displayed in Fig. 9. For calculating the total heat transfer coefficient, the required parameters that are extracted from the analysis are average temperature and average total heat flux.

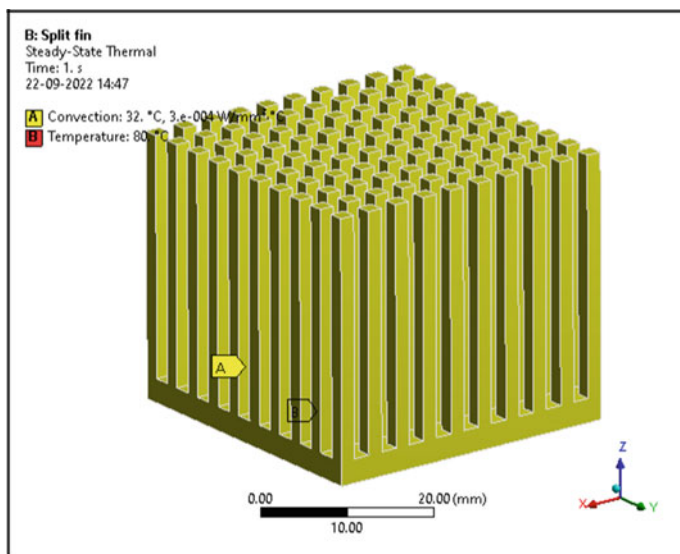


Fig. 7 Boundary conditions for split fin

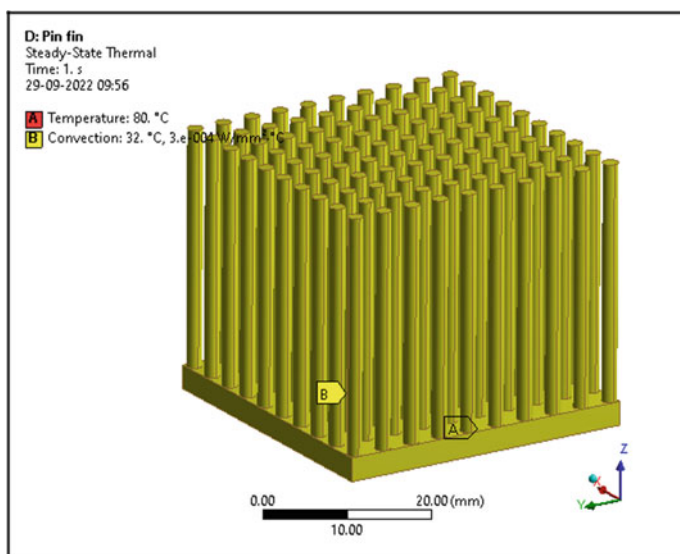


Fig. 8 Boundary conditions for pin fin

Outline of All Parameters				
	A	B	C	D
1	ID	Parameter Name	Value	Unit
2	[-] Input Parameters			
3	[-] Split fin (B1)			
4	P7	Convection Film Coefficient	0.0003	W mm ⁻² C ⁻¹
5	P8	Convection Ambient Temperature	32	C
6	P9	Temperature Magnitude	80	C
*	New input parameter	New name	New expression	
8	[+] Output Parameters			
9	[-] Split fin (B1)			
10	P1	Temperature Average	57.652	C
11	P2	Total Heat Flux Average	0.1644	W mm ⁻²
12	[-] Conventional fin (C1)			
13	P3	Temperature Average	63.346	C
14	P4	Total Heat Flux Average	0.13217	W mm ⁻²
15	[+] Pin fin (D1)			
16	P5	Temperature Average	56.811	C
17	P6	Total Heat Flux Average	0.16259	W mm ⁻²
*	New output parameter		New expression	
19	Charts			

Fig. 9 Output parameters

4 Results and Discussion

Average heat flux is obtained from the steady-state thermal analysis. Figure 10 depicts the total heat flux for conventional fins setup. Figure 11 depicts the total heat flux for the split fins setup. Figure 12 depicts the total heat flux for the pin fins setup.

To claim the most effective geometry of heat sink, the parameter required is the average heat transfer coefficient. Average heat transfer can be calculated from average heat flux and temperature difference.

For conventional fin geometry, the heat transfer coefficient is 4216.487 W/m² °C.

For split fin geometry, the heat transfer coefficient is 6408.857 W/m² °C.

For pin fin geometry, the heat transfer coefficient is 6553.405 W/m² °C.

This shows that:

$$pin_{fin} > split_{fin} > conventional_{fin}.$$

According to the study, the above comparison also shows the effectiveness of the fins in the respective orders. To validate the effectiveness of fins, a temperature drop should be obtained. The more the temperature drop, the more will be the effectiveness of the heat sink.

Figure 13 shows the temperature drop in the conventional fin is 28.1 °C. Figure 14 shows the temperature drop in the split fin is 35.6 °C. Figure 15 shows the temperature drop in the pin fin is 35.8 °C.

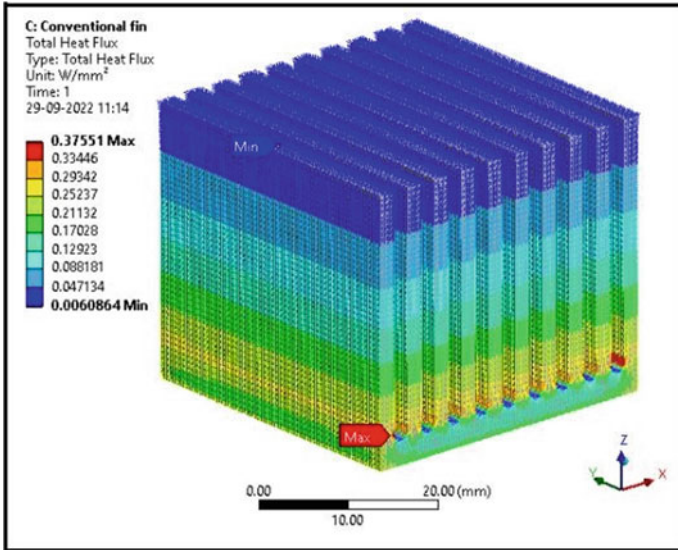


Fig. 10 Heat flux contour for conventional fin

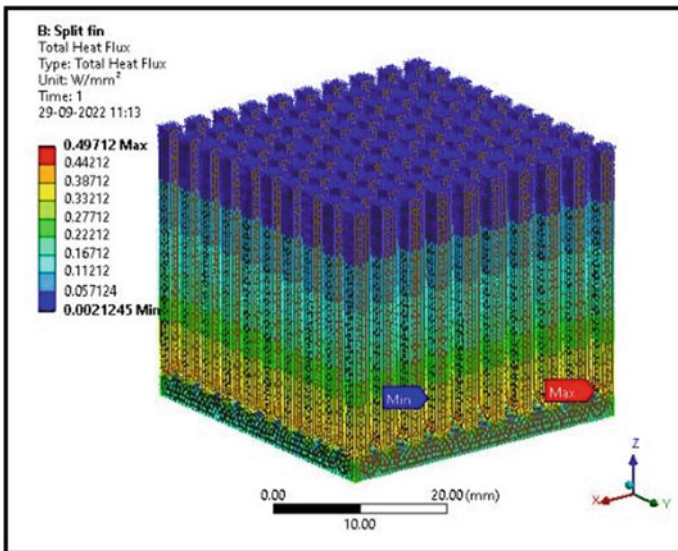


Fig. 11 Heat flux contour for split fin

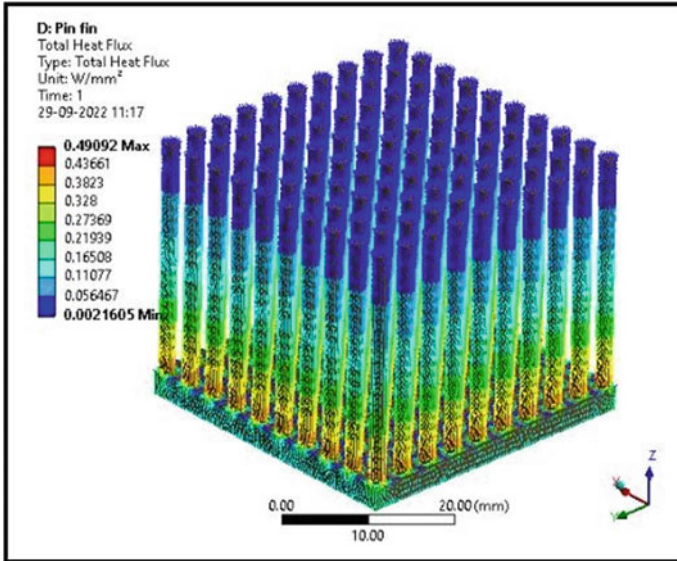


Fig. 12 Heat flux contour for pin fin

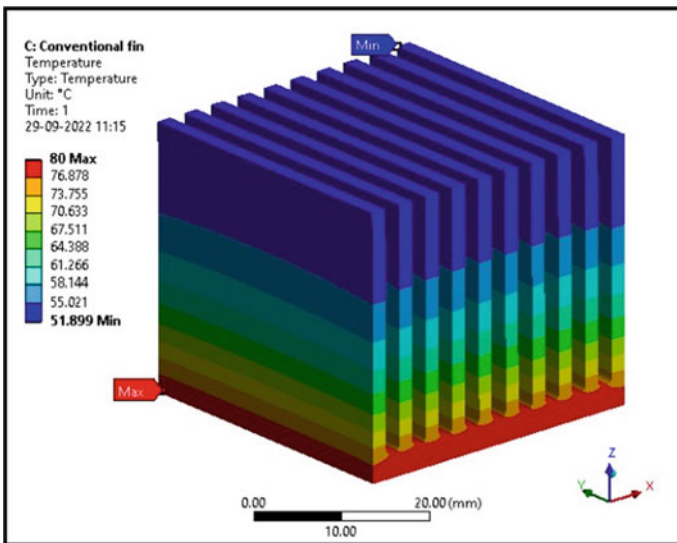


Fig. 13 Temperature contour for conventional fin

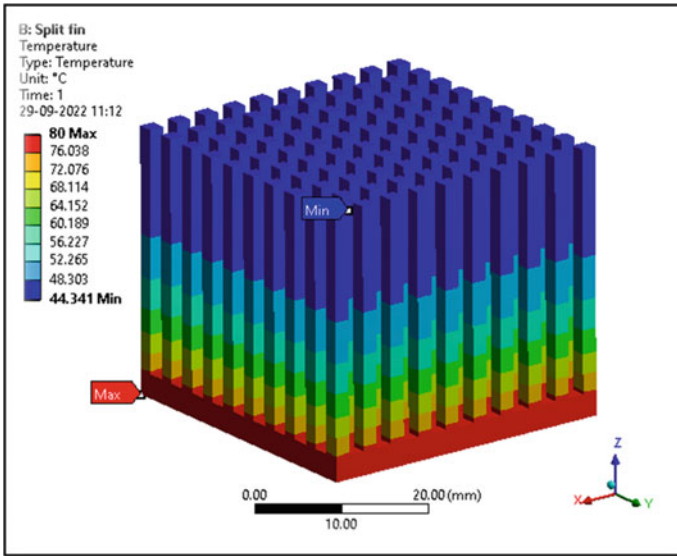


Fig. 14 Temperature contour for split fin

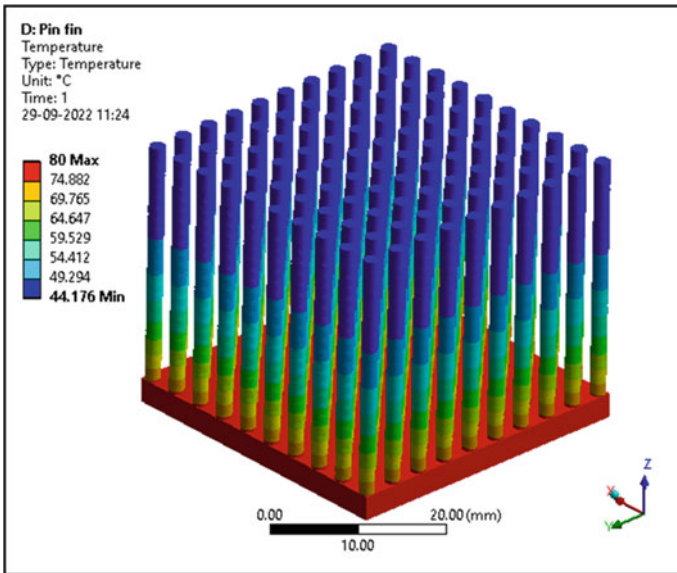


Fig. 15 Temperature contour for pin fin

The higher the temperature drop the more is the cooling. From the above discussion, the relation between the temperature drop obtained is:

$$T_{\text{pin fin}} > T_{\text{split fin}} > T_{\text{conventional fin}}$$

Hence, the results obtained are validated.

5 Conclusions

From this study, it can be concluded that the most effective fin arrangement for the CPU heat sink is the pin fin with a heat transfer coefficient being $6553.405 \text{ W/m}^2 \text{ }^\circ\text{C}$ and portraying a temperature drop of $35.8 \text{ }^\circ\text{C}$.

References

1. Khalil M et al (2022) Forced convection heat transfer in heat sinks with topologies based on triply periodic minimal surfaces. *Case Stud Therm Eng* 38:102313
2. Han XH et al (2021) Topology optimization for spider web heat sinks for electronic cooling. *Appl Therm Eng* 195:117154
3. Brahim T, Jemni A (2021) CFD analysis of hotspots copper metal foam flat heat pipe for electronic cooling applications. *Int J Therm Sci* 159:106583
4. Alam MW et al (2020) CPU heat sink cooling by triangular shape micro-pin-fin: numerical study. *Int Commun Heat Mass Transf* 112:104455
5. Shatikian V, Ziskind G, Letan R (2005) Numerical investigation of a PCM-based heat sink with internal fins. *Int J Heat Mass Transf* 48(17):3689–3706
6. Carbajal G et al (2007) A quasi-3D analysis of the thermal performance of a flat heat pipe. *Int J Heat Mass Transf* 50(21–22):4286–4296
7. Hosseinizadeh SF, Tan FL, Moosania SM (2011) Experimental and numerical studies on the performance of PCM-based heat sink with different configurations of internal fins. *Appl Therm Eng* 31(17–18):3827–3838
8. Koito Y et al (2006) Numerical analysis and experimental verification on thermal fluid phenomena in a vapor chamber. *Appl Therm Eng* 26(14–15):1669–1676
9. Irshadrshad A et al (2017) Thermal performance of phase change material (PCM) based pin-finned heat sinks for electronics devices: effect of pin thickness and PCM volume fraction. *Appl Therm Eng* 112:143–155
10. El Ghandouri I et al (2021) Thermal performance of a corrugated heat dissipation fin design: a natural convection numerical analysis. *Int J Heat Mass Transf* 180:121763

Modelling of Phase Change Material Embedded Li-Ion Battery Pack Under Different Load Conditions Using Equivalent Circuit Model



Mazhar Hussain, Mohd. Kaleem Khan, and Manabendra Pathak

1 Introduction

The soaring increase in greenhouse gas (GHG) emissions has turned the world on the verge of a climate crisis. The fossil fuel-driven automobile sector is a significant contributor to pollutants, so transformation for a greener future is essential. Electric vehicles (EVs) and hybrid electric vehicles (HEVs) are the most promising alternatives for a de-carbonized grid. The market cap size for EVs and HEVs is exponential in many nations. But, they are yet to pass the litmus tests posed by EV fires, range anxiety, charging time, and de-carbonized grid. Li-ion batteries are the prominent ones that propel EVs and HEVs. These secondary batteries have an advantage compared to their contemporaries due to their low self-discharge, no memory effect, low weight, and higher energy density. But these are susceptible to the operating temperature. The optimal temperature range for the proper functioning of the battery pack is -20 to 40 °C, and the temperature uniformity should be less than 5 °C [1]. The rise in temperatures of the battery pack over 80 °C can lead to uncontrolled exothermic chain reactions and cause fire or explosion [2]. This phenomenon is referred to as thermal runaway, the prominent reason for EV fires [3]. To restrict such catastrophic conditions, thermal analysis of the battery pack is essential, done by coupling an accurate battery model with a cooling system.

M. Hussain (✉) · Mohd. K. Khan · M. Pathak
Sustainable Energy Research Laboratory, Department of Mechanical Engineering, Indian Institute of Technology Patna, Patna 801106, India
e-mail: mazhar_2121me25@iitp.ac.in

2 Literature Review and Objective

Battery modelling is complex as a battery is a non-linear electrochemical device. Multiple coupled equations are required to address the electrochemical behaviour, which relates chemical parameters like diffusion and ion concentration to electrical and thermal parameters like voltage, current, and temperature. Fundamental modelling requires a lot of battery parameters which need state of the art facility to obtain them [4]. So, researchers have worked on building simple and accurate models with low computational costs. Electrochemical, multi-scale multi-dimensional models are prominently used for thermal analysis of the battery, later being simple and faster in computation time [5].

The dual potential multi-scale multi-dimensional (MSMD) model framework is considered in this present study. Further, MSMD has three sub-models, such as Newman, Tiedemann, Gu, and Kim (NTGK), equivalent circuit model (ECM), and pseudo-two-dimensional (P2D) models. In the literature, researchers have applied these models according to the problem statement. For stable charge–discharge conditions with low parametrical input, NTGK model is preferred. ECM is selected for varying compound cycles with fluctuating charge–discharge conditions. The P2D model is a more fundamental model analysing the internal characteristics of the battery. In this study, ECM is selected as the considered battery pack is subjected to static and dynamic conditions. The ECM has lower computational costs, but this is thermal-electrochemically not coupled as it does not solve the Arrhenius equation [6]. According to the vehicle's range and power capability, many cooling systems are used in the market. Prominent being indirect liquid and forced-air cooling [7]. Other cooling techniques like immersion, passive methods such as heat pipe, and phase change materials (PCMs) are widely researched [8]. The liquid cooling system is not a great option for low-range vehicles because additional accessories added in confined space lead to extra weight and higher parasitic loss from the battery pack. So, the PCMs can be the best alternative as they are economical and can be retrofitted easily with existing battery pack enclosures.

In the literature, the researchers have worked predominantly on PCM-based cooling by considering the battery as a constant heat generation source. Only a few studies have applied multi-scale multi-dimensional sub-models to analyse PCM cooling, providing an accurate analysis with lower computational costs. In the present work, the selection of optimal PCM thickness, the effect of higher discharge rates, and the dynamic load conditions are modelled on the battery pack with and without the PCM.

3 Design and Methods

This section discusses the battery pack's design and briefly introduces the considered models.

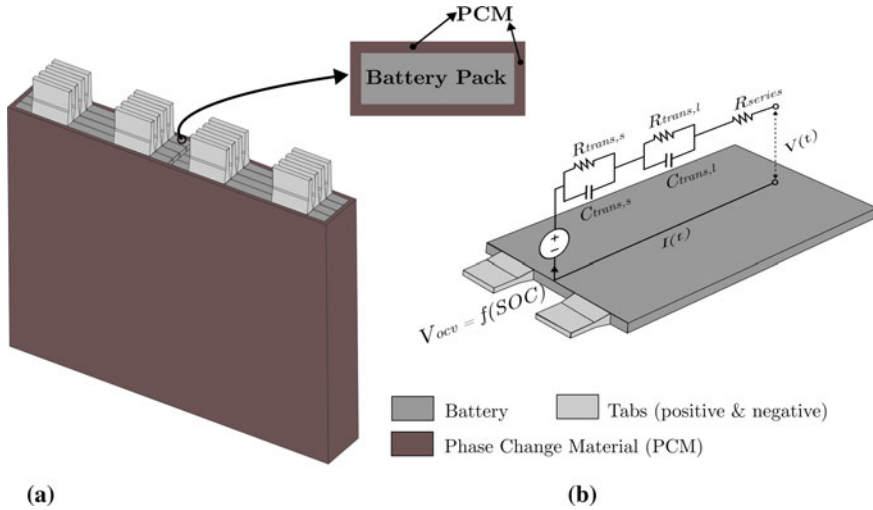


Fig. 1 a PCM embedded 4S2P battery pack model design b an equivalent electrical circuit representing a single battery

3.1 Model Design

In the present study, a scaled model is considered to replicate the battery pack installed in the vehicles. This battery pack is of 4S2P configuration where S represents the series, and P is parallel configuration. An ePLB C020 battery with a nominal capacity of 20 Ah and a nominal voltage of 3.7 V is considered. The total capacity and voltage of the 4S2P battery pack are 40 Ah and 16.6 V. A PCM is embedded around the battery pack, as shown in Fig. 1a. In this study, the battery is assumed to be a 2 RC-circuit electrical model, as depicted in Fig. 1b; further details are discussed in the next section.

3.2 Equivalent Circuit Model (ECM)

ECM considers the battery to be an electrical circuit. This circuit consists of a series resistance denoted by R_{series} accounts for the instantaneous voltage drop in the battery. Two parallel circuits constitute a resistance (R_{trans}) and capacitance (C_{trans}) which collectively consider the transient effects of the battery during its charging and/or discharging. Resistances ($R_{trans,s}$, $R_{trans,l}$) and capacitances ($C_{trans,s}$, $C_{trans,l}$) constitute the transient effects of the short-time and long-time constants in voltage variation of the battery ($V(t)$). These parameters inherently depend on the state of charge (SOC). SOC denotes the amount of the capacity still left in the battery during the discharge [4].

$$V(t) = V_{OCV} - V_{trans,s} - V_{trans,l} - R_{series}I(t) \quad (1)$$

$$\frac{dV_{trans,s}}{dt} = \frac{1}{R_{trans,s}C_{trans,s}}V_{trans,s} - \frac{1}{C_{trans,s}}I(t) \quad (2)$$

$$\frac{dV_{trans,l}}{dt} = \frac{1}{R_{trans,l}C_{trans,l}}V_{trans,l} - \frac{1}{C_{trans,l}}I(t) \quad (3)$$

$$\frac{d}{dt}(\text{SOC}) = \frac{I(t)}{3600Q_{ref}} \quad (4)$$

All the above parameters constituting the voltages (V_{OCV} , $V_{trans,s}$, $V_{trans,l}$), resistances (R_{series} , $R_{trans,s}$, $R_{trans,l}$), and capacitances ($C_{trans,s}$, $C_{trans,l}$) are considered polynomial and negatively exponential functionals of SOC [4]. The parameters that fit the functional relations are obtained from the experimental I-V performance curves of the considered battery. In this study, the ePLB C020 cell is considered [6, 9], and the parameters are obtained from the literature [4, 6, 10].

The semi-empirical equations obtained in ECM are solved, and the energy equation of the battery domain is later solved. The heat generation inside the battery constitutes irreversible heat and reversible heat. The irreversible heat is due to the over-voltage potential, whereas the reversible heat is due to the entropy generation in the battery. Additional terms in Eq. (5) constitute the heat generation in the current collectors. The volumetric current density j is related to open circuit voltage ($V_{OCV}(\text{SOC})$) obtained from the ECM equations at a given time, as shown in Eq. (6).

$$q_{gen} = j \left[(V_{OCV} - (V_P - V_N)) - T \frac{dV_{OCV}}{dT} \right] + [\sigma_+ \nabla V_P^2 + \sigma_- \nabla V_N^2] \quad (5)$$

$$j = \frac{Q_{total}}{Q_{nominal}} \cdot \frac{I(t)}{V_{OCV}} \quad (6)$$

where V_P , σ_+ and V_N , σ_- denote the potential and electrical conductivity of positive and negative electrodes, respectively. The Q_{total} and Q_{ref} represent the battery's total capacity and reference capacity. The governing energy equation in the battery pack and its components is given by:

$$\frac{\partial}{\partial t}(\rho_b c_{pb} T) = \nabla \cdot (k_b \nabla T) + (q_{gen} - q_{conv}) \quad (7)$$

The terms ρ_b , c_{pb} , and k_b denote the density, specific heat, and thermal conductivity of the battery. q_{gen} , q_{conv} denote the heat generated and convective heat dissipation in the battery at a particular SOC.

3.3 Phase Change Material Modelling

The PCM is modelled using the solidification and melting model which is based on the enthalpy porosity method. In this study, the natural convection in the liquid phase of the PCM is neglected [8]. This consideration results in solving the energy equation where the enthalpy and temperature are porosity dependent. The porosity is quantified by a liquid fraction β which is 0 for the solid phase of PCM and 1 for the liquid phase. The governing equations are listed below:

$$\frac{\partial}{\partial t}(\rho_{\text{PCM}}H) = \nabla \cdot (k_{\text{PCM}}\nabla T) \quad (8)$$

where

$$H = \int_{T_0}^T C_{\text{PCM}}dT + \beta L \quad (9)$$

$$\beta = \begin{cases} 0 & T < T_s \\ \frac{T-T_s}{T_L-T_s} & T_s < T < T_L \\ 1 & T > T_L \end{cases} \quad (10)$$

Here, ρ_{PCM} , k_{PCM} , C_{PCM} represent the porosity and temperature-dependent density, thermal conductivity, and specific heat of PCM. T , T_s , and T_L represent the PCM's temperature, solidus temperature, and liquidus temperature at a given time. T_0 represents the initial temperature of the solid-liquid PCM. Initially, the battery pack temperature is considered equal to the ambient temperature in the enclosure (T_{amb}). Convective heat transfer with a constant average convective heat transfer coefficient (' h ') of 5 W/(m²K) is considered for the exposed walls as boundary conditions.

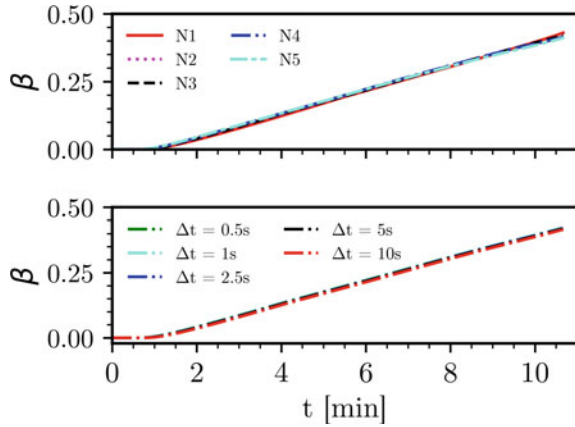
3.4 Methodology

This section establishes the reliability of the numerical simulations. PTC-CREO and ANSYS are utilised for simulations [10]. Properties of battery and PCM chosen from the literature [6, 11].

3.4.1 Grid and Time Step Independence Study

The grid independence study is done for both designs by analysing the variation of averaged liquid fraction (β) for the 4S2P battery pack without and with PCM, respectively.

Fig. 2 Grid and time step independency analysis for **a** 4S2P battery pack without PCM and **b** 4S2P battery pack embedded with PCM



Time step independence analysis is done by considering different time step values for the optimal meshes obtained from the grid independent study, as shown in Fig. 2. Larger time step values lead to instability, whereas lower values lead to higher computational time without any improvement in accuracy. The time step of $\Delta t = 2.5$ s is considered optimal for both designs.

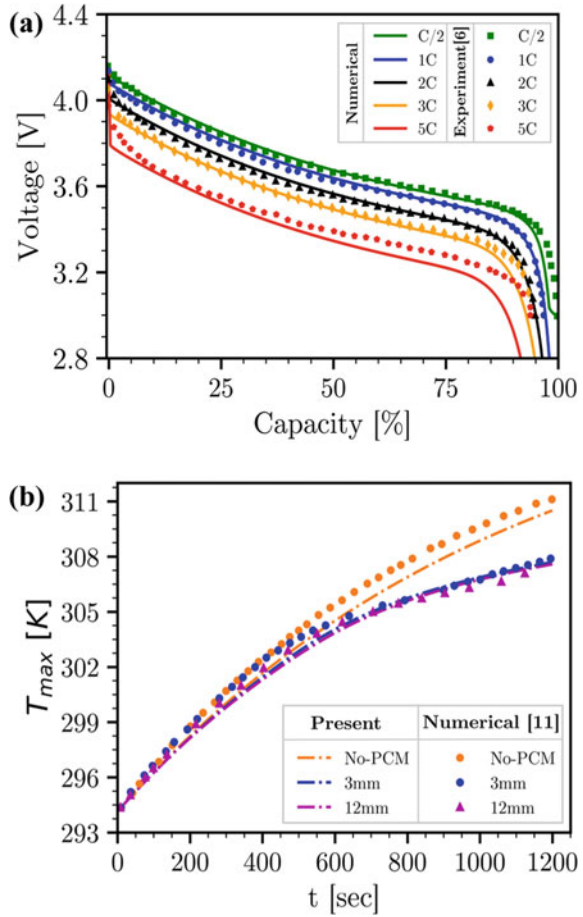
3.4.2 Validation

The current ECM is validated with Li et al.'s work [6]. The voltage variation plots of the current simulation to that of an experiment are shown in Fig. 3a. The average deviation in the results is less than 3% which signifies that the good agreement has been observed. Figure 3b shows the validation of the PCM model with Javani et al.'s work [11]. The average variation in the temperature is in the range of $\pm 0.4\%$, as shown in the subplot of Fig. 3b.

4 Results and Discussion

This section discusses the effect of phase change material thickness and the impact of higher discharge rates on the battery pack's thermal performance. Later, the current–voltage–temperature (I–V–T) variation of the battery pack with PCM under a compound cycle is analysed.

Fig. 3 a Voltage variation using ECM is validated with experimental values of Li et al. [6], and **b** Validation of the maximum temperature with and without PCM is done with numerical results of Javani et al. [11]

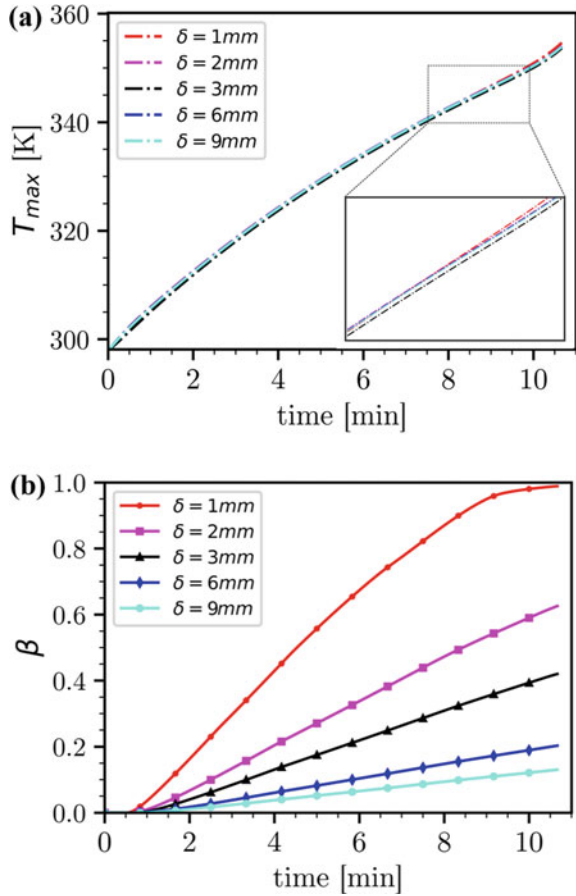


4.1 Selection of Phase Change Material’s Optimal Thickness

The phase change material (PCM) is a thermal storage device. The PCM transforms its phase by absorbing the heat generated by the battery. In this model design, the PCM is retrofitted as the outer enclosure to the battery pack. The crucial parameter is the type and thickness of PCM. The n-octadecane is the better performing PCM at the room temperature of 25 °C (298.15 K) due to its higher latent heat, so this PCM has been considered throughout the study.

The thickness is the other crucial parameter. The PCMs generally have lower thermal conductivity; with an increase in thickness, the heat storage capacity increases but the heat dissipation capacity lowers. So, simulations have been done on the 4S2P battery pack enclosed in PCM at a 10C rate with different thicknesses (δ). The maximum temperature of the battery pack (T_{max}) is lower when the δ is 3 mm, as shown in the zoomed-in plot of Fig. 4a. The averaged liquid fraction (β) reaches

Fig. 4 a Maximum temperature (T_{max}) variation of 4S2P embedded with PCM under discharge rate of 10C at 298.15 K, and **b** Averaged liquid fraction variation for various δ values



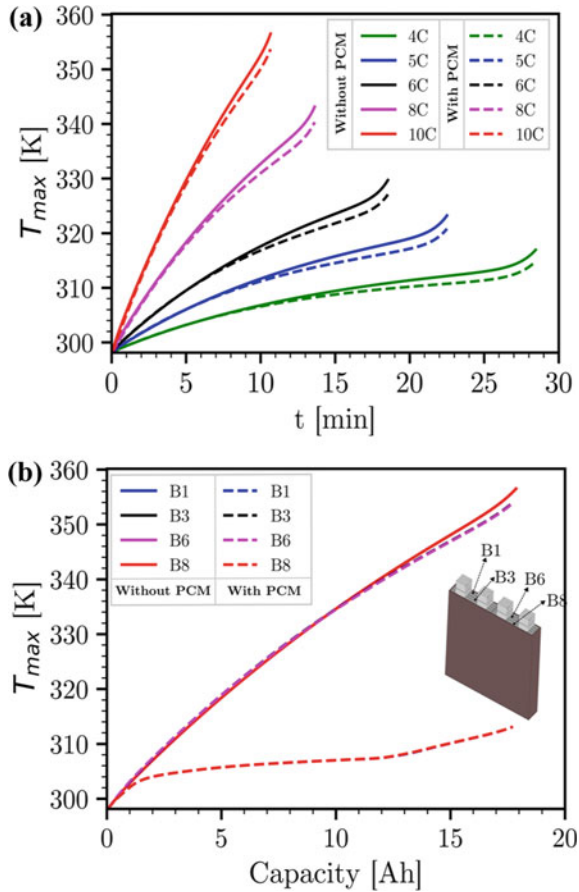
1 in the case of δ values which signifies that the PCM cannot absorb the heat further. At higher δ values, the thermal storage capacity of PCM is higher as β has lower values, but the T_{max} is higher and adds extra weight to the battery pack. Therefore, a PCM thickness of 3 mm is optimal, which is further considered in this study.

4.2 Effect of Higher Discharge Rates

The battery pack’s thermal performance is tested when discharged with higher currents (or C-rates) to power up the vehicle. As the C-rate increases, the heat generation from both ohmic and electrochemical reactions rises, pushing the battery pack to work under near-peak temperatures. The designed thermal cooling system must restrict the pack from touching the thermal runaway condition of 80 °C (353.15 K).

Figure 5a shows the maximum temperature of the battery pack (T_{max}) with and without PCM at higher discharge rates. At all the C-rates, the T_{max} reduction is evident due to the heat absorption capability of the PCM. The temperature reduction of 2.18 K, 2.42 K, 2.63 K, 2.82 K, and 2.82 K is observed when discharged with the C-rates of 4C, 5C, 6C, 8C, and 10C respectively as shown in Fig. 5a. Later, the T_{max} is evaluated for four batteries, B1, B3, B6, and B8, under 10C rate, as shown in Fig. 5b. The side-BATT groups, B1 and B8, have shown significantly lower temperatures of 313 K compared to centre batteries B3 and B6 which registered temperatures of 353 K. The PCM is effective for the batteries in immediate contact as the heat dissipation is predominantly conduction heat transfer.

Fig. 5 Maximum temperature (T_{max}) transient variation of **a** 4S2P embedded with PCM at 298.15 K for higher C-rates values and **b** different batteries for constant 10C discharge rate



4.3 I-V-T Variation on Battery Pack with PCM for Dynamic Load Conditions

A specific case study has been done to evaluate the thermal performance where the 4S2P battery pack is subjected to dynamic load conditions. At first, the battery pack is discharged with a constant C-rate of 1C, i.e. 40 A for 720 s. Later, the battery pack is subjected to a discharge of 5C-rate (200 A) for the 30 s, then rested for another 30 s. This dynamic cycle has continued up to the 1020 s.

The 4S2P battery pack's voltage and temperature variation under dynamic conditions from 720 to 1020 s is shown in Fig. 6a. The current follows the user-defined step profile, and the voltage follows a similar trajectory, but the value keeps decreasing due to depleting SOC. Here, the batteries are classified into two groups, 1. Central batteries (centre-BATT) constitute B2, B3, B6, and B7, 2. Adjacent side batteries (side-BATT) comprising batteries B1, B4, B5, and B8. All these batteries are schematically demonstrated in Fig. 6b. The maximum temperature (T_{\max}) of the centre-BATT is higher compared to the side-BATT under dynamic load conditions. The trajectory followed by the T_{\max} of both the battery groups is similar, but the side-BATT group recorded 1.24 K temperature reduction compared to the centre-BATT group reduction of 0.6 K. The reason is attributed to their presence adjacent to embedded phase change material.

The temperature contours of the PCM embedded battery pack under dynamic loading at the end of discharge are shown in Fig. 6b. Initially, the temperature isotherms are higher at the tab locations due to the ohmic heat generation at the tabs. Later, the low temperatures are recorded at the top due to the high thermal conductivity of aluminium tabs, and higher temperature isotherms are observed in the centre portion of a battery. The temperature isotherms of PCM also suggest the same. The centre-BATT group recorded higher temperatures than the side-BATT group adjacent to the PCM.

5 Conclusions

The present study focuses on the thermal analysis of PCM embedded Li-ion battery packs using ECM. The numerical simulations are performed for the 4S2P battery pack under different loading conditions of faster C-rates and dynamic loading to obtain thermal performance. The conclusions obtained are listed as follows:

1. The optimal thickness of the enclosed PCM thickness is 3 mm. A reduction of 2.8 K is observed in the maximum temperature (T_{\max}) compared to other thickness values.
2. With an increase in the C-rate, the temperature increases due to higher heat generation. With the embedded PCM, the reduction in T_{\max} is 2.82 K, 2.82 K, and 2.63 K when the battery is discharged with constant discharge rates of 10C, 8C, and 6C, respectively.

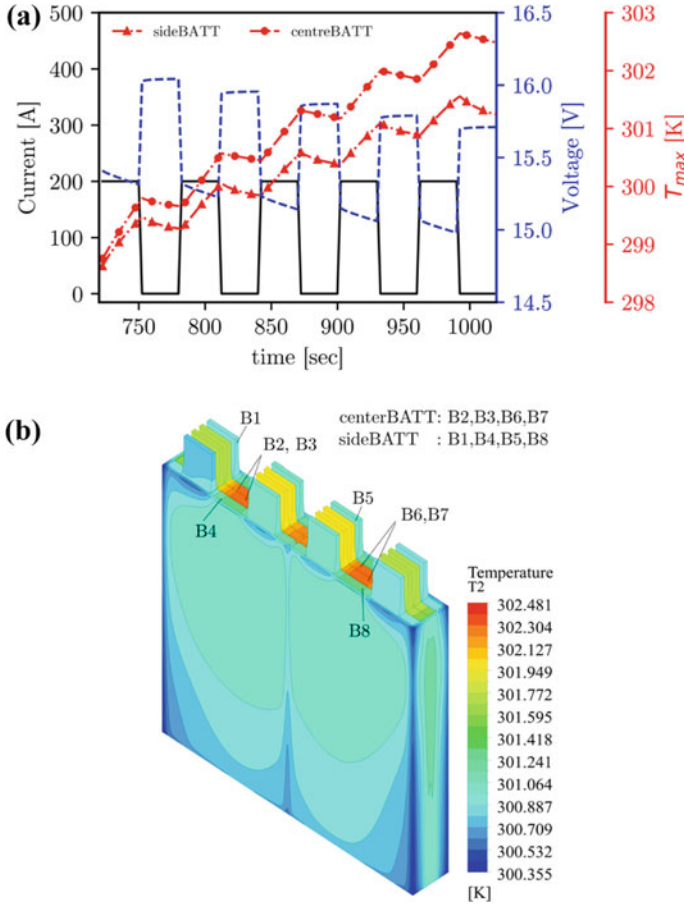


Fig. 6 **a** Transient variation of I-V-T characteristics and **b** temperature contours at the end of discharge for PCM embedded battery pack under dynamic load

3. The side-BATT group has registered lower T_{max} values than the centre-BATT group, with a reduction of 43.38 K under constant loading conditions of 10C rate.
4. For the dynamic loading conditions at the later stages, i.e. the current adopting a step profile, the voltage follows a similar trajectory but with continuous drop up to the end of the discharge.
5. The side-BATT group has shown a reduction of 1.24 K, whereas the centre-BATT group is reduced by just 0.6 K under the considered dynamic load conditions.

Nomenclature

B _n	<i>n</i> th battery
<i>C</i>	Capacitance
<i>R</i>	Resistance
<i>V</i> _{OCV}	Open circuit voltage
centre-BATT	Batteries which are placed in centre
side-BATT	Batteries which are in immediate contact with phase change material jacket

Symbols and Subscripts

σ	Electrical conductivity
β	Liquid fraction
δ	Thickness in mm
amb	Ambient conditions
conv	Convective heat transfer
trans, <i>s</i>	Transient effects of short-time constants
trans, <i>l</i>	Transient effects of long-time constants

Acronyms

BTMS	Battery thermal management system
ECM	Equivalent circuit model
SOC	State of charge
DOD	Depth of discharge
C-rate	Battery charge/discharge rate
PCM	Phase change material

References

1. Rao Z, Qian Z, Kuang Y, Li Y (2017) Thermal performance of liquid cooling based thermal management system for cylindrical lithium-ion battery module with variable contact surface. *Appl Therm Eng* 123:1514–1522
2. Wang Q, Ping P, Zhao X, Chu G, Sun J, Chen C (2012) Thermal runaway caused fire and explosion of lithium ion battery. *J Power Sources* 208:210–224
3. Sun P, Bisschop R, Niu H, Huang X (2020) A review of battery fires in electric vehicles. *Fire Technol* 56:1361–1410

4. Chen M, Rincon-Mora GA (2006) Accurate electrical battery model capable of predicting runtime and IV performance. *IEEE Trans Energy Convers* 21(2):504–511
5. Ramadesigan V, Northrop PW, De S, Santhanagopalan S, Braatz RD, Subramanian VR (2012) Modeling and simulation of lithium-ion batteries from a systems engineering perspective. *J Electrochem Soc* 159(3):R31
6. Li Y, Zhou Z, Wu WT (2019) Three-dimensional thermal modeling of Li-ion battery cell and 50 V Li-ion battery pack cooled by mini-channel cold plate. *Appl Therm Eng* 147:829–840
7. Panchal S, Dincer I, Agelin-Chaab M, Fraser R, Fowler M (2016) Experimental and theoretical investigation of temperature distributions in a prismatic lithium-ion battery. *Int J Therm Sci* 99:204–212
8. Moraga NO, Xamán JP, Araya RH (2016) Cooling Li-ion batteries of racing solar car by using multiple phase change materials. *Appl Therm Eng* 108:1041–1054
9. Taheri P, Bahrami M (2012) Temperature rise in prismatic polymer lithium-ion batteries: an analytic approach. *SAE Int J Passeng Cars-Electron Electr Syst* 5(1):164–176
10. Inc., ANSYS (2020) ANSYS Fluent Theory Guide. Available at: <https://www.ansys.com>. Accessed Sept 2022
11. Javani N, Dincer I, Naterer GF, Yilbas BS (2014) Heat transfer and thermal management with PCMs in a Li-ion battery cell for electric vehicles. *Int J Heat Mass Transf* 72:690–703

Heat Transfer Enhancement in Miniature Channels with Micro-fin Having Varying Fin Height Along the Axis of Flow



Rohit Kumar and Manmohan Pandey

1 Introduction

The advancement in high computing electronic devices has raised the concern of the immense heat flux removal requirement of the electronic cooling industry. Different active and passive high heat removal techniques have been extensively explored in the last four decades [1]. The development of microchannel heat exchanger (MCHX) as an electronic cooling device makes the system more miniaturized and enhances the efficiency of the system [2]. MCHX devices have very high heat flux removal capacity due to their large surface area to volume ratio. This feature of MCHX is widely exploited and has drawn the attention of many researchers in this field [3]. In 1981, Tuckerman and Pease [4] successfully demonstrated the removal of high heat flux from electronic devices up to 780 W/cm^2 through single-phase fluid flow in microchannels. Extensive work has been done to investigate the heat transfer and fluid flow phenomena in microchannels and minichannels. Many heat transfer augmentation techniques have been implemented by researchers to enhance the heat transfer performance and efficiency of the system [5]. Among all distinct methods, the enhancement in heat transfer through surface modification of microchannel heat exchangers is the most commonly used technique. The introduction of pin fins and roughness elements in microchannel and small-scale channels shows a large increment in heat transfer capacity and thermal performance of cooling devices.

Microfins of different geometric structures and their arrangements have been widely investigated by many investigators to propose an optimized design for better thermal performance of MCHX devices [6]. In a numerical study of microchannels with rectangular, trapezoidal, and triangular cross-sections, the rectangular microchannel shows better heat transfer characteristics than the other two configurations [7]. Prajapati [8] numerically investigated the effect of varying microfins

R. Kumar (✉) · M. Pandey
Department of Mechanical Engineering, IIT Guwahati, Guwahati 781039, India
e-mail: rohit18e@iitg.ac.in

height on fluid flow and heat transfer characteristics. It was concluded that the open microchannel heat exchanger with microfin 75–80% height shows maximum thermal performance. The microfins structure like circular, rectangular, diamond, square, triangular, cone, and hydrofoil have been studied numerically [9]. It was observed that the rectangular-shaped pin fins give better thermal performance than the other proposed structures. The microfins structure in the miniature channel facilitates the mixing of fluid at a low Reynolds number, and hence, it promotes the convection heat transfer. These roughness elements act as flow-resistant elements and cause large hydraulic losses, which creates the demand for a large pumping power of fluid for the device [10]. Thus, there is a need for a feasible and optimal design of the MCHX that offers enhanced heat transfer and low hydraulic loss. In the current work, the height of microfins is varied along the flow to propose an arrangement that offers better thermal performance. Three different arrangements are proposed where the fin height is kept constant along the flow axis in one and varied differently in the other two cases. The fin height increases along the flow in the second case and decreases along the flow in the third case.

2 Channel Design and Numerical Model

The rectangular miniature channel is designed for the numerical simulation to investigate the heat transfer and fluid flow through it. The details of channel geometry are represented in Fig. 1. The cross-section of the miniature channel ($w \times h$) is 0.4 mm \times 1 mm, and the length of the channel (L) is 10 mm. The microfins of cylindrical shape are incorporated into the channel along the axis of flow. The three cases of a miniature channel designed with varying microfins height along the flow axis are proposed as shown in Fig. 1. The diameter of the fin cross-section is 0.2 mm, kept constant in all three cases. The distance between the center of two microfins, also called pitch, is maintained as 0.4 mm. In Case-1, as shown in Fig. 1d, the height of microfins is kept constant at 0.75 mm along the flow axis. Figure 1e represents Case-2, where fins' height varied from 0.05 to 0.75 mm in increasing sequence along the axis of flow. In Case-3, the microfins height is gradually decreasing along the length from 0.75 to 0.05 mm. The three-dimensional channel geometry is created in the Design modeler of ANSYS. The conjugate heat transfer and fluid flow in all three directions is investigated numerically with the help of the commercial software ANSYS Fluent.

The finite volume method is selected for the numerical analysis of three-dimensional conjugate heat transfer and fluid flow through proposed miniature channels. The commercial software ANSYS Fluent is used for the simulation. The numerical approach implemented for the analysis, as suggested in similar work performed in the literature [11–13], predicts results with considerable accuracy and precision. The SIMPLE numerical method is employed, and the pressure–velocity coupling algorithm is used to solve the three-dimensional governing equations. The second-order upwind scheme is adopted to solve these equations. The residuals 10^{-4} are

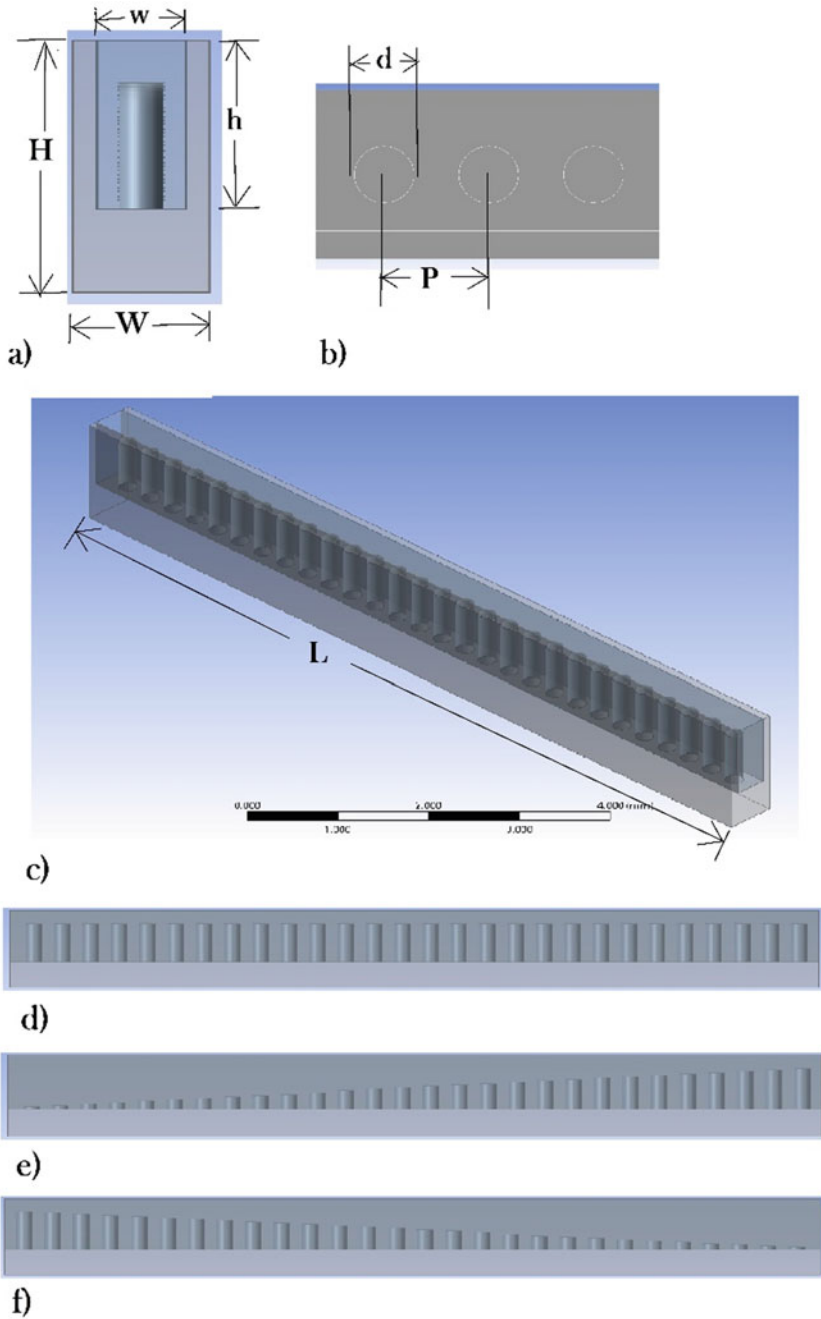


Fig. 1 a Cross-sectional view and detail of channel geometry, b top view, c isometric view, d Case-1, e Case-2, f Case-3

given for continuity, 10^{-6} for momentum equations, and 10^{-8} for energy equation is fixed as convergence criteria of the solution.

The simulation is performed in the laminar fluid flow regime, and liquid water is used as the working fluid. Copper metal is considered for solid material because it has a high conductivity and is commonly used in heat sinks for heat transfer applications. A constant heat flux is provided from the bottom surface of the wall, and a constant inlet flow velocity of the fluid is given. The boundary conditions and assumptions taken for the solution of governing equations are stated as follows:

- Constant thermophysical properties of the solid
- Fluid is viscous and incompressible
- Steady state and laminar flow model is used
- The inlet fluid temperature is constant 293 K
- No-slip condition at the channel wall
- Pressure outlet is considered at 1 atm pressure
- Constant heat flux of 250 W/cm^2 is supplied at the bottom wall of the solid.

The general governing equations solved for the simulation of three-dimensional conjugate heat transfer and fluid flow are given as [12]:

The conservation mass (continuity equation):

$$\nabla \cdot (\rho_l \vec{V}) = 0 \tag{1}$$

The conservation of momentum (Navier–Stokes equation):

$$\rho_l \vec{V} \cdot \nabla \vec{V} = -\nabla p + \nabla \cdot \mu_l \left[(\nabla \vec{V} + \nabla \vec{V}^t) - 2/3 \nabla \cdot \vec{V} \right] + \rho_l \vec{g} \tag{2}$$

Energy equation:

Conservation of energy for fluid flow:

$$\rho_l c_{p,l} \vec{V} \cdot \nabla T = \nabla \cdot (k_l \nabla T) \tag{3}$$

Conservation of energy for solid:

$$k_s \nabla^2 T = 0 \tag{4}$$

Temperature-dependent variable thermophysical properties of the fluid are incorporated in Fluent for the solution of governing equations [11]. The correlations used are given as:

$$\rho(T) = 765.33 + 1.8142T - 0.0035T^2 \tag{5}$$

$$c_p(T) = 28070 - 281.7T + 1.25T^2 - (2.48 \times 10^{-3})T^3 + (1.857 \times 10^{-6})T^4 \tag{6}$$

$$k(T) = -0.5752 + (6.397 \times 10^{-3})T - (8.151 \times 10^{-6})T^2 \quad (7)$$

$$\begin{aligned} \mu(T) = (9.67 \times 10^{-2}) - (8.207 \times 10^{-4})T + (2.344 \times 10^{-6})T^2 \\ - (2.244 \times 10^{-9})T^3 \end{aligned} \quad (8)$$

3 Model Validation and Data Reduction

3.1 Grid Independency Test

The entire computational domain of all proposed design channels is discretized into unstructured tetrahedral grid elements. Very fine meshing is done at the fluid and solid interface and microfins wall to capture the details of fluid flow and heat transfer interaction near the wall with better accuracy. The mesh sizes gradually increase on proceeding away from the wall, and coarse mesh is used for the solid domain. The optimized mesh for Case-1 is shown in Fig. 2. The minimum element size of the grid is taken as 0.05 mm and the maximum size as 0.08 mm. Figure 1a–c are a side view, top view, and an isometric view of the discretized computational domain of the channel, respectively. The test of grid independence is conducted for all the channel geometry at different mesh element sizes. Simulation for all the geometry is first conducted at the coarse mesh, and then mesh size gradually decreases to finer mesh. The results of each meshing type, from coarse grid size mesh element to fine mesh element, are compared. The optimized mesh size for a particular channel geometry which gives comparatively more accurate results and lesser computational time is selected for further analysis. The information of the selected optimized mesh for all proposed channel structures is shown in Table 2. Figure 3 represents the independency of meshing of Case-1. The simulation is done for four different mesh element sizes. The error in the value of pressure drop is more significant for the coarse mesh, which decreases on adopting a fine mesh grid, as shown in Table 2.

3.2 Validation of Numerical Model

The numerical model used for the simulation is validated by the experimental results of Qu et al. [14]. The numerical results were found in good agreement with the experimental data, and MAE (mean absolute error) is 7%. The comparison of numerical results of pressure drop with experimental data is shown in Fig. 4. The results are compared, and numerical analysis is performed for laminar range flow from Reynolds number 200–800.

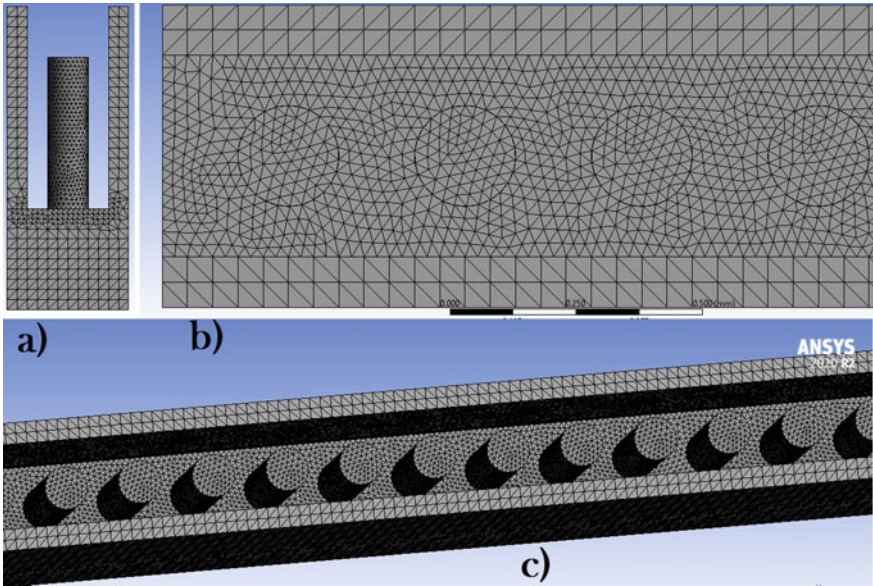
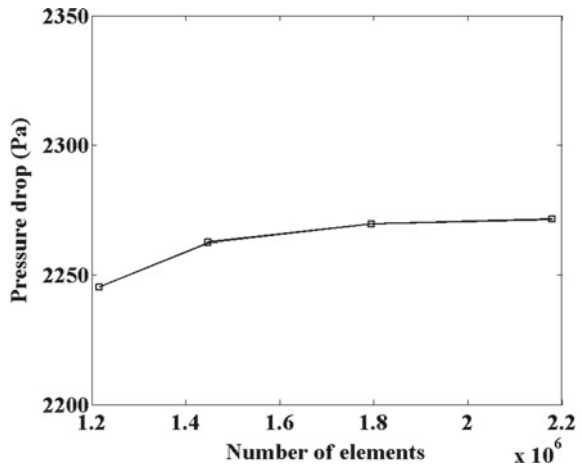


Fig. 2 Meshing of computational domain of Case-1 channel; **a** side view, **b** top view, and **c** isometric view

Fig. 3 Variation of pressure drop with number of elements

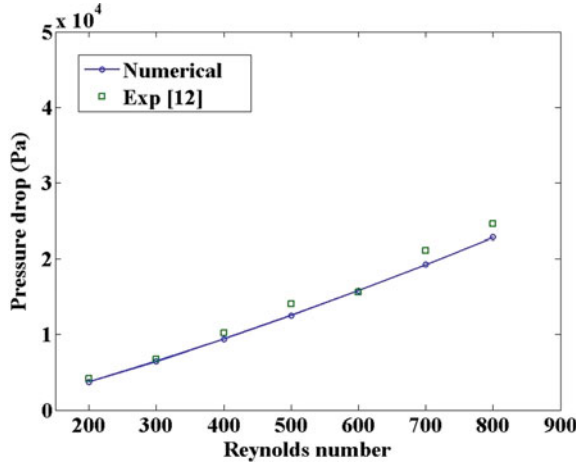


3.3 Data Reduction

The result obtained from the numerical analysis is processed to calculate the required parameters. The value of convective heat transfer is determined as

$$q = h(T_w - T_m) \tag{9}$$

Fig. 4 Validation of numerical model with experimental data



Channel wall temperature is defined as T_w , and mean bulk fluid temperature is denoted by T_m (Tables 1 and 2).

$$h = \frac{q}{(T_w - T_m)} \tag{10}$$

$$T_m = \frac{\iint u \cdot T dA}{\iint u \cdot dA} \tag{11}$$

Table 1 Detail of selected mesh for designed channels

S. No.	Channel design	Minimum mesh size (mm)	Number of elements	Number of nodes
1	Case-1	0.05	1,795,244	357,135
2	Case-2	0.05	1,341,026	235,472
3	Case-3	0.05	1,347,398	236,212

Table 2 Mesh details of Case-1 for test of grid independency

S. No.	Minimum element size (mm)	Number of elements	Number of nodes	Pressure drop (Pa)	Error (%)
1	0.06	1,216,836	211,876	2245.4	1.41
2	0.055	1,446,817	251,864	2262.5	0.387
3	0.05	1,795,244	357,135	2269.53	0.0779
4	0.045	2,180,050	378,773	2271.3	0

4 Results and Discussion

The three-dimensional numerical simulation is performed for three cases of designed miniature channels to analyze the conjugate heat transfer and fluid flow. Three cases of proposed channel design with microfins having variable fin height along the flow are investigated. The numerical results of all three cases of designed miniature channels are compared with the plain channel to analyze the enhancement in heat transfer and thermal performance. The thermal performance is determined with reference to the plain channel as [15].

$$\text{Thermal performance factor, TPF} = \frac{(\text{Nu}/\text{Nu}_0)}{(\Delta P/\Delta P_0)^{1/3}} \quad (12)$$

Here, Nu_0 and ΔP_0 is the Nusselt number and pressure drop of plain miniature channel.

Figure 5 shows the temperature contours of the proposed channels, obtained from the CFD post of ANSYS Fluent, for the simulation conducted at an inlet Reynolds number of 400, and heat flux of 250 W/cm^2 . The channel with uniform fin height along the flow has a lower maximum wall temperature than the other two microfins arrangements. The average fluid temperature of 303 K and channel wall temperature of 312 K is observed for this case, while the maximum heater wall temperature is 328.7 K. The maximum heater wall temperature for Case-2 and Case-3 are 331.2 K and 353.3 K, respectively. The velocity contour of cross-section taken at the middle position of channel length is shown in Fig. 6. The maximum flow velocity attained in Case-1 is highest, while in Case-2 it is more significant than in Case-3. The region of high-velocity area is the largest in Case-1, while in Case-2, it is more than Case-3. Therefore, the pressure drop trend for the same mass flow rate in these three geometries is as follows: Case-1 > Case-2 > Case-3. Also, the convection in Case-1 is superior to the other two geometries. The effect of change in Reynolds number on the hydraulic loss of fluid flow in all three cases is shown in Fig. 7.

With increase in the Reynolds number of the flow, the pressure drop increases. The microfins, which are uniformly distributed along the channel axis having constant fin height (Case-1), have maximum pressure drop in comparison to the other two cases. The difference in pressure drop is small at low Reynolds numbers, which become large for higher Reynolds numbers. The arrangement of microfins in Case-1 offers higher resistance toward flow than Case-2 and Case-3. Microfins arrangement in Case-3 has lower flow resistance than the other two cases. The effect of varying Reynolds numbers on the Nusselt number in all designed channels is represented in Fig. 8. The channel with microfins having uniform height along the flow axis has the higher Nusselt number than the other two cases. In contrast, the channel with decreasing fin height arrangement shows enhanced heat transfer characteristics than the channel with increasing microfins height along the flow axis. The Nusselt number of Case-3 is lower than the other two cases, which improves at higher Reynolds numbers. The Nusselt number in all three cases increases on increasing Reynolds

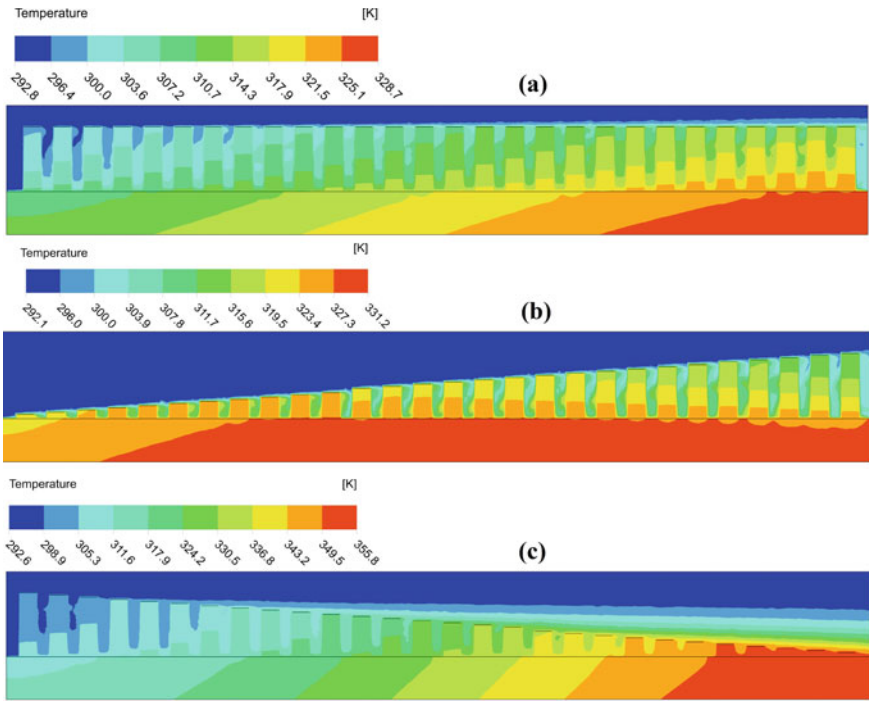


Fig. 5 a Temperature contour of Case-1, b Case-2, and c Case-3

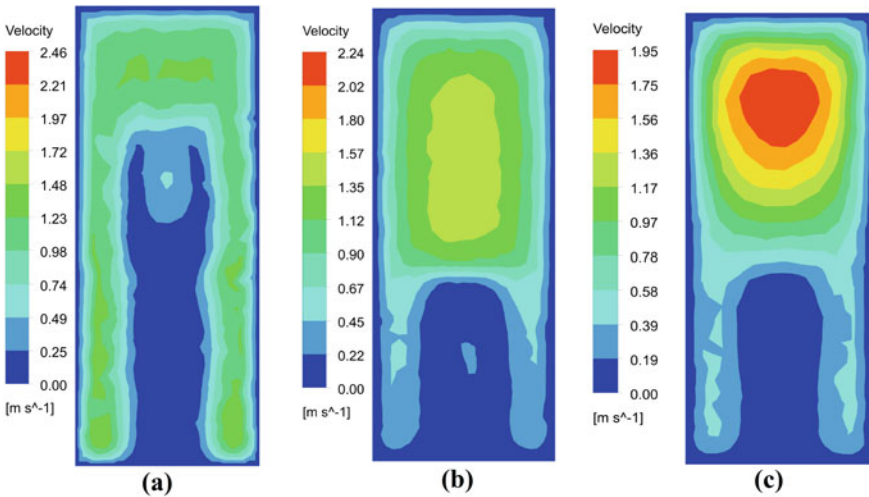


Fig. 6 a Velocity contour of Case-1, b Case-2, and c Case-3

Fig. 7 Variation of pressure drop with Reynolds number

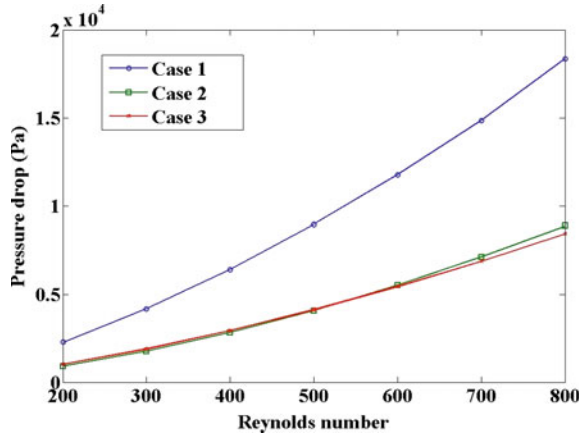
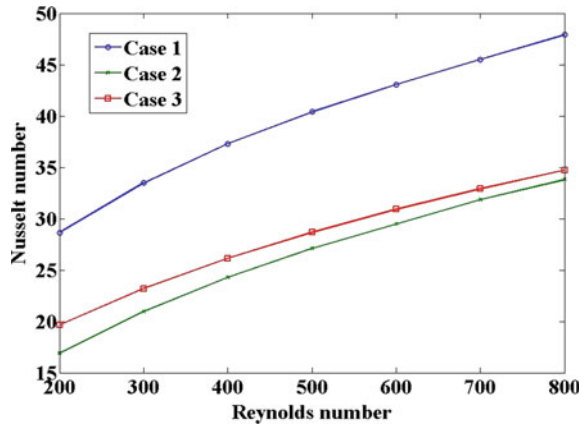
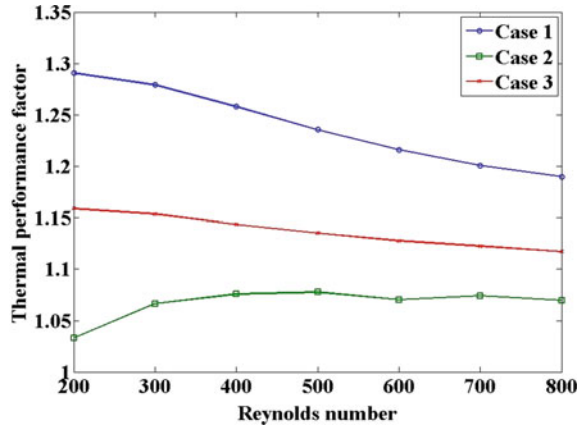


Fig. 8 Variation of Nusselt number with Reynolds number



number. The thermal performance factor of designed miniature channels varying with Reynolds number is shown in Fig. 9. The miniature channel with microfins having uniform fin height shows better thermal performance than the other two configurations. The thermal performance of Case-3 is superior to Case-2. The thermal performance of Case-1 and Case-3 decreases with an increase in Reynolds number, but the thermal performance for Case-2 is enhanced by increasing Reynolds number.

Fig. 9 Thermal performance of channel varying with Reynolds number



5 Conclusion

The effect of varying microfins height along the flow axis on heat transfer and fluid through miniature channels is investigated. The simulation is conducted to study three-dimensional conjugate heat transfer and flow behavior in the three different configurations of microfins arrangement. The results of enhanced channel surfaces are compared with plain miniature channels, and thermal performance is analyzed. The overall work is summarized as follows:

- The microfins arrangement of Case-1 offers maximum fluid flow restriction and hence shows a larger pressure drop than the other two designed miniature channels. The pressure drops in Case-2 are slightly more than the Case-3.
- The pressure drops increase with the increase in Reynolds number, but the pressure drop increment with Reynolds number in Case-1 is steeper.
- With the increase in Reynolds number, the Nusselt number also increases. The Nusselt number in Case-1 is higher than Case-3, which is superior to Case-2.
- The thermal performance factor of Case-1 is higher than the other two designed channels, and Case-3 has better thermal performance than Case-2. The thermal performance of Case-1 and Case-3 decreases with an increase in Reynolds number, but Case-1 is still superior. The thermal performance of Case-3 increases with an increase in Reynolds number.
- The proposed design with uniform microfins height (Case-1) is recommended over the other two configurations. It has better performance as well as lower maximum heater wall temperature than the other two cases. The performance of Case-3 is superior to Case-2, but the maximum wall temperature of Case-3 is higher.

Nomenclature

A	Cross-section area of channel (mm^2)
a	Depth of the channel (mm)
b	Width of the channel (mm)
d_h	Hydraulic diameter (mm)
h	Heat transfer coefficient ($\text{W}/\text{m}^2\text{K}$)
k	Thermal conductivity (W/mK)
L	Length of channel (mm)
Nu	Nusselt number
p	Pressure ($\text{kg}/\text{m}\cdot\text{s}^2$)
q	Heat flux (W/cm^2)
Re	Reynolds number
T	Temperature (K)
TPF	Thermal performance factor
V	Velocity matrix (m/s)

Special characters

ρ	Density of fluid (kg/m^3)
μ	Viscosity of fluid ($\text{kg}/\text{m}\cdot\text{s}$)

Subscripts

l	Liquid
m	Mean value
o	Plain channel
s	Solid
w	Wall interface of fluid and solid

References

1. Ramesh, Naga K, Karthikeya Sharma T, Rao G (2021) Latest advancements in heat transfer enhancement in the micro-channel heat sinks: a review. *Arch Comput Methods Eng* 28(4):3135–3165
2. Ameel TA, Warrington RO, Wegeng RS, Kevin Drost M (1997) Miniaturization technologies applied to energy systems. *Energy Convers Manage* 38(10–13):969–982
3. Garimella SV, Singhal V (2004) Single-phase flow and heat transport and pumping considerations in microchannel heat sinks. *Heat Transfer Eng* 25(1):15–25

4. Tuckerman, David B, Pease RFW (1981) High-performance heat sinking for VLSI. *IEEE Electron Device Lett* 2.5:126–129
5. Strydom JT, Van Wyk JD, Ferreira JA (2001) Some units of integrated L-C-T modules at 1MHz. *I.E.E.E Trans Ind Appl* 37(3):820–828
6. Dirker J, Liu W, Van Wyk JD, Meyer JP, Malan AG (2005) Embedded solid state heat extraction in integrated power electronic modules. *I.E.E.E. Trans Power Electron* 20(3)
7. Naquiuddin H, Saw LH, Yew MC, Yusof F, Ng TC, Yew MK (2018) Overview of micro-channel design for high heat flux application. *Renew Sustain Energy Rev* 82:901–914
8. Kosar A, Peles Y (2007) TCPT-2006-096. R2: micro scale pin fin heat sinks—parametric performance evaluation study. *IEEE Trans Compon Packag Technol* 30(4):855–865
9. Wang H, Chen Z, Gao J (2016) Influence of geometric parameters on flow and heat transfer performance of micro-channel heat sinks. *Appl Therm Eng* 107:870–879
10. Zhao J, Huang S, Gong L, Huang Z (2016) Numerical study and optimizing on micro square pin-fin heat sink for electronic cooling. *Appl Therm Eng* 93:1347–1359
11. Prajapati, Yogesh K (2019) Influence of fin height on heat transfer and fluid flow characteristics of rectangular microchannel heat sink. *Int J Heat Mass Transf* 137:1041–1052
12. İzci T, Koz M, Koşar A (2015) The effect of micro pin-fin shape on thermal and hydraulic performance of micro pin-fin heat sinks. *Heat Transfer Eng* 36(17):1447–1457
13. Bhandari P, Prajapati YK (2021) Thermal performance of open microchannel heat sink with variable pin fin height. *Int J Therm Sci* 159:106609
14. Qu W, Mudawar I (2002) Experimental and numerical study of pressure drop and heat transfer in a single-phase micro-channel heat sink. *Int J Heat Mass Transf* 45(12):2549–2565
15. Kumar R, Pandey M (2021) Effect of geometry in conjugate heat transfer and fluid flow through triangular copper miniature channels. In: *Proceedings of 26th national and 4th international ISHMT-ASTFE heat and mass transfer conference, Madras, India*

Thermo-Hydraulic Evaluation of Isothermally Heated Bluff Bodies with Different Shapes



Bibhu Bhusan Sha, Rajiva Lochan Mohanty, Dishant Chandrakant Patel, and Mihir Kumar Das

1 Introduction

The engineering applications of flow around a bluff body are extended to various fields such as air ventilation, architecture, urban structures, bridges, transmission lines, sea cables, and heat exchangers. Numerous industries utilize shell and tube heat exchangers due to their favorable qualities. The fundamental challenge of this equipment is that it must conserve energy, weight, and space. Shell and tube heat exchangers are used in chemical and biochemical facilities, bioprocessing, thermal and nuclear power plants, food processing, and pharmaceutical industries, etc. Shell and tube heat exchangers consist of tubes enclosed within a shell. It must accurately predict how heat will travel and how much pressure will drop to function correctly. For the initial prediction of thermo-hydraulic performance, the different shapes of single tube are suitable as per the applications. Based on that, it is possible to assess the effectiveness of the bank of tubes used in the shell and tube heat exchanger by choosing the tube shape that has the highest ratio of heat transfer coefficient to pressure drop.

2 Literature Study and Goal of Work

The shell and tube heat exchanger forms a circular tube in its arrangement. In cross-flow settings, numerous studies have been conducted across a circular tube in the research [1–4]. The researchers investigated natural and forced convection over the

B. B. Sha · R. L. Mohanty (✉) · D. C. Patel · M. K. Das
School of Mechanical Sciences, IIT Bhubaneswar, Khorda, Odisha 752050, India
e-mail: rajiva.mohantyfme@kiit.ac.in

R. L. Mohanty
School of Mechanical Engineering, KIIT University, Bhubaneswar, Odisha 751024, India

circular tube under conditions of cross-flow [1–4]. Hamad and He [5] reported experimental work for heat transfer over a 16-mm circular tube. They found that the heat transfer coefficient for water is more than oil for the same condition they also add air with the oil and found an enhancement in heat transfer. A limited number of investigations, including cross-flow circumstances, have been carried out over the semi-circular tube. Nada et al. [6] and Nada and Mowad [7] researched the heat transfer and fluid flow processes around a semi-circular cylinder oriented in various ways. They investigated a process known as single-phase heat transfer, which occurs when air flows from the left to the right. They concluded that curved shapes with flow directions that faced the flow direction performed significantly better than flat faces with flow directions that faced the flow direction. Forbes [8] performed a numerical simulation of an obstruction in the form of a half-circle placed on the bottom of a moving stream to ensure optimal fluid flow. Hashizume [9] researched the heat transfer and pressure drop characteristics of a finned tube operating in a cross-flow scenario. According to the study by Ibrahim and Elsayed [10], heat transfer performance in semi-circular tubes is superior to that of circular tubes. Sha et al. [11] reported that increasing the Reynolds number increases the Nusselt number and pressure drop for the non-circular tubes. Non-circular section, named Type-IV, is the most excellent option for circular tubes in heat transfer equipment. Sha et al. [12] found increased Nusselt number and decreased pressure drop for the semi-circular shape at the 90° orientation angle, as compared to the circular shape and other orientations. When compared to other cases, thermal performance and pressure drop are worst for the flat surface and curved semi-circular tube facing flow.

It is essential to highlight that, to the best of the author's knowledge from the literature study, it is observed that the study is more related to the circular tube. Significantly less work is available in the non-circular section. The primary purpose of this investigation is to undertake a numerical simulation of the flow around the non-circular bluff bodies to determine the heat transfer performance and pressure drop for various inlet velocities corresponding to different tube geometry. This work directly compares the heat transfer and pressure drop performance of various non-circular bluff bodies such as semi-circular, ellipse, hexagonal, and triangular and compared with circular sections. All bodies are compared, keeping the surface area the same to find the best performing body under single-phase heat transfer.

3 Method

3.1 Configuration of Different Bodies

In ANSYS design modular, tubes are drawn using a two-dimensional geometry. As shown in Fig. 1, many different kinds of geometry are used in this analysis.

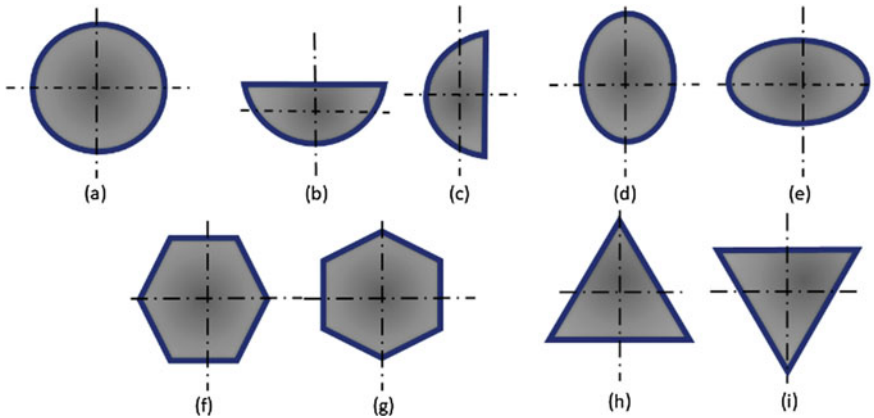


Fig. 1 Different shapes of bluff bodies geometrical surface **a** circular **b** horizontal semicircle **c** vertical semicircle **d** vertical ellipse **e** horizontal ellipse **f** hexagon **g** rotated hexagon **h** triangular **i** inverted triangular

3.2 Implemented Boundary Phenomena

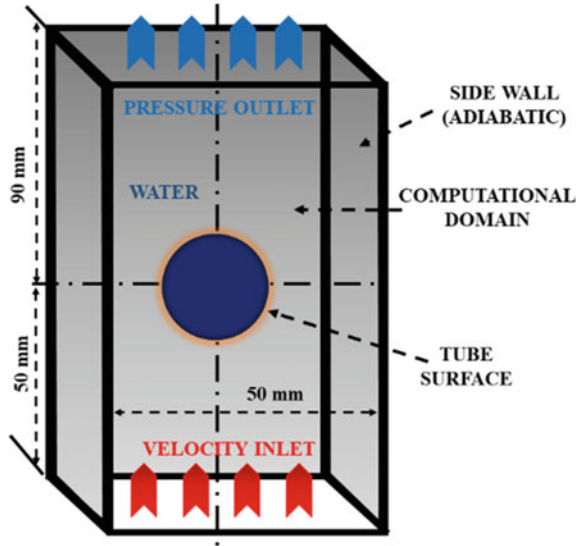
The boundary condition is shown in Fig. 2. The water comes in through the bottom as a velocity inlet at 300 K. The water leaves as a pressure outlet at 300 K and zero-gauge pressure. On both sides of the domain, walls have no heat transfer. The tube's wall temperature is always 350 K higher than the temperature of the water in the domain. To see how things work at different speeds, the speed of the air coming in ranged from 0.01 to 0.05 m/s.

3.3 Numerical Methodology

For all input velocities, the steady-state solution is used. The direction of gravity is Y. Atmospheric pressure and temperature were chosen as the operational conditions. A collection of parameters determines the inlet velocity. Aside from accepting input, the parameter dialogue box also allows for the output of values. The input is the inflow velocity, and the outputs are the heat transfer coefficient (HTC) and the pressure drop. A button labeled "hybrid type initialization" must be pressed before the calculation begins. Both the solution method and the control are kept at their default values. Maximum iterations per run are set at 2000.

The fluid enters the region at various input velocities and impacts the tube. The velocity at the flow entrance is between 0.01 and 0.05 m/s. All sorts of tube surfaces exhibit turbulent fluid flow.

Fig. 2 Boundary conditions were applied to all geometric surfaces



3.4 Governing Equations

In the whole domain, the steady-state solution is used. The finite volume method is used to solve equations involving mass, momentum, and energy. Below are the equations that describe what happens:

$$\rho(u.\nabla).u = \left[-p + \mu(\nabla u + \nabla u^T) - \frac{2}{3}\mu(\nabla.u) \right] + F \tag{1}$$

$$\nabla(\rho u) = 0 \tag{2}$$

$$\rho Cpu.\nabla T = \nabla.(k\nabla T) + Q \tag{3}$$

In order to compare the heat transmission performance, the surface areas of both circular and non-circular bodies remained constant.

3.5 Grid Test

The ANSYS fluent mesh module is used to make the grids. Edge meshing is used to create a mesh, and inflation is added through the tube’s edge. HTC is calculated for different grid numbers over a circular tube with an inlet velocity of 0.01 m/s.

The plot of the HTC for each grid sizes is displayed in Fig. 3. The grid size ranged from 2300 to 5000 grids, but it is seen that 4133 grids produce the best results. Once

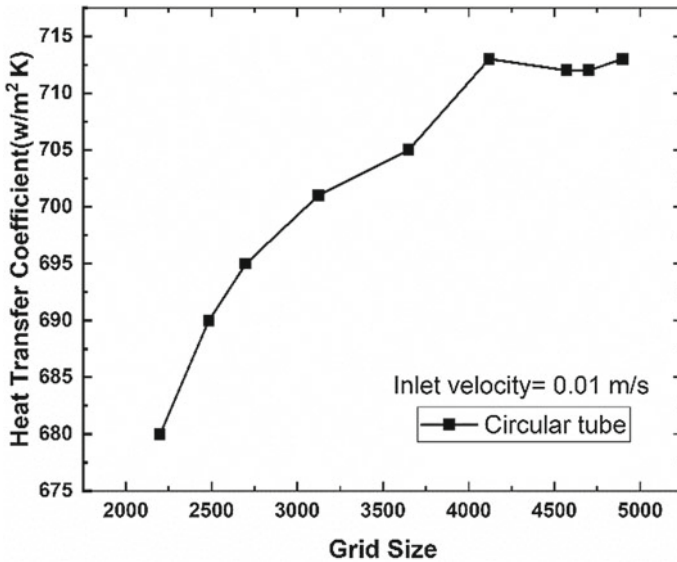


Fig. 3 HTC for the computational domain at various grid sizes

this grid number is reached, no noticeable fluctuations in the HTC produced will occur.

3.6 Validation of Present Model

A circular body of 16 mm diameter, same as the Hamad and He [5], is taken for validation. Water is taken as the working fluid for various inlet velocities flowing from the bottom side of the pipe as similar to [5]. Constant heat flux around 8500 W/m²K is supplied at the wall of the tube for comparison in the same condition. Although the results of the current study do not perfectly match the author's findings, they do agree well with Hamad and He [5], with an error range of 8–13%. The error range may be due to the numerical simulation (Fig. 4).

4 Results and Discussion

The liquid comes into the domain at varying speeds and strikes the tube. The inlet velocity can be anywhere from 0.01 to 0.05 m/s. The heat transfer performance and drop in pressure due to bluff bodies are discussed below.

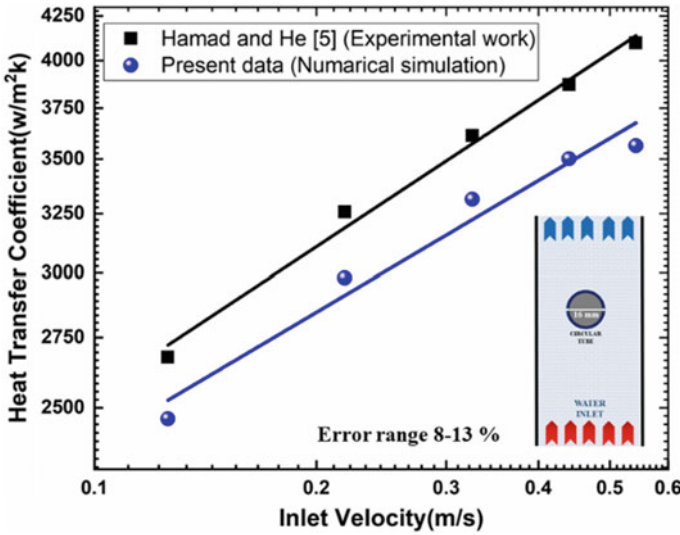


Fig. 4 Comparison of heat transfer coefficient for different inlet velocity of present study and experimental study [5]

5 Heat Transfer and Pressure Drop Performance

The bluff bodies performance is evaluated in terms of heat transfer coefficient and pressure drop. Figure 5a shows the different bluff bodies' heat transfer performances with varying input velocities. This investigation of single-phase heat transfer showed that, across all geometries, HTC increased in conjunction with increasing inlet velocity. This is due to the thinness of boundary layer as the Reynolds number rises. Most heat transfer performance indicators for a given input velocity are better for non-circular than circular orientations except triangle.

The HTC among all bluff bodies is highest in horizontal ellipse and in descending order is vertical semicircle, hexagon, vertical ellipse, inverted triangle, rotated hexagon circular, and triangle. The maximum HTC achieved by the horizontal ellipse is approximately 2500 W/m²K, whereas, for the circular shape, it is around 1800 W/m²K at an inlet velocity of 0.05 m/s. All bodies in the simulations have the same surface area. A possible explanation for the larger HTC seen in the horizontal ellipse is that it represents a region where the water hit occurred over a larger area.

The relationship between the pressure drop (PD) and the input velocity is seen in Fig. 5b. The pressure drop is proportional to the inlet velocity because higher speeds result in superior frictional losses as the fluid moves through the pipe. All non-circular shape pressure drop features have a crucial influence in heat exchanger performance.

The pressure drop of all bluff bodies is written here in descending order as horizontal ellipse, triangle, inverted triangle, rotated hexagon, horizontal semicircle,

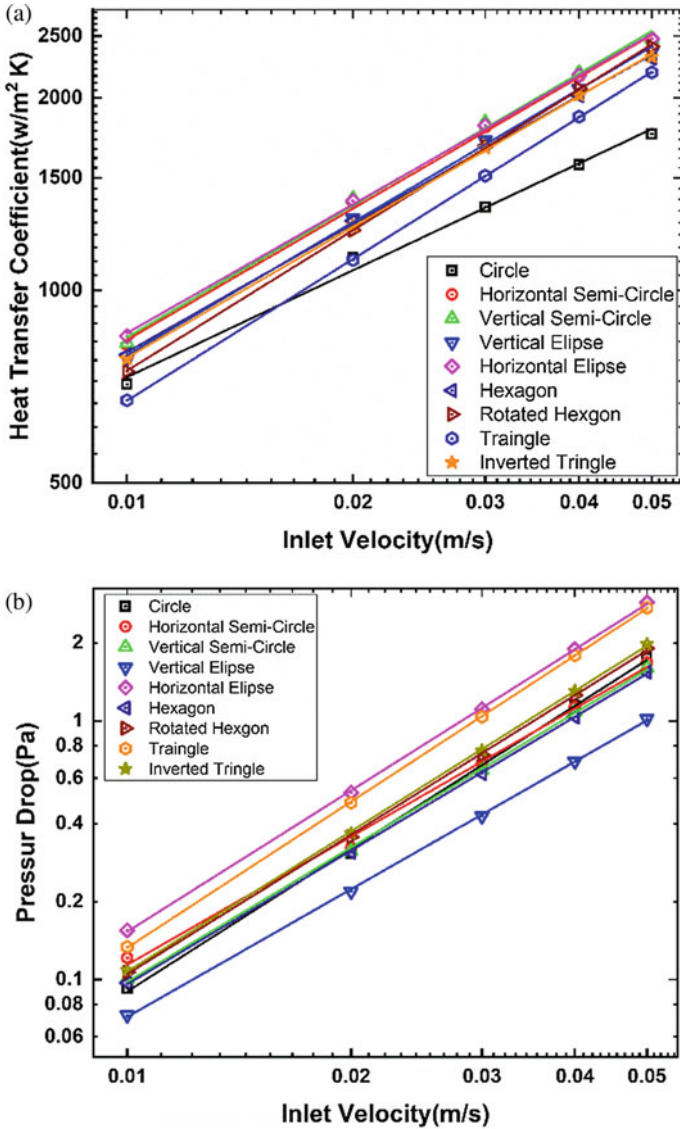


Fig. 5 a Variation of heat transfer coefficient with inlet velocity b change of pressure drop with inlet velocity

vertical semicircle, hexagon, circle, and vertical ellipse. The pressure drop is highest in horizontal ellipse as around 3 Pa and lowest at around 1 Pa at the highest inlet velocity of 0.05 m/s. The pressure drop for the circular bodies has around 1.5 Pa at the same inlet velocity.

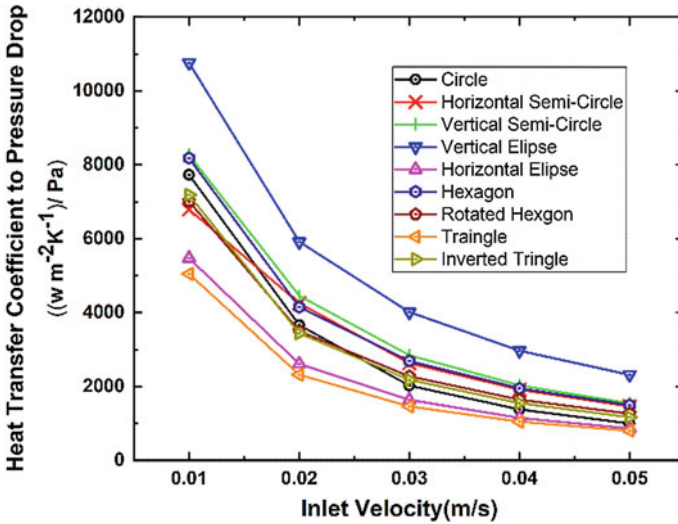


Fig. 6 Variation of heat transfer coefficient to pressure drop w.r.t. inlet velocity

Figure 6 shows the variation of heat transfer coefficient to pressure drop w.r.t. inlet velocity. With an increase in flow speed, the ratio of HTC to pressure drop value decreases. The vertical ellipse performed best, and the tringle performed the least among the bodies.

The enhancement ratio (ER) is the ratio between the HTC of non-circular bodies to the circular body. Figure 7 shows the enhancement ratio w.r.t. inlet velocity. It is seen that increase in inlet flow, the ER increases. Vertical semicircle led the best performance, and tringle performs the least among all the shapes compared to the circular tube.

The pressure drop ratio (PDR) is the ratio of pressure drop of non-circular bodies to the circular body. Figure 8 shows the pressure drop ratio w.r.t. inlet velocity. The horizontal ellipse, triangle, inverted triangle, and rotated hexagon have higher PDR than the circle. The horizontal semicircle, vertical semicircle, and vertical ellipse showed the lowest PDR than the circle.

5.1 Contour Displaying Temperature

Figure 9 shows the temperature contours for the proposed scenarios within the computational area. In every case, the top surface of the tube responds better to temperature fluctuation than the bottom half. This may be because of boundary layer forms over the tube’s surface during fluid flow. The creation of wake causes a greater temperature gradient to be observed at the tube’s upper surface.

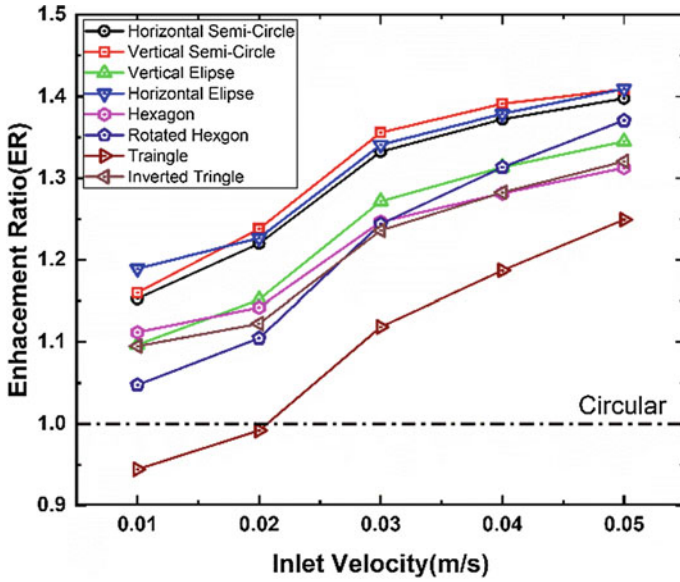


Fig. 7 Enhancement ratio w.r.t. inlet velocity for different bluff bodies

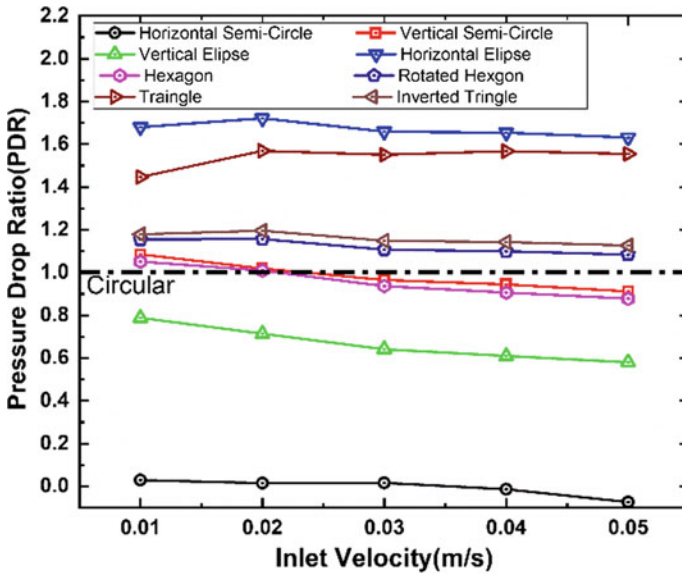


Fig. 8 Pressure drop ratio w.r.t. inlet velocity for different bluff bodies

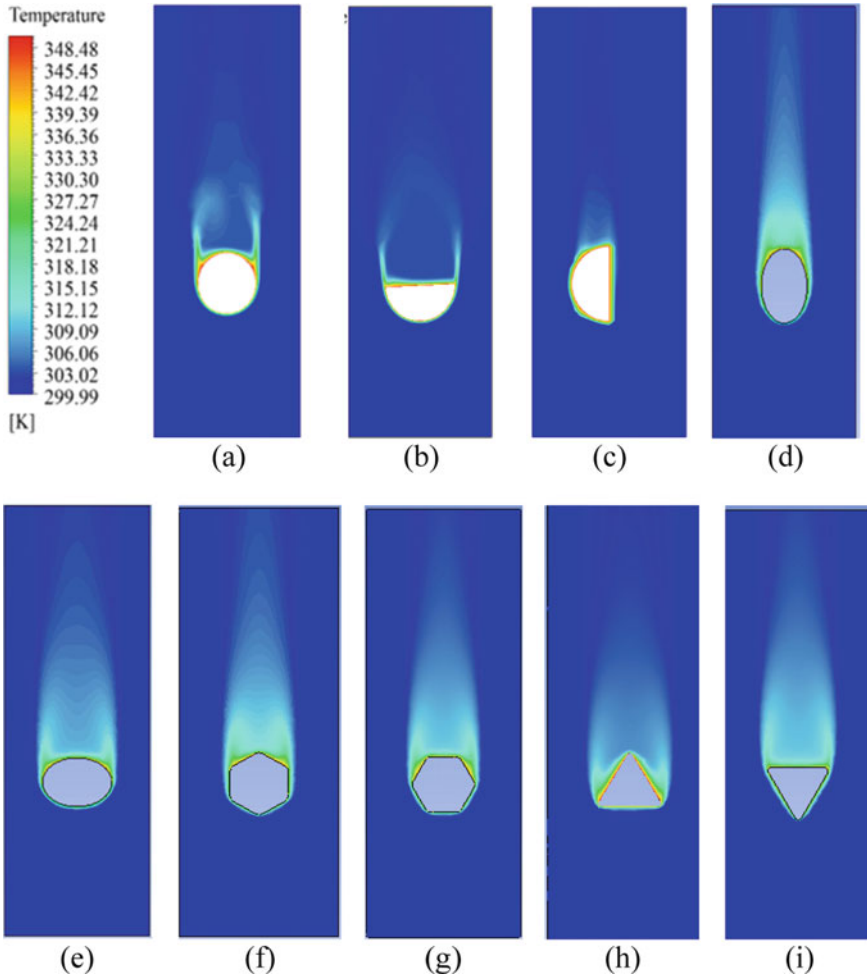


Fig. 9 Different surfaces temperature contours **a** circular **b** semi-circular horizontal cut **c** semi-circular vertical cut **d** vertical ellipse **e** horizontal ellipse **f** hexagon **g** rotated hexagon **h** triangular **i** inverted triangular velocity contour

Figure 10 presents velocity contours formed around the tube surface in the computational domain. Separation of the boundary layer occurs at the tube's upper surface, which is perpendicular to the direction of fluid flow in the computational domain. The fluid disturbance is observed at the tube's periphery in the direction against the flow, i.e., the tube's upper surface.

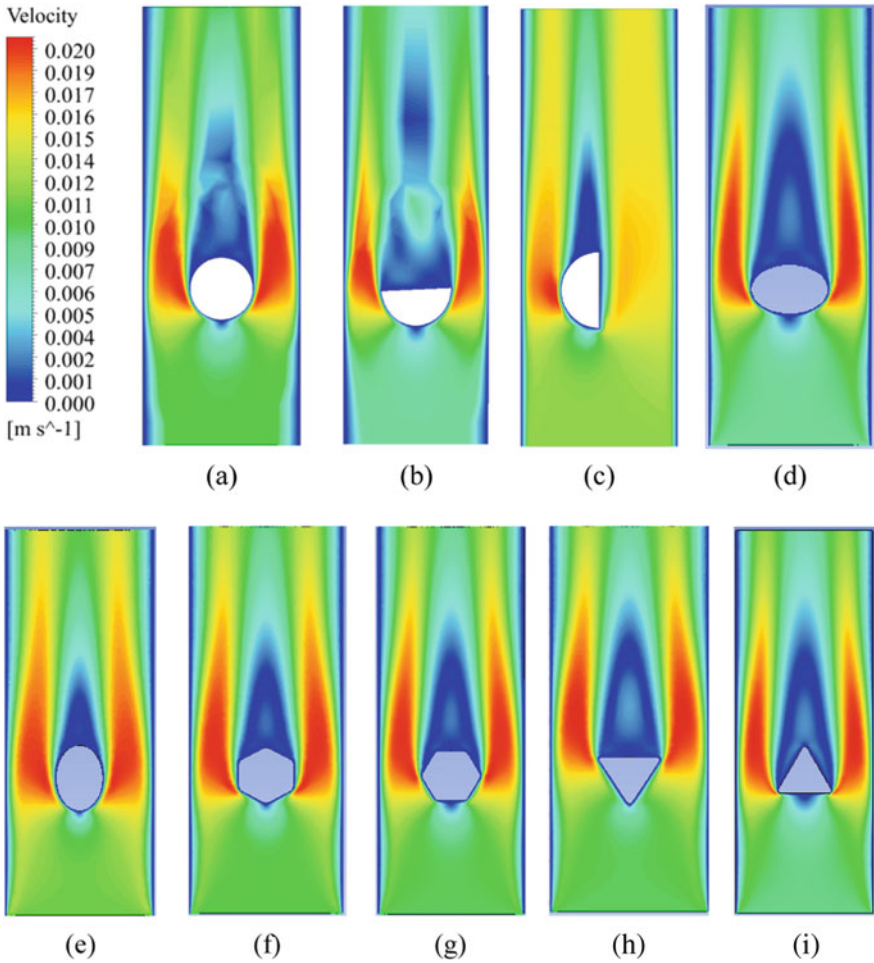


Fig. 10 Velocity contours over the different surfaces **a** circular **b** semi-circular horizontal cut **c** semi-circular vertical cut **d** vertical ellipse **e** horizontal ellipse **f** hexagon **g** rotated hexagon **h** triangular **i** inverted triangular

6 Conclusions

The thermo-hydraulic performance of bluff bodies heated isothermally is reported in this work. Using ANSYS-2020R2 software (fluent module), we investigate single-phase heat transfers and pressure drop over a 2D single tube and compare it to the circular tube. The tube’s shape and inlet velocities are altered. The following results and interpretations were uncovered as a result of the numerical simulation.

- An increase in inlet velocities increases the heat transfer coefficient (HTC) value for all the tubes.

- Increase in inlet velocities, the value of pressure drop (PD) increases for all the tubes.
- The HTC among all bluff bodies is highest in horizontal ellipse followed by vertical semicircle, horizontal semicircle, hexagon, vertical ellipse, inverted triangle, rotated hexagon, circle, and triangle.
- The maximum enhancement in HTC, about 19%, is found for horizontal ellipse than that of circular.
- The pressure drop is found highest in horizontal ellipse among all bluff bodies followed by horizontal ellipse, triangle, inverted triangle, rotated hexagon, horizontal semicircle, vertical semicircle, hexagon, circle, and vertical ellipse.
- The vertical ellipse provides a 21% lesser pressure drop among all bluff bodies than circular.
- A vertical ellipse is best for a high heat transfer coefficient and less pressure drop. The pressure drop for other bodies is reported in ascending order as a vertical semicircle, hexagon, circle, inverted triangle, rotated hexagon, horizontal semicircle, horizontal ellipse, and triangle.
- The vertical semicircle showed the highest enhancement ratio (ER), and the triangle gave the least among all the shapes compared to the circular tube.
- The pressure drop ratio (PDR) is highest for horizontal ellipse, and lowest for vertical ellipse and vertical semicircle compared to the circle.

References

1. Achenbach E (1974) Total and local heat transfer from a smooth circular cylinder in cross-flow at high Re. *Int J Heat Mass Transf* 18:1387–1390
2. Zdravkovich MM (1997) *Flow around circular cylinders vol 1*. Oxford University Press
3. Sparrow EM, Abraham JP, Tong JCK (2004) Archival correlations for average heat transfer coefficients for non-circular and circular cylinders and for spheres in cross-flow. *Int J Heat Mass Transf* 47:5285–5296
4. Mohanty RL, Swain A, Das MK (2018) Thermal performance of mixed tube bundle composed of circular and elliptical tubes. *Therm Sci Eng Prog* 5:492–505
5. Hamad F, He S (2017) Heat transfer from a cylinder in cross-flow of single and multiphase flows. *Int J Mech Aerosp Ind Mechatro Manuf Eng* 11(3):386–390
6. Nada SA, Batsh EI, Moawed H (2007) Heat transfer and fluid flow around semi-circular tube in cross flow at different orientations. *Heat Mass Transf* 43(11):1157–1169
7. Nada S, Mowad M (2003) Free convection from a vertical and inclined semi-circular cylinder at different orientations. *Alexandria Eng J* 42(3):273–282
8. Forbes LK (1988) Critical free surface flow over a semi-circular obstruction. *J Eng Math* 22(1):313
9. Hashizume K (1981) Heat transfer and pressure drop characteristics of finned tubes in cross-flow. *Heat Transf Eng* 3(2):15–20
10. Ibrahim EZ, Elsayed AO (2000) Characteristics of heat transfer from a semi-circular pipe in cross-flow. In: *Mansoura third international engineering conference, vol 2*. El- Mansoura, Egypt, pp 77–83
11. Sha BB, Mohanty RL, Das MK (2021) Thermo-hydraulics performance of isothermally heated tube composed of the flat and circular surface. In: *Proceedings of the 26th national and 4th*

- international ISHMT-ASTFE heat and mass transfer conference, Dec 17–20, IIT Madras, Chennai-600036, Tamil Nadu, India. Begel House Inc.
12. Sha BB, Mohanty RL, Das MK (2023) Heat transfer and pressure drop characteristics of semicircular tube at different orientations. In: Manik G, Kalia S, Verma OP, Sharma TK (eds) Recent advances in mechanical engineering. Lecture notes in mechanical engineering. Springer, Singapore

Study of the Effect of Single-Phase Flow Conditions on FAC for Various Feeder Bend Geometries of Pressurized Heavy Water Reactor (PHWR)



K. Premsai, Niraj Uttam, A. Moorthi, and Ankit Bangar

1 Introduction

Indian nuclear power program is currently based on indigenous pressurized heavy water reactors (PHWR). PHWR uses natural uranium as fuel eliminating the need for enrichment. PHWR is a pressure tube type reactor which means calandria is pierced by a large number of pressure tubes. These pressure tubes contain coolant at high pressure, while the moderator takes the rest of the space in calandria. Moderator and coolant (both heavy water, D_2O) are having their separate circuits. The number of pressure tubes varies depending upon the power rating of the reactor. For the case of $540 MW_e$ and $700 MW_e$ number of pressure tubes are 392.

Flow accelerated corrosion (FAC) is an electrochemical corrosion process involving chemical dissolution and mass transfer. FAC causes wall thinning of pipeline and pipe fittings. Due to wall thinning, catastrophic failure occurs leading to enormous economic loss to industries like oil and gas, nuclear power plants, and the chemical process industry [1]. The FAC of feeder pipes of PHWRs is a matter of concern since it causes thinning of the wall leading to an eventual failure. The parameters affecting the corrosion rate are water chemistry, temperature, the metallurgy of pipe, mass transfer coefficient, etc.

Given in Fig. 1 is diagram showing mechanism of FAC. In deoxygenated water flow in the circuit leads to the formation of a magnetite layer which acts as a barrier to further oxidization. In FAC, this barrier formed is dissolved in a flowing water stream which carries away dissolved ions ($FeOH^+$), creating a concentration gradient that leads to the further dissolution of the protective magnetite layer. Dissolution continues till the thickness of the piping element crosses the minimum required thickness to sustain pressure leading to the failure of a component.

K. Premsai · N. Uttam · A. Moorthi · A. Bangar (✉)
BARC Facilities, Kalpakkam 603127, India
e-mail: ankitb@barc.gov.in

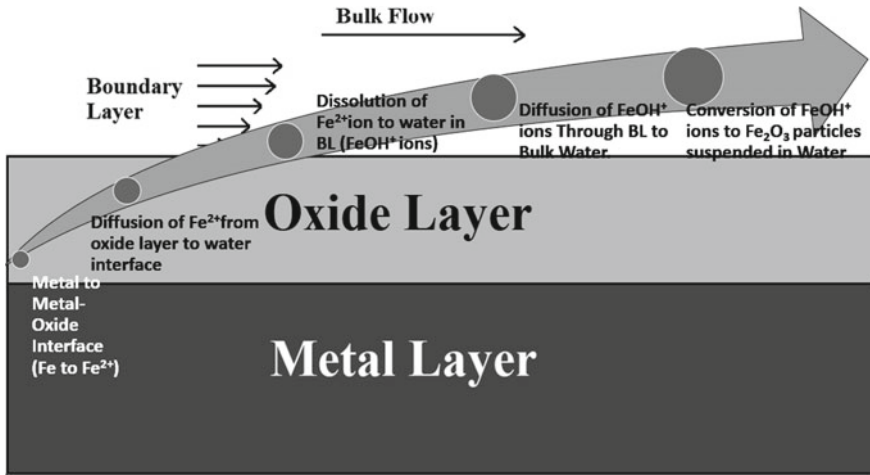


Fig. 1 Depiction of FAC mechanism

Initially, iron is present in metallic form in pipe material. This metallic iron present on the surface of the pipe undergoes oxidation in presence of oxygen content available in the coolant. Upon oxidation metallic iron (Fe) is converted into oxidized form (Fe²⁺). This ionic Fe²⁺ is soluble in the coolant which is heavy water. Although the rate of dissolution is less, but depending upon the life of the reactor and local flow conditions, it can be detrimental. Once Fe²⁺ is dissolved in coolant, formation of FeOH⁺ happens. This newly formed FeOH⁺ diffuses through the boundary layer. Chemical effects more or less cause FAC uniformly throughout the piping. But the mechanical effect can cause the localized rate of FAC to be higher. It can happen due to local flow conditions. These local flow conditions (like eddies) can cause an increase in mass transfer locally resulting in increased rate of FAC locally.

For the case of a fully developed turbulent boundary layer, mass transfer rate and wall shear stresses can be related by using Chilton- Colburn analogy [2],

$$\left(\frac{f}{2}\right)^n = \frac{Sh}{Re \cdot Sc^{1/2}}, \tag{1}$$

where

$$\text{Schmidt number} = \frac{\text{Momentum Diffusivity}}{\text{Mass Diffusivity}} \text{ or } Sc = \frac{\mu}{\rho\Gamma}, \tag{2}$$

$$\text{Sherwood number} = \frac{\text{Convective Mass Transfer}}{\text{Rate of Diffusive Mass Transfer}} \text{ or } Sh = \frac{kd}{\Gamma}, \tag{3}$$

$$\text{Reynolds Number} = \frac{\text{Inertial Force}}{\text{Viscous Force}} \text{ or } Re = \frac{\rho ud}{\mu}. \tag{4}$$

' Γ ' is the diffusion coefficient for a given species in fluid combination, ' d ' is the hydraulic length for a given geometry, ' f ' is the Fanning friction factor, ' k ' is the mass transfer coefficient, ' u ' is flow velocity, ' μ ' is the dynamic viscosity of the fluid, and ' ρ ' is the fluid density. The value of exponent ' n ' can be '1' according to [2] or between 0.5 and 1. Further Fanning friction factor ' f ' can be defined in terms of wall shear stress (τ) as,

$$\frac{f}{2} = \frac{\tau}{\rho u^2}. \quad (5)$$

From above equations mass transfer coefficient can be defined in terms of wall shear stress as,

$$k = \left(\frac{\tau}{\rho u^2} \right)^n u Sc^{-2/3}. \quad (6)$$

Equation (6) points to the fact that mass transfer coefficient is dependent on wall shear stress. This dependence is directly proportional which means higher the value of wall shear more is mass transfer. From above given arguments, it is concluded that since higher wall shear stress results in more mass transfer, so to identify the regions more susceptible to FAC, regions with higher values of wall shear stress are to be identified.

2 Literature Review and Objective

A pressurized heavy water reactor (PHWR) consists of fuel channels connected to a common inlet and outlet header. These fuel channels are connected to common headers via the arrangement of 2–2.5 inch diameter tubes (as shown in Fig. 2). The geometric design of inlet and outlet feeder pipe is the same. Each feeder pipe is clubbed into types depending upon variables like diameter, flow velocity, whether single or double bend, etc. There are '12' such types shown in Figs. 3 and 4.

The Types 7, 10 and 11 are more susceptible to FAC due to higher values of wall shear developed as a consequence of double bend geometry. Bends in feeder pipes are not lying in the same plane as shown in Fig. 5. But for simplification, both the bends are assumed to be in a single plane as shown in Fig. 6. This assumption has little effect on wall shear distribution and magnitude [4].

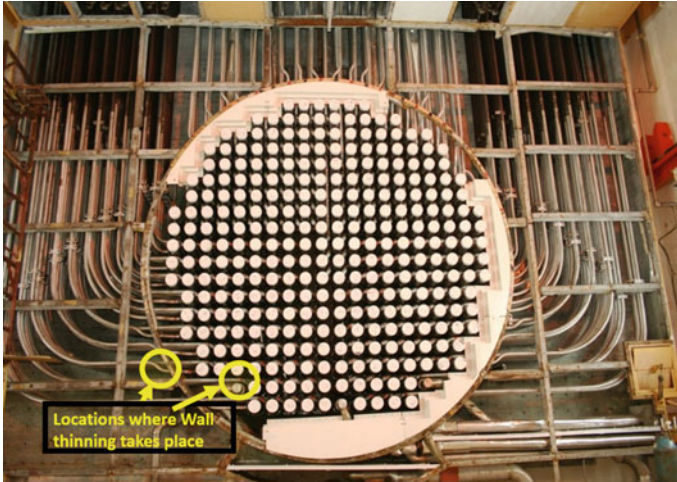


Fig. 2 Arrangement of feeder bends in PHWR

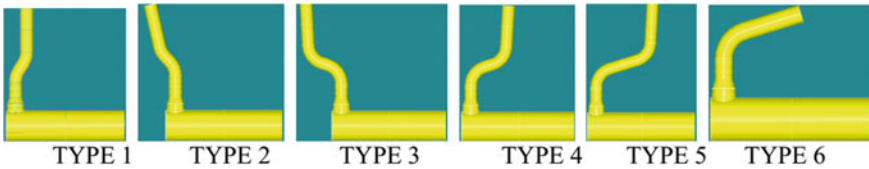


Fig. 3 2.5 inch diameter outlet feeder pipes geometric types

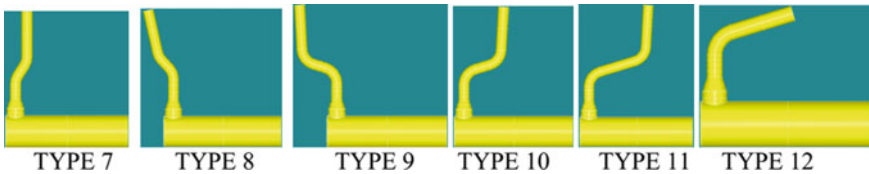


Fig. 4 2 inch diameter outlet feeder pipes geometric types

3 Material and Methods

Effect of 4 parameters are varied and their effect on wall shear distribution and magnitude is studied. These parameters are the length of the straight portion of pipe at entry, bend angle of first bend, bend angle of second bend, and length of the straight portion of pipe connecting these two bends, respectively. For simplicity entry length is represented as 'L1', interconnecting length as 'L2', first bend angle as 'BA1', and second bend angle as 'BA2'. Four data points of each of the four parameters are taken, Fig. 6. The data range (Table 1) is chosen such that the values of feeder pipe bend in

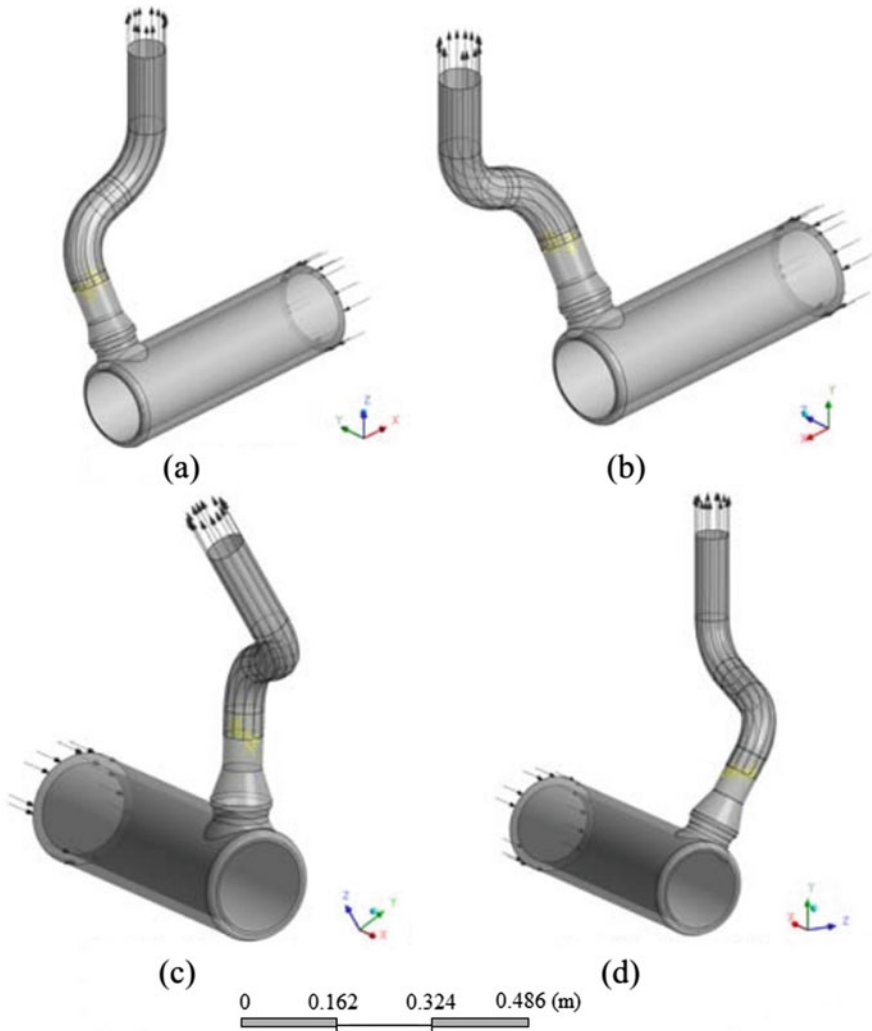


Fig. 5 Multi-planar feeder bend geometry of PHWR

PHWR lie in between the selected range of parameters. The range of parameters is taken rather than the geometries of feeder bends, so that a more holistic view of wall shear distribution and magnitude can be obtained for different geometric variables.

There are ‘four’ parameters to vary for ‘four’ values, each will result in running 256 (4^4) cases.

Since a total of 256 simulations are run splitting the fluid domain into two halves (Fig. 7) reduces computational work and also reduces the time of simulations. But it can result in erroneous results as the fluid in the upstream part will not be communicating with the fluid downstream. Also, the local conditions (like pressure, eddies,

Fig. 6 Geometric parameters varied for study of effect on wall shear

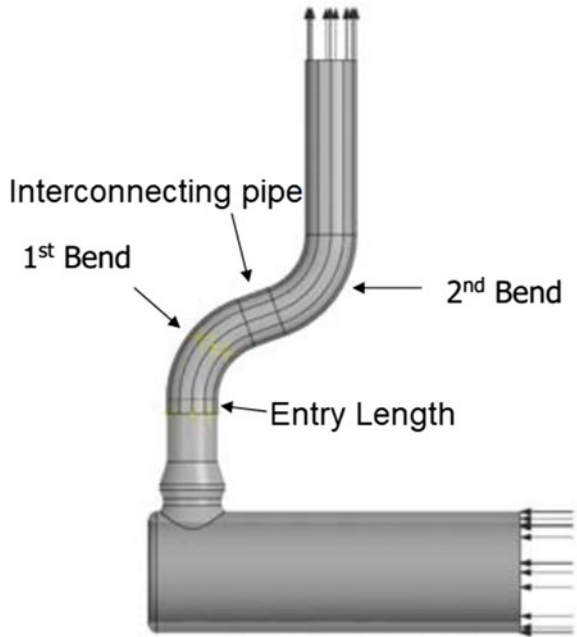


Table 1 Design points for simulation

S. No.	L1 (mm)	BA1	L2 (mm)	BA2
1	15	30°	24	30°
2	30	45°	75	45°
3	45	60°	126	60°
4	60	75°	177	75°

etc.) are altered as inlet and outlet boundary conditions are imposed at the plane of split. To take care of probable errors introduced into data due to splitting of fluid domain, simulations of the complete geometries were performed. To further reduce computational effort, only cases with a minimum entry length value, 15 mm, and minimum interconnecting length value, 24 mm are taken. Value of first bend angle is kept constant at 45°, while second bend angle is only varied. So, a total of four simulations with the complete fluid domain are performed. The average velocity in feeder pipe for different fuel channels comes out to vary in the range of 7.26–18.09 m/s [3]. Selection of inlet velocity into pressure tube is done such that average velocity in feeder bend comes out to be 15 m/s. On applying continuity equation in between the inlet to pressure tube and outlet from pressure tube, average velocity at the inlet to pressure tube taken is 4.15 m/s.

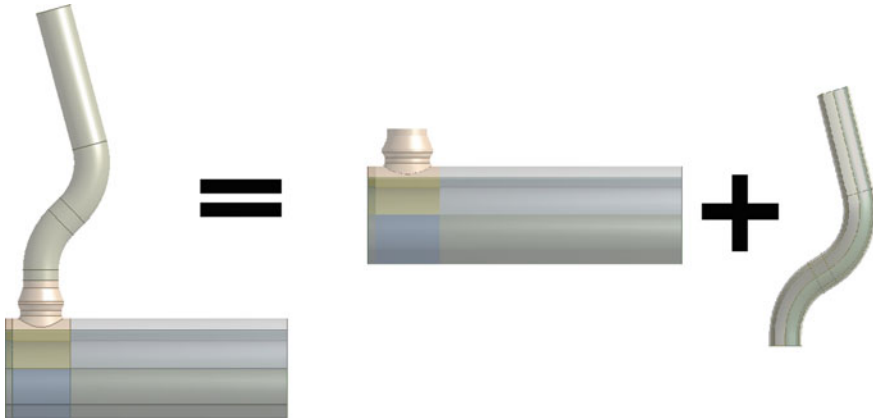


Fig. 7 Separate study of pressure tube and feeder pipe section of model

Solver settings

- Turbulent model: Realizable $k - \varepsilon$, with enhanced wall treatment.
- Density = 788.3 kg/m^3 , viscosity = $8.5 \times 10^{-5} \text{ Pa.s}$.
- Boundary conditions: Inlet velocity = 4.15 m/s , outlet pressure = 0 Pa , wall condition = no slip.
- Method: SIMPLE.
- Residual convergence criteria: $\approx 1 \times 10^{-4}$ for continuity, $\approx 1 \times 10^{-6}$ for velocity, $\approx 1 \times 10^{-5}$ for ' k ' and ' ε '.

Profile from the outlet of pressure tube is saved. Flow variables like velocity, ' k ', and ' ε ' are written in the files which are read as an inlet profile for the feeder bend section of the model. Since mesh was done to resolve the boundary layer to get results as close to reality, values of y^+ are kept as close to unity as possible (Fig. 8).

As it can be seen from the data as given in Table 2 feeder bend only simulations over-predict values of wall shears giving values more conservative in nature. Also, the maximum percentage error for maximum wall shear comes around 4%. While the maximum percentage error for average wall shear is about 8%, showing that the impact of splitting the geometry on wall shear and its distribution is not much prominent. So, remaining 255 cases were simulated using only feeder bend geometry domain (Figs. 9 and 10).

4 Results and Discussion

To know the dependence of wall shear stress on the 'four' of varied parameters, a statistical tool of linear regression is used. It works on the minimization of mean square error (MSE). The hypothesis function ' $h_\theta(x)$ ' is chosen such that it best

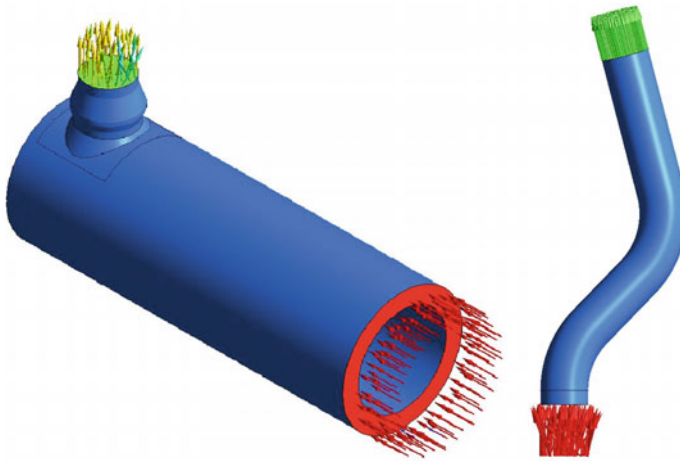


Fig. 8 Boundary conditions applied wall (blue), inlet (red) and outlet (green)

Table 2 Comparing data from feeder bend only and complete fluid domain simulations

BA 1 (°)	BA 2 (°)	Feeder bend only		Full fluid domain	
		Max. wall shear (Pa)	Avg. wall shear (Pa)	Max. wall shear (Pa)	Avg. wall shear (Pa)
45	30	659.26	324.25	644	322.88
45	45	667.56	324.8	663.89	299.37
45	60	669.36	324.73	644.33	317.6
45	75	669.08	323.94	660.47	311.54

represents the nature of variation of available data points. Hypothesis function can be linear, quadratic, cubic, or even trigonometric, logarithmic. Hypothesis function for average wall shear stress is given in Eq. (8).

Calculation of flow accelerated corrosion (FAC) is done using the Eq. (7) [3],

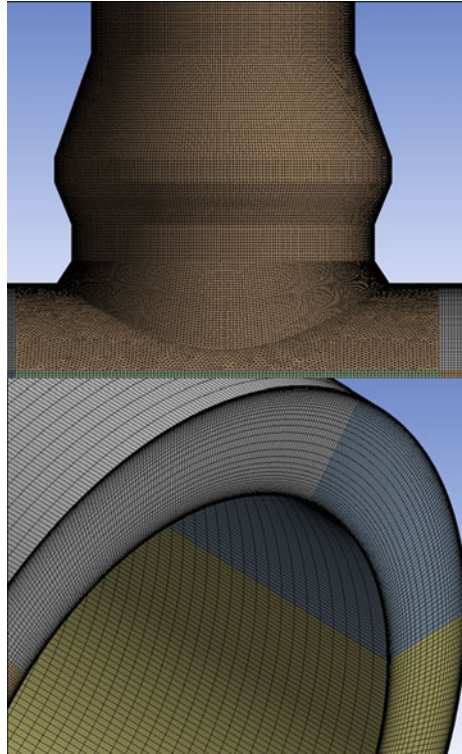
$$\text{RATE}(\mu\text{m/s}) = 7.65(1 + 0.111\tau^{0.75}).(1 + 7.15 \times 10^{-10} e^{\text{pH}}), \quad (7)$$

where ‘ τ ’ is wall shear stress and ‘pH’ is taken to be 10.4. The above equation holds for case of carbon steel A106-B. Values of FAC calculated using wall shear stress obtained from simulation are coming near to the values calculated using empirical results (Figs. 11, 12, 13 and 14).

Hypothesis function for calculation of average wall shear is,

$$h_{\theta}(x) = \left(\begin{array}{c} \theta_0 x_0 + \theta_1 x_1 + \theta_2 x_2 + \theta_3 x_3 + \theta_4 x_4 \\ + \theta_5 x_1^2 + \theta_6 x_2^2 + \theta_7 x_3^2 + \theta_8 x_4^2 + \\ \theta_9 x_1 x_2 + \theta_{10} x_2 x_3 + \theta_{11} x_3 x_4 + \theta_{12} x_4 x_1 \end{array} \right), \quad (8)$$

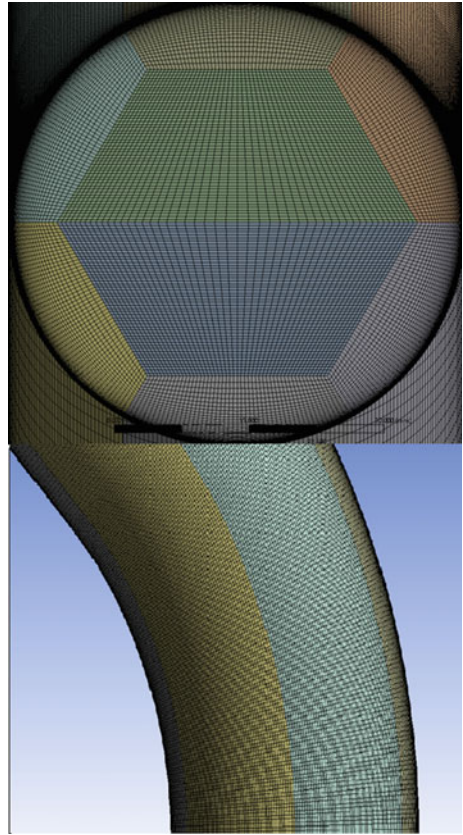
Fig. 9 Meshing of pressure tube section



where

$$\begin{bmatrix} \theta_0 \\ \theta_1 \\ \theta_2 \\ \theta_3 \\ \theta_4 \\ \theta_5 \\ \theta_6 \\ \theta_7 \\ \theta_8 \\ \theta_9 \\ \theta_{10} \\ \theta_{11} \\ \theta_{12} \end{bmatrix} = \begin{bmatrix} 351.0416 \\ -0.8159 \\ -0.4418 \\ 0.1364 \\ -0.2127 \\ 2.6466 \times 10^{-3} \\ 1.9690 \times 10^{-3} \\ -5.3634 \times 10^{-4} \\ 1.6955 \times 10^{-4} \\ 4.6846 \times 10^{-3} \\ -1.3374 \times 10^{-3} \\ -5.6222 \times 10^{-4} \\ 7.4522 \times 10^{-4} \end{bmatrix} \tag{9}$$

Fig. 10 Meshing of feeder tube section



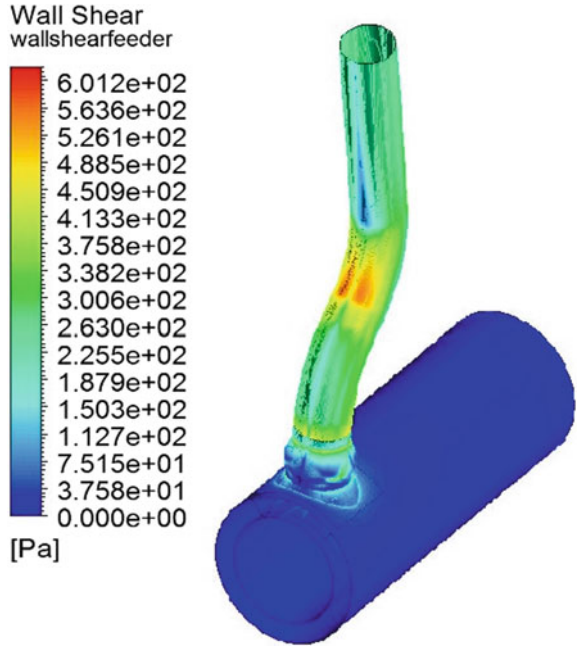
and $x_0, x_1, x_2, x_3,$ and x_4 are ‘1’, entry length (L1), first bend angle (BA1), second bend angle (BA2), and interconnecting length (L2), respectively, gives hypothesis function for prediction of average wall shear stress (Table 3, 4, 5 and 6).

Hypothesis function for maximum wall shear stress is,

$$h_{\theta}(x) = \left(\begin{array}{c} \theta_0 x_0 + \theta_1 x_1 + \theta_2 x_3 + \theta_4 x_4 \\ + \theta_5 x_1^2 + \theta_6 x_2^2 + \theta_7 x_3^2 + \theta_8 x_4^2 \\ + \theta_9 x_1 x_2 + \theta_{10} x_2 x_3 + \theta_{11} x_3 x_4 + \theta_{12} x_4 x_1 \\ \theta_{13} x_1^3 + \theta_{14} x_2^3 + \theta_{15} x_3^3 + \theta_{16} x_4^3 \end{array} \right) \quad (10)$$

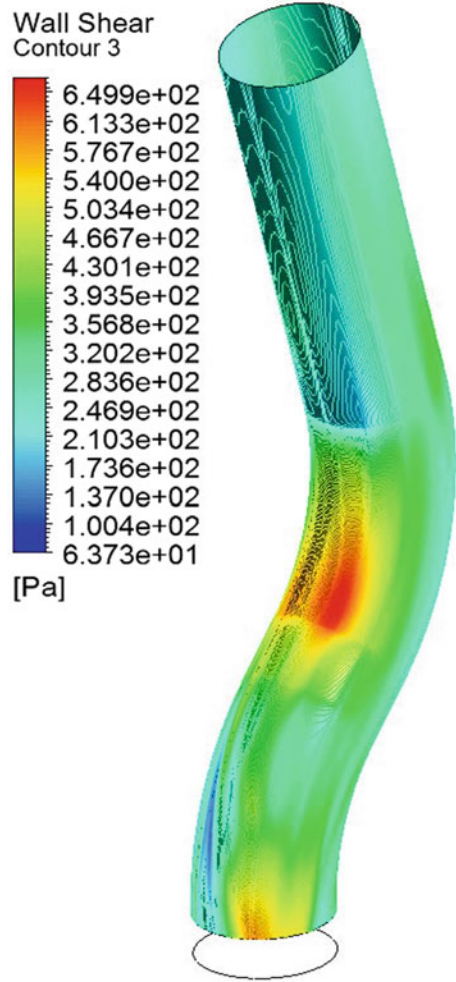
where

Fig. 11 Wall shear contour for case of L1 = 15 mm, L2 = 24 mm, BA1 = 45°, and BA2 = 60° for full fluid domain



$$\begin{bmatrix} \theta_0 \\ \theta_1 \\ \theta_2 \\ \theta_3 \\ \theta_4 \\ \theta_5 \\ \theta_6 \\ \theta_7 \\ \theta_8 \\ \theta_9 \\ \theta_{10} \\ \theta_{11} \\ \theta_{12} \\ \theta_{13} \\ \theta_{14} \\ \theta_{15} \\ \theta_{16} \end{bmatrix} = \begin{bmatrix} 713.5251 \\ -6.0822 \\ 4.5637 \\ 0.71154 \\ -2.3482 \times 10^{-2} \\ 5.7437 \times 10^{-2} \\ -0.11324 \\ -7.9722 \times 10^{-3} \\ 1.7148 \times 10^{-2} \\ 1.6643 \times 10^{-2} \\ -5.7148 \times 10^{-4} \\ -1.3687 \times 10^{-3} \\ -3.2875 \times 10^{-3} \\ -1.4134 \times 10^{-4} \\ 7.6878 \times 10^{-4} \\ 3.8562 \times 10^{-5} \\ -3.8750 \times 10^{-5} \end{bmatrix} \tag{11}$$

Fig. 12 Wall shear contour for case of $L1 = 15$ mm, $L2 = 24$ mm, $BA1 = 45^\circ$, and $BA2 = 60^\circ$ for feeder pipe only



5 Conclusions

From data obtained, following can be concluded:

1. Average wall shear stress is a nearly linear function of variables. Average wall shear stress decreases with an increase in the values of variables. Effects of variables on average wall shear stress in decreasing order are entry length ($L1$), interconnecting length ($L2$), first bend angle ($BA1$), and second bend angle ($BA2$).
2. Maximum wall shear stress variation is nonlinear in nature. Maximum wall shear stress decreases with an increase in values of variables (except for the second bend angle). The order of effects of variables on maximum wall shear stress is

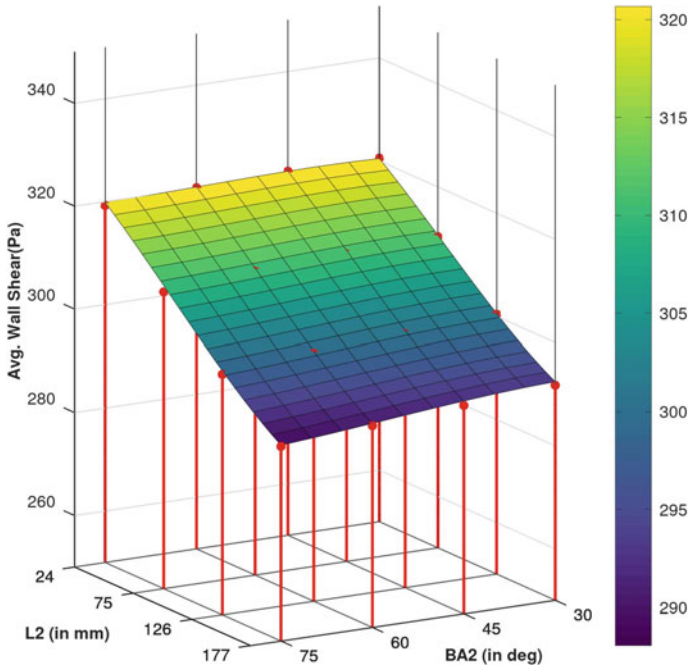


Fig. 13 Simulation data points (red dots) and linear regression fit (as surface plot) for average wall shear stress for case of $L1 = 15 \text{ mm}$ and $BA1 = 60^\circ$

the same as that of average wall shear stress. Maximum wall shear stress comes out to be 1.5–2 times the value of average wall shear stress for a given set of parameters. For all simulations, maximum wall shear stress appeared at intrados of the second bend angle.

3. Using linear regression, polynomial equations for calculating average wall shear stress and maximum wall shear stress for different values of mentioned variables were developed. These equations predict average wall shear stress and maximum wall shear stress with < 5% error for given range of parameters.
4. The dependence of average wall shear stress and maximum wall shear stress on entry length is highest among other variables. Variation as high as 15% of the average value for case of average wall shear stress and 22% of the average value for maximum wall shear stress for given set of other variables is observed. Since fluid enters the ‘entry length’ portion first its influence on flow distribution downstream is significant. Smaller entry length results in higher values of wall shear stress as the fluid doesn’t get the sufficient length for velocity gradients to normalize. For $L1 > 45 \text{ mm}$, change in the rate of FAC calculated using average wall shear stress is < 0.7% and < 7% for rate of FAC taking maximum wall shear stress values. While for $L1 < 45 \text{ mm}$, 5% variation in FAC for average wall shear stress values and > 25% for FAC calculated using maximum wall shear stress is observed. Also, it is observed from the data that the value of average wall

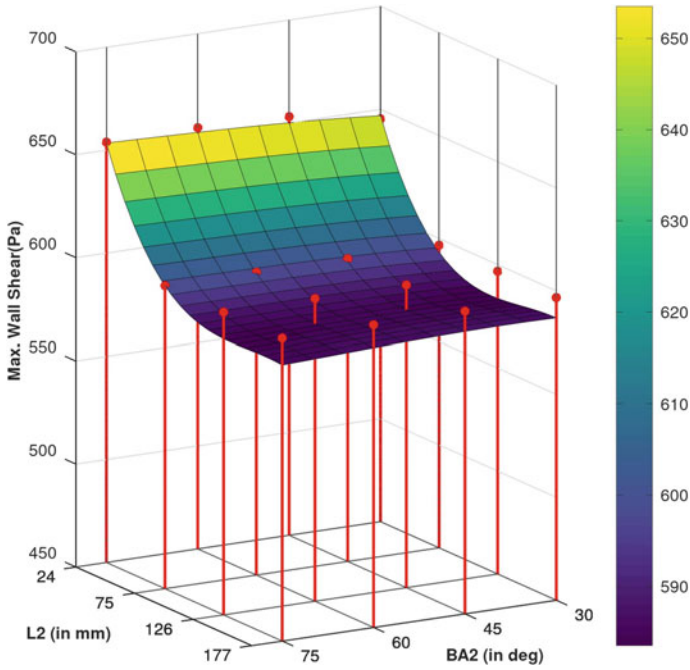


Fig. 14 Simulation data points (red dots) and linear regression fit (as surface plot) for maximum wall shear stress for case of L1 = 15 mm and BA1 = 60°

Table 3 Linear curve fitting parameters for average wall shear stress

Parameters	Value
R^2	0.9848
MSE	2.14
Error variance	2.255
Max residual	14.62
Min residual	- 9.35

Table 4 Linear curve fitting parameters for maximum wall shear stress

Parameters	Value
R^2	0.92085
MSE	179.62
Error variance	192.39
Max residual	40.984
Min residual	- 36

Table 5 Data points for first eight cases

L1 (mm)	BA1 (°)	BA2 (°)	L2 (mm)	Max. wall shear (Pa)	Avg. wall shear (Pa)
15	30	30	24	650.92	329.21
15	30	30	75	595.5	317.37
15	30	30	126	595.54	307.54
15	30	30	177	595.43	298.46
15	30	45	24	670.58	330.54
15	30	45	75	600.77	317.33
15	30	45	126	595.45	307.15
15	30	45	177	595.54	304.39

Table 6 Calculated values minimum and maximum of FAC for values of average and maximum wall shear stress

Max. wall shear (simulation)		Max. wall shear (simulation)	
Minimum value	473.20 Pa	Minimum value	278.91 Pa
Maximum value	675.48 Pa	Maximum value	330.70 Pa
FAC rate (min)	93.80 μm/a	FAC rate (min)	65.61 μm/a
FAC rate (max)	120.16 μm/a	FAC rate (max)	73.50 μm/a

shear stress is not going below the value of 280 Pa for any values of variables. These lowest values correspond to both the bend angles at the lowest 30°, at this value the pipe is essentially a straight pipe and any variation in entry length and interconnecting length causes little to no variation in wall shear stresses both average and maximum wall shear stress.

- Interconnecting length is the second most decisive parameter, leading to a maximum variation of ≈13% of average for average wall shear stress and > 20% of average for maximum wall shear stress. The effect of the increase in interconnecting length is to decrease maximum and minimum values of wall shear stress by an equal margin. As the interconnecting length increases, the effect on flow distribution due to entry length and the first bend angle decreases flow tends to become more uniform along the straight portion of the interconnecting length.
- The maximum variation introduced to average wall shear stress with a variation of first bend angle is ≈11.7% of average and for maximum wall shear stress is < 20% of average. As observed from wall shear stress contours, regions of high wall shear stresses (regions where wall shear stress is higher than the average value) are observed at entry length and first bend. Thus, geometry in the starting of the feeder pipe influences wall shear stress magnitude and distribution in a significant manner. As first bend angle increases, the length of the bend increases giving time for high-velocity gradients introduced by the pressure tube to dissipate. This causes wall shear stress to decrease with an increase in the first bend angle.
- The effect of the second bend angle is negligible for both average and maximum wall shear stresses.

8. Since effect of entry length is more prominent, entry length dimension should be more. But its effect is less for higher values of entry length. After entry length, value of interconnecting length should be kept as long as possible. At last first bend angle can be increased.

References

1. Kain V (2014) Flow accelerated corrosion: forms, mechanisms and case studies. In: BARC, 1st international conference on structural integrity, ICONS
2. Chilton TH, Colburn AP (1934) Industrial and engineering chemistry, 26th edn, pp 1183
3. Cătană A, Păuna E, Ioan M (2013) Computational fluid dynamics analysis for flow accelerated corrosion in CANDU6 feeder pipes. Institute for Nuclear Research Pitești, Romania
4. Kang DG, Jo JC (2007) Prediction of the local areas of CANDU feeder pipes highly susceptible to wall thinning due to Flow-accelerated corrosion, by Korea Institute of Nuclear Safety

Deployment of Helical Fins for Heat Transfer Enhancement in Internal Flows



Yatharth Lilhare, Amit Arora, and Himanshu Jangid

1 Introduction

Heat exchangers are widely used in commercial applications, such as automobile, HVAC, aerospace, process industry, etc., and in domestic applications, such as in fridge, air conditioners, etc. As there are advancements in technology, there is a need for more effective heat exchanger. In this quest to find solution for the same, internally finned tube have provided an effective solution. It also helps in making the system more compact. Internally finned tubes are currently used in HVAC industry for evaporators, condensers, shell and tube heat exchanger, etc. [1], and many more fields are being explored where this kind of tubes can be used [2, 3]. As of now, tubes with limited variety of helix angle are available in the market, out of which tubes with helix angle 18° and 25° are widely available. In order to obtain the best results, it is necessary to define the fin geometry at various operating conditions.

2 Literature Review and Objective

In the past, various numerical analyses have drawn comparison between a normal tube and internally finned tubes mainly by analysing convective heat transfer coefficient (h) and pressure drop (ΔP). Fahed et al. [4] and Copetti et al. [5], in their study, had recommended to use this tube in turbulent regime instead of laminar as there is very slight increment in h in laminar region.

Experimentally, internally finned tubes are not explored much as there is limitation of manufacturing such kind of tubes. Albeit, there are some experimental data [6–9] present which vouch for the numerical study. Every study has concluded that there

Y. Lilhare (✉) · A. Arora · H. Jangid
Department of Mechanical Engineering, MNIT Jaipur, Jaipur 302017, India
e-mail: 2019ume1181@mnit.ac.in

is a significant improvement in h upon using internal fins and almost each of them had given appropriate reason for their results.

The case presented in this paper has slight change in design of fins. Shakir et al. [10] has made fins after certain intervals, which is underutilization of internal surface of fins that can be further used to augment the heat transfer. Tube design presented in this case has continuous fins in order to utilize the inner surface optimally.

The objective of the following study is to get the results for continuous helical internal fins of triangular shape in turbulent region by changing some geometrical and kinematic properties, recording its enhancement in h . PEC has been used to decide the best kind of tube so as to consider both h and ΔP simultaneously in comparison to plain tube and straight triangular serrated tube.

3 Numerical Model

ANSYS Fluent software was used for this computational study. A two-equation model, i.e. standard k - ϵ model [11], is used for the numerical simulation. It is one of the widely used models in CFD. This model provides a description of turbulence with the help of two transport equations. The first transported variable is turbulent kinetic energy (k) and the second transported variable is turbulent kinetic energy's rate of dissipation (ϵ). Wall function adopted for this study is enhanced wall treatment with thermal and pressure gradient effects. For pressure velocity coupling, SIMPLE (Semi-Implicit Method for Pressure Linked Equations) algorithm is used. Spatial discretization for every variable is modelled using second-order upwind scheme and the convergence criteria was satisfied when the residual of the energy equation was 10^{-8} and 10^{-5} for other governing equations.

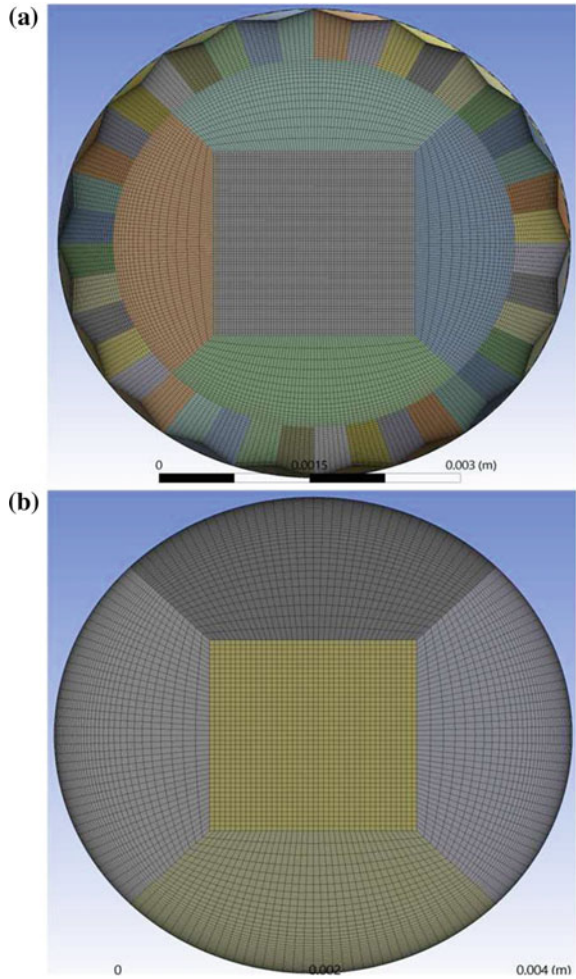
3.1 Geometrical Model

Tube with fixed fin number $N = 20$ is analysed with different helix angle(α), from 30° to 50° , is considered in this study, with a step increment of 5° . Length of the tube, $L = 75$ mm, and its pitch diameter, $D_p = 5$ mm. Apart from this, case of tube with different fin height(e), ranging from 0.05 to 0.2 mm, with a step increment of 0.05 mm, is studied.

3.2 Mesh Generation

For this analysis, mapped mesh is used for the whole domain as it contains hexahedral elements only and hexahedral elements produce more accurate solution than tetrahedral elements. An image of cross-section area of mesh is shown in Fig. 1a.

Fig. 1 Mesh distribution
a helical tube **b** normal tube



In order to decide an appropriate mesh size, a grid independence test is conducted on plain tube with $L = 75$ mm and $D = 5$ mm. Image of plain tube mesh is depicted in Fig. 1b. Table 1 shows h and ΔP corresponding to the number of elements. It can be inferred that as the number of elements has changed, ΔP and h changes negligibly. So, an appropriate number of mesh elements are selected for helically finned tube so that the results remain considerably unaffected.

Table 1 Grid independence test

Axial element length (mm)	Element no. (million)	h (W/m ² K)	ΔP (Pa)
0.2	3.008	10,760.35	1323.566
0.3	2.000	10,770.98	1318.608
0.4	1.504	10,783.88	1315.447
0.5	1.200	10,799.87	1313.678
0.6	1.000	10,818.67	1312.952
0.7	0.864	10,839.25	1312.902
0.8	0.752	10,865.38	1313.419

Table 2 Boundary conditions

Physical boundary	Fluid flow B.C.	Thermal B.C.
Tube inlet	Velocity	Temperature
Tube outlet	Outflow	Outflow
Tube wall	No slip	Temperature

3.3 Boundary Conditions

Working fluid in this study is water and its respective properties were taken into consideration. The tube material selected over here is aluminium with constant wall temperature of 80°C. In all cases, the Reynolds number (Re) is fixed to 10,000. The velocity at the tube inlet is changed according to the hydraulic diameter (D_h) (Eq. 2).

$$D_h = 4 \frac{A_c}{P_w} \quad (1)$$

$$Re = \frac{\rho v D_h}{\mu} \quad (2)$$

3.4 Model Validation

Model verification for straight triangular serrated tube is done for h by using Dittus–Boelter equation [12] as expressed below.

$$\frac{h D_h}{k_f} = Nu = 0.023 Re^{0.8} Pr^{0.4} \quad (3)$$

Fig. 2 Model validation

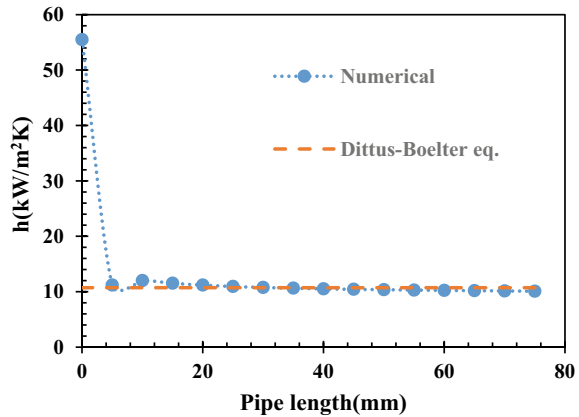


Figure 2 shows the graph for numerical value of h in comparison with the value obtained by Dittus–Boelter equation. It can be seen that the experimental and numerical values are close to each other, and hence, we can verify that the selected calculation method and its boundary condition can accurately determine the results for helically finned tube.

4 Results and Discussion

This section thoroughly explains the effect of different fin height, helix angle and Reynolds number on h and ΔP in internally finned tubes. Also, performance enhancement criteria (PEC) is used to decide the best one.

$$PEC = \frac{\left(\frac{h}{h_o}\right)}{\left(\frac{\Delta P}{\Delta P_o}\right)^{\frac{1}{3}}} \tag{4}$$

4.1 Impact of Varying Helix Angle

Figure 5 manifests the effect of helix angle upon h and ΔP along the tube length. Pitch diameter is 5 mm, and fin height is fixed to 0.2 mm and Re = 10,000 for each case.

It is evident that as the helix angle increases, h decreases and also the ΔP decreases. From the velocity contours, shown in Fig. 3, it can be seen that as the helix angle is less, more fluid is sluggish near the wall. This is because the fluid flowing in tube

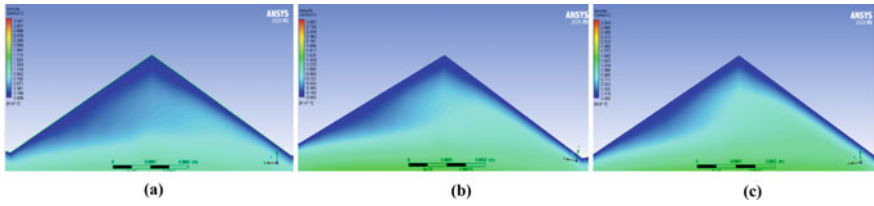


Fig. 3 Velocity contours corresponding to different helix angle a 30° b 40° c 50°

with less helix angle travels more distance, spirally, and hence experiences more skin friction. Temperature contours are shown in Fig. 4. For tubes with less helix angle, the temperature gradient at the wall is sharp which enhances the local convective heat transfer coefficient (h_x) and therefore h gets enhanced (Fig. 5).

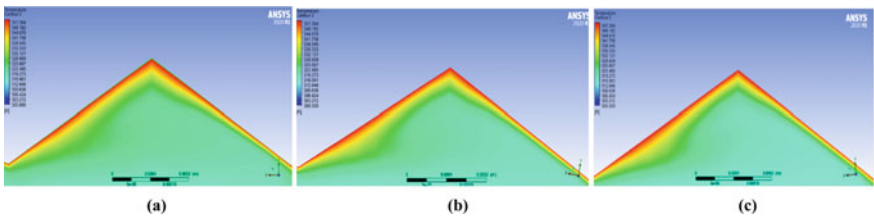


Fig. 4 Temperature contours corresponding to different helix angle a 30° b 40° c 50°

Fig. 5 Impact of helix angle
a h b ΔP

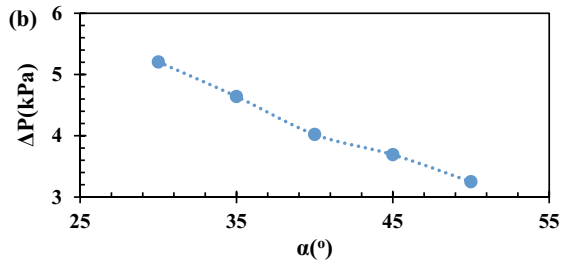
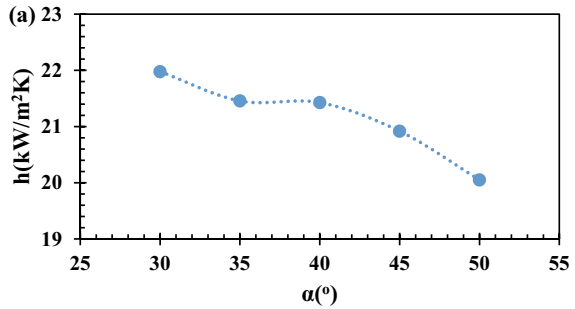
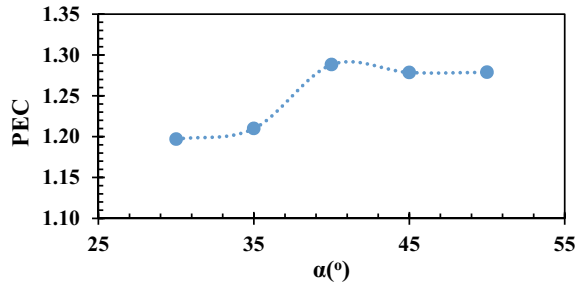


Fig. 6 Variation of PEC with different helix angle



But as per the PEC, the performance of the tube increases up to helix angle of 40° and then it starts plummeting. Figure 6 depicts the variation of PEC with helix angle, graphically, for five different cases.

4.2 Impact of Varying Fin Height

In section 4.1, we found that the tube with $\alpha = 40^\circ$ had best performance among all the variants. So, for the same helix angle, variation of fin height with the h and ΔP is studied. Figure 9 shows the plot of h and ΔP w.r.t. fin height. It can be seen that as the fin height increases, both, ΔP and h , increase. This variation can be attributed to the increase in surface area. As the fin height increases, the surface area increases, which increases the skin friction, leading to greater loss of pressure. Also, greater surface area enables more heat transfer. Velocity and temperature contour, near fins, for different cases is depicted in Figures 7 and 8, respectively.

Figure 10 shows the plot of PEC versus fin height for internally finned tubes. Here, all the tubes are compared with plain tube having $D = 5$ mm and $L = 75$ mm, having same Reynolds number. According to plot, tube with $e = 0.15$ mm has the best performance among all.

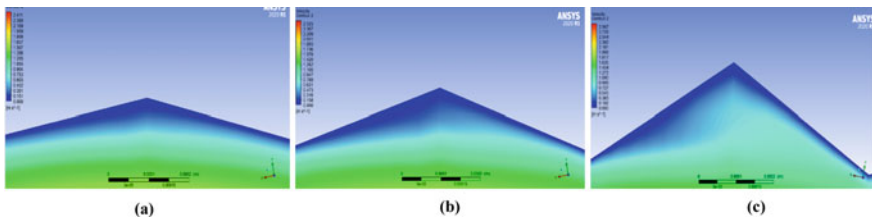


Fig. 7 Velocity contours corresponding to different fin height **a** 0.05 mm **b** 0.1 mm **c** 0.2 mm

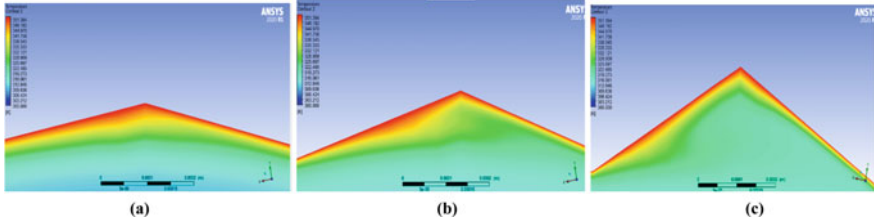


Fig. 8 Temperature contours corresponding to different fin height a 0.05 b 0.1 c 0.2 mm

Fig. 9 Impact of fin height a h b ΔP

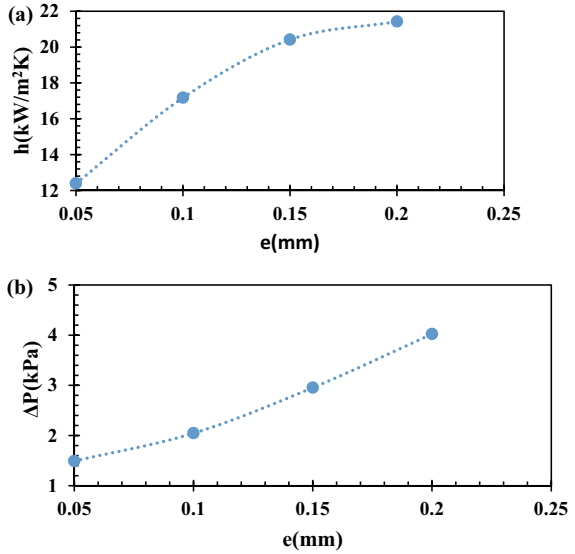
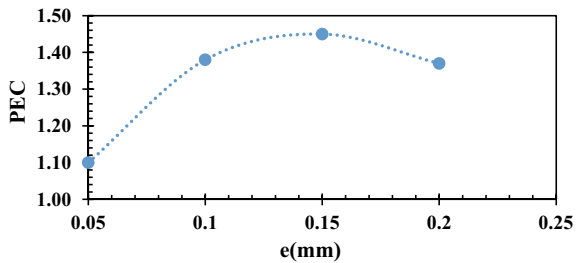


Fig. 10 Variation of PEC with different fin height



4.3 Impact of Different Reynolds Number

Here also, the best variant of tube is selected for analysing the trend of Reynolds number. So, for this tube, trend of Reynolds number with h and ΔP is shown in Figure 13.

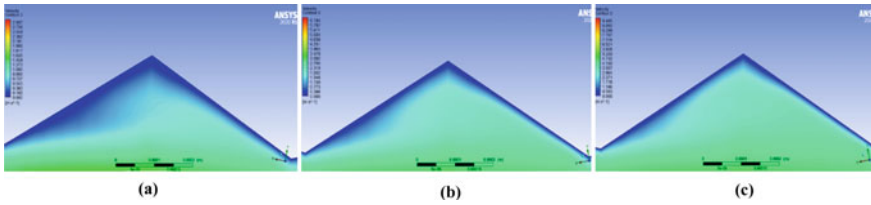


Fig. 11 Velocity contours corresponding to different Reynolds number **a** 10,000 **b** 20,000 **c** 30,000

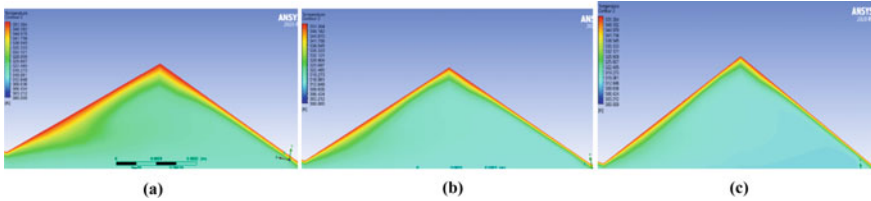


Fig. 12 Temperature contours corresponding to different Reynolds number **a** 10,000 **b** 20,000 **c** 30,000

The graph clearly indicates the increment h and also the ΔP as the Reynolds number has increased. From the velocity contour, shown in Fig. 11, it can be observed that as the Reynolds number increases, the velocity gradients at the boundary becomes sharp and hence the ΔP increases. Same can be seen from temperature contour shown in Fig. 12. As the Reynolds number increases, the temperature gradients at the boundary becomes sharp, thereby increasing the h_x and also the overall heat transfer coefficient (Fig. 13).

For comparison of performance, all tubes are compared with the plain tube of $D = 5$ mm, $L = 75$ mm and having $Re = 10,000$. PEC, shown in Fig. 14, also increases as the flow becomes more turbulent, and therefore, internally finned tubes are recommended to be used in turbulent region as mentioned by Fahed et al. [4].

5 Conclusions

Convective heat transfer coefficient, pressure drop and performance enhancement criteria were calculated numerically. A thorough study was conducted to comprehend the effect of geometric and kinematic changes on heat transfer performance in internally finned tubes. The conclusions of this study are as follows:

As the helix angle has increased, convective heat transfer coefficient and pressure drop, both, have decreased. Although, from performance enhancement criteria, we can say that the tube with helix angle of 40° was better.

Fig. 13 Impact of Reynolds number **a** h **b** ΔP

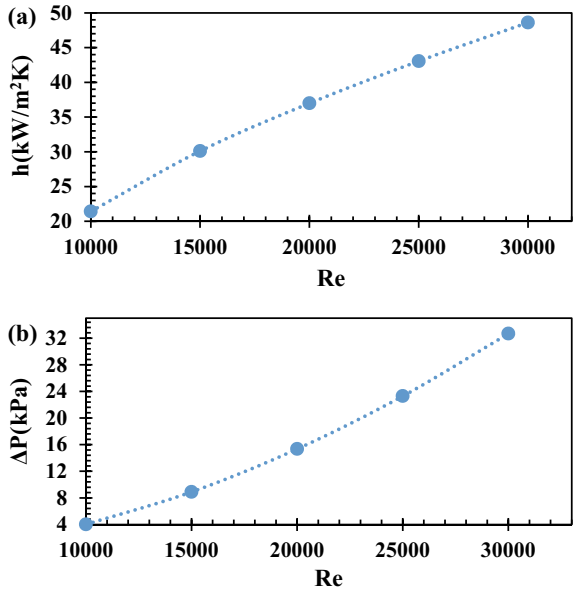
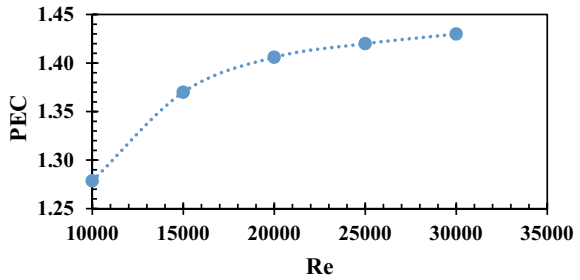


Fig. 14 Variation of PEC with different Reynolds number



Upon increasing the fin height, also, convective heat transfer coefficient and pressure drop, both, have increased. But for the fin height of 0.15 mm, the performance was best among all. As Reynolds number have increased, the performance has also been enhanced. Convective heat transfer coefficient has increased but along with it, pressure drop has also increased.

Nomenclature

- A_c Cross-section area of tube [m^2]
- D Diameter of tube [m]

D_h	Hydraulic diameter of tube [m]
D_p	Pitch diameter [m]
e	Fin height [m]
h	Average convective heat transfer coefficient [W/m ² K]
h_x	Local convective heat transfer coefficient [W/m ² K]
h_o	Convective heat transfer coefficient of reference tube [W/m ² K]
K_f	Thermal conductivity of fluid [W/mK]
L	Length of tube [m]
Nu	Nusselt number of fluid –
Pr	Prandtl number of fluid –
ΔP	Pressure drop [Pa]
ΔP_o	Pressure drop in reference tube [Pa]
PEC	Performance enhancement criteria –
Re	Reynolds number –
v	Velocity of fluid [m/s]
α	Helix angle (°)
μ	Dynamic viscosity of fluid [Pa-s]
P	Density of fluid [kg/m ³]

References

1. Dastmalchi M, Arefmanesh A, Sheikhzadeh GA (2017) Numerical investigation of heat transfer and pressure drop of heat transfer oil in smooth and micro-finned tubes. *Int J Therm Sci* 121:294–304
2. Muñoz Javier, Abánades Alberto (2011) Analysis of internal helically finned tubes for parabolic trough design by CFD tools. *Appl Energy* 88:4139–4149
3. Lin L, Zi C, Zhang C, Lin Z (2021) Experimental and numerical investigation on flow and heat transfer characteristics of a multi-waves internally spiral finned tube. *Int J Heat Mass Transf* 172:121104
4. Al-Fahed S, Chamra LM, Chakroun W (1999) Pressure drop and heat transfer comparison for both micro fin tube and twisted-tape inserts in laminar flow. *Exp Therm Fluid Sci* 18:323–333
5. Jacqueline BC, Mario Henrique M, de Daiana S, De Rejane CO (2004) Experiments with micro-fin tube in single phase. *Int J Refrigerat* 27:876–883
6. Yong-Hui W, Ji-Li Z, Zhi-Xian M (2018) Experimental study on single-phase flow in horizontal internal helically finned tubes: the critical Reynolds number for turbulent flow. *Exp Therm Fluid Sci* 92
7. Karol M (2013) Concept of a measurement and test station to determine linear pressure drop and the heat transfer coefficient of internally ribbed tubes. *J Pow Technol* 93(5)
8. Zhixian M, Anping Z, Jili Z, Yonghui W (2017) Experimental investigation on the friction characteristics of water–ethylene glycol mixture flow in internal helical finned horizontal tubes. *Exp Therm Fluid Sci* 89
9. Yonghui W, Jili Z, Zhixian M (2017) Experimental study of single-phase flow and heat transfer characteristics for a horizontal internal helically-finned tube. In: 10th international symposium on heating, ventilation and air conditioning, ISHVAC2017, 19-22 October, Jinan, China
10. Ali S, Ammar A, Nawfel M (2016) Numerical investigation for enhancement of heat transfer in internally finned tubes using ANSYS CFX program. *Basrah J Eng Sci* 16:2

11. Kyoungwoo P, Byeong SK, Hyo-Jae L, Ji WH, Park KO, Juhee L, Keun-Yeol Y (2008) Performance improvement in internally finned tube by shape optimization. *Int J Appl Sci Eng Technol* 4:3
12. Çengel Y, Ghajar A (2017) *Heat and mass transfer: fundamentals and applications*. McGraw-Hills, New York, USA

Numerical Study on Heat Transfer Through Semi-Circular Grooved Microchannel



Anshul Rajput, Zahoor Bhat, Yogesh M. Nimdeo, and Harish Pothukuchi

1 Introduction

Understanding the properties of heat transfer in microchannels is crucial for designing and improving the thermal performance of microfluidic heat transfer devices. Such electrical components produce more heat as a result of continuous operation. A fundamental barrier to the creation of next-generation electronic devices is the production of substantial heat fluxes by tiny electronic devices. In order to prevent their failure and ensure consistent performance, effective heat dissipation is crucial because the performance of electronic elements is largely dependent on their operating temperatures. There are several techniques used for controlling the temperature of electronic components, but fluid flow through microchannels has shown to be one of the most effective means of doing so. By employing microchannels to distribute heat, a number of researchers have continued their work in this area to improve the thermal performance of such constantly active electronic devices [1–4]. For example mini- and microchannels have much higher heat transfer rates than traditional cooling methods like using fans, blowers and fins.

2 Literature Review and Objective

In 1981, Tuckerman and Pease [5] employed microchannels as high-performance heat sinks for the cooling of electronic equipment, beginning in the era of microchannels. Conventional microchannels were used in the early stages of microchannel

A. Rajput · Z. Bhat · Y. M. Nimdeo (✉)
Department of Chemical Engineering, IIT Jammu, Jammu 181221, India
e-mail: yogesh.nimdeo@iitjammu.ac.in

H. Pothukuchi
Department of Mechanical Engineering, IIT Jammu, Jammu 181221, India

evolution. These had the appearance of straight channel with almost straight fluid flow streamlines. Heat transfer was ineffective as a result of the fluid's poor mixing. Therefore, changing the microchannels' structure is important. The performance of heat transfer is improved when fluid flows across curved surfaces because adequate coolant mixing and the creation of vortices prohibit the boundary layer from continuously growing. Many researchers have examined the heat transfer across circular, cylindrical and wavy channels by taking advantage of the improved thermal performance of microchannels.

They also have investigated the heat transfer across circular, cylindrical and wavy channels using both numerical and experimental methods because of the better thermal performance of microchannels. To calculate the amount of heat that will be transferred through a three-dimensional cylindrical irregularities channel, Comini et al. [6] performed a numerical analysis. They discovered that a smaller aspect ratio increases the Nusselt Number.

Suabsakul et al. [7] performed numerical simulation and studied the effect of variations in heat transfer rate and pressure drop with Reynolds number. His study also suggests that dimple improves heat sink in microchannel and the heat transfer is useful when Reynolds number is more than 125. Gulshan et al. [8] find that thermal boundary layers produced in the dimpled channel were seen to be thinner at any given Reynolds number than those in the case of the smooth channel. In contrast to the increasing nature found for the smooth channel, local disruptions caused by the presence of inward dimples led to a relatively flatter profile of the thermal boundary layer.

Manoj et al. [9] present a three-dimensional numerical investigation of the flow between a solid substrate and a rectangular microchannel. To determine the impact of channel aspect ratio on axial back conduction, a substrate with constant dimensions ($0.4 \times 0.6 \times 60$ mm) and a range of aspect ratios (0.45–4.0) was utilized. Simulations have been run for the thermal conductivity ratio k_{sf} ranging from 12.2 to 635. The findings clearly demonstrate that an average Nusselt number minimum occurs with respect to the channel aspect ratio for any flow rate and any value of k_{sf} . This minimal corresponds to a channel aspect ratio that is roughly equal to or just under 2.0.

Zekeriya Palak et al. [10] studied that wavy channel shows negligible change in the outlet temperature was seen as a result of the increase in cross-sectional area, which reduced the impacts of the heat transfer surface on the outlet temperature. However, a greater microchannel's height resulted in a lower exit temperature. The increase in the microchannel's width and height had the same impact on the direction of the inlet pressure decrease. Dharaiya et al. [1] performed simulations on smooth channel and channel with roughness. Moreover, continuous streamlines were seen in all of the rough geometries when looking at the velocity vectors for those various geometries. There were no vortices forming behind the roughness features, which would have increased heat transfer effects but also resulted in a significant pressure reduction.

To explore microchannel heat sinks with symmetric and parallel wavy microchannels in a wide range of Reynolds numbers from 50 to 700, Shuo et al. [11] employed a three-dimensional fluid–solid conjugate model. The performance of these modified

wavy configurations with secondary branches is then compared to that of the original as well as other wavy configurations after inserting the transverse gaps into ribs. According to the study, the parallel construction has a slightly higher Nu in the low Re range, but in the moderate and high Re ranges, it performs substantially worse in terms of heat transmission than the symmetric structure. For parallel wavy layouts, the introduction of transverse gaps into ribs promotes flow mixing between neighbouring microchannels which significantly boost the coolants convective heat transfer performance. The results suggest that a modified symmetric wavy arrangement with a larger gap and a low amplitude-to-wavelength ratio is advantageous.

Lin et al. [2] investigated a wavy microchannel heat sink with different wavelength and amplitude along the flow direction. The author proposed that compared to the original wavy design, the heat sink with a shorter wavelength or bigger amplitude along the flow direction has a lower thermal resistance and a smaller temperature difference on the bottom wall. When the amplitude and wavelength are changed at the same time, there is a perfect pairing of ΔA and $\Delta \lambda$ that will result in the best heat sink performance.

The features of heat transmission in a sinusoidal wavy channel with secondary corrugations are numerically investigated by Harikrishnan et al. [12]. They found that recirculation occurs in the grooves of streamwise and secondary corrugated channels but not in the grooves of spanwise corrugated channels.

Using a parametric numerical model, Minghai Xu et al. [3] studied the flow and heat transmission in a microchannel with dimples. To find the best geometric design and examine the flow field change brought on by dimples, three geometric factors—dimple depth, aspect ratio and spacing—were examined under a constant Reynolds number of 500. They conclude that transverse convection flow is caused by the existence of a dimple in the channel. For enhancing convection heat transfer in laminar flow, dimple-induced transverse convection is essential. In addition to enhancing heat transfer, dimples can lessen pressure loss. It's a good technique to improve a microchannel heat sink's overall performance.

The development of the maximum velocity zone in the flow core with rising Dimple height is the subject of the article, Isaev et al. [13]. The author demonstrated how variations in dimple depth can alter flow velocity along the flow. It has been observed that the rise in dimple depth, increases the flow velocity. It is also noticed that the highest velocity component of maximum velocity appear at dimple height of more than 0.2.

Using numerical simulations, Wang et al. [14] examined the impact of geometric parameters on the flow and heat transfer characteristics of microchannel heat sinks with triangular, rectangular, and trapezoidal shapes. The results show that the geometry and form of microchannels significantly affect the flow and heat transfer characteristics of microchannel heat sinks. The thermal resistance and pressure drop of a rectangular microchannel heat sink are significantly influenced by the channel number. When the number of channels is increased, the pressure drop increases but the thermal resistance decreases. Furthermore, triangular and trapezoidal cross section micro channel heat sinks and rectangular microchannel heat sinks with a large aspect ratio, a long-wetted perimeter, and a small hydraulic diameter frequently

exhibit low thermal resistance and significant pressure drop. The best performance can be found in rectangular microchannel heat sinks with an aspect ratio of 8.904 to 11.442.

Qifeng Zhu et al. [4] study the effects of different groove designs on fluid flow and heat transfer in microchannel heat sinks. Here the sidewalls of the silicon-based microchannel heat sinks were designed with five different types of periodic grooves: rectangular, trapezoidal, water-droplet, triangular, and semi-circular. The addition of sidewall grooves, causes vortices inside the grooves, disrupting the flow boundary layer and improving heat transfer efficiency. The vortices that form inside the grooves serve as rolling bearings for fluid flow, changing sliding friction to rolling friction, reducing flow resistance, and reducing pressure drop. The author also demonstrated that, with the exception of the rectangular grooved channel, all grooved channels achieve higher heat transfer efficiency than smooth channels over the range of Reynolds numbers varying from 190 to 610. The water-droplet grooved channel has the most potential for improving heat transfer efficiency even though the triangular grooved channel has the highest Nusselt number.

Overall, according to the literature mentioned above, the channel's geometry significantly affects the properties of heat transfer. Over straight microchannels, cylindrical and circular grooved microchannel have a large heat transfer advantages. To our knowledge, though, the relative thermal performance of the cylindrical microchannels geometries has not been discussed in detail. As a result, in this work, performance characteristics of cylindrical grooved microchannels are compared with those of a straight channel. In order to determine the thermal performances, the analysis includes velocity contours and the variation of temperature, pressure, average Nusselt number, and surface heat transfer coefficient as a function of distance along the axial length of the microchannel.

3 Methodology

This section presents the detailed methodology for the numerical study of heat transfer characteristics in a microchannel with and without the semi-circular grooves or the dimples with 0.5 mm radius. Each of the channels has a 2D geometrical section with a channel length of 75 mm and 1 mm in height. The bottom wall is maintained at a continuous heat input of 50 W/cm². The top wall is modelled as an adiabatic surface. The schematic representation and mesh distribution in the microchannel is shown in Fig. 1a and 1b, respectively. At the inlet, the temperature of the water is specified as 27 °C for all the simulations. The description of the variables used in the numerical analysis is shown in Table 1.

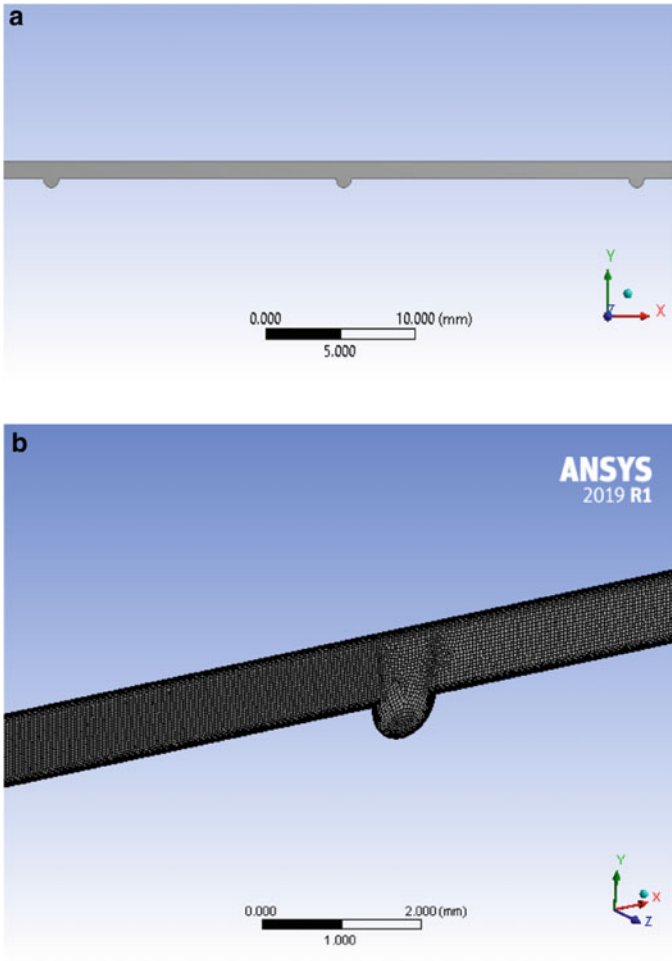


Fig. 1 a Schematic diagram of the set-up, b details of mesh distribution in a microchannel

Table 1 Boundary conditions

Variables	Values
Inlet water temperature (T_{in})	300K
Heat flux rate (Q')	50W/cm ²
Reynolds number range (Re)	150–750

3.1 Numerical Schemes

ANSYS Fluent, a finite volume-based commercial solver, is used to carry out the numerical simulations. Pressure–velocity coupling is achieved using the well-known

SIMPLE algorithm. Second-order upwind method is used for solving the momentum and energy equations. Reducing of residuals to the order of 10^{-6} is the chosen convergence criterion.

3.2 Meshing

MultiZone Quad and Tri methods are used for meshing with 0.05 mm element size. There are 51,573 discretized elements in the entire domain. Figure 1b shows the structure of the selected mesh distribution. The fluid zone near the vicinity of the heated bottom wall and the adiabatic top wall are resolved using a fine grid to capture the local gradients in velocity and temperature gradients.

3.3 Governing Equations

The steady-state mass, momentum and energy conservation equations for the fluid flow and heat transfer characteristics are given as follows:

$$\text{Mass Conservation: } \nabla \cdot (\rho u) = 0 \quad (1)$$

$$\text{Momentum conservation: } (u \cdot \nabla) \rho u = -\nabla p + \mu \nabla^2 u \quad (2)$$

$$\text{Energy conservation : } u \cdot \nabla T = \frac{k}{\rho C_p} \nabla^2 i \quad (3)$$

The average heat transfer coefficient is measured according to the Eq. (4) as follows:

$$h = \frac{Q'}{T_w - T_m} \quad (4)$$

where Q' is the applied wall heat flux

T_w = Area weighted average wall temperature.

T_i = Inlet fluid temperature.

T_m = Bulk fluid temperature.

Using the generated heat transfer coefficient data, the Nusselt number is calculated as follows:

$$Nu = \frac{h_{avg} \times D_h}{k} \quad (5)$$

Here, $D_h = \frac{4*H*W}{2*(H+W)}$ is the hydraulic diameter of the channel, and 'k' is the thermal conductivity of the fluid.

3.4 Boundary Condition

The following boundary conditions are considered for the calculation of velocity, pressure and temperature distributions.

Inlet velocity condition: $u = U_{in}$.

Outlet pressure condition: $P = P_{atm}$.

Inlet fluid temperature: 300 K.

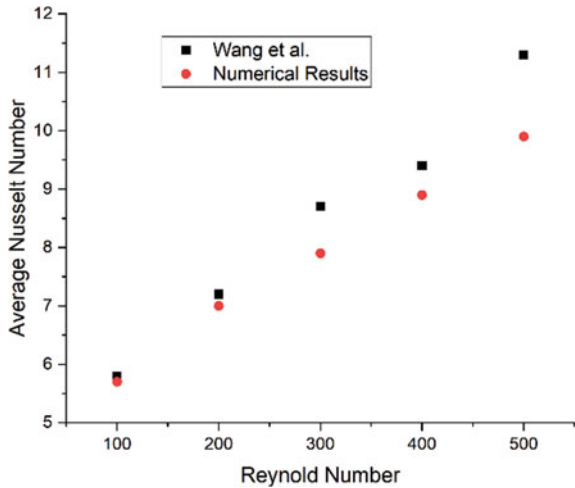
Top wall: Adiabatic.

Bottom wall: Constant heat flux condition.

3.5 Numerical Validation

In the present study, the validation studies for the numerical model framework is presented by comparing against the measured average Nusselt number as a function of Re [11] in a microchannel with similar boundary conditions. As depicted in Fig. 2, predictions are found to be in good agreement with the experimental observations of Wang et al. [11].

Fig. 2 Comparison of average Nusselt number obtained from present computation with results of Wang et al. [11]



4 Results and Discussion

This section presents the results and discussion on the flow and heat transfer characteristics in a microchannel. The simulations are performed to study the influence of varying Reynolds number on the heat transfer characteristics of a microchannel with and without dimples.

4.1 Influence of Re

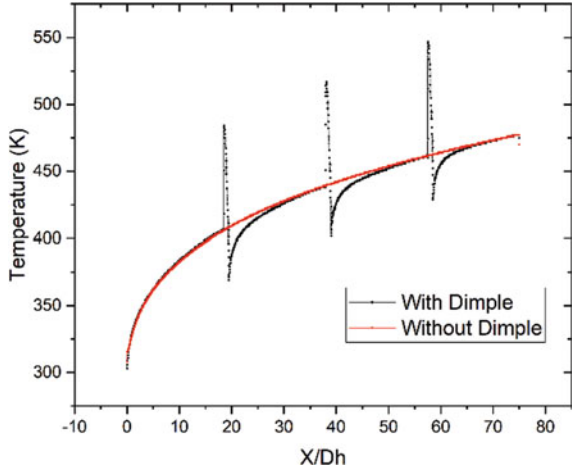
The effect of Re on the microchannel heat transfer is studied for three different values of Re ranging from 150 to 750. The variation in Re is achieved by varying the inlet velocity. As can be observed, in every situation, channel centre is where velocity is at its highest. However, in dimpled channels, the total velocity field is entirely different. Since the distance between the top and bottom walls in a simple 2D rectangular channel with flat base remains constant, the fluid's velocity streamlines direction remains constant and are nearly continuous along the axial direction. While in the case of a channel with a radius of 0.5 mm, the formation of a dimple causes non-uniformity in the space between the two walls, which results in the discontinuation of the velocity streamlines along the flow direction. As a result, in a dimpled channel, the streamlines deviate from its original path. Inside the dimple flow circulation can be noticed. Dimpled/grooved microchannels exhibit improved heat transfer over a straight microchannel due to repeated discontinuity in the creation of the velocity boundary layer.

4.2 Temperature Variation

The thickness of the isotherms (which represent the thickness of the thermal boundary layer) in the straight channel is significant and uniform along the flow direction. As a result, the temperature gradients along the flow direction weaken. On the other hand, the thermal boundary layer is not smooth along the flow direction in Dimpled grooved channels. The channel geometry causes a disruption in the thermal boundary layer's development, which improves the grooved channel's heat transfer rate.

Figure 3 depicts the temperature's graphical variation along the axial direction. The temperature is not rising steadily in these Dimpled grooved channels like it would in a straight channel. When fluid begins to flow over flat surfaces, the temperature begins to rise; however, when a grooved part arrives in the scene, the temperature profile is disrupted and mixing occurs, which implies thermal boundary layer destabilization and improves heat transport in grooved channels relative to that in straight channels. However, a grooved channel with a radius of 0.5 mm performs better in terms of heat transfer than one having radius less than 0.5 mm.

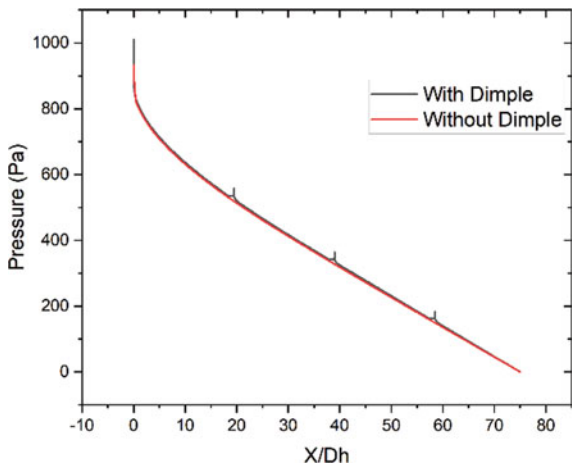
Fig. 3 Axial variation of temperature at $Re = 750$



The pressure variation along the flow direction is depicted in Fig. 4. The pressure drop in Dimpled grooved microchannels is higher than in straight microchannels at the grooved regions. This is because the channel's curved structure disrupts the entire flow field and creates an increase in turbulence and vorticity in the groove, which raises the pressure. Additionally, it is obvious that a grooved channel with a radius of 0.5 mm has a bigger pressure drop and needs more power to maintain flow than one with a plain channel.

Figure 5 depicts how the surface heat transfer coefficient varies across all channels. In Dimpled grooved channels, the tendency is to vary along the axial axis with largest peaks occurring at the just after the dimple of the channel (corresponding to the bottom wall) and lower peaks occurring at the inside portion of the channel.

Fig. 4 Variation of pressure in axial direction at $Re = 750$



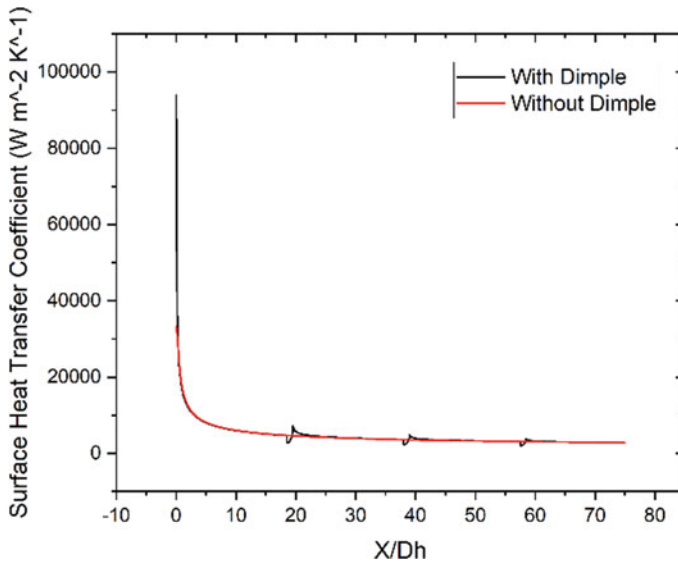


Fig. 5 Surface heat transfer coefficient at $Re = 750$

The variation of the average Nusselt number in relation to the Reynolds number is shown in Fig. 6. The relationship between Nusselt number and Reynolds number is clearly seen, and Dimpled grooved channels exhibit greater average Nusselt number fluctuation than straight channels. Grooved channels have a higher thermal efficiency because the thermal boundary layers are more dispersed as a result of the curved pattern at bottom walls. Additionally, for a given Reynolds number, the mixing of flow and the subsequent instabilities occur further upstream in grooved channels compared to straight channels. Furthermore, the average Nusselt number for channels with grooves of radius $r = 0.5$ mm is higher than for channels without grooves.

For microchannel-based heat sinks, the flow becomes regular with a significant thermal boundary layer thickness in the case of straight channels in laminar flow regions. As a result, the efficiency of heat transfer along the flow direction decreased. Vortices, on the other hand, easily form inside the grooves along the flow direction and displace the thermal boundary layer. It improves the grooved microchannel heat sinks' ability to transmit heat. For better understanding to analyse the heat transfer and fluid flow phenomena in great depth, further experimental research need be conducted.

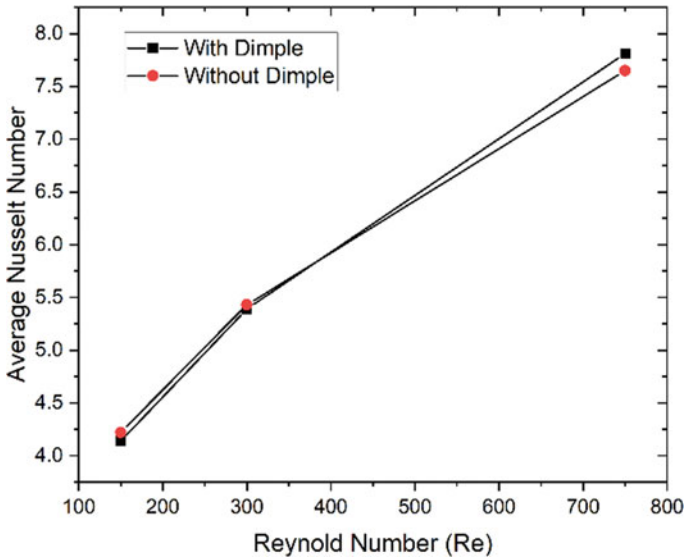


Fig. 6 Average Nusselt number w.r.t. Reynold number

5 Summary and Conclusions

Numerical simulations are performed to compare the heat transfer characteristics of a semi-circular grooved microchannels and straight microchannels. The results indicate that semi-circular grooved microchannels transfer heat more effectively than straight channels. Dimple significantly raises the local Nusselt number at its front and rear ends, which in turn improves the efficiency of the microchannel heat sink. With an increase in the Re , both the heat transfer and pressure drop increases. Compared to channel without dimple, heat transfer better takes place in channel with a circular groove of radius, $r = 0.5\text{ mm}$. However, dimpled channel provides a better heat transfer characteristics for higher Re and the corresponding pressure drop is not so significantly different compared to straight channels. Overall, the present study demonstrates that Dimpled grooved microchannel heat sinks perform better than those with straight channels at high Re only. At low Re , the heat transfer rate is found to be deteriorating due to the presence of dimples on the microchannel surface, whereas heat transfer is increased by 2.273% for higher Re values.

Acknowledgements I would like to sincerely acknowledge the Ministry of Human Resources and Development (MHRD) and the Indian Institute of Technology (IIT) Jammu for providing the financing required for the research.

Nomenclature

Re	Reynolds number-
T_{in}	Inlet water temperature[K]
Q'	Heat flux rate [W/cm ²]
p	Pressure[N/m ²]
u	Velocity[m/s]
H	Height of channel[mm]
W	Width of channel[mm]
r	Semi-circular groove radius[mm]

References

1. Dharaiya VV, Kandlikar* SG (2013) A numerical study on the effects of 2d structured sinusoidal elements on fluid flow and heat transfer at microscale. *Int J Heat Mass Transf* 57:190–201. <https://doi.org/10.1016/j.ijheatmasstransfer.2012.10.004>
2. Lin L, Zhao J, Lu G, Wang XD, Yan WM (2017) Heat transfer enhancement in microchannel heat sink by wavy channel with changing wavelength/amplitude. *Int J Therm Sci* 118:423–434. <https://doi.org/10.1016/j.ijthermalsci.2017.05.013>
3. Minghai X, Hui L, Liang G, John C, Xinyue D (2016) Parametric numerical study of the flow and heat transfer in microchannel with dimples. *Int Commun Heat Mass Transf* 76:348–357. <https://doi.org/10.1016/j.icheatmasstransfer.2016.06.002>
4. Zhu Q, Xia H, Chen J, Zhang X, Zhang KCH, Wanga H, Wan J, Jin Y (2021) Fluid flow and heat transfer characteristics of microchannel heat sinks with different groove shapes. *Int J Therm Sci* 161:106721. <https://doi.org/10.1016/j.ijthermalsci.2020.106721>
5. Tuckerman DB, Pease RFW (1981) High performance heat sinking for VLSI. *IEEE Electr Dev Lett* (2):136–129. <https://doi.org/10.1109/EDL.1981.25367>
6. Comini G, Nonino C, Savino S (2003) Effect of aspect ratio on convection enhancement in wavy channels. *Num Heat Transf Part A* 44:21–37. <https://doi.org/10.1080/713838173>
7. Gururatana S (2012) Numerical simulation of micro-channel heat sink with dimpled surfaces. *Am J Appl Sci* 9(3):399–404. <https://doi.org/10.3844/ajassp.2012.399.404>
8. Gulshan KS, Rahul HD, Haridas D (2017) Performance evaluation of compact channels with surface modifications for heat transfer enhancement: an interferometric study in developing flow regime. *Int J Heat Fluid Fl* 64:55–65. <https://doi.org/10.1016/j.ijheatfluidflow.2017.02.002>
9. Manoj Kumar M, Sameer K (2013) Effect of aspect ratio of rectangular microchannels on the axial back conduction in its solid substrate. *Int J Microscale Nanoscale Therm Fluid Transp Phenom* 4(3/4)
10. Zekeriya P (2017) Optimal design of wavy microchannel and comparison of heat transfer characteristics with zigzag and straight geometries. *Heat Mass Transf* <https://doi.org/10.1007/s00231-018-2375-6>
11. Lin Wang S, Feng Zhu J (2022) Heat transfer enhancement of symmetric and parallel wavy microchannel heat sinks with secondary branch design. *Int J Therm Sci* 171:107229. <https://doi.org/10.1016/j.ijthermalsci.2021.107229>
12. Hari Krishnan S, Shaligram T (2019) Heat transfer characteristics of sinusoidal wavy channel with secondary corrugations. *Int J Therm Sci* 145:105973. <https://doi.org/10.1016/j.ijthermalsci.2019.105973>

13. Isaev SA, Leontiev AI, Milman OO, Popov IA, Sudakov AG (2019) Influence of the depth of single-row oval-trench dimples inclined to laminar air flow on heat transfer enhancement in a narrow micro-channel. *Int J Heat Mass Transf* 134:338–358. <https://doi.org/10.1016/j.ijheatmasstransfer.2018.12.175>
14. Wang H, Chen Z, Gao J (2016) Influence of geometric parameters on flow and heat transfer performance of micro-channel heat sinks. *Appl Therm Eng* 107:870–879. <https://doi.org/10.1016/j.applthermaleng.2016.07.039>

Numerical Study of Combined Phase Change Material and Natural Air Cooling System for Lithium-Ion Battery Thermal Management



Indra Kumar Lokhande, Deepyaman Chakraborty, and Nishant Tiwari

1 Introduction

The apparent increase in the development of electrified vehicles and hybrid electrified vehicle demands a higher energy storage system with safety features [1]. Lithium-ion batteries with high-energy density have been proved to be one of the prominent energy storage options for an electric vehicle. However, during operation, the performance of lithium-ion batteries is mainly affected by two factors: (i) Excess heating of battery module due to rapid overcharging and discharging [2]. (ii) During winters [3], lithium-ion battery unveils poor discharging performance due to slow chemical reaction leading to inefficient ionic conductivity in the electrolytes and lithium-ion diffusivity within the electrodes. Hence, temperature is a crucial factor that affects performance and lifespan of lithium-ion batteries, motivating researchers to design the efficient thermal management system for lithium-ion batteries that helps to maintain the desirable temperature range of 293 to 333 Kelvin (K) for its safe and reliable functioning.

Many researchers pointed out pump driven liquid cooled systems have better heat dissipation rate than traditional air-cooled systems. However, pump-driven liquid cooled systems require higher work input to run the cooling system. Alternatively, phase change material cooling system has an advantage over pump-driven cooling systems because it does not any external work input. Considering this, Zhang et al. [4] presents a hybrid model of battery thermal management system utilizing phase change material and providing bottom liquid cooling for a large-sized power battery module. A comparison of this hybrid model with liquid cooling is done which shows that at steady state the hybrid cooling shows better thermal management [4]. Huang et al. [5] have performed a numerical and experimental investigation of a battery pack with phase change material cooling. The higher thermal conductivity and high

I. K. Lokhande · D. Chakraborty · N. Tiwari (✉)

School of Mechanical Engineering, Vellore Institute of Technology, Vellore 632014, India
e-mail: nishant.tiwari4@gmail.com

latent heat of the phase change material provides better thermal management. The optimal value of 94% was obtained for the porosity of paraffin/metal foam to attain the lowest maximum temperature [5]. Kiani et al. [6] investigated numerically and experimentally the hybrid thermal management system using copper foam along with paraffin wax (PCM) and alumina nano-fluid as active cooling fluid. The result shows that use of active coolant along with copper foam and PCM delays the setting of PCM phase transition effectively ultimately delays the melting time consequently which leads to decrease in rise of temperature [6]. A numerical investigation of a battery thermal management system using liquid pipe cooling of Phase Change Material (PCM) for maintaining the thermal performance of battery pack and found that even at ambient temperature of 318 K system removes the heat stored in PCM effectively and improves the battery pack temperature within 321 K [7]. A flexible composite stable phase change material using styrene butadiene, paraffin and expanded graphite for battery thermal management system is developed to improve the limitation of phase change material such as leakages on melting, low thermal conductivity and poor mechanical properties. During observation, it is found that the maximum temperature of a battery module is maintained below 319 K on 5C discharge process and the difference in temperature does not exceed 4 K[8].

The above discussion reveals that the thermal performance of lithium-ion battery cooling systems is improved with PCM. However, in most of the recent studies [9–11], researchers used a high volume of PCM blocks and with the melting of PCM, in the absence of a structure constricting the flow of the new form liquid, the liquid flows slowly due to the gravitational force. After solidifying, the structure will get deformed with uneven distribution of the PCM mass along the height and width; therefore, rendering the structure unused. To avoid the above situation, thin PCM block along with air cooling is proposed for the cooling of lithium-ion battery. And the thermal performance of the proposed cooling system is evaluated with different charging rates and is also compared with air-cooled battery system.

2 Numerical Modelling

Three-dimensional numerical simulation is performed to apprehension the thermal performance of PCM cooled battery system. For this purpose, a prismatic pouch cell of $192 \times 145 \times 7 \text{ mm}^3$ with a nominal capacity of 20 Ampere-hour (Ah) proposed by Kim and Yi et al. [12] is undertaken for the study. For cooling of pouch cell, a $192 \times 145 \times 2 \text{ mm}^3$ thick chamber is assembled with pouch cell. The detailed geometrical dimensions of PCM cooled battery system are presented in Fig. 1 and Table 1. Direct comparison between proposed cooling system and air-cooled system for different charging rates.

Fig. 1 Schematic diagram of pouch cell **a** cell dimensions and **b** boundary conditions

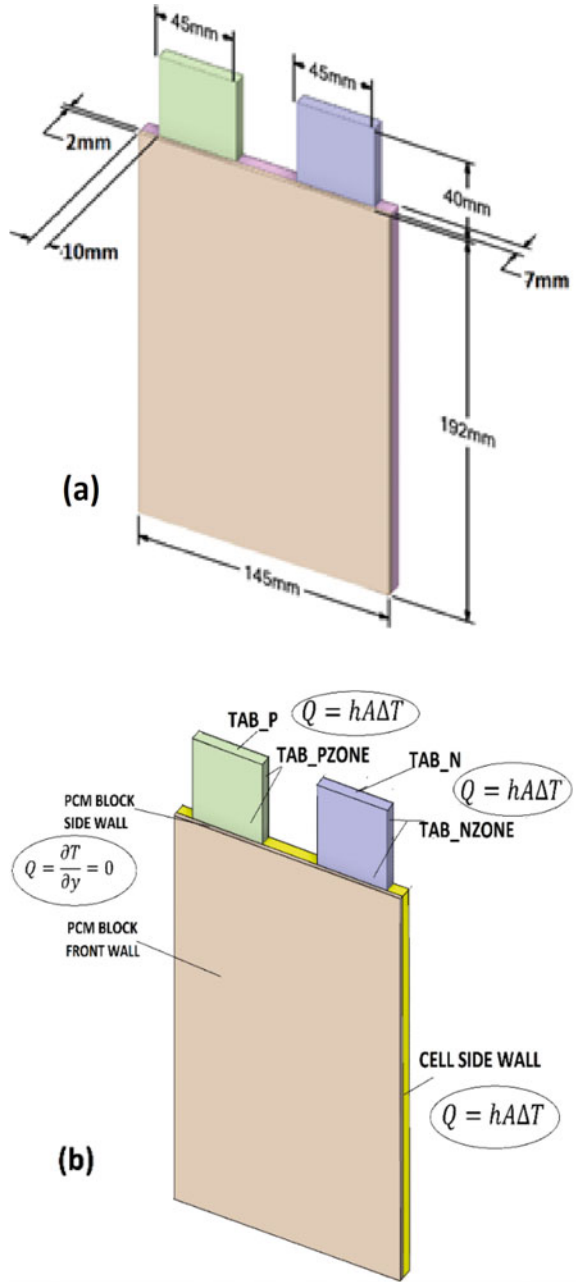


Table 1 Geometrical dimensions of PCM cooled battery system

	Length (mm)	Height (mm)	Thickness (mm)
Cell	145	192	7
Tab	45	40	7
PCM Block	145	192	2

2.1 Mathematical Modeling

To mimic the actual behavior of pouch cell, a numerical model has been developed by utilizing the ANSYS Fluent platform. A semi-empirical electro-chemical model based on the dual-potential approach of The Newman, Tiedemann, Gu, and Kim (NTGK) model proposed by Kwon [13, 14] is used. During charging potential amount of heat is generated which can be calculated by equation taken from Javani et al. [15].

$$q = J \left\{ U - (\varphi_+ - \varphi_-) - T \frac{dU}{dT} \right\} \tag{1}$$

The volumetric heat generation term is referred to as q , and φ_+ and φ_- stands for positive- and negative-phase potentials respectively. Considering the page limitation, the detailed description of NTGK model and parameters involved during electro-chemical reaction can be found in said papers [14, 15].

Further, continuity, momentum and energy equations are solved to capture the heat transfer behavior of PCM cooling system:

$$\frac{\partial \rho}{\partial t} + \nabla \cdot (\rho v) = 0 \tag{2}$$

$$\rho \frac{\partial T}{\partial t} v + \nabla \cdot (\rho v) = 0 \tag{3}$$

$$\rho \frac{\partial H}{\partial t} + \nabla \cdot (\rho v H) = \nabla \cdot (k \nabla T) + S \tag{4}$$

where v represents the velocity of the fluid, here the pcm, S is the source term.

To model the melting of PCM, the solidification and melting model [16] of the ANSYS Fluent package is being utilized. Instead of using an explicit method to track the phase change, the package uses the enthalpy porosity technique to model a variable called “liquid fraction” calculated based on enthalpy per iteration. The following equations are used in the package to measure enthalpy,

$$H = h + \Delta H \tag{5}$$

Table 2 Properties of phase change material [17]

PCM	Density	Thermal conductivity (k) (w/ m K)	Heat capacity (KJ/ kg K)	Latent heat of fusion (Kj/Kg)	Transition temperature(K)
RT 31	880(s) 770 (f)	0.2	2.0	165	300 –306

$$h = h_{ref} + \int_{T_{ref}}^T c_p dT \tag{6}$$

h_{ref} and T_{ref} are known as enthalpy and temperature at constant pressure. As the temperature increases the properties of the pcm changes, it can be defined by three states, solid, mushy and liquid, the PCM properties used are mentioned in Table 2.

The MSMD model coupled with solidification and melting model is solved using ANSYS Fluent 2020R2. The numerical simulation includes Semi-Implicit Method for Pressure-Linked Equations (SIMPLE) algorithm for pressure velocity coupling. Spatial discretization uses least square cell based for gradient, second order for pressure, momentum and energy. A residual value of $10e^{-6}$ is given to meet the convergence condition for solving the continuity, momentum and energy equation.

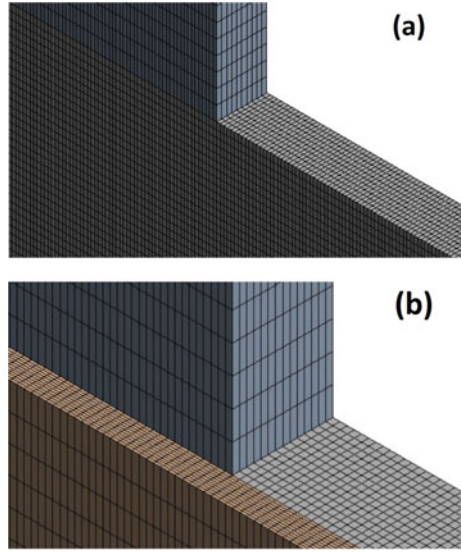
2.2 Meshing and Mesh Geometry

In the current study, a heat transfer characteristic of a cell is solved by using a numerical Finite Volume Method (FVM) in which energy equation is discretized over small element spread over the entire geometry. The quadrilateral mesh is applied over the entire geometry using ANSYS 2020R2 as shown in Fig. 2.

2.3 Initial Boundary Condition

At time $t = 0$, cell and PCM temperatures are set at 300 K; the liquid volume fraction initially taken as zero. For achieving the battery to be charged 100%, the battery initial State of Charge (SOC) is considered as 15% and the initial voltage is taken as 3.5. For substrate, front surface and side wall of the PCM block has given zero heat flux and for battery convective heat transfer coefficient is given as 25 W/m²K for battery cell and tabs.

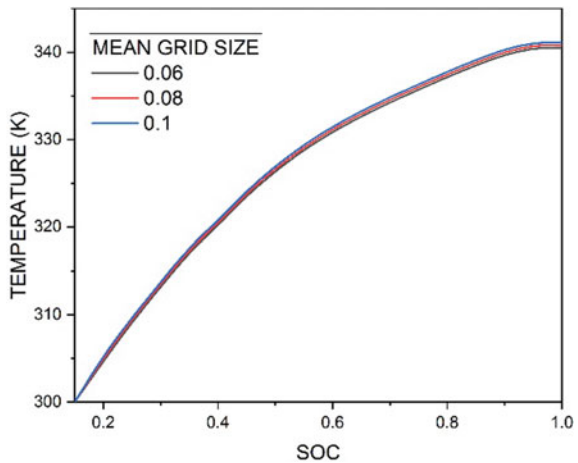
Fig. 2 Mesh applied to geometry **a** without PCM and **b** with PCM



2.4 Grid Independence Check

Hexahedral Meshing (Structured) is employed for both air-cooled and PCM-cooled systems and optimal grid size is determined by performing grid sensitivity analysis. The cell average temperature is calculated for three different mesh settings ranges from 0.04 to 0.08 mm mean cell size. It can be depicted in Fig. 3, moving from the lowest cell size to the highest cell size, less than a 2.5% change in values is observed. Therefore, mesh number two is selected for all geometry and used in further studies to save computational time.

Fig. 3 Effect of different grid size on average cell temperature as a function state of charge (SOC)



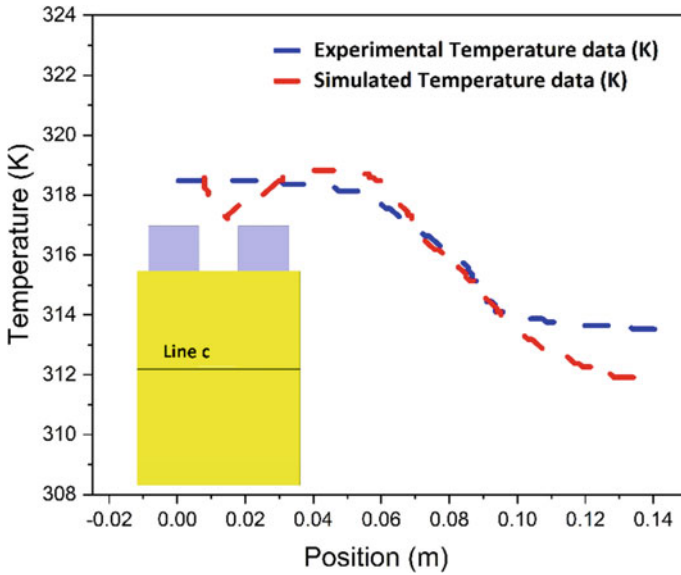


Fig. 4 Temperature profiles are compared between simulated model and experimental data (from Kim and Yi et al. [12]) to validate the current CFD model

2.5 Validation

Based on standard practice, any CFD result must be cross-checked against experimental data to validate the efficiency of the CFD model and mesh in use. For this purpose, numerical simulation is performed using a prismatic pouch cell of $192 \times 145 \times 7 \text{ mm}^3$ with a nominal capacity of 20 Ah proposed by Kim and Yi et al. [12]. The temperature results at different axial locations of cell are compared with experimental results and around 2.5% difference in the temperature values is observed which can be seen in Fig. 4.

3 Results and Discussion

The numerical simulation is carried out on a 20 Ah lithium ion pouch cell for which it is assumed that initially the temperature of the cell is considered as an atmospheric temperature of 300 K, state of charge (SOC) as 15% and voltage (V) is set at 3.5 V. The convective heat transfer coefficient (h) is taken as $25 \text{ W/m}^2\text{K}$ [18]. The performance of a cooling system is studied by evaluating the effect of phase change material, cell temperature, and cell voltage at high charging rates. The SOC of a cell or battery pack can be defined as the amount of charge remaining or the percentage of charge available within the cell or battery pack. It is important to understand the C-rates or

charging/discharging rates of the battery in the context of rechargeable lithium ion batteries. It is a measure of charging current at which battery is charging/discharging. For example, if a battery is having a capacity of 20 Ah and then charging at a current rate of 40 A it is considered as 2C rate similarly when charging at 60 A current rate it is considered as 3C rate and when charging at 80 A it is considered as 4C rate which ultimately reduces the time required for charging the battery. If the charging is performed for 20 Ah cell at 20 A it will take one hour, when it is performed at 40 A it will take 30 min similarly for 60 A and 80 A it will take 20 min and 15 min, respectively.

Figure 5 presents the temperature contour for both air cooled and PCM cooled systems when charging is performed at a current rate of 60A. It can be seen in Fig. 6, at initial stage of charging (at SOC 20%), cell temperature of both cooling systems attains a lower value. This is due to heat generation rate in cell being lower. As the time increases, cell temperature keeps rising with the State of Charging (SOC) and when cell is charged up to 80–95%, a substantial amount of heat is generated which further carried away cooling system. In Fig. 5, it can be depicted that cell temperature of PCM cooled attains a lower value compared to cell temperature of air cooled system. This happens because in PCM cooled battery system heat generated by the cell is absorbed by the latent heat of PCM.

Similarly, cell temperature of PCM-cooled and air-cooled systems are calculated and compared during charging at different current rates and presented in Fig. 8. It can be seen in the Fig. 6 that the cell temperature is keep increasing during charging for all current rates. However, for lower charging current rate of 40A, less amount of heat is generated for both cooling systems. And heat generation rate increases with an increase in current rate. When charging is performed at a current rate of 80A, cell temperature of air cooled system is higher by 6 K than the PCM cooled system.

Further, the melting rate of PCM is also captured at different stages of charging and presented in Figs. 7 and 8. It can be noticed from Fig. 8 that when charging is performed at a current rate of 40A and 60A, melting of PCM starts from 20% SOC and get completely melted at 45% SOC. However, when the charging is performed at a current rate of 80A, melting process of PCM is completed within the rage of 36% SOC. And at this situation, the heat carrying capacity of PCM gets deteriorated due to the low thermal conductivity of PCM at liquid state and increases the chance of thermal runaway. Thus, it can be concluded that forced convection system along PCM is better option than the combination of natural convection and PCM based cooling system.

4 Conclusions

The thermal behavior of lithium-ion battery is discussed in this paper using NTGK MSMD battery model of ANSYS Fluent. The present model will help identify the prone zone where the maximum heat is generated opening the way for research. The results obtained from the numerical simulation of air cooled and PCM cooled battery

Fig. 5 Temperature contour cell alone and cell with PCM at different flow time

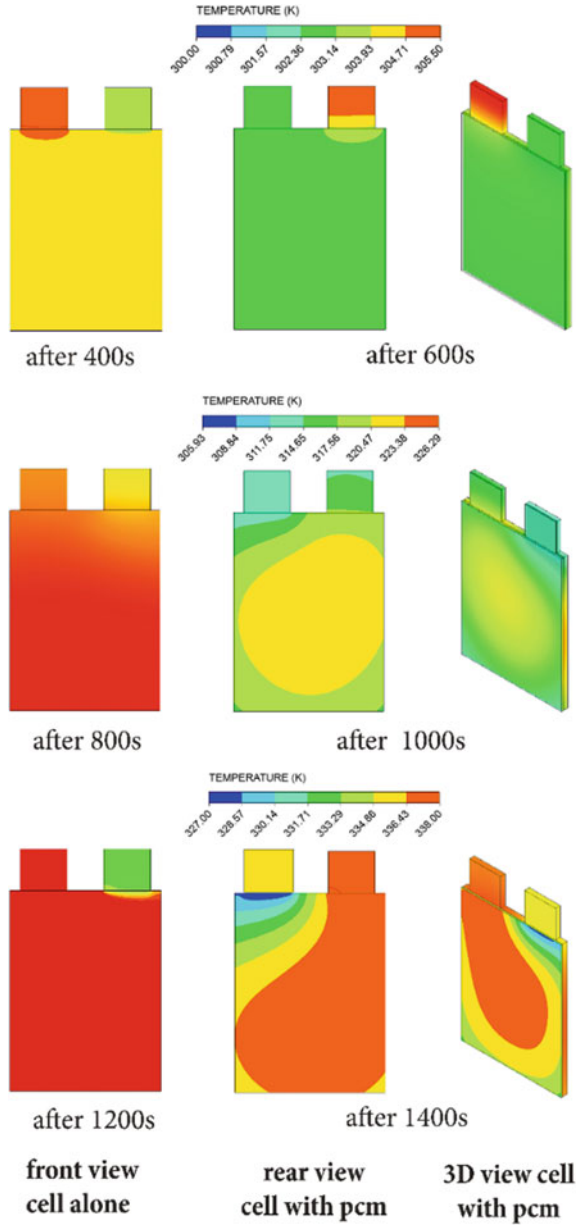
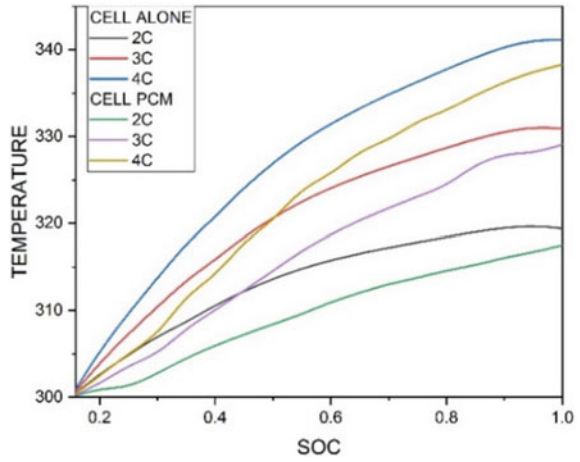


Fig. 6 Temperature plot of cell with respect to charging of battery at different current rates



at different current rates of 40, 60, and 80 A show that the maximum temperature attained when charging is performed at a current rate of 80 A, that is, 338 K which may increase the chance of thermal runaway. While charging battery at a current rate of 40 A lowers the risk and maximum temperature is about 315 K. Applying PCM along with the cell lowers the temperature of cell by 5–6 K.

Fig. 7 Mass fraction contour of cell with PCM at different State of Charge

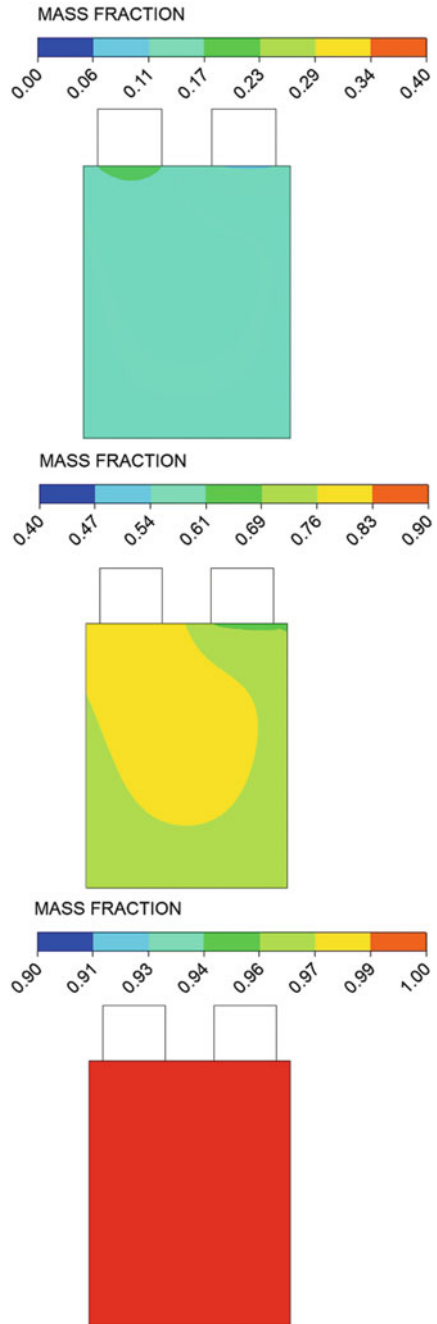
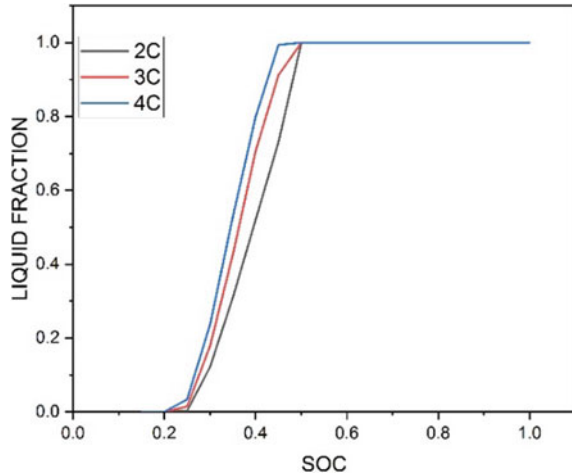


Fig. 8 Liquid fraction plot of cell at different C-rates with respect to charging of cell with PCM



Nomenclature

ρ_{PCM}	Density of PCM (kg/m^3)
$c_{p-\text{PCM}}$	Specific heat of PCM (kJ/kg K)
\vec{V}	Velocity vector
T_{PCM}	Temperature of PCM (K)
k_{PCM}	Thermal conductivity of PCM
i_p and i_n	Linear current density (A/m)
J	Current density (A/m^2)

References

1. Ai W, Kraft L, Sturm J, Jossen A, Wu B (2020) Electrochemical thermal-mechanical modelling of stress inhomogeneity in lithium-ion pouch cells. *J Electrochem Soc* 167:013512. <https://doi.org/10.1149/2.0122001jes>
2. Mali V, Saxena R, Kumar K, Kalam A, Tripathi B (2021) Review on battery thermal management systems for energy-efficient electric vehicles. *Renew Sustain Energy Rev* 151:111611. <https://doi.org/10.1016/j.rser.2021.111611>
3. Xie Y, He XJ, Hu XS, Li W, Zhang YJ, Liu B et al (2020) An improved resistance-based thermal model for a pouch lithium-ion battery considering heat generation of posts. *Appl Therm Eng* 164:114455. <https://doi.org/10.1016/j.applthermaleng.2019.114455>
4. Zhang H, Wu X, Wu Q, Xu S (2019) Experimental investigation of thermal performance of large-sized battery module using hybrid PCM and bottom liquid cooling configuration. *Appl Therm Eng* 159:113968. <https://doi.org/10.1016/j.applthermaleng.2019.113968>
5. Huang R, Li Z, Hong W, Wu Q, Yu X (2020) Experimental and numerical study of PCM thermophysical parameters on lithium-ion battery thermal management. *Energy Rep* 6:8–19. <https://doi.org/10.1016/j.egy.2019.09.060>

6. Kiani M, Ansari M, Arshad A, Ehsan A, Mehdi H (2020) Hybrid thermal management of lithium - ion batteries using nanofluid, metal foam, and phase change material: an integrated numerical—experimental approach. *J Therm Anal Calorim*. <https://doi.org/10.1007/s10973-020-09403-6>
7. Ping P, Zhang Y, Kong D, Du J (2021) Investigation on battery thermal management system combining phase changed material and liquid cooling considering non-uniform heat generation of battery. *J Energy Storage* 36:102448. <https://doi.org/10.1016/j.est.2021.102448>
8. Huang Q, Li X, Zhang G, Deng J, Wang C (2021) Thermal management of Lithium-ion battery pack through the application of flexible form-stable composite phase change materials. *Appl Therm Eng* 183:116151. <https://doi.org/10.1016/j.applthermaleng.2020.116151>
9. Chen J, Kang S, E J, Huang Z, Wei K, Zhang B et al (2019) Effects of different phase change material thermal management strategies on the cooling performance of the power lithium ion batteries: a review. *J Power Sources* 442:227228. <https://doi.org/10.1016/j.jpowsour.2019.227228>
10. Huang Q, Deng J, Li X, Zhang G, Xu F (2020) Experimental investigation on thermally induced aluminum nitride based flexible composite phase change material for battery thermal management. *J Energy Storage* 32:101755. <https://doi.org/10.1016/j.est.2020.101755>
11. Mehrabi-kermani M, Houshfar E, Ashjaee M (2019) International Journal of Thermal Sciences A novel hybrid thermal management for Li-ion batteries using phase change materials embedded in copper foams combined with forced-air convection. *Int J Therm Sci* 141:47–61. <https://doi.org/10.1016/j.ijthermalsci.2019.03.026>
12. Kim US, Yi J, Shin B, Han T, Park S (2011) Modeling the dependence of the discharge behavior of a lithium-ion battery on the environmental temperature 158:1–8. <https://doi.org/10.1149/1.3565179>
13. Hyun K, Burm C, Hyuk T, Kim C (2006) A two-dimensional modeling of a lithium-polymer battery 163:151–7. <https://doi.org/10.1016/j.jpowsour.2006.03.012>
14. Verma A, Shashidhara S, Rakshit D (2019) A comparative study on battery thermal management using phase change material (PCM). *Therm Sci Eng Prog* 11:74–83. <https://doi.org/10.1016/j.tsep.2019.03.003>
15. Javani N, Dincer I, Naterer GF, Rohrauer GL (2014) Modeling of passive thermal management for electric vehicle battery packs with PCM between cells. *Appl Therm Eng* 73:307–316. <https://doi.org/10.1016/j.applthermaleng.2014.07.037>
16. Mousavi S, Siavashi M, Zadehkabir A (2021) A new design for hybrid cooling of Li-ion battery pack utilizing PCM and mini channel cold plates. *Appl Therm Eng* 197:117398. <https://doi.org/10.1016/j.applthermaleng.2021.117398>
17. Savvakis N, Dialyna E, Tsoutsos T (2020) Investigation of the operational performance and efficiency of an alternative PV + PCM concept. *Sol Energy* 211:1283–1300. <https://doi.org/10.1016/j.solener.2020.10.053>
18. Li Q, Yang C, Santhanagopalan S, Smith K, Lamb J, Anna L et al (2019) Numerical investigation of thermal runaway mitigation through a passive thermal management system. *J Power Sources* 429:80–88. <https://doi.org/10.1016/j.jpowsour.2019.04.091>

Flow and Heat Transfer Phenomena Through Porous Media Under Turbulent Regime



Shaik Dilshad Begum, G. Trilok, and N. Gnanasekaran

Nomenclature

a_{sf}	Interfacial surface area[1/m]
c_p	Specific heat[J/KgK]
H	Channel thickness[m]
H_f	Metal foam total thickness[m]
ρ_f	Density of fluid[kg/m ³]
d_p	Diameter of hole in porous media[m]
d_f	Diameter of fibre[m]
p	Pressure[Pa]
T	Temperature[K]
u	Velocity[m/s]
h_{sf}	Interfacial heat transfer coefficient[$W/m^2 K$]
ε	Porosity[-]
λ_f	Thermal conductivity of fluid[W/mK]

1 Introduction

A wide range of potential technologies, including high efficiency heating systems, fuel cells, passive heatsinks, photovoltaic receivers, avionics cooling, etc., are accomplished by porous media comprised of metal. Foams possess large surface area, high thermal conductivity and low-density favouring heat transfer for a great extent. These unique structural characteristics open a spectrum of research to study the

S. D. Begum · G. Trilok · N. Gnanasekaran (✉)
Department of Mechanical Engineering, National Institute of Technology Karnataka, Surathkal,
India
e-mail: gnanasekaran@nitk.edu.in

physics indulged within. The heat transfer characteristics are known to enhance with increased velocities, significantly more in turbulent regimes. With this regard, the current study focuses to quantify the effect of turbulence on thermo-hydraulic behaviours in thermal systems consisting of metal foams.

2 Literature Review and Objective

In two channel topologies, parallel plates, and spherical pipes, Kazmierczak and Poulidakos researched fully developed forced-convection through a channel filled with porous matrix. The findings emphasize that the rate of heat transfer is minimum at the critical thickness, and it exists when Nu reaches a minimum. Seo and Byung [1] experimentally examined the effect of aluminium foams on transfer of heat by convection and flow of fluid through an asymmetric channel. The results indicate that for lower permeable aluminium foams, the friction factor is much higher. Pradeep et al. [2] experimental results reported that the heat transfer enhances by 2.7–3.9 times in a channel clogged with metal foams than that of the empty channel for the same inlet velocity. They also noticed an increase in heat transfer performance is only 4% in copper foam compared to aluminium foam. Simon et al. [3] considered aluminium foams of constant porosity of 0.93 and two different foam core heights (20 mm and 40 mm) for experimental study of thermal (heat transfer) and hydro-dynamic (pressure drop) behaviour. The findings state, a foam height of 20 mm shows higher heat transfer coefficients than the one with 40 mm core height, but the pressure gradient results are almost identical for both heights. Mahmoudi et al. [4] numerically examined the heat transfer enhancement due to the presence of porous media filled partially in a circular duct. They determined the optimum thickness of the porous layer under varying inertia with a reasonable pressure drop. They noticed considerably different values of Nusselt number by applying two models at the porous media and fluid interface. Nimvari et al. [5] numerically examined the heat transfer enhancement due to partially filled porous metal foam in a pipe. They determined the optimum thickness of the porous film under varying inertia with a reasonable pressure drop. They noticed considerably different values of Nusselt number by applying both thermal models at the fluid and porous media interface. The forced convective flow case was examined analytically in parallel plate heat exchangers by Tao et al. [6]. The overall heat transfer depends on the flow rate and heat transfer resistance. Many other researchers [7] numerically investigated high porosity aluminium metal foams using LTE and LTNE models. It's observed that the findings of LTNE model are in good agreement with the experimental results. With the help of two-dimensional computational fluid dynamics, Kotresha and Gnanasekaran [8] quantitatively examined the mixed-convective heat transfer through partially filled aluminium metal metal foams in an upright channel. They discovered that the Nusselt number rises as the partial filling of the metal foams increases. Helium was used as the working fluid in a computational investigation of a regenerator for a miniaturized Stirling cryocooler

by Garg et al. [9]. They contrasted the heat transfer models for Local Thermal Equilibrium (LTE) and Local Thermal Non-equilibrium (LTNE). It became evident that the LTE and LTNE models accurately forecast variations in overall temperature, but for detecting precise heat transfer parameters, such as thermal saturation, the LTNE model must be employed. Mo et al. [10] proposed an analytical study for transfer of heat in a parallel plate partially filled with porous media to study velocity contours and temperature distributions. They investigated the dependence of key parameters, which include solid, fluid thermal conductivity ratio, pore density, porosity, Re , and relative height of metal foams. Venugopal et al. [11] experimented with the prospect of a metallic porous filler to facilitate heat transmission through a vertical duct with pressured flow. Based on the experimental results, they stated new correlations for the Nu , which does not require any hydrodynamic studies information. Karimi and Mahmoudi [12] carried out analytical analysis of forced convection through partially brimmed with porous medium subjected to constant heat flux. Two-equation model is implemented for the fluid flow and porous coat. Lin et al. [13] concluded from their experimental analysis that at higher velocities, LTE model and LTNE model produce the same thermal results. Using computational and asymptotic methodologies, Hooman et al. [14] investigated the thermal propagation effects on fully formed forced heat transfer in a porous-saturated pipe. Using asymptotic technique Nusselt number can be obtained as a function of thermal dispersion coefficient if velocity and temperature are known. In this study for the plug flow, Nusselt number is found to be a linear function of thermal dispersion coefficient. The effects of pore density, input velocity, and blockage ratio on the behaviour of fluid pressure and flow drop in channel partially occupied with a porous metal block were experimentally investigated by Anu et al. [15]. It was revealed that the pressure decrease brought on by the solid block is greater at low occlusion ratios. However, the drop in pressure caused by the metal foam is greater than that of a solid block over a certain blockage ratio. In a parallel-plate channel filled with a bi-disperse porous medium, Wa et al. [16] explored the completely developed forced convective energy and mass transfer using a Darcy flow model with a constant heat flux boundary condition. The effects of flow velocity, interphase mass transfer coefficient, effective thermal conductivity ratio, Biot, Soret, and Damkohler numbers were investigated on the temperature and concentration distributions. Nihad and Ahmed [17] reviewed the thermal development in open cell aluminium metal porous media fused between two heated parallel plates. The findings suggest that while studying the heat transfer of metal foams, the thermal entering zone should be taken into consideration.

The aforementioned study highlights that there have been several research studies on the performance of metal foams, but the tortuous flow path inside porous media opens up a plethora of study that has to be done in order to fully understand the dynamic behaviour. This numerical analysis uses Kotresha and Gnanasekaran [18] prior study on the subject as a reference. In contrast to the laminar scenario, which serves as the foundation, this study focuses on examining pressure drop, flow distribution, and heat transfer properties in the turbulent realm.

3 Numerical Description

A vertical channel numerical analysis by Kotresha and Gnanasekaran [18] studying nuances of fluid flow in the presence of an aluminium porous media is chosen as the reference work as shown in Fig. 1. It can be observed that the domain is symmetrical about the Y-axis; hence, for the simulation, only one symmetrical portion of the vertical channel is considered as computations domain as shown in Fig. 2. A heater is placed between two aluminium plates. To enhance heat transfer, metal foams are placed on both sides of aluminium plates. Aluminium plates are of the size 250 mm * 150 mm * 3 mm. For filling rate by volume of 40% i.e., $H_f = 0.4H$, the dimensions of porous medium are 250 mm * 150 mm * 4 mm. Aluminium foams of various pores per inch (PPI) namely, 10PPI, 20PPI, 30PPI, 45PPI with different porosity varying from 0.9 to 0.95 are considered. Table 1 lists the properties of metal foam considered in this study. Table 1 lists the attributes of metal foam taken from Kamath et al.[19] experimental work.

Assumptions made:

1. Considering an incompressible, steady stream, the air as work fluid with an inlet temperature of 30 degrees C.
2. With barely any thermal dispersion, the metal foam is uniform and isotropic.
3. The flow blending in the porous zone is ignored in the current analysis owing to the high complexity of interconnections.

4 Results and Discussion

4.1 Governing Equations

Numerical simulations were performed in ANSYS FLUENT software. Varying the velocity in turbulent regime from 5 to 40 m/s, Reynolds number is fixed. The characteristic length is set in accordance with the dimensions of the problem domain. For the internal flow through the upright channel, $k-\epsilon$ is used.

The simulation's governing equation is provided below.

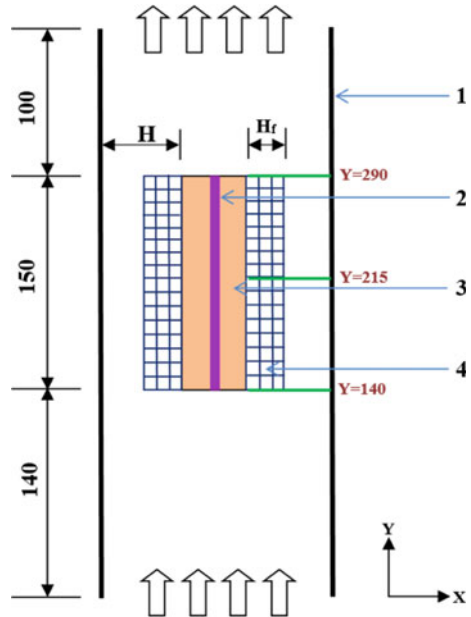
$$\frac{\partial(\rho_f u_i)}{\partial x_i} = 0$$

$$\frac{\partial(p_f u_i u_j)}{\partial x_j} = \frac{\partial p}{\partial x_j} + \frac{\partial}{\partial x_j} \left((\mu_f + \mu_t) \left(\frac{\partial u_i}{\partial x_j} + \frac{\partial u_j}{\partial x_i} \right) \right)$$

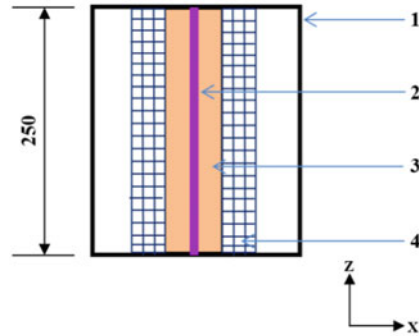
$$\frac{\partial(\rho_f u_i T)}{\partial x_j} = \frac{\partial}{\partial x_j} \left(\left(\frac{\partial}{Pr_f} + \frac{\mu_t}{Pr_t} \right) \right) \frac{\partial T}{\partial x_j}$$

Continuity equation: $\frac{\partial(\rho_f \epsilon u_i)}{\partial x_i} = 0 \quad \frac{\partial(\rho_f \epsilon u_i)}{\partial x_i} = 0$

Fig. 1 Sketch of domain considered for numerical analysis. (1) Outer wall (2) Heater (3) Aluminium plate (4) Aluminium metal foam



(a) Front view



(b) Top view

Momentum equations:

$$\frac{\partial(\rho_f u_i u_j)}{\partial x_j} = -\varepsilon \frac{\partial P}{\partial x_i} + \frac{\partial}{\partial x_i} \left((\mu_f + \mu_t) \left(\frac{\partial u_i}{\partial x_i} + \frac{\partial u_i}{\partial x_i} \right) \right) - \varepsilon \left(\frac{\mu}{K} u_i + \rho_f C |u| u_i \right)$$

Energy Equation considering LNTE model.

For fluid: $\varepsilon \frac{\partial(\rho_f C_{p,f} u_j T)}{\partial x_j} = \lambda_{fe} \frac{\partial}{\partial x_i} \left(\frac{\partial T_f}{\partial x_j} \right) + h_{sf} a_{sf} (T_s - T_f).$

Fig. 2 The boundary conditions computational domain

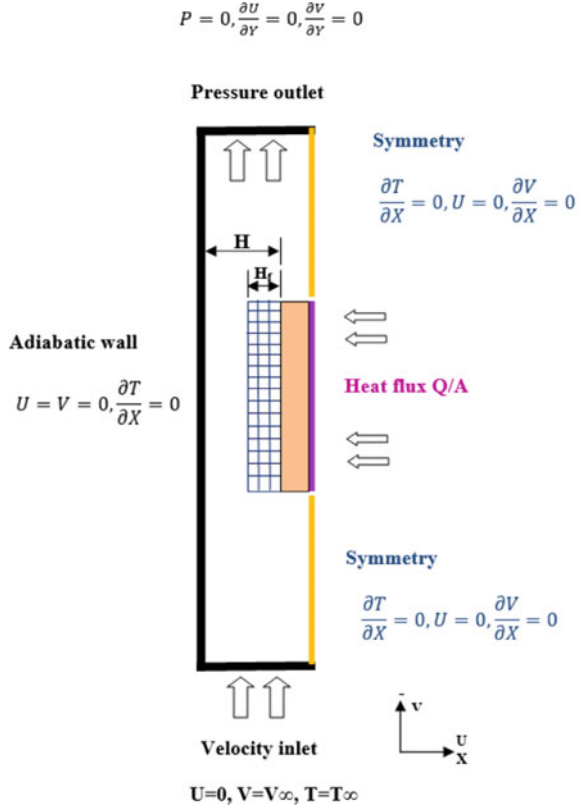


Table 1 Attributes of metal foam considered in analysis

Pore Density (PPI)	Fibre Diameter d_f (mm)	Pore Diameter d_p (mm)	Porosity ϵ	Interfacial surface area a_{sf} (m^{-1})
10	0.445	4.952	0.95	360.60
20	0.451	3.416	0.90	960.65
30	0.216	2.324	0.92	936.38
45	0.184	1.654	0.90	1671.76

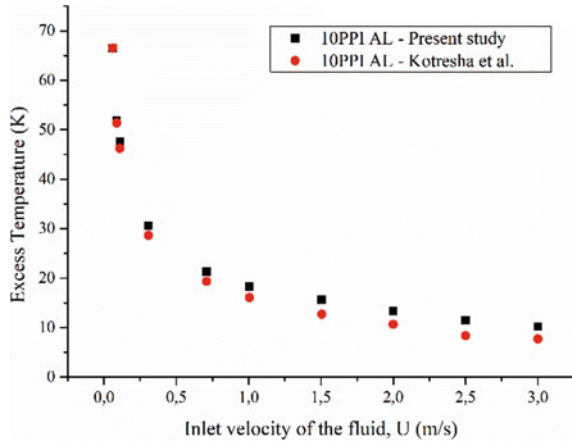
For solid: $\lambda_{fe} \frac{\partial}{\partial x_i} \left(\frac{\partial T_s}{\partial x_j} \right) = h_{sf} a_{sf} (T_s - T_f)$.

The values of specific surface area of metal foams of various PPI and porosity are tabulated in Table 2.

Table 2 Specific surface area of aluminium foams

Pore Density (PPI)	Porosity	Permeability $10^7, m^2$	Uncertainty %	Form drag Coefficient	Uncertainty %
10	0.95	4.952	± -7.95	94.98	± -2.45
20	0.90	3.416	± -9.67	208.82	± -2.21
30	0.92	2.324	± -9.83	148.97	± -3.68
45	0.90	1.654	± -5.87	397.01	± -5.80

Fig. 3 Comparison study of Excess Temperature



5 Validation

Numerical analysis of the current study is validated by the observations and findings that are already available in the literature. Figure 3. shows a comparison of temperature distribution for 10PPI. Variation of Nu is plotted against Re and validated in Fig. 4.

6 Fluid Flow and Heat Transfer

For all porous metal foam, the modulation of excess temperature vs inlet velocity of the flow, is plotted in Fig. 5. The temperature difference in the laminar investigation by [18] is in the order of tens for the laminar velocity range. However, as the velocity rises, the temperature difference greatly reduces, which is in line with the findings of Kamath et al. [19] experiments. These findings are achieved by incorporating LTNE model. In the present study it is observed that under lower turbulent velocities, the increment in heat transfer enhancement is very significant with variation in porous conditions of metal foams. Contrarily, with increase in turbulent velocity, though

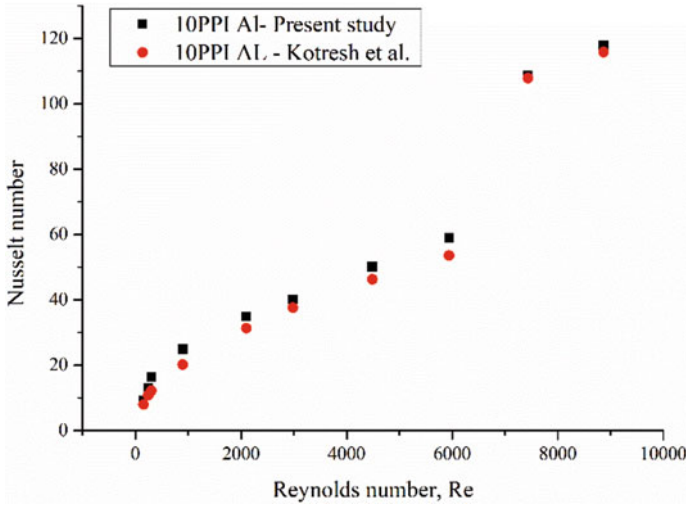


Fig. 4 Comparison study of Nu varying with Re

the heat transfer enhancement is very high, the relative deviations of heat transfer corresponding to different porous conditions of metal foams are observed to be relatively closer. Thus, while seeking higher heat transfer which could be obtained on operating at higher turbulent velocities, the metals foams could be chosen such that the corresponding pressure drop is minimum as the variation in heat transfer is comparatively less among all porous conditions.

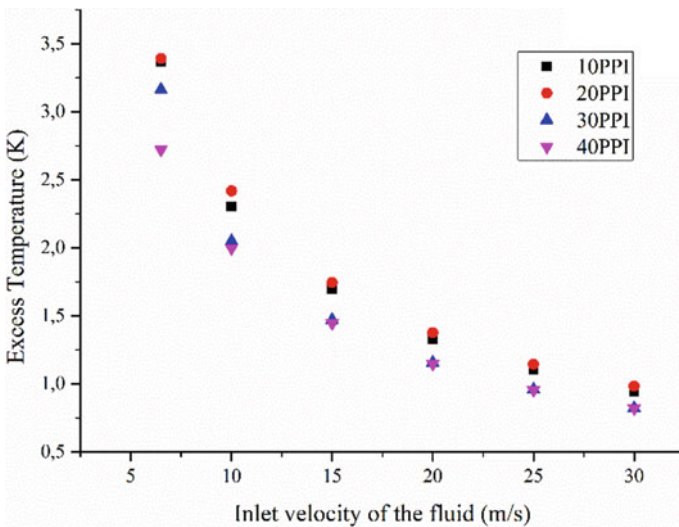


Fig. 5 Excess temperature variation for a 10PPI metal foam

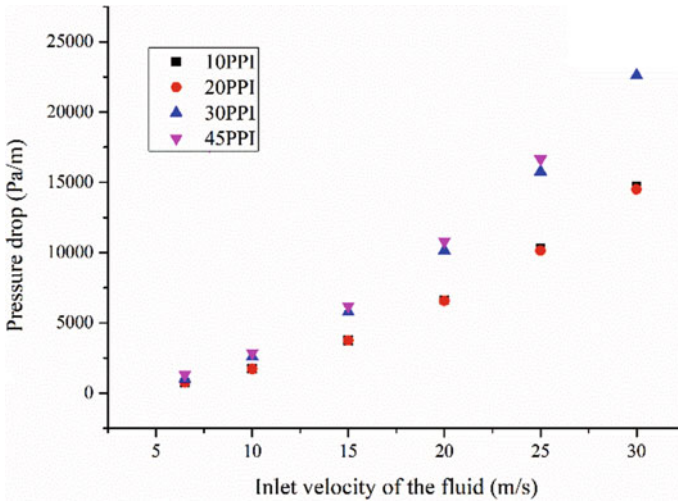


Fig. 6 Variation of pressure drop for different PPIs

The variability in pressure drop with respect to the velocity for porous metal foams with four different PPIs namely, 10, 20, 30, and 45 is shown in Fig. 6. According to the plot, all PPIs see an increase in pressure drop as velocity rises. The pressure drop generated at 45PPI is 1.6 times higher than the pressure drop recorded with a metal foam at 10PPI. This demonstrates that pressure drop in the turbulent regime from one pore density to another is not uniformly varying. Also, at higher turbulent velocities the change in the pressure drop can be seen highly significant as shown in Fig. 6, thus demonstrating the need for careful examination of metal foams particularly while working under higher turbulent velocities.

Nusselt number (Nu) variation with Reynolds number (Re) is plotted in the Fig. 7. It is evident from the figure that for the forced convection regime in turbulent region, that is, the higher Reynolds number. Strong relationship exist among Reynolds number and Nusselt's number. The metal foam with pores per inch (PPI) 30 and 45 tends to show similar results. But, there is an increase of Nu by 16.5% from a 10PPI to that of a 45 PPI one. The inter- facial area increases with increasing PPI which results in higher Nusselt number.

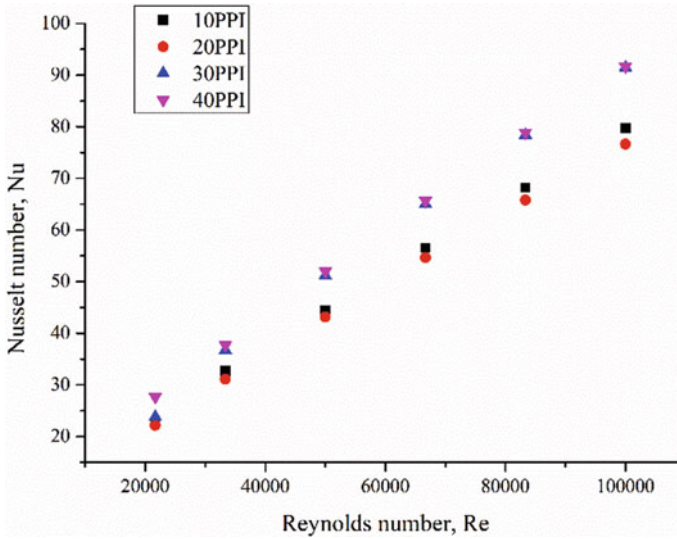


Fig. 7 Variance in Nu with Re for all PPIs of metal foams

7 Conclusion

In the current work, a hydrodynamic comparison of fluid flow characteristics and heat transfer properties between laminar and turbulent regime is made. The flow through a partially clogged metal foam through a vertical channel is predicted by incorporating the Darcy–Forchheimer model with conjugation of local thermal non-equilibrium model. The numerical model suggests that for greater PPI metals foam in turbulent regime, the rate of heat transfer increases to significant extent with a compromise in pressure drop. The flow and heat transfer characteristics in the turbulent regime is observed to be a complex behaviour exhibited differently with varying turbulent velocities. Through this study, it is observed that, though a rich heat transfer enhancement can be achieved while operating under turbulent regime, efforts in order to arrive at an optimized thermo-hydraulic performance is necessary, as the variation in the thermo-hydraulic behaviour is not uniform with change in the turbulent velocities. Thus, there is a big scope of research, yet to find the optimum combination of porosity, pores per inch, volume filling rate, and material properties to enhance heat transfer with minimal pressure drop conditions.

References

1. S. Y. Kim, H. Kang, and J.-H. Kim, “Forced convection from aluminum foam materials in an asymmetrically heated channel.” [Online]. Available: www.elsevier.com/locate/ijhmt

2. Kamath PM, Balaji C, Venkateshan SP (2011) Experimental investigation of flow assisted mixed convection in high porosity foams in vertical channels. *Int J Heat Mass Transf* 54(25–26):5231–5241. <https://doi.org/10.1016/j.ijheatmasstransfer.2011.08.020>
3. Mancin S, Zilio C, Rossetto L, Cavallini A (2012) Foam height effects on heat transfer performance of 20 ppi aluminum foams. *Appl Therm Eng* 49:55–60. <https://doi.org/10.1016/j.applthermaleng.2011.05.015>
4. Mahmoudi Y, Karimi N (2014) Numerical investigation of heat transfer enhancement in a pipe partially filled with a porous material under local thermal non-equilibrium condition. *Int J Heat Mass Transf* 68:161–173. <https://doi.org/10.1016/j.ijheatmasstransfer.2013.09.020>
5. Nimvari ME, Maerefat M, El-Hossaini MK (2012) Numerical simulation of turbulent flow and heat transfer in a channel partially filled with a porous media. *Int J Therm Sci* 60:131–141. <https://doi.org/10.1016/j.ijthermalsci.2012.05.016>
6. Lu W, Zhang T, Yang M, Wu Y (2017) Analytical solutions of force convective heat transfer in plate heat exchangers partially filled with metal foams. *Int J Heat Mass Transf* 110:476–481. <https://doi.org/10.1016/j.ijheatmasstransfer.2017.02.087>
7. Gangapatnam P, Kurian R, Venkateshan SP (2018) Numerical simulation of heat transfer in metal foams. *Heat and Mass Transfer/Waerme- und Stoffuebertragung* 54(2):553–562. <https://doi.org/10.1007/s00231-017-2149-6>
8. B. Kotresha and N. Gnanasekaran, “Investigation of Mixed Convection Heat Transfer Through Metal Foams Partially Filled in a Vertical Channel by Using Computational Fluid Dynamics,” *J Heat Transfer*, vol. 140, no. 11, Nov. 2018, doi: <https://doi.org/10.1115/1.4040614>.
9. Garg SK, Premachandran B, Singh M (2019) Numerical study of the regenerator for a miniature Stirling cryocooler using the local thermal equilibrium (LTE) and the local thermal nonequilibrium (LTNE) models. *Thermal Science and Engineering Progress* 11:150–161. <https://doi.org/10.1016/j.tsep.2019.03.005>
10. Lu W, Zhang T, Yang M (2016) Analytical solution of forced convective heat transfer in parallel-plate channel partially filled with metallic foams. *Int J Heat Mass Transf* 100:718–727. <https://doi.org/10.1016/j.ijheatmasstransfer.2016.04.047>
11. Venugopal G, Balaji C, Venkateshan SP (2010) Experimental study of mixed convection heat transfer in a vertical duct filled with metallic porous structures. *Int J Therm Sci* 49(2):340–348. <https://doi.org/10.1016/j.ijthermalsci.2009.07.018>
12. Karimi N, Mahmoudi Y, Mazaheri K (2014) Temperature fields in a channel partially filled with a porous material under local thermal non-equilibrium condition - An exact solution. *Proc Inst Mech Eng C J Mech Eng Sci* 228(15):2778–2789. <https://doi.org/10.1177/0954406214521800>
13. Lin W, Xie G, Yuan J, Sundén B (2016) Comparison and Analysis of Heat Transfer in Aluminum Foam Using Local Thermal Equilibrium or Nonequilibrium Model. *Heat Transfer Eng* 37(3–4):314–322. <https://doi.org/10.1080/01457632.2015.1052682>
14. Hooman K, Li J, Dahari M (2017) Thermal dispersion effects on forced convection in a porous-saturated pipe. *Thermal Science and Engineering Progress* 2:64–70. <https://doi.org/10.1016/j.tsep.2017.04.005>
15. F. Shikh Anuar, I. Ashtiani Abdi, M. Odabae, and K. Hooman, “Experimental study of fluid flow behaviour and pressure drop in channels partially filled with metal foams,” *Exp Therm Fluid Sci*, vol. 99, pp. 117–128, Dec. 2018, doi: <https://doi.org/10.1016/j.expthermflusci.2018.07.032>.
16. Q. Wang, K. Wang, and P. Li, “Forced convective heat and mass transfer in a bidisperse porous parallel-plate channel with a first order reaction on the wall,” *Thermal Science and Engineering Progress*, vol. 13, Oct. 2019, doi: <https://doi.org/10.1016/j.tsep.2019.100369>.
17. Dukhan N, Suleiman AS (2017) The thermally-developing region in metal foam with open pores and high porosity. *Thermal Science and Engineering Progress* 1:88–96. <https://doi.org/10.1016/j.tsep.2017.03.004>
18. K. Banjara and G. Nagarajan, “Nuances of fluid flow through a vertical channel in the presence of metal foam/solid block – A hydrodynamic analysis using CFD,” *Thermal Science and Engineering Progress*, vol. 20, Dec. 2020, doi: <https://doi.org/10.1016/j.tsep.2020.100749>.

19. Kamath PM, Balaji C, Venkateshan SP (2013) Convection heat transfer from aluminium and copper foams in a vertical channel - An experimental study. *Int J Therm Sci* 64:1–10. <https://doi.org/10.1016/j.ijthermalsci.2012.08.015>

Numerical Investigation of Heat Transfer Characteristics of CO₂ in a Vertical Divergent Tapered Annular Channel



Ashok Kumar Gond, Dipankar Narayan Basu, and Amaresh Dalal

Nomenclature

b	Bulk [m ²]
c_p	Specific heat [J/kg K]
d	Diameter [m]
G	Mass flux [kg/m ² s]
Gr	Grashoff number [kg/m ³]
g	Gravity [rad/s]
H	Bulk enthalpy [kJ/kg]
HTC	Heat transfer coefficient [kW/m ² K]
L	Length [m]
\dot{m}	Mass flow rate [kg/s]
P	Pressure [Pa]
P_c	Pseudocritical
q	Heat flux [kW/m ²]
Re	Reynolds number
T	Temperature [K]
t	Turbulent
u	Axial velocity [m/s]
v	Radial velocity [m/s]
w	Wall
y^+	Non-dimensional distance
α	Taper angle [°]
λ	Thermal conductivity [w/m K]
μ	Dynamic viscosity [Ns/m ²]
ρ	Density [kg/m ³]

A. K. Gond (✉) · D. N. Basu · A. Dalal
Department of Mechanical Engineering, IIT Guwahati, Guwahati 781039, India
e-mail: ashok1994@iitg.ac.in

1 Introduction

Since supercritical carbon dioxide (sCO₂) has unique physical properties that considerably improve heat transfer, it is used as a working fluid in thermal cycles in a variety of thermal systems. The sCO₂ Brayton cycle, which benefits from a simple system design, minimal environmental impact, and high energy conversion efficiency, represents one of the most promising applications. It has various possible uses, including air conditioning, refrigeration systems, solar power, nuclear power, and coal-fired electricity [1]. The high heat transport capacities of sCO₂ in the tubes have recently attracted the attention of numerous researchers. A substantial amount of experimental and numerical study has been done, and they have revealed that heat transfer mainly hampered by two factors buoyancy and flow acceleration. Bae et al. [2] performed experimental heat transfer studies of sCO₂ about forced and mixed convection in a vertical tube. For the buoyancy effect, the expression was used as Gr/Re^2 . Their data represented that heat transfer impairment occurred whenever the buoyancy parameter exceeded the limit 2×10^{-5} and significantly reduced the Nusselt number from 1×10^{-6} to 2×10^{-5} . Kim et al. [3] experimentally analyzed heat transfer of a vertical tube of 4.5 mm inner diameter to ascertain the influence of buoyancy and flow acceleration. In the buoyancy and acceleration effects evaluation, the ratio of the experimental and correlation Nusselt numbers was compared along the variables for buoyancy (Bo^*) and flow acceleration (q^+), respectively. Through the experiment, Wang et al. [4] looked into the convective heat transfer characteristics of sCO₂. They investigated the influence of mass flux, inlet temperature, heat flux, tube diameter and pressure on heat transfer. According to the report, buoyancy would enhance heat transfer in a downward direction while deteriorating upward. Zhang et al. [5] explored the thermal and flow characteristics of sCO₂ in simple horizontal and vertical tubes as well as helical-coiled tubes under heating conditions using numerical and experimental methods. According to experimental results, the heat transfer impairment was likewise more apparent in the vertical tube than in the horizontal. With the quick advancement of computational systems, the exploration of heat transfer characteristics of fluids at supercritical pressure has become easier [6–9]. It can gather comprehensive data on the physical aspects of many different fluids at supercritical pressure. For instance, Yang et al. [10] numerically performed three special heat transfer behaviours assessments of a long vertical tube with a 4 m heated part, including a 0.35 m adiabatic part before and after the heated section's inlet and outlet. These behaviours included normal, enhanced and deteriorated heat transfer. They evaluated seven two-equation turbulence models for low (100 kg/m²s) and normal (400 kg/m²s) mass flux values and suggested $\sqrt{2}f$ and SST $k - \omega$ turbulence models. For low mass flow conditions, the significant buoyancy effect in the low enthalpy zone reduces laminar sublayer thickness and promotes heat conduction and turbulence convection by raising turbulent kinetic energy. Li et al. [11] carried out a numerical analysis of horizontal tubes with varying cross sections while being heated. Tubes with Converging, divergent as being varied cross-sections, and straight shapes with fixed cross-section were employed. As a result, it was noticed that converging

tube HTC dropped by 4.93%, and the divergent tube rose by 19.26% against the straight tube.

In light of the above findings, this work presents a tapered divergent annular channel at a fixed outer diameter with a varying cross-section of the heat generation rod using sCO₂. And the heat transfer characteristics of a vertical divergent tapered annular channel with varying tapered angles are studied against a straight vertical annular channel. Furthermore, the heat transfer behaviour is also examined at different mass flux conditions.

2 Physical Model and Boundary Conditions

This circular divergent tapered annular channel consists of solid and fluid domains, and the solid domain has been made tapered. As a result, fluid domain cross-section continually varies over the heated length corresponding to the solid domain cross-section variation. Whereas the outermost diameter of fluid domain is kept fixed throughout adiabatic and heated sections, as illustrated in Fig. 1. The entire geometry is split into two sections: one is an adiabatic section, and the other is a heated section. A heated section of 2.5 m long has been made to study the thermalhydraulics characteristics of the sCO₂, while the adiabatic section of 0.5 m long provided for the fully developed turbulent flow. Along the flow direction, the heated and adiabatic sections are both symmetrical about their central axis. Furthermore, the dimensions of various tapered channel configurations are provided in Table 1. The boundary conditions incorporated in this vertical divergent tapered annular channel are shown in Table 2.

3 Governing Equations

Using ANSYS Fluent software, the upward-flowing sCO₂ in a vertical divergent tapered annular channel was analyzed for its thermal and flow characteristics. The study defined steady governing equations, which encompassed continuity, momentum and energy considerations.

Continuity equation:

$$\frac{\partial}{\partial x}(\rho u) + \frac{1}{r} \frac{\partial}{\partial r}(r \rho v) = 0$$

U momentum equation:

$$\frac{\partial}{\partial x}(\rho u^2) + \frac{1}{r} \frac{\partial}{\partial r}(r \rho uv) = -\frac{\partial P}{\partial x} + \rho g + 2 \frac{\partial}{\partial x} \left[\mu_e \left(\frac{\partial u}{\partial x} \right) \right]$$

Fig. 1 Schematic diagram of divergent tapered annular channel

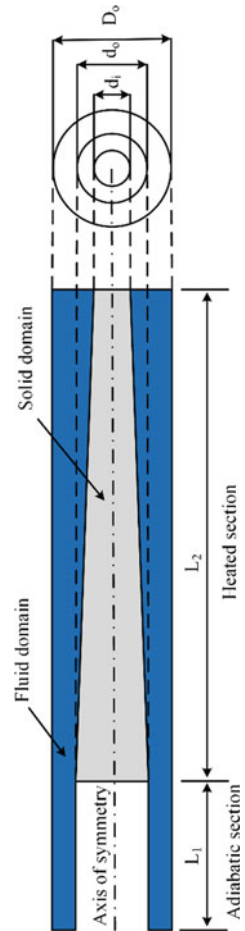


Table 1 Dimensions of different vertical tapered channel configurations (all dimensions in mm)

d_i	d_0	L_2	D_0	$\alpha = \tan^{-1}\left(\frac{d_0-d_i}{L_2}\right)$
11	11	2500	9	0
10.12	11.86	2500	9	0.02
9.2	12.69	2500	9	0.04
8.3	13.534	2500	9	0.06
7.3	14.28	2500	9	0.08

Table 2 Boundary condition of divergent tapered annular channel

Boundary	Property	Value
Inlet	Mass flux	400 to 700 kg/m ² s
Inlet	Temperature	303 K
Outlet	Pressure	8.5 MPa
Outer wall	Adiabatic	0 kW/m ²

$$+ \frac{1}{r} \frac{\partial}{\partial r} \left[r \mu_e \left(\frac{\partial u}{\partial r} + \frac{\partial v}{\partial x} \right) \right]$$

V momentum equation:

$$\begin{aligned} \frac{\partial}{\partial x} (\rho u v) + \frac{1}{r} \frac{\partial}{\partial r} (r \rho v^2) &= -\frac{\partial P}{\partial r} + \frac{\partial}{\partial x} \left[\mu_e \left(\frac{\partial u}{\partial r} + \frac{\partial v}{\partial x} \right) \right] \\ &+ 2 \frac{\partial}{\partial r} \left[r \mu_e \left(\frac{\partial v}{\partial r} \right) - 2 \frac{\mu_e v}{r^2} \right] \\ \mu_t &= \rho C_\mu f_\mu \frac{k^2}{\varepsilon} \end{aligned}$$

Energy equation:

$$\frac{\partial}{\partial x} (\rho u h) + \frac{1}{r} \frac{\partial}{\partial r} (r \rho v h) = \frac{\partial}{\partial x} \left[\left(\frac{\mu}{pr} + \frac{\mu_t}{\sigma_t} \right) \frac{\partial h}{\partial x} \right] + \frac{1}{r} \frac{\partial}{\partial r} \left[r \left(\frac{\mu}{pr} + \frac{\mu_t}{\sigma_t} \right) \frac{\partial h}{\partial r} \right]$$

4 Numerical Schemes

In the convective heat transfer study of sCO₂, the pressure and velocity fields were connected through the SIMPLE scheme method. The upwind scheme is incorporated to solve the transport equation, which provides numerical stability. In addition, the under-relaxation factors for the momentum, turbulent kinetic energy, specific dissipation rate, turbulent viscosity, and energy were imposed to 0.4, 0.8, 0.8, 1, and 0.99, respectively. The sCO₂ temperature (and pressure) dependent characteristics were determined using the NIST Standard Reference Database 23 (REFPROP) Version 9.0. The convergence criteria have been used to evaluate the numerical approaches' uncertainty. The iteration ended when the mean relative residuals of the following equations as continuity, momentum, turbulent kinetic energy, and turbulent dissipation reached a value of 1 × 10⁻⁵ or less, and for the energy, a value of 5 × 10⁻¹⁰ or less.

5 Validation and Grid Independent Test

To confirm the accuracy of the present SST $K - \omega$ model, it is necessary to validate it. The current model result was verified with both experimental and numerical wall results obtained by Liu et al. [12] and Liu et al. [13]. The employed boundary conditions included mass flux ($588.2 \text{ kg/ m}^2\text{s}$), heat flux (77.3 kW/m^2), pressure (9.04 MPa) and inlet temperature 298.9 K . In the result, Fig. 2 shows a local variation of wall temperature from fluid inlet to outlet. As shown, the wall temperatures generated by the two models rise monotonically throughout the flow, overlapping each other and closely matching both model results with experimental findings.

In the grid-independent test, four distinct meshes, numbered mesh 1 to 4, have been used, and the mesh elements of mesh 1 to 4 are 311,000, 639,000, 924,000, and 1,386,000, respectively. The wall y^+ value has been taken at 0.215 in all four meshes, which fulfil less than one criterion of the SST $K - \omega$ model. The minimum distance between the wall and the first node is approximately 1×10^{-6} . One point is noted: the separation between wall and node varies because of varying fluid domain cross-sections along the length. The simulation has been performed at operating conditions following mass flow rate (0.0797 kg/s), power (12 kW), outlet pressure (8.5 MPa) and inlet temperature 303 K . In Figs. 3 and 4, the local wall temperature and HTC are shown with the axial distance. As observed, only mesh 1 exhibits the wall temperature and HTC variations from position $X = 1.22 \text{ m}$ to 1.52 m rather than the entire flow length; in contrast, meshes 2, 3, and 4 show no variations along the whole axial length. So, in this order for further simulation, mesh 2 has been confirmed among the four different meshes.

Fig. 2 Model validation

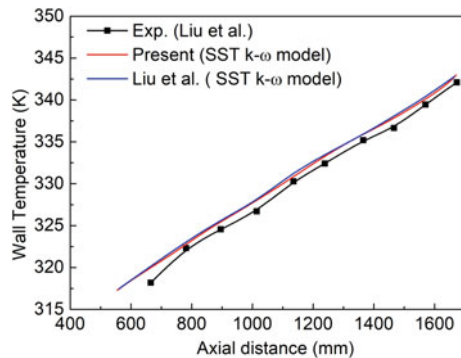


Fig. 3 Wall temperature comparison at $\dot{m} = 0.0797 \text{ kg/s}$, $E = 12 \text{ kW}$ and $P = 8.5 \text{ MPa}$

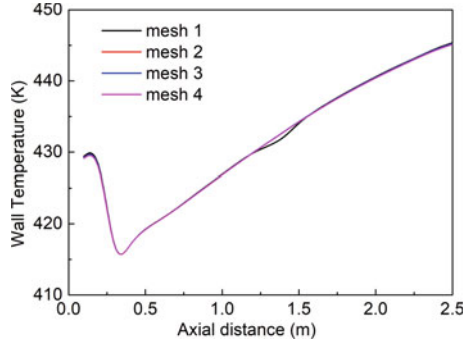
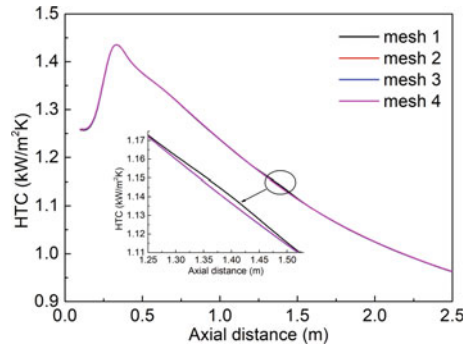


Fig. 4 HTC comparison at $\dot{m} = 0.0797 \text{ kg/s}$, $E = 12 \text{ kW}$ and $P = 8.5 \text{ MPa}$



6 Results and Discussions

This study examined the convective heat transfer properties of the divergent tapered annular channel with those of a typical cylindrical annular channel using the sCO₂. The local HTC is written as follows:

$$h = \frac{q_w}{T_w - T_b}$$

where q_w is described as wall heat flux, and T_w and T_b are temperatures of the wall and bulk fluid. The bulk mean enthalpy was estimated as average over each cross-section, and it was subsequently then utilized to calculate the T_b , written as

$$\int \frac{\rho u H dA}{\rho u dA}$$

6.1 Comparison of Cylindrical and Tapered Annular Channel

Figures 5 and 6 show a local variation of wall temperature and HTC along the fluid flow direction. To compare cylindrical and tapered annular channels, the tapered ones with different tapered angles are examined against the simple cylindrical ones under the same mass flow rate (0.0797 kg/s), power (10 kW), outlet pressure (8.5 MPa), and inlet temperature of 303 K. The effect of the tapered annular channel can be observed at distinct tapered angles level from $\alpha = 0$ to 0.08° with respect to the cylindrical annular channel in which the wall temperature reduces and HTC increases. These trends continue with increasing the tapered angle, but no result is shown after the tapered angle of $\alpha = 0.08^\circ$ because a further increment in taper angle leads to inflation layers deflected away to the wall regions of the tapered annular channel, which causes may not capture drastic change in thermophysical properties close the wall regions. Additionally, with increasing the taper angle $\alpha = 0$ to 0.08° , the wall temperature drops due to increasing velocity, which leads to a higher Reynolds number that facilitates the mixing of bulk and wall fluid regions that causes enhancement in heat transfer occurs.

Fig. 5 Wall temperature variation at different taper angles

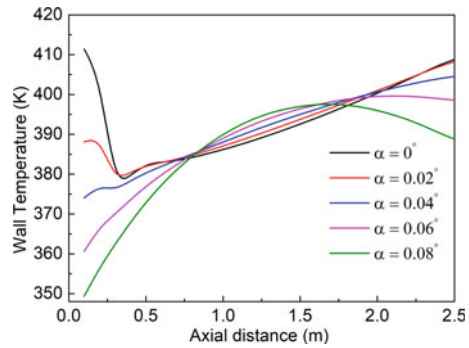
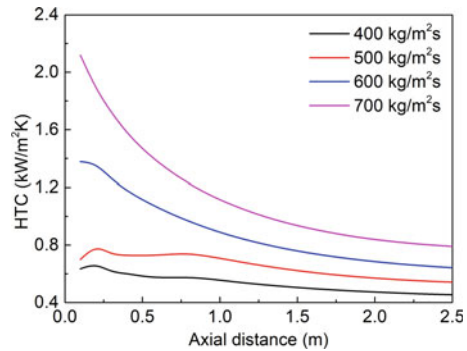


Fig. 6 HTC variation at different taper angles



6.2 Effect of Mass Flux on Heat Transfer

In this section, the mass flux effect on sCO₂ is examined to inspect heat transfer characteristics of a vertical divergent tapered annular channel at the boundary conditions of power, outlet pressure, and inlet temperature, which are 10 kW, 8.5 MPa, and 303 K, respectively, utilize a mass flux range of 400 to 700 kg/m²s. Wall temperature and HTC are shown versus axial distance in Figs. 7 and 8. The wall temperature magnitude drop over the flow length as mass flux rises from 400 to 700 kg/m²s and the HTC value increases. Furthermore, the wall temperature steadily rises at high mass flow values of 600–700 kg/m²s without any unevenness in its variation. However, at the low mass flux values of 400–500 kg/m²s, the wall temperature grows monotonically but shows some abrupt changes in its variation. This abrupt change arises primarily due to large disparities in the thermophysical characteristics between the core and wall fluids regions, which lead to strong buoyancy and flow acceleration suppressing heat transfer.

Fig. 7 Wall temperature variations with different mass fluxes at $E = 10$ kW and $P = 8.5$ MPa

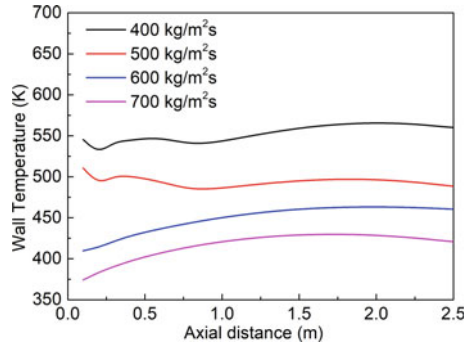
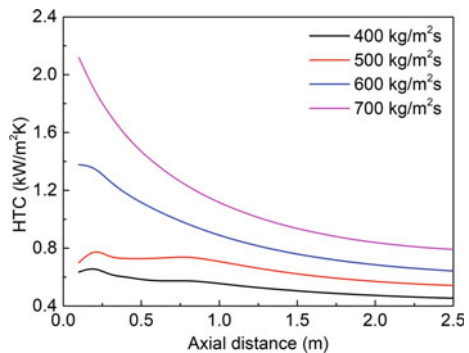


Fig. 8 HTC variations with different mass fluxes at $E = 10$ kW and $P = 8.5$ MPa



7 Conclusions

In this study, the vertical divergent tapered annular channel has been found to be better heat transfer potential than a simple cylindrical annular channel. The wall temperature reduces, and the HTC value rises as the tapered angle of the heat generation rod increases. This trend continues with increasing the tapered angle, but the wall temperature and HTC variation are shown up to taper angle $\alpha = 0.08^\circ$ due to numerical meshing tapering limitations, which prevented inflation from being used within the wall region. Furthermore, the wall temperature decline and HTC rise with different mass flux conditions as the mass flux value increases because Reynolds number and turbulent kinetic energy increase, enhancing the heat transfer. However, at relatively high mass flux cases of 600–700 kg/m²s, the wall temperature variation throughout the flow direction appears smooth. In contrast, at low mass fluxes of 400–500 kg/m²s, wall temperature unevenness occurs closer to the heated inlet region rather than across the entire flow length. This phenomenon happens may be due to the impairment of heat transfer by the strong buoyancy effect.

Acknowledgements This work was supported by the Department of Science and Technology, Government of India, Sanction Order No. TMD/CERI/Clean Coal/2017/034 (IT G).

References

1. Wang J, Guo P, Yan J, Zhu F, Luo X (2019) Experimental study on t forced convective heat transfer of supercritical carbon dioxide in a horizontal circular tube under high heat flux and low mass flux conditions. *Adv Mech Eng* 11(3):1687814019830804
2. Bae YY, Kim HY, Kang DJ (2010) Forced and mixed convection heat transfer to supercritical CO₂ vertically flowing in a uniformly-heated circular tube. *Exp Thermal Fluid Sci* 34(8):1295–1308
3. Kim DE, Kim MH (2010) Experimental study of the effects of flow acceleration and buoyancy on heat transfer in a supercritical fluid flow in a circular tube. *Nucl Eng Des* 240(10):3336–3349
4. Wang L, Pan YC, Der Lee J, Wang Y, Fu B-R, Pan C (2020) Experimental investigation in the local heat transfer of supercritical carbon dioxide in the uniformly heated horizontal miniature tubes. *Int J Heat Mass Transf* 159:120136
5. Zhang Q, Li H, Liu J, Lei X, Wu (2020) Numerical investigation of different heat transfer behaviours of supercritical CO₂ in a large vertical tube. *Int J Heat Mass Transf* 147:118944
6. Cheng H, Zhao J, Rowinski MK (2017) Study on two wall temperature peaks of supercritical fluid mixed convective heat transfer in circular tubes. *Int J Heat Mass Transf* 113:257–267
7. Yang J, Oka Y, Ishiwatari Y, Liu J, Yoo J (2007) Numerical investigation of heat transfer in upward flows of supercritical water in circular tubes and tight fuel rod bundles. *Nucl Eng Des* 237(4):420–430
8. He S, Kim W, Bae W (2008) Assessment of performance of turbulence models in predicting supercritical pressure heat transfer in a vertical tube. *Int J Heat Mass Transf* 51(19–20):4659–4675
9. Du Z, Lin W, Gu A (2010) Numerical investigation of cooling heat transfer to supercritical CO₂ in a horizontal circular tube. *J Supercrit Fluids* 55(1):116–121
10. Yang Z, Chen W, Chyu MK (2018) Numerical study on the heat transfer enhancement of supercritical CO₂ in vertical ribbed tubes. *Appl Thermal Eng* 145:705–715

11. Li C, Hao J, Wang X, Ge Z, Du X (2022) Dual-effect evaluation of heat transfer deterioration of supercritical carbon dioxide in variable cross-section horizontal tubes under heating conditions. *Int J Heat Mass Transf* 183:122103
12. Liu S, Huang Y, Liu G, Wang J, Leung LK (2017) Improvement of buoyancy and acceleration parameters for forced and mixed convective heat transfer to supercritical fluids flowing in vertical tubes. *Int J Heat Mass Transf* 106:1144–1156
13. Liu SH, Huang YP, Wang JF, Leung LK (2018) Numerical investigation of buoyancy effect on heat transfer to carbon dioxide flow in a tube at supercritical pressures. *Int J Heat Mass Transf* 117:595–606

A Numerical Study on the Combined Effect of Y-Shaped Fin and Alumina Nanoparticles on PCM Solidification



S. Abhinand, Amrita Sharma, and Hardik Kothadia

1 Introduction

Nearly 50% of the world's energy is being consumed for space heating and cooling requirements, accounting for 33% of the emission of greenhouse gases because of energy production through conventional methods. In this regard, the thermal energy storage system holds a remarkable role in maximizing the storage capacity of renewable energy sources like wind and solar. These systems are more advantageous when phase change material is incorporated into them, as PCM has a relatively high volumetric storage capability. This feature of PCM helps to make the system compact. The selection of PCM depends on the desired phase change temperature, provided no supercooling and thermal stability over several runs. Most of the PMCs have a low value of thermal conductivity, which can weaken the heat transfer rate and increase the phase-changing duration. In this regard, various improvement techniques have been incorporated in the past. Such as installing extended fin surfaces, adding metal matrix, micro-encapsulation, and multiple layers of PCM and nanoparticle-enhanced PCM.

2 Literature Review and Objective

Sheikholeslami [1] studied charging and discharging in a triplex pipe with the inclusion of triangular fin and copper oxide (CuO) nanoparticles. RT35 is the phase change material (PCM) candidate selected for this study, and water flows as HTF in the interior and exterior parts of the pipe. The results from the numerical study show that triangular fin incorporation and nanoparticle addition accelerate the solidification rate

S. Abhinand · A. Sharma · H. Kothadia (✉)
Department of Mechanical Engineering, IIT Jodhpur, Jodhpur 342030, India
e-mail: hardikothadia@iitj.ac.in

by 40.75 and 44.88%, respectively. It was also found that as nanoparticle concentration in the PCM increases, melting time decreases. Alizadeh [2] numerically found the impact of Y-shaped fins and nanoparticle inclusion in the solidification of PCM inside a triplex storage pipe. Water is selected as the PCM, fins are made of copper particles, and single-walled carbon nanotubes (SWCNT) are chosen as nanoparticle for the study. Initially, the RSM optimization technique finds the optimum configuration of the Y-shaped fin, and the most optimal fin structure for minimum solidification time is chosen for the simulations. Simulations are performed employing the standard Galerkin finite element method (SGFEM). The study concluded that fin incorporation is more effective in improving the solidification rate as compared to mixing nanoparticles in the PCM. Sharma et al. demonstrated the longitudinal fin number effect [3]. Trung [4] presented discharging process of PCM with Al_2O_3 nanoparticle addition and inclusion of Y-shaped fins. Newton–Raphson method and finite element technique were used to display the discharging phenomena of nanoparticle-enhanced phase change material (NEPCM). The study results found that NEPCM accelerates solidification due to increased thermal diffusion. Hajizadeh [5] modelled the solidification of paraffin embedded with CuO nanopowders on a wavy channel. The channel had paraffin in the outer duct, and the air was made to flow through the inner portion. The output from the study shows that wavy duct is more efficient in discharging process than a straight duct. Nanoparticle inclusion also leads to a lowering of discharging time. Keshteli [6] simulated freezing and melting phenomena in a triplex pipe system with RT82 as PCM within the interior of the triplex tube, water flowing the inside and outside of the tube. Al_2O_3 nanoparticles were added to the PCM, and the geometrical and other influencing parameters were studied. The addition of Al_2O_3 to the system leads to improved thermal conductivity and reduced time for both solidification and melting processes, and the same improvement occurs when fin addition is done in the system. Elbahjaoui [7] used rectangular storage system filled with n-octadecane to study solidification process and the effects of adding copper nanoparticles on the solidification process. Enthalpy porosity method was employed to find the freezing process numerically, and a correlation to find the solidification time based on control parameters such as aspect ratio, HTF inlet temperature, and nanoparticle volume fraction was presented. Khodadadi [8] dispersed nanoparticles in base PCM material to improve the functionality and thermal conductivity of the PCM. It was found that NEPCM has a much improved heat transfer rate as compared to base PCM.

NEPCM has greater potential to unlock high heat transfer characteristics of PCM-based storage systems and is a promising method to enhance thermal characteristics of the systems, thereby reducing the energy supply–demand gap in the future where energy demand is rapidly accelerating. The main objective of the presented paper is to examine the effects of different volume fractions of nanoparticles with Y-shaped fins on PCM solidification. The flow behaviour of the PCM is examined, and the importance of natural convection and effective region of nanoparticles in the solidification process are shown by the model based on finite volume discretization.

3 Problem Statement

An investigation on the addition of alumina nanoparticles on the discharge process of RT82 PCM is numerically done. The system is incorporated with Y-shaped fins, so that heat exchange between HTF and PCM is improved, and a minimum solidification time for the discharging process can be achieved. The impact of alumina nanoparticles and Y-shaped fin is quantitatively presented by simulating different volume fraction ratios of the nanoparticle, which are 0, 3, and 7% and comparing the minimum solidification time and liquid fraction at different time steps for each case. Figure 1 illustrates the two-dimensional domain simulated. The thermal storage system is concentric with inner diameter of 50 mm and an outer diameter of 150.8 mm. The Y-shaped fins have a base length of 19.35 and 12 mm for the branching with a thickness equal to 2 mm. The HTF fluid flows in the interior tube. The thermal energy storage system wall incorporated with fin has the same temperature as that of the HTF fluid flowing as a lumped body assumption is taken into account in the study. By this, the wall is made of a highly conducting material, copper. Thus, an isothermal condition can be applied to the wall with wall temperature equal to HTF temperature. The thermo-physical property values of RT82 PCM and alumina nanoparticle are given in Table 1.

The initial temperature of the thermal storage system is kept at 366 K, which is well above the liquidus temperature of PCM, and hence initially, the PCM is in a fully liquid state. The boundary conditions of the inner HTF tube are given a temperature of 338 K, and as the flow occurs, the transition from liquid to solid state of PCM

Fig. 1 Two-dimensional simulated domain

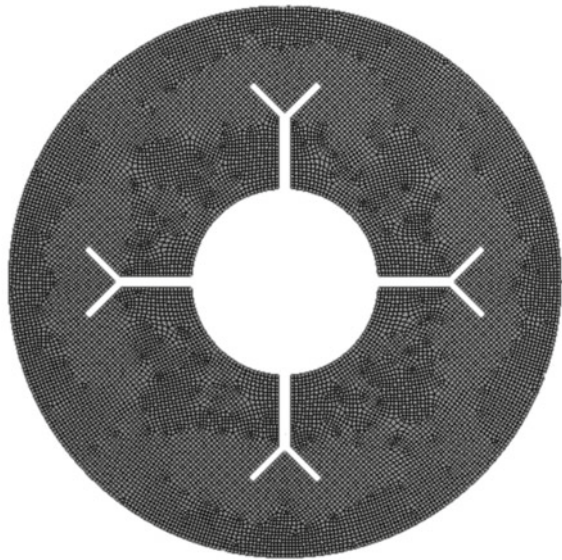


Table 1 Thermo-physical properties of the fluids

Properties/Units	RT82	Al ₂ O ₃
Density (kg/m ³)	770	3600
Specific heat (kJ/kg K)	2	0.765
Thermal conductivity (W/m K)	0.2	36
Dynamic viscosity (N s/m ²)	0.03499	–
Latent heat (kJ/kg)	176	–
Solidus temperature (K)	350	–
Liquids temperature (K)	358	–

occurs. A fully solidified PCM region is produced after an amount of energy equal to the latent heat of fusion of the PCM is discharged.

3.1 Governing Equations

As the flow of HTF in the system occurs, heat exchange happens between the PCM and HTF. The stored energy of PCM is discharged to the low-temperature HTF, and thus, solidification phenomena of the PCM occur. The equations governing the process are as follows:

$$\nabla \cdot V = 0 \tag{1}$$

$$\frac{\partial V}{\partial t} + V \cdot \nabla V = \frac{A_{mush}(1 - \gamma)^2}{\gamma^3 + 0.001} u_i + \frac{1}{\rho} (-\nabla P + \rho g \beta (T - T_{ref}) + \mu \nabla^2 V) \tag{2}$$

$$\frac{\partial H}{\partial t} + \nabla \cdot (VH) = \nabla \cdot \left(\frac{k}{\rho C_p} \nabla h \right) \tag{3}$$

During the freezing process, the liquid fraction of PCM ranges from 0 to 1, where 0 means a solid region and 1 indicates a fully liquified region. The intermediate value of liquid fraction is taken as the mushy zone, considered a porous medium for numerical modelling. The liquid fraction, γ , is given by:

$$\gamma = \begin{cases} \frac{T_s - T}{T_s - T_l} & T_s < T < T_l (\text{mushy zone}) \\ 0 & T < T_s (\text{solid}) \\ 1 & T < T_l (\text{liquid region}) \end{cases} \tag{4}$$

To model nanoparticle-enhanced PCM model, the fluid is considered as a homogeneous mixture with effective properties. The properties of nanoparticle-enhanced PCM are defined as:

$$\rho_{npcm} = \varphi\rho_{np} + (1 - \varphi)\rho_{pcm} \tag{5}$$

$$(\rho C_p)_{npcm} = \varphi(\rho C_p)_{np} + (1 - \varphi)(\rho C_p)_{pcm} \tag{6}$$

$$(\rho L)_{npcm} = (1 - \varphi)(\rho L)_{pcm} \tag{7}$$

$$(\rho\beta)_{npcm} = \varphi(\rho\beta)_{np} + (1 - \varphi)(\rho\beta)_{pcm} \tag{8}$$

Here, φ is the volume fraction of nanoparticle, and ρ , C_p , L , and β denote density, specific heat, melting heat, and thermal expansion coefficient, respectively. Subscript np refers to nanoparticle, $npcm$ indicates nano-PCM, and pcm refers base PCM. The thermal conductivity and dynamic viscosity of the NPCM are given by:

$$k_{npcm} = \frac{k_{np} + 2k_{pcm} - 2(k_{pcm} - k_{np})\varphi}{k_{np} + 2k_{pcm} + (k_{pcm} - k_{np})\varphi} k_{pcm} + 5 \times 10^4 \beta_k \varphi \rho_{pcm} C_{p,pcm} \sqrt{\frac{BT}{\rho_{np} d_{np}}} f(T, \varphi) \tag{9}$$

$$\beta_k = 8.4407(100\varphi)^{-1.07304} \tag{10}$$

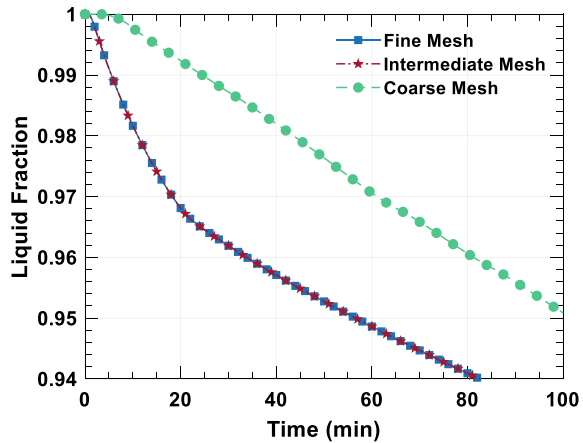
$$\mu_{npcm} = 0.983e^{12.959\varphi} \mu_{pcm} \tag{11}$$

Here, B is the Boltzmann constant, and the function in conductivity equation is given by:

$$f(T, \varphi) = (2.8217 \times 10^{-2} \varphi + 3.917 \times 10^{-3}) \frac{T}{T_{ref}} + (-3.0669 \times 10^{-2} \varphi - 3.91123 \times 10^{-3}) \tag{12}$$

Simulations were performed on commercially available ANSYS FLUENT 19R2, and the method employed to solve the solidification problem was based on enthalpy porosity, in which the mushy zone is considered as a porous medium having liquid fraction as the porosity value. Finite volume method is employed by FLUENT to discretize the system with SIMPLE and QUICK scheme applied. For correcting pressure equations, PRESTO method is employed. Gradient terms were calculated using the Green–Gauss cell method. The simulations were checked at each stage to ensure convergence of the governing equations.

Fig. 2 Grid independency test



3.2 Grid Independency Test

To study grid convergence, three meshes of grid sizes 0.5, 1, and 3 mm corresponding to fine, intermediate, and coarse were generated. ANSYS meshing software was used to mesh the geometries, and mesh factors such as aspect ratio, orthogonality, and skewness were kept well under the optimal value to get better results. Liquid fraction was plotted against flow time for three meshes generated, and the grid convergence was verified as shown in Fig. 2. From the liquid fraction plot of three simulations, it can be seen that coarse grid size deviates from the trend by a large value. Meanwhile, intermediate and fine mesh sizes have a very minimal deviation from each other, and they follow the same trend line in the plot. The average error between liquid fraction results obtained from intermediate and fine cases was found to be less than 1%. Hence, intermediate size with a 0.5 s time step was selected for the entire study.

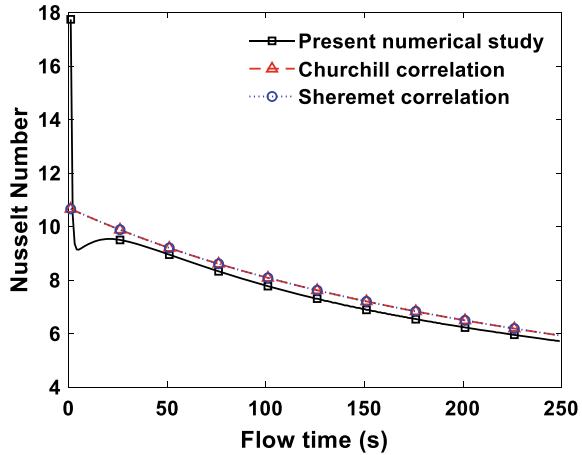
4 Results and Discussion

Impact of incorporating Y-shaped fins and varying the volume fraction of alumina nanoparticles on the discharging process are presented in this section. Also, the computational model is validated with an existing correlation to justify the computation powers.

4.1 Validation

Empirical correlations to find mean Nusselt number value of natural convection flow around circular cylinder presented by Churchill [9] and Sheremet [10] are used to

Fig. 3 Validation of the present computation powers with existing correlations for the Nusselt number



validate the numerical model used, and the correlations are as follows:

$$Nu = 0.36 + 0.518 \left[Ra / \left(1 + 1 + \left(\frac{0.559}{Pr} \right)^{\frac{9}{16}} \right)^{\frac{16}{9}} \right]^{1/4} \tag{13}$$

$$Nu = 0.34Ra^{0.265} \tag{14}$$

The Nusselt number was plotted against time employing the present numerical model and compared with the correlations presented above. The combined plot is presented in Fig. 3. The average error of the Nusselt number value obtained by present simulation and that of correlation was found to be below 5%, and thus, the present numerical model is validated.

4.2 Impact of Y-Shaped Fins and Nanofluid on Discharging Process

The impact of varying volume fraction of nanoparticle in the PCM on the solidification process was simulated by using RT82 as PCM and alumina as nanoparticle. Y-shaped fin is incorporated in the thermal storage system to improve the discharging process. The inner HTF tube is given a temperature of 338 K, and all other boundaries are given adiabatic conditions. The PCM domain is initially given a temperature of 366 K. The volume fraction of nanoparticles in PCM was varied as 0, 3, and 7% to find the effect of increasing nanoparticle concentration in the PCM with the fin. The HTF and PCM interface of the thermal energy storage system was given isothermal

boundary conditions. As low-temperature HTF passes through the system, the solidification of PCM takes place, and the initial liquid PCM system is converted to solid.

As low-temperature HTF passes through the system, the solidification of PCM takes place, and the initial liquid PCM system is converted to solid. This process is governed mainly by conduction and natural convection process. Natural convection is the initial dominating heat transfer mode. As solidified PCM starts accumulating in the HTF tube walls, the conduction process also comes into account. The contours of discharging process for Y-shaped fin-assisted domain under 0, 3, and 7% nanoparticles at different time steps of 500, 10,000, 20,000, and 25,000 s are shown in Fig. 4. The amount of solidified PCM, interface growth, the impact of fin, and temperature distribution in the thermal storage system can be visualized from the contours. The case has a higher region of blue indicating higher solidified PCM and thus is more effective in enhancing the solidification process. The temperature contour on the right half side also follows the same trend as the liquid fraction contour. The lower temperature implies more effective freezing process for the system.

At any given time step, it can be seen that a nanoparticle concentration of 7% gives the highest amount of solidified mass of PCM. Also, the blue region in the temperature contour corresponds to a value of lower temperature. The transition from red to blue in the temperature plot is also greater for 7% of nanoparticle cases, justifying that it is the most optimal case amongst the three cases to achieve enhanced heat transfer performance of the thermal storage system. Also, Y-shaped fins also have an impact on the solidification process. As Y-shaped fin is incorporated, a greater surface area of the PCM is in contact with the HTF tube compared to without a fin case. Thus, the cooling characteristics of the thermal storage system are improved.

The temporal variation of liquid fraction and mean temperature of the thermal storage system during the discharging phenomena are depicted in Figs. 5 and 6, respectively. The liquid fraction is essential in quantifying the thermal discharge process as it defines how much solid is converted to liquid at a particular time. Also, the mean temperature of the thermal storage system during the discharge phenomena represents the quantity of PCM which has undergone phase change as lower average temperature implies more mass of PCM converted from liquid to solid phase. The graph shows that with 7% nanoparticle concentration is highest with 27,195.9 s for complete solidification. Whilst with no nanoparticle, it takes the highest time of 35,620.8 s to complete conversion of liquid PCM to solid PCM. The case of 3% nanofluid takes 31,292.6 s to complete full solidification, thus justifying the trend. It can also be seen from the graph that at the initial stage of the freezing process, all the graphs follow the same trend and values, which indicates that the nanoparticle enhancement is effective in the later stages of discharge process or when conduction mode of heat transfer becomes dominant than natural convection.

Nanoparticles have a high value of specific heat, thermal conductivity, and viscosity; thus, the addition of nanoparticles to base PCM results in the creation of nano-PCM with enhanced thermal properties. The viscosity increase may hinder thermal performance as it reduces the velocity gradient and affects the movement of the PCM in the liquid state, but this reduction surpassed by the greater increase

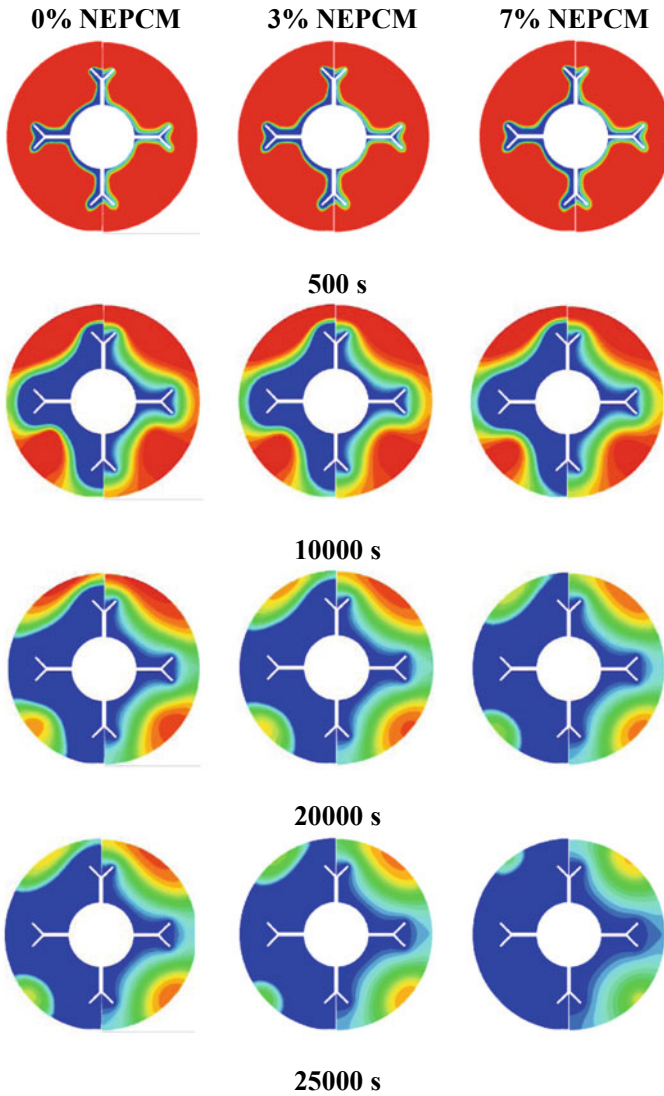


Fig. 4 Liquid fraction (left) and temperature (right) contours at different time steps under different volume fractions of nanoparticles in PCM

in thermal conductivity value. The time for complete solidification for all cases simulated is pictorially shown in Fig. 7.

Fig. 5 Liquid fraction profiles under different volume fractions of alumina nanoparticles in PCM with Y-shaped fins

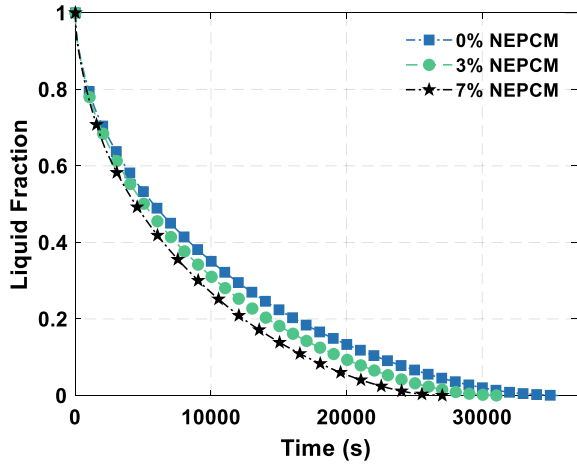


Fig. 6 Average temperature under different volume fractions of alumina nanoparticles in PCM with Y-shaped fins

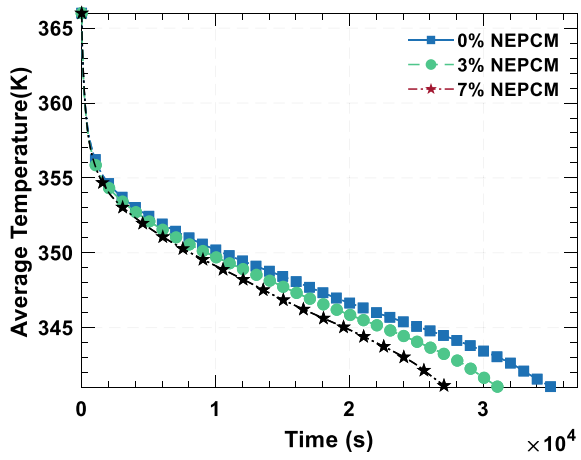
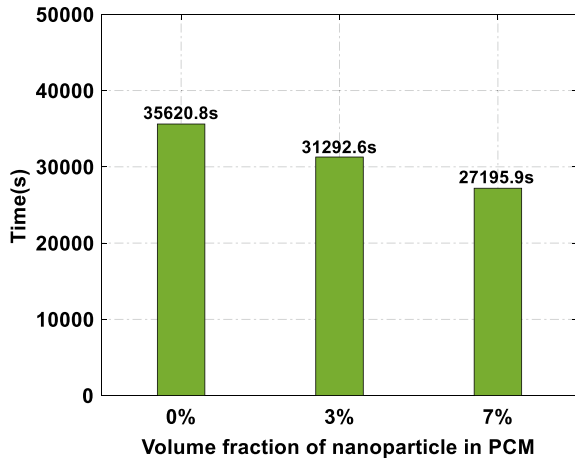


Fig. 7 Time taken for complete solidification for different amounts of nanoparticle volume fraction in PCM



5 Conclusion

In the present work, a 2D transient numerical simulations were performed to study the flow and thermal behaviour of discharging process of nanoparticle-enhanced PCM in a Y-shaped fin-aided thermal storage system. The impact of dispersing alumina on the solidification of RT82 PCM was computationally modelled and validated with standard correlations. The PCM storage system was isothermally cooled from the interior HTF tube, and Y-shaped fins were incorporated to the interior of the HTF tube to enhance the solidification rate. Simulation results conclude that better heat transfer and flow performance of RT82 are present when alumina particles are dispersed in the base PCM. Increasing the amount of volume fraction of nanoparticles in the base PCM leads to decrease in the time taken by the system for complete solidification. Thus, nanoparticles can be effectively used to improve the heat transfer performance of a thermal storage system and save time in discharging process applications. The simulation results also show that the impact of adding nanoparticles is profound in the later stages of freezing or when the conduction mode of heat transfer comes into play as the solidified layer of PCM settles at the HTF tube, and the convection process slows down. Thus, it can also be concluded that nanoparticle addition is an effective way to improve the thermal conductivity of PCM whose base thermal conductivity value is comparatively less, which acts as a disadvantage for the heat transfer processes in the PCM.

Nomenclature

A_{mush} Mushy zone constant
 B Boltzmann constant [J/K]

C_p	Specific heat [kJ/kg K]
d_{np}	Diameter of nanoparticle [mm]
g	Gravity due to acceleration [m/s^2]
H	Enthalpy [J/kg]
<i>HTF</i>	Heat transfer fluid
k	Thermal conductivity [W/ m K]
L	Latent heat [J/kg]
l	Liquid
np	Nanoparticle
$npcm$	Nanoparticle-enhanced PCM
Nu	Nusselt number
P	Pressure [Pa]
<i>PCM</i>	Phase change material
Pr	Prandtl number
Ra	Rayleigh number
s	Solid
T	Temperature [K]
V	Velocity components [m/s]
ρ	Density [kg/m^3]
β	Thermal expansion coefficient [K^{-1}]
μ	Dynamic viscosity [Pa s]
γ	Liquid fraction
φ	Nanoparticle volume fraction

References

1. Sheikholeslami M, Keshteli AN, Shafee A (2020) Melting and solidification within an energy storage unit with triangular fin and CuO nanoparticles. *J Energy Storage* 32:101716
2. Alizadeh M, Pahlavani MH, Tohidi M, Ganji DD (2020) Solidification expedition of phase change material in a triplex-tube storage unit via novel fins and SWCNT nanoparticles. *J Energy Storage* 28:101188
3. Sharma A, Parth P, Shobhana S, Bobin M, Hardik BK (2022) Numerical study of ice freezing process on fin aided thermal energy storage system. *Int Commun Heat Mass Transf* 130:105792
4. Nguyen-Thoi T, Bhatti M, Ali JA, Hamad SM, Sheikholeslami M, Shafee A, Rul H (2019) Analysis on the heat storage unit through a Y-shaped fin for solidification of NEPCM. *J Mol Liq* 292:111378
5. Hajizadeh MR, Selimefendigil F, Muhammad T, Ramzan M, Babazadeh H, Li Z (2020) Solidification of PCM with nano powders inside a heat exchanger. *J Mol Liq* 306:112892
6. Keshteli AN, Sheikholeslami M (2020) Influence of Al₂O₃ nanoparticle and Y-shaped fins on melting and solidification of paraffin. *J Mol Liq* 314:113798
7. Elbahjaoui R, El Qarnia H (2017) Thermal analysis of nanoparticle-enhanced phase change material solidification in a rectangular latent heat storage unit including natural convection. *Energy Build* 153:1–17
8. Khodadadi JM, Hosseinizadeh SF (2007) Nanoparticle-enhanced phase change materials (NEPCM) with great potential for improved thermal energy storage. *Int Commun Heat Mass Transf* 34:534–543

9. Churchill SW, Chu HHS (1975) Correlating equations for laminar and turbulent free convection from a horizontal cylinder. *Int J Heat Mass Transf* 18:1049–1053
10. Sheremet MA (2012) Laminar natural convection in an inclined cylindrical enclosure having finite thickness walls. *Int J Heat Mass Transf* 55:3582–3600

Effect of Interruption on a Shrouded Fin Heat Sink: A Numerical Study



Rahul Ray, Arovinda Mohanty, and Pandab Patro

1 Introduction

Nowadays, performance of electronic components increases rapidly and their functioning generates unwanted heat. This unwanted heat leads to break down their operation and also reduces their performance and operational life. This unwanted heat should be extracted from the electronic components for better performance. It can be possible by installing heat sink on the heated surface. Active or passive cooling heat sinks are preferred for heat removal from the surface [1]. Both cooling methods gained popularity as per their usage. Active cooling needs external force to drive fluid flow, which extracts more heat than passive cooling, but it also gets popularity due to its easy installation and operation. It extracts heat from heated surface by conduction and dissipates heat to the surrounding by convection through its surface area, so surface area and its geometry play important role to dissipate heat. Therefore, heat sink becomes popular amongst the researchers, and they are giving continuous effort to increase the heat sink surface area and reduce the manufacturing cost.

R. Ray (✉) · A. Mohanty · P. Patro
Department of Mechanical Engineering, Veer Surendra Sai University of Technology Burla,
Odisha 768018, India
e-mail: rahulray.mu01@gmail.com

A. Mohanty
e-mail: amohanty_me@gmail.com

P. Patro
e-mail: ppatro_me@vssut.ac.in

2 Literature Review and Objective

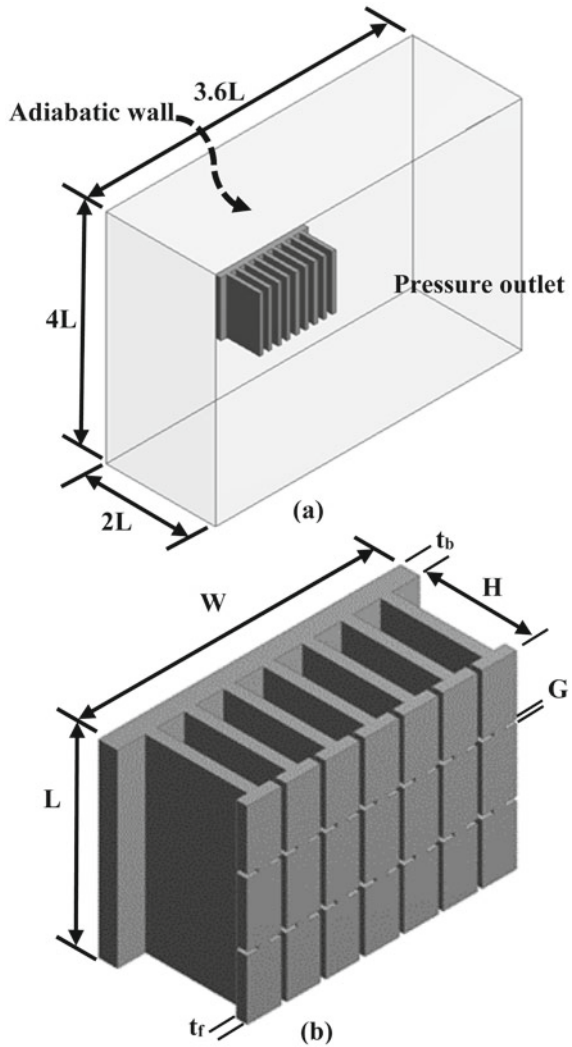
Several studies have done by various researchers on the heat sink design; few of those discussed here. Baskaya et al. [2] investigated the conventional (continuous plate fin) heat sink mounted on the horizontal base plate. They found that overall heat transfer rate depends on the various parameters, i.e., fin spacing, fin height, and surrounding temperature. Tari et al. [3] studied rectangular plate fin heat sinks mounted on horizontal and slightly inclined base plate and developed a correlation which covers all inclined angles. Yazicioğlu et al. [4] investigated the rectangular plate fin heat sink mounted on vertical base plate and found the optimum fin spacing between 6.1 and 11.9 mm. They also found the maximum heat transfer occurs on the vertical base plate. Branched fin heat sinks studied by various researchers and found to dissipate heat transfer than conventional rectangular plate fin heat sinks [5–7]. Branched and interrupted fins on vertical base plate increase surface area and enhance the overall heat transfer rate [8, 9]. Karlapalem et al. [10] investigated the perforated branched fins and found maximum heat transfer rate with vertical base.

3 Problem Descriptions

The present simulation deals with numerical simulation for the effect of interruptions on secondary branched fins (shrouded fins) mounted on vertical base. The dimensions of the schematic diagram of computational domain and proposed heat sink base plate are $4L \times 3.6L \times 2L$ and $L \times 1.6L \times 0.1L$ with fin height and thickness that are 30 and 3 mm, respectively (Fig. 1a). The domain base is considered as adiabatic wall, attached to the fin base, and rest of the surfaces are considered as pressure outlets. Ahmadi et al. [8] and Ray et al. [9] studied conventional plate fin heat sink, branched and interrupted heat sink, and interrupted secondary branched fin. Secondary branched fin on primary branched rectangular plate fin heat sinks has been considered to investigate the effect of interruption of the secondary branched fins on the overall thermal performance. The objective of this study is to identify the optimum number of interruption on secondary branched fins.

Figure 1 shows the conventional (rectangular plate fin) heat sink, and its physics is well defined in the literature. Figure 2 shows four different proposed heat sinks. On the secondary branched fin (case III), number of interruptions (i.e., 1, 2, 3, 4, 5) imposed on the secondary branched fins are shown in Fig. 2. The objective of this study is to calculate heat transfer rate and Nusselt number on the above proposed heat sinks and compare it with the conventional heat sink. The ambient temperature is considered 300 K and ΔT (temperature difference between surrounding and base plate) varied 10–60 °C.

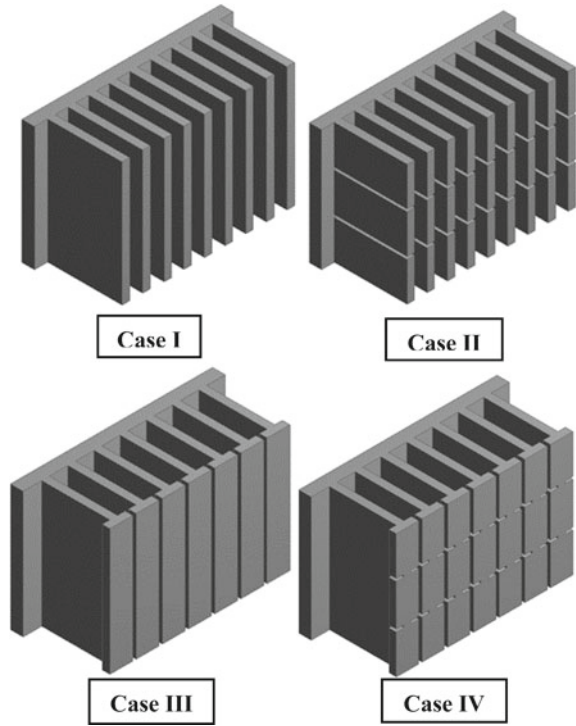
Fig. 1 a Schematic diagram of the computational domain and b detailed diagram of the novel heat sink



4 Mathematical Modelling

Suitable boundary conditions and governing equations have taken to solve three-dimensional numerical model. This computational study is performed within the Rayleigh number ranges from $1.1 \times 10^5 \leq Ra \leq 6.1 \times 10^5$. For this simulation, laminar incompressible flow and steady-state flow condition have been considered. Heat transfer through radiation is negligible also considered.

Fig. 2 Schematic diagram of all fin configurations



To solve all governing equations, the algebraic equation multi-grid solver is used in the ANSYS Fluent 15. The following equations can be expressed for steady flow conditions with incompressible fluid (air):

5 Continuity Equation:

$$\frac{\partial u}{\partial x} + \frac{\partial v}{\partial y} + \frac{\partial w}{\partial z} = 0 \tag{1}$$

6 Momentum Equations:

$$\rho \left(u \frac{\partial u}{\partial x} + v \frac{\partial v}{\partial y} + w \frac{\partial w}{\partial z} \right) = -\frac{\partial p}{\partial x} + \mu \nabla^2 u \tag{2}$$

$$\rho \left(u \frac{\partial u}{\partial x} + v \frac{\partial v}{\partial y} + w \frac{\partial w}{\partial z} \right) = -\frac{\partial p}{\partial y} + \mu \nabla^2 v - \beta g(T - T_\infty) \tag{3}$$

$$\rho \left(u \frac{\partial u}{\partial x} + v \frac{\partial v}{\partial y} + w \frac{\partial w}{\partial z} \right) = -\frac{\partial p}{\partial z} + \mu \nabla^2 w \quad (4)$$

Energy equation:

$$\rho C_p \left(u \frac{\partial T}{\partial x} + v \frac{\partial T}{\partial y} + w \frac{\partial T}{\partial z} \right) = k \left(u \frac{\partial^2 T}{\partial x^2} + v \frac{\partial^2 T}{\partial y^2} + w \frac{\partial^2 T}{\partial z^2} \right) \quad (5)$$

Boundary conditions:

To solve governing equations, following boundary conditions are used:

- Constant base plate temperature should be maintained, i.e., $T = T_w$.
- The domain wall should be insulated or adiabatic, on which base plate mounted, i.e., $\frac{\partial T}{\partial n} = 0$.
- The walls should be in no-slip and no-penetration condition, i.e., $v_t = 0$ and $v_n = 0$.
- The coupled condition should be used to maintain flux and temperature constant, i.e., $(K_s \frac{\partial T_s}{\partial n})_{interface} = (K_f \frac{\partial T_f}{\partial n})_{interface}$ and $T_s = T_f$.
- Pressure outlet boundary condition is selected for the outer domain, where $T = T_\infty$ and $p = P_{atm}$.
- The mean value of the base plate temperature and surrounding temperature was utilized to compute all of the thermo-physical properties used in this simulation. There is a temperature difference between inside and outside. As a result, the film temperature can be expressed as $T_{film} = \frac{1}{2}(T_{base} + T_\infty)$.

The equation is used to calculate the following:

$h = \frac{Q}{A(T_{base} - T_\infty)}$, where Q is the heat transferred from the heat sink to the surrounding, which is computed during simulation.

The average value of Nusselt number for the heat sink has been defined as, $Nu = \frac{hL}{k}$.

7 Numerical Methodology

7.1 Computational Model

In this simulation, a finite volume approach is used. Over each control volume, the differential equations are discretized to generate a set of algebraic equations. To discretize the diffusion and pressure terms, governing equations used the central difference scheme and body force weighted scheme, respectively. To ensure convergence of convective terms, the first-order upwind method is utilized at the start of the iteration. To increase accuracy in the solution, the second-order upwind approach

Table 1 Under-relaxation factors

Pressure	Density	Body forces	Momentum	Energy
0.35	0.97	0.98	0.6	1.0

Table 2 Sensitivity of Nu on domain size

Domain size (in L)	1.5	2	3	4	5	6
Nu	15.04	15.19	15.27	15.318	15.324	15.325
Relative difference %	–	0.997	0.526	0.314	0.0391	0.00653

is used once convergence is reached. The SIMPLE algorithm is used to couple the velocity and pressure fields. For the continuity and momentum equations, the normalized residuals were set to 10^{-4} , whereas for the energy equation, limited at 10^{-6} . The under-relaxation factors used for this simulation are as follows (Table 1):

7.2 Domain-Independent Test and Sensitivity Test

A domain-independent analysis was conducted to determine the optimal domain size so that calculated heat transfer rate becomes domain size independent. Several domain sizes were chosen to investigate the relationship between domain size and key parameters like heat transfer. Separate simulations were carried out for each domain at the same operating conditions. When the domain size is sufficiently large enough (i.e., domain size greater than $4L$), domain reliance becomes negligible, as shown in Table 2.

7.3 Grid Independent Test and Sensitivity Test

In the mesh generation process, tetrahedral meshes were formed which are later converted to polyhedral mesh. Because heat and velocity gradients are considerably high close to the contact region of solid wall and fluid zone, fine grids are used.

The grids along the surface of the fins were made fine so that velocity and temperature gradients can be accurately captured. As near the domain boundary, the cell becomes increasingly fine-grained. Eight distinct grid sizes were used to test grid sensitivity. To better capture the thermal plumes, a coarser grid is initially used and then refined. Table 3 indicates heat dissipation rate which becomes grid independent beyond grid 3. The chosen grid for computation is grid 3 with a cell count of 11.13

Table 3 Sensitivity of Nu on grid size

Number of cells	3.61×10^5 Grid 1	6×10^5 Grid 2	11.13×10^5 Grid 3	14×10^5 Grid 4	20.45×10^5 Grid 5
Nu	15.66	15.48	15.318	15.317	15.314
Relative difference %	-1.3072	-1.1353	-1.0526	-0.0097	-0.0048

$\times 10^5$. Nusselt number and heat transfer rate have been calculated using the same method in this study for all other heat sink configurations.

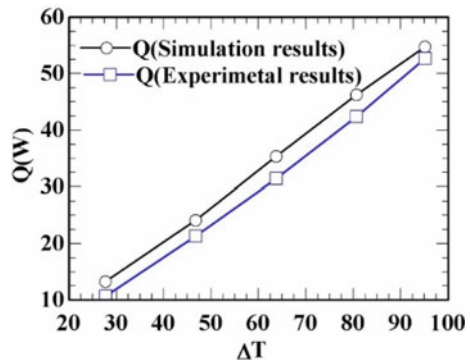
7.4 Validation of Present Simulation

Simulations employing a plate fin heat sink with similar configurations to those reported by [4] were investigated to validate the present numerical simulation. The variation of heat transfer rate with base temperature is depicted in Fig. 3. The heat transfer calculated from the simulation coincides well with Yazicioglu and Yuncu’s experimental study with a maximum error of 6.89 per cent as shown in Fig. 3.

8 Results and Discussion

The thermal behaviour of secondary branched interrupted fin heat sink studied numerically under natural convection. This study concluded the comparison of overall heat transfer rate, Nusselt number, and fin effectiveness with convectioal heat sink.

Fig. 3 Comparison of present simulation with experimental work [4]



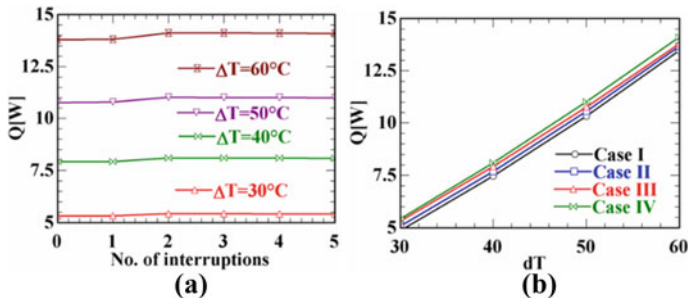


Fig. 4 Variation of overall heat transfer with number of interruptions and ΔT

8.1 Effect of Interruption of Secondary Branched Fin on Overall Heat Transfer Rate

Figure 4 shows the variation of overall heat transfer rate with number of interruptions at different temperature differences between ambient temperature and the base plate temperature, i.e., 10–60 °C, for all cases. When secondary branching placed at the extreme end of the vertical fin, i.e., case III, heat transfer rate is maximum as reported by Ray et al. [9]. When interruptions are used, the secondary branched fin, where the temperature difference between fin surface and ambient air is more, increases heat transfer rate up to the optimum number of interruptions (i.e., 2, Fig. 4a), and further interruption, decreases the surface area, which reduce the heat transfer rate. It helps to circulate more cold air to the inner surface of the heated fin and extract more heat to the surrounding. It also disturbs the flow and breaks the thermal plumes near the extreme end of the vertical fins which increase the cold air flow as shown in Figs. 6 and 7. Figure 6 shows the thermal plumes for all cases. It shows the cold air circulation is more in case IV amongst all cases and case I (conventional heat sink) circulates less. Figure 7 shows the flow velocity due to density difference. Case IV shows highest velocity amongst all cases and minimum in case I. Heat dissipation rate and Nusselt number at low ΔT are minimum and maximum at high ΔT as shown in Figs. 4a and 5a, respectively.

8.2 Effect of Interruption of Secondary Branched Fin on Nusselt Number with Number of Interruptions and ΔT .

The effect of interruptions of secondary branched fin on the Nusselt number at different ΔT is shown in Fig. 5. Figure 5a, b shows the Nusselt number gradually increases with number of interruptions and ΔT , respectively.

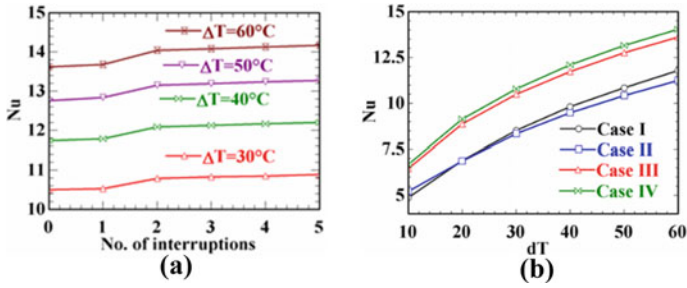


Fig. 5 Variation of Nusselt number with number of interruptions and ΔT

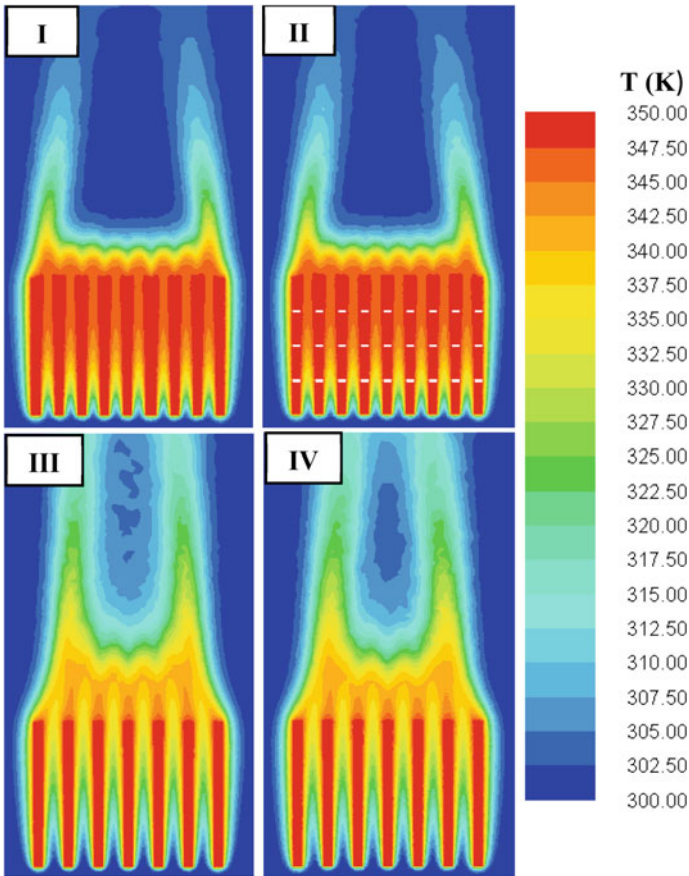


Fig. 6 Thermal plumes for all cases

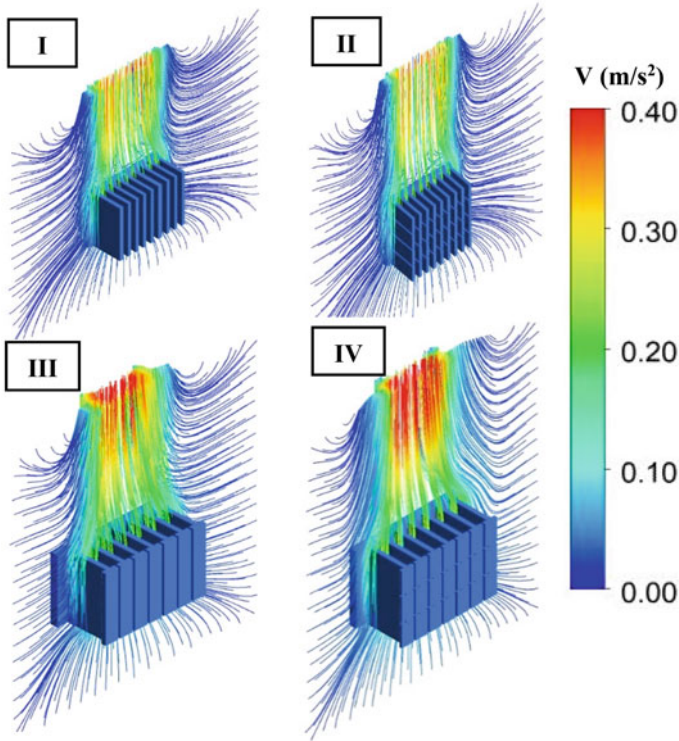


Fig. 7 Streamline velocity for all cases

9 Conclusions

In this simulation work, three-dimensional computational model was studied for four different cases of plate fin heat sinks as shown in Fig. 2.

The simulation work is in close agreement with results obtained by experiments reported in the literature, with a maximum error of 6.89%. Overall heat transfer rate and Nusselt number were evaluated with the temperature range, i.e., 10–60 °C. The following results were concluded from this investigation as follows:

- Overall heat dissipation improves as interruptions on the secondary branched fins increase and reach maximum. Further interruptions reduce the heat transfer rate.
- At lower ΔT , heat dissipation rate is low and maximum at higher ΔT .
- The overall heat transfer rate for novel heat sink, i.e., case IV, is 7.62% higher than the conventional heat sink(case I) and 4.77% higher than secondary branched fin heat sink(case III).
- Nusselt number gradually increases with number of interruptions and ΔT , respectively.

Acknowledgements We would like to appreciate Dr. Santosh kumar Senapati for his valuable suggestions.

NOMENCLATURE

A	Fin surface area[m ²]
L	Fin lengthmm
W	Fin widthmm
H	Fin heightmm
G	Interruption gap lengthmm
t_b	Base plate thicknessMm
t_f	Fin thicknessMm
x, y, z	Coordinate axes
u, v, w	Velocity components in x, y, z directions, respectivelym/s
T_s	Solid temperature at the interfaceK
T_{base}	Heat sink base temperatureK
T_{film}	Film temperatureK
T_{∞}	Ambient temperatureK
ΔT	Difference in fin base and ambient temperatureK
C_p	Specific heat capacityJ/K
k	Thermal conductivity of airW/m-K
g	Acceleration due to gravitym/s ²
P	PressureN/m ²
P_{atm}	Ambient pressureN/m ²
K_s	Thermal conductivity of the finW/m-K
K_f	Thermal conductivity of the fluidW/m-K
Nu	Average Nusselt number
B	Thermal expansion coefficient1/K
μ	Molecular viscosityKg/m-s
ρ	DensityKg/m ³
ν	Kinematic viscositym ² /s

References

1. Şevik S, Özdilli Ö (2021) Experimental and numerical analysis of the splay impact on the performance of splayed cross-cut fin heat sink. Int J Therm Sci 170
2. Baskaya S, Sivrioglu M, Ozek M (2000) Parametric study of natural convection heat transfer from horizontal rectangular fin arrays. Int J Therm Sci 39(8):797-805
3. Tari I, Mehrtash M (2013) Natural convection heat transfer from horizontal and slightly inclined plate-fin heat sinks. Appl Therm Eng 61(2):728-736
4. Yazicioğlu B, Yüncü H (2007) Optimum fin spacing of rectangular fins on a vertical base in free convection heat transfer. Heat Mass Transf und Stoffuebertragung 44(1):11-21

5. Karlapalem V, Rath S, Dash SK (2019) Orientation effects on laminar natural convection heat transfer from branching-fins. *Int J Therm Sci* 142:89–105
6. Park SJ, Jang D, Yook SJ, Lee KS (2015) Optimization of a staggered pin-fin for a radial heat sink under free convection. *Int J Heat Mass Transf* 87:184–188
7. Joo Y, Lee I, Kim SJ (2018) Efficient three-dimensional topology optimization of heat sinks in natural convection using the shape-dependent convection model. *Int J Heat Mass Transf* 127:32–40
8. Ahmadi M, Mostafavi G, Bahrami M (2014) Natural convection from rectangular interrupted fins. *Int J Therm Sci* 82(1):62–71
9. Ray R, Mohanty A, Patro P, Chandra K (2022) Performance enhancement of heat sink with branched and interrupted fins. *Int Commun Heat Mass Transf* 133:105945
10. Karlapalem V, Dash SK (2021) Design of perforated branching fins in laminar natural convection. *Int Commun Heat Mass Transf* 120:105071

Study on Melting of Beeswax Dispersed with Ferro-Nanoparticles Inside a Square Annulus Cavity Under an External Magnetic Field



Amit Kumar Ghosh and Pabitra Halder

1 Introduction

Energy is the foundation of entire globe since it satisfies all of society's needs. As the world's population grows at an exponential rate, so does the need for energy. Non-renewable resources are scarce and cannot be exploited indefinitely. The use of renewable energy resources is growing, and researchers are working to find more effective ways to use natural resources. Because some energy supplies, such as solar energy, are only available during the day, their deployment is inefficient. This is the most efficient technique to use thermal energy storage systems to improve renewable energy application performance. Latent heat thermal storage system (LHTES) is gaining attentions in the last few decades. The phase change material (PCM) has been shown to be essential for usage in LHTES, waste heat recovery systems and heat sinks. The PCM's low thermal conductivity is a significant disadvantage which can reduce the heat transfer performances. A large variety of approaches are used to improve heat transfer in PCM, like encapsulation of PCM, adopting metal matrix, using high conductivity composite of PCM, addition of nanoparticles with PCM.

A. K. Ghosh (✉) · P. Halder

Department of Aerospace Engineering and Applied Mechanics, IIST-Shibpur, Howrah 711103, India

e-mail: iamamit222@gmail.com; 2021amp002.amit@students.iiests.ac.in

P. Halder

e-mail: pabitrah@aero.iiests.ac.in

2 Literature Review and Objective

Phase change problem specially from solid to liquid started in eighteenth centuries. Jožef Stefan, a renowned scientist, studied melting of polar ice cap overtime period (1889–1891). In honour of Stefan works, Šarler [1] reported involving solid–liquid phase change or free and moving boundary problems. Different types of experimental and numerical works have been performed by different researchers. Gau and Viskanta [2] experimented and reported the effect of natural convection on heat transport and the mobility of the solid–liquid melt front in the melting and solidification of gallium. Brent et al. [3] studied numerically the melting of pure gallium using enthalpy porosity approach. Isothermal phase change has been studied under the influence of natural convection. The outcomes of numerical study are matched with experimental observation. Suspension of solid particles in the convectational PCM can improve the thermal conductivity which influence the heat transfer performances. Enhancement of thermal conductivity by introducing some micro-sized solid particles in the base fluid was first experimented by Maxwell [4]. Later, Choi and Eastman [5] proposed the addition of some nanosized solid particle in the base fluid for overcoming the sedimentation, erosion and high-pressure loss problems. The usage of nanofluid by Eastman et al. [6] was successful with very low-pressure loss and a greater rate of heat transfer due to improved thermal conductivity. Nguyen et al. [7] raised the question whether using nanofluid for heat transfer enhancement is reliable or not. From last three decades, an enormous number of researches have carried out the effect of magnetic field on electrically conducting fluid. Ghasemi et al. [8] investigated free convection in an Al_2O_3 –water nanofluid-filled square enclosure applied to a magnetic field. Kumar et al. [9] investigated cu–paraffin NePCM and reported that using a magnetic field reduced the melting rate.

The objective of the present study is to analyse the combined effect of nanoparticle volume fraction and magnetic field at different sets of thermal boundary conditions. The effect of dispersion of nanoparticles on the melting of PCM at different temperature differences is the motivation of the present study. Besides, the magnetic field effect on melting at different temperature differences is also significant parameter in this present study.

3 Problem Formulation

3.1 Physical Model

Figure 1 depicts a square annular cavity taken into consideration in the current study. Beeswax is considered as a phase change material that is contained in a square annulus. Consequently, nano-enhanced phase change material dispersion with a volume fraction of 0.5, 1, 1.5 or 2% ferro-nanoparticles is under consideration.

Table 1 summarizes the thermophysical properties of beeswax and Fe_3O_4 nanoparticles. Four sets of thermal boundary conditions are assumed in the current study. In the four different cases, inner walls are maintained higher temperature of 10, 20, 30 and 40 K above the melting temperature of beeswax. Outer walls are kept at ambient temperature (300.15 K). A constant magnetic field B_0 is subjected to the horizontal direction.

All the boundaries are electrically insulated. The effects of induced magnetic field, viscous dissipation, volume expansion during PCM melting, radiation effect and Joule heating are not considered in this study.

Fig. 1 Schematic diagram of square annulus filled with beeswax and Fe_3O_4 nanoparticles

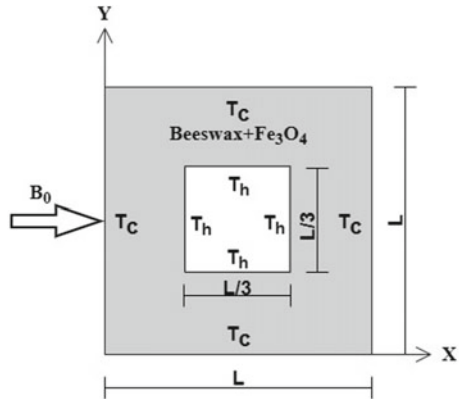


Table 1 Thermophysical properties of beeswax and Fe_3O_4

Properties	Beeswax	Fe_3O_4
Density, ρ (kg/m^3)	961	5200
Specific heat at constant pressure, C_p (J/Kg-K)	2093	670
Thermal conductivity, k (W/m-K)	0.3	6
Solidification temperature, T_S (K)	331	-
Liquefaction temperature, T_L (K)	333.6	-
Latent heat of fusion, L (J/kg)	141,490	-
Dynamic viscosity, μ (kg/m-sec)	0.02461	-
Thermal expansion coefficient, β (1/K)	0.00034	1.3×10^{-5}
Electrical conductivity, σ ($\Omega.m$) ⁻¹	2×10^{-13}	25,000

3.2 Mathematical Model

The solid–liquid phase transition process is modelled using the enthalpy porosity technique. The following are the forms of the governing equations for two-dimensional transient fluid flow and heat transfer that are numerically solved.

Continuity equation:

$$\frac{\partial u}{\partial x} + \frac{\partial v}{\partial y} = 0 \quad (1)$$

Momentum equation:

$$\rho_{npcm} \left(\frac{\partial u}{\partial t} + u \frac{\partial u}{\partial x} + v \frac{\partial u}{\partial y} \right) = \mu_{npcm} \left(\frac{\partial^2 u}{\partial x^2} + \frac{\partial^2 u}{\partial y^2} \right) - \frac{\partial P}{\partial x} + S_u \quad (2)$$

$$\rho_{npcm} \left(\frac{\partial v}{\partial t} + u \frac{\partial v}{\partial x} + v \frac{\partial v}{\partial y} \right) = \mu_{npcm} \left(\frac{\partial^2 v}{\partial x^2} + \frac{\partial^2 v}{\partial y^2} \right) - \frac{\partial P}{\partial y} + S_v \quad (3)$$

Here,

$$S_u = Au \quad (4)$$

$$S_v = Av + \rho_{npcm} g B (T - T_{npcm}) - \sigma_{npcm} B_0^2 v \quad (5)$$

$$A = -A_{mush} \frac{(1 - \delta)^2}{\delta^3 + b} \quad (6)$$

A_{mush} is the mushy zone parameter, b is computation constant, and δ is liquid fraction that can be obtained by

$$\delta = \begin{cases} 0, & T \leq T_s \\ 1, & T \geq T_L \\ \frac{T - T_s}{T_L - T_s}, & T_s < T < T_L \end{cases} \quad (7)$$

Energy equation:

$$\rho_{npcm} c_{pnpcm} \left(\frac{\partial T}{\partial t} + u \frac{\partial T}{\partial x} + v \frac{\partial T}{\partial y} \right) = k_{npcm} \left(\frac{\partial^2 T}{\partial x^2} + \frac{\partial^2 T}{\partial y^2} \right) + S_T \quad (8)$$

Here,

$$S_T = \rho \frac{\partial \Delta H}{\partial t} \quad (9)$$

Boundary conditions are given as follows:

Inner walls: $u = 0, v = 0, T = T_h$.

Outer walls: $u = 0, v = 0, T = T_c$.

σ_{npcm} and B_0 are the electrical conductivity of the NePCM and constant external magnetic field, respectively. In the present study, the magnetic field's strength is changed by varying the Hartmann number value that is defined as follows:

$$Ha = B_0 L \sqrt{\frac{\sigma}{\mu}} \quad (10)$$

The effective thermophysical properties equations of composite PCM are given as follows:

$$\rho_{npcm} = (1 - \phi)\rho_{pcm} + \phi\rho_{np} \quad (11)$$

$$(\rho C_p)_{npcm} = (1 - \phi)(\rho C_p)_{pcm} + \phi(\rho C_p)_{np} \quad (12)$$

$$(\rho\beta)_{npcm} = (1 - \phi)(\rho\beta)_{pcm} + \phi(\rho\beta)_{np} \quad (13)$$

$$(\rho L)_{npcm} = (1 - \phi)(\rho L)_{pcm} \quad (14)$$

$$k_{ff} = k_{pcm} \left[\frac{(k_{np} + 2k_{pcm}) - 2\phi(k_{pcm} - k_{np})}{(k_{np} + 2k_{pcm}) + \phi(k_{pcm} - k_{np})} \right] + 5.10^4 \rho_{pcm} \theta C_{p_{pcm}} \sqrt{\frac{K_B T_{npcm}}{\rho_{np} d_{np}}} f(T, \theta) \quad (15)$$

Here, K_B is Boltzmann constant of value 1.38×10^{-23} and d_{np} nanoparticle diameter of 47 nm. $f(T, \theta)$ is a correction factor which is defined as follows:

$$f(T, \theta) = (2.8217 \times 10^{-2}\theta + 3.917 \times 10^{-3}) \frac{T_{npcm}}{T_{ref}} + (-3.0669 \times 10^{-2}\theta - 3.91123 \times 10^{-3}) \quad (16)$$

Dynamic viscosity of composite can be calculated by

$$\mu_{npcm} = 0.983e^{(12.958\phi)} \cdot \mu_{pcm} \quad (17)$$

Electrical conductivity of composite can be calculated by

$$\frac{\sigma_{npcm}}{\sigma_{pcm}} = 1 + \frac{3\left(\frac{\sigma_{np}}{\sigma_{pcm}} - 1\right)\phi}{\left(\frac{\sigma_{np}}{\sigma_{pcm}} + 2\right) - \left(\frac{\sigma_{np}}{\sigma_{pcm}} - 1\right)\phi} \quad (18)$$

4 Numerical Methodology and Grid Independence Test

The coupled nonlinear equation and the aforementioned boundary conditions are numerically solved using finite volume method commercial package ANSYS Fluent. SIMPLE algorithm is used to couple pressure and velocity. Power law is applied for the spatially discretization of momentum and energy equation. The time step is 0.1 for the time component of the unsteady governing equation. Pressure, momentum and energy each have under-relaxation factors fixed at 0.3, 0.7 and 1, respectively. Criteria for convergence of continuity, momentum and energy are considered as 10^{-3} , 10^{-3} , 10^{-6} , respectively. Mushy zone parameter for solidification and melting is set as default value of 10^5 . A grid independence test is performed considering different number of elements of 6480, 8262, 10,764, 14,400. Melt fraction has been calculated at different cases. It is observed that there is no significant change of melt fraction after 10,764 element numbers, so the number of elements in the current study is fixed at 10,764.

5 Validation

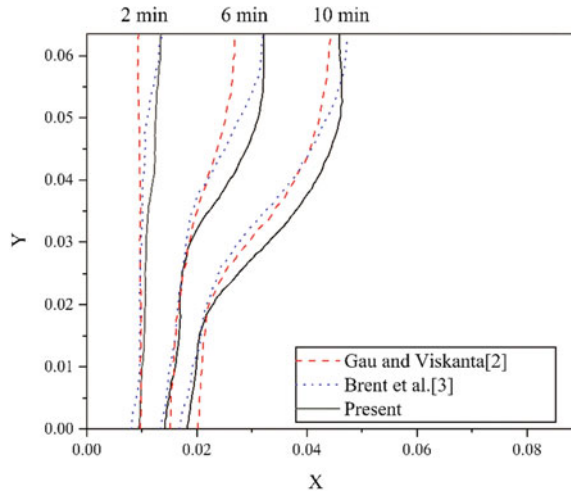
5.1 Validation of Phase Change Model

The first verification study is performed to check the reliability of the present phase change model. An experimental investigation on the melting and solidification of gallium was performed by Gau and Viskanta [2]. The study was conducted in a rectangular enclosure of 8.89×6.35 cm size. The left and right walls of the enclosure are maintained at isothermal conditions of 38 and 28.3 °C, respectively, whilst the top and bottom walls are maintained at adiabatic conditions. The melt front at different times elapsed is reported. Brent et al. [3] performed a numerical study adopting the enthalpy porosity method to compare the results reported by Gau and Viskanta [2]. In the present study, the same flow domain and boundary conditions are replicated to validate the phase change model. Figure 2 illustrates the comparison of the melt front at 2 min, 6 min and 10 min time instances of experimental, numerical and present study. The study results exhibit good agreement with the previously published results. This validation model may now be used to expand the current problem.

5.2 Validation of MHD Model

The present mathematical model includes an additional source term for the external magnetic field in the momentum conservation equation. Consequently, a second verification confirms the correctness of the solution to the free convective heat transfer problem using nanofluid underneath the effect of an external magnetic field. The

Fig. 2 Comparison of melt front at different time instances of melting of gallium in a rectangular enclosure



comparison of isotherms and stream function of the present study with Ghasemi et al. [8] for Rayleigh number, $Ra = 10^5$, and volume fraction of nanoparticles, $\phi = 0.03$, is shown in Fig. 3.

Ghasemi et al. [8] present

6 Results and Discussion

6.1 Effect of Nanoparticles Volume Fraction on Melt Fraction

Figure 4 illustrates the temporal variation of melt fraction at different nanoparticles volume fraction. There are four different cases based on temperature difference that has been represented. From Fig. 4a at $\Delta T = 10$ K, it is observed that melt fraction enhances with nanoparticles volume fraction.

When temperature difference increases, a contradictory observation has been found. Figure 4b, c at $\Delta T = 20$ and 30 K shows that initially melt fraction increases with volume fraction of nanoparticles but after some time elapse increasing nanoparticles volume fraction deteriorates the melt fraction. Finally, from Fig. 4d, it can clearly found that at higher temperature difference, increasing volume fraction of nanoparticles decreases the melt fraction.

Figure 6 shows combined contours of melt profile and streamlines. It can be seen that at $\Delta T = 30$ K, $Ha = 0$, $\phi = 0$, $t = 200$ s, two equally and opposite rotating streamlines are created near the two sides of inner vertical walls. At $t = 1000$ s, the strength of these two circulations increases due to natural convection. Consequently, another two equally and opposite rotating streamlines formed near

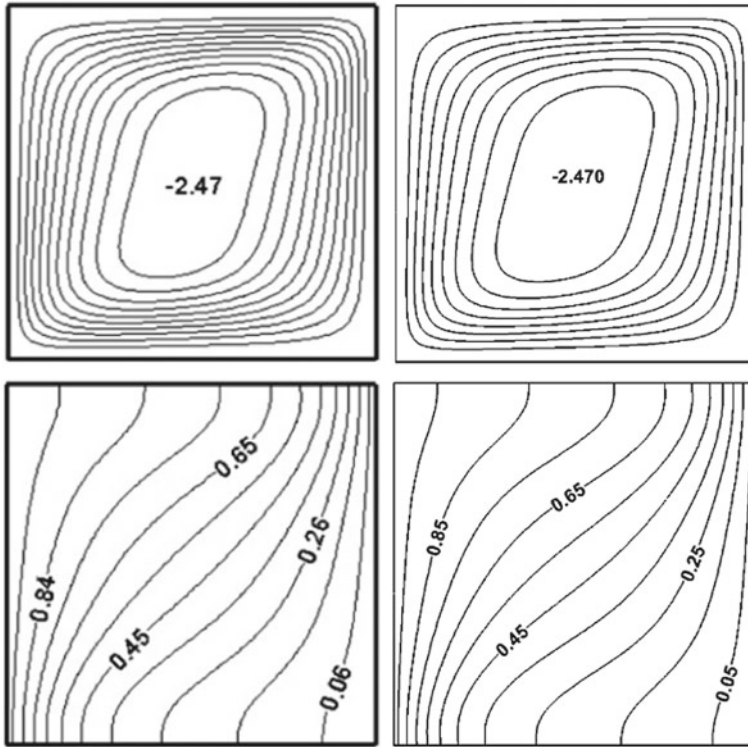


Fig. 3 Comparison of streamlines and isotherms at $Ra = 10^5$, $Ha = 60$, $\phi = 0.03$

the top inner horizontal wall. As time progress, the buoyancy force dominated over viscous force and the streamlines tend to move upward direction. At $\Delta T = 30$ K, $Ha = 0$, $\phi = 0.02$, $t = 1000$ s, the value of the maximum stream function (Ψ_{max}) decreases which results in weaker convective circulation inside the melted zone. As a result, melt front suppressed and deterioration of melt fraction observed.

6.2 Effect of Magnetic Field on Melt Fraction

Figure 5 shows the temporal variation of melt fraction at various Hartmann number (Ha) and different ΔT . It can be found that with increasing Hartmann number, melt fraction decreases. Initially, at $\Delta T = 10$ and 20 K, no effect of magnetic field on melt fraction is observed. As time progressed, the natural convections are dominated. The impact of magnetic field on the melt fraction is negligible up to $t = 400$ s because of weaker natural convective flow and heat transfer. After $t = 400$ s, change of melt fraction with increasing Hartmann number is noticeable. The effect of magnetic field on melt fraction is more influential at $\Delta T = 30$ K and 40 K. As ΔT increases, natural

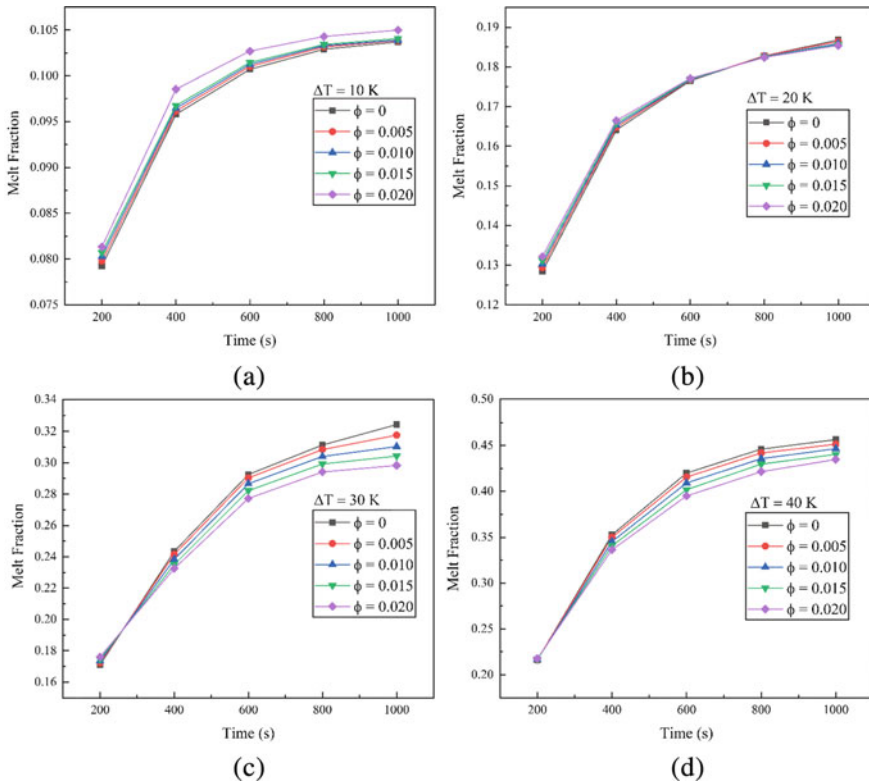


Fig. 4 Temporal variation of melt fraction at different volume fractions of nanoparticles and different temperature **a** $\Delta T = 10$ K, **b** $\Delta T = 20$ K, **c** $\Delta T = 30$ K, **d** $\Delta T = 40$ K

convective flow inside the domain increases. The restricted motion of electrically conducted NePCM caused by an external magnetic field is what causes the drop in melt fraction with a rise in Hartmann number.

From the Fig. 6, it can be observed that with increasing Hartmann number, the strength of streamline decreases. At $t = 200$ s, the effect of Hartmann number on streamlines and melt profile are very negligible. At $Ha = 40$, $t = 1000$ s, all the four equally and opposite rotating streamlines are combined and formed two equally and opposite rotating streamlines. Maximum stream function values (Ψ_{max}) also reduced, resulting in melt front suppressed, and deterioration of melt fraction observed.

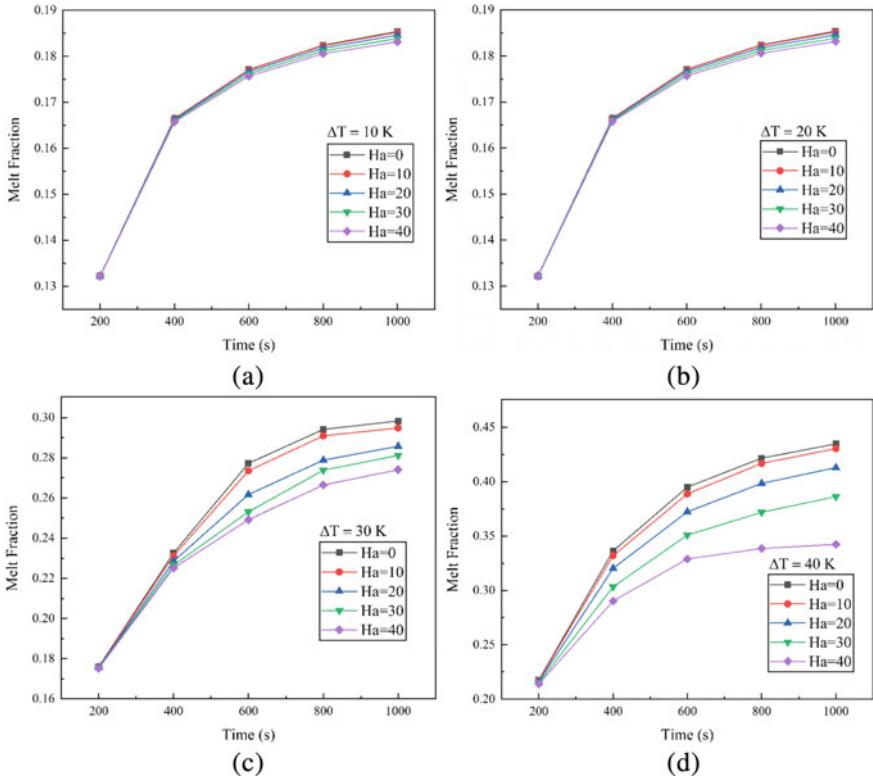


Fig. 5 Temporal variation of melt fraction at $\phi = 0.02$ and different Hartmann numbers and different temperatures **a** $\Delta T = 10$ K, **b** $\Delta T = 20$ K, **c** $\Delta T = 30$ K, **d** $\Delta T = 40$ K

7 Conclusions

In this present study, a numerical investigation on the melting of beeswax with ferro-nanoparticles in the presence of magnetic field is performed. It is seen that an increase in melt fraction with nanoparticle volume fraction at a lower temperature difference is observed. A contradictory observation has been found at a higher temperature difference. Melt fraction decreasing with nanoparticle volume fraction at a higher temperature difference is observed. It can also be found that the external magnetic field has an influential role in the reduction of melt fraction.

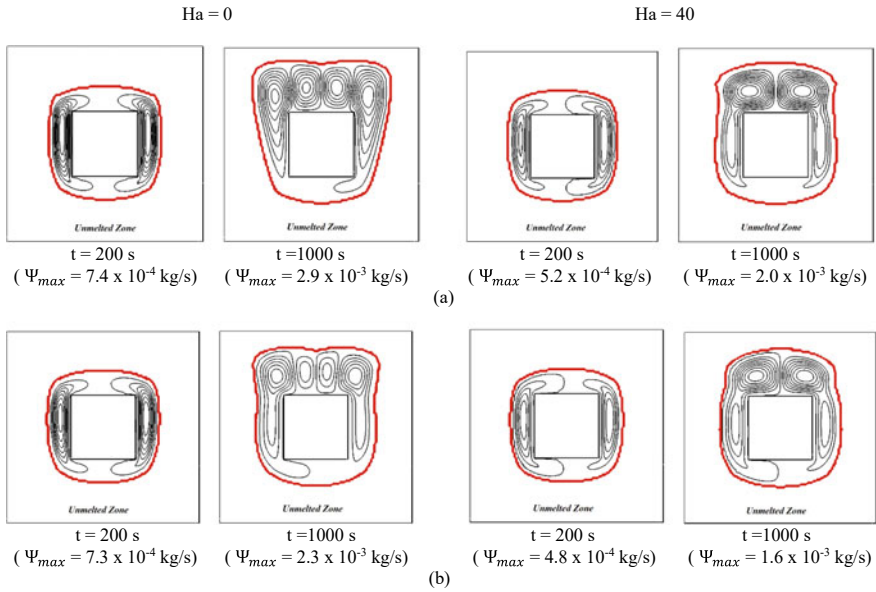


Fig. 6 Combined contour of streamline and melt profile at $\Delta T = 30$, $Ha = 0, 40$ and **a** $\phi = 0$ **b** $\phi = 0.02$

Acknowledgements We would like to thank Department of Aerospace Engineering and Applied Mechanics, IEST-Shibpur, for the support provided during this research work.

NOMENCLATURE

- ϕ Volume fraction of nanoparticles–
- T_h Temperature of inner hot walls[K]
- T_c Temperature of outer cold walls[K]
- T_L PCM melting temperature[K]
- ΔT Temperature difference, $T_h - T_L$ [K]
- t Time[S]

References

1. Šarler B (1995) Stefan’s work on solid-liquid phase changes. Eng Anal Boundary Elem 16:83–92
2. Gau C, Viskanta R (1986) Melting and solidification of a pure metal on a vertical wall
3. Brent AD, Voller VR, Reid KTJ (1988) Enthalpy-porosity technique for modeling convection-diffusion phase change: application to the melting of a pure metal. Num Heat Transf Part A Applcat 13:297–318

4. Maxwell JC (1873) A treatise on electricity and magnetism. vol 1, Clarendon press
5. Choi SUS, Eastman JA (1995) Enhancing thermal conductivity of fluids with nanoparticles
6. Eastman JA, Choi SUS, Li S, Yu W, Thompson LJ (2001) Anomalous increased effective thermal conductivities of ethylene glycol-based nanofluids containing copper nanoparticles. *Appl Phys Lett* 78:718–720
7. Nguyen CT, Desgranges F, Galanis N, Roy G, Maré T, Boucher S, Mintsa HA (2008) Viscosity data for Al_2O_3 -water nanofluid—hysteresis: is heat transfer enhancement using nanofluids reliable? *Int J Therm Sci* 47:103–111
8. Ghasemi B, Aminossadati SM, Raisi A (2011) Magnetic field effect on natural convection in a nanofluid-filled square enclosure. *Int J Therm Sci* 50:1748–1756
9. Kumar A, Saha SK, Kumar KR, Rakshit D (2022) Study of melting of paraffin dispersed with copper nanoparticles in square cavity subjected to external magnetic field. *J Energy Stor* 50:104338

Numerical and Experimental Analysis of Liquid Cold Plate Thermal Management System for High-Powered Electronics



Rehan Ansari, Mohammad Saqlain Fakhri, Osama Khan, Uzair Sain, and Arnab Ganguly

1 Introduction

Since decades, there has been an exponential increase in the number of transistors in integrated circuits, resulting in a significant increase in computing performance [1]. Development in miniaturization of electronic components for less material and operational cost has also seen a significant rise. All these factors have resulted in a substantial increase in power consumption and heat dissipation, as observed in Fig. 1. Thus, thermal management using traditional air-cooling methods is not quite sufficient for these devices at its nominal and high operating temperature. Although ICs are highly capable for thermal throttling, the traditional air-cooling method becomes a bottleneck for drawing out maximum performance out of them.

Thus, to solve this issue, liquid cooling-based thermal management systems are used. Liquid cooling uses the qualities of the fluid to effectively reduce the heat dissipation and increase the performance. Depending on the application, different coolants may be employed along with different liquid cooling techniques, such as direct or indirect cooling. In cooling of high-powered electronics, liquid cooling involves a closed system that carries the liquid from one component to another. These systems are usually referred to as loops or circuits. For high heat dissipation rates, various other techniques such as jet impingement, heat pipe, microheat sink, and microchannel have also been found to be effective.

Khandlikar et al. [2] discussed the types of liquid-cooled cold plates for industrial high-power electronic devices and the various thermal design and manufacturing considerations associated with them. The cold plates were classified into four types: formed tube cold plates, deep drilled cold plates, machined channel cold plates, and pocketed folded-fin cold plates. The authors also discussed the selection of cold plate

R. Ansari (✉) · M. S. Fakhri · O. Khan · U. Sain · A. Ganguly
Department of Mechanical Engineering, Rizvi College of Engineering, Mumbai 400050, India
e-mail: ansarirehan892@gmail.com

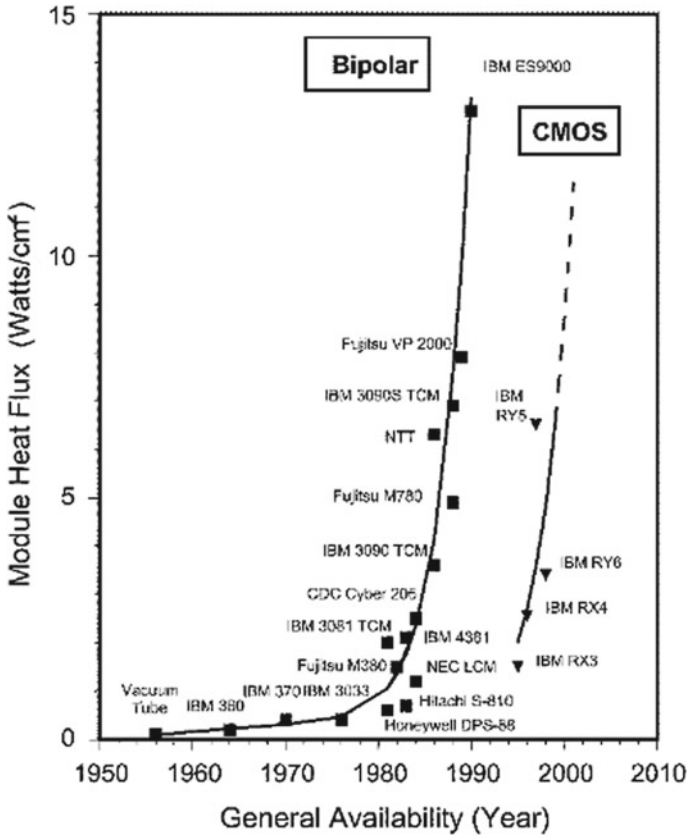


Fig. 1 Trend in module heat flux by Chu et al. [1]

type and channel configuration, as well as some of the relevant manufacturing issues, in this paper. The authors have also provided information on how to avoid general design issues and the liquid type or coolant used.

Khatak et al. [3] worked on a spray cooling method using nanofluids. The cooling occurred when liquid was forced through a small orifice, shattering into a dispersion of small droplets which then impacts onto the heated surface. In this experiment, water was first impacted over the heated surface at various heat inputs and at different velocities and heat fluxes. The surface temperature was measured for each case. An insulation box was also used so that the heat transfer is in one direction. The heat input varied between 140 and 180 W, and the flow rate varied between 15 and 25 ml/min. As flow rate increased (more fluid encounters the heated surface) and heat flux increased, the temperature at the surface decreased. Thus, ZnO fluid was used at a heat input of 180 W and 20 ml/min. Suspended particles of ZnO in the base fluid of water increased thermal conductivity, thus resulting in high heat transfer.

Lie et al. [4] performed a numerical analysis of a mini-channel heat sink for single-phase laminar flow of water as coolant through small hydraulic diameters, with a constant heat flux boundary condition. The pressure drop, thermal resistance, and maximum allowable heat flux were all affected by channel dimensions, channel wall thickness, bottom thickness, and inlet velocity. The findings showed that a narrow and deep channel with a thin bottom thickness and a relatively thin channel wall thickness improves heat transfer performance while maintaining a relatively high but acceptable pressure drop. A nearly optimized heat sink configuration is discovered that can cool a chip with a heat flux of 256 W/cm^2 at a pumping power of 0.205 W . With a maximum difference of 12%, the simulated thermal resistance agreed quite well with the result of the conventional correlation method.

Thus, in the current work, a $40 \text{ mm} \times 40 \text{ mm}$ mini-channel cold plate has been designed for heat dissipation of 300 W . The cold plate was numerically simulated for its heat transfer characteristics using commercial CFD software, ANSYS Fluent. Using experimentation, operating temperatures of mini-channel cold plate were demonstrated to be less than $70 \text{ }^\circ\text{C}$ for fluid flow rates of 12, 15, and 20 lpm , which had close agreement with analytical and numerical analysis.

2 Methodology

Firstly, an analytical examination of the design and performance of the cold plate was done, followed by the requisite numerical and experimental analysis.

2.1 Analytical Study for Mini-channel Cold Plate

See (Fig. 2).

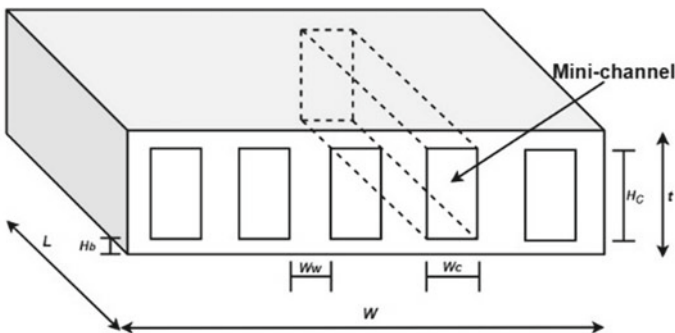


Fig. 2 Diagrammatic representation of mini-channel cold plate

Before designing, it is important to evaluate the number of mini-channels, maximum temperature, and thermal resistance of cold plate at varying flow rate for the requisite design criteria. Thus, a 1D steady-state heat transfer analysis is carried out [4–9].

The Reynolds number of the flow in the channels is given by:

$$\text{Re} = \frac{\rho v D}{\mu} \quad (1)$$

The hydraulic diameter of the mini-channel can be written as:

$$D = \frac{2H_c W_c}{H_c + W_c} \quad (2)$$

Also, the Prandtl number (Pr) of fluid can be calculated as:

$$\text{Pr} = \frac{\mu C_p}{k} \quad (3)$$

Since Re and Pr are known, Nusselt number (Nu) can be calculated using the correlation given [9]. The reason for using this correlation is because of the very small size of the channels which makes the flow almost laminar, thus making analytical calculations much simpler.

$$\text{Nu} = 1.86 \times \left(\frac{\text{Re} \times \text{Pr}}{\frac{L}{D}} \right)^{\frac{1}{3}} \quad (4)$$

Thus, using Nusselt number, the average heat transfer coefficient can be easily calculated as:

$$h = \frac{\text{Nu} \times k_f}{L} \quad (5)$$

The total thermal resistance offered by the cold plate is as follows:

$$\theta = \frac{\Delta T}{Q} = \frac{T_{\max} - T_{\text{in}}}{q \times A_b} \quad (6)$$

It can be observed from the Fig. 1 that the wall between the two channels acts as a fin. Thus, using insulated tip-fin criteria, the efficiency in heat transfer can be evaluated.

$$\eta = \frac{\tanh(ml)}{ml} \quad (7)$$

$$m = \left(\frac{H_c + W_w}{H_c \times W_w} \right) \times \left(\frac{Nu \times k_f}{k_s} \right)^{\frac{1}{2}} \tag{8}$$

Thus, the total thermal resistance offered by the cold plate will be as follows:

$$\theta = \theta_{cond} + \theta_{conv} + \theta_{heat} \tag{9}$$

$$\theta = \frac{H_b}{k_s A_b} + \frac{1}{h A_{sf}} + \frac{1}{\dot{m} C_p} \tag{10}$$

The dimension of the cold plate is considered as 44 mm × 40 mm since the standard size of a modern high computing CPU available in market is around 40 mm × 40 mm. The important parameter to characterize is the number of mini-channels which gives high heat transfer performance at comparatively less pressure drop and thermal resistance while maintaining the optimum surface temperature. Thus, a study for the same was carried out for choosing the number of channels for our design points. Aluminum is considered for the design of cold plate due to its high-thermal conductivity and less cost as compared to copper. The fluid is considered as water at STP.

It was observed from Fig. 3 that the optimum thermal resistance and pressure drop are with channels close to 5 and 6. Thus, for ease of manufacturing, five channels are considered for the design of cold plate. Also, the maximum temperature with five channels is close to 70 °C for a flow rate of 10 lpm. Intuitively, for higher flow rates, the temperature drops, and heat transfer would be comparatively more. Thus, the dimensions of the mini-channel cold plate are tabulated in Table 1.

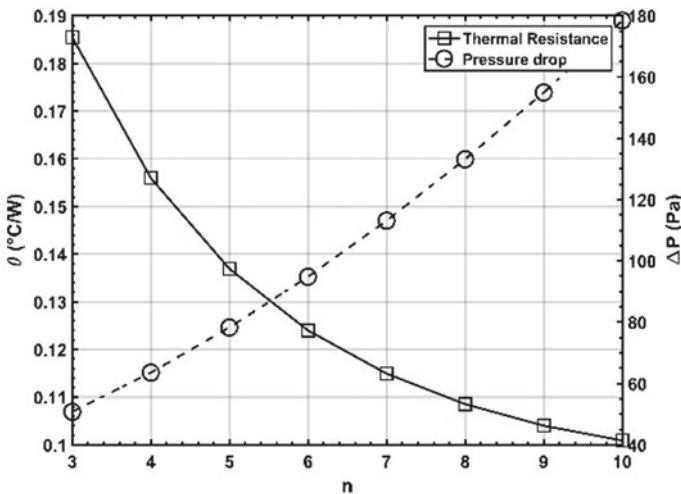


Fig. 3 Variation of number channels with thermal resistance and pressure drop

Table 1 Dimensions of cold plate

Parameter	Value (mm)
Length (L)	40
Width (W)	44
Thickness (t)	10
Channel height (H_c)	6
Channel width (W_c)	4
Base thickness (H_b)	2

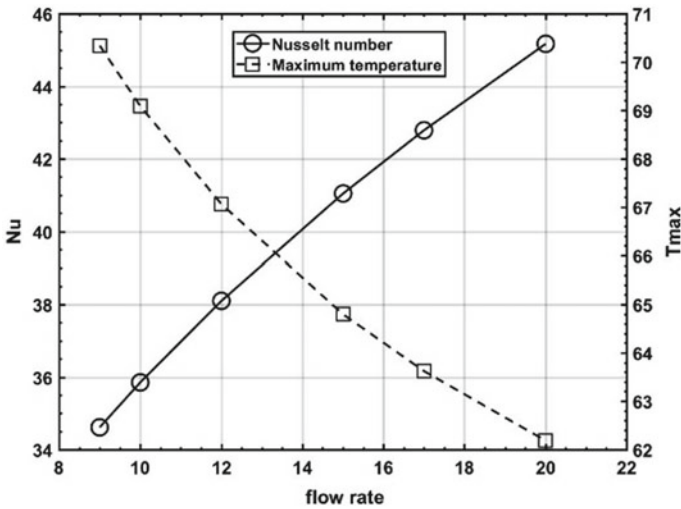


Fig. 4 Variation of Nusselt number and maximum temperature with increasing flow rates

The variation of Nusselt number and maximum temperature with varying fluid rate is observed in Fig. 4. It is critical to understand the variation of Nusselt number because it estimates the overall heat transfer performance. Evaluation is done at a heat dissipation of 300 W or a heat flux of 171 kW/m². Figure 4 shows that increasing the flow rate results in a decrease in temperature and an increase in the Nusselt number, implying that maximum heat is extracted. Thus, temperatures below 70 °C are observed for all cases.

2.2 Numerical Simulation

To validate the analytical calculations, numerical simulations are performed on commercial CFD solver, ANSYS Fluent. The domain of the cold plate consists of solid and liquid sub-domains. Thus, each domain is to be discretized for solving them

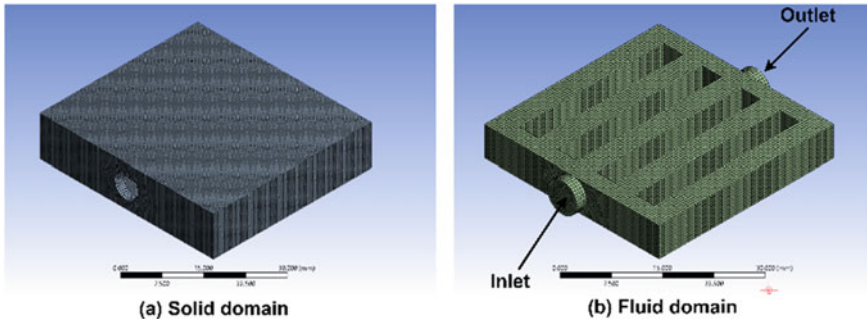


Fig. 5 Discretization of solid and fluid domains

numerically. Using ICEMCFD, the fluid and solid domain is uniformly discretized with a mesh size of 0.5 mm. Using hex-dominant meshing algorithm, the entire domain is linearly meshed with quadrilateral and triangular elements as shown in Fig. 5. The total nodes were 2,12,188, and the total elements were 2,11,139.

A uniform heat flux of 171 kW/m² is applied on the bottom face of the cold plate. Other walls of the cold plate are assigned to adiabatic wall condition. The cold plate consists of an inlet and outlet. Thus, at inlet, velocity corresponding to the respective flow rates of 12, 15, and 20 lpm has been assigned. Also, the temperature of fluid at inlet is 303.15 K. The outlet has been assigned as a ‘pressure outlet’ with atmospheric pressure of 101,325 Pa.

The governing differential equations for the numerical solutions which involve fluid flow and heat transfer are as follows:

1. Continuity equation

$$\nabla \vec{V} = 0 \tag{11}$$

2. Momentum conservation equation

$$\nabla \cdot (\rho \vec{V} \cdot \nabla \vec{V}) = \nabla \cdot [-p + \mu(\nabla \vec{V} + \nabla \vec{V}^t)] \tag{12}$$

3. Energy conservation equation

$$\rho C_p (\vec{V} \cdot \nabla T) = k_f \nabla^2 T \tag{13}$$

For solving the governing equations, SIMPLE algorithm in ANSYS Fluent was used [10, 11]. Also, Gauss–Seidel iterative technique was used to solve the resulting algebraic equations. Furthermore, a second-order upwind scheme is used for discretizing the momentum–energy equations. A convergence criterion of 10⁻⁶ was set for continuity, momentum, and energy conservation equations.

2.3 Experimental Apparatus

The experimental setup consists of a mini-channel cold plate, a heating module, a heat exchanger (radiator), a flow sensor, a submersible pump, and a fluid reservoir, as shown in Fig. 6. The temperature of the cold plate is measured using a k-type thermocouple ($\pm 2\text{ }^\circ\text{C}$). To record the maximum surface temperature, thermocouple is attached between the heating module and the cold plate, with the help of thermal paste. A hall-effect flow sensor is used to record the flow rate of water entering the cold plate. Both the k-type thermocouple and the flow sensor are connected to Arduino UNO for data collection.

To simulate the heat dissipated from high-powered electronics and IC's, a heating module is used. The heating module consists of three nichrome wire-based heating elements, each of 100 W. The three heating elements are connected in parallel, to create 300 W heating module [8, 11–13]. The heating module is connected to AC supply, with the help of a VARIAC. The pump and the fan for radiator are connected to the DC supply, as shown in Fig. 7.

The mini-channel cold plate is fabricated using aluminum grade 6061. The cold plate is fabricated using CNC machining, as shown in Fig. 8. The machined halves of the mini-channel cold plate are bonded using industrial epoxy, Araldite. No seepage of water from the bonded cold plate was observed during the entire testing phase. The flow loop is created using flexible PVC tubes, to provide water to the cold plate at the

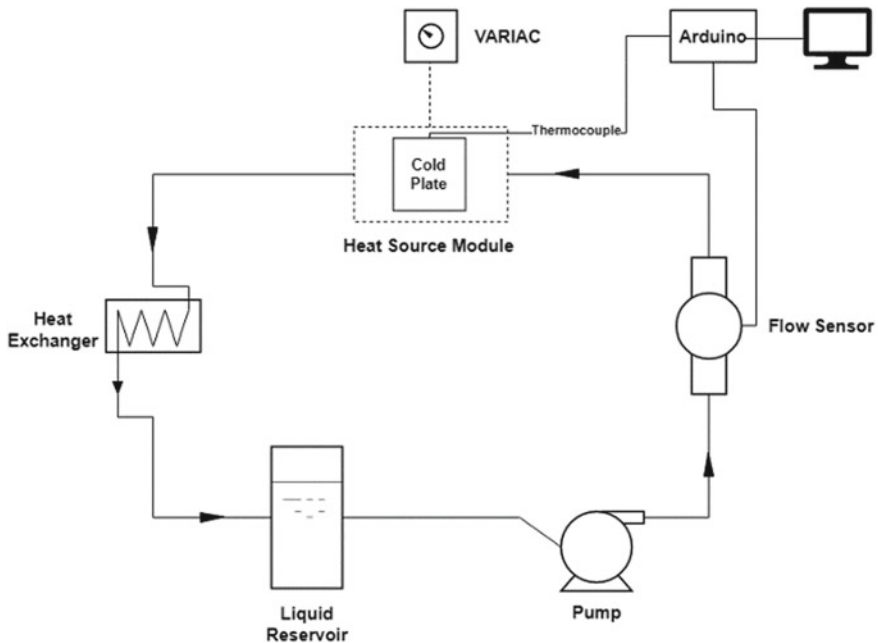


Fig. 6 Schematic of experimental setup

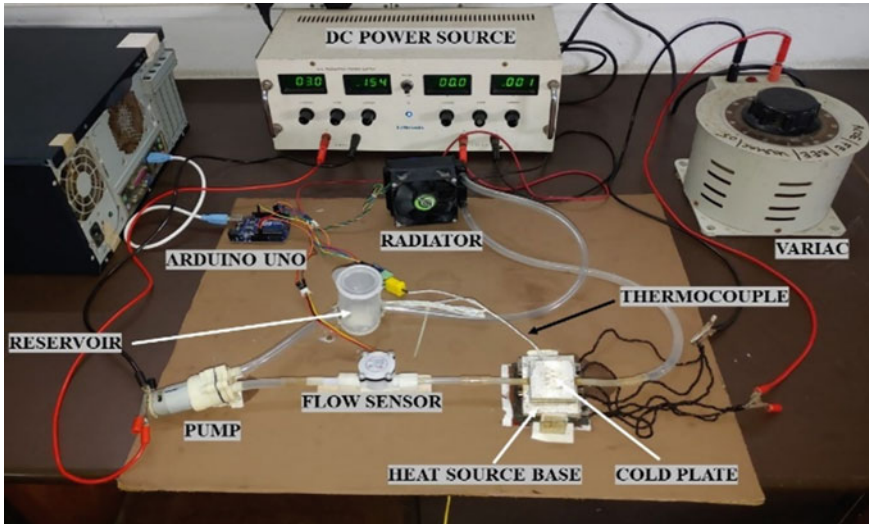


Fig. 7 Photographic view of experimental setup

ideal temperature and flow rate. With the aid of a VARIAC, the heat source module coupled to the cold plate is intended to generate the requisite 300 W of power. The heat produced by the heating module is conducted to the cold plate. In addition to this, readings from the k-type thermocouple are used to monitor the temperature of the cold plate.

A pattern is followed to test the system. Firstly, the heating is initiated for several seconds, to have steady heat generation. Once the surface temperature reaches approximately 100 °C, the system is activated by powering the pump and radiator. Temperature is observed till it reaches a steady state.

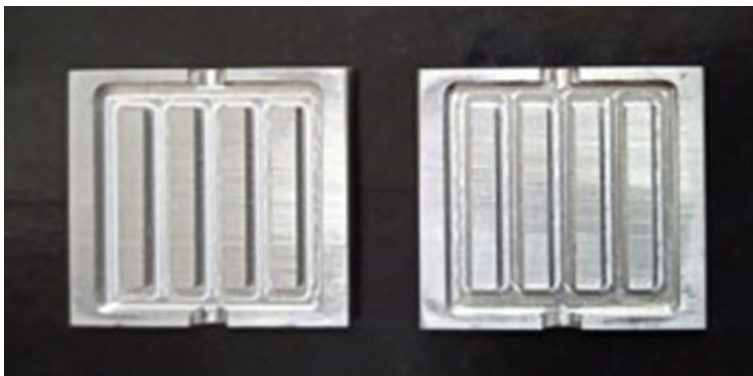


Fig. 8 Machined mini-channel cold plate halves

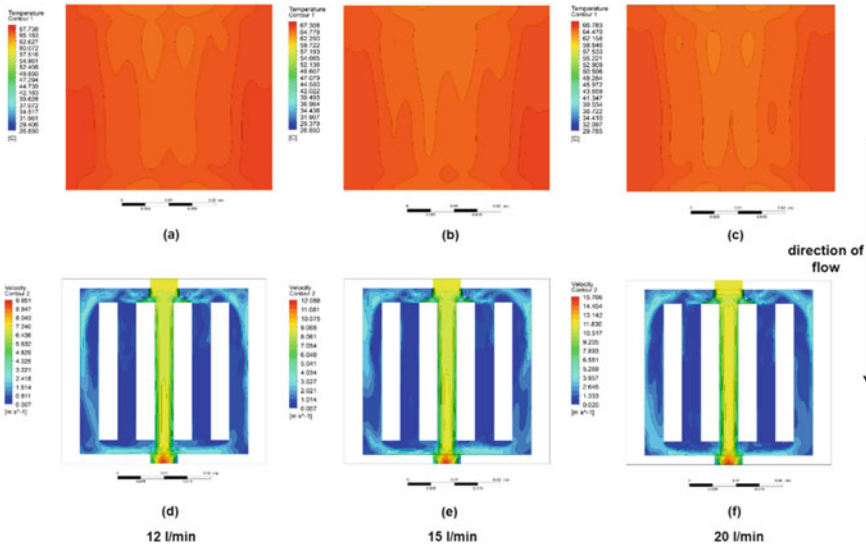


Fig. 9 Temperature and velocity contours

3 Results and Discussion

3.1 Results of CFD

After numerical computations, the results of the CFD simulation were post-processed, as shown in Fig. 9. The temperature contour at the base of the cold plate and the velocity contour in the mini-channels were plotted. It was observed from Fig. 9a that the maximum temperature at flow rate of 12 lpm was 67.738 °C. For flow rates of 15 and 20 lpm, the maximum temperature, from Fig. 9b, c, was observed as 67.308 °C and 66.783 °C, respectively. It is clearly observed that an increase in flow rate furthermore increased the thermal performance. It was also discovered that the flow rate of fluid in each channel varied due to flow maldistributions, causing the temperature along the cold plate surface to vary. Maximum flow rate was observed in the middle channel, thus decreasing the flow rate in adjacent channels, as observed in Fig. 9d–f. Approximately 80% of the flow was observed in the middle channel, with the remainder forming other channels.

3.2 Experimental Results

As discussed earlier, three test cases with flow rates of 12, 15, and 20 lpm were run with heat dissipation of 300 W. Initially, the heating module was turned on for

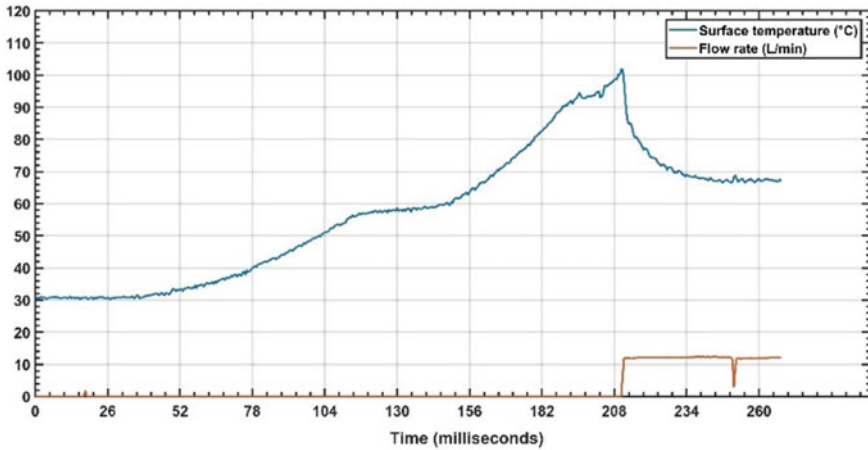


Fig. 10 Cooling characteristics at 12 lpm

several seconds for steady heat generation. Once the maximum surface temperature reached 100 °C, the system was activated to check for its thermal performance. Using a VARIAC, 160 V AC supply was provided to the heating module, and the total current was measured as 1.9 A. Thus, uniform heat generation of 304 watts was achieved using the heating module. The flow rate of water was varied by altering the voltage of DC supply to the pump.

It is observed in Fig. 10 that the maximum surface temperature of the cold plate drops instantly from 100 °C and reaches steadily to 67.26 °C, when the flow rate is maintained at 12 lpm. Within milliseconds, a temperature drop of around 20 °C is reported, indicating superior heat transfer performance of the system.

Similarly, when the system is turned on for flow rate of 15 lpm, the maximum surface temperature of the cold plate drops instantly from 100 °C and steadily reaches 66.3 °C, as observed in Fig. 11.

When the system is turned on for fluid flow rate of 20 lpm, the maximum surface temperature of the cold plate steadily reaches 65.24 °C, as observed in Fig. 12.

3.3 Overall Comparison

See (Fig. 13).

The error between the analytical, numerical, and experimental values for the maximum surface temperature was found to be the smallest at a flow rate of 12 lpm. The maximum difference in the values was at a flow rate of 20 lpm. Table 2 summarizes the reported error between different studies.

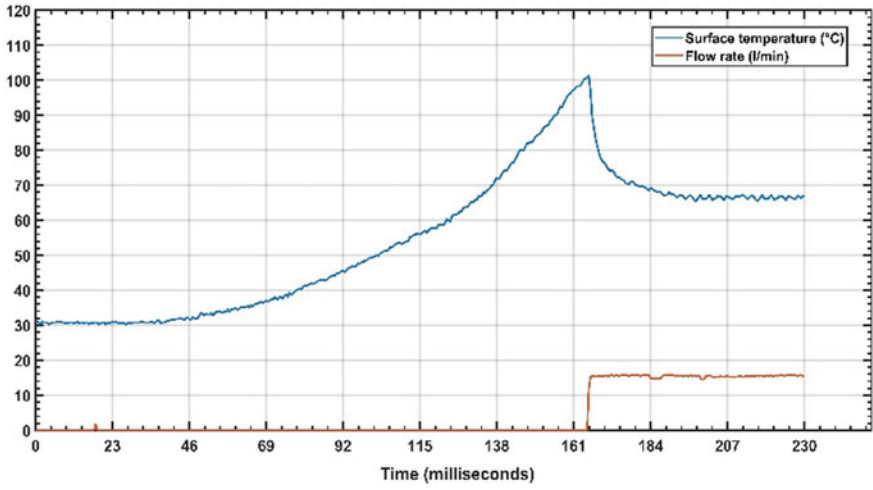


Fig. 11 Cooling characteristics at 15 lpm

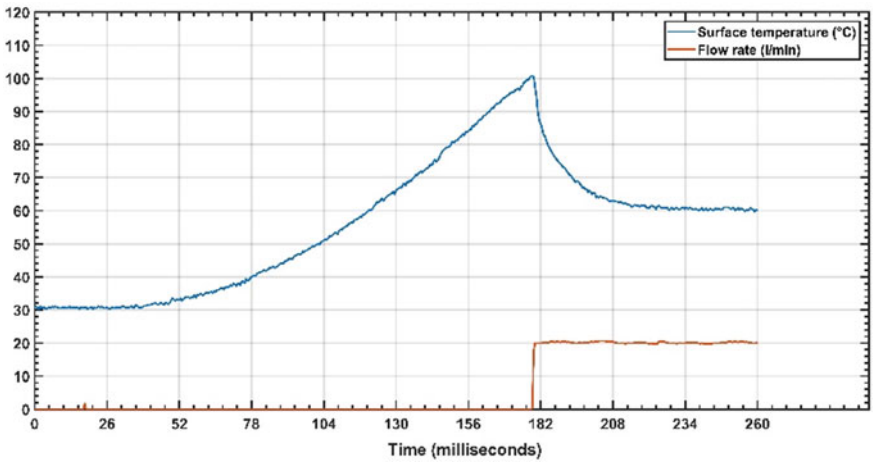


Fig. 12 Cooling characteristics at 20 lpm

Fig. 13 Comparison between analytical, numerical, and experimental results

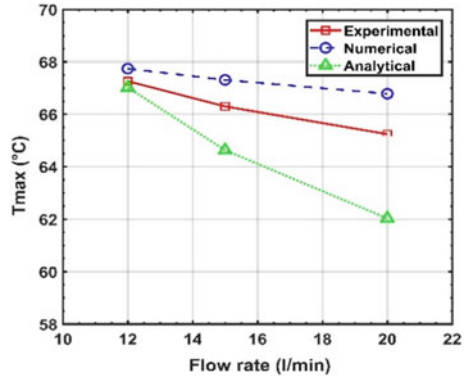


Table 2 Error comparison

Comparative data	Maximum error (%)
Analytical versus numerical	7.6
Analytical versus experimental	5.2
Numerical versus experimental	2.3

4 Conclusion

The heat transfer performance of a mini-channel cold plate-based thermal management system at heat dissipation of 300 W was investigated. Numerical simulations and experimental analysis of the cold plate were carried out as well. The analytical, numerical, and experimental analysis revealed the following conclusions:

1. Increasing the number of channels in the cold plate improved thermal performance but also increased the pressure drop. Thus, the designer must make necessary trade-offs while designing the cold plate.
2. Increasing Nusselt number decreased the thermal resistance of the cold plate, thus improving its heat transfer performance.
3. Analytical calculations predicted maximum surface temperatures of 67.02 °C, 64.63 °C, and 62.03 °C at flow rates of 12 lpm, 15 lpm, and 20 lpm, respectively, while numerical solutions predicted temperatures of 67.738 °C, 67.308 °C, and 66.783 °C at flow rates of 12 lpm, 15 lpm, and 20 lpm, respectively, with a maximum error of 7.6%.
4. Using experimentation, maximum surface temperatures of 67.26 °C, 66.3 °C, and 65.24 °C were measured at flow rates of 12 lpm, 15 lpm, and 20 lpm, respectively, which corresponded well with analytical and numerical results with a maximum error of 5.2% and 2.3%.
5. Due to flow maldistribution, the surface of the cold plate is observed with various temperature hot spots.

- Use of different coolants as well as nanofluids can furthermore increase the thermal performance of the system at comparatively less flow rates and higher heat dissipation rates.

Nomenclature

Q	Heat dissipation (W)
q	Heat flux (W/m^2)
Re	Reynold number
Pr	Prandtl number
Nu	Nusselt number
μ	Dynamic viscosity (Pa.s)
D	Hydraulic diameter of channel (m)
W_c	Width of the channel (m)
W_w	Width of wall adjacent to channel (m)
H_c	Height of the channel (m)
H_b	Bottom thickness (m)
ρ	Density of fluid (kg/m^3)
k_f	Thermal conductivity of fluid ($\text{W}/\text{m K}$)
k_s	Thermal conductivity of solid ($\text{W}/\text{m K}$)
h	Average heat transfer coefficient ($\text{W}/\text{m}^2 \text{ K}$)
W	Width of cold plate (m)
L	Length of cold plate (m)
η	Efficiency of wall acting as fin
θ	Total thermal resistance ($^\circ\text{C}/\text{W}$)
θ_{cond}	Conductive thermal resistance ($^\circ\text{C}/\text{W}$)
θ_{conv}	Convective thermal resistance ($^\circ\text{C}/\text{W}$)
θ_{heat}	Capacitive thermal resistance ($^\circ\text{C}/\text{W}$)
A_b	Channel bottom surface area (m^2)
A_{sf}	Channel area in contact with fluid (m^2)
\dot{m}	Mass flow rate of fluid (kg/s)
C_p	Specific heat of fluid ($\text{J}/\text{kg K}$)
T_{max}	Maximum surface temperature ($^\circ\text{C}$)
T_{in}	Inlet temperature of fluid ($^\circ\text{C}$)
\vec{V}	Velocity matrix (m/s)
\vec{V}^t	Transpose of velocity matrix (m/s)
∇	Gradient operator

References

1. Chu RC, Simons RE, Ellsworth MJ, Schmidt RR, Cozzolino V (2004) Review of cooling technologies for computer products. *IEEE Trans Device Mater Reliab* 4:568–585
2. Kandlikar SG, Hayner CN (2009) Liquid cooled cold plates for industrial high-power electronic devices—thermal design and manufacturing considerations. *Heat Transf Eng* 30:918–930
3. Khatak P, Jakhar R, Kumar M (2015) Enhancement in cooling of electronic components by nanofluids. *J Inst Eng (India) Ser C* 96:245–251
4. Xie XL, Liu ZJ, He YL, Tao WQ (2009) Numerical study of laminar heat transfer and pressure drop characteristics in a water-cooled minichannel heat sink. *Appl Therm Eng* 29:64–74
5. Tuckerman DB, Pease RFW (1981) High-performance heat sinking for VLSI. *IEEE Electron Device Lett* 2:126–129
6. Ijam A, Saidur R, Ganesan P (2012) Cooling of minichannel heat sink using nanofluids. *Int Commun Heat Mass Transf* 39:1188–1194
7. Yang X-H, Tan S-C, Ding Y-J, Liu J (2017) Flow and thermal modeling and optimization of micro/mini-channel heat sink. *Appl Therm Eng* 117:289–296
8. Li H, Ding X, Meng F, Jing D, Xiong M (2019) Optimal design and thermal modelling for liquid-cooled heat sink based on multi-objective topology optimization: An experimental and numerical study. *Int J Heat Mass Transf* 144:118638
9. Incropera FP, DeWitt DP, Theodore LB, Lavine AS et al (1996) *Fundamentals of heat and mass transfer* 6
10. Bhandari P, Prajapati YK (2021) Thermal performance of open microchannel heat sink with variable pin fin height. *Int J Therm Sci* 159:106609
11. Fazeli SA, Hashemi SMH, Zirakzadeh H, Ashjaee M (2012) Experimental and numerical investigation of heat transfer in a miniature heat sink utilizing silica nanofluid. *Superlattices Microstruct* 51:247–264
12. Jajja SA, Ali W, Ali HM, Ali AM (2014) Water cooled minichannel heat sinks for microprocessor cooling: effect of fin spacing. *Appl Therm Eng* 64:76–82
13. Weilin Q, Mudawar I (2002) Experimental and numerical study of pressure drop and heat transfer in a single-phase micro-channel heat sink. *Int J Heat Mass Transf* 45:2549–2565

Investigation on Passive Thermal Management Using Phase Change Materials Encapsulated Over 18,650 Lithium-Ion Battery



Saumendra Nath Mishra, Siddhartha Banerjee, Sourav Sarkar, Achintya Mukhopadhyay, and Swarnendu Sen

1 Introduction

In recent years, lithium-ion battery (LIB) has become popular because of their inherent advantages over conventional battery systems, including high specific capacity, zero memory, exceptional cycling wide temperature range, low self-discharge, and performance operational mode [1, 2]. However, the performance of LIB is temperature dependent, and it gives the best performance when the battery temperature is maintained within 20–40 °C [3]. Therefore, a battery thermal management system (BTMS) is required to keep the battery temperature within the optimum range [4, 5].

The battery thermal management can be classified as active or passive based on the power consumption [6, 7]. Air cooling [5], liquid-based cooling [4], and mist cooling [8] are active cooling systems, whereas phase-changing material (PCM)-based cooling is categorized under passive cooling because it extracts large amount of heat in the latent form and thus does not require external power input [9]. Thermal management techniques that properly incorporate PCM into the battery design allow battery packs to be kept at their ideal operating temperature [10].

Wang et al. [11] revealed that the PCM thermal conductivity, PCM encapsulation thickness, and PCM melting temperature are the important design criteria while designing the PCM-based cooling system. The thermal conductivity of PCM can be improvised by adding metal foam, a carbon-based material, nanoparticles [6]. The high thermal conductivity of the PCM results in good temperature homogeneity during the melting process. Bai et al. [12] looked at the thermal behavior of a PCM-based BTM system. They investigated the impact of battery gap spacing,

S. N. Mishra · S. Banerjee · S. Sarkar (✉) · A. Mukhopadhyay · S. Sen
Department of Mechanical Engineering, Jadavpur University, Kolkata, India
e-mail: souravsarkar.mech@jadavpuruniversity.in

PCM melting point, and thermal conductivity on cooling effectiveness. The findings demonstrated that maximum temperature and temperature gradient dropped when gap spacing and thermal conductivity increased, whereas maximum temperature rises and temperature gradient falls as PCM melting point increases. Choudhuri et al. [13] in their numerical investigation found that the battery temperature remains the minimum thickness of the PCM module and is kept near critical thickness. The critical thickness can be calculated as the difference between the battery radius and the ratio of PCM thermal conductivity to ambient heat transfer coefficient. Weng et al. [14] found that the process of resting, also known as laying aside time, is crucial to dynamic battery cycling. For instance, during cycles with a 5 min rest period, the temperature is around 1 C lower than during cycles without a rest period. Also, increasing the rest time further decreases the temperature [14]. However, a limited number of investigations are found that address the melting and solidification time magnitude comparison during the dynamic battery cycling. Hence, the present numerical analysis emphasizes on melting and solidification of PCM encapsulation corresponding to the critical thicknesses of insulation.

In the present study, a numerical investigation is carried out on the passive cooling of 18,650 LIB encapsulated in PCM. The thickness of PCM is kept as 2, 5, and 8 mm. The steady-state temperature of the cells obtained during the operational conditions are compared for the above-defined PCM modules. Also, the optimum PCM module thickness obtained from the above comparison is used further to quantify the PCM's total melting time and solidification time under 3 C charging and discharging rate.

2 Numerical Modeling

2.1 Problem Formulation

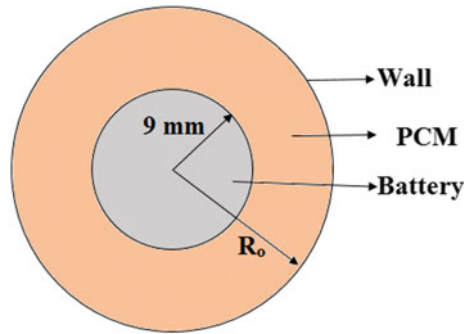
The present study considers a single 18,650 lithium-ion battery (capacity 2.4Ah and nominal voltage of 3.6 V). The properties of the lithium-ion battery (LIB) are taken from the literature [12]. An envelope of PCM is wrapped around the cell to extract the heat generated during the operational condition. The PCM used is lauric acid. The thermophysical properties of the lauric acid are enlisted in Table 1. The geometrical dimension of the battery with the PCM module is illustrated in Fig. 1.

Therefore, the geometry for the numerical analyses contains two domains: (i) cell and (ii) PCM encapsulation. The radius of the battery is 9 mm, whereas the radii of PCM encapsulation (R_o) are taken as 11 mm, 14 mm, and 17 mm, which corresponds to the PCM encapsulation thickness of 2 mm, 5 mm, and 8 mm, respectively. The cooling of the battery is performed for charging and discharging rates of 1 C-rate, 2 C-rate, and 3 C-rate. The outside ambient condition is kept identical during the entire analysis.

Table 1 Thermophysical properties of Lauric acid [13]

Property	Solid	Liquid	Unit
Liquidus temperature (T_l)	–	321.35	K
Solidus temperature (T_s)	316.65		K
Melting temperature (T_m)	319		K
Density (ρ)	940	885	Kg/m ³
Specific heat, (C_p)	2180	2390	J/Kg K
Thermal conductivity (k)	0.16	0.14	W/m k
Viscosity (μ)		0.008	N-s/m ²
Latent heat of fusion, (L)	187,210		J/kg

Fig. 1 Schematic diagram of the battery with PCM encapsulation



2.2 Governing Equations

From Fig. 1, it can be realized that there are two domains: (i) cell which is a solid domain, (ii) phase-changing material covering the cell, which is a fluid domain. When the battery is under operational condition, heat is generated within battery due to the resistance which is known as the Joule heating. To find the spatial and the temporal variation of temperature for the single cell, general two-dimensional heat transfer equation (Eq. 1) is solved in the cell domain, and it is represented as:

$$\frac{\partial}{\partial x} \left(k \frac{\partial T}{\partial x} \right) + \frac{\partial}{\partial y} \left(k \frac{\partial T}{\partial y} \right) + \dot{Q}_{gen} = v_{cell} \rho_{jr} C_{jr} \frac{\partial T}{\partial t} \tag{1}$$

The term \dot{Q}_{gen} mentioned in Eq. 1 accounts for the Joule heating. The volumetric heat generation magnitudes corresponding to the 1 C-rate, 2 C-rate, and 3 C-rate are mentioned in 10,447 W/m³, 41,788.37 W/m³, and 94,023.8 W/m³ [13].

The heat generated during the operational condition increases the battery temperature, and the PCM absorbs the heat. So, in the beginning, the PCM is in solid state and absorbs heat in the form of sensible heat. As soon as it reaches its melting temperature, it melts and absorbs a large amount of heat in the latent form. Therefore,

there is phase transition from solid to liquid for the PCM through a narrow transition zone known as mushy zone. The spatial and temporal variation of the temperature in the liquid–solid and liquid domain can be modeled through the enthalpy porosity approach. This approach does not explicitly consider liquid–solid; thus, a single equation can be solved to find the temperature as a function as space and time. The enthalpy porosity-based approach is applied by considering the following assumptions: (i) PCM behaves as a Newtonian fluid, (ii) PCM is homogenous and isotropic, and (iii) viscous effect and the thermal radiation is neglected, and (iv) PCM domain is considered as porous zone. Considering the above assumptions, the PCM domain’s continuity, momentum, and energy equation are solved [10]. The energy equation (Eq. 2) containing the enthalpy porosity approach is defined as [10, 13]:

$$\frac{\partial \rho H}{\partial t} + \nabla \cdot (\rho \nabla H) = \nabla \cdot (k \nabla T) \tag{2}$$

Here

$$H = H_{\text{ref}} + \int_{T_{\text{ref}}}^T C_p dT + \Delta H \tag{3}$$

H_{ref} is reference enthalpy at the referred temperature T_{ref} .
The term ΔH is the latent heat and can be expressed as:

$$\Delta H = \beta L \tag{4}$$

Here, β is the liquid fraction and can be represented as:

$$\beta = \left\{ \begin{array}{l} 0 \text{ if } T < T_s \\ \frac{T - T_s}{T_l - T_s} \text{ if } T_s < T < T_L \\ 1 \text{ if } T > T_l \end{array} \right\} \tag{5}$$

The heat exchange between the PCM and surrounding takes place via convection. The value of the convective heat transfer coefficient was set as 10 W/m² K at the wall for all the cases during the entire simulation.

2.3 Numerical Methodology

The above governing conditions are solved in the specified domain, and the simulation is being carried out in ANSYS Fluent. An interface is created between the cell and PCM module to enable the conjugate heat transfer between them. The heat transfer equation is solved in the cell domain, whereas energy equation enthalpy porosity

form was solved for the PCM domain along with the continuity and momentum equations. The semi-implicit technique for the pressure-linked equations (SIMPLE) was used to couple pressure and velocity, and the PRESTO (pressure staggering option) scheme was used to spatially discretize and interpolate the pressure terms. The transient term was discretized using a second-order implicit discretization methodology, and the advection component was discretized using a second-order upwind method. For density, momentum, pressure correction, thermal energy, and melt fraction, the under-relaxation factors used were 1, 0.7, 0.3, 1, and 0.9, respectively.

2.4 Grid Independence and Time Step Size Independence Study

Grid independence study and time step size independence study were performed to nullify the effect of the grid number and time step size on solution strategy. The geometry considered is shown in Fig. 1. The grid independence study was carried out for 874 cells, 2801 cells, and 5414 cells (Fig. 2), whereas the time step size independence study was carried out for 0.01 s and 0.1 s. (Fig. 3). It is visible from Figs. 2 and 3 that both temperature and melting fraction lines have coincided for different cell numbers and time step sizes. Hence, 874 cells with 0.1 s time step size are chosen to perform simulations.

Fig. 2 Grid independence study

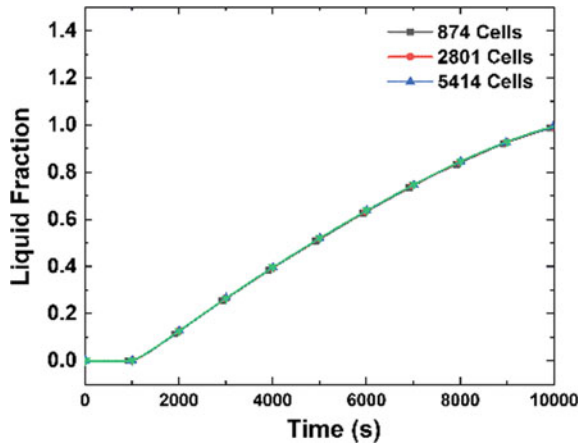
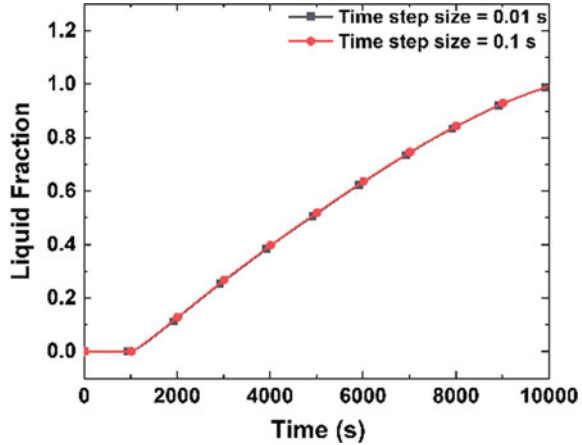


Fig. 3 Time step size independence study



3 Results and Discussions

3.1 Validation

In the present study, the melting of an annular region filled with PCM was validated with the analytical result. The internal radius and outer radius of the annular were kept as 2.5 mm, and external radius was kept as 50 mm, respectively. Initial temperature PCM region was set as 300 K and the outer wall (i.e., the boundary form by the outer radius was fixed at 300 K). Heat flux of magnitude $90,000 \text{ W/m}^2$ was applied at the inner radius to initiate the melting in the vicinity of inner wall. The formulation to find the temperature distribution within the PCM is adapted from Choudhuri et al. [12].

The value of λ^2 needed to find the temperature distribution [13, 15] was calculated as 1.5894. The numerical model was found to be in good agreement with the analytical result. While performing the validation, it was found that the deviation of the CFD result from the analytical solution solutions was higher in the initial transient phase and decreased with an increase in time (Fig. 4). In fact, after 1000 s from the beginning, the maximum deviation was recorded as 5.03%.

3.2 Effect of PCM Module Thickness on Cell Temperature

The thickness of PCM module is an important design criterion while performing PCM cooling. In this section, an investigation is being carried out where three different thicknesses of PCM, 2, 5, and 8 mm, were taken. Joule heating corresponding to 3 C-rate was incorporated, and cell temperature was monitored for different insulation thicknesses and is shown in Fig. 5.

Fig. 4 Validation of numerical model

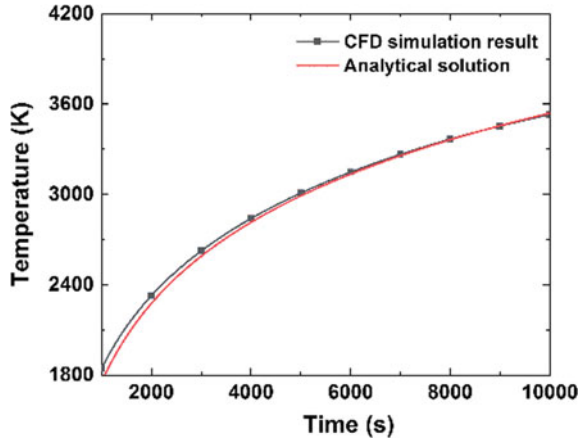
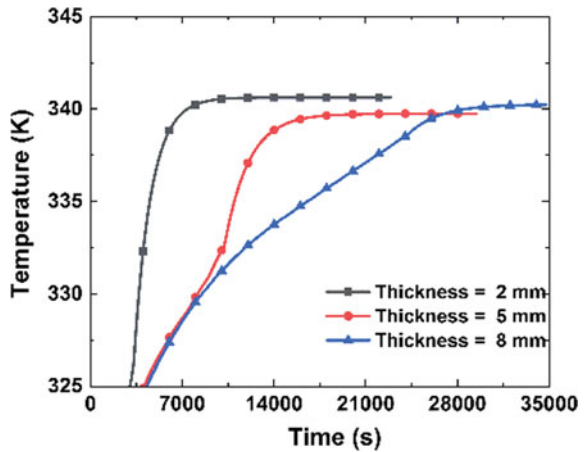


Fig. 5 Effect of PCM encapsulation thickness

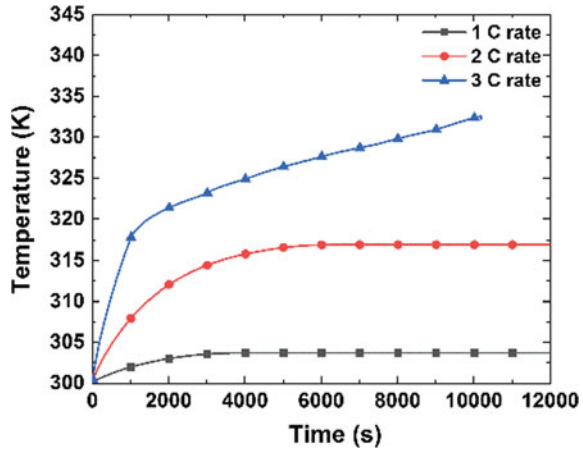


From Fig. 5, it can be observed that the temperature rise of the cell was minimum corresponding to thickness of 5 mm. In heat transfer, there is well known equation to find the critical radius:

$$R_{critical} = \frac{k}{h}$$

where, 'k' is the thermal conductivity of PCM, and 'h' is the heat transfer coefficient. In our case, value of k is 0.14 W/m k and h is 10 W/m²/K. Therefore, critical radius comes out to be 14 mm (i.e., 5 mm thickness). From our numerical model, we get the minimum cell temperature for the PCM consistency of 5 mm. It is because the PCM insulation offers minimum thermal resistance for critical insulation thickness.

Fig. 6 Cell temperature under different C-rates



3.3 Effectiveness of PCM Cooling Under Different C-Rates

LIB gives the best performance for certain temperature ranges. Therefore, to investigate the effectiveness PCM cooling for different C-rates, temperature of the cell is tracked (Fig. 6). When the power current flow rate increases, the heat generation within the cell increases. In this section, investigations are performed to visualize the effectiveness of PCM cooling under different C-rates. From Fig. 6, it can be observed that the battery achieves a steady-state temperature under 1 C-rate and 2 C-rate. The steady-state battery temperature recorded under 1 C-rate and 2 C-rate is around 303 K and 316 K, respectively. However, PCM cooling at a higher C-rate (3 C-rate) cannot bring it at steady state, and the maximum battery temperature is recorded around 332 K. It was also found that the PCM does not melts under 1 C-rate and 2 C-rate.

However, the whole PCM domain takes 10,180 s (~ 170 min), absorbing large amount of heat in latent form (Fig. 7) Therefore, it can be inferred from the above analysis that PCM cooling becomes essential only at higher charging–discharging rates.

3.4 Melting and Solidification Time Under 3 C-Rate

When entire PCM has melted during operational condition, it is to be solidified again to reuse its latent heat absorbing capacity. In this section, the regeneration of PCM is performed keeping the boundary conditions identical with melting conditions. Simulations were performed to see the magnitude of the melting and solidification time.

Fig. 7 Temporal variation of PCM melt fraction during the solidification and melting

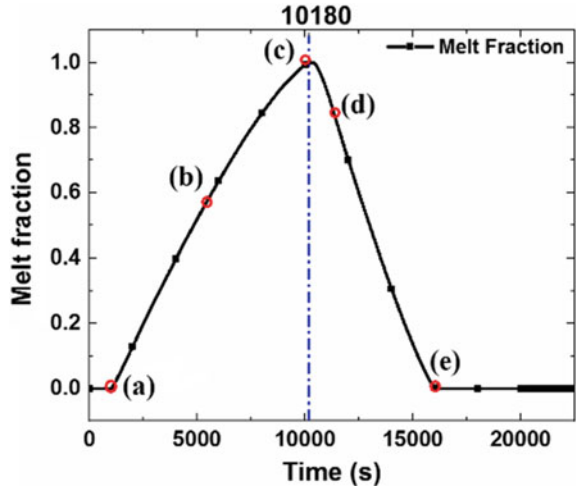
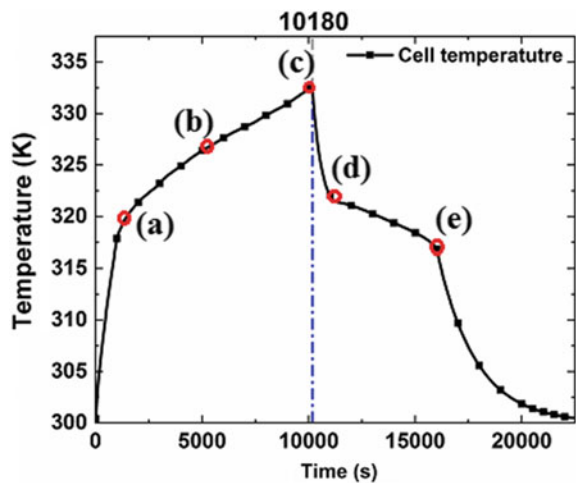


Figure 8 shows the temporal variation of the cell temperature where point (a) corresponds to 1100 s when PCM starts to melt, point (b) refers to 6000 s when solid-to-liquid transition is taking place, point (c) refers to 10,180 s when entire PCM has melted and current in the cell is switched off, point (d) refers to 11,000 s when PCM begins to solidify, and point (e) refers to 16,030 s where almost PCM has solidified. The liquid/melt fraction and the temperature contours corresponding to the above times instant are shown in Fig. 9.

The solidification and melting cycle takes 370 min. The PCM was found to melt completely at about 10,180 s (Fig. 7), and the cell temperature was about 332 K (Fig. 8). At this instant, the current in cell was switched off, and the PCM begins

Fig. 8 Temporal variation of battery temperature during the solidification and melting



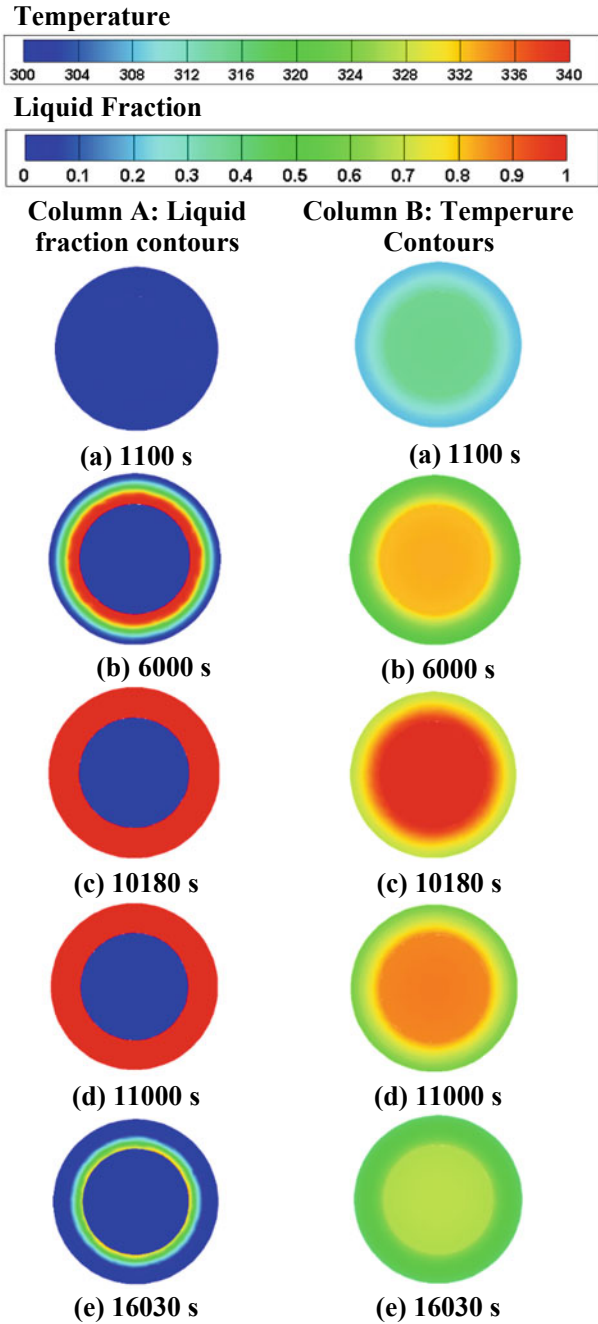


Fig. 9 Contours of liquid fraction (left column) and temperature (right column)

to solidify from the outer wall toward the inner radius by losing heat in convective form. PCM took around 5850 s (~ 97 min) to solidify completely. However, during this instant, the cell's temperature dropped to 316.75 K. Beyond this instant, the cell loses heat to come to its initial temperature and PCM during this phase loses heat to the surroundings as sensible heat. It takes around 12,320 s (~ 200 min) to regain its initial configuration.

The following observations can also be inferred from Fig. 8 that there is a steep temperature rise up to 1100 s followed by a decrease in the slope of temperature rise up to 10,180 s. It is because the solid–liquid transition occurs between this time period (Fig. 9), and PCM absorbs heat in the latent form, which drops the temperature rise. At 10,180 s, the current in the battery is switched off, and heat generation becomes zero. The cell temperature starts to fall at this instant. However, the PCM has yet to begin to solidify and losses heat in the sensible form. Thus, we get a steep fall in temperature up to 11,000 s where the liquid-to-solid transition of PCM begins (Fig. 9). At 16,030 s, the PCM almost solidifies and during this time period (i.e., between 1100 s and 16,030 s), it leaves the latent heat absorbed without undergoing appreciable temperature fall. After that, the temperature fall again becomes steep because PCM begins to lose heat sensible form.

4 Conclusions

Passive cooling using phase-changing materials is carried out in the current numerical investigation. The numerical model is initially verified with the analytical results. Henceforth, the study was performed to determine the impact insulating thickness of PCM for various charging and discharging speeds (1C, 2C, and 3C) and quantify the PCM module's melting and solidification times. Consequently, the following conclusions can be drawn from the present numerical study: (i) The steady-state temperature of the cell is minimum when the thickness of PCM module is kept equal to critical thickness of insulation and (ii) for slower charging and discharging rates (1C and 2C), the PCM module maintains the cell temperature at steady state without melting. Therefore, PCM cooling is not necessary at lower charging and discharging rates. (iii) However, the battery temperature does not stabilize at a 3C-rate charging and discharging rate, and the PCM melts completely after approximately 10,180 s (around 170 min). (iv) The current in the battery is switched off when the entire PCM melts. Hereafter, it regains its solid state at about 5850 s (~ 97 min), and the cell temperature achieves its initial temperature (i.e., 300 K) in 12,320 s (~ 200 min). The ambient condition was identical for the melting and solidification. Hence, with PCM as the only cooling medium, laying aside time becomes essential. However, if 2N number of batteries are employed, the magnitude of solidification and melting time can be used to transform intermittent operation into continuous operation. When one battery row operates, the electricity in the other row is turned off. The PCM nearby an inoperative battery will renew and get prepared to absorb for the following cycle. (iv) During the melting process, the slope of cell temperature

rises or falls during sensible heating/cooling of PCM and is found to be greater than latent heating/cooling (solid-to-liquid transition).

Nomenclature

BTM	Battery thermal management
C-rate	Charging/discharging rate
H	Enthalpy (J/s)
LIB	Lithium-ion battery
k	Thermal conductivity (W/m K)
PCM	Phase changing material
T	Temperature (K)
ρ	Density (kg/m^3)

References

1. Wang Y, Liu C, Pan R, Chen Z (2017) Modeling and state-of-charge prediction of lithium-ion battery and ultracapacitor hybrids with a co-estimator. *Energy* 121:739–750
2. Yang J, Liu X, Tian J, Jianliya M, Xiao W, Baofeng J, Li W (2017) Adhesive nanocomposites of hypergravity induced Co_3O_4 nanoparticles and natural gels as Li-ion battery anode materials with high capacitance and low resistance. *RSC Adv* 7:21061–21067
3. Bubbico R, D'annibale F, Mazzarotta B, Menale C (2017) Air cooling of lithium-ion battery: an experimental analysis. *Chem Eng Trans* 57:379–384
4. Wang L, Tao T, Xu J, Shi H, Mei X, Gou P (2022) Thermal performance of a liquid-immersed battery thermal management system for lithium-ion pouch batteries. *J Energy Storage* 46:103835
5. Sharma DK, Prabhakar A (2021) A review on air cooled and air centric hybrid thermal management techniques for Li-ion battery packs in electric vehicles. *J Energy Storage* 41:102885
6. Tete PR, Gupta MM, Joshi SS (2021) Developments in battery thermal management systems for electric vehicles. *A Tech Rev J Energy Storage* 35:102255
7. Kim J, Oh J, Lee H (2020) Review on battery thermal management system for electric vehicles. *Appl Therm Eng* 149:192–212
8. Jana A, Saha R, Pal D, Sarkar S, Mukhopadhyay S (2023) Early detection and management of thermal runaway in batteries using water mist for air precooling. *Int J Energy Clean Environ* 24(4)
9. Jilte RD, Kumar R, Ma L (2019) Thermal performance of a novel confined flow Li-ion battery module. *Appl Therm Eng* 146:1–11
10. Al-Hallaj S, Selman J (2000) A novel thermal management system for electric vehicle batteries using phase-change material. *J Electrochem Soc* 3231
11. Wang X, Xie Y, Day R, Wu H, Hu Z, Zhu J, Wen D (2018) Performance analysis of a novel thermal management system with composite phase change material for a lithium-ion battery pack. *Energy* 156:154–168
12. Bai FF, Chen MB, Song WJ, Li Y, Feng ZP, Li Y (2019) Thermal performance of pouch Lithium-ion battery module cooled by phase change materials. *Energy Procedia* 158:3682–3689

13. Choudhari VG, Dhoble AS, Panchal S (2020) Numerical analysis of different fin structures in phase change material module for battery thermal management system and its optimization. *Int J Heat Mass Transf* 163:120434
14. Weng J, Yang X, Zhang G, Ouyang D, Chen M, Wang J (2019) Optimization of the detailed factors in a phase-change-material module for battery thermal management. *Int J Heat Mass Transf* 138:126–134
15. Ozisik MN (1993) *Heat conduction*. Wiley, New York

Thermal and Hydraulic Study of Mini-Channel with Irregular Surface Topology



Vishwajeetsinh Rahevar, Prayag Desai, Sheetal Pandya, Amit Arora,
and Niraj Shah

Nomenclature

m_f	Mass flow rate [m ³ /s]
Re	Reynolds number-
D_h	Average channel hydraulic diameter [m]
A	Average channel cross-section area [m ²]
d_i	Inlet plenum diameter[m]
d_o	Outlet plenum diameter[m]
l	Length of channel[m]
L	Length of substrate[m]
w	Width of channel [m]
W	Width of substrate[m]
h	Height of channel[m]
H	Height of substrate[m]
q	Heat flux[w/m ²]
ΔP	Pressure drop between inlet and outlet plenums [N/m ²]
ΔT	Temperature rise of water[K]
h	Heat transfer coefficient [W/m ² K]
f	Fanning friction factor -
i	Running index

V. Rahevar · P. Desai · N. Shah (✉)
Department of Mechanical Engineering, Nirma University, Ahmedabad, India
e-mail: niraj.shah@nirmauni.ac.in

S. Pandya · A. Arora
Department of Material Science and Engineering, Indian Institute of Technology, Gandhinagar,
India

1 Introduction

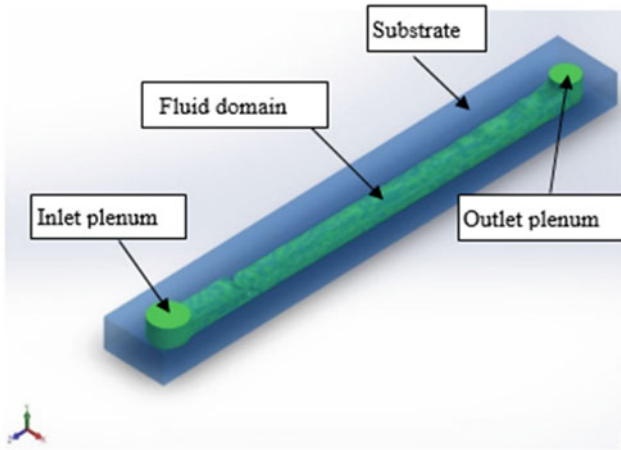
Day by day with the development of hardware and software of computational resources, heat dissipation problem is becoming bottleneck in its further advancements. To cater this need, various researches are going on and out of that one of the areas is to enhance the heat dissipation from such devices using mini- and micro-channel heat sinks (MCHSs). The developments in this area are occurring at a faster rate since last decade with development of such channels by Tuckerman and Pease [1]. Use of MCHS has been proved to be promising for removing heat fluxes from microprocessor units of computers.

2 Literature Review and Objective

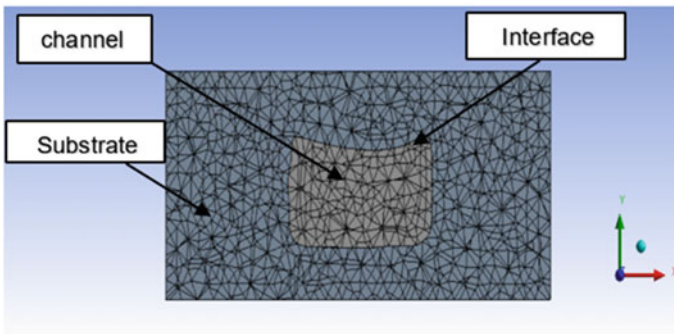
Various studies have claimed for heat dissipation rate of 2×10^6 – 4×10^6 Watts/m² [2, 3]. MCHS due to its high surface area-to-volume ratio helps in removal of high heat flux [4]. The growth of various fabrication techniques and methodologies contributed a lot in fabrication of MCHS [5, 6]. This has led to active research related to hydraulic and thermal aspects of the single-phase and multiphase flows for different flow regimes. [7, 8]. Many researchers studied single-phase and multiphase flow and thermal characteristics using regular shaped channels in continuum and rarefied flow regimes [9–11]. Many of them worked on single-phase heat enhancement techniques [12, 13]. However, such studies using mini-channels with irregular surface topology is found to be very limited. Thus, it is motivated to carry out study of such mini-channel, and the objectives of present work are (i) to carry out numerical investigations of fluid flow and heat transfer for single-phase flow mini-channel with irregular surface, (ii) to analyse the effect of different mass flow rate, (iii) to determine the critical Reynolds number at which flow transits to turbulent flow.

3 Numerical Modelling

Figure 1 (a) shows the CAD model of mini-channel with irregular surface. It can be observed from the figure that geometry includes inlet and outlet plenums, substrate, and irregular shaped mini-channel. The diameter of inlet (d_i) and outlet plenum (d_o) is 8 mm and 6 mm, respectively. The height of the both plenums is kept as 4 mm from the base of channel base. The hydraulic diameter of the channel is found to be 4–2 mm which varies non-uniformly along its length. The average cross-sectional area of the channel (A) is 11.17 mm². Other data related to geometric parameters of the channel used in the present work are mentioned in an abstract. Water is used as working fluid.



(a)



(b)

Fig. 1 CAD model of (a) mini-channel with substrate and (b) cross-sectional view of mini-channel with grid

ANSYS meshing is used to discretize the computational domain of the mini-channel. Due to channel irregularity, unstructured tetrahedral mesh (Fig. 1 (b)) is used with maximum grid size 0.6 mm which ended up with total 460,030 cells. Numbers of nodes generated are 666,490. Simulations are performed using ANSYS Fluent. Mass, momentum, and energy equations are solved under steady-state condition. As due to irregular surface turbulence occurs at low Reynolds number, standard $k-\epsilon$ turbulence model is applied to model turbulent flow. Conjugate model is used to account for heat exchange between solid and fluid. For this mesh interface is coupled to solve conduction equation in substrate domain and convection equation in fluid domain. The SIMPLE scheme is used to resolve pressure-velocity coupling. The implicit pressure-based solver is used with first-order upwind scheme. Convergence criteria for continuity, x, y, and z velocities are kept as 10^{-3} , while for energy, it is kept at 10^{-5} . Mass flow rate and outflow boundary conditions are applied at inlet

Table 1 Temperature difference between inlet and outlet of mini-channel with mass flow rate

Mass flow rate (kg/sec)	Experimental temperature difference (K)	Numerical temperature difference (K)	% Error
0.00130	26.08	28.30	8.51
0.00442	7.58	7.99	5.40

and outlet. Bottom wall is modelled as convection boundary condition with heat flux of 200W, whereas other walls are kept adiabatic. To study the hydrodynamic and thermal characteristic of such irregular surface, simulations are performed at four mass flow rates, i.e. 0.0013, 0.0026, 0.0039, and 0.00494 kg/sec.

4 Results and Discussion

4.1 Validation

Simulation and experimental results of the temperature difference (ΔT) between the outlet and inlet are tabulated in Table 1. From the data of two mass flow rate, it is depicted that simulation results are matching within 10% with experimental one. Thus, the numerical model applied in the present work is in good agreement with the actual conditions.

4.2 Velocity Distributions

In order to explore the hydrodynamic behaviour of fluid inside the mini-channel with irregular surface topology, stream-wise velocity contour along the channel length at $x/W = 0.5$ is plotted in Fig. 2.

From velocity contour at inlet, it can be seen that velocity of water increases rapidly when the water enters from an inlet plenum to the channel interior due to sudden contraction. This is alike when the water flows through an orifice creating a vena contracta at the downstream of the orifice. Hence, for this case too, vena contracta occurs at the interior of channel near to the end of inlet plenum. Similar effect due to inlet plenum was also noted by Sahar et al. [14]. Further velocity increases with increase in length due to reduction in the cross-section area and the velocity suddenly jumps to higher value due to sudden contraction in the channel. After contraction, the contours of velocity almost remain similar, so it can be said that the flow became developed after this length. From the velocity contour, it can be also noted that nearer to outlet plenum, the velocity gets decreases as the flow is expanding due to increase in the area in this zone. When the surface irregularities along the channel length is found intermediately at that locations, flow gets disturbed.

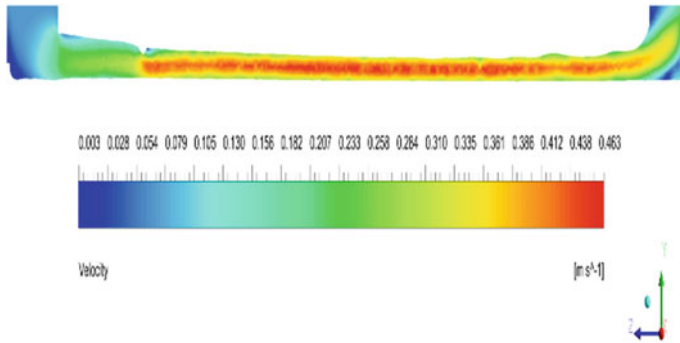


Fig. 2 Velocity contours along the channel length at $x/W = 0.5$ for mass flow rate 0.00338 kg/sec

4.3 Pressure Distributions

High-pressure drops in mini and micro-channels have been reported in past [15]. Pressure contours at along the channel length at location $x/W = 0.5$ are shown in Fig. 3. Pressure decreases along the channel length. Here, pressure drop observed is high accounting to the various head losses observed due to bends in flow at inlet and outlet, sudden contraction near inlet, and roughness of the surface. Negative pressures are obtained in outlet region as zero-gauge pressure is applied at the inlet. The pressure contours obtained validate the Bernoulli's effect as with flow restrictions (due to sudden contraction and channel irregularities) pressure drop increases.

Figure 4 shows that as mass flow rate increases, the pressure drop also increases nonlinearly due to increase in inertia of flow.

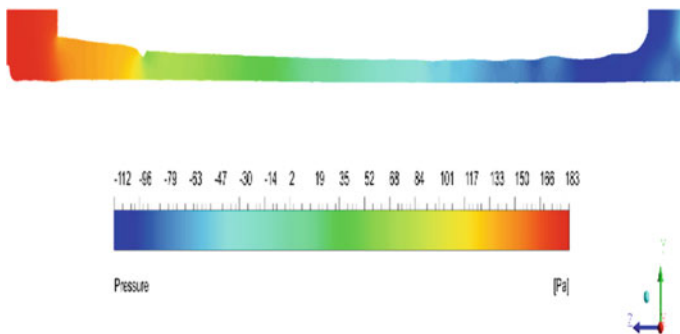
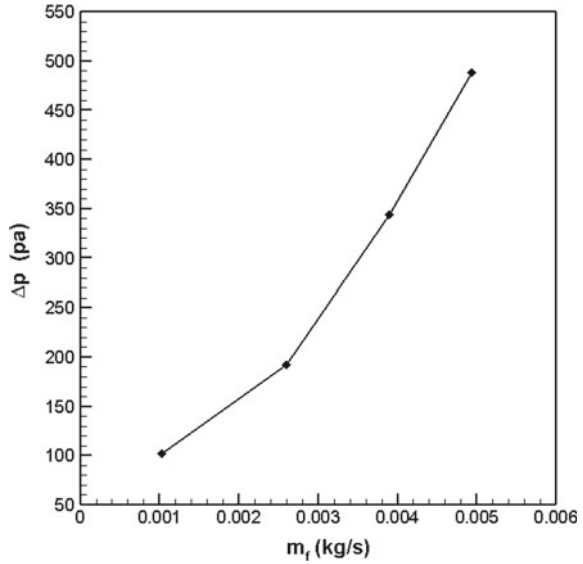


Fig. 3 Pressure contours along the channel length at $x/W = 0.5$ for mass flow rate 0.00338 kg/sec

Fig. 4 Effect of variation of the mass flow rate on the pressure drop



4.4 Temperature Distributions

The temperature contours for a particular mass flow rate are plotted in Fig. 5. Due to heat transfer from bottom wall, temperature of water increases as it flows through the mini-channel.

The temperature drop between outlet and inlet is found to be 308 K. The temperature drop obtained using simulation is validated with the experimental results; thus, it proves that the modelling of conjugate heat transfer is done effectively.

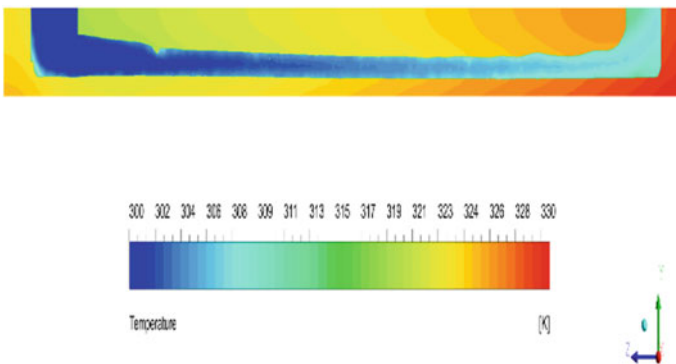
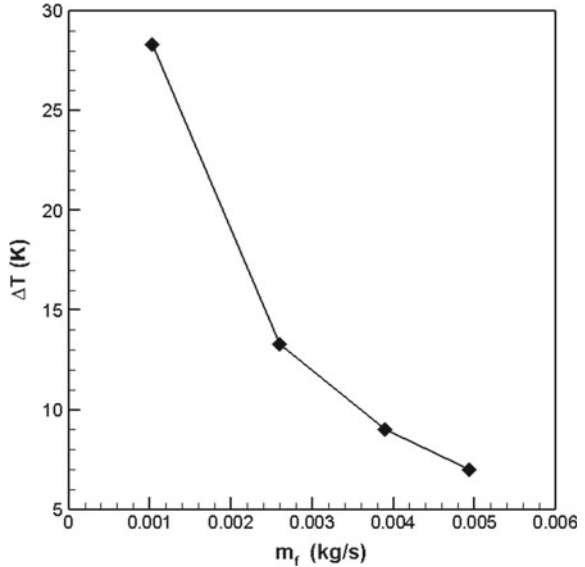


Fig. 5 Temperature contours along the channel length at $x/W = 0.5$ for mass flow rate 0.00338 kg/sec

Fig. 6 Effect of variation of the mass flow rate on the temperature difference



Due to irregularities, thermal boundary layer disturbs very often not allowing flow to become thermally developed. It can be observed from the contour that the temperature in solid in axial direction does not remain constant. This is termed as axial back conduction as heat is flowing in reverse direction to that of convective heat transfer in the fluid flow, i.e. from outlet to inlet. This is the cause to offset constant heat flux condition at interface.

The effect of increase of mass flow rate on temperature drop is plotted in Fig. 6. It is found that with increase in mass flow rate, temperature gained by the water decreases nonlinearly.

4.5 Heat Transfer Coefficient

Heat transfer coefficient generally increases with increase in Reynolds number (mass flow rate) in laminar regime while remains nearly constant in turbulent regime. Figure 7 presents variation of heat transfer coefficient with the mass flow rate. It can be inferred that as mass flow rate increases, the heat transfer coefficient also increases; however, after mass flow rate of 0.0039, the rise in heat transfer coefficient is less which depicts the fall of transition regime in between mass flow rates 0.0025 and 0.0045 kg/sec (i.e. between Reynolds numbers 900 and 1500).

Data for the comparison of rise of pressure and heat transfer coefficient with increase in the mass flow rate are tabulated in Table 2. Here, the ratio of mass flow rate represents the mass flow rate of next case (presented using variable i) with the initial case (presented using variable 1). Similarly, the ratio of pressure drop and

Fig. 7 Variation of heat transfer coefficient with mass flow rate

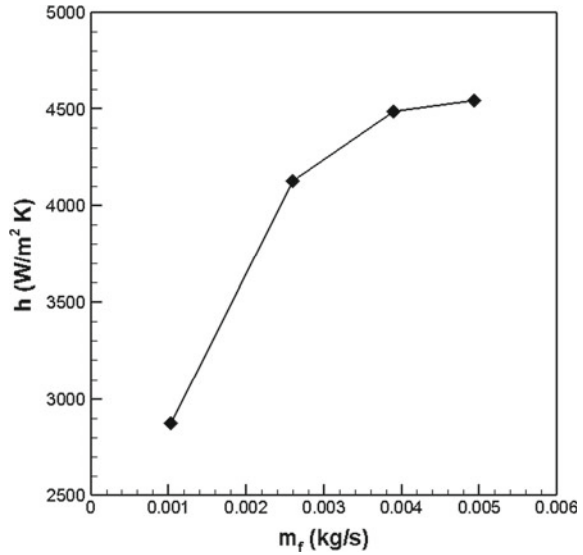


Table 2 Effect of increase in the mass flow rate on increase in the pressure and heat transfer coefficient

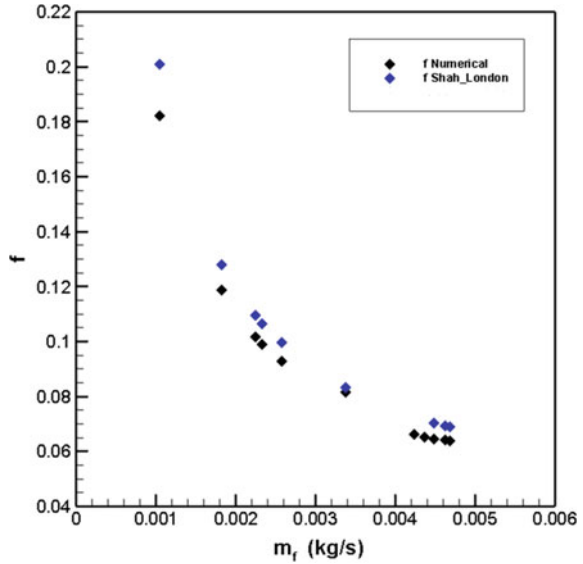
Mass flow rate ratio (m_{f_i}/m_{f_1})	Pressure ratio P_i/P_1	Heat transfer rate h_i/h_1
1	1	1
2.52	1.89	1.43
3.78	3.37	1.55
4.79	4.79	1.57

heat transfer coefficient are defined. It can be inferred from results that with increase in the mass flow rate, rate of heat transfer does not increase as the pumping power requirement increases due to rise in the pressure drop. This may be due to involvement of the inlet and outlet plenums which play a role in increasing the pressure drop due to entrance, exit, and bends, whereas the effect of plenum on the heat transfer coefficient is limited. Also, over and above it, due to irregular surface topology, the flow resistance and surface roughness increase which affect the pressure drop more as compared to the heat transfer coefficient.

4.6 Friction Factor

The variation of heat transfer coefficient with the mass flow rate depicted that flow regime changes from laminar to transition for the mass flow rate where Reynolds number is below 2300 (critical Reynolds number for pipe flow). In order to find the

Fig. 8 Variation of friction factor with mass flow rate and comparison with correlation proposed by Shah and London [16]



critical Reynolds number, more simulations are carried out in between the mentioned mass flow rates in Sect. 2. The behaviour of friction factor with mass flow rate is studied using Fig. 8. It is notable that initially friction factor decreases asymptotically with increase in the mass flow rate referring to the laminar regime. However, after then with further increase in mass flow rate, friction factor tends to remain almost constant which refers to the turbulence regime. The transition regime observed from the figure falls between the mass flow rates 0.0026 kg/sec and 0.0040 kg/sec (i.e. between Reynolds numbers 1000 and 1500). The results of the friction factors are verified with an analytical solution given by Shah and London [16] for developing laminar flow inside non-circular duct. Similar methodology to predict transition regime is adopted by many researchers [17, 18].

5 Conclusions

Numerical investigation is carried out to determine the fluid flow and thermal characteristics for mini-channels with irregular surfaces. From the study, the following conclusions are derived:

- i. The convective heat transfer coefficient is observed to increase with the increase in the mass flow rate; however, the increase in the pressure drop supersedes it. Such characteristic is accounted for the flow restrictions in passage in terms of surface irregularities and sudden change in geometry of channel (viz., sudden contraction and expansion).

- ii. The transition is found early for the case of mini-channel with irregular surfaces at low Reynolds number ranging from 1000 to 1500, whereas for conventional channels, it is nearly about 2300.

Early transition and irregular surface topology has attributed to removal of high heat rates using these mini-channels.

References

1. Tuckerman, D. B., and Pease, R. F. W. "High-performance heat sinking for VLSI." *IEEE Electron device letters* 2, Vol. EDL-2, No. 5 (1981): pp. 126–129.
2. Karayiannis TG, Mahmoud MM (2017) Flow boiling in microchannels: Fundamentals and applications. *Appl Therm Eng* 115:1372–1397
3. Kandlikar, S. G., Garimella, S., Li, D., Colin, S., and King, M. R. "Heat transfer and fluid flow in minichannels and microchannel. Elsevier, (2005).
4. Fan Y, Luo L (2008) Recent Applications of Advances in Microchannel Heat Exchangers and Multi-Scale Design Optimization. *Heat Transf Eng* 29(5):461–474
5. Satish G. Kandlikar and William J. Grande, "Evolution of Microchannel Flow Passages Thermohydraulic Performance and Fabrication Technology", *Heat Transfer Engineering* Vol 24, 2003 – Issue 1
6. Ghani IA, Sidik NAC, Kamaruzaman N (2017) Hydrothermal performance of microchannel heat sink: The effect of channel design. *Int J Heat Mass Transf* 107:21–44
7. Steinke, M. E., and Kandlikar, S. G. "Single-phase heat transfer enhancement techniques in microchannel and minichannel flows." *Proceedings of ASME ICMM2004. ICMM2004–2328*: pp. 141–148. Rochester, NY, June 1719, 2004.
8. Kandlikar SG (2002) Fundamental issues related to flow boiling in minichannels and microchannels. *Exper. Therm. Fluid Sci.* 26:389–407
9. Agrawal A (2011) A comprehensive review on gas flow in microchannels. *Int. J. Micro-Nano Scale Transp.* 2(1):1–40
10. Agarwal RK, Yun KY, Balakrishnan R (2001) Beyond Navier-Stokes Burnett equations for flows in the continuum transition regime. *Phys Fluids* 13:3061–3085
11. Lee P-S, Garimella SV (2006) Thermally developing flow and heat transfer in rectangular microchannels of different aspect ratios. *Int J Heat Mass Transf* 49(17–18):3060–3067
12. Steinke ME, Kandlikar SG (2004) Review of single-phase heat transfer enhancement techniques for application in microchannels, minichannels and microdevices. *Heat and Technology* 22(2):3–11
13. M.E. Steinke, S.G. Kandlikar, "Single-Phase Liquid Heat Transfer in Plain and Enhanced Microchannels" *Proceedings of Fourth International Conference on Nanochannels, Microchannels and Minichannels, Limerick, Ireland, 2006.*
14. A. M. Sahar, J. Wissink, M. M. Mahmoud, T. G. Karayiannis, and M. S. Ashrul Ishak, "Effect of hydraulic diameter and aspect ratio on single phase flow and heat transfer in a rectangular microchannel," *Appl. Therm. Eng.*, vol. 115, pp. 793–814, 2017.
15. Hwang YW, Kim MS (2006) The pressure drops in microtubes and the correlation Development. *Int. J. Heat Mass Transfer* 49:1804–1812
16. Shah RK, London AL (1978) *Laminar Flow Forced Convection in Ducts*. Academic Press, New York
17. Steinke ME, Kandlikar SG (2006) Single-phase liquid friction factors in microchannel. *Int J Therm Sci* 45:1073–1083
18. Dirker J, Meyer JP, Garach DV (2014) Inlet flow effects in micro-channels in the laminar and transitional regime on single-phase heat transfer coefficient and friction factors. *Int J Heat Mass Transf* 77:612–662

Thermo-hydraulic Assessment of Fin Profiles in Internally Finned Tubes



Himanshu Jangid, Amit Arora, and Yatharth Lilhare

1 Introduction

Efforts are being made to maximize the effectiveness of heat exchanging systems. Putting fins inside the tube of a heat exchanger is one way to improve the coefficient of heat transmission and in turn, the heat exchanger's efficiency [1]. They provide additional heat transfer surface and reduce thermal boundary layer to enhance heat transfer, which make heat exchanger more compact and cost efficient. Also, they must be operated with clean working fluid or fluid with nearly no contaminants for optimal performance.

2 Literature Review and Objective

To achieve the best results, fin geometry must be defined under a variety of operating conditions. Several experiments and studies have been conducted on internally finned tubes, in order to compute the pressure drop, frictional factor, and heat transfer coefficient. To make the flow fully developed, Braga et al. [2] have considered the entry and exit part of the tube unfinned. By varying the velocity pattern, heat transfer improves which was studied by Zeitoun and Hegazy [3], by arranging two successive fins of unequal heights with an even number of fins. Wavy finned tubes were also explored to study laminar convective heat transfer performance using air as a working fluid and with varying the Reynolds number [4]. The consequences of internally star fins with varying fin numbers and configurations are studied by Khanmohammadi et al. [5]. Many researchers have also focused on using different types of fluids, for example, Choi et al. [6] studied the same but with refrigerants, such as R134a and

H. Jangid (✉) · A. Arora · Y. Lilhare
Department of Mechanical Engineering, MNIT Jaipur, Jaipur 302017, India
e-mail: 2019ume1729@mnit.ac.in

R12, and Wang et al [7] studied with water–ethylene–glycol. A significant rise in the heat transfer coefficient has been found in every study that had used internal fins, and nearly all of these studies provided convincing justifications for their findings.

In this study, we present a similar case as presented by Bellos et al. [8], using three geometries for the internal fins, triangular, annular-sector, and curved but with a change in the design of the fins. Rather than having fins with intermittent spacing between them, we create fins on the entire internal surface of the tube to fully utilize the surface area available for heat transfer and hence increase in heat transfer coefficient.

The objective of this assessment is to determine the optimal configuration of an internally longitudinal finned tube in order to improve the coefficient of heat transmission and pressure drop. Optimal configuration depends upon the shape of fins, number of fins, and fin height. The impacts of all these parameters are examined by varying them within a predetermined range to find the best value. The optimized configuration of the tube is then examined under turbulent flow by varying Reynolds number to obtain the optimal condition to operate this tube too. Performance Evaluation Criteria were used to figure out which tube did the best out of all the ones that were examined.

3 Numerical Model

The numerical simulation employs a two-equation model, i.e., the standard k – ε model [9]. It is one of the most widely used CFD models. Utilizing two transport equations, this model provides a description of turbulence. The first transported variable is turbulent kinetic energy (k), and the second is the rate of dissipation of turbulent kinetic energy (ε). This study employs an enhanced wall treatment with thermal and pressure gradient effects as the wall function. The Semi-Implicit Method for Pressure-Linked Equations (SIMPLE) algorithm is utilized for pressure–velocity coupling. The spatial discretization of all variables is modeled using a second-order upwind scheme, and convergence criteria are met when the residual of the energy equation is 10^{-8} and other governing equations are 10^{-5} .

3.1 Geometrical Model

Three tubes with curved, triangular, and annular-sector geometries of internal fins are analyzed at same surface area nearly equal to 1536 mm^2 and pitch diameter $D_p = 5 \text{ mm}$. Length of all the tubes $L = 75 \text{ mm}$ and outer diameter $D_o = 5.5 \text{ mm}$. Apart from this, number of fins in curved-finned tube is varied from 18 to 42 with the step increment of six fins. For smooth tube (without fins), length $L = 75 \text{ mm}$, $D_i = 5 \text{ mm}$, and $D_o = 5.5 \text{ mm}$ (Fig. 1).

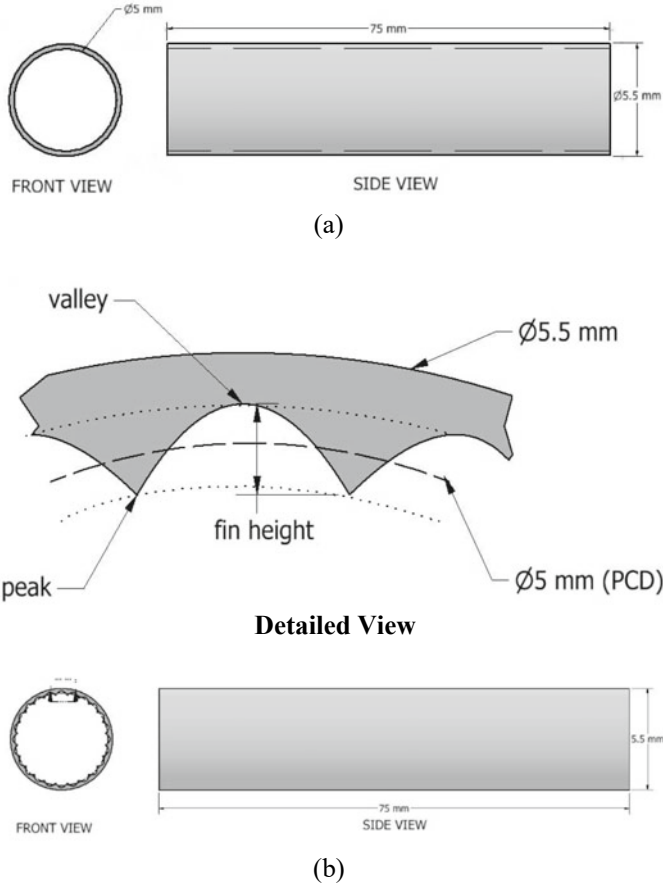


Fig. 1 Orthographic projection **a** Smooth tube, **b** curved-finned tube

3.2 Mesh Generation

The mapped mesh is used for the entire domain for the respective analysis because it only contains hexahedral elements and hexahedral elements produce more accurate solutions than their tetrahedral counterpart. Figures 2 and 3 depicts a cross-section area of a mesh of all four tubes.

3.3 Boundary Conditions

Water is taken as a working fluid, with its all properties into consideration. Material of the tube is aluminum with the constant wall temperature 353 K. Analysis of all

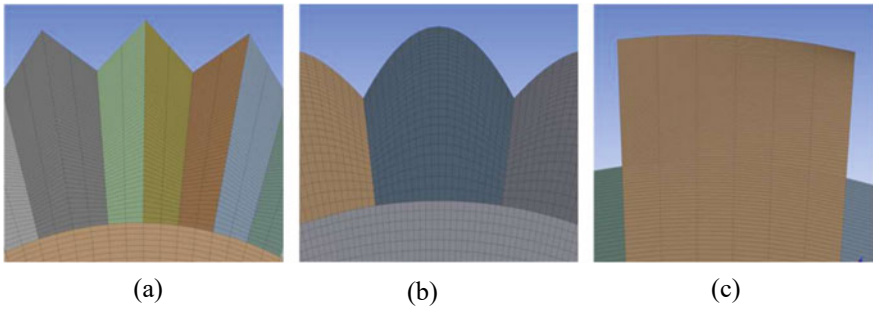


Fig. 2 Mapped mesh **a** Triangular fin, **b** curved fin, **c** annular-sector fin

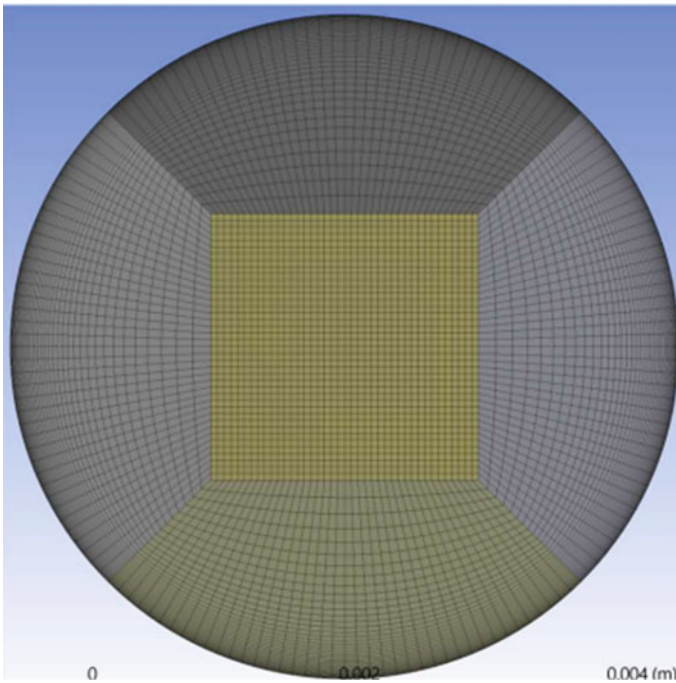


Fig. 3 Mapped mesh of smooth tube

cases is done at a fixed Reynolds number, i.e., $Re = 10,000$. Velocity at the inlet of each tube is determined from the hydraulic diameter (D_h) of the same tube (Table 1).

$$D_h = \frac{4A_c}{P_w}, \quad (1)$$

$$R = \frac{\rho v D_h}{\mu}. \quad (2)$$

Table 1 Boundary conditions

Physical boundary	Fluid flow B.C	Thermal B.C
Tube inlet	Velocity	Temperature
Tube outlet	Outflow	Outflow
Wall	No slip	Temperature

3.4 Model Validation

Using the Dittus–Boelter equation [10], model verification for all three types of serrated tube is conducted for the convective heat transfer coefficient. The graph shown in Figs. 4 and 5 compares the numerical value of the heat transfer coefficient to the value calculated using the Dittus–Boelter equation for triangular serrated tube and rest are not shown due to space limitation. By comparing the experimental and numerical values, we find that they are reasonably close. Hence, it proves that the chosen calculation method and its boundary condition can reliably predict the outcomes of the serrated tubes.

$$\frac{hD_h}{K_f} = Nu = 0.023Re^{0.8}Pr^{0.4}. \tag{3}$$

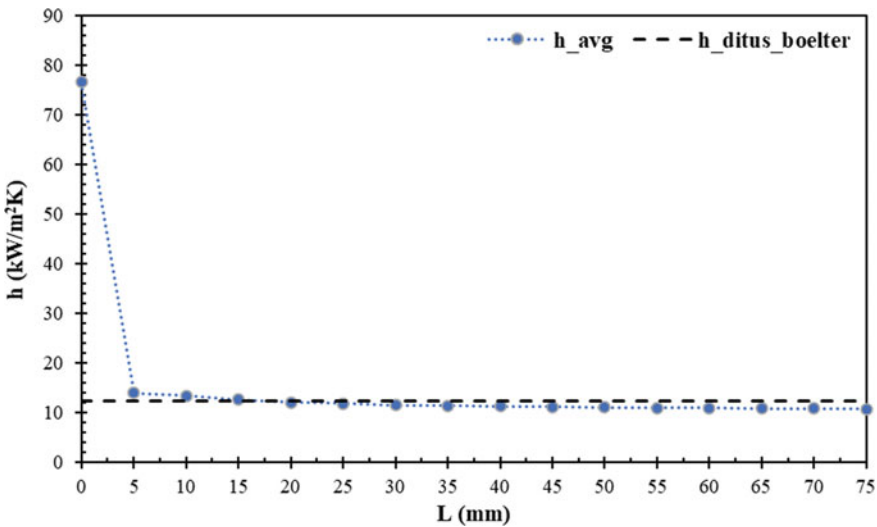


Fig. 4 Model validation

4 Results and Discussion

In this section, the effect of fin profile, number, height, width, and Reynolds number on the heat transfer properties of straight internal finned tubes is studied. Performance Evaluation Criteria (PEC) are used to choose best option from the rest.

$$PEC = \frac{\left(\frac{h}{h_o}\right)}{\left(\frac{\Delta P}{\Delta P_o}\right)^{\frac{1}{3}}} \tag{4}$$

4.1 Effect of Fin Shape

Figure 6 shows the impact of fin shape on the coefficient of heat transmission and pressure loss along the tube’s axial length. Surface area and pitch diameter remain constant across all shapes. It can be seen from Fig. 5 that the triangle-finned tube has the greatest increase in heat transfer coefficient. The entering fluid flow has the greatest effect on the sharp angles of triangular fins, which considerably improves heat transmission in the region. But, PEC is maximum for the curved fins as shown in Fig. 6; hence, curved-finned tube is selected for the further study.

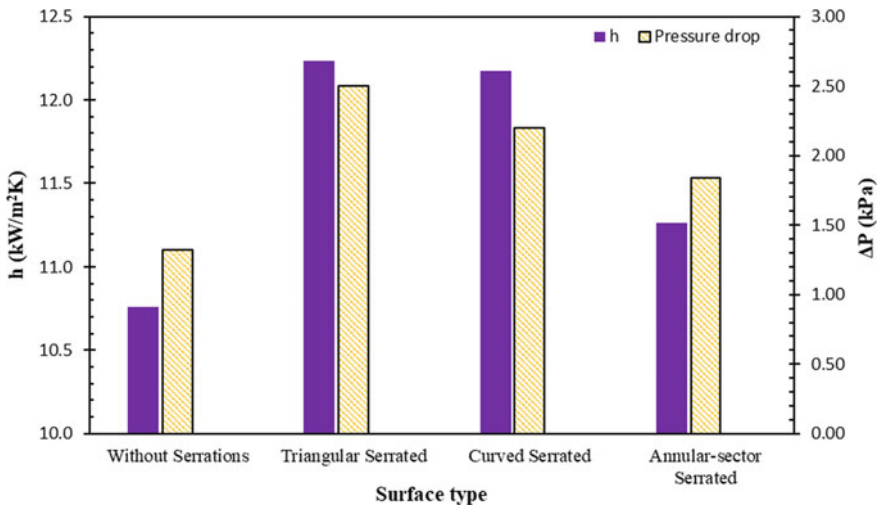


Fig. 5 Comparison of coefficient of heat transmission and pressure drop for different types of geometries

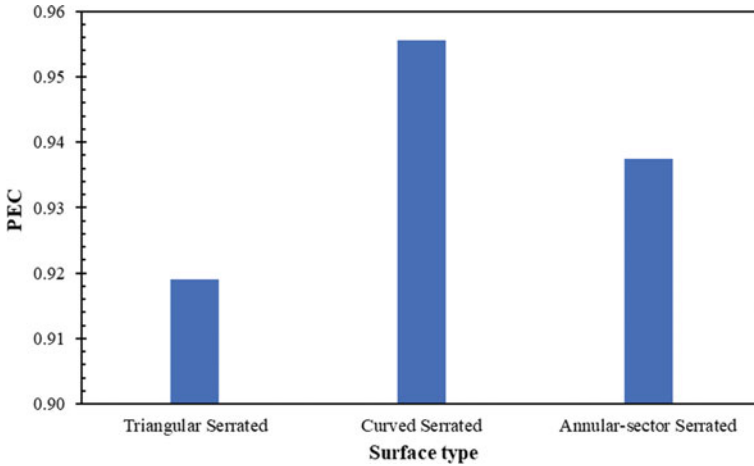


Fig. 6 Comparison of PEC for different fin geometries

4.2 Effect of Fin Numbers

In this section, we would find the optimal number of fins in the tube. For that, we did study on tubes with 18, 24, 30, 36, and 42 fins, keeping all the other parameters same. As described by Liu et al. [1], at the corners, there was a great energy loss due to the convective heat transfer and pressure loss being maximum. Due to the increase in fin numbers, the number of corners increases that result in increase in shear stress which ultimately increases pressure drop. More number of fins means greater surface area for heat transfer which increases heat transfer coefficient as shown in Fig. 9. From Fig. 10, we observed that there will be an optimal number of fins for a tube. After which, with the increase in fin numbers, fluid flow counters greater obstruction; the fluid viscosity at the fin tips decreases; the boundary layer thickens and inhibits heat exchange. Now, the pressure drops significantly, and hence, PEC decreases. The discovery yields an optimal condition with 24 fins. Velocity and temperature contours for different number of fins are shown in Figs. 7 and 8, respectively.

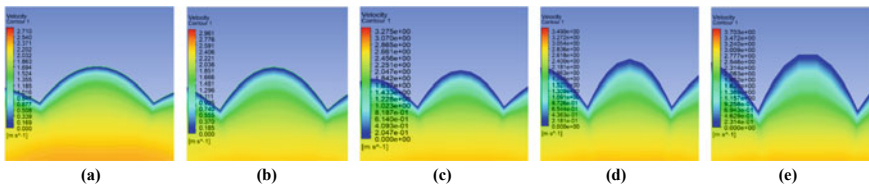


Fig. 7 Velocity contour in developed region of tube a 18 fins, b 24 fins, c 30 fins, d 36 fins, e 42 fins

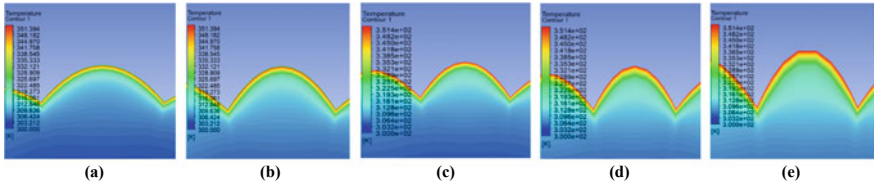


Fig. 8 Temperature contour in developed region of tube **a** 18 fins, **b** 24 fins, **c** 30 fins, **d** 36 fins, **e** 42 fins

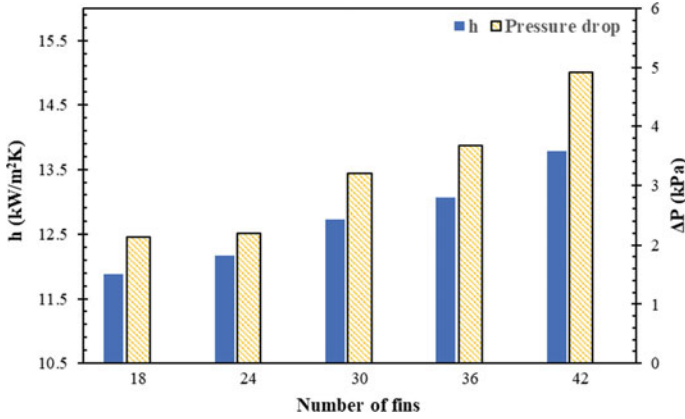


Fig. 9 Comparison of transfer coefficient and pressure drop for different fin numbers

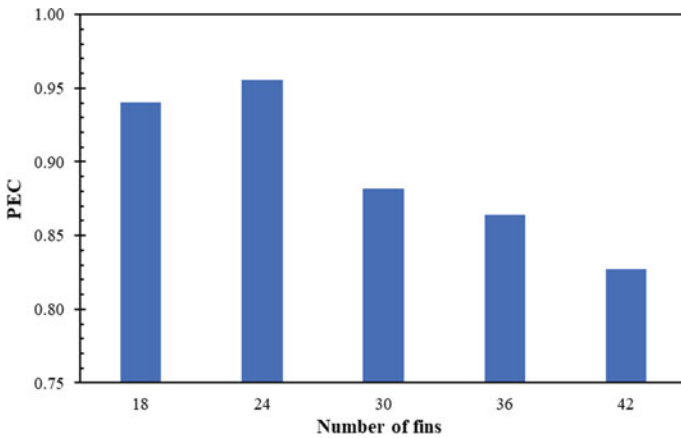


Fig. 10 Comparison of PEC for different fin numbers

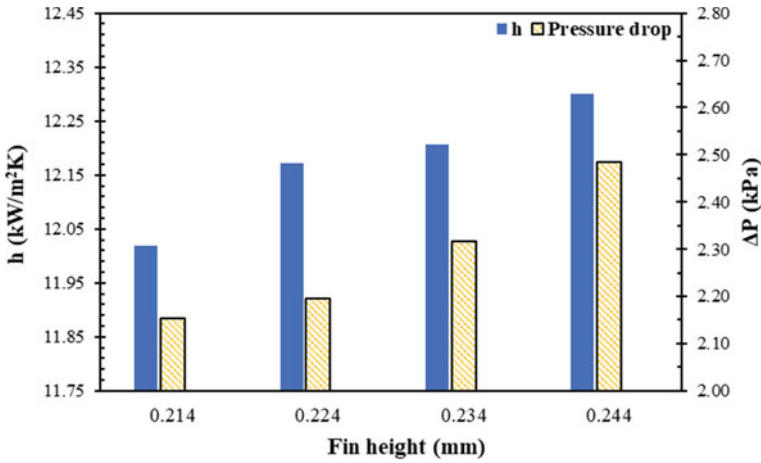


Fig. 11 Comparison of heat transfer coefficient and pressure drop for different fin heights

4.3 Effect of Fin Height

The curved-finned tube with 24 fins (best in Sect. 4.2) is selected for analysis at four different fin heights; 0.214 mm, 0.224 mm, 0.234 mm, and 0.244 mm, respectively. The larger the fin height, the higher the exposed surface on both sides of the fins and the greater the disruption to the fluid flow at the surface of the wall. This results in an increase in the heat transfer coefficient and also the pressure drops as the fin height increases, as depicted below in Fig. 11. But, as the fin height goes up, the Performance Evaluation Criteria gradually falls due to the predominance of pressure drop over the rise in heat transfer coefficient, shown in Fig. 12.

4.4 Effect of Different Reynolds Numbers

Graph shown in Figs. 13 and 14 clearly depicts the variation of coefficient of heat transmission and pressure loss with the Reynolds number. Both go up with the rise in Reynolds number. From the velocity contour also as shown in Fig. 15, we can observe that boundary layer becomes thinner and velocity gradients gradually increase as Reynolds number increases resulting in higher pressure drop. Also, from the temperature contours as shown in Fig. 16, it is quite evident that the boundary layer becomes narrower and temperature gradient increases which enhances coefficient of local heat transmission and hence is augmenting overall heat transmission coefficient.

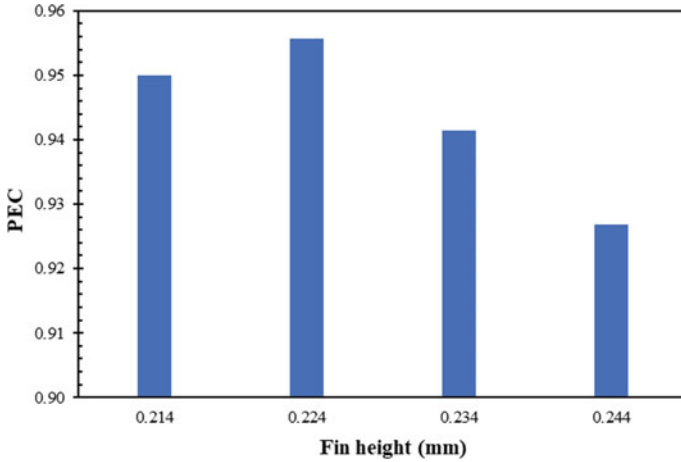


Fig. 12 Comparison of PEC for different fin heights

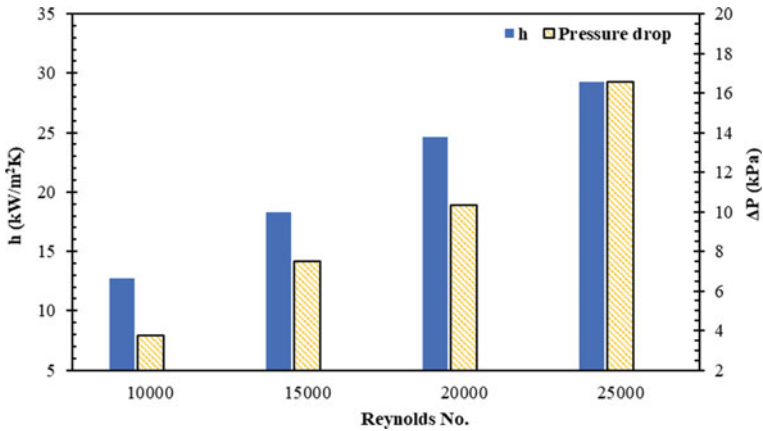


Fig. 13 Comparison of heat transfer coefficient and pressure drop for different Reynolds numbers

5 Conclusions

In this computational study, heat transfer enhancement in internal flows is analyzed by using fins of different geometries. A parametric investigation was carried out to determine the effect of fin type, its height and density, and operating conditions on the heat transfer performance of internally finned tubes. The conclusions of this study are as follows:

- (a) Compared to their triangular and annular-sector counterparts, curved-finned tubes are clearly superior. Fins' increased efficiency at transferring heat is a result of their geometry, which features sharp ends.

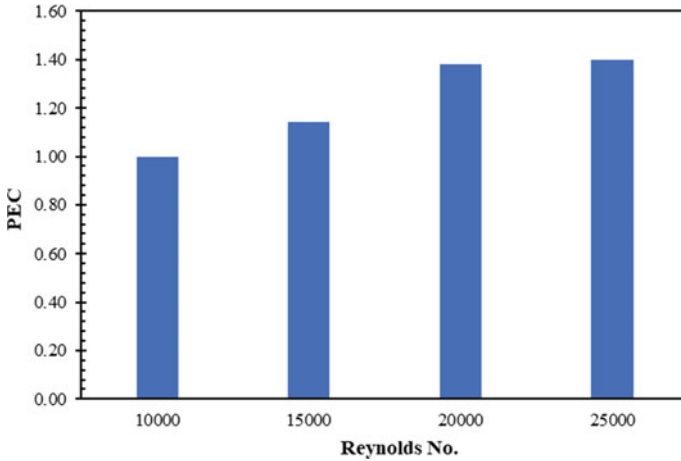


Fig. 14 Comparison of PEC for different Reynolds numbers

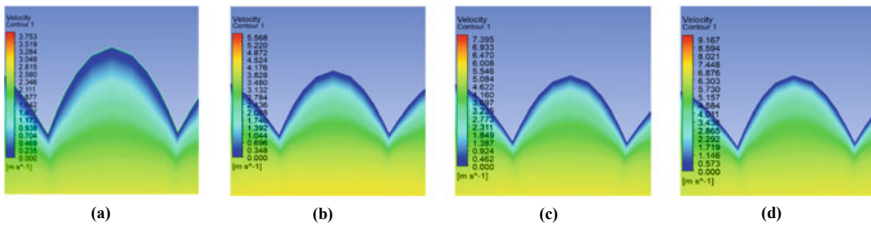


Fig. 15 Velocity contour in developed region of tube with Reynolds no. a 10,000, b 15,000, c 20,000, d 25,000

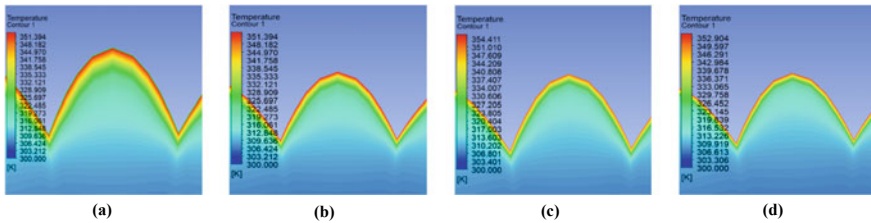


Fig. 16 Temperature contour in developed region of tube with Reynolds no. a 10,000, b 15,000, c 20,000, d 25,000

(b) Both the pressure drop and the coefficient of heat transmission increase with increasing fin number, but once the optimal number of fins is reached, the pressure drop starts to dominate and the Performance Evaluation Criteria begins to decrease. As a result, out of all the tubes with different fin numbers, tube with 24 fins is the best option.

- (c) As the fin height increases, convective heat transfer coefficient and pressure drop both have increased.
- (d) As Reynolds number had gone up, the heat transfer coefficient and pressure drop, both, have increased simultaneously. This has caused Performance Evaluation Criteria to go up.

Nomenclature

A_c	Cross-section area of tube	[m ²]
a	Fin height	[m]
D	Diameter of tube	[m]
D_h	Hydraulic diameter of tube	[m]
h	Average convective heat transfer coefficient	[W/m ² K]
h_s	Local convective heat transfer coefficient	[W/m ² K]
h_o	Convective heat transfer coefficient of reference tube	[W/m ² K]
K_f	Thermal conductivity of fluid	[W/m K]
L	Length of tube	[m]
Nu	Nusselt number of fluids	
PCD	Pitch Circle Diameter	[m]
Pr	Prandtl number of fluids	
ΔP	Pressure drops	[Pa]
ΔP_o	Pressure drops in reference tube	[Pa]
PEC	Performance Enhancement Criteria	
Re	Reynolds number	
v	Velocity of fluid	[m/s]
μ	Dynamic viscosity of fluid	[Pa-s]
ρ	Density of fluid	[Kg/m ³]

References

1. Liu Z, Yue Y, She L, Fan G (2019) Numerical analysis of turbulent flow and heat transfer in internally finned tubes. *Front. Energy Res* 7:64
2. Braga CVM, Saboya FEM (1999) Turbulent heat transfer, pressure drop and fin efficiency in annular regions with continuous longitudinal rectangular fins. *Exp Thermal Fluid Sci* 20:55–65
3. Zeitoun O, Hegazy AS (2004) Heat transfer for laminar flow in internally finned pipes with different fin heights and uniform wall temperature. *Heat Mass Transf* 40:253–259
4. Lin M, Tian L, Wang QW (2011) Laminar heat transfer characteristics of internally finned tube with sinusoidal wavy fin. *Heat Mass Transf* 47:641–653
5. Khanmohammadi F, Farhadi M, Ali Rabienataj Darzi A (2019) Numerical investigation of heat transfer and fluid flow characteristics inside tube with internally star fins. *Heat Mass Transf* 55:1901–1911

6. Choi JY, Kedzierski MA, Domanski PA (2001) Generalized pressure drop correlation for evaporation and condensation in smooth and micro-fin tubes, IIF—IIR—Commission B1—Paderborn, Germany—2001/5
7. Wang Y-H, Zhang J-L, Ma Z-X (2018) Experimental study on single-phase flow in horizontal internal helically-finned tubes: the critical Reynolds number for turbulent flow. *Exp Thermal Fluid Sci* 92:402–408
8. Bellos E, Lykas P, Tzivanidis C (2022) Heat and flow study of the internally finned tubes with different fin geometries. *Appl. Syst. Innov.* 5:50
9. Bellos E, Tzivanidis C, Daniil I, Antonopoulos KA (2017) The impact of internal longitudinal fins in parabolic trough collectors operating with gases. *Energy Convers Manage* 135:35–54
10. Çengel Y, Ghajar A (2017) Heat and mass transfer: fundamentals and applications. McGraw-Hills, New York, USA

Loss of Electric Power Supply Transient in an Irradiation Test Loop of HFRR



Amitanshu Mishra, Paban Kumar Guchhait, and Samiran Sengupta

1 Introduction

High flux research reactor (HFRR) is a 40 MW pool type research reactor. It uses low enriched uranium (LEU) U_3Si_2 dispersed in aluminium matrix as fuel and aluminium alloy as clad. The reactor core is cooled using light water which also acts as a moderator. Heavy water is used as reflector in an annular reflector vessel surrounding the reactor core. The reflector vessel has irradiation positions/thimbles for material and fuel testing.

Irradiation test loop (ITL) is a self-contained independent system designed to support various material and fuel tests under simulated light water power reactor conditions. It is a high pressure loop with maximum operating pressure as 17.5 MPa and maximum operating temperature is 330 °C, respectively. The ITL consists of in-pile test section and out-of-pile process system. The test section is located in an irradiation position in the reflector tank. The thermal and the fast flux at the ITL location are of the order of 2×10^{14} n/cm²/s and 2.6×10^{12} n/cm²/s, respectively. In-pile test section provides a pressure boundary enclosure to the test fuel bundles and also a separation between high temperature & high pressure water inside the test section and the pool water. The in-pile test section has an internally insulated pressure tube surrounded by jacket tube. Details of the in-pile test section are shown in Fig. 1. Irradiation samples such as test fuel cluster and materials for irradiation testing are installed in the fuel tube section. The coolant flows through the annulus created by the fuel tube inside the pressure tube; the coolant flows downwards through the outer annulus region between fuel tube and the pressure tube; after reaching the bottom of pressure tube, the flow reverses in the upwards direction through the fuel tube where the irradiation sample is located to remove nuclear heat generated during reactor

A. Mishra (✉) · P. K. Guchhait · S. Sengupta
Research Reactor Design and Projects Division, Bhabha Atomic Research Centre, Trombay,
Mumbai 400085, India
e-mail: mishraa@barc.gov.in

operation. The in-pile components are made of Zircaloy (Zirconium tin alloy) for better neutron economy.

Out-of-pool section consists of various process systems (such as main loop system, purification and sampling system, pressurizer system, jacket coolant system, etc.), piping and equipment necessary to maintain the required temperature, pressure and flow conditions inside the in-pile test section. Process system schematic of the ITL is shown in Fig. 2.

The main loop system of ITL was designed to provide cooling flow up to 4.5 kg/s with heat removal capacity of 800 kW. The cooling medium of main loop system is DM water. Main loop system of ITL mainly comprises of a shell-and-tube heat exchanger, a pressurizer, a canned motor pump and other auxiliary equipment. The main loop system also has a decay heat removal pump for removal of residual heat of irradiation test samples during reactor shut down and off-normal conditions. The decay heat removal pumps are provided with Class II (battery operated) power supply to ensure cooling to the test fuel in the event of Class IV power failure.

The main loop system transfers heat to the Dowtherm cooling system through the shell-&-tube heat exchanger; Dowtherm cooling system is an intermediate cooling system with Dowtherm-A as a cooling medium. It was chosen due to its high boiling point (257 °C) for the system pressure. To regulate temperature of the main loop coolant at the inlet of test section, a flow control valve is provided to regulate flow of Dowtherm coolant to the main loop heat exchanger. The Dowtherm cooling system transfers heat to the secondary cooling system of HFRR which rejects the heat to atmosphere via cooling towers.

Loop heater is provided at the test section inlet to maintain the temperature of loop water at the desired value as per the set point. It is also used for warming up the loop to the required operating temperature during start-ups.

The pressurizer maintains main loop system pressure and accommodates the volumetric changes occurring in the main loop due to temperature changes as well as due to feed or bleed in the system. The system pressure is maintained by generating saturated steam by evaporation of water in the pressurizer vessel using electrical heating elements.

To mitigate the radiological consequences of test fuel failure in the event of loss of coolant accident (LOCA) due to breach of primary loop pressure boundary, a two-stage emergency cooling system (ECS) has been provided which comprises of high pressure light water injection from gas pressurized storage tanks called accumulators and also low pressure water injection by virtue of gravity head from emergency water storage tank (EWST) located at higher elevation in HFRR reactor building. Safety relief valves are also provided in the main loop system for the protection of system equipment and piping during over-pressurization transient.

Loss of normal Class IV electric power supply is identified as one of postulated initiating event (PIE) for evaluation of ITL process system design. In this case, a test fuel is considered being irradiated at ITL and thermal hydraulic analysis is carried out using RELAP5/MOD 3.2 to determine fuel & clad temperatures and thermal margin during loss of power failure.

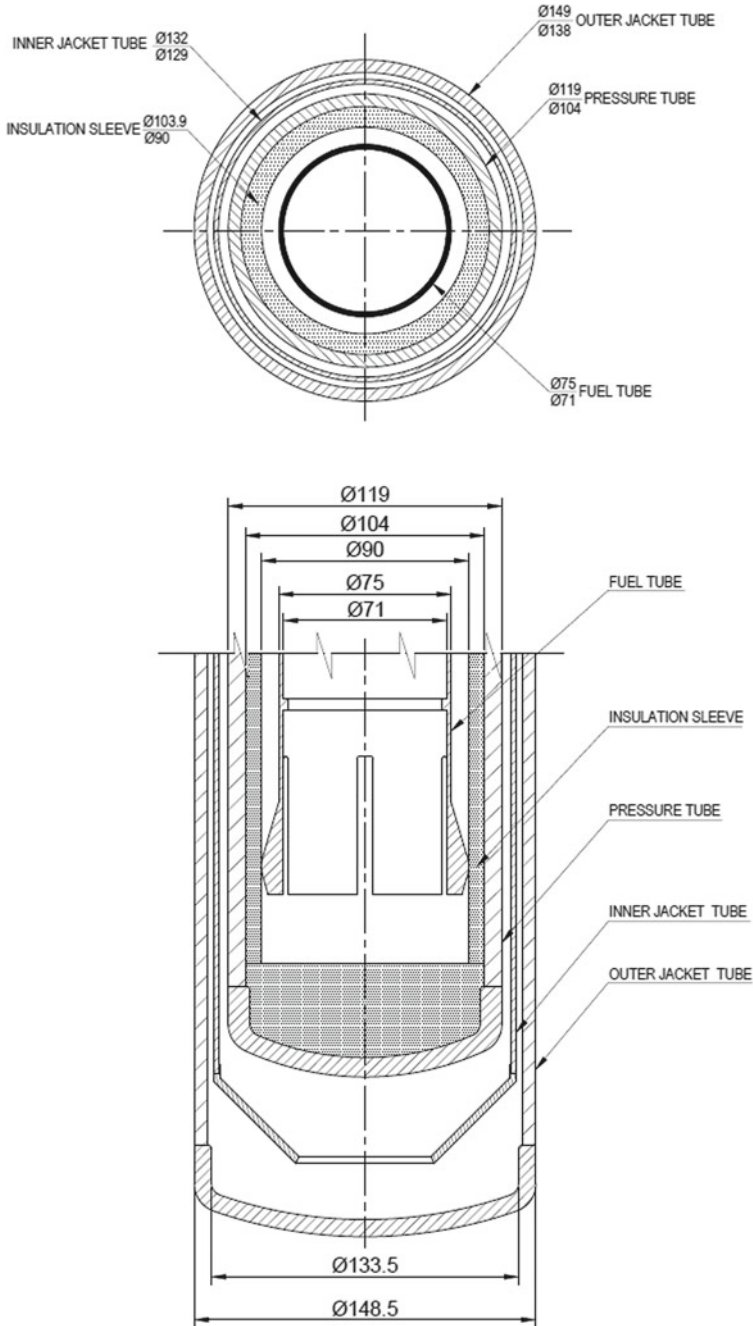


Fig. 1 Section diagram of in-pile test section

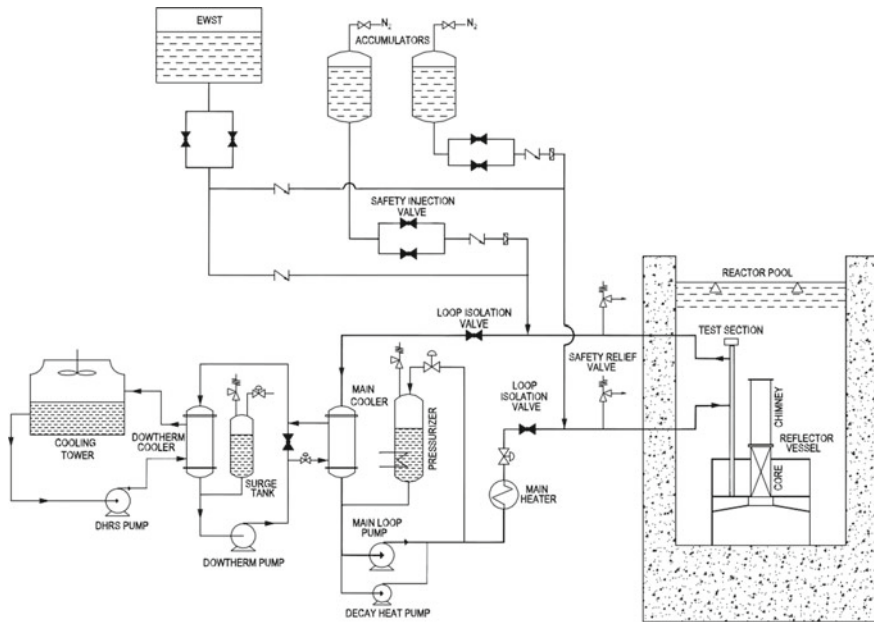


Fig. 2 Schematic diagram of process system of ITL

2 System Modelling

2.1 Test Fuel Details

A test fuel cluster was considered for the qualification study. The fuel pin has Zircaloy-4 clad enveloping the uranium oxide fuel pellets. The fuel cluster has spacers to maintain uniform distance between the fuel pins to allow proper distribution of coolant so that formation of hotspots could be avoided.

2.2 RELAP5 Modelling

Thermal hydraulic analysis is carried out using best estimate code RELAP5/MOD3.2 developed by the Idaho National Engineering Laboratory. The code is extensively used for analyzing transients and postulated accidents in light water reactor systems. It has capability to model the coupled behaviour of the reactor core and the coolant system. It uses a two-fluid, non-equilibrium, non-homogeneous, hydrodynamic model for transient simulation of the two-phase system behaviour [1].

In-pile test section and main loop piping were modelled as PIPE component. Pressurizer is modelled as PIPE component along with heat structures for pressurizer

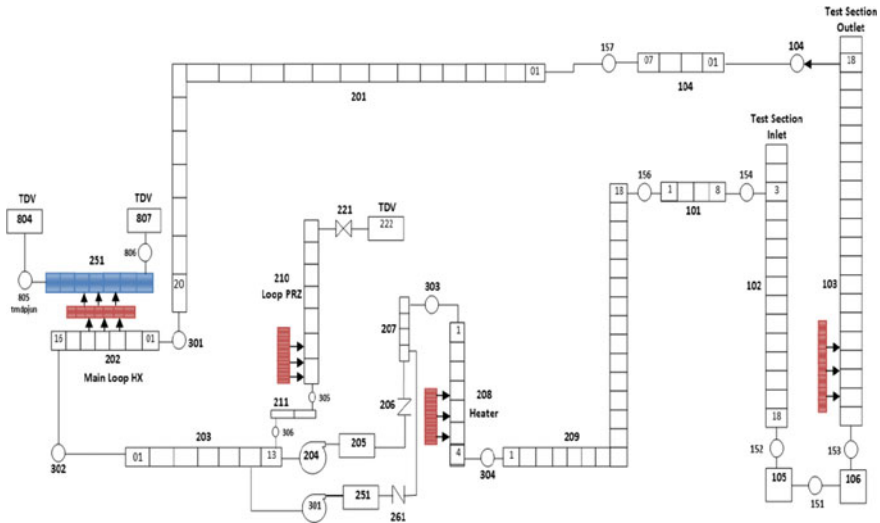


Fig. 3 Nodalization diagram of ITL process system

heater. Similarly, loop heater is modelled as PIPE component with associated heat structures. Pump characteristics of canned motor pumps (main loop pump and decay heat removal pump) of main loop system were incorporated in the hydrodynamic model. The test fuel was modelled as heat structures and highest power pin was modelled separately. Nuclear peaking factors due to variation in axial and radial variation in neutron flux in the test fuel clusters were taken into account. Reactor trips and controls were also incorporated in model. The heat loss from ITL process piping to the atmosphere and reactor pool is not considered for conservative estimate. Nodalization diagram of the ITL process system is shown in Fig. 3.

3 Acceptance Criteria

Loss of normal power supply is considered under anticipated operation occurrence (AOO) category. The acceptance criterion taken for the transient analysis of ITL main loop system being used for nuclear fuel irradiation is as follows:

- (a) Clad temperature shall be less than 500 °C.
- (b) Minimum DNBR shall be greater than 1.3.

4 Event Sequence

The transient initiates at the loss of Class IV power supply resulting in the tripping of the main loop pump. Under normal operation, only one main loop pump is operating and another pump was kept on stand-by. The coolant inlet temperature during normal operation is maintained at 260 °C. The total heat load from nuclear heating is considered as 800 kW in the steady-state operation.

Tripping of main loop pump will result in continuous reduction of coolant flow through the test section. The first reactor trip generated on power supply failure is ignored. The second reactor trip is initiated on main loop cooling flow reaching below 90% of its nominal value. During the power failure, the decay heat removal pump will start on Class II power supply (battery operated pump). Normally, two decay heat removal pumps are available for operation. However, in the analysis, operation of one decay heat removal pump is considered. Decay heat removal pump will continue to operate during the initial phase of electric power failure to limit the clad and fuel temperatures below the acceptable limits. The Dowtherm flow to main loop heat exchanger secondary side will get interrupted due to the power failure as the Dowtherm pumps are provided with Class III power supply based on diesel generators. The pumps will start once the electric power from diesel generator is supplied. Dowtherm pumps usually start operating after 180 s (3 min) of electric power failure as the Class III power supplied by diesel generators will come into effect and it will restore transfer of decay heat to the secondary cooling system of HFRR via Dowtherm heat exchanger. However, for conservative estimate, it was considered that Dowtherm cooling on the secondary side of main loop heat exchanger is not available till $t = 300$ s.

5 Analysis Results and Discussion

After the loss of electric power, the main loop pump and loop heater will trip. The Dowtherm cooling pump, which removes heat from the main loop and transfer it to Dowtherm cooling system, will also trip. In the analysis, reactor trip generated on electrical signal based on power under voltage is ignored. Variation in clad temperature, loop flow and reactor power with time during power failure transient is shown in Fig. 4.

Due to the pump trip, the cooling flow in the main loop will decrease rapidly which will generate second reactor trip signal on low main loop flow (90% of nominal flow). However, till the initiation of reactor trip, the clad temperature will increase due to reduction in cooling flow, while reactor is being operated at full power. On the initiation of reactor trip, the heat generated in the test fuel and in-pile structures will instantly reduce to lower level which will lead to reduction in clad temperature. Decay heat pump will start on Class II power provided by battery banks after Class IV power failure to remove the residual decay heat from the test fuel. This will

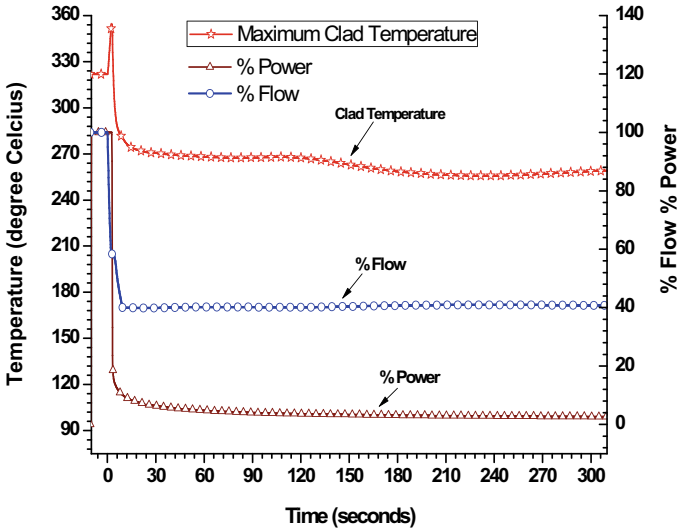


Fig. 4 Variation in clad temperature with time

provide adequate cooling to the test fuel while maintaining the clad temperature within acceptable limits till the restoration of normal power supply.

It is observed that the clad temperature reaches near the saturation temperature for very short time during the transient as shown in Fig. 5. The pressurizer is able to maintain the main loop system pressure of 17.5 MPa in the event of power failure till the restoration of power supply to the pressurizer heater from diesel generators (Class III).

Minimum critical heat flux (CHF) reaches to 5.6 MW/m² as obtained from Groen-veld look-up table (LUT) [2]. This corresponds to minimum DNBR ratio of 3.5 which meets the acceptance criteria for the analysis.

6 Conclusions

It was found that maximum clad temperature of the test fuel rises to 354 °C during electric power failure. The maximum clad temperature was found to be less than acceptable limit. The minimum DNB ratio was also well above the acceptable limit during the transient. The transient analysis has demonstrated that the main cooling system will be able to maintain sufficient cooling to the test fuel so that the clad and fuel temperatures were maintained within the acceptable limits and fuel-clad integrity remained intact throughout the transient.

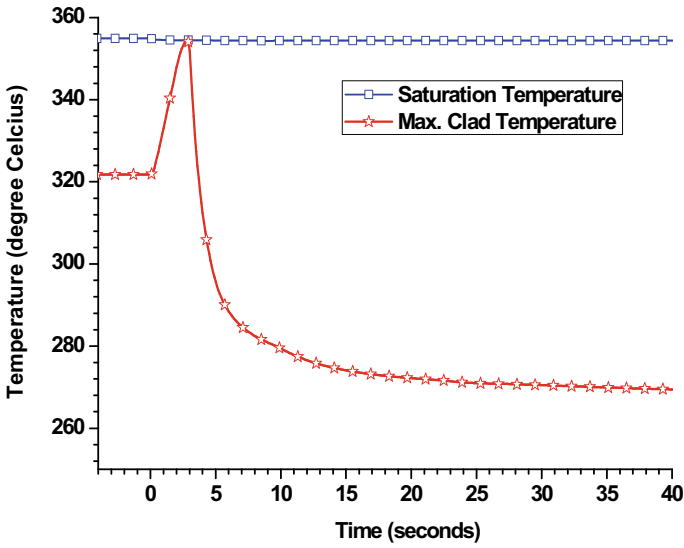


Fig. 5 Variation in clad and local saturation temperature

References

1. RELAP5/MOD3 Code manual volume I: code structure, system models, and solution methods
2. Groeneveld DC, Cheng SC, Doan T (1986) 1986 AECL-UO critical heat flux lookup table. Heat Transf Eng 7:46–62

Toward Analysis of Corium Hydraulics in Liquid Sodium



Ram Kumar Maity, T. Sundararajan, M. Rajendrakumar, and K. Natesan

1 Introduction

Fast reactors are a type of nuclear reactors in which the nuclear fission reaction that produces thermal energy is sustained by fast (energetic) neutrons. In order to limit neutron flux and fissile inventory, fast reactors work with compact cores with enriched fuel. Because of low core volume, the power density and linear power rating of fuel becomes high for such reactors (typical power density is 400–500 kW/liter and linear power rating is 400 to 500 W/cm of pin length). Such high-power densities warrant use of a highly efficient coolant medium. Many operational fast reactors around the world therefore use liquid metal in the form of liquid sodium as the coolant. A pool type reactor is characterized by a large pool of sodium which holds the primary heat transport system. A large capacity fast reactor is preferentially designed as a pool type reactor due to the large thermal inertia of reactor pool and associated enhancements in reactor safety. Details of design of Indian fast reactors can be found in ref. [1].

Accidents leading to core meltdown that can release molten corium into reactor pool are rare events with very low probability and is considered as beyond design basis event [2]. However, in the eventuality of an incident that leads to core meltdown and release of molten corium into reactor pool the transport of the same becomes important and needs to be characterized. Corium is the material created in a nuclear reactor during core meltdown accident and would primarily be a mixture of reactor fuel, fission products and structural material. An expected post-accident scenario with respect to movement of molten corium and its relocation is depicted in Fig. 1

R. K. Maity (✉) · M. Rajendrakumar · K. Natesan
Thermal Hydraulics Division, Indira Gandhi Centre for Atomic Research, Kalpakkam 603102,
India
e-mail: rammaity@gmail.com

T. Sundararajan
Department of Mechanical Engineering, IIT Palakkad, Palakkad 678557, India

[2, 3]. Moreover, during such an accident christened as a severe accident in a fast reactor in addition to molten corium, large volumes of fission gases are released into reactor pool as well. Accident progression in the fast reactor is expected to be distinct from that in the thermal reactor. Accidents, which can lead to degradation and melting of the whole core, are classified as severe accidents and specifically called a Core Disruptive Accident (CDA) in the context of fast reactors. Due to the extreme low probability of occurrence of CDA, it is often referred to as a hypothetical accident [4]. Despite such low frequency, an accident like CDA needs to be analyzed in view of its possible serious impact on the reactor systems and its surroundings. It is to be demonstrated that any radioactivity release to environment stays within specified limits [4].

It is necessary to develop tools that allow characterization of transport of various species after a severe accident in a fast reactor. Such characterization would allow to improve and optimize accident management strategies. For example, one of the major tasks after release of corium in sodium pool is to avoid clumping (aggregation of fuel fragments) that may result in re-criticality and further large energy release. Development of such tools becomes even more pertinent in view of the planned expansion of the Indian fast reactor program [2]. The understanding of severe accident

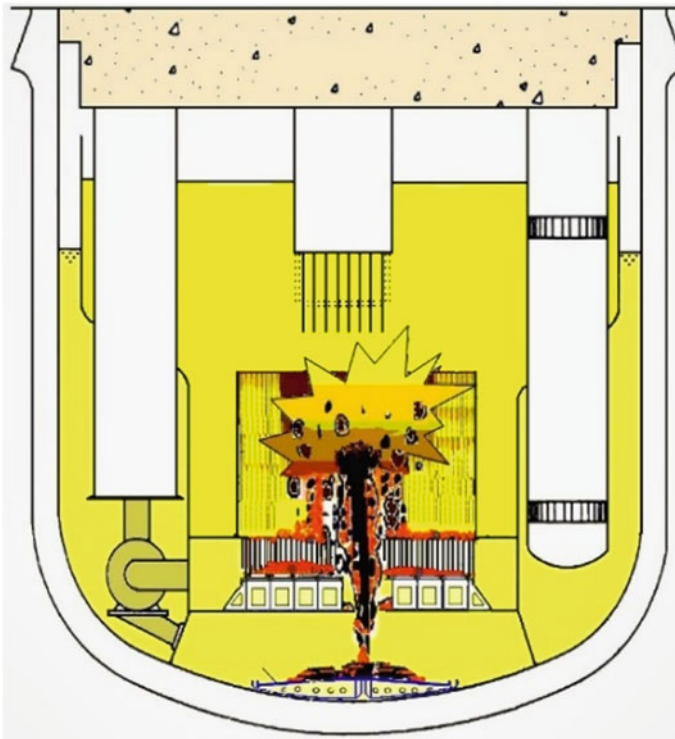


Fig. 1 Schematic showing transport of molten corium after a severe accident (top) [3]

related phenomena need to be improved substantially as a part future advanced reactor designs. The focus of the present study is on the movement of corium in liquid state within liquid sodium with resolution of flow structures resulting from two phase instabilities. Phase change is beyond the scope of the present study. The studies are done using an in-house force balanced two phase flow solver based on the volume of fluid (VOF) method called THYC-MP.

2 Literature Review and Objective

A brief description of numerical studies on movement of corium in coolant using two phase analysis methods with capabilities similar to VOF method is presented here. The motion of a jet of corium in coolant takes place primarily after a severe accident has occurred. A majority of the studies till now have been experimental in nature. This is due to the complex physics involved and the lack of adequate computational power along with suitable development on numerical algorithms. The aim of these experiments includes determination of jet instabilities and jet breakup length and characterization of corium spread on structures like core catcher. A comprehensive review of experimental works on jet break-up and fragmentation phenomena can be found in ref. [5].

Oh et al. [6] described a study on the break-up behavior of a molten metal jet in still gas when in the presence of sinusoidal oscillations. The studies that included amplitude-modulated waveform were done using a VOF based method. Thakre et al. [7] presented a two-dimensional VOF analysis of melt jet fragmentation using commercial CFD code FLUENT. The study included identification of jet fragmentation pattern, influence of Weber number and physical properties. Lin et al. [8] described studies using a VOF-based method when a melt droplet has a vapor film and is exposed to a pressure pulse. The effect of surface tension is studied and found to be insignificant. The results also indicated that the vapor film can be neglected as well with material density and pressure pulse playing the most important role in droplet deformation and surface wave growth.

Zhou et al. [9] presented a paper on metal jet breakup that also analyzed cooling and solidification behavior. Solidification was modeled using an enthalpy based approach. The results were found to be in good agreement with experimental observations at different Weber numbers. More recently, using the color-gradient Lattice Boltzmann method, a very detailed study on corium jet break-up and fragmentation in sodium has been studied by Cheng et al. [10].

Several recent advances and application of two phase flow algorithms to study the interactions of two immiscible liquid metals or equivalent materials have been described in literature. They also prove the viability of using two phase flow analysis tools for characterization of corium behavior in liquid sodium. Corium interaction with liquid sodium involves several intricate interfacial and phase change phenomena. For the present study a force balanced two phase solver based on the VOF method is developed and described in more detail in the next section. The code

developed in applied to analyze movement of simulant material (wood's metal) in water and corium in sodium. Preliminary results from these studies are presented.

3 Materials and Methods

Out of the different fixed grid two-phase flow analysis methods, the VOF method sees widespread use. This method is capable of accurate conservation of mass for each phase. Volume conservation is a very important aspect in two-phase flows and must be ensured in order to capture the right flow physics. In two-phase problems, methods to track the physics of an interface between the two phases present within the domain need to be implemented in addition to the solving the flow. As a results, two-phase flow problems are in general more challenging than single phase flow problems. The VOF method is a fixed grid "one-fluid" approach that makes use of a marker function to separate the two phases within the domain. Integration of the marker function within a control volume or computational cell gives the value of volume fraction ' f '. If the presence of phase designated ' k ' is specified by the marker function $\alpha_k(x, y, z, t)$, then the volume occupied by this phase and subsequently the volume fraction (f_k) within a cell can be calculated using the following expressions:

$$V_k = \int_{\Omega} \alpha_k(x, y, z, t) dV, f_k = V_k / V \quad (1)$$

The value of volume fraction can take any value from 0 to 1. The implications of the values taken by the variable are listed:

- $f = 1$ Cell completely filled with primary phase.
- $0 < f < 1$ Mixed cell containing both phases.
- $f = 0$ Cell completely filled with secondary phase.

The primary fluid is also referred to as the dark fluid. The first step of the overall method, involves reconstruction of the interface between the primary and secondary fluids. This is done using the volume fraction values of mixed cells. The interface would pass through mixed cells and is a zone of discontinuity across which a large change in fluid properties occurs. Either with the help of the reconstructed interface or directly operating upon the values of volume fractions, the next step involves calculation of curvature. The calculated curvature of interface is required for calculation of surface tension forces. These forces arise due to the existence of the discontinuity in medium at interface and need to be imbibed into the momentum equations as part of the flow solver using special force balanced schemes. After the flow field advances, the interface is advected based on the prevalent flow velocities. Thus, a single time step or iteration of calculations for two-phase flow is completed. The present implementation is on a fully staggered grid that stores quantities like pressure, volume fraction, temperature, fluid properties and curvature at center of continuity cells. Two separate cells viz. u-momentum and v-momentum cells are used for integration

of u , v momentum equations and for storage of u and v velocities. Specifically, u -momentum cells are centered around centers of left and right faces and v -momentum cells are centered around centers of top and bottom faces of a continuity cell. Further details of the main steps of the VOF method along with their implementation as part of the present work are described in the succeeding sections.

3.1 Interface Reconstruction

The first step is reconstruction of interface using the prevailing volume fraction field. An interface will lie within mixed cells alone and is defined using piecewise linear segments. Such methods are called Piecewise Linear Interface Construction (PLIC) methods. The equation of a line segment can be defined in terms of components of normal and a constant as: $n_x x + n_y y + \rho = 0$. Thus, defining a linear segment representative of the interface within a mixed cell requires values of interface normals (n_x, n_y) and a line constant (ρ). The method used for the present work for determination of interface normals is the E-PLIC method. This has been discussed in detail in ref. [11]. The method uses a c_0 correction template (shown in Fig. 2) that is imposed over a primary PLIC interface.

For the present study this primary PLIC interface is the Linear least squares (LLS) method [12]. The LLS method is known to be one of the most accurate PLIC methods reported in literature. The application of the c_0 correction template has been shown to further improve the accuracy of PLIC reconstruction [11].

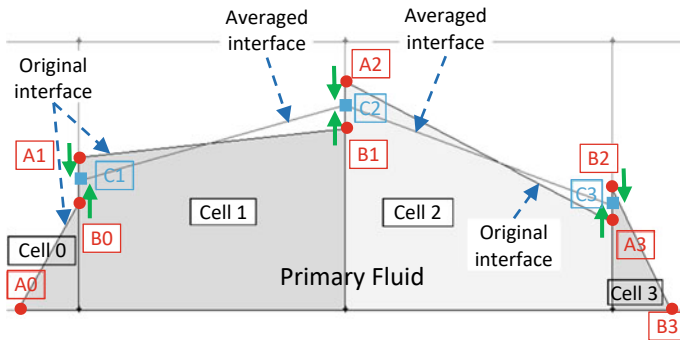


Fig. 2 c_0 correction template for PLIC interface

3.2 Interface Advection

A major step in two phase flow simulation is the computation of two phase interface kinematics. This requires obtaining a solution for the equation of conservation of volume fraction shown below:

$$\frac{\partial f}{\partial t} + \vec{u} \cdot \nabla f = 0 \quad (2)$$

where \vec{u} is the velocity vector, f is the volume fraction. The equation is integrated and discretized geometrically to allow a diffusion free advection of the interface. This maintains sharpness of interface through a two phase flow transient being studied. For the present work the edge matched flux polygon algorithm (EMFPA) proposed by Lopez et al. [13] is implemented. The method requires the following constraints are respected during construction of the flux polygons (referring to Fig. 3).

$$\begin{aligned} m_{23} &= \frac{v_2^{n+1/2}}{u_2^{n+1/2}}, m_{14} = \frac{v_1^{n+1/2}}{u_1^{n+1/2}} \\ m_{34} &= \frac{(y_1 - y_2) - (v_1^{n+1/2} - v_2^{n+1/2})}{(x_1 - x_2) - (u_1^{n+1/2} - u_2^{n+1/2})} \\ m_{12} &= \frac{y_1 - y_2}{x_1 - x_2} \end{aligned} \quad (3)$$

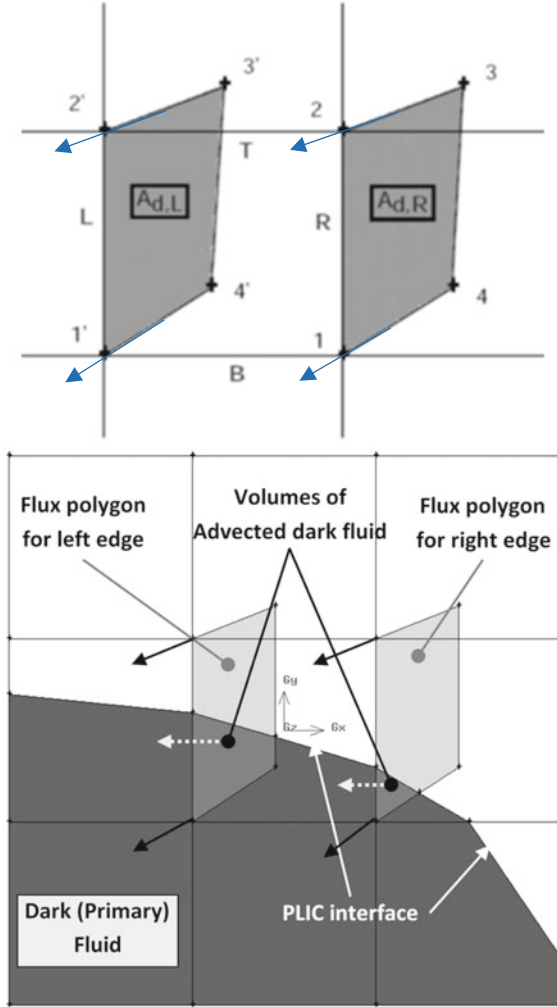
These relations are relevant for right face (marked as R) of the computational cell and are used to determine coordinates of points 3 (x_3, y_3) and 4 (x_4, y_4) with respect to coordinates of points 1 (x_1, y_1) and 2 (x_2, y_2). Flux polygons are constructed for all other sides of the cell sussing similar relations. The method is an unsplit advection method that is mass conserving and uses edge matched flux polygons with no overlap or uncovered region. Geometric integration requires the construction of flux polygons from the prevailing velocity field and subsequently, the area of intersection between the flux polygon and the dark polygon (region covered by primary/dark fluid) derived from the interface reconstruction step is calculated that gives the flux of primary fluid through respective face. This is depicted in a schematic as given in Fig. 3. The area of flux polygon represents the total fluid flux passing through each edge of cell. The sum of these areas over must be zero (to satisfy overall continuity).

$$A_{d,R} = \frac{1}{4} (u_1^{n+1} + u_1^n + u_2^{n+1} + u_2^n) \Delta y \Delta t \quad (4)$$

Similar relations are used to derive $A_{d,L}$, $A_{d,T}$, $A_{d,B}$ with the following condition to be satisfied (L-left, T-top, B-Bottom):

$$A_{d,R} + A_{d,L} + A_{d,T} + A_{d,B} = 0 \quad (5)$$

Fig. 3 Flux polygons constructed using EMFPA (top) and method used to calculate geometric advection using flux polygon and dark polygon



In the present work, a set of analytical relations are developed to derive the flux polygons [14]. This makes the implementation of the method highly efficient. The integration of Eq. 2 is done over a continuity cell. Using Gauss Divergence theorem and integrating Eq. 2, we get:

$$f_i^{n+1} = f_i^n + \frac{1}{A_{ij}} \sum_{k=R,L,T,B} (\delta A_{i,k}) \tag{6}$$

Here, A_{ij} represents area of cell (i, j) . The second term of Eq. 3 represents the area of intersection of flux and dark polygons as shown in Fig. 3.

3.3 Calculation of Curvature

Calculation of curvature required for the determination of surface tension force is done using the Height Functions method. The height functions used here is the variable template version of Hernandez et al. [15]. The basic principle of the method involves the following three steps:

1. The dominant component of interface normal is found in order to orient the direction of height functions. For the present study components of normal from Young's PLIC are used.
2. Next the volume fractions are summed up along the dominant direction of the interface normal from step 1. This gives the local values of height functions $X(y)$ or $Y(x)$.
3. Differentiation of height functions gives the value of Curvature. This step is valid only when the height function lies within the cell dimensions.

Thus, if $n_x < n_y$, Three height functions viz. $Y_{i-1,j}$, $Y_{i,j}$, $Y_{i+1,j}$ can be defined:

$$Y_{i,j} = \sum_{j-3}^{j+3} f_{i,j}(y_j - y_{j-1}) \quad (7)$$

Curvature can be calculated from height functions as:

$$\kappa = \text{Sign}(n_y) \left[\partial^2 Y / \partial x^2 / \left(1 + \left(\partial y / \partial x \right)^2 \right)^{\frac{3}{2}} \right] \quad (8)$$

The original height functions [16] uses a stencil of size 7×3 cells. The version used in this work is a more accurate version that uses a variable stencil size depending on the volume fraction field. The steps for these can be found in ref. [15]. The surface tension force for u-momentum equation (for u-momentum cell (ui, uj) on the left face of continuity cell (i, j)) is given by:

$$F_{ST_x} = -\sigma \kappa_{ui,uj} \left(\frac{\partial f}{\partial x} \right)_{ui,uj} \quad (9)$$

Local curvatures are calculated and stored for continuity cells and are to be interpolated to u-momentum cells using and v-momentum cells. The surface tension forces are calculated using these curvature values.

3.4 Flow Solver

The inclusion of surface tension forces need to be carefully implemented using a “well balanced” or a “force balanced” method. This means the discretized form of the momentum equation(s) should be able to describe the Laplace equilibrium correctly. In the present work, the scheme (PROST) proposed by Renardy and Renardy [17] is implemented for a staggered grid system. Components of velocity viz. u-velocity is stored on the left and right faces of a continuity cell with the v-velocity being stored at the top and bottom faces of the same. In this method, the pressure is divided into two components ($P = P_1 + P_2$) where component P_1 represents the capillary pressure component arising due to presence of surface tension. The value of capillary pressure (P_1) is determined such that the surface tension force is equal to the derivative of P_1 . The divergence of the difference between surface tension force and gradient of capillary pressure is made zero as shown in the following equation:

$$\nabla \cdot (\vec{F}_{ST} - \nabla P_1) = 0 \Rightarrow \nabla \cdot \vec{F}_{ST} = \nabla \cdot \nabla P_1 \quad (10)$$

The above equation is integrated and discretized over the continuity cell. The equation is discretized as an implicit (in time) equation and is stored by using a matrix solver. The velocity and pressure fields are coupled using a projection method described in detail in ref. [17].

The discretization scheme for volume fraction (f) and capillary pressure (P_1) follows the same exact discretization in order to maintain perfect force balance. The time integration of all conservation equations including the energy equation is done using fully implicit schemes. After discretization these are solved using matrix solvers. For the present study, a Bi-Conjugate Gradient stabilized (Bi-CGSTAB) linear solver is used. The flow solver has been validated extensively against complex two phase flow problems not described as part of the present study. In the next section results from application to the problem of movement of corium in sodium and simulant wood’s metal in water is presented. The standard energy equation is solved along with flow equations. The buoyancy forces due to temperature differences are not turned on due to the large buoyancy forces imparted by the density differences between the primary and secondary fluids. The code is named as Thermal Hydraulics Code—Multi-Phase viz. THYC-MP.

3.5 Calculation Domain and Properties

Two systems of fluids viz. Wood’s metal-water and corium-sodium are studied. The former system is a popular choice as simulant system to study hydraulics of the later. It must be noted that no phase change is considered as part of this work. Phase change is otherwise expected to occur and is the subject of future extension. The flow domain, boundary conditions and fluid properties are similar to those used in

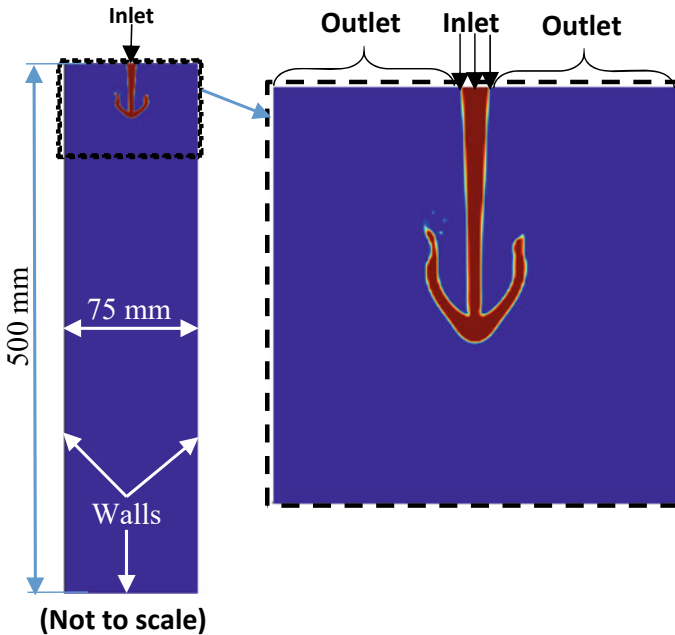


Fig. 4 Details of domain and boundary conditions

ref. [7]. The domain selected is a 75 mm width \times 500 mm depth column of fluid (secondary fluid—water and sodium in study 1 and 2, respectively) as shown in Fig. 4 kept at an initial temperature of T_{ambient} . A slot jet of width 5 mm is injected at 0.5 m/s and temperature of T_{jet} . The top boundary otherwise (excluding faces through which jet is injected) is an outlet boundary. All the remaining walls (side and bottom) are adiabatic walls. Flow and thermal properties for the present study are listed in Table 1 and are sourced from ref. [18]. A uniform grid of 150×1000 cells is used along with a time step of $1e-4$ s for the numerical studies. The Woods metal-water system corresponds to an Ambient Weber number (We_a) of 1.25 while that for Corium Sodium study is 2.2.

4 Results and Discussion

The evolution of volume fractions of corium (in sodium) and woods metal (in water) as predicted by THYC-MP code is shown in Fig. 5. The computational elements used for the present study are of size 0.5 mm. The total number of elements used is 1.5 lakhs. The studies reported here are preliminary in nature designed to be more like demonstration studies. From the contours of volume fraction in Fig. 5 it can be seen that both large scale and smaller scale instabilities are present. Due to the

Table 1 Properties for the present study

Property		Woods Metal–Water	Corium–Sodium
Density (kg/m ³)	ρ_{primary}	9700	8756
	$\rho_{\text{secondary}}$	998.16	857
Dynamic viscosity (Ns/m ²)	μ_{primary}	1.94e-3	6.49e-3
	$\mu_{\text{secondary}}$	1.002e-3	0.281e-3
Specific heat (J/kgK)	cp_{primary}	168	460
	$cp_{\text{secondary}}$	4180	1278.5
Thermal conductivity (W/mK)	k_{primary}	18.8	2.5
	$k_{\text{secondary}}$	0.59953	71.2
	T_{jet}	200 °C	3000 °C
	T_{ambient}	50 °C	460 °C
Surface tension coefficient	σ	1	0.484

deceleration of the jet as it enters further into the secondary fluid, the whole jet tends to bend and eventually breakup. Smaller structures continuously break and separate from the main jet. These structure mainly arise from the trailing edge of the mushroom cloud like structure that arises in both the cases studied. The mushroom like structure at the leading edge of the jet of primary fluid can be ascribed to the presence of Rayleigh Taylor instability modes. As the jet travels further blobs of primary fluid break out from the trailing edge as can be seen clearly from the plots of Fig. 5. It must be remembered that the smallest structures predicted as part of this study is limited by the mesh size used. The mesh size is limited by the computational resources available and the efficiency of the code. At present steps are being taken to improve the efficiency of the code in addition to parallelization that would allow studies on finer grids. The jets of corium and woods metal are injected into respective secondary fluids at the same velocity. This makes the Weber number for the corium studies significantly higher than that for the wood metal studies. It can also be seen that jet breakup is seen later and at longer jet lengths in the case of corium studies. Moreover, there is similarity between the behavior of the two primary fluids.

In addition, the shedding of blobs of primary fluid from the trailing edge of the mushroom like structure is much more pronounced in the case of corium-sodium combination. This can be explained by the significantly higher Weber number for corium flow in sodium. Even though the velocity of the jet injection is same, the movement of corium is significantly faster into the column of secondary fluid. From the contours of temperature, the effect of high thermal conductivity of sodium with respect to water can be clearly seen. This can be concluded from the significantly cooler corium jet w.r.t the woods metal jet after 0.3 s. The range for the two plots is decided by the extreme domain temperatures (T_{jet} to T_{ambient}). Both the jet and ambient temperatures in the case of corium-sodium study is significantly higher. In addition, phase change is not modelled. Thus, these results are indicative in nature. Thus, as seen in both the case studies the jet of corium (or woods metal) becomes

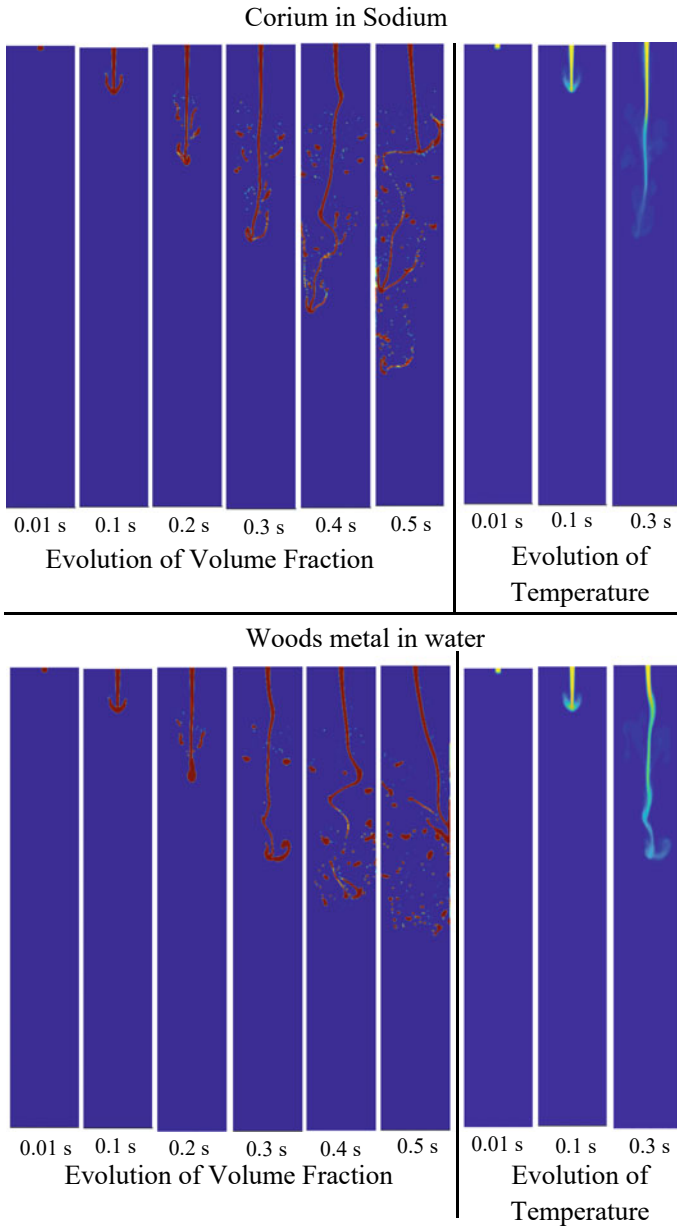


Fig. 5 Evolution of volume fraction and temperature for the two fluid systems studied

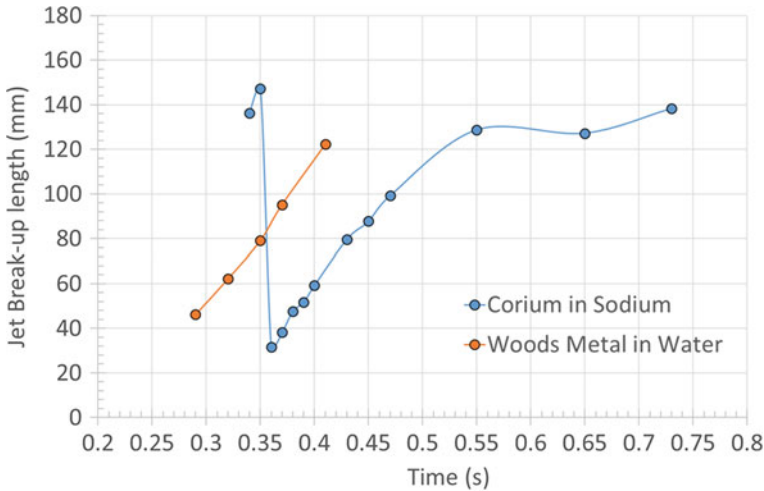


Fig. 6 Jet break-up length with respect to time for the two fluid systems studied

completely fragmented after penetrating into the column of secondary fluid for a distance of about half of the column depth. This is desirable as it proves that corium jet would be completely fragmented before reaching tank bottom and would be well distributed without any clumping.

The jet break-up length extracted from plots of jet interface are presented in Fig. 6. It is seen that jet break-up length increases i.e. the jet grows in time, eventually breaking at an intermediate length. This leads to sudden shortening of the jet. The corium and woods metal jets grow at similar rates even though the length of corium jet is slightly greater.

5 Conclusion

The development of a VOF-based code for simulation of two phase flow and heat transfer (THYC-MP) is described. The code developed uses advanced algorithms for interface reconstruction, advection and curvature calculations. The flow solver is force balanced and is capable of reproducing Laplace equilibrium conditions exactly. Application on the important problem of corium movement in sodium arising as a result of a severe accident in fast reactor is shown. The results show the capability of the developed code towards capturing important jet instability modes. Further extension in the form of including phase change physics and speeding up through parallelization is in progress.

References

1. Chetal SC et al (2006) The design of the prototype fast breeder reactor. *Nucl Eng Des* 236(7–8):852–860
2. Raj B, Chellapandi P, Rao PRV (2015) Sodium fast reactors with closed fuel cycle. CRC Press Taylor and Francis Group, LLC, Boca Raton
3. Sudha AJ et al (2017) Progress in nuclear energy experimental simulation of downward molten material relocation by jet ablation of structures and fuel coolant interaction in a fast reactor. *Prog Nucl Energy* 105:194–201
4. Rouault J et al (2010) Severe accidents. In: Cacuci DG (ed) Handbook of nuclear engineering. Springer Science+BusinessMedia LLC, New York, pp 2651–2661
5. Iwasawa Y, Abe Y (2018) Progress in nuclear energy melt jet-breakup and fragmentation phenomena in nuclear reactors: a review of experimental works and solidification effects. *Prog Nucl Energy* 108:188–203
6. Oh YS et al (2014) Breakup behavior of a molten metal jet. *Int J Heat Fluid Flow* 50:27–37
7. Thakre S, Manickam L, Ma W (2015) A numerical simulation of jet breakup in melt coolant interactions. *Ann Nucl Energy* 80:467–475
8. Lin M, Zhong M, Li Y, Yuan M, Yang Y (2015) Numerical analysis on molten droplet hydrodynamic deformation and surface waves under high pressure pulse. *Ann Nucl Energy* 77:133–141
9. Zhou Y, Chen J, Zhong M, Wang J, Lv M (2017) Numerical simulation of metal jet breakup, cooling and solidification in water. *Int J Heat Mass Transf* 109:1100–1109
10. Cheng H, Cheng S, Zhao J (2020) Study on corium jet breakup and fragmentation in sodium with a GPU-accelerated color-gradient lattice Boltzmann solver. *Int J Multiph Flow* 126:103264
11. Maity RK, Sundararajan T, Velusamy K (2021) An enhanced piecewise linear interface construction template based on c0 correction. In: Proceedings of 48th National conference on fluid mechanics and fluid power (FMFP)
12. Scardovelli R, Zaleski S (2003) Interface reconstruction with least-square fit and split Eulerian-Lagrangian advection. *Int J Numer Methods Fluids* 41(3):251–274
13. López J, Hernández J, Gómez P, Faura F (2004) A volume of fluid method based on multidimensional advection and spline interface reconstruction. *J Comput Phys* 195(2):718–742
14. Maity RK, Sundararajan T, Velusamy K (2020) An accurate interface reconstruction method using piecewise circular arcs. *Int J Numer Methods Fluids* 93(1):93–126
15. Hernández J, López J, Gómez P, Zanzi C, Faura F (2008) A new volume of fluid method in three dimensions—Part I: Multidimensional advection method with face-matched flux polyhedra. *Int J Numer Methods Fluids* 58(8):897–921
16. Cummins SJ, Francois MM, Kothe DB (2005) Estimating curvature from volume fractions. *Comput Struct* 83(6–7):425–434
17. Renardy Y, Renardy M (2002) PROST: A parabolic reconstruction of surface tension for the volume-of-fluid method. *J Comput Phys* 183(2):400–421
18. Manickam L, Bechta S, Ma W (2017) On the fragmentation characteristics of melt jets quenched in water. *Int J Multiph Flow* 91:262–275

Effect of Porous-Fin on Performance Enhancement of Shell-Tube Latent Heat Thermal Storage System



C. Suresh and Sandip K. Saha

Nomenclature

A_m	Numerical coefficient for damping velocity
C_p	Specific heat capacity (J/kg. k)
CE	Inertial coefficient (m^{-1})
D_f	Diameter of ligament or fibre (m)
d_p	Pore size or diameter of pore (m)
g	Gravitational acceleration (m/s^2)
h_{sf}	Interstitial heat transfer co efficient (w/m^2K)
K	Permeability of copper foam (m^2)
L	Latent heat of fusion (kJ/kg)
P	Pressure (pa)
Pr	Prandtl number
Re	Reynolds number
t	Time (s)
T	Temperature (K)
u	Velocity component (m/s)
v	Velocity vector (m/s)
α_{sf}	Interfacial surface area (m^2)
β	Thermal expansion coefficient (K^{-1})
γ	Liquid fraction
λ	Thermal conductivity (w/m K)
μ	Dynamic viscosity (kg/ (m s))

C. Suresh (✉) · S. K. Saha

Department of Mechanical Engineering, Indian Institute of Technology Bombay,
Mumbai 400076, India

e-mail: csuresh428@gmail.com

ρ	Density (kg/m ³)
CF	Copper foam
FP	Fluid phase

1 Introduction

Energy consumption has significantly grown as a result of the economy and industry rapid expansion. In order to meet the growing energy demand, the utilization of fossil fuels have been increased which resulted in damaging the environment and intensifies global warming. Therefore, renewable energy is the sustainable energy source which can alternate the fossil fuels. But these renewable energy sources are intermittent in nature and the energy production and demand cannot be matched at every time. Hence, to match the supply and demand and also to ensure continuous energy supply, an integration of Thermal Energy Storage (TES) to the solar thermal systems is much needed [1]. The TES systems are classified categorized as sensible, latent and chemical TES. Among those TES technologies, PCM-based latent TES received much attention due to their greater storage density, constant temperature and compact size. However, the drawback of low thermal conductivity of PCM hinders the application of latent TES systems in real-time conditions. Therefore, many researchers have introduced the different heat transfer augmentation techniques in order to improve the heat transfer of latent TES [2]. Some of the heat transfer augmentation techniques that includes are addition of fins, metal meshes, porous-foams, heat pipes, expanded graphite, nano-encapsulation and Nano-additives [3]. From all these methods, addition of fins is the most prominent applied technique due to its simple in construction, better performance and lower cost. Numerous studies on latent TES employing fins have been carried under various fin parameters and configurations such as annular/circular fin, shape of fins, fin material, fin numbers and size [4].

2 Literature Review and Objective

Wu et al. [5] numerically studied the effect of thermal conductivity, inlet velocity and temperature, fin length and distribution on the thermal performance of novel latent TES. Further, performance parameters were evaluated in terms of melting time, storage intensity and storage capacity. The findings shown that fin arrangement has a more significant influence in improving the storage performance of system than the PCM thermal conductivity. Compared to the case of no-fins, the storage intensity of non-uniform fin length and distribution was enhanced by 104.33% and 61.06% for the uniform fin length and distribution.

Zhang et al. [6] carried out the work by employing novel fin geometry and Al_2O_3 as a heat transfer augmentation for improving the performance of latent TES. The effect of various fin configurations and nanoparticles volumes fractions were also evaluated. The results show that employing novel fins and nanoparticles improved the melting characteristic of latent TES system. Four different novel fins have melting times that are lowered by 80.35%, 77.62%, 77.33%, and 80.65%, respectively, compared to the without fin system. It was concluded that the fins and nanoparticles are the efficient ways to improve the melting process.

Mahdi et al. [7] proposed a novel fin assisted metal foam strips as a heat transfer enhancement method for latent TES system. Further, a comparative study has been performed by comparing with the metal foam with PCM, fins, uniform and non-uniform fins assisted with metal foam strips. Incorporating fins with a considerably smaller volume percentage compared to metal-foam impregnation improves the heat transfer between the heat source and PCM. The addition of uniform fin-foam strips increases the melting and solidification rates more effectively than alone adding fins. It was concluded that employing fins with metal foam strip rather than fins alone or foam alone under the same volume, PCM often solidifies more quickly and recovers heat more rapidly.

Nematpour et al. [8] studied the melting process of triplex shell and tube latent TES system under different enhancement methods that includes addition of fins, Nano-particles, metal foams and combination of methods. The findings demonstrate that a PCM-metal foam composite with porosities ranging from 0.98 to 0.92 achieves the shorter melting than the pure PCM. As compared to pure PCM, the melting time was reduced by 69.52% with the addition of nanoparticles and metal foam. Metal foam combined with nano-particles has a greater rate of heat storage as compared to all methods.

From the literature studies, it has been found that metal foam has gained more attraction due to the increased thermal conductivity and heat transfer through the increase of heat transfer surface. Based on the studies, it was found that most of the works are carried on fins and metal foams for enhancing the heat transfer of PCM. The findings showed that the inclusion of fins won't result in a uniform temperature distribution and that copper foam embedded in the PCM can significantly reduce the mass of the PCM resulted in reduction of the storage capacity. Therefore, a novel copper porous-fin implanted in the PCM TES has been developed in order to attain the uniform temperature distribution and to increase the storage capacity. To accomplish this, a two-dimensional axisymmetric numerical model has been developed to examine the performance of the porous-fin TES.

3 Numerical and Physical Model

3.1 Physical Model

The TES storage with porous copper foam fin embedded in the PCM was designed. A 2-D axisymmetric physical domain for the shell and tube TES tank has been developed in order to save computing time and expense, as illustrated in Fig. 1. The storage tank has a height of 350 mm and the inner radius of shell and tube are 73 mm and 11 mm, respectively. Further, the shell and tube have a thickness of 3 and 1.5 mm. The porous fin TES comprises of 4 number of porous fins with a thickness of each 5 mm and a pitch distance of 70 mm. The water as a Heat Transfer Fluid (HTF) and technical grade paraffin as a PCM is selected for the present study. During the charging, the HTF at high temperature enters at top and leaves at bottom of the storage tank as show in Fig. 1. The thermo-physical properties of paraffin and copper foam are given in the Table 1.

Fig. 1 Schematic of 2-D axisymmetric model

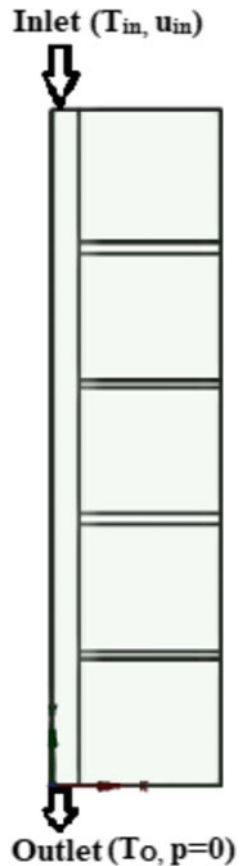


Table 1 The thermo-physical properties of paraffin and copper

Material	Properties	Values
Paraffin	Melting temperature (°C)	48.43–58.7
	Latent heat (kJ/kg)	250
	Density (kg/m ³) (Solid/liquid)	800/760
	Specific heat capacity (J/ (kg K))	1800/2000
	Thermal conductivity (W/(m K)) (Solid/liquid)	0.24/0.2
	Dynamic viscosity (kg/ (m s))	2.508 × 10 ⁻³
	Thermal expansion coefficient (K ⁻¹)	7.5 × 10 ⁻⁴
Copper	Density (kg/m ³)	8960
	Specific heat capacity (J/ (kg K))	390
	Thermal conductivity (W/ (m K))	401

Based on the above-mentioned physical model, numerical simulation was carried out under the following assumptions: the flow of liquid PCM and HTF was two-dimensional, laminar, unsteady, incompressible, and Newtonian. The temperature of HTF at inlet is kept constant. The buoyancy driven convection was applied through Boussinesq approximation, which assumes that there is no change in properties of material other than the density. Thermal non-equilibrium was emerged for the local heat transfer between the working fluid and metal foam fin.

3.2 Governing Equations

In the copper-foam composite PCM TES system, the inclusion of copper foam will unquestionably increase the flow resistance. Therefore, Forchheimer extended Darcy model is adopted for governing the flow resistance. By considering Darcy model, the governing equations of continuity, momentum and the energy for PCM and copper foam are presented as follows;

$$\frac{\partial \rho_P}{\partial t} + \nabla(\rho_P v) = 0 \tag{1}$$

$$\begin{aligned} \frac{\rho_P}{\varepsilon \gamma} \frac{\partial u_i}{\partial t} + \frac{\rho_P}{\varepsilon \gamma^2} (v \cdot \nabla) u_i = -\nabla P + \frac{\mu_P}{\varepsilon \gamma} \nabla^2 u_i - \left(\frac{\mu_P}{K} + \frac{\mu_P C_E}{\sqrt{K}} |v| \right) u_i \\ - \frac{(1 - \gamma)^2}{\gamma^3 + 0.001} A_m u_i + \rho_P g_i \beta_P \end{aligned} \tag{2}$$

$$\rho_P \left(C_P + L \frac{d\gamma}{dt} \right) \frac{\partial T_P}{\partial t} + \rho_P C_P (v \cdot \nabla) T_P = \nabla[\lambda_{eFP} + \lambda_{TD} \nabla T_P]$$

$$- h_{sf} \alpha_{sf} (T_P - T_{CF}) \quad (3)$$

$$(1 - \varepsilon) \rho_{CF} C_{CF} \frac{\partial T_{CF}}{\partial t} = \nabla (\lambda_{eCF} T_{CF}) - h_{sf} \alpha_{sf} (T_{CF} - T_P) \quad (4)$$

For pure PCM, the metal foam related elements can be eliminated in the governing equations and further simulations can be performed.

Pore size or diameter (d_p)

$$d_p = \frac{22.4 \times 10^{-3}}{\omega} \quad (5)$$

Ligament or fibre diameter (d_f)

$$d_f = 1.18 d_p \frac{\sqrt{(1 - \varepsilon)/(3\pi)}}{\left\{1 - \exp \frac{\varepsilon - 1}{0.004}\right\}} \quad (6)$$

Interstitial surface area between PCM and metal foam

$$\alpha_{sf} = 3\pi d_f \frac{\sqrt{(1 - \varepsilon)/(3\pi)} \left\{1 - \exp \frac{\varepsilon - 1}{0.004}\right\}}{(0.59 d_p)^2} \quad (7)$$

Permeability

$$K = 0.00073 (1 - \varepsilon)^{-0.224} \left(\frac{d_f}{d_p}\right)^{-1.11} d_p^2 \quad (8)$$

Inertial co-efficient

$$C_E = 0.00212 (1 - \varepsilon)^{-0.132} \left(\frac{d_f}{d_p}\right)^{-1.63} \quad (9)$$

The interstitial heat transfer co-efficient can be determined by following equation

$$h_{sf} = \begin{cases} 0.76 \text{Re}^{0.4} \text{Pr}^{0.37} \lambda_{l,PCM}/d_f, & 0 < \text{Re} \leq 40 \\ 0.52 \text{Re}^{0.5} \text{Pr}^{0.37} \lambda_{l,PCM}/d_f, & 40 \leq \text{Re} \leq 1000 \\ 0.26 \text{Re}^{0.6} \text{Pr}^{0.37} \lambda_{l,PCM}/d_f, & 1000 < \text{Re} \leq 2000 \end{cases} \quad (10)$$

Effective thermal conductivity of PCM and metal foam can be calculated by using given equation

$$\lambda_{\text{eff}} = \frac{1}{\sqrt{2}(R_A + R_B + R_C + R_D)} \quad (11)$$

$$R_A = \frac{4\sigma}{(2e^2 + \pi\sigma(1 - e))\lambda_{CF} + (4e - 2e^2 - \pi\sigma(1 - e))\lambda_{l,PCM}}$$

$$R_B = \frac{(e - 2\sigma)^2}{(e - 2\sigma)e^2\lambda_{CF} + (2e - 4\sigma - (e - 2\sigma)e^2)\lambda_{l,PCM}}$$

$$R_C = \frac{(\sqrt{2} - 2e)^2}{2\pi\sigma^2(1 - 2\sqrt{2}e)\lambda_{CF} + 2(\sqrt{2} - 2e - \pi\sigma^2(1 - 2\sqrt{2}e))\lambda_{l,PCM}}$$

$$R_D = \frac{2e}{e^2\lambda_{CF} + (4 - e^2)\lambda_{FP}}$$

$$\text{Where, } \sigma = \sqrt{\frac{\sqrt{2(2 - (\frac{5}{8})e^3\sqrt{2} - 2\varepsilon)}}{\pi(3 - 4\sqrt{2}e - e)}}, e = 0.339$$

The effective thermal conductivity for PCM and copper foam can be defined as

$$\lambda_{eFP} = \lambda_{\text{eff}}|\lambda_{CF} = 0$$

$$\lambda_{eCF} = \lambda_{\text{eff}}|\lambda_{l,PCM} = 0$$

Thermal dispersion conductivity

$$\lambda_{TD} = \frac{0.36}{1 - \varepsilon} \rho_{FP} C_{pFP} d_f |v| \quad (12)$$

3.3 Initial and Boundary Conditions

Initial Condition

$t = 0$ s, $T = 298$ K $v = 0$ m/s.

Boundary Condition

- No-slip condition at wall
- Inlet of TES, $v = 0.011$ m/s, constant inlet temperature $T_{in} = 343$ K, during melting
- Outlet of TES, $P = 0$
- Walls are insulated and no heat loss.

3.4 Independence Study and Validation

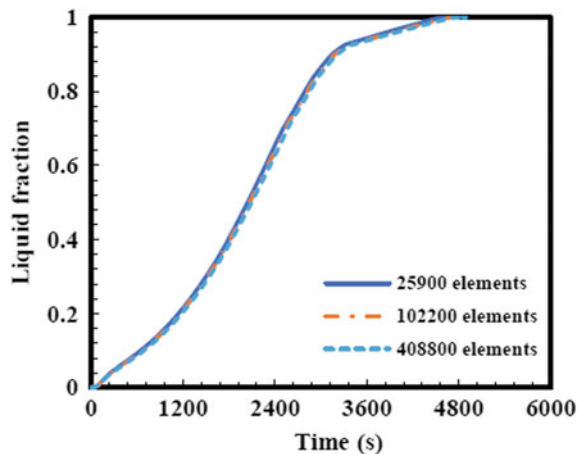
The accuracy of the numerical simulations is directly depending on the number of grid elements. In order to ensure that simulations are computationally efficient, it is important to run a grid independent test on the model and to select an appropriate number of grids. For the grid independent test in this study, three distinct grid sizes—normal, fine, and extremely fine were taken into the consideration. Figure 2 shows the liquid fraction of porous-fin TES for various grid numbers. As the grid number grew from 102,200 to 408,800, the liquid fraction was shown to have the minimum error, with an average variation of 0.47%, respectively.

Additionally, a numerical simulation of the paraffin melting process in a porous-fin shell-tube TES system was initially carried out to validate the current 2D simulation model. Figure 3 shows the comparison of present numerical model results with previous studied results of liquid fraction versus time [9]. In comparison to the results of previous research, the established models provide a good agreement of the shape and location of the solid–liquid front. As a result, the current established model could be used for computation of composite copper foam TES with non-thermal equilibrium condition.

4 Results and Discussion

Studies are carried out to investigate the potential of porous-fin TES on enhancement of melting process during charging. Further, comparative study has been performed by comparing porous-fin TES with the without-fin shell-tube TES system.

Fig. 2 Grid independence test



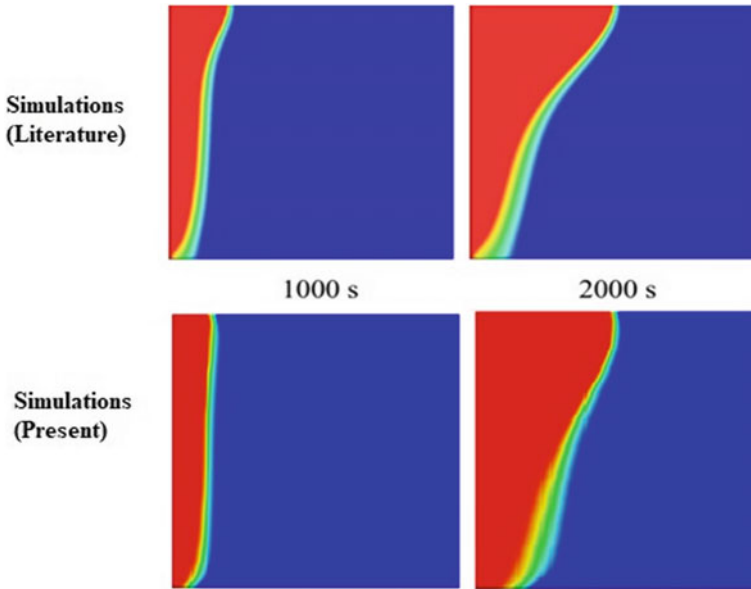


Fig. 3 Comparison of present numerical results of solid–liquid interface with the previous results [9]

4.1 Propagation of Solid Front

During charging process, the HTF at a temperature of 343 K was circulated through the HTF tube and the heat transfer will take place from the HTF to the PCM accordingly. Figure 4 depicts the comparison of solid–liquid phase transitions at 600, 1800 and 3000 s for porous-fin and without-fin TES systems. As observed in the figure, natural convection and buoyancy allow the greater temperature of the liquid PCM to move upward, which leads to a faster melting of PCM in the top section than the lower. It can be seen that as the TES is incorporated with porous-fin, the PCM melts more rapidly in the fin direction as compared to the without-fin TES. This is because copper porous fin has superior thermal conductivities, which improves heat transfer in the system. Therefore, higher liquid fraction values have been found with porous-fin TES than the without-fin TES.

4.2 Temperature Contours

Figures 5 shows the temperature contours of without-fin and porous-fin TES systems during melting 600 s, 1800s, and 3000 s, respectively. As the system is being charged, the PCM close to the heat transfer tube observes more energy and starts to increase its temperature until it melts. The higher temperatures are observed at top of the storage

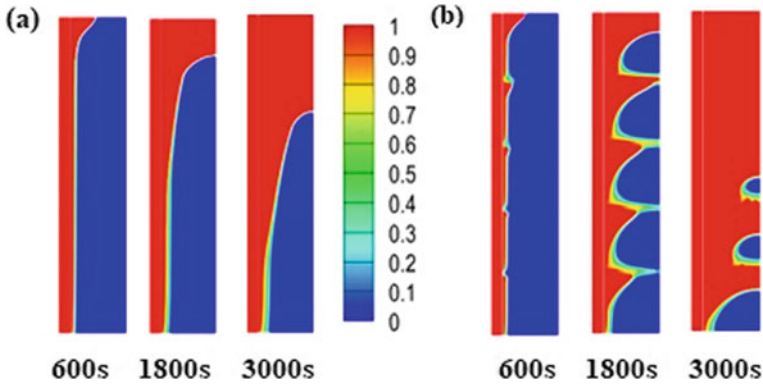


Fig. 4 Schematic of PCM solid-liquid phase interface of a without-fin and b porous-fin TES

tank than the bottom storage tank. This is due to the availability of greater potential of TES at inlet of storage. As the charging time progress, the thermal gradient in the storage tank has been reduced that results in increase of temperature at the bottom the tank. This is the fact that as the thermal gradient decreases, the amount of energy available for bottom of the storage tank increases results in temperature increment. From the comparison of without-fin TES, porous-fin TES is found to have higher temperatures and also observed uniform temperature distribution in PCM. This is due to the existence of porous-fin which has higher specific surface are for heat transfer and also the pores in the copper foam restricts the flow of PCM, which may increase the conduction heat transfer also. Because of this reasons, higher temperatures have been achieved at shorter period for porous-fin TES system.

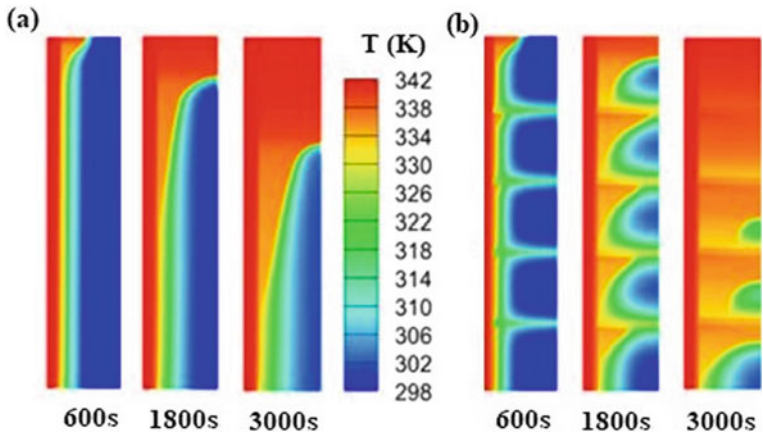
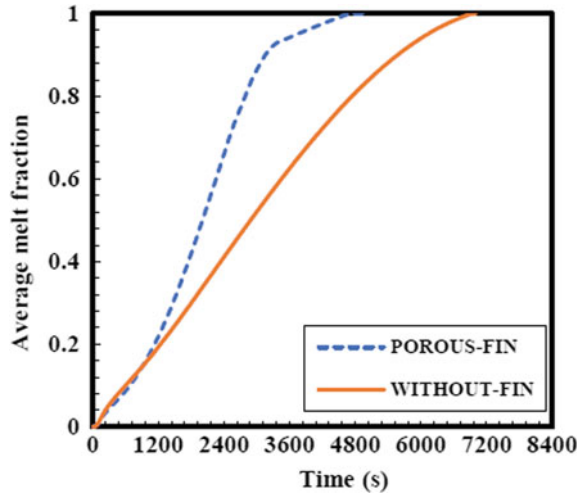


Fig. 5 Schematic of temperature contours for a without-fin b porous-fin

Fig. 6 Variation of liquid fraction for without-fin and porous-fin TES systems



4.3 Liquid Fraction

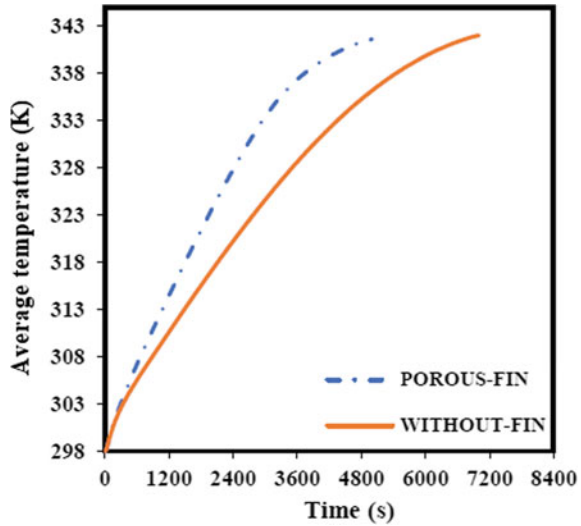
The variation of liquid fraction over time for without-fin and porous-fin TES configurations at an inlet velocity of 0.011 m/s is shown in Fig. 6.

As seen in the figure, the liquid fraction progressively grew from 0 to 1 during melting process. The TES without a fin is found to have a greater liquid fraction values at the beginning of melting, while porous fin shown lower values. This is due to that, without-fin TES transfer the thermal energy directly from heat transfer tube to PCM, while in porous-fin TES, the thermal energy is initially transferred to the fins and then it is transferred to the PCM. Therefore, at initial stage without-fin exhibits higher values than the porous-fin. The liquid fraction of PCM is found to rise over time for the both TES systems, and porous-fin is found to have the highest liquid fraction values than the without-fin TES. Further, porous-fin TES is found with shorter melting time of 4800 s, whereas without-fin TES system has 7800 s, respectively. From these results, it was that porous-fin TES system has higher melting rate and shorten melting than the without-fin TES system.

4.4 Temperature Distribution

The temperature distribution of without-fin and porous-fin TES systems are compared in the Fig. 7. It has been noticed that the increase in PCM average temperature during melting is identical for both the system up to the first 100 s. After that, faster rate of increment in temperature was found with the porous-fin TES system than the without-fin TES. This is mainly due to the high thermal conductivity of porous-fin and larger heat transfer surface area. Further, the existence of pores in the porous-fin

Fig. 7 Variation of liquid fraction for without-fin and porous-fin TES system



constrain the PCM flow during melting which resulted in an increase of conduction heat transfer. From the Fig. 7, it has been found that lower temperature values were found in the without-fin TES system. This is due to the presence of lower thermal conductivity of pure PCM that leads to a poor heat transfer from the HTF to the PCM. As a result, higher temperatures are reported on shorter period of time in porous-fin TES than the without-fin TES.

5 Conclusions

Under the current study, shell and tube TES system without-fin and porous fin foam were investigated numerically and compared. The effect of porous-fin on melting performance was evaluated by using 2-D axisymmetric numerical model. Based on the numerical results, the following conclusions have been drawn;

- It was found that, the existence of porous fin in porous-fin TES enhanced the conduction heat transfer in the system as compared to the without-fin TES system. Further, higher liquid fraction values were found with the porous-fin TES.
- From the results, it was found that the melting time of porous-fin is shortened by 32.39%, respectively as compared to the without-fin TES.
- Based on the temperature contours, porous-fin TES system is found to have uniform temperature distribution during melting over without-fin TES system.
- The porous-fin TES system found with faster rate of temperature increment at shorter time period over the without-fin TES.

Based on the conclusions, it has been evident that porous-fin showed better performance than the pure PCM TES. Therefore, porous-fin TES system can be utilized for thermal applications and thermal management.

Acknowledgements Authors acknowledge the financial support from the Indian Institute of Technology Bombay, Mumbai, India.

References

1. Leong KY, Hasbi S, Gurunathan BA (2021) State of art review on the solidification and melting characteristics of phase change material in triplex-tube thermal energy storage. *J Energy Storage* 41:1–21
2. Li Q, Li C, Du Z, Jiang F, Ding Y (2019) A review of performance investigation and enhancement of shell and tube thermal energy storage device containing molten salt-based phase change materials for medium and high temperature applications. *Appl Energy* 255:113806
3. Teggari M, Ajarostaghi SSM, Yıldız Ç, Arıcı M, Ismail KAR, Niyas H, Lino FAM, Mert MS, Khalid M (2021) Performance enhancement of latent heat storage systems by using extended surfaces and porous materials: a state-of-the-art review. *J Energy Storage* 44:103340
4. Abdulateef AM, Mat S, Abdulateef J, Sopian K, Al-Abidi AA (2018) Geometric and design parameters of fins employed for enhancing thermal energy storage systems: a review. *Renew Sustain Energy Rev* 82:1620–1635
5. Wu Y, Li D, Jiang W, Zhu S, Zhao X, Arıcı M, Tunçbilek E (2022) Energy storage and exergy efficiency analysis of a shell and tube latent thermal energy storage unit with non-uniform length and distributed fins. *Sustain Energy Technol Assess* 53:102362
6. Zhang J, Cao Z, Huang S, Huang X, Liang K, Yang Y, Zhang H, Tian M, Akrami M, Wen C (2022) Improving the melting performance of phase change materials using novel fins and nanoparticles in tubular energy storage systems. *Appl Energy* 322:119416
7. Mahdi JM, Najim FT, Aljubury IMA, Mohammed HI, ben Khedher N, Alshammari NK, Cairns A, Talebizadehsardari P (2022) Intensifying the thermal response of PCM via fin-assisted foam strips in the shell-and-tube heat storage system. *J Energy Storage* 45:103733
8. NematpourKeshтели A, Iasiello M, Langella G, Bianco N (2022) Enhancing PCMs thermal conductivity: a comparison among porous metal foams, nanoparticles and finned surfaces in triplex tube heat exchangers. *Appl Therm Eng* 212:118623
9. Zhang P, Meng ZN, Zhu H, Wang YL, Peng SP (2017) Melting heat transfer characteristics of a composite phase change material fabricated by paraffin and metal foam. *Appl Energy* 185:1971–1983

Effect of an Asymmetrically Confined Rotating Cylinder on Heat Transfer



Shruti Gautam, Aruna Thakur, and Pooja Thakur

Nomenclature

C_D	Drag coefficient
C_{DF}	Friction drag coefficient
C_{DP}	Pressure drag coefficient
C_L	Lift coefficient
d	Diameter (m)
F_D	Drag force per unit length of the cylinder (Nm^{-1})
H	Channel height (m)
L_d	Downstream length
L_u	Upstream length
m	Power-law consistency index (Pa.sn)
n	Power-law index
Nu	Nusselt number
P	Pressure (Pa)
Pe	Peclet number
Pr	Prandtl number
Re	Reynold's number
V_x, V_y, V_z	Velocity in x, y, and z directions (ms^{-1})
X, Y	Cartesian coordinates
α	Rotational velocity
β	Blockage ratio

S. Gautam · P. Thakur (✉)

Department of Chemical Engineering, National Institute of Technology, Hamirpur, Himachal Pradesh 177005, India

e-mail: pooja@nith.ac.in

A. Thakur

Department of Mechanical and Manufacturing Engineering, National Institute of Advanced Manufacturing Technology, Hatia, Ranchi, Jharkhand 834003, India

γ	Asymmetry
δ	Minimum gap between the channel wall and the cylinder (m)
η	Viscosity (Pa.s)
ρ	Density (Kg.m^{-3})
ϕ	Non dimensional temperature
τ_{ij}	Extra stress tensor (Pa)
Ω	Angular velocity (Rad.s^{-1})
θ	Azimuthal angle ($^{\circ}$)

1 Introduction

The effects produced by the asymmetric confinement of rotating cylinder on the flow of power-law fluids are shown in this study. As we know that, the rotating cylinder has a wide range of application in our day-to-day life, for example, in slurries filtration, drying of rotary drum, sheet making process in polymers, in plastic industries, etc. The flow in a tubular heat exchanger, instrumentation technology used in hot-wire anemometry, and flow past dividers in the manufacturing of plastics, the installation of pipes, offshore cylindrical drilling rigs, etc. are all the typical examples of it. In this situation, bulk and angular velocity of the cylinder are used to describe the dynamics of the flow. All these above stated applications require high mixing which is formed by the asymmetric confinement of rotating cylinder because the flow field located far from the cylinder experience less effect of rotation [1].

Many researchers did a lot of studies over the combined effects of the channel confinement on the cylinder as well as the cylinder asymmetric positioning within the channel. For shear thinning fluids over a stationary cylinder, Nirmalkar et al. [2] studied the effect of Prandtl number, power-law index, blockage ratio, Reynolds number and gap ratio on the momentum and heat transfer properties of the asymmetrical cylinder. The work shows that, in steady flow region the net lift force act in positive direction because of the asymmetric distribution of tangential and normal forces over the cylinder and the cylinder gets a repulsive force due to the wall closer to it. By using the air as the working fluid Prasad et al. [3] have investigated the characteristics of flow and heat transfer in an isothermally rotating cylinder and observe that because of the confinement of the channel, shear layer reduces and with increment of the blockage ratio, drag coefficient increases too. In the context of this, Bijjam et al. [4] work for the shear-thickening fluids, researcher finds that average Nusselt number increases when the Prandtl number goes from 1 to 50 at constant γ .

For the momentum and heat transfer Prasad et al. [3] and Mettu et al. [5] did computational work for circular cylinder placed asymmetrically in a confined channel. Mettu et al. [5] concluded that at critical Re flow transition increases from steady to unsteady by decreasing the value of γ at constant β . When Re kept constant, an increase in β results in a reduction in the amplitude of the oscillations that occur

in the lift coefficient. Cliffe et al. [6] observed the gradual spinning of the cylinder on its axis and concludes that when the rotational speed is high enough, a vortex street can be completely removed even when the flow rate remains the same.

As per the literature, less work has been done for the flow around a rotating cylinder with the implementation design constraints that is asymmetric and blockage for the power-law fluid. The dimensionless parameters used to solve the governing equations numerically are Reynolds number, Prandtl number, power law index which has the range of values as $0.1 \leq Re \leq 40$, $0.7 \leq Pr \leq 100$, and $0.3 \leq n \leq 1$ respectively, asymmetric ratio $0.1 \leq \Upsilon \leq 1$ and blockage ratio $0.2 \leq \beta \leq 0.6$.

2 Methodology

A long cylinder, constricted asymmetrically by two plane walls, which are parallel with each other, has taken into account, and shown in Fig. 1. The cylinder of diameter d , rotating in counter clockwise direction having an angular velocity ω . The average inlet velocity of bulk fluid and the linear rotational velocity of the cylinder kept identical ($2V_{avg}/d$). In the channel, asymmetry ratio Υ tells us about the position of the cylinder, which is defined as $\delta/(H/2-d/2)$, where δ is spacing between the channel wall and the surface of the cylinder. Blockage ratio β tells us about the channel's confinement ($\beta = d/H$).

In the non-dimensional version, the governing equations for a time-dependent, laminar, two-dimensional, incompressible flow of a power-law fluid are expressed as follows:

Continuity equation:

$$\frac{\partial V_x}{\partial X} + \frac{\partial V_y}{\partial Y} = 0$$

Momentum in x direction:

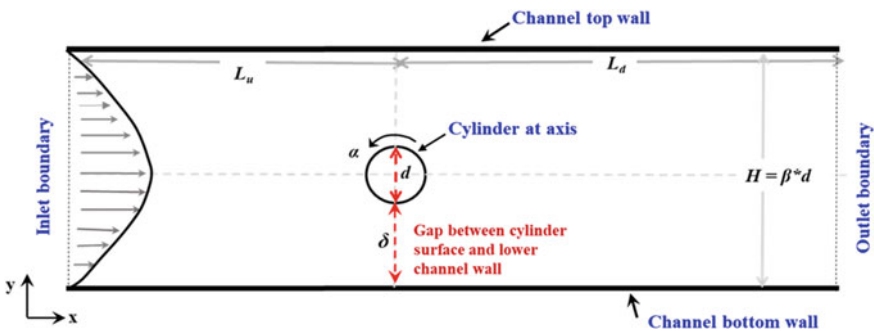


Fig. 1 Schematic form of the domain

$$V_x \frac{\partial V_x}{\partial X} + V_y \frac{\partial V_x}{\partial Y} + \frac{\partial V_x}{\partial t} = -\frac{\partial P}{\partial X} + \frac{1}{Re} \left(\frac{\partial \zeta_{xx}}{\partial X} + \frac{\partial \zeta_{yx}}{\partial Y} \right)$$

Momentum in y direction

$$V_x \frac{\partial V_y}{\partial X} + V_y \frac{\partial V_y}{\partial Y} + \frac{\partial V_y}{\partial t} = -\frac{\partial P}{\partial Y} + \frac{1}{Re} \left(\frac{\partial \zeta_{xy}}{\partial X} + \frac{\partial \zeta_{yy}}{\partial Y} \right)$$

For incompressible fluid, the rheological state’s equation is:

$$\tau_{ij} = 2\eta_{ij}$$

where τ_{ij} is extra stress tensor, ε_{ij} is rate of strain tensor component which is shown in terms of velocity field and X and Y coordinates are represented by i and j .

$$\varepsilon_{ij} = \frac{1}{2} \left(\frac{\partial V_i}{\partial j} + \frac{\partial V_j}{\partial i} \right)$$

The viscosity for the power-law fluid is:

$$\eta = m \left(\frac{I_2}{2} \right)^{\frac{n-1}{2}}$$

where n is power-law index and m is power-law consistency index. n defines the behaviour of fluid i.e., if $n = 1$ means Newtonian fluid, $n < 1$ means shear-thinning fluids and $n > 1$ means shear thickening fluids. I_2 is second invariant of rate of strain tensor ε_{ij} .

$$I_2 = \sum_i \sum_i \varepsilon_{ij} \cdot \varepsilon_{ji} = (\varepsilon_{xx}^2 + \varepsilon_{yy}^2 + \varepsilon_{xy}^2 + \varepsilon_{yx}^2)$$

The boundary conditions for this flow are given as:

1. At inlet ($x = 0$): In x -direction, fully developed velocity profile is assumed, velocity in y - direction is zero and temperature at inlet is also zero.

$$V_x = \left[1 - \left(\left| 1 - \frac{2y}{H} \right| \right)^{\frac{n+1}{n}} \right], \phi = 0 \text{ for } 0 \leq y \leq 1/\beta$$

where, $V_x = V_{avg} \left(\frac{2n+1}{n+1} \right)$.

2. At the top and bottom of walls ($y = 0$ and $y = 1/\beta$): No slip and no penetration conditions are applied.

$$V_x = 0, \phi = 0$$

3. At the exit ($x = L_u + L_d$): Excluding the pressure term all the other dependent variables have zero diffusion flux.

$$\frac{\partial \xi}{\partial X} = 0 \quad \text{where } \xi = (V_x, V_y, T)$$

4. At the surface of the cylinder: No slip condition is applied

$$V_x = -\alpha \sin \theta, V_y = -\alpha \cos \theta, \phi = 1$$

By adopting characteristic length as d and velocity scale V_{avg} , the variables shown in governing equations and boundary conditions have been made dimensionless. So, the scale for pressure is ρV_{avg}^2 , for stress $m(V_{\text{avg}}/d)^2$ and for time d/V_{avg} . The flow is affected by two Reynold's number Re_{avg} and Re_{Ω} and six dimensionless parameters. The Reynold's numbers are given as:

$$\text{Re}_{V_{\text{avg}}} = \frac{\rho d^n V_{\text{avg}}^{n-2}}{m}$$

$$\text{Re}_{\Omega} = \frac{\rho d^2 \Omega^{2-n}}{2^{2-n} m}$$

$$\text{Re}_{\Omega} = \alpha^{2-n} \text{Re}_{V_{\text{avg}}}$$

α represent the dimensionless angular velocity ($\Omega d/2 V_{\text{avg}}$). The Reynolds number for the fluid and Reynolds number for the rotating cylinder are same.

$$\text{Re}_{V_{\text{avg}}} = \text{Re}_{\Omega} = \text{Re}$$

Total drag coefficient C_D and lift coefficient C_L are used to define the overall hydrodynamic behaviour. The coefficient of drag is calculated by adding the friction and pressure drag components, as shown in the following:

$$C_D = C_{DP} + C_{DF} = \frac{F_D}{\frac{1}{8} \rho \Omega^2 d^3}$$

$$C_{DP} = \frac{F_{DP}}{\frac{1}{8} \rho \Omega^2 d^3}$$

$$C_{DF} = \frac{F_{DF}}{\frac{1}{8} \rho \Omega^2 d^3}$$

3 Numerical Details

COMSOL Multiphasic software (5.5 versions) has been used to solve the governing continuity and momentum equations which are based on Finite Element Method, so we need to generate mesh in the vicinity of the cylinder. Because of the asymmetric and confined conditions, we need to use the extremely fined triangular meshing around the cylinder and as we move far from the cylinder the mesh will gradually become coarser. For the proper convergence of governing equations, a relative tolerance of 10^{-8} has been used. Usually, PARDISO (parallel direct linear solver) is chosen for algebraic equations.

3.1 Domain and Grid Independency Test

The choice of numerical parameters, that is, the length of domain affects the precision and consistency of the results because small region will have an impact on the flow field while an excessively large region will demand significant computing efforts. Likewise, meshing round the cylinders also affects the accuracy of results. Therefore, for getting the optimum values of upstream and downstream length, domain independency test has been performed at the lower values of Reynolds number and Prandtl number, that is, $Re = 0.1$ and $Pr = 0.7$. And the grid independency test has been performed at the higher values of Reynolds number and Prandtl number, that is, $Re = 40$ and $Pr = 100$. Tables 1 and 2 sum up the results for domain test. An analysis of these results tells that the values of drag and lift coefficients and average Nusselt number changes less than 2%, on increasing the length of L_d from 60 to 70, so the optimum value for upstream and downstream length are $L_u = 40$ and $L_d = 60$. While Table 3 summarized the results for grid independence tests for three different grids G1, G2 and G3. The results do not show any significant variation on changing the grid from G2 to G3. Thus, Grid G2 with 480 nodes on the periphery of the cylinder is appropriate for computing the other results. The detail study has been reported in the literature done by Thakur et al. [8]. The bold values shown in Tables 1, 2 and 3 are the optimum values for upstream and downstream length and number of grid opted for the further simulation respectively.

4 Results and Discussion

The range of various non-dimensional parameters used to obtain the new results are Reynolds number, $0.1 \leq Re \leq 40$; Prandtl number, $0.7 \leq Pr \leq 100$; power-law index $0.3 \leq n \leq 1$; asymmetrical ratio, $0.1 \leq \gamma \leq 1$ and blockage ratio, $0.2 \leq \beta \leq 0.6$. The results discussed further describe the effect of these numerical parameters over the heat transfer and fluid mechanics. So, before going towards the new results, it is

Table 1 Effect of upstream length at $Re = 0.1, Pr = 0.7$

L_u	$n = 1, \beta = 0.2$					
	$\gamma = 0.1$			$\gamma = 1$		
	C_D	Nu_{avg}	C_L	C_D	Nu_{avg}	C_L
10	2600.982	2.80447	0.18651	32.70712	1.06473	0.022
50	2601.331	2.80519	0.35952	32.70262	1.06472	0.00377
60	2601.336	2.80521	0.35872	32.70262	1.06472	0.00385
70	2598.221	2.80412	0.35822	32.70262	1.06472	0.00392

Table 2 Effect of downstream length at $Re = 0.1, Pr = 0.7$

$Re = 0.1, Pr = 0.7, L_u = 60$

L_d	$n = 1, \beta = 0.2$					
	$\gamma = 0.1$			$\gamma = 1$		
	C_D	Nu_{avg}	C_L	C_D	Nu_{avg}	C_L
10	2607.453	2.80576	0.35632	32.52644	1.06884	0.00437
30	2607.459	2.80576	0.35222	32.52645	1.06885	0.00452
40	2607.460	2.80576	0.3513	32.52645	1.06885	0.00464
45	2607.461	2.80576	0.35056	32.52645	1.06885	0.00463

Table 3 Effect of grid on results at $Re = 40, Pr = 100$

$Re = 40, Pr = 100, L_u = 60, L_d = 40, \beta = 0.2$

Grid no	N_p	Δ/d	$n = 1$			
			C_D	Cd_p	Nu_{avg}	C_L
$\gamma = 0.1$						
G1	400	0.015708	0.04636	0.05737	5.634	0.25379
G2	480	0.01309	0.04634	0.05737	5.6343	0.25381
G3	600	0.010472	0.04633	0.05736	5.63454	0.25382
$\gamma = 1$						
G1	400	0.015708	0.00234	7.40E-04	1.14741	-0.00443
G2	480	0.01309	0.00234	7.42E-04	1.14746	-0.00443
G3	600	0.010472	0.00234	7.44E-04	1.14747	-0.00443

important to validate the present results and methodology with the results available in the literature.

Table 4 Comparison of present results with that of Bharti et al. [7] at $n = 1, \gamma = 1$

Values of β	Values of Re	Ref. [7]	Present
0.625	1	9.02	8.95
	10	19.67	19.59
	40	32.0	32.34
0.25	1	5.78	5.73
	10	12.1	12.18
	40	23.6	23.67

Table 5 Comparison of present results with that of Prasad [3] at $n = 1, Re = 40, Pr = 0.7, \gamma = 1$

α	β	C_D		C_L		Nu_{avg}	
		Present	Ref. [3]	Present	Ref. [3]	Present	Ref. [3]
0	0.1	2.9856	2.9905	–	–	3.87637	3.88533
	0.2	3.33258	3.37626	–	–	4.01652	4.13067
	0.3	4.25629	4.21227	–	–	4.23856	4.23733
	0.5	8.345752	8.4566	–	–	5.1438	5.26133
2	0.1	2.29013	2.12225	–7.4199	–7.4055	3.78178	3.80214
	0.2	2.83476	2.82972	–7.58137	–7.57802	3.86515	3.84761
	0.3	4.04389	4.01951	–7.78115	–7.75064	3.9873	3.95722
	0.5	9.09183	9.13192	–10.6563	–10.7673	5.04193	5.18182

4.1 Validation of Result

For validating the results, a comparison has been done with Bharti et al. [7] for non-rotating asymmetrically confined cylinder for $\beta = 0.625$ and $\beta = 0.25$ at $n = 1$ and $\gamma = 1$, shown in Table 4. Similarly, Table 5 shows the comparison of drag and lift coefficients and average Nusselt number with that of Prasad et al. [3] for rotating cylinders in Newtonian fluids and it has been observed that the present results are within 1–2% of the literature values.

4.2 Streamlines

The behaviour of flowing fluid can be determined with the help of streamlines in the proximity of rotating cylinder. Figure 2 show the effects of Re, n, γ and β on the cylinder rotating in power-law fluid. For Newtonian fluids, at low Reynolds number rear and front vortices formed for asymmetrically placed cylinder $\gamma = 0.001$ and with increasing Reynolds number wake length increases [9]. As the value of γ increases the vortices almost disappears and the fluid follows the shape of rotating cylinder.

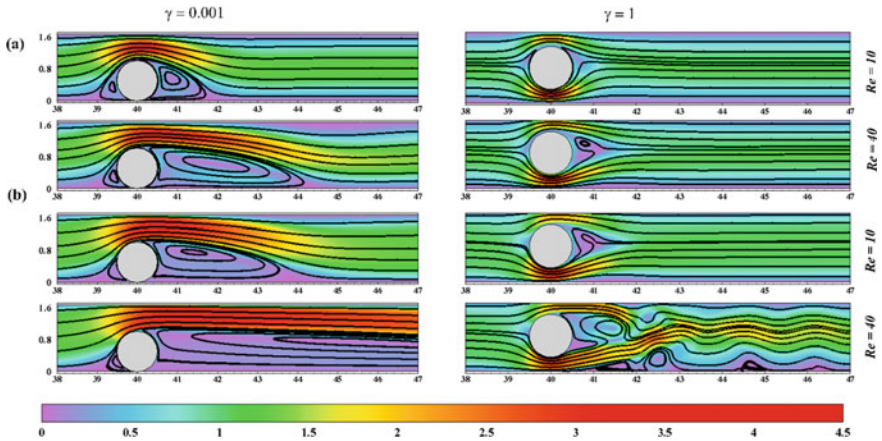


Fig. 2 Streamlines and velocity contours at $\beta = 0.6$ (a) $n = 1$, (b) $n = 0.3$

Whereas, for shear thinning fluids $n = 0.3$, wakes forms even at low Reynolds number. At $\beta = 0.6$, $Re = 40$ and $\gamma = 1$ strong wall vortex has formed and fluid leaves the cylinder. With decreasing the degree of confinement, the size of wakes reduces however an additional wall wakes forms near the channel walls specially for high shear thinning fluids i.e., $n = 0.3$. In the Fig. 2, the velocity contours shows that in recirculation regions, the velocity gradients are low hence pressure gradient become high which rise to develop the adverse pressure gradient near the walls and from the wall wakes.

4.3 Temperature Profile

Isotherm helps us in visualising the temperature field. The Figs. 3 and 4 shows the profile of isotherms near around the rotating cylinder for different value of Prandtl number, power-law index, blockage ratio and degree of asymmetry at $Re = 40$. At low Prandtl number $Pr = 0.7$, the thermal boundary layer becomes thick as the velocity gradient is low around the cylinder, hence, the convective heat transfer is poor. The contours show that when the blockage ratio increases, the isotherms close to the cylinder get more crowded and bend in upward direction. But the bending of isotherms decreases with increasing the asymmetry ratio for Newtonian fluids. Whereas, for shear thinning fluids the fluid become unsteady at $\gamma = 1$ and isotherms become wavy in the downstream. At high Prandtl number $Pr = 100$, boundary layer becomes thin, and isotherms form a tail at the rear of the cylinder which shows that the heat transfer is dominated by convection because of the thinning of the thermal boundary layer. This impact is seen to be significant in Newtonian fluids, implying that heat transfer in Newtonian fluids is greater than that in power law fluids.

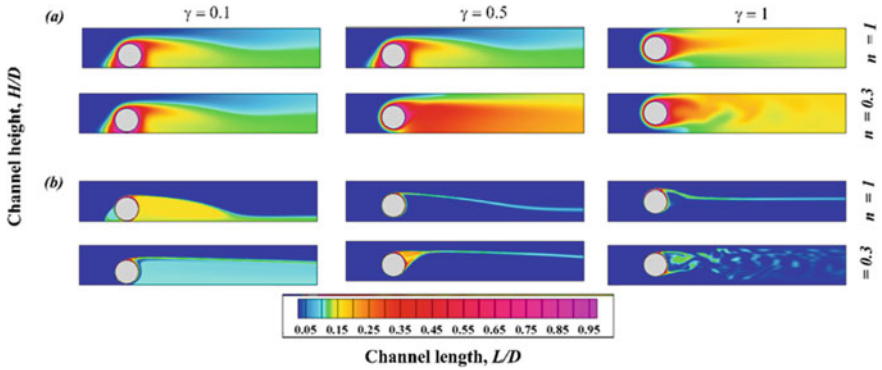


Fig. 3 Isotherms contours at $Re = 40$ for $\beta = 0.6$ (a) $Pr = 0.7$, (b) $Pr = 100$

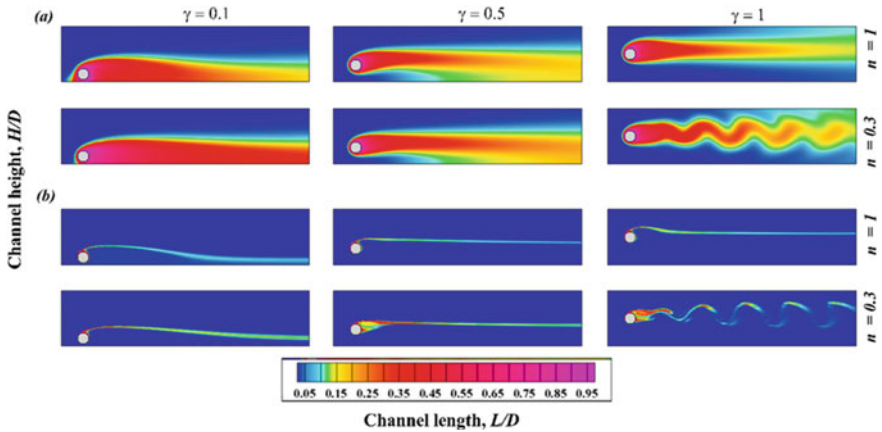


Fig. 4 Isotherms contours at $Re = 40$ for $\beta = 0.2$ (a) $Pr = 0.7$, (b) $Pr = 100$

4.4 Local Nusselt Number

Figure 5 shows the effect of Re , Pr , n and γ on the Nusselt number on rotating cylinder's surface. At the front stagnation point, Nusselt number is higher for $n = 0.3$, $\beta = 0.6$ at $Re = 40$. For Newtonian fluids, at $\theta = 90^\circ$ and 270° the plot of local Nusselt number shows two peaks. The peak formed at $\theta = 90^\circ$ is higher than the other peak and there is no way for shearing to change the viscosity, the Nusselt number changes much less from the surface of the cylinder. But in shear-thinning fluids, this behaviour is now affected by both the shear-dependent viscosities and the changing temperature gradient on the surface of the fluid. Here, at $\beta = 0.6$ and $n = 0.3$ the plot has a lot of variation which indicates that the strong vortex has formed and fluid separates from the cylinder at that point.

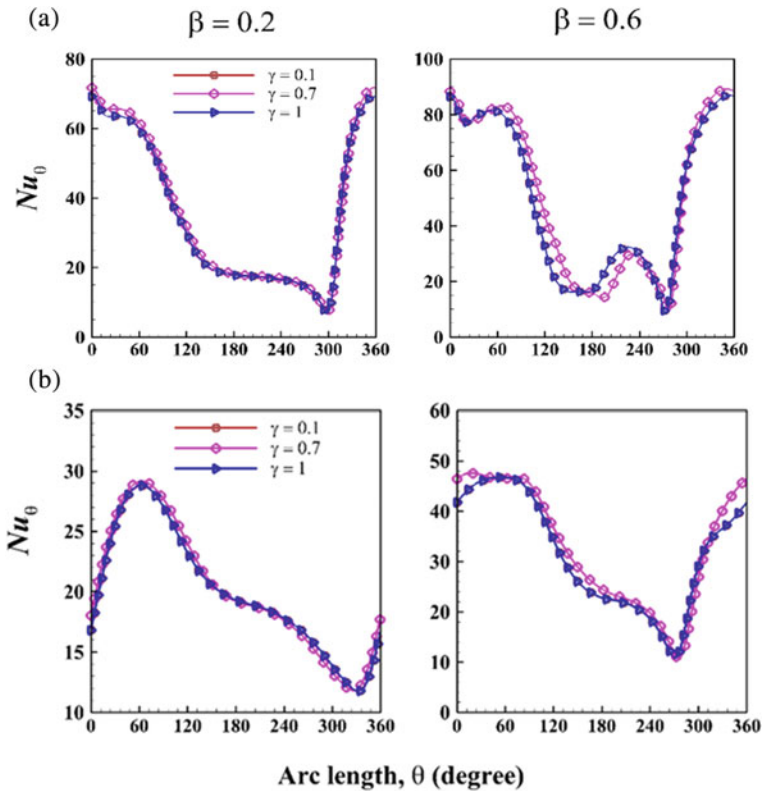


Fig. 5 Variation of local Nusselt number at $Re = 40$, $Pr = 100$ (a) $n = 0.3$, (b) $n = 1$

4.5 Average Nusselt Number

Integrating the local values of the Nusselt number throughout the surface of the cylinder provides the average value of the Nusselt number. These average values should obviously be the functions of Reynolds number, Prandtl number, blockage ratio, asymmetry ratio and power-law index. Figure 6 shows the plot of average Nusselt number for different values of blockage ratio at $\gamma = 0.1$ and $\gamma = 1$ and it tells that the average Nusselt number always increases with increasing Peclet number and channel confinement. However, asymmetry positioning makes relatively linear dependency of the Nusselt number on Peclet number.

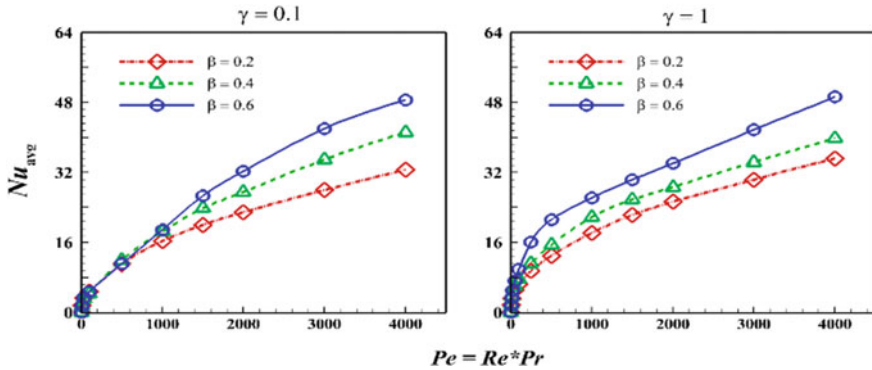


Fig. 6 Variation of average Nusselt number at $Re = 40$, $\gamma = 0.1$ and 1

5 Conclusion

Asymmetrically confined rotating cylinder placed in between of power-law fluid has been numerically investigated for the following range of parameters $0.1 \leq Re \leq 40$, $0.7 \leq Pr \leq 100$, $0.3 \leq n \leq 1$, $0.1 \leq \gamma \leq 1$ and $0.2 \leq \beta \leq 0.6$. Flow characteristics has been describing in terms of streamlines. Similarly, isotherms, average and local Nusselt number are used to describe the characteristics of heat transfer. Thus, it has been concluded that more confiner the channel more heat will transfer and as the asymmetry increases flow become stabilize. The maximum heat transfer occurs at $\gamma = 0.1$ for $n = 0.3$ and at $\gamma = 0.5$ for $n = 1$ and to enhance the heat transfer in rotating cylinder maximum confined channel and moderate asymmetric rotating cylinder is suggested.

References

1. Thakur P, Tiwari N, Chhabra RP (2018) Flow of a power-law fluid across a rotating cylinder in a confinement. *J Non-Newtonian Fluid Mech* 251:145–161
2. Nirmalkar N, Chhabra RP (2012) Forced convection in power-law fluids from an asymmetrically confined heated circular cylinder. *J Non-Newtonian Fluid Mech* 55:235–250
3. Prasad K, Paramane SB, Agrawal A, Sharma A (2011) Effect of channel-confinement and rotation on the two-dimensional laminar flow and heat transfer across a cylinder. *Numer Heat Transfer Part A Appl* 60:699–726
4. Bijjam S, Dhiman A, Gautam V (2015) Laminar momentum, and heat transfer phenomena of power-law dilatant fluids around an asymmetrically confined cylinder. *Int J Therm Sci* 88:110–127
5. Mettu S, Verma N, Chhabra RP (2006) Momentum and heat transfer from an asymmetrically confined circular cylinder in a plane channel. *Heat Mass Transfer* 42:1037–1048
6. Cliffe KA, Tavener SJ (2004) The effect of cylinder rotation and blockage ratio on the onset of periodic flows. *J Fluid Mech* 501:125–133
7. Bharti RP, Chhabra RP, Eswaran V (2007) Effect of blockage on heat transfer from a cylinder to power law liquids. *Chem Eng Sci* 62:4729–4741

8. Thakur P, Tiwari N, Chhabra RP (2019) Momentum and heat transfer from an asymmetrically confined rotating cylinder in a power-law fluid. *Int J Therm Sci* 137:401–430
9. Zovatto L, Pedrizzetti G (2001) Flow about a circular cylinder between parallel walls. *J Fluid Mech* 440:1–25

Flow and Heat Transfer Investigation of Liquid Heat Sink for an IGBT Module



Puja Koch, Alankrita Singh, and Sudhakar Subudhi

Nomenclature

AR	Aspect ratio
H	Height of mini channel (m)
Q	Power supplied (W)
R_{th}	Thermal resistance ($^{\circ}\text{C}/\text{W}$)
T_j	Junction temperature ($^{\circ}\text{C}$)
T_{in}	Inlet temperature of water ($^{\circ}\text{C}$)
W	Width of mini channel (m)

1 Introduction

In today's world, electronic components like resistors, transistors, diodes, and integrated circuits are used in most devices. These power electronic devices generate heat while operating and fail to function properly beyond their operating temperature. With advanced technology, electronic devices are getting smaller, therefore overheating components cause devices less functional and longevity. Reducing the operating temperature of the device by 10°C doubles its expected life [1].

There are different cooling methods used for heat dissipation in electronic devices. Existing cooling methods can be classified as natural & forced convection and liquid evaporation. Among these, forced convection liquid cooling and liquid evaporation methods are the most effective techniques for high heat flux. Many researchers are using forced convection liquid cooling method for its operation at micro-scale

P. Koch (✉) · A. Singh · S. Subudhi
Department of Mechanical and Industrial Engineering, IIT Roorkee, Roorkee 247667, India
e-mail: puja_k@me.iitr.ac.in

level. Micro-channel and mini channel heat sinks have high heat transfer capability. Microchannel-based cooling systems have drawn a lot of attention due to its exceptional cooling performance, very tiny size, and suitability for small electronic devices.

In liquid cooling, it is important to choose a coolant with good thermophysical properties such as high specific heat, high thermal conductivity, low viscosity, non-corrosiveness, thermal stability, etc. Water has a wide range of applications for its suitable nature as a coolant. The first microchannel heat sink was introduced by Tuckerman and Pease [2] in 1981. They conducted analytical and experimental work on water-cooled heat sink consolidated into an integrated chip. Xie et al. [3] numerically investigated the turbulent heat transfer and pressure drop characteristics of a mini channel heat sink with water as coolant. They claimed pressure drop as an important parameter for design of heat sink and is sensitive to channel geometry. The heat transfer performance by deep and narrow channels was better than shallow and wide channels at the expense of lower pressure drop. Jajja et al. [4] experimentally investigated water-cooled finned mini channel heat sinks for microprocessor cooling. They confirmed that geometrically improved heat sinks with water as coolant have huge scope for cooling microprocessors which generate around 300 W of heat.

Limited reported work could be found on performance of heat sinks using actual electronic components. Shi et al. [5] had compared the thermal performance of H-CFMC (Horizontal counter-flow microchannel) and L-CFMC (Longitudinal counter-flow microchannel) base plate for IGBT module using microchannel cooling. The H-CFMC baseplate gave lower junction temperature along with lower pressure drop due to its shorter channel length. Mohammadi et al. [6] performed water cooled mini-channel heat sink experiment to study thermal management of electronic chipset of Inter® Core™ i7-940XM CPU. They found that the cooling performance of coolant decreases with increase in heat flux of the electronic chipset.

From the above discussion, it can be said that heat transfer performance of liquid heat sink depends on multiple parameters and existing data are not sufficient to predict the performance of any random liquid heat sink. Further most of the studies have pertained to consideration of uniform heat flux or uniform temperature at base of heat sink instead of considering real electronic devices which need to be cooled. It is a known fact that any electronic device fails when the temperature of any one of the components reach beyond its operating temperature. Hence the prime objective of any heat sink design should be to reduce the junction temperature of devices rather than reducing the average temperature of component. Therefore, the present study is devoted to design and investigation of different configurations of mini-channel of liquid heat sink for cooling of real IGBT.

2 Numerical Modelling

In this chapter, an industry-based model of IGBT is used for thermal management investigation. A 1200 V/115 A IGBT module (SKM75GB12T4, made by Semikron) [7] is considered for the numerical analysis. A schematic diagram of the multi-layered IGBT module used in present study are shown in Fig. 1. The dimensions and corresponding mechanical properties of various layer of the IGBT module is described in Table 1.

The computational model consists of a mini channel copper heat sink for cooling of IGBT module. The dimension of the heat sink is $100 \times 50 \times 3 \text{ mm}^3$. Forty-nine mini channels are aligned along the length of the heat sink whose one end acts as inlet and other end as outlet. In the present work two different shapes of mini channels; rectangular and circular shaped are numerically analysed. A single rectangular mini channel is 0.8 mm in height and 0.5 mm in width. By keeping the same cross-sectional area in both the shapes, a circular mini channel is designed for a radius of 0.36 mm. The computational model of the IGBT package with heat sink is illustrated in Fig. 2. Liquid water is passed through these mini channels as a coolant for forced convection of IGBT module.

In the present work, the heat transfer from the IGBT package to a mini channel heat sink is analysed. A three-dimensional computational model is developed; then

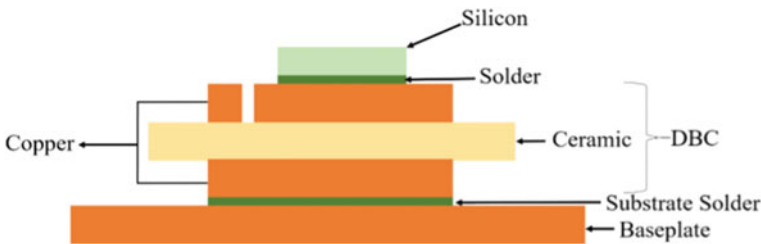


Fig. 1 Schematic diagram of SKM75GB12T4 module used in the present study

Table 1 Geometric and material details of the module

Material layer	Thickness (mm)	Length (mm)	Width (mm)	Thermal conductivity (W/mK)
Silicon	0.15	7.24	6.9	153
Solder	0.12	7.24	6.9	66.8
Copper	0.3	28.5	25.8	401
Alumina	0.38	30.6	28	26
Copper	0.3	28.5	25.8	401
Solder	0.12	28.5	25.8	66.8
Baseplate (Copper)	2.8	91.4	31.4	401

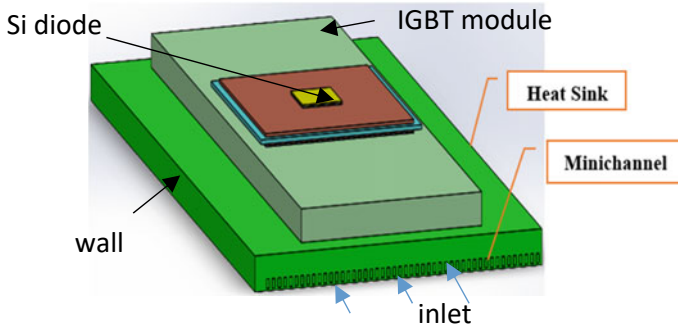


Fig. 2 Numerical model of IGBT module with heat sink fitted with rectangular mini channel

numerically simulated in CFD-based software ANSYS Icepak 2021. Here the model comprises of IGBT module (Diode chip, DBC substrate, baseplate), the solid domain of copper heat sink and water channels in the liquid domain. Following assumptions are made during the modelling-

- (1) The fluid flow in the mini channels is steady, incompressible and laminar with no-slip boundary condition at the channel wall.
- (2) The effect of body force and gravity force is neglected.
- (3) Heat dissipation is neglected and the thermophysical property of liquid is assumed to be constant.

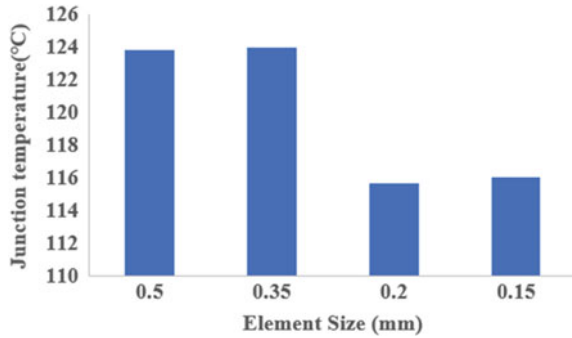
The CFD solver of ANSYS Icepak is used to discretize continuity, steady, incompressible Navier–Stokes equation and energy equation with second order upwind scheme. The coupled algorithm is used for pressure-velocity coupling. Pressure field terms are solved using the SIMPLE algorithm. The solution is assumed to be converged when sum of residuals fall below 10^{-5} for continuity, momentum and turbulence equations and 10^{-7} for energy equation.

Table 2 enlists the boundary conditions applied to the computational model of Fig. 3 for IGBT cooling using mini channel heat sink design.

Table 2 Boundary conditions

Location	Boundary condition
Silicon diode	Constant power input (200W)
Inlet	Inlet velocity-Re = 396–989 Inlet fluid temperature = 305 K
Outlet	Gauge pressure is zero
Heat sink	All external walls are adiabatic
IGBT module	All externals walls are adiabatic

Fig. 3 Mesh independence test for junction temperature of IGBT



2.1 Mesh Independence Test

A mesh independence study is conducted for the 3D computational model. Four different mesh sizes are developed and the automatic mesh method is applied to all the meshing. Here average temperature of the silicon diode (Table 3) and junction temperature of IGBT module (Fig. 4) with rectangular mini channel is compared. As seen from Table 3 and Fig. 4 with element size of 0.2 and 0.15 mm the percentage variation in average temperature is negligible and the variation in junction temperature is below 1%. In order to save computational time without losing accuracy mesh with element size of 0.2 mm is considered for the numerical simulations.

Table 3 Different mesh sizes and nodes for mesh independence study

Mesh	Element size (mm)	Nodes	Junction temperature (°C)
1	0.5	364,288	123.802
2	0.35	947,228	124
3	0.2	3,677,568	115.674
4	0.15	8,960,876	116

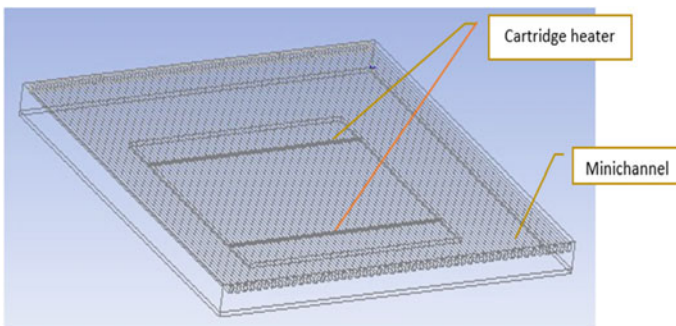


Fig. 4 Schematic diagram of the model adopted from the work of Sohel et al. [8]

2.2 Numerical Model Validation

The current numerical work is validated with the experimental work of Sohel et al. [8]. They worked on a rectangular mini channel heat sink made up of copper with water as a coolant. The inlet temperature of water is set at 32 °C and two constant power supply (cartridge heater) each of 200 W is applied below the heat sink which acted as a power source of IGBT. The width of the channel was kept constant with value of 0.5 mm while the height was 0.8 mm. A computational model depicting the design of heat sink is shown in Fig. 4.

The boundary condition in the numerical model was kept similar to experiment of interest. The experimental result of baseplate temperature of the heat sink for range of Reynolds number is compared with the present numerical model. The maximum and average variation between experimental result of Sohel et al. [8] and the present numerical study are 2.9% and 1% respectively. Such variations are expected to arise because of certain external conditions of experiments which cannot be considered during numerical simulation (Fig. 5).

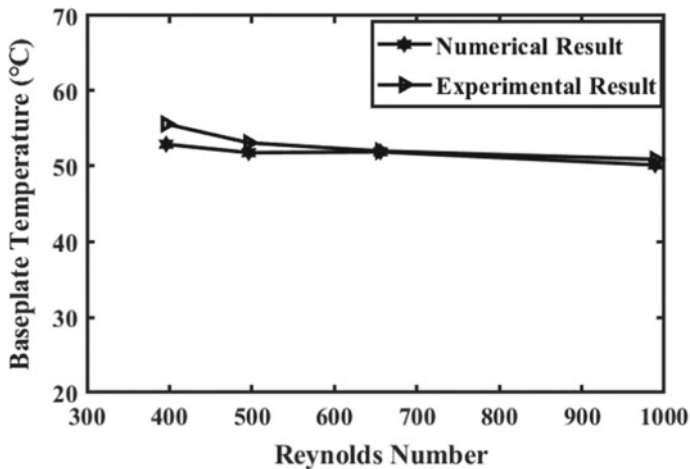


Fig. 5 Comparison of baseplate temperature from experimental work

3 Results and Discussion

3.1 Different Shapes of Mini Channel

A numerical study is conducted to investigate the conjugate heat transfer analysis of cooling of real IGBT module with water cooled minichannel heat sink. In this study, two different shapes of mini channel are compared for determining the heat transfer performance. The Reynolds number are varied from 396 to 989.

The variation of baseplate temperature and junction temperature of the IGBT module for different Reynolds numbers are demonstrated in Figs. 6 and 7 respectively.

Findings reveal that the rectangular mini channel has more heat transfer capacity to water than the circular channel. This result is consistent with result of Naquiuddin.et al. [9]. Rectangular mini channel has a higher surface area to cross-sectional area ratio than circular mini channel, that is why heat dissipation is more in the case of the rectangular-shaped channel. As expected, the heat transfer from the IGBT module to the heat sink significantly increases with the increase of Reynolds number in both rectangular and circular channels. The temperature contour of IGBT module with circular and rectangular channel heat sink at a cut section is shown in Figs. 8 and 9, respectively. As seen from the contours the rectangular mini channel is able to bring down the junction temperature to greater extent compared to that of the circular mini channel.

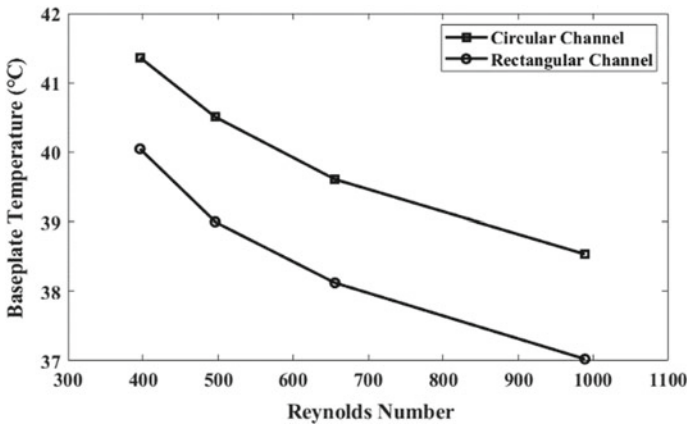


Fig. 6 Baseplate temperature of IGBT module for rectangular and circular mini channel at different Reynolds numbers

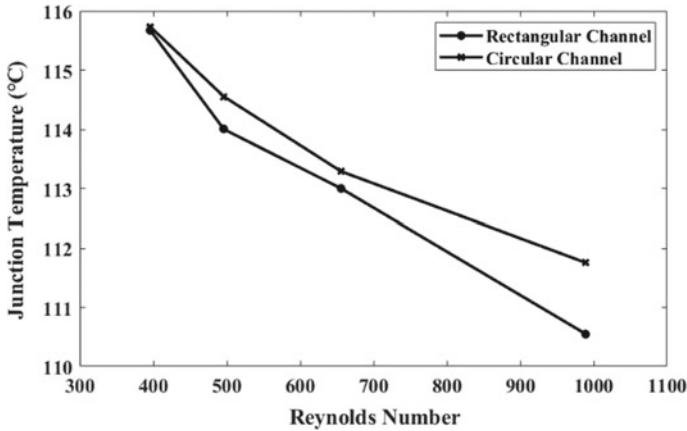


Fig. 7 Junction temperature of IGBT module for rectangular and circular mini channel at different Reynolds numbers

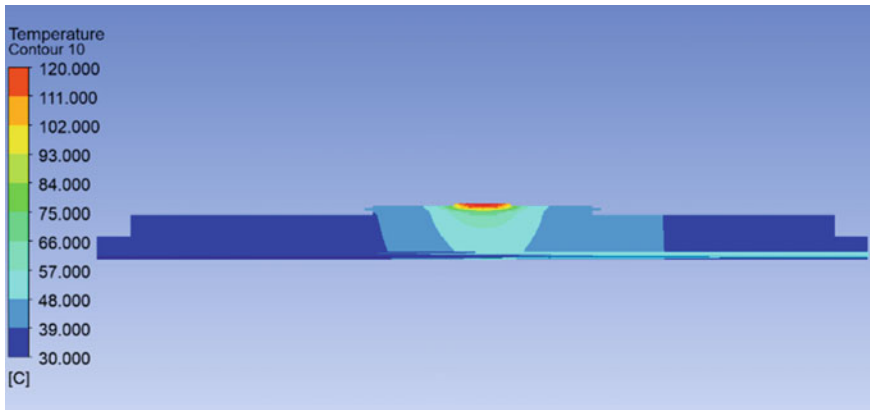


Fig. 8 Temperature contour of IGBT module with circular channel cut-section at $Re = 989$

3.2 Aspect Ratio of Rectangular Mini Channel

Rectangular mini channels have high heat dissipating capacity but the ratio of height to width of a rectangular channel affects lot in its heat transfer efficiency. In the current study the effect of aspect ratio on rectangular channel’s heat transfer is investigated. Aspect Ratio (AR) of rectangular channel is defined as the ratio of Height to Width (H/W) of the channel. Four different aspect ratios (0.8–1.6) are analysed to investigate their effect on baseplate temperature and junction temperature as depicted in Fig. 10 and 11 respectively. It is seen from the figure that as the AR increases the effectiveness of heat transfer also increases. This can be attributed to the fact that the height of the channel act as a fin which facilitates more heat dissipation. But there is a limitation

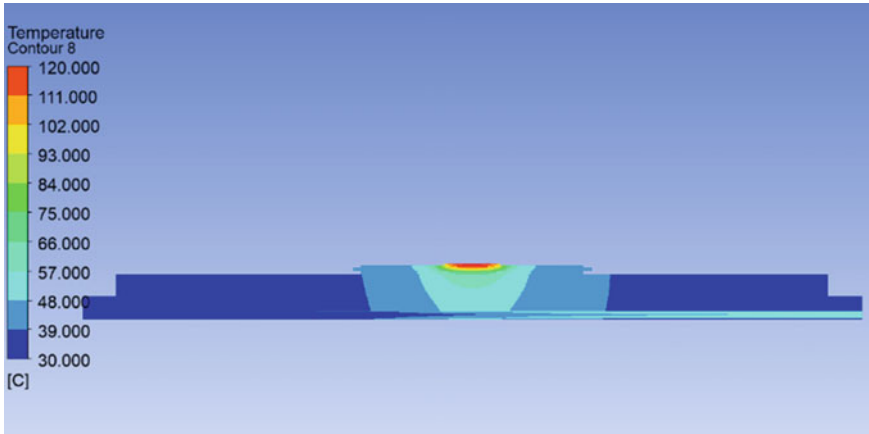
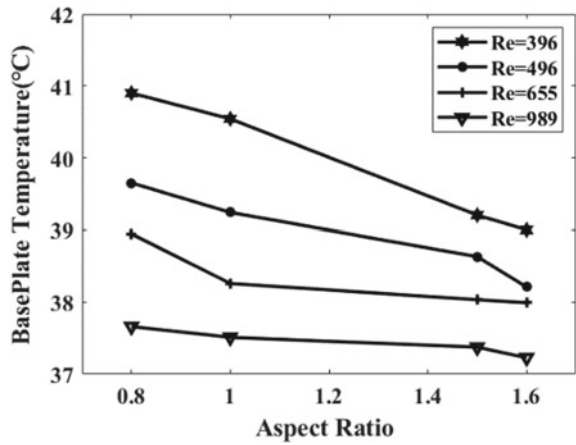


Fig. 9 Temperature contour of IGBT module with rectangular channel cut-section at Re = 989

Fig. 10 Effect of various AR on baseplate temperature at different Reynolds numbers



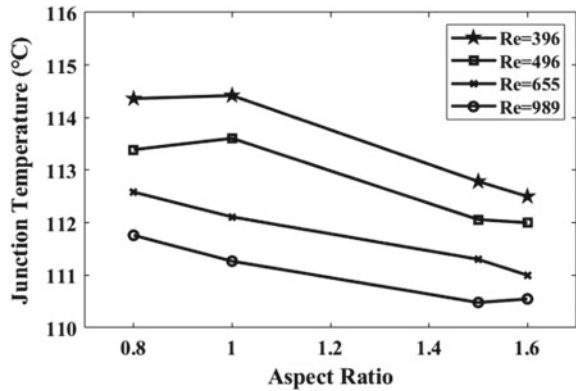
in height increment; beyond the point of the optimum height of the channel, the heat transfer enhancement is found stagnant.

3.3 Thermal Resistance

The junction-to-case thermal resistance of the model is calculated as,

$$R_{th} = \frac{T_j - T_{in}}{Q} \tag{1}$$

Fig. 11 Effect of various AR on junction temperature at different Reynolds numbers



The thermal resistance for rectangular and circular mini channel is evaluated at different Reynolds numbers. Results show that the circular channel offers more thermal resistance than that of the rectangular channel as illustrated in Fig. 12. The convection thermal resistance plays a more dominant role than conduction and capacitive thermal resistance [10]. As the convective heat transfer in the circular channel is less than that of rectangular channel, thus generating more thermal resistance than rectangular channel.

Figure 13 shows the effect of channel height on thermal resistance. It can be seen that the thermal resistance decreases with increasing height up to its optimum height beyond which no much change occurs.

As per the datasheet of IGBT provided by the manufacturer [7] the maximum allowed junction temperature is 150 °C with a required junction-to-case thermal resistance value of 0.38 K/W. To meet this requirement, among all cases the rectangular channel with aspect ratio of 1.5 at Reynolds number of 989 gives junction temperature and junction-to-case thermal resistance values of 110.5 °C and 0.39 °C/W respectively.

Fig. 12 Variation in thermal resistance for rectangular and circular minichannel at different Reynolds numbers

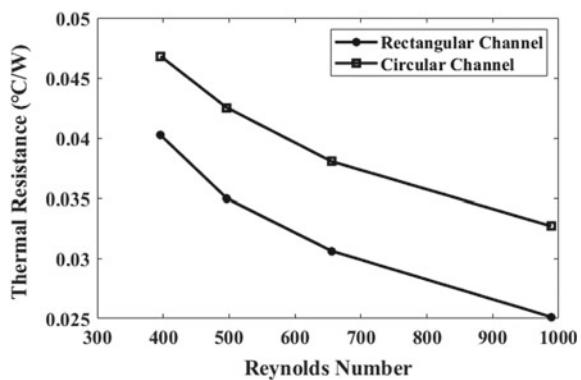
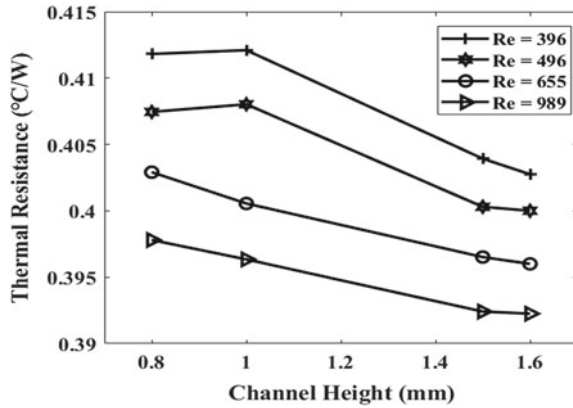


Fig. 13 Effect of channel height on thermal resistance at different Reynolds numbers



4 Conclusions

In the present study, thermal management of IGBT module integrated with mini channel heat sink was studied. Heat transfer analysis for two different shapes, rectangular and circular shaped mini channel was conducted at different Reynolds numbers. The effect of aspect ratio on the cooling performance of rectangular mini channel and thermal resistance of the model is elaborately investigated. Statement from the above result can be concluded into following points-

- (1) Rectangular mini channel has better heat transfer capability than circular mini channel having a lower baseplate and junction temperature of IGBT module, as rectangular channel has higher surface area to cross-sectional ratio than circular channel.
- (2) Higher aspect ratio of rectangular mini channel is more convenient for cooling performance. Channel height act as fin in a higher aspect ratio, thus enhancing heat dissipation. Also, it was noticed that beyond the optimum point, there was no change in temperature.
- (3) Thermal resistance of circular channels was found to be higher, because of its low convective heat transfer than rectangular channel. Higher channel height has lower thermal resistance comparatively.
- (4) Among all cases the rectangular channel with an aspect ratio of 1.5 at Reynolds number of 989 gives junction temperature and junction-to-case thermal resistance values of 110.5 °C and 0.39 °C/W respectively which is meeting the actual requirements of the selected IGBT module as per its datasheet.

Acknowledgements The authors acknowledge the High-Performance Computing Facility provided by IIT Roorkee to carry out the computational work.

References

1. Electronics cooling methods for PCB thermal management, system analysis blog, Cadence
2. Tuckerman DB, Pease RFW (1981) High-performance heat sinking for VLSI. *IEEE Electron Device Lett* 2(5):126–129
3. Xie XL, Tao WQ, He YL (2007) Numerical study of turbulent heat transfer and pressure drop characteristics in a water-cooled minichannel heat sink. *J Electron Packaging* 129(3):247–255
4. Jajja SA, Ali W, Ali H, Ali A (2014) Water cooled minichannel heat sinks for microprocessor cooling: effect of fin spacing. *Appl Therm Eng* 64(1–2):76–82
5. Shi M, Yu X, Tan Y, Wang X, Zhang X, Li J (2022) *Appl Therm Eng* 201:117718
6. Mohammadi M, Taheri A, Passandideh-Fard M, Sardarabadi M (2020) Electronic chipset thermal management using a nanofluid-based mini-channel heat sink: an experimental study. *Int Commun Heat Mass Transfer* 118(September):104836
7. SKM75GB12T4—Semikron—IGBT Module, Half Bridge, 115 A.
8. Sohel MR, Khaleduzzaman SS, Saidur R, Hepbasli A, Sabri MFM, Mahbubu IM (2014) An experimental investigation of heat transfer enhancement of a minichannel heat sink using $\text{Al}_2\text{O}_3\text{-H}_2\text{O}$ nanofluid. *Int J Heat Mass Transfer* 74:164–172
9. Naquiuddin NH, Saw LH, Yew MC, Yusof F, Ng TC, Yew MK (2018) Overview of micro-channel design for high heat flux application. *Renew Sustain Energy Rev* 82:901–914
10. Soudagar M, Kalam MA, Sajid M, Afzal A, Banapurmath NR, Akram N, Mane SD, Saleel A (2020) Thermal analyses of minichannels and use of mathematical and numerical models. *Numer Heat Transfer Part A Appl* 77(5):497–537

Numerical Investigation of Laminar Fluid Flow and Heat Transmission in a Filleted Grooved Channel



Ananya Mandal, Auronil Mukherjee, Soumen Chakraborty, and Supratim Saha

Abbreviations

Nomenclature

l	Groove length (mm)
C_p	Specific heat at constant pressure (J (kg.K ⁻¹))
L	Periodic length of the module (mm)
R	Fillet radius (mm)
h	The grooved channel's half height (mm)
Nu	Local Nusselt number
Nu_p	Nusselt number for the parallel-plate channel
Nu_m	Space-averaged Nusselt number
Pr	Prandtl number
Pe	Peclet number
ν	Kinematic viscosity
Re	Reynolds number
T	Temperature (K)
S	Distance along the grooved channel wall from the inlet (mm)
p	Pressure (Pa)
u	Velocity components in X-direction
v	Velocity components in Y-direction
U	Maximum velocity (ms ⁻¹)
U_m	Mean velocity (ms ⁻¹)

A. Mandal · S. Chakraborty · S. Saha (✉)
Department of Mechanical Engineering, MSIT, Kolkata 700150, India
e-mail: Supratimiitm@gmail.com

A. Mukherjee
Department of Applied Mechanics, IIT Madras, Chennai 600036, India

U	Velocity vector
Δp	Pressure drop (Pa)
α	Heat transfer coefficient of surface ($\text{W. (m}^2\cdot\text{K)}^{-1}$)
η	Efficiency
ρ	Density of the fluid (kg m^{-3})
k	Thermal conductivity of fluid (W. (m.K)^{-1})
μ	Dynamic viscosity

Subscripts

m	Mean
w	Wall
out	Outlet
in	Inlet
avg	Average

1 Introduction

For long-term energy security which has less emissions, renewable energy sources are essential. Utilizing the temperature differential between deep sea water (3–10 °C) and surface water (20–30 °C), ocean thermal energy conversion (OTEC) proves to be an exceptionally efficient method for generating clean energy [1]. In order to optimize heat transfer, much study and analysis has been done for better understanding of the geometric pattern of the channels [2]. Most researchers have taken into account the channel geometry of the contracted and extended types. Several academics are conducting experimental studies to determine the relationship between pressure drop and heat transmission in converging and diverging tubes [3–5]. To analyze the flow of water in channels, Pereira and others [6] employed a rectangular groove on a plate. They conducted study on fluid flow deflection and various complex flow patterns. Using statistical methods [7], the investigation conducted by Farhanieh focused on the analysis of heat transfer and fluid flow in steady laminar channels containing trapezoidal grooves. Wirtz et al. [8] researched about the performance of heat transfer and the measured pressure drops on both walls for the V-grooved channel. Using symmetric and asymmetric grooves in channels, the heat transfer and fluid flow were examined by Adachi et al. [9]. They proposed a correlation between heat transmission and pressure drop using statistical techniques to identify the most effective channel layouts with coherent grooved segments. Deflectors promote heat transfer by increasing the mixing of fluid between the main flow and grooved zone, according to Gutierrez et al. [10] investigation of their effect in a grooved channel. By observing temperature fields while varying the Reynolds numbers, Herman et al. [11] conducted

an experiment to investigate the characteristics of the local heat transfer coefficient in a grooved channel. The Tollmien Schlichting (T-S) wave causes instability and self-sustaining oscillations when the Reynolds number surpasses a particular threshold, as demonstrated in this work. At 1054 value of Reynolds number, the oscillations of flow were first observed here. Huang et al. [12] employed both computational and experimental methods to establish the highest heat transfer coefficient achievable for different groove lengths in grooved channels subjected to pulsatile flow. A shorter downstream reversed flow zone results [13, 16] during flow contraction from filters restricting fluid flow toward channel walls. The introduction of fillet to grooved channels increases heat transfer and efficiency for OTEC application [16]. There is a need for understanding about the locations which influence the characteristics of heat transmission in a grooved channel and how spatial modification to sharp corners enhance performance parameters.

The goal of the study is to enhance heat transmission rate in consistently grooved channels by adding fillet at various sharp locations in the channel. Keeping the Reynolds number between 50 and 250, a continuous flow is used for the simulation. Fillets were introduced at each corner except inlet and outlet of the channel, and the crucial site for fillet introduction is identified. The heat transfer and efficiency of different cases of filleted configurations were compared with the current sharp-cornered conventional channel geometry. At various Reynolds numbers, the insertion effect of the fillet on Nusselt number, pressure drop, and efficiency is investigated.

2 Methodology

2.1 Two-Dimensional Computational Details

According to Fig. 1, the computational domain for this investigation consists of 25 grooves. The periodic length (L), length (l), and height (h) of the groove are 20 mm, 10 mm, and 2.5 mm, respectively, according to literature [14]. The fillet under investigation in this study has a radius of 1 mm is shown in Fig. 2. The working fluid, water, enters the module through a far-upstream intake before passing through the entrance zone and flowing into the module. In the accompanying diagram, the X-axis represents the direction of flow, while the Y-axis is perpendicular to it, with the origin at point O. The fluid is assumed to be incompressible, and the flow is modeled as two-dimensional (2-D) [9]. Throughout the simulation, it is assumed that water's thermal conductivity remains constant [14].

The governing equations for the laminar incompressible 2-D steady flow are shown below in the Cartesian coordinate system.

Conservation of mass:

$$\frac{\partial u}{\partial x} + \frac{\partial v}{\partial y} = 0 \quad (1)$$

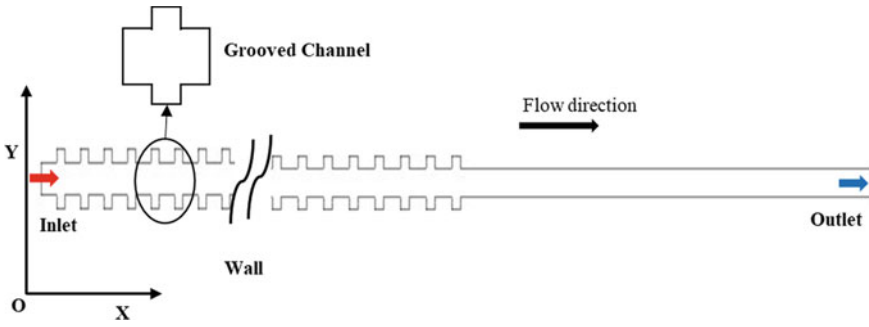
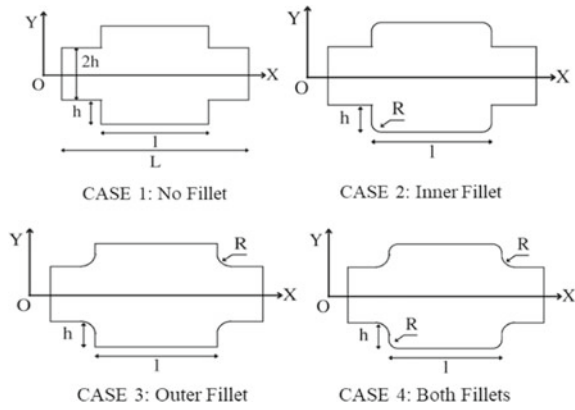


Fig. 1 Illustrative diagram of the computational domain

Fig. 2 Different cases of grooved channel considered in the study



(l = 10mm, L = 10mm, h = 2.5 mm, R = 1 mm)

Conservation of momentum:

$$\rho \left(u \frac{\partial u}{\partial x} + v \frac{\partial u}{\partial y} \right) = - \frac{\partial p}{\partial x} + \left(\frac{\partial^2 u}{\partial x^2} + \frac{\partial^2 u}{\partial y^2} \right) \tag{2}$$

$$\rho \left(u \frac{\partial v}{\partial x} + v \frac{\partial v}{\partial y} \right) = - \frac{\partial p}{\partial y} + \left(\frac{\partial^2 v}{\partial x^2} + \frac{\partial^2 v}{\partial y^2} \right) \tag{3}$$

The energy equation of this two-dimensional arrangement is:

$$\rho C_p \left(u \frac{\partial T}{\partial x} + v \frac{\partial T}{\partial y} \right) = k \left(\frac{\partial^2 T}{\partial x^2} + \frac{\partial^2 T}{\partial y^2} \right) \tag{4}$$

Reynolds number along with Prandtl number averages are calculated as follows: $Re = U_m \frac{2h}{\nu}$ and $Pr = \frac{\mu C_p}{k}$, where ν is the fluid’s kinematic viscosity, and k is thermal conductivity.

2.2 *Boundary and Initial Conditions*

- (1) At the entrance of the channel, the fluid enters at a constant temperature, T_0 . A constant velocity profile in correspondence with the maximal velocity is applied depending on the Reynolds number. The temperature of inlet is similar to the heat exchanger temperatures found in the OTEC system. The following are the boundary conditions of the inlet:

$$u = U, v = 0, T_0 = 283 \text{ K} \quad (5)$$

- (2) At the computational domain's outlet, the condition of outflow is applied. A boundary condition with constant pressure is being imposed [14].

$$\partial T / \partial x = 0 \text{ and } p_{\text{out}} = 0.01 \text{ Pa} \quad (6)$$

- (3) The top and lower walls of the grooved channel, which are maintained at the same temperature, are subjected to a no slip boundary condition. The following are the boundary requirements at the walls:

$$u = U, v = 0, T_w = 303 \text{ K} \quad (7)$$

In this study, the wall temperature was set at a level similar to the heat exchanger temperatures utilized in OTEC applications [14].

2.3 *Numerical Validation*

Using the original geometry and undertaking the same circumstances [9, 14] as in previously published literature studies, the numerical solver is verified in this work for steady flow at $Re = 260$. As stated in the literature, periodic heating conditions are created after groove number 9, and hence, the 20th groove is taken into account for validation [14].

Figure 3 displays the results and compares them to prior research using $Nu_p = 7.54$ as found by the literature [14]. The simulation results demonstrate a remarkable similarity to the findings reported in the literature results.

To showcase the local heat transfer capability, the Nusselt number (Nu) is plotted along the inner surface of the groove on the wall, S. The velocity and temperature fields, presented in Figs. 4 and 5, appear to closely align with the research work conducted by Adachi et al. [9]. No deflection to one side of the channel is detected, and it is seen that the fluid flow is symmetrical with that line.

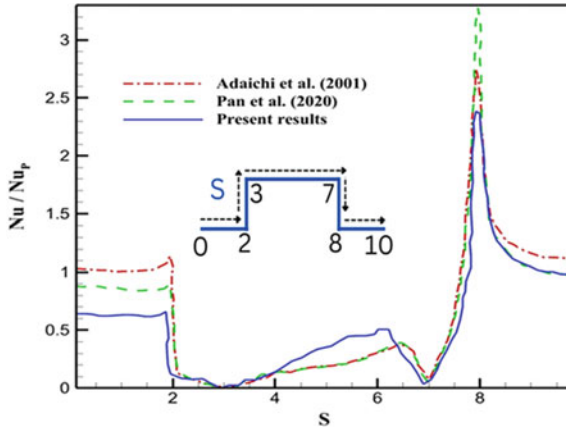


Fig. 3 Comparison between numerical results for the 20th groove and the local Nusselt number distribution as collected from the literature [9, 14]

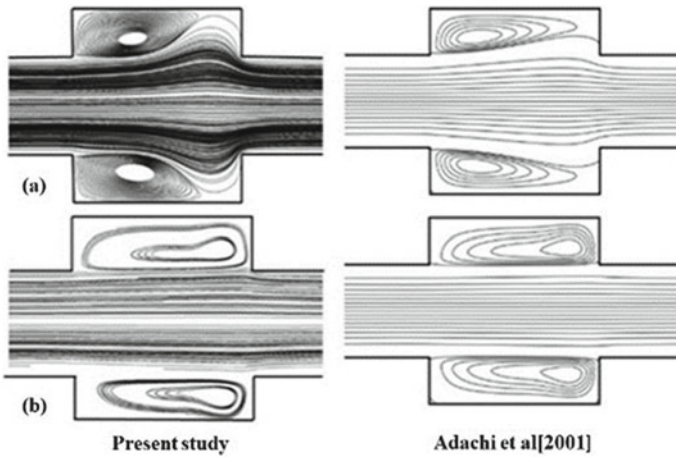


Fig. 4 Velocity fields comparison with Adaichi et al. [9] **a** $Re = 50$ and **b** $Re = 260$

2.4 Grid-Independence Analysis

In order to conduct the grid-independence study, five types of mesh were produced for a fluid flow with $Re = 50$. In that order, they were nodes around 90,000, 500,000, 700,000, 800,000, and 980,000. Figure 6 shows how the space-averaged Nusselt number (Nu_m) varies with different grid sizes. The mesh sizes beyond 800,000 are considered in this investigation as the Nusselt number is not changing due to further increment of grid size. Similar to that, this method is tailored for each case to ensure mesh independence result. The calculation for space-averaged Nu_m is as follows:

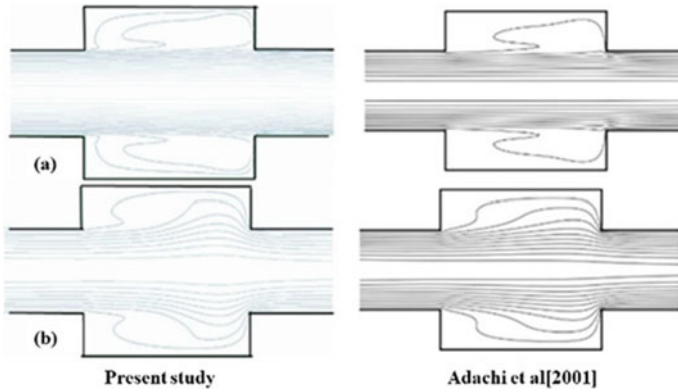
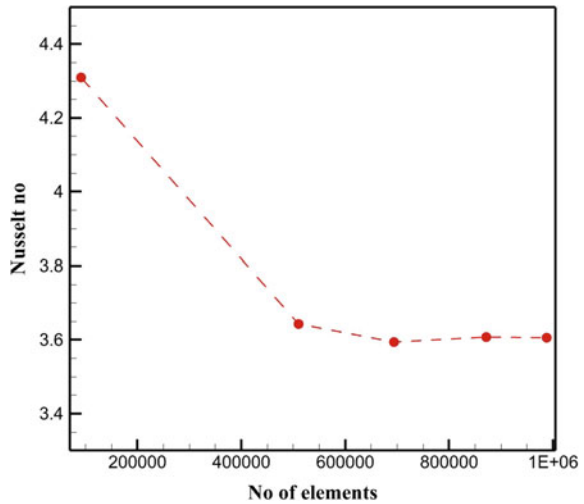


Fig. 5 Temperature fields comparison with Adachi et al. [9] **a** Re = 50 and **b** Re = 260

Fig. 6 Demonstration of grid independence for various mesh sizes



$$Nu_m = \left[\frac{(2h + 4h)/2}{k} \right] \alpha_{\text{avg, wall}}$$

2.5 Numerical Methods

The Ansys Fluent 19.2, a software for computational fluid dynamics (CFD), was used to apply the finite volume method in order to solve the governing equations. The SIMPLE method was used to establish the relationship between pressure and velocity. The momentum problem was discretized using the second-order upwind

technique, which ensured a reliable and stable solution. The energy equation was considered to have converged when the threshold of 10^{-6} was reached, while all other variables in each case were considered to have converged at a threshold on the order of 10^{-3} .

3 Results and Discussion

Figures 7 and 8 illustrates the velocity and temperature contours for four distinct configurations for the 20th groove with the flow having Reynolds numbers equal to 100. As the Reynolds number increases, the fluid flows into the region of the groove which is expanding. On the other hand, the phenomena of enhanced heat transmission are visible in the contours shown below in Figs. 7, 8, 9, and 10.

According to the velocity contours for various Reynolds numbers, the presence of fillets at the corners which are sharp increased the velocity magnitude in the extended grooved region. Due to the fillet's presence, the fluid flow is increased around the corners, improving the temperature distribution as the fluid temperature rises in the extended grooved sections. The existence of fillet configuration at sharp corners has a considerable impact on the incidence of the abovementioned occurrences. Figure 11 shows the pressure drop across the channel for different configurations, and it is seen that the pressure drop is significantly reduced by using the fillets. With regard to the position of the fillet inserted for various cases, the pressure loss change variation

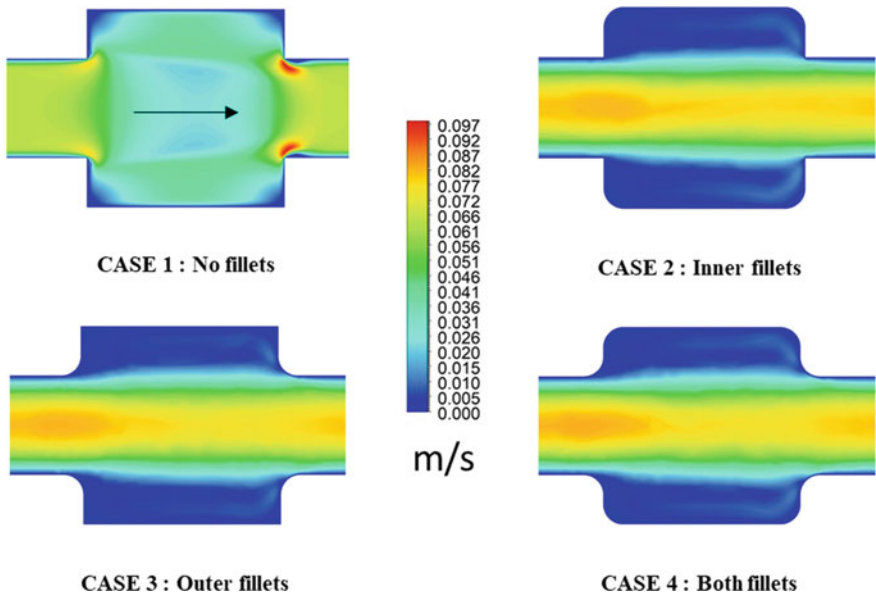


Fig. 7 Velocity contour plots for Re = 100

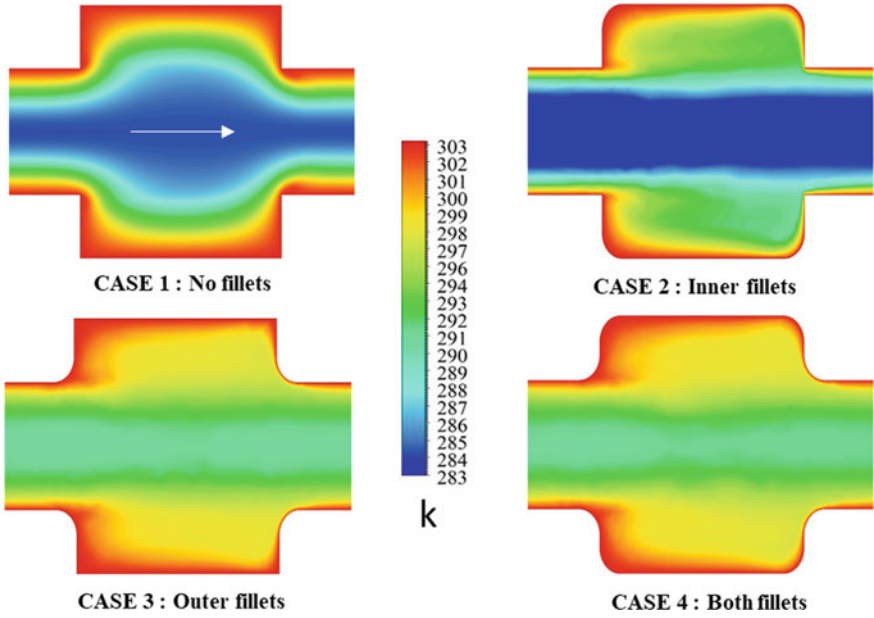


Fig. 8 Temperature contour plots for $Re = 100$

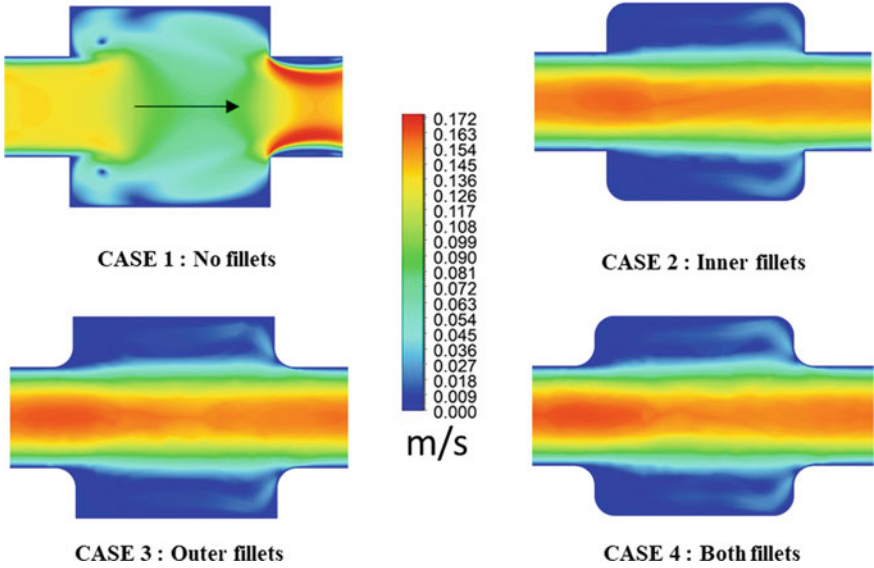


Fig. 9 Velocity contour plots for $Re = 200$

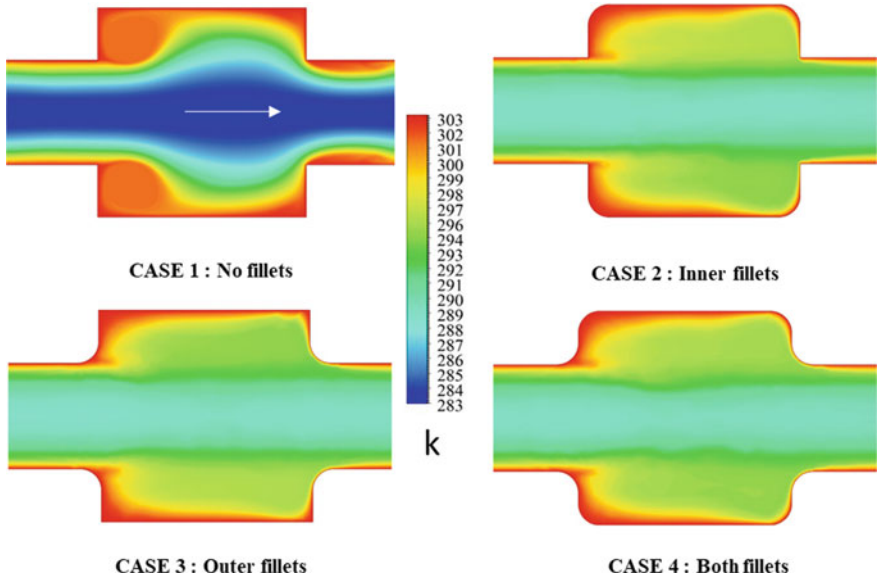


Fig. 10 Temperature contour plots for $Re = 200$

with Reynolds number is nearly same plot in Fig. 12 illustrates how the spatial mean Nusselt number changes with Reynolds number. The fillets play a crucial role in improving heat transfer since they raise the average heat transfer coefficient at the wall, leading to an increase in the Nusselt number.

Fig. 11 Pressure drop with respect to Reynolds number

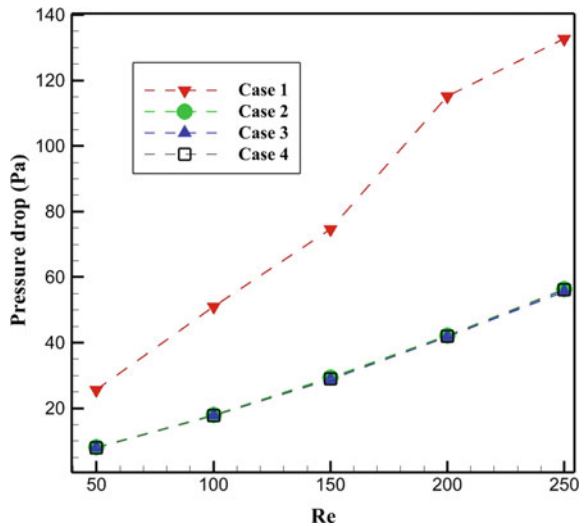
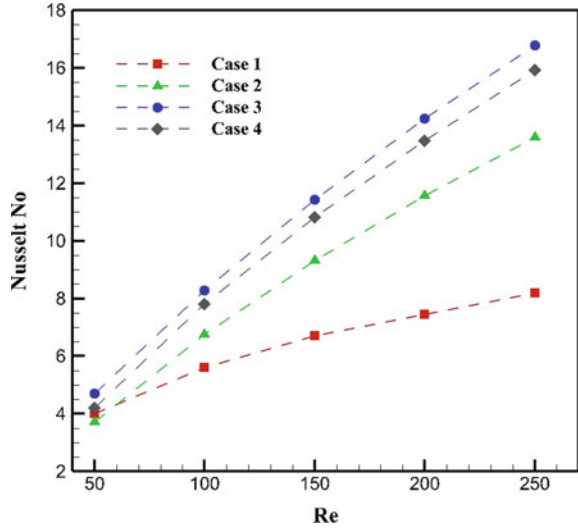


Fig. 12 Nusselt number variation in relation to the Reynolds number in space



The Nusselt number also increases as the Reynolds number does which is consistent with literature [16]. All cases of filleted configuration improved heat transfer performance in comparison with the conventional grooved channel. The field synergy idea of heat transfer improvement, suggested by Guo et al. [15], may be utilized to decipher a basic improvement mechanism of heat transfer. Fillets facilitate convective heat transfer by establishing a reasonably strong synergy between the fields of the temperature and velocity gradients. The energy equation is integrated across the entire computational domain V , and the condition imposed on boundary is modified to form the field synergy method:

$$\iiint_p \rho C_p (U \cdot \nabla T) dV = -k dT/dn_{wall} = \alpha (T_w - T_m) \tag{8}$$

The variables in the equation above are represented by the characters T , U , C_p , and n , which also stand for the specific heat capacity at constant pressure and the directional vector of the heat flux. The heat transfer coefficient is related to the value of the dot product, UT . If the velocity flow field is more parallel to the direction of temperature gradient, heat transmission will be improved. Having a parameter that can improve both pressure loss and heat transfer performance is significant [9]. Efficiency can be determined by calculating the ratio of improved heat transmission to improved pressure drop. It is plotted against Peclet number, i.e., $Pe = Re * Pr$ for all the cases, and the qualitative trend is the same as that of Adachi et al. [8, 9].

$$\eta = \frac{Nu_m / Nu_p}{\Delta p / \Delta p_p} \tag{9}$$

In this work, we employ the space-averaged Nusselt number for a constant flow scenario. In a parallel-plate channel having height of 2 h, the pressure losses can be compared to an equivalent pressure drop of Δp_p , which is equal to $2L/Re$ in magnitude. This graph illustrates the reasonable increase in channel efficiency caused by the presence of a fillet. The divergence is more pronounced in low Reynolds number regimes and basically unchanged as the Reynolds number (Re) increases (Fig. 13).

Table 1 shows the percentage change of pressure drop and Nusselt number of different filleted cases as compared to conventional groove channel. As demonstrated in Table 1, Case 2, Case 3, and Case 4 exhibit pressure drop reductions of 62.93%, 63.56%, and 63.39%, respectively. Likewise, these cases show an increase in Nusselt numbers, with Case 2, Case 3, and Case 4 experiencing improvements of 34.67%, 66.22%, and 56.24%, respectively, as indicated in Table 1. The increase in heat transfer along with decrease of pressure drop by introducing fillet similarly reported literature in heat sink application in microchannel [17].

Fig. 13 Efficiency between heat transfer and pressure drops to Peclet number

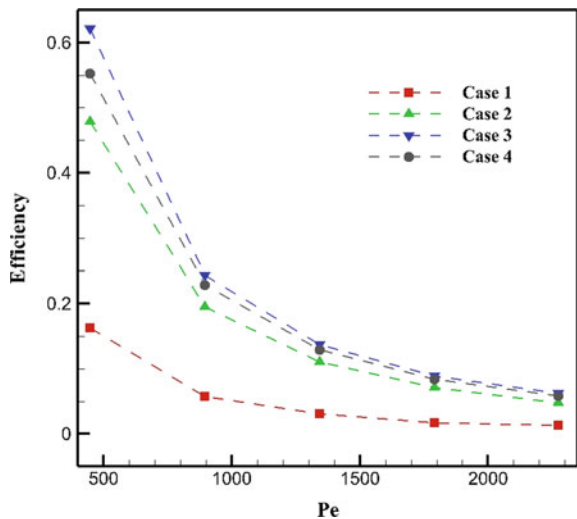


Table 1 Percentage change of engineering relevant parameters with respect to conventional grooved channel (Case 1)

Cases	Pressure drops (%)	Nu_m (%)
Case 2	62.93	34.67
Case 3	63.56	66.22
Case 4	63.30	56.24

4 Conclusions

An analysis of the flow velocity and temperature field in a channel with uniformly spaced grooves that faces the stream direction was implemented computationally using a simplified model of plate-type heat exchangers used in OTEC applications. Using computational fluid dynamics (CFD) concept, several filleted and non-filleted channels having grooved surface with variation of Reynolds numbers from 50 to 250 were computed. Temperature and velocity fields in two dimensions are modeled using a finite volume method. According to numerical findings, adding fillets at any channel's sharp edges enhances heat transmission mechanism and improves pressure drop. Previous research suggests that a significant correlation exists between the velocity of fluid flow and the temperature gradient, which results in an increase in heat transfer through convection. When dealing with low Reynolds numbers, the inclusion of a fillet in a grooved channel significantly enhances the efficiency of heat transfer. The grooved channel having outer fillet (Case 3) has the maximal heat transfer performance. The pressure drop reduction and heat transfer enhancement found to be at least around 60% and 30%, respectively, for different cases in comparison with the conventional channel with groove surfaces.

References

1. Khan N et al (2017) Review of ocean tidal, wave and thermal energy technologies. *Renew Sustain Energy Rev* 72:590–604
2. Derakhshanpour K, Kamali R, Eslami M (2020) Effect of rib shape and fillet radius on thermohydrodynamic performance of microchannel heat sinks: a CFD study. *Int Commun Heat Mass Transfer* 119:104928
3. Souza Mendes P, Sparrow EM (1984) Periodically converging-diverging tubes and their turbulent heat transfer, pressure drop, fluid flow, and enhancement characteristics. *J Heat Transfer* 106(1):55–63
4. Ghaddar NK et al (1986) Numerical investigation of incompressible flow in grooved channels. Part I. Stability and self-sustained oscillations. *J Fluid Mech* 163:99–127
5. Sunden B, Trollheden S (1989) Periodic laminar flow and heat transfer in a corrugated twodimensional channel. *Int Commun Heat Mass Transfer* 16(2):215–225
6. Pereira JCF, Sousa JMM (1993) Finite volume calculations of self-sustained oscillations in a grooved channel. *J Comput Phys* 106(1):19–29
7. Farhanieh B (1991) Numerical investigation of periodic laminar heat transfer and fluid characteristics in parallel plate ducts with streamwise-periodic cavities. *Int J Num Meth Heat Fluid Flow* 1:143–157
8. Wirtz RA, Huang F, Greiner M (1999) Correlation of fully developed heat transfer and pressure drop in a symmetrically grooved channel, pp 236–239
9. Adachi T, Uehara H (2001) Correlation between heat transfer and pressure drop in channels with periodically grooved parts. *Int J Heat Mass Transfer* 44(22):4333–4343
10. Lorenzini-Gutierrez D et al (2015) Numerical and experimental analysis of heat transfer enhancement in a grooved channel with curved flow deflectors. *Appl Therm Eng* 75:800–808
11. Herman C, Kang E (2001) Experimental visualization of temperature fields and study of heat transfer enhancement in oscillatory flow in a grooved channel. *Heat Mass Transfer* 37(1):87–99

12. Huang H et al (2018) Numerical and experimental analysis of heat transfer enhancement and pressure drop characteristics of laminar pulsatile flow in grooved channel with different groove lengths. *Appl Therm Eng* 137:632–643
13. Derakhshanpour K, Kamali R, Eslami M (2020) Effect of rib shape and fillet radius on thermalhydrodynamic performance of microchannel heat sinks: a CFD study. In: *International communications in heat and mass transfer*, vol 119, p 104928
14. Pan J et al (2020) Characteristics of flow behaviour and heat transfer in the grooved channel for pulsatile flow with a reverse flow. *Int J Heat Mass Transfer* 147:118932
15. Guo ZY, Li DY, Wang BX (1998) A novel concept for convective heat transfer enhancement. *Int J Heat Mass Transfer* 41(14):2221–2225
16. Mukherjee A, Saha S (2021) Effect of fillet on fluid flow and heat transfer characteristics in a grooved channel: a numerical study. In: *Proceedings of the 26th National and 4th International ISHMT-ASTFE heat and mass transfer conference*, December 17–20, 2021, IIT Madras, Chennai, 600036, Tamil Nadu, India. Begel House Inc
17. Egab K, Oudah SK, Salman AS (2021) The effect of fillet profile on heat transfer characteristics of heat sink. In: *Heat transfer summer conference*, vol 84874. American Society of Mechanical Engineers

Local Heat Transfer and Fluid Flow Characteristics Over Cylinder in the Presence of Vortex Generator Acting as Flow Guides



Arravaram Lakshman, Sandeep Mantri, and Satyanand Abraham

Nomenclature

D	Diameter of cylinder (m)
h	Heat transfer coefficient ($\text{W}/\text{m}^2\text{K}$)
k	Thermal conductivity of air (W/mK)
Nu	Nusselt number
T_w	Time-averaged cylinder surface temperature ($^{\circ}\text{C}$)
T_a	Air temperature ($^{\circ}\text{C}$)
VG	Vortex generator
θ	Angle of attack of vortex generator ($^{\circ}$)

1 Introduction

Fluid flow over cylinder is a very common situation that has many engineering applications. The heat transfer between the cylinder and the fluid is important in many engineering problems such as cooling of electric vehicle battery and flow in heat exchangers. When air is used as the fluid, heat transfer enhancement techniques are required for improved heat transfer between cylinder and fluid. A widely applied technique is use of vortex generator to increase the turbulence.

The feasibility of using vortex generators to increase turbulence and to divert some mainstream flow over to cylinder surface to enhancement of heat transfer from the cylinders with air as coolant is the objective of the current study. This is proposed as a

A. Lakshman · S. Mantri · S. Abraham (✉)
Department of Mechanical Engineering, National Institute of Technology Warangal,
Hanamkonda, Telangana 506004, India
e-mail: abrahams@nitw.ac.in

method to enhance the heat transfer from the Li-ion battery by air cooling in electric vehicle battery arrangement. Numerical simulations for a single cylinder with one and two flow guides with different configurations were conducted and compared the results with the data obtained for without vortex generator.

2 Literature Review and Objective

Various methods to cool the electric vehicle batteries are mentioned by Kuper et al. [1]. Among those various methods, air cooling is the simplest. However, heat transfer enhancement techniques are required for effective cooling with air. Shuanglong et al. [2] reported the heat generation rates inside vehicle battery for various discharge rates. The problem of vehicle battery cooling can therefore be considered as flow over bundle of cylinders with uniform heat flux condition. The local variation of temperature and the Nusselt number over the cylinder surface is important and needs to be checked for the uniformity in cooling. Intention of the present study is to well understand the flow and local heat transfer over surface in the presence of vortex generators functioning also as flow guides.

Numerical and experimental studies on flow over bare cylinders are available in open literature. Toukir et al. [3] studied flow separation over a cylinder in steady state for low Reynolds numbers. Buyruk et al. [4] conducted experimental study for calculation of average Nusselt number during cooling of cylinder. Haeri and Shrimpton [5] and Jain and Goel [6] conducted numerical studies to investigate the Nusselt number variation at low Reynolds numbers.

Studies on the effect of using vortex generators on the flow over cylinder are also available in literature. Joubert and Hoffman [7] and Unal and Atlar [8] reported considerable drag reduction over the cylinder surface by placing vortex generators at different locations. Hussain et al. [9] performed experimental study of cylinder cooling using vortex generator, and the results show that the heat transfer is increased when the vortex generators were used. Many studies were available on the heat transfer characteristics of circular fins in the presence of vortex generators for the performance enhancement of heat exchangers. Introduction of vortex generators is shown to have increased the heat transfer and reduction in the irreversibility to heat transfer [10–12].

All the studies mentioned above focus mainly on the overall heat transfer coefficient over the cylinder. However, in many conditions, the local variation along the circumference of cylinder is important. Such a condition is cooling of vehicle battery, where the temperature of the battery should be kept at a constant value as possible. In the present study, the local heat transfer along the circumference of a single cylinder is analysed due to the flow over it in the presence of one and two vortex generators acting also as flow guides. The present study is a basis for the future studies on bundle of cylinders with flow guides.

3 Methodology

Numerical investigation on flow over cylinder was conducted using ANSYS 16. Air is taken as the fluid. The initial studies were conducted for a bare cylinder without vortex generators over which air is flowing as shown in Fig. 1. The domain was also considered as circular with diameter of 50 times the diameter of cylinder (D). This case was studied as the base condition and to validate the present methodology. The meshing of the geometry was done using ANSYS meshing tool with wall Y^+ value less than 1.

The present study was conducted with incompressible flow assumption under transient condition. The turbulence model used for the entire study is SST $k-\omega$ as reported in [13]. The governing equations available in the ANSYS guide [14] were used and are not shown here for the sake of brevity.

The inlet condition was given as velocity in the x -direction, and the thermal boundary condition over the cylinder surface was given as constant heat flux. The top and bottom walls were given symmetry boundary condition. A time step of 0.02 s was given for all the conditions. The simulations were conducted to the time till which the lift coefficient variation is identical for several peaks and valleys. The Strouhal number was calculated based on the frequency of the lift coefficient variation. Heat transfer coefficient at any location on the surface was calculated using the Eq. (1)

$$h = \frac{q''}{(T_w - T_a)} \tag{1}$$

where T_w is the time-averaged wall temperature at any location over a period corresponding to two full fluctuation of lift coefficient, i.e. two times the time corresponding to the Strouhal number.

Fig. 1 Domain and boundary conditions without vortex generators

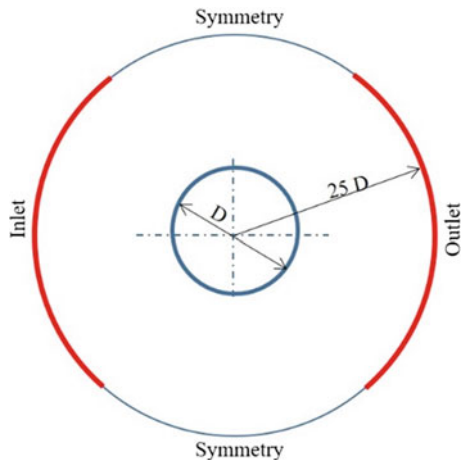
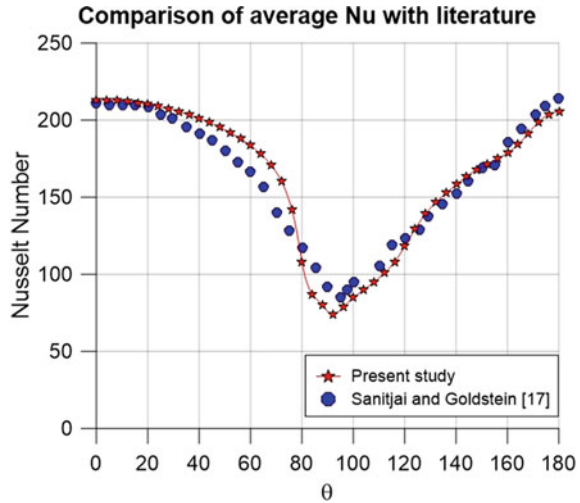


Fig. 2 Nusselt number comparison with Sanitjai and Goldstein [17]



Nusselt number was calculated using Eq. (2) by taking cylinder diameter as the characteristics length.

$$Nu = \frac{hD}{k} \tag{2}$$

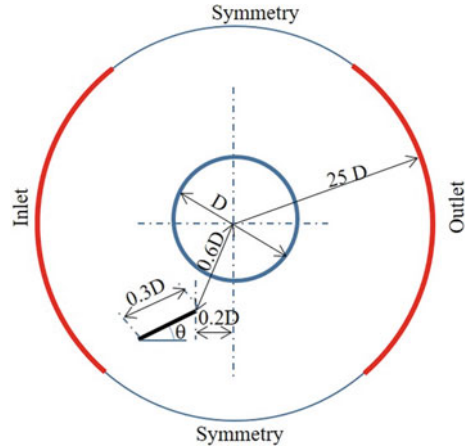
The grid independence test was performed and model showed grid independence after 200,000 meshes by converging the drag coefficient to 1.129, which is the value reported by Incropera and Dewitt [15] at $Re = 3800$. Strouhal number was calculated to be 0.22 based on the lift coefficient variation, which is matching well with the data reported by Sridhar and Patnaik [16]. The circumferential variation of time-averaged Nusselt number (Nu) at Reynolds number equal to 44,800 was compared to the data reported by Sanitjai and Goldstein [17]. The comparison is shown in Fig. 2 and the match found to be satisfactory.

3.1 Problem Modelling

Studies were conducted with vortex generators acting as flow guide only on one side and on both sides of the cylinder. The geometric configurations for single vortex generator (VG) set-up are shown in Fig. 3. As the intension is to divert some main-stream fluid towards the cylinder surface to break boundary layer growth and to increase the turbulence near the surface, the vortex generators were positioned in the favourable pressure gradient region.

For the single flow guide configuration, the vortex generator was placed on the bottom portion of the cylinder. For two flow guide configuration, one vortex generator

Fig. 3 Geometric configuration and boundary conditions for single vortex generator set-up



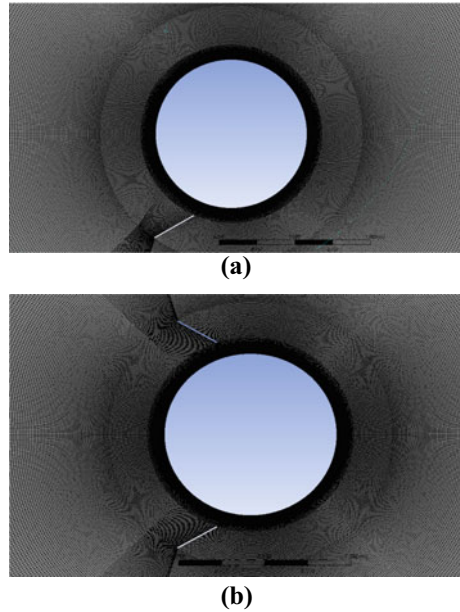
was placed each on top and bottom portions of the cylinder in symmetric manner. Top portion of cylinder is identified as 0° to 180° measured along the top surface of the cylinder from the geometry, where 0° is the stagnation point for bare cylinder. Bottom side is identified with 0° to 180° measured along the bottom surface of the cylinder. The vortex generator was positioned at a distance $0.6D$ from the cylinder centre and $0.2D$ upstream of it. The length of the vortex generator was also fixed as $0.3D$. The angle of attack, which is measured with respect to horizontal, was varied from 30° to 60° in steps of 5° . These geometric values are same for both single and double vortex generators configurations. The Reynolds number was kept constant at 44,800 for all the studied conducted.

The mesh generated for single and double vortex generator configurations is shown in Fig. 4a and b. Structured meshing was done by dividing the domain into several blocks. Grid independency study shows that the number of cells required for one and two vortex generators is 250,000 and 270,000 for angle of attack of 50° , where the drag coefficient converges to 1.6 and 2 for one and two vortex generators, respectively. The same number of cells was maintained for other angle of attacks also.

4 Results and Discussion

The results of both single and double flow guide configurations are discussed here and are compared to the no vortex generator case. The case of one vortex generator (VG) is split into two separate sections, i.e. bottom portion of the cylinder and top portion of the cylinder. The two vortex generators case will be discussed in a single section as it gives symmetric results on both top and bottom sides of the cylinder.

Fig. 4 Mesh for cylinder with **a** one VG, **b** two VG



4.1 *Bottom Side of Cylinder with Single Vortex Generator*

Figure 5 shows the time-averaged Nusselt number (Nu) variation along the circumference of the bottom portion of cylinder with single vortex generator (VG). As the flow guide is placed on the bottom region, a direct impact can be observed on the Nusselt number distribution. It can be observed that for all angle of attacks, the Nusselt number at 0° is same as that for no vortex generator case. However, the initial decrease in Nusselt number is at higher rate than that observed for no vortex condition. The Nusselt number reduces till circumferential location of 52° to 54° and then increases and shows a local maxima near 80° . After this, the Nusselt number fluctuates, and the values are different for different angle of attack. The peak value is Nusselt number is observed between 155° and 160° , depending on the angle of attack. The high value of Nusselt number is observed for angle of attack of 50° and higher.

The behaviour in the Nusselt number variation can be explained based on the flow behaviour around the cylinder. Figure 6a and b shows, respectively, the velocity vectors at an instant around the cylinder for no vortex generator condition and with one vortex generator with 50° angle of attack. The flow is symmetrically distributed to top and bottom regions for no vortex generator condition. Whereas, the presence of single vortex generator as flow guide on the bottom side causes a shift in the stagnation point towards the bottom side. This causes a higher flow rate towards the top side. The diversion of flow towards the cylinder bottom surface due to the flow diverter is also evident from the contour.

Fig. 5 Variation of time-averaged Nusselt number on bottom side with single VG

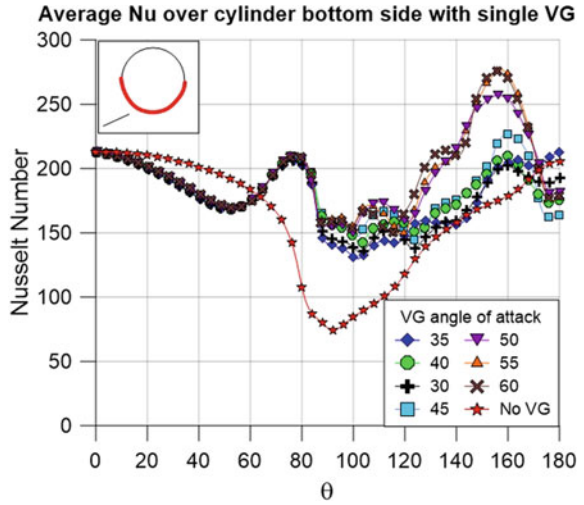


Fig. 6 Velocity vectors at an instant: **a** no VG, **b** single VG with angle of attack of 50°

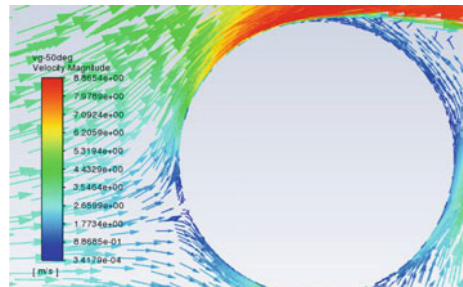
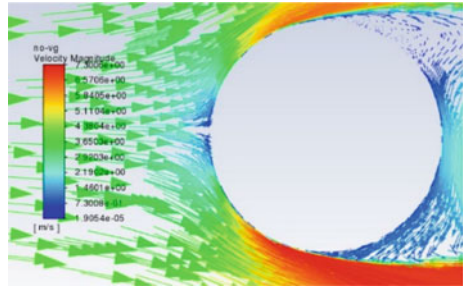


Fig. 7 Time-averaged velocity magnitude around cylinder with single VG at 50° angle of attack

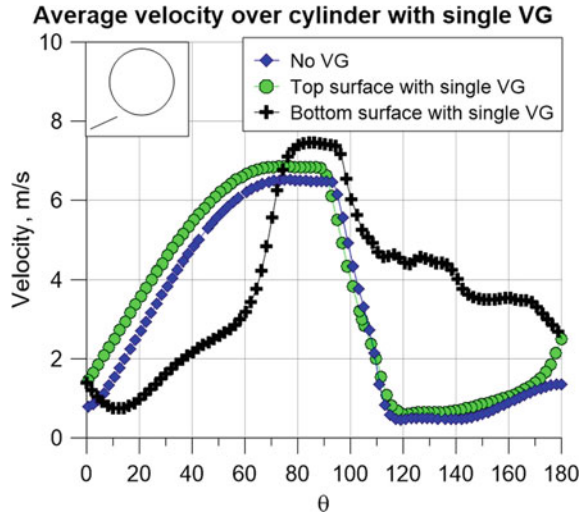


Figure 7 shows the time-averaged velocity vectors along a curve at a distance $0.05D$ from the cylinder surface for both top and bottom surfaces for angle of attack of 50° . This curve goes through the location at midway between cylinder and the vortex generator. Velocity at every location was averaged over time corresponding to two times the Strouhal number.

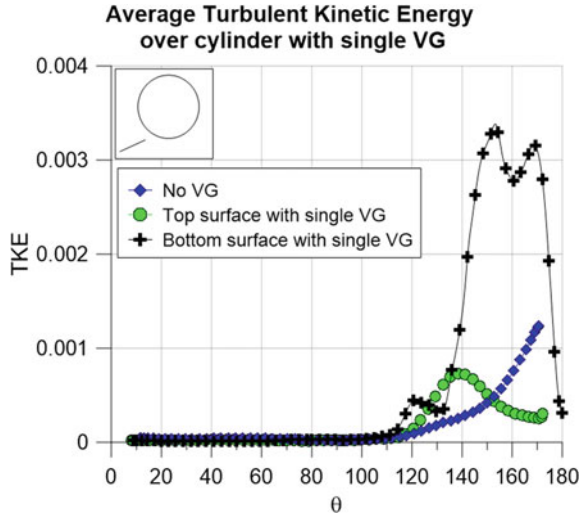
The flow behaviour is similar for other angle of attacks also and is not reported here for the sake of brevity. The velocity values can be observed to be lower on bottom portion compared to no vortex generator condition. The decrease in the flow rate towards the bottom side, and shift in the stagnation point causes higher rate of drop in Nusselt number compared to no vortex generator case at low circumferential angles as shown in Fig. 5.

Figure 8 shows the time-averaged turbulent kinetic energy (TKE) on the cylinder surface with and without single vortex generator for angle of attack of 50° . The increase in the TKE for bottom surface is much higher than no vortex generator condition. TKE peaks at 150° to 155° depending on the angle of attack, which coincides with the peak Nusselt number on the bottom surface as shown in Fig. 5. Thus, the reduction in the flow to the bottom portion is compensated by the increase in the TKE.

4.2 Top Side of Cylinder with Single Vortex Generator

Figure 9 shows the time-averaged Nusselt number variation on the top region of cylinder with single vortex generator. The Nusselt number variations on the top region with and without single vortex generators are similar for low circumferential distances, but with small difference in the values. The higher values on the top region

Fig. 8 Time-averaged TKE around cylinder with single VG at 50° angle of attack



at low circumferential angles are due to the higher velocity to the top region with placement of single vortex generator on bottom as shown in Figs. 6b and 7. However, the local minimum occurs at various circumferential location depending on the angle of attack. This can be attributed to the shift in the stagnation point towards bottom portion due to presence of vortex generator as shown in Fig. 6b.

Considerable difference in the Nusselt number behaviour can be observed for different angle of attack beyond a circumferential location of 120°. Even though no vortex generator is placed on the top side, there is a major increase in Nusselt number on the top side, and as the angle of attack increases the Nusselt number also

Fig. 9 Variation of time-averaged Nusselt number on top side with single VG

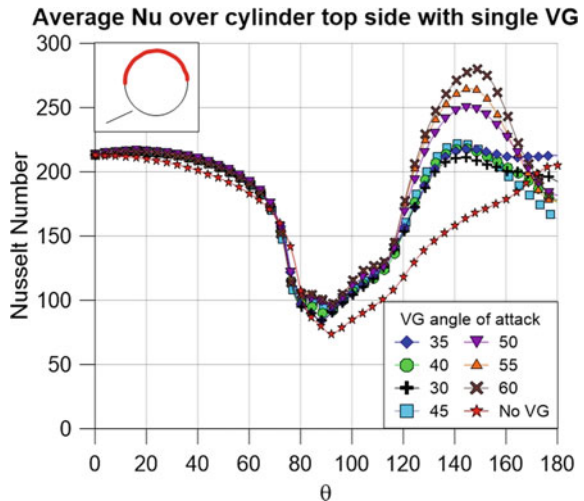
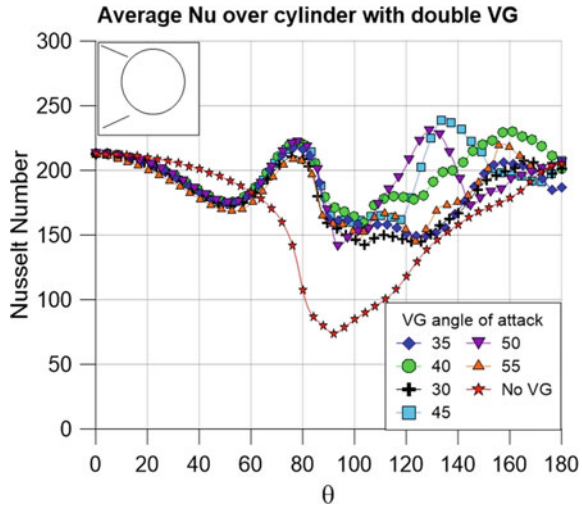


Fig. 10 Variation of time-averaged Nusselt number with double VG



increases. The Nusselt number behaviour becomes more and more similar to that of high Reynolds number with peak value after 140° [14]. This can be due to the increase in the flow rate to the top region. The TKE as shown in Fig. 8 also shows an increase in the value at 140° on top region of cylinder, which coincides with the increase in Nusselt number.

4.3 Cylinder with Two Vortex Generators

Figure 10 shows the Nusselt number variation for double vortex generator configuration. This case gave almost symmetric results when time averaged and therefore results from only one side of the cylinder is discussed.

It can be observed from Fig. 10 that up to a circumferential location of 60° the Nusselt number trend for all attack angles is similar and is less than the case of no vortex generator. After this location, the Nusselt number values show fluctuations, and the values are higher than no vortex conditions. The Nusselt number values variations are very chaotic in nature, and effect of angle of attack is not easily differentiable.

Figure 11 shows the velocity vectors at an instant for double vortex generator configuration. The stagnation point can be observed to be same as that for bare cylinder as shown in Fig. 6a. More flow is diverted away from the cylinder near the stagnation region due to the blockage by vortex generator. However, near to the vortex generator region, more mainstream flow is guided towards the cylinder surface, and the velocity is increased near to the surface. This is clearer from the time-averaged velocity over the surface as shown in Fig. 12.

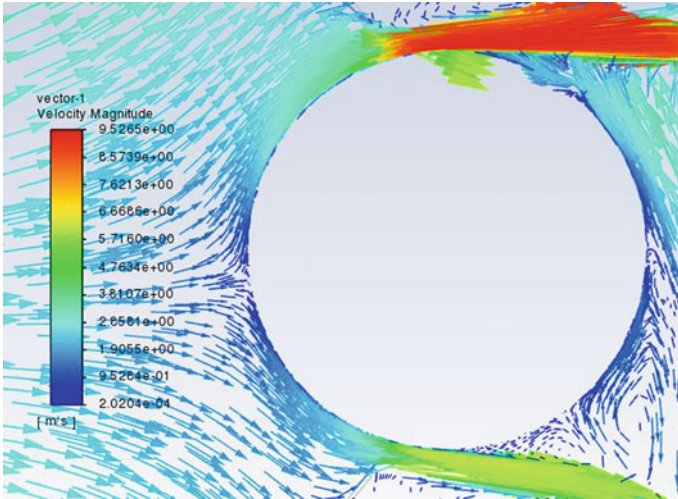
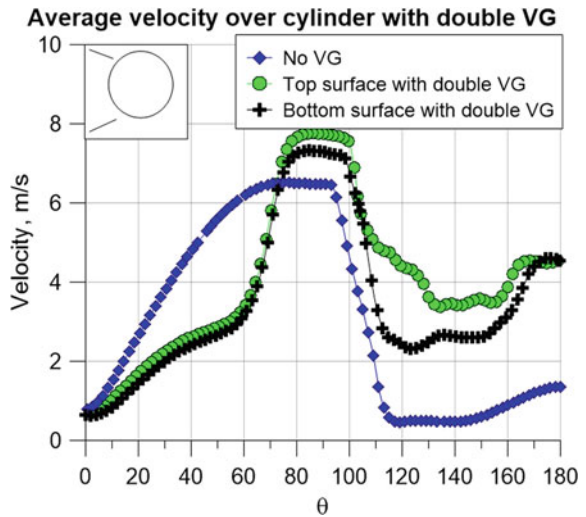


Fig. 11 Velocity vectors at an instant with double VG with angle of attack of 50°

Fig. 12 Time-averaged velocity magnitude around cylinder with double VG at 50° angle of attack



From the above information, it can be said that using of vortex generators is increasing the rate of heat dissipation from the cylinder, and this occurs for both single and double vortex generator cases. Although double vortex generators case is showing an increase in Nusselt number, it is not showing regularity in the trend when the various angle of attacks are being compared. One vortex generator case on the other hand is showing regularity in the Nusselt number patterns with angle of attack.

5 Conclusion

The heat transfer and flow characteristics of flow over cylinder in the presence of vortex generators were studied by numerical methodology. The vortex generators were used to divert some mainstream flow towards the cylinder surface to interrupt the boundary layer growth on the surface in addition to the increase in the turbulence.

Introducing a single vortex generator near one side of cylinder increases the Nusselt number on that side and reduces the fluctuations in the value along the circumference. The opposite side of cylinder also shows an increase in the Nusselt number due to the increase flow rate towards that side. The stagnation point shifts along the circumference towards the location near to the vortex generator. The Nusselt number variations along the surface show good relation with turbulence on the surface in terms of turbulent kinetic energy. Angle of attack more than 45° shows almost same peak Nusselt number values.

The case of cylinder cooling with two vortex generators also increases the Nusselt number. However, it is difficult to get an optimum configuration as the results obtained for various angle of attacks are very similar to each other.

References

1. Kuper C, Hoh M, Miller GH (2008) Thermal management of hybrid vehicle battery systems. In: 24th International battery, hybrid and fuel cell electric vehicle conference and exhibition (EVS-24), Stavanger, Norway
2. Du S, Lai Y, Ai L, Cheng Y, Tang Y, Jia M (2017) An investigation of irreversible heat generation in lithium ion batteries based on a thermo-electrochemical coupling method. *Appl Therm Eng* 121:501–510
3. Islam T, Hassan SMR, Ali M, Islam Q (2013) Finite volume study of flow separation phenomena for steady flow over a circular cylinder at low Reynolds number. In: 10th International conference on mechanical engineering, pp 282–287
4. Buyruk E, Johnson MW, Owen I (1998) Numerical and experimental study of flow and heat transfer around a tube in cross-flow at low Reynolds number. *Int J Heat Fluid Flow* 19(3):223–232
5. Haeri S, Shrimpton JS (2013) A correlation for the calculation of the local Nusselt number around circular cylinders in the range $10 < Re < 250$ and $0.1 < Pr < 40$. *Int J Heat Mass Transfer* 59:219–229
6. Jain PC, Goel BS (1976) A numerical study of unsteady laminar forced convection from a circular cylinder. *J Heat Transfer* 98(2):303–307
7. Joubert PN, Hoffman ER (1962) Drag on circular cylinder with vortex generators. *J Roy Aeronaut Soc* 66(619):456–457
8. Unal UO, Atlar M (2010) An experimental investigation into the effect of VG on the near-wake flow of a circular cylinder. *Exp Fluids* 48(6):1059–1079
9. Hussain S, Liu J, Wang L, Sundén B (2017) Endwall heat transfer enhancement around cylinders with a wall-mounted vortex generator pair, Paper No. IMECE2017-70244, V008T10A014, Proceedings of the ASME International mechanical engineering congress and exposition, November 3–9, 2017
10. Wang LC, Su M, Hu W-L, Lin Z-M, Wang L-B, Wang Y (2011) The characteristic temperature in the definition of heat transfer coefficient on the fin side surface in tube bank fin heat exchanger. *Numer Heat Transfer Part A* 60(10):848–866

11. Ghazikhani M, Khazaei I, Monazzam SMS, Takdehghan H (2016) Exergy destruction analysis of a vortices generator in a gas liquid finned tube heat exchanger: an experimental study. *Heat Mass Transfer* 52(11):2531–2539
12. Wu XH, Yuan P, Luo Z-M, Wang L-X, Lu Y-L (2016). Heat transfer and thermal resistance characteristics of fin with built-in interrupted delta winglet type. *Heat Transfer Eng* 37(2):172–182
13. Ahn J, Sparrow EM, Gorman JM (2017) Turbulence intensity effects on heat transfer and fluid-flow for a circular cylinder in crossflow. *Int J Heat Mass Transfer* 113:613–621
14. Ansys Fluent Theory Guide, Release 15.0, November 2013.
15. Incropera FP, DeWitt DP (2002) *Fundamentals of heat and mass transfer*. Wiley, New York
16. Muddada S, Patnaik BSV (2010) An assessment of turbulence models for the prediction of flow past a circular cylinder with momentum injection. *J Wind Eng Ind Aerodyn* 98(10–11):575–591
17. Sanitjai S, Goldstein RJ (2004) Forced convection heat transfer from a circular cylinder in crossflow to air and liquids. *Int J Heat Mass Transfer* 47(22):4795–4805

Estimating Baking Time for a Bakery Furnace Using Radiation Network Analysis



Guru Bachan Satsangi, Sunny Jagdish Shiyal, Bamaniya Jayesh Pravinbhai, Narayan Jaiswal, and Amit Patel

1 Introduction

The use of the bread is an inevitable part of the diet, and hence, baking is the most fundamental and the most generic need of mankind. Large amount of wood is still being used to bake the bread, and this is especially true for developing nations of Africa and certain parts of Asia. The use of firewood for the baking of the bread is a major incentive in the rural area due to its large availability and at almost zero cost.

Figure 1 shows a typical wood-fired furnace that is commonly used for baking bread in several parts of Africa and Asia [1]. For the purpose of baking, the furnace is first heated up to 400 °C. The time taken for this heating is known as charging time which is typically up to 3 to 8 h [1]. The charging is carried out by supplying hot flue gases in the furnace resulting from the combustion of the wood stocks until the required baking temperature is attained. After the charging of the furnace, the trays filled with the dough are inserted in the furnace to start the baking process. During the baking process, the door is kept closed. However, during a baking process, the operator has a tendency to open and close the door. This is carried out to judge the quality of baking and decide the baking time for a given batch of the bread, and this is decided by the operator intuitively just by a visual inspection. The time required to bake depends largely on the furnace wall temperature. It is required that the bread has a fine and crispy top crust and for that the bread should have low moisture content. This requirement can be achieved by operating the furnace at a high furnace temperature and keeping a low baking time. On the other hand, low quality bread has a thick crust and has a high moisture content. This is resulted due to having a low furnace wall temperature and allowing a high baking time. It is very critical for an operator to constantly visualize a baking process and get an idea of these parameters

G. B. Satsangi · S. J. Shiyal · B. J. Pravinbhai · N. Jaiswal · A. Patel (✉)

Department of Mechanical Engineering, Faculty of Technology and Engineering, The Maharaja Sayajirao University of Baroda, Vadodara, Gujarat, India

e-mail: a.r.patel-med@msubaroda.ac.in

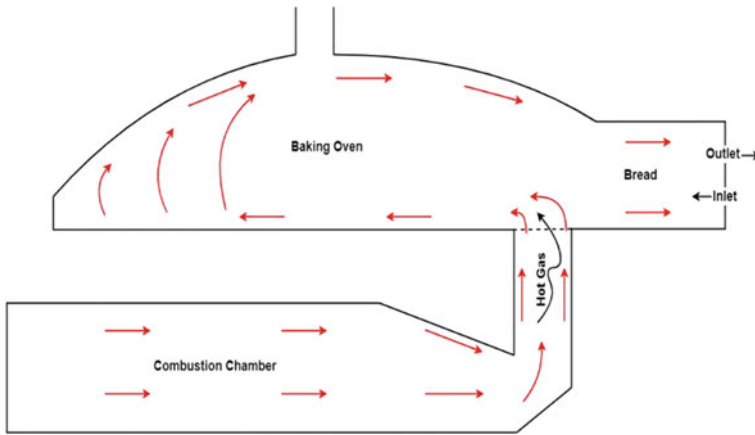


Fig. 1 Cross-sectional view of a typical wood-fired bakery furnace [1]

and continuously assess if a state of correct baking process is accomplished or not. An expert operator usually judges the quality of the bread quickly just by a visual inspection with minimum frequency of opening and closing of the door of the furnace. However, it is very difficult to execute such an ideal baking cycle, and it is found that during an actual operation of a typical baking cycle an average operator opens or close the door with an average frequency of 'three' [1]. In doing so almost 30% of total heat that is required for the backing of the bread is lost [1]. Such thermally inefficient baking process may rapidly bring down the temperature of the furnace and can result in the lengthening of the baking time not only for the ongoing batch but also for each subsequent batch.

2 Heat and Mass Transfer in Baking of Bread

Figure 2 shows components of heat and mass transfer taking place during a baking process [2]. All the fundamental mode of heat transfer involved during the baking process. The furnace walls surrounding the dough radiate its heat to the dough via radiation. The same is added by the heat supplied through convection mode surrounding the dough by means of hot stagnant air. The surface of dough conducts the heat further inside by conduction. As a result of this, the moisture from the dough diffuses through mass transfer towards the outer surface of the dough slowly turning the dough in a bread. A balanced supply of the heat in the form of wall radiation towards the dough is essential. Its smooth penetration into the dough is essential for a good texture and a crispy taste of the bread. Since the inner environment is not aided by a circulating fan, the heat transfer by convection always has a small quantity. Therefore, a controlled and a definite amount of thermal radiation from the wall towards the dough will decide the transformation of dough into an adequate quality

of the bread. This necessitates an estimate of a radiative heat transfer a key as it is the dominating heat transfer mode.

The heat transfer from the furnace walls to the dough for the present case is investigated by following an electrical analogy for the radiation network.

The baking time of a bread can be obtained by solving the radiation network for a simplified furnace. Hassan et al. proposed a simplified method to analyse the radiative heat transfer occurring inside the furnace [3]. The method proposed the use of electrical network analogy of radiative heat transfer considering a simple box type furnace. The method is modified, and the same is applied in the present case. Figure 3 shows a schematic and pictorial view of a simplified model of the box type furnace.

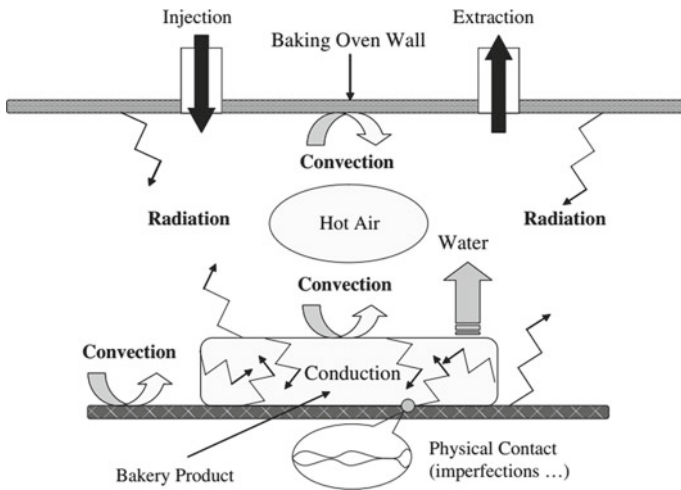


Fig. 2 Heat and mass transfer process in baking [2]

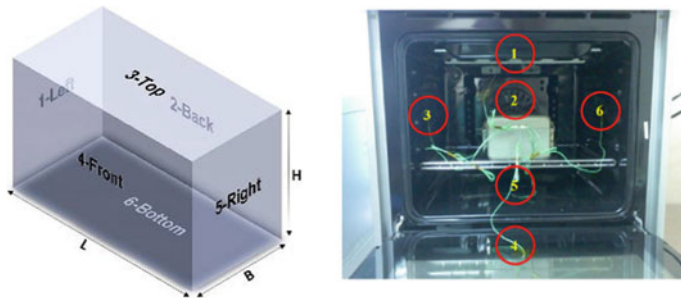


Fig. 3 Simplified baking furnace, schematic (left), and pictorial (right) view

3 Estimating Radiative Heat Flux Available at the Furnace Walls Using Network Analogy

Ibrahim et al. [4] proposed a network diagram for radiation network analogy for rectangular furnace involving six surfaces. Based on this, a modified network for the present work is worked out and is as shown in Fig. 4. The resulting view factors of different walls for the given dimensions of the furnace are as shown in Table 1 and discussed in following section. Heat transfer to dough through conduction and convection effects within the furnace during baking process are neglected. Also, the heat loss from the furnace is assumed to be of a small value is also neglected. The walls of the furnace are assumed to be diffused, opaque and made up of grey surfaces. Each surface of the furnace is assumed to behave as an isothermal wall and having uniform radiosity. The medium within the space inside the furnace is taken to be a non-participating.

The radiative heat flux (q_i) available at the furnace walls is the difference between the radiosity (J_i) and the irradiation (G_i) of the surface i of the furnace wall which can be evaluated using the following equation:

$$q_i = A_i(J_i - G_i) \tag{1}$$

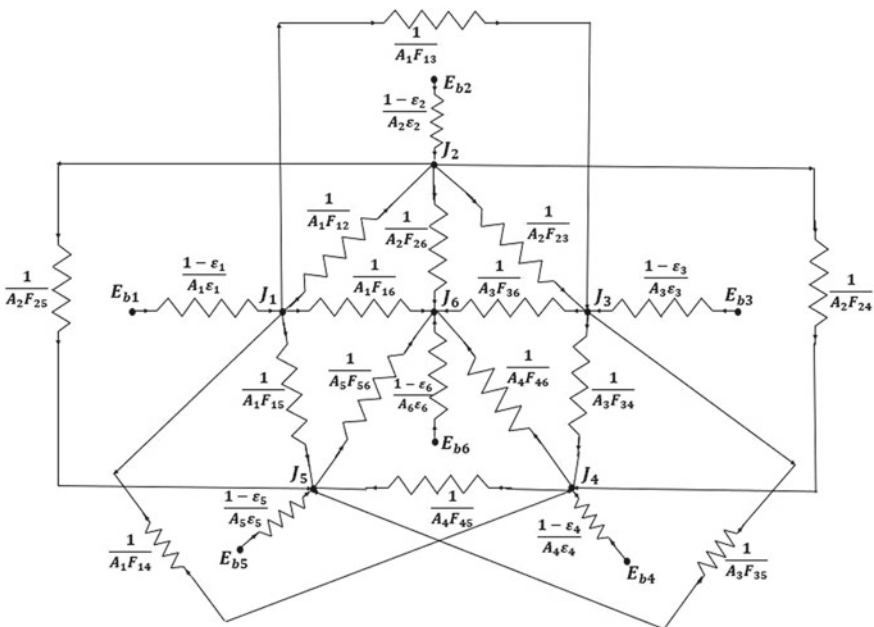


Fig. 4 Radiation network for the furnace

Table 1 View factors obtained for the furnace

F_{ij}	1	2	3	4	5	6
1	0	0.15	0.30	0.15	0.10	0.30
2	0.15	0	0.30	0.10	0.15	0.30
3	0.15	0.15	0	0.15	0.15	0.40
4	0.10	0.15	0.30	0	0.15	0.30
5	0.10	0.15	0.30	0.15	0	0.30
6	0.15	0.15	0.40	0.15	0.15	0

Radiosity of the surface i of the furnace wall can be calculated by adding the heat emitted by the surface (E_i) and the portion of the irradiative heat reflected from the surface.

$$J_i = E_i + \rho_i G_i \tag{2}$$

By substituting the value of radiosity in Eq. (1), the net radiative heat transfer from the surface i of the furnace wall can be calculated from the following equation:

$$q_i = A_i(E_i - \alpha_i G_i) \tag{3}$$

For an opaque surface, the radiosity in terms of emissivity (ϵ_i) can be written down as following:

$$J_i = \epsilon_i E_{bi} + (1 - \epsilon_i) G_i \tag{4}$$

where

$$E_{bi} = \sigma T_i^4 \tag{5}$$

Substituting the value of G_i by solving the above equation and substituting back into Eq. (1), the final equation for the radiative heat transfer from the surface i of the furnace wall can be obtained as following:

$$q_i = (E_{bi} - J_i)/((1 - \epsilon_i)/\epsilon_i A_i) \tag{6}$$

The following alternate expression in terms of shape factor can be used to calculate the heat transfer from the surface i towards j of the furnace wall:

$$q_i = \sum_{j=1}^N A_i F_{ij} (J_i - J_j) \tag{7}$$

By combining the Eq. (6) and (7), an expression can be evaluated to obtain the value of the radiosity which is given below:

$$(E_{bi} - J_i)/((1 - \varepsilon_i)/\varepsilon_i A_i) = \sum_{j=1}^N A_i F_{ij} (J_i - J_j) \quad (8)$$

In the radiation network analogy, there are two types of resistance (a) Surface resistance (c_i) (between E_b and J) and (b) Space resistance (b_i) (between two surfaces). Surface resistance purely depends on emissivity of the surface, whereas space resistance depends on view factor or shape factor (F_{ij}) from surface 1 towards surface 2 which are given below.

$$c_i = \frac{1 - \varepsilon_i}{\varepsilon_i A_i} \quad (9)$$

$$b_{ij} = A_i F_{ij} \quad (10)$$

To find the value of radiosity to estimate the radiative heat flux available at the furnace walls, the following equation is used which was derived for surface 1 by expanding and rearranging Eq. (8):

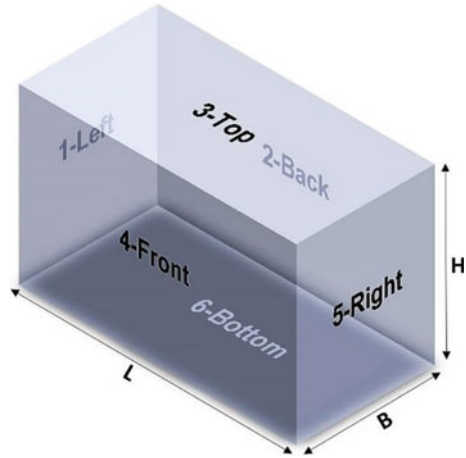
$$J_1 = \frac{\left(\frac{E_{b1}}{c_1}\right) + b_{12}J_2 + b_{13}J_3 + b_{14}J_4 + b_{15}J_5 + b_{16}J_6}{b_{12} + b_{13} + b_{14} + b_{15} + b_{16} + \left(\frac{1}{c_1}\right)} \quad (11)$$

To find the value of radiosity for particular surface, one needs to calculate the shape factor which is discussed in the following subsection. The radiosity equations (J_1 to J_6) were solved by finding the view factors for respective surface of the furnace wall simultaneously using Gauss–Seidel iterative method. Once radiosity value is obtained, the radiation heat transfer at surface i (q_1 to q_6) can be calculated using Eq. (7).

3.1 View Factor Calculations for the Furnace

During the radiation exchange in an enclosure, radiation leaving any surface of the enclosure incidents on that surface itself or incidents on another surface of the enclosure. The net rate of radiation heat transfer depends on the surface temperatures, the emissivity of the surfaces, and the areas of the surfaces. This spatial geometric relationship of the surfaces is called view factor. View factor (configuration or shape factor) is a geometrical term for a system in which two surfaces exchange energy by radiation. View factor (F_{ij}) is calculated between two surfaces of the furnace as shown in Table 1. The calculation of view factors involves three methods which are

Fig. 5 Simplified geometry of baking furnace



(a) aligned parallel rectangle, (b) perpendicular rectangles with common edges, and (c) reciprocity rules. The furnace dimensions considered for the present study are as shown in Fig. 5. The length, breadth, and height considered are 1 m, 1 m, and 0.5 m, respectively.

(a) Aligned parallel rectangle method

$$\bar{x} = \frac{X}{L}, \bar{y} = \frac{Y}{L}$$

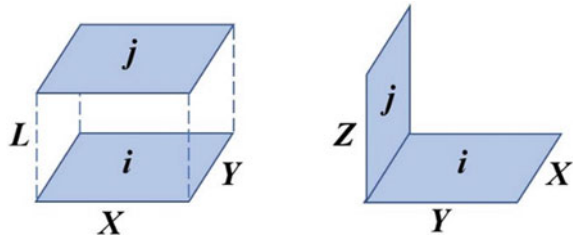
$$F_{ij} = \frac{2}{\pi xy} \left[\begin{aligned} & \ln \left[\frac{(1 + \bar{x}^2)(1 + \bar{y}^2)}{1 + \bar{x}^2 + \bar{y}^2} \right]^{0.5} + \bar{x}(1 + \bar{y}^2)^{0.5} \tan^{-1} \left(\frac{\bar{x}}{(1 + \bar{y}^2)^{0.5}} \right) \\ & + \bar{y}(1 + \bar{x}^2)^{0.5} \tan^{-1} \left(\frac{\bar{y}}{(1 + \bar{x}^2)^{0.5}} \right) \\ & - \bar{x} \tan^{-1}(\bar{x}) - \bar{y} \tan^{-1}(\bar{y}) \end{aligned} \right] \tag{12}$$

(b) Perpendicular rectangle with common edges:

$$h = \frac{Z}{X}, w = \frac{Y}{X}$$

$$F_{ij} = \frac{1}{\pi w} \left[\begin{aligned} & w \tan^{-1} \left(\frac{1}{w} \right) + h \tan^{-1} \left(\frac{1}{h} \right) - (h^2 + w^2)^{0.5} \tan^{-1} \left(\frac{1}{(h^2 + w^2)^{0.5}} \right) \\ & + \frac{1}{4} \ln \left\{ \frac{(1 + w^2)(1 + h^2)}{1 + w^2 + h^2} \left[\frac{w^2(1 + w^2 + h^2)}{(1 + w^2)(w^2 + h^2)} \right]^{w^2} \left[\frac{h^2(1 + w^2 + h^2)}{(1 + h^2)(w^2 + h^2)} \right]^{h^2} \right\} \end{aligned} \right] \tag{13}$$

Fig. 6 Aligned parallel rectangular method (left) and perpendicular rectangle with common edges (right)



(c) Reciprocity rule:

$$A_i F_{i,j} = A_j F_{j,i} \quad (14)$$

Figure 6 shows the respective cases for aligned parallel surfaces and perpendicular rectangle having common edge. The final view factor obtained using above three methods and applying dimensions of the furnace is presented in Table 1.

4 Estimating Time to Bake

After estimating the radiative heat flux available at the furnace walls, the time (in seconds) taken to bake each batch of bread is to be estimated next. The area occupied by an average sized loaf of bread considered in the study is 0.04 m^2 . The clearance or gap between the two loaves on the baking plate is considered as 12%. The total area available at the base of the baking furnace is 1 m^2 . Calculation shows that an average of 21 loaves of breads can be accommodated in the furnace in one batch. Energy required to bake 1 kg of loaf considered is 475 kJ [1], and the energy absorbed by tin plate over which the loaves are placed for baking is around 95 kJ. This makes the total energy required to bake 1 kg of loaf of bread as 570 kJ. Average mass of a loaf estimated is 0.93 kg. The total amount of energy required to bake for one batch of loaves of bread (E_{total}) for the present furnace is 11,132 kJ. In the present study, two cases of the operation of the furnace are considered which are Case-I, baking with feeding door closed thought the baking process. The time required and quality of the bread baked in this case are decided based on intuition of the operator. While Case-II, in which baking is carried out in a conventional manner, i.e. with frequent opening and closing of the door thought the baking process, to assess the time required and quality of the bread being baked. It is noted in the literature that during the second case of baking of bread, there is 30% more energy consumption takes place [5]. The consumption of energy for baking during later case is estimated by adding this heat loss to the total basic energy required for baking of the bread. The time required to bake a batch of loaves is now estimated by the following equation:

$$t = \frac{\text{Energy required to bake a batch of loaf } (E_{\text{total}})}{\text{Radiative heat recieved at the bottom surface } (q_6)} \quad (15)$$

Amount of baking load is kept constant for each baking cycle. After each baking cycle of batch of loaves, the heat supplied for the baking of breads is subtracted from the total available stored energy of the walls. The reduction in the temperature of the furnace walls is once again determined at the starting of a new baking cycle and the same is assumed to remain same during that baking cycle.

5 Results and Discussions

As per the conventional baking procedure, the furnace is first charged or heated using the heat from the combustion of wood. It is assumed in the present study that the heat possessed by each wall at the end of the charging period is same and it is equivalent to 50,000 kW of energy available, for a simplicity an arbitrary value is assigned towards the energy storage to the walls. Additionally, each wall of the furnace is considered to acquire an average temperature of 300 °C at the end of the charging period because of this heat addition. After the charging period is over, the first batch of baking load is supplied to the furnace, and the baking cycle is allowed to take place. The full load condition of furnace is considered for baking cycle, i.e. 21 loaves of breads considered for one baking cycle. The baking of bread is allowed to perform only till the average wall temperature is above 140 °C, this is due to the fact that below this temperature the time required to bake will be large, for this period the quality of bread baked will not produce a top crispy crust for the bread, and the bread without this crispy top layer will reduce the acceptability from the customers.

Figures 7 and 8 show the effect of average furnace wall temperature on the cumulative baking time of furnace for different baking cycles for the Case-I and Case-II, respectively. It is observed that with decrease in the wall temperature the baking time for each batch increases for every subsequent batch. This is due to the reduction in the wall temperature requires more time for each batch in the furnace until it acquires the required heat to bake the bread. The trend is as shown in Figs. 7 and 8; both are in the form of an exponential decay curve. It is observed that corresponding to the upper and lower temperature limits imposed for the operation of the furnace a total of 16 numbers of baking cycles is possible for Case-I while for Case-II only 13 number of baking cycle is possible. This is due to a large heat is wasted and lost during frequent opening and closing of door in Case-II. This results in a smaller number of possible baking cycles.

The time taken to bake the first batch of bread in Case-I was around 150 s, whereas the same for Case-II is around 190 s. Similarly, the time taken for last baking cycle in Case-I was around 930 s, and the same for Case-II was around 1230 s. The percentage increase in time required for the first baking cycle in Case-II compared to Case-I was 26%, and the same for the last baking cycle was 32%.

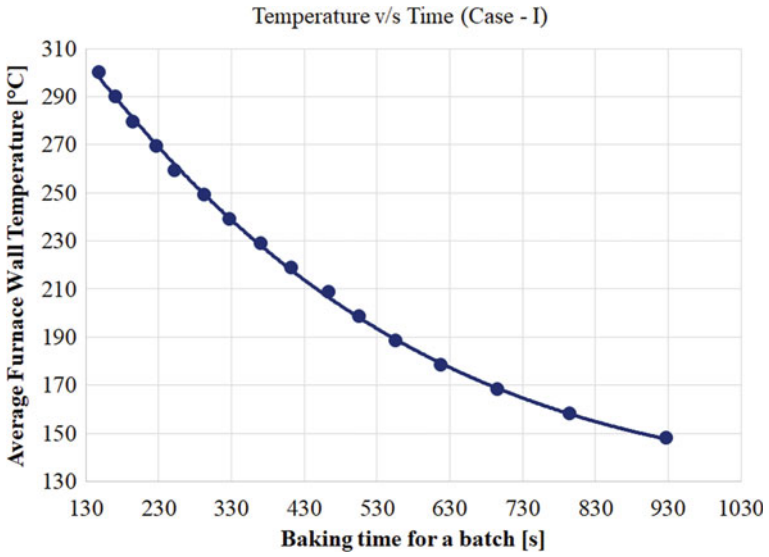


Fig. 7 Variation in wall temperature with cumulative baking time for Case-I

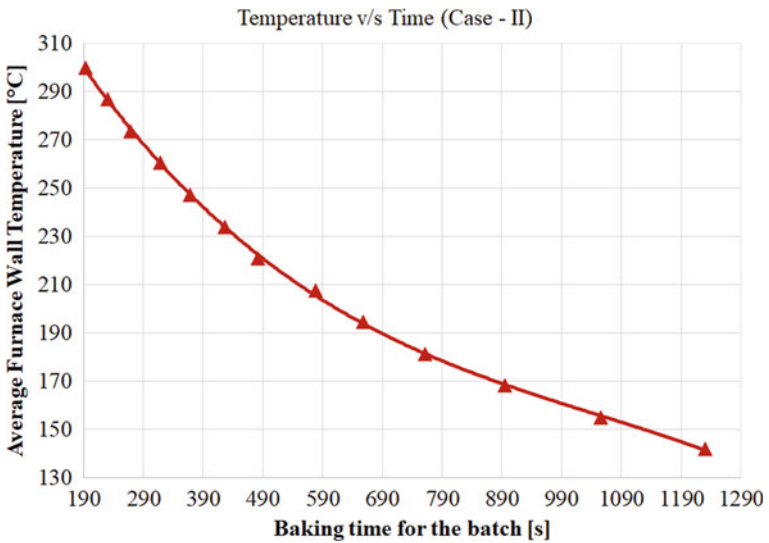


Fig. 8 Variation of wall temperature with cumulative baking time for Case-II

In order to investigate the contributions of heat supplied by each wall of furnace in the overall baking process, a dimensionless heat capacity factor (Ω) is proposed. It is the ratio of heat capacity of the wall at any instance of time to the heat capacity of the wall at the beginning of the first baking cycle operation (or at the end of charging period). Figure 9 represents variation in Ω for each wall with the cumulative baking time. Ω represents the stored heat drained from each wall of furnace during the baking. From the results, it was found that wall 2 which is at the back side of the furnace (Fig. 3) contributes the least heat transfer in terms of radiative heat transfer during the baking operation. This is also observed from the fact that the wall has low view factor with respect to the base (where the dough is placed for the baking) and hence contributes less in form of radiation leaving the wall and reaching to the base for both the cases Case-I and Case-II (as shown in Fig. 10).

Figure 11 compares the cumulative time of operation of the furnace for Case-I and Case-II. It is observed that Case-I offers not only large number of possible baking cycles but also offers smaller baking time for each baking cycle. This is due to the fact that the average furnace wall temperature for the baking operation is large for Case-I. This gives lower specific wood consumption in kg of wood used per kg of bread produced. This improves economics of operation as well as reduction in emission from the operation of furnace.

Figure 12 shows the comparison of baking time for Case-I and Case-II and also percentage increase in the cycle time for each batch under Case-I and Case-II. The trend shows that rate of increase in the percentage increase in the baking time increases continuously and the slope of the curve becomes steeper and steeper with each increase in the baking cycle. This represents the fact that as the batch increases

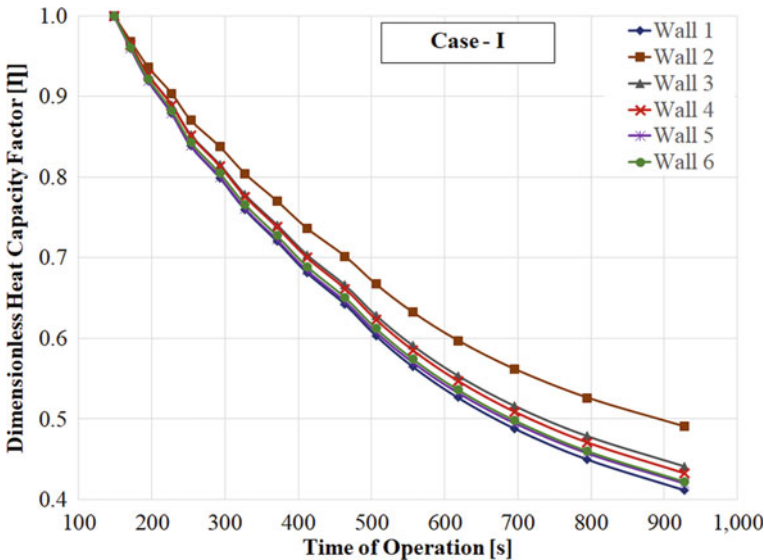


Fig. 9 Variation in Ω for the furnace walls Case-I

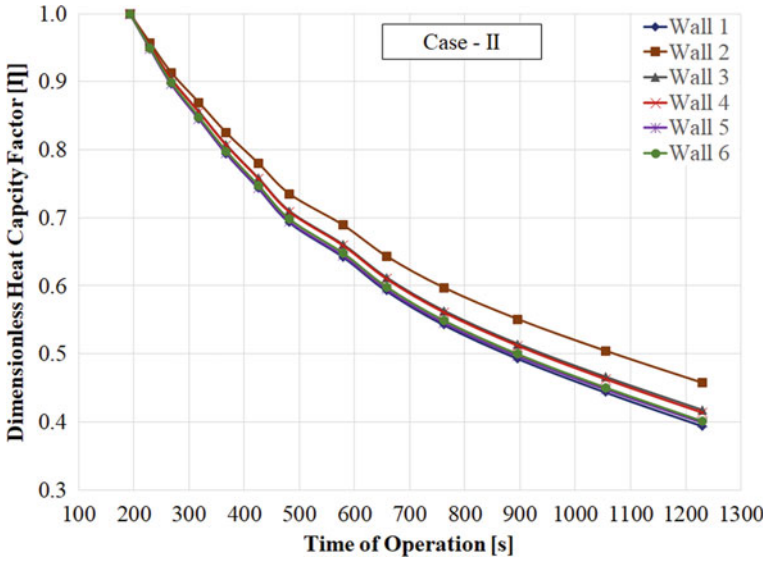


Fig. 10 Variation in η for the furnace walls Case-II

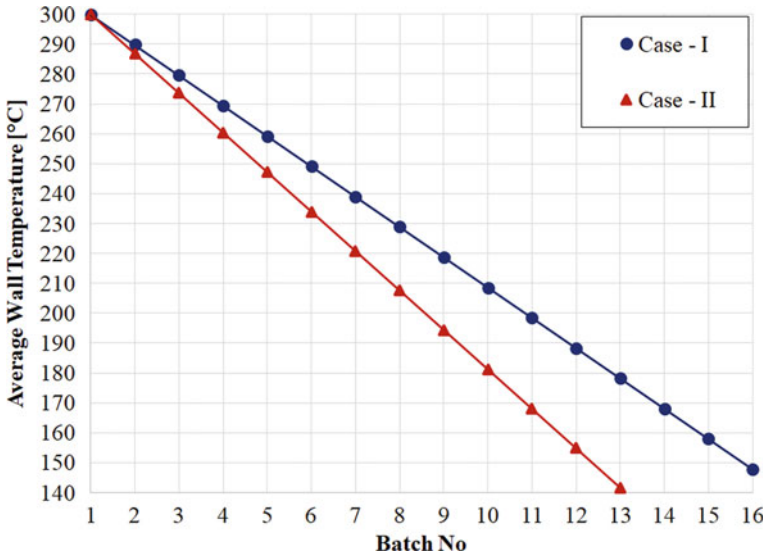


Fig. 11 Number of batches and average wall temperature for Case-I and Case-II

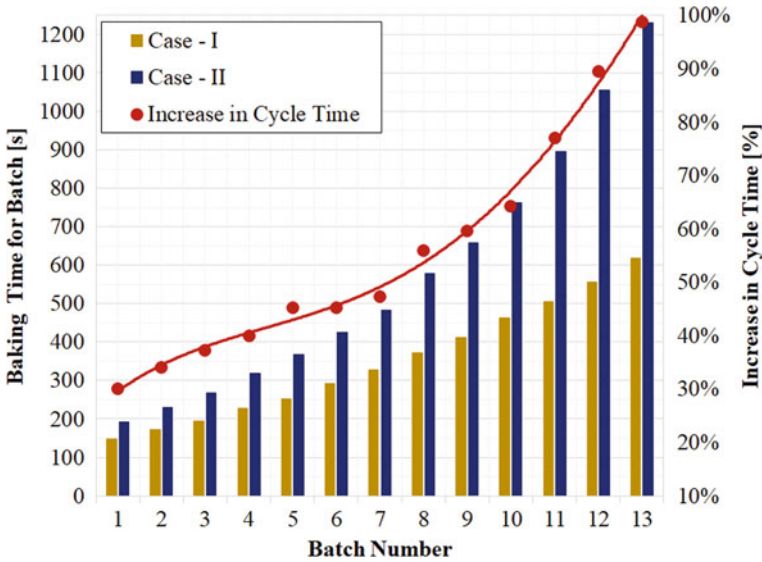


Fig. 12 Comparison of baking time

the difference in the time required for a baking cycle under Case-II compared to Case-I also increases. This difference in the time for baking reaches to such a level that for the batch number 13 the baking time required under Case-II is almost double compared to Case-I. Additionally, after the completion of 13th cycle of baking the wall temperature of furnace is still 180 °C for Case-I, while the same in case of Case-II it is already reached to minimum operating furnace of the temperature, and this limits any further baking process.

6 Conclusions

The present study concludes that the human intervention in the form of the door opening and closing of the furnace just to assess the quality of bread is a very cost sensitive issue and can significantly affect the operation of the furnace.

The study also points to the fact that there is a possibility of improvement in the heat utilization by way of modifying the dimensions of the furnace, e.g. heat stored in the wall 2 is not fully utilized. A cubical or hemispherical top shape of furnace may resolve this issue. By this study if an operator is provided with appropriate temperature display showing average wall temperature along with a chart showing approximate baking time for different average wall temperature, may be in that case the operator will not require to go for frequent opening and closing of the furnace and the operation of furnace in that case will be independent of intervention of operator.

Under this case the consumption of wood and the overall cost of bread making will be reduced to a great extent, and at the same time the emission footprint of the bread will also be minimum.

Nomenclature

q_i	Radiative heat flux at walls (W)
J_i	Radiosity of the surface (W)
G_i	Irradiation of the surface (W)
E_i	Heat emitted by the surface (W)
ε_i	Emissivity of surface
T_i	Temperature of the surface (K)
A_i	Area of the wall (m^2)
F_{ij}	View factor
L	Length of the wall (m)
B	Breadth of the wall (m)
H	Height of the wall (m)

References

1. MANHIÇAC FA (2015) Efficiency of a wood-fired bakery oven—improvement by theoretical and practical. Forest Products and Chemical Engineering, Department of Chemical and Biological Engineering, Sweden
2. Marcotte M (2007) Chapter 8: Heat and mass transfer during baking. In: WIT Transactions on state of the art in science and engineering, vol 13. Quebec, Canada
3. Hassan NH, Salleh RM, Ibrahim UK (2013) Effect of convection mode on radiation heat transfer distribution in domestic baking oven. Int J Chem Eng Appl 3(6)
4. Ibrahim UK, Salleh RM (2012) Application of network representation model for radiation analysis. Int J Chem Eng Appl 3(3):195–200
5. Akinoso R, Aremu AK, Ismaila AR (2014) Energetic analysis of clay oven used for bread baking. J Agric Eng Technol 22 (4)

Experimental Investigation of Elliptical Air-Jet Impingement on Metal-Foamed Surface



Pradeep Kumar Singh, Jaykumar Joshi, Pawan Sharma,
and Santosh Kumar Sahu

Nomenclature

A	Area of target plate (mm^2)
AR	Aspect ratio
d	Equivalent diameter of the nozzle (mm)
h	Local heat transfer coefficient ($\text{W}/\text{m}^2\text{K}$)
h_{avg}	Average heat transfer coefficient ($\text{W}/\text{m}^2\text{K}$)
I	Current (A)
K	Thermal conductivity of fluid (W/mK)
l	Nozzle length (mm)
\dot{m}	Flow rate of air (kg/s)
Nu	Nusselt number
Re	Reynolds number
T_{jet}	Temperature of fluid leaving the nozzle (K)
T_p	Temperature of the plate (K)
x	Longitudinal distance from the stagnation (mm)

1 Introduction

Heat dissipation from the smaller areas of heat transfer and electronic devices has been a challenge with the increasing compactness of the devices. Air-jet impingement cooling applies to both the steady and unsteady concentrated heat load. Devices dissipating high heat flux may be maintained at a constant low temperature using air-jet impingement cooling. Air-jet impingement cooling is relevant in many industrial

P. K. Singh (✉) · J. Joshi · P. Sharma · S. K. Sahu
Department of Mechanical Engineering, IIT Indore, Indore 453552, India
e-mail: phd2001103005@iiti.ac.in

© The Author(s), under exclusive license to Springer Nature Singapore Pte Ltd. 2024
K. M. Singh et al. (eds.), *Fluid Mechanics and Fluid Power, Volume 1*, Lecture Notes
in Mechanical Engineering, https://doi.org/10.1007/978-981-99-7827-4_54

applications, including the cooling of gas turbine blades, electronics component cooling, and the paper and textile industries [1–3]. Thermal management of electronic devices poses a significant challenge by virtue of its compactness and limitations with other coolants except for air. Air-jet impingement with the modified surface, to some extent, has been successful in the dissipation of unwanted heat. The geometry and specifications of the nozzles used in impinging jets vary widely in practice. The use of a circular axisymmetric nozzle surpasses the other categories of nozzles.

2 Literature Review and Objective

Extended and modified surfaces are ubiquitous in augmenting the thermal performance of the devices [4]. To further enhance the ability of heat dissipation, open-cell metal foam (OCMF) is commonly used nowadays [5]. An OCMF is a solid, porous metallic structure comprising open voids for the passage of fluids. Depending on the percentage of the space occupied by the voids and the number of pores per inch, it can be classified based on porosity and pore density (PPI—pores per inch) [6, 7].

The present analysis focuses on combining the merits of both the jet impingement and the modified surface in the form of metal foam to augment the cooling rate of the test surface. The use of OCMF has shown tremendous improvement in the thermal management of compact heat transfer devices [8, 9]. Chou and Yang [8] experimentally studied the heat sink combined with the OCMF. They found the effectiveness to be 25% higher than the conventional arrangement. Calmidi and Mahajan [10] formulated an empirical correlation for the characterization of the foam thermal conductivity. Hsieh et al. [11] investigated the effect of porosity and pore density on the heat transfer efficacy of aluminum foam heat sinks. They found them to have a better dissipation rate than conventional ones. The thermal performance of aluminum foam with different PPI using a circular nozzle was studied by Yogi et al. [12]. They concluded that the 10 PPI aluminum foam with 90% porosity has better thermal performance than the higher PPI foam of the same porosity. The influence of the local thermal performance on the geometry of the nozzle and exit boundary conditions was investigated by Yang et al. [13]. They concluded that the exit conditions significantly affect the turbulence intensity and the potential core length. Singh et al. [14] performed experiments to identify the effect of thin foam. They concluded that thinner foams augment the heat transfer in a metal foam-plate arrangement [15].

Caliskan et al. [16] studied the heat transfer performance of the smooth plate using elliptical and rectangular impinging jet arrays. They concluded that the elliptical nozzles provide higher heat transfer coefficients than the rectangular ones. Also, the increased aspect ratio (AR) resulted in a higher heat transfer enhancement in the stagnation region. The use of metallic foam with elliptical nozzles in jet impingement is very limited in the literature. Hence, this study analyzes the thermal performance of the elliptical nozzles of different aspect ratios using flat plate impinging jet conditions.

3 Materials and Methods

3.1 Test Facility

The present experimental analysis is carried out using an experimental arrangement as depicted in Fig. 1. It consists of a fluid flow system, test surface assembly, power supply, and other devices to measure the temperature of the heated specimen plate. The test plate used in the experiment is a thin stainless-steel foil, and the plate characteristics are depicted in Table 1. The copper foam used in the current analysis is embedded over the flat plate. The metal foam consists of open pores through which fluid on impingement gets further accelerated before coming in contact with the heated plate. Porosity, pore density, and the size of the pores are used to characterize the foam. The current investigation uses open-cell copper foam of 90% porosity with a pore density of 12 pores per inch. The foam of thickness 4 mm is glued to the SS-304 foil. The microscopic image of the foam used in the present investigation is depicted in Fig. 2.

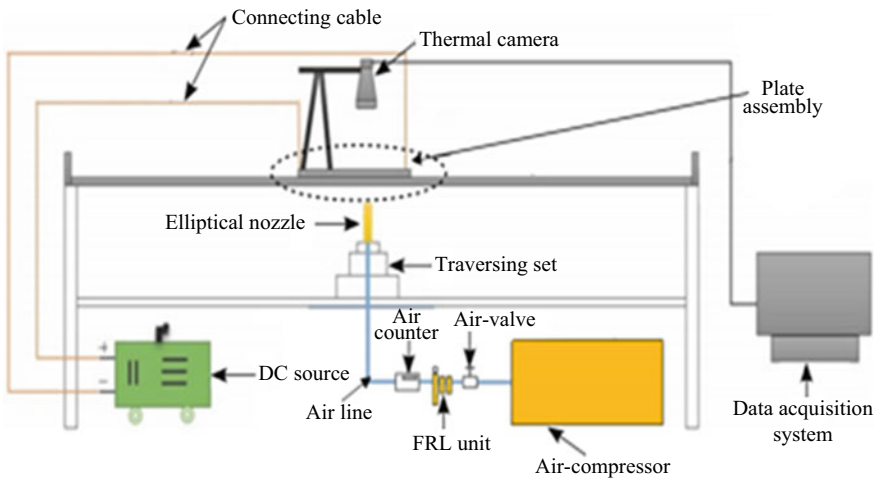
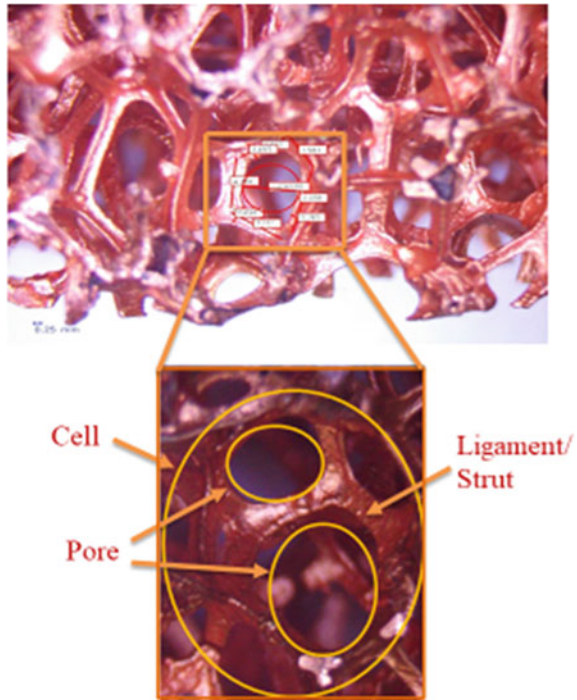


Fig. 1 Diagram of the experimental setup

Table 1 Test surface characteristics

Material of test specimen	SS-304
Area (A), mm ²	130 × 80
Thickness (δ), mm	0.15
Density (ρ), kg/m ³	8000
Specific heat capacity (C_p), J/kgK	500

Fig. 2 Microscopic image of metal foam



The test specimen is attached to the pair of copper bus bars, which are then secured to the setup between the L-shaped aluminum structure. The elliptical nozzles have an equivalent diameter of 1.5 mm and an aspect ratio of 1 and 4, respectively. The test specimen is heated using a DC power source. Power consumption and voltage are measured using a digital multimeter.

3.2 *Experimental Methodology*

An experimental investigation is carried out using ambient air as the working fluid. The fluid is supplied using a reciprocating air compressor and is metered through the FRL unit. The compressed air is passed through the elliptical nozzle and is then impinged onto the heated specimen maintained in steady-state conditions. The experiments are carried out at higher Reynolds number (Re) 40,000 and 50,000, respectively. The nozzle-to-plate distance (z/d) is kept at 3 and 7, respectively. The experimental operational variables considered in the present investigation are displayed in Table 2. A thermal imaging camera (Model: A655sc) with a resolution of 640×480 pixels is used to record the thermal image. The IR camera is fixed at a distance of 0.5 m above the test specimen to record the thermal image. The emissivity and the reflected ambient temperature of the camera are 0.95 and 30°C , respectively.

Table 2 Operational variables

Parameter	Operating range
Aspect ratio	1 and 4
Nozzle equivalent diameter d , (mm)	1.5 mm
Nozzle-to-plate distance (z/d)	3 and 7
Input heat flux (W/m^2)	4000
Reynolds number	40,000 and 50,000

The Nusselt number (Nu) and Reynolds number (Re) for the present assessment are calculated as follows:

$$Nu = \frac{hd}{k} \tag{1}$$

$$h = \frac{q_{conv}}{T_p - T_{jet}} \tag{2}$$

$$q_{conv} = q_{supplied} - q_{loss} \tag{3}$$

$$q_{supplied} = \frac{VI}{A} \tag{4}$$

Experimental determination of q_{loss} is carried out as per reference [12]:

$$Re = \frac{\rho vd}{\mu} = \frac{4\dot{m}}{\pi \mu d} \tag{5}$$

where h , d , k , μ , ρ represent heat transfer coefficient of the fluid, equivalent diameter of the nozzle, thermal conductivity of the fluid, dynamic viscosity, and density of the air, respectively.

For the current analysis, various parameters like length, width, thickness of the stainless-steel foil, nozzle dimensions, and temperature using a thermal camera were measured. Thereafter, for a given Re, the corresponding Nu were evaluated for the different impinging distances. The errors associated with the above measurement were analyzed using the method suggested by Coleman and Steele [17]. The corresponding uncertainty in the measurements is reported in Table 3.

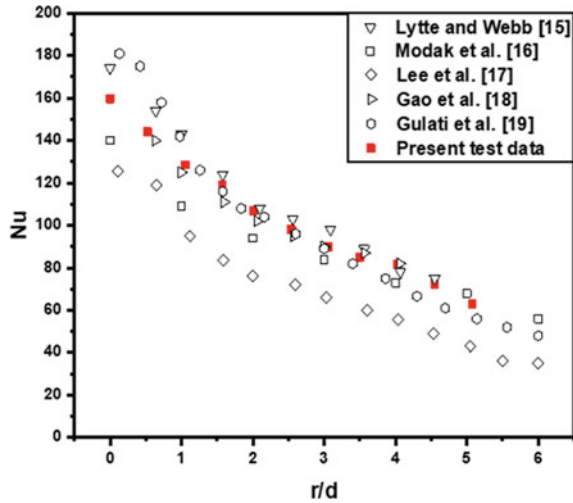
4 Results and Discussion

The thermal performance of the flat plate using an elliptical air-jet arrangement is analyzed for the higher Reynolds number of 40,000 and 50,000, respectively. Also, the nozzle-to-plate distance is maintained at 3 and 7, respectively. The foam under consideration is an OCMF of 90% porosity and 12 PPI, respectively.

Table 3 Uncertainties of various parameters

Variable	% Uncertainty
Reynolds number	3.6
Temperature measurement	2.0
Heat loss	2.8
Convective heat transfer coefficient	3.8
Heat flux	4.8
Nusselt number	5.7

Fig. 3 Comparison of the results



4.1 Endorsement of the Investigational Approach

The experimental setup is validated by performing the experiments at $Re = 23,000$ and $z/d = 6$ for the plate without foam. The test results are plotted as shown in Fig. 3. The present results relate well with the findings of the researchers Lytle and Webb [18], Modak et al. [19], Lee et al. [20], and Gao et al. [21].

4.2 Local Heat Transfer Assessment

The distribution of the local Nusselt number (Nu) in the longitudinal direction (x/d) for the cases under consideration is represented in Figs. 4 and 5. As observed in Fig. 4 and 5, the local Nu is found to be maximum in the stagnation region, and the Nu decreases along x/d for both nozzles with an aspect ratio (AR) of 1 and 4, respectively. The reasons for the same may be attributed to the drop in the momentum of the fluid upon striking as it flows outwards, losing its flowability, thus reducing its

Fig. 4 Local Nusselt number distribution for $Re = 40,000$ and $z/d = 3$

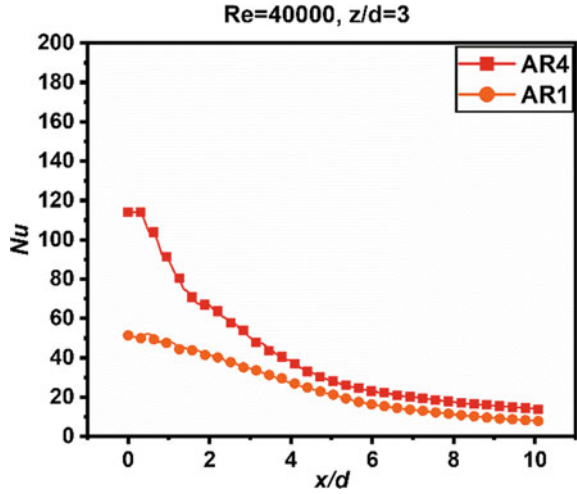
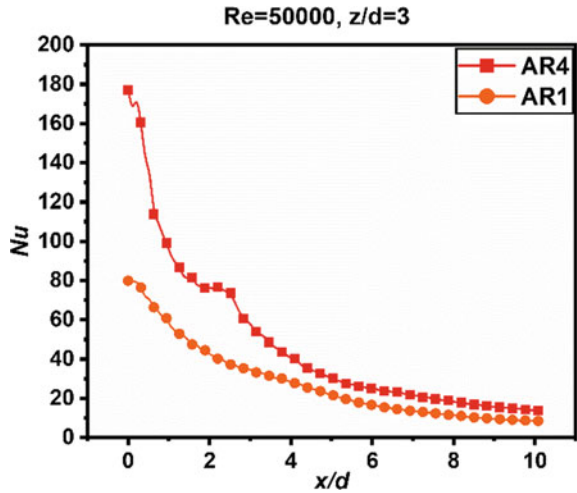


Fig. 5 Local Nusselt number distribution for $Re = 50,000$ and $z/d = 3$



heat dissipation ability. The Nu with AR 4 is found to be higher than AR 1. Similar trends are visible for the variation of Nu with x/d for $Re = 50,000$ at $z/d = 3$. The magnitude of Nu is found to increase with the increase in Re.

4.3 Average Heat Transfer Assessment

The average Nu has been calculated for the plate impinged with the nozzle with AR 4 and AR 1 while varying the impinging distance (z/d) from 3 to 7, as depicted in

Fig. 6 Average Nusselt number distribution

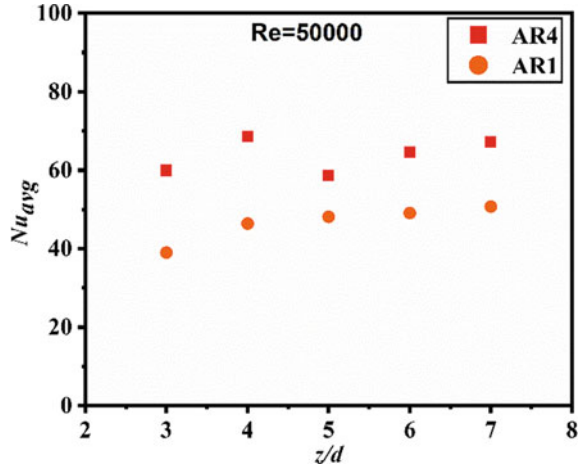


Fig. 5. It is observed that the average Nu is greater for the case with the AR 4 nozzle in comparison with the nozzle with AR 1. The improvement in thermal performance at higher AR is due to the better mixing of the jet fluid with the ambient air. The Nu is also found to increase with the increasing distance between the nozzle and the plate upto $z/d = 4$. (Fig. 6).

5 Conclusions

An experimental investigation has been carried out to assess the thermal performance of the flat plate amalgamated with the open-cell metal foam using elliptical nozzles. Tests are conducted for the higher Reynolds number 40000 and 50,000 for the nozzle aspect ratio of 1 and 4. The conclusions from the present investigations are listed below:

- Thermal performance is observed to be better with a higher aspect ratio (AR 4).
- The thermal performance improves with an increase in the impinging distances for the given nozzle aspect ratio.
- The enhancement with $Re = 50,000$ is found to be higher than $Re = 40,000$ for both the nozzles.
- The enhancement in the peak value of the stagnation Nusselt number is found to be 61.42% and 54% for Reynolds number 40000 and 50,000, respectively, by varying the AR from 1 to 4.

References

1. Viskanta R (1993) Nusselt-Reynolds prize paper heat transfer to impinging isothermal gas and flame jets. *Exp Therm Fluid Sci* 6:111–134
2. Katti V, Prabhu SV (2008) Experimental study and theoretical analysis of local heat transfer distribution between smooth flat surface and impinging air jet from a circular straight pipe nozzle. *Int J Heat Mass Transfer* 51(17–18):4480–4495
3. Rajamuthu VP, Panse SS, Ekkad SV (2020) Thermal hydraulic performance of high porosity high pore density thin copper foams subject to array jet impingement. In: Intersociety conference on thermal and thermomechanical phenomena in electronic systems (ITHERM), vol 202, pp 15–22.
4. Hansen LG, Webb BW (1993) Air jet impingement heat transfer from modified surfaces. *Int J Heat Mass Transfer* 36(4):989–997
5. Kumari N, Krishnan S, Garimella SV (2007) Analysis and performance comparison of competing desktop cooling technologies. In: 2007 Proceedings of ASME InterPack Conference (IPACK 2007), vol 2, pp 1018–1027
6. Wang J, Kong H, Xu Y, Wu J (2019) Experimental investigation of heat transfer and flow characteristics in finned copper foam heat sinks subjected to jet impingement cooling. *Appl Energy* 241:433–443
7. Yakkatelli R, Wu Q, Fleischer AS (2010) A visualization study of the flow dynamics of a single round jet impinging on porous media. *Exp Therm Fluid Sci* 34(8):1008–1015
8. Chou SF, Yang SF (1993) Heat transfer characteristics of aluminum foam metal. In: International symposium on transport phenomena in thermal engineering, pp 215–220
9. Singh P, Zhang M, Mahajan RL (2019) Effect of metal foam thickness and pore density on array jet impingement heat transfer. In: ASME International mechanical engineering congress and exposition, proceedings (IMECE), vol 8
10. Calmidi VV, Campmode RLM (2000) Forced convection in high porosity metal foams. *J Heat Transfer* 122(3):557–565
11. Shih WH, Liu CC, Hsieh WH (2016) Heat-transfer characteristics of aluminum-foam heat sinks with a solid aluminum core. *Int J Heat Mass Transfer* 97:742–750
12. Yogi K, Godase MM, Shetty M, Krishnan S, Prabhu SV (2020) Experimental investigation on the local heat transfer with a circular jet impinging on a metal foamed flat plate. *Int J Heat Mass Transfer* 162:120405
13. Yang G, Choi M, Lee JS (1999) An experimental study of slot jet impingement cooling on concave surface: Effects of nozzle configuration and curvature. *Int J Heat Mass Transfer* 42(12):2199–2209
14. Singh PK, Joshi J, Sahu SK (2021) Experimental investigation to identify the effect of thin metal foam on heat transfer characteristics of a heated plate. In: Proceedings of the 26th National and 4th International ISHMT-ASTFE heat and mass transfer conference, December 17–20, 2021, IIT Madras, Chennai, 600036, Tamil Nadu, India, pp 2541–2546
15. Singh PK, Joshi J, Sahu SK (2023) Heat transfer characteristics of the flat plate integrated with metal foam of varying thickness using an unconfined circular air-jet impingement. *Therm Sci Eng Prog* 41:101810. <https://doi.org/10.1016/j.tsep.2023.101810>
16. Caliskan S, Baskaya S, Calisir T (2014) Experimental and numerical investigation of geometry effects on multiple impinging air jets. *Int J Heat Mass Transfer* 75:685–703
17. Coleman HW, Steele WG (2018) Experimentation, validation, and uncertainty analysis for engineers, 4th ed, pp 1–368
18. Lytle D, Webb BW (1994) Air jet impingement heat transfer at low nozzle-plate spacings. *Int J Heat Mass Transfer* 37(12):1687–1697
19. Modak M, Srinivasan S, Garg K, Chougule SS, Agarwal MK, Sahu SK (2015) Experimental investigation of heat transfer characteristics of the hot surface using Al₂O₃-water nanofluids, vol 91. Elsevier BV
20. Lee DH, Song J, Jo MC (2004) The effects of nozzle diameter on impinging jet heat transfer and fluid flow. *J Heat Transfer* 126(4):554–557

21. Gao N, Sun H, Ewing D (2003) Heat transfer to impinging round jets with triangular tabs. *Int J Heat Mass Transfer* 46(14):2557–2569

Comparative Numerical Analysis of ZnO and Ag/ZnO Nanofluids Flowing Through Automobile Radiator



Sandip Dhumal, Krantisinha Jagtap, Shubham Malkunjikar, Mahesh Shindge, and Surendra D. Barewar

Nomenclature

C_p	Specific heat (kJ/kgk)
k	Thermal conductivity ([W/mk)
Nu	Nusselt number
p	Fluid pressure (Pa)
Dh	Hydraulic diameter (kg/m^3)
Pr	Prandtl number
Re	Reynold number
T	Temperature (k)
ρ	Density (kg/m^3)
μ	Dynamic viscosity (N.s/ m^2)
ν	Kinematic viscosity (m^2 / s)
\emptyset	Volume concentration (Vc)
HTC	Heat transfer coefficient ($\text{W/m}^2\text{k}$)

1 Introduction

Energy conservation and the rising cost of fuel are giving more attention today to the design of thermal systems that are energy efficient. A radiator is a type of heat exchanger that plays a crucial role in the cooling system of a vehicle. Water is often used as a coolant in automobile radiators, but it is bad for engines. The heat generated by engines damages pistons, connecting rods, and other internal parts. Different

S. Dhumal · K. Jagtap (✉) · S. Malkunjikar · M. Shindge · S. D. Barewar
School of Mechanical Engineering, MIT Academy of Engineering, Alandi 412105, India
e-mail: krantisinha.jagtap@mitaoe.ac.in

nanofluids can be used in commercial vehicles to enhance heat transfer to overcome this issue [1]. Through the use of nanofluid, heat can be easily absorbed from the engine and transferred to the atmosphere via a radiator. As a result, the engine's life and performance may be extended, as well as maintenance costs reduced.

Alternative to water, ZnO nanoparticles are added to water in car radiators. This study indicates that the heat transfer rate increases, which provides opportunities to make car radiators more compact, reducing their size and material requirements [2]. A horizontal flat tube radiator uses four different water-based nanofluids (Al_2O_3 , TiO_2 , ZnO, and SiO_2). In order to predict the rate at which heat is transferred across the radiator and the pressure drop across it, various researchers used computational fluid dynamics (CFD).

1.1 Thermophysical Properties of Working Nanofluids

1.1.1 Thermal Conductivity and Dynamic Viscosity of ZnO

Thermal conductivity is an essential factor for improving the heat transfer performance of a working fluid. It was found that when temperature and ZnO nanoparticle increased which increases the thermal conductivity at different nanofluid concentrations. It is observed that the thermal conductivity for ZnO nanofluid is increased with the increasing volume concentration and temperature [3]. The thermal conductivity is determined at various 0.02, 0.04, 0.06, 0.08, and 0.1% volume concentration. In a Newtonian fluid, viscosity is constant at different shear rates. The measurement of viscosity is very important as pumping cost increases with an increase in viscosity (Figs. 1 and 2).

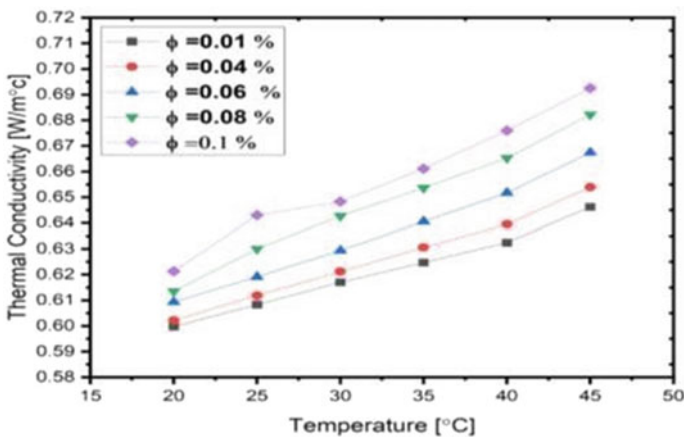


Fig. 1 Thermal conductivity of ZnO at different temperature and Vc [3]

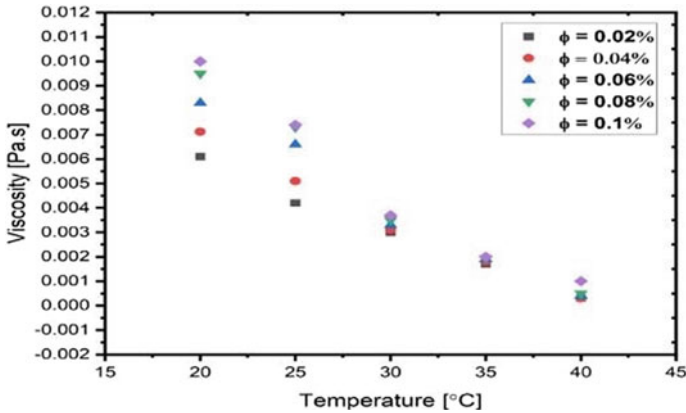


Fig. 2 Viscosity of ZnO at different temperature and Vc [4]

According to researchers, nanofluid viscosity increases with increasing volume fractions at the same temperature when nanoparticles are added and reached at various volume fractions. Whenever the volume concentration of nanoparticles was increasing at a constant temperature, the viscosity of the nanofluid increased as well.

1.1.2 Thermal Conductivity and Dynamic Viscosity of Ag/ZnO

The combination of Ag and ZnO hybrid nanoparticles was adopted for the ongoing investigation because ZnO increased chemical stability and Ag enhanced thermal conductivity. The increased thermal conductivity and stability of Ag/ZnO nanofluid contribute to enhancing the heat transfer. Brownian motion among nanoparticles is initiated by any rise in temperature, but it gradually increases the nanofluid's thermal conductivity [5]. It has been observed that when temperature and volume concentration increase, thermal conductivity increases. In Ag/ZnO nanofluid, at constant temperature and increase in volume concentration (0.02, 0.04, 0.06, 0.08, 0.1) resulting in a large amount of increase in viscosity but the stability is reduced (Figs. 3 and 4).

2 Literature Review and Objective

The CFD analyses revealed that nanofluids improve heat transfer, with ZnO and Al_2O_3 exhibiting a 4.9–15% increase. However, higher nanoparticle volume fractions led to increased pressure drops in the radiator [6]. In a car radiator under laminar flow conditions ($100 \leq Re \leq 1000$), experiments revealed that CuO/water nanofluid exhibited a higher overall heat transfer coefficient compared to the base

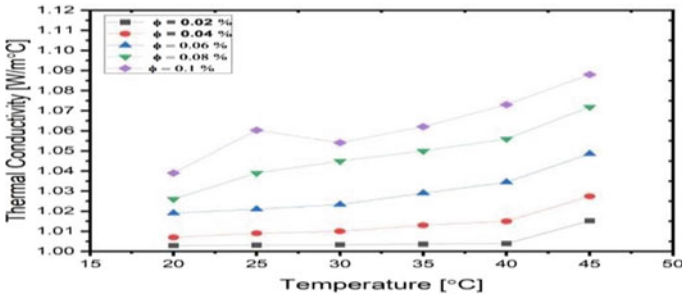


Fig. 3 Thermal conductivity of Ag/ZnO at different temperature and Vc

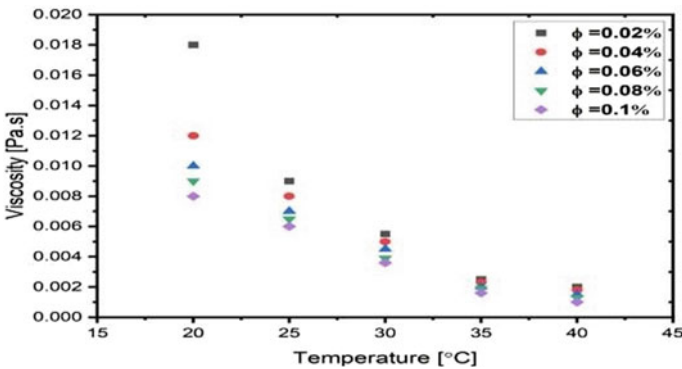


Fig. 4 Viscosity of Ag/ZnO at different temperature and Vc

fluid. Additionally, an increase in nanofluid concentration from 0 to 0.4 vol.% positively affected the overall heat transfer coefficient [7]. The numerical investigation employs computational fluid dynamics (CFD) to simulate heat transfer in nanofluids (Al_2O_3 particles in water and ethylene glycol-based fluid) passing through a three-dimensional flat tube, considering both laminar and turbulent flow conditions. The study examines single- and two-phase approaches and observes a minor discrepancy in tube friction factors between the two approaches. Moreover, the Nusselt number differs between the two-phase and single-phase models [8]. The heat transfer and flow performance of a hybrid nanofluid through a combination of experimental analysis and computational fluid dynamics (CFD) simulations were carried out. The study focuses on the coating of ‘Ag’ nanoparticles with graphene to create Ag/graphene nanofluids, employing a 0.1% mass concentration of nanoparticles in water as the base fluid. Notably, the investigation reveals a substantial enhancement of 22.22% in thermal conductivity at a temperature of 40 °C [9]. The aim is to investigate the heat transfer characteristics of a less commonly used heat transfer fluid, specifically ZnO-water nanofluid, in the context of natural convection within a closed rectangular enclosure. The numerical analysis focuses on exploring various parameters,

including the position of the heating wall, volume concentration of nanoparticles, and Rayleigh number. The findings indicate that a substantial increase in entropy generation leads to improved heat transfer rates [10]. This study examines the heat transfer and flow characteristics of ZnO ethylene glycol (EG)/water nanofluid in two multiport mini channels. The nanofluid is created by dispersing ZnO nanoparticles (30 nm average diameter) into a 40/60% EG/water solution, resulting in nanofluids with volume concentrations of 0.75 and 1.5% [11]. Researchers have conducted studies on ZnO nanomaterial due to its desirable characteristics, including corrosion resistance, high thermal conductivity, wide availability in purity ranges of 94% to 99.9%, versatile size and shape options, and cost effectiveness [12].

It is evident from the literature that a lot of studies has been done on the different nanofluid and hybrid nanofluid but no one can do the CFD analysis on Ag/ZnO hybrid nanofluid, so it is a novel work and then it compares the performance of Ag/ZnO and ZnO nanofluid. In this study, hybrid nanofluid Ag/ZnO is employed as a fluid, and CFD analysis is performed on it as well. ZnO is used as a nanofluid to accomplish the CFD analysis. Analytical results were employed for the comparison because, in computational fluid dynamics, it is necessary to compare the numerical analysis results with either experimental results or analytical calculations.

3 Methodology

The analysis of the research problem is shown in Fig. 5. One horizontal radiator tube without fins was modelled for this investigation. The fluid flows from the radiator through the internal side. Air flow around the radiator causes heat transfer, and cooling fluid enters in the radiator through the intake and exits from the radiator. In this investigation, only the radiator tube is considered for analysis, and the whole radiator is not taken into consideration for analysis. Figure 5 shows radiator tubes with circular sections. The cooling liquid enters in the pipe from one side and exits from the opposite side. The airflow was circling through tube. For a circular tube, the radiator material is of aluminium and total thickness of 1 mm, as depicted in Fig. 5. The specifications of the horizontal radiator are shown in Table 1. The model was built in fusion 360 with 6 mm inner and 8 mm outer diameter having 7 tubes and length of the tube is 230 mm.

3.1 Mesh Selection

In this study, Ansys workbench is used for analysis of the radiator, and tetrahedron meshing was developed. The corner of the radiator's tube is finely meshed using an inflation tool so that it does not obstruct the meshing's flow throughout the radiator. Fine meshing is utilised for getting proper/accurate results after meshing geometry.

Fig. 5 Geometry of radiator tube



Table 1 Specifications of automobile radiator

Parameters	Measurement (mm)
Radiator tube length	230
Radiator tube height	100
Radiator width	20
Tube width	22.5
Tube height	480
Distance between two tubes	5

Table 2 Meshing parameters

Domain	Nodes	Elements
Solid_Wall	184,911	564,741
Volume_Volume	178,772	807,568
All Domains	363,683	1,372,309

The meshing parameters are summarised in Table 2. The fluid domain had the most elements possible to the use of fine mesh, which also contributed to the flow’s greatest possible accuracy.

3.2 Boundary Condition

Numerical calculations were performed in a water-based turbulent regime, with volume contents of ZnO and Ag/ZnO nanoparticles from 0 to 1%. The velocity input, pressure exit, wall, and symmetry were all implemented using the boundary conditions shown in Table 3. To accurately display fluid bulk heat transfer close to the wall, cell density near the wall was throughout to be higher. Because it demonstrates higher density surrounding the wall, a square grid was chosen. The simulations can apply an upgraded wall treatment with pressure gradient and thermal effects since the turbulent flow of pure water and water-based nanofluids is at a Reynolds number of less than 10^6 .

Table 3 Boundary condition for the radiator analysis

Type of nanofluid	Parameters			
	Inlet temperature (k)	Inlet velocity (m/s)	Wall temperature (k)	Gauge pressure (Pa)
ZnO	320	0.5	355	0
Ag/ZnO	320	0.5	355	0

The temperature and velocity at the input are known, the hydraulic diameter of the circular tube was 4 mm, and the turbulence intensity was 5%. The wall of the computational domain was supposed to have a convection boundary condition with an assumed air temperature of 355 K and a heat transfer coefficient of 150 W/m²k. Table 3 presents detailed information about the boundary conditions.

3.3 Governing Equations

The steady state with pressure-focused methodologies was used to carry out the numerical simulation. The values of mass and momentum under steady-state conditions are determined using the partial differential equation. Basic methods are used to determine pressure and velocity, and second-order discretion equations are employed. On the basis of all the governing equations, numerous experiments have been carried out using simulation. Since the *k-ω* model predicts well far from the boundaries (wall) and the *k-ε* model predicts well close to the wall, it was chosen for this analysis. Equations (1–5) are used to find the conditions for fluid flow in the radiator tube using continuity, energy, and Navier–Stokes equations (5).

The conservation of mass is described by the continuity equation and is given by

$$\frac{\partial p}{\partial t} + \frac{\partial p U_1}{\partial x_1} + \frac{\partial p U_2}{\partial x_2} + \frac{\partial p U_3}{\partial x_3} = 0 \tag{1}$$

$$\frac{\partial p}{\partial x} + \frac{\partial v}{\partial x_1} = 0 \tag{2}$$

For compressible flow

$$\frac{\partial p}{\partial t} = 0 \tag{3}$$

Newton’s second law is followed by the momentum balance. The body and surface pressures are under the influence of two forces. The momentum equation is given by CFD software,

$$\rho \left(u \frac{\partial u}{\partial x} + v \frac{\partial v}{\partial x} \right) = -\rho g - \frac{\partial p}{\partial x} + u \frac{\partial^2 y}{\partial x^2} \quad (4)$$

The governing energy equation is given by

$$\rho C_p \left(u \frac{\partial t}{\partial x} + v \frac{\partial T}{\partial x} \right) = k \left(\frac{\partial^2 T}{\partial y^2} \right) \quad (5)$$

3.4 Data Processing

In this paper, imperial correlations from heat transfer have been taken and applied to achieve desired outcomes from analytical calculation which will further be compared with the numerical results.

Hydraulic diameter,

$$Dh = \frac{4A}{P} = \frac{4 \times \frac{\pi}{4} \times D^2}{\pi D} = D \quad (6)$$

$Dh = D$.

Reynolds number,

$$\Re = \frac{\rho v D}{\mu} \quad (7)$$

Prandtl number,

$$Pr = \frac{u c_p}{k} \quad (8)$$

Nusselt number,

For cylinder tube,

$$Nu = 0.023 \times Re^{0.8} \times Pr^{0.3} \quad (9)$$

Heat transfer coefficient,

$$Nu = \frac{h D_h}{k} \quad (10)$$

Surface rate,

$$A_s = \frac{\Pi}{4} \times D_h^2 \times L \quad (11)$$

Heat transfer rate,

$$Q = h A_s \Delta t \tag{12}$$

4 Results and Discussion

In this section, the laminar flow through the radiator tube with two different fluids is simulated. Main intimation is to understand the flow distribution in the radiator tube. In Fig. 6, it is shown that the velocity at the curved section of tube for nanofluid and hybrid nanofluid is more as compared to the other part of the tube. It investigated that when the shape of the tube changed then velocity also changed but losses due to shape change process are increased and that losses directly affect the pressure drop inside the tube which is reasonable for increasing pumping cost.

The temperature variation inside the radiator tube is shown in Fig. 7. When ZnO is a fluid at that time the temperature difference between inlet and outlet is decreasing with respect to change in volume concentration. It is happened due to the change in thermophysical property of ZnO. When the volume concentration of ZnO increases in the base fluid, it will decrease the thermal conductivity because thermal conductivity of Zn nanoparticles is less than the other nanoparticles, but stability is more while it will mix in the base fluid. In the Ag/ZnO hybrid nanofluid, the temperature difference between the inlet and outlet temperature increases with respect to increase in the volume concentration. From this study, it is proved that the Ag/ZnO has a high ability to transfer the heat to the surrounding because of good thermal conductivity. With increase in the volume concentration of Ag nanoparticles in the ZnO nanofluid, it increased the thermal conductivity of ZnO nanofluid. Ag/ZnO has good thermal conductivity and stability, and it is suitable to use as a thermofluid.

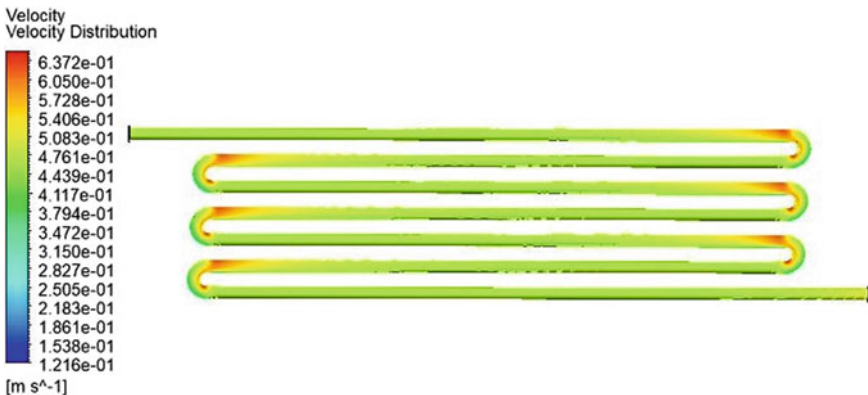


Fig. 6 Velocity contour for ZnO

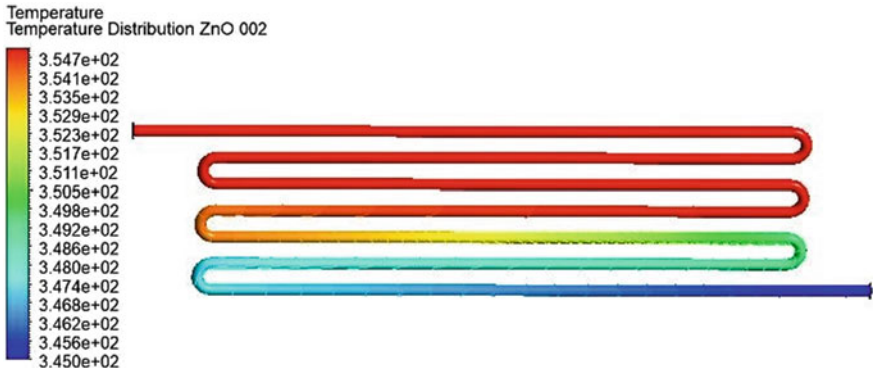


Fig. 7 Temperature distribution as a ZnO

Pressure drop is a very sensitive phenomenon in the heat exchanger, and it depends on the various parameters of the fluid and geometry. Figure 8 depicts that the pressure distribution for ZnO nanofluid, contour shows that the pressure at the inlet of the radiator is much higher than the outlet which happens due to the diameter of the tube, length of the tube, and the property of the nanofluid. The tube diameter is very less up to 4 mm, and length is about 230 mm. While travelling inside the tube it will enhance the friction, so that reduction in pressure happens at the outlet of the tube (Fig. 9).

The Nusselt number is dependent on the thermal conductivity and length of the tube. An increase in the length of the tube increases the Nusselt number. Figure 10a, b shows that increasing the Nusselt number increases the heat transfer coefficient. The same happens in the case of the Ag/ZnO nanofluid, which will cause an increase

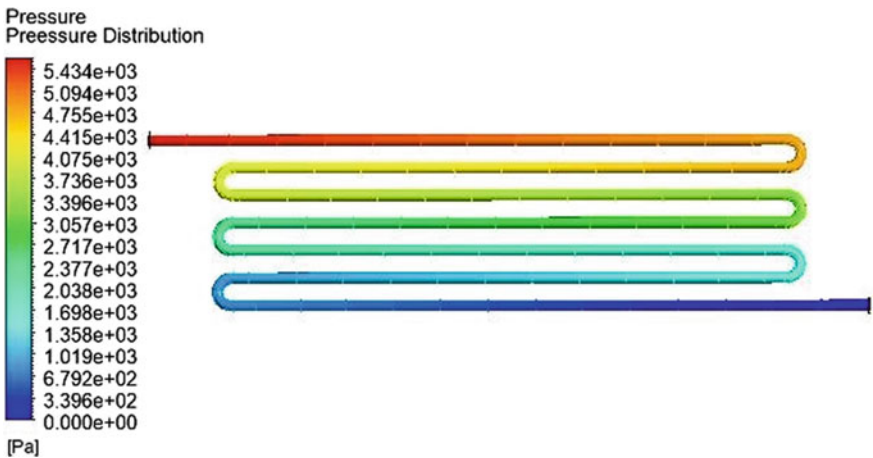


Fig. 8 Pressure drop as a ZnO nanofluid

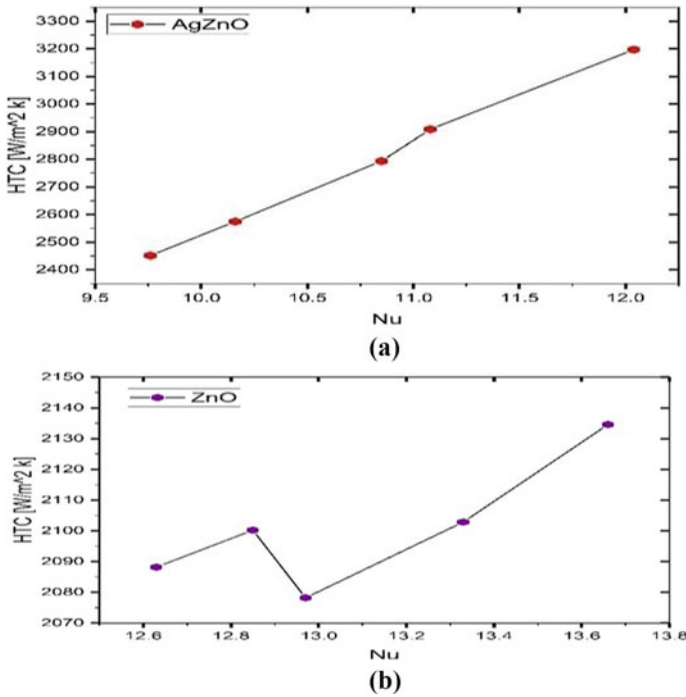


Fig. 9 a Nu versus HTC for Ag/ZnO, b Nu versus HTC for ZnO

in heat transfer coefficient. In ZnO nanofluid, the Nusselt number is greater than the hybrid nanofluid, and it has a lower heat transfer coefficient than the hybrid nanofluid. The variation in the Nusselt number and the Reynolds number is shown in Fig. 11 a, b. The effect of increased Nusselt number in nanofluids and hybrid nanofluids increases the Reynolds number. The Reynolds number is dependent on the viscosity, and the Nusselt number is dependent on the thermal conductivity. In the case of ZnO, the Reynolds and Nusselt numbers are greater, and they increase proportionally to each other. Ag/ZnO shows the variation of the Nusselt number with the Reynolds number, which is less than the ZnO. An increase in the Reynolds number results in an increase in the Nusselt number and a reduction in pressure drop. It shows that both fluids have the ability to transfer heat with a minimum pressure drop and a higher heat transfer rate [12].

The enhancement in the heat transfer rate with respect to the volume concentration studied by analytical and numerical method. In the case of ZnO, HTC increased by 0.1% Vc using the numerical method, but it decreased slightly using the analytical method. ZnO had a 27% error in analytical and numerical methods. In the Ag/ZnO, the heat transfer rate gradually increased with respect to the increase in the volume concentrations. It is shown in Fig. 11. That at the 0.1% Vc solution, results are equal for both methods, and the error is 0%. Numerical results show a higher heat transfer rate than analytical for Ag/ZnO. From numerical and analytical analysis, it shows

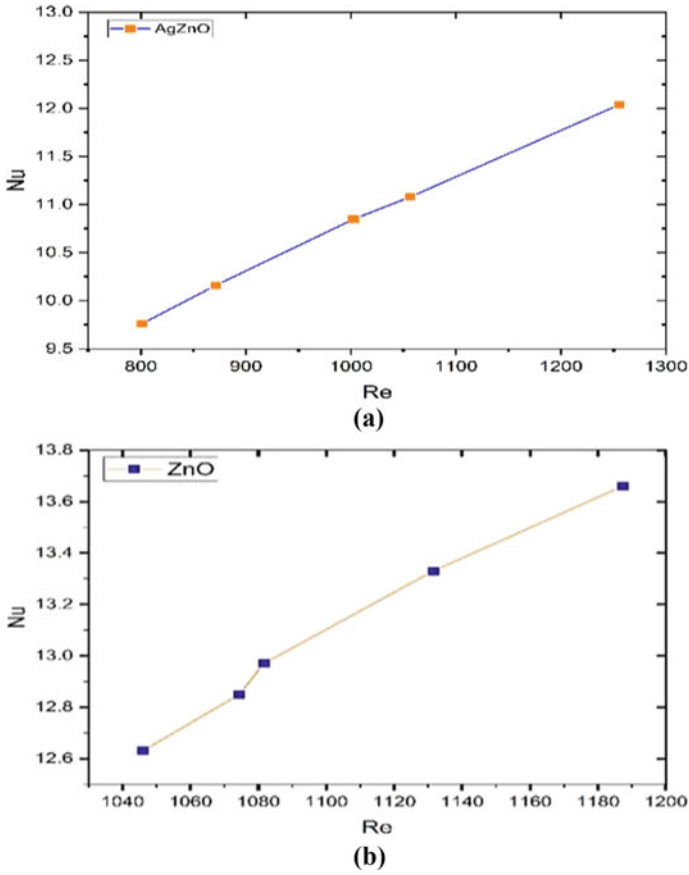


Fig. 10 a Re versus Nu for Ag/ZnO, b Re versus Nu for ZnO

that the increase in volume concentration is helpful for enhancing the heat transfer rate in the Ag/ZnO hybrid nanofluid. In the case of ZnO nanofluid, the heat transfer rate increases with respect to V_c , but only from 0.08% to 0.1% before decreasing with respect to V_c . Thus, it concludes that the heat transfer rate for the hybrid nanofluid is more satisfactory than the nanofluid.

5 Conclusions

In this study, the pressure drops, the Nusselt number, and the heat transfer coefficient for the ZnO nanofluid and Ag/ZnO hybrid nanofluid were obtained by using properties. The results are summarised as below:

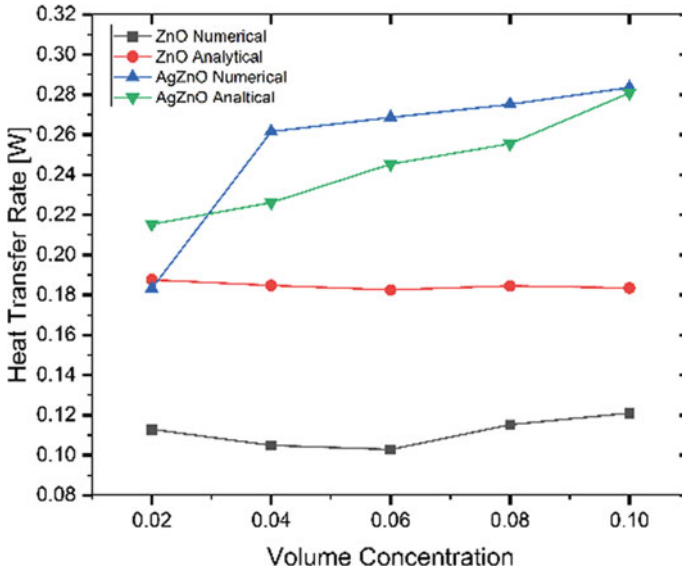


Fig. 11 Vc versus HTC for ZnO & Ag/ZnO

- From this study, it can be concluded that a car radiator tube can be simulated numerically and analytically by considering internal flow.
- It is observed that by using hybrid nanofluid (Ag/ZnO) as a coolant, the HTC is enhanced by 34.68% more than with nanofluid (ZnO and pressure drop was reduced by 18.03%. Thus, the hybrid nanofluid (Ag/ZnO) is more efficient than the nanofluid (ZnO) and base fluid (H₂O) for coolant applications.
- Hybrid nanofluid has a maximum heat transfer rate at (0.1%) volume concentration by both methods.
- However, as the Nusselt number increased, the heat transfer coefficient also increased. Due to an increase in length and heat transfer coefficient, the Nusselt number increases, and thermal conductivity decreases for the coolant.

Finally, it has been proved that the increase in Reynolds number causes the decrease in the pressure drop for both nanofluid and hybrid nanofluid. But in case of the ZnO nanofluid, increase in the volume concentration results in increase in pressure drop.

References

1. Sonage BK, Mohanan P (2015) Miniaturization of automobile radiator by using zinc-water and zinc oxide-water nanofluids. *J Mech Sci Technol* 29(5):2177–2185. <https://doi.org/10.1007/s12206-015-0438-x>

2. Pawar Amol D, Sarup J, Mittal SK (2016) Application of GIS for flood mapping: a case study of Pune city. *Int J Modern Trends Eng Res* 2349:28–30
3. Barewar SD, Tawri S, Chougule SS (2020) Experimental investigation of thermal conductivity and its ANN modeling for glycol-based Ag/ZnO hybrid nanofluids with low concentration. *J Therm Anal Calorim* 139(3):1779–1790. <https://doi.org/10.1007/s10973-019-08618-6>
4. Barewar SD, Kotwani A, Chougule SS, Unune DR (2021) Investigating a novel Ag/ZnO based hybrid nanofluid for sustainable machining of inconel 718 under nanofluid based minimum quantity lubrication. *J Manuf Process* 66:313–324. <https://doi.org/10.1016/j.jmapro.2021.04.017>
5. Barewar SD, Tawri S, Chougule SS (2018) Heat transfer characteristics of free nanofluid impinging jet on flat surface with different jet to plate distance: An experimental investigation. *Chem Eng Process Process Intensif* 136:1–10. <https://doi.org/10.1016/j.cep.2018.12.001>
6. Khan TA, Ahmad H (2019) CFD-based comparative performance analysis of different nanofluids used in automobile radiators. *Arab J Sci Eng* 44(6):5787–5799. <https://doi.org/10.1007/s13369-019-03750-9>
7. Naraki M, Peyghambarzadeh SM, Hashemabadi SH, Vermahmoudi Y (2013) Parametric study of overall heat transfer coefficient of CuO/water nanofluids in a car radiator. *Int J Therm Sci* 66:82–90. <https://doi.org/10.1016/j.ijthermalsci.2012.11.013>
8. Delavari V, Hashemabadi SH (2014) CFD simulation of heat transfer enhancement of Al₂O₃/water and Al₂O₃/ethylene glycol nanofluids in a car radiator. *Appl Therm Eng* 73(1):380–390. <https://doi.org/10.1016/j.applthermaleng.2014.07.061>
9. Yarmand H et al (2015) Graphene nanoplatelets-silver hybrid nanofluids for enhanced heat transfer. *Energy Convers Manage* 100:419–428. <https://doi.org/10.1016/j.enconman.2015.05.023>
10. Minea AA, Lorenzini G (2017) A numerical study on ZnO based nanofluids behavior on natural convection. *Int J Heat Mass Transf* 114:286–296. <https://doi.org/10.1016/j.ijheatmasstransfer.2017.06.069>
11. Wen T, Lu L, Zhang S, Zhong H (2021) Experimental study and CFD modelling on the thermal and flow behavior of EG/water ZnO nanofluid in multiport mini channels. *Appl Therm Eng* 182. <https://doi.org/10.1016/j.applthermaleng.2020.116089>
12. Safir NH et al (2018) Fluid flows for heat transfer enhancement by using ZnO/water nanofluids with different concentrations. *IOP Conf Ser Mater Sci Eng* 429(1). <https://doi.org/10.1088/1757-899X/429/1/012076>
13. Barewar SD, Chougule SS, Jadhav J, Biswas S (2018) Synthesis and thermo-physical properties of water-based novel Ag/ZnO hybrid nanofluids. *J Therm Anal Calorim* 134(3):1493–1504. <https://doi.org/10.1007/s10973-018-7883-6>

Role of Buoyancy and Acceleration Parameters in the Heat Transfer Deterioration of Supercritical Carbon-Dioxide Under Natural Circulation



Kapil Bodkha, D. S. Pilkhwal, and N. K. Maheshwari

Nomenclature

d	Diameter (m)
G	Mass flux ($\text{kg}/\text{m}^2 \text{ s}$)
H	Enthalpy (kJ/kg)
htc_a	Heat transfer coefficient of air ($\text{W}/\text{m}^2 \text{ K}$)
k	Thermal conductivity ($\text{W}/\text{m K}$)
m	Mass flow rate (kg/s)
Q_n	Net power to the heater (kW)
q	Heat flux (kW/m^2)
q_v	Volumetric heat generation rate (W/m^3)
T	Temperature ($^{\circ}\text{C}$)
x	Distance from heater inlet (m)

K. Bodkha (✉)

Engineering Sciences Discipline, Homi Bhabha National Institute, Mumbai 400094, India
e-mail: kapil585@rediffmail.com

D. S. Pilkhwal

Ex-Head, Cryo-Technology Division, Bhabha Atomic Research Centre, Mumbai 400085, India

K. Bodkha · N. K. Maheshwari

Reactor Design & Development Group, Bhabha Atomic Research Centre, Mumbai 400085, India

1 Introduction

Supercritical fluids (SCFs) find extensive proposed applications in the industries as well as in the upcoming generation of nuclear reactors due to numerous advantages associated with them. Supercritical carbon-dioxide (SC-CO₂) finds applications in heat pumps for district heating [1], advanced air-conditioning system [2], solar [3] and geothermal [4] power conversion system besides the one in SC-CO₂-based Brayton cycle which is proposed in the secondary cycles of sodium-cooled fast reactor, lead-cooled fast reactor and molten salt reactors. Similarly, supercritical water (SCW) and supercritical helium (SC-He) also find applications in the upcoming generation (i.e. generation-IV) of the nuclear reactor based on the direct cycles for power production. SC-CO₂ is a good simulant for SCW due to analogous property in the supercritical region. This offers relatively ease of performing experiments with CO₂ due to its lower critical pressure (7.38 MPa) as compared to that of water (22.06 MPa).

With specific reference to application of SCFs in nuclear reactor systems, the safety studies with SCFs face challenges due to certain ambiguities in the heat transfer behaviour of these fluids. The SCFs undergo drastic changes in the thermos-physical properties while they pass through the pseudo-critical region. The changes in properties may cause to have normal heat transfer (NHT), enhanced heat transfer (EHT) or deteriorated heat transfer (DHT) for these fluids.

SCFs fluids operate above the critical point; therefore, the problem of critical heat flux (CHF), as encountered for sub-critical fluids, disappears for SCFs. However, there may exist a deteriorated heat transfer (DHT) regime in the pseudo-critical region where the SCFs may undergo deterioration in the heat transfer which may not be as severe as CHF but still can affect the safe operation of the nuclear reactor. Thus, a thorough understanding for the DHT phenomena is essential from design and safety point of view of nuclear reactors.

2 Literature Review and Objective

There have been various studies in the literature for investigating DHT. Vikhrev et al. [5], Kim et al. [6], Liu et al. [7] and Zhang et al. [8] experimentally investigated the DHT for upward flows and noted varying observations. Kim et al. [6] observed the HTD for SC-CO₂ at lower mass flux, whereas at higher mass flux the heat transfer was found to be normal for the almost same heat loads (i.e. ratio of heat flux to mass flux); however, Zhang et al. [8] noted the HTD occurrence at higher mass fluxes for the same heat load of 0.16 kJ/kg as compared to the lower mass flux. Zhao [9] studied the HTD for upward and downward flows and observed the wall temperatures are higher for the upward flows as compared to that in the case of downward flow. The wall temperatures were found to increase with increase in heat flux for the upward flows. Similar observations were noted by Yang et al. [10] for their studies with SCW in an annular test section. The role of buoyancy parameter, Bu, as suggested

by Jackson and Hall [11] in the insignificant heat transfer impairment (for $Bu < 10^{-5}$) was also discussed by Yang et al. [10] for upward and downward flows, and a significant role of buoyancy was found even when $Bu < 10^{-5}$.

Based on experimental studies, many criteria for onset of DHT have been suggested in the literature. Such criteria are available for SC-CO₂ in a limited manner [12–15]. However, owing to the complex phenomena of heat transfer none of such criteria can be applied with full confidence for safety studies of supercritical energy systems. Observations noted in one set of experiments can differ to those in another set of experiments as the DHT is strongly coupled to the heat flux, mass flux and operating pressure and temperature. Moreover, it can be noted that the criteria available in the literature for onset of HTD have been derived for the forced convection systems. Their applicability to natural circulation (NC) systems is uncertain. Kiss et al. [16] with their studies under NC assessed criteria of Yamagata et al. [17] developed for forced convection systems for SCW and found the same as invalid for NC systems. This calls for extensive studies on NC systems requiring a substantial support of experimental data. With this background, the experiments are performed in the present paper with SC-CO₂ under NC for investigation of HTD and studying the role of buoyancy parameter, Bu on the same.

The details of the experimental set-up, procedure, experimental observations and results obtained for the DHT of SC-CO₂ in the present studies are reported in this paper.

3 Experimental Set-Up and Tests

Experimental studies have been performed in a uniform diameter rectangular loop, viz. supercritical pressure natural circulation loop (SPNCL) set-up at BARC. The loop has two heaters (one vertical and one horizontal) and two coolers (one vertical and one horizontal) and can be operated for any of the four combinations of heater and cooler orientations (horizontal heater horizontal cooler (HHHC), horizontal heater vertical cooler (HHVC), vertical heater horizontal cooler (VHHC) and vertical heater vertical cooler (VHVC)). The loop also facilitates to conduct experiments with either of two fluids, viz. water and CO₂. Besides, the loop hardware consists of a pressurizer and adiabatic pipes to connect heaters and coolers. Pressurizer takes care of thermal expansion in the loop apart from housing pressurizing cover gas. Schematic of the loop is shown in Fig. 1. Heating sections are directly heated electrical resistance type heaters, whereas coolers are tube in tube type configurations with chilled water flowing in the annulus region. The loop is adequately insulated to take care of heat losses.

The loop is extensively instrumented to measure different parameters. K-type thermocouples are used to measure the bulk fluid temperature at different locations in the loop. Besides, in order to evaluate HTC thermocouples have also been brazed on the surface of the heater sections at 12 different locations as shown in Fig. 2. Kellar make pressure transducer is installed to measure the loop pressure. Uncertainty in the

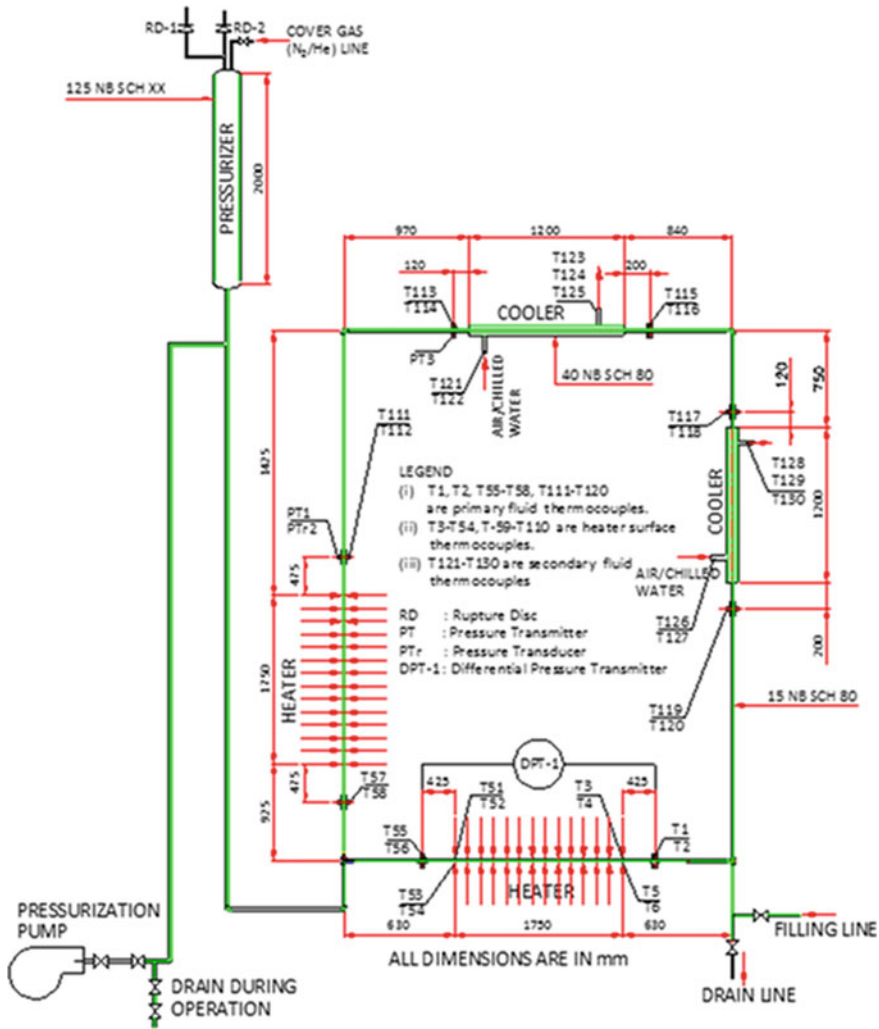
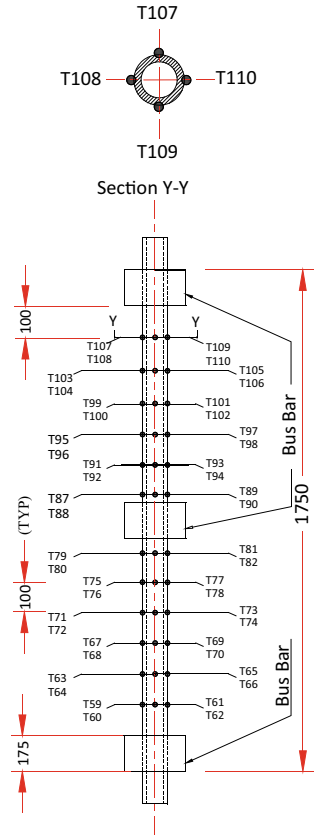


Fig. 1 Schematic diagram of the SPNCL

temperature measurement is $\pm 1.5\text{ }^{\circ}\text{C}$ for $T \leq 375\text{ }^{\circ}\text{C}$ and $\pm 0.4\%$ of the measurement for $T > 375\text{ }^{\circ}\text{C}$ as per standard IEC 584.2 Class-1, whereas uncertainty in the pressure measurement is $\pm 0.06\%$. Voltage and current which are used for power measurement have uncertainties of $\pm 0.5\%$ and $\pm 0.1\%$, respectively.

Fig. 2 Scheme for measurement of surface temperatures in the heater section



3.1 Operating Procedure

Initially the loop was charged with CO₂ and then with the help of helium (as a cover gas in the pressurizer) up to the desired operating pressure. The desired cooler was valved-in, and the loop was cooled at no power condition to achieve uniform temperature condition in the loop. Subsequently, the power was raised in steps, and at each step, the loop was maintained for sufficient duration to achieve steady-state condition. The operating pressure of the system was controlled within ± 0.1 MPa at each of the power step by venting the cover gas inventory from the pressurizer. After reaching at the maximum (dictated by safety limits on high surface temperature) power level in this way, the power was reduced back to zero again in the steps while passing through several steady states. Experiments performed separately for the VHHC, and VHVC orientations at 10.0 ± 0.1 MPa are discussed here to investigate the role of buoyancy parameter and acceleration parameter in HTD under NC conditions.

3.2 Data Reduction

Voltage, current, pressure and temperatures have been obtained during the experiments. Temperature measurements included bulk fluid temperature at various locations in the loop and outer wall temperature of the heater section as depicted in Figs. 1 and 2. Steady-state natural circulation mass flow rates generated during the experiments have been evaluated using the heat balance method across the heater section as given in (1). Temperatures measured at heater inlet and outlet have been utilized to evaluate enthalpy, H , the respective locations.

$$m = \frac{Q_n}{H_{\text{out}} - H_{\text{in}}} \quad (1)$$

Inner wall temperature, T_{wi} , of the heater section has been evaluated with the help of measured temperature of outer wall, T_{wo} , using Eq. (2) obtained by conduction analysis considering temperature-dependent thermal conductivity of the Inconel-625, $k(T) = a + bT = 9.2985 + 0.0156 T$ and the heat loss to the surrounding.

$$T_{\text{iw}} = \frac{-a + \sqrt{(a + b \cdot T_{\text{ow}})^2 + b \cdot q_v \left(\frac{d_o^2 - d_i^2}{8} \right) - b \cdot d_o \cdot \ln \left(\frac{d_o}{d_i} \right) \left[\frac{q_v \cdot d_o}{4} + \frac{(a + b \cdot T_{\text{ow}})(T_{\text{amb}} - T_{\text{ow}})d_{\text{ins}}}{\frac{2k_{\text{ins}}}{h_{\text{tc}a}} + d_{\text{ins}} \cdot \ln \left(\frac{d_{\text{ins}}}{d_o} \right)} \right]}}{b} \quad (2)$$

Detailed derivation of (2) can be referred from supplementary material provided with the author's earlier publication [18].

4 Results and Discussion

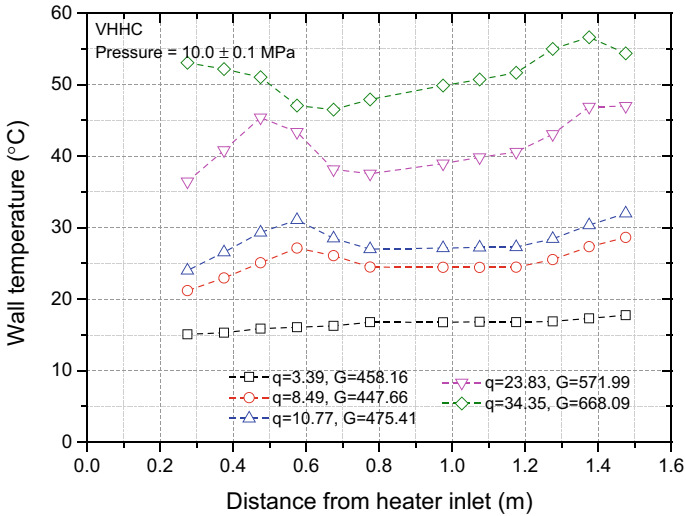
This section discusses the results obtained for the set of experiments mentioned earlier. It may be noted here that as the experiments are conducted under NC conditions, the flow rate could not be controlled during the experiments unlike in the case of forced convection systems. The flow in a NC system depends on the buoyancy head generated in the system due to temperature difference between hot and cold segments of the loop which in turn depends on the power (i.e. heat flux) supplied to the heater. Therefore, the mass flux corresponding to various heat fluxes varies and represents the flow generated in the system due to buoyancy head. The flow generated in a NC system with SCF first increases with power, attains a peak and then starts decreasing. Detailed investigations for flow behaviour of SC-CO₂ under NC have been conducted by the authors in [18], the same may be referred for the details related to the SC-CO₂ flow rate under NC for the present set of experiments. The occurrence of HTD can be identified by various methods given in the literature

wherein besides the classical method of observation of axial wall temperature profile, typically the heat transfer coefficient (*htc*) (or Nusselt No.) of the SCF obtained in experiments is normalized with that obtained using Dittus–Boelter correlation which is applicable for convective flows at sub-critical pressures. In the present paper, the HTD is identified using method of observation of axial temperature profile. The HTD is believed to occur at a location when the wall temperature there exceeds that at a location which is downstream. While making observation, the measurement uncertainty of the thermocouples is also considered, and a minimum of $\pm 3\text{ }^{\circ}\text{C}$ (i.e. twice of the uncertainty of $\pm 1.5\text{ }^{\circ}\text{C}$) is considered for the purpose.

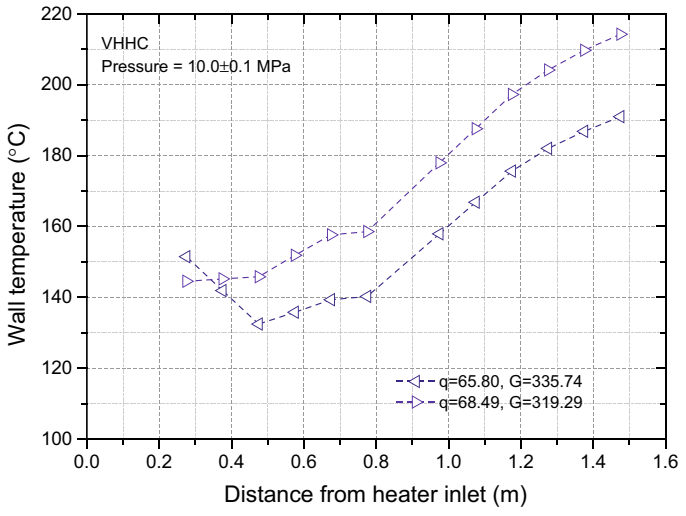
The experimentally obtained inner wall temperature profile has been depicted in Fig. 3a and b at various heat fluxes. Since the temperature data is spread in a large range, it is appropriate to show the same in separate plots with different scales. As the power is fed to the heater section, $q = 3.39\text{ kW/m}^2$, the wall temperatures start rising smoothly. As the power is raised in steps up to 10.77 kW/m^2 , the HTD sets-in at $x = 0.575\text{ m}$ (HTD is not considered to set-in at $q = 8.49\text{ kW/m}^2$ due to uncertainty consideration explained above). As the power is further increased, the extent of HTD increases with the peak in wall temperature at $x = 0.575\text{ m}$ (however, this is not shown in the Fig. 3a to avoid repetition of observations). With further increase of the heat flux to $q = 23.83\text{ kW/m}^2$, the location of the HTD shifts at $x = 0.475\text{ m}$, i.e. towards inlet of the heater section. The HTD occurs at the same location for higher heat fluxes (not shown here) until the heat flux is raised up to $q = 34.35\text{ kW/m}^2$ at which the HTD locations shifts to $x = 0.275\text{ m}$. The HTD location remains same for further high heat fluxes, and the temperature peaks at $x = 0.275\text{ m}$ when the heat flux is raised up to 65.80 kW/m^2 . The HTD disappears for the heat fluxes up to the maximum heat flux achieved during the experiments. After this, the power to the test section was reduced in the steps up to zero. Similar trends of shifting HTD locations have been observed in the reverse manner confirming the repeatability of the HTD phenomena. It may be noted here that the mass flux varies at different heat fluxes owing to the dependency of NC flow rate on the power.

As per literature, the HTD mechanism has been attributed to the combination of variation of different thermos-physical properties leading to the buoyancy and acceleration effects which in turn alter the turbulence production causing the degradation in the heat transfer. In the pseudo-critical region (PCR), the thermos-physical properties vary drastically. During this, the steep rise in specific heat and fall in dynamic viscosity assist the heat transfer improvement; however, considerable reduction in thermal conductivity together with sharp reduction in density causes the heat transfer to degrade. As a combined effect of all these along with operating parameters improvement or impairment of the heat transfer occurs as the turbulence production gets altered.

Jackson [19] explained the influencing role of buoyancy and acceleration in the HTD. In the case of upward flow, with increase in the heat flux in the PCR the near wall layers of fluid experience a buoyancy force which causes increase in local fluid velocity leading to lower shear stress and hence lesser turbulence production. With further increase in the heat flux, the velocity profile tends to achieve M-shaped curve, and the shear stress becomes negative. The peak in surface temperature is



(a)



(b)

Fig. 3 Axial temperature profiles for heater wall for experiment at 10.0 MPa pressure for VVHC orientation (q : kW/m²; G : kg/m²s)

expected in the vicinity of operating range. However, negative shear stress causes the flow to become unstable, and thus, the turbulence production recovers. Thus, the wall temperature at the locations where HTD occurred reduces, and the HTD disappears. Similarly, acceleration effects also cause reduction in the radial shear stress gradients. For maintaining flow conservation, an additional pressure gradient

(stream wise) is required for acceleration effects in a heated flow. Since the additional pressure gradient is greater in the boundary layer than that in the core region, the radial shear stress gradient in the near wall region reduced sufficiently to reduce the turbulence production and cause the HTD. For quantification of buoyancy and acceleration effects, various forms of buoyancy parameter (*Bu*) and acceleration parameter (*Ac*) have been proposed by different researchers. In the present paper, the *Bu* [11] and *Ac* [20] as given by (3) and (4) have been utilized to study their effect on HTD.

$$Bu = \frac{\overline{Gr}_b}{Re_b^{2.7}} \tag{3}$$

where $\overline{Gr}_b = \left(\frac{\rho_b(\rho_b - \overline{\rho})d^3g}{\mu_b^2} \right)$ and $Re_b = \left(\frac{GD}{\mu_b} \right)$.

$$Ac = \frac{q_b^*}{Re_b^{0.625}} \left(\frac{\rho_b}{\rho_w} \right)^{0.5} \left(\frac{\mu_w}{\mu_b} \right) \tag{4}$$

where $q_b^* = \left(\frac{q\beta_b}{GC_{p,b}} \right)$ and β , ρ and μ are thermal expansion coefficient, density and viscosity, respectively.

Figure 4a and b shows the variation of *Bu* and *Ac*, respectively, for the test data generated at 10.0 MPa pressure with VHHC orientation. These variations correspond to the temperature profiles given in Fig. 3. *Bu* and *Ac* signify the reduction in shear stress due to buoyancy and acceleration effects, respectively. These are being discussed here to examine and apprehend the HTD mechanism explained earlier in the context of present set of experiments under NC condition.

A close observation of Fig. 4a shows that the *Bu* profile at $q = 3.39 \text{ kW/m}^2$ appears to be smooth. As the flux is increased, the *Bu* profile also gets modified to include peaks and valleys. It is interesting to note that at $q = 10.77 \text{ kW/m}^2$, the *Bu* attains a peak at $x = 0.575 \text{ m}$ which happens to be the HTD location as observed from Fig. 3a. Moreover, with increase of heat flux, as the HTD location keeps on shifting towards heater inlet, the *Bu* also follows the similar trend and attains the peak values at the corresponding locations of HTD for various heat fluxes. The maximum peak value of *Bu* is observed at $q = 23.83 \text{ kW/m}^2$ at $x = 0.475 \text{ m}$. Beyond this heat flux the peak values of *Bu* obtained at various heat fluxes decreases. Finally, when the HTD disappears at $q = 68.49 \text{ kW/m}^2$, the *Bu* has maximum value at $x = 0.275 \text{ m}$ which is lesser than that obtained for $q = 65.80 \text{ kW/m}^2$ at which the HTD was observed for the last instance. However, at $q = 68.49 \text{ kW/m}^2$, the maximum value of *Bu* is not sufficient to sustain the HTD, and the heat transfer recovers.

The above set of observations indicates that the *Bu* has a strong influence on the HTD under NC conditions too. The *Bu* peaks at the onset of HTD ($q = 10.77 \text{ kW/m}^2$), *Bu* peaks attain maxima at higher heat flux ($q = 23.83 \text{ kW/m}^2$), and the quanta of these peaks keeps on decreasing with even higher heat fluxes. These observations

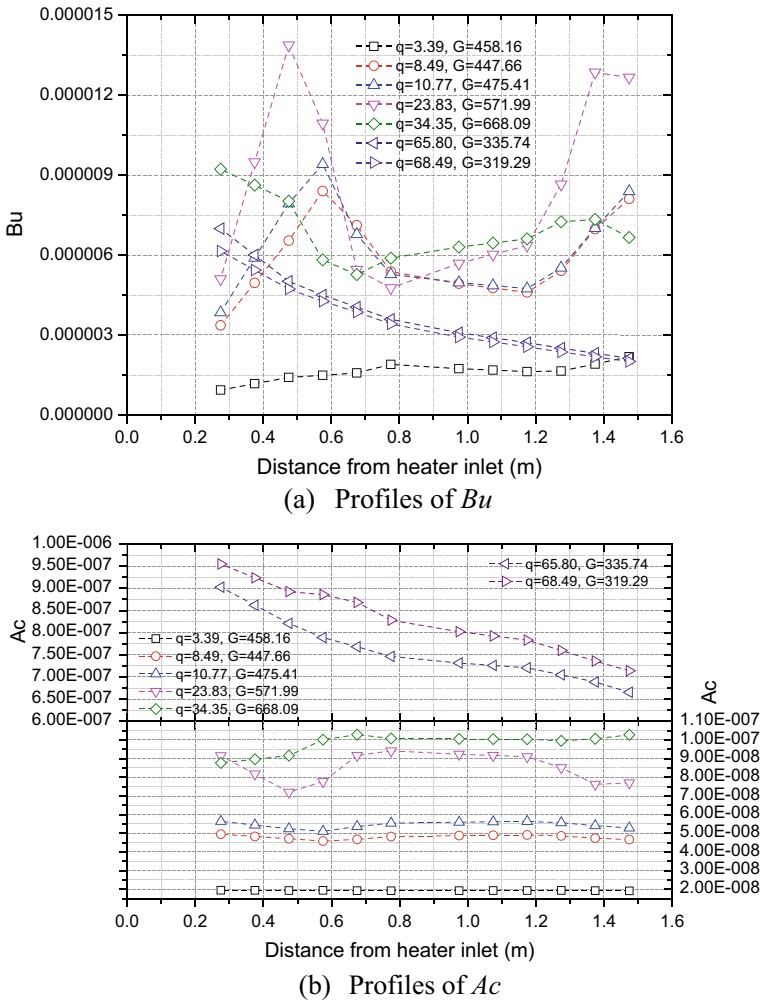


Fig. 4 Axial variation of Bu and Ac at 10.0 MPa pressure for VHHC orientation (q : kW/m²; G : kg/m²s)

confirm the role of Bu , and the trend of Bu is found in-line with the HTD mechanism discussed by Jackson [19].

Figure 4b shows the variation of Ac along the heater length at different heat fluxes to study its effect on HTD. As observed from Fig. 4b, no clearly identifiable peak has been obtained for the Ac profiles. However, the maximum value for a given profile at a heat flux does not correspond to the HTD location identified in Fig. 3. In fact, the location for peak value of Ac corresponds to that of NHT or EHT. Also, the HTD has been observed when the Ac is at its minimum value at given location and heat flux (e.g. $q = 10.77$ kW/m², $x = 0.575$ m; $q = 23.83$ kW/m², $x = 0.475$ m etc.). Thus,

there is no observation which can directly attribute the role of Ac in the HTD for the present set of experiment. In contrast to the observations made with Bu , Ac does not peak at the HTD location. Jackson [21] suggested a critical value of Ac as 4×10^{-6} for the onset of considerable HTD. Maximum value of Ac obtained in the present experiments is lower than this critical value. The observations indicate that there is no negative impact of Ac on the heat transfer in fact it is observed to assist the heat transfer in the present experiments. Lower values of Ac obtained in the experiments could be incapable of altering turbulence production to cause the HTD.

Figure 5a shows the axial variations of wall temperature, Bu and Ac , for the experiment conducted with VHVC orientation at the same pressure of 10.0 MPa. For demonstration purpose, profiles have been shown only at selected heat flux values. The HTD onsets at $x = 0.775$ m when $q = 21.86$ kW/m², and subsequently shift in its location is also observed at higher heat fluxes. The HTD onset is observed at higher heat flux value as compared to that in the case of VHHC orientation. This may be due to the fact that the flow rates generated in the VHVC are lower as compared to those in VHHC due to lesser elevation difference between heater and cooler. This results in higher loop average temperature in the case of VHVC. Thus, lower mass flux values call for higher heat fluxes to generate necessary non-uniformity in the density distribution to affect shear stress distribution and turbulence production.

Figure 5b shows the variation of Bu and Ac . As observed in earlier case, the Bu is found to peak at the HTD location at different heat fluxes signifying its major role in the HTD, whereas observations for Ac also remain similar as reported for the case of experiment at VHHC orientation. Ac is found irrelevant to cause HTD.

5 Conclusions

Experiments conducted for VHHC and VHVC orientations under NC conditions are presented. The HTD location was found to shift towards heater inlet with the increase in heat flux. Role of Bu and Ac is brought out with reference to HTD under NC conditions. Bu is found to have a significant role in the HTD, whereas Ac is not found to cause HTD for present set of experiment. Instead, it was found to assist the heat transfer. Lower values of Ac in these experiments could be attributed to this.

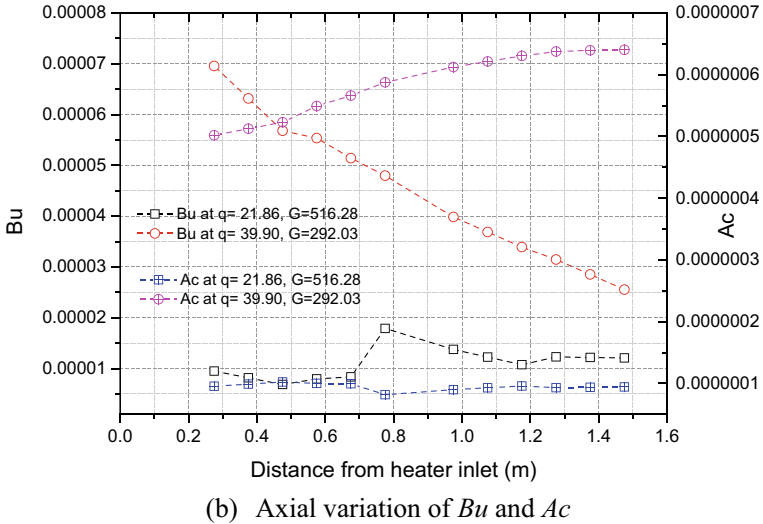
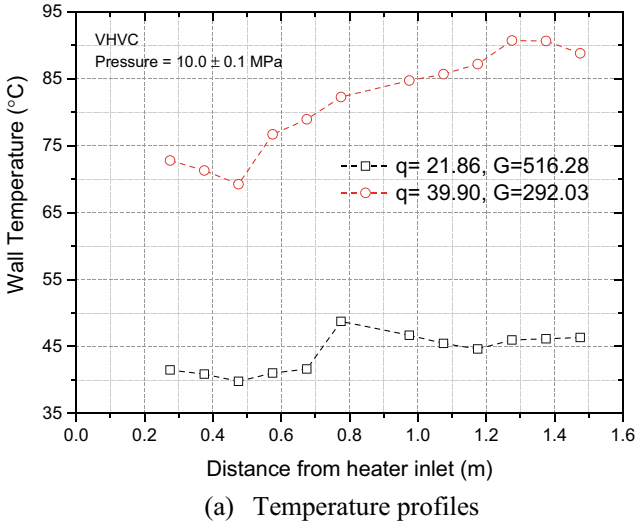


Fig. 5 Axial profiles at 10.0 MPa pressure for VHVC orientation (q : kW/m^2 ; G : $\text{kg}/\text{m}^2\text{s}$)

Acknowledgements Authors hereby acknowledge the support of Dr. Manish Sharma, Mr. S.S. Jana and Dr. R.D. Kulkarni of Reactor Engineering Division in providing resources to conduct the experiments.

References

1. Kalnin IM, Pustovalov SB, Krivtsov DV (2013) CO₂ heat pump technology for heating supply system (presentation). In: European heat pump summit, October 15–26, 2013, Nurnberg, Germany
2. Lorentzen G (1994) Revival of carbon dioxide as a refrigerant. *Int J Refrig* 17(5):292–301
3. Chapman DJ, Arias DA (2009) An assessment of the supercritical carbon dioxide cycle for use in a solar parabolic trough power plant. In: Proceedings of SC-CO₂ power cycle symposium, No. 09SC1-4, Apr. 29–30, 2009. Troy, NY
4. Wan Y, Xu T, Pruess K (2011) Impact of fluid-rock interactions on enhanced geothermal systems with CO₂ as heat transmission fluid. In: Proceedings of the 36th workshop on geothermal reservoir engineering. Stanford University, Paper No. SGP-TR-191, Jan. 31–Feb. 2, 2011, Stanford, CA
5. Vikhrev Y, Barulin Y, Konkov A (1967) A study of heat transfer in vertical tubes at supercritical pressure. *Thermal Eng* 14(9):116–119
6. Kim JK, Jeon HK, Lee JS (2007) Wall temperature measurements with turbulent flow in heated vertical circular/non-circular channels of supercritical pressure carbon-dioxide. *Int J Heat Mass Transfer* 50:4908–4911
7. Liu SH, Huang YP, Liu GX, Wang JF, Leung LKH (2017) Improvement of buoyancy and acceleration parameters for forced and mixed convective heat transfer to supercritical fluids flowing in vertical tubes. *Int J Heat Mass Transfer* 106:1144–1156
8. Zhang SJ, Xu XX, Liu C, Liu XX, Dang CB (2019) Experimental investigation on the heat transfer characteristics of supercritical CO₂ at various mass flow rates in heated vertical-flow tube. *Appl Therm Eng* 157:113687
9. Zhao CR, Liu QF, Zhang Z, Jiang PX, Bo HL (2018) Investigation of buoyancy-enhanced heat transfer of supercritical CO₂ in upward and downward tube flows. *J Suprcrit Fluid* 138:154–166
10. Yang Z, Bi Q, Wang H, Wu G, Hu R (2013) Experiment of heat transfer to supercritical water flowing in vertical annular channels. *J Heat Transf* 135:042504
11. Jackson JD, Hall WB (1979) Influences of buoyancy on heat transfer to fluids flowing in vertical tubes under turbulent conditions. In: Kakac S, Spalding DB (eds) *Turbulent forced convection in channels and bundles*. Hemisphere, pp 613–640
12. Shiralkar BS, Griffith P (1968) The deterioration in heat transfer to fluids at super-critical pressure and high heat fluxes. MIT Engineering Project Laboratory, Massachusetts, Report No. 70332
13. Kim JK, Jeon HK, Lee JS (2007) Wall temperature measurement and heat transfer correlation of turbulent supercritical carbon dioxide flow in vertical circular/non-circular tubes. *Nucl Eng Des* 237:1795–1802
14. Grabezhnaya VA, Kirillov PL (2006) Heat transfer under supercritical pressures and heat transfer deterioration boundaries. *Therm Eng* 53(4):296–301
15. Kline N, Feuerstein F, Tavoularis S (2018) Onset of heat transfer deterioration in vertical pipe flows of CO₂ at supercritical pressures. *Int J Heat Mass Transfer* 118:1056–1068
16. Kiss A, Balaskó M, Horváth L, Kis Z, Aszódi A (2017) Experimental investigation of the thermal hydraulics of supercritical water under natural circulation in a closed loop. *Ann Nucl Energy* 100:178–203
17. Yamagata K, Nishikawa K, Hasegawa S, Fujii T, Yoshida S (1972) Forced convective heat transfer to supercritical water flowing in tubes. *Int J Heat Mass Transfer* 15:2575–2593.
18. Bodkha K, Pikhwal DS, Maheshwari NK (2022) Experimental investigations on thermal-hydraulics of supercritical carbon dioxide under natural circulation vertical flows. *J Heat Transfer* 144:082601
19. Jackson JD (2017) Models of heat transfer to fluids at supercritical pressure with influences of buoyancy and acceleration. *Appl Therm Eng* 124:1481–1491

20. Kim DE, Kim MH (2010) Experimental study of the effects of flow acceleration and buoyancy on heat transfer in a supercritical fluid flow in a circular tube. *Nucl Eng Des* 240:3336–3349
21. Jackson JD (2013) Fluid flow and convective heat transfer to fluids at supercritical pressure. *Nucl Eng Des* 264:24–40

Experimental Investigations on the Thermal Contact Conductance Using Al₂O₃ Nanoparticles in the Interfacial Material



Rajesh Choudhary, Aman Singh, Aditya Kumar, and Sudhakar Subudhi

1 Introduction

The knowledge of thermal contact conductance (TCC) is very essential in designing thermal components like compact heat exchangers, heat sinks, and multiple interfaces that are widely used in compound reactor walls, building constructions, furnaces, multilayer insulations in pipes for heating as well as cryogenic applications, and many more. The uniform heat flow between two similar or dissimilar metallic surfaces is restricted to conduction through the different contact spots. These limited contact spots and gaps between two surfaces applied a thermal contact resistance (TCR) to the heat transfer. The range of interfacial TCC varies from 2000 to 2×10^5 W/m²K [1]. This variation in the range is because of the different methods used to improve the interfacial thermal conductance, such as coating the small size particles of the different materials on the solid surface, or applying a large amount of pressure to press the solid surface against each other, or by deforming the surfaces in the contact.

R. Choudhary (✉)

Department of Mechanical Engineering, SVNIT Surat, Surat 395007, India
e-mail: rchoudhary@med.svnit.ac.in

A. Singh

School of Mechanical Engineering, Lovely Professional University, Phagwara 144411, India

A. Kumar

Department of Energy & Environment, NIT Tiruchirappalli, Trichy 620015, India

S. Subudhi

Department of Mechanical and Industrial Engineering, IIT Roorkee, Roorkee 247667, India

2 Literature Review and Objectives

TCR is an imperative research topic for scientists and researchers over the last hundred years [2, 3]. Numerous theoretical and experimental research emphasizing the measurement of TCR have been reported in the literature [4–7]. Zheng et al. [8] measured the TCR of the micro pin fins located near the heat source, which were used to increase the heat dissipation in the microchannel heat sink. Parikh et al. [9] used experimental and numerical methods to estimate the TCC for one-dimensional heat conduction problems and for two periodically contacted bodies. Dai et al. [10] proposed a mechanical–thermal–mechanical–thermal dual-iterative coupling method based on the thermal expansion of the pellet in cladding to predict the TCR. The surface roughness and pressure were correlated with the TCR of the phase change material and their encapsulation material by Feng et al. [11]. The interfaces of erythritol and different thin metal plates were prepared using conventional solidification, and a reduction in the TCR was reported with the decrease in the surface roughness and rise in the pressure. By modifying the lattice Boltzmann method through an inserted layer treatment, the thermal conduction of a packed bed with the TCR was simulated by Li et al. [12] to investigate the effect of surface roughness.

A lot of work has been done to improve the thermal contact using the nanocoating, but it increases the cost, as advanced manufacturing techniques are used to prepare the nanocoating, and the perfect contact is also not achieved at the microscopic level. All these processes need technological advancement and a very high initial cost. Along with these, the presence of air cannot be avoided at the interface, which further creates interfacial thermal resistance. Shojaefard and Goudarzi [13] numerically studied the dependence of TCR on the pressure and texture of the specimen surfaces. Chen et al. [14] studied the TCR between two thin metal sheets of battery tabs as a function of contact pressure. Another option is to use the liquid at the interface, which can fill the space presented between the solid surface and remove all the air or gases available at the interface. But, as mentioned earlier, when the rate of heat transfer is very high, the thermal conductivity of the filled liquid must be very high to avoid the chances of burnout of the filler. Different types of fillers are used in the literature, such as silicon oil and glycerin but are unable to achieve a significant change in the rate of heat transfer. Wang et al. [15] studied the effects of interface material on the TCR in thermoelectric generators, experimentally. Thermal grease was used to overcome the air gaps at the contact interfaces, and, due to this TCR decreased.

A quantitative experimental assessment of interface material and pressure on the TCR of a thermoelectric module was conducted by Wang et al. [15]. In the presence of thermal grease, an increased temperature difference at the interface and power output was reported, for the constant temperature difference between the hot and cold source. In addition, by increasing the loading pressure, a reduction in the TCR and a 33% enhancement in the power output were also measured. Beltrán-Pitarch et al. [16] also measured the TCR of a thermoelectric device for a small temperature difference by performing three current–voltage (I–V) curves at different conditions. The accuracy

of the approach was further examined through experiments on a commercial Bi-Te module using the thermal interfacial material.

Liu et al. [17] prepared a novel phase change thermal interface material (TIM), using graphene, olefin block copolymer, and paraffin, to increase the wetting between two solid surfaces to reduce the TCR. By employing the prepared TIM to heat dissipation of a microelectronic device, Liu et al. [17] found a reduction of more than 90% in TCR for the rise in the temperature from 37 to 45 °C. Another phase change TIM was also designed and prepared using polyethylene glycol, unsaturated polyester resin, and graphene by Liu et al. [18]. It was reported that a thin molten layer of polyethylene glycol wetted the solid surface when temperature increased and filled the micro gaps and bumps to reduce the TCR. In addition, TCR was further reduced by increasing the pressure, but the reduction was more for the phase change TIM. Grujicic et al. [19] studied the effect of TCR on heat management between the central processing unit assembly and the heat sink. They reported that the use of thermal interface materials eliminates the micro gap significantly which leads to abatement in the TCR and expedites the heat transfer. Thermally conductive fluids may reduce this contact resistance between the surface.

Nanofluids are the new generation of smart fluids consisting of enhanced thermophysical properties. The fascinating feature of the nanofluids is the anomalously enhanced and tunable thermal conductivity. The plentiful literature shows that the thermal conductivity of the nanofluids improved and was consistent [20–23]. The high thermal conductivity of nanofluids may enhance the heat transfer between the thermal contacts. The thermal conductivity of nanofluids has been studied by a number of researchers during the last decade [21–23]. Lee et al. [24], Das et al. [25], Chon et al. [26], Chandrasekar et al. [27], Esfe et al. [28] and Elias et al. [29] studied the thermal conductivity of nanofluids containing Al_2O_3 nanoparticles and reported that the thermal conductivity of the nanofluids is enhanced with the nanoparticle's concentrations.

Thermal contact conductance is a primary parameter for the improvement of electronic cooling. A higher value TCC results in better cooling of the electronic components and further increases the life and reliability of the electric devices. In the present work, an experimental approach is used to investigate the enhancement of TCC using different thermal interface materials. The primary objectives of the present study were to determine the effect of the interface filler material (glycerin and Silvo) and the use of Al_2O_3 nanoparticles, having a particle diameter of 40 nm, suspended in the thermal interface material on the TCC at the interface. In the present work, a mixture of nanoparticles in the base fluid was employed as a thermally conducting liquid to improve the thermal contact to enhance the thermal conductance and diminish the TCR between the two solid plates. The effect of the concentration of the nanoparticles on thermal conductance was also calculated.

3 Experimental Facility and Preparation of Nanoparticle Mixture

The experimental setup has been fabricated to measure the thermal conductance between the two copper plates at low pressure and low heat flux conditions, as per the ASTM D5470 standard [30]. A schematic diagram of the experimental setup has been depicted in Fig. 1. Both the copper plates are plane in geometry, and at the contact interface of these plates, the thermal conductance will be estimated. Both copper plates are of the same dimensions of $50 \text{ mm} \times 25 \text{ mm} \times 5 \text{ m}$. The upper copper plate is connected to the electrical plate heater (make: Lakshmi Electrical Industries, Thane; material: mild steel) of 100 W and 230 V capacity and behaves as a hot surface of dimensions of $50 \times 25 \times 10 \text{ mm}$. While the lower copper plate is connected to the water jacket with dimensions of $50 \times 25 \times 70 \text{ mm}$ and behaves as a cold surface.

The electric power is supplied to the plate heater from a variac, which is used to step down the line voltage to a smaller scale. The ammeter and voltmeter are further connected to measure the current and voltage of the electric power supplied. A mica sheet is kept over the plate heater to provide insulation. Over the mica sheet, a dead weight of 3.5 kg is put to maintain uniform and constant pressure on the upper and lower plates. The water jacket is used to take away the heat transferred to the lower plate through the interface. The water jacket is fabricated as a rectangular cavity using the acrylic sheet and connected to the lower plate as one side of the jacket, as shown in Fig. 2, in which water at $20 \text{ }^\circ\text{C}$ is supplied from the constant temperature

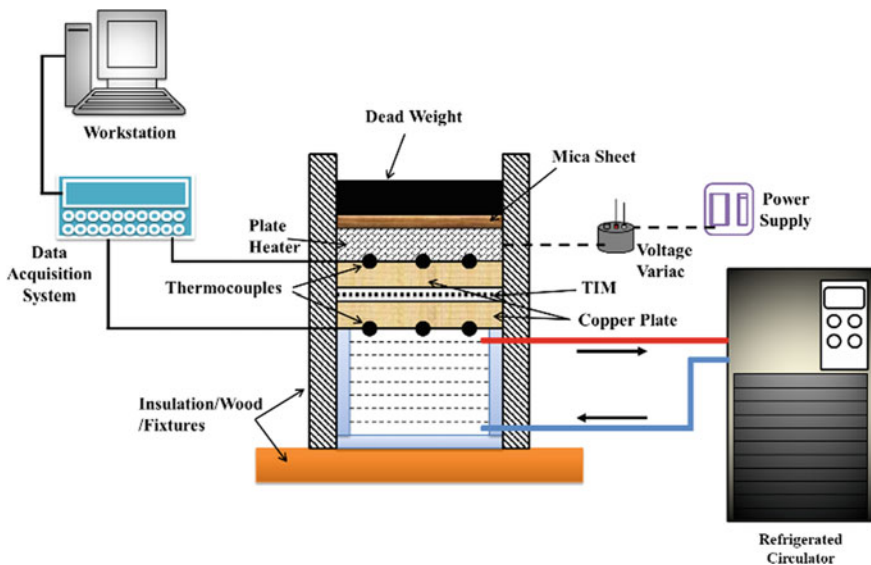


Fig. 1 Schematic diagram of the setup

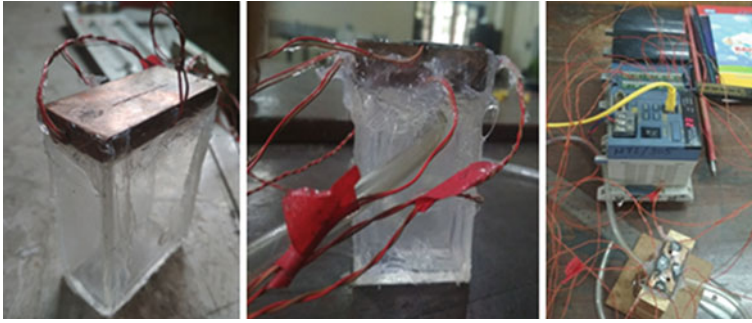
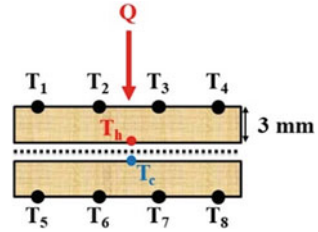


Fig. 2 Different components of the experimental setup: (left) water tank with lower copper plate, (center) water tank with upper and lower copper plates with thermocouples, and (right) DAQ system

circulator. As the cold water absorbed the heat from the bottom plate, the temperature difference between the copper plates increased, heat transfer resistance reduces, and heat flow was improved. By regulating the flow rate of cold water and power supply to the plate heater, the temperatures of both copper plates were controlled during the experiments.

To measure the temperature of the interface, a groove of 2 mm was prepared to connect the T-type thermocouples at the four locations of the upper plate and four locations of the lower plate. Along with the corresponding temperature, voltage and current were also recorded from the power supply. The measured temperature data were recorded using the DAQ system (make: Yokogawa Japan, model: MW100) and stored in to a workstation. To prepare the nanofluids, the Al_2O_3 nanoparticles having a diameter of 40 nm were used, procured from Nanoshell, USA. Silvo (thermal grease) and glycerine were used as base fluids. Silvo thermal paste has a thermal conductivity in the range of 3–8 W/mK, due to the presence of silver compound. To prepare the nano-suspension of fixed weight percentage, an accurate measurement of nanoparticles was done by the electric weighing balance device (make: Wensar; model: DAB220). For the preparation of Al_2O_3 nano-suspension at different weight percentages, the two-step method was adopted. The nanoparticles were dispersed in base fluids and mixed by a magnetic stir device at 2000 rpm. An ultrasonic probe sonicator (make: BioMatrix; model: BMS—750 T) of frequency 19.2 ± 2 kHz at the power of 750 W was utilized to break down the agglomerates of nanoparticles in base fluids for 10 min. The thermal conductivity of the base fluid and nano-suspension was measured by a thermal conductivity analyzer (make: Decagon, USA; model: KD2—pro) with an accuracy of ± 0.01 W/m $^\circ\text{C}$.

Fig. 3 Measurement of temperature at different locations in the experimental facility and direction of heat transfer



3.1 Data Reduction

As stated earlier, the temperature was measured at 4 different locations on the hot and cold plate, each, as shown in Fig. 3, and an average of 4 temperature readings was calculated to find the temperature of the upper and lower surfaces of the hot and cold copper plates, respectively.

$$T_{h1} = \frac{(T_1 + T_2 + T_3 + T_4)}{4} \tag{1}$$

$$T_{c1} = \frac{(T_5 + T_6 + T_7 + T_8)}{4} \tag{2}$$

From the Fourier’s law of heat conduction,

$$\frac{Q}{A} = k \frac{(T_{h1} - T_h)}{l} = k \frac{(T_c - T_{c1})}{l} \tag{3}$$

The temperature at the interface on hot plate and cold plate can be derived from Eq. (3), given as

$$T_h = T_{h1} - Ql/kA \tag{4}$$

$$T_c = T_{c1} + Ql/kA \tag{5}$$

The thermal contact conductance or resistance was calculated using the temperature difference at the interface, $[\Delta T]_{interface} = (T_h - T_c)$.

$$TCC = \frac{1}{TCR} = \frac{\frac{Q}{A}}{\Delta T_{interface}} \tag{6}$$

4 Results and Discussion

In the present work, a suspension of nanoparticles is employed as a thermally conducting liquid to improve the thermal contact to increase the thermal conductance between the two solid plates. The glycerin-based Al_2O_3 nanofluid is synthesized by the two-step method. In the thermophysical characterization, the thermal conductivity of the thermal interface material, with and without the suspension of nanoparticles, was measured, and it was found that the thermal conductivity increases with the particle concentration of the nanoparticles. For the glycerin, a maximum of 10.9% enhancement in the thermal conductivity was measured for the 10% wt. of nanoparticles, whereas the enhancement was about 3.52% for the 1.96% wt.

The TCC at the interface of two copper plates is estimated with respect to the heat flux and the use of different thermal interface materials. The measurement of the variable is conducted under steady-state conditions. Figure 4 shows the value of TCC with the heat flux in the absence of any thermal interface material between the two smooth copper plates. The TCC was measured in the absence of any thermal interface material, and it was found that the TCC increases with the heat flux at the interface. Simultaneously, the temperature difference at the interface was also increases with the heat flux, which would increase the TCR. At this contradiction, it can be predicted that the increment in the TCC may be due to radiation heat transfer takes place at the interface.

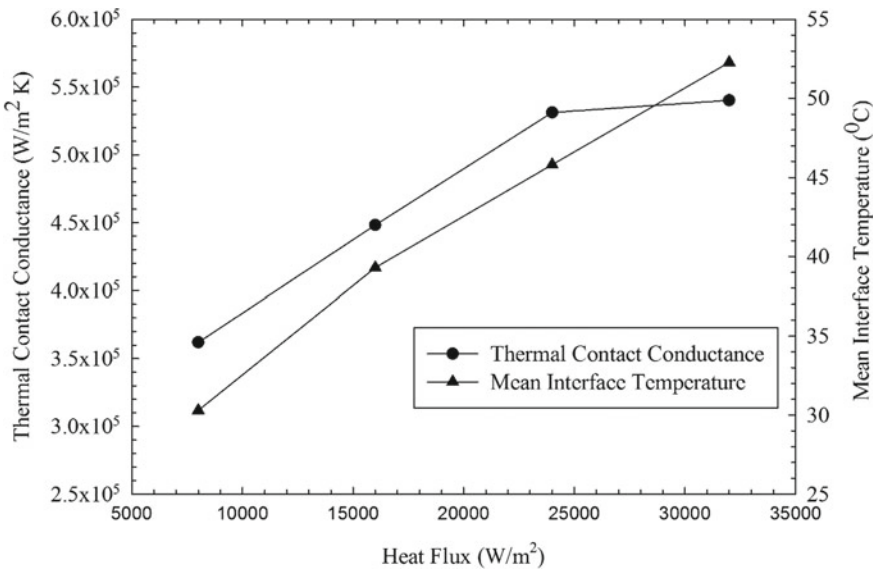


Fig. 4 Variation in thermal contact conductance and mean interface temperature with heat flux in the absence of interface materials between the plates

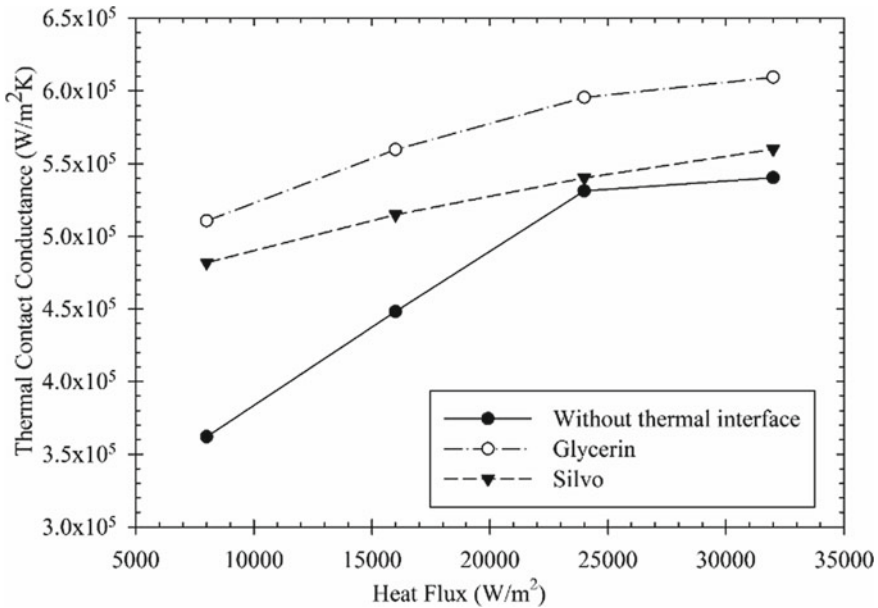


Fig. 5 Thermal contact conductance versus heat flux for the glycerine and silver paste (Silvo)

The values of TCC for the glycerine and Silvo thermal paste between the plates are shown in Fig. 5. The TCC increased more for the glycerine and Silvo than that without thermal interface material. The maximum enhancement of 40% for the glycerine and about 30% for Silvo was observed at the lowest heat flux of 8000 W/m², and this enhancement became constant at the higher heat fluxes. As the glycerine was in a semi-fluid state, it filled all the gaps by removing the air between the solid copper plates and making better contact, resulting in higher values of TCC. The increment in the TCC was smaller for the Silvo due to its semi-solid state.

The effect of mixing of Al₂O₃ nanoparticles in the different concentrations in glycerine on the TCC is depicted in Fig. 6. The values of the TCC were enhanced with the concentration of the nanoparticles in the glycerine. The maximum enhancement of 16% was observed at the nanoparticle concentration of 10 wt. % in the TCC value at the heat flux of 32,000 W/m². The thermal conductivity of the mixture was increased with the nanoparticle concentrations and plays an important role in the increment of the TCC. As compared to the glycerine, a maximum increment of 14% was observed for the particle concentration of 1.96% wt. at higher heat flux (12,000 W/m²). But, at the low heat fluxes, the TCC was decreased for the all-particles concentrations of nanoparticles suspended in the glycerine.

The effect of Al₂O₃ nanoparticles in the Silvo thermal paste was also measured, as shown in Fig. 7. By suspending the Al₂O₃ nanoparticles to the Silvo, the TCC was decreased with the weight percentage of the nanoparticles. This conflicting behavior might be due to the higher viscosity of the Silvo, due to which the motion

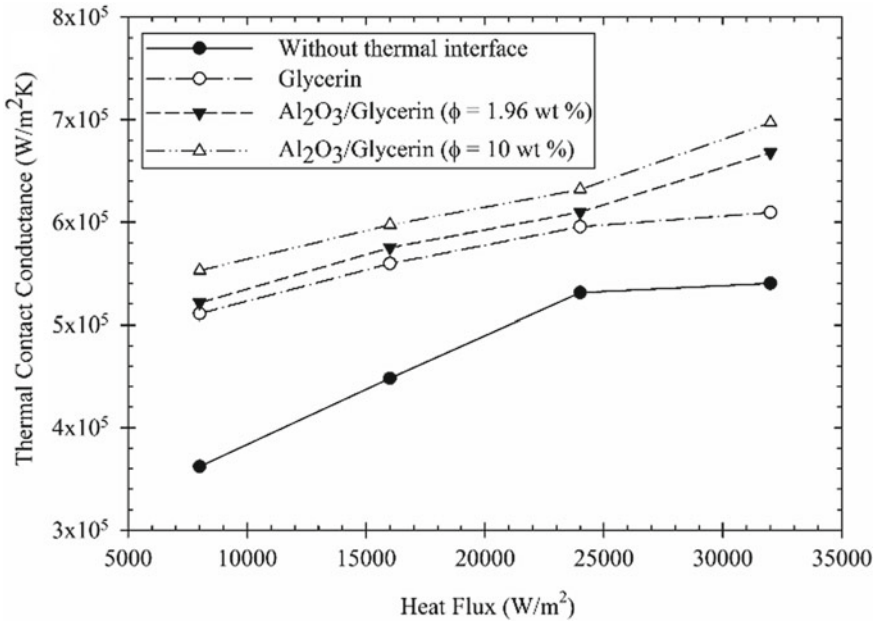


Fig. 6 Thermal contact conductance with heat flux for the Al₂O₃/glycerine nanofluids

of nanoparticles is constrained. But with the increase in heat flux, the value of TCC and temperature difference at interface was increased. By comparing the nanoparticle suspension in to the glycerin and Silvo, the TCC increased with the heat flux for the glycerin, while decreases for the Silvo. The temperature difference at the interface was increased with the heat flux for all the thermal interface materials. For some cases, such as glycerin and nanoparticle suspension in glycerin, the TCC and temperature differences increase, and simultaneously, it might be due to the increase in radiation heat transfer, but authors did not have any proof in the support of the claim.

5 Conclusions

The effect of different thermal interface materials such as glycerin, Silvo thermal paste, and the mixture of nanoparticles in these interface materials is investigated between the copper plates, subjected to a constant dead weight. From the present investigation, the following key points were observed:

- The temperature difference at the interface was increased with the heat flux for all the thermal interface materials, indicating a higher rate of heat transfer across the interface.

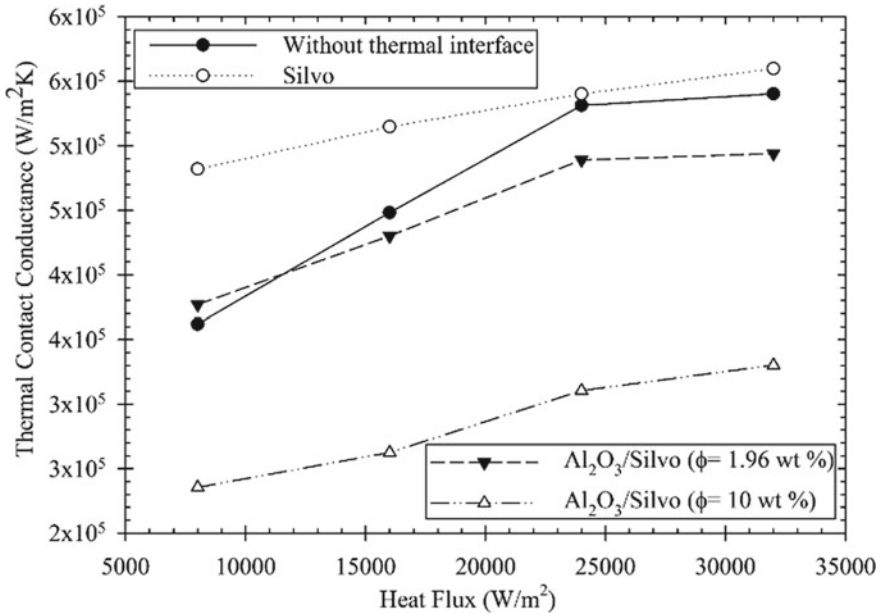


Fig. 7 Thermal contact conductance with heat flux for Al₂O₃/silvo paste

- The TCC was increased with the use of nanoparticles suspension in the base material for the glycerine, resulting in the reduction of the resistance at the interface.
- At the low heat fluxes, the TCC was decreased for all particle concentrations of nanoparticles mixed in the Silvo.
- The thermal interface material should be in semi-fluid state to fill all the gaps between the solid surfaces.

To make the electronic devices reliable and efficient with a long life, different types of nanoparticles such as CuO, carbon nanotubes, and TiO₂, can be used to improve the thermal contact conductance at the interface. More combinations of the nanoparticle concentration and particle size should be used with different thermal interface material. For more accurate measurement of the thermal contact conductance, transient study should be used. While the present work was the steady-state study.

Acknowledgements This work was supported by the Sardar Vallabhbai National Institute of Technology Surat under the Seed Grant Project No. 2021-22/DoME/21 and Sustainable Power & Energy System Lab, Department of Mechanical & Industrial Engineering, IIT Roorkee.

References

1. Çengel YA (2002) Heat transfer—a practical approach, 2nd edn. McGraw Hill Higher Education, New York
2. Barratt T (1913) Thermal and electrical conductivities of some of the rarer metals and alloys. *Proc Phys Soc London* 26:347–371
3. Barratt T (1915) The magnitude of the thermal resistance introduced at the slightly conical junction of two solids, and its variation with the nature of the surfaces in contact. *Proc Phys Soc London* 28:14–20
4. Savija I, Culham JR, Yovanovich MM, Marotta EE (2003) Review of thermal conductance models for joints incorporating enhancement materials. *J Thermophys Heat Transf* 17:43–52
5. Bahrami M, Culham JR, Yovanovich MM, Schneider GE (2006) Review of thermal joint resistance models for nonconforming rough surfaces. *Appl Mech Rev* 59:1–12
6. Lambert MA, Fletcher LS (1993) Review of the thermal contact conductance of junctions with metallic coatings and films. *J Thermophys Heat Transf* 7:547–554
7. Prasher RS, Phelan PE (1997) Review of thermal boundary resistance of high-temperature superconductors. *J Supercond* 10:473–484
8. Zheng R, Wu Y, Li Y, Wang G, Ding G, Sun Y (2022) Development of a hierarchical microchannel heat sink with flow field reconstruction and low thermal resistance for high heat flux dissipation. *Int J Heat Mass Transf* 182:121925. <https://doi.org/10.1016/j.ijheatmasstransfer.2021.121925>
9. Parikh M, Shah S, Vaghela H, Parwani AK (2022) A comprehensive experimental and numerical estimation of thermal contact conductance. *Int J Therm Sci* 172:107285. <https://doi.org/10.1016/j.ijthermalsci.2021.107285>
10. Dai YJ, Ren XJ, Wang Y, Xiao Q, Tao WQ (2021) Effect of thermal expansion on thermal contact resistance prediction based on the dual-iterative thermal–mechanical coupling method. *Int J Heat Mass Transf* 173:121243. <https://doi.org/10.1016/j.ijheatmasstransfer.2021.121243>
11. Feng B, Zhang YH, Tu J, Fan LW, Yu ZT (2021) Correlating the thermal contact resistance between metal/erythritol interfaces with surface roughness and contact pressure. *Int J Heat Mass Transf* 176:121407. <https://doi.org/10.1016/j.ijheatmasstransfer.2021.121407>
12. Li X, Gao D, Hou B, Wang X (2021) An inserted layer LBM for thermal conduction with contact resistances. *Chem Eng Sci* 233:116431. <https://doi.org/10.1016/j.ces.2020.116431>
13. Shojaefard MH, Goudarzi K (2008) The numerical estimation of thermal contact resistance in contacting surfaces. *Am J Appl Sci* 5:1566–1571
14. Chen J, Zhang W, Feng Z, Cai W (2014) Determination of thermal contact conductance between thin metal sheets of battery tabs. *Int J Heat Mass Transf* 69:473–480
15. Wang S, Xie T, Xie H (2018) Experimental study of the effects of the thermal contact resistance on the performance of thermoelectric generator. *Appl Therm Eng* 130:847–853
16. Beltrán-Pitarch B, Vidan F, García-Cañadas J (2021) Thermal contact resistance evaluation of a thermoelectric system by means of three I-V curves. *Int J Heat Mass Transf* 173:121247. <https://doi.org/10.1016/j.ijheatmasstransfer.2021.121247>
17. Liu C, Yu W, Chen C, Xie H, Cao B (2020) Remarkably reduced thermal contact resistance of graphene/olefin block copolymer/paraffin form stable phase change thermal interface material. *Int J Heat Mass Transf* 163:120393. <https://doi.org/10.1016/j.ijheatmasstransfer.2020.120393>
18. Liu C, Yu W, Yang J, Zhang Y, Xie H (2021) Reducing thermal contact resistance by a novel elastomeric polyethylen glycol/unsaturated polyester resin/graphene thermal interface materials. *Int Commun Heat Mass Transfer* 127:105553. <https://doi.org/10.1016/j.icheatmasstransfer.2021.105553>
19. Grujicic M, Zhao CL, Dusel EC (2005) The effect of thermal contact resistance on heat management in the electronic packaging. *Appl Surf Sci* 246:290–302. <https://doi.org/10.1016/j.apsusc.2004.11.030>
20. Choi SUS, Eastman JA (1995) Enhancing thermal conductivity of fluids with nanoparticles. In: International mechanical engineering congress and exhibition, San Francisco, CA (United States)

21. Kumar A, Subudhi S (2018) Preparation, characteristics, convection and applications of magnetic nanofluids: a review. *Heat Mass Transfer* 54:241–265. <https://doi.org/10.1007/s00231-017-2114-4>
22. Kumar A, Subudhi S (2019) Preparation, characterization and heat transfer analysis of nanofluids used for engine cooling. *Appl Therm Eng* 160:114092
23. Khurana D, Choudhary R, Subudhi S (2016) Investigation of thermal conductivity and viscosity of Al_2O_3 /water nanofluids using full factorial design and utility concept. *NANO* 11:1650093
24. Lee S, Choi SU-S, Li S, Eastman JA (1999) Measuring thermal conductivity of fluids containing oxide nanoparticles. *J Heat Transfer* 121:280–289
25. Das SK, Putra N, Thiesen P, Roetzel W (2003) Temperature dependence of thermal conductivity enhancement for nanofluids. *J Heat Transfer* 125:567–574
26. Chon CH, Kihm KD, Lee SP, Choi SUS (2005) Empirical correlation finding the role of temperature and particle size for nanofluid (Al_2O_3) thermal conductivity enhancement. *Appl Phys Lett* 87:153107
27. Chandrasekar M, Suresh S, Chandra Bose A (2010) Experimental investigations and theoretical determination of thermal conductivity and viscosity of Al_2O_3 /water nanofluid. *Exp Therm Fluid Sci* 34:210–216
28. Hemmat Esfe M, Karimipour A, Yan WM, Akbari M, Safaei MR, Dahari M (2015) Experimental study on thermal conductivity of ethylene glycol based nanofluids containing Al_2O_3 nanoparticles. *Int J Heat Mass Transf* 88:728–734
29. Elias MM, Mahbulul IM, Saidur R, Sohel MR, Shahrul IM, Khaleduzzaman SS, Sadeghipour S (2014) Experimental investigation on the thermo-physical properties of Al_2O_3 nanoparticles suspended in car radiator coolant. *Int Commun Heat Mass Transf* 54:48–53
30. ASTM D5470–06 (2006) Standard test method for thermal transmission properties of thin thermally conductive solid electrical insulation materials. *ASTM Int.* <https://doi.org/10.1520/D5470-06>

Propulsion and Power

Design and Analysis of Optimized Solid Propellant Grain



Mohammed Akbar and Prabhat Dattakumar Phondekar

1 Introduction

Propellants are employed in rocket motors for the purpose of undergoing combustion and providing thrust to the rocket [1]. In the case of solid rocket motors, this is achieved with solid propellant grain [2], which is the combination of solid fuel and/or oxidizer cast and cured into a semi-solid state inside the combustion chamber.

For achieving different types of combustion, there are many different designs created specifically. There are four types of burning: progressive, neutral, regressive, and multi-step thrust [1]. For progressive burning, there is the hollow cylindrical geometry. For neutral burning, the geometry of the rod-in-tube is implemented. Regressive burning utilizes various geometries such as double anchor and cross shape hollow geometry [3].

While these geometries have been designed since the early days of rocket making craft, they certainly function as intended, despite not being optimized designs [4].

In this paper, the creation of new and optimized designs [5] with calculus methods is investigated and analyzed using finite element analysis for greater surface area and to encompass a greater quantity of propellant inside the combustion chamber. In these aspects, two models are theorized, designed, and observed in analysis software for their various parameters such as internal surface area, volume, and their pressure vs time curves.

This paper is organized as follows: The literature review and research targets are enlisted in Sect. 2, and the methods to achieve these are discussed in detail in Sect. 3,

M. Akbar (✉)

Department of Mechanical Engineering, Medi-Caps University, Indore 453331, India

e-mail: mohammed.akbar0207@gmail.com

P. D. Phondekar

Department of Space Engineering and Rocketry, Birla Institute of Technology, Mesra 835215, India

including the derivations, covering the mathematical calculations. The results of the analysis are discussed in Sect. 4.

2 Literature Review and Objective

In the world of rocketry, the primary fuel sources of rockets are the propellant materials that undergo combustion and produce the required thrust for liftoff [3]. These solid rockets or booster stages utilize the propellant that is cast and cured into the combustion chamber into a specific geometry to serve a particular purpose [6], such as liftoff and landing a reusable shuttle. However, these geometries are standard and have been used since their development, but there is now a huge room to improve it with the availability of agile software and applying innovative optimization techniques to the existing geometry.

This brings us to the question: What if a propellant geometry is created and optimized for a particular parameter? This optimization of propellant geometry would aid in creating better propellant geometries [7] in the aspect of greater internal surface area or to have more propellants in the same combustion chamber space.

The goals of this research in solid propellant grain design for solid rocket motors are detailed as follows:

- (1) Theorizing of solid propellant grain geometries with the aim of optimization.
- (2) Create mathematical formulation using derivative calculus, of the theorized solid propellant grain models.
- (3) Design the models of hypothetical solid propellant grain geometries in 3D design software.
- (4) Perform FEA analysis of said models of theorized grain geometries.
- (5) Compare the FEA analysis results with a conventional solid rocket motor's propellant grain geometry to observe the difference.
- (6) Arrive at a conclusion based on the results from the analysis of the models.

Objectives (1) and (2) will be accomplished by utilizing maximizing and minimizing concepts from derivative calculus. That is, first and second derivative tests will be used to come up with an equation that determines the dimensions of maxima or minima in the solid propellant grain geometry.

Objective (3) utilizes 3D design software for creating the solid propellant grain geometry from the dimensions obtained from the prior calculation and mathematical formulation.

And for Objectives (4), (5), and (6) finite element analysis software such as ANSYS Fluent and ANSYS CFD-Post will be applied to the 3D designs to obtain results and arrive at conclusions.

Two models will be theorized and optimized in such a way that: first model can contain more propellant material compared to conventional propellant grain geometry.

The second model will be optimized so that it has a greater surface area for combustion compared to a conventional propellant grain geometry.

3 Methodology

Meshing method—patch conforming method—common to both propellant models discussed below in Sects. 3.1 and 3.3. Flow visualization from CFD solver—K-epsilon two-equation model common to both propellant designs in Sects. 3.1 and 3.3. Meshing details for both propellant designs are shown in Tables 1 and 2.

3.1 Hollow Spherical Chain Geometry

The mathematical formulation of this geometry is obtained with the help of the following problem statement:

In a given arrangement as shown in Fig. 1, a certain number of spheres are to be placed in a solid cylinder such that when the volume of said spheres is subtracted from the solid cylinder’s volume, the new volume that is left over should be maximum. And determine how many maximum numbers of spheres can be placed in the cylinder for the volume subtraction.

Let volume of new solid be V , radius of the cylinder be R , length of cylinder be l , radius of spherical cavity be r , and number of spherical cavities be n .

$$V = \{[\pi R^2 l] - [n(\frac{4}{3})\pi r^3]\} \tag{1}$$

Table 1 Mesh details hollow spherical chain geometry

Cells	Faces	Nodes
86,958	177,568	16,441

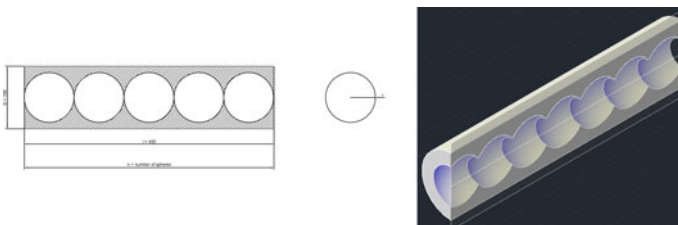


Fig. 1 Hollow spherical chain geometry and 3D section view

Also,

$$l = n(2r) \quad (2)$$

$$V = \left\{ [2\pi R^2 nr] - \left[n\left(\frac{4}{3}\right)\pi r^3 \right] \right\} \quad (3)$$

On differentiating with respect to r and then equating $V' = 0$,

$$\frac{dV}{dr} = V' = \left\{ [2\pi R^2 n] - [4\pi nr^2] \right\} \quad (4)$$

$$V' = 0 \quad (5)$$

$$[2\pi n R^2] - [4\pi nr^2] = 0 \quad (6)$$

$$[2\pi n R^2] = [4\pi nr^2] \quad (7)$$

$$R = r\sqrt{2} \quad (8)$$

$$r = \frac{R}{\sqrt{2}} \quad (9)$$

On differentiating again with respect to r ,

$$\frac{d^2V}{dr^2} = V'' = 0 - [8n\pi r^2] \quad (10)$$

$$V'' = -8n\pi r \quad (11)$$

$$V''_{r=\frac{R}{\sqrt{2}}} = -8n\pi \left[\frac{R}{\sqrt{2}} \right] \quad (12)$$

$$V''_{r=\frac{50}{\sqrt{2}}} = -8n\pi \left[\frac{50}{\sqrt{2}} \right] \quad (13)$$

$$V''_{r=\frac{50}{\sqrt{2}}} = -888.57658n \text{ (approximately)} \quad (14)$$

$$\text{i.e., } V''_{r=\frac{R}{\sqrt{2}}} < 0 \text{ (negative)} \quad (15)$$

At $V = \text{maximum}$,

$$n = \frac{2\pi R^2 r}{\frac{4}{3}\pi r^3} \quad (16)$$

$$n = 3 \text{ (or multiples of three)} \tag{17}$$

And also, the value of r or radius of spherical cavity,

$$r = \frac{50}{\sqrt{2}} \tag{18}$$

$$r = 35.3553906 \text{ mm (approximately)} \tag{19}$$

Therefore, the volume of the new resulting solid is maximum.

In other words, ideally it should have maximum propellant, in terms of volume. Considering its low web thickness $(R-r)/2$ which is approximately 7 mm, pressure casting technique [8] can be used for casting this type of propellant geometry.

3.2 Calculation of Dimensions for Hollow Spherical Chain Geometry

Let us consider the dimensions of propellant geometry’s length $l = 400$ mm and its radius $R = 50$ mm. Also, consider the number of spheres as $n = 7$ because of design constraint of test model so that there are open passages on both sides of propellant geometry for flow.

So,

$$R = 50 \text{ mm} \tag{20}$$

$$\text{sphere cavity radius} = 35.3553906 \text{ mm} \tag{21}$$

$$l = 400 \text{ mm} \tag{22}$$

Such that surface area of hollow cylindrical propellant grain is the same as new hollow spherical chain geometry.

And now on computing hollow cylindrical grains’ dimensions,

Surface area hollow spherical chain cylinder = Surface area hollow cylinder

$$A = 2\pi l(R + r) + 2\pi(R^2 - r^2) \tag{23}$$

$$225760 = [(2\pi(400))(50 + r)] + [(2\pi)(50^2 - r^2)] \tag{24}$$

Approximate value of area from ANSYS,

$$35390.819952426 = [20000 + 400r] + [2500 - r^2] \tag{25}$$

$$r^2 - 400r = -13430.81995 \tag{26}$$

$$r^2 - 400r + 13430.81995 = 0 \tag{27}$$

Solving for r , the value is obtained,

$$\therefore r = 36.9994477 \text{ mm} \tag{28}$$

These dimensions are used for creating geometries for the purpose of comparison.

3.3 Hollow Cuboidal Cavity Geometry

The mathematical formulation of this particular geometry is obtained with this problem statement:

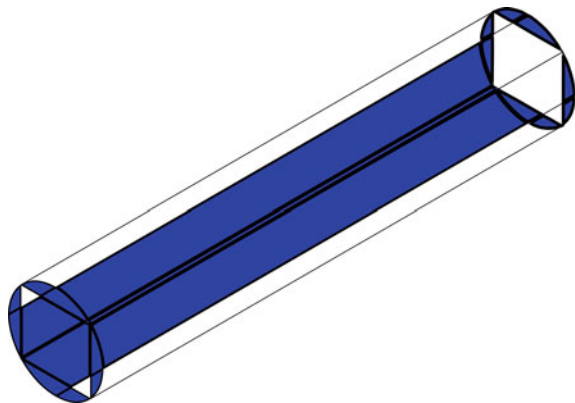
In this certain and unconventional configuration of solid propellant grain geometry as visualized in Fig. 3, the difference in areas of circle and rectangle of cross-section of propellant is to be minimized, to obtain a new hollow internal burning geometry visualized in Fig. 2 with hollow cuboidal cavity such that the internal surface area of this hollow cuboidal cavity is maximum.

Minimizing the area A in novel Eq. 29 on cross-section of propellant theoretically implies that the internal burning surface area will be maximum.

Table 2 Mesh details hollow cuboidal cavity geometry

Cells	Faces	Nodes
53,241	108,298	9,857

Fig. 2 Hollow cuboidal cavity highlighted in geometry



Visualizing the cross-section as shown in Fig. 3 let the area of rectangle ABFG be S , the area of circle be C , and the area of new geometry be denoted as A .

$$A = C - S \tag{29}$$

$$A = [\pi R^2] - [xy] \tag{30}$$

From triangle AMO,

$$R^2 = \left(\frac{x}{2}\right)^2 + \left(\frac{y}{2}\right)^2 \tag{31}$$

Substituting this value in the very first equation,

$$A = \left\{ [\pi] \left[\left(\frac{x}{2}\right)^2 + \left(\frac{y}{2}\right)^2 \right] \right\} - \{xy\} \tag{32}$$

$$A = \left[\left(\frac{\pi x^2}{4}\right) + \left(\frac{\pi y^2}{4}\right) - (xy) \right] \tag{33}$$

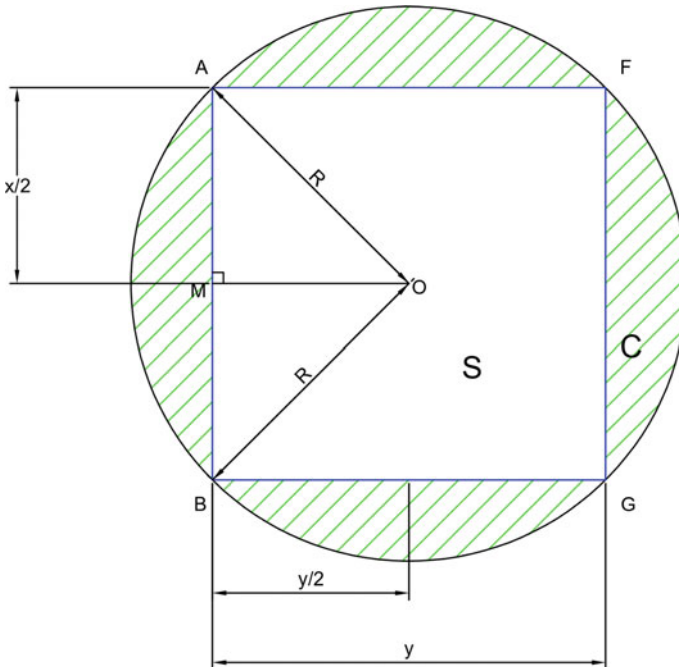


Fig. 3 Cross-section of the Hollow cuboidal cavity geometry. The shaded area A is the propellant mass with cuboidal cavity in center

On differentiating with respect to x ,

$$\frac{dA}{dx} = A' = \left(\frac{\pi x}{2}\right) + 0 - y \quad (34)$$

$$\frac{\pi x}{2} - y = 0 \quad (35)$$

$$y = \frac{\pi x}{2} \quad (36)$$

This equation gives the dimensions of rectangle ABFG such that the area A of cross-section (Fig. 3) of new geometry will be minimum.

On differentiating A' with respect to x ,

$$A'' = \frac{d\left(\frac{\pi x}{2} - y\right)}{dx} \quad (37)$$

$$A'' = \frac{\pi}{2} \text{(positive)} \quad (38)$$

This value is positive; therefore, the cross-section area A of new geometry is minimum.

This implies that the internal surface area of the hollow cuboidal space would be maximum, or in other words, the internal surface area in this case would be greater than that of a simple hollow cylindrical solid propellant grain of same volume.

Now for the purpose of comparison, take a simple hollow cylindrical propellant grain of these dimensions:

$$R = 50 \text{ mm} \quad (39)$$

$$r = 35.3553906 \text{ mm (approximately)} \quad (40)$$

$$l = 400 \text{ mm} \quad (41)$$

Such that the volume of hollow cylindrical propellant grain is the same as new cuboidal hollow propellant grain.

And now computing the cuboidal hollow propellant grain's dimensions,

Volume hol. cylinder = Volume hol. cuboidal propellant grain

$$1570791.747 = (400)(A) \quad (42)$$

Approximate value from 3D model in ANSYS

$$A = 3926.979368 \text{ mm}^2 \quad (43)$$

$$A = \frac{\pi x^2}{4} + \frac{\pi y^2}{4} - xy \quad (44)$$

$$y = \frac{\pi x}{2} \quad (45)$$

$$A = \frac{\pi x^2}{4} + \frac{\pi^3 x^2}{4^2} - \frac{\pi x^2}{2} \quad (46)$$

$$3926.979368 = (x^2) \left(\frac{\pi}{4} + \frac{\pi^3}{16} - \frac{\pi}{2} \right) \quad (47)$$

$$x^2 = \frac{3926.979368}{1.152494129} \quad (48)$$

$$x^2 = 3407.374726 \quad (49)$$

$$x = 58.37272245 - 15 \quad (50)$$

Adjusted for propellant grain dimensions

$$x = 43.37272245 \text{ mm} \quad (51)$$

$$y = \frac{\pi x}{2} \quad (52)$$

$$y = 91.69165801 - 15 \quad (53)$$

Factor of 15 is subtracted to account for design constraints of test propellant model for x and y dimensions.

$$y = 76.69165801 \text{ mm} \quad (54)$$

These dimensions are later used for creating geometries for the purpose of comparison of new propellant geometries with the conventional ones.

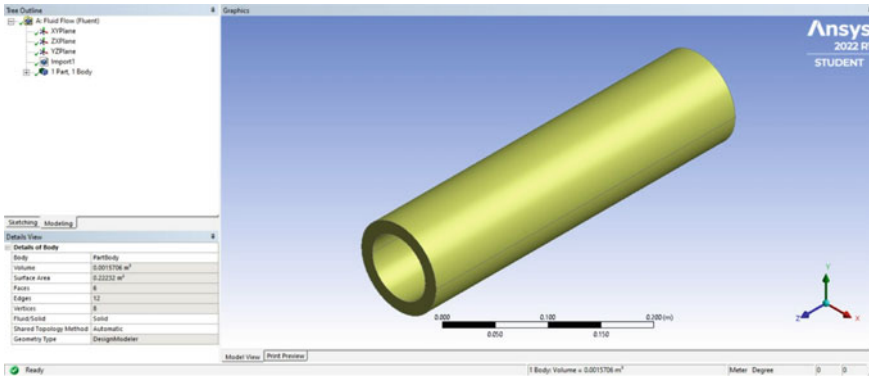


Fig. 4 Hollow cylinder of volume 0.0015706 m³ and surface area 0.22 m²

4 Results and Discussion

4.1 Analysis Results of Hollow Spherical Chain Geometry

After FEA analysis of the first unconventional propellant grain design and comparison with a simple hollow cylinder geometry of the same surface area, the unconventional geometry has a significantly larger volume as shown in Figs. 4 and 5. If these geometrical dimensions are used, more propellant can be stored in the same combustion chamber. Another finding is that there is an initial spike in combustion chamber pressure, but after that period the pressure vs time curve in Fig. 6 reflects the behavior of a regressive combustion type propellant grain. Wind flow simulation is in Fig. 7.

$$\% \text{ increase vol} = \left[\left(\frac{0.001922 - 0.0015706}{0.0015706} \right) * 100 \right] \tag{55}$$

$$\% \text{ increase in volume} = 22.3736\% \tag{56}$$

4.2 Analysis Results of Hollow Cuboid Propellant Grain Geometry

Compared to a simple hollow cylinder geometry of the same volume, this unconventional propellant geometry has a greater internal surface area as shown in Figs. 8 and 9. This exposes more propellant surface in the combustion chamber, which implies greater combustion. This geometry’s pressure–time plot shown in Fig. 10 is an intriguing FEA result. The curve indicates two peaks in pressure during flow. One,

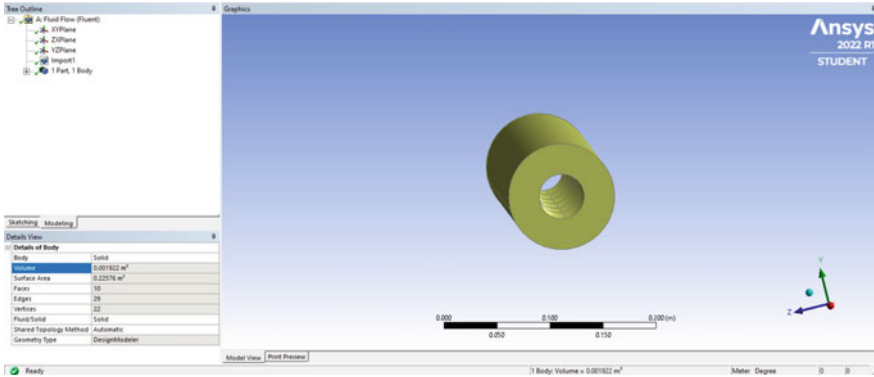


Fig. 5 Hollow spherical chain propellant geometry of volume 0.001922 m³ and surface area 0.22 m²

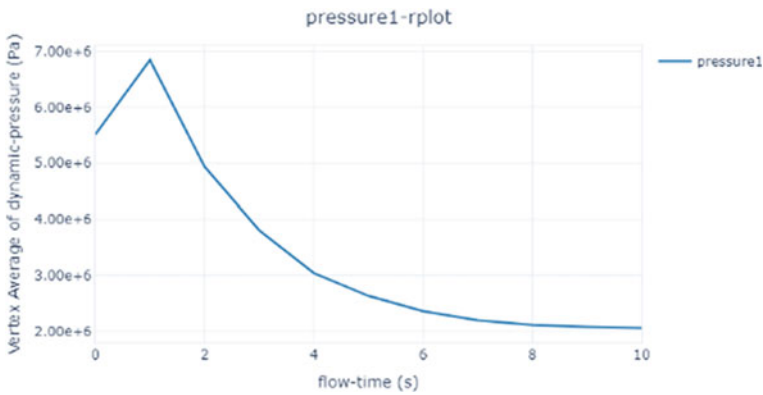


Fig. 6 P–t curve of hollow spherical chain geometry

initially, and the second peak occurs afterward. The pressure–time curve will deviate slightly as there is a notable increase in surface area as per calculations, compared to standard hollow cylindrical propellant geometry [9]. It is not conclusive whether or not it is a progressive or a regressive burning type geometry, but it is determined that it is a multi-step thrust burning type of propellant geometry. Visualization of wind flow is in Fig. 11.

$$\% \text{ increase surface} = \left[\left(\frac{0.0961 - 0.088833}{0.088833} \right) * 100 \right] \tag{57}$$

$$\% \text{ increase in internal surface area} = 8.1805\% \tag{58}$$

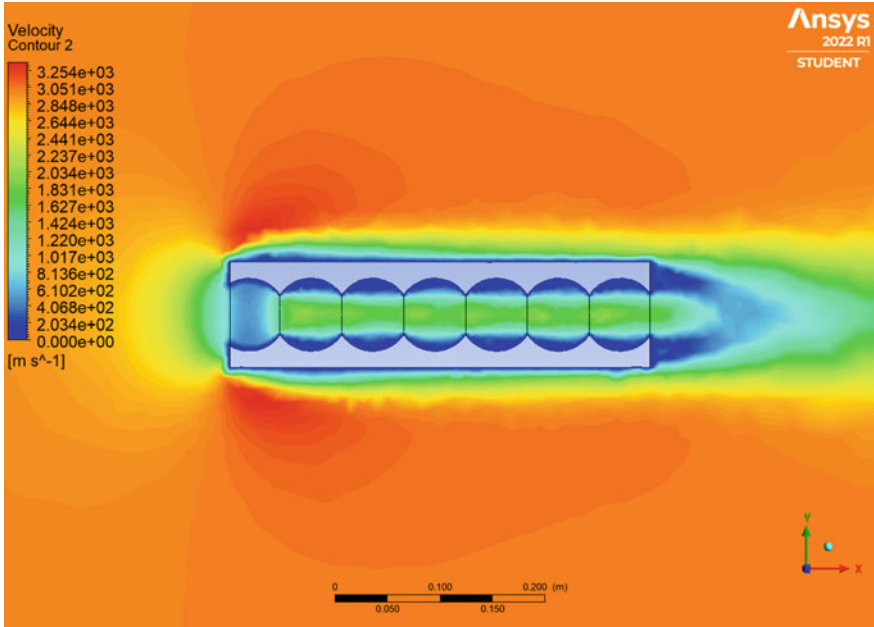


Fig. 7 Wind flow simulation of propellant geometry 1

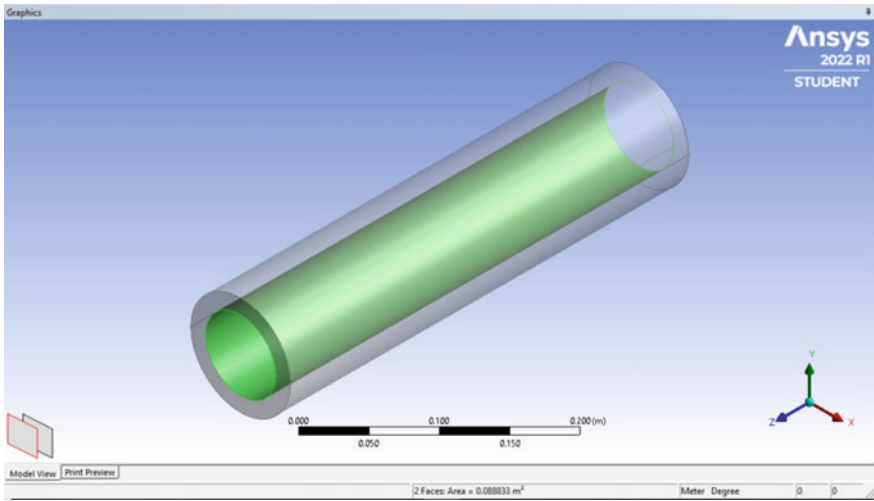


Fig. 8 Hollow cylinder geometry of internal surface area 0.088833 m^2

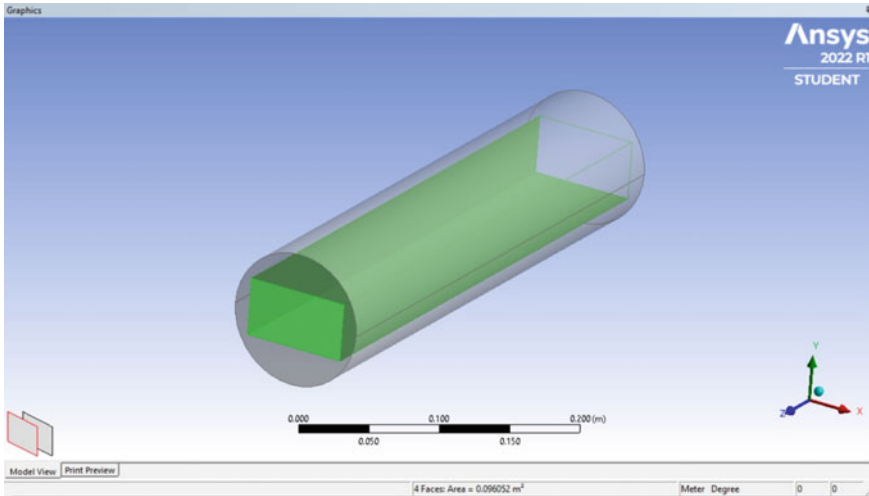


Fig. 9 Hollow cuboidal propellant geometry of internal surface area 0.0961 m²

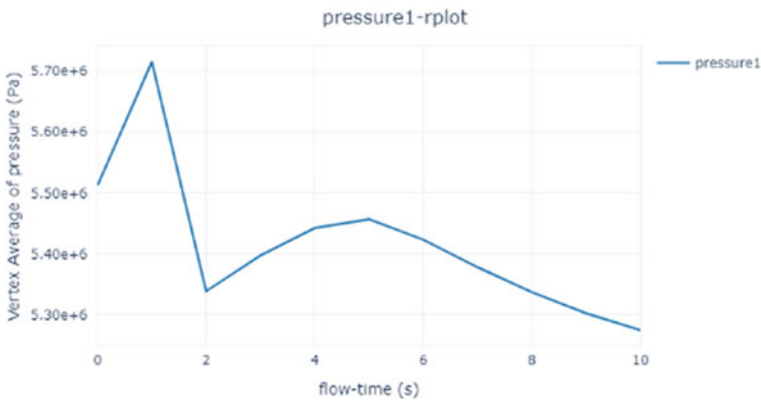


Fig. 10 P–t curve of hollow cuboidal geometry

5 Conclusions

There are various propellant geometries that are used in solid rocket motors for propulsion. The solid propellant grain geometries designed in this paper have yielded better results as they are optimized geometries. The various findings in this research are as follows:

- (1) The optimized hollow spherical chain geometry can accommodate up to 23.37% more propellant material in the combustion chamber as compared to the conventional propellant geometry design of the same surface area.

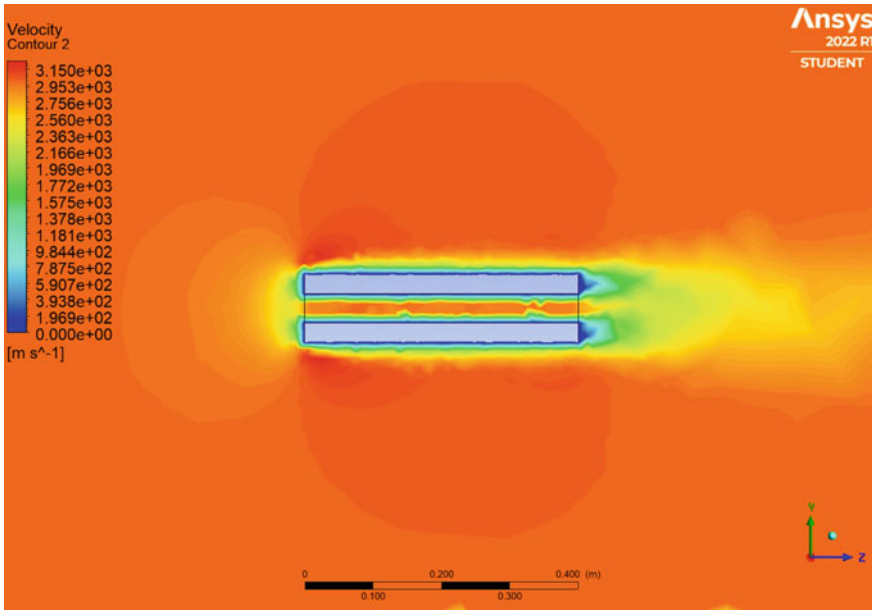


Fig. 11 Wind flow simulation of propellant geometry 2

- (2) The hollow spherical geometry has been identified as a regressive combustion type solid propellant grain geometry.
- (3) And in the case of the cuboidal hollow geometry the internal surface has increased by 8.18% compared to a simple hollow cylindrical geometry of the same volume.
- (4) This means that, as there is more surface area available, there will be greater combustion of the propellant inside the combustion chamber.
- (5) Another result of this optimization means that the volume of the cuboidal hollow propellant geometry will be less compared to a conventional propellant geometry of the same surface area.
- (6) Therefore, propellant geometries with this design will be having greater surface area for better combustion and as complementary will also be lightweight in the propulsion payload systems.
- (7) The cuboidal hollow geometry is found to be an inconclusive, yet multi-step thrust combustion type of geometry as it shows two pressure peaks with the passage of time.
- (8) The wind flow is better in the case of hollow cuboidal propellant geometry seen in Fig. 11. Whereas in hollow spherical chain propellant geometry (Fig. 7), the air flow is more restricted than the hollow cuboidal model.

Acknowledgements This work acknowledges technical support from MARS Exploration Pvt Ltd for software training.

Nomenclature

Model 1	Hollow spherical chain geometry
V	Volume of new solid [m ³]
R	Radius of cylinder [m]
l	Length of the cylinder [m]
r	Radius of the spherical cavity [m]
N	Number of spherical cavities
$\frac{dV}{dr}$ or V'	Rate of change of volume with respect to radius OR derivative of volume with respect to radius
$\frac{d^2V}{dr^2}$ or V''	Rate of change of rate of change of volume with respect to radius OR second derivative of volume with respect to radius
$V''_{r=\frac{R}{2}}$	Value of second derivative at condition radius of spherical cavity is same as half the radius of cylinder
A	Surface area of hollow spherical chain propellant geometry
Model-2	Hollow cuboidal cavity geometry
S	Area of rectangle ABFG [m ²]
C	Area of circle [m ²]
A	Difference between the areas of circle and rectangle ABFG [m ²]
x	Side 1 of rectangle ABFG [m]
y	Side 2 of rectangle ABFG [m]
R	Radius of cylinder r[m]
$\frac{dA}{dx}$ or A'	Rate of change of area with respect to side 1 rectangle ABFG OR derivative of area with respect to x
$\frac{d^2A}{dx^2}$ or A''	Rate of rate of change of area with respect to side 1 rectangle ABFG OR second derivative of area with respect to x

References

1. Pandey KM, Bose P (2013) Mathematical modelling of solid propellant grain geometry suitable for multi barrel rocket launcher applications. *J Environ Res Develop* 7(4):1407–1412
2. Rossi C, Orioux S, Larangot B, Conto TD, Estève D (2002) Design, fabrication and modeling of solid propellant microrocket-application to micropropulsion, Elsevier. *J Sen Act A: Physic* 99(1–2):125–133
3. Makled A (2015) Experimental and design considerations for solid propellant gas generator. In: International conference on aerospace sciences and aviation technology ASAT vol 16, pp 1–13
4. Mahjub A, Azam Q, Abdullah MZ, Mazlan NM (2019) Design optimization of solid rocket propulsion: a survey of recent advancements. *J Spacecr Rocket* 57(1):3–11
5. Douglas HW, Collins JH, Brooks WT, Keller RB, Chan GO, Chase CA, Speak CA (1972) Solid propellant grain design and internal ballistics. NASA Space Veh Design Criteria (Chemical Propulsion), NASA SP-8076
6. Summerfield M, Gaveny LH, Ohlemiller TJ, Kubota N, Battista RN (1973) Solid propellant combustion mechanism research. Princeton university unclassified department of aerospace & mechanical science SZB. Group, Annual rept. 1 Nov 1972–30, 01 August 1973

7. Shekhar H (2009) Design of funnel port tubular propellant grain for neutral burning profile in rockets. *Def Sci J* 59(5):494–498
8. Dombé G, Jain M, Singh PP, Radhakrishnan KK, Bhattacharya B (2008) Pressure casting of composite propellant. *NIScPR Online Periodic Reposit* 15:420–423
9. Kallmeyer T, Sayer L (2012) Differences between actual and predicted pressure-time histories of solid rocket motors. In: *Joint propulsion conferences, AIAA*, vol 18

Role of Piezoelectric Coupling Factor on FIV-Based Energy Harvesting of a Piezoelectric Flag



Rajanya Chatterjee, Chhote Lal Shah, Sayan Gupta, and Sunetra Sarkar

1 Introduction

Piezoelectric materials possess the unique ability to convert strain energy to electrical energy and vice-versa. Therefore, they are being extensively used as vibration energy harvesters [1], as sensors [2], or as actuators now a days. These materials are often layered on beam substrates to form a composite structure, which can generate voltage when the beam is deformed by various types of external disturbances like base actuation [3], moving loads [4], etc. The performance of such models is enhanced by various strategies, such as, by introducing a proof mass [5], or coupled bending and torsion [6], etc. However, all these models require an external actuation and hence can harvest energy only at expense of some input energy. But, when the external actuation is modelled by the fluid loads, emerging from downstream of bluff bodies, or waves, or from self-sustained flow-induced vibration (FIV), which is abundantly available in nature, the harvester models become capable of extracting energy without any artificial actuation.

In recent times, a lot of attention have been drawn towards the FIV-based energy harvesting [7–9] using different configurations of flexible structures, layered with piezo materials. Akcabay and Young [8] studied a cantilever beam in viscous flow and identified parametric regimes of the flexible beam, where the self-sustained oscillations are observed, and energy harvesting is beneficial. Shoele and Mittal [10] studied an inverted cantilever configuration and found that there exists a critical

R. Chatterjee (✉) · S. Gupta

Department of Applied Mechanics and Biomedical Engineering, IIT Madras, Chennai 600036, India

e-mail: rajanya02@gmail.com

C. L. Shah · S. Sarkar

Department of Aerospace Engineering, IIT Madras, Chennai 600036, India

S. Gupta · S. Sarkar

Complex Systems and Dynamics Group, IIT Madras, Chennai 600036, India

angle of inclination above which the performance gets affected. Akaydin et al. [7, 11] experimentally tested a bluff body with a downstream inverted cantilever plate configuration to enhance energy harvesting efficiency. In recent studies in our group [12], a cylinder-flapper model was used for energy harvesting from wind tunnel experiments, and the intermediate gap, Strouhal number, and length of the beam were seen to play a crucial role in the performance.

In most of the aforementioned literature [7, 8], the numerical investigations are often limited to studying the coupled dynamics of the fluid–structure interactions (FSI) problem to identify the higher oscillation regimes, where they often employ a two-way coupled solver to study the variation in the efficiency. However, there have been very few studies [10] focused on simulating the models with a fully coupled fluid–structure–energy equations solver. Hence, the effect of the piezoelectric coupling on dynamical transitions has not attracted the attention much in the literature. To the best of the authors' knowledge, no study has been done for varying piezoelectric coupling factor to identify the variation in the harvesting regime. In context of vibration energy harvesters, the effect of the piezoelectric properties on the harvesting performance, owing to the choice of piezoelectric materials, *e.g.* lead zirconate titanate (PZT) fibres, polyvinylidene fluoride (PVDF)s, etc., is widely tested in the energy harvesting community [13]. On the other hand, in the FIV-based energy harvesting literature, such study is scarce. Although the choice of piezoelectric materials comes with ensuing challenges of choosing a number of material properties, coupling factor is considered as one of the main influencing factors towards determining the scale of harvested energy as well as feedback forcing to the structure.

The present study focuses on examining the crucial role played by the coupling factor in affecting the vibration dynamics for a range of inertia and stiffness values. To this end, a flexible flag of length $L = 1.0$, layered with piezoelectric material on both sides, is kept in an incoming viscous flow at $Re = 200$. The primary objectives of this study are: (i) to identify the parametric regime where the energy harvesting is conducive and (ii) to see the effect of piezoelectric coupling on dynamical transitions in the system and corresponding flow field behaviour. The beam exhibits three different types of dynamics; a damped oscillation, a self-sustained oscillation, and a very high oscillation state leading to failure or damage of the material. At low flexibility and inertial range, a higher coupling factor is seen to take the system to self-sustained oscillation state from a damped oscillation state. On the other hand, in presence of the piezoelectric coupling, the system is also seen to transition from a periodic response to an aperiodic state for $\beta \geq 5$. It is important to mention that for a broader range of parametric values, the coupling factor does not have any considerable effect on the oscillation of the beam.

The rest of the paper is arranged as follows: Sect 2 discusses the solver details and methodology. The validation of the three-way coupled fluid–structure–energy solver is given in Sect 2-A. Section 3 presents the detailed analyses of the result, and finally the conclusions from the present study are derived in Sect 4.

2 Methodology

An inextensible two-dimensional (2-D) flexible flag of length $L = 1.0$ layered with PZT-5A on both sides (bimorph configuration) is considered in the present study. The leading-edge of the flag is fixed, and the rest of the body is free to oscillate in the fluid. The non-dimensional governing equation of motion for the flexible flag is given by [8].

$$\beta \frac{\partial^2 \mathbf{X}}{\partial t^2} = \frac{\partial}{\partial s} \left(T_s \frac{\partial \mathbf{X}}{\partial s} \right) - \frac{\partial^2}{\partial s^2} \left(\gamma \frac{\partial^2 \mathbf{X}}{\partial s^2} \right) + \nu V \frac{d}{ds} [\delta s - \delta(s - L)] + \mathbf{F}, \quad (1)$$

$$\frac{\partial \mathbf{X}}{\partial s} \cdot \frac{\partial \mathbf{X}}{\partial s} = 1, \quad (2)$$

where $\mathbf{X} = (X(s, t), Y(s, t))$ is the instantaneous position of the flag, s is the arc length, δ is a Dirac-Delta function, $\beta = \rho_s q / \rho_f L_s$ is the mass ratio, and $(\rho_s, \rho_f, q$ and $L_s)$ are the structural density, fluid density, thickness, and reference length of the flag, respectively). $\rho_f U_\infty^2 L_s$ is used to non-dimensionalize tension coefficient (T_s), $\rho_f U_\infty^2 L_s^3$ is used to non-dimensionalize bending stiffness (γ), t is the non-dimensional time, V is the voltage output non-dimensionalized by $L_s U_\infty (\rho_f / \epsilon)^{\frac{1}{2}}$, ν is the piezoelectric coupling term non-dimensionalized by $L_s U_\infty (\rho_f \epsilon)^{\frac{1}{2}}$, and \mathbf{F} is the Lagrangian forcing acting on the solid body non-dimensionalized by $\rho_f U_\infty^2$. The inextensibility condition is satisfied by Eq. 2. The non-dimensional energy equation for bimorph is given by

$$\frac{1}{2} \frac{\partial V}{\partial t} + \frac{q q_p}{R_b} V(t) = - \int_0^1 \nu \frac{(q q_p (1 - q_p))}{2} \frac{\partial^3 \mathbf{X}}{\partial t \partial s^2} ds, \quad (3)$$

where q_p is ratio of the thickness of one piezoelectric layer with the total thickness of the beam (piezo + substrate), and R_b is the non-dimensional resistance of the piezoelectric circuit. The structural equation (Eq. 1) and the energy equation (Eq. 3) have been discretized using finite difference method (FDM) following Huang et al. [14].

The viscous flow around the flexible flag is governed by the unsteady Navier-Stokes (N-S) equations. In the discrete forcing IBM framework, the momentum conservation and continuity equations in non-dimensional form can be written as

$$\frac{\partial \mathbf{u}}{\partial t} + \nabla \cdot (\mathbf{u}\mathbf{u}) = -\nabla p + \frac{1}{Re} \nabla^2 \mathbf{u} + \mathbf{f} \quad (4)$$

$$\nabla \cdot \mathbf{u} - q_s = 0. \quad (5)$$

where \mathbf{u} is the flow velocity vector non-dimensionalized by U_∞ , $Re = \rho_f U_\infty L_s / \mu$ is the Reynolds number (μ being the dynamic viscosity), and pressure p is non-dimensionalized by $\rho_f U_\infty^2$. The momentum forcing term \mathbf{f} is added throughout the solid domain to ensure no-slip and no-penetration boundary conditions are satisfied at the solid boundary, and mass conservation is satisfied by adding a mass source/sink term (q_s) to the continuity equation [15]. The fluid, structure, and energy equations are coupled in a staggered manner where they exchange their information at every time-step. Further, red–black successive over-relaxation (RB-SOR) method is applied to divide the fluid domain into two sets of nodes, independent of their previous iteration and are alternatively demarcated with the labels ‘red’ and ‘black’. This allows us to use OpenMP pragma directives to parallelize the computationally extensive part of the solver to enhance the simulation speed. Details can be found in Shah et al. [16].

2.1 Validation

The computational domain is considered sufficiently large so that the boundary effects on the solid body are rudimentary. The schematic representation of computational domain with boundary conditions and the non-uniform Cartesian mesh grid are presented in Fig. 1a and b, respectively. The minimum grid size ($\Delta x = \Delta y = 0.005$) and time-step ($\Delta t = 0.0002$) are chosen after performing mesh and time convergence, respectively, which are not presented here for the sake of brevity.

The detailed qualitative and quantitative validations of only flow solver and the two-way coupled FSI solver are presented in our recent studies [15, 17, 18], and therefore, it is not repeated here. Instead, the three-way coupled solver has been validated by simulating the piezoelectric flapper with the surrounding free-stream at $Re = 210$. The other parameters considered for the simulations are $\gamma = 1/36$, $\beta = 10$, and $\nu = 5.3$. The symbols follow the same definitions as given in [8]. The

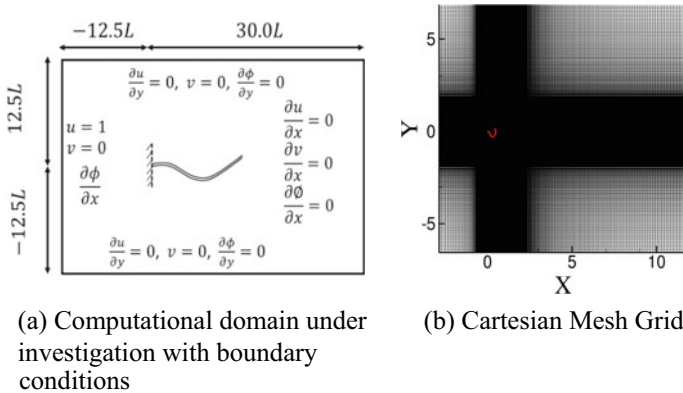
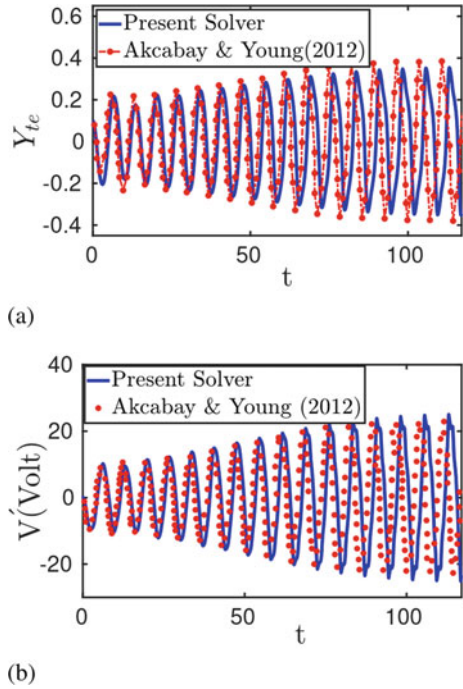


Fig. 1 Computational domain and mesh for current model

Fig. 2 Validation of the present solver in terms of **a** tip of trailing-edge (Y_{te}) displacement and **b** voltage (V') time histories with that of Akcabay and Young [8]



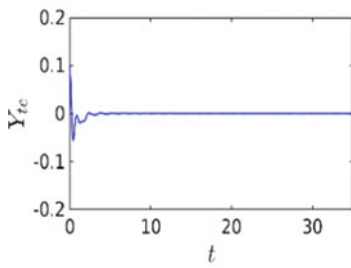
tip of trailing-edge (Y_{te}) displacement and voltage (V') time histories from current simulations are compared with the result obtained from Akcabay and Young [8] in Fig. 2a, b, respectively. The close match between the results proves the efficacy of the present three-way coupled solver.

3 Results and Discussion

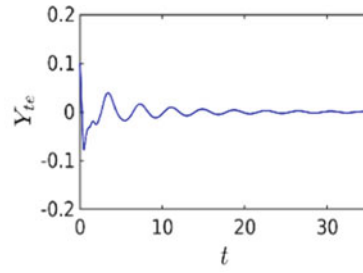
The flexible flag is subjected to an incoming uniform flow at $Re = 200$. The structure is initially placed in 2nd mode of deformation such that the tip deflection is 1% of its length. A series circuit connection of piezoelectric is considered with a non-dimensional resistance of $R_b = 3 \times 10^{-3}$. Simulations have been performed for a wide range of β and γ parameters to see the effect of piezoelectric coupling on the oscillation states of the system where energy harvesting can be conducive.

It is observed that for a very low β and high γ values, the system damps down to zero oscillation with/without piezoelectric coupling due to viscous damping being dominant. However, for a certain range of β and γ values, the presence of piezoelectric coupling takes the system to a self-sustained oscillation state; otherwise, it damps down to zero oscillations. For example, at $\gamma = 10^{-3}$ & $\beta = 0.05$, the system response in terms of the displacement of tip of the trailing-edge (Y_{te}) is seen to die down to zero

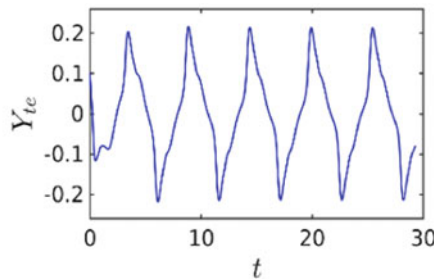
oscillation without piezoelectric coupling factor ($\nu = 0$); see Fig. 3a. As a voltage feedback was introduced with $\nu = 5.3$, Y_{te} is seen to undergo a prolonged transient state before settling to zero oscillations; see Fig. 3b. Interestingly, when the coupling factor is further increased to $\nu = 10$, the system attained self-sustained oscillations as shown in Fig. 3c. The corresponding voltage output for $\nu = 10$ is presented in Fig. 4, and it is seen to follow the periodic dynamics as that of Y_{te} .



(a) For $\gamma = 10^{-3}, \beta = 0.05,$
 $\nu = 0.$



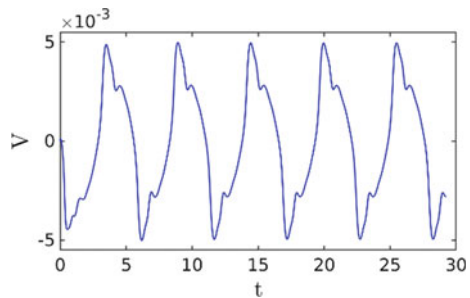
(b) For $\gamma = 10^{-3}, \beta = 0.05,$
 $\nu = 5.3.$



(c) For $\gamma = 10^{-3}, \beta = 0.05, \nu = 10.$

Fig. 3 Tip displacement (Y_{te}) of the flexible flag of identical structural properties, at varying coupling coefficient values (ν)

Fig. 4 Voltage time history for $\gamma = 10^{-3}, \beta = 0.05, \nu = 10$



Next, we have considered the parametric regime where the flag attains self-sustained oscillations due to FSI coupling to understand effect of ν on dynamical transitions in the system. The periodic oscillations for $\gamma = 10^{-2}, \beta = 5$ without piezoelectric coupling ($\nu = 0$) transitions into an aperiodic state as the FSI system is coupled with the energy equations, with $\nu = 5.3$. The unmodulated Y_{te} time history in Fig. 5a is the signature of periodic dynamics, and the corresponding deformation envelope is seen to have a clear second mode shape; see Fig. 5b. On the other hand, for a coupling factor of $\nu = 5.3$, the modulated Y_{te} time history in Fig. 5c is the signature of aperiodic dynamics, and the corresponding deformation envelope show an irregular structural bending behaviour (Fig. 5d).

The flow fields for the above two cases are also examined to see the effect on the vortex structures due to the change in the dynamics. A well-organized flow field with a ‘2P’ vortex street (marked by rectangular boxes in 6a) where two pairs of vortices shed in a single flapping cycle is observed for the periodic case without the piezoelectric coupling. As the beam response becomes aperiodic, and the deformation envelope traverses among multiple mode shapes, as a result ‘2P’ vortex street is seen to get distorted to become an aperiodic vortex street in the far field; see Fig. 6b. The periodic dynamics are normally considered as the suitable regime for energy harvesting from piezoelectric flag as the material may easily incur damages in the aperiodic regime. Therefore, the present study highlights the important parametric regime conducive for energy harvesting-based flow-induced vibration.

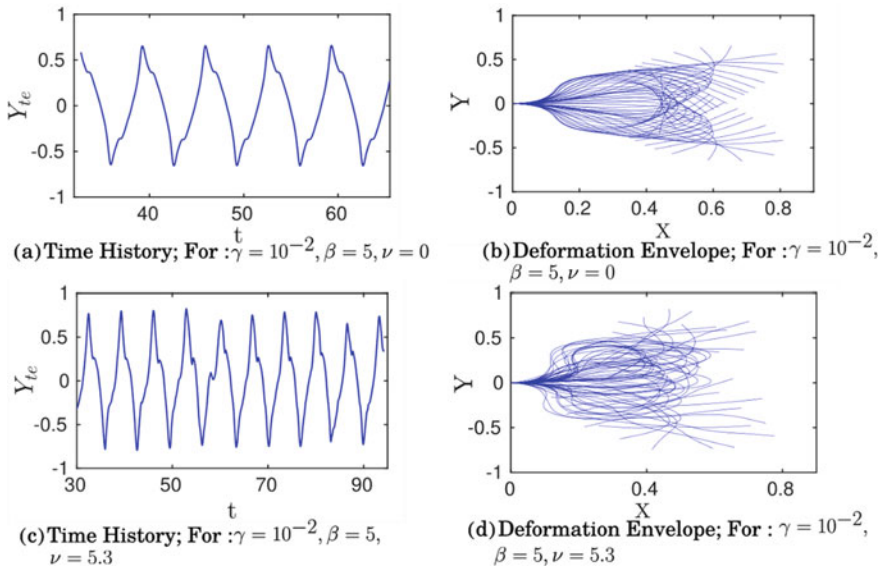


Fig. 5 Tip time histories with corresponding deformation envelopes of the flag without and with piezoelectric coupling

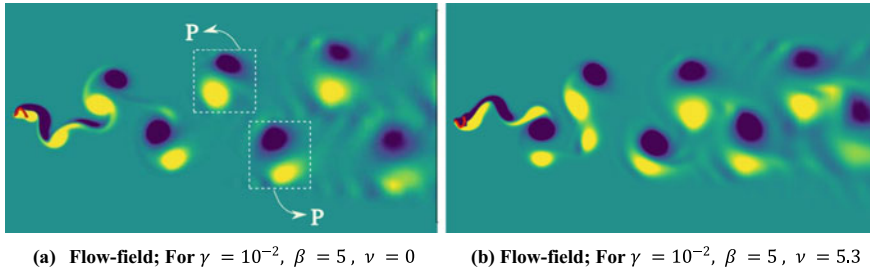


Fig. 6 Effect on the flow fields due to dynamical changes in structural response

4 Conclusions

The effect of piezoelectric coupling on the dynamical transitions of the three-way coupled fluid–structure–energy system has been investigated in the present study. It is observed that the damped oscillations state transitions into self-sustained oscillations with the introduction of piezoelectric coupling for a certain range of flexibility and inertia. On the contrary, the FSI system exhibiting self-sustained oscillations, transitions into an aperiodic state in the presence of piezoelectric coupling through fluid–structure–energy feedback. The corresponding flow fields in these regimes also show similar dynamical transitions where the periodic ‘2P’ vortex street gets distorted through near-field interactions giving rise to an aperiodic flow field. Therefore, a proper selection of piezoelectric coupling coefficient is essential to enhance the voltage extraction, improve efficiency, and avoid scenarios where the system goes into an aperiodic state. The irregular and large deformations in the flag during the aperiodic regime severely affect the health of piezoelectric material and may lead to damage and failure. Moreover, irregular voltage output during aperiodic regime might not be useful for the practical purposes. Hence, this study is of importance to identify the suitable parametric regime in terms of mass ratio, piezoelectric coupling, and bending rigidity in which energy can be harvested efficiently.

Acknowledgements Authors would like to acknowledge the partial funding received from the Science and Engineering Board, Department of Science and Technology, Govt of India for project no. EMR/2016/007500 and from Ministry of Education, Govt of India towards Institute of Eminence, project no. SP2021077/DRMHRD/DIRIIT and the high performance computing facility (HPCE) of IIT Madras.

Nomenclature

- γ Non-dimensional stiffness
- β Non-dimensional inertia
- L Non-dimensional length of flag

- q Total non-dimensional thickness of the piezoelectric flag
 Re Reynolds number
 q_p Ratio of thickness of one piezoelectric layer to the total thickness of the composite
 ν Piezoelectric coupling coefficient
 R_b Non-dimensional resistance

References

1. Erturk A, Inman DJ (2008) A distributed parameter electromechanical model for cantilevered piezoelectric energy harvesters. *J Vibrat Acoust* 130(4)
2. Tressler JF, Alkoy S, Newnham RE (1998) Piezoelectric sensors and sensor materials. *J Electroceram* 2(4):257–272
3. Erturk A, Inman DJ (2009) An experimentally validated bimorph cantilever model for piezoelectric energy harvesting from base excitations. *Smart Mater Struct* 18(2):025009
4. Amini Y, Heshmati M, Fatehi P, Habibi SE (2017) Piezoelectric energy harvesting from vibrations of a beam subjected to multimoving loads. *Appl Math Model* 49:1–16
5. Chun-Liang K, Shun-Chiu L, Wen-Jong W (2016) Fabrication and performance evaluation of a metal-based bimorph piezoelectric mems generator for vibration energy harvesting. *Smart Mater Struct* 25(10):105016
6. Abdelkefi A, Najaf F, Nayfeh AH, Ayed SB (2011) An energy harvester using piezoelectric cantilever beams undergoing coupled bending–torsion vibrations. *Smart Mater Struct* 20(11):115007
7. Akaydin HD, Elvin N, Andreopoulos Y (2010) Wake of a cylinder: a paradigm for energy harvesting with piezoelectric materials. *Exp Fluids* 49(1):291–304
8. Akcabay DT, Young YL (2012) Hydroelastic response and energy harvesting potential of flexible piezoelectric beams in viscous flow. *Phys Fluids* 24(5):054106
9. Michelin S, Doare O (2013) Energy harvesting efficiency of piezoelectric flags in axial flows. *J Fluid Mech* 714:489–504
10. Shoele K, Mittal R (2016) Energy harvesting by flow-induced flutter in a simple model of an inverted piezoelectric flag. *J Fluid Mech* 790:582–606
11. Akaydin HD, Elvin N, Andreopoulos Y (2010) Energy harvesting from highly unsteady fluid flows using piezoelectric materials. *J Intell Mater Syst Struct* 21(13):1263–1278
12. Krishna Kumar S, Bose C, Ali SF, Sarkar S, Gupta S (2017) Investigations on a vortex induced vibration based energy harvester. *Appl Phys Lett* 111(24):243903
13. Anton SR, Sodano HA (2007) A review of power harvesting using piezoelectric materials (2003–2006). *Smart Mater Struct* 16(3):R1
14. Wei-Xi H, Shin SJ, Sung HJ (2007) Simulation of flexible filaments in a uniform flow by the immersed boundary method. *J Computat Phys* 226(2):2206–2228
15. Majumdar D, Bose C, Sarkar S (2020) Capturing the dynamical transitions in the flow-field of a flapping foil using immersed boundary method. *J Fluids Struct* 95:102999
16. Shah CL, Majumdar D, Sarkar S (2019) Performance enhancement of an immersed boundary method based fsi solver using openmp. In: 21st annual CFD symposium. NAL, Bangalore, India
17. Shah CL, Majumdar D, Bose C, Sarkar S (2022) Chordwise flexible aft-tail suppresses jet-switching by reinstating wake periodicity in a flapping foil. *J Fluid Mech* 946
18. Shah CL, Majumdar D, Sarkar S (2020) Delaying the chaotic onset in the flow-field of flapping foil with flexible Aft Tail. In: ASME international mechanical engineering congress and exposition, vol 7A: dynamics, vibration, and control, 11 2020, V07AT07A027

Flow Features of Propeller Wakes Impinging on a Circular Disk Through Unsteady Simulations



Bhavin Patel and Rajesh Ranjan

1 Introduction

The influence of propeller slipstream on a downstream body is of relevance to several aeronautical and marine applications. In aeronautics, propeller–wing interactions are seen in turboprop aircraft in both pusher and tractor configurations [3]. In naval hydrodynamics, propeller wakes interact with the rudder, which is used for maneuvering purposes [7]. The physical mechanisms that characterize these interactions are very complex. These propeller wakes are highly vortical and have multiple coherent structures. Simulations of these propeller wakes are computationally challenging. In the literature, attempts are made to study these interactions through numerical simulations of both idealized and practical configurations. Some examples include propeller–wing interactions [3], rudder–propeller interactions [7, 12], propeller–hydrofoil interactions [8], propeller–hull interactions [6].

In this work, we numerically study the vortex–body interaction by setting up a simplified configuration of a marine propeller wake impinging normal to a thin circular disk (aspect ratio, $\xi = d/t = 10$, where d is the diameter, and t is the thickness) using Unsteady Reynolds Averaged Navier–Stokes (URANS) approach. There have been numerous studies on isolated propellers [5, 11] as well as isolated disks [10, 13]—an interaction between these two wakes brings interesting aspects of fluid dynamics, which is the scope of this work. The wake created by a circular disk is typical of three-dimensional bluff body wakes and provides insights into shear-layer separation, bifurcation dynamics, and transition-to-turbulence. This wake behaviour gets modified due to incoming propeller vortices and depends on the blade passing frequency or the rotational speed of the propeller.

For description and future reference, we show the numerical set-up in Fig. 1. The diameter of the circular disk, d , is comparable to the propeller diameter, D_p .

B. Patel (✉) · R. Ranjan

Department of Aerospace Engineering, IIT Kanpur, Kanpur, India

e-mail: bhavinpatel6160@gmail.com

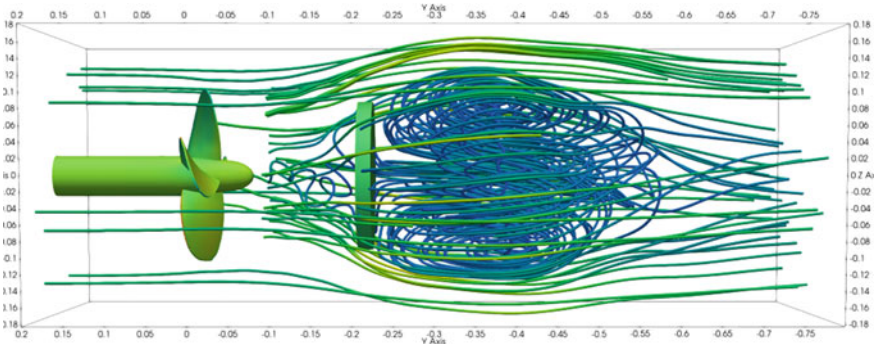


Fig. 1 Set-up of propeller–disk interaction in the current simulation

Further, the disk is kept at a distance of one disk diameter from the propeller. The convoluted streamlines behind the disk are due to the incoming periodic propeller wakes. Although not clear from this figure, the recirculating region in front of the disk also gets significantly modified due to upstream propeller effects.

The paper is arranged as follows. Section 2 discusses the numerical approach along with the details of the propeller. Results, Sect. 3, are presented for three flows: pure disk, only propeller, and propeller–disk. Primary flow features in all three cases are described, and mechanisms for propeller–disk interactions are discussed. Finally, conclusions are given in Sect. 4.

2 Numerical Methodology

The numerical model considers the incompressible Navier–Stokes equations, governing the conservation laws of mass and momentum, with the Boussinesq approximation as follows

$$\frac{\partial u_i}{\partial x_i} = 0 \tag{1}$$

$$\frac{\partial u_i}{\partial t} + \frac{\partial (u_i u_j)}{\partial x_j} = -\frac{1}{\rho_0} \frac{\partial p}{\partial x_i} + \frac{\partial \tau_{ij}}{\partial x_j} + \tau_{Re} \tag{2}$$

where $i = 1, 2, 3$ denotes the spatial coordinates in three directions. The stress tensor τ is based on the fluid’s kinematic viscosity $\nu = 10^{-6} \text{ m}^2/\text{s}$. τ_{Re} is the Reynolds stress tensor which is obtained using turbulence models described below.

2.1 Solver Details

The numerical investigation is carried out in an opensource CFD tool, OpenFOAM-v9 distributed by The OpenFOAM Foundation. pimpleFoam, a transient solver for incompressible, turbulent flow of Newtonian fluids with optional mesh motion and mesh topology alterations, is employed for the simulation. The PIMPLE algorithm, which combines PISO and the SIMPLE algorithms, is used by pimpleFoam. Although the problem may be a transient one, pimpleFoam allows for a steady-state solution at each time step using the SIMPLE (steady-state) approach. The details of schemes used for the current simulations are listed in Table 1.

For modelling turbulence, we employed the $k-\epsilon$ model. This two-equation solves the transport equations for two turbulence quantities—turbulence kinetic energy k and dissipation rate ϵ . Length scale ($L = k^{3/2}/\epsilon$), turbulence viscosity ($\nu_t = k^2/\epsilon$), and a timescale ($\tau = k/\epsilon$) are formed from k and ϵ .

Propeller Modelling: There are several ways to model a propeller including the actuator disk theory, blade element theory, and moving frame of reference approach (MRF). In this work, we employ a more accurate but relatively expensive approach based on Cyclic Arbitrary Mesh Interface (CyclicAMI). In flows with rotating geometries such as propellers, CyclicAMI allows for different meshes for rotating and stationary sections of geometry and connects through patch boundaries.

In the current cyclicAMI approach, a patch near the propeller with 22,416 faces are interpolated in every time step. However, PimpleFoam implementation in OpenFOAM allows for relatively larger time steps [1]. For our simulation, we have used an adjustable time step approach based on the maximum Courant number fixed at 2.

Table 1 Details of fvSchemes

Name	Term	Symbol	Scheme
ddtSchemes	ddt	$\frac{\partial}{\partial t}$	Euler
Grad schemes	grad(p)	∇p	GaussLinear
	grad(U)	∇U	CellLimited GaussLinear
divSchemes	div(phi, U)	$\nabla \cdot (\phi U)$	GaussLinear upwind grad(U)
	div(phi, k)	$\nabla \cdot (\phi k)$	Gauss upwind
	div(phi, epsilon)	$\nabla \cdot (\phi \epsilon)$	Gauss upwind
Laplacian schemes	Laplacian()	∇^2	GaussLinear Limited corrected
Interpolation schemes	–	–	Linear
snGrad schemes	–	–	Limited corrected

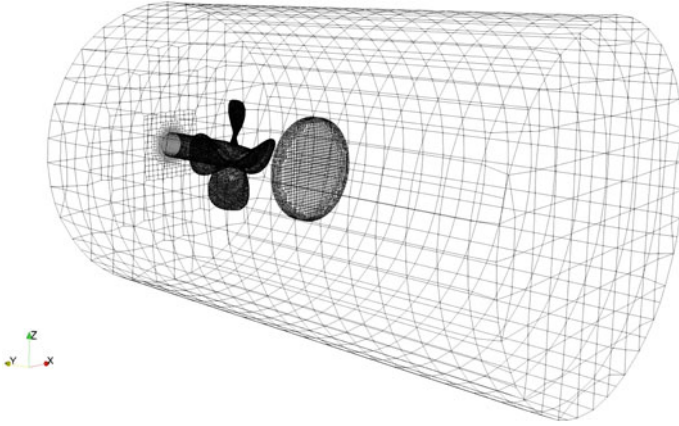


Fig. 2 Propeller–disk flow mesh

2.2 Computational Domain

We employ a cylindrical domain for our computations as shown in Fig. 2. The diameter of this external cylinder is $2.643D_p$, while the axial domain length is $4.4D_p$. The propeller plane is positioned at about $0.88D_p$ from the inflow, leaving about $3.5D_p$ length in the wake for the swirling flow to develop. The cylindrical disk of diameter comparable to the propeller diameter is kept in the swirling region at about one propeller diameter from the propeller. snappyHexMesh approach available in OpenFOAM is used for meshing that ensures dense regions around the propeller. The total mesh size of both propeller only and propeller with disk simulations is about 0.52 million. Numerical convergence is ensured in the case of propeller-only simulation by altering the mesh with mesh size up to 0.95 million.

2.3 Propeller Details

The current study employs INSEAN E779A marine propeller, which has been employed in several experimental and numerical studies [4]. This propeller is a four-bladed, fixed-pitch, right-handed propeller and has a nominally constant pitch distribution and a very low skew angle.

The characteristics of the propeller are listed in Table 2. The rotational speed of the propeller is fixed at 1500 rpm. The advance ratio, $J = U_\infty/nD_p$, is taken as 0.88, which gives the incoming flow velocity of $U_\infty = 5$ m/s.

Table 2 E779A propeller details

Parameter	Value
Propeller dia, D_p	227.27 mm
Number of blades	4
Pitch ratio, P/D_p	1
Hub ratio	0.2
Rotation	Right-handed

3 Results and Discussion

All the simulations performed in this study were run up to dimensional time $t = 1$ s, when steady (for disk only) or quasi-steady (for propeller) states were reached. The average computing time for each run is about 30 h with 10 processors.

3.1 Propeller Flow

First, we describe the results of the propeller-only simulation. Figure 3 shows the propeller wake region at the end of the simulation using the Q -criterion at $Q = 1000$. We note the tip vortices that form a helical shape and stay in the circular region. Hub vortex can also be seen in the middle. The shapes of these vortices are comparable to those observed in experiments [4]. However, the computational domain may not be long enough to capture the instability of vortices as observed in the experiments [4].

Figure 4 shows the development of the flow in the wake region through axial velocity contours. These shapes are comparable to those reported through PIV and LDV measurements [2].

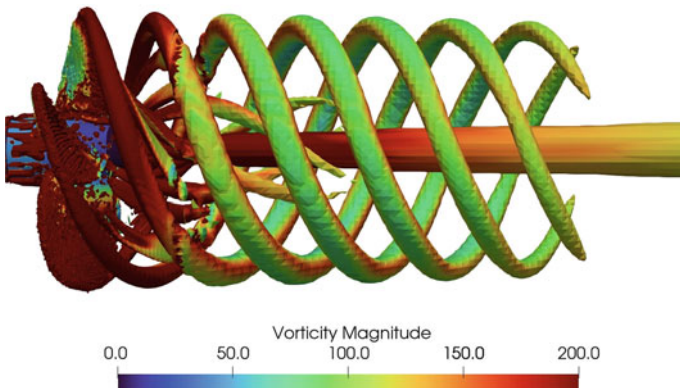


Fig. 3 Hub and tip vortices behind the propeller using the Q -criterion at $Q = 1000$

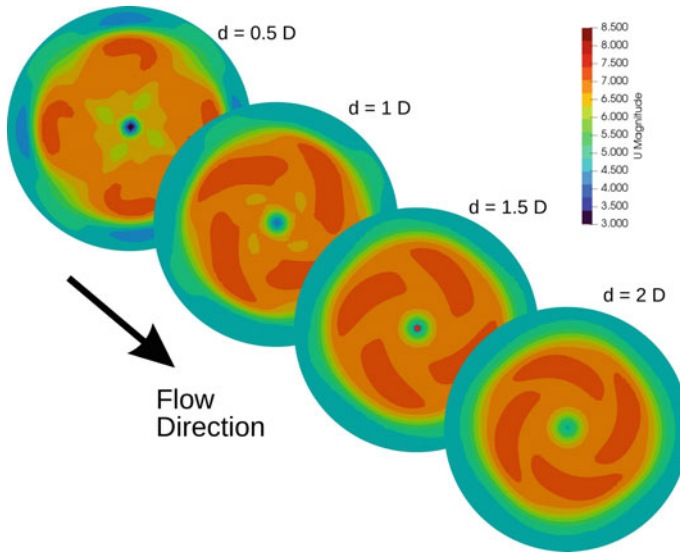


Fig. 4 Propeller wake region shown at different planes using the velocity magnitude

3.2 Disk Flow

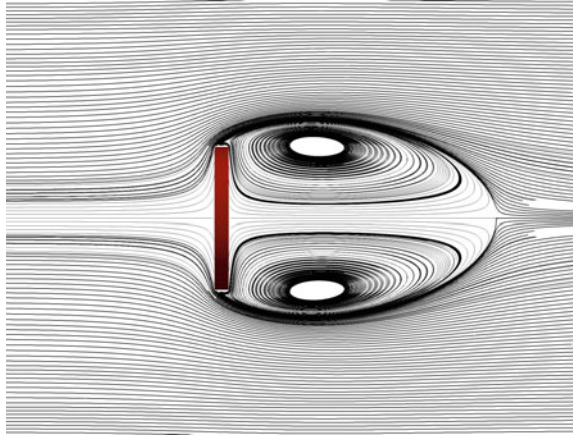
For the disk-only simulation, all the flow parameters remain unaltered except for the absence of the propeller.

This gives the flow Reynolds number (Re) based on the disk diameter as 10^6 . The aspect ratio of the disk, $\xi = 10$, is the same as what has been widely studied in the literature [9]. Figure 5 shows the flow behind the disk. The flow has become steady before the end of simulation time. The streamlines clearly indicate a recirculating region as expected, which shows the steady vortices structure. The width of this region is 0.275 m, and the length is 0.376 m. The vortex centres are placed symmetric to the disk centre and do not change with time.

3.3 Propeller–Disk Flow

When the disk is placed in the propeller slipstream, the flow field gets significantly modified. Numerous studies have described the effect of propeller slipstream on other configurations, like rudder [12], hull [6]. Figure 1, described earlier, shows the overall flow features through volumetric streamlines. The propeller imparts a swirl to the incoming flow in the disk. The hub vortex primarily modifies the streamlines behind the disk, while the tip vortices interact with the disk shear layer.

Fig. 5 Symmetric recirculating region for flow normal to a disk



To understand the complex flow behaviour and vortex ring structure development in the disk wake region, we describe the development of flow from initial interactions to the formation of the recirculation region. The flow development, shown in Fig. 6a, starts from the individual vortex ring forming in the disk wake region near the periphery. The vortex ring starts peripheral growth while also rotating under the influence of incoming swirl motion (Fig. 6b). As the size of the outermost ring grows, multiple concentric rings form simultaneously (Fig. 6c). Lastly, these rings interact with each other to form a large recirculating region (Fig. 6d). Unlike the cylindrical disk wake without any upstream propeller effects, these recirculating regions are only quasi-steady. There is an asymmetry in the locations of centres of two vortices (not shown) and the positions interchange based on the blade passing frequency.

The complex three-dimensional interaction of vortices can be explained by considering an isolated vortex ring. Figure 7 shows this ring through streamlines plotted in front of the disk.

Vortex rings adjust themselves while it grows and rotates under the influence of the swirling motion of the fluid. This ring also expands itself in 360° rotational domain, and its width of rotation adjusts on its own axis throughout the rotation. This happens for all the vortex rings in the disk wake region in the propeller–disk flow which leads to the development of continuously interacting vortex rings structure in the disk wake region.

The propeller wake also changes the aerodynamic characteristics of the disk. In Fig. 8, pressures on the centreline of the disk are compared between pure disk and propeller–disk flows. The plots are shown behind and front sides of the disk, respectively, in Fig. 8a, b. The comparison shows that pressure drag behind the disk does not change significantly as the plots are close except near the edge of the disk.

The hub vortices only slightly influence the overall aerodynamic field. In comparison, the pressure field in front of the disk is significantly modified due to tip vortices shown in Fig. 3. The influence of these vortices reaches the centreline of the disk due

Fig. 6 Propeller-disk interaction

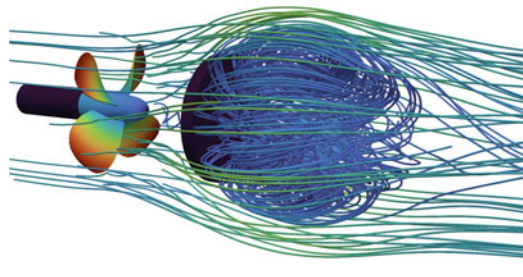
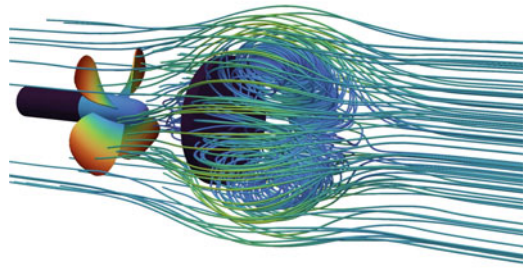
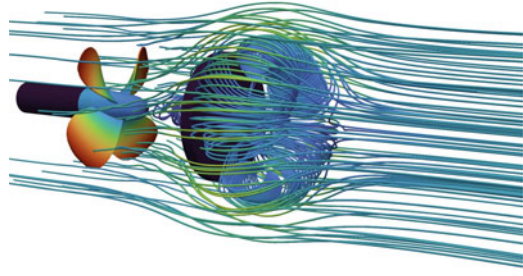
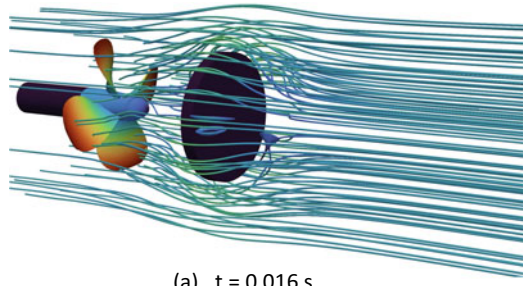
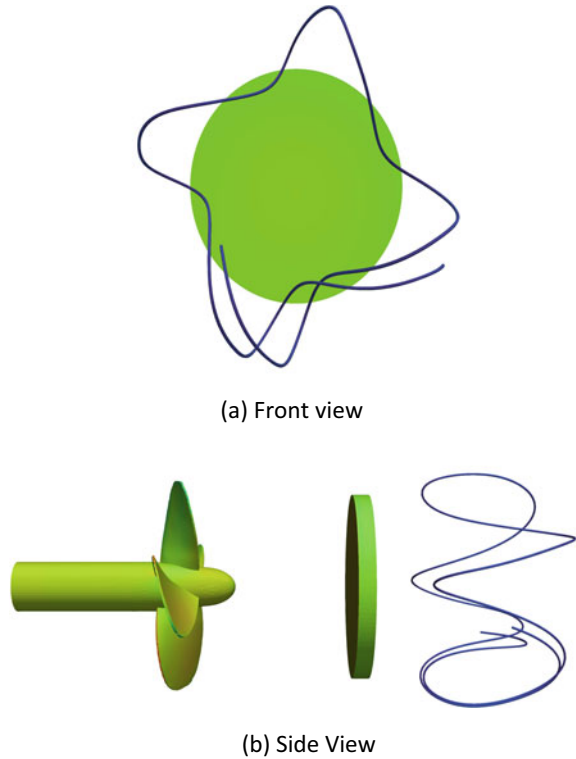


Fig. 7 Vortex formation and interaction of the disk



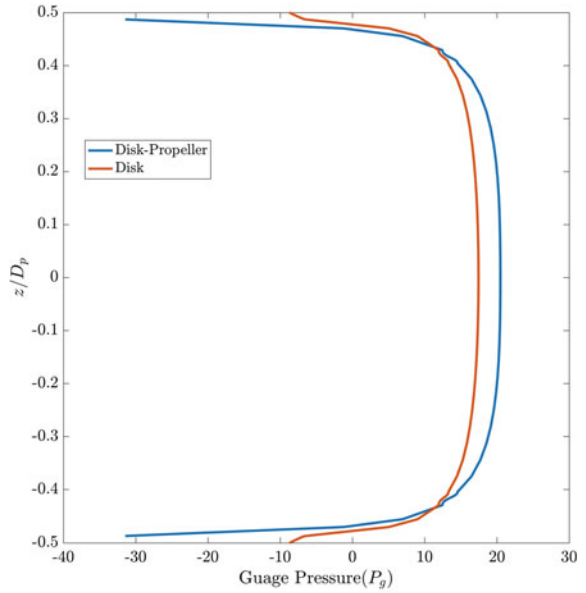
to the interacting vortex rings described earlier. The slight asymmetry in propeller–disk flow is due to the periodic wake influence, which changes based on blade passing frequency. We have calculated the overall normal force on the disk by integrating the pressure multiplied by the area normal. This force increases by about 5% due to the presence of the propeller.

The length of the recirculation bubble also gets modified under the influence of impinging wakes. Table 3 shows the bubble characteristics including the bubble width and length for pure disk and propeller–disk flows. The propeller wakes lead to an increase in the size of the bubble. For the current study, the bubble size increases by about 5% in both width and size due to the upstream propeller.

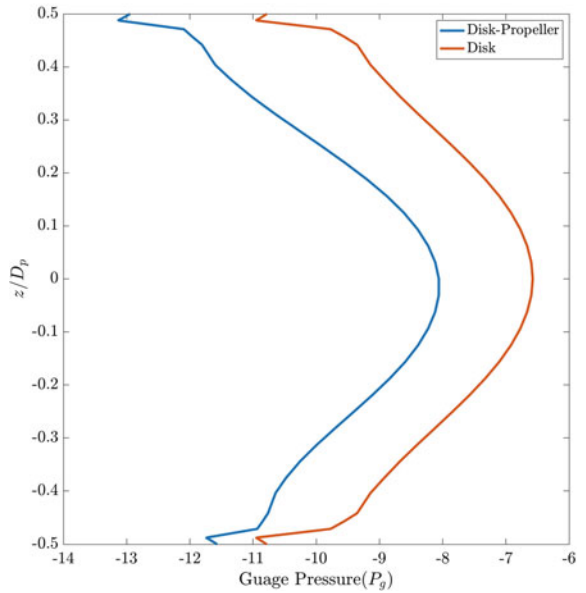
4 Conclusions

In the present work, we numerically investigate the modifications in flow features of the disk due to the presence of an upstream propeller. A thin disk, with an aspect ratio 10, is kept in the slipstream of INSEAN E779A propeller. The disk diameter is comparable to the propeller size and is kept at one disk diameter away. The propeller

Fig. 8 Pressure comparison between pure disk and propeller-disk flows



(a) Behind the disk



(b) In front of the disk

Table 3 Effect of propeller slipstream on disk

Case	Bubble Length	Bubble width
Disk-only	1.88 <i>d</i>	1.38 <i>d</i>
Propeller-disk	1.98 <i>d</i>	1.41 <i>d</i>

tip vortices dynamically interact with the disk shear layer and modify overall features. The propeller-disk flow is not steady, and the symmetry of the recirculation bubble in front of the disk gets disturbed with propeller wakes. This asymmetry is related to the blade passing frequency. Further, the size of the recirculation bubble increases due to the presence of the propeller. The pressure profile behind the disk is not changed greatly. However, the profile in front of the disk gets significantly modified. These changes in the flow features depend on the positioning of the disk in the propeller stream. Our future work will study this effect by changing the propeller and disk separation distance.

Acknowledgements Authors acknowledge the support from SERB Start-up Research Grant SRG/2021/000636.

The support and the resources provided by PARAM Sanganak under the National Supercomputing Mission, Government of India, at the Indian Institute of Technology, Kanpur, are gratefully acknowledged.

Nomenclature

A	Frontal area of rotor [m^2]
Re	Reynolds number
D_p	Propeller diameter [m]
d	Disk diameter [m]
t	Disk thickness [m]
ξ	Aspect ratio
k	Turbulent kinetic energy [J/kg]
ϵ	Dissipation [J/(kg s)]
T	Time scale [s]
L	Length scale [m]

References

1. Ashim Ali M (2020) Effect of ship motions on propeller-hull interaction, Ph.D. thesis, Memorial University of Newfoundland
2. Calcagno G, Di Felice F, Felli M, Franchi S, Pereira F, Salvatore F (2003) The INSEAN e779a propeller test case: a database for cfd validation. In: Proceedings of the Marnet-CFD final workshop

3. de Vries R, van Arnhem N, Avallone F, Ragni D, Vos R, Eitelberg G, Veldhuis LLM (2021) Experimental investigation of over-the-wing propeller–boundary-layer interaction. *AIAA J* 59(6):2169–2182
4. Felli M, Camussi R, Di Felice F (2011) Mechanisms of evolution of the propeller wake in the transition and far fields. *J Fluid Mech* 682:5–53
5. Guilmineau E, Deng GB, Leroyer A, Queutey P, Visonneau M, Wackers J (2018) Numerical simulations for the wake prediction of a marine propeller in straight-ahead flow and oblique flow. *J Fluids Eng* 140(2)
6. Mehdipour R (2014) Simulating propeller and propeller-hull interaction in openfoam
7. Muscari R, Dubbioso G, Di Mascio A (2017) Analysis of the flow field around a rudder in the wake of a simplified marine propeller. *J Fluid Mech* 814:547–569
8. Posa A, Broglia R (2022) Near wake of a propeller across a hydrofoil at incidence. *Phys Fluids* 34(6):065141
9. Shenoy AR, Kleinstreuer C (2008) Flow over a thin circular disk at low to moderate reynolds numbers. *J Fluid Mech* 605:253–262
10. Tian X, Ong MC, Yang J, Myrhaug D (2016) Large-eddy simulations of flow normal to a circular disk at $re = 1.5 \times 10^5$. *Comput Fluids* 140:422–434
11. Turunen T, Siikonen T, Lundberg J, Bensow R (2014) Open-water computations of a marine propeller using openfoam. In: *ECFD VI-6th European congress on computational fluid dynamics, Barcelona, Spain, 20–25 July 2014*, pp 1123–1134
12. Villa D, Franceschi A, Viviani M (2020) Numerical analysis of the rudder–propeller interaction. *J Mar Sci Eng* 8(12):990
13. Yang J, Liu M, Wu G, Zhong W, Zhang X (2014) Numerical study on coherent structure behind a circular disk. *J Fluids Struct* 51:172–188

Experiment on Hydraulic Power Take-Off Unit (PTO) for Point Absorber Wave Energy Converter (PA-WEC)



Shivam Gupta, Sumana Ghosh, Parmod Vaishnav, Priti Sarkar, Deepak Kumar, and Bharat Sitaram Mendhe

1 Introduction

Oceans are huge and offer a tremendous source of energy that can be harnessed into a useful form of energy. The other forms of renewable energy sources are hydro, wind, and solar. The technologies associated with hydro, wind, and solar are very much matured. However, in terms of power density, ocean energy offers tremendous potential. Ocean energy has power density of 2–3 kW/m², while wind (0.4–0.6 kW/m²) and solar has 0.1–0.2 kW/m² [1]. India has a vast coastline and thus offers a great advantage in utilizing wave energy as a useful form of energy. There are many types of wave energy converters (WEC) to harness ocean energy. Broadly, they can be classified as, attenuators, point absorbers, and terminators [2]. Attenuators are long structure devices placed along the wavelength's direction. The point absorber is a device whose length is smaller than the wave's wavelength. Terminators are long structure devices placed perpendicular to the direction of the wavelength. Based on the location [2], they can be classified as nearshore devices, onshore, and offshore devices. Onshore devices are located on the shore along the coastal line, e.g., oscillating water column (OWC) devices. Nearshore devices are placed a few hundred meters from the shore where the water depth ranges from 10 to 15 m, whereas offshore devices are located where the water depth is more than 40 m.

Point absorbers are the simplest wave energy converters in terms of operation. A point absorber wave energy converter is comprised of two parts. The first is the float, which interacts directly with waves, and the second is the power take-off system (PTO) which converts incidence wave energy to electricity. The hydraulic PTO system is the most widely used among the various PTO systems. It involves

S. Gupta · S. Ghosh (✉)

Department of Chemical Engineering, IIT Roorkee, Roorkee 247667, India
e-mail: sumana.gosh@ch.iitr.ac.in

P. Vaishnav · P. Sarkar · D. Kumar · B. S. Mendhe
ONGC Energy Centre Trust, Delhi 110092, India

hydraulic fluid, which works on the principle of pascal's law. The reported efficiency of the hydraulic PTO system is up to 90% [3].

2 Literature Review

An initial literature review was conducted to find out the various existing technologies in the PTO system. Based on the findings of the PTO system, an experimental facility to test the hydraulic fluid is constructed in the chemical engineering department at IIT Roorkee, India. Hydraulic PTO can be classified into parts: (1) variable pressure PTO and (2) constant pressure PTO. Based on rectification, hydraulic PTO systems can be classified as two-check valve concepts, four-check valve concepts, and the directional control valve concept. The constant pressure PTO received more attention than variable pressure PTO because it has added advantage of efficiency and reliability. Hence, various concepts of hydraulic PTO systems are based on the constant pressure system. The constant pressure type-1 (CP-Type-1) is inefficient as the hydraulic system has a single-acting hydraulic cylinder in which the flows move in one direction. The generator rotates in only one direction [4]. The adjustable slope angle wave energy convertor uses the hydraulic oil PTO system, which has one directional hydraulic motor, an oil tank, and a relief valve [5]. The variable pressure PTO is used in the wave star point absorber system, consisting of a double-acting double-rod hydraulic cylinder connected to a bi-directional variable displacement motor. The variable displacement motor drives the rotary generator [6]. To overcome the disadvantage associated with rectification associated with the two-check valve, a hydraulic PTO system with four-check valve system is studied [7], which involves the double-acting single rod, four-check valves for rectification, high- and low-pressure accumulator, a hydraulic motor coupled with the rotary generator. The unbalanced forces are generated due to the use of a single rod in the double-acting hydraulic cylinder. To overcome the shortcoming of a double-acting single rod, double-acting double-rod is used in the development of WEC-Sim tool software [8]. In some wave energy converters, the low-pressure accumulator is replaced by the oil tank; such a hydraulic PTO system is used in the Pelamis wave energy converter [9]. Since the current work requires the testing of the hydraulic fluid under the recreational condition of the ocean, the experiment facility constructed is of four-check valve system with a double-acting double-rod with high- and low-pressure accumulators.

3 Experiments on Hydraulic PTO System

One of the major PTO facilities used globally for wave generators is hydraulic PTO. In this system, ocean energy conversion to electricity is done through a hydraulic system. The mechanism works on the principle of Pascal's law. Hydraulic fluid played

a vital role in this PTO. Therefore, experiments are performed to select a suitable liquid available in the market.

The experiment facility is on a constant pressure type system. The schematic of the experiment facility is shown in Fig. 1. The hydraulic fluid under consideration is HLP-68 and HLP-46. The HLP is the code letter of the hydraulic fluid under DIN-51524-2. Two hydraulic fluids are selected based on their availability and accessibility in the market, and they are most widely used in hydraulic-based systems. The hydraulic term 68 represents the kinematic viscosity. The physio-chemical properties of the selected fluid are shown in Table 1.

To check the performance of the hydraulic fluid, two temperature sensors and three pressure sensors are installed in the setup shown in Fig. 2. The temperature sensor is installed at the entry and exit of the hydraulic motor. The hydraulic motor is coupled with a rotary generator which generates electricity. The hydraulic motor rotates due to the pressure difference at the hydraulic motor. The temperature and pressure data are collected through the data acquisition systems (DAQ) of the National Instrument (NI).

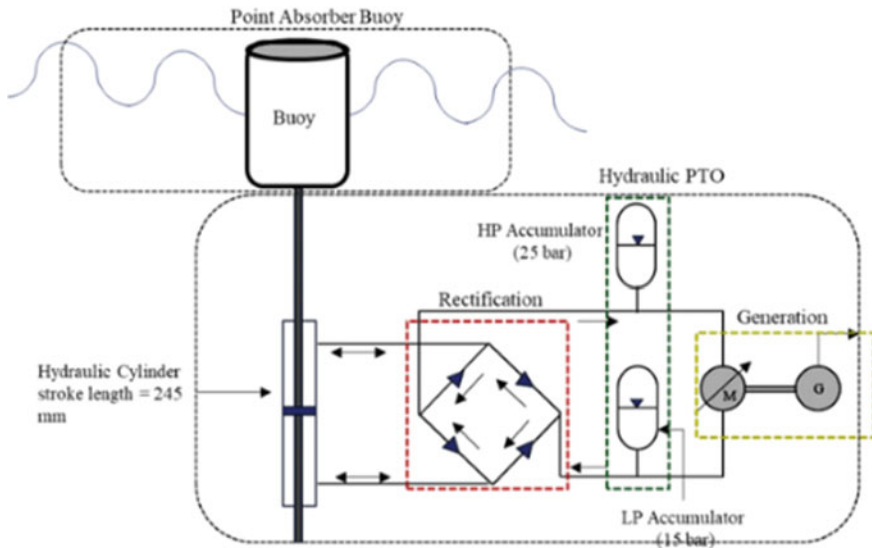


Fig. 1 Schematic of hydraulic PTO system

Table 1 Physio-chemical properties

Viscosity, kinematic, cSt, (@40 °C)	Viscosity index, Min	Flash point (COC), °C, Min	Pour point, °C	Copper strip corrosion, @ 100 °C For 3 h
68	90	210	-12	1
46	90	200	-15	1

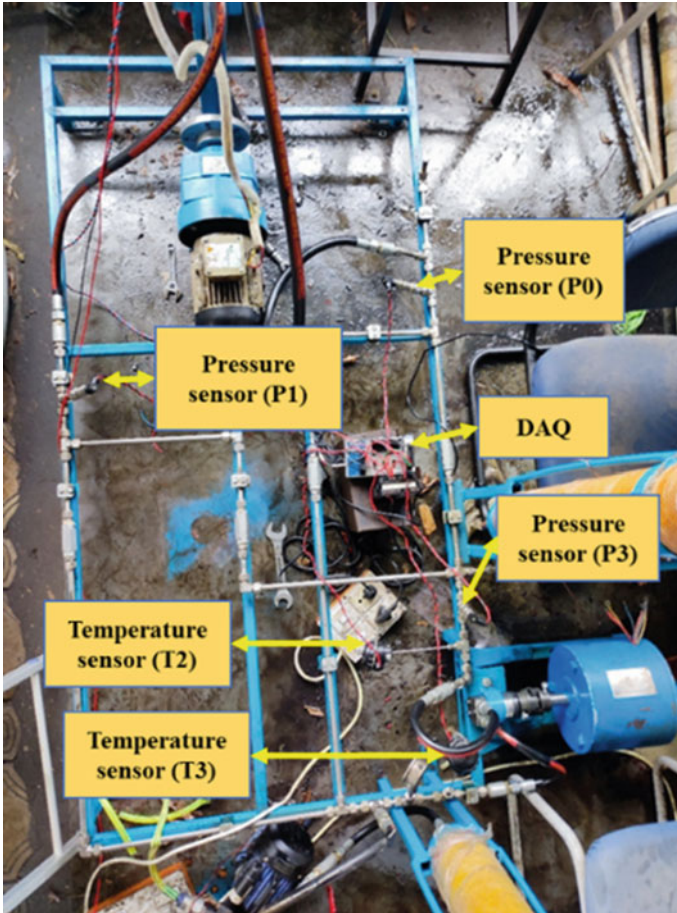


Fig. 2 Pressure and temperature sensors of PTO experiment setup

After data collection, Noise removal is done through the fast Fourier transformation. Fast Fourier transformation of raw pressure signal gives the number of the different frequencies of cosine wave from which the original signal is composed off. It converts a time domain signal to a frequency domain signal. Through the use of the inverse filter, the frequency domain model is converted back to the time domain model. Figure 2 shows the location of the temperature sensors, pressure sensors, and DAQ. The two temperature sensor is termed T2 and T3 at the inlet and outlet of the hydraulic motor, respectively.

The pressure sensors are termed P0, P1, and P2. The pressure sensors P0 and P1 are installed in the line connected to the hydraulic cylinder. The pressure sensor P3 is installed at the entrance of the hydraulic motor. The hydraulic fluid under consideration is tested for different displacements, namely 13 and 10 cm. These two different heights are scaled-down conditions of significant wave height of ocean

Fig. 3 Rheology test of the hydraulic fluid HLP-46 and HLP-68

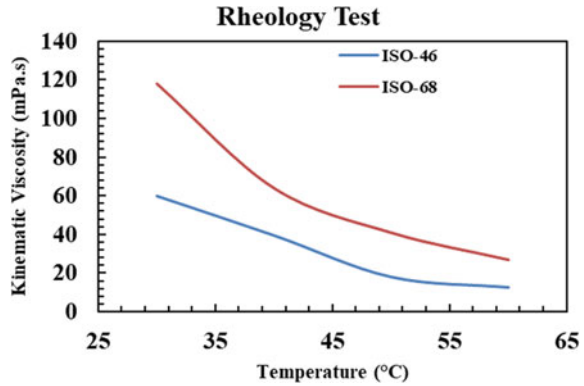


Table 2 Uncertainty analysis

Parameters	Uncertainty (%)
Pressure	0.25%
Temperature	± 0.5 °C
Kinematic viscosity	± 1%

conditions. Different displacements are obtained by varying the connecting rod of the hydraulic cylinder and the electric motor which drives the hydraulic cylinder. Image processing calculates the time period for each displacement setting of the hydraulic cylinder. Each experiment is run for about one hour to see the temperature variation in the hydraulic fluid. The voltage generated by the rotary generator is measured through the digital storage oscilloscope (DSO).

The rheology study of the hydraulic fluids under consideration is performed at the central testing facility in the chemical engineering department. For hydraulic fluid HLP-68 and 46, in the experiment, the kinematic viscosity at 40 °C is found to be 64.903 and 39.641 mPa.s, while the reported kinematic viscosity is 68 and 46 cSt. Figure 3 represents the variation of the kinematic viscosity with the temperature of both hydraulic fluids.

The uncertainty of all the experimental parameters is estimated by a single error propagation method and reported in Table 2

4 Results and Discussion

All the experiments of hydraulic PTO run for one hour. At a given time period of 0.8 s, there is a steady increase in temperature for hydraulic oil of HLP-68 compared to the HLP-46, in which temperature becomes stable after a certain time.

For both the hydraulic fluid HLP-46 and 68, respectively, the variation in temperature of HLP-68 is more as compared to the HLP-46, as shown in Figs. 4a and

5a. For the hydraulic fluid HLP-68 and 46, the maximum average temperature for the duration of 1 h. cycle run is 40 and 37 °C, respectively, for the same hydraulic displacement of 13 cm. The fluids are further compared for different average parameters as a function of the time period at the same displacement in Figs. 6 and 7. Corresponding voltage ranges are given in Fig. 8. It can be seen from the figures that as the time period increases, average temperature, pressure, and V_{rms} decrease steadily for 13 cm displacement. On the other hand, slight fluctuations are noted for 10 cm. A close look at the figures reveals that the maximum average temperature for the same time period is less in HLP-46 than in HLP-68.

The V_{rms} produced in the HLP-68 range from 66 to 80 V, while for HLP-46, the V_{rms} vary from 45 to 75 V. Figure 8 shows V_{rms} measured through the DSO. The maximum V_{rms} of 87.5 V is produced at a time period of 0.7 s for HLP-68, while for HLP-46, the maximum V_{rms} is 74.07 V at time period of 0.5 and 0.8 s. Considering factors like temperature and keeping the pressure variation small, the performance of HLP-46 is better compared to HLP-68. The overall maximum average temperature at different time periods is small in HLP-46 compared to HLP-68. Although the V_{rms} induced at different time periods in HLP-46 is less than HLP-68 but for long duration of cycle hour in ocean conditions, the system with hydraulic oil HLP-46 may perform better compared to HLP-68.

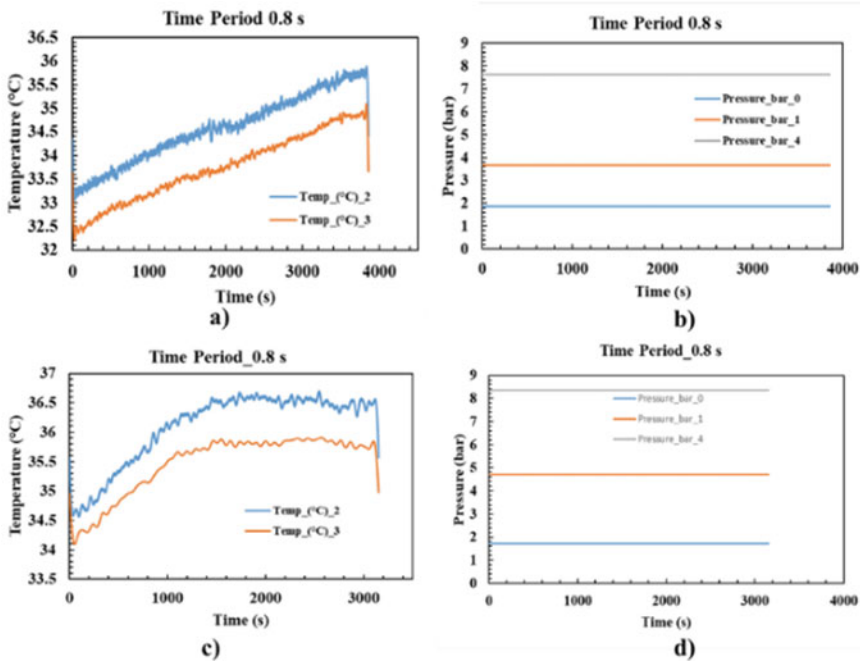


Fig. 4 HLP-68, Displacement 13 **a** Temperature variation, **b** pressure variation, displacement 10 cm **c** temperature variation, **d** pressure variation

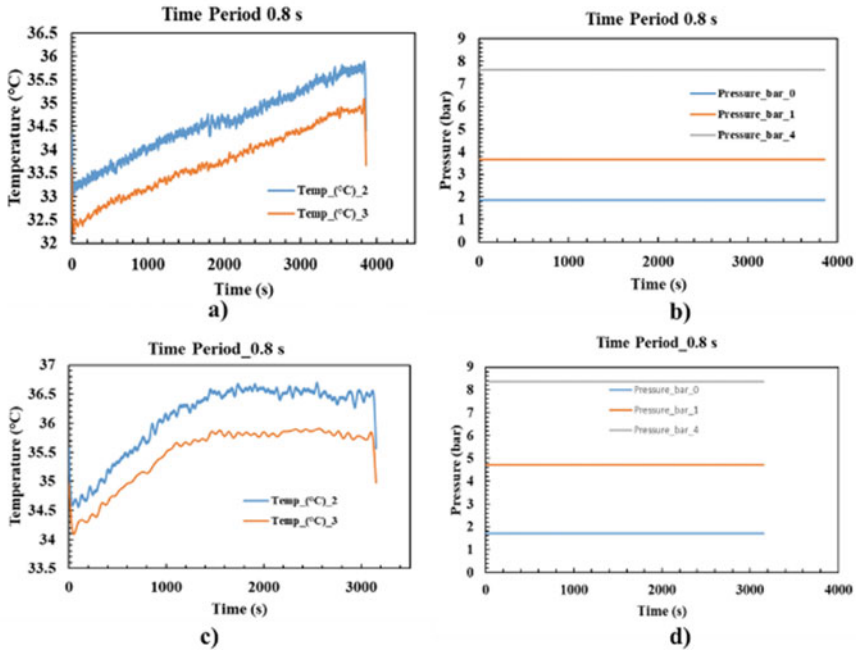


Fig. 5 HLP-46, displacement 13 a temperature variation, b pressure variation, displacement 10 cm c temperature variation, d pressure variation

5 Conclusions

The research involves studying the hydraulic PTO system in which hydraulic fluid selection is to be undertaken based on the experiment. The PTO experiment facility is installed to carry out the result. The ocean is turbulent and hydraulic fluid needs to sustain its properties for a long time. Thus, testing hydraulic fluid is of utmost importance. The fluid under consideration is DIN-51524-part2. Two hydraulic fluids of HLP-68 and 46 are used in the experiment. The initial experiment reveals that, in terms of temperature, as a hydraulic fluid in PTO works for long operating cycles, hydraulic fluid HLP-46 performs better than HLP-68. The temperature increases more in HLP-68 as compared to HLP-46 of hydraulic fluid.

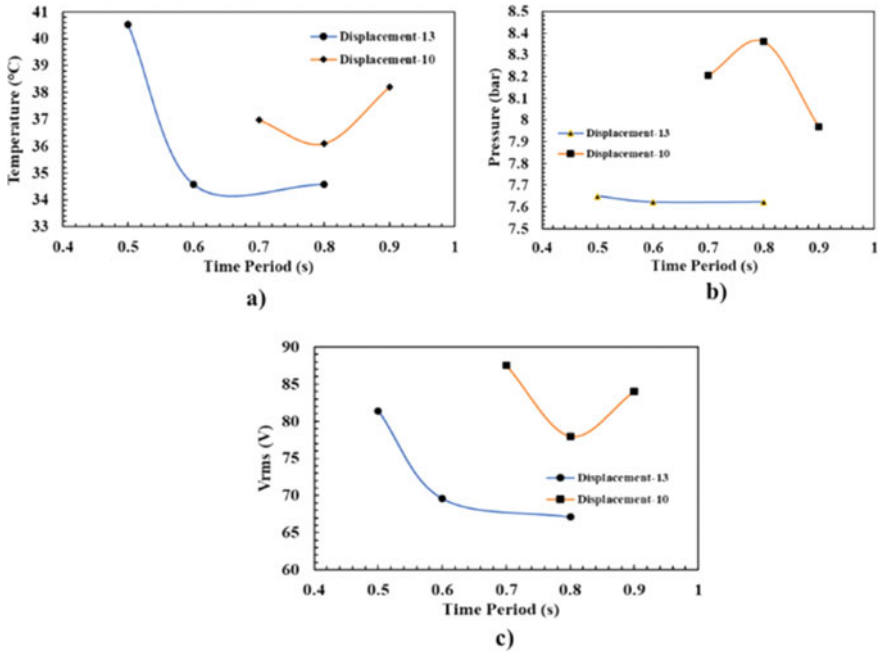


Fig. 6 HLP-68, **a** temperature versus time period, **b** pressure versus time period, **c** V_{rms} versus time period

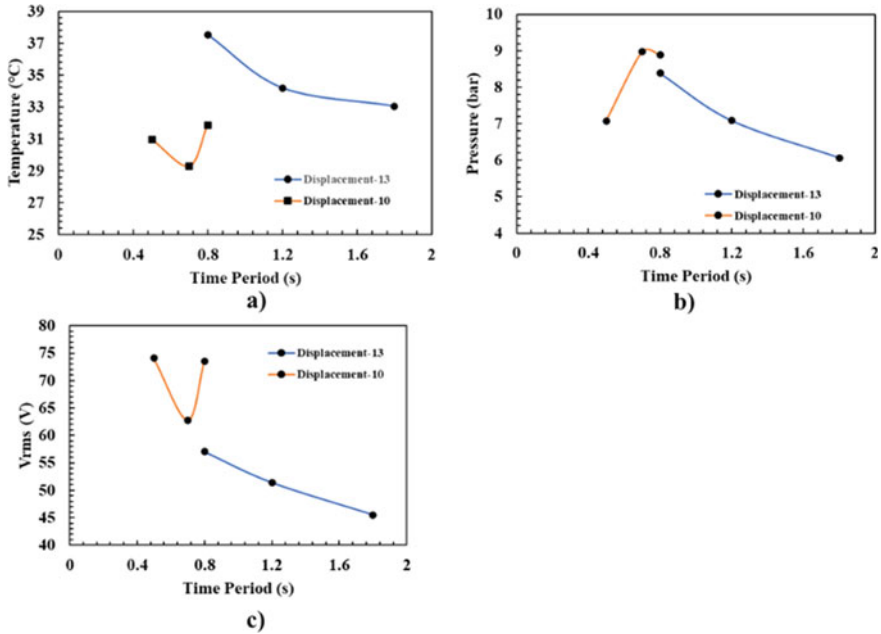


Fig. 7 HLP-46, a temperature versus time period, b pressure versus time period, c V_{rms} versus time period



Fig. 8 Voltage wavsshape form of a HPL-68, b HLP-46

Acknowledgements The research project is funded by ONGC Energy Centre Trust (OECT), India.

Nomenclature

- WEC* Wave energy converter
- PTO* Power take-off

<i>OWC</i>	Oscillating water column
<i>OBREC</i>	Overhead breakwater for energy conversion
<i>SSG</i>	Sea wave slot-cone generator
<i>DAQ</i>	Data acquisition systems
<i>NI</i>	National Instrument
<i>DSO</i>	Digital storage oscilloscope

References

1. Drew B, Plummer AR, Sahinkaya MN (2009) A review of wave energy converter technology proceedings of the institution of mechanical engineering. Part A: J Pow Energy 223:887–902
2. López I, Andreu J, Ceballos S, Martínez De Alegría I, Kortabarria I (2013) Review of wave energy technologies and the necessary power-equipment. Renew Sustain Energy Rev 27:413–434
3. Hansen RH, Kramer MM, Vidal E (2013) Discrete displacement hydraulic power take-off system for the wavestar wave energy converter. Energies 6:4001–4044
4. Jusoh MA, Ibrahim MZ, Daud MZ, Albani A, Yusop ZM (2019) Hydraulic power take-off concepts for wave energy conversion system: a review. Energies 12
5. Tri NM, Truong DQ, Thinh DH, Binh PC, Dung DT, Lee S, Park HG, Ahn KK (2016) A novel control method to maximize the energy-harvesting capability of an adjustable slope angle wave energy converter. Renew Energy 97:518–531
6. Andersen TO, Pedersen HC, Rico Hansen H, Henrik Pedersen C (2011) Model based design of efficient power take-off systems for wave energy converters
7. António AF (2007) Modelling and control of oscillating-body wave energy converters with hydraulic power take-off and gas accumulator. Ocean Eng 34:2021–2032
8. So R, Casey S, Kanner S, Simmons A, Brekken TKA PTO-Sim: development of a power take off modeling tool for ocean wave energy conversion
9. Henderson R (2006) Design, simulation, and testing of a novel hydraulic power take-off system for the Pelamis wave energy converter. Renew Energy 271–283

Micro-hydropower Generation for Sustainable Development: A Review



Anmol Jamakhandikar, Rahulkumar Painter, Ashish Doshi, and Mukund Bade

1 Introduction

There have been different types of renewable energy studied, including geothermal, hydro, solar, and wave power. These are substitutes for fossil fuels, which are running out because of pollution and the desire for sustainability on the part of humanity [1]. One of the renewable energy sources, power from water in mini-/micro-hydroelectricity is usually the most popular choice—both for its environmental friendliness and its efficiency and economy when it comes to small-scale rural electrification projects [2]. Water energy is a cost-effective, environmentally friendly, and sustainable way to generate power [3]. However, Indonesia still struggles with generating enough of its own cleaner energy sources. About 96% of the energy relied upon by power stations comes from burning fuel (mostly coal, but also some gas). Renewable energy sources like solar power produce an increasingly high percentage.

From 2003–2013, the average growth rate for a power plant in Indonesia was 7.3%. This can be broken down and analyzed by whether it is gas, steam, or another type of power plant. Gas plants saw the highest average year-over-year growth at 10%, while steam plants saw an average yearly growth rate of 9.3%. Steam power plants account for the most amount of consumers, at 46.7%. They are followed closely by gas and steam power plants (19.3%) as well as diesel power plants (11.6%). The consumption of renewable energy power plants is still low. For example, 9.9% for hydropower, 2.6% for geothermal, 0.2% for mini-hydro, and 0.1% for micro-hydro [4]. As Indonesia's energy sector transforms, it presents both challenges and opportunities. DI's need for energy is growing in step with economic growth. However, this means there is an ongoing search for a way to procure enough energy at a

A. Jamakhandikar (✉) · R. Painter · A. Doshi · M. Bade
Department of Mechanical Engineering, SVNIT Surat, Surat 395007, India
e-mail: p21tm012@med.svnit.ac.in

cost that is affordable to businesses and the public. We need new energy technologies, increased use of renewable energy sources, and increased efficiency to be successful at this challenge. Indonesia is located between degrees North Latitude and South Latitude, and between degrees East Latitude. Hundreds of thousands of islands make up this country, where the equator line runs through it. Indonesia is located in Southeastern Asia and borders the following countries: North–Malaysia, Singapore, Vietnam, Philippines, and Thailand; South–Australia and Timor Leste; West–Indian Ocean; East–Papua New Guinea and the Pacific Ocean. With a total area of 1,913,578.68 km², it can be categorized as follows: North: The content quality they provide is also similar to that of professional copywriters. Indonesia has a tropical climate that gets extremely humid. If you are traveling to the highlands, the weather may be more moderate, depending on what month it is and whether or not it is past the rainy season. The consistency in climate varies by region; depending on where you are in Indonesia, there will either be a dry season or a rainy season. One of the things that make Sucre stand out is its location. The city is in the Andes and has a big cold season [5]. That’s why it’s important to prepare for it by investing in renewable sources of energy, like micro-hydropower plants. Micro-hydropower generators are playing an increasingly important role in Indonesia’s energy supply.

2 Literature Review and Objective

There are a lot of hydropower components spread across Indonesia, with a total potential of 75,000 MW. However, only about 9% of that potential has been exploited for large-scale power plants and smaller ones. In 2005, Indonesia began developing micro-hydropower plants for the country. By 2006 and 2007, such power plants were being run in small quantities of 0.45 MW. They were eventually developed to 0.69 MW by 2008 and 2010 [6]. One strategy the Indonesian Government is taking to use more renewable energy is by adding a cumulative capacity of 20 MW from the hydropower plant in the Eastern region of Indonesia and also from mini-hydropower generation. The Eastern region has a potential capacity to generate 20 MW (mainly on a mountainside), whereas Java-Bali can generate 500 MW and Sumatra with 480 MW. However, while the construction of hydropower plants began in early 2015, there was no hydropower plant set up until last August. Some construction of hydropower plants began in the Eastern region of Indonesia with 800–1300 MW (including). Thanks to environmental risks like the protection of fish and other biota within the water, it is not safe to make large-scale power plants. It is possible to use a grid on one island to provide electricity, however, because, on plenty of islands in Indonesia, hydropower plants in style of small hydropower until pico-hydro powerhouse may well be will become the simplest solution for using that hydro. If you are looking for more sustainable energy sources, we can help! Many rivers in Indonesia have the potential to be used for a mini-/micro-hydropower plant. There is no agreement on what constitutes small hydropower. The most common figures are between 2 and 10 MW, but there is an upper limit of 25 MW. It can be seen from Table 1 that Indonesia

is the country with the most potential for hydropower production, with a total of 143,845.30 kW from small power plants ranging from 15–500 kW.

It can be seen from Table 2 that only around 1.8% of potential micro-hydropower plants are installed and built, which is rather low. Out of this data, several micro-hydropower plants have also been built. There is a hydroelectric dam in the Van Der Wick irrigation channel in Yogyakarta Bay that has a capacity of 11 kW. In the province of West Java, there is a micro-hydropower plant Rimba Lestari in Tangsi Jaya Hamlet which is located within Gunung Hall, Bandung Barat. Mendola hamlet and Pekalongan, Jawa Tengah became the newest locations of micro-hydropower plants installed in Indonesia. With an estimated total capacity of 22 kW, the two MHPPs use a cross-flow turbine [7]. There are already several micro-hydropower plants in Indonesia, including one in West Sumatra. This region has three plants with a total of 100 kW. Out of these power plants, a couple is in West Kalimantan: Pancuang Taba (40 kWh), Muaro Air (30 kWh), and Koto Ranah (30 kWh). These potential sites in the river include Kapuas Hulu, which has 18 locations from 100 watts to 5.2 MW.

Table 1 Potential of micro-hydro energy from the river in Indonesia [8]

S. No.	Province	Number of location	Potential capacity 1 kW
1	Aceh	3	2862.4
2	Sumatera Utara	11	9329.2
3	Sumatera Barat	4	26,819.0
4	Sumatera Selatan	2	10,238.0
5	Jambi	2	1360
6	Bengkulu	13	21,458.4
7	Lampung	3	3494.0
8	Jawa Timur	1	2486.9
9	Kalimantan Barat	3	2079.8
10	Kalimantan Selatan	4	2743.9
11	Kalimantan Timur	4	980.0
12	Kalimantan Tengah	6	2.838.0
13	Sulawesi Utara	5	5059.4
14	Sulawesi Tengah	12	10.225.0
15	Sulawesi Selatan	14	14.135.3
16	Sulawesi Tenggara	2	1154.4
17	Nusa Tenggara Barat	10	4143.6
18	Nusa Tenggara Timur	18	14.849.8
19	Maluku	5	1809.0
20	Papua	8	5743.2
Total			143,845.3

Table 2 Installed micro-hydro plant in Indonesia period 2011–2014 [9]

S. No.	Province	Location	Capacity (kW)
1	Sumatera Utara	Samosir Tapanuli Selatan	56.2
2	Sumatera Barat	Pasaman Barat, Mentawai Solok	54
3	Riau	Kampar	8
4	Jambi	Sarolangun	18
5	Sumatera Selatan	OKU Selatan, Muara Enim	43
6	Lampung	Lampung Barat	80
7	Jawa Barat	Ciamis	24.4
8	Jawa Timur	Situbondo	15
9	Nusa Tenggara Barat	Lombok, Lombok Timur, Sumbawa	350
10	Nusa Tenggara Timur	Ngada, Manggarai Timur, Rote, Tengah, Sumba Tengah, Timur Tengah Selatan	273
11	Kalimantan Barat	Kapuas Hulu, Landak	450
12	Kalimantan Tengah	Gunung Mas, Lamandau	48.9
13	Sulawesi Utara	Sangihe	14.1
14	Gorontalo	Gorontalo, Gorontalo Utara, Bone Bolango	145.2
15	Sulawesi Tengah	Lamatoli Morowali	20.6
16	Sulawesi Barat	Mamasa	120
17	Sulawesi Selatan	Luw Utara	40
18	Sulawesi Tenggara	Konawe Utara, Buton Utara	28
19	Maluku	Seram Bagian Barat	30
20	Papua Barat	Sorong Selatan, Maybrat, Manokwari	596
21	Papua	Pegunungan Bintang, Teluk Bintuni, Yalimo Jayapura	186.36
Total			2,600.75

The utilization of micro-hydropower seems to be slowing in Indonesia, even though there are many opportunities for this type of electricity generation. Meanwhile, the electrification ratio in Indonesia shows that several regions are still facing problems. In 2010, Indonesia's electrification ratio was 67.15%. It then increased to 84.35% in early 2014.

Java and Sumatra, areas with an electrification ratio of over 70%, are followed by Kalimantan, Sulawesi, and Maluku, who score 60%. West Lesser Sunda Islands (50%) are next in line followed by East Lesser Sunda Islands, which reach 40%,

and Papua which barely reaches 35%. The electrification ratio needs to be extended by improving infrastructures for electricity. One way to improve the electrification rate by giving more effort to set up more renewable energy sources like micro-hydro, which benefits both communities and the environment. Another alternative renewable energy source in Indonesia that has already been explored is the use of geothermal energy, wind energy, and also alternative renewable energy sources. These are some of the first sources of renewables. Geothermal energy, the potential of which is estimated at 29 GW, includes 270 locations. Sumatra Island has the largest representation with 51% of those sites; Java & Bali is 34.26% and 7.4%. The whole installed capacity of geothermal power is 1226 MW. Wind power in Indonesia has been steadily increasing, with a current installed capacity of 1.9MW. About 85% of wind plants are in Eastern Indonesia and generally have speeds ranging from 3–6 m per second. Besides being used for alternative energy, solar energy is also collected for electricity in Indonesia but the intensity of radiation varies throughout the year, and it is different in each place. On average, high solar irradiation occurs in the eastern part of Indonesia, while medium and low solar irradiation occurs in the western part. About 4.2 kWh/m² is both the all-time low and the highest radiation intensity value.

Table 3 displays the classification of SHP in India, and Table 4 displays the country’s progress in integrating small hydropower with other renewable energy sources to produce grid-connected renewable power [10]. Mini-hydropower comes in three different sizes: micro, pico, and nano. These capture the kinetic energy of the water through miniature turbines to create electricity. A single turbine cannot generate much power individually, but several turbines working in tandem can work well for a project like this. There are two general types of hydropower turbines: the impulse turbine and the reaction turbine. Both of these types are found in a variety of impulse-type turbines such as the Turgo, Pelton, and cross-flow turbine, whereas Francis and Kaplan turbine among the reaction turbines. There are several pump types that can be converted to turbines such as split pipe reactions, screws, and pump as turbine (PAT). The geographical location of some region has many rivers that can be converted into hydropower. Consequently, all of those types of turbines can be applied with a head lower than 5 m and this means that there is the potential to establish some power nuclei even in some irrigation infrastructures.

Northeast India has a high potential for SHP. It is often called the “future powerhouse of India.” Table 5 shows the tariff figures for SHP in the year 2020–21 and the size of a plant will determine its capital cost. The Indian Government has been

Table 3 Classification of SHP

S. No.	Plant capacity (kW)	Type
1	Up to 5	Pico
2	Up to 100	Micro
3	101–2000	Mini
4	2001–250,000	Small

Table 4 Region-wise attainment of SHP with capital cost [10]

Renewable source	Attainment (MW) (April–December 2019)	Cumulative attainment (MW) as on 31 December 2019
Bio-power	83.00	9861.31
Solar power—ground mounted	5013.00	31,379.30
SHP	78.40	4671.55
Solar power—roof top	536.88	2333.23
Wind power	1879.21	37,505.18
Waste to power	1.50	139.80
Total	7591.99	85,908.37

Table 5 Region-wise attainment of SHP with capital cost [10]

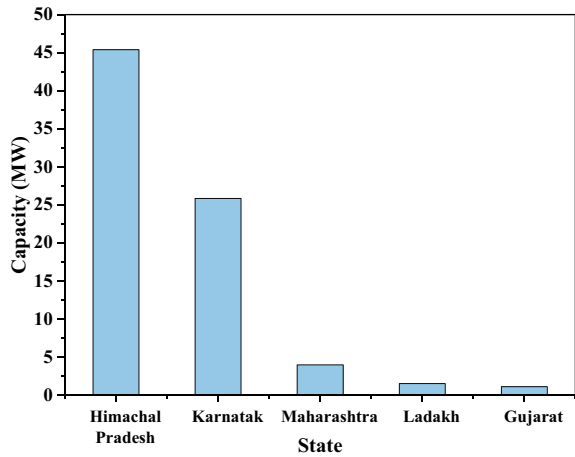
S. No.	Region	SHP size (MW)	Capital cost	
			(INR Million/MW)	(USD Million/MW)
1	Himachal Pradesh, Uttarakhand, West Bengal and Northeastern States	Less than 5	100	1.39
2	Himachal Pradesh, Uttarakhand, West Bengal and Northeastern States	Between 5 to 25	90	1.25
3	Other states	Less than 5	77.9	1.08
4	Other states	Between 5 to 25	70.7	0.98

aggressively pushing for the development of solar power, and as a result, 12 SHP projects were commissioned in 2019–2020. In total, 6 of those projects are located in Himachal Pradesh, which has a capacity of 45.9 MW illustrated in Fig. 1.

3 Results and Discussion

Based on Indonesian National Energy Policy, renewable energy will contribute 31% of the energy mix in 2050. Biomass, biodiesel, geothermal, hydropower, and nuclear will, respectively, provide 23, 21, 20, 10, and 7%. Fuel methane will carry with it 6%. Bioethanol and biogas, respectively, provide 4% each [11]. Each type of renewable energy has its own set of benefits and drawbacks to it which can lead to a difficult decision on which type is the best for you. However, in Indonesia, hydropower is regarded as the best choice; coming from geothermal sources [12]. Micro-/mini-hydropower is a form of electricity generation that is more efficient than other forms

Fig. 1 SHP commissioned between 2019 and 2020 [10]



such as wind power or solar. Solar cells convert 10–12% of sunlight, while micro-hydro units convert a range between 60 and 90% [13]. Economic analysis of several micro-hydropower is different reckoning on the placement and capacity of the station [14]. Present that it consumed an entire cost of 393 K euros with a payback time of six years, this power generation also helps with the regulation of watercourses aside from just the economy of this micro-hydro station [15]. Presented two economical sites in Iran. Initial economic costs for hydropower systems include the worth and expenses of powerhouse construction, setup, and equipment. For micro-sized power stations, the cost per kilowatts can be \$670 with a payback period that could be as short as a year. Below are some renewable energy resources and their respective minimum and maximum payback periods: micro-hydro at 1–6 years; wind energy at 8–13 years; solar energy at 12–21 years. It is shown that micro-hydropower stations have a bottom minimum payback period than other resources. To all of that benefit, the Indian Government should promote the event of micro-hydropower just like the other sources of renewable energy.

4 Conclusions

Developing nations such as India is working hard in order to reduce its dependency on fossil fuels with increasing the use of renewable sources of power, these include solar, geothermal, wind, and hydropower. However, this is not a problem-free solution: in some places, there are small hydroelectric power plants and so much untapped potential for small hydroelectric power plants in India. The current obstacles to overcome are exactly why there needs to be a serious effort put into the future of micro-hydropower plants in India. The Indian Government is developing hydroelectric power, a renewable energy source to turn micro-hydro into a sustainable

form of energy. Micro-hydro power constitutes about 1% of India's current energy production, so expanding this source could increase the percentage of renewable energies in total output to 16%.

The Indian summer monsoon typically lasts from June–September with large areas of western and central India receiving over 90% of their total annual precipitation. Southern and northwestern India receive 50%–70% rainfall. During this month, one can switch to micro hydro turbines to generate power. The benefits include reduced concerns about water availability and enhanced power generation. Moreover, it is also recommended to use a typical turbine if water availability is not an issue.

Nomenclature

<i>SHP</i>	Small hydropower
<i>PAT</i>	Pump as turbine
<i>MHPP</i>	Micro hydro power plant

References

1. Erinofiardi MS, Prayitno A (2015) Electric power generation from low head simple turbine for remote area power supply. *J Teknolologi (Sci Eng)* 74(5):21–25
2. Laghari JA, Mokhlis H, Bakar AHA, Mohammad H (2013) A comprehensive overview of new designs in the hydraulic, electrical equipment and controllers of mini hydro power plants making it cost effective technology. *J Renew and Sustain Energy Reviews* 20:279–293
3. Date A, Akbarzadeh A (2009) Design and cost analysis of low head simple reaction hydro turbine for remote area power supply. *J Renew Energy* 34:409–415
4. Dewan Energi Nasional Republik Indonesia. *Outlook Energi Indonesia 2014*
5. Sub-directorate of Statistical Compilation and Publication. *Statistical yearbook of Indonesia 2016*. BPS-Statistic Indonesia 2016
6. Agung Wahyu Kencono, Dwinugroho MP. *Handbook of energy and economic statistics of Indonesia 2015*. Ministry of Energy and Mineral Resources Republik of Indonesia, Jakarta 2015
7. Widodo Wahyu Purwanto, Nok Afifah. Assessing the impact of techno socioeconomic factors on sustainability indicators of microhydro power projects in Indonesia: a comparative study. *J Renewable Energy* 2016;93:312–22
8. Widodo WP, Yulianto SN, Rinaldi D, Harsono AS (2006) *Indonesia energy outlook and statistics 2006*, Jakarta: PEUI
9. MEMR. *Statistik EBTKE 2015*. Jakarta: Ministry of energy and mineral resources of Indonesia; 2015
10. *Annual Report 2019–20*, Ministry of New and Renewable Energy, Govt. of India. Available from: https://mnre.gov.in/img/documents/uploads/file_f-1585710569965.pdf
11. Agung Wahyu Kencono, Sugeng Mujiyanto, Aang Darmawan. *Perkembangan penyediaan dan pemanfaatan migas batubara energy baru terbarukan dan listrik*. Pusat data dan teknologi informasi Kementerian ESDM Jakarta, 2015
12. Tasri A, Susilawati A (2014) Selection among renewable energy alternatives based on a fuzzy analytic hierarchy process in Indonesia. *J Sustain Energy Technol Assessments* 7:34–44

13. Kusakana K, Munda JL, Jimoh AA. Economic and environmental analysis of micro hydropower system for rural area power supply. In: Proceedings of the IEEE 2nd international power and energy conference, 2008, pp 441–444
14. Roque A, Sousa DMM, Casimiro C, Margato E. Technical and economic analysis of a micro hydro power plant; a case study. In: Proceedings of the 7th international conference on the European energy market (EEM);2010: pp. 1–6
15. Ghadimi AA, Razavi F, Mohammadian B (2011) Determining optimum location and capacity for micro hydropower plants in Lorestan province in Iran. *J Renew Sustain Energy Rev* 15:4125–4131

Numerical Investigation of Unsteady Performance of a High-Pressure Transonic Turbine Stage of a Small Engine



Ssheshan Pugazhendhi and Shyama Prasad Das

1 Introduction

The flow inside a turbomachine is very complex. From a designer's perspective, it is crucial to understand the flow physics and to know the relative contribution of different components of losses at different operating points. Also, there is a constant need to improve the efficiency of the machine. We choose to study the first stage of an uncooled high-pressure transonic turbine. There is ample literature on studying the effects on the downstream rotor component due to the presence of stator upstream. Selected literature on this topic has been listed on the reference section [1–9]. But the upstream interactions due to the downstream components in a turbine caught less attention in the past decades. Due to unsteady phenomena, an appreciable amount of pressure and temperature fluctuations at the upstream stator is possible. Such an increase in temperature may lead to an increase in thermal loads on the stator vane, affecting its performance and life.

2 Literature Review and Objective

One of the earlier studies in this area is done by Dring et al. [10] where they studied both upstream and downstream influences of a component in a subsonic turbine. They found that, with a low axial gap between stator and rotor, there are increased pressure fluctuations upstream and increased Stanton number on the vanes. Williamson et al. [11] studied a low aspect ratio high-pressure transonic turbine stage and found that the presence of a rotor downstream improves the performance of the stator vane. It greatly reduced the hub secondary flow losses and improved the flow deviation. Miller et al.

S. Pugazhendhi (✉) · S. P. Das
Department of Mechanical Engineering, IIT Madras, Chennai 600036, India
e-mail: ssheshan.pugal@gmail.com

[12] studied the wake, shocks, and potential field interaction in a 1.5 stage transonic turbine and found that the presence of a downstream vane influences the rotor flow field downstream of its throat. They also found that the wake interaction did not show any appreciable change in rotor surface pressure. Gaetani and Persico [13] studied the influence of the downstream rotor on the stator exit flow field under subsonic flow conditions. It was found that the relative motion of the rotor induces fluctuations of pressure and velocities upstream, thereby affecting the stagnation properties, and found this phenomenon to be quasi-isentropic. It has been observed that the stagnation temperature fluctuations of about $\pm 8\%$ of the drop across the stage. Gaetani et al. [14] studied experimentally the effect of expansion ratio and blade loading on the turbine. It was found that, for the same flow exit angle, an increase in expansion ratio mitigates the effects of secondary flows, thereby increasing efficiency. Also, low stator exit Mach number condition increases unsteadiness at the rotor inlet in the moving frame of reference. Korakianitis [15] studied the influence of the stator-to-rotor pitch ratio, R in the nature of unsteady interaction in the turbine. It was found that for higher values of R (> 3), the unsteadiness in the flow field will be dominated by potential field interaction; and for low values of R (< 1), viscous interactions will dominate. From the details of the geometry of the turbine chosen for the present study, the value of R leans toward the higher side, meaning a significant potential field interaction can be expected.

Upon reviewing the literature, it is found that there exists a need to understand the unsteady phenomena inside a turbine stage better. Hence, it is the intent of this study to investigate the unsteady interactions in a high-pressure transonic turbine stage with application to a small engine. This work covers the evaluation of the time-averaged performance of the machine at various operating points and investigation of the influence of stage pressure ratio and rotor speed on the temporal fluctuations of total temperature upstream of the rotor.

3 Computational Methodology

3.1 Geometry and Setup

The turbine stage geometry consists of 19 stator vanes and 50 rotor blades, making the stator-to-rotor pitch ratio, $SRPR = 2.63$. The arrangement is shown in Fig. 1. The turbine blade has a flat tip with a constant tip gap. Additional details regarding the stage are provided in Table 1.

The stage operates between the total-to-total pressure ratios of 1.75–3.2, where the design point lies at 2.78. The inlet is assumed to have a constant total pressure and temperature. The blades are modeled in ANSYS Design Modeler with blade modeler features and exported to TurboGrid, where high-quality hexahedral cells were generated. The simulation setup was made in CFX, with 2 stator and 5 rotor blades, to maintain a pitch ratio close to 1. The setup made is as shown in Fig. 2. Steady-state

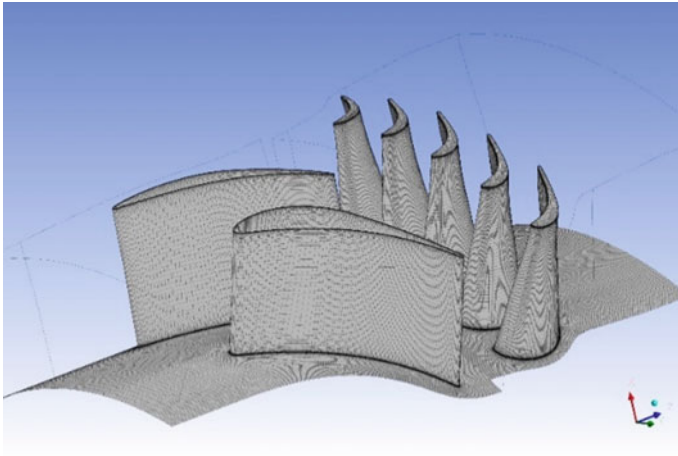


Fig. 1 Mesh with the turbine stage geometry setup

Table 1 Details of the turbine stage

Parameter	Stator	Rotor
Number of blades	19	50
Aspect ratio	0.621	1.886
Hub-to-tip ratio	0.764	0.734
L/C at midspan	0.769	0.783
Reynolds number	0.89×10^6	0.21×10^6
Axial gap	$0.55 \times C_{ax}$ of stator at midspan	
Tip gap	–	$\approx 1\%$ of the height
Reaction at midspan	–	0.48

simulations were run, and the result obtained was given as initial condition for the respective transient simulations. Transient blade row (TBR) with time-transformation methodology is utilized for unsteady simulations. One hundred timesteps per passing period are chosen with 20 inner loop iterations for each timestep. Monitors were set at the exit of both components to check if the simulation has achieved temporal periodicity in results. Most simulations achieved periodicity after 8 passing periods, as per monitor data. But the simulation run was allowed to complete one full revolution. The five cases chosen for simulation are design point (DP), low pressure ratio (LP), high pressure ratio (HP), low rotor speed (LS), and high rotor speed (HS). Table 2 provides the details of these cases.

Fig. 2 Grid independence study

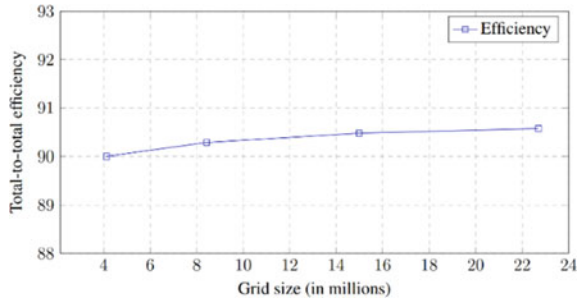


Table 2 Details of simulation runs

Case	P_{01}/P_{exit}	% N_{des}
DP	3.13	100
LP	1.85	100
HP	3.89	100
LS	3.13	90
HS	3.13	105

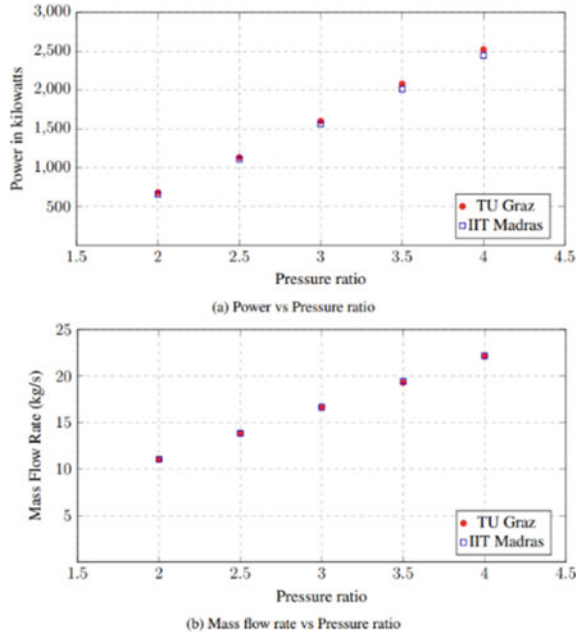
3.2 Grid Independence

The computational domain modeled with 2 stator vanes and 5 rotor vanes was discretized with hexahedral mesh using ANSYS TurboGrid. Four different grids were made with the number of nodes of around 4.1 million, 8.4 million, 15 million, and 22.3 million. The spanwise mesh count was kept constant for all the cases, and the mesh was varied in other two directions. The three-dimensional steady-state RANS equation was solved using ANSYS CFX 18.1. High-resolution schemes were chosen for advection and turbulence. SST $k-\omega$ was chosen for turbulence closure. The inlet turbulence intensity was set to medium (5%), and the length scale was chosen to be 10% of the inlet height. The high-speed numerics option is selected for the solver to better suit the compressible flow with shocks. The efficiency at the design point is plotted for the four mesh sizes. The differences in efficiency for the subsequent finer mesh are 0.5%, 0.2%, and 0.1%, respectively. Hence, the mesh with 15 million nodes is taken to be grid-independent. The plot for grid independence is shown in Fig. 2.

3.3 Validation

TU Graz turbine from Erhard [16] has been chosen for the purpose of validation. It is a single-stage high-pressure turbine with 24 stators and 36 rotors. Although the original model has a squealer at the turbine tip, it has been made flat for the purpose

Fig. 3 Validation with TU Graz geometry [16]



of simplification, and the filets were removed. It was run for different speeds and pressure ratios, and those results are compared for power and mass flow rate with their CFD result. A good agreement is found with their result (Fig. 3).

4 Results and Discussion

4.1 Definition of Normalized Quantities

For the purpose of generalization, all the quantities are normalized accordingly. For loss measurements, the static entropy has been normalized with the expected isentropic enthalpy drop across the component. The definitions are different for the stator and the stage. For stator, the isentropic enthalpy drop is the difference between inlet total enthalpy and the exit static enthalpy that is derived from the isentropic relations for the corresponding static pressure at the exit of the component. For the stage, this is replaced by the isentropic total enthalpy drop across the stage derived from the isentropic relations for the corresponding total pressure in stationary frame at the measurement plane downstream of rotor. This is because the performance of the machine is estimated in terms of total-to-total efficiency for the HP turbine stage. It is to be noted that all of the normalizing parameters are time-averaged. The definitions of entropy loss coefficients are different from that of Denton [17] and Mansour et al.

[18] as the isentropic enthalpy drop is considered for normalizing instead of the exit kinetic energy which is dependent on the exit flow field. The definitions for stator and stage entropy loss coefficients respectively are as follows:

$$\xi_{ngv} = \frac{T_{2,avg} \Delta S_{1-2}}{h_{01,avg} \left(1 - \left(\frac{P_{2,avg}}{P_{01,avg}} \right)^{(\gamma-1)/\gamma} \right)}$$

$$\xi_{st} = \frac{T_{3,avg} \Delta S_{1-3}}{h_{01,avg} \left(1 - \left(\frac{P_{03,avg}}{P_{01,avg}} \right)^{(\gamma-1)/\gamma} \right)}$$

Total temperature measurements were made at the exit of stator. For the purpose of normalizing, time-averaged total temperature drop across the stage for the respective cases is used. The definition is as follows:

$$\theta = \frac{T_{02} - T_{01,avg}}{T_{01,avg} - T_{03,avg}}$$

The above definition shows that the local instantaneous value of total temperature is subtracted by the time-averaged stage inlet total temperature, in order to visualize the variation above and below the mean inlet temperature.

4.2 Analysis of Statistical Quantities

This section includes the discussion on the statistical average and deviation quantities of performance parameters. Static entropy is normalized with the area-averaged entropy increase across the stage at the design point. The total temperature values have been normalized with the area-averaged total temperature drop across the stage.

Design Point (DP): The time-averaged entropy increase across the stator at the design point is shown in Fig. 4. The wake region extends across the span for two stator components. It can be seen that hub secondary flows generate more losses at the hub. The tip passage vortex is also visible from the contour at about 70% of the span. The pattern remains the same for all cases, except for the low-pressure case, where the losses are less.

Figure 5 shows the entropy increase across the rotor. Five distinct wake regions can be identified to extend across the span. Tip leakage vortex region marks the highest losses extending from span 100–80%. The tip passage vortex can be seen just below the tip leakage vortex that extends the secondary flow region to a further 15%. This is followed by the midspan loss region, where the primary source of loss is profile loss. The bottom 30% of the span is occupied by the hub secondary flows, which mark the second highest loss region. Hub passage vortex region can be clearly seen from the contour, and no distinct stator wake structures can be observed.

Fig. 4 Normalized entropy loss parameter at the exit of stator at design point

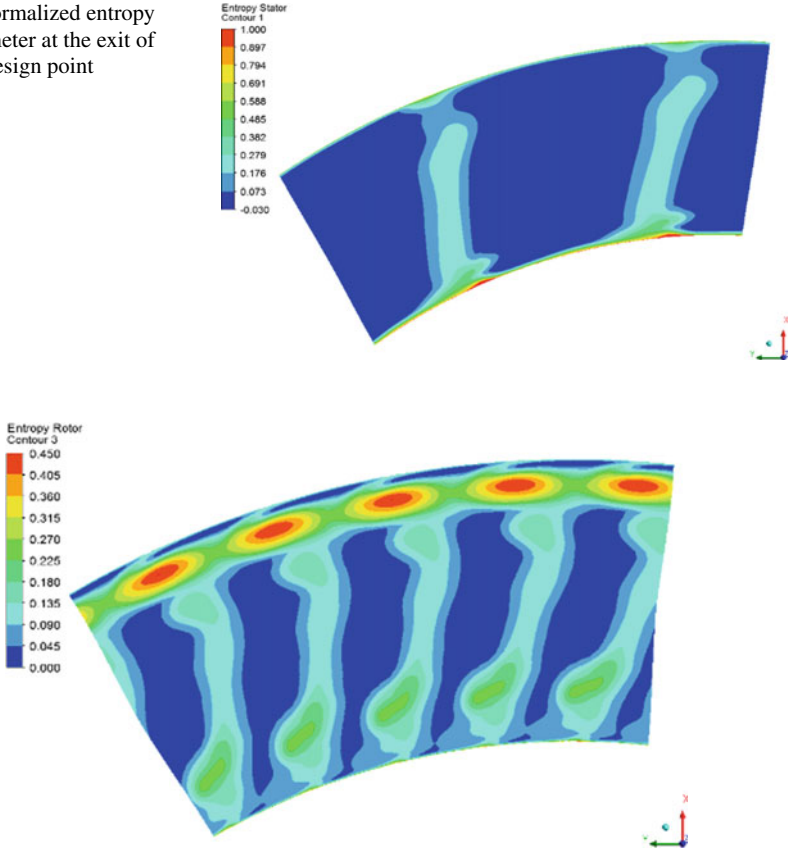


Fig. 5 Normalized entropy loss parameter at the exit of rotor at design point

Comparison of time-averaged entropy loss parameters circumferentially averaged at each span for stator and rotor for different cases is shown in Figs. 6 and 7. These figures are helpful in understanding the flow phenomena’s contribution to losses at each span.

Although the entropy loss coefficient is measured across the stage in Fig. 7, the stator loss is very small in comparison with that of rotor loss. Hence, the figure primarily shows the effect of different loss mechanisms in the rotor on entropy generation.

Low Pressure Ratio (LP): The entropy change across the stator for the low pressure (LP) case can be seen from Fig. 6. The losses are low in comparison with the design point, but the pattern remains the same. Figure 7 shows the loss regions at the rotor exit. The hub secondary loss region penetrates further upward to around 40% of the span. The tip leakage loss region occupies the same range of span as in other cases, as the tip leakage mass flow is limited by choking of the flow. It can be observed

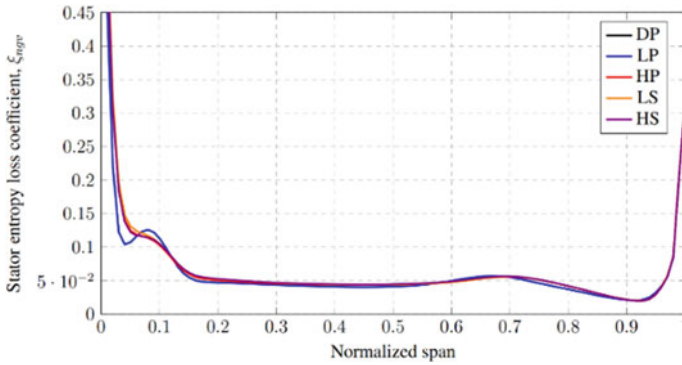


Fig. 6 Spanwise variation of circumferentially averaged time-averaged entropy loss parameter at the exit of stator

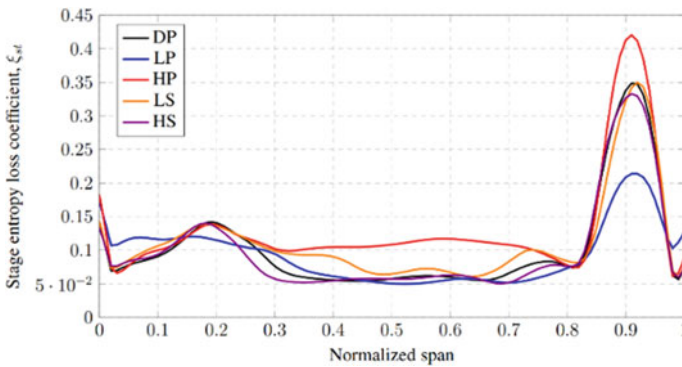


Fig. 7 Spanwise variation of circumferentially averaged time-averaged entropy loss parameter at the exit of rotor

that the losses in the tip leakage region and that of tip passage vortex region appear less pronounced in comparison with that of the design point case. One of the reasons behind this is the shock losses at the tip are minimal due to low pressure ratio. The midspan loss and tip leakage loss are the least for the case of LP. The nozzle exit condition for the rest of the cases remains the same as the design point, and the plot appears almost identical. Hence, the following discussions are restricted to rotor exit conditions only.

High Pressure Ratio (HP): With reference to Fig. 7 on loss across stage, it can be observed that the hub secondary losses appear to be similar to that of the design point case. This is due to the flow choking near that region, and it inhibits the secondary flow from penetrating any further into the higher rotor span. A significant increase in midspan losses can be observed due to an increase in shock losses and shock-induced separation near the trailing edge of the rotor blade. Due to such high losses, the passage vortex region is overshadowed by wake losses. The tip leakage losses in

this case mark the highest of losses in comparison with the rest of the cases under consideration. This is due to the strong compression shocks in the near tip region due to high pressure ratio across the rotor.

Lower Rotor Speed (LS): Figure 7 shows that the hub secondary losses increase, and the penetration of hub secondary flows extends close to midspan. The tip passage vortex appears relatively more prominent in comparison with other cases. This is primarily caused by the change in flow angle at the inlet of the rotor due to a reduction in rotor speed. The rotor encounters a positive incidence as a result, which increases the profile losses in the mid-portion of the blade and creates a condition that facilitates an increase in secondary flows in the near end-wall region.

Higher Rotor Speed (HS): It can be observed from Fig. 7 that the loss patterns are very similar to that of the design point. A small reduction in secondary flow losses is observed. The penetration of secondary flows into the domain is also observed to have reduced. The passage vortex and tip leakage vortex losses have reduced by a small amount in comparison with that of design point case.

4.3 Analysis of Instantaneous Quantities

Monitor Locations: Three span locations are chosen, one near hub (named SH01, SH02, and SH03), one near midspan (named SM01, SM02, and SM03), and another near tip (named ST01, ST02, and ST03). The angular positions of monitor points are chosen and such divides the stator pitch into three equal regions, one point for each region.

Design Point (DP): Due to the relative motion of the rotor, there is unsteadiness in flow that travels upstream of the rotor. It is observed that there is significant total temperature fluctuation upstream. Figure 8a–c show the variation of total temperature normalized with stage total temperature drop. In all cases, the monitors near the hub have a high value of total temperature. Its range extends from 8% on the positive side to 5% on the negative side approximately, making around 13% variation on total. For near midspan, the range extends from 3% on the positive side to 4% on the negative side. The least variation in all cases is seen at near tip monitor points. The range extends to 2% on both sides of the axis.

It is to be noted that the stator exit is subsonic at this span. It can be observed from the plots that we get five peaks for two passing periods, which corresponds to the ratio of rotors to that of stator $\sim 5:2$. Figure 9 shows the standard deviation of the total temperature variation at the exit of the stator. It shows the relative extent of the variation of the quantity in the plane/location. It can be seen that the near hub side has the highest values, whereas the tip side, the lowest. The wake regions also show some high values. It can be said that the most of change in total temperature happens in the secondary flow region. Figure 10 shows the contour the normalized total temperature in the rotor relative frame close to the leading edge of the rotor. It can be seen that

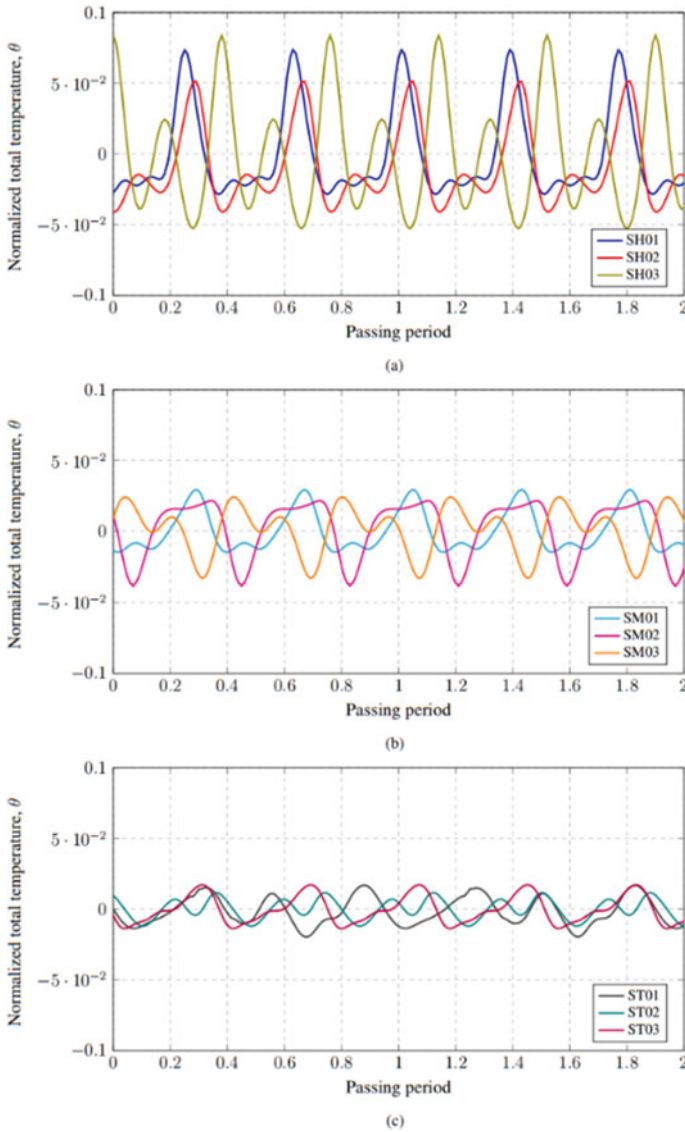


Fig. 8 Normalized local total temperature variation at monitor points at the stator exit at design point **a** near hub, **b** at near midspan, and **c** at near tip region

the five pillars, indicating the positions of the five rotors. The suction side of the rotor has the higher/positive total temperature, whereas the pressure side has the negative ones. This phenomenon is due to the energy separation effect [19], and it is a quasi-isentropic [13] and does not lead to any irreversible entropy generation in an inviscid flow. It can be observed that the near hub region has the higher values

of total temperature. This is because the rotor leading edge at the hub is closer to this plane than in the tip region. It can also be noted that the values near the rotor are much higher than that of at the interface. From the Fig. 8a–c, it can be seen that the near portion has the most variation and the tip region, the least. This trend is followed in all other cases as well. As the near hub portion shows more prominent interaction, the following discussions for other cases include only near hub variation of total temperature.

The distribution of total temperature normalized (θ) at midspan is shown in Fig. 11. The values of θ are very high near the rotor leading edge. A cloud of high θ can be

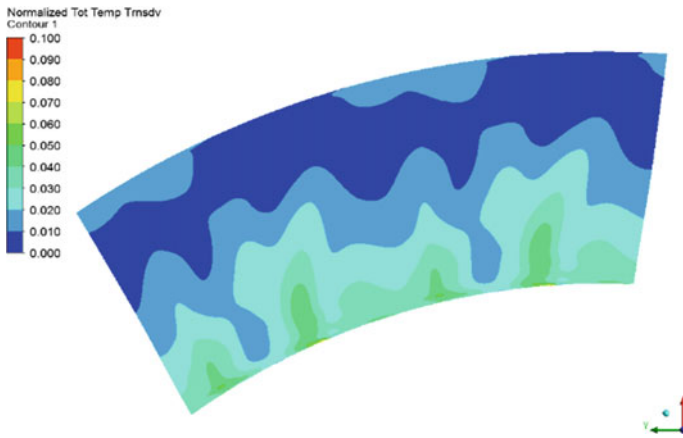


Fig. 9 Standard deviation of total temperature variation at the exit of stator for the design point case

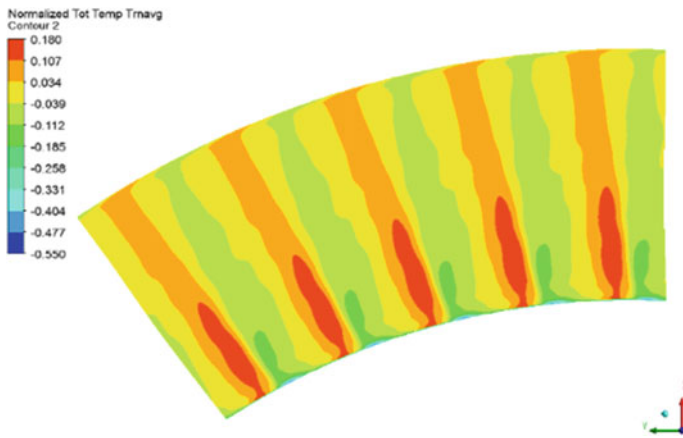


Fig. 10 Time-averaged normalized total temperature in stationary frame near rotor leading edge relative to the frame of rotor

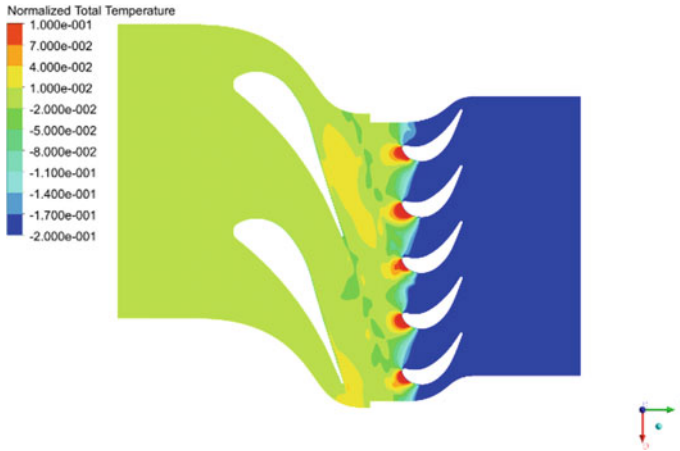


Fig. 11 Normalized total temperature in stationary frame distribution in midspan at the design point

seen upstream of rotor which moves toward the stator. Alternating high and low values of θ can be seen from the stator vortex shedding as well.

Effect of Pressure Ratio: For the case of low pressure ratio (LP), the total temperature fluctuations are less than $\pm 1\%$ even locally for all the cases, which can be seen from Fig. 12. Hence, the prediction is that there is no significant perturbations traveling upstream. For the case of high pressure ratio (HP), the total temperature monitor looks only marginally different from that of the design point case. This is due to the nozzle exit condition being almost the same for both design point as well as high pressure ratio cases.

Effect of Rotation Speed: Figure 13 shows the plane-averaged total temperature in percentages of total temperature drop of corresponding cases at every instant. This will provide the detail of the change in total temperature or inlet total energy received by the rotor on average at every instant. For the case of 90% of rotor speed, the total temperature values are lower than that of the design point. And for the case of 105%

Fig. 12 Normalized local total temperature variation at near hub monitor points for the low pressure ratio case

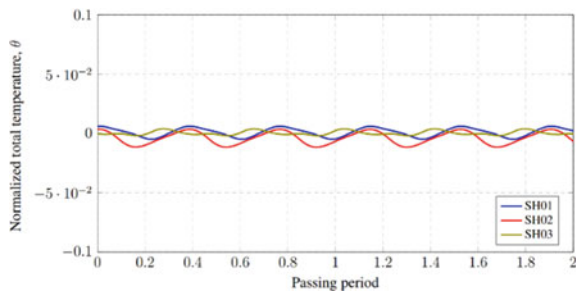
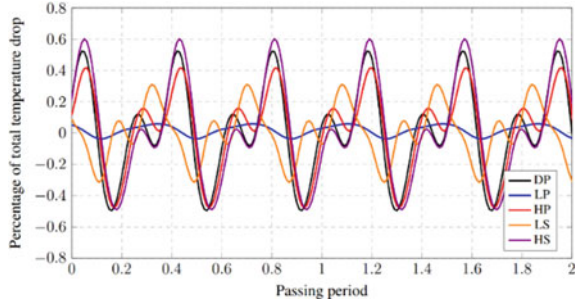


Fig. 13 Plane-averaged total temperature variation with time in terms of percentage of total temperature drop for corresponding cases



of rotor speed, the values are slightly higher than the design point. This indicates that the magnitude of the total temperature fluctuation perceived by the stator is dependent on rotor speed.

It can be observed from Fig. 13 that the average variation of total temperature at the interface plane is approx. 0.5% of total temperature drop for the design point case. The figure also shows that the case of LP has the least variation with less than 0.1% of total temperature drop and HS has the most variation with about 0.6%. By comparing the variations in LS, DP, and HS cases, LS having the least variation and HS having the most, it can be said that the variation of average total temperature is a function of rotor speed, within the investigated range.

5 Conclusions

Three-dimensional unsteady CFD simulations were performed on a high-pressure transonic turbine stage with application to a small engine. Five different conditions (DP, LP, HP, LS, HS) were chosen by varying the pressure ratio and rotor speeds to investigate their influence on the performance of the machine. For the purpose of generalization, all quantities are normalized appropriately. A qualitative assessment of relative contributions of different loss regions, viz., tip leakage, tip passage vortex, hub secondary flows, and midspan loss regions, across both components for different conditions under consideration is made. The rotor generates total pressure fluctuations upstream, thereby affecting the nozzle exit flow field. The local fluctuations at the interface are about 13% of total temperature drop locally for the design point and high pressure ratio case, whereas for the low pressure ratio case, the value is less than $\pm 2\%$. This suggests that the fluctuations might increase from the subsonic operating conditions till the transonic condition and remain almost the same for any further increase in pressure ratio. It is also observed that these fluctuations closer to the rotor are as high as $\pm 10\%$. The low rotor speed case shows around $\pm 5\%$ local total temperature variation at the interface, and it is slightly higher than the design point for the high rotor speed case. This shows the dependency of these fluctuations

on rotor speed. Within the range of rotor speeds investigated, the plane average of total temperature fluctuations at the interface is proportional to rotor speed.

Acknowledgements High-Performance Computing Environment (HPCE) facility at the institute is used for running CFD simulations. The authors would like to acknowledge the contributions of late Prof. B. V. S. S. Prasad, Department of Mechanical Engineering, Indian Institute of Technology Madras.

Nomenclature

C	Chord [m]
h	Specific enthalpy [J/kg]
L	Circumferential pitch [m]
N	Rotor speed [rpm]
P	Pressure [Pa]
S	Static entropy [J/kg K]
T	Temperature [K]
θ	Normalized total temperature
ξ	Normalized entropy change

Suffix

avg	Time-averaged
ax	Axial
des	Design point
exit	Exit of rotor domain
ngv	Stator
St	Stage
0x	Stagnation property
1	Inlet of stage
2	Exit of stator (or) stator–rotor interface
3	Measurement plane downstream of rotor

Abbreviations

DP	Design point case
LP	Low pressure ratio case
LS	Low speed case
HP	High pressure ratio case

HS High-speed case
SRPR Stator-to-rotor pitch ratio

References

1. Denos R, Arts T, Paniagua G, Michelassi V, Martelli F (2001) Investigation of the unsteady rotor aerodynamics in a transonic turbine stage. *J Turbomach* 123:81–89
2. Chaluvadi VSP, Kalfas AI, Benieghbal MR, Hodson HP, Denton JD (2001) Blade-row interaction in a high-pressure turbine. *J Propul Power* 17:892–901
3. Chaluvadi VSP, Kalfas AI, Hodson HP, Ohyama H, Watanabe E (2003) Blade row interaction in a high-pressure steam turbine. *J Turbomach* 125:14–24
4. Schlienger J, Kalfas AI, Abhari RS (2005) Vortex-wake-blade interaction in a shrouded axial turbine. *J Turbomach* 127:699–707
5. Miller RJ, Moss RW, Ainsworth RW, Horwood CK (2003) Time-resolved vane-rotor interaction in a high-pressure turbine stage. *J Turbomach* 125:1–13
6. Gaetani P, Persico G, Dossena V, Osnaghi C (2007) Investigation of the flow field in a high-pressure turbine stage for two stator-rotor axial gaps—part I: three-dimensional time-averaged flow field. *J Turbomach* 129:572–579
7. Gaetani P, Persico G, Dossena V, Osnaghi C (2007) Investigation of the flow field in a HP turbine stage for two stator-rotor axial gaps: part II—unsteady flow field. *J Turbomach* 129:580–590
8. Persico G (2007) Unsteady aerodynamic rotor-stator interaction in high pressure turbines. Doctoral thesis, Politecnico di Milano, VKI Report
9. Paniagua G, Yasa T, La Loma AD, Castillon L, Coton T (2008) Unsteady strong shock interactions in a transonic turbine: experimental and numerical analysis. *J Propul Power* 24(4):722–731
10. Dring RP, Joslyn HD, Hardin LW, Wagner JH (1982) Turbine rotor-stator interaction. *J Eng Power* 104:729–742
11. Williamson RG, Moustapha SH, Hout JP (1986) The effect of downstream rotor on the measured performance of a transonic turbine nozzle. *J Turbomach* 108:269–274
12. Miller RJ, Moss RW, Ainsworth RW, Harvey NW (2003) Wake, shock, and potential field interaction in a 1.5 stage turbine—part I: vane-rotor and rotor-vane interaction. *J Turbomach* 125:33–39
13. Gaetani P, Persico G (2021) Influence of the rotor-driven perturbation on the stator-exit flow within a high-pressure gas turbine stage. *Int J Turbomach Propulsion Power* 6(28):2021
14. Gaetani P, Persico G, Spinelli A (2017) Coupled effect of expansion ratio and blade loading on the aerodynamics of a high-pressure gas turbine. *MDPI Appl Sci* 7. ISSN 2076-3417
15. Korakianitis T (1993) On the propagation of viscous wakes and potential flow in axial-turbine cascades. *J Turbomach* 115:118–127
16. Erhard J (2000) Design, construction and commissioning of a transonic test-turbine facility. Doctoral Thesis, TU Graz
17. Denton JD (1993) The 1993 IGTI scholar lecture: loss mechanisms in turbomachines. *J Turbomach* 115:621–656
18. Mansour M, Chokani N, Kalfas AI, Abhari RS (2012) Impact of time-resolved entropy measurements on a one-and-one-half-stage axial turbine performance. *J Turbomach* 134(2):021008
19. Eckert ERG (1987) Cross transport of energy in fluid streams. *Wärme-und Stoffübertragung* 21:73–81

Effect of Divergence Angle, Carrier Gas, and Back Pressure on Species Separation Using Convergent Divergent Micro-Nozzle



Manu K. Sukesan, Ashok Kumar, and S. R. Shine

1 Introduction

Species separation devices have a variety of applications, including the removal of impurities from micro reactor feeds or product streams, MEMS-based separation devices, pre-concentrators, and so on. A newly emerging field is the separation of species using supersonic flow through micro-nozzles in a rarefied environment. Toxic gases and pollutants in a mixture can be detected in real time by passing the mixture through the micro-nozzle. In recent times, a little research has been conducted on the micro-nozzle to study the effect of expansion ratio, wall temperature, etc. on species separation. The current study focused on the effect of divergent angle, back pressure, and the impact of heavier carrier gases on species separation.

2 Literature Review and Objective

Schwan et al. [1] studied the non-equilibrium effects between heavy isotopes and light carrier gases in a cylindrical separation nozzle by using a tracer Monte Carlo procedure. The results indicated that the separation processes are functions of Knudsen, Mach number, and deflection angle. Guy [2] conducted an experimental and numerical investigation on the molecular separation effect in a pitot-type sampling probe, and the results showed the presence of radial diffusion currents in the stagnation zone created by strong temperature and pressure gradients. Chatwani et al. [3] used the

M. K. Sukesan (✉) · A. Kumar · S. R. Shine
Department of Aerospace Engineering, Indian Institute of Space Science and Technology, IIST,
Thiruvananthapuram 695547, India
e-mail: manuksukesan.19@res.iist.ac.in

S. R. Shine
e-mail: shine@iist.ac.in

tracer Monte Carlo procedure to study the isotope separation in a curved nozzle, and the results suggest that the strong non-equilibrium effects will be present for typical operating conditions of actual separation nozzles used for uranium isotope enrichment. They [4] also studied the spherical source expansion of binary and ternary mixtures of monatomic gases by using the direct simulation Monte Carlo method, and the results are compared with the previous sudden-freeze, moment-method, and Monte Carlo predictions. Anderson and Malling [5] investigated the separation of isotopes in opposed-jet flows from slits, and they concluded that the separation factors of high accuracy were obtained using a test particle method.

Sabouri and Darbandi [6] conducted a study on a linear 2D nozzle, and they discussed the effect of geometrical expansion ratio (2–4), the wall temperature (200–400 K) and inlet Knudsen number (0.003–1.454) variation on species separation. They proposed two distinct separation phenomena, one in the lateral direction and the other in the streamwise direction. Kosyanchuk and Yakunchikov [7] studied the effect of geometrical features on species separation of Ar and He mixtures by varying nozzle angles, nozzle lengths, and expansion ratios. Separation efficiency was found to be higher at higher exit velocities, higher curvature at the exit, and at higher speed ratios of species. They [8] also studied the effect of carrier gas on species separation by using a lighter gas as a carrier gas. Significant improvement in separation was noticed for lighter carrier gas concentrations (> 70%). Bykov and Zakharov [9] studied the flow of the binary gas mixture through an orifice into the vacuum. Two binary mixtures (Au–Ne and Au–He) with a large specific mass ratio were selected for the study. They observed that an increase in the parameter species mass ratio causes an increase in the characteristic longitudinal size of the jet. This effect is more pronounced for the transition regime and a large (greater than 0.9) mole fraction of the light species. Sukesan and Shine [10] recently studied the impact of throat height and the divergent shape of the micro-nozzle on species separation. They observed that the lateral separation effect is influenced by the nozzle divergent section shape, and from the study, they concluded that the divergent section with a trumpet shape is preferred for the species separation performance.

There are only a limited number of studies conducted on species separation in convergent divergent micro-nozzles. The presence of heavier carrier gases has unexplored effects on species separation. So numerical simulations are conducted to study the effects of divergence angle, carrier gas, and back pressure on species separation.

3 Methodology

All the simulations have been carried out by using a Direct Simulation Monte Carlo method (DSMC). The DSMC technique, a type of particle method that replicates the Boltzmann equation, is well known as an effective approach for statistically solving rarefied flow issues. For a simple dilute gas, the Boltzmann equation has the following form:

$$\begin{aligned} & \frac{\partial(nf)}{\partial t} + \vec{c} \cdot \frac{\partial(nf)}{\partial \vec{r}} + \vec{F} \cdot \frac{\partial(nf)}{\partial \vec{c}} \\ & = \int_{-\infty}^{\infty} \int_0^{4\pi} n^2 [f^* f_1^* - f f_1] c_r \sigma d\Omega d\vec{c}_1 \end{aligned} \tag{1}$$

where f and f_1 stand for the velocity distribution function at c and c_1 , respectively. $d\vec{c}_1$ is the infinitesimal velocity of the field molecules, and $d\Omega$ is the infinitesimal velocity space solid angle. Post-collision characteristics are indicated by the superscript $*$. The initial setup condition, indexing and moving the particles, enabling the collision of particles, and computing the thermodynamic parameters of the cells based on particles present within the cells are the many phases involved in DSMC simulations. The current simulation was conducted using the openFOAM software framework and the open-source DSMC solver “dsmcFoam+” [11]. The collision partner selection model has been based on the Bird’s NTC method. The Variable Soft Sphere model with a reference temperature of 273 K has been chosen as the binary collision model. The energy redistribution following an elastic collision is modelled using Larsen and Borgnakke’s equations. Based on the molecule’s mean free path, the entire domain is divided into a number of cells, each of which has a size that is comparable to the mean free path. To choose the collision pairs, the NTC algorithm will further divide the cells into sub-cells, making sure that each sub-cell size is less than $\lambda/3$. According to earlier studies, the inaccuracy resulting from cell dimension would be minimised as long as the size of the cell is less than $\lambda/3$. At the inlet and outlet, the dsmcFoamPlus solver’s built-in pressure boundary conditions have been applied. The ratio of real to the simulated number of particles was 2×10^7 , which will ensure more than 20 particles per cell. Figure 1 depicts the computational domain used for the numerical investigation. The blockMesh tool of openFOAM 2.4.0 was used to construct the structured mesh, and Paraview 5.6.2 was used to post-process the output.

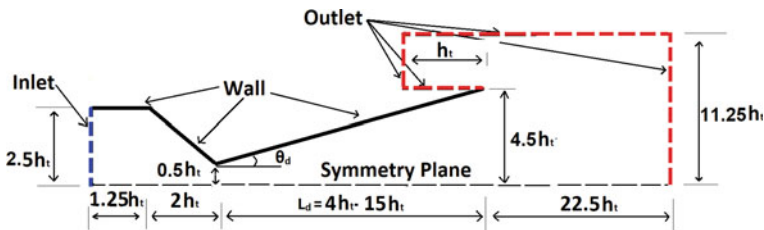


Fig. 1 Computational domain

3.1 Validation

The current numerical methodology has been validated with the experimental results of Hao et al. [12] where the experimental mass flow rate of the 20 μm nozzle was compared with the DSMC results for different back pressures ranging from 0 to 90 kPa. The inlet of the micro-nozzle is kept at 100 kPa and 300 K. For all the simulations, a constant wall temperature of 300 K is maintained. The maximum deviation of the numerical mass flow rate from the experimental results is found to be less than 2%. The numerically validated mass flow rate is shown in Fig. 2, and details of the experiment are shown in Table 1.

Fig. 2 Comparison of mass flow rate with experimental result of Hao et al. [12]

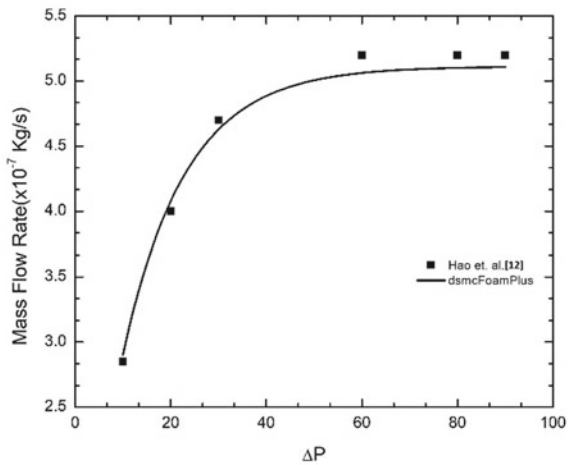


Table 1 Summary of the experimental methods

S. No.	Details	Hao et al. [12]
1	Methodology	Measurement of pressure and mass flow rate
2	Nozzle dimensions	$h_t = 20 \mu\text{m}$ expansion ratio = 1.7
3	Type of nozzle	Rectangular nozzle
4	Pressure and temperature	$P_i = 100 \text{ kPa}$, $P_e = 0\text{-}100 \text{ kPa}$, inlet and wall temperature = 300 K
5	Test gas	Air
6	Measured parameters	Mass flow

4 Results and Discussion

The present study is carried out on a $2\ \mu\text{m}$ h_t 2D micro-nozzle by varying divergence angle ($15\text{--}45^\circ$), in the absence and presence of carrier gas N_2 and Kr , for two exit back pressures condition 0 and 30 kPa. At the inlet of the nozzle, an equimolar mixture of Ar and He is applied at a pressure of 120 kPa and 300 K. Walls are assumed as fully diffuse and kept at 300 K temperature. The mole fraction of argon (X_{Ar}) is defined as.

$$X_{\text{Ar}} = \frac{n_{\text{Ar}}}{n_{\text{Ar}} + n_{\text{He}}} \tag{2}$$

4.1 Divergence Angle Study

The effect of divergence angle for a constant expansion ratio is studied with different divergence angles 15, 30, and 45° for micro-nozzle having $h_t = 2\ \mu\text{m}$. The expansion ratio is defined as the ratio of outlet to throat width. The length of the divergent section has been varied to maintain a constant expansion ratio. Inlet pressure of 120 kPa and hard vacuum at exit are maintained for all simulations. Figure 3 shows the centreline mole fraction of Ar for the three cases. The highest mole fraction is observed for the higher divergence angle. The peak value shifted more downstream of the throat as the divergence angle increased. No significant differences are observed in the convergent part of the micro-nozzle. Considerable enhancement in Ar mole fraction is noticed for the 45° towards the exit. Since the expansion ratio is kept constant, the length of the divergent section varies for the three cases.

Fig. 3 Ar mole fraction along the centreline for micro-nozzles having different divergence angles 15, 30, and 45°

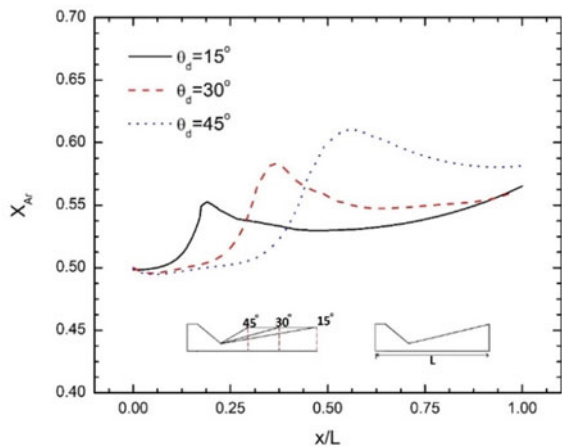
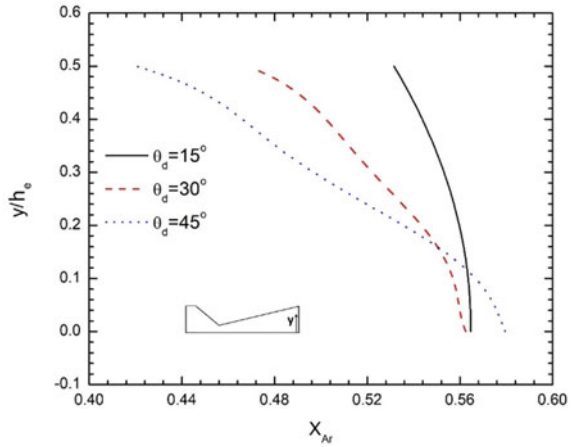


Fig. 4 Ar mole fraction along the vertical plane at exit for micro-nozzles having different divergence angles 15, 30, and 45°



The higher length of the 15° nozzle promotes more velocity slip and separation towards the exit. Figure 4 shows the Ar concentration at the exit vertical plane for the three cases. For the 45° divergent angle, wall deflection is more, resulting in higher lateral separation effects. The curvature of the streamlines is higher; the heavier molecules cannot bend so easily and therefore remains in the axis region.

Figure 5 shows the stream lines for Ar and He species. The bending of the He streamlines was found to be higher compared to Ar, and the deviation is more visible at the outlet of the micro-nozzle. The highest bending of the stream lines in the 45° nozzle creates higher pressure gradient towards the centre of the nozzle, and as a result, 45° nozzle shows highest Ar concentration.

The Ar mole fraction contour shown in Fig. 6 indicates the clear separation of the species. The maximum Ar mole fraction is observed to be 0.69, and it is located near the axis of the nozzle.

The Mach contour shown in Fig. 7 indicates that the exit Mach number is highest in the 45° nozzle. If higher the exit velocity, velocity slip will also be higher and which will facilitate the increased mole fraction of heavier species [6, 10]. More subsonic layer is found to be covered in the divergent section of the 15° nozzle, causing a reduction in the average Mach number.

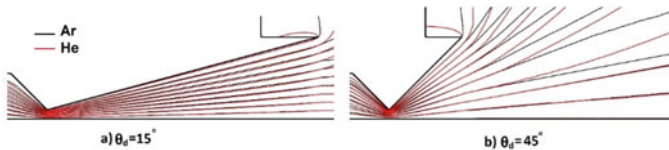
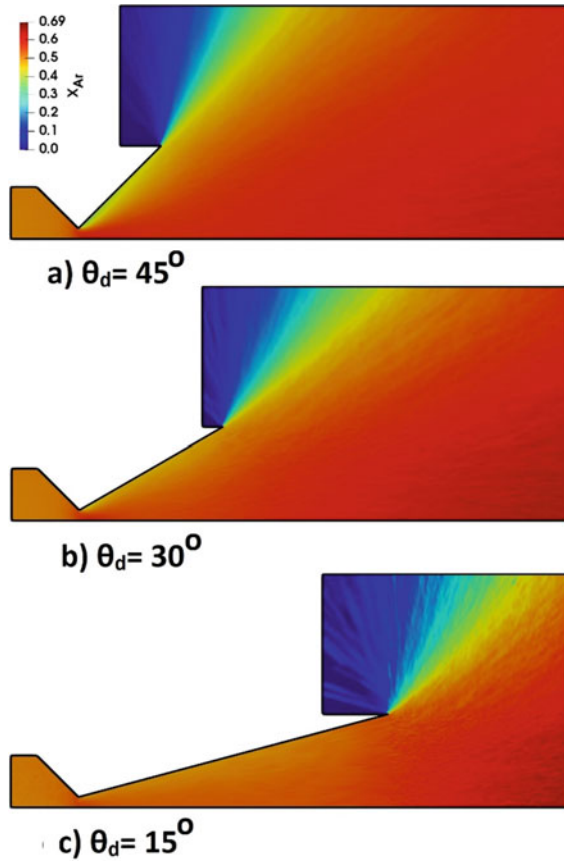


Fig. 5 Ar and He streamlines for micro-nozzles having different divergence angles

Fig. 6 Ar mole fraction contour for micro-nozzles having different divergence angles 15, 30, and 45°



4.2 Carrier Gas Study

To study the effect of carrier gas on species separation, a third gas is introduced along with helium and argon. Nitrogen is selected as the carrier gas as it has molar mass between He and Ar. Different simulations are conducted with varying percentages of carrier gas, such as 0, 33, 70, and 90%. Inlet pressure of 120 kPa and hard vacuum at exit are maintained for all simulations. The normalised argon mole fraction on a vertical plane at a distance of $2h_t$ from the nozzle exit is plotted and is shown in Fig. 8. Normalised Ar mole fraction is defined as

$$X_{n,Ar} = \frac{n_{Ar}}{(n_{Ar}) + (n_{He})_{inlet}} \tag{3}$$

The introduction of carrier gas has decreased the species separation effect at the nozzle exit. As the percentage of N_2 increases, the species separation is reduced at

Fig. 7 Mach contour for micro-nozzles having different divergence angles 15, 30, and 45°

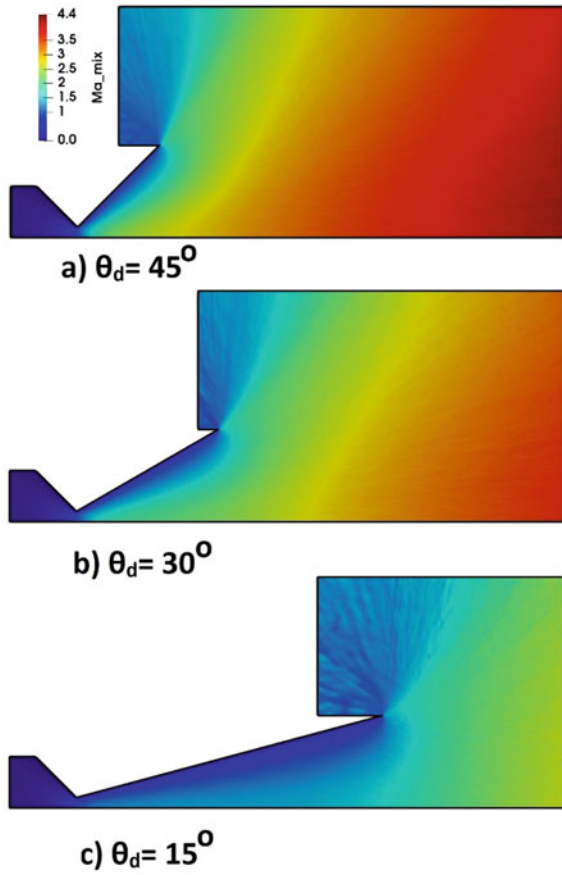


Fig. 8 Micro-nozzle axis argon and helium mole fraction for linear nozzle with N₂ as carrier gas

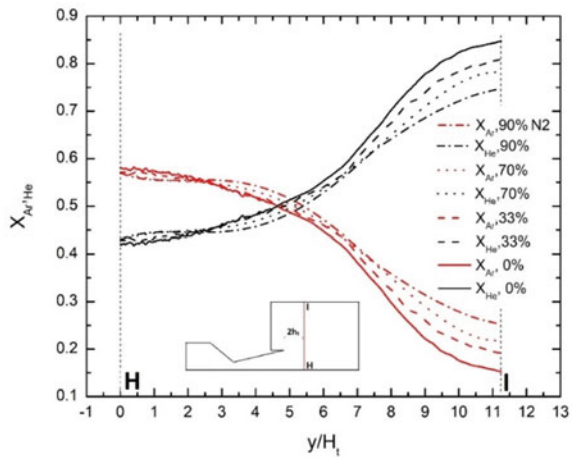
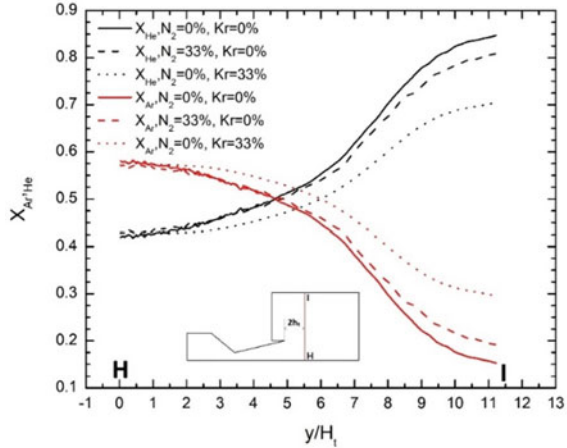


Fig. 9 Micro-nozzle axis argon and helium mole fraction for linear nozzle with Kr and N₂ as carrier gas



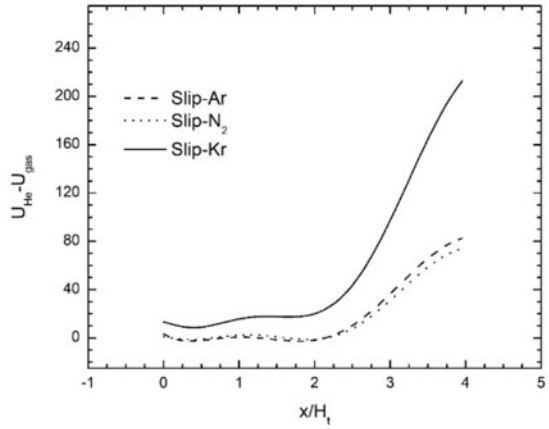
the exit of the domain. Simulations are conducted with a heavier carrier gas such as krypton (Kr), and the results are shown in Fig. 9. As the carrier gas becomes heavier, the species separation is suppressed. Krypton is almost heavier by two times Ar and 20 times He. Adding a heavier component reduces the lateral separation effect due to the low turning of streamlines. Lower species streamline divergence is noticed with heavier carrier gas.

Figure 10a shows the difference in velocity (slip velocity) between He and other heavier species along the nozzle axis and Fig. 10b indicates a representative streamline for different species. The slip velocity is highest when the difference in molecular weight is highest. There is more bending for the lighter gas (He) and least for the heavier gas (Kr). N₂ and Ar almost traced the same path because of the slight mass difference.

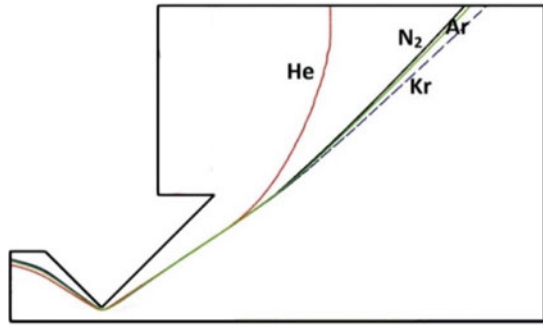
4.3 Back Pressure Study

The simulation was conducted with an inlet pressure of 120 kPa and exit pressures of 0 and 30 kPa to study the effect of back pressure on species separation. All the studies have been conducted on a 2 μm h_t micro-nozzle. The static mole fraction of Ar is measured on a vertical plane HI and is shown in Fig. 11. Near to the exit of the domain, the lower helium concentration is observed at higher back pressures. The species separation is found to be decreased with an increase in back pressure. The streamlines shown in Fig. 12 indicate the higher bending of the streamline at high back pressures. This will increase the pressure gradient towards the exit from the wall, causing heavier argon species to accumulate in this area. It may be the reason for the higher mole fraction of argon near the exit domain at 30 kPa compared to vacuum boundary conditions.

Fig. 10 a Slip velocity of helium and b bending of streamline for different species

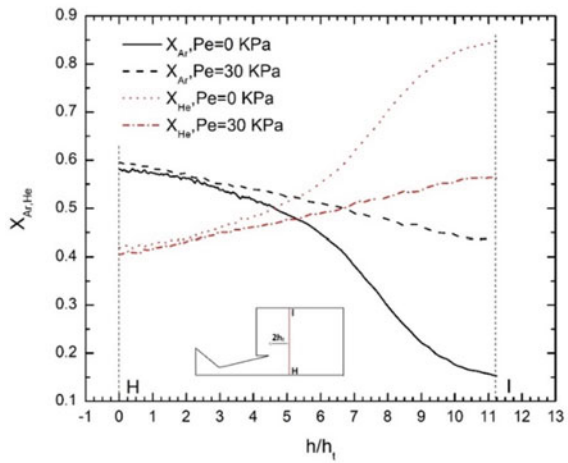


(a)



(b)

Fig. 11 Static mole fraction variation at the exit plane at two back pressure conditions (30 kPa and vacuum) for 2 μm h_t micro-nozzle



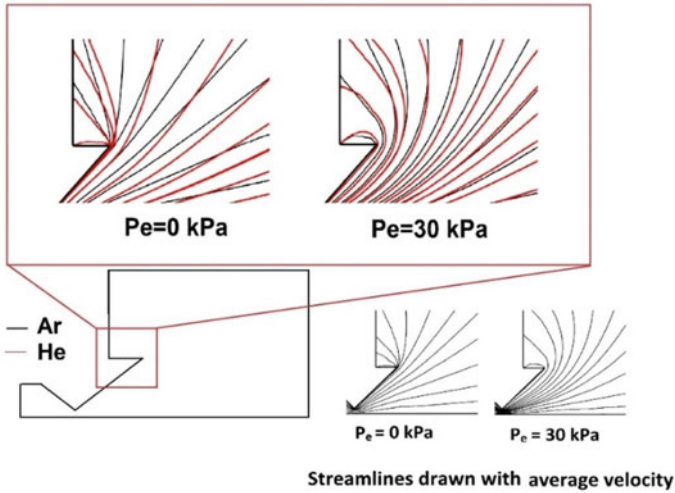


Fig. 12 He and Ar streamlines at the exit plane at two back pressure conditions (30 and 0 kPa) for $2 \mu\text{m } h_t$ micro-nozzle

5 Conclusions

The primary objective of the present computational study is to understand the binary separation characteristics of converging–diverging 2D planar micro-nozzles under various conditions. The effect of different divergence angle, nozzle back pressures and the impact of heavier carrier gas, etc., on the separation phenomenon are analysed. The study of aerodynamic separation of the binary equimolar mixture of argon and helium is done with Direct Simulation Monte Carlo approach. The DSMC approach is validated utilising experimental findings that are documented in the literature. The divergence angle of the nozzle is varied from 15 to 45° for vacuum exit boundary conditions. Krypton and nitrogen are used as the carrier gas to understand the effect of heavier gases on species separation. The highest centreline argon mole fraction is observed for the highest divergence angle (i.e. 45°) studied. The higher length of the 15° nozzle promotes more velocity slip and separation towards the exit. The argon concentration on the line HI at a distance $2h_t$ from the exit of the nozzle found to be decreasing with increase in carrier gas nitrogen concentration. Due to the higher mass of krypton, the species separation is further suppressed. The species separation is found to be decreased with an increase in back pressure.

Nomenclature

- h_t Throat height [μm]
- X Static mole fraction

θ_d	Divergence angle ($^\circ$)
L_d	Divergence length [μm]
P	Pressure [Pa]
n	Number density [m^{-3}]
Kn	Knudsen number

References

- Schwan W, Fiebig M, Mitra NK, Chatwani AU (1985) Investigation of nonequilibrium effects in separation nozzles by Monte-Carlo simulation. In: Belotserkovskii OM, Kogan MN, Kutateladze SS, Rebrov AK (eds) *Rarefied gas dynamics*, vol 2. Springer US, Boston, MA, pp 1327–1339
- Guy TB (1975) Correlation of the probe-induced molecular separation effect in supersonic gas mixtures. *J Phys D Appl Phys* 8(18):2208–2223
- Chatwani AU, Fiebig M, Mitra NK, Schwan W, Bley P, Ehrfeld W, Fritz W (1981) Tracer Monte-Carlo simulation for an isotope separation nozzle. In: Fisher SS (ed) *Rarefied gas dynamics*, parts I and II, progress in astronautics and aeronautics, vol 74. AIAA, New York, pp 541–557
- Chatwani AU, Fiebig M (1981) Source expansion of monatomic gas mixtures. In: Fisher SS (ed) *Rarefied gas dynamics*, parts I and II, progress in astronautics and aeronautics, vol 74. AIAA, New York, pp 785–801
- Anderson JB, Malling GF (1981) Monte-Carlo simulation of isotope separation in opposed jets. In: Fisher SS (ed) *Rarefied gas dynamics*, parts I and II, progress in astronautics and aeronautics, vol 74. AIAA, New York, pp 598–606
- Sabouri M, Darbandi M (2019) Numerical study of species separation in rarefied gas mixture flow through micronozzles using dsmc. *Phys Fluids* 31:042004
- Kosyanchuk V, Yakunchikov A (2021) Separation of a binary gas mixture outflowing into vacuum through a micronozzle. *Phys Fluids* 33:082007
- Kosyanchuk V, Yakunchikov A (2022) Aeroseparation of gas mixture during supersonic outflow in vacuumed reservoir with skimmer. *Vacuum* 199:110959
- Bykov NY, Zakharov VV (2022) Rarefied gas mixtures with large species mass ratio: outflow into vacuum. *Phys Fluids* 34:057106
- Sukesan MK, Shine SR (2022) Effect of back pressure and divergent section contours on aerodynamic mixture separation using convergent–divergent micronozzles. *AIP Adv* 12:085207
- White C, Borg MK, Scanlon TJ, Longshaw SM, John B, Emerson DR, Reese JM (2018) DsmcFoam+: an openFoam based direct simulation Monte Carlo solver. *Comput Phys Commun* 224:22–43
- Hao P-F, Ding Y-T, Yao Z-H, He F, Zhu K-Q (2005) Size effect on gas flow in micro nozzles. *J Micromech Microeng* 15:2069

The Effect of Hot Gas Injection on Thrust Vector Control in a Double-Divergent Nozzle—A Numerical Investigation



B. S. Bijo and S. Kumar Ranjith

1 Introduction

A nozzle is a device, which is a specially designed tube through which the combustion products flow. Commonly, rockets use a convergent-divergent nozzle to create thrust. Often, these nozzles are designed for a fixed expansion ratio, thereby it gives an optimum performance only at particular altitude. During the ascent, the ambient pressure reduces continuously, thereby over expansion and under expansion occur sequentially. In order to avoid such conditions, altitude adapting nozzles such as a dual bell nozzle, extendable nozzle, and double-divergent nozzle are used. These nozzles have good performance and can be used for single stage rockets. A planar double-divergent nozzle is an altitude adaptive nozzle which is simple in construction and have rectangular cross section.

Direction or path control is essential for rockets, and a thrust vector control mechanism is used for controlling the flight path. Here, the core jet flow is deflected from the main axis to accomplish the vectoring. Typically, jet vanes, jetavators, and hinged nozzle are conventionally used as thrust vector control (TVC) methods. These mechanically operated systems have some drawbacks such as high mass, less durable, and high energy consumption. Fluidic thrust vectoring (FTV) is the one of the effective alternative for the attitude control. It has no mechanical moving parts and has less weight. Secondary injection thrust vector control is a type of FTV, in which a secondary fluid is injected to the main flow to create lateral force by deflecting the core flow. Secondary injection thrust vector control (SITVC), counter flow, Coanda effect, and throat skewing are different type of fluid thrust vectoring approaches. Various FTV techniques in 2D convergent-divergent nozzle were investigated by Deere et al. [10] to shed light into the problem.

B. S. Bijo (✉) · S. Kumar Ranjith
Micro/Nanofluidics Research Laboratory, Department of Mechanical Engineering, College of Engineering Trivandrum, Thiruvananthapuram, Kerala 695016, India
e-mail: bijobaijus@gmail.com

Among these techniques, secondary injection thrust vector control is an effective technique and has less space requirement. Several studies were conducted to understand the effect of SITVC. Many analytical, experimental, and computational studies were conducted in conventional nozzle [3, 9]. Spaid et al. [12] proposed a model called bluff body and found that secondary injection into a supersonic flow created a bluff body flow. Zmijanovic et al. [11] and Sellam et al. [8] conducted both experimental and numerical studies to evaluate the SITVC performance. These studies reported that, SITVC requires costly equipment, and also large vibration is created due to strong shock formation.

Meanwhile, numerical methods provided great insight into the flow characteristics at microscopic level. Initially, Balu et al. [2] estimated the performance parameters by solving Euler equation. Dhinagram and Bose [4] did the simulations using Euler and Navier–Stokes equation in a conventional CD nozzle and noted that Navier–Stokes equations have better accuracy. Later et al. [5] conducted a performance analysis by solving 3D Navier–Stokes equation with Bladwin Lomax turbulence model and $k-\epsilon$ turbulence model. Thereafter, Salehifar et al. [7] conducted a numerical study of hot gas injection thrust vector control (HGITV) in a three-dimensional convergent-divergent nozzle using $k-\omega$ SST turbulence model. Waithe and Deere [10] performed both computational and experimental studies to investigate the effect of multiple injection. Recently, Lee et al. [6] introduced the application of hydrogen peroxide (H_2O_2) to a liquid injection thrust vector control (LITVC) system for a hybrid rocket.

Although there are various research works carried out on the performance of SITVC on convergent-divergent or dual-bell nozzles, however, studies on the planar double-divergent nozzle are minimal. Thereby, the current study is conducted to understand the effect of hot gas injection on TVC in a planar double-divergent nozzle. Here, various influencing parameters are secondary pressure ratio, the injector location, injector angle, nozzle inflection angle, and the type of injectant on SITVC performance.

2 Methodology

2.1 Governing Equations

The field variable in the computational domain is solved using continuum-based mass, momentum, and energy balance equations by assuming the flow is compressible, steady, turbulent, and two-dimensional (2D). To properly capture the laminar to turbulent transitional behavior, that occurs while the fluid moves from converging to diverging section, a turbulent model also is used. Further, the continuity equation is written as

$$\frac{\partial}{\partial x_i}(\rho u_i) = 0$$

where ρ is the density and U is the time averaged velocity. Next, the RANS equation is

$$\frac{\partial}{\partial x_j}(\rho u_i u_j) = -\frac{\partial P}{\partial x_i} + \frac{\partial}{\partial x_j} \left[\mu \left(\frac{\partial u_i}{\partial x_j} + \frac{\partial u_j}{\partial x_i} - \frac{2}{3} \delta_{ij} \frac{\partial u_l}{\partial x_l} \right) \right] + \frac{\partial}{\partial x_j} \left(-\overline{\rho u'_i u'_j} \right)$$

where μ is the viscosity and P is the static pressure. The temperature field is obtained from the energy equation

$$\frac{\partial}{\partial x_i} [u_i (\rho E + P)] = \frac{\partial}{\partial x_j} \left[\left(k + \frac{c_p \mu_t}{0.85} \right) \frac{\partial T}{\partial x_j} + u_i (-\overline{\rho u'_i u'_j}) \right]$$

where T is the local temperature, k is the thermal conductivity, C is the specific heat of the fluid, and u' is the fluctuating quantity. The turbulence modeling is conducted using k - ω SST model and transition k - k_1 - ω models. The transport equations for transition k - k_1 - ω are given below. The turbulent kinetic energy is represented as

$$\frac{\partial(\rho u_j k_T)}{\partial x_j} = \rho(P_{kT} + R + R_{\text{NAT}} - \omega k_T - D_T) + \frac{\partial \left[\left(\mu + \frac{\rho \alpha T}{\sigma_k} \right) \frac{\partial k_T}{\partial x_j} \right]}{\partial x_j}$$

while the laminar kinetic energy is obtained from

$$\frac{\partial(\rho u_j k_L)}{\partial x_j} = \rho(P_{kL} - R - R_{\text{NAT}} - D_L) + \frac{\partial \left(\mu \frac{\partial k_L}{\partial x_j} \right)}{\partial x_j}$$

Further, the specific dissipation rate is given by

$$\frac{\partial(\rho u_j \omega)}{\partial x_j} = \rho \left[C_{\omega 1} \frac{\omega}{k_T} P_{kT} + \left(\frac{C_{\omega} R}{f_w} - 1 \right) \frac{\omega}{k_T} (R + R_{\text{NAT}}) \right] + \rho \left[-C_{\omega 2} \omega^2 + C_{\omega 3} f \omega \alpha_T f_w^2 \frac{\sqrt{k_T}}{d^3} \right] + \frac{\partial \left[\left(\mu + \frac{\rho \alpha T}{\alpha \omega} \right) \frac{\partial \omega}{\partial x_j} \right]}{\partial x_j}$$

where k_T and k_L are turbulent and laminar kinetic energy and R and R_{NAT} are the bypass and natural transition. Moreover, P_{kT} and P_{kL} are the production rate of turbulent and laminar kinetic energy. Furthermore, D_T and D_L are the near wall

dissipation terms, where f_ω and α_T is the kinematic damping function and turbulent scalar diffusivity. Note that, the simulation parameters selected are $C_{\omega 1} = 0.44$, $C_{\omega 2} = 0.92$, $C_{\omega 3} = 0.3$, and $C_{\omega R} = 1$.

2.2 Validation

A validation study was conducted on a CD nozzle with secondary injection to check the accuracy of numerical procedure. Here, RANS and eddy viscosity models are used to simulate a CD nozzle with fluidic injection. The wall pressure distribution from the simulation is shown in Fig. 1. The experimental data is extracted from Waithe et al. [10] and is compared with the numerical simulation. The numerical result is in close agreement with the experimental results. Suitability of transition $k-k_1-\omega$ turbulence model is demonstrated, and this model is used for further investigations.

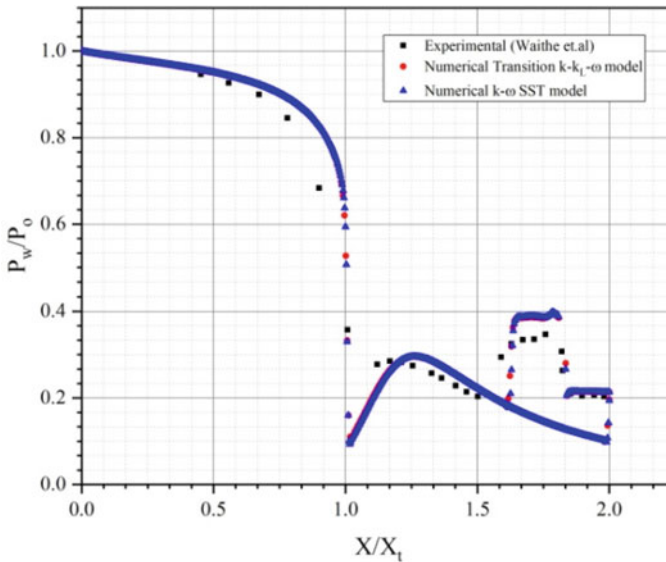


Fig. 1 Comparison between experimental data for static pressure distribution [10] and numerical results. Note that X_t is the throat length of nozzle, and P_w is the wall pressure. Here, the injector location is $X_i/L = 0.9$, nozzle pressure ratio = 4.6, and secondary pressure ratio = 0.7

3 Secondary Injection in DDN

3.1 Nozzle Geometry and Computational Domain

The computational domain and the nozzle geometry are shown in Fig. 2. The DDN geometry for the current study is taken from the paper of Arora et al. [1], and the dimensions are shown in the figure. The length of the base nozzle is 55 mm and extension nozzle is 45 mm. The total length of diverging section is denoted as L_d as well as horizontal distance between injection port and nozzle throat is taken as X_i . The area ratio of nozzle exit to the throat is 3.6, and area ratio of inflection point to throat is 1.4.

In this study, the injector is placed at four different locations ($X_i/L_d = 0.55, 0.65, 0.75,$ and 0.85) to study its effect L_d on thrust vectoring. The effect of inflection

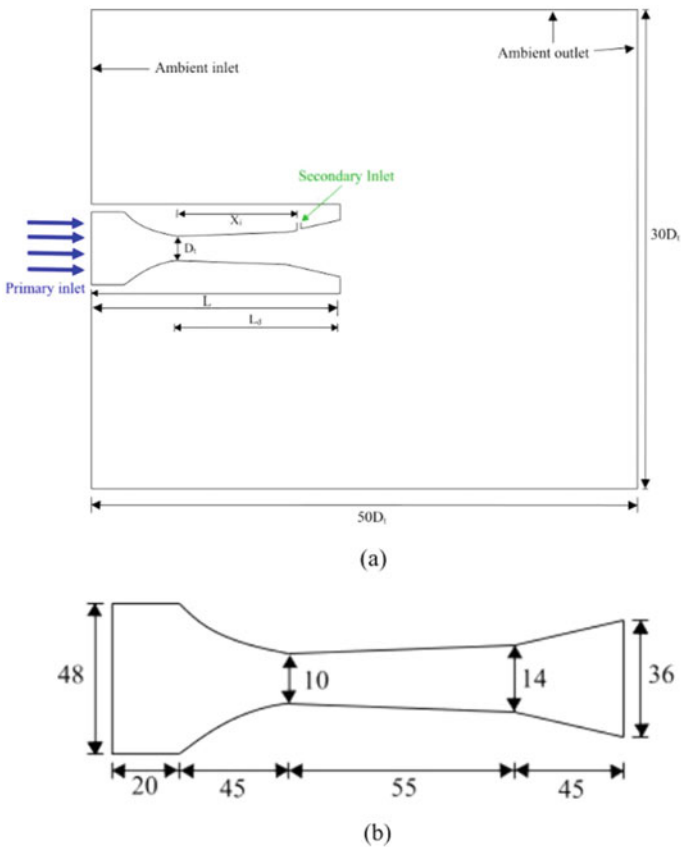


Fig. 2 a Computational domain and the nozzle geometry. b Enlarged view of the DDN (all dimensions are in mm)

Table 1 Wall static pressure for different grid size

No.	Grid size	First cell height	$\left(\frac{P_w}{P_0}\right) \frac{A=1.1}{A}$
1	150 × 500	3.08×10^{-4}	0.285
2	250 × 550	1.4×10^{-4}	0.327
3	300 × 585	1×10^{-5}	0.350
4	400 × 650	9×10^{-5}	0.389
5	500 × 700	7.2×10^{-5}	0.391

Table 2 Boundary conditions

NPR	SPR				
	0.3 (bar)	0.4 (bar)	0.5 (bar)	0.6 (bar)	0.7 (bar)
4	1.2	1.6	2	2.4	2.8
4.5	1.35	1.8	2.25	2.7	3.15
5	1.5	2	2.5	3	3.5

angle was studied with different angles $\theta = 8.76^\circ$, 11.7° , and 15.68° . Furthermore, the injection angles ($\theta_{inj} = 45^\circ$, 90° , and 135°) are varied to study its effect on thrust vectoring.

ANSYS meshing software is used to mesh the computational domain with structured rectangular elements, the physics preference is CFD, and the solver preference is Fluent. To obtain effective mesh, a grid-independent study is conducted on five different grid sizes which are shown in Table 1. By comparing the experimental and numerical results of pressure ratios, the fourth set (400×650) has an accurate result with lower computational time. Hence, this mesh is used for further examinations.

This study is carried out with three different nozzle pressure ratios (NPR). The outlet boundary is considered as ambient condition with pressure 1 bar and temperature 300 K. The boundary conditions chosen for the simulation are shown in Table 2. The pressure inlet is given to the secondary fluid inlet.

3.2 SITVC Performance Parameters

In this study, several parameters are used to evaluate SITVC performance of DDN. Firstly, an important simulation parameter is secondary pressure ratio (SPR), which is the ratio of stagnation pressures of secondary and primary fluids.

Thrust ratio: It is the ratio between lateral force (F_y) and axial force (F_x). Figure 3 shows the schematic diagram of axial and lateral forces and the deflection angle.

$$TR = \frac{F_y}{F_x} \quad (7)$$

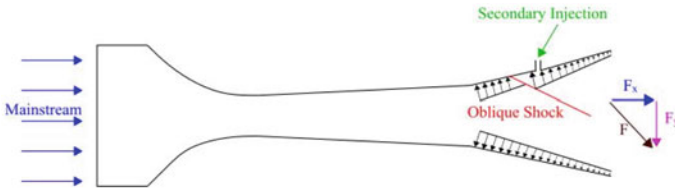


Fig. 3 Schematic of pressure variation along the nozzle wall with secondary injection

Thrust angle/deflection: It represents the core flow deviation with respect to the axial coordinate.

$$\delta = \tan^{-1} \frac{F_y}{F_x} \tag{8}$$

4 Results and Discussion

In this section, the numerical simulation of the hot gas injection in double-divergent nozzle and the SITVC performance under various working conditions are discussed.

4.1 Effect of Injectant

At first, the effect of different types of injectants on lateral force generation is examined in this section. For a given injection location, the effect of injectant on SITVC performance is discussed. For a given NPR, different injectants are used as secondary fluid for different SPRs. The simulation was carried out using H₂O₂, LOX/LH₂, and LOX/RP₁ propellants. The variation of thrust ratio and thrust angle with respect to SPR is shown in Fig. 4. Hydrogen peroxide shows more effective in producing lateral thrust. Hence, H₂O₂ is used as working fluid in remaining studies. The shock strength is noted to be higher for hydrogen peroxide than other hot gases. It is observed that, the temperature of injectant also influences vectoring. If the temperature raised, the vectoring performance is found to be decreased.

4.2 Effect of NPR and SPR

Next, the influence of injection pressure on SITVC performance for a given injection position is explored. The Mach contour for the flow field at SPR = 0.3 and 0.7 is shown in Fig. 5. Note that, the injector is placed at $X_i/L_d = 0.85$. Here, the

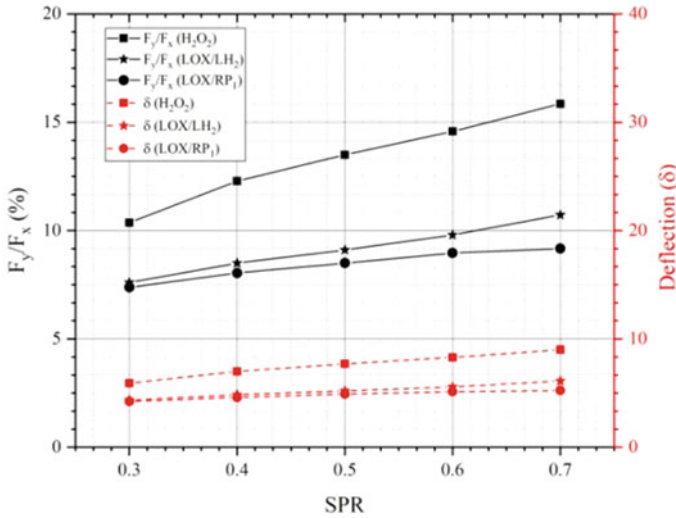


Fig. 4 Effect of propellant on thrust vectoring

injection pressure has a considerable influence on the core flow deflection; as the secondary injection pressure increases, the flow deflects further. As the injection pressure rises, the oblique and separation shocks shift upstream, thereby the shock strength increased. Owing to the increased injection pressure and consequent rise in oblique shock strength, the Mach disk created in the downstream injector grows stronger, see Fig. 5.

Figure 6 shows the variation of thrust ratio and thrust angle with injection pressure. When the injection pressure increases, the shock strength enhanced; hence, a pressure imbalance is created between upper and lower walls; subsequently, the lateral force is improved. In case of elevated NPRs, the axial force is increased considerably and lateral force generation is lowered. Thus, the deflection is noted to be reduced as NPR increased.

4.3 Effect of Injection Location

Effect of injection location is studied by placing injector at different location in the diverging section of DDN. Figure 8 shows the flow field of injector location at $X_i/L_d = 0.55$ and $X_i/L_d = 0.85$ for a constant NPR = 5 and SPR = 0.7. When the injector is placed near to the exit, the deflection is maximum. The penetration of secondary fluid into primary fluid is more when the injector placed in downstream location. If the injector is placed upstream, near to the inflection point there is chance of shock reflection, which indeed adversely affects the thrust vectoring performance.

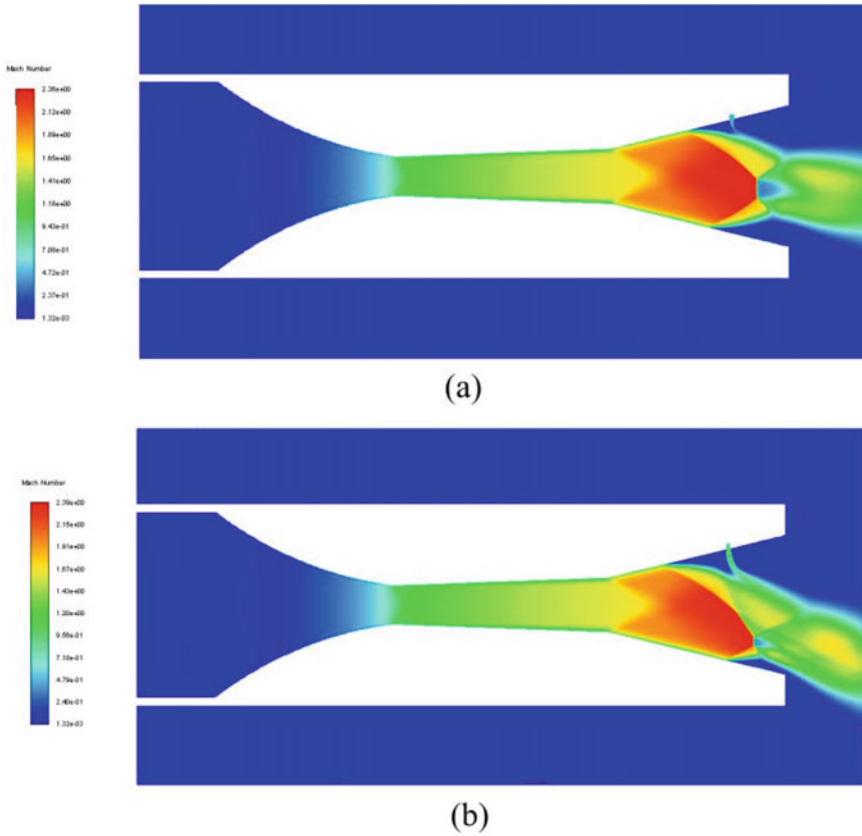


Fig. 5 Comparison of Mach contour for different SPRs **a** SPR = 0.3, **b** SPR = 0.7

The variation of deflection and thrust ratio with respect to the injector position is shown in Fig. 8. Here, as injector is moving downstream direction the thrust ratio and deflection is increased along with the lateral force. While the injector is in the upstream region, negative thrust vectoring is occurred due to the shock reflection.

4.4 Effect of Injection Angle

Finally, the influence of the secondary injector angle (θ_{inj}) with respect to the nozzle axis is investigated. The Mach contour is obtained when injection angles $\theta_{inj} = 45^\circ$ and 135° are shown in Fig. 9. As the injection angle increases, the location of separation shock advanced. And also the bow shock formed near the injection port is bent more toward the lower wall. In addition, the thrust ratio and thrust angle increased with increase in angle.

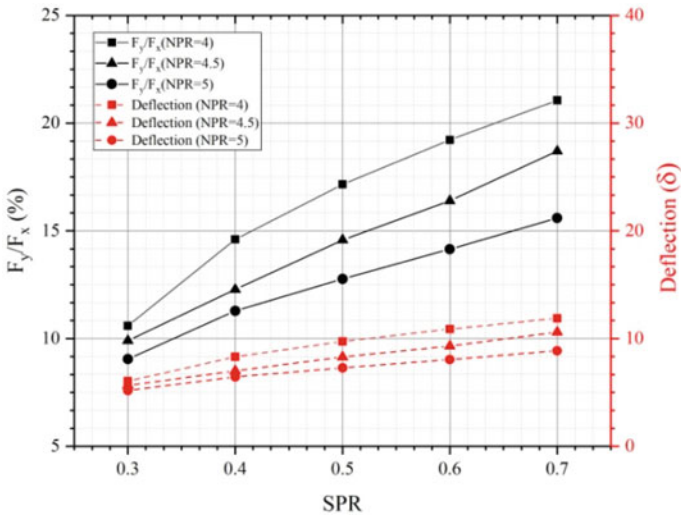


Fig. 6 Effect of NPR and SPR on thrust ratio and thrust angle

At higher angles, elevated flow obstruction is created and shock strength increased. Figure 10 shows the variation of thrust angle and thrust ratio due to the influence of injection angle. It is evident that as injection angle increased, the deflection is enhanced (Fig. 7).

4.5 Effect of Inflection Angle

This section discusses about the effect of inflection angle on thrust vectoring performance. Figure 11 shows the Mach contours for $\theta = 8.76^\circ$ and 15.68° . As the angle increases, the separation shock moves upstream and the shock strength is increased. The size of primary upstream vortex region increased and flow separation is raised. Therefore, more deflection is created at high inflection angles. Figure 12 shows the variation of thrust ratio and deflection for three different inflection angles. Here, the deflection as well as the thrust ratio is increased with rise in inflection angle. Most importantly, when inflection angle increases, the side force also is noticed to be improved.

5 Conclusions

A numerical analysis was performed to evaluate the thrust vector control by hot gas injection in a DDN. The findings are enlisted below.

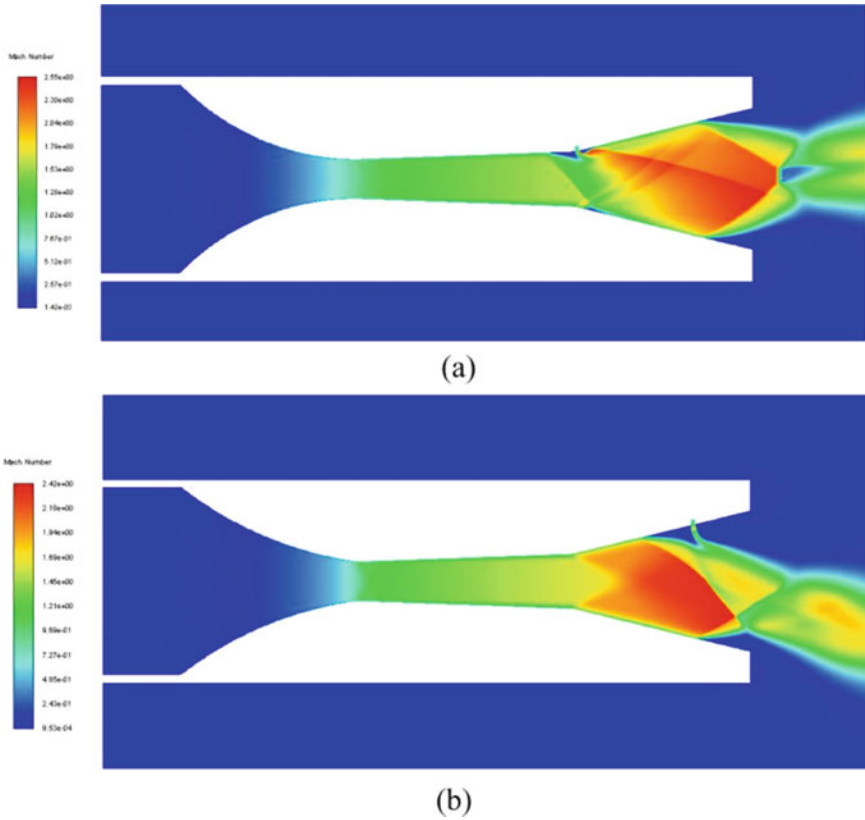


Fig. 7 Mach contour comparison **a** $X_i/L_d = 0.55$, **b** $X_i/L_d = 0.85$

- By comparing the effect of propellant type on SITVC performance, it is found that H_2O_2 is having better efficiency than its counterparts.
- To obtain high lateral thrust, the injection pressure should be increased, which in turn gives high shock strength and good vectoring performance.
- The injector needed to be placed in downstream region to avoid shock reflection and to get maximum deflection.
- High injection angles create elevated obstruction to the core flow and its help to achieve enhanced deflection.
- Furthermore, as the inflection angle increases the vectoring performance also found to be improved.

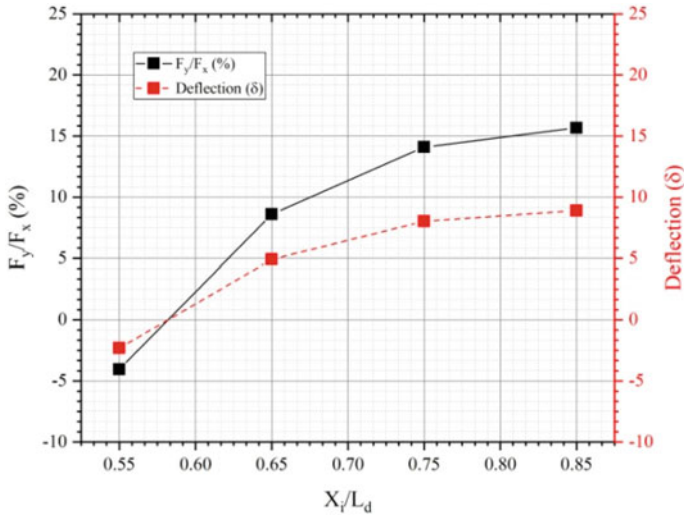


Fig. 8 Variation of thrust ratio and deflection with injector position

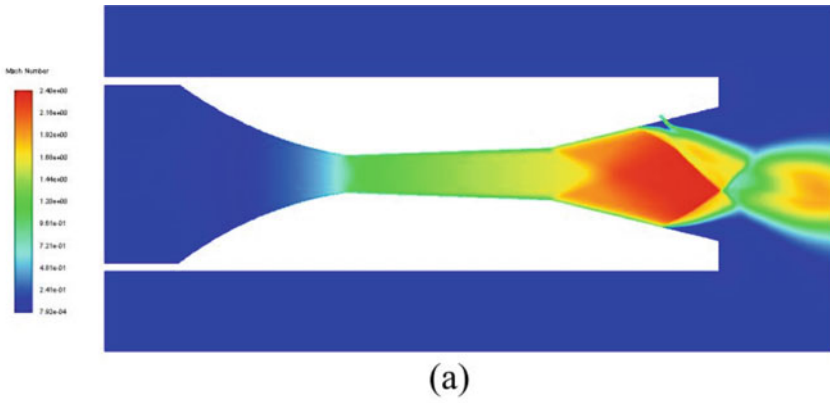


Fig. 9 Mach contour comparison **a** $\theta_{inj} = 45^\circ$, **b** $\theta_{inj} = 135^\circ$

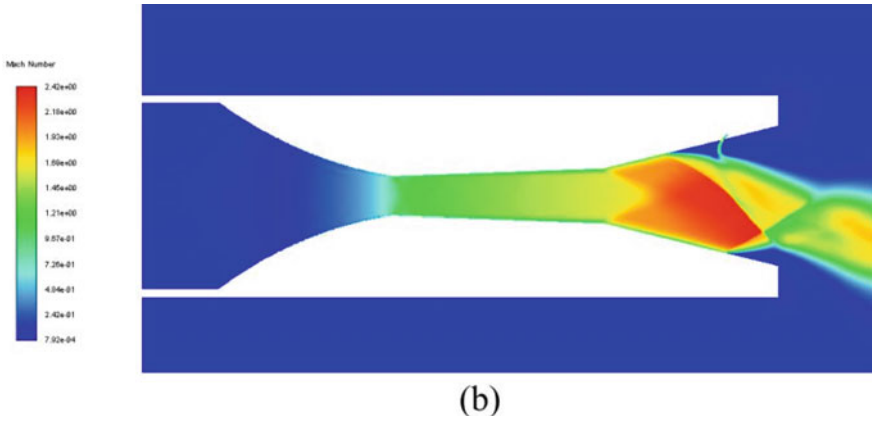


Fig. 9 (continued)

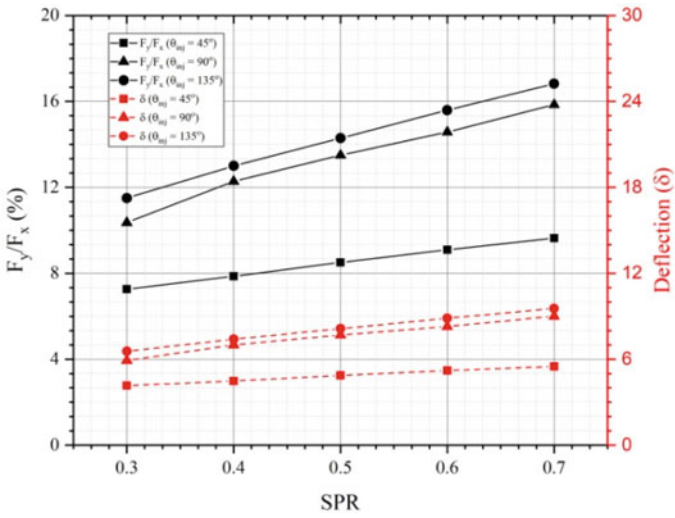
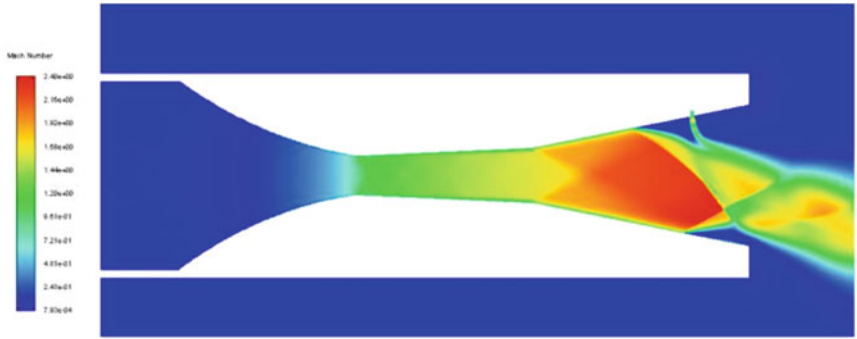
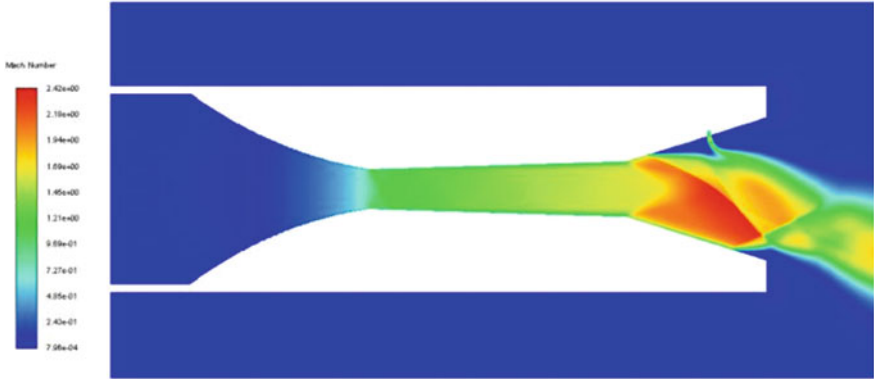


Fig. 10 Effect of injection angle



(a)



(b)

Fig. 11 Mach contour **a** $\theta = 8.76^\circ$, **b** $\theta = 15.68^\circ$

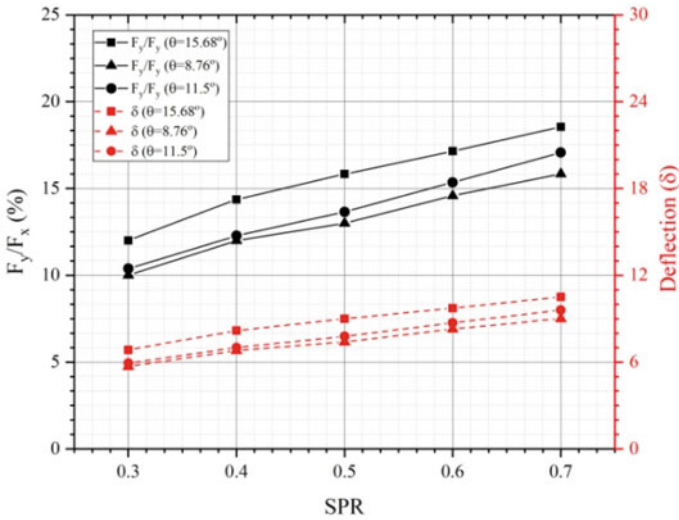


Fig. 12 Influence of inflection angle on thrust ratio and thrust angle

Nomenclature

- 2D Two dimension
- 3D Three dimension
- A Cross-sectional area [m^2]
- c Specific heat of fluids
- F Force [N]
- k_T Turbulent kinetic energy [J/kg]
- k_L Laminar kinetic energy (J/kg)
- P Pressure [Pa]
- T Temperature [K]
- TR Thrust ratio
- t Time [s]
- μ Dynamic viscosity [kg/m s]
- $^p k_T$ Production of turbulent kinetic energy
- $^p k_L$ Production of laminar kinetic energy
- R Bypass transition
- $^R NAT$ Natural transition

References

1. Arora R, Vaidyanathan A (2015) Experimental investigation of flow through planar double divergent nozzles. *Acta Astronautica*: 200–216
2. Balu R, Marathe AG, Paul PJ, Mukunda HS (1991) Analysis of performance of a hot gas injection thrust vector control system. *J Propul Power* 7(4):580–585
3. Choi J, Moon T, Choi J, Park S, Kim H, Huh H (2018) Technology and patent trends of altitude compensation nozzles. *J Korean Soc Aeronaut Space Sci* 46(8):662–670
4. Dhinakaran R, Bose T (1996) Comparison of Euler and Navier-Stokes solutions for nozzle flows with secondary injection. In: 34th aerospace sciences meeting and exhibit, p 453
5. Ko H, Yoon W-S (2002) Performance analysis of secondary gas injection into a conical rocket nozzle. *J Propul Power* 18(3):585–591
6. Lee E, Kang H, Kwon S (2019) Demonstration of thrust vector control by hydrogen peroxide injection in hybrid rockets. *J Propul Power* 35(1):109–114
7. Salehifar M, Tahani M, Hojaji M, Dartoomian A (2016) CFD modeling for flow field characterization and performance analysis of hgivc. *Appl Therm Eng* 103:291–304
8. Sellam M, Chpoun A, Zmijanovic V, Lago V (2012) Fluidic thrust vectoring of an axisymmetrical nozzle: an analytical model. *Int J Aerodyn* 2(2–4):193–209
9. Semlitsch B, Mihăescu M (2018) Fluidic injection scenarios for shock pattern manipulation in exhausts. *AIAA J* 56(12):4640–4644
10. Waithe K, Deere K (2003) An experimental and computational investigation of multiple injection ports in a convergent-divergent nozzle for fluidic thrust vectoring. In: 21st AIAA applied aerodynamics conference, p 3802
11. Zmijanovic V, Leger L, Depussay E, Sellam M, Chpoun A (2016) Experimental–numerical parametric investigation of a rocket nozzle secondary injection thrust vectoring. *J Propul Power* 32(1):196–213
12. Zukoski EE, Spaid FW (1964) Secondary injection of gases into a supersonic flow, *AIAA J* 2(10):1689–1696

Study and Computational Analysis of RS-25 Engine's Nozzle and Find Out Data of RS-25 Engine



Jaykumar I. Adalja, Krutarth T. Soni, Mehul K. Rana, and Jignesh R. Vala

1 Introduction

A nozzle is a device designed to control the direction of exit flow or characteristics of a fluid flow (especially increase velocity) as it exits (or enters) an enclosed chamber. The nozzle is delivered or propelled combustion products at high-speed pressure, and the temperature is lower at the exit section to the high supersonic velocities. Pressure and temperature difference is the main key factor of the nozzle due to delivering high velocity at the exit part. In 1890 Carl Gustaf Patrik developed a de Laval convergent-divergent nozzle, a design he created that has the ability to deliver a steam jet to a supersonic stage [1]. This nozzle was termed a de Laval nozzle and was later widely used for rocket propulsion. An American engineer Robert Goddard was the first to integrate or developed such a high-level de Laval nozzle with a combustion chamber, in a combustion chamber two different types of liquid come together such as high pressure and generate pressure at a higher level, thereby increasing the velocity value and decreasing pressure and temperature at the exit part, so due to this, rocket efficiency is increasing and attaining the supersonic velocities in the region of Mach 7 or some case; it is a possibility to above this [2]. Rocket engine generally starts from a combustion chamber (there is a lot of component and system above the combustion chamber such as a compressor, impellor, pump, etc., but they are attached above the combustion chamber; these all are whole part of the engine but, generally some of it is not considered as part of the engine when especially working on the geometry and shape of the nozzle) and then throat and then after comes a massive divergent section. So, we can say that the rocket engine generated thrust itself accelerating gases outside and producing the desired power. That massive chemical process occurs in the combustion chamber and produces high temperature and pressure and then all

J. I. Adalja · K. T. Soni · M. K. Rana (✉) · J. R. Vala
Aeronautical Engineering Department, Sardar Vallabhbhai Patel Institute of Technology,
Vasad 388306, India
e-mail: mehulrana.aero@svitvasad.ac.in

accelerated toward a throat section; at this point, value of velocity Mach 1 must be achieved for getting maximum thrust, and further flow is reached at a divergent section and then exit to the atmosphere; there will be Mach value which is so high, and it may be supersonic or hypersonic Mach number [3].

Developing and designing a rocket nozzle is not easy, because there are so many complexities and challenging designs in curvature shape, and all things are connected perfectly based on the design and engine configuration. This is to be very helpful if the nozzle pressure ratio is too high, and the flow will reach a sonic value at the narrowest point (i.e., nozzle throat region) in the nozzle. Exit velocity is directly proportional to the square root of temperature.

$$M_e = \frac{V_e}{\sqrt{\gamma RT_e}}$$

In the combustion chamber, ratios of the fuel and oxidizer are to be fixed because there are the main ingredients of the engine and burning processes occurring in the chamber with maintained all parameters with the proper ratio of the propellants (generally all industries use fuel as liquid hydrogen and oxidizer as liquid oxygen). Some industries use rocket grade kerosine (RP-1), sue-cooled liquid methane, unsymmetrical di-methyl hydrazine (UDMH), monomethyl hydrazine (MMH), etc. [4].

RS-25 is one of the most powerful rocket engines ever created by humans. This engine's total length is 168 inches, and the diameter of the nozzle section is 96 inches. It performs very well at sea level as well as at vacuum level. Designed and manufactured in the United States by Rocketdyne (Later Pratt & Whitney Rocketdyne and Aerojet Rocketdyne), the RS-25 is a cryogenic engine; it uses liquid hydrogen as a fuel and liquid oxygen as an oxidizer, and this engine produces 1859 kN (lbf) thrust during lift-off (Fig. 1).

Furthermore, the specific impulse is 452 s (4.43 kN- sec/kg) in a vacuum and 366 s (3.59 kN-sec/kg) at sea level. It is capable of throttling 67% to 109% of its rated power level in one-percent increments. This engine was used in space shuttles in the early times, but now many modifications and many advanced features have been implemented by the company, and now this engine is used in next-generation missions such as the moon and further missions by NASA; moreover, now this engine's throttling capability is increasing 111–113%. And the most important thing is that it is a reusable engine, so it may reduce the total cost of the mission, so it is cost-effective. Some of the other details related to the RS-25 engine are mentioned in the materials and method section.

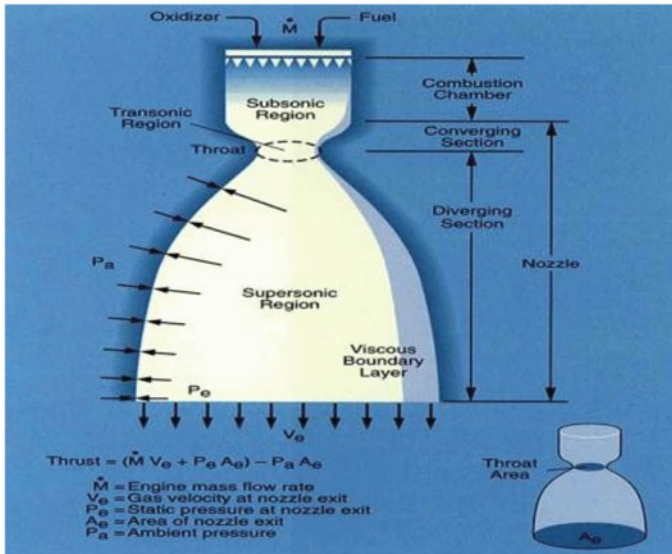


Fig. 1 Typical rocket nozzle section

2 Literature Review and Objective

K. P. S. S. Narayana and K. S. Reddy worked on a “simulation of convergent-divergent rocket nozzle using CFD analysis” in which they observed that by changing the quality of mesh and number of divisions (Nodes & Element), i.e., with refinement in mesh, Mach number is increased, and also pressure, temperature, velocity, density, and also shockwave are varied [5].

Y. R. Maddu, S. Saidulu, Md. Azeem and S. Jabiulla worked on “Design and fluid flow analysis of Convergent-divergent Nozzle” in which it was observed that pressure, temperature, velocity, density, and also variation in shockwave had been observed based on changes in the mesh quality and related iterations [6].

Chelouati, M., Jha, M. S., Galeotta, M., and Theilliol, D. (2021). “5th International Conference on Control and Fault-Tolerant Systems”. In recent years, liquid propulsion rocket engines (LPREs) have gained considerable attention for their reusability. LPRE combustion chambers are automatically evaluated for their remaining useful lives based on the cracking of their internal walls caused by thermo-mechanical stresses.

Using simulated data from a fictive LPRE engine model, this work develops an extended Kalman filter based on the simulated data. An approximate degradation model and actual sensor measurements are fused for failure prognostics [7].

Hötte, F., Sethe, C. V., Fiedler, T., Haupt, M. C., Haidn, O. J., and Rohdenburg, M. (2020). “Experimental lifetime study of regeneratively cooled rocket chamber walls”. Understanding the life-limiting mechanisms of regeneratively cooled rocket

combustion chambers can improve the safety, thrust-to-weight ratio, and cost efficiency of future rocket engines. This article discusses the life-limiting processes of creeping, yielding, abrasion, blanching, and thermal aging [8].

Z. X. He, W. J. Zhong, Q. Wang, Z. C. Jiang, Y. N. Fu, "An investigation of transient nature of the cavitating flow in injector nozzles". Additionally, numerical simulation has proved effective in understanding the flow characteristics of cavitating flows in nozzles, which impacts fuel atomization characteristics and subsequent combustion and exhaust emissions. Based on experimental injection rate data, a 3D simulation of nozzle cavitating flow was conducted using a moving mesh generation strategy [6].

Shin C. S., Kim H. D., Setoguchi T., et al. "A computational study of thrust vectoring control using dual throat nozzle". Furthermore, dual throat nozzles have become increasingly popular for thrust vectoring. There are two throats in the DTN, an upstream and a downstream minimum at the nozzle exit, separated by a cavity. In the computational analysis of dual throat nozzle performance at various secondary flow rates and nozzle pressure ratios, it was observed that computational work has been carried out [9].

Wang Y. S., Xu J. L., Huang S., et al. "Computational study of axisymmetric divergent bypass dual throat nozzle". Bypass dual throat nozzles (BDTN) and fluidic thrust vectoring nozzles (FTVN) descended from conventional dual throat nozzles (DTN). In addition to providing high thrust vectoring (TV) efficiency with low thrust loss, the BDTN does not require additional secondary flow. With axisymmetric divergent BDTNs (ADBDTNs), not only is TV efficiency high in pitch and yaw directions but also the flow adaptability of the BDTN means the engine can be operated at high performance without significantly changing its working state. Also discussed are the TV mechanism and effects of expanding ratio, bypass widths, and rounding radii at the throat and cavity bottom of the nozzle under vectored operation, which deflects the primary flow through the separation zone. Due to the high discharge coefficient and large pitch thrust vector angle, larger expansion ratios and rounding radii at the nozzle throat contribute to these characteristics. The thrust coefficient can be improved by reducing the expansion ratio and increasing the rounding radius at the nozzle throat. Increasing bypass width increases thrust and discharge coefficients, increasing pitch thrust vector angles, and increasing pitch thrust vector angles [10].

Dawei L., Jun H., Zhiqiang S., Jinzu J. Nevertheless, when designing and manufacturing these nozzles, achieving a smooth motion between the components while maintaining nozzle sealing poses a challenge. It was determined that spoilers would affect the jet mixing of lobed nozzles [11].

The principal model of the lobed nozzle was equipped with spoilers. In order to achieve the different widths of spoilers, the mixer tube was mounted with the same axial position, but the spoilers were mounted circumferentially. Numerical analysis was conducted to analyze what effect spoilers had on the jet mixing of lobe nozzles, and the results showed that stream ratios were not significantly affected either before or after installation. There was a corresponding improvement in thermal mixing efficiency and total pressure recovery coefficient. Consequently, mixing was accelerated due to the spoilers increasing the borderline area between the primary and

secondary streams. By avoiding high-temperature primary stream impingement on mixing tube walls, spoilers significantly reduced the mixing tube wall's temperature.

3 Materials and Methods

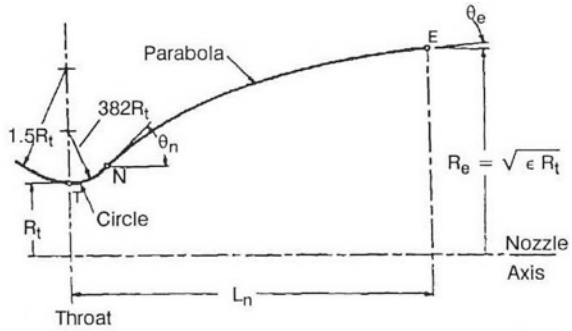
A rocket engine is generally engineered to expand the hot gases generated by burning propellants to an extremely high pressure, in order to provide needed thrust by expanding the gases at a high velocity. It is essential that exhaust gases have sufficient kinetic energy to generate a greater amount of exhaust velocity due to the fact that a large value of specific thrust requires a high value of kinetic energy. Essentially, the expansion ratio will be determined by the pressure ratio across the nozzle. It was comprised of three parts: a convergent part (narrowing down from a wide diameter to a smaller diameter in the flow direction), a throat part (the tiniest narrow area within the nozzle), and a divergent part (expanding from a smaller to a larger diameter). Several processes occur in the combustion chamber, and then the flow is passed into the throat section. Together, they are called the convergent section or the combustion chamber. This divergent section is included to increase its velocity even more because the gas velocity in the convergent section is limited to the speed of sound, and the divergent section is added to improve its velocity further. Hence, CD nozzle configuration involves a convergent duct followed by a divergent duct.

High flow will strive the engine's throat region, even though it is the smallest part, after the combustion chamber process. The flow of fluid reaches the noise velocity at the throat under supersonic flow conditions [12]. De Laval, one of Sweden's pioneering engineers, devised the first nozzle in 1886 with this design. Consequently, CD nozzles are used in rocket engines to accomplish higher exhaust speeds beyond sonic speed, which is approximately 2–4.5 km per second [13].

Using semi-empirical parabolic approximation methods, Rao designed a bell-shaped nozzle for maximum thrust [14]. It is dependent on ambient pressure, the curvature of the nozzle in the throat region, the length, and the composition of the gas, as well as other factors, as to what contour is optimal. According to Fig. 2, the divergent section of the contour between the throat and point N comprises a circular arc with a radius of $0.382 R_t$, while the nozzle contour just after upstream of the throat is defined by a circular arc with a radius of $1.5 R_t$. In this case, the expansion ratio is found to match the parabola formed till the nozzle exit. As an interesting point to note, a bell-shaped nozzle is also capable of generating an angle downstream of its throat that is much larger than 30° . As compared to a conical nozzle with the same divergent angle, the bell-shaped nozzle has a significantly shorter length by approximately 20%. The main objective is to change the shape and design of the engine nozzle.

The main objective is to change the shape and design of the engine nozzle. So, first, we have to take them as paradigm nozzle (RS-25) and try to get the original value according to their requirement, run the process using analysis software, and then compare it with the newly modified nozzle design. So, the reference nozzle is taken

Fig. 2 Geometry of standard nozzle



as the SLS rocket RS-25 engine’s nozzle. Now, in this engine, some modifications were done by the firm, and now this engine uses by NASA for the upcoming Moon mission and beyond that is called Artemis Mission. So, some basic details about the RS-25 engine are as under.

3.1 RS-25 Rocket Engine

This nozzle is developed by Aerojet Rocketdyne and Whitney & Pratt Rocketdyne Company, a USA company, and almost every rocket engine and fighter jet engine is developed by these companies. This is a liquid fuel-type engine or a cryogenic rocket engine. This engine’s nozzle design is a de Laval nozzle or a bell-shaped extension nozzle. The chamber pressure of this engine is exceptionally high. In this fuel is liquid hydrogen and the oxidizer used liquid oxygen. The inner surface is cooled by liquid hydrogen, that is flowing through a brazed stainless steel tube, and this tube is convoluted around the outside of the nozzle area (Fig. 3).

For making the design of this nozzle computer-aided design (CAD) software is used, such as Fusion 360, CREO, SolidWorks, and CATIA. This software is very attentive to detail. So, users can make designs properly and get accurate results as per their requirements. So, this software is largely recognizable by many industries, and it has also a large option for editing and manufacturing different components as CAD models. In this task, CATIA is used for the designing part.

This is standard geometry, and tackling all the dimensions is a standard dimension for creating a bell-type De Laval nozzle, so this data is used for creating an engine geometry that is RS-25. So, here is the geometry that is created with the help of CATIA software.

1. $\frac{T_c}{T_t} = 1 + \frac{(\text{Gama}-1)}{2} M^2$
2. $\frac{P_c}{P_t} = \left(\frac{T_c}{T_t}\right)^{\frac{\text{Gama}}{(\text{Gama}-1)}}$
3. $P_{\text{atm}} = \rho gh$
4. $I_{\text{sp}} = \frac{F}{mg}$

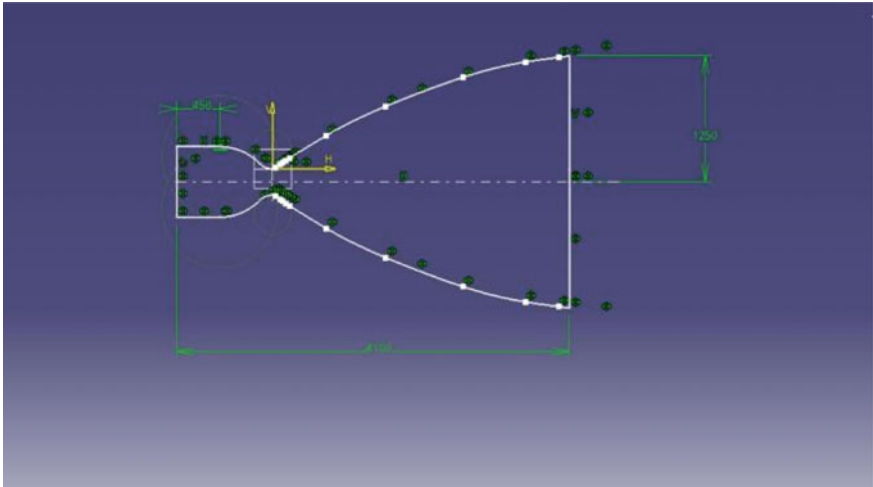


Fig. 3 2D design of RS-25 in CATIA-V5

5. $F_{thrust} = V_e * m$
6. $T_t = \frac{T_c}{\frac{(Gamma+1)}{2}}$
7. $P_t = P_c \frac{(Gamma+1)}{2} \frac{1}{(Gamma-1)^{\frac{Gamma}{Gamma-1}}}$
8. $M_e = \frac{V_e}{(Gamma * R * T_c)}$
9. For an ideal Gas

$$P_0 = \rho * R * T_0$$

3.2 Different Types of Nozzles

Nozzles with A part boundary include:

- (a) The Expansion-Deflection Nozzle
- (b) The Plug Nozzle
- (c) The Aero Spike Nozzle
- (d) Single Enlargement Ramp Nozzle (SERN).

Controlled nozzles:

- (a) The increasing nozzle,
- (b) Bell nozzles with a removable insert and
- (c) The stepped nozzles or dual-bell nozzles.

Dual-mode nozzles include:

- (a) The dual-expander nozzle

- (b) The dual throat nozzle.

3.3 *Computational Fluid Dynamics Analysis*

The CFD analysis software was used for predicting how a model will behave or for standardizing the working conditions. Rather than making a prototype, the software was designed without it. Researchers and industries almost exclusively use CFD as a tool. As a result of recent advancements in computing power, combined with powerful graphics and interactive 3D manipulation of models, creating and analyzing CFD models have become much easier, which in turn has reduced time and cost. Furthermore, advanced solvers are equipped with algorithms that allow them to engender robust solutions to the flow field in a reasonable amount of time [15]. As a result of these characteristics, computational fluid dynamics was already a well-established industrial design tool. It helps to shorten design timescales and enhance processes throughout the engineering sector. Typically, Ansys users break down labyrinthine structures into little components that are modeled and tested independently. A user can begin by setting the dimensions of objects and then add as many data, features, and characteristics as needed. As a result, the Ansys program simulates and examines movement, fatigue, fracture, fluid flow, temperature distribution, electromagnetic efficiency, and other related impacts and values throughout time.

In order to determine the characteristics of rocket engines, the following equations need to be used. Equations play a significant role in defining many of the values used in analysis and mathematical methods as well. Additionally, different numerical methods are available to achieve the desired result.

Table 1 contains the provided data. Although the engine's dimensions and characteristics are taken from NASA's official website [12], the remaining data (nozzle) is obtained by deriving and calculating numerous equations. Formulas are mentioned above, and they are imperative for useful data.

As a first step, a design was created in the ANSYS workbench or design modeler or can be directly imported from any design software, such as SolidWorks, CATIA, and Crio using the design modeler. In the following step, meshing has been the most paramount part since all factors affecting the results are directly related to meshing. To get accurate results, need to do mesh properly using the veracious methods, using different types of mesh depending on the characteristics, and checking the number of nodes and elements. Furthermore, results are more accurate if the number of nodes and elements in the mesh was high, so a more convoluted structure has been very advantageous for achieving desired results.

As an atmospheric condition for supervising the shock diamonds, the meshing of the RS-25 nozzle and surrounding portions was taken into account. Whenever there was an analysis, meshing plays a crucial role since everything was connected to it. Structured meshes were used in this case, with approximately eighty thousand nodes and elements.

Table 1 RS-25 nozzle dimension and boundary condition

$R_{throat} = 0.13 \text{ m}$	
$R_{exit} = 1.15 \text{ m}$	
$P_0 = 20,640,000 \text{ Pa}$	
$T_0 = 3573.15 \text{ K}$	
$\dot{m} = 514.49 \text{ kg/s}$	
$T = 1,859,000 \text{ N}$	
$\Gamma = 1.26$	
$R = 831.4 \text{ J/Kg K}$	
Exit velocity (V_e) = 3590 m/s	
Exit Mach number (Me) = 10.5495151	
Throat pressure (P_t) = 11,415,000 Pa	
Throat temperature (T_t) = 3161.946 K	
Exit temperature = 110.5460 K	
Exit pressure = 0.998810 Pa	

In order to create this geometry, face meshes and edge meshes were used. When a mesh is good, convergence can be achieved faster, and the results can be inevitable (Fig. 4).

In the next step, boundary conditions were applied after the meshing has been completed. The fluid models and values should be checked with different fluid types and models, followed by the application of appropriate conditions based on analyses and situations. The design analysis is an integral part of any project. As a result, the boundary conditions must be accurate and fair so that the outcome can be derived. Thus, Figs. 5, 6 and 7 show the pressure, velocity, and temperature contours based on the analysis data found in Table 2.

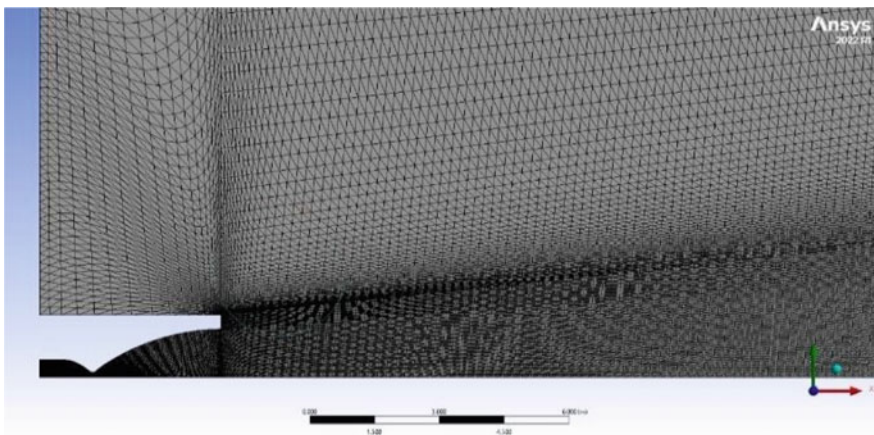


Fig. 4 Meshing part of RS-25 engine (rocket nozzle)

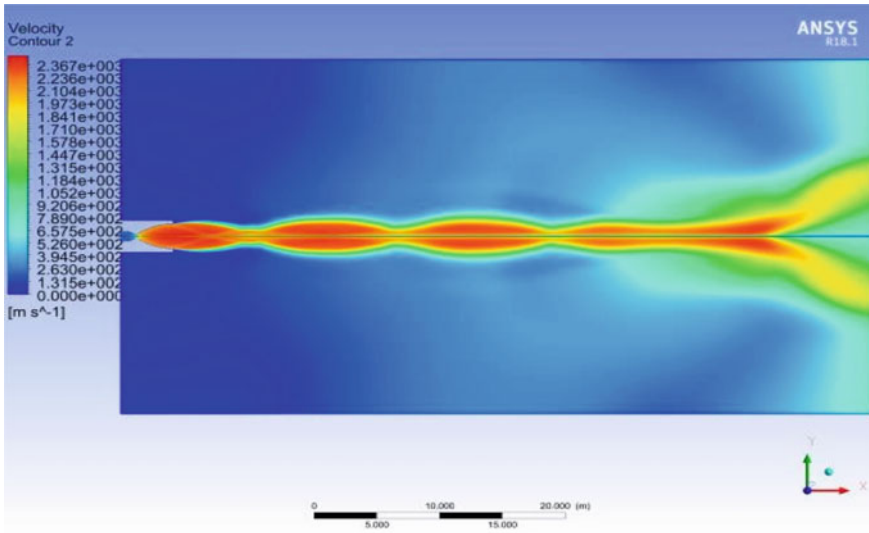


Fig. 5 Velocity contour

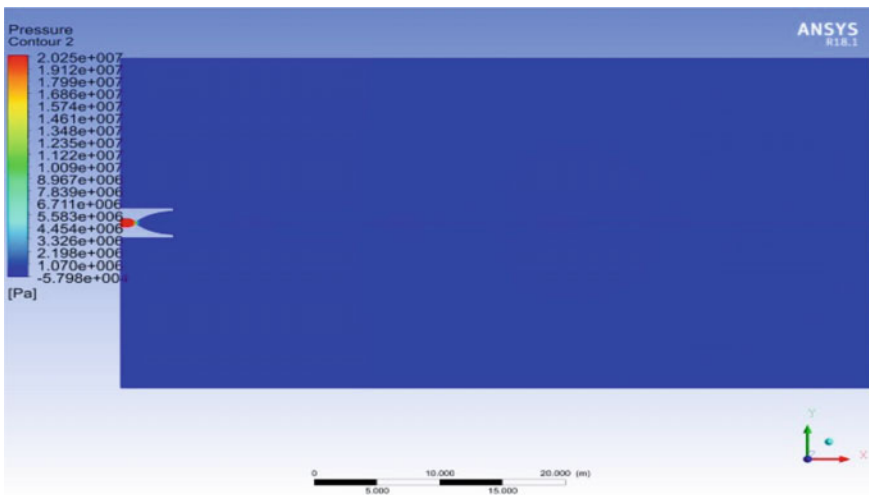


Fig. 6 Pressure contour

According to Figs. 5, 6 and 7, all values perfectly match not only with the available values (provided in Table 2) but also with reference values from various sources. It had been evident from the analysis derivation that the values received from the computational analysis are correct and are depicted in the figures.

Physical phenomena such as the relationship between velocity, temperature, and pressure can be demonstrated by these figures.

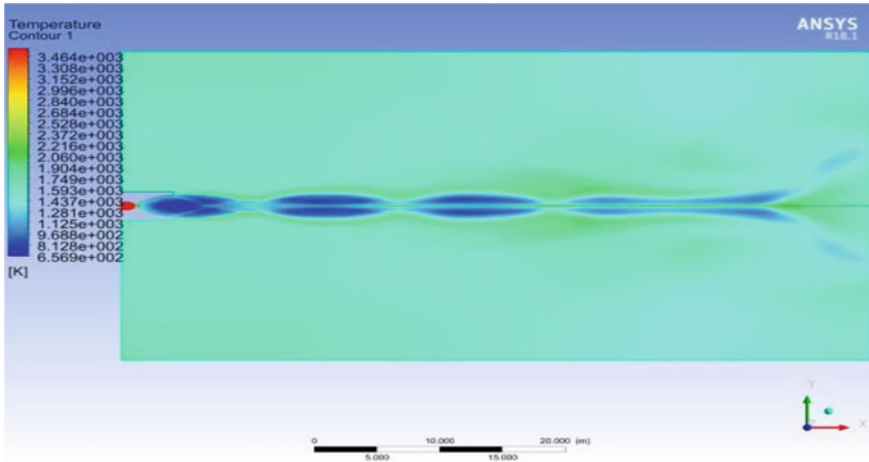


Fig. 7 Temperature contour

Table 2 Computational fluid dynamics analysis data

Procedure	Details
Problem setup	Type: Density Based Velocity: Absolute Time: Steady 2D space: Planar
Models	Energy: On Viscous: Realizable k-epsilon, Standard wall treatment
Material	Fluid: Air Density: Ideal Gas Viscosity: Sutherland
Boundary condition	Inlet: Pressure Inlet Gauge Total Pressure (pa): 20,640,000 Inlet Total temperature (K): 3573.15 Outlet: Outlet Pressure Gauge Total Pressure (pa): 0.99881 Outlet Temperature (K): 110.564
Reference value	Compute from: Inlet
Initialization	Standard Initialization Compute from: Inlet
Solution	Run calculation: Enter the iteration number and calculate until the solution converges

A cross-sectional view of the rocket engine was typically accompanied by a map depicting velocity and pressure. Software that simulates the flow of gases through the engine and calculates the pressure distribution across its flow field uses computational fluid dynamics techniques to color code each point in the flow field. Higher velocities or pressure are indicated by warmer colors, while lower velocities or pressure are indicated by cooler colors [7].

A rocket engine's performance can be better understood by analyzing its velocity or pressure contours. For example, a high velocity or pressure can cause erosion or damage to the engine components or indicate inefficient fuel combustion or other functioning issues, as well as areas of low velocity or pressure that can indicate inefficient fuel combustion or other troubles.

Having taken a close look at Fig. 7, it becomes apparent that temperature variation follows a similar trend as pressure.

A temperature contour shows the distribution of temperature within a system, and Ansys Workbench lets you create and analyze temperature contours for rocket engines, so they can be optimized for performance and safe operation.

All values in Figs. 5, 6 and 7 are perfectly matched with those given in Table 2 and also with other references. In addition, the values have been calculated in an accurate manner, and this has all been confirmed by the analysis. Not only do these graphs illustrate properties like velocity, pressure, and temperature throughout the nozzle, but they also show variations among the sections of the nozzle.

3.4 Innovation and Modification

The major goal of this work is to modify or change a nozzle design if it becomes necessary. Since the nozzle shape or geometry of rocket engines has remained the same for the past several decades, with all industries using bell- or De Laval-shaped nozzles, none of the modifications mentioned in this section are guaranteed to occur. However, they do provide a brief idea of what might happen. Every day, numerous new technologies and adjustments are created. Therefore, the primary goal of this section is to provide some potential alterations and provide the results of the analysis performed using CFD software. Thrust is produced from the exhaust part of the rocket engine nozzle. This part is a divergent section of the nozzle.

Therefore, only the divergent section has been modified; and all other sections, including the convergent and throat regions, have remained unchanged.

The CFD part has also undergone alterations, including meshing, nodes, and element sections. Possible changes are in the divergent section. All different modifications to the actual design require a different kind of treatment in order to acquire profitable results. So, CFD analytical steps are as equal as others though the process in each step is quite different from each other. An apt example of this is the meshing part and boundary condition.

- I. Change in divergent angle.
- II. Attached convergent section just after the divergent section.
- III. Change the parabola curve of the divergent section.
- IV. Make a spike in the divergent section.

Because the overall length and nozzle diameter have not changed, there have been no design changes other than the inlet data being the same. The only difference between the measurements and the actual design (RS-25) is in the diverging section's

geometry design. Due to the variable changes in the design portion, the analytical boundary value for the inlet remains the same, while only the outlet section varies. The value for the outflow portion is therefore regarded as an atmospheric value.

For the rocket thrust equation,

$$F = \dot{m} u_e + p_e A_e - p_a A_e \tag{1}$$

For maximum thrust slope (thrust vs. exit area graph) = 0.

fluctuation. After the analysis, it appears that the results are accurate and that the equations have been derived correctly. Energy equations are obeyed correctly by these data

$$\frac{dF}{dA_e} = 0 \tag{2}$$

Take differentiation for Eq. (1)

$$dF = \dot{m} du_e + u_e d\dot{m} + p_e dA_e + A_e dp_e - p_a dA_e - A_e dp_a \tag{3}$$

$\dot{m} = \text{Constant}$
 $p_a = \text{Constant.}$

$$dF = \dot{m} du_e + p_e dA_e + A_e dp_e - p_a dA_e \tag{4}$$

Use conservation of mass + momentum at the nozzle exit

$$dp + \rho u du = 0 \quad \text{so,} \quad dp_e + \rho_e u_e du_e = 0$$

$$\dot{m} = \rho u A \quad \text{so,} \quad \dot{m} = \rho_e u_e A_e$$

Form Eq. (4)

$$dF = \rho_e u_e A_e du_e + p_e dA_e + A_e dp_e - p_a dA_e$$

$$dF = (\rho_e u_e du_e + dp_e) A_e + p_e dA_e - p_a dA_e$$

$$dF = p_e dA_e - p_a dA_e$$

$$dF = (p_e - p_a) dA_e$$

From Eq. (2)

$$\frac{dF}{dA_e} = p_e - p_a = 0$$

So, $p_e = p_a$ for maximum thrust (Fig. 8).

The diverging section's parabola curve has been modified in this design by being somewhat lengthened. Therefore, the key goal is that, if the weight of the nozzle

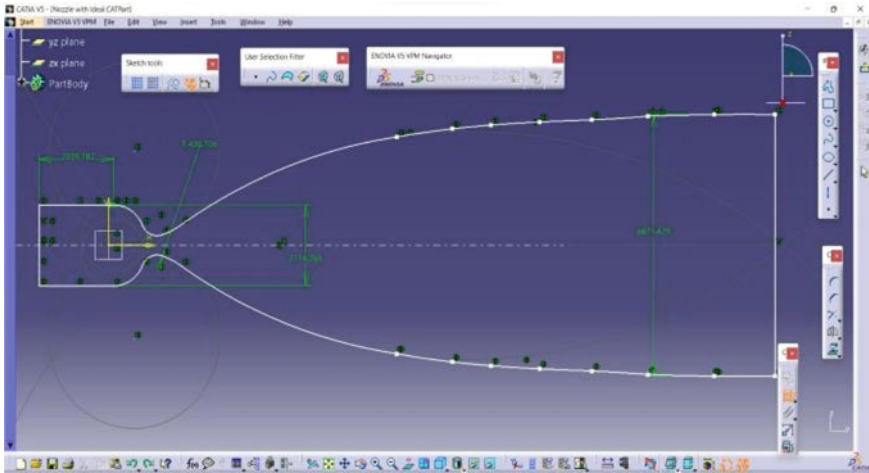


Fig. 8 Change in divergent section

is ignored due to the lengthening of the nozzle, the Mach number always rises as the lengthening of the nozzle occurs since the pressure is further reduced as a result of the lengthening and the likelihood of producing shock is reduced. However, also maintain the stress–stress graph for maintaining the structure of the nozzle. So, the designed nozzle structure should be lengthened or elongated instead of increasing the nozzle diameter [16] (Fig. 9).

Introduced in the nozzle area is the spike. Since every activity that takes place in the chamber takes place several times, the pressure is high, the temperature is

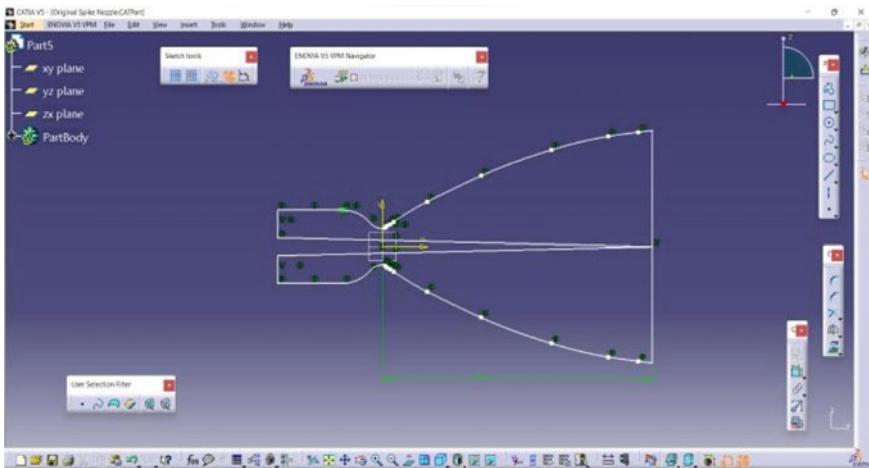


Fig. 9 Made a spike in the nozzle

immensely produced, and the velocity increases at the very end, this chamber is better suited for low altitudes where the pressure is constrained by the exhaust gas's expansion. It can be called a "bell nozzle with a central spike" or "spike nozzle".

Typically, a spike is placed at the throat of the nozzle, i.e., the narrowest area of the nozzle. Spike helps to improve the efficiency of the nozzle by reducing the amount of energy lost due to shock waves that form when the supersonic gas flow is abruptly slowed down at the nozzle throat. In addition, it disrupts the flow, so shockwaves move downstream of the nozzle throat and reduce their strength and allow the gas to expand more smoothly and efficiently. It helps to optimize the expansion of the exhaust gases that are left in the nozzle. This is headed toward the higher exhaust velocities and greater thrust [8].

This type of engine is used to increase the expansion ratio of the nozzle, which can help to increase the power of the engine. The spike nozzle engine also helps to improve the performance of the engine at high altitudes and low atmospheric pressures.

The design of a spike nozzle needs careful consideration of the shape and size of the spike, as well as the geometry of the nozzle itself. Computational fluid dynamics simulations are also often used to optimize the design of the nozzle and spike for significant engine and mission requirements.

Overall, designing this type of engine is not an easy task, and it is a complex procedure and ensures that during production it does not create any catastrophic effects, such as flow separation, and uneven heat transfer to the wall of the nozzle. Nevertheless, it is certainly possible and will be successfully used in various rocket engines and space missions.

3.5 Some Other Possible Modifications

Another way to change that is to provide or add a second combustion process, similar to an afterburner in a jet engine. A propellant is supplied externally from the outside of the nozzle's divergent section, the same as an afterburner process occurs in a jet engine. As a result, all variables are changed like velocity, pressure, temperature, and all values that depend on it can change, but one essential factor is that the nozzle in this instance needs to be longer than other nozzles. So, every step can be appropriately completed during the process, and it has to design and modify more precisely any uncertainty that is not acceptable. These improvements apply only to the liquid fuel engine. It may be also required to strengthen the material to the bottom portion because, after the twice combustion process, the exhaust flow's temperature is very high. These types of engines are also used as a replacement for solid rocket boosters. Though, this type of engine must be made with significant condition and as per the mission requirement. Most probably, this engine is suitable for space travel missions because this kind of mission does not require a higher altitude. Also, it is more acceptable for a short-duration mission, because it requires a high fuel rate and consumption.

If we see further modification or improvement, which is to use a multi-engine instead of using the one giant nozzle, the use of the multi-engine in any mission is more favorable. There are many reasons to use this type of engine. It can be easier to the on-off engine off as per the requirement which means we can stop the propellantumping and save the fuel for further tasks, so we have control over the flow or velocity, especially, during the vacuum or space travel. Generally, if there is more than one engine attached to the rocket, it uses a multi-propellant tank. So, if during the mission out of this, any tank is the failure of some circumstances, we have another tank and working engine. Hence, it can work properly with properly other engines. So, the chance of failure is very less as compared use one gigantic engine [9]. Due to the multi-nozzles being attached on the bottom side of the spaceship using uneven combustion, take control spaceship, so no more need for a thrust vector controlling system during the first stage. More important is that get the maximum amount of thrust and distribute exhaust gases evenly. Have full control of changing the direction of the rocket and the ratio of the fuel oxidizer during the ignition. One of the most prosperous points is the efficiency of the engine is so high, because the engine is optimized at the different level as per the requirement as well as the sea level and vacuum level, and it can be increasing the speed of the rocket due to proper amount of the propellants that are burning. Redundancy decreases at the lowest level because there many engines are available as a backup if any engine becomes dead or shut down for any reason, so chances of failure are so less; moreover, it operates with multiple nozzles. If safety comes into the mission, it is given maximum safety due to the high level of structure and minimum redundancy [10]. However, there are some points against this implementation, such as complexity, weight, and ground control, but in the future, it can be sure that all the negative points will be solved by supercharged technology and advancement. Even, this type of structure uses by many companies nowadays in the first stage as well as the second stage, and they have accomplished their mission with a minimum level of disaster or failure. Therefore, in the future, many companies will use this type of arrangement.

4 Results and Discussion

Here, you may compare all of the data that resulted from changes to the meshing element. The conclusion drawn from this data is that results will be closer to our intended value or more accurate when the mesh is more tortuous, and convergence will occur in a shorter amount of time and iterations. Here, Table 3 indicates how will affect nodes and elements sizes on pressure value.

One of the major goals is to find the data about the RS-25 rocket engine that is available in Table 1 and also derived a graph with the help of the analysis method, which is shown in Figs. 10 and 11.

Nowadays, space technology is growing more rapidly, and everyday new technology comes and makes incredible objects that make enormous changes in every field. Some experts believe that our planet (Earth) no longer become habitual for

Table 3 Changing in meshing (nodes and elements)

Nodes	Elements	Pressure
240	195	32,541
869	780	6939
21,777	20,652	1829
39,390	38,900	1013

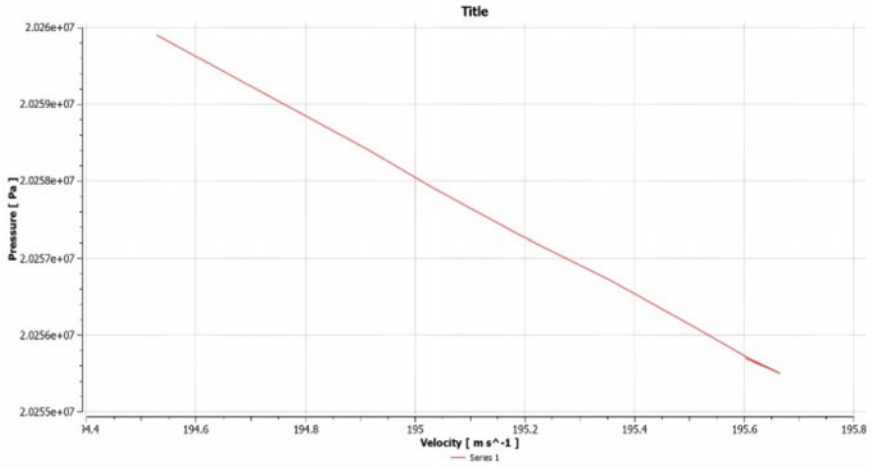


Fig. 10 Pressure vs. velocity graph (RS-25)

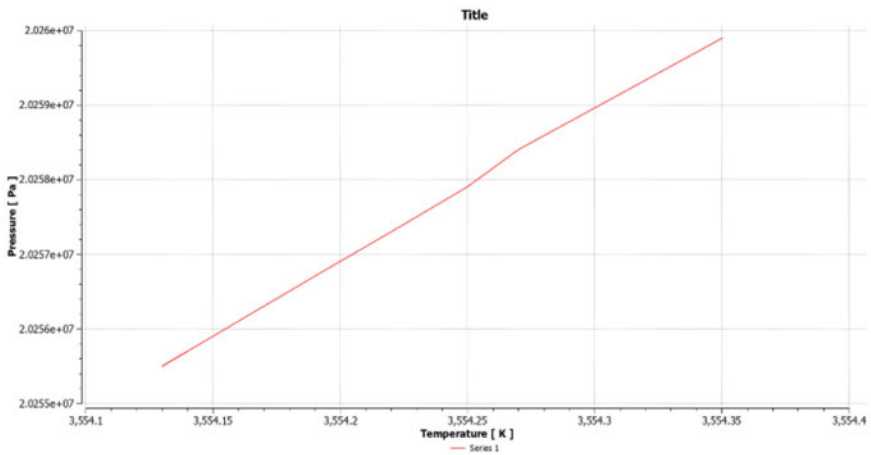


Fig. 11 Pressure vs. temperature graph (RS-25)

future generations. And in the universe, all space objects are too far from each other, and traveling takes a huge amount of time, so here propulsion system plays a major role. In any place, if we want to commute between these two places propulsion systems are used. Hence, if we want to travel faster in space, we have to establish an appropriate propulsion system.

Some industries try to make changes in propellant and using this they research in this field and make the engine more efficient and increase the power of it. Others are working on the engine's geometry and design and making it expeditious. Some space industries are takes part in completely modifying the whole design of the engine and using new materials and manufacturing technologies to reduce weight and increase durability and try to increase thrust-to-weight ratio. If we talk about the new propulsion system for space vehicles, the newest technology is electric propulsion or plasma thruster system. It is a safer, more convenient, more efficient, and more powerful system. While NASA is working on the laser technology for the propulsion system, they enunciate that it is the fastest propulsion system ever and it is used in the Mars mission, and beyond it reduces the huge amount of traveling time [11].

However, all the firms are trying to improve the efficiency and performance of the engine, while others are working then safer and more reliably. In addition, the development of new fuel and propellant and using new computational models optimize engine design and performance. The results of research into rocket engines and their modification have the potential to revolutionize space travel and exploration, making it more affordable, efficient, and accessible to a wider range of people and organizations.

4.1 Actual Nozzle Contour

From the result and graph creation option in Ansys software, given properties comparison can be drawn. This graph elucidates velocity vs. pressure value throughout the nozzle. As per previous Figs. 5, 6, and 7, actual design values have been found.

Considering those figures as references, this graph pattern indicates authenticity. The graph also proving the phenomenon that velocity and pressure are directly proportional to each other.

Now referring to Fig. 11, it is visible that temperature follows similarly to pressure quantity. Thus, the temperature is also inversely proportional to the velocity of the flow.

As a result, both graphs are derived from the computational analysis for the RS-25 engine and can say that this is advantageous because of the differences in graphs (whenever the temperature is decreased, pressure is also decreased, and velocity is increased, or vice versa), and both graphs are in agreement with the actual data that are provided by various companies and available resources [17, 18] (Fig. 12).

This spike nozzle travels at a higher velocity than a true nozzle (RS-25) because combustion takes place twice, increasing the pressure inside the chamber as a result

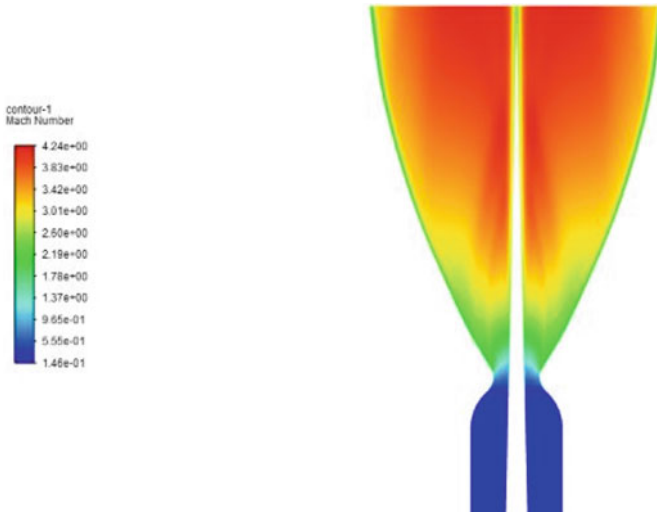


Fig. 12 Analytical result of nozzle with spike

of the spike and the excessively high temperature, and this kind of nozzle operates most effectively at low altitude (Fig. 13).

Here, it is an elongated nozzle and from this getting higher velocity, because the length of the convergent section is large as compared to the actual type nozzle (RS-25), Furthermore, velocity is increased, and pressure is reduced as a result of the length being extended. When the length is increased at one point, it reaches a limit, and if it exceeds the limit, the nozzle becomes fatigued.

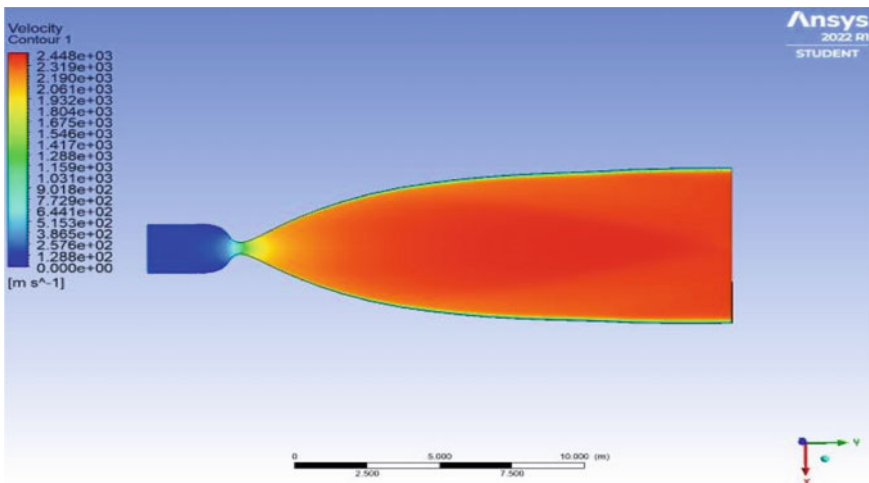


Fig. 13 Simulation in nozzle's divergent section

5 Conclusions

As a result, all of the major factors depend on the nozzle geometry, and any changes made to the geometry directly impact the nozzle's efficiency. There are numerous ways to modify geometry, but some limitations prevent the nozzle from performing optimally. All of the changes that are not guaranteed to work perfectly are listed here. The intention behind this is to demonstrate that different changes have occurred in section geometry and to examine the variation. All the modifications are done in the divergent section and a 5–10% improvement is in velocity as compared to the actual RS-25 engine. Moreover, the main goal is to find out all the data on the RS-25 engine, and these data are found by numerical methods that are accurate and completely match the analysis.

Acknowledgements Authors are sincerely thankful to Sardar Patel Institute of Technology, Vasad Gujarat, India for their CFD lab facilities. We also thank ph.d scholar Anand Darji for his continuous support and guidance.

Nomenclature

p_0	Total pressure (pa)
p_a	Atmospheric pressure (pa)
Me	Exit Mach number
V_e	Exit velocity (m/s)
T_0	Total temperature (k)
\dot{m}	Mass flow rate (kg/s)
A_e	Exit area (m ²)
p_e	Exit pressure (pa)
ρ	Density of air (kg/m ³)
F_{thrust}	Thrust (N)

References

1. Sutton GP (2006) History of liquid propellant rocket engines. American Institute of Aeronautics and Astronautics Inc., Reston, Virginia
2. Parthiban P, RobertSagayadoss M, Ambikapathi T (2015) Design and analysis of rocket engine nozzle by using CFD and optimization of nozzle parameters. Int J Eng Res online, 3(5)
3. Anderson JD (2003) Modern compressible flow with historical perspective. McGraw Hill, 3rd edn. Boston
4. Frey M, Hagemann G (1998) Status of flow separation prediction in rocket nozzles. AIAA-98-3619
5. Space Ref Editor, Aerojet Rocketdyne Completes Successful Space Launch System Rocket Engine Test Series, SPACE REF*, Aerojet Rocketdyne, Commerce, USA

6. He ZX, Zhong WJ, Wang Q, Jiang ZC, Fu YN (2013) An investigation of transient nature of the cavitating flow in injector nozzles. *Appl Therm Eng* 54(1):56–64
7. Versteeg H, Malalasekera W (2009) An introduction to computational fluid dynamics, the finite volume method, 2nd edn
8. Chelouati M, Jha MS, Galeotta M, Theilliol D (2021) Remaining useful life prediction for liquid propulsion rocket engine combustion chamber. In: 2021 5th International conference on control and fault-tolerant systems (SysTol), pp 225–230
9. Shin CS, Kim HD, Setoguchi T et al (2010) A computational study of thrust vectoring control using dual throat nozzle. *J Therm Sci* 19(6):486–490
10. Wang YS, Xu JL, Huang S et al (2019) Computational study of axisymmetric divergent bypass dual throat nozzle. *Aerosp Sci Technol* 86:177–190
11. Dawei L, Jun H, Zhiqiang S, Jinzu J (2016) The effect of spoilers on jet mixing of lobed nozzles. *J Aerosp Technol Manag* 8(4):459–466
12. Barrere M, Jaumotte A, Fraeijs De Veubeke B, Vandenkerckhove J (1960) Rocket propulsion. Elsevier Publishing Company, Amsterdam, pp 9–21
13. NASA New RS-25 Rocket Engine Series Wikipedia
14. Htte F, Sethe CV, Fiedler T, Haupt MC, Haidn OJ, Rohdenburg M (2020) Experimental lifetime study of regeneratively cooled rocket chamber walls. *Int J Fatigue* 138:105649
15. Mason MS, Crowther WJ (2002) Fluidic thrust vectoring on low observable aircraft. In: CEAS aerospace aerodynamics research conference, 10–12 June 2002, Cambridge, UK
16. Surya Narayana KPS, Sadhashiva Reddy K (2016) Simulation of convergent divergent rocket nozzle using CFD analysis. *IOSR J Mech Civ Eng (IOSR-JMCE)* eISSN: 2278-1684, p-ISSN: 2320-334X, 13(4) Ver. I (Jul. - Aug. 2016), pp 58–65
17. Tudor M, Raghu S, Space launch system core stage engine (RS-25) at the University of Alabama in Huntsville
18. Maddu YR, Saidulu S, Azeem Md., Jabiulla S (2018) Design and fluid flow analysis of convergent divergent nozzle. *Int J Eng Technol Sci Res IJETS* 5(4):903–909. www.ijetsr.com ISSN 2394-3386